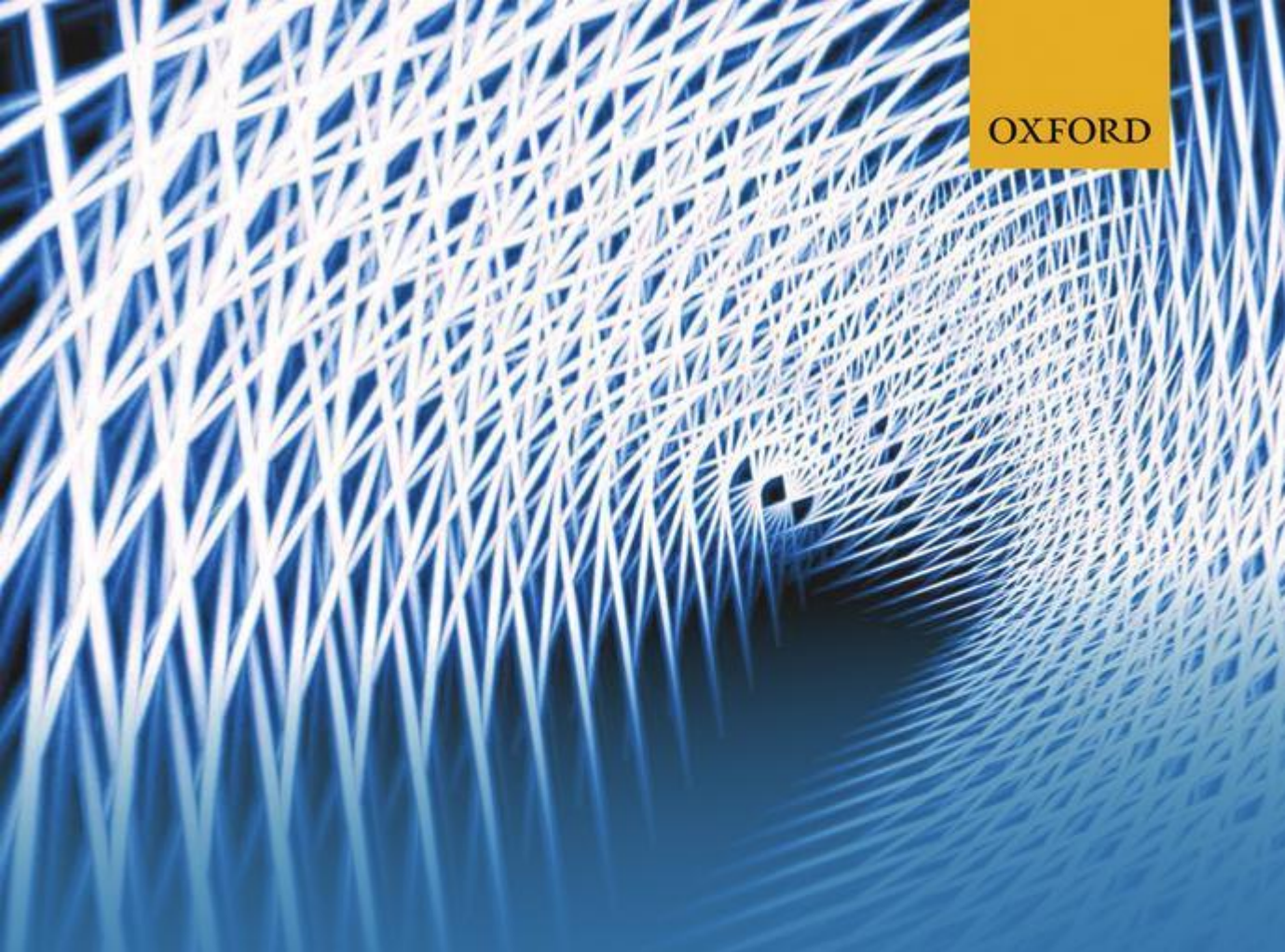

OXFORD

modern optics

SECOND EDITION

B. D. GUENTHER

MODERN OPTICS

Modern Optics

Second Edition

B. D. Guenther

Duke University, USA

OXFORD
UNIVERSITY PRESS

OXFORD
UNIVERSITY PRESS

Great Clarendon Street, Oxford, OX2 6DP,
United Kingdom

Oxford University Press is a department of the University of Oxford.
It furthers the University's objective of excellence in research, scholarship,
and education by publishing worldwide. Oxford is a registered trade mark of
Oxford University Press in the UK and in certain other countries

© B. D. Guenther 2015

The moral rights of the author have been asserted

First Edition published by Wiley in 1990
Second Edition published in 2015

Impression: 1

All rights reserved. No part of this publication may be reproduced, stored in
a retrieval system, or transmitted, in any form or by any means, without the
prior permission in writing of Oxford University Press, or as expressly permitted
by law, by licence or under terms agreed with the appropriate reprographics
rights organization. Enquiries concerning reproduction outside the scope of the
above should be sent to the Rights Department, Oxford University Press, at the
address above

You must not circulate this work in any other form
and you must impose this same condition on any acquirer

Published in the United States of America by Oxford University Press
198 Madison Avenue, New York, NY 10016, United States of America

British Library Cataloguing in Publication Data

Data available

Library of Congress Control Number: 2014957917

ISBN 978–0–19–873877–0

Printed and bound by
CPI Group (UK) Ltd, Croydon, CR0 4YY

Links to third party websites are provided by Oxford in good faith and
for information only. Oxford disclaims any responsibility for the materials
contained in any third party website referenced in this work.

Preface

The second edition of this textbook is designed for use in a standard physics course on optics. The book is the result of a one-semester elective course that has been taught to juniors, seniors, and first-year graduate students in physics and engineering at Duke University for 13 years and has been used as a graduate text in a number of universities. Students who take this course should have completed an introductory physics course and mathematics courses through differential equations. Electricity and magnetism can be taken concurrently.

Modern Optics differs from the classical approach of most textbooks on this subject in that its treatment of optics includes some material that is not found in more conventional textbooks. These topics include nonlinear optics, guided waves, Gaussian and Bessel beams, photonic structures, surface plasmons, imaging and computational imaging, and light modulation. Moreover, a selection of optional material is provided for the instructor so that the course content can reflect the interest of the instructor and the students. Basic derivations are included to make the book appealing to physics departments, and design concepts are included to make the book appealing to engineering departments. Because of the material covered here, the electrical engineering and biomedical engineering departments at Duke have made the corresponding optics course a prerequisite for some of their advanced courses in optical communications and medical imaging.

Before the 1960s, the only contact that the average person had with optics was a camera lens or eyeglasses. Geometrical optics was quite adequate for the design of these systems, and it was natural to emphasize this aspect of optics in a curriculum. The approach used introduced the students to the theory and to examples of the application of the theory, accomplished by a description of a large variety of optical instruments. The reason for this approach was that lens design is found to be quite tedious, and the optimization of a lens design is more easily described than accomplished.

Today, the student is exposed to many more optical systems. Everyone encounters supermarket scanners, copying machines, compact disk players, holograms, and discussions of fiber-optic communications. In the research environment, lasers, optical modulators, fiber-optic interconnects, and nonlinear optics have become important. Upon graduation, many students will be called on to participate in the use or development of these modern optical systems. An elementary discussion of geometrical optics and a review of classical optical instruments will not adequately prepare the student for these demands.

The second edition retains the emphasis on both fundamental principles of optics and an exposure to actual optics engineering problems and solutions. A large portion of the conventional treatment of geometrical optics and a discussion of classical optical systems is not included. In their place, a geometrical optics discussion of fiber optics has been included and, in this second edition, a discussion of photonic structures with holography being considered as a special case of photonic structures. Rather than describe a host of optical systems, a few systems, such as the Fabry–Perot interferometer, are examined using a variety of theories. The second edition retains its emphasis on diffraction and the use of Fourier theory to describe the operation of an optical system.

To allow the development of a one-year course in modern optics, a number of topics have been added or expanded. The classical theory of the interaction of light and materials

has been expanded to include surface plasmons. A discussion of electro-optic and magneto-optic effects is used to introduce optical modulators, and a discussion of nonlinear optics is constructed around second-harmonic generation. Because of the importance of birefringence in optical modulators and nonlinear optics, an expanded discussion of optical anisotropy has been included. This is a departure from most texts, which ignore anisotropy because of the need to use tensors. In modern optics, anisotropy is an important design tool, and its treatment allows a discussion of the design of optical modulators and phase matching in nonlinear materials.

The first two chapters review wave theory and electromagnetic theory. Except for the section on polarization in Chapter 2, these chapters could be used as reading assignments for well-prepared students. Chapter 3 discusses reflection and refraction and utilizes the boundary conditions of Maxwell's equations to obtain the fraction of light reflected and refracted at a surface.

Chapter 4 discusses interference of waves and describes several instruments that are used to measure interference. Two of the interferometers—Young's two-slit experiment and the Fabry–Perot interferometer—should receive emphasis in discussions of this chapter because of the role they play in later discussions. An appendix to this chapter provides a brief introduction to some of the design techniques that are used to produce multilayer interference filters. All of the appendices in the book are included to fill in gaps in students' knowledge and to provide some flexibility for the instructor. The appendices may therefore be ignored or used as the subject matter for special assignments.

The treatment of geometrical optics, presented in Chapter 5, is not traditional. It was through the reduction of traditional subject matter that space has been freed to allow the introduction of more modern topics. A brief introduction to the matrix formalism used in lens design is presented, and its use is demonstrated by analyzing a confocal Fabry–Perot resonator. Geometrical optics and the concept of interference are used to analyze the propagation of light in a fiber. This introduction to fiber optics is then extended through the use of the Lagrangian formulation to propagation in a graded-index optical fiber. The connection between the matrix equations and the more familiar lens equations is established in Appendix 5A. Because of their importance in the Graduate Records Exam, aberrations are treated in Appendix 5B.

A formal connection between geometrical and wave optics was presented in Chapter 5 in the first edition. It has been removed from this edition because it was not found useful in the classroom.

The Fourier theory in Chapter 6 is presented as a review of and refresher on the subject. It is an important element in the discussions of the concept of coherence in Chapter 8 and of Fraunhofer diffraction in Chapter 10. The discussions of optical signal processing in Appendix 10A and of imaging in Appendix 10B draw heavily on Fourier theory. The treatment of imaging has been expanded to include computational imaging and coded apertures.

The discussion of dispersion given in Chapter 7 could be delayed and combined with the other chapters on material interactions (Chapters 13 and 15). It is included here to justify the discussion of coherence in Chapter 8. The discussion of dispersion in materials had as its objective the development by the student of a unifying view of the interaction of light and matter. It has been expanded to include surface plasmons.

The development of coherence theory in Chapter 8 is built around applications of the theory to spectroscopy and astronomy. It is a very difficult subject, but building the theory around the methods used to measure coherence should make the subject more intelligible.

Both the Fresnel and Gaussian wave formalisms of diffraction are introduced in Chapter 9. The Gaussian wave formalism is used to analyze a Fabry–Perot cavity and

thin lens. This chapter can be skipped, and the material introducing the Fresnel–Huygens integral can be covered in a single lecture.

The Fresnel formalism is expanded and discussed in Chapters 10 and 11. Fraunhofer diffraction is treated from a linear system viewpoint in Chapter 10, and applications of the theory to signal processing and imaging are presented in Appendices 10A and 10B. These two appendices are the most important in the book. Fresnel diffraction is introduced in Chapter 11, where it is used to interpret Fermat's principle and analyze zone plates and pinhole cameras.

In this second edition, Chapter 12 is constructed around a presentation of photonic structures. Guided by the presentation found in the book *Photonic Crystals: Molding the Flow of Light* by Joannopoulos, Johnson, Winn, and Meade (Princeton University Press, Second Edition, 2008), an overview of diffractive structures and their applications is given. Multidimensional periodic modulation of the index of refraction is shown to produce light propagation properties similar to the behavior of electrons in crystals. The similarity to holograms is discussed. A simple theory of holography is presented, and Fresnel theory is used to discuss the operation of a hologram. To generate the space needed to discuss photonic structures, much of the material on holography found in the first edition has been removed.

Chapter 13 uses the introduction of polarizers and retarders as a basis for the development of the theory of the propagation of light in anisotropic materials. The treatment of anisotropic materials is expanded over the conventional presentation to allow an easy transition into the discussion of light modulation in Chapter 14. The many geometrical constructions used in the discussion of anisotropy are confusing to everyone. To try to make the material understandable, only one construction is used in Chapter 13. To provide the student with reference material to aid in reading other books and papers, the other constructions are discussed in the appendices.

The discussion of modulators in Chapter 14 provides an application-based introduction to electro- and magneto-optic interactions. The design of an electro-optic modulator provides the student with an example of the use of tensors. The material interactions presented in Chapters 14 and 15 require the use of tensors, a subject normally avoided in an undergraduate curriculum. Tensor notation has been used in this book because it is key in the understanding of many optical devices. Some familiarity with tensors removes much of the "magic" associated with the design of modulators and the applications of phase matching discussed in Chapter 15.

The subject of nonlinear optics in Chapter 15 is developed by using examples based on frequency doubling. Only a few brief comments are made about third-order nonlinearities. The additional discussion of third-order processes is best presented from a quantum mechanical viewpoint. It was thought that this would be best done in a separate course. The material presented in this chapter should prepare the student to immediately undertake a course in nonlinear optics.

Enough material has been included for a one-year course in optics. Chapters 2–4, 6, 9 (excluding Gaussian waves), and 10 contain the core material and could be used in a one-quarter course. By adding Chapters 7 and 8 along with Appendices 10A and 10B, a one-semester course can be created. The instructor can alter the subjects discussed from year to year by adding topics such as Appendix 4A, the guided wave discussion of Chapter 5, or the discussion of holography in Chapter 12 in place of Appendices 10A and 10B. A less demanding one-semester course can be created by ignoring Chapter 8 and substituting Chapter 5, Appendix 4A, or possibly Chapter 12. In anticipation of developing skill and knowledge, the subject matter and problems increase in difficulty as the student moves through the book.

A number of people provided help in the preparation of this book. Those who provided photographs or drawings are identified in the figure captions. Their generosity is most appreciated. Dr. Frank DeLucia provided the initial motivation for writing the book. Many ideas and concepts are the result of breakfast discussions with A. VanderLugt. The book would never have gone past the note stage without the equation writer written by Dennis Venable. Duncan Steel reviewed some of the additions to the second edition, and I want to thank him for that effort. Thomas Stone provided ideas, photographic skills, and encouragement during the preparation of most of the photographs in this book. His enthusiasm kept me working.

Very special thanks must go to Nicholas George. He loaned me equipment and laboratory space to prepare many of the photographs. His encouragement prevented me from shelving the project, and his technical discussions provided me with an improved understanding of optics.

ROBERT D. GUENTHER

Contents

1 Wave Theory 1

1.1 Introduction 1
1.2 Traveling Waves 1
1.3 Wave Equation 4
1.4 Transmission of Energy 5
1.5 Three Dimensions 6
1.6 Attenuation of Waves 10
1.7 Summary 11
1.8 Problems 12

2 Electromagnetic Theory 15

2.1 Introduction 15
2.2 Maxwell's Equations 16
2.2.1 Gauss's Law 16
2.2.1.1 Gauss's (Coulomb's) Law for the Electric Field 16
2.2.1.2 Gauss's Law for the Magnetic Field 17
2.2.2 Faraday's Law 17
2.2.3 Ampére's Law (Law of Biot and Savart) 17
2.2.4 Constitutive Relations 18
2.3 Free Space 19
2.4 Wave Equation 19
2.5 Transverse Waves 21
2.6 Interdependence of **E** and **B** 22
2.7 Energy Density and Flow 24
2.8 Polarization 28
2.8.1 Polarization Ellipse 29
2.8.1.1 Linear Polarization 32
2.8.1.2 Circular Polarization 33
2.8.2 Stokes Parameters 36
2.8.3 Jones Vector 39
2.9 Propagation in a Conducting Medium 40
2.10 Summary 44
2.11 Problems 45
References 47
Appendix 2A: Vectors 47
2A.1 Products 48
2A.2 Derivatives 48
Appendix 2B: Electromagnetic Units 50

3 Reflection and Refraction 52

3.1 Introduction 52
3.2 Reflection and Transmission at a Discontinuity 53

3.3 Laws of Reflection and Refraction 56
3.4 Fresnel's Formula 58
3.4.1 σ Case (Perpendicular Polarization) 60
3.4.2 π Case (Parallel Polarization) 61
3.5 Reflected and Transmitted Energy 63
3.6 Normal Incidence 65
3.7 Polarization by Reflection 68
3.8 Total Reflection 69
3.9 Reflection from a Conductor 73
3.10 Summary 75
3.11 Problems 77
References 78

4 Interference 79

4.1 Introduction 79
4.2 Addition of Waves 79
4.2.1 Trigonometric Approach 80
4.2.2 Complex Approach 81
4.2.3 Vector Approach 81
4.3 Interference 82
4.4 Young's Interference 86
4.5 Dielectric Layer 89
4.5.1 Fizeau Fringes 91
4.5.2 Color Fringes 91
4.5.3 Haidinger's Fringes 94
4.5.4 Antireflection coating 94
4.5.5 Newton's Rings 95
4.6 Michelson Interferometer 97
4.7 Interference by Multiple Reflection 101
4.7.1 Fabry–Perot Interferometer 106
4.8 Summary 112
4.9 Problems 114
References 116
Appendix 4A: Multilayer Dielectric Coatings 116
4A.1 Vector Approach 117
4A.2 Matrix Approach 121

5 Geometrical Optics 126

5.1 Introduction 126
5.2 Eikonal Equation 128
5.3 Fermat's Principle 129
5.4 Applications of Fermat's Principle 132
5.4.1 Law of Reflection 132
5.4.2 Law of Refraction 133
5.4.3 Propagation through an Optical System 134
5.5 Lens Design and Matrix Algebra 135
5.6 Geometrical Optics of Resonators 141

5.7 Guided Waves 146
5.7.1 End Coupling 149
5.7.2 Guided Modes 153
5.7.3 Propagation Vector Formalism 157
5.7.4 Solution for Asymmetric Guide 158
5.7.5 Solution for Symmetric Guide 160
5.7.6 Cutoff Condition 162
5.7.7 Coupling into Guided Wave Modes 162
5.7.7.1 Fiber Coupling 163
5.7.7.2 Evanescent Wave Coupling 164
5.8 Lagrangian Formulation of Optics 165
5.8.1 Hamilton's Principle 166
5.8.2 Rectilinear Propagation 168
5.8.3 Law of Refraction 168
5.9 Propagation in a Graded-Index Optical Fiber 169
5.10 Summary 177
5.11 Problems 179
References 182
Appendix 5A: The *ABCD* Matrix 183
5A.1 Thin-Lens Equation 184
5A.2 Optical Invariant 184
5A.3 Lensmaker's Equation 185
5A.4 Gaussian Formalism 186
5A.5 Newtonian Formalism 186
5A.6 Principal Planes 187
5A.6.1 Nodal Points 189
5A.7 Aperture Stop and Pupil 189
Appendix 5B: Aberrations 191
5B.1 Wavefront Aberration Coefficients 194
5B.1.1 Optical Path Difference 196
5B.1.2 Transverse Ray Coefficients 197
5B.2 Spherical Aberrations 198
5B.2.1 Ray Intercept Plot 201
5B.3 Coma 202
5B.3.1 Optical Sine Theorem 204
5B.3.2 Spot Diagram 205
5B.4 Astigmatism 206
5B.5 Field Curvature 207
5B.6 Distortion 209
5B.7 Aberration Reduction 210
5B.7.1 Coddington Shape Factor 210
5B.7.2 Coddington Position Factor 211

6 Fourier Analysis 214

6.1 Introduction 214
6.2 Fourier Series 215
6.2.1 DC Term 216
6.2.2 Cosine Series 216
6.2.3 Sine Series 217

6.2.4 Even and Odd Functions 217
6.2.5 Exponential Representation 218
6.3 Periodic Square Wave 219
6.4 The Fourier Integral 222
6.4.1 Dirichlet Conditions 223
6.4.2 Evaluation of the Fourier Transform 224
6.5 Rectangular Pulse 225
6.6 Pulse Modulation Wave Trains 227
6.7 Dirac Delta Function 230
6.8 Replication and Sampling 234
6.9 Correlation 237
6.10 Convolution Integrals 239
6.11 Linear System Theory 242
6.12 Fourier Transforms in Two Dimensions 244
6.13 Summary 246
6.14 Problems 249
References 251
Appendix 6A: Fourier Transform Properties 252
6A.1 Linearity 252
6A.2 Scaling 252
6A.3 Shifting 252
6A.4 Conjugation 252
6A.5 Differentiation 252
6A.6 Convolution 252
6A.7 Parseval's Theorem 252
6A.8 Correlation 252
6A.9 Common Fourier Transform Pairs 253
6A.10 Convolution Properties 253

7 **Dispersion** 254
7.1 Introduction 254
7.2 Stiff Strings 256
7.3 Group Velocity 258
7.4 Dispersion of Guided Waves 264
7.5 Material Dispersion 266
7.5.1 Conductive Gas 267
7.5.1.1 Plasma Frequency 268
7.5.2 Molecular Gas 271
7.5.3 Dense Dielectric 277
7.5.4 Metals 283
7.6 Plasmons and Polaritons 283
7.7 Lorenz–Lorentz Law 287
7.8 Signal Velocity, Superluminal Propagation 289
7.9 Summary 293
7.10 Problems 295
References 298
Appendix 7A: Chromatic Aberrations 298

8 Coherence 306

8.1 Introduction 306
8.2 Photoelectric Mixing 307
8.3 Interference Spectroscopy 310
8.4 Fourier Transform Spectroscopy 312
8.4.1 Gaussian Spectral Distribution 315
8.5 Fringe Contrast and Coherence 316
8.6 Temporal Coherence Time 318
8.7 Autocorrelation Function 320
8.8 Spatial Coherence 323
8.8.1 A Line Source 325
8.8.2 van Cittert–Zernike Theorem 327
8.9 Spatial Coherence Length 329
8.10 Stellar Interferometer 330
8.11 Intensity Interferometry 332
8.12 Summary 335
8.13 Problems 338
References 340

9 Diffraction and Gaussian Beams 341

9.1 Introduction 341
9.2 Huygens' Principle 343
9.2.1 Rectilinear Propagation 345
9.2.2 Law of Reflection 345
9.2.3 Snell's Law 346
9.3 Fresnel Formulation 347
9.4 The Obliquity Factor 350
9.4.1 Approximate Solutions of the Huygens–Fresnel integral 355
9.5 Gaussian Beams 356
9.6 Higher-Order Gaussian Modes and Bessel Beams 363
9.6.1 Hermite–Gaussian Waves 363
9.6.2 Laguerre–Gaussian Waves 364
9.6.3 Bessel Beams 364
9.7 Beam Propagation 365
9.7.1 The *ABCD* Law 366
9.7.2 Thin Lens 368
9.7.3 Fabry–Perot Resonator 369
9.7.4 Laser Cavity 371
9.8 Summary 372
9.9 Problems 373
References 375
Appendix 9A: Fresnel–Kirchhoff Diffraction 375
Appendix 9B: Rayleigh–Sommerfeld Formula 381

10 Fraunhofer Diffraction 384

10.1 Introduction 384
10.2 Fraunhofer Diffraction 385

10.3 Fourier Transforms via a Lens 388
10.4 Plane Wave Representation 391
10.5 Diffraction by a Rectangular Aperture 392
10.6 Diffraction by a Circular Aperture 394
10.7 Array Theorem 398
10.8 *N* Rectangular Slits 401
10.8.1 Young's Double Slit 402
10.8.2 The Diffraction Grating 403
10.9 Summary 411
10.10 Problems 413
References 416
Appendix 10A: Abbe Theory and Optical Processing 417
10A.1 Introduction 417
10A.2 Abbe's Theory of Imaging 417
10A.3 Amplitude Spatial Filtering 428
10A.4 Apodization 432
10A.5 Phase Filtering 434
10A.6 Phase and Amplitude Filter 437
Appendix 10B: Imaging 442
10B.1 Introduction 442
10B.2 Incoherent Imaging 443
10B.2.1 Resolution Criteria 444
10B.2.2 Optical Transfer Function 447
10B.2.3 Modulation Transfer Function 450
10B.3 Coherent Imaging 451
10B.4 Computational Imaging 455

11 Fresnel Diffraction 459

11.1 Introduction 459
11.2 Fresnel Approximation 460
11.3 Rectangular Apertures 464
11.4 Fresnel Zones 469
11.4.1 Incident Plane Wave 476
11.5 Circular Aperture 477
11.5.1 Intensity near the Aperture 478
11.5.2 Off-Axis Intensity 479
11.6 Opaque Screen 479
11.7 Zone Plate 481
11.8 Pinhole Camera 484
11.9 Fermat's Principle 485
11.10 Comparison of Techniques 486
11.11 Summary 487
11.12 Problems 488
References 489
Appendix 11A: Babinet's Principle 490
11A.1 Fraunhofer Diffraction 490
11A.2 Fresnel Diffraction 491

Appendix 11B: Fresnel Integral Solutions 493
11B.1 Table of Fresnel Integrals 493
11B.2 Cornu Spiral 495

12 Periodic Index of Refraction 496

12.1 Introduction 496
12.2 Holography 497
12.3 Holographic Recording 502
12.4 Off-Axis Holography 505
12.4.1 Recording 505
12.4.2 Development 507
12.4.3 Reconstruction 507
12.5 Spatial Spectrum of Off-Axis Holograms 508
12.6 Classification of Holograms 511
12.7 Diffraction Efficiency 512
12.8 Holography and Zone Plates 513
12.9 Resolution Requirements 517
12.10 Coherence Requirements 519
12.10.1 Temporal Coherence 519
12.10.2 Spatial Coherence 520
12.11 Photonic Crystals 522
12.11.1 Maxwell's Equations for Sinusoidal ε 522
12.12 The Bloch (or Floquet) Theorem 524
12.13 Multilayer Photonic Crystal 526
12.13.1 Photonic Crystal Defect 527
12.14 Numerical Techniques 529
12.15 Two-Dimensional Periodic Structure 530
12.16 Three-Dimensional Periodic Structure 533
12.17 Fabrication Defects 533
12.18 Natural Photonic Crystals 533
12.19 Summary 533
12.20 Problems 536
References 539
Appendix 12A: Phase Holograms 540
Appendix 12B: VanderLugt Filter 543

13 Anisotropy 549

13.1 Introduction 549
13.2 Dichroic Polarizers 551
13.2.1 Crystals 551
13.2.2 Wire Grids 552
13.2.3 Polaroid Sheet 552
13.3 Reflection Polarizers 554
13.3.1 Brewster's Angle Polarizers 555
13.3.2 Interference Polarizers 555
13.4 Polarization by Birefringence 559
13.5 Optical Indicatrix 564

13.6 Fresnel's Equation 568
13.6.1 Transverse Waves 569
13.6.2 Interdependence of **D** and **H** 569
13.6.3 Fresnel's Equation 569
13.7 Retarder 572
13.7.1 Quarter-Wave Plate 572
13.7.2 Compensator 573
13.7.3 Rhomb 575
13.8 Mueller Calculus 575
13.9 Jones Calculus 577
13.10 Optical Activity 578
13.11 Summary 585
13.12 Problems 586
References 588
Appendix 13A: Tensors 588
13A.1 Scalars 589
13A.2 Vectors 589
13A.3 Second-Rank Tensors 589
13A.4 Higher-Rank Tensors 589
13A.5 Coordinate Transformations 590
13A.6 Geometrical Representation 590
13A.7 Crystal Symmetry 591
Appendix 13B: Poynting Vector in an Anisotropic Dielectric 592
13B.1 Ray Ellipsoid 594
Appendix 13C: Normal Surfaces 595
13C.1 Biaxial Crystal 595
13C.2 Uniaxial Crystal 595
13C.3 Refraction in Crystals 597
Appendix 13D: Ray Surfaces 599

14 Optical Modulation 602

14.1 Introduction 602
14.2 Electro-optic Effect 604
14.3 Electro-optic Indicatrix 606
14.3.1 Pockels Effect 606
14.3.2 Kerr Effect 610
14.4 Amplitude Modulation 612
14.4.1 Kerr Modulation 615
14.4.2 Pockels Modulation 616
14.5 Modulator Design 621
14.5.1 Kerr Modulator 621
14.5.2 Pockels Modulator 621
14.5.3 Longitudinal Modulator 622
14.5.4 Transverse Modulator 623
14.6 Magneto-optic Effect 623
14.6.1 Cotton–Mouton and Voigt Effects 629
14.7 Photoelastic Effect 630

14.8 Acousto-optics 634
14.8.1 Bragg Scattering 637
14.8.2 Raman–Nath Scattering 638
14.8.3 Acousto-optic Modulator 640
14.8.4 Spectrum Analyzer 643
14.8.5 Acousto-optic Beam Deflector 644
14.9 Summary 646
14.10 Problems 648
References 649
Appendix 14A: Pockels and Kerr Tensors 649
Appendix 14B: Phenomenological Acousto-optic Theory 653
14B.1 Bragg Region 656
14B.2 Raman–Nath Region 659
Appendix 14C: Acoustic Figure of Merit 662

15 Nonlinear Optics 664

15.1 Introduction 664
15.2 Nonlinear Polarization 667
15.3 Nonlinear Optical Coefficient 670
15.4 Symmetry Properties 671
15.5 Wave Propagation in a Nonlinear Medium 673
15.6 Conservation of Energy 676
15.6.1 Manley–Rowe Relation 676
15.7 Conservation of Momentum 677
15.7.1 Poynting Vector 677
15.7.2 Phase Matching 680
15.8 Second-Harmonic Generation 682
15.9 Methods of Phase Matching 684
15.9.1 Quasi-Phase Matching (QPM) 684
15.9.2 Total Internal Reflection 685
15.9.3 Dielectric Waveguide 686
15.9.4 Noncollinear Phase Matching 686
15.9.5 Birefringent Phase Matching 688
15.10 Phase Conjugation 693
15.11 Summary 698
15.12 Problems 701
References 702
Appendix 15A: Nonlinear Optical Medium 703
15A.1 Introduction 703
15A.2 Generalized Linear Theory 704
15A.3 Nonlinear Equation of Motion 704
15A.4 Perturbation Technique 705
15A.5 Second-Order Nonlinearity 708
Appendix 15B: Miller's Rule 710
Appendix 15C: Nonlinear Polarization in the 32 Point Group 711

Index 714

Wave Theory

1

1.1 Introduction 1
1.2 Traveling Waves 1
1.3 Wave Equation 4
1.4 Transmission of Energy 5
1.5 Three Dimensions 6
1.6 Attenuation of Waves 10
1.7 Summary 11
1.8 Problems 12

1.1 Introduction

The theory of wave motion is an important mathematical model in many areas of physics. A large number of seemingly unrelated phenomena can be explained using the solution of the wave equation, the basic equation of wave theory. The equation was first used to describe the behavior of a vibrating violin string by Daniel Bernoulli and Jean d'Alembert in the eighteenth century. Wave theory is a fundamental part of modern quantum theory, and solutions of the wave equation are used to explain a number of classical phenomena. Familiarity with wave theory developed in the study of light will aid in the understanding of such diverse physical processes as water waves, vibrating drums and strings, traffic dynamics, and seismic waves.

Mathematically, the basis of wave theory is a second-order partial differential equation called the wave equation. In this chapter, a traveling wave on a string will be used to find the functional form of a one-dimensional wave. Following a discussion of the energy associated with the traveling wave, the one-dimensional model associated with the string illustration will be expanded to three dimensions. The displacement of the wave discussed in this chapter is assumed to be a scalar function, and the theory is called a *scalar wave theory*. In Chapter 2, the vector wave theory will be discussed.

Christian Huygens (1629–1695) developed the wave theory of light in 1678. **Isaac Newton (1642–1727)** proposed a counter theory based on a particle view of light. Because of Newton's scientific stature, only a few scientists during the eighteenth century, for example **Leonard Euler (1707–1783)** and **Benjamin Franklin (1706–1790)**, accepted the wave theory and rejected Newton's particle theory. **Thomas Young (1773–1829)** in 1801 and **Augustin Jean Fresnel (1788–1827)** in 1814 utilized experiments to demonstrate interference and diffraction of light and presented a theoretical explanation of these experiments in terms of the wave theory. Fresnel was able to explain rectilinear propagation using the wave theory, thereby removing Newton's main objection to the theory. Acceptance of Fresnel's theory came very slowly, and the final rejection of Newton's theory did not come until the measurement of the speed of light in water and air by **Jean Bernard Léon Foucault (1819–1868)**. The velocity measurements were a key element in the rejection of Newton's theory, because the particle theory required the speed of light in a medium to exceed the speed of light in a vacuum in order to explain refraction. The measurements by Foucault showed the propagation velocity in a vacuum to exceed that in water.

1.2 Traveling Waves

Before the equation of motion of a wave is discussed, a mathematical expression for a wave will be obtained. We will assume that a disturbance propagates without change along a string and that each point on the string undergoes simple harmonic motion. This assumption will allow us to obtain a simple mathematical expression for a wave that will be used to define the parameters that characterize a wave.

Modern Optics. Second Edition. B. D. Guenther.

© B. D. Guenther 2015. Published in 2015 by Oxford University Press.

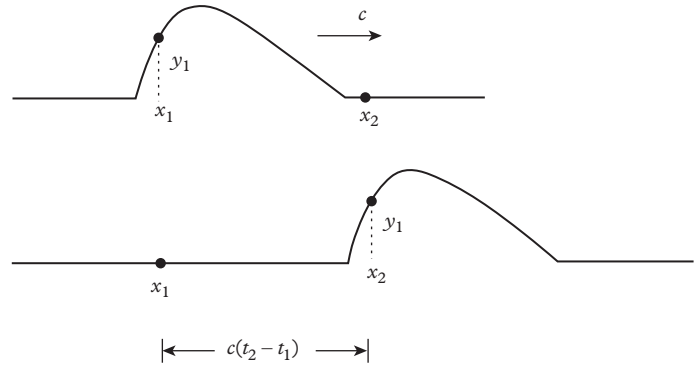

Figure 1.1 *Propagation of a pulse on a guitar string. We assume that the amplitude does not change as the pulse propagates along the string.*

A guitar string is plucked, creating a pulse, which travels to the right and left along the x-axis at a constant speed c. In Figure 1.1, the pulse traveling toward the right is shown. The pulse's amplitude is defined as

$$y \equiv f(x, t)$$

and equals y_1 at position x_1 and time t_1. This amplitude travels a distance $c(t_2 - t_1)$ to the right of x_1 and is shown graphically in Figure 1.1.

Assume the pulse does not change in amplitude as it propagates:

$$f(x_1, t_1) = f(x_2, t_2),$$

where $x_2 = x_1 + c(t_2 - t_1)$. If the function has the form

$$y = f(ct - x), \tag{1.1}$$

then the requirement that the pulse does not change is satisfied because

$$\begin{aligned} f(x_1, t_1) &= f(ct_1 - x_1), \\ f(x_2, t_2) &= f(ct_2 - x_2) = f(ct_2 - x_1 c(t_2 - t_1)) \\ &= f(ct_1 - x_1). \end{aligned}$$

Using the same reasoning, we can show that an unchanging pulse traveling from right to left, along the x-axis, with speed c is described by

$$y = g(x + ct).$$

The expression $y = f(ct - x)$ is a shorthand notation to denote a function that contains x and t only in the combination $ct - x$; i.e., the function can contain combinations of the form $2(ct - x)$, $t \pm x/c$, $x - ct$, $(ct - x)^2$, $\sin(ct - x)$, etc. but not expressions such as $2ct - x$ or $ct^2 - x^2$.

To the assumption of an unchanging propagating disturbance is now added the requirement that each point on the guitar string oscillate transversely, i.e., perpendicular to the direction of propagation, with simple harmonic motion:

$$m\frac{d^2y}{dt^2} + sy = 0,$$

where s is often called the spring constant. The string in Figure 1.1 lies along the x-axis, and the harmonic motion will be in the y-direction. The point on the string at the origin ($x = 0$) undergoes simple harmonic motion with amplitude Y and frequency ω. Note that throughout this book, we shall use the angular frequency $\omega = 2\pi\nu$, where the linear frequency ν is defined as the reciprocal of the period of oscillation:

$$\nu = \frac{1}{T} = \frac{1}{2\pi}\sqrt{\frac{s}{m}}.$$

The equation describing the motion of the origin is

$$y = Y\cos\omega t.$$

The origin acts as a source of a continuous train of pulses (a wave train) moving to the right.

A function of $ct - x$ that will reduce to harmonic motion at $x = 0$ is

$$y = f(ct - x) = Y\cos\left[\frac{\omega}{c}(ct - x)\right].$$

This is called a ***harmonic wave***.

A number of different notations are used for a harmonic wave; the one used in this book involves a constant

$$k = \frac{\omega}{c}, \tag{1.2}$$

called the ***propagation constant*** or the ***wavenumber***. The harmonic wave is written

$$y = Y\cos(\omega t - kx). \tag{1.3}$$

The change in the value of x for which the phase $\omega t - kx$ changes by 2π and thus leaves the right-hand side of (1.3) unchanged is the ***spatial period*** and is called the ***wavelength*** λ. Let $x_2 = x_1 + \lambda$, so that

$$\omega t - kx_2 = \omega t - kx_1 - k\lambda = \omega t - kx_1 - 2\pi;$$

thus,

$$k = \frac{2\pi}{\lambda}. \tag{1.4}$$

Since $k = \omega/c = 2\pi\nu/c$, we also have the relationship $c = \nu\lambda$.

To determine the speed of the wave in space, a point on the wave is selected, and the time it takes to go some distance is measured. This is equivalent to asking how fast a given value of phase propagates in space. Assume that in the time $\Delta t = t_2 - t_1$, the disturbance y_1 travels a distance $\Delta x = x_2 - x_1$, as shown in Figure 1.1. Since the disturbance at the two points is the same, i.e., y_1, the phases must be equal:

$$\omega t - kx = \omega(t + \Delta t) - k(x + \Delta x),$$

$$\frac{\Delta x}{\Delta t} = \frac{\omega}{k}.$$

In the limit as $\Delta t \to 0$, we obtain the ***phase velocity***

$$c \equiv \frac{dx}{dt} = \frac{\omega}{k}.$$

The adjective "phase" is used because this velocity describes the motion of a preselected phase of the wave. Another method that can be used to obtain the propagation speed associated with a wave is to define the phase velocity using the following result from partial differential calculus:

$$\left(\frac{\partial x}{\partial t}\right)_y = -\frac{\left(\dfrac{\partial y}{\partial t}\right)_x}{\left(\dfrac{\partial y}{\partial x}\right)_t} = \frac{\omega}{k}. \tag{1.5}$$

This equation may be verified by applying it to (1.3).

1.3 Wave Equation

We may write the wave equation as

$$\frac{\partial^2 y}{\partial x^2} = \frac{1}{c^2}\frac{\partial^2 y}{\partial t^2}. \tag{1.6}$$

This differential equation describes a number of physical situations: a vibrating string, sound waves, a vibrating drum head, elastic waves in solids such as seismic waves in the earth, electric signals in a cable, and electromagnetic waves—the subject of this book.

We said earlier that the motion of a vibrating string was described by equations of the form (1.1):

$$y_1 = f(ct - x) \quad \text{or} \quad y_2 = g(ct + x).$$

To show that y_1 is a solution, we substitute it into the wave equation (we will denote derivatives with respect to the argument of the function f, i.e., $ct - x$, by a prime):

$$\frac{\partial f}{\partial t} = \frac{\partial f}{\partial (ct-x)}\frac{\partial (ct-x)}{\partial t} = cf', \ \frac{\partial f}{\partial x} = \frac{\partial f}{\partial (ct-x)}\frac{\partial (ct-x)}{\partial x} = (-1)f',$$

$$\frac{\partial^2 f}{\partial t^2} = c^2 f'', \ \frac{\partial^2 f}{\partial x^2} = f'',$$

$$\frac{\partial^2 f}{\partial x^2} - \frac{1}{c^2}\frac{\partial^2 f}{\partial t^2} = f'' - \frac{1}{c^2}\left(c^2 f''\right) = 0.$$

The same procedure is used to prove that $g(ct + x)$ is a solution.

Another important property of the wave equation is the ***superposition principle***. This states that the sum of two solutions is also a solution. Proof of the superposition principle is the objective of Problem 1.10.

1.4 Transmission of Energy

Each element of a string, with a harmonic wave propagating along it, moves up and down in the y-direction, undergoing simple harmonic motion. This can be seen by selecting a coordinate position to observe, say x_1, and replacing kx_1 in (1.3) by a constant δ, i.e., $y = Y\cos(\omega t - \delta)$. Equation (1.3) now assumes the same form as the equation for a harmonic oscillator:

$$x = A\cos(\omega_0 t + \delta), \tag{1.7}$$

$$v = -\omega_0 A\ \sin(\omega_0 t + \delta), \tag{1.8}$$

$$a = -\omega_0^2 A\ \cos(\omega_0 t + \delta). \tag{1.9}$$

The elements of the string do not move in the direction of wave motion (the x-direction). Even though the elements are not translated along the direction of propagation, energy is transmitted. An aid to understanding how this occurs can be obtained by imagining yourself at the end of a long line of people waiting to purchase tickets. To communicate with a friend at the front of the line, you could pass a note from hand to hand until it reaches your friend at the front of the line. No one need move in the direction of your friend, and yet the note arrives.

Energy is transmitted by a wave in the same way as the note. To discover the wave characteristics that determine the energy transmitted by a wave, consider a string, under tension T, as shown in Figure 1.2: point "a" on the string has work done on it by the point to its left and it does work on the point on its right. The work done on point "a" is

$$dW = F\,dy = (T\sin\theta)(v\,dt).$$

The work done is equal to the change in energy, allowing us to write the instantaneous power transmitted as

$$P = \frac{dE}{dt} = Tv\ \sin\theta.$$

From (1.3), we can write

$$\frac{dE}{dt} = YT\sin\theta[-\omega\sin(\omega t - kx)].$$

We continue to assume small-amplitude waves, so that the tension at point "a" in Figure 1.2 is parallel to the slope of the wave at "a":

$$\sin\theta \approx \tan\theta \approx -\tan\phi = -\frac{dy}{dx} = -kY\sin(\omega t - kx),$$

$$\frac{dE}{dt} = T[-kY\sin(\omega t - kx)][-\omega Y\sin(\omega t - kx)],$$

$$\frac{dE}{dt} = Tk\omega Y^2\sin^2(\omega t - kx).$$

The average power transmitted in one period $(2\pi/\omega)$ is

$$P_{\text{avg}} = \langle E\rangle = \frac{\omega}{2\pi}\int_0^{2\pi/\omega} P\,dt = \frac{Tk\omega^2 Y^2}{2\pi}\int_0^{2\pi/\omega}\sin^2(\omega t - kx)\,dt,$$

$$P_{\text{avg}} = \frac{Tk\omega Y^2}{2} = \frac{T\omega^2 Y^2}{2c}. \tag{1.10}$$

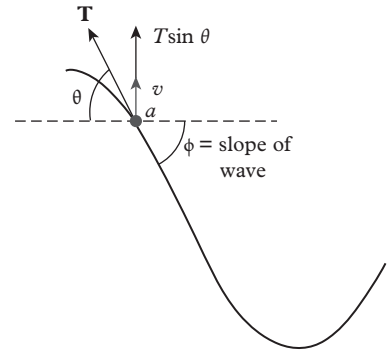

Figure 1.2 *Forces acting on point "a" of a string.*

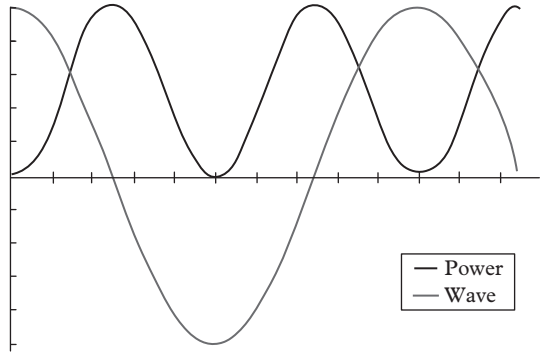

Figure 1.3 *A traveling wave and its instantaneous power are plotted with their amplitudes normalized to one.*

For a given string, the tension T and the phase velocity c are constants, and the average power transmitted is proportional to the square of the frequency and the square of the amplitude. In Figure 1.3, we plot the wave and its instantaneous power, demonstrating that the power travels along with the wave.

1.5 Three Dimensions

While the wave traveling along a string can be described with only one dimension, we will need a three-dimensional model in our discussion of light. The one-dimensional model (1.6) generalizes to a three-dimensional wave equation

$$\frac{\partial^2 f(\mathbf{r},t)}{\partial x^2}+\frac{\partial^2 f(\mathbf{r},t)}{\partial y^2}+\frac{\partial^2 f(\mathbf{r},t)}{\partial z^2}=\frac{1}{c^2}\frac{\partial^2 f(\mathbf{r},t)}{\partial t^2}, \tag{1.11}$$

or, in vector notation [see (2A.8) in Appendix 2A],

$$\nabla^2 f(\mathbf{r},t)=\frac{1}{c^2}\frac{\partial^2 f(\mathbf{r},t)}{\partial t^2}. \tag{1.12}$$

A generalized harmonic wave solution of (1.12) is

$$f(\mathbf{r},t)=E(\mathbf{r})\cos[\omega t-\mathcal{S}(\mathbf{r})].$$

At a fixed time, the surfaces for which $\mathcal{S}(\mathbf{r})=$ constant are called ***wavefronts***. If $E(\mathbf{r})$, the amplitude of the wave, is a constant over the wavefront, then the wave is said to be ***homogeneous***; if not, then the wave is ***inhomogeneous***. The average power defined by (1.10) is defined for the three-dimensional case as the average power transmitted per unit cross-sectional area. This quantity is called the ***intensity*** of the wave.

Another notation we will find useful in the study of waves is complex notation. The generalized solution of the wave equation can be expressed in complex notation as

$$f(\mathbf{r},t)=\mathcal{E}(\mathbf{r})e^{i\omega t},$$

where

$$\mathcal{E}(\mathbf{r})=E(\mathbf{r})e^{-i[\mathcal{S}(\mathbf{r})+\delta]}$$

and δ is an arbitrary phase angle. If we substitute $f(\mathbf{r}, t)$ into the wave equation, we obtain

$$\frac{\partial^2 f(\mathbf{r}, t)}{\partial t^2} = -\omega^2 \mathcal{E}(\mathbf{r}) e^{i\omega t},$$
$$\nabla^2 f(\mathbf{r}, t) = e^{i\omega t} \nabla^2 \mathcal{E}(\mathbf{r}).$$

Using the relationship $\omega/c = k$, the wave equation becomes

$$(\nabla^2 + k^2)\mathcal{E}(\mathbf{r}) = 0. \tag{1.13}$$

If we are interested in the spatial properties of the wave but not the temporal properties, we need only seek solutions of this equation, which is called the ***Helmholtz equation***.

The evaluation of the phase velocity of the three-dimensional wave is more complicated than it was for the one-dimensional case because we must monitor the motion of a surface. As we show below, it is possible to derive the phase velocity of an arbitrary wavefront. In this book, however, we will restrict our consideration to two simple wavefronts: a plane (called a plane wave) and a sphere (called a spherical wave).

To calculate the phase velocity of an arbitrary wavefront, we must follow a point of constant phase as the wave moves through space and time. If the phase at ($\mathbf{r}$, t) is equal to the phase at ($\mathbf{r} + \Delta\mathbf{r}$, $t + \Delta t$), then

$$\omega t - \mathcal{S}(\mathbf{r}) = \omega t + \omega\, \Delta t - \mathcal{S}(\mathbf{r} + \Delta\mathbf{r}),$$
$$\omega \Delta t - \left[\frac{\mathcal{S}(\mathbf{r} + \Delta\mathbf{r}) - \mathcal{S}(\mathbf{r})}{\Delta\mathbf{r}}\right] \Delta\mathbf{r} = 0,$$

and in the limit as $\Delta t \Delta\mathbf{r} \to 0$, the term in square brackets becomes the gradient of $\mathcal{S}(\mathbf{r})$:

$$\omega dt - \nabla \mathcal{S}(\mathbf{r}) \cdot d\mathbf{r} = 0. \tag{1.14}$$

If we define a unit vector $\hat{\mathbf{n}}$ in the direction of $d\mathbf{r}$, so that $d\mathbf{r} = \hat{\mathbf{n}}\, ds$, where ds is the distance between the surfaces $\mathcal{S}(\mathbf{r})$ and $\mathcal{S}(\mathbf{r} + d\mathbf{r})$, then the velocity of the surface is

$$\frac{ds}{dt} = \frac{\omega}{\hat{\mathbf{n}} \cdot \nabla \boldsymbol{\mathcal{S}}(\mathbf{r})}.$$

Figure 1.4 shows these parameters for a plane surface. This derivative has its smallest value when $\hat{\mathbf{n}}$ is normal to the wavefront,

$$\hat{\mathbf{n}} = \frac{\nabla \boldsymbol{\mathcal{S}}(\mathbf{r})}{|\nabla \boldsymbol{\mathcal{S}}(\mathbf{r})|}.$$

We then have an equation for the phase velocity of the wavefront, c:

$$\frac{ds}{dt} = c = \frac{\omega}{|\nabla \mathcal{S}(\mathbf{r})|}. \tag{1.15}$$

Note that the phase velocity is not a vector. We must exercise care in assigning any physical significance to this velocity.

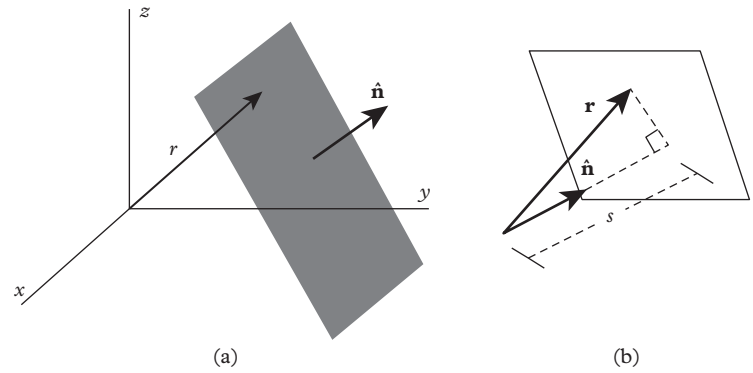

Figure 1.4 *(a) A plane wave. Its normal is the unit vector* $\hat{\mathbf{n}}$*, which points in the direction of propagation. A surface of constant phase is the shaded plane passing through the point defined by the vector* $\mathbf{r}$*. (b) The projection of* $\mathbf{r}$ *on the plane's normal defines the distance s from the origin.*

Mathematically, a plane is described by the equation

$$\mathbf{r} \cdot \hat{\mathbf{n}} = s$$

where $\mathbf{r}$ is the position vector of a point in the plane, $\hat{\mathbf{n}}$ is a unit vector normal to the plane, and s is a constant equal to the distance from the origin to the plane, as shown in Figure 1.4. For a wavefront to be a plane, we must have $S(\mathbf{r}) = k(\mathbf{n} \cdot \mathbf{r})$. For convenience, we define the wavevector $\mathbf{k} = k\hat{\mathbf{n}}$, and we write our plane wave solution of the wave equation as

$$f(\omega t - \mathbf{k} \cdot \mathbf{r}) + g(\omega t + \mathbf{k} \cdot \mathbf{r}).$$

The harmonic plane wave solution is

$$f(\mathbf{r}, t) = E(\mathbf{r}) \cos(\omega t - \mathbf{k} \cdot \mathbf{r}). \tag{1.16}$$

In complex notation, the harmonic plane wave is written as

$$f(\mathbf{r}, t) = E(\mathbf{r}) e^{i(\omega t - \mathbf{k} \cdot \mathbf{r})}. \tag{1.17}$$

We will find this harmonic plane wave important because, as we will see later, any three-dimensional wave can be written as a combination of plane waves of different amplitudes, directions, and frequencies.

The second three-dimensional wave we will find useful is one with spherical symmetry:

$$f(\mathbf{r}, t) = f(r, \theta, \phi, t) = f(r, t),$$

where

$$r = \sqrt{x^2 + y^2 + z^2}.$$

For example, a point source located at the origin would produce a wave with a wavefront that is a sphere. In this case, the wavefront is given by $S(\mathbf{r}) = S(r) = kr =$ constant (the equation for a sphere). The wave equation can be obtained by converting from rectangular to

spherical coordinates (we only have to obtain the r component, because f is not a function of θ and ϕ if it has spherical symmetry):

$$\begin{aligned}\frac{\partial f}{\partial x} &= \frac{\partial f}{\partial r}\frac{\partial r}{\partial x} = \frac{x}{r}\frac{\partial f}{\partial r},\\ \frac{\partial^2 f}{\partial x^2} &= \frac{\partial}{\partial r}\left(\frac{x}{r}\frac{\partial f}{\partial r}\right)\frac{\partial r}{\partial x} = \frac{x}{r}\left[\frac{x}{r}\frac{\partial^2 f}{\partial r^2} + \frac{\partial f}{\partial r}\frac{\partial}{\partial r}\left(\frac{x}{r}\right)\right],\\ &= \frac{x^2}{r^2}\frac{\partial^2 f}{\partial r^2} + \left(\frac{1}{r} - \frac{x^2}{r^3}\right)\frac{\partial f}{\partial r}. \end{aligned} \tag{1.18}$$

We do the same for the derivatives with respect to y and z and add the results to (1.18):

$$\begin{aligned}\frac{\partial^2 f}{\partial x^2} + \frac{\partial^2 f}{\partial y^2} + \frac{\partial^2 f}{\partial z^2} &= \frac{1}{r^2}\frac{\partial^2 f}{\partial r^2}\left(x^2 + y^2 + z^2\right) + \frac{3}{r}\frac{\partial f}{\partial r} - \frac{x^2 + y^2 + z^2}{r^3}\frac{\partial f}{\partial r},\\ &= \frac{\partial^2 f}{\partial r^2} + \frac{2}{r}\frac{\partial f}{\partial r}.\end{aligned}$$

The wave equation for spherically symmetric solutions becomes

$$\frac{\partial^2 f}{\partial r^2} + \frac{2}{r}\frac{\partial f}{\partial r} = \frac{1}{c^2}\frac{\partial^2 f}{\partial t^2},$$

or, equivalently,

$$\frac{\partial^2}{\partial r^2}(rf) = \frac{1}{c^2}\frac{\partial^2}{\partial t^2}(rf).$$

This is the one-dimensional wave equation with a general solution

$$rf(r,t) = f(ct - r) + g(ct + r).$$

The harmonic spherical wave is

$$f(r,t) = \frac{A}{r}\cos(\omega t - kr). \tag{1.19}$$

It is easy to find physical examples of the spherical wave. One realization that everyone has seen is the water wave formed on the surface of a still pool by a drop of water striking the surface, as shown in Figure 1.5. As the wave moves out from its source, it forms circles of ever increasing radii. This water wave can be thought of as a representation of the intersection of the spherical wavefront and a plane that cuts through the wave and contains the source. If we assume that there are no losses, then the total power in the wave is a constant, P_0, given by the product of the power per unit area, P, and the area of the spherical wave, $4\pi r^2$:

$$P_0 = P\left(4\pi r^2\right).$$

This leads to the conclusion that the power per unit area is inversely proportional to the radius r of the spherical wave's phase front:

$$P = \frac{P_0}{4\pi r^2}.$$

Figure 1.5 *Spherical wavefront. Uploaded from Flickr by Jacopo Werther, taken by Davide Restivo.* http://commons.wikimedia.org/wiki/File:Water_drop_impact_on_a_water-surface_-_(5).jpg.

Since r is also the distance that the wave has traveled from the source, we have that the power per unit area in a spherical wave is inversely proportional to the square of the distance the wave has propagated. The power per unit area of a spherical wave can also be obtained by using (1.19) in (1.10) and is given by

$$P \propto \frac{A^2}{r^2}.$$

Conservation of energy and the wave model both yield the inverse square law behavior.

1.6 Attenuation of Waves

Physical systems dissipate a wave's energy as it propagates. We can take the effect of a dissipative force into account by adding a loss or damping term to the wave equation. We will use the same functional form for the loss term as is used for a damped harmonic oscillator:

$$m\frac{d^2y}{dt^2} = -sy - b\frac{dy}{dt},$$

where b is a positive constant of proportionality, with units of kg/s, called the ***damping constant***. The solutions of this equation behave as shown in Figure 1.6. The new equation of motion is then

$$\frac{\partial^2 f}{\partial x^2} - \gamma\frac{\partial f}{\partial t} - \frac{1}{c^2}\frac{\partial^2 f}{\partial t^2} = 0, \tag{1.20}$$

where $\gamma = b/m$ is the resistance per unit time. Is this equation still a wave equation? We can find out by testing if the one-dimensional representation of a plane wave (1.17),

$$f(x,t) = Ae^{i(\omega t - kx + \phi)}, \tag{1.21}$$

is a solution of (1.20). If we differentiate (1.21), we obtain

$$\frac{\partial^n f}{\partial x^n} = (-ik)^n Ae^{i(\omega t - kx + \phi)} = (-ik)^n f(x,t), \tag{1.22}$$

$$\frac{\partial^n f}{\partial t^n} = (i\omega)^n Ae^{i(\omega t - kx + \phi)} = (i\omega)^n f(x,t). \tag{1.23}$$

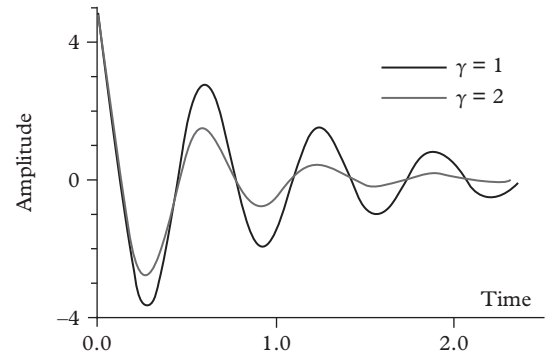

Figure 1.6 *Damped harmonic oscillator with two different size loss terms.*

Here the usefulness of complex notation becomes apparent. The untidy equations obtained when differentiating sine and cosine functions are avoided. Substituting the above results into (1.20) yields

$$k^2 = \left(\frac{\omega}{c}\right)^2 - i\omega\gamma.$$

This type of equation is called a ***dispersion equation*** or ***dispersion relation***. We see that for (1.20) to have a plane wave solution of the form (1.21), k must be complex. If we write the complex k as

$$\tilde{k} = \kappa_1 - i\kappa_2 \tag{1.24}$$

and substitute this into (1.21), we obtain

$$f(x,t) = Ae^{-\kappa_2 x}e^{i(\omega t - \kappa_1 x + \phi)}.$$

A solution of (1.21) is a harmonic wave whose amplitude is attenuated as it propagates in the positive x-direction. κ_2 is an attenuation constant whose reciprocal equals the distance the wave will propagate before its amplitude falls to $1/e$ of the value it had at $x = 0$.

1.7 Summary

We developed a one-dimensional model of a wave whose properties are described by the wave equation

$$\frac{\partial^2 f(x,t)}{\partial x^2} = \frac{1}{c^2}\frac{\partial^2 f(x,t)}{\partial t^2}.$$

We extended this equation to three dimensions:

$$\nabla^2 f(\mathbf{r},t) = \frac{1}{c^2}\frac{\partial^2 f(\mathbf{r},t)}{\partial t^2}.$$

A special case of the wave equation called the Helmholtz equation

$$(\nabla^2 + k^2)E(\mathbf{r}) = 0$$

was introduced for those situations where only the spatial properties of the wave are to be discussed.

The most important solution of the wave equation for the discussions in this book is the harmonic plane wave

$$f(\mathbf{r},t) = E(\mathbf{r})\cos(\omega t - \mathbf{k}\cdot\mathbf{r}),$$

or, in complex notation,

$$f(\mathbf{r},t) = E(\mathbf{r})e^{i(\omega t - \mathbf{k}\cdot\mathbf{r})}.$$

The solution of the wave equation is modified if the propagation medium has some loss mechanism. A plane harmonic wave propagating in the x-direction then has an amplitude that is attenuated as it propagates:

$$f(x,t) = Ae^{-\kappa_2 x}e^{i(\omega t-\kappa_1 x+\phi)}$$

where

$$\tilde{k} = \kappa_1 - i\kappa_2$$

is the complex wavevector for the wave propagating in the dissipative medium.

The average power per unit area (equivalently the energy per unit time per unit area) was defined as the intensity of the wave and was shown to be proportional to the amplitude squared.

1.8 Problems

1.1. Assume a sine wave with an amplitude of 10 cm and a wavelength of 200 cm moving with a velocity of 100 cm/s:

(a) What is the frequency, both ν and ω?

(b) What is the value of k?

(c) What is the wave equation?

(d) Assume the left end is at the origin and moving down at $t = 0$. What is the equation of motion at the left end?

(e) What is the equation of motion of the point 150 cm to the right of the origin?

1.2. The wavelength of light ranges from 390 to 780 nm and its velocity (in a vacuum) is about 3×10^8 m/s. What is the corresponding frequency range?

1.3. Given the complex number

$$\tilde{z}_1 = \frac{1}{2i}(1-4i),$$

what are its real part and its modulus? Calculate

$$\tilde{z}_1\tilde{z}_1^*.$$

What is the imaginary part of

$$\tilde{z}_2 = \frac{e^{i\omega t}-e^{-i\omega t}}{2} \quad ?$$

1.4. If

$$f(x,t) = Ae^{i(kx-\omega t)},$$

what are the expressions for $\mathcal{R}e\{|f|^2\}$ and $[\mathcal{R}e\{f\}]^2$?

1.5. Show that

$$s(x, t) = Ae^{-(2x+3t)^2}$$

is a solution of the wave equation. What is the velocity? In what direction is the wave moving?

1.6. The thickness of a human hair is about 4×10^{-2} mm. Compare its dimension with that of a light wave.

1.7. Find the direction of travel of the following two waves:

$$s(x, t) = A \sin(kx - \omega t),$$
$$s(x, t) = A \cos(\omega t - kx).$$

1.8. If we write the wavefunction in complex notation

$$s(x, t) = Ae^{i\phi},$$

show that s is unchanged when its phase increases or decreases by 2π.

1.9. Given the wave

$$\varphi(x, t) = 10 \cos\left\{2\pi\left[\frac{x}{2 \times 10^{-7}} - (1.5 \times 10^{15})t\right]\right\},$$

determine its speed, wavelength, and frequency in MKS units.

1.10. If s_1 and s_2 are solutions of the wave equation

$$\frac{\partial^2 s}{\partial x^2} = \frac{1}{v^2}\frac{\partial^2 s}{\partial t^2},$$

prove the superposition principle, i.e., that $as_1 + bs_2$ is also a solution, where a and b are both constants.

1.11. A simple harmonic oscillator has a mass m of 0.01 kg and a force constant s of 36 N/m. At $t = 0$, the mass is displaced 50 mm to the right of its equilibrium position and is moving to the right at a speed of 1.7 m/s. Calculate (a) the frequency, (b) the period, (c) the amplitude, and (d) the phase constant.

1.12. The HCl molecule, to first order, acts like a simple harmonic oscillator. The hydrogen, which does all the vibrating, has a mass of 1.67×10^{-27} kg, and the force constant is 840 N/m. What is the vibration frequency?

1.13. Assume the motion of an oscillator is described by

$$y = 2 \cos 6\pi t + \sin 5\pi t.$$

If the mass of the oscillator is 10 g, what are the maximum and minimum kinetic energies?

1.14. When playing a guitar, harmonics of the open string are generated by placing a finger lightly on the string above the 12th fret (this is at the halfway point between the supports of the guitar string, i.e., the nut and the saddle). What other positions, in terms of string length, would be useful for harmonic generation?

1.15. A mass of 10 g is attached to a spring and causes it to stretch 1 cm downward. If the attached mass is moved downward another 1 cm and released, what will be its period and maximum velocity?

1.16. A spring has a spring constant $k = 2.5$ N/m and a damping force constant $b = 1$ kg/m. A mass of 25 g is attached to the spring, and the spring is released at $t = 0$ from a position at $x = -5$ cm. Find (a) the frequency and (b) the epoch angle (the initial phase at $t = 0$). (c) Write an expression for the displacement as a function of time of the oscillator.

1.17. Find the times when the maximum displacements occur and the values of the maximum displacement for the first three excursions of the oscillator in Problem 1.16.

1.18. A particle of mass m that is constrained to move along the x-axis experiences a force toward the origin equal to mkx. Upon release, the particle undergoes simple harmonic motion about the origin with a period of 6 s. At time $t = 2$ s, the particle reaches the origin. At $t = 3$ s, the particle is found to have a velocity of 5 cm/s. (a) What is the force constant? (b) What is the maximum distance from the origin reached by the particle?

1.19. A string 3 m long and weighing 300 g is held under a tension of 10 N. How long does it take a wave to travel the string's length?

1.20. A string is held under tension by passing it over a pulley and attaching a 2 kg weight. An 8 m-long segment of the string, which weighs 600 g, has a wave of amplitude 10 cm and wavelength 3 m traveling along its length. (a) What is the velocity of the wave? (b) What is the maximum transverse velocity of a point on the wave?

1.21. A string with mass per unit length $\mu = 0.1$ kg/m and $T = 90$ N has a wave of amplitude 30 cm and frequency 1 Hz propagating along it. How much energy is transmitted by the wave?

Electromagnetic Theory

2

2.1 Introduction

2.1 Introduction 15
2.2 Maxwell's Equations 16
2.3 Free Space 19
2.4 Wave Equation 19
2.5 Transverse Waves 21
2.6 Interdependence of E and B 22
2.7 Energy Density and Flow 24
2.8 Polarization 28
2.9 Propagation in a Conducting Medium 40
2.10 Summary 44
2.11 Problems 45
References 47
Appendix 2A: Vectors 47
Appendix 2B: Electromagnetic Units 50

The scalar wave theory that we discussed in Chapter 1 was applied to the study of light before the development of the theory of electromagnetism. At that time, it was assumed that light waves were longitudinal, in analogy with sound waves; i.e., the wave displacements were in the direction of propagation. A further assumption, that light propagated through some type of medium, was made because the scientists of that time approached all problems from a mechanistic point of view. The scalar theory was successful in explaining diffraction (see Chapter 9), but problems arose in interpretation of the effects of polarization in interference experiments (discussed in Chapter 4). Young was able to resolve the difficulties by suggesting that light waves could be transverse, like the waves on a vibrating string. Using this idea, Fresnel developed a mechanistic description of light that could explain the amount of reflected and transmitted light from the interface between two media (see Chapter 3).

Independent of this activity, the theory of electromagnetism was under development. **Michael Faraday (1791–1867)** observed in 1845 that a magnetic field would rotate the plane of polarization of light waves passing through the magnetized region. This observation led Faraday to associate light with electromagnetic radiation, but he was unable to quantify this association. Faraday attempted to develop electromagnetic theory by treating the field as lines pointing in the direction of the force that the field would exert on a test charge. The lines were given a mechanical interpretation with a tension along each line and a pressure normal to the line. **James Clerk Maxwell (1831–1879)** furnished a mathematical framework for Faraday's model in a paper read in 1864 and published a year later [1]. In this paper, Maxwell identified light as "an electromagnetic disturbance in the form of waves propagated through the electromagnetic field according to electromagnetic laws" and demonstrated that the propagation velocity of light was given by the electromagnetic properties of the material.

Maxwell was not the first to recognize the connection between the electromagnetic properties of materials and the speed of light. Kirchhoff (**Gustav Robert Kirchhoff: 1824–1887**) recognized in 1857 that the speed of light could be obtained from electromagnetic properties. Riemann (**Georg Friedrich Bernhard Riemann: 1826–1866**), in 1858, assumed that electromagnetic forces propagated at a finite velocity and derived a propagation velocity given by the electromagnetic properties of the medium. However, it was Maxwell who demonstrated that the electric and magnetic fields are waves that travel at the speed of light. It was not until 1887 that an experimental observation of electromagnetic waves, other than light, was obtained by **Heinrich Rudolf Hertz (1857–1894)**.

The classical electromagnetic theory is successful in explaining all of the experimental observations to be discussed in this book. There are, however, experiments that cannot be explained by classical wave theory, especially those conducted at short wavelengths or very low light levels. Quantum electrodynamics (QED) is capable of predicting the outcome of all optical experiments; its shortcoming is that it does not explain why or how. An excellent elementary introduction to QED has been written by Richard Feynman [2].

Modern Optics. Second Edition. B. D. Guenther.

© B. D. Guenther 2015. Published in 2015 by Oxford University Press.

In this chapter, we will borrow, from electromagnetic theory, Maxwell's equations and Poynting's theorem to derive properties of light waves. Details of the origins of these fundamental electromagnetic relationships are not needed for our study of light but can be obtained by consulting any electricity and magnetism text (e.g., [3]).

The basic properties that will be derived are

- the wave nature of light;
- the fact that light is a transverse wave;
- the velocity of light in terms of fundamental electromagnetic properties of materials;
- the relative magnitude of the electric and magnetic fields and relationships between the two fields;
- the energy associated with a light wave.

The concept of polarized light and a geometrical construction used to visualize its behavior will be introduced. In the seventeenth century, Hooke postulated that light waves might be transverse, but his idea was forgotten. Young and Fresnel made the same postulate in the nineteenth century and accompanied this with a theoretical description of light based on transverse waves. Forty years later, Maxwell proved that light must be a transverse wave and that **E** and **H**, for a plane wave in an isotropic medium with no free charges and no currents, are mutually perpendicular and lie in a plane normal to the direction of propagation, **k**.

Convention requires that we use the electric vector to label the direction of the electromagnetic wave's polarization. The direction of the displacement vector is called the *direction of polarization*, and the plane containing the direction of polarization and the propagation vector is called the *plane of polarization*. The selection of the electric field is not completely arbitrary—except for relativistic situations, when $v \approx c$, the interaction of the electromagnetic wave with matter will be dominated by the electric field. Both a vector and a matrix notation for describing polarization will be presented in this chapter, but details on the manipulation of light polarization will not be discussed until Chapter 14. The chapter will conclude with a discussion of the propagation of light in a conducting medium.

2.2 Maxwell's Equations

The bases of electromagnetic theory are Maxwell's equations. They allow the derivation of the properties of light. In our study of optics, we will treat these equations as axioms, but we provide the reader with a reference source here that can be consulted if information on the origin of the equations is desired.

In rationalized MKS units, Maxwell's equations are as follows.

2.2.1 Gauss's Law

2.2.1.1 Gauss's (Coulomb's) Law for the Electric Field

Coulomb's law provides a means for calculating the force between two charges (see Chapter 2 of [3]),

$$\mathbf{F} = \frac{q_0}{4\pi\varepsilon_0}\int \frac{dq}{r^2}\hat{\mathbf{n}},$$

where dq is the charge on an infinitesimal surface and $\hat{\mathbf{n}}$ is a unit vector in the direction of the line connecting the charges q_0 and dq. The electric field

$$\mathbf{E} = \frac{\mathbf{F}}{q_0}$$

is obtained using Coulomb's law (see Chapter 3 of [3]). We view this field as Michael Faraday did, as lines of flux, called lines of force, originating on positive charges and terminating on negative charges. Gauss's Law states that the quantity of charge contained within a closed surface is equal to the number of flux lines passing outward through the surface (see Chapter 4 of [3]). This view of the electric field leads to

$$\nabla \cdot \mathbf{D} = \rho, \tag{2.1}$$

where ρ is the charge density and $\mathbf{D}$ is the electric displacement (see Chapter 10, Section 5 of [3]). The use of the displacement allows the equation to be applied to any material.

2.2.1.2 Gauss's Law for the Magnetic Field

Charges at rest led to (2.1). Charges in motion, i.e., a current $\mathbf{i}$ or a current density $\mathbf{J}$, create a magnetic field $\mathbf{B}$ (see Chapter 14 of [3]). As we did for the electric field, we treat the magnetic field as flux lines, called lines of induction, and we assume that the current density is a constant so that $\nabla \cdot \mathbf{J} = 0$. This leads to (see Chapter 16 of [3])

$$\nabla \cdot \mathbf{B} = 0. \tag{2.2}$$

The zero is due to the fact that the magnetic equivalent of a single charge has never been observed.

2.2.2 Faraday's Law

The previous two equations are associated with electric and magnetic fields that are constant with respect to time. The next equation, an experimentally derived equation, deals with a magnetic field that is time-varying or equivalently a conductor moving through a static magnetic field:

$$\nabla \times \mathbf{E} + \frac{\partial \mathbf{B}}{\partial t} = 0. \tag{2.3}$$

In terms of the concept of flux, it states that an electric field around a circuit is associated with a change in the magnetic flux contained within the circuit.

2.2.3 Ampére's Law (Law of Biot and Savart)

An electric charge in motion creates a magnetic field around its path. The law of Biot and Savart allows us to calculate the magnetic field at a point located a distance $\mathbf{R}$ from a conductor carrying a current density $\mathbf{J}$. Ampère's law is the inverse relationship used to calculate the current in a conductor due to the magnetic field contained in a loop about the conductor. Neither relationship is

adequate when the current is a function of time. Maxwell's major contribution to physics was to observe that the addition of a *displacement current* to Ampère's law allowed fluctuating currents to be explained. The relationship became (see Chapter 21 of [3])

$$\nabla \times \mathbf{H} = \mathbf{J} + \frac{\partial \mathbf{D}}{\partial t}, \tag{2.4}$$

As discussed in Appendix 2B, the constants in Maxwell's equations depend on the units used. Many optics books use c.g.s. units, which result in a form for Maxwell's equations shown in Appendix 2B.

2.2.4 Constitutive Relations

The dynamic responses of atoms and molecules in the propagation medium are taken into account through what are called the *constitutive relations*:

$$\mathbf{D} = f(\mathbf{E}),$$
$$\mathbf{J} = g(\mathbf{E}),$$
$$\mathbf{B} = h(\mathbf{H}).$$

Here we will assume that the functional relations are independent of space and time, and we will write the constitutive relations as

$$\mathbf{D} = \varepsilon \mathbf{E}, \quad \varepsilon = \text{dielectric constant},$$
$$\mathbf{J} = \sigma \mathbf{E}, \quad \sigma = \text{conductivity (Ohm's law)},$$
$$\mathbf{B} = \mu \mathbf{H}, \quad \mu = \text{permeability},$$

where the constants ε, σ, and μ contain the description of the material. Later, we will explore the effects resulting from the constitutive relations having a temporal or a spatial dependence.

Often, **D** and **B** are defined as

$$\mathbf{D} = \varepsilon_0 \mathbf{E} + \mathbf{P}, \tag{2.5}$$
$$\mathbf{B} = \mu_0 \mathbf{H} + \mathbf{M},$$

where **P** is the polarization and **M** is the magnetization. This formulation emphasizes that the internal field of a material is due not only to the applied field but also due to a field created by the atoms and molecules that make up the material. We will find (2.5) useful in Chapters 7 and 15. We will not use the relationship involving **M** in this book.

By manipulating Maxwell's equations, we can obtain a number of the properties of light, such as its wave nature, the fact that it is a transverse wave, and the relationship between the **E** and **B** fields. We will make a number of simplifying assumptions about the medium in which the light is propagating to allow a quick derivation of the properties of light. Later, we will see what happens if we modify these assumptions.

2.3 Free Space

We assume that the light is propagating in a medium that we will call *free space* and that is

(1) uniform: ε and μ have the same value at all points;
(2) isotropic: ε and μ do not depend upon the direction of propagation;
(3) nonconducting: $\sigma = 0$, and thus $\mathbf{J} = 0$;
(4) free from charge: $\rho = 0$;
(5) nondispersive: ε and μ are not functions of frequency, i.e., they have no time dependence.

Our definition departs somewhat from other definitions of free space in that we include in the definition not only the vacuum, where $\varepsilon = \varepsilon_0$ and $\mu = \mu_0$, but also dielectrics, where $\sigma = 0$ but the other electromagnetic constants can have arbitrary values.

Using the above assumptions, Maxwell's equations and the constitutive relations simplify to

$$\nabla \cdot \mathbf{E} = 0, \tag{2.6a}$$

$$\nabla \cdot \mathbf{B} = 0, \tag{2.6b}$$

$$\nabla \times \mathbf{E} = -\frac{\partial \mathbf{B}}{\partial t}, \tag{2.6c}$$

$$\nabla \times \mathbf{H} = \frac{\partial \mathbf{D}}{\partial t}, \tag{2.6d}$$

$$\mathbf{B} = \mu \mathbf{H}, \tag{2.6e}$$

$$\varepsilon \mathbf{E} = \mathbf{D}. \tag{2.6f}$$

These simplified equations can now be used to derive some of the basic properties of a light wave.

2.4 Wave Equation

To find how the electromagnetic wave described by (2.6) propagates in free space, Maxwell's equations must be rearranged to display explicitly the time and coordinate dependence. Using (2.6e, f), we can rewrite (2.6d) as

$$\frac{1}{\mu} \nabla \times \mathbf{B} = \varepsilon \frac{\partial \mathbf{E}}{\partial t}.$$

The curl of (2.6c) is taken and the magnetic field dependence is eliminated by using the rewritten (2.6d):

$$\nabla \times (\nabla \times \mathbf{E}) = \nabla \times \left(-\frac{\partial \mathbf{B}}{\partial t} \right) = -\frac{\partial}{\partial t} (\nabla \times \mathbf{B}) = -\frac{\partial}{\partial t} \left(\varepsilon \mu \frac{\partial \mathbf{E}}{\partial t} \right).$$

The assumption that ε and μ are independent of time allows this equation to be rewritten as

$$\nabla \times (\nabla \times \mathbf{E}) = -\varepsilon \mu \frac{\partial^2 \mathbf{E}}{\partial t^2}.$$

Using the vector identity (2A.12) from Appendix 2A, we can write

$$\nabla (\nabla \cdot \mathbf{E}) - \nabla^2 \mathbf{E} = -\varepsilon \mu \frac{\partial^2 \mathbf{E}}{\partial t^2}.$$

Because free space is free of charge, $\nabla \cdot \mathbf{E} = 0$, giving us

$$\nabla^2 \mathbf{E} = \mu\varepsilon \frac{\partial^2 \mathbf{E}}{\partial t^2}. \tag{2.7}$$

We can use the same procedure to obtain

$$\nabla^2 \mathbf{B} = \mu\varepsilon \frac{\partial^2 \mathbf{B}}{\partial t^2}. \tag{2.8}$$

These equations are wave equations, with the wave's velocity being given by

$$v = \frac{1}{\sqrt{\mu\varepsilon}}. \tag{2.9}$$

The connection of the velocity of light with the electric and magnetic properties of a material was one of the most important results of Maxwell's theory. In a vacuum,

$$\mu_0\varepsilon_0 = \left(4\pi \times 10^{-7}\right)\left(8.8542 \times 10^{-12}\right) = 1.113 \times 10^{-17}\ \mathrm{s^2/m^2},$$

$$\frac{1}{\sqrt{\mu_0\varepsilon_0}} = 2.998 \times 10^8\ \mathrm{m/s} = c. \tag{2.10}$$

In a material, the velocity of light is less than c. We can characterize a material by defining the *index of refraction*, the ratio of the speed of light in a vacuum to its speed in a medium:

$$n = \frac{c}{v} = \sqrt{\frac{\varepsilon\mu}{\varepsilon_0\mu_0}}. \tag{2.11}$$

The data in Table 2.1 demonstrate that if magnetic materials are not considered, then $\mu/\mu_0 \approx 1$, so that

$$n = \sqrt{\frac{\varepsilon}{\varepsilon_0}}.$$

Table 2.1 *Representative magnetic permeabilities*

Material	μ/μ_0	Class
Silver	0.99998	Diamagnetic
Copper	0.99999	Diamagnetic
Water	0.99999	Diamagnetic
Air	1.00000036	Paramagnetic
Aluminum	1.000021	Paramagnetic
Iron	5000	Ferromagnetic
Nickel	600	Ferromagnetic

Table 2.2 *Selected indices of refraction*

Material	n (yellow light)	$\sqrt{\varepsilon/\varepsilon_0}$ (static)
Air	1.000294	1.000295
CO_2	1.000449	1.000473
C_6H_6 (benzene)	1.482	1.489
He	1.000036	1.000034
H_2	1.000131	1.000132

The data displayed in Table 2.2 demonstrate that, at least for some materials, the theory agrees with experimental results. The materials whose indices are listed in Table 2.2 have been specially selected to demonstrate good agreement; we will see in Chapter 7 that the assumption that ε, μ, and σ are independent of frequency results in a theory that neglects the response time of the system to the electromagnetic signal.

2.5 Transverse Waves

Hooke postulated, in the seventeenth century, that light waves might be transverse, but his idea was forgotten. In the nineteenth century, Young and Fresnel made the same postulate and provided a theoretical description of light based on transverse waves. Forty years later, Maxwell proved that light must be a transverse wave. We can demonstrate the transverse nature of light by substitution of the plane wave solution of the wave equation into Gauss's law:

$$\nabla \cdot \mathbf{E} = \frac{\partial E_x}{\partial x} + \frac{\partial E_y}{\partial y} + \frac{\partial E_z}{\partial z} = 0.$$

To complete the demonstration, we consider the divergence of the electric component of the plane wave. We will examine only the x-coordinate of the divergence in detail:

$$\frac{\partial E_x}{\partial x} = \frac{\partial}{\partial x}\left(E_{0x}e^{i(\omega t - \mathbf{k}\cdot\mathbf{r}+\phi)}\right) = iE_{0x}e^{i(\omega t-\mathbf{k}\cdot\mathbf{r}+\phi)}\frac{\partial}{\partial x}(\omega t - k_x x - k_y y - k_z z + \phi)$$
$$= -ik_x E_x.$$

We easily obtain similar results for E_y and E_z, allowing the divergence of $\mathbf{E}$ to be rewritten as a dot product of $\mathbf{k}$ and $\mathbf{E}$. Gauss's law for the electric field states that the divergence of $\mathbf{E}$ is zero, which for a plane wave can be written

$$\nabla \cdot \mathbf{E} = -i\mathbf{k} \cdot \mathbf{E} = 0. \tag{2.12}$$

If the dot product of two vectors $\mathbf{E}$ and $\mathbf{k}$, is zero, then the vectors $\mathbf{E}$ and $\mathbf{k}$ must be perpendicular [see (2A.1) in Appendix 2A]. In the same manner, substituting the plane wave into $\nabla \cdot \mathbf{B} = 0$ yields $\mathbf{k} \cdot \mathbf{B} = 0$. Therefore, Maxwell's equations require light to be a transverse wave; i.e., the vector displacements $\mathbf{E}$ and $\mathbf{B}$ are perpendicular to the direction of propagation, $\mathbf{k}$.

2.6 Interdependence of E and B

The electric and magnetic fields are not independent, as we can see by continuing our examination of the plane wave solutions of Maxwell's equations. First, let us calculate several derivatives of the plane wave. We will need

$$\frac{\partial \mathbf{B}}{\partial t} = \frac{\partial}{\partial t}\mathbf{B}_0 e^{i(\omega t - \mathbf{k}\cdot\mathbf{r}+\phi)} = i\mathbf{B}\frac{\partial}{\partial t}(\omega t - \mathbf{k}\cdot\mathbf{r} + \phi)$$
$$= i\omega\mathbf{B} \tag{2.13}$$

and, similarly,

$$\frac{\partial \mathbf{E}}{\partial t} = i\omega\mathbf{E}. \tag{2.14}$$

A simple expression for the curl of $\mathbf{E}$, $\nabla \times \mathbf{E}$, can be obtained when we use the derivatives just calculated. The expression for the curl of $\mathbf{E}$ is given by (2A.7) from Appendix 2A and is rewritten here:

$$\nabla \times \mathbf{E} = \left(\frac{\partial E_z}{\partial y} - \frac{\partial E_y}{\partial z}\right)\hat{\mathbf{i}} + \left(\frac{\partial E_x}{\partial z} - \frac{\partial E_z}{\partial x}\right)\hat{\mathbf{j}} + \left(\frac{\partial E_y}{\partial x} - \frac{\partial E_x}{\partial y}\right)\hat{\mathbf{k}}.$$

The terms making up the *x*-component of the curl are

$$\frac{\partial E_z}{\partial y} = E_{0z}\frac{\partial}{\partial y}e^{i(\omega t - \mathbf{k}\cdot\mathbf{r}+\phi)} = -ik_y E_z$$

and

$$\frac{\partial E_y}{\partial z} = -ik_z E_y.$$

By evaluating each component, we find that the curl of $\mathbf{E}$ for a plane wave is

$$\nabla \times \mathbf{E} = -i\mathbf{k} \times \mathbf{E}. \tag{2.15}$$

A similar derivation leads to the curl of $\mathbf{B}$ for a plane wave:

$$\nabla \times \mathbf{B} = -i\mathbf{k} \times \mathbf{B}. \tag{2.16}$$

With these vector operations on a plane wave defined, we can evaluate (2.6c) for a plane wave. The left-hand side of

$$\nabla \times \mathbf{E} = -\frac{\partial \mathbf{B}}{\partial t}$$

is replaced with (2.15) and the right-hand side by (2.13), resulting in an equation connecting the electric and magnetic fields:

$$-i\mathbf{k} \times \mathbf{E} = -i\omega\mathbf{B}.$$

Using the relationship between ω and $\mathbf{k}$ given by (1.2) from Chapter 1 and the relationship for the wave velocity in terms of the electromagnetic properties of the material, (2.9), we can write

$$\frac{\sqrt{\mu\varepsilon}}{k}\mathbf{k} \times \mathbf{E} = \mathbf{B}. \tag{2.17}$$

A second relationship between the magnetic and electric fields can be generated by using the same procedure to rewrite

$$\nabla \times \mathbf{B} = \mu\varepsilon\frac{\partial \mathbf{E}}{\partial t}$$

for a plane wave as

$$-i\mathbf{k} \times \mathbf{B} = i\varepsilon\mu\omega\mathbf{E};$$

that is,

$$\frac{1}{k\sqrt{\mu\varepsilon}}\mathbf{k} \times \mathbf{B} = -\mathbf{E}. \tag{2.18}$$

From the definition of the cross product given by (2A.2) in Appendix 2A, we see that the electric and magnetic fields are perpendicular to each other, are in phase, and form a right-handed coordinate system with propagation direction $\mathbf{k}$ (see Figure 2.1).

If we are only interested in the magnitude of the two fields, we can use (2.11) to write

$$n|\mathbf{E}| = c|\mathbf{B}|. \tag{2.19}$$

In a vacuum, we take $n = 1$ in (2.19). For our plane wave, the ratio of the field magnitudes is

$$\frac{|\mathbf{E}|}{|\mathbf{H}|} = \sqrt{\frac{\mu}{\varepsilon}}. \tag{2.20}$$

This ratio has units of ohms ($\mu \Rightarrow \text{ml/Q}^2$, $\varepsilon \Rightarrow \text{Q}^2\text{t}^2/\text{ml}^3$, and $\Omega \Rightarrow \text{ml}^2/\text{Q}^2\text{t}$) and is called the impedance of the medium. In a vacuum,

$$Z_0 = \sqrt{\frac{\mu_0}{\varepsilon_0}} = 377\ \Omega.$$

When the ratio is a real quantity, as it is here, **E** and **H** are in phase.

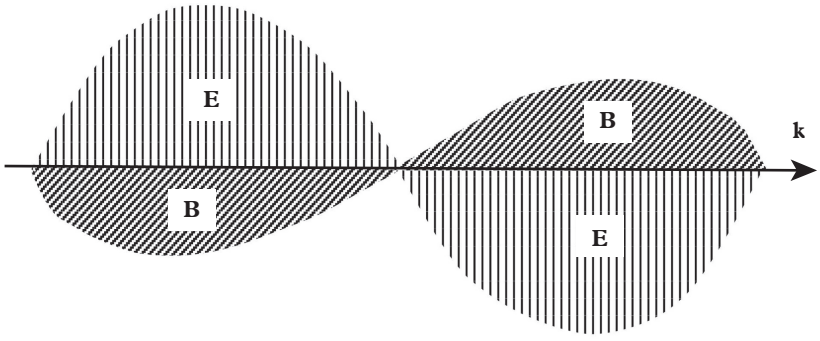

Figure 2.1 *Graphical representation of an electromagnetic plane wave. Note that* **E** *and* **B** *are perpendicular to each other and individually perpendicular to the propagation vector* **k**, *are in phase, and form a right-handed coordinate system as required by (2.17) and (2.18).*

2.7 Energy Density and Flow

We saw in our discussion of waves propagating along strings that the power transmitted by a wave is proportional to the square of the amplitude of the wave. Any text on electromagnetic theory (see, e.g., Chapter 21 of [3]) demonstrates that the energy density (in J/m^3) associated with an electromagnetic wave is given by

$$U = \frac{\mathbf{D}\cdot\mathbf{E} + \mathbf{B}\cdot\mathbf{H}}{2}. \tag{2.21}$$

We can simplify (2.21) by using the simple constitutive relations $\mathbf{D} = \varepsilon\mathbf{E}$ and $\mathbf{B} = \mu\mathbf{H}$, if they apply to the propagation medium:

$$U = \frac{1}{2}\left(\varepsilon E^2 + \frac{B^2}{\mu}\right) = \frac{1}{2}\left(\varepsilon + \frac{1}{\mu c^2}\right)E^2.$$

In a vacuum, further simplification is possible:

$$U = \varepsilon_0 E^2 = \frac{B^2}{\mu_0}.$$

John Henry Poynting (1852–1914), an English professor of physics at Mason Science College, now the University of Birmingham, demonstrated that the presence of both an electric and a magnetic field at the same point in space results in a flow of the field energy. This fact is called the Poynting theorem, and the flow is completely described by the *Poynting vector*

$$\mathbf{S} = \mathbf{E}\times\mathbf{H}. \tag{2.22}$$

The Poynting vector has units of J/(m^2·s). We will use a plane wave to determine some of the properties of this vector. Since $\mathbf{S}$ will involve terms quadratic in $\mathbf{E}$, it will be necessary to use the real form of $\mathbf{E}$ (see Problem 1.4). We have

$$\mathbf{H} = \frac{\mathbf{B}}{\mu} = \frac{\sqrt{\mu\varepsilon}}{\mu k}\mathbf{k}\times\mathbf{E},$$

where

$$\mathbf{E} = \mathbf{E}_0\cos(\omega t - \mathbf{k}\cdot\mathbf{r} + \phi).$$

Then,

$$\begin{aligned}\mathbf{S} &= \frac{\sqrt{\mu\varepsilon}}{\mu k}\mathbf{E}_0\times(\mathbf{k}\times\mathbf{E}_0)\cos^2(\omega t - \mathbf{k}\cdot\mathbf{r} + \phi)\\ &= \frac{n}{\mu c}|\mathbf{E}_0|^2\frac{\mathbf{k}}{k}\cos^2(\omega t - \mathbf{k}\cdot\mathbf{r} + \phi).\end{aligned} \tag{2.23}$$

Note that the energy is flowing in the direction of propagation (indicated by the unit vector $\mathbf{k}/k$).

We normally do not detect $\mathbf{S}$ at the very high frequencies associated with light ($\approx 10^{15}$ Hz) but rather detect a temporal average of $\mathbf{S}$ taken over a time T determined by the response time of the detector used. We must obtain the time average of $\mathbf{S}$ to relate theory to actual measurements. The time average of $\mathbf{S}$ is called the *flux density* and has units of W/m^2. We will call this quantity the ***intensity*** of the light wave,

$$I = |\langle \mathbf{S} \rangle| = \left| \frac{1}{T} \int_{t_0}^{t_0+T} \mathbf{A} \cos^2(\omega t - \mathbf{k} \cdot \mathbf{r} + \phi)\, dt \right|, \tag{2.24}$$

where we have defined

$$\mathbf{A} = \frac{n}{\mu c} |\mathbf{E}_0|^2 \frac{\mathbf{k}}{k}$$

to simplify the notation.

The units used for the flux density are a confusing mess in optics. One area of optics is interested in measuring the physical effects of light, and the measurement of energy is called *radiometry*. In radiometry, the flux density is called the *irradiance*, with units of W/m^2. Another area of optics is interested in the psychophysical effects of light, and the measurement of energy is called *photometry*. For this group, the flux density is called *illuminance*, with units of a lumen/m^2 (lm/m^2) or a lux. Each of these two group has its own set of units, but both desire to measure the energy flow of a field that is not well defined in frequency or phase. Much research in modern optics belong to a third area that is associated with the use of a light source that has both a well-defined frequency and a well-defined phase—the laser. In this area of optics, common usage defines the time-averaged flux density as the intensity. In this book, all of the waves discussed are uniquely defined in terms of the electric field and the electromagnetic properties of the material in which the wave is propagating. To emphasize that the results of our theory are immediately applicable only to a light source with a well-defined frequency and phase, we will use the term *intensity* for the magnitude of the Poynting vector.

We will assume that $\mathbf{k}$ is independent of time over the period T:

$$\langle \mathbf{S} \rangle = \frac{\mathbf{A}}{\omega T} \int_{t_0\omega}^{(t_0+T)\omega} \cos^2(\omega t - \mathbf{k} \cdot \mathbf{r} + \phi)\, d(\omega t).$$

Using the trigonometric identity

$$\cos^2\theta = \frac{1}{2}(1 + \cos 2\theta)$$

and evaluating the integral results in the expression

$$\langle \mathbf{S} \rangle = \frac{\mathbf{A}}{2} + \frac{\mathbf{A}}{4\omega T} [\sin 2(\omega t_0 + \omega T - \mathbf{k} \cdot \mathbf{r} + \phi) - \sin 2(\omega t_0 - \mathbf{k} \cdot \mathbf{r} + \phi)]. \tag{2.25}$$

The largest value that the term in square brackets can assume is 2. The period T is the response time of the detector to the light wave. Normally, it is much longer than the period of light oscillations, so $\omega T \gg 1$ and we can neglect the second term in (2.25). As an example,

suppose our detection system has a 1 GHz bandwidth, yielding a response time of $T = 10^{-9}$ s (the reciprocal of the bandwidth). Green light has a frequency of $\nu = 6 \times 10^{14}$ Hz or $\omega \approx 4 \times 10^{15}$ rad/s. With these values, $\omega T = 4 \times 10^{5}$, and the neglected term would be no larger than 10^{-6} of the first term. Therefore, in optics, the assumption that $\omega T \gg 1$ is reasonable and allows the average Poynting vector to be written as

$$\langle \mathbf{S} \rangle = \frac{\mathbf{A}}{2} = \frac{n}{2\mu c} |\mathbf{E}_0|^2 \frac{\mathbf{k}}{k}. \tag{2.26}$$

The energy per unit time per unit area depends on the square of the amplitude of the wave.

The energy calculation was done with plane waves of **E** and **H** that are in phase. We will later see that materials with nonzero conductivity $\sigma \neq 0$ will yield a complex impedance because **E** and **H** are no longer in phase. If the two waves are 90° out of phase, then the integral in (2.24) will contain $\sin x \cos x$ as its integrand, resulting in $\langle \mathbf{S} \rangle = 0$. Therefore, no energy is transmitted.

In quantum mechanics, the energy of light is carried by discrete particles called photons. If the light has a frequency ν, then the energy of a photon is $h\nu$. The intensity of the light is equal to the number of photons, striking unit area in unit time, N, multiplied by the energy of an individual photon:

$$I = Nh\nu.$$

The intensity of a 10 mW HeNe laser beam, 2 mm in diameter, is

$$I = \frac{\text{power}}{\text{area}} = \frac{10^{-2}}{\pi \left(10^{-3}\right)^2} = 3.18 \times 10^3 \,\text{W m}^{-2}.$$

The number of photons in this beam can be calculated once we know that the wavelength of the light is 632.8 nm:

$$N = \frac{I}{h\nu} \cdot \text{area} = \frac{10^{-2}\lambda}{hc} = \frac{10^{-2}\left(632.8 \times 10^{-9}\right)}{\left(6.6 \times 10^{-34}\right)\left(3 \times 10^{8}\right)} = 32 \times 10^{15}.$$

We can get a perspective on how large this number is by comparing it with the number of molecules in a mole of a molecule, i.e., Avogadro's constant

$$N_A = 6.02214129 \times 10^{23}.$$

For carbon-12, a mole is 12 g.

The energy crossing a unit area A in a time Δt is contained in a volume $A(v\Delta t)$ (in a vacuum $v = c$), as shown in Figure 2.2. To find the magnitude of this energy, we must multiply this volume by the average energy density $|\langle \mathbf{S} \rangle|$. Thus, we expect the energy flow to be given by

$$|\langle \mathbf{S} \rangle| = \frac{\text{energy}}{A\Delta t} \propto \frac{Av\Delta t \langle U \rangle}{A\Delta t} = v \langle U \rangle.$$

We may use the definitions of the wave velocity

$$v = \frac{1}{\sqrt{\mu\varepsilon}}$$

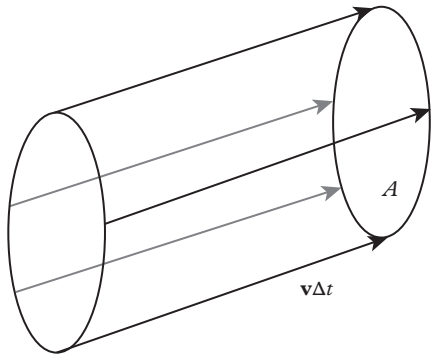

Figure 2.2 *The energy of a wave crossing a unit area A in a time* Δt.

and index of refraction $n = c/v$ to rewrite (2.26) as

$$|\langle \mathbf{S} \rangle| = \frac{\varepsilon v E_0^2}{2} = v \langle U \rangle, \tag{2.27}$$

giving the expected result that the energy is flowing through space at the speed of light in the medium. The relationship defined by (2.27), (energy flow) = (wave velocity) · (energy density), is a general property of waves.

At the Earth's surface, the flux density of full sunlight is 1.34×10^3 J/(m^2·s). It is not completely correct to do so, but if we associate this flux with the time average of the Poynting vector, then the electric field associated with the sunlight is $E_0 = 10^3$ V/m.

Our discussion of the time average of the Poynting vector provides an opportunity to discover one of the advantages of the use of complex notation. To obtain the time average of the product of two waves A and B, where

$$A = \mathcal{R}e\{\tilde{A}\} = \mathcal{R}e\{A_0 e^{i(\omega t + \phi_1)}\},$$
$$B = \mathcal{R}e\{\tilde{B}\} = \mathcal{R}e\{B_0 e^{i(\omega t + \phi_2)}\},$$

we use

$$\mathcal{R}e\{\tilde{z}\} = x = r\cos\phi = \frac{\tilde{z} + \tilde{z}^*}{2},$$
$$Im\{\tilde{z}\} = y = r\sin\phi = \frac{\tilde{z} - \tilde{z}^*}{2i}$$

to write the average over one period as

$$\langle AB \rangle = \frac{1}{T}\int_0^T \left(\frac{\tilde{A} + \tilde{A}^*}{2}\right)\left(\frac{\tilde{B} + \tilde{B}^*}{2}\right) dt,$$

$$\left(\tilde{A} + \tilde{A}^*\right)\left(\tilde{B} + \tilde{B}^*\right) = \tilde{A}\tilde{B} + \tilde{A}^*\tilde{B}^* + \tilde{A}\tilde{B}^* + \tilde{A}^*\tilde{B},$$

where

$$\tilde{A}\tilde{B} = A_0 B_0 e^{i(2\omega t+\phi_1+\phi_2)},$$

$$\tilde{A}^*\tilde{B}^* = A_0 B_0 e^{-i(2\omega t+\phi_1+\phi_2)}.$$

The time averages of the latter two terms are zero, and we are left with

$$\langle AB\rangle = \frac{1}{T}\int_0^T \frac{\tilde{A}\tilde{B}^* + \tilde{A}^*\tilde{B}}{4}\, dt.$$

Again using $\mathcal{R}e\{\tilde{z}\} = (\tilde{z} + \tilde{z}^*)/2$, we may rewrite this as

$$\langle AB\rangle = \frac{1}{2}\mathcal{R}e\left\{\tilde{A}\tilde{B}^*\right\}. \tag{2.28}$$

The reader may find this quite general relation easier to use than performing an integration such as (1.24).

2.8 Polarization

The displacement of a transverse wave is a vector quantity. We must therefore specify the frequency, phase, and direction of the wave along with the magnitude and direction of the displacement. The direction of the displacement vector is called the *direction of polarization*, and the plane containing the direction of polarization and the propagation vector is called the *plane of polarization*. This quantity has the same name as the field quantity introduced in (2.5). Because the two terms describe completely different physical phenomena, there should be no danger of confusion.

From our study of Maxwell's equations, we know that **E** and **H**, for a plane wave in free space, are mutually perpendicular and lie in a plane normal to the direction of propagation, **k**. We also know that, given one of the two vectors, we can use (2.17) to obtain the other. Convention requires that we use the electric vector to label the direction of the electromagnetic wave's polarization. The selection of the electric field is not completely arbitrary.

The electric field of the electromagnetic wave acts on a charged particle in the material with a force

$$\mathbf{F}_E = q\mathbf{E}. \tag{2.29}$$

This force accelerates the charged particle to a velocity v in a direction transverse to the direction of light propagation and parallel to the electric field. The moving charge interacts with the magnetic field of the electromagnetic wave with a force

$$\mathbf{F}_H = q(\mathbf{v}\times\mathbf{B}), \tag{2.30}$$

parallel to the propagation vector. We can write the ratio of the forces on a moving charge in an electromagnetic field due to the electric and magnetic fields as

$$\frac{F_E}{F_H} = \frac{eE}{evB}.$$

We can replace B using (2.19) to obtain

$$\frac{F_E}{F_H} = \frac{c}{nv}, \tag{2.31}$$

where v is the velocity of the moving charge. Assuming that a charged particle is traveling in air at the speed of sound, so that $v = 335$ m/s, the force due to the electric field of a light wave on that particle will therefore be 8.9×10^5 times larger than the force due to the magnetic field. The size of this numbers demonstrates that, except in relativistic situations, when $v \approx c$, the interaction of an electromagnetic wave with matter will be dominated by the electric field.

A conventional vector notation is used to describe the polarization of a light wave; however, to visualize the behavior of the electric field vector as light propagates, a geometrical construction is useful. The geometrical construction, called a Lissajous figure, describes the path followed by the tip of the electric field vector.

2.8.1 Polarization Ellipse

Assume that a plane wave is propagating in the z-direction and that the electric field, determining the direction of polarization, is oriented in the (x, y) plane. In complex notation, the plane wave is given by

$$\tilde{\mathbf{E}} = \mathbf{E}_0 e^{i(\omega t - \mathbf{k}\cdot\mathbf{r} + \phi)} = \mathbf{E}_0 e^{i(\omega t - kz + \phi)}.$$

This wave can be written in terms of the x- and y-components of $\mathbf{E}_0$:

$$\tilde{\mathbf{E}} = E_{0x} e^{i(\omega t - kz + \phi_1)} \hat{\mathbf{i}} + E_{0y} e^{i(\omega t - kz + \phi_2)} \hat{\mathbf{j}}. \tag{2.32}$$

(To prevent errors, we will use only the real part of $\mathbf{E}$ for manipulation.) We divide each component of the electric field by its maximum value so that the problem is reduced to one of the following two sinusoidally varying unit vectors:

$$\frac{E_x}{E_{0x}} = \cos(\omega t - kz + \phi_1) = \cos(\omega t - kz)\cos\phi_1 - \sin(\omega t - kz)\sin\phi_1,$$

$$\frac{E_y}{E_{0y}} = \cos(\omega t - kz)\cos\phi_2 - \sin(\omega t - kz)\sin\phi_2.$$

When these unit vectors are added together, the result will be a set of figures called *Lissajous figures* (**Jules Antoine Lissajous: 1822–1880**). The geometrical construction shown in Figure 2.3 can be used to visualize the generation of the Lissajous figure. The harmonic motion along the x-axis is found by projecting a vector rotating around a circle of diameter E_{0x} onto the x-axis. The harmonic motion, along the y-axis is generated the same way using a circle of diameter E_{0y}. The resulting x- and y-components are added to obtain $\mathbf{E}$. In Figure 2.3, the two harmonic oscillators both have the same frequency, $\omega t - kz$, but differ in phase by

$$\delta = \phi_2 - \phi_1 = -\frac{\pi}{2}.$$

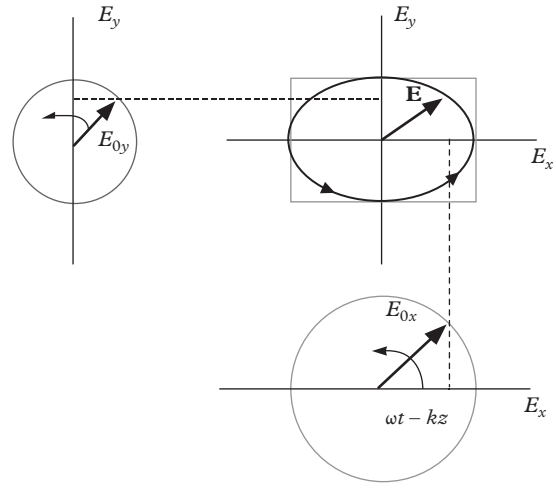

Figure 2.3 *Geometrical construction showing how the Lissajous figure is constructed from harmonic motion along the x- and y-coordinate axes. The harmonic motion along each coordinate axis is created by projecting a vector rotating around a circle onto the axis.*

The tip of the electric field **E** in Figure 2.3 traces out an ellipse, with its axes aligned with the coordinate axes. To determine the direction of the rotation of the vector, assume that $\phi_1 = 0$, $\phi_2 = -\pi/2$, and $z = 0$, so that

$$\frac{E_x}{E_{0x}} = \cos\omega t, \quad \frac{E_y}{E_{0y}} = \sin\omega t$$

$$\mathbf{E} = \left(\frac{E_x}{E_{0x}}\right)\hat{\mathbf{i}} + \left(\frac{E_y}{E_{0y}}\right)\hat{\mathbf{j}}.$$

Table 2.3 *Rotating electric field vector* **E**

ωt	**E**
0	$\hat{\mathbf{i}}$
$\frac{\pi}{4}$	$\frac{1}{\sqrt{2}}\left(\hat{\mathbf{i}}+\hat{\mathbf{j}}\right)$
$\frac{\pi}{2}$	$\hat{\mathbf{j}}$
$\frac{3\pi}{4}$	$\frac{1}{\sqrt{2}}\left(-\hat{\mathbf{i}}+\hat{\mathbf{j}}\right)$
π	$-\hat{\mathbf{i}}$

The normalized vector **E** can easily be evaluated at a number of values of ωt to discover the direction of rotation. Table 2.3 shows the value of the vector as ωt increases.

The rotation of the vector **E** in Figure 2.3 is seen to be in a counterclockwise direction, moving from the positive x-direction, to the y-direction, and finally to the negative x-direction.

To obtain the equation for the Lissajous figure, we eliminate the dependence of the unit vectors on $\omega t - kz$. First, we multiply the two equations by $\sin\phi_2$ and $\sin\phi_1$, respectively, and then subtract the resulting equations. Second, we multiply the two equations by $\cos\phi_2$ and $\cos\phi_1$, respectively, and then subtract the resulting equations. These two operations yield the following pair of equations;

$$\frac{E_x}{E_{0x}}\sin\phi_2 - \frac{E_y}{E_{0y}}\sin\phi_1 = \cos(\omega t - kz)\,[\cos\phi_1\sin\phi_2 - \sin\phi_1\cos\phi_2],$$

$$\frac{E_x}{E_{0x}}\cos\phi_2 - \frac{E_y}{E_{0y}}\cos\phi_1 = \sin(\omega t - kz)\,[\cos\phi_1\sin\phi_2 - \sin\phi_1\cos\phi_2].$$

The term in square brackets can be simplified using the trigonometric identity

$$\sin\delta = \sin(\phi_2 - \phi_1) = \cos\phi_1\sin\phi_2 - \sin\phi_1\cos\phi_2.$$

After replacing the term in square brackets by $\sin\delta$, the two equations are squared and added, yielding the equation for the Lissajous figure:

$$\left(\frac{E_x}{E_{0x}}\right)^2 + \left(\frac{E_y}{E_{0y}}\right)^2 - \left(\frac{2E_xE_y}{E_{0x}E_{0y}}\right)\cos\delta = \sin^2\delta. \tag{2.33}$$

The trigonometric identity

$$\cos\delta = \cos(\phi_2 - \phi_1) = \cos\phi_1\cos\phi_2 + \sin\phi_1\sin\phi_2$$

was also used here to further simplify (2.33).

Equation (2.33) has the same form as the equation of a conic,

$$Ax^2 + Bxy + Cy^2 + Dx + Ey + F = 0.$$

The conic here can be seen to be an ellipse because, from (2.33),

$$B^2 - 4AC = \frac{4}{E_{0x}^2E_{0y}^2}(\cos^2\delta - 1) < 0.$$

This ellipse is called the *polarization ellipse*. Its orientation with respect to the x-axis is given by

$$\tan 2\theta = \frac{B}{A-C} = \frac{2E_{0x}E_{0y}\cos\delta}{E_{0x}^2 - E_{0y}^2}. \tag{2.34}$$

If $A = C$ and $B \neq 0$ then $\theta = 45°$. When $\delta = \pm\pi/2$, then $\theta = 0°$, as shown in Figure 2.3.

The tip of the resultant electric field vector obtained from (2.34) traces out the polarization ellipse in the plane normal to **k**, as predicted by (2.33). A generalized polarization ellipse is shown in Figure 2.4. The x- and y-coordinates of the electric field are bounded by $\pm E_{0x}$ and $\pm E_{0y}$. The rectangle in Figure 2.4 illustrates these limits. The component of the electric field along the major axis of the ellipse is

$$E_M = E_x\cos\theta + E_y\sin\theta$$

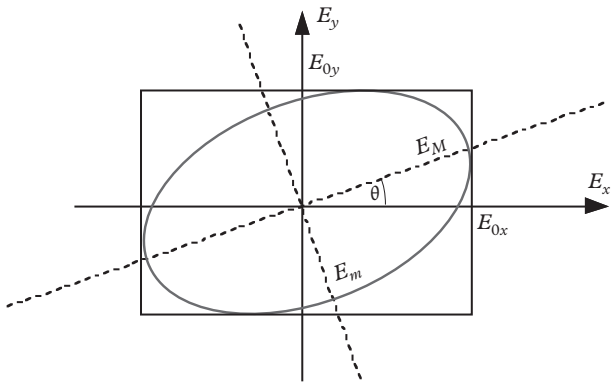

Figure 2.4 *General form of the ellipse described by (2.33).*

and that along the minor axis is

$$E_m = -E_x \sin\theta + E_y \cos\theta,$$

where θ is obtained from (2.34). The ratio of the length of the minor axis to that of the major axis is related to the ellipticity φ, which measures the amount of deviation of the ellipse from a circle:

$$\tan\varphi = \pm\left(\frac{E_m}{E_M}\right) = \frac{E_{0x}\sin\phi_1\sin\theta - E_{0y}\sin\phi_2\cos\theta}{E_{0x}\cos\phi_1\cos\theta + E_{0y}\cos\phi_2\sin\theta}. \tag{2.35}$$

To find the time dependence of the vector **E**, we rewrite (2.32) in complex form:

$$\tilde{\mathbf{E}} = e^{i(\omega t - kz)}\left(\hat{\mathbf{i}}E_{0x}e^{i\phi_1} + \hat{\mathbf{j}}E_{0y}e^{i\phi_2}\right). \tag{2.36}$$

This equation shows explicitly that the electric vector moves about the ellipse in a sinusoidal motion.

By specifying the parameters that characterize the polarization ellipse (θ and φ), we completely characterize the polarization of a wave. A review of two special cases will aid in understanding the polarization ellipse.

2.8.1.1 Linear Polarization

First consider the cases when $\delta = 0$ or π. Then (2.33) becomes

$$\left(\frac{E_x}{E_{0x}}\right)^2 + \left(\frac{E_y}{E_{0y}}\right)^2 \mp \frac{2E_xE_y}{E_{0x}E_{0y}} = 0.$$

The ellipse collapses into a straight line with slope E_{0y}/E_{0x}. The equation of the straight line is

$$\frac{E_x}{E_{0x}} = \mp\frac{E_y}{E_{0y}}.$$

Figure 2.5 displays the straight-line Lissajous figures for the two phase differences. The θ-parameter of the ellipse is the slope of the straight line,

$$\tan\theta = \frac{E_{0y}}{E_{0x}},$$

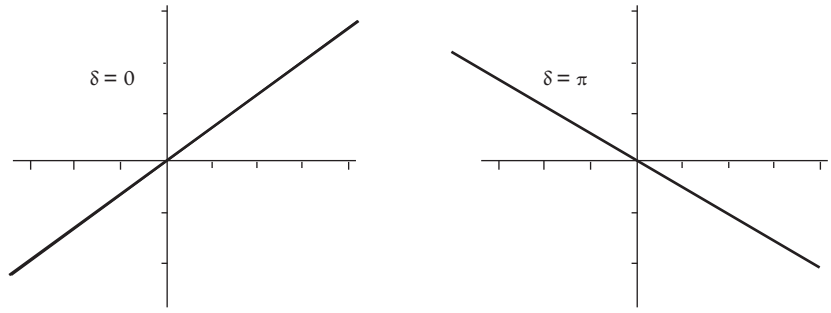

Figure 2.5 *Lissajous figures for phase differences between the y- and x-components of oscillation of 0 and* π.

resulting in the value of (2.34) being given by

$$\tan 2\theta = \frac{2\tan\theta}{1-\tan^2\theta} = \frac{2E_{0x}E_{0y}}{E_{0x}^2 - E_{0y}^2}.$$

The φ-parameter is given by (2.35) as $\tan\varphi = 0$.

The time dependence of the **E** vector shown in Figure 2.5 is given by (2.36). The real component is

$$\mathbf{E} = \left(E_{0x}\hat{\mathbf{i}} \pm E_{0y}\hat{\mathbf{j}}\right)\cos(\omega t - kz).$$

At a fixed point in space, the x- and y-components oscillate in phase (or 180° out of phase) according to the equation

$$\mathbf{E} = \left(E_{0x}\hat{\mathbf{i}} \pm E_{0y}\hat{\mathbf{j}}\right)\cos(\omega t - \phi).$$

The electric vector undergoes simple harmonic motion along the line defined by E_{0x} and E_{0y}. At a fixed time, the electric field varies sinusoidally along the propagation path (the z-axis) according to the equation

$$\mathbf{E} = \left(E_{0x}\hat{\mathbf{i}} \pm E_{0y}\hat{\mathbf{j}}\right)\cos(\phi - kz).$$

This light is said to be *linearly polarized.*

2.8.1.2 Circular Polarization

The second case occurs when $E_{0x} = E_{0y} = E_0$ and $\delta = \pm\pi/2$. From (2.33),

$$\left(\frac{E_x}{E_0}\right)^2 + \left(\frac{E_y}{E_0}\right)^2 = 1.$$

The ellipse becomes a circle as shown in Figure 2.6. For this polarization, $\tan 2\theta$ is indeterminate and $\tan\varphi = 1$.

From (2.38), the temporal behavior is given by

$$\mathbf{E} = E_0[\cos(\omega t - kz)\,\hat{\mathbf{i}} \pm \sin(\omega t - kz)\,\hat{\mathbf{j}}].$$

The time dependence of the angle ψ that the **E** field makes with the x-axis in Figure 2.6 can be obtained by finding the tangent of ψ:

$$\tan\psi = \frac{E_y}{E_x} = \pm\frac{\sin(\omega t - kz)}{\cos(\omega t - kz)} = \pm\tan(\omega t - kz).$$

The interpretation of this result is that at a fixed point in space, the **E** vector rotates in a clockwise direction if $\delta = \pi/2$ and a counterclockwise direction if $\delta = -\pi/2$.

In particle physics, the light would be said to have a negative helicity if it rotated in a clockwise direction. If we look at the source, the electric vector seems to follow the threads of a left-handed screw, agreeing with the nomenclature that left-handed quantities are negative.

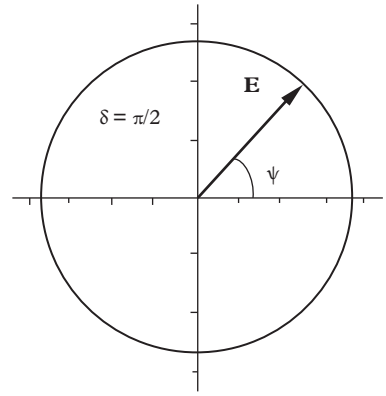

Figure 2.6 *Lissajous figure for the case when the phase differences between the y- and x-components of oscillation differ by* $\pm\pi/2$ *and the amplitudes of the two components are equal. The tip of the electric field vector moves along the circular path shown in the figure.*

However, in optics, the light that rotates clockwise as we view it traveling toward us from the source is said to be *right-circularly polarized*. The counterclockwise-rotating light is *left-circularly polarized*.

The association of right-circularly polarized light with "right-handedness" in optics came about by looking at the path of the electric vector in space at a fixed time: then $\tan\psi = \tan(\phi - kz)$; see Figure 2.7. As shown in Figure 2.7, right-circularly polarized light at a fixed time seems to spiral in a counterclockwise fashion along the z-direction, following the threads of a right-handed screw.

This motion can be generalized to include elliptically polarized light when $E_{0x} \neq E_{0y}$. Figure 2.3 schematically displays the generation of the Lissajous figure for the case $\delta = \pi/2$ but with unequal values of E_{0x} and E_{0y}. Figure 2.8 shows two calculated Lissajous figures. If the electric vector moves around the ellipse in a clockwise direction, as we face the source, then the phase difference and ellipticity are

$$0 \leq \delta \leq \pi \qquad \text{and} \qquad 0 < \varphi < \frac{\pi}{4},$$

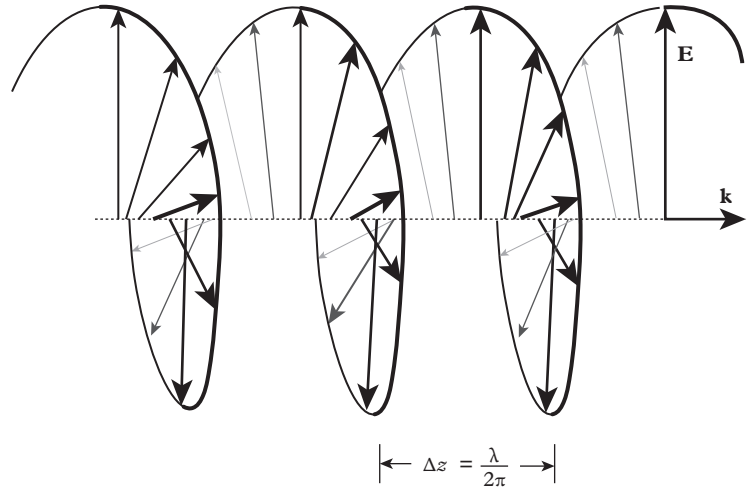

Figure 2.7 *The path of the electric vector of right-circularly polarized light at a fixed time.*

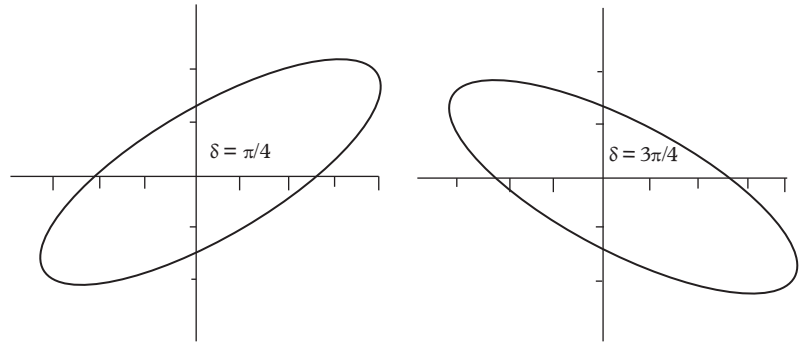

Figure 2.8 *Lissajous figures for elliptically polarized light. These were calculated with $E_{0x} = 0.75$ and $E_{0y} = 0.25$.*

and the polarization is right-handed. If the motion of the electric vector is moving in a counterclockwise direction, then the phase difference and ellipticity are

$$-\pi \leq \delta \leq 0 \qquad \text{and} \qquad -\frac{\pi}{4} < \varphi < 0.$$

The orientation of either ellipse, with respect to the x-axis, is given by (2.34) and depends upon the relative magnitudes of E_{0x} and E_{0y}.

The procedure used to decompose an arbitrary polarization into polarizations parallel to two axes of a Cartesian coordinate system is a technique used extensively in vector algebra to simplify mathematical calculations. According to the mathematical formalism associated with this technique, the polarization is described in terms of a set of basis vectors $\mathbf{e}_i$. An arbitrary polarization would be expressed as

$$\mathbf{E} = \sum_{i=1}^{2} a_i \mathbf{e}_i. \tag{2.37}$$

The set of basis vectors $\mathbf{e}_i$ are orthonormal, i.e.,

$$\mathbf{e}_i \mathbf{e}_j^* = \delta_{ij} = \begin{cases} 1 & (i = j), \\ 0 & (i \neq j), \end{cases}$$

where we have assumed that the basis vectors could be complex. We mention this mathematical formalism because an identical formalism is encountered in elementary particle physics, where it is used to describe spin [4].

In a Cartesian coordinate system, the $\mathbf{e}_i$'s are the unit vectors $\hat{\mathbf{i}}$, $\hat{\mathbf{j}}$, $\hat{\mathbf{k}}$. The summation in (2.36) extends over only two terms because the electromagnetic wave is transverse, confining $\mathbf{E}$ to a plane normal to the direction of propagation [according to the coordinate convention we have selected, the $\mathbf{E}$ field is in the (x, y) plane].

The polarization can also be described in terms of basis vectors consisting of a right-circularly polarized component

$$\mathbf{E}_{\mathcal{R}} = E_{0\mathcal{R}}[\cos(\omega t - kz)\,\hat{\mathbf{i}} - \sin(\omega t - kz)\,\hat{\mathbf{j}}]$$

and a left-circularly polarized component

$$\mathbf{E}_{\mathcal{L}} = E_{0\mathcal{L}}[\cos(\omega t - kz)\,\hat{\mathbf{i}} + \sin(\omega t - kz)\,\hat{\mathbf{j}}].$$

An arbitrary elliptical polarization can then be written as

$$\begin{aligned} \mathbf{E} &= \mathbf{E}_{\mathcal{R}} + \mathbf{E}_{\mathcal{L}} \\ &= (E_{0\mathcal{R}} + E_{0\mathcal{L}})\cos(\omega t - kz)\,\hat{\mathbf{i}} - (E_{0\mathcal{R}} - E_{0\mathcal{L}})\sin(\omega t - kz)\,\hat{\mathbf{j}}. \end{aligned} \tag{2.38}$$

The geometrical construction that demonstrates the expression of an arbitrary elliptically polarized light wave in terms of right- and left-circularly polarized waves is shown in Figure 2.9. The use of circularly polarized waves as the basis set for describing polarization is discussed by Klein and Furtak [5].

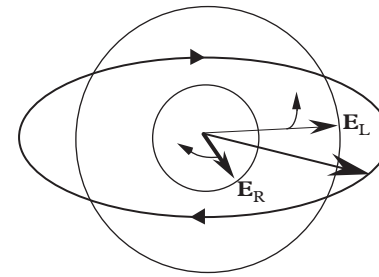

Figure 2.9 *Construction of elliptically polarized light from two circularly polarized waves.*

In the formalism associated with (2.37), the expansion coefficients a_i can be used to form a 2×2 matrix that in statistical mechanics is called the density matrix and in optics the coherency matrix [6]. The elements of this matrix are formed by the rule

$$\rho_{ij} = \mathbf{a}_i \mathbf{a}_j^*.$$

We will not develop the theory of polarization using the coherency matrix, but will simply use this matrix to justify the need for four independent measurements to characterize polarization. There is no unique set of measurements required by theory, but normally measurements made are of the *Stokes parameters*, which are directly related to the polarization ellipse of Figure 2.4. (We will see shortly that only three of the four measurements are independent. This will be in agreement with the definition of the coherency matrix, where $\rho_{ij} = \rho_{ij}^*$, i.e., the matrix is Hermitian.)

2.8.2 Stokes Parameters

The Stokes parameters (**Sir George Gabriel Stokes: 1819–1903**) of a light wave are measurable quantities, defined as follows:

- s_0 total flux density;
- s_1 difference between flux densities transmitted by a linear polarizer oriented parallel to the x-axis and one oriented parallel to the y-axis (the x- and y-axes are usually selected to be parallel to the horizontal and vertical directions in the laboratory);
- s_2 difference between flux densities transmitted by a linear polarizer oriented at 45° to the x-axis and one oriented at 135°;
- s_3 difference between flux densities transmitted by a right-circular polarizer and a left-circular polarizer.

The physical instruments that can be used to measure the parameters will be discussed in Chapter 13.

If the Stokes parameters are to characterize the polarization of a wave, they must be related to the parameters of the polarization ellipse. It is therefore important to establish that the Stokes parameters are variables of the polarization ellipse (2.33). In its current form, (2.33) contains no measurable quantities and thus must be modified if it is to be associated with the Stokes parameters. In the discussion of the Poynting vector, it was pointed out that the time average of the Poynting vector is the quantity observed when measurements are made of light waves. We must, therefore, find the time average of (2.33) if we wish to relate its parameters to observable quantities. To simplify the discussion, let us assume that the amplitudes of the orthogonally polarized waves E_{0x} and E_{0y} and their relative phase δ are constants. We will also use the shorthand notation for a time average introduced in (2.24):

$$\langle E_x^2 \rangle = \frac{1}{T} \int_{t_0}^{t_0+T} E_{0x}^2 [\cos(\omega t - kz) \cos\phi_1 - \sin(\omega t - kz) \sin\phi_1]^2 dt.$$

The time average of (2.33) can now be written as

$$\frac{\langle E_x^2 \rangle}{E_{0x}^2} + \frac{\langle E_y^2 \rangle}{E_{0y}^2} - 2\frac{\langle E_x E_y \rangle}{E_{0x} E_{0y}} \cos\delta = \sin^2\delta. \tag{2.39}$$

Multiplying both sides of (2.39) by $(2E_{0x}E_{0y})^2$ removes the terms in the denominators to give

$$4E_{0y}^2\langle E_x^2\rangle + 4E_{0x}^2\langle E_y^2\rangle - 8E_{0x}E_{0y}\langle E_xE_y\rangle\cos\delta = (2E_{0x}E_{0y}\sin\delta)^2.$$

The same argument that was used to simplify (2.25) can be used to obtain the time averages for the first two terms:

$$\langle E_x^2\rangle = \frac{E_{0x}^2}{2}, \qquad \langle E_y^2\rangle = \frac{E_{0y}^2}{2}.$$

The calculation of the time average in the third term,

$$\langle E_xE_y\rangle = \frac{1}{2}E_{0x}E_{0y}\cos\delta, \tag{2.40}$$

is left as Problem 2.12. With these time averages, (2.39) can be written as

$$4E_{0x}^2E_{0y}^2 - \left(2E_{0x}E_{0y}\cos\delta\right)^2 = \left(2E_{0x}E_{0y}\sin\delta\right)^2.$$

If $E_{0x}^2 + E_{0y}^2$ is added to both sides of this equation, it can be rewritten as

$$\left(E_{0x}^2 + E_{0y}^2\right)^2 - \left(E_{0x}^2 - E_{0y}^2\right)^2 - \left(2E_{0x}E_{0y}\cos\delta\right)^2 = \left(2E_{0x}E_{0y}\sin\delta\right)^2. \tag{2.41}$$

Each term in this equation can be identified with a Stokes parameter.

In our derivation we required that the amplitudes and relative phase of the two orthogonally polarized waves be constant, but we can relax this requirement and instead define the Stokes parameters as temporal averages. With this modification, the terms of (2.41) become

$$\begin{aligned} s_0 &= \langle E_{0x}^2\rangle + \langle E_{0y}^2\rangle, \quad s_1 = \langle E_{0x}^2\rangle - \langle E_{0y}^2\rangle, \\ s_2 &= \langle 2E_{0x}E_{0y}\cos\delta\rangle, \quad s_3 = \langle 2E_{0x}E_{0y}\sin\delta\rangle. \end{aligned} \tag{2.42}$$

Equation (2.41) can now be written as

$$s_0^2 - s_1^2 - s_2^2 = s_3^2. \tag{2.43}$$

For a polarized wave, only three of the Stokes parameters are independent. This agrees with the requirement placed upon elements of the Hermitian coherency matrix, introduced above.

With this demonstration of the connection between the Stokes parameters and the polarization ellipse, the Stokes parameters can be written in terms of the parameters of the polarization ellipse in Figure 2.4:

$$\begin{aligned} s_1 &= s_0\cos 2\varphi\cos 2\theta, \\ s_2 &= s_0\cos 2\varphi\sin 2\theta, \\ s_3 &= s_0\sin 2\varphi. \end{aligned} \tag{2.44}$$

It is this close relationship between the Stokes parameters and the polarization ellipse that makes the Stokes parameters a useful characterization of polarization.

The Stokes parameters can be used to define the *degree of polarization*

$$V = \frac{1}{s_0}\sqrt{s_1^2 + s_2^2 + s_3^2}. \tag{2.45}$$

[The equality (2.43) applies to completely polarized light, when $V = 1$.] The degree of polarization can be used to characterize any light source that is physically realizable. If the time averages in the definition of the Stokes parameters s_2 and s_3 in (2.42) are zero and if $\langle E_{0x}^2 \rangle = \langle E_{0y}^2 \rangle$, so that

$$s_0 = 2\langle E_{0x}^2 \rangle, \quad s_1 = s_2 = s_3 = 0,$$

then the light wave is said to be unpolarized and $V = 0$.

Hans Mueller, a physics professor at MIT [6], pointed out that the Stokes parameters can be thought of as elements of a column matrix or 4-vector

$$\begin{bmatrix} s_0 \\ s_1 \\ s_2 \\ s_3 \end{bmatrix}.$$

This view will allow us to follow a polarized wave through a series of optical devices by using matrix algebra, as we will see later.

Poincaré's sphere (Henri Poincaré: 1854–1912) Before it was discovered that the Stokes parameters could be treated as elements of a column matrix, a geometrical construction was used to determine the effect of an anisotropic medium on polarized light. The parameters s_1, s_2, s_3 are viewed as the Cartesian coordinates of a point on a sphere of radius s_0. This sphere is called the *Poincaré sphere* [7] and is shown in Figure 2.10. On the sphere, right-hand polarized light is represented by points on the upper hemisphere. Linear polarization is represented by points on the equator. Circular polarization is represented by the poles.

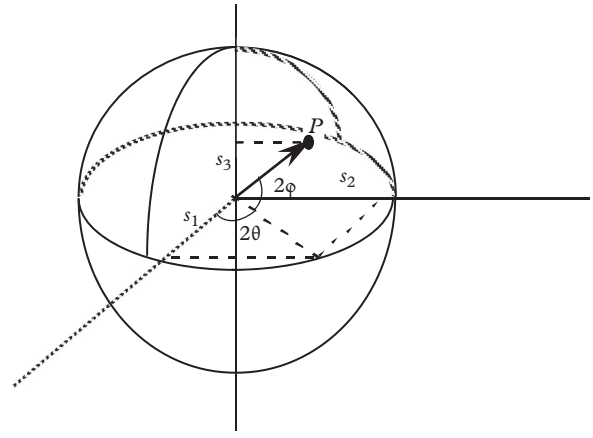

Figure 2.10 *Poincaré sphere.*

2.8.3 Jones Vector

There is one other representation of polarized light, complementary to the Stokes parameters, developed by **R. Clark Jones (1916–2004)** in 1941 and called the *Jones vector*. It is superior to the Stokes vector in that it handles light of a known phase and amplitude with a reduced number of parameters. It is inferior to the Stokes vector in that, unlike the Stokes representation, which is experimentally determined, the Jones representation cannot handle unpolarized or partially polarized light. The Jones vector is a theoretical construct that can only describe light with a well-defined phase and frequency. The density matrix formalism can be used to correct the shortcomings of the Jones vector, but then the simplicity of the Jones representation is lost.

It was shown earlier that if it is assumed that the coordinate system is such that the electromagnetic wave is propagating along the z-axis, then any polarization can be decomposed

Table 2.4 *Jones and Stokes vectors*

Jones vector	**Stokes vector**
Horizontal polarization	
$\begin{bmatrix} 1 \\ 0 \end{bmatrix}$	$\begin{bmatrix} 1 \\ 1 \\ 0 \\ 0 \end{bmatrix}$
Vertical polarization	
$\begin{bmatrix} 0 \\ 1 \end{bmatrix}$	$\begin{bmatrix} 1 \\ -1 \\ 0 \\ 0 \end{bmatrix}$
+45° polarization	
$\frac{1}{\sqrt{2}}\begin{bmatrix} 1 \\ 1 \end{bmatrix}$	$\begin{bmatrix} 1 \\ 0 \\ 1 \\ 0 \end{bmatrix}$
–45° polarization	
$\frac{1}{\sqrt{2}}\begin{bmatrix} 1 \\ -1 \end{bmatrix}$	$\begin{bmatrix} 1 \\ 0 \\ -1 \\ 0 \end{bmatrix}$
Right-circular polarization	
$\frac{1}{\sqrt{2}}\begin{bmatrix} 1 \\ i \end{bmatrix}$	$\begin{bmatrix} 1 \\ 0 \\ 0 \\ 1 \end{bmatrix}$
Left-circular polarization	
$\frac{1}{\sqrt{2}}\begin{bmatrix} 1 \\ -i \end{bmatrix}$	$\begin{bmatrix} 1 \\ 0 \\ 0 \\ -1 \end{bmatrix}$

into two orthogonal **E** vectors, say, for the purposes of this discussion, parallel to the *x*- and *y*-directions. The Jones vector is defined as a two-row column matrix consisting of the complex components in the *x*- and *y*-directions:

$$\mathbf{E} = \begin{bmatrix} E_{0x}e^{i(\omega t - \mathbf{k}\cdot\mathbf{r}+\phi_1)} \\ E_{0y}e^{i(\omega t - \mathbf{k}\cdot\mathbf{r}+\phi_2)} \end{bmatrix}. \tag{2.46}$$

If absolute phase is not an issue, then we may normalize this vector by dividing it by that number that simplifies the components but keeps the sum of the squared magnitudes of the components equal to one. For example, assuming that $E_{0x} = E_{0y}$, then

$$\mathbf{E} = E_{0x}e^{i(\omega t - \mathbf{k}\cdot\mathbf{r}+\phi_1)} \begin{bmatrix} 1 \\ e^{i\delta} \end{bmatrix}.$$

The normalized vector would comprise the terms contained within the square brackets, each divided by $\sqrt{2}$. The general form of the Jones vector is

$$\mathbf{E} = \begin{bmatrix} \mathbf{A} \\ \mathbf{B} \end{bmatrix}, \qquad \mathbf{E}^* = \begin{bmatrix} \mathbf{A}^* & \mathbf{B}^* \end{bmatrix}.$$

Some examples of Jones vectors and Stokes vectors are shown in Table 2.4.

2.9 Propagation in a Conducting Medium

In Chapter 1, we discussed the propagation of a wave with attenuation. In our discussion of the propagation of light, however, we have ensured that we would experience no loss by assuming $\sigma = 0$. We now relax that assumption and allow $\sigma \neq 0$. Maxwell's equations become

$$\nabla \cdot \mathbf{D} = 0, \qquad \nabla \cdot \mathbf{B} = 0,$$

$$\nabla \times \mathbf{H} = \mathbf{J} + \frac{\partial \mathbf{D}}{\partial t}, \qquad \nabla \times \mathbf{E} = -\frac{\partial \mathbf{B}}{\partial t}.$$

We continue to neglect dynamic or resonant effects so that we may use the simple constitutive relations

$$\mathbf{J} = \sigma\mathbf{E}, \quad \mathbf{D} = \varepsilon\mathbf{E}, \quad \mathbf{B} = \mu\mathbf{H}.$$

where ε, μ, and σ are scalars, independent of time. Maxwell's equations in a medium with dissipation can be rewritten using these constitutive relations as

$$\begin{aligned} \nabla \cdot \mathbf{E} &= 0, & \nabla \cdot \mathbf{H} &= 0, \\ \nabla \times \mathbf{H} &= \sigma\mathbf{E} + \varepsilon\frac{\partial \mathbf{E}}{\partial t}, & \nabla \times \mathbf{E} &= -\mu\frac{\partial \mathbf{H}}{\partial t}. \end{aligned} \tag{2.47}$$

We now apply the same procedure used to derive the wave equation for free space,

$$\nabla \times (\nabla \times \mathbf{E}) = \nabla \times \left(-\mu \frac{\partial \mathbf{H}}{\partial t}\right) = -\mu \frac{\partial}{\partial t}(\nabla \times \mathbf{H}),$$

$$-\mu \frac{\partial}{\partial t}(\nabla \times \mathbf{H}) = -\mu \frac{\partial}{\partial t}\left(\sigma \mathbf{E} + \varepsilon \frac{\partial \mathbf{E}}{\partial t}\right),$$

$$\nabla \times (\nabla \times \mathbf{E}) = \nabla(\nabla \cdot \mathbf{E}) - \nabla^2 \mathbf{E}.$$

yielding the wave equation in a conducting medium:

$$\nabla^2 \mathbf{E} = \mu\sigma \frac{\partial \mathbf{E}}{\partial t} + \mu\varepsilon \frac{\partial^2 \mathbf{E}}{\partial t^2}. \tag{2.48}$$

This wave equation is of the same form as (1.20). We can derive a similar equation for the magnetic field:

$$\nabla^2 \mathbf{B} = \mu\sigma \frac{\partial \mathbf{B}}{\partial t} + \mu\varepsilon \frac{\partial^2 \mathbf{B}}{\partial t^2}. \tag{2.49}$$

Equations (2.48) and (2.49) are called the *telegraph equations* and were developed by Oliver Heaviside (1850–1925). They are wave equations derived to explain the propagation of pulses on telegraph lines.

We see that the wave equation (2.48) contains a damping term $\partial \mathbf{E}/\partial t$ when we allow $\sigma \neq 0$. By comparing (2.48) and (1.20), we can see that the solution of (2.48) will be an electromagnetic wave that will experience attenuation proportional to $\mu\sigma$ as it propagates. Using (1.22) and (1.23), we can rewrite (2.47), for plane wave solutions, as

$$\begin{aligned} \nabla \times \mathbf{E} = -\mu \frac{\partial \mathbf{H}}{\partial t} \quad &\Rightarrow \quad \nabla \times \mathbf{E} = -i\omega\mu \mathbf{H}, \\ \nabla \times \mathbf{H} = \sigma \mathbf{E} + \varepsilon \frac{\partial \mathbf{E}}{\partial t} \quad &\Rightarrow \quad \nabla \times \mathbf{H} = i\omega\left(\varepsilon - \frac{i\sigma}{\omega}\right)\mathbf{E}. \end{aligned} \tag{2.50}$$

We can rewrite (2.48) in terms of these expressions for the curls of **E** and **H**:

$$\nabla^2 \mathbf{E} + \omega^2 \mu \left(\varepsilon - \frac{i\sigma}{\omega}\right)\mathbf{E} = 0. \tag{2.51}$$

This has the form of the Helmholtz equation (1.13) if we replace k^2 in the latter by the complex function

$$\tilde{k}^2 = \omega^2 \mu \left(\varepsilon - i\frac{\sigma}{\omega}\right). \tag{2.52}$$

We use the identity

$$k = \frac{n\omega}{c} = \omega\sqrt{\mu\varepsilon},$$

to demonstrate that the equations for conducting media are identical to those derived for nonconducting media if the dielectric constant ε is replaced by a complex dielectric constant

$$\tilde{\varepsilon} = \varepsilon - i\left(\frac{\sigma}{\omega}\right). \tag{2.53}$$

This equation suggests that σ may contain a frequency dependence (in fact, in the c.g.s. system, the units of σ are s^{-1}; for copper, in c.g.s. units, $\sigma = 5.14 \times 10^{17}\ s^{-1}$). In condensed matter physics, one finds that the mobility of the electrons creates a frequency dependence that shows up in σ.

Since we have replaced k by the complex quantity

$$\tilde{k} = \omega\sqrt{\mu\left(\varepsilon - i\frac{\sigma}{\omega}\right)},$$

we must replace the index of refraction by a complex index. In the literature, this is accomplished in two ways:

$$\tilde{n} = n(1 - i\kappa), \tag{2.54}$$

$$\tilde{n} = n_1 - in_2.$$

We will use the notation in (2.54).

To find out how a plane wave propagates in this conductive medium, we simply replace the propagation constant k by

$$\tilde{k} = \tilde{n}\frac{\omega}{c} = \left(\frac{\omega n}{c}\right)(1 - i\kappa),$$

as we did with (1.24). κ is called the *extinction coefficient* and $n\kappa$ is called the *absorption coefficient*.

If we assume that **k** is parallel to the z-axis, then the plane wave is

$$\mathbf{E} = \mathbf{E}_0 e^{i\omega t} e^{-i\omega(n/c)(1-i\kappa)z},$$

$$\mathbf{E} = \mathbf{E}_0 e^{-(\omega n\kappa/c)z} e^{-i\omega(t-nz/c)}, \tag{2.55}$$

$$\mathcal{R}e\{\mathbf{E}\} = \mathbf{E}_0 e^{-(\omega n\kappa/c)z}\cos(\omega t - kz). \tag{2.56}$$

The wave described by (2.56) is a plane wave, attenuated by the exponential factor

$$e^{-(\omega/c)n\kappa z}. \tag{2.57}$$

Figure 2.11 displays the exponential decay of a light wave propagating in an absorbing medium. A layer of xylene floats upon water containing the dye rhodamine 6G in solution. The dye strongly absorbes a beam of blue light from a HeCd laser (440 nm). As can be seen in Figure 2.11, the blue light is rapidly attenuated once it enters the water. Some of the energy absorbed by the rhodamine is reemitted at longer wavelengths. The reemitted light travels in all directions, since it has no memory of the direction traveled by the blue light. For this reason, the beam of light in the water appears diffuse, and as can be seen, is orange in color.

Figure 2.11 *Blue laser light is shown propagating in xylene (above) and water (below). The water contains the dye rhodamine 6G in solution. The red rhodamine dye absorbs the blue light, and the beam rapidly decays to zero. Some of the energy absorbed by the dye is reemitted in the yellow to red region of the spectrum. This reemitted light caused the diffuse appearance of the light as it propagates in the water.*

To evaluate the absorption coefficient $n\kappa$ in terms of electromagnetic properties of the medium, we will derive a relationship between $n\kappa$ and σ. We rewrite (2.54) as

$$\tilde{n}^2 = n^2(1-\kappa^2-2i\kappa) = \frac{c^2}{\omega^2}\tilde{k}^2.$$

This can be used to express n^2 in terms of the constants of the material:

$$\tilde{n}^2 = c^2\mu\left(\varepsilon - i\frac{\sigma}{\omega}\right). \tag{2.58}$$

Equating real and imaginary terms, we obtain

$$n^2(1-\kappa^2) = c^2\mu\varepsilon, \quad 2n^2\kappa = c^2\frac{\mu\sigma}{\omega}.$$

We can use these two relationships to find

$$n^2 = \frac{c^2}{2}\left[\sqrt{\mu^2\varepsilon^2 + \left(\frac{\mu\sigma}{\omega}\right)^2} + \mu\varepsilon\right], \tag{2.59}$$

$$n^2\kappa^2 = \frac{c^2}{2}\left[\sqrt{\mu^2\varepsilon^2 + \left(\frac{\mu\sigma}{\omega}\right)^2} - \mu\varepsilon\right]. \tag{2.60}$$

Note that when $\sigma = 0$, $\kappa = 0$, and we obtain the free-space result, (2.11):

$$n^2 = \frac{\mu\varepsilon}{\mu_0\varepsilon_0}.$$

An estimate of the magnitude of the quantities under the radicals in (2.59) and (2.60) can be obtained by using values for copper, where, in MKS units, $\sigma = 5.8 \times 10^7$ mho/m and $n = 0.62$ at $\lambda = 589.3$ nm. (The index of refraction is less than one, which implies that the phase velocity is greater than the speed of light. This apparent contradiction of a fundamental postulate of the theory of relativity will be discussed during the study of dispersion in Chapter 7.) The two terms under the radical are

$$\frac{\mu\sigma}{\omega} = \frac{\left(4\pi \times 10^{-7}\right)\left(5.8 \times 10^7\right)\left(5.893 \times 10^{-7}\right)}{(2\pi)\left(3 \times 10^8\right)} = 2.3 \times 10^{-14}\ \mathrm{s^2/m^2},$$

$$\mu\varepsilon = \mu_0\varepsilon_0 n^2 = \left(4\pi \times 10^{-7}\right)\left(8.8542 \times 10^{-12}\right)(0.62)^2 = 4.3 \times 10^{-18}\ \mathrm{s^2/m^2}.$$

By comparing the relative magnitude of these two terms, we are justified in assuming that $\sigma/\omega \gg \varepsilon$ and can make the approximation

$$n^2\kappa^2 \approx \frac{c^2\mu\sigma}{2\omega},$$

$$n\kappa = c\sqrt{\frac{\mu\sigma}{2\omega}}. \tag{2.61}$$

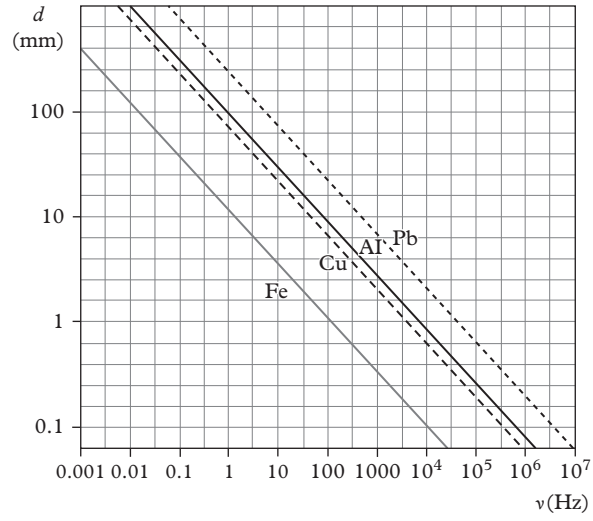

Figure 2.12 *Skin depth for a few metals.*

We use (2.61) to find the depth at which an electromagnetic wave is attenuated, to $1/e$ of its original energy, when propagating into a conductor. At that depth, denoted by d, the exponent in (2.57) will equal 1, and thus

$$\frac{\omega}{c} n\kappa d = \frac{2\pi}{\lambda_0} n\kappa d = 1,$$

$$d = \frac{\lambda_0}{2\pi n\kappa} \approx \frac{\lambda_0}{2\pi c}\sqrt{\frac{2\omega}{\mu\sigma}},$$

$$d = \sqrt{\frac{2}{\mu\sigma\omega}}. \tag{2.62}$$

The depth d is called the *skin depth*. Figure 2.12 shows the dependence of skin depth on frequency for some metals.

2.10 Summary

In this chapter, Maxwell's equations were used to obtain the wave equation for free space,

$$\nabla^2 \mathbf{E} = \mu\varepsilon \frac{\partial^2 \mathbf{E}}{\partial t^2}.$$

and for a conductive medium,

$$\nabla^2 \mathbf{E} = \mu\sigma \frac{\partial \mathbf{E}}{\partial t} + \mu\varepsilon \frac{\partial^2 \mathbf{E}}{\partial t^2}.$$

While the forms of these two equations appear quite different, we demonstrated that plane wave solutions existed for both equations when the dielectric constant of the conductive medium was replaced by a complex constant

$$\tilde{\varepsilon} = \varepsilon - i\left(\frac{\sigma}{\omega}\right).$$

This replacement means that the optical properties of a conductive material are described by a complex index of refraction

$$\tilde{n} = n(1 - i\kappa).$$

A plane wave propagating in conductive material has an amplitude attenuated by the exponential factor

$$e^{-(\omega/c)n\kappa z}.$$

By manipulation of Maxwell's equations, we were able to show that the propagation velocity of a light wave is governed by the electrical properties of the medium. The index of refraction was used to indicate the propagation velocity in the medium, relative to the propagation velocity in a vacuum:

$$n = \frac{c}{v} = \sqrt{\frac{\varepsilon\mu}{\varepsilon_0\mu_0}}.$$

Also, we were able to demonstrate that light waves must be transverse waves and that the magnitudes of the electric and magnetic fields are related by

$$n|\mathbf{E}| = c|\mathbf{B}|.$$

By comparing the forces experienced by a charged particle in an electromagnetic field, we found that we could describe the polarization of an electromagnetic wave by the electric field vector. We developed the formalism necessary for discussion of polarization, but delayed a discussion of the manipulation of a light wave's polarization until Chapter 13.

2.11 Problems

2.1. Light is traveling in glass ($n = 1.5$). If the amplitude of the electric field of the light is 100 V/m, what is the amplitude of the magnetic field? What is the magnitude of the Poynting vector?

2.2. A 60 W monochromatic point source is radiating equally in all directions in a vacuum. What is the electric field amplitude 2 m from the source?

2.3. The flux density at the Earth's surface due to sunlight is $I = 1.34 \times 10^3$ J/(m^2·s). Calculate the electric and magnetic fields at the Earth's surface by assuming that the average Poynting vector is equal to this flux density.

2.4. What is the flux density of light needed to keep a glass sphere of mass 10^{-8} g and diameter 2×10^{-5} m floating in midair?

2.5. An 85 kg astronaut has only a flashlight to propel him in space. If the flashlight emits 1 W of light in a parallel beam for one hour, how fast will the astronaut be going at the end of the hour, assuming he started at rest?

2.6. What are the polarizations of the following waves:

$$\mathbf{E} = E_0\left[\cos(\omega t - kz)\,\hat{\mathbf{i}} + \cos\left(\omega t - kz + \frac{5}{4}\pi\right)\hat{\mathbf{j}}\right],$$

$$\mathbf{E} = E_0\left[\cos(\omega t + kz)\,\hat{\mathbf{i}} + \cos\left(\omega t + kz - \frac{1}{4}\pi\right)\hat{\mathbf{j}}\right],$$

$$\mathbf{E} = E_0\left[\cos(\omega t - kz)\,\hat{\mathbf{i}} - \cos\left(\omega t - kz + \frac{1}{6}\pi\right)\hat{\mathbf{j}}\right]?$$

2.7. Show that the addition of two elliptically polarized waves propagating along the z-axis results in another elliptically polarized wave.

2.8. Write an expression, in MKS units, for a plane electromagnetic wave, with a wavelength of 500 nm and an intensity of 53.2 W/m^2, propagating in the z-direction. Assume that the wave is linearly polarized at an angle of 45° to the x-axis.

2.9. Using conventional vector notation, prove that a right- and a left-circularly polarized wave can be combined to yield a linearly polarized wave. Carry out the same demonstration using the Jones vector notation. What requirement must be placed on the two circularly polarized waves? Sketch the geometrical construction that demonstrates the combination of circularly polarized waves to generate a linearly polarized wave.

2.10. Write the equation for a plane wave propagating in the positive z-direction that has right elliptical polarization with the major axis of the ellipse parallel to the x-axis. Use both the conventional vector and the Jones vector notation.

2.11. Describe the polarization of a wave with the Jones vector

$$\begin{bmatrix} -i \\ 2 \end{bmatrix}.$$

Write the Jones vector that is orthogonal to this vector and describe its polarization.

2.12. Prove that (2.42) is correct using the expressions

$$E_x = E_{0x}[\cos(\omega t - kz)\cos\phi_1 - \sin(\omega t - kz)\sin\phi_1],$$

$$E_y = E_{0y}[\cos(\omega t - kz)\cos\phi_2 - \sin(\omega t - kz)\sin\phi_2]$$

for the two orthogonally polarized electric fields.

2.13. Demonstrate, using the Jones vector notation, that right- and left-circularly polarized light waves are orthogonal.

2.14. Find the skin depth for seawater with a resistivity $\rho = 0.20\,\Omega$/m for $\nu = 30$ kHz and 30 MHz. What frequency should we use to communicate with a submarine that will not be deeper than 100 m?

2.15. At what frequency would the approximation used to obtain (2.26) produce a 10% error?

2.16. If a 1 kW laser beam is focused to a spot with an area of 10^{-9} m^2, what is the amplitude of the electric field at the focus?

2.17. The human eye is sensitive to light of wavelengths from approximately 600 nm (red) to 400 nm (blue). (a) Calculate the frequency of both wavelengths. (b) Find the energy of the photons associated with the red and blue wavelength limits.

2.18. If green light, 500 nm, could be frequency modulated to 0.1% of the light wave's frequency, calculate the number of 6 MHz bandwidth TV channels that could be carried by the modulation.

2.19. Given the Stokes vector

$$\begin{bmatrix} 1 \\ 0 \\ -\frac{3}{5} \\ \frac{4}{5} \end{bmatrix},$$

(a) calculate the degree of polarization, (b) determine the orthogonal vector, and (c) draw the polarization ellipse.

2.20. How thin must a sheet of iron be if it is one skin depth thick? How many atoms thick is such a sheet?

REFERENCES

1. Maxwell, J.C., *A dynamical theory of the electromagnetic field*. Phil. Trans. R. Soc. Lond., 1865. **155**: p. 459–512.
2. Feynman, R.P., *QED, The Strange Theory of Light and Matter*. 2006: Princeton University Press: p. 192.
3. Wangsness, R.K., *Electromagnetic Fields*. 2nd ed. 1986: Wiley.
4. McMaster, W.H., *Polarization and the Stokes parameters*. Am. J. Phys., 1954. **22**: p. 351–362.
5. Klein, M.V. and T.E. Furtak, *Optics*. 2nd ed. 1986: Wiley.
6. Mueller, H., *The foundation of optics*. J. Opt. Soc. Am, 1948. **38**: p. 661.
7. Poincaré, H., *Théorie mathématique de la lumiére*. Vol. 2. 1892: Georges Carré.

Appendix 2A Vectors

We will review a few properties of vectors that will be of use in our discussion of light. A vector is a quantity with both magnitude and direction; it can be defined in terms of unit vectors along the three orthogonal axes of a Cartesian coordinate system:

$$\mathbf{E} = E_x\hat{\mathbf{i}} + E_y\hat{\mathbf{j}} + E_z\hat{\mathbf{k}}.$$

To add two vectors, we add like components:

$$\mathbf{E}_1 + \mathbf{E}_2 = (E_{1x} + E_{2x})\hat{\mathbf{i}} + (E_{1y} + E_{2y})\hat{\mathbf{j}} + (E_{1z} + E_{2z})\hat{\mathbf{k}}.$$

2A.1 Products

There are two ways to multiply vectors:

- The *scalar (dot) product* is given by

$$\mathbf{E} \cdot \mathbf{H} = EH \cos\theta = E_x H_x + E_y H_y + E_z H_z, \tag{2A.1}$$

  where θ is the angle between $\mathbf{E}$ and $\mathbf{H}$. This product is a scalar quantity that gives the projection of one vector onto the second vector. If $\mathbf{E}$ and $\mathbf{H}$ are perpendicular, then their dot product is zero.

- The *vector (cross) product* is given by

$$\mathbf{E} \times \mathbf{H} = EH \sin\theta\, \hat{\mathbf{n}},$$

  where $\hat{\mathbf{n}}$ is a unit vector normal to the plane formed by $\mathbf{E}$ and $\mathbf{H}$. The cross product is a vector with a magnitude equal to the area of the parallelogram formed by $\mathbf{E}$ and $\mathbf{H}$; it is zero if the two vectors are parallel. The components of this vector are calculated as follows:

$$\mathbf{E} \times \mathbf{H} = \begin{bmatrix} \hat{\mathbf{i}} & \hat{\mathbf{j}} & \hat{\mathbf{k}} \\ E_x & E_y & E_z \\ H_x & H_y & H_z \end{bmatrix}$$

$$= (E_y H_z - E_z H_y)\hat{\mathbf{i}} - (E_x H_z - E_z H_x)\hat{\mathbf{j}} + (E_x H_y - E_y H_x)\hat{\mathbf{k}}. \tag{2A.2}$$

  We will find use for the vector triple product relationship

$$\mathbf{A} \times (\mathbf{B} \times \mathbf{C}) = (\mathbf{A} \cdot \mathbf{C})\mathbf{B} - (\mathbf{A} \cdot \mathbf{B})\mathbf{C}. \tag{2A.3}$$

2A.2 Derivatives

A vector operator called the *del operator* is defined in a Cartesian coordinate system as

$$\nabla = \hat{\mathbf{i}}\frac{\partial}{\partial x} + \hat{\mathbf{j}}\frac{\partial}{\partial y} + \hat{\mathbf{k}}\frac{\partial}{\partial z}. \tag{2A.4}$$

We can treat this operator as a vector and calculate three products of use in optics:

- The *gradient* of a scalar:

$$\nabla V = \frac{\partial V}{\partial x}\hat{\mathbf{i}} + \frac{\partial V}{\partial y}\hat{\mathbf{j}} + \frac{\partial V}{\partial z}\hat{\mathbf{k}}. \tag{2A.5}$$

  The gradient is a vector giving the magnitude and direction of the fastest rate of change of the scalar quantity V.

- The *divergence* of a vector:

$$\nabla \cdot \mathbf{E} = \frac{\partial E_x}{\partial x} + \frac{\partial E_y}{\partial y} + \frac{\partial E_z}{\partial z}. \tag{2A.6}$$

The divergence gives the amount of flux flowing toward (negative) or away from (positive) a point. If the divergence is zero, then there are no sources or sinks in the volume.

- The *curl* of a vector:

$$\nabla \times \mathbf{E} = \left(\frac{\partial E_z}{\partial y} - \frac{\partial E_y}{\partial z}\right)\hat{\mathbf{i}} + \left(\frac{\partial E_x}{\partial z} - \frac{\partial E_z}{\partial x}\right)\hat{\mathbf{j}} + \left(\frac{\partial E_y}{\partial x} - \frac{\partial E_x}{\partial y}\right)\hat{\mathbf{k}}. \tag{2A.7}$$

A physical interpretation of this operation can be made easily if the vector is a velocity, then when the curl of the velocity is nonzero, rotation is also occurring.

If we calculate the divergence of a gradient of a scalar, we obtain a scalar function, the *Laplacian*:

$$\nabla \cdot \nabla V = \nabla^2 V = \frac{\partial^2 V}{\partial x^2} + \frac{\partial^2 V}{\partial y^2} + \frac{\partial^2 V}{\partial z^2}. \tag{2A.8}$$

For a vector quantity, we have

$$\nabla^2 \mathbf{E} = \nabla^2 E_x \hat{\mathbf{i}} + \nabla^2 E_y \hat{\mathbf{j}} + \nabla^2 E_z \hat{\mathbf{k}}. \tag{2A.9}$$

Table 2A.1 *Operations with the del operator in spherical coordinates (r, θ, ϕ), where subscripts r, θ, and ϕ denote the respective components*

$$(\nabla V)_r = \frac{\partial V}{\partial r} \qquad (\nabla V)_\theta = \frac{1}{r}\left(\frac{\partial V}{\partial \theta}\right) \qquad (\nabla V)_\phi = \frac{1}{r\sin\theta}\left(\frac{\partial V}{\partial \phi}\right)$$

$$\nabla \cdot \mathbf{E} = \frac{1}{r}\left[\frac{\partial (rE_r)}{\partial r}\right] + \frac{1}{r\sin\theta}\left[\frac{\partial (E_\theta \sin\theta)}{\partial \theta}\right] + \frac{1}{r\sin\theta}\left(\frac{\partial E_\phi}{\partial \phi}\right)$$

$$\nabla^2 V = \frac{1}{r^2}\frac{\partial}{\partial r}\left(r^2 \frac{\partial V}{\partial r}\right) + \frac{1}{r^2\sin\theta}\frac{\partial}{\partial \theta}\left(\sin\theta \frac{\partial V}{\partial \theta}\right) + \frac{1}{r^2\sin^2\theta}\frac{\partial^2 V}{\partial \phi^2}$$

$$(\nabla \times \mathbf{E})_r = \frac{1}{r\sin\theta}\left[\frac{\partial}{\partial \theta}(E_\phi \sin\theta) - \frac{\partial E_\theta}{\partial \phi}\right]$$

$$(\nabla \times \mathbf{E})_\theta = \frac{1}{r}\left[\frac{1}{\sin\theta}\frac{\partial E_r}{\partial \phi} - \frac{\partial}{\partial r}(rE_\phi)\right]$$

$$(\nabla \times \mathbf{E})_\phi = \frac{1}{r}\left[\frac{\partial}{\partial r}(rE_\theta) - \frac{\partial E_r}{\partial \theta}\right]$$

$$(\nabla^2 \mathbf{E})_r = \nabla^2 E_r - \frac{2E_r}{r^2} - \frac{2}{r^2\sin\theta}\frac{\partial (E_\theta \sin\theta)}{\partial \theta} - \frac{2}{r^2\sin\theta}\frac{\partial E_\phi}{\partial \phi}$$

$$(\nabla^2 \mathbf{E})_\theta = \nabla^2 E_\theta + \frac{2}{r^2}\frac{\partial E_r}{\partial \theta} - \frac{E_\theta}{r^2\sin^2\theta} - \frac{2\cos\theta}{r^2\sin^2\theta}\frac{\partial E_\phi}{\partial \phi}$$

$$(\nabla^2 \mathbf{E})_\phi = \nabla^2 E_\phi + \frac{2}{r^2\sin\theta}\frac{\partial E_r}{\partial \phi} + \frac{2\cos\theta}{r^2\sin^2\theta}\frac{\partial E_\theta}{\partial \phi} - \frac{E_\phi}{r^2\sin^2\theta}$$

Several other identities involving the del operator will come in handy in our study of optics:

$$\nabla \times \nabla V = 0, \tag{2A.10}$$

$$\nabla \cdot \nabla \times \mathbf{E} = 0, \tag{2A.11}$$

$$\nabla \times (\nabla \times \mathbf{E}) = \nabla(\nabla \cdot \mathbf{E}) - \nabla^2 \mathbf{E}, \tag{2A.12}$$

$$\nabla \cdot (\mathbf{A} \times \mathbf{B}) = \mathbf{A} \cdot (\nabla \times \mathbf{B}) + \mathbf{B} \cdot (\nabla \times \mathbf{A}). \tag{2A.13}$$

We have displayed all of the above relations in a Cartesian coordinate system; similar expressions can be derived using spherical coordinates. We list them in Table 2A.1 for the reader's convenience.

Appendix 2B Electromagnetic Units

Of all topics in physics, perhaps the one that introduces the most confusion is the subject of electromagnetic units. In this book, we use MKS units, but the reader will find most older optics books will use c.g.s. units.

Table 2B.1 *Electromagnetic units*

c.g.s.	Units	MKS	Units
c	cm/s	$\dfrac{1}{\sqrt{\mu_0 \varepsilon_0}}$	m/s
$\mathbf{D}$	$12\pi \times 10^{-5}$ statcoulomb/cm^2	$\sqrt{4\pi\varepsilon_0}\ \mathbf{D}$	coulomb/m
$\mathbf{B}$	10^4 gauss	$\sqrt{\dfrac{4\pi}{\mu_0}}\,\mathbf{B}$	weber/m^2
$\mathbf{H}$	$4\pi \times 10^{-3}$ oersted	$\sqrt{4\pi\mu_0}\,\mathbf{H}$	amp-turn/m
$\mathbf{E}$	$\dfrac{1}{3} \times 10^{-4}$ statcoulomb/cm	$\sqrt{4\pi\varepsilon_0}\,\mathbf{E}$	volt/m
$\mathbf{J}$	3×10^5 statamp/cm^2	$\dfrac{\mathbf{J}}{\sqrt{4\pi\varepsilon_0}}$	amp/m^2
σ	9×10^9 s^{-1}	$\dfrac{\sigma}{4\pi\varepsilon_0}$	mho/m
ρ	3×10^3 statcoulomb/cm^3	$\dfrac{\rho}{\sqrt{4\pi\varepsilon_0}}$	coulomb/m^3
ε		$\dfrac{\varepsilon}{\varepsilon_0}$	
μ		$\dfrac{\mu}{\mu_0}$	

In rationalized MKS units, ε and μ in a vacuum have the following values

$$\varepsilon_0 = 8.8542 \times 10^{-12}\ \mathrm{C/(N \cdot m^2)}\ \ (= \mathrm{F/m})$$
$$\approx \left(\frac{1}{36\pi}\right) \times 10^{-9}\ \mathrm{F/m},$$
$$\mu_0 = 4\pi \times 10^{-7}\mathrm{N \cdot s^2/C^2}\ \ (= \mathrm{H/m}).$$

In c.g.s. units, $\varepsilon_0 = \mu_0 = 1$.

Maxwell's equations in c.g.s. units are written as

$$\nabla \cdot \mathbf{D} = 4\pi\rho,$$
$$\nabla \cdot \mathbf{B} = 0,$$
$$\nabla \times \mathbf{H} = \frac{4\pi}{c}\mathbf{J} + \frac{1}{c}\frac{\partial \mathbf{D}}{\partial t},$$
$$\nabla \times \mathbf{E} + \frac{1}{c}\frac{\partial \mathbf{B}}{\partial t} = 0.$$

A good discussion of the subject of units can be found in Jackson [1]. Here, we provide a brief table to aid the reader in converting from one system to the other.

REFERENCE

1. Jackson, J.D., *Clasical Electrodynamics*. 3rd ed. 1998: Wiley.

3

Reflection and Refraction

3.1 Introduction 52
3.2 Reflection and Transmission at a Discontinuity 53
3.3 Laws of Reflection and Refraction 56
3.4 Fresnel's Formula 58
3.5 Reflected and Transmitted Energy 63
3.6 Normal Incidence 65
3.7 Polarization by Reflection 68
3.8 Total Reflection 69
3.9 Reflection from a Conductor 73
3.10 Summary 75
3.11 Problems 77
References 78

3.1 Introduction

In Chapter 2, we treated the propagation of light in a uniform medium using Maxwell's equations. In this chapter, we wish to explore what happens to the propagation of a light wave when the electrical properties of the medium change in a discontinuous way. We will find that the wave will experience reflection at the boundary between two media with different electromagnetic properties. The light transmitted across the boundary will undergo a change in propagation direction. This direction change is called *refraction*. We will make the first of several derivations of the laws of refraction and reflection, here relying only on the wave properties of light to obtain these laws. To obtain the amplitude of the reflected and refracted light waves, we will use boundary conditions developed in classical electromagnetic theory for Maxwell's equations.

Once equations for the reflected and transmitted amplitudes have been obtained, we will consider light incident normal to the boundary to simplify the equations for the amplitudes of reflected and transmitted waves. With this simplification, it will become obvious that the fractions of the wave reflected and transmitted at the boundary between two media depend on the relative propagation velocities of the wave in the two media.

We will find that there is an angle, called Brewster's angle, for which light reflected from a boundary will be linearly polarized. There is also a set of conditions for which all light incident on a boundary will be reflected. A few of the properties of this reflected wave, called a totally reflected wave, will be discussed.

Use of reflection existed before written history, as is evidenced by the discovery of a mirror in Turkey from the period around 8000 years ago [1]. Some of the earliest written comments about reflection can be found in *Exodus* 38:8 and *Job* 37:18. **Euclid** in about 300 BC discussed the focus of a spherical mirror in his book *Catoptrics*. **Cleomedes** (AD 50) discussed refraction of light at an air–water interface. He described an experiment whereby a coin at the bottom of a bowl, and hidden by the bowl's sides, could be made visible by pouring water in the bowl.

Claudius Ptolemy of Alexandria (AD 139) made tables of the angles of incidence and refraction. His work is one of the few examples of experiment during that time. The concept of the sine of an angle was not yet developed, so his tables were only approximately correct. One of the most interesting individuals active in optics during the Middle Ages was **Alhazen** (Abû 'Alî al Hasan ibn al Hasan ibn Al Haitam, **965–1038**), who developed optics during the golden age of the Arabic empire. He added, to the law of reflection developed by Ptolemy, the fact that the incident angle and the reflected angle lie in the same plane, called the plane of incidence. He also corrected Ptolemy's tables of incident and refracted angles. Alhazen failed, however, to discover the law of refraction. (Alhazen was a successful optical scientist, but some of his civil engineering projects got him into trouble with his caliph, and Alhazen had to feign insanity and hide to escape the caliph's wrath.)

Vitello (in 1270) repeated Ptolemy's experiments, but also failed to discover the law of refraction. **Johannes Kepler (1571–1630)** gave a broad outline of the correct theory of the telescope and discussed total internal reflection without knowledge of the law of refraction. He used an empirical expression, $\theta_i = n\theta_r$, where $n = 3/2$.

Modern Optics. Second Edition. B. D. Guenther.

© B. D. Guenther 2015. Published in 2015 by Oxford University Press.

The law of refraction was discovered, evidently through experimentation, by **Willebrord Snellius (Willebrord Snel van Royen: 1580–1626)**, a professor of mathematics at Leiden. He never published, but Huygens and Isaak Voss claimed to have examined Snell's manuscript. Ibn Sahl is credited with the first discovery in 984, but he failed to get credit. **René Descartes (1596–1650)**, in 1637, deduced the law of refraction theoretically and expressed it in its present form. It is interesting that one of his assumptions was wrong. He often confidently deduced theory without allowing himself to be disturbed by any possible discrepancy between his final conclusions and the actual facts. Later, **Pierre de Fermat (1601–1665)** deduced the law of refraction from the assumption that light travels from a point in one medium to a point in another medium in the least time.

3.2 Reflection and Transmission at a Discontinuity

To develop the laws of reflection and refraction, we will first consider the one-dimensional problem of a vibrating string where the string has a discontinuous change in its mass/unit length at the origin of an (x, y) coordinate system (Figure 3.1). The string is stretched along the x-direction, and a wave propagating along the string in the positive x-direction creates a displacement in the y-direction. An example of such a string might be an "A" string of a guitar with part of its winding removed. In a string under tension T, the phase velocity of a wave is

$$\sqrt{\frac{T}{\mu}}. \tag{3.1}$$

[A dimensional analysis of this ratio,

$$T/\mu \Rightarrow (\text{kg} \cdot \text{m/s}^2)/(\text{kg/m}) = \text{m}^2/\text{s}^2 = (\text{velocity})^2,$$

supports the association of the ratio with velocity.] Therefore, a nonuniform wave propagation velocity will result from a nonuniform mass/unit length. What happens to the wave motion on a string with a nonuniform propagation velocity? Assume that the tension is the same throughout the string and that the mass/unit length is μ_1 for $x < 0$ and μ_2 for $x > 0$, as shown in Figure 3.1. We have two boundary conditions that must be satisfied at $x = 0$.

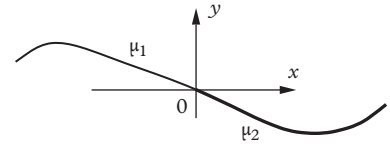

Figure 3.1 *String with a nonuniform mass/unit length. For $x < 0$, the mass/unit length is μ_1, while for $x > 0$, the mass/unit length is μ_2. The tension is the same throughout the string.*

1. The displacement at $x = 0$ must be the same for the two strings. If this were not the case, the string would be broken.
2. The slopes of the two strings must be the same at $x = 0$. We assume that the string undergoes small displacements so $\sin\theta \approx \tan\theta = dy/dx$. The vertical force at any point is therefore $T_y = T dy/dx$. If the slopes were not equal, there would be a finite vertical force acting on an infinitesimal mass, and the acceleration at $x = 0$ would be infinite.

Initially, we will assume that there are two waves present. One wave is incident from the left and propagating toward $x = 0$, traveling from left to right in Figure 3.1. This incident wave is given by

$$y_i = Y_i \cos(\omega_i t - k_i x), \qquad x < 0.$$

The speed of the wave is

$$c_1 = \sqrt{\frac{T}{\mu_1}}.$$

At the origin, $x = 0$, the wave and its first derivative are

$$y_i\Big|_{x=0} = Y_i \cos \omega_i t, \qquad \frac{dy_i}{dx}\Big|_{x=0} = k_i Y_i \sin \omega_i t.$$

The second wave, called the transmitted wave, is one that has propagated past $x = 0$, also traveling from left to right in Figure 3.1. The transmitted wave is represented by

$$y_t = Y_t \cos(\omega_t t - k_t x), \qquad x > 0,$$

with a propagation velocity given by {1}. At $x = 0$, the wave and its first derivative are

$$y_t\Big|_{x=0} = Y_t \cos \omega_t t, \qquad \frac{dy_t}{dx}\Big|_{x=0} = k_t Y_t \sin \omega_t t.$$

We will attempt to satisfy the boundary conditions with these two waves, but will discover that a third wave will be needed if the boundary conditions are to be satisfied.

The first boundary condition requires that the waves be equal at $x = 0$ and is met if $Y_i = Y_t$. Since the boundary condition must hold for all time, the frequencies of the waves propagating at the two different velocities must be the same, $\omega_i = \omega_t$.

The second boundary condition requires that the first derivatives of the two waves must be equal at $x = 0$, and we find again that $\omega_i = \omega_t$, since the equality must hold for all time. The second boundary condition also requires that

$$k_i Y_i = k_t Y_t,$$

but, because $Y_i = Y_t$ from the first boundary condition, we must have $k_i = k_t$. The definition (1.2) allows the replacement of the propagation constants by $\omega_i/c_1 = \omega_t/c_2$. Because the two frequencies are required to be equal by the boundary conditions, we are led to a contradiction of the initial assumption that the propagation velocities in the two dissimilar string segments are unequal, $c_1 \neq c_2$.

To overcome this contradiction and satisfy the boundary conditions, a reflected wave must be introduced, traveling from right to left and originating at $x = 0$. The reflected wave is defined as

$$y_r = Y_r \cos(\omega_r + k_r x), \qquad x < 0.$$

Its propagation velocity is c_1. The evaluation of the wave and its first derivative at the origin yields

$$y_r\Big|_{x=0} = Y_r \cos \omega_r t, \qquad \frac{dy_r}{dx}\Big|_{x=0} = -k_r Y_r \sin \omega_r t.$$

With the new wave, the boundary conditions are written

$$y_i + y_r - y_t\Big|_{x=0} = 0, \qquad \frac{dy_i}{dt} + \frac{dy_r}{dt} + \frac{dy_t}{dt}\Big|_{x=0} = 0.$$

These two equations are satisfied if

$$\omega_i = \omega_r = \omega_t, \tag{3.2}$$

$$Y_i + Y_r = Y_t, \tag{3.3}$$

$$k_i Y_i - k_r Y_r = k_t Y_t. \tag{3.4}$$

Solving (3.3) and (3.4) simultaneously yields

$$Y_t = \frac{k_i + k_r}{k_t + k_r} Y_i = \frac{\omega\left(\frac{1}{c_1} + \frac{1}{c_1}\right)}{\omega\left(\frac{1}{c_1} + \frac{1}{c_2}\right)} Y_i = \frac{2\frac{\omega}{c_1}}{\left(\frac{\omega}{c_1 c_2}\right)(c_1 + c_2)} Y_i.$$

The transmission coefficient at the junction of the two dissimilar strings is defined as $\tau = Y_t / Y_i$ and is given by

$$\tau = \frac{2c_2}{c_1 + c_2}. \tag{3.5}$$

In the same way, a reflection coefficient can also be defined at the junction where the mass/unit length of the string changes:

$$\rho = \frac{Y_r}{Y_i} = \frac{c_2 - c_1}{c_1 + c_2}. \tag{3.6}$$

If $c_1 = c_2$ then $Y_r = 0$, there is no reflected wave, and the incident and transmitted waves have equal amplitudes, $Y_i = Y_t$. The wave propagates pass the point $x = 0$ without change. Note that the transmission and reflection coefficients are functions only of the wave velocities. This same dependence upon propagation velocity will be found for light waves.

The frequency across the discontinuity is required, by the boundary conditions, to be a constant, but the velocity changes. This means that the wavelength must also change, as is shown in Figure 3.2. There are two waves to the left of the origin. From the principle of superposition, the displacement of the string at any time is a sum of these two waves: the incident wave and the reflected wave. The addition of the incident and reflected waves leads to a standing wave if the wave is totally reflected at the discontinuity.

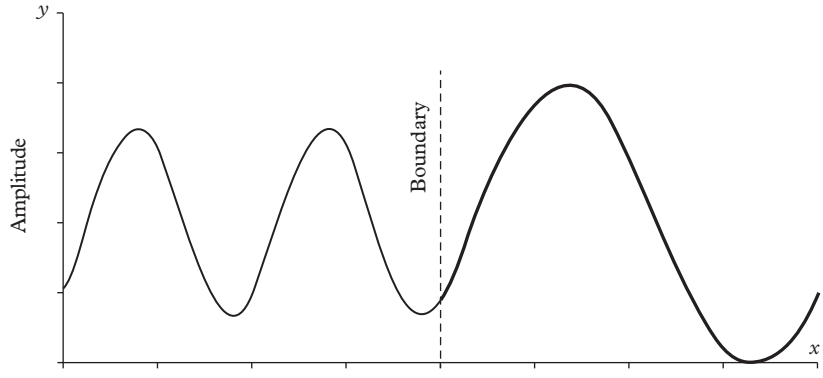

Figure 3.2 *Two strings of unequal mass/unit length joined at x = 0. The wave velocity of the string to the left is 20 m/s and that to the right is 10 m/s. The wave is incident onto the junction from the left and has amplitude of 3 cm and a wavelength of 1 m. The plot shows the resultant waves: on the right of x = 0 the transmitted wave and on the left of x = 0 the sum of the incident and reflected waves.*

Total reflection will occur if the string on the right of Figure 3.1 is replaced by a rigid support. The rigid support is equivalent to a string with an infinite mass/unit length, $\mu_2 = \infty$. Since T, the tension in the string, is finite, the propagation velocity is zero, $c_2 = 0$. The transmitted amplitude is then $Y_t = 0$, and $Y_i = -Y_r = Y$. The wave is totally reflected, i.e., $\rho = -1$ and $\tau = 0$. From the superposition principle, the incident and reflected waves add together to produce the resultant wave, a standing wave:

$$\begin{aligned} y &= y_i + y_r \\ &= Y[\cos(\omega t - kx) - \cos(\omega t + kx)] \\ &= 2Y \sin \omega t \sin kx. \end{aligned}$$

(The addition of waves will be discussed in more detail in Chapter 4.)

3.3 Laws of Reflection and Refraction

The three-dimensional problem of a wave propagating across a boundary, where a discontinuous change of propagation velocity occurs, can be studied by using the coordinate system shown in Figure 3.3. The result will be an extension, to three dimensions, of the one-dimensional laws of reflection and refraction we have just derived. We will perform the derivation by only requiring the phase of the wave to vary smoothly across the boundary.

The wave velocity in the medium in the upper half-plane of Figure 3.3 is v_i. For a light wave, this propagation velocity can be indicated by characterizing the medium with the index of refraction $n_i = c/v_i$, (2.11). The incident wave is assumed to be a plane wave, defined in (1.16) to be of the form $F(\omega t - \mathbf{k} \cdot \mathbf{r})$. To learn something about the geometry of the reflective and refractive waves, we require that the phases of the three wavefunctions,

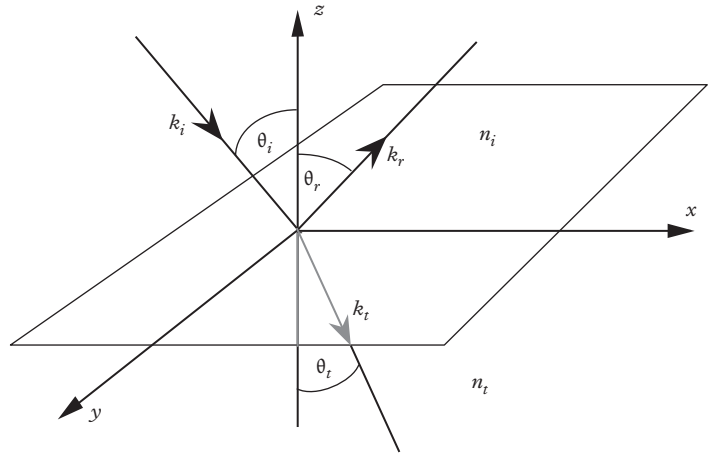

Figure 3.3 *Coordinate diagram for light reflection and transmission across a boundary. The index of refraction in the upper half-plane is n_i and that in the lower half-plane is n_t.*

incident, reflected, and transmitted, be the same on the boundary between the two half-planes (at $z = 0$):

$$\omega_i t - \mathbf{k}_i \cdot \mathbf{r}|_{z=0} = \omega_i t - \mathbf{k}_r \cdot \mathbf{r}|_{z=0} = \omega_t t - \mathbf{k}_t \cdot \mathbf{r}|_{z=0}\,. \tag{3.7}$$

Since the equality (3.7) must hold for all time, the frequency of the wave across the boundary does not change, $\omega_i = \omega_t = \omega$. At $z = 0$, we have

$$\mathbf{r} \to (x, y, 0), \qquad \mathbf{k}_i \to \left(\frac{n_i\omega}{c}\right)(k_x^i, k_y^i, k_z^i),$$

$$\mathbf{k}_r \to \left(\frac{n_i\omega}{c}\right)(k_x^r, k_y^r, k_z^r), \qquad \mathbf{k}_t \to \left(\frac{n_t\omega}{c}\right)(k_x^t, k_y^t, k_z^t),$$

where the (k_x^i, k_y^i, k_z^i) and (k_x^t, k_y^t, k_z^t) are the direction cosines of the incident and transmitted waves, i.e., for the incident wave in a rectangular coordinate system,

$$\mathbf{k}_i = \left(\frac{n_i\omega}{c}\right)(k_x^i\hat{\mathbf{i}} + k_y^i\hat{\mathbf{j}} + k_z^i\hat{\mathbf{k}}).$$

The spatial part of the phase must meet the equality in (3.7), independent of the temporal part; therefore, since the boundary has been positioned at $z = 0$,

$$\frac{n_i\omega}{c}(k_x^i x + k_y^i y) = \frac{n_i\omega}{c}(k_x^r x + k_y^r y) = \frac{n_t\omega}{c}(k_x^t x + k_y^t y).$$

This relationship must hold independently for all values of x and y:

$$n_i k_x^i = n_i k_x^r = n_t k_x^t, \qquad n_i k_y^i = n_i k_y^r = n_t k_y^t. \tag{3.8}$$

The relationships in (3.8) require that both the transmitted and reflected waves lie in the same plane as the incident wave. We call this plane the *plane of incidence* and define it as the plane containing the incident wave vector $\mathbf{k}_i$ and the normal to the boundary, at the point where $\mathbf{k}_i$ intersects the boundary.

In this discussion, the boundary is taken to be the $z = 0$, (x, y) plane; the normal to the plane is the unit vector $\hat{\mathbf{k}}$ parallel to the z-axis. (Note that $\hat{\mathbf{k}}$ is the unit vector along the z-direction and that $\mathbf{k}$ is the wavevector—the "hat" on the unit vector and the context of the discussion should prevent confusion.) The plane of incidence is arranged to lie in the (x, z) plane, as shown in Figure 3.3. The direction cosines associated with the propagation vectors are thus

$$\begin{aligned} k_x^i &= \sin\theta_i, & k_y^i &= 0, & k_z^i &= \cos\theta_i, \\ k_x^r &= \sin\theta_r, & k_y^r &= 0, & k_z^r &= \cos\theta_r, \\ k_x^t &= \sin\theta_t, & k_y^t &= 0, & k_z^t &= \cos\theta_t. \end{aligned}$$

Equation (3.8) can now be written

$$n_i \sin\theta_i = n_i \sin\theta_r = n_t \sin\theta_t.$$

From this expression, we have, in the first medium,

$$\sin\theta_i = \sin\theta_r \tag{3.9}$$

If the coordinate system is selected so that $\mathbf{k}_i$ is propagating in the positive direction and $\cos\theta_i \geq 0$, then it is apparent from Figure 3.3 that $\mathbf{k}_r$ is in the negative direction and $\cos\theta_r \leq 0$, resulting in $\theta_r = \pi - \theta_i$. The statement that the reflected wave is in the same plane as the incident wave together with (3.9) form the *law of reflection*.

Returning to (3.8), the second relationship is

$$n_i \sin\theta_i = n_t \sin\theta_t, \tag{3.10}$$

which is the *law of refraction* or *Snell's law.*

By requiring phase continuity across the boundary, we have obtained the laws of reflection and refraction. These relations hold for any solution of the wave equation and are not dependent upon the electromagnetic properties of light waves. Later, we will use other approaches to obtain these laws.

3.4 Fresnel's Formula

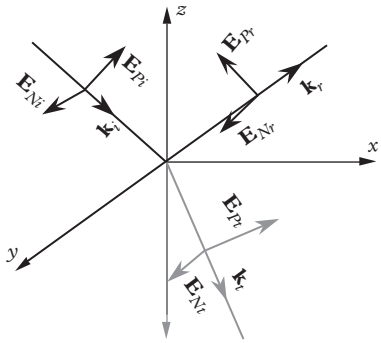

Figure 3.4 *Orientation of the electric field and wave vectors in the coordinate system we have selected for the discussion of reflection and refraction. The plane of incidence is the (x, z)-plane.*

The geometry of reflected and transmitted waves have been obtained using only the wave character of light; however, nothing about the amplitudes of the waves has been determined. We must use Maxwell's equations and the boundary conditions associated with these equations to learn about the amplitudes of the reflected and transmitted waves. The geometry to be used in this discussion is shown in Figure 3.4. Two media are separated by an interface, the (x, y) plane at $z = 0$, whose normal, $\hat{\mathbf{n}} = \hat{\mathbf{k}}$, is the unit vector along the z-direction. The incident wave is labeled with an i, the reflected wave with an r, and the transmitted wave with a t. The incident wave's propagation vector $\mathbf{k}_i$, which we assume to lie in the (x, z) plane, and the normal to the interface establish the plane of incidence.

The electric field vectors for each of the three waves have been decomposed into two components: one in the plane of incidence, labeled P, and one normal to the plane and parallel to the unit vector $\hat{\mathbf{j}}$ along the y-axis, labeled N. This is an extension of the technique, discussed in Chapter 2, of using orthogonal vectors to describe the polarization of a light wave. [According to custom, the two polarizations are labeled π for parallel to the plane of incidence and σ for perpendicular to the plane of incidence (the Greek letter sigma σ denotes perpendicular because "s" is the first letter of the German word *senkrecht*). However, we will use N and P in this book in place of the Greek letters.] The upper half-plane has a velocity of propagation v_i and an index n_i, and the lower half-plane has a velocity of propagation v_t and an index n_t.

The actual vectors to be used are as follows:

- **incident wave**

$$\mathbf{k}_i = k_i\left(\hat{\mathbf{i}}\sin\theta_i - \hat{\mathbf{k}}\cos\theta_i\right), \tag{3.11}$$

$$\mathbf{E}_i = E_{Pi}\left(\hat{\mathbf{i}}\cos\theta_i + \hat{\mathbf{k}}\sin\theta_i\right) + E_{Ni}\hat{\mathbf{j}}; \tag{3.12}$$

- **reflected wave**

$$\mathbf{k}_r = k_i\left(\hat{\mathbf{i}}\sin\theta_i + \hat{\mathbf{k}}\cos\theta_i\right), \tag{3.13}$$

$$\mathbf{E}_r = E_{Pr}\left(-\hat{\mathbf{i}}\cos\theta_i + \hat{\mathbf{k}}\sin\theta_i\right) + E_{Nr}\hat{\mathbf{j}}; \tag{3.14}$$

- **transmitted wave**

$$\mathbf{k}_t = k_t\left(\hat{\mathbf{i}}\sin\theta_t - \hat{\mathbf{k}}\cos\theta_t\right), \tag{3.15}$$

$$\mathbf{E}_t = E_{Pt}\left(\hat{\mathbf{i}}\cos\theta_t + \hat{\mathbf{k}}\sin\theta_t\right) + E_{Nt}\hat{\mathbf{j}}. \tag{3.16}$$

The boundary conditions associated with Maxwell's equations are as follows:

1. From $\nabla \cdot \mathbf{D} = \rho$, the normal components of $\mathbf{D}$ must be continuous if there are no surface charges. We use $\mathbf{D} = \varepsilon \mathbf{E}$ to write this boundary condition:

$$[\varepsilon_i(\mathbf{E}_i + \mathbf{E}_r) - \varepsilon_t \mathbf{E}_t] \cdot \hat{\mathbf{n}} = 0. \tag{3.17}$$

   Evaluating the dot product yields

$$\varepsilon_i \sin\theta_i \, (E_{Pi} + E_{Pr}) = \varepsilon_t \sin\theta_t E_{Pt}. \tag{3.18}$$

2. From Maxwell's equation containing $\nabla \times \mathbf{E}$, the tangential component of $\mathbf{E}$ is continuous. This boundary condition is written

$$(\mathbf{E}_i + \mathbf{E}_r + \mathbf{E}_t) \times \hat{\mathbf{n}} = 0. \tag{3.19}$$

   Each of the vector products is of the form

$$\mathbf{E} \times \hat{\mathbf{n}} = E_y \hat{\mathbf{i}} - E_x \hat{\mathbf{j}}.$$

   Evaluating the cross product yields

$$(E_{Ni} + E_{Nr} - E_{Nt})\hat{\mathbf{i}} - (E_{Pi}\cos\theta_i - E_{Pr}\cos\theta_i - E_{Pt}\cos\theta_t)\hat{\mathbf{j}} = 0.$$

   Both vector components must be equal to zero, and thus

$$E_{Ni} + E_{Nr} = E_{Nt}, \tag{3.20}$$

$$(E_{Pi} - E_{Pr})\cos\theta_i = E_{Pt}\cos\theta_t. \tag{3.21}$$

3. From $\nabla \cdot \mathbf{B} = 0$, the normal component of $\mathbf{B}$ must be continuous. We use (2.17) to rewrite the normal component of $\mathbf{B}$ in terms of $\mathbf{E}$:

$$\mathbf{B} \cdot \hat{\mathbf{n}} = \left(\frac{\sqrt{\mu\varepsilon}}{k}\right)\mathbf{k} \times \mathbf{E} \cdot \hat{\mathbf{n}}.$$

   The boundary condition is then written

$$\left[\frac{\sqrt{\mu_i\varepsilon_i}}{k_i}(\mathbf{k}_i \times \mathbf{E}_i + \mathbf{k}_r \times \mathbf{E}_r) - \frac{\sqrt{\mu_t\varepsilon_t}}{k_t}(\mathbf{k}_t \times \mathbf{E}_t)\right] \cdot \hat{\mathbf{n}} = 0. \tag{3.22}$$

   Each of the vectors will be of the form

$$(\mathbf{k} \times \mathbf{E}) \cdot \hat{\mathbf{n}} = [(E_y k_z - E_z k_y)\hat{\mathbf{i}} + (E_z k_x - E_x k_z)\hat{\mathbf{j}} + (E_x k_y - E_y k_x)\hat{\mathbf{k}}] \cdot \hat{\mathbf{k}} = -E_y k_x,$$

$$\sqrt{\mu_i\varepsilon_i}\,(E_{Ni} + E_{Nr})\sin\theta_i = \sqrt{\mu_t\varepsilon_t}\,E_{Nt}\sin\theta_t. \tag{3.23}$$

   We can simplify this relationship by rewriting Snell's law (3.10) as

$$\frac{\sin\theta_t}{\sin\theta_i} = \sqrt{\frac{\mu_i\varepsilon_i}{\mu_t\varepsilon_t}}. \tag{3.24}$$

   Equation (3.23) can then be seen to be the same as (3.20). This boundary condition is redundant, and we need not use it.

4. From Maxwell's equation containing $\nabla \times \mathbf{H}$, the tangential component of $\mathbf{H}$ is continuous if there are no surface currents. The tangential component of $\mathbf{H}$ can be written in terms of the electric field:

$$\mathbf{H} \times \hat{\mathbf{n}} = \frac{\mathbf{B}}{\mu} \times \hat{\mathbf{n}} = \frac{\sqrt{\mu\varepsilon}}{\mu k} \mathbf{k} \times \mathbf{E} \times \hat{\mathbf{n}}. \tag{3.25}$$

The boundary condition is then written

$$\left[\frac{1}{k_i} \sqrt{\frac{\varepsilon_i}{\mu_i}} (\mathbf{k}_i \times \mathbf{E}_i + \mathbf{k}_r \times \mathbf{E}_r) - \frac{1}{k_t} \sqrt{\frac{\varepsilon_t}{\mu_t}} (\mathbf{k}_t \times \mathbf{E}_t) \right] \times \hat{\mathbf{n}} = 0,$$

$$\begin{aligned} (\mathbf{k} \times \mathbf{E}) \times \hat{\mathbf{n}} &= [(E_y k_z - E_z k_y)\hat{\mathbf{i}} + (E_z k_x - E_x k_z)\hat{\mathbf{j}} + (E_x k_y - E_y k_x)\hat{\mathbf{k}}] \times \hat{\mathbf{k}} \\ &= (E_z k_x - E_x k_z)\hat{\mathbf{i}} - E_y k_z \hat{\mathbf{j}} = 0. \end{aligned} \tag{3.26}$$

Each vector component must equal zero. The x-component gives

$$\sqrt{\frac{\varepsilon_i}{\mu_i}} (E_{Pi} + E_{Pr}) = \sqrt{\frac{\varepsilon_t}{\mu_t}} E_{Pt}. \tag{3.27}$$

If we apply Snell's law (3.24) to (3.18), we obtain the same equation as (3.27). Therefore, we do not need boundary condition 1. The y-component of (3.26) gives

$$\sqrt{\frac{\varepsilon_i}{\mu_i}} (E_{Ni} - E_{Nr}) \cos\theta_i = \sqrt{\frac{\varepsilon_t}{\mu_t}} E_{Nt} \cos\theta_t. \tag{3.28}$$

Of the four boundary conditions for Maxwell's equations, only two are needed to obtain the relationships between the incident, reflected, and transmitted waves; the conditions utilized are that the tangential components of $\mathbf{E}$ and $\mathbf{H}$ be continuous across the boundary. The boundary conditions place independent requirements on the polarizations parallel to and normal to the plane of incidence and generate two pair of equations that are treated separately. There are three unknowns but only two equations for each polarization; thus, the amplitudes of the reflected and transmitted light can only be found in terms of the incident amplitude.

3.4.1 σ Case (Perpendicular Polarization)

For this component of the polarization, $\mathbf{E}$ is perpendicular to the plane of incidence, i.e., the (x, z) plane. This means that $\mathbf{E}$ is everywhere normal to $\hat{\mathbf{n}}$ and parallel to the boundary surface between the two media. [This case could be labeled the *transverse electric field* (TE) case. However, we do not use this notation, because it implies that the wave may not be a transverse electromagnetic wave (a TEM wave); instead, we use the subscript N, and the TE notation will be reserved for inhomogeneous waves in a guiding structure, discussed in Chapter 5.]

The second and fourth boundary conditions provide, in (3.20) and (3.28), relationships between the various normal electric fields. The amplitudes of reflected and transmitted light will be found, using these equations, in terms of the incident amplitude. We use Snell's law (3.24) to modify (3.28):

$$E_{Ni} - E_{Nr} = \frac{\mu_i \sin\theta_i}{\mu_t \cos\theta_i} \frac{\cos\theta_t}{\sin\theta_t} E_{Nt} = \frac{\mu_i \tan\theta_i}{\mu_t \tan\theta_t} E_{Nt}. \tag{3.29}$$

Adding (3.29) to (3.20) yields

$$2E_{Ni} = \left(1 + \frac{\mu_i \tan\theta_i}{\mu_t \tan\theta_t}\right) E_{Ni},$$

$$\frac{E_{Nt}}{E_{Ni}} = \frac{2}{1 + \dfrac{\mu_i \tan\theta_i}{\mu_t \tan\theta_t}}. \tag{3.30}$$

As was shown in Chapter 2, for the majority of optical materials, $\mu_i \approx \mu_t$, and the equation simplifies to

$$t_N = \frac{E_{Nt}}{E_{Ni}} = \frac{2\sin\theta_t \cos\theta_i}{\sin(\theta_i + \theta_t)}. \tag{3.31}$$

The amplitude ratio t_N is called the amplitude transmission coefficient for perpendicular polarization.

Now, (3.30) can be substituted back into (3.20) to obtain the amplitude ratio for the reflected light:

$$E_{Ni} + E_{Nr} = \frac{2E_{Ni}}{1 + \dfrac{\mu_i \tan\theta_i}{\mu_t \tan\theta_t}},$$

$$\frac{E_{Nr}}{E_{Ni}} = \frac{1 - \left(\dfrac{\mu_i \tan\theta_i}{\mu_t \tan\theta_t}\right)}{1 + \left(\dfrac{\mu_i \tan\theta_i}{\mu_t \tan\theta_t}\right)}. \tag{3.32}$$

Again, when $\mu_i \approx \mu_t$, we obtain the ratio of reflected amplitude to the incident amplitude, which is called the amplitude reflection coefficient for perpendicular polarization:

$$r_N = \frac{E_{Nr}}{E_{Ni}} = \frac{-\sin(\theta_i - \theta_t)}{\sin(\theta_i + \theta_t)}. \tag{3.33}$$

3.4.2 π Case (Parallel Polarization)

For this component of polarization, **E** is everywhere parallel to the plane of incidence; however, **B** and **H** are everywhere normal to $\hat{\mathbf{n}}$ and parallel to the boundary between the two media. [This case could be labeled the *transverse magnetic field* (TM) case, but we will use the subscript *P* for the same reason we did not use the TE notation; see Chapter 5, where the TM notation is utilized for inhomogeneous waves.] The second boundary condition provides (3.21), which can be written

$$E_{Pi} - E_{Pr} = \frac{\cos\theta_t}{\cos\theta_i} E_{Pt}. \tag{3.34}$$

Applying Snell's law (3.24) to (3.27) yields

$$E_{Pi} + E_{Pr} = \sqrt{\frac{\mu_i \varepsilon_t}{\mu_t \varepsilon_i}}\, E_{Pt} = \frac{\mu_i \sin\theta_i}{\mu_t \sin\theta_t} E_{Pt}. \tag{3.35}$$

Adding this equation to (3.34) yields the desired ratio of amplitudes

$$\frac{E_{Pt}}{E_{Pi}} = \frac{2\cos\theta_i \sin\theta_t}{\cos\theta_t \sin\theta_t + \dfrac{\mu_i}{\mu_t}\cos\theta_i \sin\theta_i}. \tag{3.36}$$

For the usual situation of $\mu_i \approx \mu_t$, the amplitude transmission coefficient for parallel polarization is

$$t_P = \frac{E_{Pt}}{E_{Pi}} = \frac{2\cos\theta_i \sin\theta_t}{\sin(\theta_i + \theta_t)\cos(\theta_i - \theta_t)}. \tag{3.37}$$

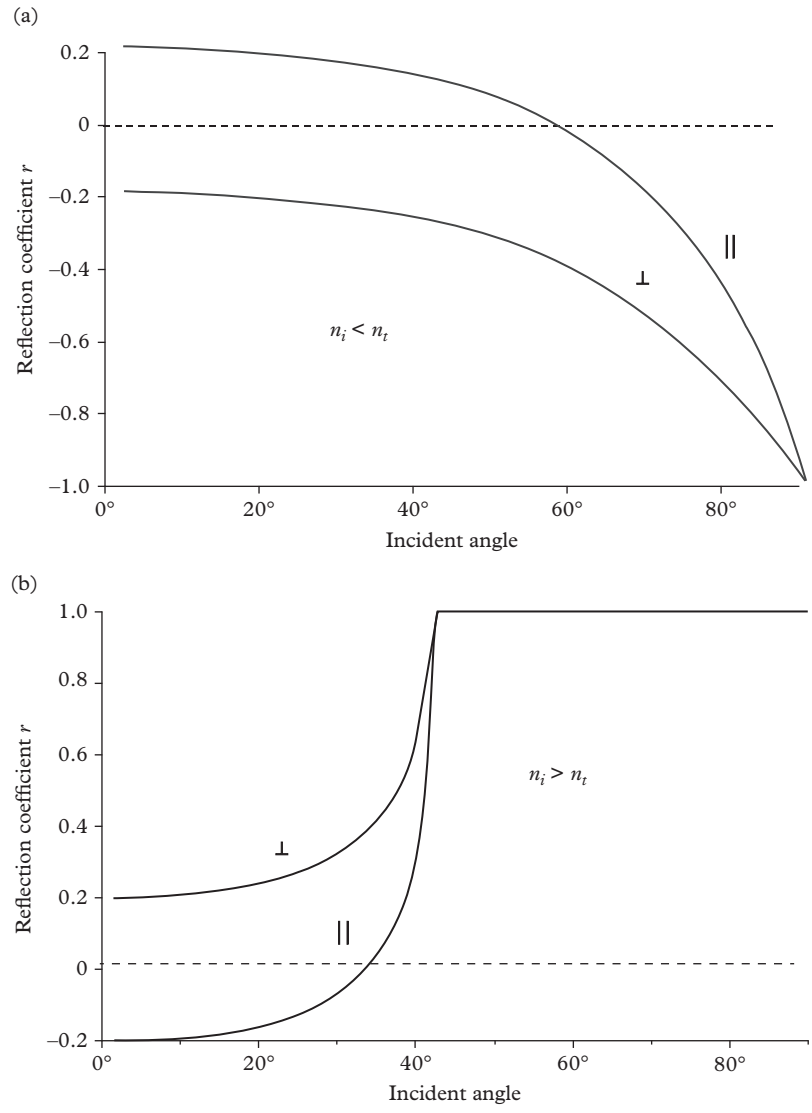

Figure 3.5 *(a) Reflection coefficient for $n_i = 1.0$ and $n_t = 1.5$, i.e., the ratio of index of refraction is 1.5. (b) Reflection coefficient for $n_i = 1.5$ and $n_t = 1$, i.e., the ratio of index of refraction is 0.67.*

Substituting (3.37) into (3.35) produces the amplitude reflection ratio

$$\frac{E_{Pr}}{E_{Pi}} = \frac{\left(\frac{\mu_i}{\mu_t}\right)\sin 2\theta_i - \sin 2\theta_t}{\sin 2\theta_t + \left(\frac{\mu_i}{\mu_t}\right)\sin 2\theta_i}. \tag{3.38}$$

The assumption of $\mu_i \approx \mu_t$ (this assumption will be used from now on) results in a reflection coefficient for parallel polarization of

$$r_P = \frac{E_{Pr}}{E_{Pi}} = \frac{\tan(\theta_i - \theta_t)}{\tan(\theta_i + \theta_t)}. \tag{3.39}$$

The amplitude reflection coefficients are plotted as functions of incident angle in Figure 3.5. Figure 3.5(a) corresponds to the condition $n_i < n_t$ and 3.5(b) to the condition $n_i > n_t$. As can be seen by examining the two figures, the behavior of the reflection coefficient is quite different for these two conditions.

The plots of the reflection coefficients shown in Figure 3.5 demonstrate that a sign change occurs for r_P, labeled II in the figure, and the angle where the transition occurs depends on the relative index of refraction. This phase change is important, because r_P must pass through zero for the phase change to occur.

We will discuss in detail the behavior of the amplitude reflectance coefficient when $\theta \approx 0°$, when $r_P = 0$, and when $r = 1$, which occurs if $n_i > n_t$, as shown in Figure 3.5(b).

3.5 Reflected and Transmitted Energy

The fractions of the incident amplitude reflected and transmitted at a surface are not experimentally available. The parameter that can be measured is the energy. At first, we might think that we could simply square the ratios we have derived to obtain the energies, but this would lead to erroneous results. The correct way to proceed is to use the average Poynting vector incident on a unit area, given by

$$\langle \mathbf{S} \rangle \cdot \hat{\mathbf{n}} = |\langle \mathbf{S} \rangle| \cos\theta_i,$$

where the expression for the average Poynting vector is obtained from (2.26). (We assume that $\mu \approx \mu_0$, resulting in

$$\mu c = \sqrt{\frac{\mu_0}{\varepsilon_0}} \approx 377 \text{ ohms},$$

which is defined as the impedance of the vacuum.) The energy flow across the boundary can be obtained from the equations

$$v_i \langle U_i \rangle = \langle S_i \rangle \cos\theta_i = \frac{n_i}{2}\sqrt{\frac{\varepsilon_0}{\mu_0}}\,|E_i^2| \cos\theta_i, \tag{3.40}$$

$$v_r \langle U_r \rangle = \langle S_r \rangle \cos\theta_i = \frac{n_i}{2}\sqrt{\frac{\varepsilon_0}{\mu_0}}\,|E_r^2| \cos\theta_i, \tag{3.41}$$

$$v_t \langle U_t \rangle = \langle S_t \rangle \cos\theta_t = \frac{n_t}{2}\sqrt{\frac{\varepsilon_0}{\mu_0}}\,|E_t^2| \cos\theta_t. \tag{3.42}$$

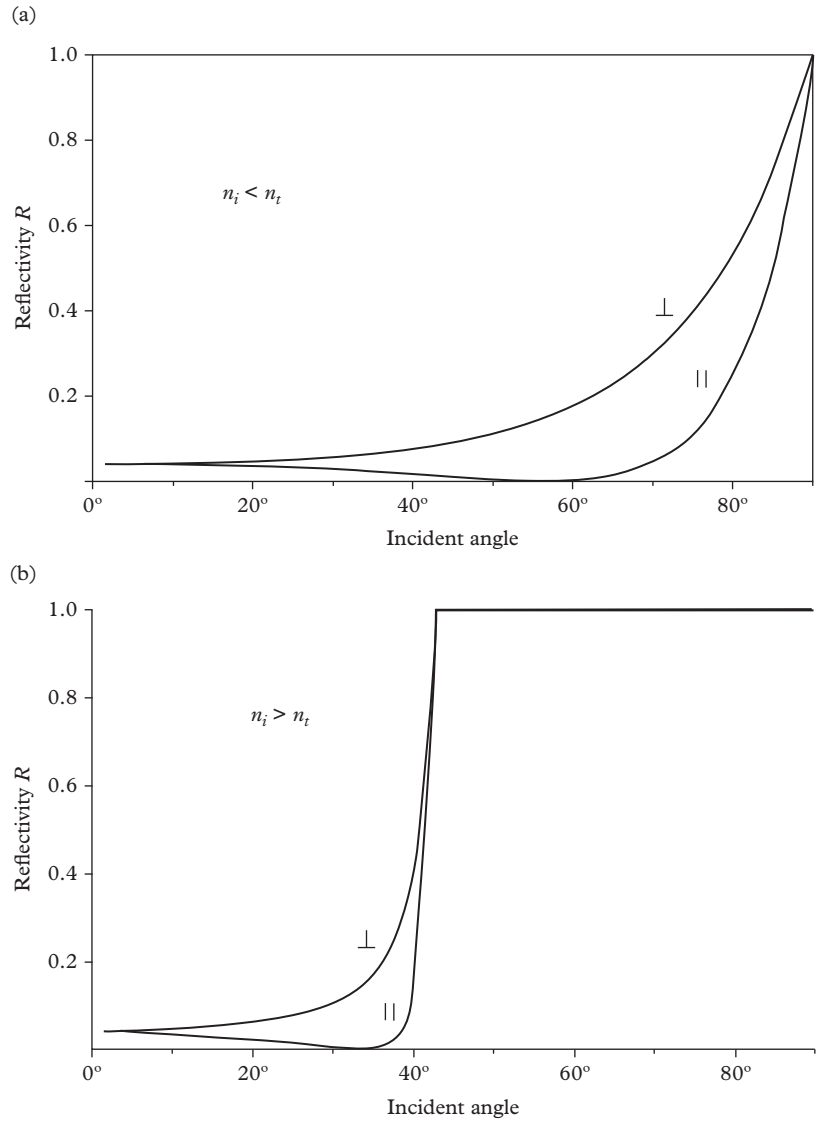

Figure 3.6 *Reflectivity as a function of incident angle: (a) for $n_i = 1.0$ and $n_t = 1.5$; (b) for $n_i = 1.5$ and $n_t = 1$.*

Each of these three equations applies separately to the normal and parallel components of polarization, resulting in six equations for the description of reflected and transmitted energy at a boundary.

We define the *reflectivity* as

$$R = \frac{\langle U_r \rangle}{\langle U_i \rangle} = \frac{|E_r|^2}{|E_i|^2} \tag{3.43}$$

and the *transmissivity* as

$$T = \frac{v_t \langle U_t \rangle}{v_i \langle U_i \rangle} = \left(\frac{n_t}{n_i}\right) \frac{\cos\theta_t}{\cos\theta_i} \frac{|E_t|^2}{|E_i|^2}. \tag{3.44}$$

[The quantities defined by (3.43) and (3.44) are ratios of the Poynting vectors and therefore assume a wave of known frequency and phase. Experimentally, the ratios of the incident flux to the reflected and transmitted flux are determined using radiometric units called the *reflectance* and the *transmittance*.] The expressions for the reflectivity and the transmissivity can be used to demonstrate that energy is conserved, $T + R = 1$, when light encounters a boundary (see Problem 3.9).

Figure 3.6 displays the dependence of the reflectivity on the angle of incidence for both polarizations. Here, as was done for the amplitude reflection coefficient, the conditions $n_i < n_t$ and $n_i > n_t$ are shown. The special cases when $r_N^2 = r_P^2 = 1$ and $r_P^2 = 0$ are quite noticeable. After first discussing reflection and transmission when a light wave is incident normal to the boundary, we will examine these special cases.

3.6 Normal Incidence

The meaning of a plane of incidence is lost for an incident angle of $\theta \approx 0$, since the two vectors that are suppose to define the plane are parallel and thus cannot define a plane. Upon examining Figure 3.6, it can be seen that $R_N = R_P$ when $\theta < 10°$. For these reasons, at normal incidence, i.e., when $\theta_i \approx 0$, the distinction between the normal and parallel polarizations is lost.

The reflection and transmission coefficients at $\theta = 0°$ can be found if the limit of the coefficients is taken as $\theta \to 0°$. The sine in the denominator of (3.37) can be eliminated by using Snell's law and the two trigonometric identities

$$\sin(\theta_i + \theta_t) = \sin\theta_i \cos\theta_t + \cos\theta_i \sin\theta_t,$$
$$\cos(\theta_i - \theta_t) = \cos\theta_i \cos\theta_t + \sin\theta_i \sin\theta_t.$$

This gives

$$\frac{E_{Pt}}{E_{Pi}} = \frac{2\cos\theta_i \sin\theta_t}{\sin\theta_t \left[\left(\frac{n_t}{n_i}\right)\cos\theta_t + \cos\theta_i\right][\cos\theta_i \cos\theta_t + \sin\theta_i \sin\theta_t]}.$$

$\sin\theta_t$ cancels out of the numerator and denominator, so that the limit of the ratio as θ_i and $\theta_t \to 0°$ is found to be

$$\frac{E_{Pt}}{E_{Pi}} = \frac{2n_i}{n_t + n_i}. \tag{3.45}$$

In the same way, the limit of (3.31) as $\theta \to 0°$ is found to be

$$\frac{E_{Nt}}{E_{Ni}} = \frac{2n_i}{n_t + n_i},$$

yielding the same transmission coefficient for the two polarizations.

The limit of (3.33) as $\theta \to 0°$ can also be obtained using the above identities:

$$\frac{E_{Nr}}{E_{Ni}} = \frac{-\sin\theta_t \left[\left(\frac{n_t}{n_i}\right)\cos\theta_t - \cos\theta_i\right]}{\sin\theta_t \left[\left(\frac{n_t}{n_i}\right)\cos\theta_t + \cos\theta_i\right]} = \frac{-(n_t - n_i)}{n_t + n_i}. \tag{3.46}$$

The limit of (3.39) is a little more difficult to obtain because terms that go to zero as θ approaches zero do not cancel out of the equation

$$\frac{E_{Pr}}{E_{Pi}} = \frac{\left[\frac{\sin(\theta_i - \theta_t)}{\cos(\theta_i - \theta_t)}\right]}{\left[\frac{\sin(\theta_i + \theta_t)}{\cos(\theta_i + \theta_t)}\right]}.$$

Near normal incidence, $\theta_i \approx \theta_t \approx 0$ and we have $\cos\theta_i = \cos\theta_t \approx 1$ and $\sin\theta_t \approx \theta_t$, leading to

$$\sin\theta_i = \left(\frac{n_t}{n_i}\right)\sin\theta_t = \left(\frac{n_t}{n_i}\right)\theta_t.$$

We can write

$$\begin{aligned}\frac{\sin(\theta_i \pm \theta_t)}{\cos(\theta_i \pm \theta_t)} &\approx \frac{\sin\theta_i\cos\theta_t \pm \cos\theta_i\sin\theta_t}{\cos\theta_i\cos\theta_t - \sin\theta_i\sin\theta_t}, \\ &\approx \frac{\left(\frac{n_t}{n_i}\right)\theta_t \pm \theta_t}{1 - \left(\frac{n_t}{n_i}\right)\theta_t^2}.\end{aligned}$$

Keeping only terms linear in θ_t gives

$$\frac{E_{Pr}}{E_{Pi}} = \frac{n_t - n_i}{n_t + n_i}. \tag{3.47}$$

The reflection coefficient is directly proportional to the difference between the propagation velocities of the two media forming the interface—a result identical to the one obtained for waves on a string, (3.5). Experimental proof of this result is shown in Figure 3.7. A glass rod, with an index of refraction of about 1.5, is seen passing through air ($n = 1.0$), xylene ($n = 1.5$), and water ($n = 1.3$). The rod is easily seen in air and water because of light reflected from its surface. The glass rod is nearly invisible in the xylene because the index of refraction of the rod and the liquid are nearly equal.

The reflection coefficients for the two polarizations have the same magnitude; the difference in sign between (3.46) and (3.47) is due to the geometry and sign convention used in Figure 3.4. [Upon reflection, the normal polarization, along the y-axis, is not affected by the change in propagation direction, but the parallel polarization, in the (x, z) plane, has its x-component reversed in sign.]

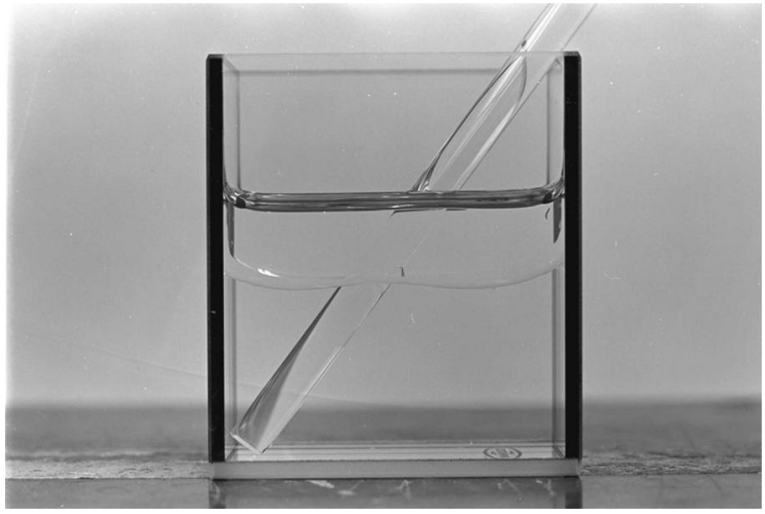

Figure 3.7 *A glass rod rests in a beaker containing water with xylene floating on its surface. The rod is invisible in the xylene because no light is reflected from its surface.*

Most optical glasses have an index of refraction of about 1.5, and air has an index of 1.0; therefore, $n_t/n_i = 1.5$ and

$$R = \left(\frac{n_t - n_i}{n_t + n_i}\right)^2 = \left(\frac{1 - 1.5}{1 + 1.5}\right)^2 = (-0.2)^2 = 0.04.$$

This means that at each glass–air interface, 4% of the incident light is reflected. The efficiencies of solar collectors are affected by this loss, and a trade-off between thermal conduction loss to the surrounding air, reduced by multiple glass panes, and reflective loss must be made when designing solar collectors. Early camera lenses required the use of optical designs with few elements because of the problems created by reflections at air–glass interfaces.

If we calculate the transmissivity for a glass–air interface, we find that $T = 0.96$; thus $T + R = 1.0$ and energy is conserved. It can be shown in general that this is true (see Problem 3.15).

In electromagnetic theory, the ability to transmit energy from a source, say an oscillator, to a load is affected by the impedance of the source, the transmission medium, and the load. The same formalism can be used to describe the transmission of light. The equations for reflection and refraction can be reformulated in terms of the impedance of each medium (see Problem 3-10), yielding new definitions for the reflectivity and transmissivity

$$R = \left(\frac{Z_t - Z_i}{Z_t + Z_i}\right)^2, \tag{3.48}$$

$$T = \frac{4Z_iZ_t}{(Z_t + Z_i)^2}. \tag{3.49}$$

The choice of using the impedance formulation or the index of refraction formulation for optics problems is one of personal preference.

3.7 Polarization by Reflection

In Figure 3.8 we replot the reflectivity of a wave polarized in the plane of incidence to emphasize the region where the amplitude of the reflected wave goes to zero. For the component of polarization parallel to the plane of incidence, the angle of incidence for which there is no reflected wave is named after **Sir David Brewster (1781–1868)**, the inventor of the kaleidoscope.

From the equation for the reflection coefficient, (3.39), we see that the reflection coefficient is zero whenever $\tan(\theta_i + \theta_t) = \infty$. This occurs if the sum of the angles is 90°, i.e., when $\theta_i + \theta_t = \pi/2$. To calculate *Brewster's angle*, we use Snell's law:

$$\frac{n_t}{n_i} = \frac{\sin\theta_i}{\sin\theta_t} = \frac{\sin\theta_i}{\sin\left(\frac{1}{2}\pi - \theta_i\right)} = \frac{\sin\theta_i}{\cos\theta_i} = \tan\theta_B. \tag{3.50}$$

Brewster's angle is therefore given by

$$\theta_B = \tan^{-1}\left(\frac{n_t}{n_i}\right).$$

In Figure 3.8, when $n_t > n_i$, the ratio of indices is $n_t/n_i = 1.5$ and Brewster's angle is $\theta_B = 56.3°$. When $n_i > n_t$, the ratio of the indices is $n_t/n_i = 0.67$ and Brewster's angle is the complement of the previous angle, $\theta_B = 33.7°$. As can be seen in Figure 3.8, the reflectivity remains near zero over a large range of angles, making the effect quite easy to observe.

Some laser designs use windows or crystal surfaces set at the Brewster's angle to reduce the reflective losses in the laser cavity for one polarization. Some brands of sunglasses are designed to take advantage of the fact that light of one polarization is not reflected strongly from dielectric surfaces. These sunglasses use a material (Polaroid) that transmits light polarized in one direction and absorbs light polarized normal to that direction (see Chapter 13 for a discussion of Polaroid).

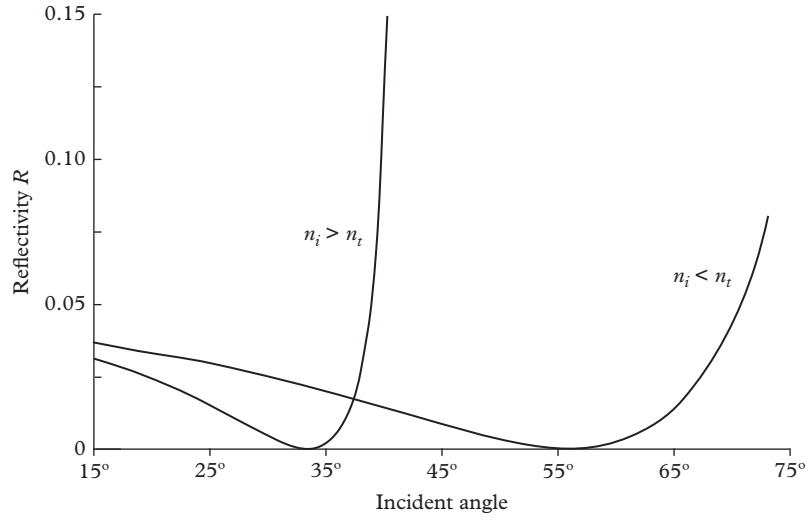

Figure 3.8 *The reflectivity of a wave polarized in the plane of incidence as a function of the incident angle around the Brewster's angle. The two indices are 1.0 and 1.5.*

A simple physical explanation can be given for Brewster's angle [2]. In Figure 3.9, the angle between $\mathbf{k}_r$ and $\mathbf{k}_t$ is

$$\left(\frac{1}{2}\pi - \theta_i\right) - \left(-\frac{1}{2}\pi + \theta_t\right) = \pi - (\theta_i + \theta_t).$$

At Brewster's angle $\theta_i + \theta_t = \pi/2$, the angle between $\mathbf{k}_r$ and $\mathbf{k}_t$ is $\pi/2$, so $\mathbf{E}_t$ is parallel to $\mathbf{k}_r$. When light is incident on a medium, the electric field causes the electrons to vibrate in the direction of the field of the transmitted wave, $\mathbf{E}_t$. The vibrating electrons radiate an electromagnetic wave that propagates back into the first medium; this is the origin of the reflected wave. There is no radiation produced in the direction of vibration [3] of the electrons. Thus, when the reflected and transmitted waves are propagating at right angles to each other, the reflected wave does not receive any energy from oscillations in the plane of incidence. The geometry of the waves at Brewster's angle, shown in Figure 3.9, demonstrates that no radiation will be observed. Magnetic materials complicate the problem [4], but the mathematics needed to describe the effects is a straightforward extension of this derivation.

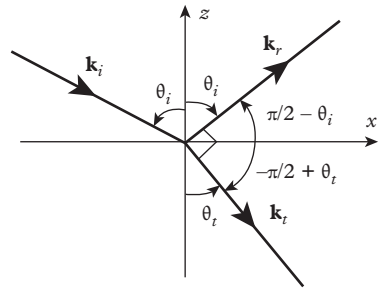

Figure 3.9 *Geometry used to explain the occurrence of Brewster's angle.*

3.8 Total Reflection

From Figure 3.6(a), it is apparent that when light is incident upon a denser (larger value of index n) medium from a less dense one, the reflectivity for the perpendicular polarization is a monotonically increasing function of the incident angle. The reflectivity for the parallel polarization decreases to zero at Brewster's angle and then exhibits the same behavior as the reflectivity for the perpendicular polarization.

When light is incident upon a less dense medium from a denser one, Figure 3.6(b) shows that the reflectivity is 1 beyond a critical angle. Beyond this critical angle, the light is said to undergo *total reflection*. If you are underwater and look toward the surface, you will see that much of what you observe is reflection from items under the water (Figure 3.10).

A schematic representation of refraction and total reflection is shown in Figure 3.11. When $n_i > n_t$, Snell's law states that $\theta_t > \theta_i$, because, for θ between 0° and $\pi/2$, $\sin\theta$ is a

Figure 3.10 *Total reflection dominates what we can see when in the high-index medium. The turtle is a Chelonia mydas. (Inaglory, B., Total internal reflection of Chelonia mydas. 2008: Wikimedia Commons; <http://commons.wikimedia.org/wiki/File:Total_internal_reflection_of_Chelonia_mydas.jpg#>.)*

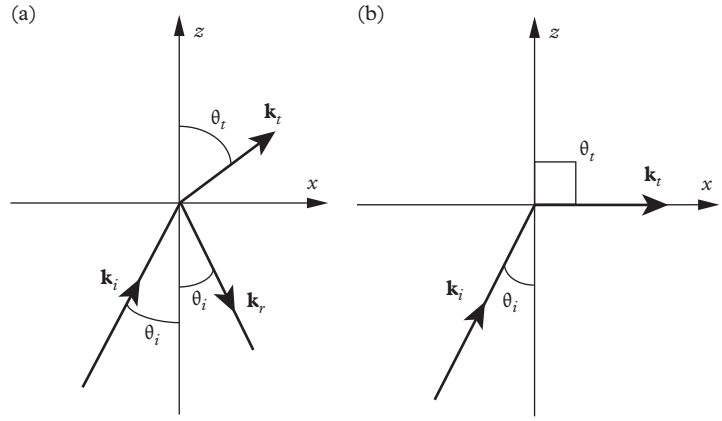

Figure 3.11 *(a) A wave incident at an angle well below the critical angle; this is normal refraction. (b) A wave incident at the critical angle at which total reflection occurs.*

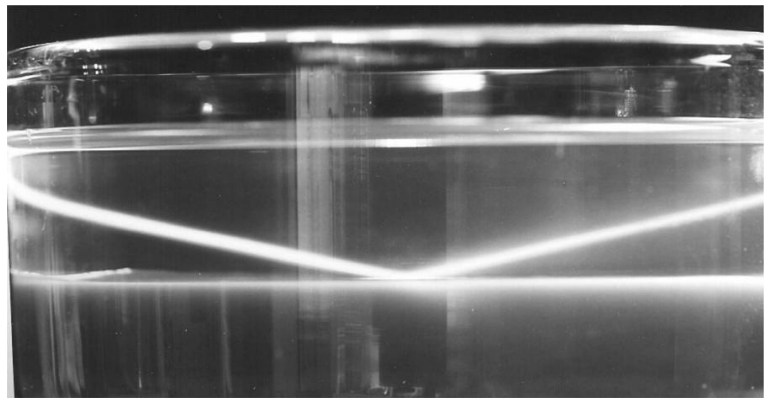

Figure 3.12 *Total reflection occurring at a water–xylene interface. Light from a HeCd laser is incident on the interface from the xylene. The water contains the dye rhodamine 6G in solution. If the blue laser light propagates in the water, it is absorbed by the rhodamine,which then produces a red fluorescence. At angles of incidence greater than the critical angle, no radiation propagates into the water and no red light is visible. At angles of incidence less than the critical angle, light travels into the water and red radiation is observed.*

monotonically increasing function. The angle θ_t reaches $\pi/2$ and $\sin\theta_t$ reaches 1 when the incident angle is equal to $\theta_c (< \pi/2)$ obtained from Snell's law:

$$\theta_c = \sin^{-1}\left(\frac{n_t}{n_i}\right). \tag{3.51}$$

Figure 3.12 shows an experimental demonstration of total reflection. In the experiment, a water–xylene interface is formed by floating a layer of xylene on water. When light is incident at an angle less than the critical angle

$$\theta_c \approx \sin^{-1}\left(\frac{1.3}{1.5}\right) = 62.7°,$$

conventional reflection and refraction takes place. When light is incident at an angle greater than the critical angle, total internal reflection takes place as shown in Figure 3.12. The water contains the dye rhodamine 6G in solution. The dye strongly absorbs the blue light from the HeCd laser used to produce the incident beam and reemits light in the yellow to red region of the spectrum. The dye complicates the calculation of θ_c because n_t is now complex; however, it makes a dramatic demonstration. At angles less than θ_c, a rapidly decaying beam of orange light is seen propagating in the water (see Figure 2.11). For angles equal to or greater than θ_c, the orange beam disappears and only blue light is seen.

Total reflection occurs when $\theta_c < \theta_i \leq \pi/2$. Beyond the critical angle θ_c, the angle θ_t becomes imaginary. To understand how this happens and the physical significance of the imaginary angle, recall that

$$\cos\theta_t = \sqrt{1 - \sin^2\theta_t}.$$

Snell's law can be used to rewrite this identity as

$$\cos\theta_t = \sqrt{1 - \left(\frac{n_i}{n_t}\right)^2 \sin^2\theta_i} = \sqrt{1 - \left(\frac{\sin\theta_i}{\sin\theta_c}\right)^2}.$$

Over the interval $0 \leq \theta \leq \pi/2$, we have $0 \leq \sin\theta \leq 1$ so that $\sin\theta_i/\sin\theta_c > 1$ when $\theta_c < \theta_i$. This leads to the conclusion that $\cos\theta_t$ is an imaginary function:

$$\cos\theta_t = i\sqrt{\left(\frac{\sin\theta_i}{\sin\theta_c}\right)^2 - 1}, \qquad \theta_c < \theta_i \leq \frac{1}{2}\pi.$$

For notational convenience, define $-i\alpha = \cos\theta_t$. The transmitted wave, represented in Figure 3.11 by its propagation vector $\mathbf{k}_t$, can be written in this notation as

$$E_t \propto e^{-i\mathbf{k}_t\cdot\mathbf{r}} = e^{-ik_t(x\sin\theta_t + z\cos\theta_t)},$$

$$E_t = \underbrace{e^{-k_t\alpha z}}_{\text{attenuation}}\ \underbrace{e^{-ik_t x\sqrt{1+\alpha^2}}}_{x\text{–propagation}}.$$

The transmitted wave propagates parallel to the surface (i.e., along the x-axis) and is attenuated exponentially in the z-direction, i.e., normal to the propagation direction. This is called an inhomogeneous plane wave. As we will see in a moment, the wave is not transverse but has a component of the field parallel to $\mathbf{k}$.

The reflectivities for the two polarizations are

$$R_P = \frac{\tan^2(\theta_i - \theta_t)}{\tan^2(\theta_i + \theta_t)} = \frac{\tan^2\left(\theta_i - \frac{1}{2}\pi\right)}{\tan^2\left(\theta_i + \frac{1}{2}\pi\right)} = \frac{\cot^2\theta_i}{\cot^2\theta_i} = 1,$$

$$R_N = \frac{\sin^2(\theta_i - \theta_t)}{\sin^2(\theta_i + \theta_t)} = \frac{\sin^2\left(\theta_i - \frac{1}{2}\pi\right)}{\sin^2\left(\theta_i + \frac{1}{2}\pi\right)} = \frac{\cos^2\theta_i}{\cos^2\theta_i} = 1.$$

Since the reflectivities are 1, there should be no energy flow across the boundary. Calculation of the z-component of the Poynting vector will verify this.

To calculate the Poynting vector, we use the geometry of Figure 3.11 and assume that the wave is incident with perpendicular polarization, i.e., that $\mathbf{E}$ is parallel to the y-axis:

$$E_{yt} \propto e^{-k_t\alpha z}e^{-ik_t x\sqrt{1+\alpha^2}},$$

$$\mathbf{H} \propto \mathbf{k}\times\mathbf{E} = -E_y k_z\hat{\mathbf{i}} + E_y k_x\hat{\mathbf{k}},$$

$$H_{zt} \propto \sqrt{1+\alpha^2}\sqrt{\frac{\varepsilon_t}{\mu_t}}E_{yt},$$

$$H_{xt} \propto i\alpha E_{yt}\sqrt{\frac{\varepsilon_t}{\mu_t}}.$$

The Poynting vector is

$$\mathbf{S} = \mathbf{E} \times \mathbf{H} = E_y H_z \hat{\mathbf{i}} - E_y H_x \hat{\mathbf{k}},$$

$$S_x \propto E_{yt}^2 \sqrt{1+\alpha^2} \sqrt{\frac{\varepsilon_t}{\mu_t}}.$$

$$S_z \propto -E_{yt}^2 i\alpha \sqrt{\frac{\varepsilon_t}{\mu_t}}.$$

Energy flows along the x-direction but not the z–direction because the Poynting vector in the z-direction is imaginary. An inhomogeneous wave attached to the surface and decaying exponentially normal to the surface, such as this one, is called an evanescent wave.

We can define a penetration depth $z = 1/\gamma$ as the value of z where the amplitude of the wave drops to $1/e$ of its original value; γ is called the decay constant:

$$\frac{1}{\gamma} = \frac{1}{k_t \alpha}.$$

We can detect this exponentially decaying wave by bringing another high-index material within a few penetration depths of the first material. This is called *frustrated total reflection* and is analogous to quantum mechanical tunneling [5]. Figure 3.13 shows two applications of frustrated total reflection: a variable attenuator and a prism coupler for launching into an optical waveguide or creating surface plasmons [6].

While the amplitude of the wave is not modified when the light undergoes total reflection, the phase of the light is modified. We can examine this phase change by looking at the reflection coefficients. The phase will be important in Chapter 5 where the propagation of light in an optical fiber is discussed. We rewrite (3.33) and (3.39) to get

$$\begin{aligned} r_N &= -\frac{\sin\theta_i \cos\theta_t - \cos\theta_i \sin\theta_t}{\sin\theta_i \cos\theta_t + \cos\theta_i \sin\theta_t} \\ &= \frac{\sqrt{1+\alpha^2}\cos\theta_i + i\alpha \sin\theta_i}{\sqrt{1+\alpha^2}\cos\theta_i - i\alpha \sin\theta_i}, \end{aligned} \tag{3.52}$$

$$\begin{aligned} r_P &= \frac{\sin\theta_i \cos\theta_i - \cos\theta_t \sin\theta_t}{\sin\theta_i \cos\theta_i + \cos\theta_t \sin\theta_t} \\ &= \frac{\sin\theta_i \cos\theta_i + i\alpha\sqrt{1+\alpha^2}}{\sin\theta_i \cos\theta_i - i\alpha\sqrt{1+\alpha^2}}. \end{aligned} \tag{3.53}$$

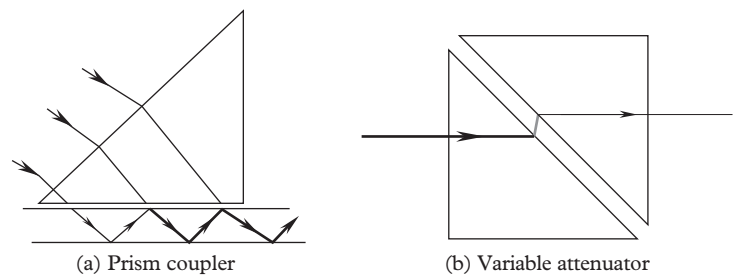

Figure 3.13 *Two examples of frustrated total reflection. (a) The evanescent wave from a light beam undergoing total internal reflection in a prism is coupled into a waveguide mode of an optical waveguide. (b) Two identical prisms are used to make a variable attenuator by varying the amount of evanescent wave coupled into the second prism.*

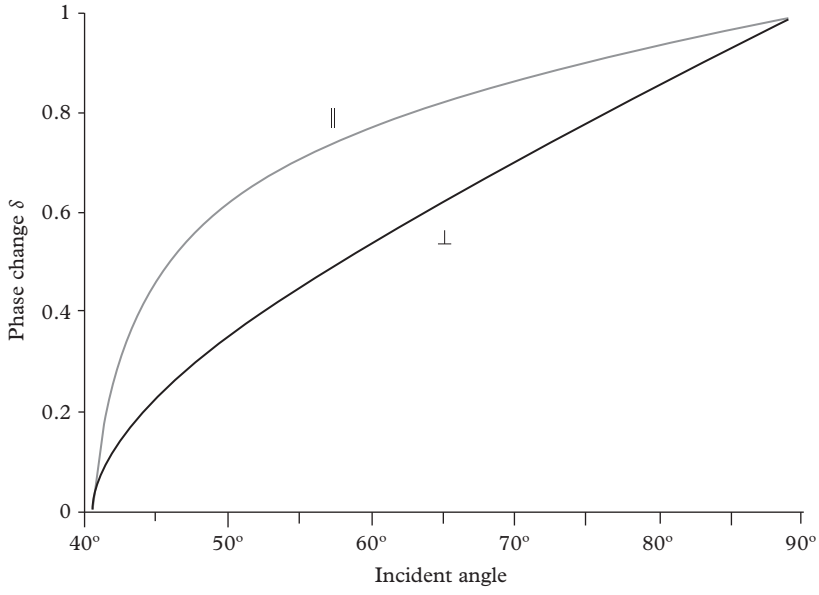

Figure 3.14 *The phase change upon total reflection for each of the two polarizations. For this calculation, we assumed that the index of the dense medium was 1.5 and the index of the less dense medium was 1.0.*

Both r_N and r_P are complex numbers of the form $(a+ib)/(a-ib)$. These complex variables can be written as

$$\frac{ae^{i\varphi}}{ae^{-i\varphi}} = e^{2i\varphi}.$$

We then define $\delta/2 = \varphi$ and $\tan(\delta/2) = b/a$. This leads to phase shifts of

$$\tan\left(\frac{\delta_N}{2}\right) = \frac{\alpha \sin\theta_i}{\sqrt{1+\alpha^2}\cos\theta_i}, \tag{3.54}$$

$$\tan\left(\frac{\delta_P}{2}\right) = \frac{\alpha\sqrt{1+\alpha^2}}{\sin\theta_i \cos\theta_i}. \tag{3.55}$$

The phase shifts as functions of incident angle are shown in Figure 3.14 for the case $n_i = 1.5$ and $n_t = 1.0$.

3.9 Reflection from a Conductor

The results derived for reflection and transmission from a boundary apply to materials with a complex index of refraction as well as to those with a real index. To use the derived equations for materials with complex indices, we simply replace the real index by the equivalent complex one. We will demonstrate the procedure by finding the reflectivity of a metal that has a complex index of refraction. We will limit our discussion to the near-normal reflection from an air–metal interface where $n_t = \tilde{n}$ (a complex index of refraction) and $n_i = 1$.

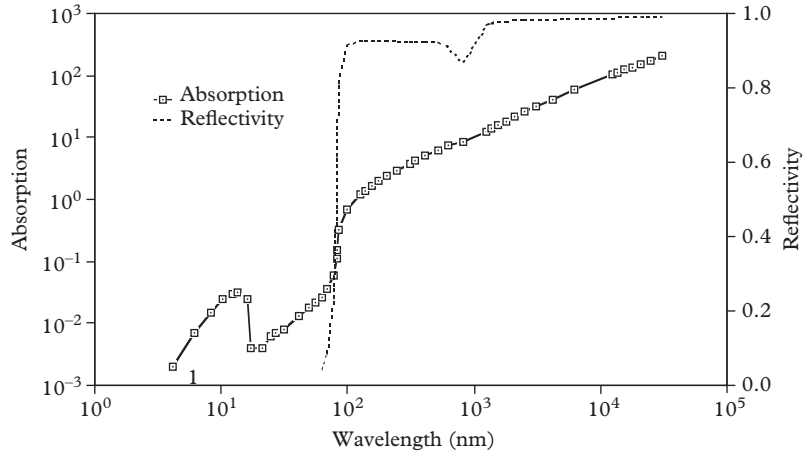

Figure 3.15 *Reflectivity and absorption as a function of wavelength in aluminum.*

Replacing the real index in (3.46) by a complex index, we have

$$R = \frac{(\tilde{n}-1)(\tilde{n}^*-1)}{(\tilde{n}+1)(\tilde{n}^*+1)} = \frac{(n-1+in\kappa)(n-1-in\kappa)}{(n+1+in\kappa)(n+1-in\kappa)} = \frac{(n-1)^2+(n\kappa)^2}{(n+1)^2+(n\kappa)^2},$$

$$R = 1 - \frac{4n}{(n+1)^2+(n\kappa)^2}. \tag{3.56}$$

The association of R and the absorption in a material can be observed in Figure 3.15, where $n\kappa$ and R are plotted as functions of wavelength for the metal, aluminum. The reason for the dependence of $n\kappa$ on wavelength will be discussed in Chapter 7.

If the index of refraction were purely imaginary, then we would have

$$\tilde{n} = in\kappa,$$

$$R = \frac{(in\kappa-1)(-in\kappa-1)}{(in\kappa+1)(-in\kappa+1)} = \frac{-(in\kappa-1)(in\kappa+1)}{-(in\kappa+1)(in\kappa-1)} = 1,$$

and the material would be a perfect reflector.

Let us look at a real metal mirror made out of aluminum. The values of n and κ as functions of wavelength are shown in Figure 3.16. We will strike an aluminum mirror from air at an angle near normal. The reflection coefficient is

$$r_1 = \frac{n_0-(n_1-in_1\kappa_1)}{n_0+(n_1-in_1\kappa_1)}.$$

We will pick a wavelength of light of 546 nm, yielding $n_1 = 0.8$ and $\kappa_1 = 6$. This give us $n_1\kappa_1 = 4.91$, and so

$$r_1 = \frac{1-(0.82-i4.91)}{1+(0.82-i4.91)} = -0.87+i0.36$$

$$= 0.94e^{i(\pi-0.39)} = -0.94e^{-0.39i},$$

$$R_1 = 0.88.$$

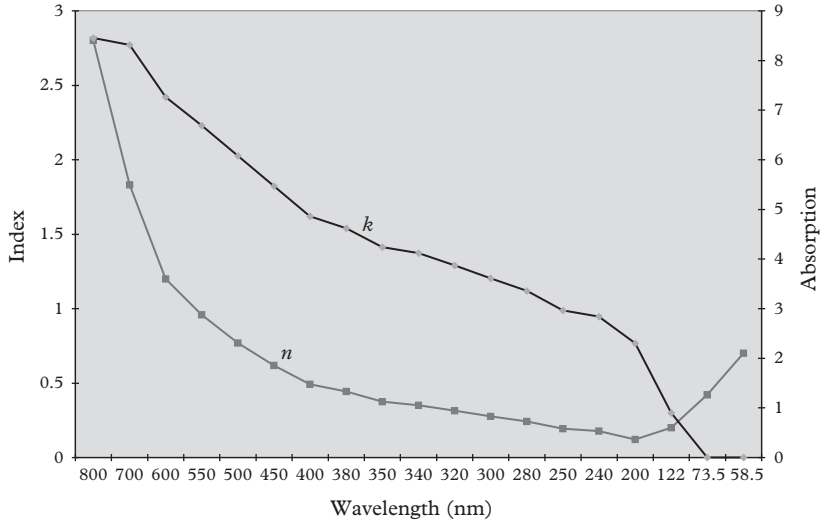

Figure 3.16 *Complex index of refraction for aluminum.*

Aluminum oxidizes in air, so it might be interesting to see what would happen if we put a glass overcoat over the aluminum. Now,

$$r_2 = \frac{1.5 - 0.82 + i4.91}{1.5 + 0.82 - i4.91} = -0.76 + i0.5$$

$$= -0.91e^{-0.58i},$$

$$R_2 = 0.83.$$

Some of the light also reflects from the glass/air surface so that the measured reflectivity is

$$\frac{I_f}{I_0} = (1 - R_1)R_2(1 - R_1)$$

$$= (1 - 0.04)(0.83)(1 - 0.04)$$

$$= 0.76.$$

We have a much lower reflectivity when we put the protective coating on the aluminum. We will learn in Chapter 4 that there is a way to beat this loss in reflectivity and still protect the metal surface.

3.10 Summary

By requiring that the phase of a wave be continuous across the boundary between media with different wave propagation velocities, the laws of reflection and refraction were derived. The media's propagation velocities are used to define the indices of refraction of the medium containing the incident wave, n_i, and of the medium containing the transmitted wave, n_t.

Law of Reflection

1. The reflected wave's propagation vector lies in the plane defined by the incident wave's propagation vector and the normal to the boundary at the point where the incident wave intersects the boundary. This plane is called the plane of incidence.
2. The angle between the reflected wave's propagation vector and the normal to the boundary, θ_r, is equal to the angle between the incident wave's propagation vector and the normal, θ_i:

$$\sin\theta_i = \sin\theta_r.$$

Law of Refraction

1. The propagation vector of the wave transmitted across the boundary lies in the plane of incidence.
2. The angle between the transmitted wave's propagation vector and the normal to the boundary, θ_t, is given by Snell's law:

$$\sin\theta_t = \frac{n_i}{n_t}\sin\theta_i.$$

Maxwell's equations and their boundary conditions were used to derive the amplitudes of the reflected and transmitted waves for the electric field in the plane of incidence,

$$t_P = \frac{E_{Pt}}{E_{Pi}} = \frac{2\cos\theta_i \sin\theta_t}{\sin(\theta_i+\theta_t)\cos(\theta_i-\theta_t)},$$

$$r_P = \frac{E_{Pr}}{E_{Pi}} = \frac{\tan(\theta_i-\theta_t)}{\tan(\theta_i+\theta_t)},$$

and normal to the plane of incidence,

$$t_N = \frac{E_{Nt}}{E_{Ni}} = \frac{2\sin\theta_t\cos\theta_i}{\sin(\theta_i+\theta_t)},$$

$$r_N = \frac{E_{Nr}}{E_{Ni}} = -\frac{\sin(\theta_i-\theta_t)}{\sin(\theta_i+\theta_t)}.$$

The reflections from a surface under several special conditions were discussed. The condition of normal incidence reduces the two equations to a single equation

$$R = \left(\frac{n_t-n_i}{n_t+n_i}\right)^2,$$

which demonstrates that the reflectivity depends upon the relative propagation velocities in the two media.

There is an angle for which a wave, polarized parallel to the plane of incidence, is not reflected. The angle is called Brewster's angle and is given by

$$\theta_B = \tan^{-1}\left(\frac{n_t}{n_i}\right).$$

If the incident wave strikes a boundary with a medium that has an index of refraction less than the index of the incident wave's medium, then when the angle of incidence is greater than a critical angle given by

$$\theta_c = \sin^{-1}\left(\frac{n_t}{n_i}\right),$$

the incident wave will be totally reflected. The totally reflected wave will experience a phase shift given by

$$\tan\left(\frac{\delta_N}{2}\right) = \frac{\alpha \sin\theta_i}{\sqrt{1+\alpha^2}\cos\theta_i}, \quad \tan\left(\frac{\delta_P}{2}\right) = \frac{\alpha\sqrt{1+\alpha^2}}{\sin\theta_i \cos\theta_i}.$$

3.11 Problems

3.1. An unpolarized beam of light is one whose Stokes vectors are $s_1 = s_2 = s_3 = 0$. If such a beam in air is incident at an angle of 30° on glass with an index of 1.50, what is the percentage of light energy refracted in the normal and parallel polarized components? What is the degree of polarization?

3.2. Light is incident on a medium of index $n = 1.682$ from air. What is Brewster's angle?

3.3. Assume we have two strings joined at the origin. The velocity of the wave in the string on the left is $v_1 = 20$ m/s. The velocity for the string on the right is $v_2 = 10$ m/s. The string on the right has a wave with an amplitude of 3 cm and a wavelength of 1 m moving toward the junction.

(a) What are the amplitudes of the transmitted and reflected waves and the wavelength of the transmitted wave?

(b) What is the ratio of the power transmitted to the power reflected?

3.4. A Gaussian displacement traveling along a string,

$$s(x,t) = A\exp\left[-\frac{(t-x/v_1)^2}{t_1^2}\right],$$

is incident from the left onto a junction at $x = 0$ where the linear mass density of the string changes from μ_1 to μ_2 and the velocity of propagation of a wave along the string changes from v_1 to v_2. Write down s_{trans} and s_{refl}.

3.5. Calculate the critical angle and Brewster's angle for water ($n = 1.33$) and for dense flint glass ($n = 1.75$) when light propagating in the medium is incident on an interface with air.

3.6. Use the computer to generate a plot of R_P and R_N for an air–glass interface ($n_1 = 1$ and $n_2 = 1.5$) for two cases:

(a) when the light is incident from the air side;

(b) when the light is incident from the glass side.

3.7. A tank of water is covered with a 1 cm thick layer of oil ($n_0 = 1.48$); above the oil is air. If a beam of light originates in the water, what angle must the light beam make at the water–oil interface if no light is to escape into the air?

3.8. As the sun rises over a still pond, an angle will be reached when its image on the water's surface is completely linearly polarized in a plane parallel to the water's surface. What is the incident angle?

3.9. Use (3.43) and (3.44) to prove that energy is conserved at the interface between two dielectrics, i.e., $T + R = 1$.

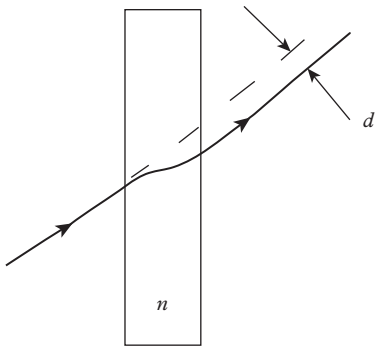

Figure 3.17 *Displacement of light after passing through a dielectric medium.*

3.10. Derive (3.48) and (3.49) using the definitions of impedance, found in the discussion following (2.20), and of reflectivity and transmissivity.

3.11. Derive an expression for the displacement of a light wave's propagation vector after it passes through a plane parallel glass plate of index n and thickness t (Figure 3.17). Show that for small n, the displacement is

$$d \approx t \sin\theta \left(1 - \frac{1}{n}\right).$$

3.12. Derive an expression for the transmittance of light normally through a stack of N glass plates, each separated by a small air space. Assume that there is no absorption and that all the plates have an index of refraction n.

3.13. Derive Brewster's law for the case when we cannot assume $\mu_1 = \mu_2 = \mu_0$. Carry out the derivation for both polarization states.

3.14. The index of refraction of germanium at $\lambda = 500$ nm is $3.47 - i(1.4)$. What is the reflection coefficient of a polished germanium surface at normal incidence?

3.15. Use the equations for transmissivity and reflectivity for normal incidence to prove that energy is conserved.

3.16. Determine the value of the amplitude reflection coefficients for light incident at 30° on an air–glass interface where $n_i = 1.0$ and $n_t = 1.5$. Write the Stokes vector for the reflected light.

3.17. Mirrors used in X-ray optics are often based upon total reflection. The index of refraction for X-rays of wavelength 0.15 nm in a vacuum is 1.0. For silver, the index is 0.99998. What is the angle for total reflection? Sketch the experimental arrangement needed to take advantage of total reflection.

3.18. What is the refractive index of a glass plate that polarizes light reflected at 57.5°?

3.19. A beam of light passes normally through one side and is totally reflected off the hypotenuse of a $45° - 90° - 45°$ glass prism of index 1.6. What is the decay constant for the evanescent wave at the point of total reflection, assuming the prism is in air? What happens if the prism is in water?

3.20. A glass container of index 1.65 is filled with carbon tetrachloride with an index of 1.46. If a beam of light stikes the contained normally, how much light is transmitted through the container?

REFERENCES

1. Enoch, J.M., *History of mirrors dating back 8000 years.* Optometry Vision Sci., 2006. **83**: p. 775–781.
2. Doyle, W.T., *Scattering approach to Fresnel's equations and Brewster's law.* Am. J. Phys., 1985. **53**: p. 463–468.
3. Wangsness, R.K., *Electromagnetic Fields*. 2nd ed. 1986: Wiley.
4. Giles, C.L. and W.J. Wild, *Brewster angles for magnetic media.* Int. J. Infrared Millimeter Waves, 1985. **6**: p. 187–197.
5. Zhu, S., et al., *Frustrated total internal reflection: a demonstration and review.* Am. J. Phys., 1986. **54**: p. 601–607.
6. Tien, P.K. and R. Ulrich, *Theory of prism-film coupler and thin-film guides.* J. Opt. Soc. Am., 1970. **60**: p. 1325–1337.

Interference

4

4.1 Introduction 79
4.2 Addition of Waves 79
4.3 Interference 82
4.4 Young's Interference 86
4.5 Dielectric Layer 89
4.6 Michelson Interferometer 97
4.7 Interference by Multiple Reflection 101
4.8 Summary 112
4.9 Problems 114
References 116
Appendix 4A: Multilayer Dielectric Coatings 116

4.1 Introduction

The superposition principle, introduced in Chapter 1, states that the sum of solutions of the wave equation is also a solution to the wave equation. In this chapter, a general approach to the addition of waves of the same frequency will be developed so that the superposition principle may be applied to a large number of three-dimensional waves traveling in a variety of directions.

The physical consequence of the superposition principle is the observation of bright and dark bands of light called ***fringes*** when a number of waves coexist in a region in space. These fringes are commonly observed in soap bubbles or on oil films on a wet roadway.[1] The bright regions occur when a number of waves add together to produce an intensity maximum of the resultant wave; this is called ***constructive interference***. ***Destructive interference*** occurs when a number of waves add together to produce an intensity minimum of the resultant wave.

Collectively, the distribution of fringes is called an ***interference pattern***. In this chapter, techniques for adding waves will be used to develop a theoretical explanation of the interference patterns produced by a number of simple physical systems. The systems to be treated are the interference between waves originating from two slits illuminated by a single, small, light source (called Young's two-slit experiment) and reflections from the front and back surfaces of a thin dielectric layer. The interference of waves reflected from a dielectric layer is used as a model to explain the operation of a Michelson interferometer and a Fabry–Perot interferometer. The results for the dielectric layer are also used in Appendix 4A to describe the design of dielectric mirrors and antireflection coatings. The results of Appendix 4A will also be used in Chapter 12 in our discussion of photonic crystals.

The first observation of interference was made by **Robert Boyle (1627–1691)** in 1663. He saw what are now called Newton's rings. **Robert Hooke (1635–1703)** was a co-discoverer of the rings, but it is Newton who has his name associated with the interference pattern because he performed a number of experiments on the effect. The first experiments involving interference effects in light were performed by **Thomas Young (1773–1829)** in 1802 [1]. His experiments disagreed with the then-accepted particle theory developed by Newton, and were rejected by most of the scientific community, sometimes rudely. Young's experiments were not decisive in establishing the wave theory because the observed intensity patterns could have originated from processes other than interference. Ten years after Young's experiments, Fresnel performed experiments that confirmed Young's results and eliminated all other possible sources of the observed patterns. These experiments led to the rejection of the particle theory of Newton and its replacement by the wave theory of light.

4.2 Addition of Waves

In the discussion of the reflection of a wave on a vibrating string in Chapter 3, a simple algebraic technique was used to combine multiple waves. The addition of these waves was

[1] Discussion of the factors that determine when the fringes can be observed must be delayed until Chapter 8, when we will examine the addition of waves of different frequencies.

Modern Optics. Second Edition. B. D. Guenther.

© B. D. Guenther 2015. Published in 2015 by Oxford University Press.

accomplished for each instant in time by adding the amplitudes of the waves algebraically, at each value of x, to obtain the resultant wave. There are two additional ways to add waves of the same frequency that are sometimes easier to apply to a general three-dimensional wave. We will demonstrate the three approaches by applying them to the addition of two or more scalar plane waves of the form

$$y = Y\cos(\omega t - \mathbf{k}\cdot\mathbf{r} + \varphi).$$

All of the waves will have the same frequency ω, and all of the sources of phase differences between the various waves will be in the phase

$$\phi_i = -\mathbf{k}_i\cdot\mathbf{r}_i + \varphi_i.$$

The differences in ϕ could arise from differences in propagation paths, phase change upon reflection, etc.

4.2.1 Trigonometric Approach

The two scalar waves

$$y_1 = Y_1\cos(\omega t + \phi_1), \quad y_2 = Y_2\cos(\omega t + \phi_2), \tag{4.1}$$

can be added algebraically to produce the resultant wave

$$\begin{aligned} y &= y_1 + y_2 \\ &= (Y_1\cos\phi_1 + Y_2\cos\phi_2)\cos\omega t - (Y_1\sin\phi_1 + Y_2\sin\phi_2)\sin\omega t. \end{aligned}$$

By defining two new variables, Y and δ, through the equations

$$Y\cos\delta = Y_1\cos\phi_1 + Y_2\cos\phi_2, \tag{4.2}$$

$$Y\sin\delta = Y_1\sin\phi_1 + Y_2\sin\phi_2, \tag{4.3}$$

the sum of the two waves can be rewritten as

$$\begin{aligned} y &= Y\cos\delta\cos\omega t - Y\sin\delta\sin\omega t, \\ &= Y\cos(\omega t + \delta). \end{aligned} \tag{4.4}$$

The resultant (4.4) obtained by adding together two sinusoidal waves of frequency ω is a sinusoidal wave of the same frequency ω. To solve for Y, we add the squares of (4.2) and (4.3) together to obtain

$$Y^2 = (Y_1\cos\phi_1 + Y_2\cos\phi_2)^2 + (Y_1\sin\phi_1 + Y_2\sin\phi_2)^2.$$

To solve for δ, we divide (4.3) by (4.2):

$$\tan\delta = \frac{Y_1\sin\phi_1 + Y_2\sin\phi_2}{Y_1\cos\phi_1 + Y_2\cos\phi_2}.$$

This wave addition technique is the one used in Chapter 3 to generate Figure 3.2 and to obtain the equation for a standing wave, (3.6). The origin of the difference in phase ϕ between the incident and reflected waves for that example was reflection.

This technique is not useful for adding a large number of waves, because of the bookkeeping required when manipulating a large number of trigonometric functions; therefore, two other techniques will be introduced.

4.2.2 Complex Approach

Starting with N waves of the form (4.1), they can be rewritten in complex notation as

$$\tilde{y}_1 = Y_1 e^{i(\omega t+\phi_1)}, \quad \ldots, \quad \tilde{y}_i = Y_i e^{i(\omega t+\phi_i)}, \quad \ldots, \quad \tilde{y}_N = Y_N e^{i(\omega t+\phi_N)}. \tag{4.5}$$

To simplify the discussion, we assume that the phase of each wave is ϕ_0 larger than the preceding wave and that the amplitude of each wave is identical and equal to the value Y_0. (Waves with these properties will be encountered when discussing multiple reflections in a dielectric film later in this chapter.) The sum of N waves of this type is written as

$$\tilde{y} = \sum_{j=1}^{N} \tilde{y}_j = Y_0 e^{i\omega t}(e^{i\phi_0} + e^{2i\phi_0} + \ldots + e^{Ni\phi_0}) = Y_0 e^{i\omega t} \sum_{j=1}^{N} e^{j(i\phi_0)} \tag{4.6}$$

and can be shown (Problem 4.16) to be equal to

$$\tilde{y} = Y_0 e^{i(\omega t+\phi_0)} \frac{1 - e^{Ni\phi_0}}{1 - e^{i\phi_0}}. \tag{4.7}$$

To obtain the real part of $\tilde{y}$, (4.7) must be placed in standard form by eliminating the complex term from the denominator:

$$\tilde{y} = Y_0 e^{i(\omega t+\phi_0)} \frac{e^{i\phi_0} - e^{i(N+1)\phi_0} - 1 + e^{iN\phi_0}}{2(1 - \cos\phi_0)}.$$

Now the real part of $\tilde{y}$ can be separated from the imaginary part and, through the use of some trigonometric identities, placed in the form

$$\mathcal{R}e\{\tilde{y}\} = \frac{Y_0 \sin(N\phi_0/2)}{\sin(\phi_0/2)} \cos[\omega t + (N+1)\phi_0/2]. \tag{4.8}$$

Again, the sum of a number of harmonic waves of the same frequency ω leads to a resultant wave that is also a sinusoidal wave with frequency ω and with an amplitude and phase given by

$$Y = Y_0 \frac{\sin(N\phi_0/2)}{\sin(\phi_0/2)}, \quad \delta = (N+1)\phi_0/2.$$

The results obtained by applying the trigonometric approach are identical to these if we set $N = 2$, $Y_1 = Y_2 = Y_0$, $\phi_1 = \phi_0$, and $\phi_2 = 2\phi_0$.

4.2.3 Vector Approach

Waves described in complex notation in (4.5) can be represented, at a time t_1, by vectors. The length of each vector is equal to the maximum amplitude of the wave, and the angle that each vector makes with the abscissa is equal to the phase $\omega t_1 + \phi_n$. If these vectors are drawn in a coordinate system rotating about the axis normal to the plane of the figure at a frequency ω, the vectors will appear stationary. Figure 4.1 shows the vector representation of two waves (a) in a fixed coordinate system and (b) in a coordinate system rotating at an angular velocity ω.

Vectors are added graphically by placing the vectors tail to head as shown in Figure 4.2. The resultant wave is then drawn from the tail of the first wave to the head of the last wave.

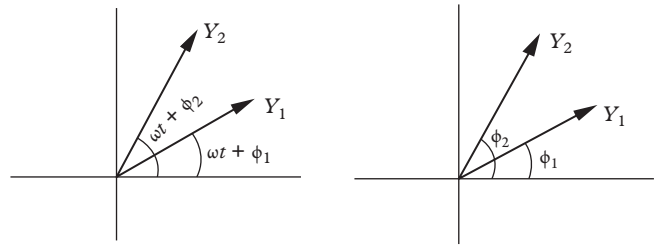

(a) Stationary coordinates at t (b) Coordinates rotating at ωt

Figure 4.1 *Vector representation of two waves with the same frequency and different phase. The coordinate system in (a) is stationary, whereas that in (b) is rotating at an angular frequency equal to the waves' frequency ω so the vectors appear stationary in this frame.*

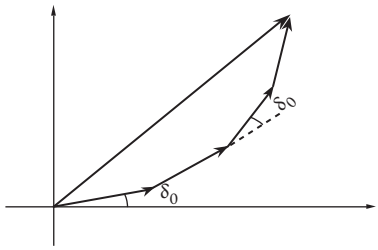

Figure 4.2 *Vector representation of four waves with equal amplitudes and phases in an arithmetic progression starting at δ_0. The coordinate system is rotating at a frequency ω.*

The resultant vector shown in Figure 4.2 is stationary in the rotating frame and rotating at a frequency ω in the fixed coordinate system; therefore, the resultant wave is a harmonic wave of frequency ω. This graphical implementation of the complex approach provides visual insight into the interference process.

4.3 Interference

To add light waves, attention must be paid to the fact that light wave displacements are vector quantities. We need to evaluate what effect this complication has on the techniques developed for adding scalar waves. We will represent the addition of two electromagnetic plane waves in its most general form. We will then discover, if we limit our attention to plane electromagnetic waves propagating in free space, that orthogonal polarizations will not interfere,because light waves are transverse.

We will represent two electromagnetic waves by

$$\tilde{\mathbf{E}}_1 = \tilde{\mathbf{A}}e^{i\omega t} \qquad \text{and} \qquad \tilde{\mathbf{E}}_2 = \tilde{\mathbf{B}}e^{i\omega t}.$$

As we stated earlier in this chapter, we will assume that the waves all have the same frequency and will need only to concern ourselves with the ***complex amplitudes*** of the waves. The components of the complex amplitudes of the two waves are

$$\tilde{A}_x = a_1 e^{-ig_1}, \quad \tilde{A}_y = a_2 e^{-ig_2}, \quad \tilde{A}_z = a_3 e^{-ig_3}, \tag{4.9}$$

$$\tilde{B}_x = b_1 e^{-ih_1}, \quad \tilde{B}_y = b_2 e^{-ih_2}, \quad \tilde{B}_z = b_3 e^{-ih_3}. \tag{4.10}$$

where g and h are of the form $\mathbf{k}\cdot\mathbf{r} + \phi$. The vector $\mathbf{r}$ represents the position of the point in space where the wave amplitudes are added. Since we can only measure the intensity of the light wave, the time average of the square of the sum of the two waves must be calculated before the theoretical result can be compared with experiment,

$$\langle \mathbf{E}^2 \rangle = \langle (\mathbf{E}_1 + \mathbf{E}_2)\cdot(\mathbf{E}_1 + \mathbf{E}_2) \rangle = \langle \mathbf{E}_1^2 \rangle + \langle \mathbf{E}_2^2 \rangle + 2\langle \mathbf{E}_1 \cdot \mathbf{E}_2 \rangle. \tag{4.11}$$

Equation (2.26) defines the intensity of the wave as proportional to the square of the electric field of the light wave. We are only interested in relative intensities, so we will replace $\langle \mathbf{E}^2 \rangle$ by I and neglect the constants of proportionality.

The intensity of the resultant wave is given by

$$I = I_1 + I_2 + 2\langle \mathbf{E}_1 \cdot \mathbf{E}_2 \rangle.$$

I_1 and I_2 are the intensities of each wave, independent of the other. All information about interference is contained in the third term of this equation. If the third term is zero at all positions, the waves do not interfere and are said to be *incoherent*. (Details of this concept will be given in Chapter 8). We will evaluate the third, interference, term using the complex notation of (2.28); the third term becomes

$$2\langle \mathbf{E}_1 \cdot \mathbf{E}_2 \rangle = \mathcal{R}e\left\{\tilde{\mathbf{E}}_1 \cdot \tilde{\mathbf{E}}_2^*\right\} = \frac{1}{2}\left(\tilde{\mathbf{E}}_1 \cdot \tilde{\mathbf{E}}_2^* + \tilde{\mathbf{E}}_1^* \cdot \tilde{\mathbf{E}}_2\right)$$
$$= a_1 b_1 \cos(g_1 - h_1) + a_2 b_2 \cos(g_2 - h_2) + a_3 b_3 \cos(g_3 - h_3).$$

(This general result will be of use not only in our discussion of interference but also in the discussion of holography in Chapter 12.)

Assume that the two waves to be added together are plane waves, of the same frequency, orthogonally polarized, and propagating parallel to one another along the z-axis. One wave is assumed to have its **E** vector located in the (x, z)-plane so that $a_2 = 0$ and the other is assumed to have its **E** vector in the (y, z)-plane so that $b_1 = 0$. With these assumptions, the interference term is

$$2\langle \mathbf{E}_1 \cdot \mathbf{E}_2 \rangle = a_3 b_3 \cos(g_3 - h_3).$$

Up to now, the electromagnetic properties of the waves have been ignored. Now, we will use the physical fact that light waves are transverse in free space. The transverse nature of light requires that $a_3 = b_3 = 0$ for the waves represented by $\mathbf{E}_1$ and $\mathbf{E}_2$ and results in the interference term being equal to zero for orthogonal polarizations.

Maxwell's equations provide the key result for interference that light waves propagating in free space and polarized at right angles to each other will not interfere. The key assumptions applied to Maxwell's equations leading to this result are that the medium is isotropic and free of charge; thus, the result applies to many simple dielectrics. (There are materials in which an electromagnetic wave can have a longitudinal component, and for those special cases, the above result must be modified.)

Since only parallel polarized waves interfere with one another, we can simplify the notation without loss of generality by assuming that all light waves are linearly polarized in the y-direction and the waves are propagating in the (x, z)-plane:

$$a_1 = a_3 = b_1 = b_3 = 0.$$
$$I_1 = \frac{a_2^2}{2}, \qquad I_2 = \frac{b_2^2}{2}.$$
$$2\langle \mathbf{E}_1 \cdot \mathbf{E}_2 \rangle = a_2 b_2 \cos(g_2 - h_2) = 2\sqrt{I_1 I_2}\cos\delta,$$

allowing the relation for the intensity of the resultant wave to be written as

$$I = I_1 + I_2 + 2\sqrt{I_1 I_2}\cos\delta, \tag{4.12}$$

where

$$\delta = [(\mathbf{k}_1 \cdot \mathbf{r}_1 - \mathbf{k}_2 \cdot \mathbf{r}_2) + (\phi_1 - \phi_2)] = \Delta + \Delta\phi. \tag{4.13}$$

Two electromagnetic waves have been added using the complex approach and have been used to demonstrate that only parallel components of the electric field contribute to the interference term. The interference term has been shown to be a function of the amplitudes of the two waves and a harmonic function of the phase difference δ between the two waves.

In (4.13), we have separated the phase difference δ into two components: $\Delta\phi = \phi_1 - \phi_2$, which is the phase difference due to differences in the epoch angles of the oscillators producing the waves, and a component $\Delta = \mathbf{k}_1 \cdot \mathbf{r}_1 - \mathbf{k}_2 \cdot \mathbf{r}_2$, which is the phase difference due to propagation path differences. The propagation paths for the two waves are measured in units of wavelength since $|\mathbf{k}| = 2\pi/\lambda$.

We know from the discussion of reflection and refraction in Chapter 3 that the wavelength of light depends upon the propagation velocity in the medium (see Figure 3.2). In order to allow the light to propagate along paths in media with different indices of refraction and still evaluate their phase differences, all path lengths are converted to an equivalent path length in a vacuum. The equivalent path length, the *optical path length,* between points A and B in a medium with an index of refraction n is defined as the distance a wave in a vacuum would travel during the time it took light to travel from A to B in the actual medium. If the distance between A and B is r and the velocity of propagation in the medium is v, then the time to travel from A to B is $\tau = r/v$. The distance light would travel in a vacuum in the time τ, i.e., the optical path length, is given by

$$c\tau = \frac{cr}{v} = nr. \tag{4.14}$$

This equation provides the mathematical definition of the optical path length.

The phase difference Δ can now be expressed in terms of the optical path length. Both waves were assumed to have the same frequency, and therefore the propagation constant of wave i is

$$|\mathbf{k}_i| = \frac{n_i 2\pi}{\lambda_0},$$

where λ_0 is the wavelength of the waves in a vacuum and n_i is the index of refraction associated with the path of the ith wave. With the definitions just introduced, it is apparent that Δ is the difference in optical path lengths of the two waves:

$$\Delta = \mathbf{k}_1 \cdot \mathbf{r}_1 - \mathbf{k}_2 \cdot \mathbf{r}_2 = \mathbf{k}_0 \cdot (n_1\mathbf{r}_1 - n_2\mathbf{r}_2),$$

where the subscript 0 denotes the propagation vector in a vacuum.

When the two waves have the same amplitude, (4.12) can be rewritten as

$$I = 4I_1 \cos^2 \frac{\delta}{2}. \tag{4.15}$$

Figure 4.3 shows a plot of the intensity distribution described by (4.15). The maximum intensity is $4I_1$ when constructive interference occurs because the phase difference between the two waves is $\delta = m \cdot 2\pi$, and the minimum intensity is zero when destructive interference occurs because the phase difference between the two waves is $\delta = (2m + 1)\pi$, where m is an integer given by the path in wavelengths. Thus, constructive interference occurs when the wave amplitudes add to produce a maximum in the observed light distribution, and destructive interference occurs when the wave amplitudes add to produce a minimum. Conservation of energy requires the energy in the combined beams to be $2I_1$ if the energy in each beam is I_1. Is conservation of energy violated when the observed intensity reaches a value of $4I_1$? The answer is no: the energy has had its spatial distribution modified by interference, but over the entire cross section of the resultant wave the energy is still $2I_1$ (the average of $\cos^2 \delta$ is equal to 1/2).

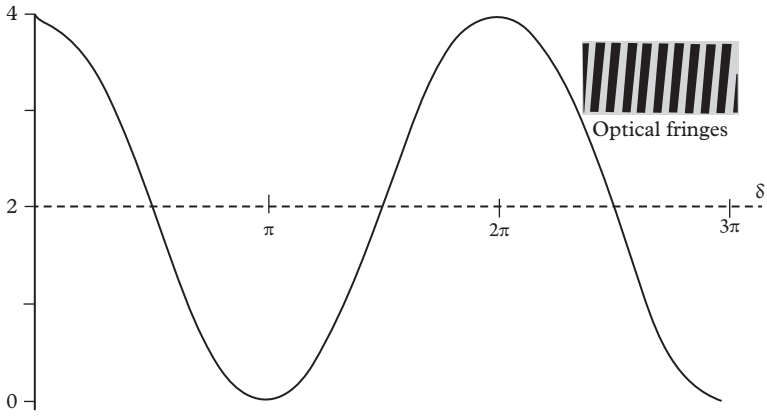

Figure 4.3 *Interference of two waves of equal intensity as described by (4.15). The insert is a photograph of optically generated fringes.*

The importance of the time average in the equations for interference cannot be overemphasized. If interference is to be observed, temporal variations of δ must be small during the period T over which we take the temporal average. From an operational viewpoint, the detector used to observe interference must respond in a time T that is shorter than the time for the intensity variations of the interference process to occur if interference is to be observed. We can define a time τ_c that characterizes the temporal variations of the phase: if $\tau_c > T$, then the waves are said to be *coherent*, and interference effects are observable and the interference term is nonzero. (We will have more to say about the subject of coherence in Chapter 8; in this chapter, all temporal effects will be assumed to be negligible, with $\tau_c \gg T$.)

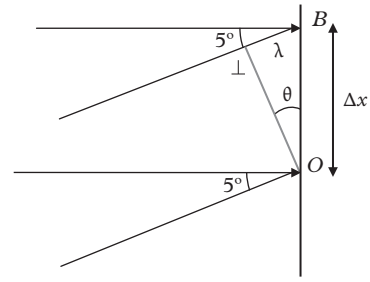

Figure 4.4 *Two plane waves intersecting on the plane OB. Note that the angle as drawn is four times too large.*

The significance of fringe structure can be understood by looking at a simple fringe pattern produced by two plane waves, as shown in Figure 4.4. The fringes that occur along the plane of intersection OB are shown in Figure 4.5. The intensity distribution described by (4.15) and shown in Figure 4.3 varies periodically between $4I$ and 0. The change in phase between two maxima (bright bands) is given by

$$\delta_{m+1} - \delta_m = (m+1)2\pi - (m)2\pi = 2\pi,$$

which corresponds to a change in the difference in optical path length of the two waves equal to one wavelength, since

$$\Delta = \mathbf{k}_0 \cdot n(\mathbf{r}_1 - \mathbf{r}_2) \propto \frac{2\pi}{\lambda_0}.$$

We have selected the geometry in Figure 4.4 because it is easy to convert the phase change to a dimension in the experimental configuration. At point O, the two waves are assumed to be in phase. They are in phase again at point B, where the wave traveling at an angle has

Figure 4.5 *Interference fringes occurring on the plane OB.*

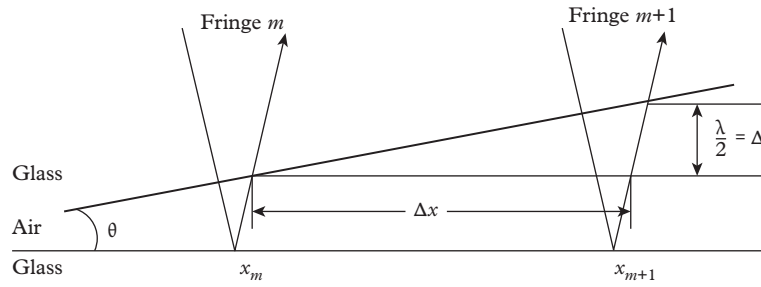

Figure 4.6 *Two glass plates with a wedge of air between them.*

traveled an additional full wavelength. The spacing between bright bands if the plane waves have a wavelength of 632.8 nm and intersect at an angle of 5° is given by

$$\sin\theta = \frac{\overline{AP}}{\overline{OP}} = \frac{\lambda}{\Delta x},$$

$$\Delta x = \frac{\lambda}{\sin\theta} \approx \frac{\lambda}{\theta},$$

$$\Delta x = 7\ \mu\text{m}.$$

Our eyes cannot resolve a spacing this small but could resolve a fringe spacing of 1 mm. The angle between the two beams that would produce fringes similar to Figure 4.5 with 1 mm spacing would be

$$\sin\theta = \frac{632.8 \times 10^{-9}}{10^{-3}},$$

$$\theta \approx 0.04°.$$

To produce the required two plane waves, we could simply reflect a plane wave from two glass plates—one tilted at an angle θ with respect to the other. To produce the small angle required to see the fringes, we could place a tissue between the two plates, along one edge. Figure 4.6 shows the experimental arrangement. The first thing to note is that the value of m is not needed to obtain the angle between the two waves. We only need the change in m, Δm, the number of fringes we cross while measuring the distance Δx in the plane OB containing the fringes. The second observation to make is that by generating fringes, we have produced a ruler with wavelength accuracy that allows us to measure very small physical parameters. In the remaining part of this chapter, we will develop physical models that will allow the use of the wavelength accuracy provided by interference to measure useful properties of physical objects.

4.4 Young's Interference

There are a number of ways to produce two waves that exhibit interference. One way is to mix samples of a single wavefront. This approach was first used by **Francesco Maria Grimaldi (1618–63)**, who used an extended source to illuminate a pair of pinholes. The variations in the light distribution observed by Grimaldi could be explained not only by the theory of interference, but also by the theory of diffraction (we will discuss the theory of

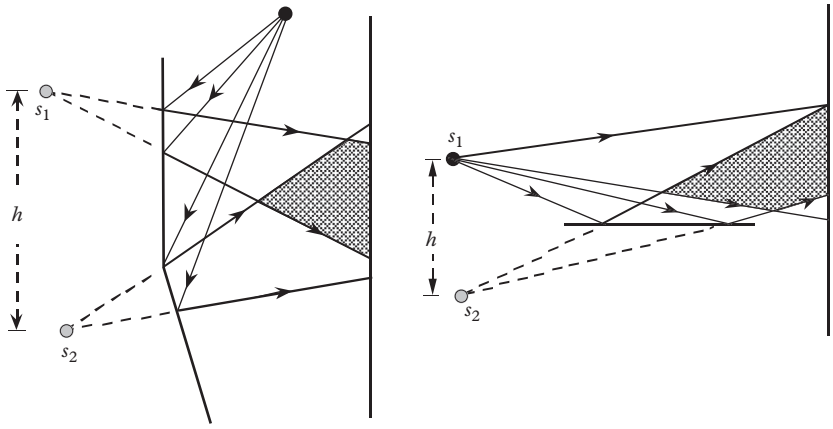

Figure 4.7 *Fresnel's mirrors and Lloyd's mirror. The shaded area is the region where fringes are observed.*

diffraction in Chapters 9–11). Thomas Young attempted to discriminate between the two theories by placing a pinhole between the source and the pair of pinholes. While Young's experiment was an improvement over Grimaldi's, it did not remove the possibility that diffraction created the observed light distribution. Fresnel and Lloyd each developed an experimental arrangement (Figure 4.7) that removed all question as to the origin of the observed dark and light bands. The interference pattern from a Lloyd's mirror experiment is shown in Figure 4.8.

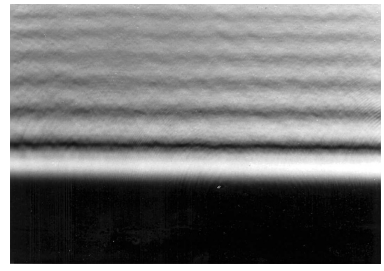

Figure 4.8 *Interference fringes from a Lloyd's mirror experiment. A HeNe laser was focused onto a pinhole, and the light transmitted through the pinhole illuminated a flat mirror. The fringe at the plane established by the mirror surface is a dark fringe.*

We will examine Young's experiment in detail because of its simplicity. The experiments of Fresnel and Lloyd can be explained by the theory of Young's experiment and the law of reflection. All discussion of diffraction in Young's experiment will be delayed until we develop diffraction theory in Chapter 9.

The experimental geometry of Young's experiment is shown in Figure 4.9. The origin of the (x, z) coordinate system is centered between two slits, labeled s_1 and s_2, separated by

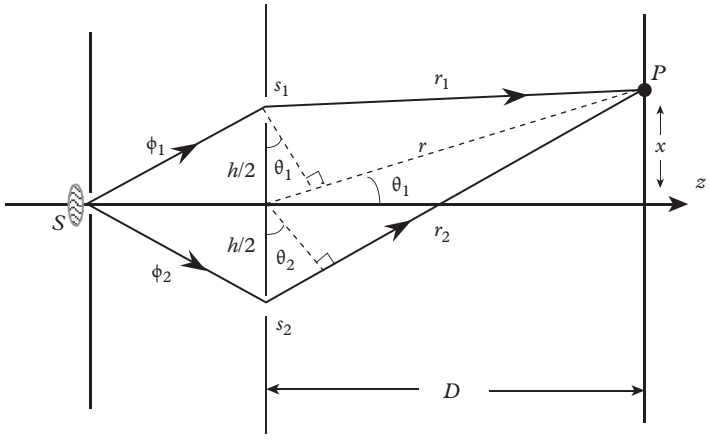

Figure 4.9 *Young's two-slit experiment.*

a distance h and extending out of the sheet of paper. (Slits make the interference pattern much easier to observe than the interference pattern produced by two pinholes by increasing the length of the interference fringes.) These slits are illuminated by a light source S, which produces a single frequency and whose extent is limited by a pinhole. The light, upon reaching s_1 and s_2, differs in phase by $\phi_2 - \phi_1$. (This phase difference is zero; it would be nonzero if the pinhole at the source were not centered with respect to the two slits.) The two slits obtain samples of the wavefront that is emitted from the pinhole. We observe the interference produced by the two wave samples after they have propagated through the distance D. We will depend upon diffraction, the subject of later chapters, to overlap the two waves; however, a lens could be used to image the source pinhole on the observation screen and thereby overlap the waves from s_1 and s_2.

The light from s_1 travels a path r_1 and the light from s_2 travels the path r_2 to the observation point P in the observation plane, a distance D from the slit plane. The intensity at P is determined by the total phase difference

$$\delta = \phi_2 - \phi_1 + k(r_2 - r_1).$$

The distances r_1 and r_2 are not easy to measure; however, the angles are experimentally more accessible. The angles shown in Figure 4.9 are defined by the equations

$$\sin\theta_1 = \frac{r - r_1}{h/2}, \qquad \sin\theta_2 = \frac{r_2 - r}{h/2}.$$

These angles are defined using distances that are not easily measured. To define the angles in terms of easily measured parameters, we assume that the distance D from the slits to the observation screen is much larger than the height of the observation point above the z-axis, i.e., $x < D$. With this assumption, $\sin\theta_1 \approx \tan\theta_1$, and we may write the distances r_1 and r_2 in terms of quantities that are easy to measure:

$$\sin\theta_1 = \frac{r - r_1}{h/2} \approx \tan\theta_1 = \frac{x}{D}$$

and

$$\sin\theta_2 = \frac{r_2 - r}{h/2} \approx \tan\theta_2 = \frac{x + h/2}{D}.$$

We further assume that $h < x < D$ so that we may neglect terms that involve h^2:

$$r_2 - r \approx \frac{xh}{2D}.$$

Now adding $(r_2 - r) + (r - r_1)$, we obtain the difference in the path lengths from s_1 to P and from s_2 to P in terms of easily measured experimental parameters:

$$r_2 - r_1 = \frac{xh}{D}.$$

The interference term

$$2\sqrt{I_1 I_2}\cos\delta$$

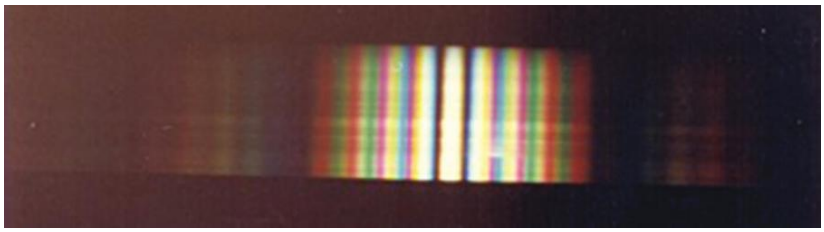

Figure 4.10 *Fringes from a two-slit experiment, made with white light.*

from (4.12) can now be evaluated by using

$$\delta = \phi_2 - \phi_1 + k(r_2 - r_1) = \Delta\phi + \frac{2\pi xh}{\lambda D}. \tag{4.16}$$

The interference pattern that results consists of bright and dark bands perpendicular to the plane of Figure 4.9. An experimental example of Young's fringes, generated using white light, is shown in Figure 4.10.

As stated in our introductory arguments about interference, whenever the argument of the cosine changes by 2π, the intensity on the screen passes through one cycle in intensity, say maximum to minimum and back to maximum:

$$\left(\frac{2\pi x_1 h}{\lambda D} + \Delta\phi\right) - \left(\frac{2\pi x_2 h}{\lambda D} + \Delta\phi\right) = 2\pi.$$

A single cycle in intensity that we have defined as a *fringe* corresponds to spacing between two bright or two dark bands. The spatial period of a fringe, i.e., its repeat distance, is given by

$$x_1 - x_2 = \frac{\lambda D}{h}. \tag{4.17}$$

From (4.17), we see that the spacing of the fringes on the viewing screen is inversely proportional to the slit spacing. Note also that the fringe spacing is a linear function of the wavelength. The fringes in Figure 4.10 were produced with white light that allows the wavelength dependence of these fringes to be seen.

The fringes are generated by adding waves originating from two samples of a wavefront obtained by using the two slits. For this reason, the term *interference by division of wavefront* is often used to describe this type of interference. Another view of the interference process is that it performs a comparison of two waves and provides a measure of their similarity; here the comparison would be between two different parts of the same wavefront. (We will discuss this view of interference during the discussion of coherence in Chapter 8.)

4.5 Dielectric Layer

Nature produces interference in a configuration that we encounter in our everyday lives. The interference is produced by waves reflecting from two surfaces of a thin dielectric film. In contrast to Young's experiment, the two interfering waves come from the same transverse position on a wavefront, resulting in this type of interference being labeled *interference by division of amplitude.*

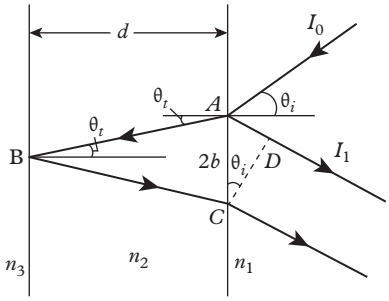

Figure 4.11 *Dielectric layer of index n_2 and thickness d separating a medium of index n_1 and a medium of index n_3.*

The geometrical model that will be used to discuss interference by reflection from a thin dielectric layer is shown in Figure 4.11. Light enters a thin dielectric film of thickness d at point A. A portion of the amplitude of the wave is reflected toward D, remaining in the medium with index n_1, while another portion proceeds from A to B and then to C in the medium with index n_2. A lens is assumed to gather the waves at C and D and bring them together on a viewing screen, as shown in Figure 4.12. The paths taken from C and D to the viewing screen are the same for both waves; therefore, this portion of the two paths will not contribute to the phase difference δ between the two waves and may be ignored. Using the geometry in Figure 4.11, the optical path lengths for the waves from A to D and from A to C via B will be obtained. These optical path lengths will then be used to find δ for use in (4.13).

The optical path as light travels from A to B in the thin film is

$$\frac{k_2 d}{\cos\theta_t} = \frac{\omega n_2 d}{c\cos\theta_t}.$$

Light is reflected off the back surface of the dielectric film at point B and travels an equivalent optical path from B to C. Thus, the optical path from A to B to C in the medium with index n_2 is

$$\overline{ABC} = \frac{2\omega n_2 d}{c\cos\theta_t}. \tag{4.18}$$

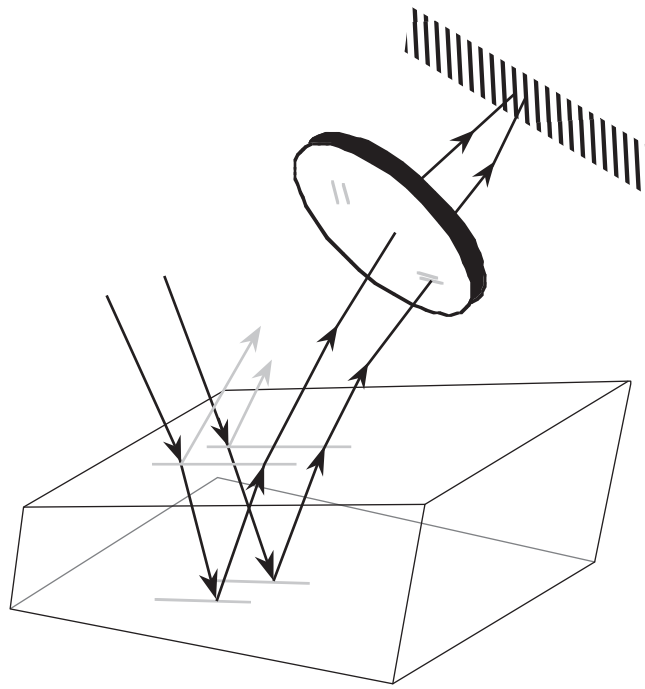

Figure 4.12 *Use of a lens to produce fringes from a dielectric layer.*

The optical path length from A to D in the medium with index n_1 is

$$\overline{AD} = k_1 2b \sin\theta_i = 2k_1 d \tan\theta_t \sin\theta_i$$

$$= \frac{2\omega n_1 d}{c} \frac{\sin\theta_i \sin\theta_t}{\cos\theta_t}. \tag{4.19}$$

Applying Snell's law, we can rewrite (4.19) as

$$\overline{AD} = 2\omega d n_2 \frac{\sin^2\theta_t}{c\cos\theta_t}.$$

Since the source for the two waves is identical, $\Delta\phi = 0$, and the phase difference between the waves at points C and D will determine the value of the interference term:

$$\delta = \overline{ABC} - \overline{AD} = \frac{4\pi n_2 d}{\lambda_0} \cos\theta_t. \tag{4.20}$$

There is an additional phase change of π upon reflection from a dense medium (see Figure 3.5 and remember that we earlier assumed that the polarization will be normal to the plane of incidence for all interference problems). If $n_2 > n_1$, the reflection at A will experience this additional phase change, and if $n_3 > n_2$, the reflection at B will experience a phase change. We will assume $n_3 < n_2$ and $n_2 > n_1$ for our discussion so that the only phase change due to reflection occurs at A. A bright band will occur when $\delta = 2\pi m$:

$$\delta = 2\pi m = \frac{2n_2 d}{\lambda_0} 2\pi \cos\theta_t + \pi.$$

Three of the parameters in this equation could independently cause δ to vary and produce a set of interference fringes. These parameters are d, λ_0, and θ_t.

4.5.1 Fizeau Fringes

If we illuminate the dielectric layer with a plane wave, with a single frequency, then $\cos\theta_t$ is constant over the layer, and each bright or dark band will show a region of constant optical thickness. The thickness associated with a particular bright band is given by

$$d = \frac{\lambda_0 (2m-1)}{4n_2 \cos\theta_t}. \tag{4.21}$$

These are called *Fizeau fringes* or fringes of constant thickness.

The geometry that could produce Fizeau fringes is shown schematically in Figure 4.13(a), where a plane wave is assumed to illuminate a dielectric film with a nonuniform thickness. The fringes, as observed by the eye, are produced by reflections of the wave in the film. Figure 4.13(b) displays fringes in a vertical soap film illuminated by sodium light (see Problem 4.13).

4.5.2 Color Fringes

The thickness of the dielectric film could be a constant and the illumination could be from a source producing a range of wavelengths—for example, an oil film floating on a the surface

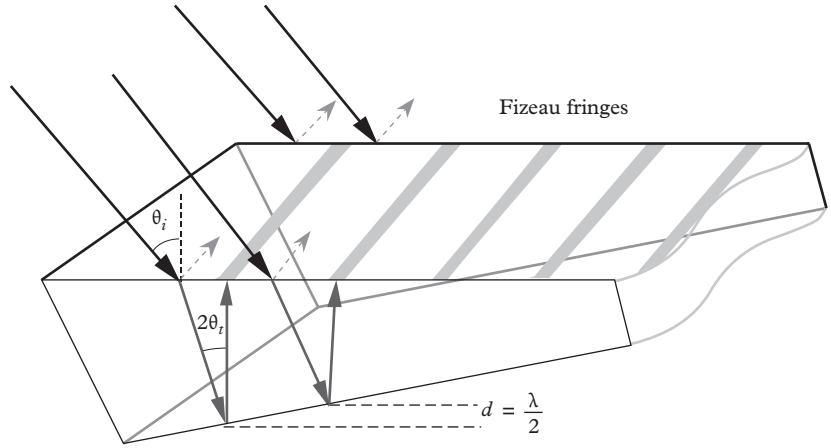

(a)

(b)

Figure 4.13 *(a) The production of Fizeau fringes in a dielectric layer with a nonuniform thickness. The fringes appear to be located at the dielectric layer but originate because of the interference of light collected by a lens such as the eye. (b) Fizeau fringes produced by illuminating a vertical soap film with sodium light. Gravity creates a nearly linear thickness change in the film.*

of a flooded river and illuminated by sunlight, as in Figure 4.14(a), or a vertical soap film illuminated by an incandescent bulb, as in Figure 4.14(b). Those regions of the film with the same thickness display the same color band; the color pattern repeats when the thickness changes by one wavelength. The wavelength for a bright band is given by

$$\lambda_0 = \frac{4n_2 d\cos\theta_t}{2m-1}. \tag{4.22}$$

(a)

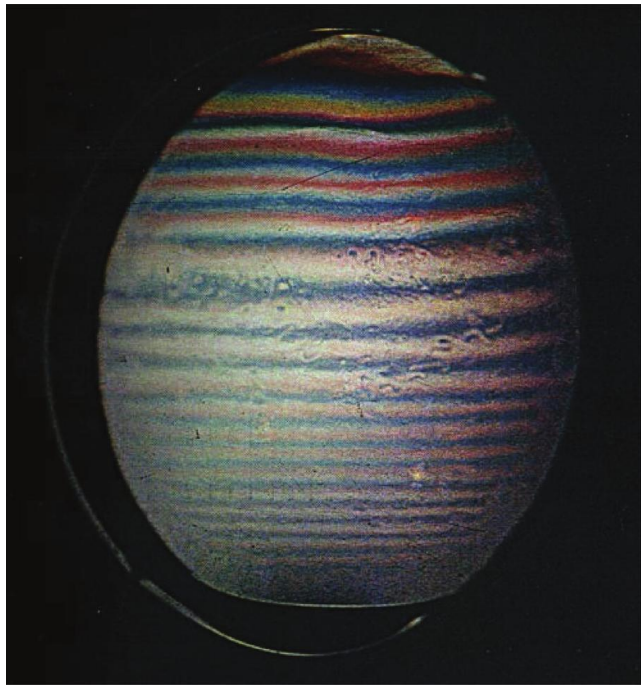

(b)

Figure 4.14 *(a) An oil film created by diesel fuel on water. (John [CC BY-SA 2.5], via Wikimedia Commons <http://commons.wikimedia.org/wiki/File:Dieselrainbow.jpg>.) (b) A soap film similar to the one shown in Figure 4.10(b), but here the soap film is illuminated by white light. The color pattern repeats when the thickness changes by one wavelength, and thus each cycle in color corresponds to one order, m, in the interference pattern.*

4.5.3 Haidinger's Fringes

If the thickness and the wavelength of the illumination are constant, then fringes of constant inclination, *Haidinger's fringes*, will be observed. The fringes will be concentric circles if the line of sight, from the viewing point to the dielectric layer, is normal to the surface and if the incident wave is nearly parallel to the line of sight. Bright bands will occur at an angle given by

$$\cos\theta_t = \frac{(2m-1)\lambda_0}{4n_2 d}.$$

We can rewrite this in terms of the angle of incidence by using Snell's law:

$$\sin\theta_i = \frac{1}{n_1}\sqrt{n_2^2 - \frac{n_2\,(2m-1)\lambda_0}{4d}}. \tag{4.23}$$

An example of these fringes is shown in Figure 4.17(c).

4.5.4 Antireflection coating

The interference resulting from light reflected by the surfaces of a dielectric layer can be used to reduce the reflectivity of the substrate supporting the layer. This is accomplished by selecting a layer thickness that results in destructive interference between the waves reflected by the front and back surfaces. The antireflection coating was invented by Olexander Smakula (1900–1983) (in English, it is Alexander) in 1935 while at Zeiss. Assume that light is incident normal to the surface of the dielectric, so that $\theta_t \approx 0$ and $\cos\theta_t \approx 1$; also assume that $n_1 < n_2 < n_3$ so that there is an equal phase change for reflections from the two surfaces of the dielectric film. To observe a dark band, we require (4.20) to fulfill the condition

$$\delta = (2m+1)\pi = \frac{2n_2 d \cdot 2\pi\cos\theta_t}{\lambda_0}.$$

Thus, the film thickness required to produce destructive interference for light incident normal to the surface is

$$d = \frac{2m+1}{4}\frac{\lambda_0}{n_2} = (2m+1)\frac{\lambda}{4}.$$

This equation is identical to (4.21), but now the bands are dark bands. This change in intensity of a band is due to the assumption made about the relative size of the various indices. The film layer is usually called a quarter-wave layer for obvious reasons.

The dielectric film thickness must be an odd multiple of $\lambda/4$ for there to be destructive interference between the light reflected from the front and back surfaces of the layer. When this condition is met, there will be no light reflected from the front surface, and the dielectric layer will be an antireflection coating (Figure 4.15). The index n_2 of the film appears in the equation to correct the wavelength for the velocity of propagation in the medium.

We have said nothing about the amount of light reflected at the surfaces. If equal amounts of light are not reflected by the two surfaces, then total cancellation of the reflected component will not occur. Fresnel's formula can be used to determine the condition for which equal fractions of light will be reflected from the two surfaces. If we require that the reflectivities of the two surfaces be equal, then, for normal incidence, (3.46) yields

$$\frac{n_2 - n_1}{n_2 + n_1} = \frac{n_3 - n_2}{n_3 + n_2}.$$

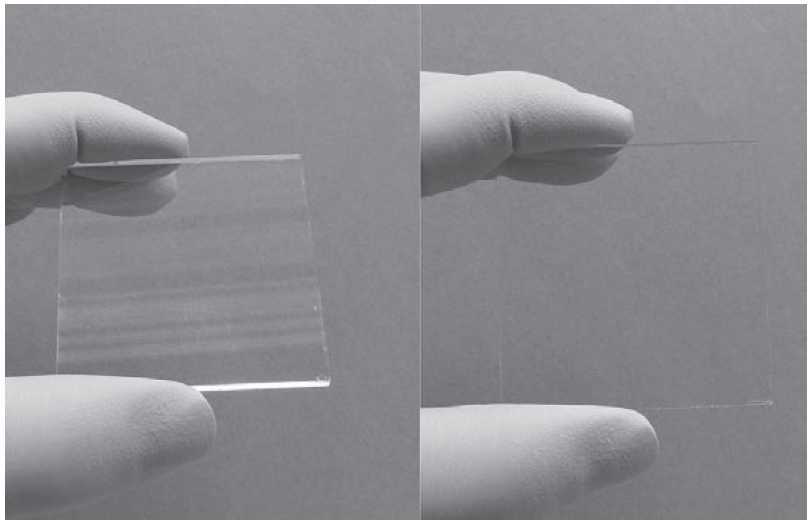

Figure 4.15 *Use of antireflection coating. (Antireflection coating split pic by Zaereth—Own work. Licensed under Creative Commons Zero, Public Domain Dedication via Wikimedia Commons <http://commons.wikimedia.org/wiki/File:Antireflection_coating_split_pic.jpg#mediaviewer/File:Antireflection_coating_split_pic.jpg>.)*

We can assume $n_1 = 1$ since most optical surfaces are used in air. With this assumption, the equation reduces to

$$n_2 = \sqrt{n_3}.$$

For some flint glasses, $n = 1.7$ and $\sqrt{n} = 1.305$. Magnesium fluoride has an index $n = 1.38$ that is reasonably close to the desired index n_2, and therefore it should act as a good antireflection coating for glasses with $n = 1.7$. For many years, magnesium fluoride was used as an antireflection coating for glasses of all indices because it was easy to apply and relatively rugged. On a typical crown glass, the reflection will be reduced from 4% to 1%. (Additional details on the design of antireflection coatings and high-reflectivity mirrors are given in Appendix 4A.)

4.5.5 Newton's Rings

The dielectric film need not have an index of refraction larger than its surroundings. Newton's rings are an example of interference fringes produced by a dielectric film whose index of refraction is less than its surroundings. Newton's rings are Fizeau fringes or fringes of constant thickness and can be obtained by placing a convex lens in contact with a flat glass plate to form an air wedge. Circular interference fringes are formed about the point of contact—point O in Figure 4.16. The radius of a dark or light band of the fringes can be calculated in terms of the radius of curvature of the lens.

In Figure 4.16, the radius of curvature of the lens is R and the radius of a band making up one of Newton's rings is ρ. These two parameters can be related by the Pythagorean theorem:

$$R^2 = \rho^2 + (R - d)^2,$$

where d is the thickness of the air gap at the fringe. Thus,

$$\rho^2 = d(2R - d),$$

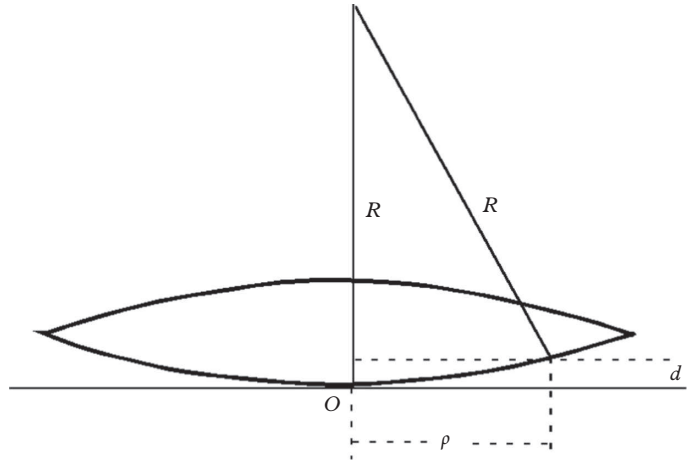

(a)

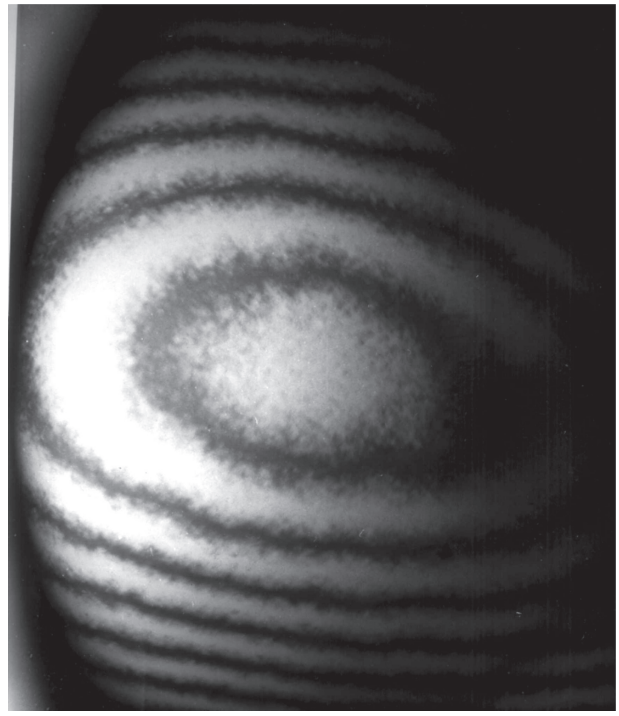

(b)

Figure 4.16 *(a) Experimental set-up for the observation of Newton's rings. (b) Newton's rings produced by the air film between a lens and an optical flat.*

and since $d \ll R$, we can write

$$d = \frac{\rho^2}{2R}. \tag{4.24}$$

We assume normal incidence, so $\cos\theta_t \approx 1$ and we get from (4.21) that the dark bands will be rings with radii given by

$$\rho^2 = \frac{m\lambda_0 R}{n_2}, \qquad m = 0, 1, 2, \ldots, \tag{4.25}$$

and the bright bands will be rings with radii given by

$$\rho^2 = \frac{\left(m + \frac{1}{2}\right)\lambda_0 R}{n_2}, \qquad m = 0, 1, 2, \ldots . \tag{4.26}$$

Usually, the gap between the test plate and the lens is air, so $n_2 = 1$. Note that here, because we see the contact point of the lens and the test plate, we actually know the value of m, which starts at $m = 0$ at the contact point. In other interference measurements, the value of m is the path length measured in wavelengths and is not known. Instead, we measure Δm, which is the number of dark fringes between two points on the interferogram.

Modern lens grinders use these fringes to monitor their work [2, 3]. Newton's rings can provide not only a qualitative idea of the quality of the lens but also a quantitative measure by providing the lens designer with a measurable parameter that will relate to the radius of curvature of the lens under construction. The parameter is the radius of a Newton's ring. Through the use of either (4.25) or (4.26), the optician can measure the radius of a Newton's ring to determine if the lens being ground has reached the proper curvature. If the Newton's rings are not symmetric, then errors in the figure of the lens can be identified and corrected. (The *figure* of an optical surface refers to how well the actual shape of the surface conforms to the desired shape.)

4.6 Michelson Interferometer

Albert Abraham Michelson (1852–1931), the first American scientist to win the Nobel Prize in Physics, developed the design for an interferometer that has found a number of useful applications. The interferometer will work with a much larger source than one can use with the two-slit arrangement of Young's experiment, giving much brighter interference fringes. A beam splitter (a semitransparent mirror) is used to divide the light into two beams, as shown in Figure 4.17(a). The two beams are directed along orthogonal paths, usually called the arms of the interferometer, where they strike two mirrors, M_1 and M_2, and then return to the beam splitter, where they interfere. Looking at the beam splitter from the detector, we see an image of mirror M_2 near mirror M_1. The image M_2' and the mirror M_1 form a dielectric layer of thickness d. The interferometer is assumed to be in air, so the dielectric layer has an index of refraction $n_2 = 1$. Also, light reflected from M_1 and M_2 experiences the same phase change upon reflection, and thus no additional phase shift need

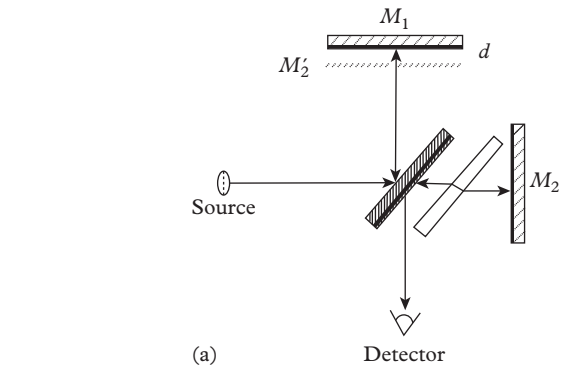

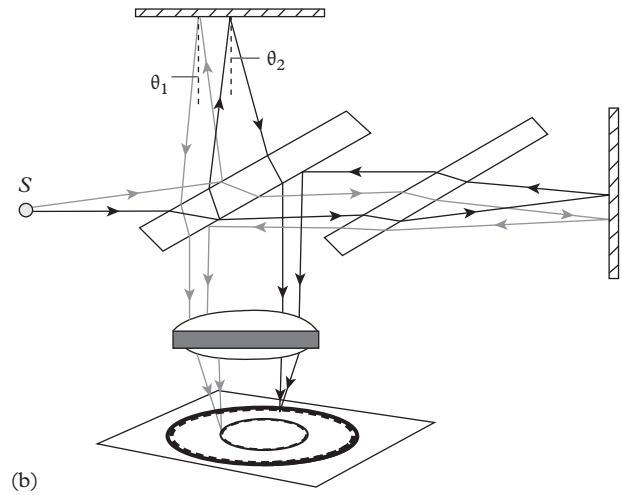

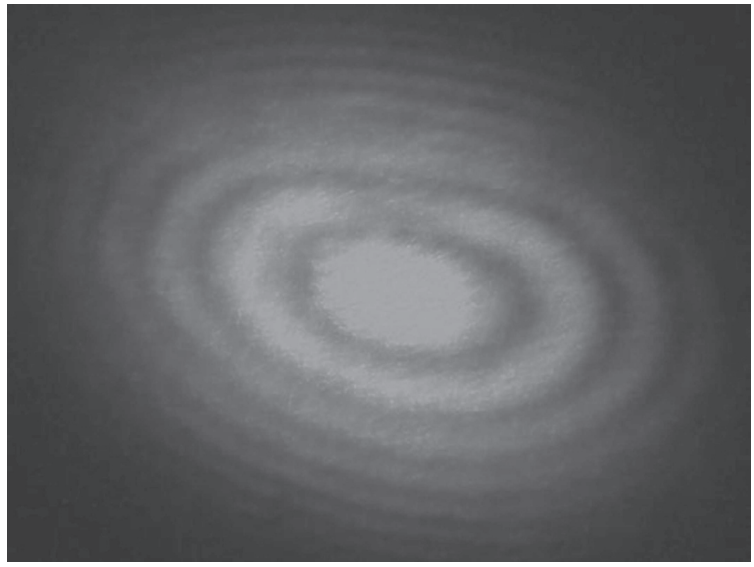
(c)

Figure 4.17 *(a) Michelson interferometer. The diagonal plate with one solid surface is a beam splitter and the solid surface represents a partially reflective coating. It creates two beams traveling toward mirrors M_1 and M_2. The second diagonal plate is called the compensating plate. The compensating plate is made of the same material and thickness as the beam splitter. Its purpose is to equalize the optical path length of the two arms of the interferometer. (b) Haidinger's fringes produced in a Michelson interferometer. Both mirror surfaces are assumed to be normal to the axis of the interferometer. The light source is a point source producing spherical waves. The gray line has a smaller angle of incidence on the mirrors than has the black line, $\theta_1 < \theta_2$. (c) Interferogram from a Michelson interferometer.*

be added to δ when calculating the phase difference between the two waves. The total phase difference for a bright band is

$$\delta = 2\pi m = \frac{2d \cdot 2\pi \cos\theta_t}{\lambda_0}.$$

The source shown in Figure 4.17(a) is nearly a point source, generating spherical waves that produce fringes of constant inclination, (4.23). The fringes are circularly symmetric, as shown in Figure 4.17(b), if d is constant across the aperture. As we stated earlier, we really do not need to know the value of m, but we can figure it out. The maximum value of m, the order of the fringe, occurs at the center of the set of fringe rings, where $\theta_t = 0$,

$$m_{\max} = \frac{2d}{\lambda_0}, \tag{4.27}$$

and the order of the fringes decreases as we move out from the center fringe in the viewing plane. The order of the fringe is shown by (4.27) to be equal to the difference in lengths of the two interferometer arms expressed in the number of wavelengths of light contained in d.

As d increases, a bright band will move out from the center of the aperture and a new bright band of higher order will take its place at the center. If we placed a detector at the position of the center fringe and monitored the intensity as we moved one of the mirrors, and thereby changed d, we would see

$$I = I_1 + I_2 + 2\sqrt{I_1 I_2}\cos\left(\frac{2\omega d}{c}\right), \tag{4.28}$$

where we have substituted

$$\frac{\omega}{c} = \frac{2\pi}{\lambda_0}.$$

If the beam splitter is a 50:50 splitter, then the intensities of light in the two arms will be the same and we can write

$$I = I_0\left[1 + \cos\left(\frac{2\omega d}{c}\right)\right]. \tag{4.29}$$

Using the physical arrangement shown in Figure 4.17, the light in the M_1 arm of the interferometer travels an extra distance, $2d$, to reach the detector. This means that two waves are added together that originated at different times; the difference in time between the origination of the two waves is

$$\tau = \frac{2d}{c}, \tag{4.30}$$

which is called the *retardation time* (the light wave in arm M_1 has been delayed or retarded with respect to the wave in arm M_2). Using the definition (4.30), we can rewrite (4.29) as

$$I = I_0(1 + \cos\omega\tau). \tag{4.31}$$

The signal is made up of a constant term plus an oscillatory term. The oscillatory term will provide information about the coherence properties of the light, as we will see in Chapter 8.

The Michelson interferometer has a number of shortcomings that have been overcome by modifying its design. The Twyman–Green interferometer (Figure 4.18) is a Michelson interferometer that utilizes a plane wave, produced by a collimating lens. The simple fringe pattern makes the Twyman–Green interferometer useful for the evaluation of optical components. Without the collimating lens, a large number of fringes (Haidinger's fringes) would be present, making interpretation of the data difficult. By the addition of a collimating lens, θ_t is converted from a variable to a constant. This means that since the angle of incidence is constant, the fringes are of equal thickness (Fizeau fringes) and (4.21) applies.

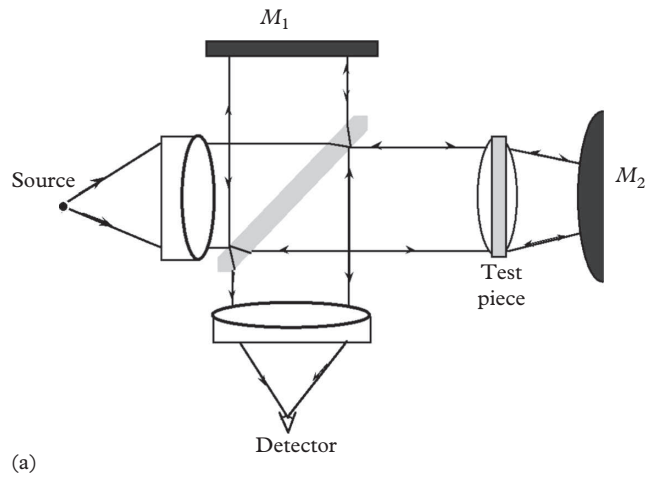

(a)

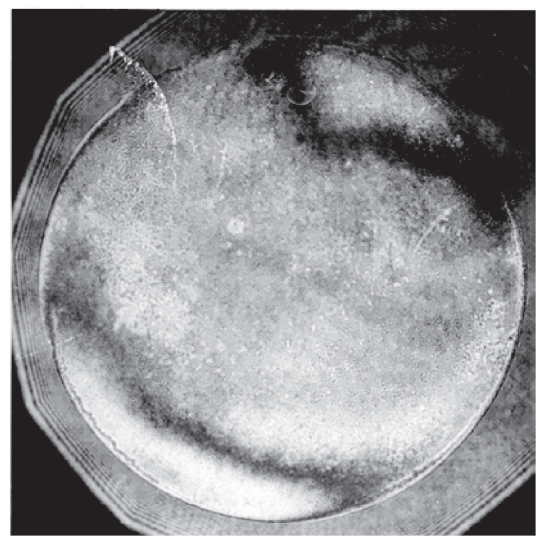

(b)

Figure 4.18 *(a) An improvement on the Michelson interferometer for the testing of optical components. If the test piece is perfect, the waves interfering on the beam splitter are plane waves. M_2 can be either a plane mirror or spherical mirror. The spherical mirror has several experimental advantages. (b) The Twyman–Green interferometer can be used to test a mirror surface by replacing the "test piece" and M_2, shown in (a), by the test mirror. Here is shown a mirror in just such a configuration. The mirror was designed for use at 10 μm, but the wavelength used in the interferometer was 0.44 μm. Thus the fringes in the interferogram correspond to 1/25 of a fringe at the mirror's operating wavelength.*

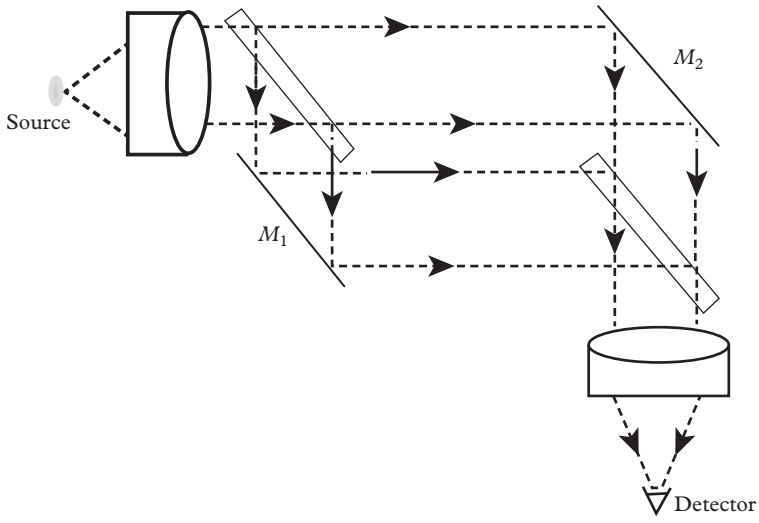

Figure 4.19 *A Mach–Zehnder interferometer configured to use plane waves. Either of the arms can be used as the test area.*

The Mach–Zehnder interferometer (Figure 4.19) also uses collimated light, but further simplifies the understanding of the observed fringes by passing light through the test area only once. By separating the two optical paths, very large objects such as wind tunnels can be tested. Either arm of the interferometer can contain the test area.

Measurements using interferometers are expressed in fringes per unit length. One fringe spacing equals the distance between adjacent dark bands.

4.7 Interference by Multiple Reflection

In our previous discussion of a thin dielectric film, we neglected multiple reflections. We now wish to consider what effect multiple reflections have on interference. We will find that the dielectric layer forms a resonant cavity. If the losses at each reflection are not too great, a set of standing waves are created in the dielectric layer, similar to a set of standing waves that form on a guitar string. The mathematics become somewhat involved, but once completed it demonstrates that the dielectric layer acts like a wavelength filter, transmitting some frequencies and rejecting others.

Before looking at the optical problem, consider a guitar string fixed, at each end, to rigid mounts, the bridges. The boundary conditions for the wave equation become $y = 0$ at $x = 0$ and $x = L$. The boundary conditions are met if

$$\frac{2\pi L}{\lambda} = kL = m\pi, \quad m = 1, 2, 3, \ldots . \tag{4.32}$$

The solutions to the wave equation become

$$y(x, t) = Y_m \sin\left(\frac{m\pi x}{L}\right)\cos \omega_m t, \tag{4.33}$$

where

$$\omega_m = \frac{\pi mc}{L}$$

and c is the wave velocity. The solutions (4.33) are called the normal modes of vibration of the string and are standing waves of the form (3.6). The spatial dependence of a standing wave is

$$y(x) = Y_m \sin\left(\frac{m\pi}{L}\right)x.$$

These functions are the eigenmodes of the string, and the frequencies ω_n are the eigenvalues.

In a dielectric layer (Figure 4.20), the light waves reflecting back and forth between the boundaries of the dielectric layer will result in solutions of the same form as (4.33), causing the dielectric layer to behave as a resonant structure. We will ignore the fields in the dielectric layer and direct our attention toward the light transmitted through the layer. Assume that a wave of amplitude A is incident upon the layer. We let f_1 be the fraction of A that is reflected from the surface, f_2 the fraction transmitted into the layer, and f_3 the fraction transmitted out of the film. [If the wave were incident normally to the layer, Fresnel's equations would give

$$f_2 = \frac{2n_1}{n_1 + n_2}, \quad f_3 = \frac{2n_2}{n_1 + n_2}, \quad f_1 = \frac{\pm(n_2 - n_1)}{n_1 + n_2},$$

but we will retain the current notation to allow the results to be applied to any illumination angle. A second method of handling the notation required for multiple reflections is introduced in Appendix 4A.]

We will determine the interference of the transmitted waves by calculating the amplitude and phase of each transmitted wave. The waves will then be added using the complex approach. As shown in Figure 4.12, a lens will be used to collect all of the transmitted waves and bring them together at a viewing screen. All of the waves are assumed to travel the same optical path length upon exit from the dielectric so that the wave combining process can be neglected.

We will represent the first transmitted wave by

$$\tilde{E} = Af_2f_3e^{i(\omega t - \mathbf{k}\cdot\mathbf{r})}.$$

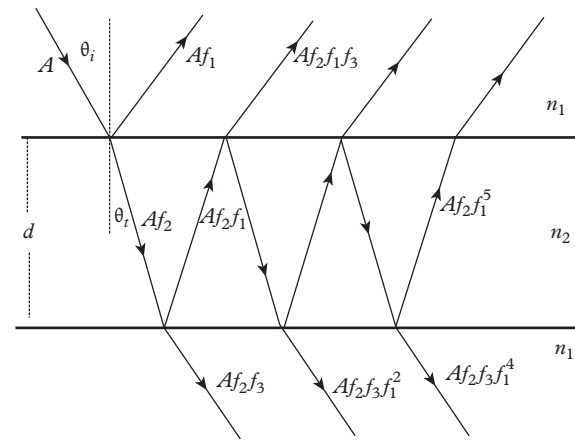

Figure 4.20 *Reflection of a plane wave in a plane parallel dielectric layer.*

The reflection coefficient of the dielectric layer is defined as $r = f_1$ and the reflectivity of the layer as r^2. The transmitted amplitudes for the various reflected waves form a geometric progression (sequence) in terms of the reflectivity:

$$\tilde{E}, \quad \tilde{E}r^2, \quad \tilde{E}r^4, \quad \tilde{E}r^6, \ldots .$$

Each transmitted wave will have a constant phase difference, relative to its neighbor, given by (4.20):

$$\delta = \frac{4\pi d n_2 \cos\theta_t}{\lambda_0}. \tag{4.34}$$

The general, nth, transmitted wave is of the form

$$\tilde{E}r^{2n}e^{i\delta_n} = r^{2n}Af_2f_3e^{i(\omega t - \mathbf{k}\cdot\mathbf{r})}e^{in\delta}, \tag{4.35}$$

where $n = 0, 1, 2, \ldots$. To add all of the transmitted waves, we use the complex method (the vector approach is used in Problem 4.19). In adding the transmitted waves, we can factor $\tilde{E}$ outside the summation because all of the transmitted waves are at the same frequency and all are propagating in a parallel direction:

$$\begin{aligned}\tilde{A} &= \tilde{E}\left(1 + r^2e^{i\delta} + r^4e^{i2\delta} + r^6e^{i3\delta} + \ldots\right)\\ &= \tilde{E}\left(1 + r^2\cos\delta + r^4\cos 2\delta + \ldots\right) + i\tilde{E}\left(r^2\sin\delta + r^4\sin 2\delta + r^5\sin 3\delta + \ldots\right).\end{aligned} \tag{4.36}$$

To evaluate this equation, we use the identity

$$\frac{1}{1+x} = 1 - x + x^2 - x^3 + x^4 - \ldots, \qquad -1 < x < 1,$$

to write

$$\frac{1}{1 - r^2e^{i\delta}} = 1 + r^2e^{i\delta} + r^4e^{i2\delta} + r^6e^{i3\delta} + \ldots, \qquad r^2 < 1.$$

The right-hand side of this equation is identical to (4.36) if we multiply by $\tilde{E}$, and the left-hand side can be rewritten as

$$\frac{1}{1 - r^2e^{i\delta}} = \frac{1}{1 - r^2e^{i\delta}}\,\frac{1 - r^2e^{-i\delta}}{1 - r^2e^{-i\delta}} = \frac{1 - r^2e^{-i\delta}}{1 - r^2\left(e^{i\delta} + e^{-i\delta}\right) + r^4}.$$

Using the identity

$$e^{\pm i\delta} = \cos\delta \pm i\sin\delta,$$

we have

$$\frac{1}{1 - r^2e^{i\delta}} = \frac{1 - r^2\cos\delta + ir^2\sin\delta}{1 - 2r^2\cos\delta + r^4}. \tag{4.37}$$

Equating real and imaginary parts of (4.36) and (4.37), we obtain for the real part

$$\frac{1 - r^2\cos\delta}{1 - 2r^2\cos\delta + r^4} = 1 + r^2\cos\delta + r^4\cos 2\delta + \ldots, \tag{4.38}$$

and for the imaginary part

$$\frac{r^2 \sin\delta}{1 - 2r^2\cos\delta + r^4} = r^2\sin\delta + r^4\sin 2\delta + r^6\sin 3\delta + \dots \,. \tag{4.39}$$

The intensity of the transmitted light is

$$I \propto \tilde{A}\tilde{A}^*,$$

which is the sum of the squares of the real and the imaginary terms we have just calculated:

$$I \propto \frac{\tilde{E}^2\left[\left(1 - r^2\cos\delta\right)^2 + r^4\sin^2\delta\right]}{\left(1 - 2r^2\cos\delta + r^4\right)^2} = \frac{\tilde{E}^2}{1 - 2r^2\cos\delta + r^4}. \tag{4.40}$$

To obtain the form of the transmitted wave normally used, the denominator of (4.40) is rewritten as

$$\begin{aligned} 1 - 2r^2\cos\delta + r^4 &= \left(1 - 2r^2\cos\delta + r^4\right) - 2r^2 + 2r^2 \\ &= 2r^2(1 - \cos\delta) + \left(1 - 2r^2 + r^4\right). \end{aligned}$$

This new expression allows (4.40) to be written in the form

$$I \propto \frac{\tilde{E}^2}{\left(1 - r^2\right)^2 + 4r^2\sin^2(\delta/2)}. \tag{4.41}$$

When $\delta = 0, 2\pi, 4\pi, \dots,$

$$I_{\max} \propto \frac{\tilde{E}^2}{\left(1 - r^2\right)^2}. \tag{4.42}$$

When $\delta = \pi, 3\pi, 5\pi, \dots,$

$$I_{\min} \propto \frac{\tilde{E}^2}{\left(1 + r^2\right)^2}. \tag{4.43}$$

We define the fringe visibility as

$$\vartheta = \frac{I_{\max} - I_{\min}}{I_{\max} + I_{\min}}. \tag{4.44}$$

The fringe visibility is a useful characterization of interference; the larger the value of this parameter, the easier it is to observe the fringe pattern. The maximum value of ϑ is 1 and occurs when $I_{\min} = 0$. The minimum value is zero, because $I_{\max} = I_{\min}$. Using (4.42) and (4.43) in (4.44), we obtain the fringe visibility in terms of the reflectivity of the film surface:

$$\vartheta = \frac{2r^2}{1 + r^4}.$$

As the reflectivity r^2 approaches 1, the fringe visibility approaches its maximum value of 1.

We can write the intensity transmitted through the dielectric layer in terms of $I_{\max}$:

$$I = \frac{I_{\max}}{1 + \dfrac{4r^2}{\left(1 - r^2\right)^2} \sin^2 \dfrac{\delta}{2}}.$$

The factor

$$F = \frac{4r^2}{\left(1 - r^2\right)^2}$$

is called the *coefficient of finesse*, and its use allows the relative transmission of the dielectric layer to be expressed in a format called the *Airy function*:

$$\frac{I}{I_{\max}} = \frac{1}{1 + F \sin^2(\delta/2)}. \tag{4.45}$$

If we plot the Airy function for different values of the reflectivity r^2, we obtain Figure 4.21, which displays a periodic maximum in the transmission of the dielectric layer as δ is varied. The peak in transmission occurs when d is equal to a multiple of $\lambda/2$, where λ is the illuminating wavelength. Thus, the maximum transmission of the film occurs when the film thickness will support standing waves in the layer; i.e., the transmission maxima occur for eigenvalues of the layer.

The peak in transmission in Figure 4.21 narrows as the reflectivity r^2 increases. The value of δ over which I goes from $I_{\max}$ to $I_{\max}/2$ is a measure of the fringe sharpness and can be obtained by noting $I = I_{\max}$ when $\delta = 0$. When $I = I_{\max}/2$,

$$\frac{4r^2 \sin^2(\delta/2)}{(1 - r^2)^2} = 1.$$

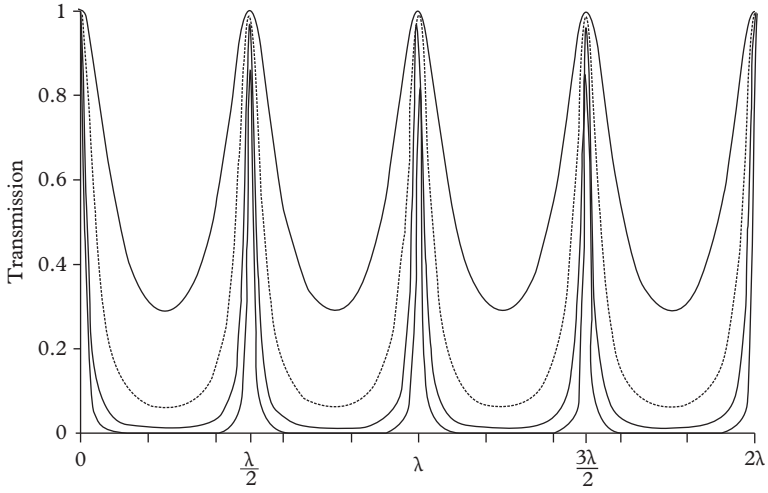

Figure 4.21 *This is a plot of the fraction of transmitted light as a function of nd for reflectivities of 0.3, 0.6, 0.8, and 0.9. The fringes become narrower as the reflectivity increases.*

The fringe sharpness is given by

$$\delta_{1/2} = 2\sin^{-1}\left(\frac{1-r^2}{2r}\right) = 2\sin^{-1}\left(\frac{1}{\sqrt{F}}\right). \tag{4.46}$$

The sharpness of the fringes increases and $\delta_{1/2}$ decreases with increasing reflectivity. If the reflectivity $r^2 = 0.9$, then

$$\delta_{1/2} = 0.211 \text{ rad}.$$

The multiple reflections are the cause of the sharp fringes as we can see by comparing the fringe sharpness of the dielectric layer with multiple reflections to a Michelson interferometer that was modeled as a dielectric layer with one reflection. Rewriting (4.29) as

$$I = I_{\max}\cos^2\frac{\delta}{2}.$$

The sharpness of the fringes for a Michelson interferometer can be obtained by noting that $I = I_{\max}$ whenever $\delta = 0$ and that $I = I_{\max}/2$ whenever

$$\delta_{1/2} = 2\cos^{-1}\left(\frac{1}{\sqrt{2}}\right) = \frac{\pi}{2} = 1.57 \text{ rad}.$$

This value for the fringe sharpness is much larger than the value obtained for the dielectric layer, and thus the fringes of a Michelson interferometer are much broader.

It is obvious that a device constructed as a dielectric layer could be used to accurately measure wavelength. Such a device was first constructed by **Marie Paul Auguste Charles Fabry (1867–1945)** and **Jean Baptiste Gaspard Gustave Alfred Perot (1863–1925)**.

4.7.1 Fabry–Perot Interferometer

The Fabry–Perot interferometer is constructed using two highly reflective surfaces usually separated by air. Figure 4.22 shows a typical experimental arrangement. Two plane glass plates separated by a distance d have reflective dielectric mirrors on their facing surfaces.

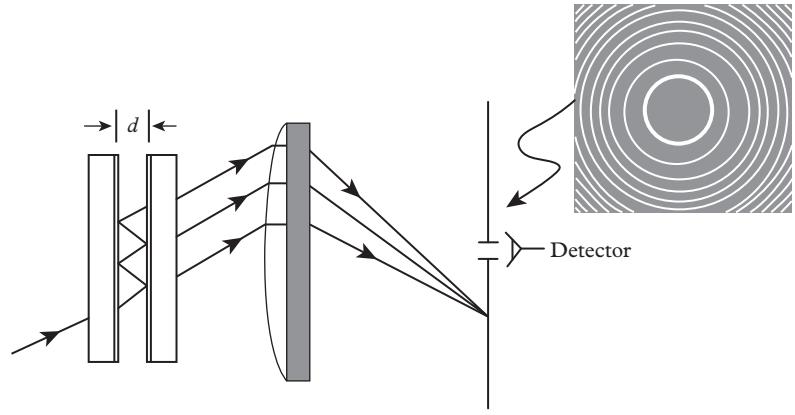

Figure 4.22 *The experimental arrangement of a Fabry–Perot interferometer. Shown on the right are the fringes observed on the screen for laser illumination.*

(We will limit our attention here to interferometers constructed using plane parallel plates, but interferometers are also constructed using spherical mirrors and we will discuss some of their properties in Chapter 5.) The waves exiting the plates, after multiple reflections, are collected by the lens and imaged on an observation screen. Only one propagation vector, incident at an angle θ, is followed through the system in Figure 4.22. Other incident propagation vectors will result in a bright fringe if $\delta = 2\pi m$. The incident angle of the propagation vectors forming the bright fringes must satisfy the equation

$$m\lambda = 2nd\cos\theta.$$

The observed fringes, such as those in Figure 4.23, are circularly symmetric if the illumination is symmetric about the symmetry axis of the optical system.

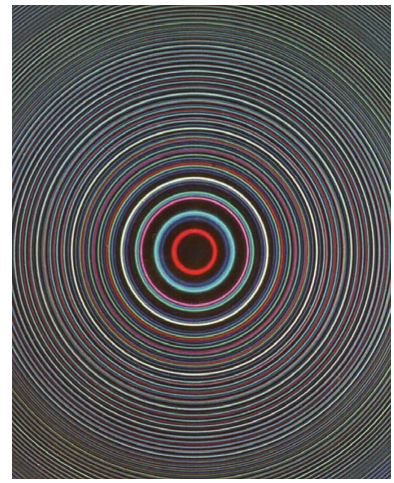

Figure 4.23 *The output fringes from a Fabry–Perot interferometer. Several sets of fringes due to multiple colors in the light source are present in this photograph. (Courtesy of Fredrick L. Roesler.)*

To use the Fabry–Perot interferometer as a wavelength-measuring instrument, a detector behind an aperture in the screen measures the light passing through the screen as the optical path length $n_2 d$ is varied by either varying the pressure of the air surrounding the interferometer or using piezoelectric translators to move one mirror relative to the other (see Figure 4.22). If a single wavelength illuminates the mirrors, then the signal recorded by the detector will look like one of the curves in Figure 4.21.

The accuracy with which an interferometer can measure the wavelength of its illumination is called its *chromatic resolving power* $\mathcal{R}$ and is defined as $\lambda/\Delta\lambda$, where λ is the mean wavelength of the illumination and $\Delta\lambda$ is the wavelength difference that can be resolved. We need a criterion for resolution, and the one we will use assumes that two wavelengths λ_1 and λ_2 of equal intensity are present. The criterion for resolution of the two wavelengths states that they are just resolved if the half maximum intensity of a fringe produced by λ_1 falls on the half maximum intensity of a fringe produced by λ_2 if we slide λ_2 closer to λ_1 in Figure 4.24. When this occurs, the transmitted intensity is a constant as d is varied from the resonant condition of λ_1 to the resonant condition of λ_2. The phase shift going from the intensity maximum for λ_1 to the intensity maximum for λ_2 is then $\Delta\delta = 2\delta_{1/2}$. The fringes are assumed to be narrow, so this is a small value and we may make the approximation

$$\sin\delta_{1/2} = \sin\frac{\Delta}{2} \approx \frac{\Delta}{2}$$

and

$$\sin\left(\frac{\delta_{1/2}}{2}\right) = \frac{\Delta\delta}{4}.$$

Using (4.46),

$$\frac{\Delta\delta}{4} \approx \frac{1}{\sqrt{F}} = \frac{1-r^2}{2r}. \tag{4.47}$$

Differentiating (4.34) gives a relationship between $\Delta\delta$ and $\Delta\theta$:

$$\Delta\delta = -4\pi n_2 d\sin\theta_t\frac{\Delta\theta_t}{\lambda_0}. \tag{4.48}$$

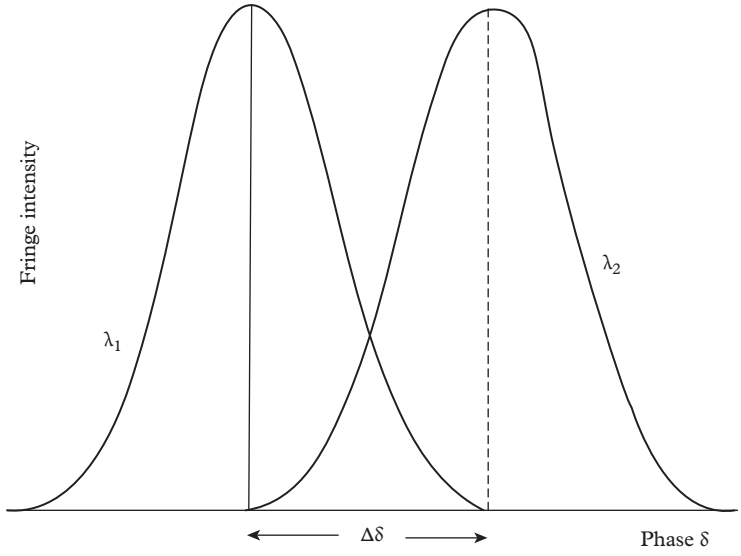

Figure 4.24 *Resolving power of a Fabry–Perot interferometer.*

A bright fringe will occur whenever

$$2n_2 d\cos\theta_t = m\lambda. \tag{4.49}$$

If we differentiate this equation we will obtain a relationship between $\Delta\theta$ and $\Delta\lambda$

$$-2n_2 d\sin\theta_t\,\Delta\theta_t = m\Delta\lambda,$$

$$-\sin\theta_t\,\Delta\theta_t = \frac{m\Delta\lambda}{2n_2 d}. \tag{4.50}$$

Using (4.50) in (4.48) and then equating with (4.47), we get

$$\Delta\delta = 2\pi m\frac{\Delta\lambda}{\lambda} = \frac{2(1-r^2)}{r}.$$

The resolving power is thus

$$\mathcal{R} = \frac{\lambda}{\Delta\lambda} = \frac{m\pi r}{1-r^2} = \frac{m\pi}{2}\sqrt{F}. \tag{4.51}$$

We see from (4.49) that the order number m has a maximum value whenever $\cos\theta_t = 1$; i.e., m is a maximum at the center of the Fabry–Perot fringe pattern, and this maximum is given by

$$m_{\max} = \frac{2n_2 d}{\lambda_0}. \tag{4.52}$$

Physically, m corresponds to the number of wavelengths of light that can fit between the two mirrors.

As an example of the chromatic resolving power of a Fabry–Perot interferometer, assume that $r^2 = 0.9$, the reflecting surfaces are separated by $d = 1$ cm, the dielectric between the two reflecting surfaces is air, $n_2 = 1.0$, and the illuminating wavelength $\lambda_0 = 500$ nm. The resolving power is

$$\frac{\lambda}{\Delta\lambda} = 1.2 \times 10^6,$$

and the smallest wavelength difference that can be measured by the instrument is

$$\Delta\lambda = 4.2 \times 10^{-4} \text{ nm}.$$

The peaks in the transmitted intensity shown in Figure 4.21 occur when the spacing d is a multiple of $\lambda/2$, where λ is the illuminating wavelength. Every time d is changed by $\lambda/2$, another peak in the intensity corresponding to the wavelength λ is recorded by the detector. The wavelength difference $(\Delta\lambda)_{SR}$, corresponding to a change in d of $\lambda/2$, or a change in m of 1, is called the *free spectral range* of the interferometer. This parameter is the maximum wavelength difference that can be unambiguously measured by the interferometer. When we change the order m by 1, we change the phase $\Delta\delta = 2\pi$. We have just derived the relationship

$$\Delta\delta = 2\pi m \frac{\Delta\lambda}{\lambda}. \tag{4.53}$$

This allows us to write for the free spectral range

$$(\Delta\lambda)_{SR} = \frac{\lambda}{m}.$$

Substituting the maximum value for m into the equation will give us the minimum free spectral range

$$(\Delta\lambda)_{SR} = \frac{\lambda^2}{2n_2 d} \tag{4.54}$$

or, in terms of frequency,

$$(\Delta\nu)_{SR} = \frac{c}{2n_2 d}.$$

If we substitute (4.52) into (4.51), we see that increasing the separation d increases the resolving power of the Fabry–Perot interferometer but accompanying that increase is a decrease in the free spectral range as shown by (4.54). If two wavelengths are separated by more than the free spectral range, we will obtain an incorrect value for their wavelength difference, identifiable in Figure 4.23, because our eye can identify the overlap using color. The overlap occurs because the order m in Fabry–Perot interferometers is very large and there is no tag labeling the order of the fringe. We cannot discriminate between, say, the fringe associated with $(m + 1)\lambda_1$ and the fringe associated with $(m - 1)\lambda_2$. This means that the separation between fringes may yield a multiple of the true wavelength separation. In Figure 4.25, we show a Fabry–Perot output of the sodium doublet. Where should we measure the distance between the observed fringe maxima? To ensure that we know where we are, another wavelength-selective device is often used as a prefilter of the light incident on the Fabry–Perot interferometer.

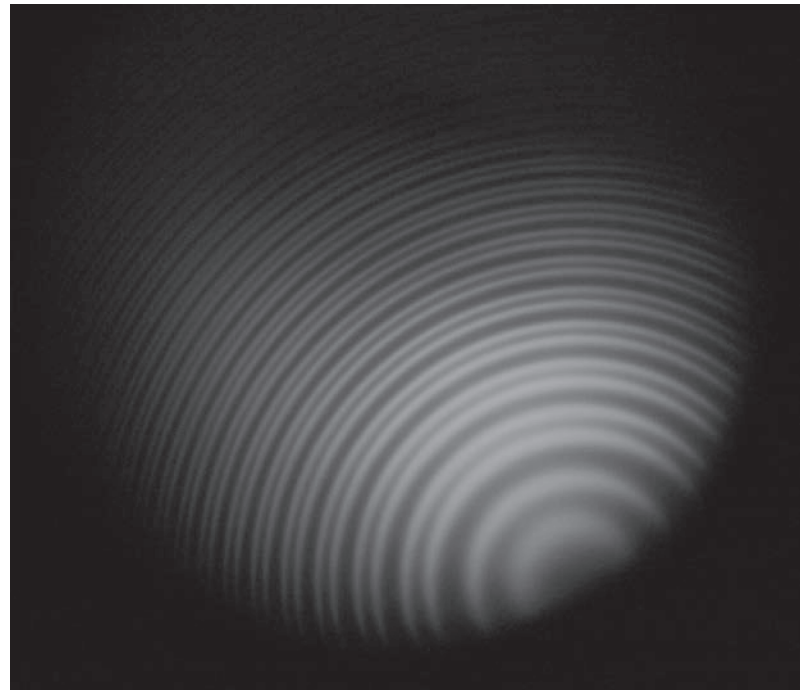

Figure 4.25 *Fabry–Perot output of the sodium doublet spectrum. The pairs of lines disappear in the center of the image because the exposure saturates. (From HyperPhysics by Rod Nave, Georgia State University <http://hyperphysics.phy-astr.gsu.edu/hbase/hframe.html>.)*

The ratio of the free spectral range to the minimum resolvable wavelength is called the ***finesse*** $\mathcal{F}$. Using (4.51) and (4.54), we can write

$$\mathcal{F} = \frac{(\Delta\lambda)_{\mathrm{SR}}}{\Delta\lambda} = \frac{\pi}{2}\sqrt{F}. \tag{4.55}$$

The finesse is the key measure of performance of the interferometer, and, as it should be, it is independent of the spacing d.

In terms of frequency, the finesse is

$$\mathcal{F} = \frac{(\Delta\nu)_{\mathrm{SR}}}{\Delta\nu}.$$

Since the finesse is proportional to the reciprocal of the minimum resolvable bandwidth of the instrument, the finesse can be thought of as proportional to the decay time of the Fabry–Perot interferometer, i.e., the time taken for the optical fields associated with the standing waves in the interferometer to fall from their steady-state value to zero after light is removed from the interferometer. The relaxation time is given by

$$\tau_D = \frac{1}{2\pi\Delta\nu} = \frac{d/c}{\delta_{\mathrm{loss}}},$$

where we assume all losses are reflective losses, $\delta_{\text{loss}} = 1 - R$. This allows us to associate the finesse of the Fabry–Perot cavity with the Q of a classical oscillator,

$$Q = \frac{\nu}{\Delta\nu} = \frac{\text{energy stored}}{\text{energy loss/s}},$$

$$Q = \frac{c}{\lambda} 2\pi \left(\frac{d}{c\delta_{\text{loss}}} \right) = \frac{2\pi d}{\lambda \delta_{\text{loss}}} = \frac{2\pi d}{\lambda(1-R)}.$$

From (4.55), we can write the reflective finesse as

$$\mathcal{F} = \frac{\pi r}{1 - r^2},$$

and the Q for a Fabry-Perot is

$$Q = \frac{2d\mathcal{F}}{\lambda\sqrt{\mathcal{R}}}.$$

The resolution in terms of the cavity Q is thus

$$\mathcal{R} = \frac{n_2 \lambda r}{4} Q$$

Two other interpretation that can be given to the finesse are: that it is the effective number of interfering beams involved in forming the interference fringe, or that it is a measure of the photon lifetime.

It would appear that by increasing the reflectivity, and thus the coefficient of finesse, F, we could continue to increase the finesse without limit. This is not the case; the figure of the mirrors, i.e., the flatness of the mirrors, will place an ultimate limit on the resolving power of the interferometer. To see why, return to the expression for the phase difference of each transmitted wave, (4.35), and assume that the index in the interferometer is $n_2 = 1$, the operating wavelength is the vacuum wavelength $\lambda = \lambda_0$, and the illumination is a plane wave so that $\cos\theta_t = 1$; then

$$\delta = \frac{4\pi d}{\lambda}.$$

The variation of δ with mirror spacing d is

$$\Delta\delta = \frac{4\pi \Delta d}{\lambda}.$$

We assume that because the mirrors are not perfectly flat, d varies across the interferometer's aperture by a fraction of a wavelength given by $\Delta d = \lambda/\mathcal{M}$. The phase variation due to the *mirror figure* (the variation in surface flatness) is given by

$$\Delta\delta = \frac{4\pi}{\mathcal{M}}.$$

Using the relation (4.53), we can write the resolving power in terms of the mirror figure:

$$\mathcal{R} = \frac{\lambda}{\Delta\lambda} = \frac{m}{2}\mathcal{M}.$$

In calculating the resolution due to mirror reflectivity, we found that the variation in phase due to the mirror's reflectivity is

$$\Delta\delta < \frac{2\left(1-r^2\right)}{r}.$$

If we have

$$\frac{1}{\mathcal{M}} < \frac{1-r^2}{2\pi r} = \frac{1/\pi}{\sqrt{F}} = \frac{1}{2\mathcal{F}},$$

then the mirror figure, not its reflectivity, will determine the wavelength resolution. We define a new finesse called the figure finesse to characterize the performance of a Fabry–Perot interferometer limited by mirror flatness:

$$\mathcal{F}_F = \frac{\mathcal{M}}{2}.$$

The size a of the pinhole used in Figure 4.18 to limit the view of the detector can also determine the wavelength resolution. There is a pinhole finesse, defined as

$$\mathcal{F}_P = \frac{4\lambda f^2}{a^2 d},$$

where f is the focal length of the lens. (The origin of this relationship is diffraction.)

The net finesse due to the pinhole size, mirror figure, and reflectivity is called the *instrument finesse* $\mathcal{F}_\mathbf{I}$,

$$\frac{1}{\mathcal{F}_I^2} = \frac{1}{\mathcal{F}^2} + \frac{1}{\mathcal{F}_F^2} + \frac{1}{\mathcal{F}_P^2}.$$

4.8 Summary

The addition of overlapping electromagnetic waves led to the result that the intensity of the resultant wave was the sum of the intensities of the individual waves unless

$$\langle \mathbf{E}_1 \cdot \mathbf{E}_2 \rangle \neq 0.$$

The term is zero if the polarizations of the two waves are orthogonal and the propagation medium is isotropic and free of charge. When the term is nonzero, the waves are said to interfere. Two experimental realizations of interference analyzed in this chapter were Young's two-slit experiment and the thin dielectric layer.

The geometry associated with Young's two-slit experiment is shown in Figure 4.9. The result of the analysis demonstrates that if the intensity passed by each slit is I_0, then the intensity a distance D from the two slits and a height x above the optical axis is

$$I = 4I_0 \cos^2\left(\frac{\pi x h}{\lambda D}\right),$$

where h is the spacing between the slits. The distance between two bright fringes was found to be

$$\Delta x = \frac{\lambda D}{h}.$$

The geometry associated with the dielectric layer model is shown in Figure 4.11. The spatial intensity distribution of the light reflected from the dielectric layer was found to be a function of the incident angle, the layer's thickness, and the wavelength of the illumination. When λ and θ_t are held constant, the fringes are called Fizeau fringes or fringes of constant thickness. When θ_t and d are held constant, then color fringes are created. Finally, when d and λ are held constant, Haidinger's fringes or fringes of equal inclination are generated. The phase difference between a wave reflected off the front and back surfaces of the layer was shown to be given by

$$\delta = \left(\frac{4\pi n_2 d}{\lambda_0}\right)\cos\theta_t.$$

To this phase shift must be added any phase change that occurs on reflection from an interface. The intensity of the light reflected from the dielectric layer depends upon the phase shift produced by the layer

$$I = I_1 + I_2 + 2\sqrt{I_1 I_2}\cos\delta,$$

where the two intensities are due to the light reflected from each interface of the dielectric layer.

The dielectric layer was found to be a useful model to explain antireflection coatings, Newton's rings, the Michelson interferometer, and the Fabry–Perot interferometer.

By using the dielectric layer model, the Michelson interferometer's output intensity was found to be

$$\frac{I}{I_0} = 1 + \cos\left(\frac{2\omega d}{c}\right),$$

where the Michelson interferometer was assumed to have a 50:50 beam splitter so that the intensity in each arm of the interferometer was equal. The variable ω in this equation is the angular frequency of the illuminating radiation and d is the difference in length of the two arms of the interferometer.

The Fabry–Perot interferometer was explained by allowing multiple reflections to occur in the dielectric layer. The transmission of light through the interferometer was found to be

$$\frac{I}{I_{\max}} = \frac{1}{1 + F\sin^2(\delta/2)},$$

where the coefficient of finesse is

$$F = \frac{4r^2}{\left(1 - r^2\right)^2} = \left(\frac{2\mathcal{F}}{\pi}\right)^2,$$

The parameter $\mathcal{F}$ is called the reflective finesse of the Fabry–Perot interferometer. The instrument finesse $\mathcal{F}_I$ was defined as the ratio of the free spectral range and the minimum resolvable wavelength of the instrument. The reflective finesse is not the only contributor to the instrument finesse. Other contributions to the instrument finesse, such as the mirror figure, add in the reciprocal:

$$\frac{1}{\mathcal{F}_I^2} = \sum_i \frac{1}{\mathcal{F}_i^2}.$$

The finesse was shown to be a measure of the resolving power of the Fabry–Perot interferometer"

$$\mathcal{R} = \frac{2n_2 d}{\lambda_0}\mathcal{F},$$

where $\mathcal{R}$ was defined as the ratio $\lambda/\Delta\lambda$.

4.9 Problems

4.1. Eight interference fringes are spread over 2 cm on a screen 100 cm away from a double slit with 0.2 mm separation. What is λ?

4.2. When a glass plate with $n = 1.517$ is placed in one of the arms of a Michelson interferometer, 18.5 fringes are displaced. What is the glass thickness if $\lambda = 589.3$ nm?

4.3. Light with a wavelength $\lambda = 514.53$ nm is incident normal to a soap film ($n = 4/3$). The first order is strongly reflected. What is the film thickness? What is λ in the film?

4.4. Two flat glass plates touch at one edge and are separated by a hair at the other. Light with $\lambda = 632.8$ nm is incident normal and nine fringes are visible. What is the hair thickness?

4.5. The equivalent of a Lloyd's mirror experiment occurs in radar when the receiver R and the source S are close to the ground (Figure 4.26). In radar, the observed interference pattern is called a "multipath." Assume that the source with a frequency of 12 GHz is located 1 m above the ground and the receiver is 30 m from the source. How high above the ground will the receiver see the first maximum in the received signal?

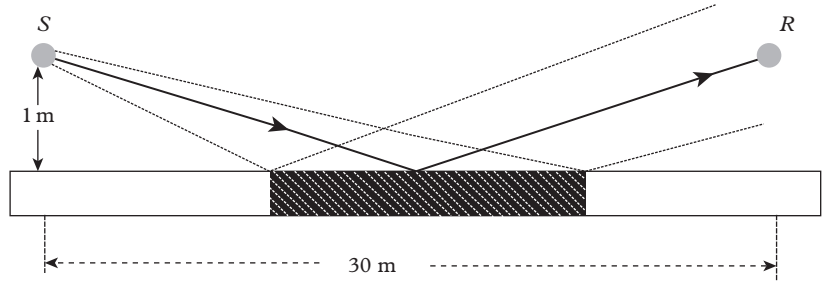

Figure 4.26 *A radiofrequency source is located 1 m above the ground and 30 m from a receiver of variable height above the ground.*

4.6. If we coat glass ($n = 1.5$) with another material ($n = 2.0$), what thicknesses gives maximum reflection? Minimum reflection? Assume that $\lambda = 500$ nm.

4.7. A solid Fabry–Perot interferometer is made of an uncoated 2 cm thick slab of material ($n = 4.5$). Relying only on the reflectivities of the air–material interface, what are the fringe contrast and the resolving power at $\lambda = 500$ nm? A glass slab such as this, often with reflective coatings, is called a *solid etalon* and is used as a wavelength-selective filter.

4.8. Assume we move one mirror of a Michelson interferometer through a distance of 3.142×10^{-4} m and we see 850 bright fringes pass by. What is the illuminating wavelength?

4.9. What is the smallest thickness that a film of index 1.455 may have if it is to generate a minimum in reflected light under normal illumination, with $\lambda = 500$ nm? The film has air on both sides. What would the transmission of this film be like at $\lambda = 500$ nm?

4.10. A glass chamber 25 mm long filled with air is placed in front of one of the slits in Young's two-slit experiment. The air is removed and replaced by a gas. On comparing the two fringe systems, we find that when the gas is present, the fringes are displaced by 21 bright bands toward the side with the chamber. If $\lambda = 656.2816$ nm and n for air is 1.000276, what is the index of refraction of the gas?

4.11. Assume the mirrors of a Michelson interferometer are not perfectly aligned. We see as an output a 3 cm $\times$ 3 cm illuminated field containing 24 vertical bright fringes. What is the angle that the two mirrors make with each other? Assume $\lambda = 632.8$ nm.

4.12. Looking into a Michelson interferometer, we see a dark central disk surrounded by concentric light and dark rings. If one mirror is 2 cm farther from the beam splitter than the other, and $\lambda = 500$ nm, what is the order of the central disk and the sixth dark ring?

4.13. A metal ring is dipped into a soap solution ($n = 1.34$) and held in a vertical plane so that a wedge-shaped film forms under the influence of gravity. At near-normal illumination with blue–green light ($\lambda = 488$ nm) from an argon laser, one can see 12 fringes per centimeter. Determine the wedge angle of the soap film. Compare this result with what is seen in Figure 4.13(b).

4.14. A positive lens with a radius of curvature of 20 cm rests on an optical flat and is illuminated, with the incident wave normal to the surface, by sodium D light ($\lambda = 589.29$ nm). The gap between the two surfaces is then filled with carbon tetrachloride ($n = 1.461$). What is the ratio of the radius of the 23rd dark band before introducing the liquid to the radius after introducing the liquid?

4.15. Two narrow parallel slits illuminated by yellow sodium light ($\lambda = 589.29$ nm) are found to produce fringes with a separation of 0.5 mm on a screen 2.25 m away. What is the distance between the slits?

4.16. Prove that the sum shown in (4.6) is given by (4.7).

4.17. Assume two plane waves of the same wavelength $\lambda = 632.8$ nm are polarized with their electric fields parallel to the y-axis. The propagation vectors for the two waves are shown in Figure 4.27. Calculate the separations of intensity maxima along the x- and z-axes.

4.18. A plane wave is incident at an angle of θ with respect to the normal of a thin parallel slab of glass with index of refraction $n = 1.5$. What glass thicknesses d will result in maximum transmission? With the derived equation, find the incident angle that will yield maximum transmission of a wave with wavelength 514.5 nm for a plate that exhibits a maximum in transmission for light of wavelength of 632.8 nm at an angle of incidence of 30°. The variation of the incident angle is often used to tune dielectric filters or etalons.

4.19. Add seven harmonic waves together graphically. The waves have the same wavelength and amplitude, but each differs in phase from the next by 20°. Assuming equal phase differences between each wave and its neighbor, for what value of the phase difference would the resultant wave have zero amplitude? What would happen to the resultant amplitude if the phase of each wave differed by 2π? By extending this problem to N waves, we could develop a theory of the Fabry–Perot interferometer using the vector approach to wave addition.

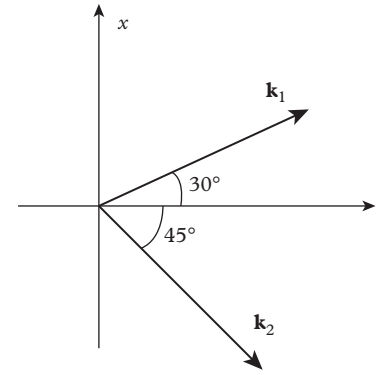

Figure 4.27 *Propagation vectors of waves to be added together as described in Problem 4.17.*

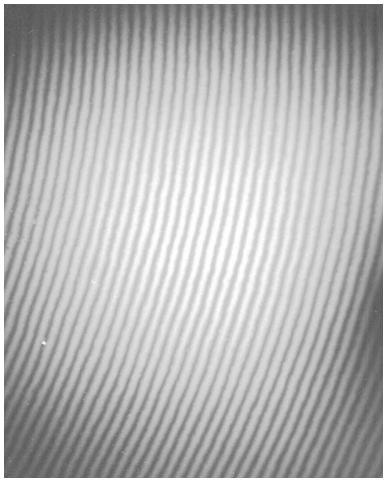

Figure 4.28 *Fringes for Problem 4.20.*

4.20. The fringes shown in Figure 4.28 were produced using a wavelength of 589 nm. The fringes are due to an air gap between two flat glass plates created by placing a scrap of tissue between the plates, along one edge. What is the angle of the air gap?

REFERENCES

1. Young, T., *Experiments and calculations relative to physical optics.* Philos. Trans. R. Soc. Lond., 1803. **94**: p. 1–16.
2. Smith, W.J., *How flat is flat*. Optical Spectra, April 1974, May 1974, August 1978.
3. Hayes, J., *Interference*, in *Encylopedia of Optical Engineering*, R.G. Driggers, Editor. 2003: CRC Press. p. 945–965.

Appendix 4A Multilayer Dielectric Coatings

Interference between waves reflected from the interfaces of a dielectric film can be used to reduce the reflection from an optical surface. This concept can be extended to a multilayer dielectric coating to produce any desired reflection property and in this appendix, several procedures for designing multilayer coatings will be described.

Fraunhofer produced antireflection layers on glass surfaces by acid etching in 1817, but it was not until 1891 that **Dennis Taylor** associated the reduced reflectivity with an increased transparency. Full utilization of the concept of interference filters had to wait until the late 1940s and early 1950s, when techniques were developed that allowed the production of rugged dielectric films. Cold mirrors designed to reflect visible wavelengths and transmit infrared wavelengths were one of the first products of this technology and today are found in every dentist's lamp. In the 1970s, multilayer coating technology had developed to a point that allowed mass production of laser mirrors with very low absorption. Coating technology is now being used to produce durable mirrors for copy machines and conductive coatings to provide frost-free aircraft windshields.

We have introduced the theory of multilayer interference filters in Chapters 3 and 4. This theory will now be used to develop several methods for designing a filter. Only the reflectivity of the filter will be considered, but enough information will be given to allow transmission to also be calculated. We need a notation that will allow the manipulation of a large number of dielectric layers. To see how the notation is generated, we rewrite (3.33) as

$$r_N = \frac{E_{Nr}}{E_{Ni}} = \frac{n_i \cos\theta_i - n_t \cos\theta_t}{n_i \cos\theta_i + n_t \cos\theta_t}$$

and (3.39) as

$$r_P = \frac{E_{Pr}}{E_{Pi}} = \frac{\dfrac{n_i}{\cos\theta_i} - \dfrac{n_t}{\cos\theta_t}}{\dfrac{n_i}{\cos\theta_i} + \dfrac{n_t}{\cos\theta_t}}.$$

First, we define the ith medium as the incident medium and the $(i+1)$th medium as the transmitted medium. The two reflection coefficients can be written as one coefficient by defining an effective index. The effective index for normal polarization is

$$N_j = \tilde{n}_j \cos\theta_j$$

and that for parallel polarization is

$$N_j = \frac{\tilde{n}_j}{\cos\theta_j},$$

where the notation indicates that the dielectric films can have a complex index of refraction. This notation allows generalized equations for the amplitude reflection coefficient and transmission coefficient to be defined at the interface between medium i and medium $i+1$:

$$r_i = \frac{N_i - N_{i+1}}{N_i + N_{i+1}}, \qquad r_i' = -r_i = \frac{N_{i+1} - N_i}{N_i + N_{i+1}}, \tag{4A.1a}$$

$$t_i = \frac{2N_i}{N_i + N_{i+1}}, \qquad t_i' = \frac{2N_{i+1}}{N_i + N_{i+1}}. \tag{4A.1b}$$

[When $\theta_j = 0$, the generalized equations (4A.1a, b) agree with (3.45) and (3.46).] The subscripts allow an unlimited number of interfaces. We will start at $j = 0$, and for m layers there will be $m + 2$ indices of refraction, $n_0, n_1, \ldots, n_m, n_{m+1}$, where n_0 is the refractive index in the incident medium and n_{m+1} is the refractive index of the substrate medium, i.e., the medium on which the dielectric layers will be deposited. This notation has allowed the design and construction of multilayer stacks as large as $m > 100$.

4A.1 Vector Approach

The vector approach to designing multilayer interference filters allows only an approximate determination of the reflectivity, but provides the designer with a means for visualizing the operation of the multilayer stack.

We begin by revisiting the problem of interference by multiple reflections discussed in Chapter 4. In Chapter 4, we formulated the problem in terms of the transmitted wave; here, we wish to reformulate the effect in terms of the reflected wave and limit our attention to the first reflection from the front and back surface of the film. Redrawing Figure 4.11 for this problem, we produce Figure 4A.1. To add the reflected waves, we must include the phase shift for the wave that is reflected from the back surface. From Figure 4A.1, the reflection coefficient is

$$\rho = \frac{1}{A}\left(Ar_0 + At_0t_0'r_1e^{-i\delta_1}\right).$$

From energy conservation, we can write

$$t_0 = 1 - r_0, \quad t_0' = 1 - r_0' = 1 + r_0,$$

thus,

$$t_0t_0' = 1 - r_0^2,$$

and we may rewrite the reflection coefficient as

$$\rho = r_0 + r_1e^{-\delta_1} - r_0^2r_1e^{-i\delta_1}.$$

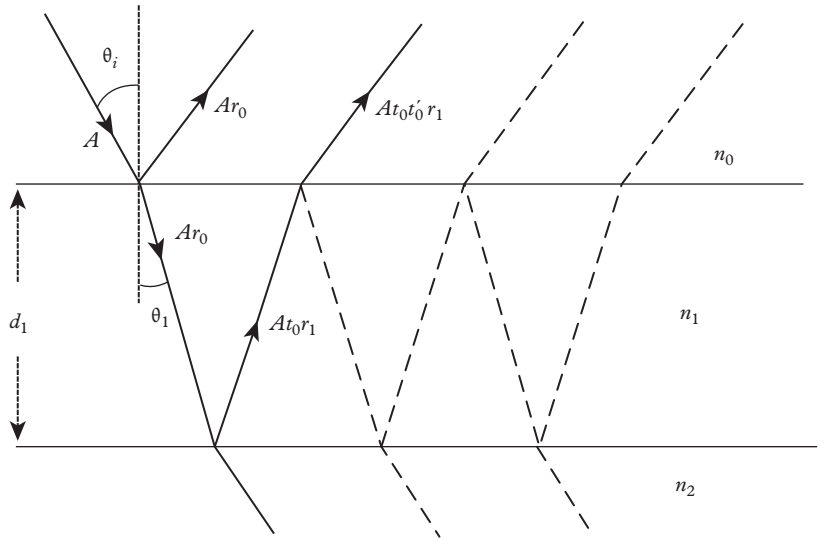

Figure 4A.1 *Reflection from a dielectric layer. We ignore the multiple reflections shown by the dashed lines.*

Only the first two terms of this expansion will be retained; i.e., we will limit our analysis to a single reflection from each interface:

$$\rho = r_0 + r_1 e^{-i\delta_1}. \tag{4A.2}$$

From (4.34), we have

$$\delta_1 = \frac{4\pi d_1 n_1 \cos\theta_1}{\lambda_0}.$$

It is quite simple to extend (4A.2) to multilayers. An m-layer stack is

$$\rho = r_0 + \sum_{j=1}^{m} r_j e^{\sum_{k=1}^{j} \delta_k}. \tag{4A.3}$$

We can perform the summation graphically according to the procedure shown in Figure 4.2. In Figure 4A.2, a graphical addition of the reflection coefficients for a two-layer stack is shown.

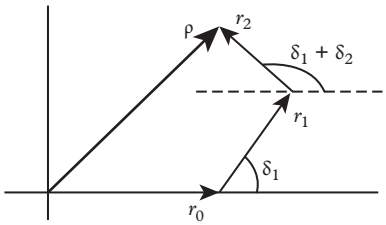

Figure 4A.2 *Graphical formulation of (4A.3).*

As an example, we will design antireflection coatings using one and two layers. Table 4A.1 lists some of the coating materials we can select for our design. The index of refraction of many of the films depends upon how the films were prepared; the table gives average values.

First we will graphically design a single-layer antireflection coating for a glass of index 1.70 using MgF_2. The glass is to be used in air, so $n_0 = 1.0$, $n_1 = 1.38$, and $n_2 = 1.7$. We have

$$r_0 = \frac{n_0 - n_1}{n_0 + n_1} = \frac{1 - 1.38}{1 + 1.38} = -0.16, \quad r_1 = \frac{1.38 - 1.7}{1.38 + 1.7} = -0.1.$$

We know from our discussion in Chapter 4 that we should make $n_1 d_1 = \lambda/4$. We will design for a wavelength $\lambda = 500$ nm, resulting in $d_1 = 910$ nm. The phase change upon

Table 4A.1 *Thin-film materials*

Material	Index of refraction	Wavelength range
Cryolite (Na_3AlF_6)	1.35	0.15–14
Magnesium fluoride (MgF_2)	1.38	0.12–8
Silicon dioxide (SiO_2)	1.46	0.17–8
Thorium fluoride (ThF_4)	1.52	0.15–13
Aluminum oxide (Al_2O_3)	1.62	0.15–6
Silicon monoxide (SiO)	1.9	0.5–8
Zirconium dioxide (ZrO_2)	2.00	0.3–7
Cerium dioxide (CeO_2)	2.2	0.4–16
Titanium dioxide (TiO_2)	2.3	0.4–12
Zinc sulfide (ZnS)	2.3	0.4–12
Zinc selenide (ZnSe)	2.44	0.5–20
Cadmium telluride (CdTe)	2.69	1.0–30
Silicon (Si)	3.5	1.1–10
Germanium (Ge)	4.05	1.5–20
Lead telluride (PbTe)	5.1	3.9–20+

passing through the film will be calculated, assuming normal incidence, for $\lambda = 500$ nm and $\lambda = 650$ nm to allow an estimate of the bandpass of the antireflection coating:

$$\delta_1(500) = \frac{4\pi d_1 n_1}{\lambda_0} = \frac{4\pi\left(9.1 \times 10^{-7}\right)(1.38)}{5 \times 10^{-7}} = 180°,$$

$$\delta_1(650) = \frac{4\pi\left(9.1 \times 10^{-7}\right)(1.38)}{6.5 \times 10^{-7}} = 140°.$$

The vector diagram for these two cases, following the procedure for vector addition outlined in Figure 4.2, are shown in Figure 4A.3.

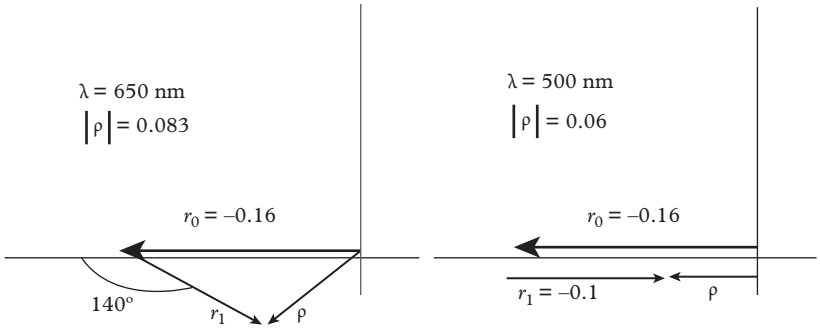

Figure 4A.3 *Design of an antireflection coating for a glass of index 1.7 using a film of index 1.38. The design wavelength that was used to select the film thickness was 500 nm.*

When the film's thickness is set to produce a phase shift of 180°, as it was for the wavelength of $\lambda = 500$ nm, then the vectors associated with the reflection coefficients r_0 and r_1 are antiparallel. For this case, it is possible to make the resultant reflection coefficient ρ zero if the reflection coefficients from the two interfaces can be made equal. When the phase shift produced by propagation through the dielectric film is not 180°, there is no possibility of obtaining a resultant reflection coefficient that is zero.

A little more challenging design is a two-layer antireflection coating (Figure 4A.4). The glass will be used in air ($n_0 = 1$), the topmost layer, A, will be SiO_2 ($n_1 = 1.46$), the second layer, B, will be TiO_2 ($n_2 = 2.3$), and the films are to be deposited on a glass substrate called BK-7 ($n_3 = 1.517$). Using these index values in (4A.1) yields

$$r_0 = -0.187, \quad r_1 = -0.213, \quad r_2 = 0.195.$$

We do not know the proper thicknesses for the two layers, so we will draw two circles of radii r_1 and r_2 as shown in Figure 4A.5. As shown in the figure, we center the circle of radius

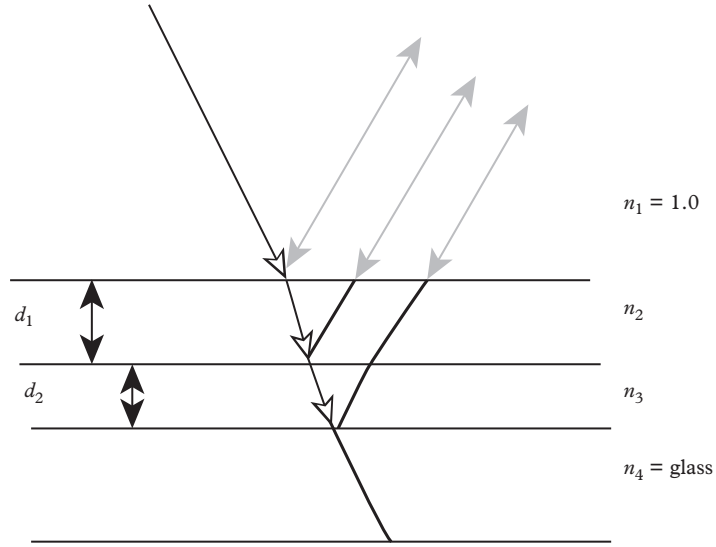

Figure 4A.4 *A antireflection coating using two dielectric layers.*

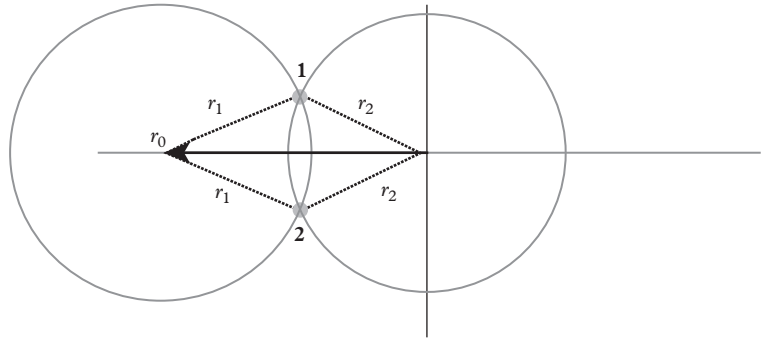

Figure 4A.5 *Design of a two-layer antireflection coating on a glass of index 1.517 using films with indices 1.46 and 2.3.*

$|r_1|$ at the head of r_0 and the circle of radius $|r_2|$ at the tail of r_0. The intersections of the two circles, labeled 1 and 2, represent two solutions to the design problem. Point 1 has

$$\delta(SiO_2) = 118°, \quad \delta(TiO_2) = 26.5°$$

and Point 2 has

$$\delta'(SiO_2) = 61.5°, \quad \delta'(TiO_2) = 153.5°.$$

The solution associated with Point 2 is easier to manufacture because it is thicker, but the solution associated with Point 1 is less sensitive to wavelength changes.

Smith chart approach: A number of other graphical means of designing multilayer filters are used [1]. One that electrical engineering students would recognize is the use of the Smith chart. The Smith chart is a graphical calculator used in microwave design for the solution of impedance matching problems. The problem of reflection reduction (or enhancement) can be approached as an impedance matching problem, as was pointed out by the introduction of (3.48) and (3.49). The design equations for thin films are similar to those used by the microwave engineer, and thus the Smith chart is found useful and is used extensively by thin-film designers. We will not discuss the Smith chart approach, however, since it offers little advantage over the vector approach and a discussion of its use would take us far afield from optics.

4A.2 Matrix Approach

A quantitative approach to designing multilayer filters that allows computer generation of the spectral characteristics of the filters, is the use of matrices. This approach is called the *method of resultant waves* or the E^+, E^- *matrix method* [2]. The boundary conditions associated with Maxwell's equations, as stated in Chapter 4, are placed into a matrix equation format. To accomplish the reformulation, the boundary conditions are manipulated so that the information about the angle of incidence and the polarization is placed into an effective index of refraction as defined in (4A.1). The fields on each side of the boundary can then be represented by plane waves incident normal to the interface as shown in Figure 4A.6.

Each dielectric layer has two interfaces, but, as shown in Figure 4A.6, these are formally identical, so we need only configure the problem for a general interface and repeat the calculation m times for the m interfaces of a dielectric stack $m-1$ layers high.

We use the boundary conditions (3.20), (3.21), (3.27), and (3.28) from Chapter 3 to produce the boundary conditions at a generalized interface:

$$n_i \cos\theta_i \left(E^i_{N+} - E^i_{N-}\right) = n_{i+1} \cos\theta_{i+1} \left(E^{i+1}_{N+} - E^{i+1}_{N-}\right), \tag{4A.4}$$

$$E^i_{N+} + E^i_{N-} = E^{i+1}_{N+} + E^{i+1}_{N-}, \tag{4A.5}$$

$$\left(E^i_{P+} - E^i_{P-}\right)\cos\theta_i = \left(E^{i+1}_{P+} - E^{i+1}_{P-}\right)\cos\theta_{i+1}, \tag{4A.6}$$

$$\left(E^i_{P+} + E^i_{P-}\right)n_i = \left(E^{i+1}_{P+} + E^{i+1}_{P-}\right)n_{i+1}. \tag{4A.7}$$

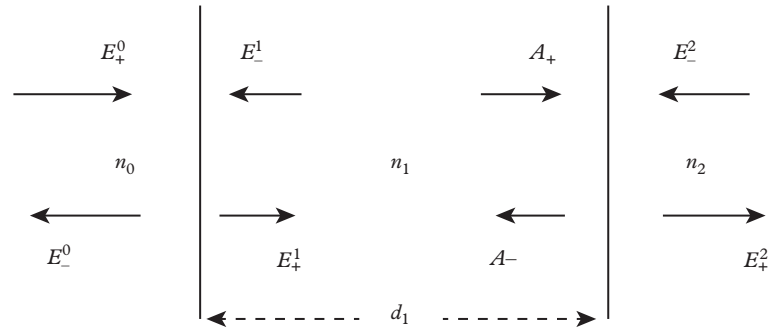

Figure 4A.6 *Geometry for waves in a dielectric film.*

For the normal components,

$$E_{N+}^i = \left(\frac{n_i \cos\theta_i + n_{i+1}\cos\theta_{i+1}}{2n_i \cos\theta_i}\right) E_{N+}^{i+1} + \left(\frac{n_i \cos\theta_i - n_{i+1}\cos\theta_{i+1}}{2n_i \cos\theta_i}\right) E_{N-}^{i+1}, \tag{4A.8}$$

$$E_{N-}^i = \left(\frac{n_i \cos\theta_i - n_{i+1}\cos\theta_{i+1}}{2n_i \cos\theta_i}\right) E_{N+}^{i+1} + \left(\frac{n_i \cos\theta_i + n_{i+1}\cos\theta_{i+1}}{2n_i \cos\theta_i}\right) E_{N-}^{i+1}. \tag{4A.9}$$

For the parallel components,

$$E_{P+}^i = \left(\frac{n_i \cos\theta_{i+1} + n_{i+1}\cos\theta_i}{2n_i \cos\theta_i}\right) E_{P+}^{i+1} + \left(\frac{n_{i+1} \cos\theta_i - n_i\cos\theta_{i+1}}{2n_i \cos\theta_i}\right) E_{P-}^{i+1}, \tag{4A.10}$$

$$E_{P-}^i = \left(\frac{n_{i+1} \cos\theta_i - n_i \cos\theta_{i+1}}{2n_i \cos\theta_i}\right) E_{P+}^{i+1} + \left(\frac{n_i \cos\theta_{i+1} + n_{i+1}\cos\theta_i}{2n_i \cos\theta_i}\right) E_{P-}^{i+1}. \tag{4A.11}$$

Using the definitions in (4A.1), we can simplify our notation and reduce (4A.8)–(4A.11) to the following two equations:

$$E_+^i = \frac{E_+^{i+1} + r_i E_-^{i+1}}{t_i}, \tag{4A.12}$$

$$E_-^i = \frac{r_i E_+^{i+1} + E_-^{i+1}}{t_i}. \tag{4A.13}$$

We may combine these into a matrix equation for the interface:

$$\begin{bmatrix} E_+^i \\ E_-^i \end{bmatrix} = \begin{bmatrix} \frac{1}{t_i} & \frac{r_i}{t_i} \\ \frac{r_i}{t_i} & \frac{1}{t_i} \end{bmatrix} \begin{bmatrix} E_+^{i+1} \\ E_-^{i+1} \end{bmatrix}.$$

Normally this is written in a more compact notation

$$\mathbf{E}^i = \mathbf{I}_i \mathbf{E}^{i+1},$$

where $\mathbf{I}_i$ is the ith interface matrix,

$$\mathbf{I}_i = \begin{bmatrix} \dfrac{1}{t_i} & \dfrac{r_i}{t_i} \\ \dfrac{r_i}{t_i} & \dfrac{1}{t_i} \end{bmatrix}. \tag{4A.14}$$

The problem of finding the values of A_+ and A_- in Figure 4A.5 is a simple propagation problem. The fields A_+ and E_- must be modified by the phase shift they experience after propagating through the dielectric layer, here labeled 1:

$$A_+ = e^{i\delta_1} E_+^1, \qquad E_-^1 = e^{i\delta_1} A_-, \quad \text{or} \quad A_- = e^{-i\delta_1} E_-^1 .$$

These equations can be combined into a matrix equation

$$\mathbf{A} = \mathbf{T}_1 \mathbf{E}^1,$$

which can be generalized for the ith dielectric layer by defining a transmission matrix of the form

$$\mathbf{T}_i = \begin{bmatrix} e^{i\delta_i} & 0 \\ 0 & e^{-i\delta_i} \end{bmatrix}. \tag{4A.15}$$

The effect of an m-layer dielectric film can be described by the matrix equation

$$\begin{bmatrix} E_+^0 \\ E_-^0 \end{bmatrix} = \mathbf{M} \begin{bmatrix} E_+^f \\ E_-^f \end{bmatrix}, \tag{4A.16}$$

where

$$\mathbf{M} = \mathbf{I}_0 \mathbf{T}_1 \mathbf{I}_1 \mathbf{T}_2 \cdots \mathbf{I}_{m-1} \mathbf{T}_m \mathbf{I}_m,$$

and the E^f are the fields in the final medium. The reflection coefficient of the stack is

$$\rho = \frac{E_-^0}{E_+^0}. \tag{4A.17}$$

To simplify the problem without affecting the desired ratios, we normally assume $E_+^f = 1$ and $E_-^f = 0$.

It is simple to program a personal computer to explore the properties of various combinations of films. We will sketch out a very simple example. The objective is to design a multilayer stack made up of alternating layers of indices n_1 and n_2 with the light incident normal to the stack. The thickness of each layer is selected to be one-quarter wavelength thick at the design wavelength. A schematic representation of the film stack would have the following index layers:

$$n_0 \mid \ n_1 \mid \ n_2 \mid \ n_1 \mid \ \ldots \ \mid \ n_1 \mid \ n_g$$

The first step in the solution of the problem is to form three matrices. The front layer matrix is

$$\mathbf{F} = \mathbf{I}_0 \mathbf{T}_1 = \frac{i}{2} \begin{bmatrix} 1 + n_1 & -(1 - n_1) \\ 1 - n_1 & -(1 + n_1) \end{bmatrix}.$$

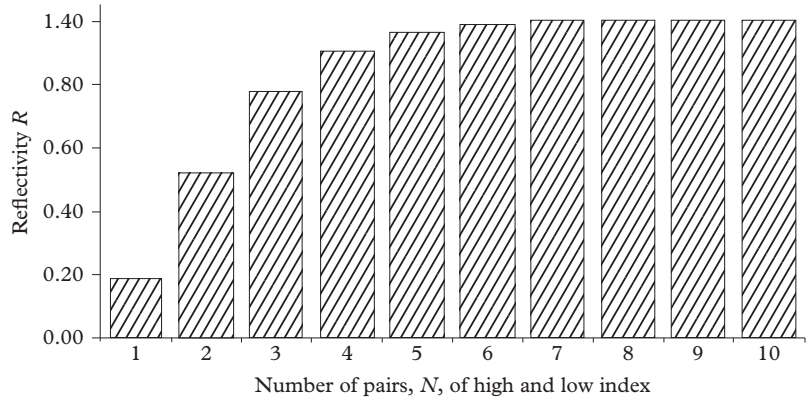

Figure 4A.7 *The reflectivity as a function of the number of pairs of low-index and high-index films, N, for a stack with a low-index film of 1.46 and a high-index film of 2.3.*

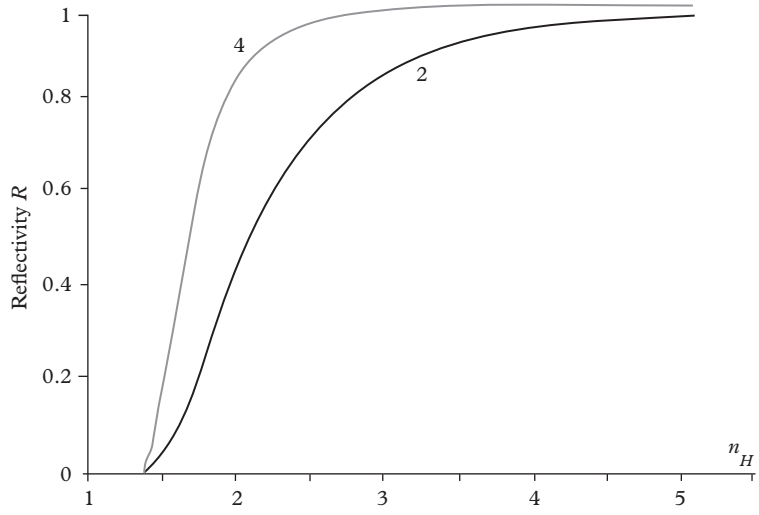

Figure 4A.8 *The reflectivity of a dielectric stack as a function of the ratio of the indices of refraction of the two materials used to construct the stack. The low-index layer was set at 1.35 and the high-index layer was allowed to range from 1.38 to 5.1. Two different-size stacks were used, one with N = 2 and the other with N = 4.*

The back-layer matrix is

$$\mathbf{B} = \mathbf{T}_{N+1}\mathbf{I}_{N+1} = \frac{i}{2n_1}\begin{bmatrix} n_1 + n_g & n_1 - n_g \\ -(n_1 - n_g) & -(n_1 + n_g) \end{bmatrix}.$$

There are N pairs of layers of indices n_1 and n_2, and the matrix for one pair is

$$\mathbf{M} = \mathbf{I}_1\mathbf{T}_2\mathbf{I}_2\mathbf{T}_1 = -\frac{1}{2}\begin{bmatrix} \frac{n_1}{n_2} + \frac{n_2}{n_1} & \frac{n_1}{n_2} - \frac{n_2}{n_1} \\ \frac{n_1}{n_2} - \frac{n_2}{n_1} & \frac{n_1}{n_2} + \frac{n_2}{n_1} \end{bmatrix}.$$

For N pairs of the $n_1 \mid n_2$ layers,

$$\mathbf{M}^N = \frac{(-1)^N}{2}\begin{bmatrix} \left(\frac{n_1}{n_2}\right)^N + \left(\frac{n_2}{n_1}\right)^N & \left(\frac{n_1}{n_2}\right)^N - \left(\frac{n_2}{n_1}\right)^N \\ \left(\frac{n_1}{n_2}\right)^N - \left(\frac{n_2}{n_1}\right)^N & \left(\frac{n_1}{n_2}\right)^N + \left(\frac{n_2}{n_1}\right)^N \end{bmatrix}.$$

We will assume that $n_g = 1$, which allows us to write the transmission (4A.15) for this problem as

$$\begin{bmatrix} E_+^0 \\ E_-^0 \end{bmatrix} = \frac{(-1)^{N+1}}{8}\begin{bmatrix} \left(\frac{n_1}{n_2}\right)^N + \left(\frac{n_2}{n_1}\right)^N & \left(\frac{n_1}{n_2}\right)^N - \left(\frac{n_2}{n_1}\right)^N \\ \left(\frac{n_1}{n_2}\right)^N - \left(\frac{n_2}{n_1}\right)^N & \left(\frac{n_1}{n_2}\right)^N + \left(\frac{n_2}{n_1}\right)^N \end{bmatrix}\begin{bmatrix} E_+^f \\ E_-^f \end{bmatrix}.$$

We can now write the reflection coefficient of the stack as

$$\rho = \frac{\left(\frac{n_1}{n_2}\right)^N - \left(\frac{n_2}{n_1}\right)^N}{\left(\frac{n_1}{n_2}\right)^N + \left(\frac{n_2}{n_1}\right)^N}. \tag{4A.18}$$

We know that one of the indices is larger than the other. For large N, one of the two ratios will dominate and the reflectivity will approach 1, as shown in Figure 4A.7, where the reflectivities for $N = 1, \ldots, 10$ are displayed. As the difference between n_1 and n_2, increases so does the wavelength range over which the reflectivity can be made nearly 1. A simple computer model using (4A.18) generated the curve in Figure 4A.8 which demonstrates the dependence of the reflectivity on the index ratio.

REFERENCES

1. Delano, E. and R.J. Pegis, *Methods of synthesis for dielectric multilayer filters*. Prog. Opt., 1969. 7: p. 67–137.
2. Heavens, O.S., *Optical Properties of Thin Solid Films*. 1965: Dover.

5 Geometrical Optics

5.1 Introduction 126
5.2 Eikonal Equation 128
5.3 Fermat's Principle 129
5.4 Applications of Fermat's Principle 132
5.5 Lens Design and Matrix Algebra 135
5.6 Geometrical Optics of Resonators 141
5.7 Guided Waves 146
5.8 Lagrangian Formulation of Optics 165
5.9 Propagation in a Graded-Index Optical Fiber 169
5.10 Summary 177
5.11 Problems 179
References 182
Appendix 5A: The *ABCD* Matrix 183
Appendix 5B: Aberrations 191

5.1 Introduction

The wavelength of light is on the order of 10^{-7} m. In terms of the size of objects in our daily lives, this is a very small dimension. The contribution to our observations from such a small wavelength should be negligible much of the time. In this chapter, we will assume that the wavelength is zero, which will lead to a geometrical theory of optics.

It is common to observe light rays, such as sunlight filtering through trees or headlights shining through the rain, that appear to travel in straight lines. These common experiences are the origin of the assumption that light propagation is rectilinear. Based on the assumption of rectilinear propagation, geometrical constructions using straight lines are used to represent the propagation path. Early man must have used the geometrical concepts of light to construct his optical instruments.

One of the oldest (3000 years) optical instruments is a converging lens of rock crystal that was found at the Assyrian city of Nimrud. There are historical references to the use of magnifying lenses and mirrors to start fires in Greece at least as early as 424 BC—see Act II of *The Clouds*, by Aristophanes. The first actual references to a geometric theory of light were by the Greeks and Romans. The Platonic school taught the theory of rectilinear propagation of light, and **Cleomedes**, a Roman who lived around the time of Augustus, discussed atmospheric refraction from a geometrical optics viewpoint.

The first optical instruments were probably reading glasses made from parts of glass spheres. Eyeglasses are thought to have been invented between 1268 and 1289 in Pisa, Italy. A number of nations claim the inventor of the telescope—one of the first complex refractive optical systems. **Hans Lippershey** of Wesel, Holland, constructed one of the first telescopes in 1608. He used crystal rather than glass for the refractive elements. Upon application for a patent on October 2, 1608, he was told to make a binocular telescope, which he quickly did, suggesting that he had a good grasp of geometrical optics. **Galileo Galilei** (1564–1642) was the first to use the telescope to make important scientific discoveries using his version of the Lippershey telescope. His astronomical discoveries in 1610 were not popular. In fact, those who were invited to look through the telescope either refused to look through the instrument or refused to believe what they saw. Another complex optical instrument, the microscope, was probably invented by **Zacharias Joannides** around 1590.

The theoretical foundation of geometrical optics was established by **Pierre de Fermat (1601–1665)**, who deduced the laws of reflection and refraction from the assumption (now called Fermat's principle) that light travels from a point in one medium to a point in another medium in the least time. Fermat did not publish, and in fact refused to do so, but instead wrote his thoughts in letters to his friends and in the margins of books. Fermat's notes were published by his son five years after Fermat's death.

The success of Fermat's principle in optics led to its application in classical mechanics by **William Rowan Hamilton** in 1831. This in turn led to the use of the same mathematical formalism for both areas of physics. The formal theory is called the Lagrangian formulation of optics, and it allows the calculation of the ray trajectories when the index of refraction is a function of position.

Modern Optics. Second Edition. B. D. Guenther.

© B. D. Guenther 2015. Published in 2015 by Oxford University Press.

Figure 5.1 *Rays of light. (By Brocken Inaglory (Own work) via Wikimedia Commons.)*

The frequent observation that light traveled in straight lines caused Newton to reject the wave theory of Huygens because of its apparent inability to explain rectilinear motion. Today, the geometrical theory of light can be formally connected to the wave theory, removing the objections of Newton. When the wavelength is allowed to approach zero, the wave equation is found to take on the form of an equation for the trajectory of a classical particle. As was mentioned earlier, narrow beams of light called *light rays* are often observed, and we associate the derived trajectories with these light rays. For example, we will discover that when the index of refraction is independent of position (a homogeneous medium), the predicted trajectory is a straight line.

The equation for a ray trajectory, obtained from the wave equation, leads to the statement of Fermat's principle. Fermat's principle is then used to derive the laws of reflection and refraction. These laws are used to develop the matrix formalism of geometrical optics. A matrix, called the *ABCD* matrix, is derived which can be used to describe any optical system. To demonstrate the use of the *ABCD* matrix, the operating parameters of a Fabry-Perot laser resonator are calculated. The connection between the *ABCD* matrix and the more traditional formulations of geometrical optics based on the thin-lens equation is presented in Appendix 5A.

The theory of geometrical optics as presented here is associated with rays that propagate at small angles where the sine of the angle can be replaced by the angle in radians. This theory, which is called the paraxial theory, fails to describe the actual performance of an optical system. The departures of the paraxial predictions from actual performance are called aberrations. An introduction to aberrations is given in Appendix 5B.

The use of geometrical optics and the concept of total reflection are used to derive a simple theory of guided waves. Some of the basic properties of guided waves are obtained by using this simple theory. The Lagrangian formulation of geometrical optics is used to prove that rectilinear propagation is obtained when the propagation medium is homogeneous and to derive the propagation in an optical fiber with an index of refraction that varies in the radial direction.

5.2 Eikonal Equation

In this section, we will derive the effect on the wave equation of allowing the wavelength to approach zero. We will find that in the limit as $\lambda \to 0$, the wave equation leads to an expression that describes the path taken by the normal to the wave surface of constant phase. This normal is called the ***optical ray*** and its equation of motion is called the ***eikonal equation***. This discussion will provide a justification for geometrical optics, but is not needed to understand or utilize the ray approach to optics.

It is the spatial rather than the temporal behavior of the light wave that is of interest in geometrical optics. For this reason, we assume that the light has a well-defined frequency and look at the behavior of the complex amplitude, which must obey the Helmholtz equation (1.13):

$$\left(\nabla^2 + k^2\right)\mathcal{E}(\mathbf{r}) = 0,$$

where

$$k = \frac{\omega}{c} = \omega\sqrt{\varepsilon\mu} = \frac{2\pi}{\lambda}.$$

If we simply allow $\lambda \to 0$, then $k \to \infty$ and the Helmholtz equation becomes indeterminate. We can draw quantitative conclusions about the equation by being more careful about taking the limit.

Assume that the solution of the Helmholtz equation is of the form

$$\tilde{E} = Ae^{ik_0 S}, \tag{5.1}$$

where the zero subscript denotes the wavelength measured in a vacuum. Comparing $\boldsymbol{S}$ with the function $\boldsymbol{S}(\mathbf{r})$ introduced in Chapter 1 suggests that $\boldsymbol{S}$ can be interpreted as the function describing the phasefront of the wave. The parameters A and $\boldsymbol{S}$ will be assumed to be slowly varying functions of x, y, and z that do not go to infinity with k_0. Substituting the assumed solution into the Helmholtz equation requires that we obtain the second spatial derivative of (5.1). For the x-derivative,

$$\frac{\partial \tilde{E}}{\partial x} = ik_0\tilde{E}\frac{\partial S}{\partial x} + e^{ik_0 S}\frac{\partial A}{\partial x} = ik_0\tilde{E}\frac{\partial S}{\partial x} + \frac{\tilde{E}}{A}\frac{\partial A}{\partial x},$$

$$\frac{\partial \tilde{E}}{\partial x} = \left(ik_0\frac{\partial S}{\partial x} + \frac{\partial \ln A}{\partial x}\right)\tilde{E},$$

$$\frac{\partial^2 \tilde{E}}{\partial x^2} = \left[-k_0^2\left(\frac{\partial S}{\partial x}\right)^2 + 2ik_0\left(\frac{1}{2}\frac{\partial^2 S}{\partial x^2} + \frac{\partial \ln A}{\partial x}\frac{\partial S}{\partial x}\right) + \left(\frac{\partial \ln A}{\partial x}\right)^2\right]\tilde{E}.$$

We get similar results for y and z. Substituting these results into the Helmholtz equation yields

$$(\nabla^2 + k^2)\tilde{E} = -k_0^2\left[\left(\frac{\partial S}{\partial x}\right)^2 + \left(\frac{\partial S}{\partial y}\right)^2 + \left(\frac{\partial S}{\partial z}\right)^2 - \frac{k^2}{k_0^2}\right]\tilde{E}$$

$$+ 2ik_0\left[\frac{\nabla^2 S}{2} + \nabla \ln A \cdot \nabla S\right]\tilde{E} + \left[\nabla^2 \ln A + (\nabla \ln A)^2\right]\tilde{E}. \tag{5.2}$$

The third term on the right-hand side here does not contain k_0 and thus creates no problem when we let $k_0 \to \infty$. The first two terms will not create any problems if the quantities in square brackets are zero and if k/k_0 remains finite and equal to the index of refraction as k_0 approaches the limit.

Since

$$\nabla \mathcal{S} \cdot \nabla \mathcal{S} = |\nabla \mathcal{S}|^2 ,$$

setting the first bracket equal to zero yields

$$|\nabla \mathcal{S}|^2 = \left(\frac{k}{k_0} \right)^2 = n^2. \tag{5.3}$$

Surfaces of constant $\boldsymbol{\mathcal{S}}$ are surfaces of constant phase, i.e., phasefronts. The normals to these surfaces are given by $\nabla \mathcal{S}$ in (5.3) and represent the rays of geometrical optics. The equation

$$\nabla \mathcal{S} = n\hat{\mathbf{s}} \tag{5.4}$$

is the ***eikonal equation*** and $\mathcal{S}$ is called the ***eikonal***. We define $\hat{\mathbf{s}}$ as a unit vector, normal to the phasefronts and tangent to the light ray.

By taking the limit of the Helmholtz Equation when $\lambda \to 0$, as we have done here, we implicitly assume that the electromagnetic wave, in the region around the ray, is a plane wave whose normal is the ray. We follow this normal to determine the propagation of the wave.

Setting the second bracket of (5.2) equal to zero yields an equation

$$\nabla \ln A \cdot \nabla \mathcal{S} = -\frac{\nabla^2 \mathcal{S}}{2}, \tag{5.5}$$

which describes, through a hydrodynamic model, how optical energy propagates. The energy is found to flow along the path of the geometrical rays, in a manner similar to a fluid flowing along flow lines. The Poynting vector is everywhere parallel to the geometrical ray. Problem 5.17 asks the reader to show that the use of

$$\tilde{E} = E_0 e^{ik_0 \mathcal{S}}, \qquad \tilde{B} = B e^{ik_0 \mathcal{S}},$$

in Maxwell's equations will demonstrate this fact by proving that $\nabla \mathcal{S}$ is proportional to the Poynting vector. We will not concern ourselves further with (5.5).

5.3 Fermat's Principle

Fermat's principle states that

> *light travels the path that takes the least time.*

Historically, geometrical optics developed from Fermat's principle and not from the wave theory as the above discussion might imply. Fermat was inspired by the book *Catoptrica*, written by **Hero of Alexandria** (***ca.* AD 100**) to apply the concept of least time to refraction. Hero was an Egyptian or Greek who proved the law of reflection using geometry from the premise that the rays of light take the shortest path between any two points.

To discuss Fermat's principle, we must use the concept of optical path length introduced in Chapter 4. The optical path length is the distance light would travel in a vacuum during the same time it takes to go a distance ℓ in a medium with index of refraction n. In Chapter 4, we used this concept to aid in the calculation of phase differences between two beams of light that start from the same point but travel different paths before they meet again. The definition of Fermat's principle is a statement of minimization; the optical path length will be the quantity that will be minimized.

In a homogeneous medium with index n, light travels a distance

$$\ell = \int_1^2 ds$$

in a time ℓ/v, where $v = c/n$ is the speed of light in the medium. In a vacuum, during this same time, light would travel

$$\frac{\ell c}{v} = n\ell = \Delta = s(\mathbf{r}_1) - s(\mathbf{r}_2).$$

If light is traveling over a path C, then the optical path length is the path integral

$$\Delta = \oint_C n\, ds,$$

where n is the index of refraction and ds is an increment of path length. In Figure 5.2, we see that the optical path length is the separation between the wavefronts at positions $\mathbf{r}_1$ and $\mathbf{r}_2$ along the optical ray.

Fermat's principle states that the optical path length of an actual ray between any two points "1" and "2" is a minimum; i.e., any curve we choose that joins these points and lies in a "neighborhood" of the proper path has the same optical path length. The time required to traverse any of the paths in this neighborhood is the same. (A physical interpretation of the "neighborhood" of the optical path will be given in Chapter 11.) Mathematically, this path is found through the calculus of variations.[1] The mathematical statement of Fermat's principle is

$$\delta\Delta = \delta \int_{P_1}^{P_2} n\, ds = 0,$$

where the symbol δ indicates that the variation has been taken.

Actually, the statement that Δ is a minimum is not entirely true, but rather Δ is a stationary value. To understand how a stationary optical path length can occur, consider an

[1] See [1] for an excellent introduction to this subject.

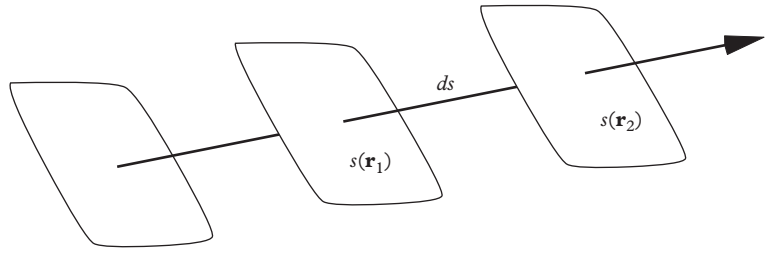

Figure 5.2 *The integral along the optical ray between the wavefronts at* r_1 *and at* r_2 *is the optical path length.*

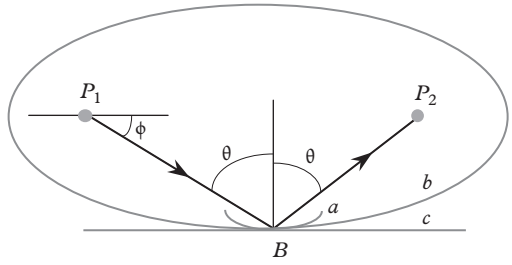

Figure 5.3 *An elliptical reflector, curve b, with a light source at one focus of the ellipse and a detector at the other. Light is reflected at point B, and the angle of incidence and reflection at point B are shown. Two other surfaces with the same surface normal at B are shown. Curve a is assumed to be a sphere with a larger curvature and curve c, a plane, with a smaller curvature than curve b.*

elliptical reflector (Figure 5.3), such as is used in some optically pumped laser designs. We wish to apply Fermat's principle to determine the optical path taken by light traveling from one focus, P_1, of the elliptical reflector to the other focus, P_2.

The actual optical path length for a reflection from point B in the elliptical optical reflector is given by the line P_1BP_2. This path results in an angle of reflection that equals the angle of incidence. If the angle ϕ a ray from P_1 is varied, then light will strike the elliptical reflector at points to the left or right of point B. For the elliptical surface, the distance from P_1 to surface b in Figure 5.4(a) and then to P_2 is unchanged. The optical path length Δ that will result is shown to as curve b in Figure 5.4(b).

Now consider a more tightly curved surface a, here a spherical surface, and the lesser curved surface of a plane c. Each surface is positioned so that it has the same surface normal as surface b at point B. If the shape of the reflector is modified so it now has the curvature of surface a, then, as ϕ is varied, the optical path length decreases in size from the correct path length; see curve a in Figure 5.4(b). The proper optical path is the maximum path length.

Finally, replace the elliptical reflector with a flat mirror, surface c. As already stated, the normal to surface c is the same as the normal of the elliptical reflector at point B. For this surface, as ϕ is varied, the optical path length increases, as is shown by curve c in Figure 5.4(b). Here, the proper optical path is the minimum path length.

Fermat's principle can be expressed in terms of the time taken to traverse the optical path:

$$\delta\Delta = \delta \int_{P_1}^{P_2} n\, ds = c\delta \int_{t_1}^{t_2} dt = 0. \tag{5.6}$$

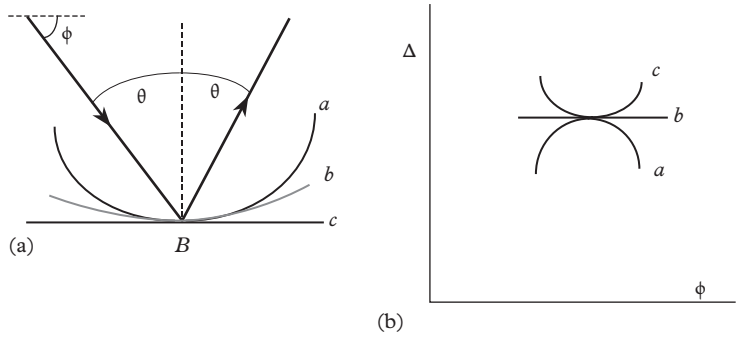

Figure 5.4 *(a) Enlarged picture of the reflection point from Figure 5.3. (b) Change in optical path length as we vary the angle at which light leaves the origin at point P_1. The labels a, b, and c refer to the three surfaces, spherical, elliptical, and planar, discussed in the text and shown in Figure 5.3. Fermat's principle predicts an optical path that is the same for all three surfaces.*

From this, we see that minimizing the optical path length is equivalent to minimizing the propagation time. In the following examples, we will minimize the propagation time in the application of Fermat's principle. From these examples, we will learn that Fermat's principle requires the time taken to traverse an optical path to remain constant, to first order, for incremental changes in the path length. Mathematically, this means that the first derivative of the time with respect to the optical path length must equal zero.

A question that arises is how does the light know to take the proper path? The answer lies in the fact that these rays are, in reality, waves. The waves traverse all possible paths. When the various waves reach their destination, they interfere. The phase differences for those waves that travel over the "wrong" paths are such that they destructively interfere, while those waves traveling over the "correct" paths constructively interfere. We can prevent light from traversing all possible paths by the use of obstructions; when we do, we observe light in regions that geometrical optics says should be dark. This behavior is called diffraction, a property of waves introduced in Chapter 9. Theoretical support for this interpretation of Fermat's principle will be given in Chapter 11.

5.4 Applications of Fermat's Principle

The Fermat's principle makes some of the laws of optics self-evident. For example, the *principle of reciprocity* says that if light travels from point P_1 to P_2 over a path, then it will travel over the same path in going from P_2 to P_1. Since light travels at the same speed in both directions, the path of least time must be the same between P_1 and P_2, no matter in which direction the light travels.

The laws of reflection and refraction can be quickly derived using Fermat's principle.

5.4.1 Law of Reflection

Consider the optical path taken by light originating at point P_1, a distance a above the mirror M, and reflected by the mirror to point P_2, a distance c from point P_1 and a distance b above the mirror, as shown in Figure 5.5. The time for light to travel from P_1 to P_2 over the path P_1OP_2 of Figure 5.5 is

$$t = \frac{\overline{P_1O} + \overline{OP_2}}{v} = \frac{1}{v}\left[\sqrt{b^2 + x^2} + \sqrt{a^2 + (c-x)^2}\right].$$

For this time to be stationary, the first derivative of the time with respect to the path length must be zero, where a, b, and c are constants since P_1 and P_2 are fixed:

$$\frac{dt}{dx} = \frac{1}{v}\left[\frac{x}{\sqrt{b^2 + x^2}} - \frac{c-x}{\sqrt{a^2 + (c-x)^2}}\right] = 0,$$

$$\frac{x}{\sqrt{b^2 + x^2}} = \frac{c-x}{\sqrt{a^2 + (c-x)^2}},$$

$$\sin i = \sin r.$$

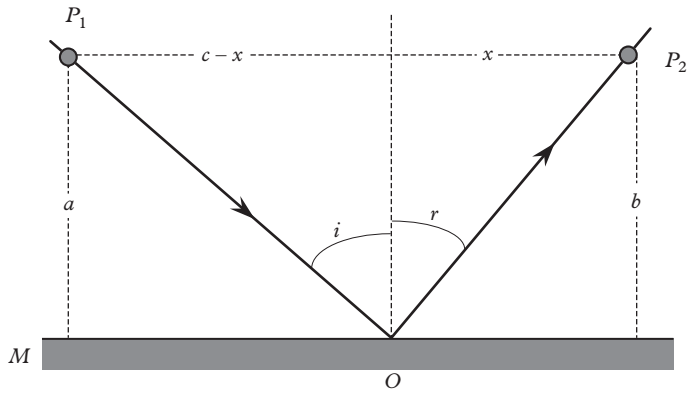

Figure 5.5 *Geometry for use of Fermat's principle to derive the law of reflection.*

Thus, the angle of incidence equals the angle of reflection. The second derivative, d^2t/dx^2, is greater than zero, so the function is a minimum, as Hero stated 1800 years ago.

5.4.2 Law of Refraction

To obtain the law of refraction using Fermat's principle, consider the path of a ray of light P_1OP_2 in Figure 5.6. All of the paths under consideration start at P_1, a distance a above the interface, and end at P_2, a distance b below the interface, so that a, b, and c are constants. The time to travel from P_1 to P_2 is

$$t = \frac{\overline{P_1O}}{v_1} + \frac{\overline{OP_2}}{v_2} = \frac{1}{v_1}\sqrt{a^2 + (c-x)^2} + \frac{1}{v_2}\sqrt{b^2 + x^2},$$

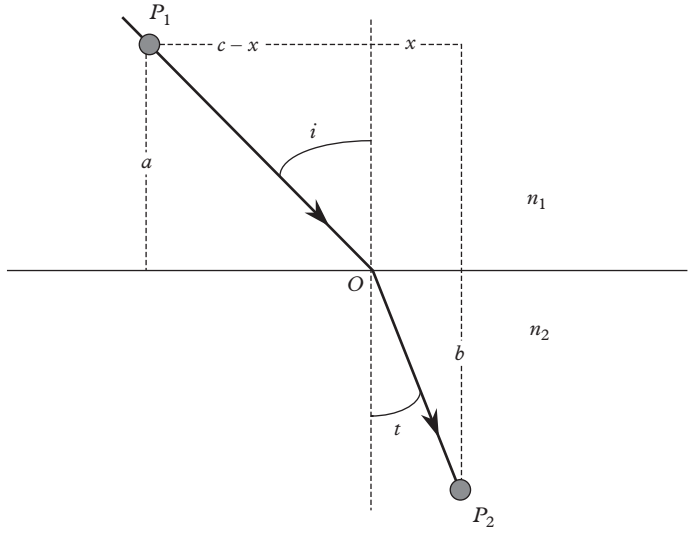

Figure 5.6 *Geometrical arrangement for using Fermat's principle to derive the law of refraction.*

where v_1 is the velocity of propagation of light in the upper medium of Figure 5.6 and v_2 is the velocity of propagation of the lower medium. The first derivative of the time with respect to the path length is

$$\frac{dt}{dx} = \frac{-(c-x)}{v_1\sqrt{a^2+(c-x)^2}} + \frac{x}{v_2\sqrt{b^2+x^2}} = 0,$$

$$\frac{\sin t}{v_2} = \frac{\sin i}{v_1},$$

$$\frac{\sin i}{\sin t} = \frac{v_1}{v_2} = \frac{n_2}{n_1}.$$

which is Snell's law.

5.4.3 Propagation through an Optical System

Assume that a spherical wave diverging from a source s enters an optical system, represented by the shaded area in Figure 5.7. The optical system forms an image of s at point P, with the wave converging to an image of the source at point P. Fermat's principle states that the light will traverse the minimum optical path length in going from s to P; however, the light from s to P in Figure 5.7 travels a large number of paths. For agreement with Fermat's principle to occur, all the rays, from the object s to the image P, must traverse identical optical path lengths—no matter how complicated the optical system.

In the simplest application of this fact, Fermat's principle can be used to generate a single surface that will image point s onto point P as shown in Figure 5.7. Fermat's principle can also be used to prove that ellipsoidal and hyperbolic surfaces will convert spherical waves into plane waves.

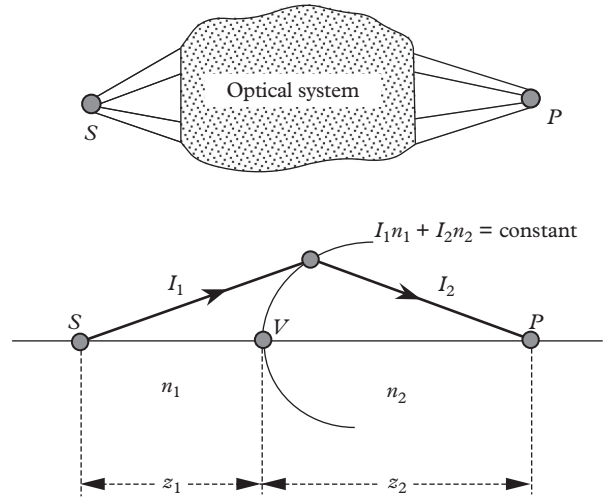

Figure 5.7 *Fermat's principle for an imaging system requires that the optical path lengths for all rays connecting the object s and the image P must be equal. For a single surface, this requirement results in a Cartesian oval.*

5.5 Lens Design and Matrix Algebra

The lens designer uses geometrical optics to trace rays through an optical system to determine the system's performance before it is constructed. Ideally, the optical system would collect light from an object point and focus it to an image point. In practice, the image point is blurred. The lens designer adjusts the lens' material, shape, and position in an attempt to reduce the blur to an acceptable size. Before the computer, this was a labor-intensive process, and every attempt was made to minimize the number of rays that needed to be traced [2]. Now, modern lens design programs generate an optical system with desired performance criteria by varying selected lens parameters and tracing many rays [3]. Figure 5.8 presents the output of a typical lens design program [4], showing a two-lens optical system optimized to produce minimum spherical aberration.

The ray tracing formulas used by lens designers are developed by applying the laws of refraction and ray propagation, as obtained from Fermat's principle. We will write the resulting equations in matrix formalism to produce a generalized presentation of the propagation of light through any optical system, from an optical fiber to a complex zoom lens.

In this section, we will, in a stepwise fashion, follow a ray through two surfaces of a lens. It is possible to formulate an exact matrix formulation involving sine, cosine and tangent functions [5, 6]; we will not do so. Our goal is to become familiar with the general process used within a modern optical design program but not to study the procedure [3, 7]. We will restrict the discussion to an approximation that allows the sine and tangent functions to be replaced by their angle in radians.

The sine, cosine, and tangent of a small angle γ can be approximated by the Taylor series

$$\sin\gamma = \gamma - \frac{\gamma^3}{3!} + \frac{\gamma^5}{5!} - \frac{\gamma^7}{7!} + \ldots,$$

$$\cos\gamma = 1 - \frac{\gamma^2}{2!} + \frac{\gamma^4}{4!} - \frac{\gamma^6}{6!} + \ldots,$$

$$\tan\gamma = \gamma + \frac{\gamma^3}{3} + \frac{2\gamma^5}{15} + \frac{17\gamma^7}{315} + \ldots.$$

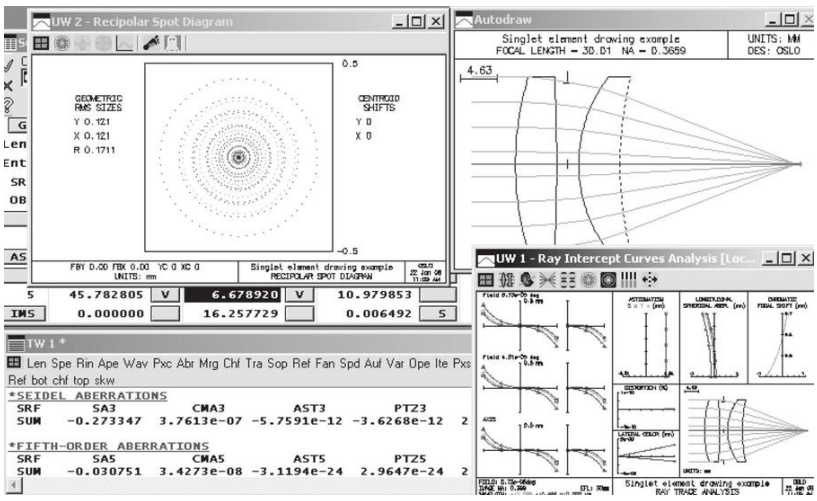

Figure 5.8 *Graphical presentation of the optical performance of a two-lens optical system. The lens design program, Oslo, was asked to minimize both spherical aberration and coma.*

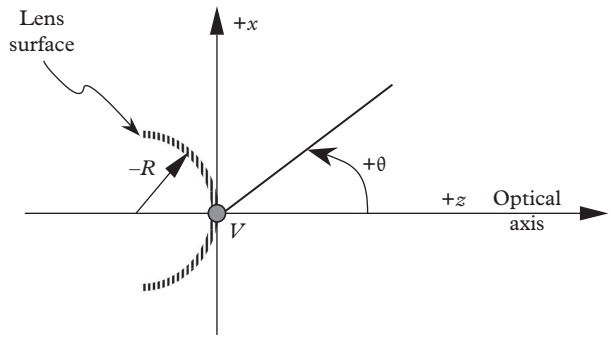

Figure 5.9 *Coordinate system that establishes the sign convention used for geometrical optics. Distances to the right of V and above the z-axis are positive. Angles measured counterclockwise from the positive z-axis are positive. The optical surface under consideration intersects the z-axis at the position V and is rotationally symmetric about the z-axis. The z-axis is defined as the optical axis. The radius of curvature of the optical surface is defined as being negative if the center of curvature is to the left of V.*

The *paraxial approximation* assumes that γ is small so that only the first term of each expansion is needed. The paraxial approximation is also called the first-order theory; retention of higher-order terms lead to third-, fifth-, seventh-order, etc., theories. We will use the paraxial approximation to construct a matrix that describes the propagation of a ray through an optical system.

Before we begin, we will establish a sign convention.[2] We assume that the optical surfaces all have spherical curvature with radius of curvature R. The position of the origin of the (x, z) coordinate system of Figure 5.9 is such that the z-axis lies along the axis of rotational symmetry of the optical components called the *optical axis.* The optical surface under consideration is assumed to intersect the optical axis at the point V, called the *vertex* of the optical surface. The origin of the (x, z) coordinate system is positioned at the vertex of the optical surface. The sign convention will be the same as that used in a Cartesian system. As is shown in Figure 5.9, all distances along z to the right of v and all distances along x above the optical axis (the z-axis) are positive, as are angles measured counterclockwise from the positive z-axis, as shown in Figure 5.9. (Normally the sign of the incident, reflected, and refracted angles are not specified but assume the sign dictated by the ray tracing procedure.) The radius of curvature of the optical surface is measured from the surface to the center of curvature and is negative if the center of curvature of the surface is to the left of the vertex V. The index of refraction to the left of the optical surface has a lower subscript than the index to the right of the surface, i.e., the indices are ordered n_1, n_2, n_3, etc.

We will analyze a general lens by considering each surface independently. This will require that a new coordinate system be constructed at each surface. Figure 5.10 contains the first optical surface to be considered, with the previously defined coordinate system constructed at its vertex, labeled V in Figure 5.10. Light will travel from the object point O in Figure 5.10 toward the right, hitting the image point I after refraction at the optical surface a distance x_1 above the optical axis. Any ray, such as the one just defined, that has as its origin the object/optical axis intersection is called an *axial ray*. The first surface has a positive radius of curvature R_1, centered on point C of Figure 5.10. The radius of curvature through the point where the light ray intersects the optical surface makes an angle ϕ with the optical axis

$$\sin\phi = \frac{x_1}{R_1}.$$

We will use the paraxial approximation that $\sin\phi \approx \phi$.

In the paraxial theory, all rays leaving the object point arrive at the image point; however, this is not the case in the exact theory. The failure of all the light rays from an object to converge to a single image point after passing through an optical system is called optical

[2] The sign convention used here is tied to the Cartesian coordinate system and was selected because it is easy to remember. There is no "best" sign convention, and a large number of other conventions are used in geometrical optics. Moving from one convention to another can be a source of confusion.

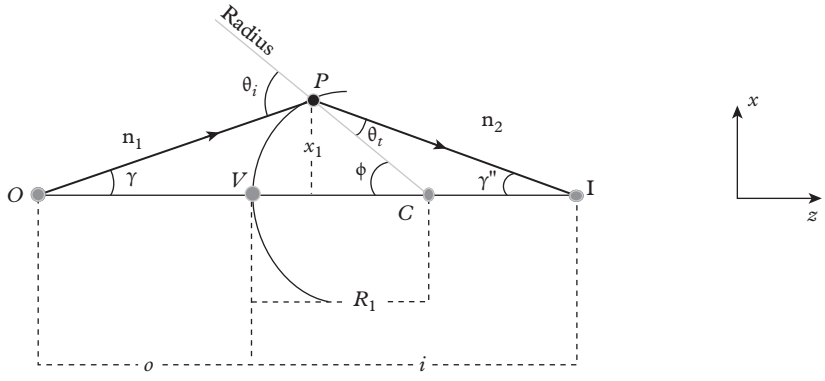

Figure 5.10 *Geometry used for the development of the lens design equations.*

aberration. To treat the aberrations mathematically, we extend the paraxial theory to third, fifth, seventh order, etc. by including additional terms in the expansion of the sine function.[3]

Snell's law is applied using the angle, shown in Figure 5.11, between the incident ray and the normal to the curved surface, the line "radius", at the point P where the ray intersects the optical surface. Using the first-order approximation,

$$n_1\theta_i = n_2\theta_t.$$

[3] A treatment of aberrations consistent with the present analysis can be found in [5], where computer routines are provided for calculating the various aberrations of an optical system. Appendix 5B provides a brief introduction to the subject.

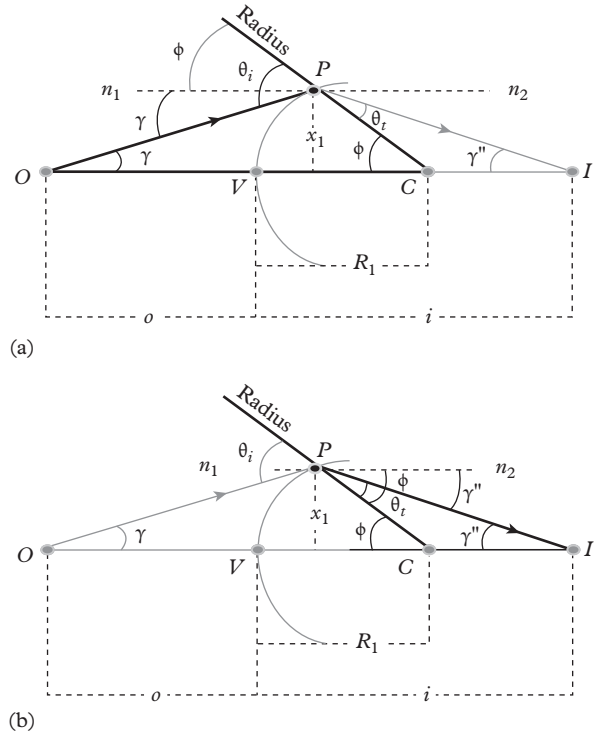

Figure 5.11 *(a) Triangle constructed using the incident ray from the object O, the optical axis from point O to point I, and the radius of curvature of the optical surface. (b) Triangle constructed using the transmitted ray traveling toward the image point I, the optical axis, and the radius of curvature of the optical surface.*

The angle of incidence θ_i and the angle of transmission θ_t can be written in terms of known angles using triangles from Figure 5.10. The triangles are redrawn in Figure 5.11 with their boundaries highlighted for clarity. Figure 5.11(a) is the triangle used to find the angle of incidence at point P, where ϕ is measured from the horizontal to the normal:

$$\theta_i = \gamma - \phi.$$

Figure 5.11(b) is the triangle used to find the angle of transmission at point P, where again ϕ is measured from the horizontal to the normal:

$$\theta_t = -\phi - (-\gamma''),$$

$$\theta_t = \gamma'' - \phi.$$

Note from Figure 5.10 that γ is the angle that the ray from the object O makes with the optical axis, and γ'', which is negative in this sign convention, is the angle that the ray traveling toward the image I makes with the optical axis. From Figure 5.10, we have

$$\sin\phi = -\frac{x_1}{R_1}.$$

The paraxial approximation allows us to write

$$\phi \approx -\frac{x_1}{R_1}.$$

Snell's law can now be written

$$n_1\left(\gamma + \frac{x_1}{R_1}\right) = n_2\left(\gamma'' + \frac{x_1}{R_1}\right).$$

Solving this equation for γ'' yields

$$\gamma'' = \frac{n_1}{n_2}\gamma + \frac{x_1(n_1 - n_2)}{n_2 R_1}. \tag{5.7a}$$

The quantity

$$\Phi = \frac{n_2 - n_1}{R_1}$$

is called the *power* of the surface, with units of *diopters* when R_1 is in meters. If the lens under consideration is located in air, then $n_1 = 1$ and the power for this surface is a positive number when the radius is positive:

$$\Phi_1 = \frac{n_2 - 1}{R_1} > 0.$$

There is no change in the ray's height above the optical axis, x_1, across the surface, so

$$x_1 = x_1'', \tag{5.7b}$$

where the double prime denotes that we are now across the boundary into the material with index n_2. Each ray is characterized by its slope and its distance from the optical axis. These can be combined into a vector, allowing (5.7a, b) to be written in matrix form as

$$\begin{bmatrix} 1 & 0 \\ \dfrac{n_1 - n_2}{n_2 R_1} & \dfrac{n_1}{n_2} \end{bmatrix} \begin{bmatrix} x_1 \\ \gamma \end{bmatrix} = \begin{bmatrix} x_1'' \\ \gamma'' \end{bmatrix}.$$

The matrix multiplying the ray vector describes refraction across the interface and is called the *refraction matrix*:

$$\mathbf{R}_1 = \begin{bmatrix} 1 & 0 \\ \dfrac{n_1 - n_2}{n_2 R_1} & \dfrac{n_1}{n_2} \end{bmatrix}. \tag{5.8}$$

This matrix defines the ray's new direction after it has undergone refraction. The determinant of $\mathbf{R}_1$ is

$$\|\mathbf{R}_1\| = (1)\left(\frac{n_1}{n_2}\right) - (0)\left(\frac{n_1 - n_2}{n_2 R_1}\right) = \frac{n_1}{n_2}.$$

[Many lens design text modify (5.7a, b) so that the index of the medium is combined with the ray slope, i.e., γn_2. Also, the ray tracing is usually done in the (y, z) plane rather than the (x, z) plane. The equations are easily modified by the reader who prefers the other convention.]

We now must consider the translation from the front surface to the back surface in the lens medium of index n_2. We will denote in Figure 5.12 the entry point into the lens as point A and the exit point from the lens as point B. We will retain the same coordinate system, with its origin at V_1, for this part of the ray tracing problem. Referring to Figure 5.12, we can write

$$x_2'' - x_1'' = \Delta x = d \tan \gamma_2'' \approx d\gamma_2''$$

where d is a positive number because the light ray is traveling in the positive z direction, from left to right ($d = z_2 - z_1$). As can be seen in Figure 5.12, because of rectilinear propagation, the angle γ'' does not change from A to B, but the height above the optical axis changes from x_1'' to x_2'':

$$x_2'' = x_1'' + d\gamma_2'', \tag{5.9a}$$

$$\gamma'' = \gamma_2''. \tag{5.9b}$$

These equations can be rewritten in matrix form as

$$\begin{bmatrix} 1 & d \\ 0 & 1 \end{bmatrix} \begin{bmatrix} x_1'' \\ \gamma_2'' \end{bmatrix} = \begin{bmatrix} x_2'' \\ \gamma'' \end{bmatrix}.$$

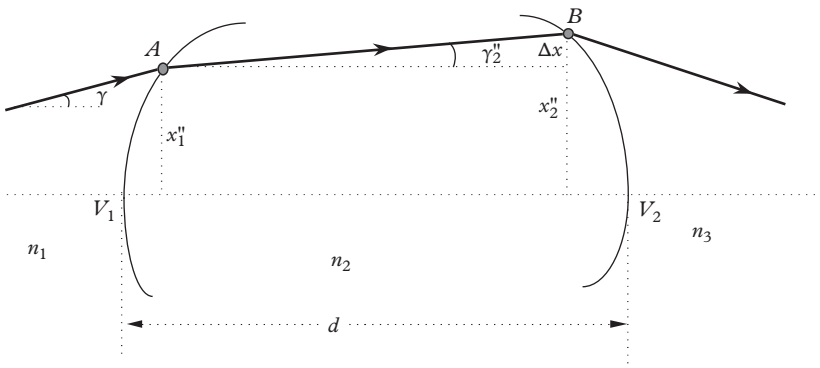

Figure 5.12 *Geometrical construction for propagation of a light ray in the lens. The first surface has radius of curvature R_1 and the second surface has radius of curvature R_2, a negative quantity in this drawing.*

The matrix that describes the propagation from one surface to another is called the *transfer matrix*

$$\mathbf{T} = \begin{bmatrix} 1 & d \\ 0 & 1 \end{bmatrix}. \tag{5.10}$$

Its determinant **T** is

$$\|\mathbf{T}\| = 1.$$

To follow the ray across the surface at B, we must construct another refraction matrix using the same procedure as was used to construct (5.8). The origin of the coordinate system is moved to the vertex of the second surface, V_2 in Figure 5.12, and the following matrix equation is constructed:

$$\begin{bmatrix} 1 & 0 \\ \dfrac{n_2 - n_3}{n_3 R_2} & \dfrac{n_2}{n_3} \end{bmatrix} \begin{bmatrix} x_2'' \\ \gamma'' \end{bmatrix} = \begin{bmatrix} x_2' \\ \gamma' \end{bmatrix}.$$

The refraction matrix for the second surface is therefore

$$\mathbf{R}_2 = \begin{bmatrix} 1 & 0 \\ \dfrac{n_2 - n_3}{n_3 R_2} & \dfrac{n_2}{n_3} \end{bmatrix}. \tag{5.11}$$

The radius of curvature of this second surface is negative according to the sign convention we have adopted. If the lens is in air, then $n_3 = 1$, and the power for this surface is

$$\Phi_2 = \frac{n_3 - n_2}{R_2} = \frac{1 - n_2}{-R_2} > 0.$$

The power of the lens is the sum of the powers of the two surfaces: $\Phi = \Phi_1 + \Phi_2$.

A lens with a positive power such as the one shown in Figure 5.12 is called a *converging lens*. If a plane wave is incident onto a converging lens, the lens will focus the plane wave to a spot; the distance from the vertex to the spot defines the *focal length* of the lens, and the plane normal to the optical axis at this distance is called the *focal plane*. If the lens is a converging lens, then the focal distance is positive.

A *diverging lens* will modify a plane wave such that the wave will appear to originate from a position in front of the lens, i.e., on the object side, a distance equal to the focal length of the lens. The focal distance of a diverging lens is negative, as is the power.

The product of the three matrices (5.8), (5.10), and (5.11) is called the *ray transfer matrix*

$$\mathbf{S} = \mathbf{R}_2\mathbf{T}\mathbf{R}_1$$

or the *ABCD matrix*

$$\begin{bmatrix} A & B \\ C & D \end{bmatrix} = \begin{bmatrix} 1 & 0 \\ \dfrac{n_2 - n_3}{n_3 R_2} & \dfrac{n_2}{n_3} \end{bmatrix} \begin{bmatrix} 1 & d \\ 0 & 1 \end{bmatrix} \begin{bmatrix} 1 & 0 \\ \dfrac{n_1 - n_2}{n_2 R_1} & \dfrac{n_1}{n_2} \end{bmatrix}. \tag{5.12}$$

The elements of the system matrix are known as the *Gaussian constants*

$$A = 1 + \frac{d(n_1 - n_2)}{n_2 R_1}, \quad B = \frac{d n_1}{n_2},$$

$$C = \frac{1}{n_3}\left[\frac{n_2 - n_3}{R_2} + \frac{n_1 - n_2}{R_1} + \frac{d(n_1 - n_2)(n_2 - n_3)}{n_2 R_1 R_2}\right],$$

$$D = \frac{n_1}{n_3}\left[1 + \frac{d(n_2 - n_3)}{n_2 R_2}\right].$$

The determinant of the system matrix is

$$\|\mathbf{S}\| = \|\mathbf{R}_2\| \cdot \|\mathbf{T}\| \cdot \|\mathbf{R}_1\| = AD - BC = \frac{n_1}{n_3}.$$

If the index of refraction is the same at the beginning and end of the ray path, the determinant of the system matrix is 1.

The use of the paraxial *ABCD* matrix to evaluate an optical system is the first step taken in optical design. It can be used to determine the size of the optical system and the general properties of the optical components and to estimate the light throughput of the optical system. Additional information about this matrix, such as its connection to the thin-lens equation and to the principal planes of the optical system, is given in Appendix 5A. Here, we will apply the matrix to the Fabry–Perot resonator used as the resonant cavity in lasers.

5.6 Geometrical Optics of Resonators

As an example of the use of the *ABCD* matrix, we will evaluate a Fabry–Perot resonator used in laser designs and a more general realization of the Fabry–Perot interferometer studied in Chapter 4. The resonator consists of two mirrors, which may have spherical curvature, separated by a distance d, as shown in Figure 5.13. The resonator performs a role similar to a resonant cavity in a microwave system by producing large internal fields with small power input. It does this by trapping energy in the region between the mirrors. The trapped energy is distributed over the eigenmodes of the cavity (also called the resonant modes of the cavity).

The *ABCD* matrix will be used to determine the importance of the three parameters R_1, R_2, and d for the design of the resonator. We will discover that the parameters must meet a "stability condition" for a resonant mode to exist in the resonator. This stability condition is associated with the trapping of a ray inside the resonator; the trapped ray establishes a resonator mode. This calculation will tell us when a mode will exist, but the physical process behind the loss of stability can only be discussed through the use of the diffraction theory developed in Chapter 9 [8].

Before the system can be evaluated, an *ABCD* matrix for a mirror must be obtained. The refraction matrix (5.8) can be used to obtain the reflection matrix by setting $n_2 = -n$. A negative index of refraction, $-n$, can be interpreted physically as being associated with a

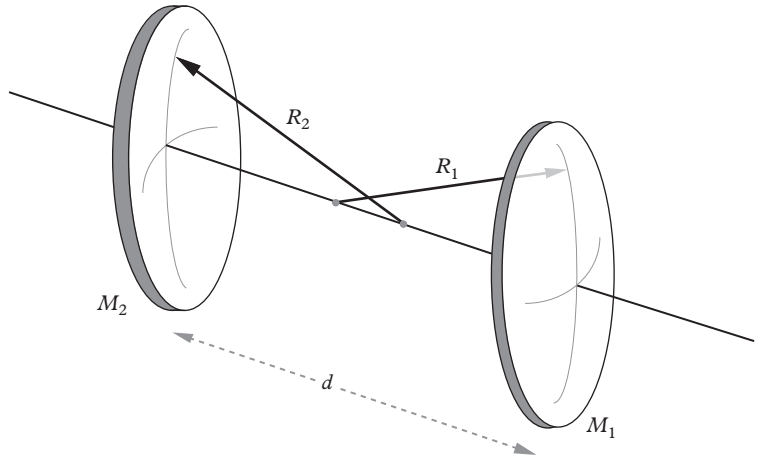

Figure 5.13 *A Fabry–Perot resonator made of a mirror M_1 with radius of curvature R_1 separated by a distance d from mirror M_2 with radius of curvature R_2.*

ray traveling in the opposite direction from the ray associated with the positive index, n. (If this modification is used on the equation for the power of a surface, we find that a mirror with a positive power must have a negative radius of curvature, which is in agreement with the knowledge that a concave mirror will focus sunlight.) The reflection matrix for a mirror of radius R in a medium of index n is

$$\mathbf{M} = \begin{bmatrix} 1 & 0 \\ \dfrac{2n}{-nR} & \dfrac{n}{-n} \end{bmatrix} = \begin{bmatrix} 1 & 0 \\ \dfrac{-2}{R} & -1 \end{bmatrix}.$$

The element M_{22} is negative because the angle of reflection is measured in the opposite sense to the angle of incidence. (A summary of the various *ABCD* matrices that we use is given in Figure 5A.4.)

To follow a light ray through a Fabry–Perot resonator, we start the light ray at mirror M_1 traveling toward mirror M_2. Let the origin of the coordinate system be at the vertex of M_2. Mirror M_1 acts as an object that is to be imaged by M_2, and the ray is followed through its reflection at mirror M_2. The transfer matrix describing the passage of the ray through the Fabry–Perot cavity is

$$\mathbf{T}_1 = \begin{bmatrix} 1 & -d \\ 0 & 1 \end{bmatrix}.$$

Reflection takes place at mirror M_2, which has a positive spherical curvature R_2. The reflection matrix is

$$\mathbf{M}_2 = \begin{bmatrix} 1 & 0 \\ -\dfrac{2}{R_2} & -1 \end{bmatrix},$$

where we assume that the index between the two mirrors is 1. In the next step of this ray tracing problem, mirror M_2 is treated as an object and we follow the ray from this new

object through its reflection at mirror M_1. The light propagates through the cavity toward mirror M_1, and the second transfer matrix becomes

$$\mathbf{T}_2 = \begin{bmatrix} 1 & d \\ 0 & 1 \end{bmatrix}.$$

Finally, the light completes its round trip by reflecting off of mirror M_1. Mirror M_1 has a negative radius of curvature since the distance from the mirror surface to the center of curvature is a negative quantity. The reflection matrix for mirror M_1 is

$$\mathbf{M}_1 = \begin{bmatrix} 1 & 0 \\ \dfrac{2}{R_1} & -1 \end{bmatrix}.$$

The *ABCD* matrix of the system is obtained by multiplying the matrices together in the matrix equation:

$$\begin{bmatrix} x_1 \\ \gamma_1 \end{bmatrix} = \begin{bmatrix} 1 & 0 \\ \dfrac{2}{R_1} & -1 \end{bmatrix} \begin{bmatrix} 1 & d \\ 0 & 1 \end{bmatrix} \begin{bmatrix} 1 & 0 \\ -\dfrac{2}{R_2} & -1 \end{bmatrix} \begin{bmatrix} 1 & -d \\ 0 & 1 \end{bmatrix} \begin{bmatrix} x_0 \\ \gamma_0 \end{bmatrix}.$$

To simplify the notation, we replace the mirror's radius of curvature with its focal length $f_i = R_i/2$:

$$\begin{bmatrix} x_1 \\ \gamma_1 \end{bmatrix} = \begin{bmatrix} 1 - \dfrac{d}{f_2} & d\left(\dfrac{d}{f_2} - 2\right) \\ \dfrac{1}{f_1} + \dfrac{1}{f_2}\left(1 - \dfrac{d}{f_1}\right) & 1 - \dfrac{2d}{f_1} - \dfrac{d}{f_2}\left(1 - \dfrac{d}{f_1}\right) \end{bmatrix} \begin{bmatrix} x_0 \\ \gamma_0 \end{bmatrix}. \tag{5.13}$$

In equation form,

$$x_1 = Ax_0 + B\gamma_0, \tag{5.14a}$$

$$\gamma_1 = Cx_0 + D\gamma_0, \tag{5.14b}$$

where

$$A = 1 - \frac{d}{f_2}, \quad B = d\left(\frac{d}{f_2} - 2\right),$$

$$C = \frac{1}{f_1} + \frac{1}{f_2}\left(1 - \frac{d}{f_1}\right), \quad D = 1 - \frac{2d}{f_1} - \frac{d}{f_2}\left(1 - \frac{d}{f_1}\right).$$

Rewriting the first ray equation, (5.14a),

$$\gamma_0 = \frac{dx_0}{dz} = \frac{1}{B}(x_1 - Ax_0).$$

If we pass through the resonator a second time, we obtain

$$\gamma_1 = \frac{1}{B}(x_2 - Ax_1). \tag{5.15}$$

From (5.14b), we obtain

$$\gamma_1 = \frac{dx_1}{dz} = Cx_0 + \frac{D}{B}(x_1 - Ax_0). \tag{5.16}$$

Equating (5.15) and (5.16) yields

$$\frac{1}{B}(x_2 - Ax_1) = Cx_0 + \frac{D}{B}(x_1 - Ax_0),$$

or

$$x_2 - (A + D)x_1 + (AD - BC)x_0 = 0. \tag{5.17}$$

The quantity $AD - BC$ is the determinant of the $ABCD$ matrix. (It is easy to show that the determinant of the resonator's system matrix, $AD - BC$, is equal to 1, as it should be since the indices of refraction of the origin and endpoint are the same.) Equation (5.17) is called a recurrence relation; it defines a sequence (x_2, x_1, x_0) by defining each term of the sequence as a function of the preceding terms. This type of recurrence relation is called a difference equation because the relationships are functions of the differences between sequence members [8].

The difference equation (5.17) is equivalent in form to the differential equation for a harmonic oscillator,

$$m\frac{d^2x}{dt^2} + sx = 0.$$

The solution of the differential equation for the harmonic oscillator, using complex notation, is

$$x = x_0 e^{\pm i\sqrt{s/m}\,x}.$$

Therefore, a reasonable guess for a solution to (5.17) is a function of the form

$$x_n = x_0 e^{in\theta},$$

where n is the number of trips the light has made through the cavity. Substituting this function into (5.17) yields

$$e^{i2\theta} - (A + D)e^{i\theta} + 1 = 0,$$

which gives

$$\begin{aligned} e^{\pm i\theta} &= \frac{1}{2}\left[(A + D) \pm \sqrt{(A + D)^2 - 4}\right] \\ &= \frac{A + D}{2} \pm i\sqrt{1 - \frac{(A + D)^2}{4}}. \end{aligned} \tag{5.18}$$

Using the Euler formula,

$$e^{i\theta} = \cos\theta + i\sin\theta,$$

we can write

$$\cos\theta = \frac{A+D}{2}. \tag{5.19}$$

The general solution of the difference equation is therefore

$$x_n = x_0\left(e^{in\theta} + e^{-in\theta}\right) = 2x_0\cos n\theta.$$

The function x_n equals the height above the optical axis where the ray strikes the mirror on pass n through the cavity. It cycles periodically through a set of values, retracing its path after one cycle but never exceeding $\pm 2x_0$. To obtain this harmonic behavior, the radical in (5.18) must be imaginary:

$$-1 \le \frac{A+D}{2} \le 1.$$

The harmonic behavior of x is associated with the stability of the cavity modes. For a mode to be stable, the ray associated with the mode must never miss a mirror as it reflects to and for in the cavity. If the ray missed the mirror after a number of reflections, then the fields in the Fabry–Perot interferometer would not build up to large values and we would not have a resonator. Using the relationships for A and D, the stability condition can be rewritten as

$$-1 \le \left[\frac{d^2}{2f_1f_2} - d\left(\frac{1}{f_1}+\frac{1}{f_2}\right)+1\right] \le 1 \tag{5.20}$$

The inequality can be simplified by using the identity

$$2\left(1-\frac{d}{2f_1}\right)\left(1-\frac{d}{2f_2}\right) = \frac{d^2}{2f_1f_2} - d\left(\frac{1}{f_1}+\frac{1}{f_2}\right)+2.$$

The left side of the inequality is

$$\begin{aligned} 0 &\le \frac{d^2}{2f_1f_2} - d\left(\frac{1}{f_1}+\frac{1}{f_2}\right)+2, \\ 0 &\le \left(1-\frac{d}{2f_1}\right)\left(1-\frac{d}{2f_2}\right). \end{aligned} \tag{5.21}$$

The right side of the inequality can be rewritten

$$\begin{aligned} \frac{d^2}{2f_1f_2} - d\left(\frac{1}{f_1}+\frac{1}{f_2}\right)+2 &\le 2, \\ \left(1-\frac{d}{2f_1}\right)\left(1-\frac{d}{2f_2}\right) &\le 1. \end{aligned} \tag{5.22}$$

Combining these two inequalities, we obtain the stability condition for the Fabry–Perot resonator:

$$0 \le \left(1-\frac{d}{2f_1}\right)\left(1-\frac{d}{2f_2}\right) \le 1. \tag{5.23}$$

In applying this stability condition, it must be kept in mind that the sign convention requires facing mirrors to have radii of curvatures of opposite signs.

If the stability condition (5.23) is not met then (5.18) is no longer complex. The identification of $(A + D)/2$ with a cosine function, (5.19), is no longer valid and, analogous to the differential equation, the solution of (5.17) becomes a function of two exponentials:

$$x_n = C_1 e^{a+x} + C_2 e^{a-x},$$

$$e^{a\pm x} = \frac{A+D}{2} \pm \sqrt{\left(\frac{A+D}{2}\right)^2 - 1}.$$

At some value of x, one of the two terms of x_n will exceed the mirror's radius and the beam will escape from the resonator.

5.7 Guided Waves

In the discussion of the Fabry–Perot interferometer, a light wave was assumed to undergo multiple reflections at the boundaries of a lossless dielectric (see Figure 4.20). The wave trapped in the dielectric layer slowly died away because of the light transmitted out of the dielectric layer at each reflection from a boundary. If the incident angle of the wave in the layer met the requirement for total reflection, (3.51), then the wave would not experience loss but would propagate along the dielectric layer; such a wave, confined to the layer, is called a *guided wave* and the dielectric layer is called a *waveguide*.

In this section, we will use geometrical optics to discover the properties of guided waves. The theory to be used is not a "pure" geometrical theory, because we borrow the concepts of interference and of phase change upon total reflection from the wave theory. Another way to view this approach is that we assume that the waves are plane waves and that the "rays" are normal to these plane waves.

We will discuss the requirements placed on the angle of incidence in the waveguide and briefly review techniques for introducing guided waves into the waveguide. The discussion will be limited to a one-dimensional problem by assuming that the waveguide (Figure 5.14) has a thickness d in the x-direction and extends to infinity in the y- and z-directions, with light propagating along the z-direction. The results for the dielectric slab of Figure 5.14 in general will not apply to optical fibers that have cylindrical symmetry. However, the results derived here will apply to those rays in a fiber that pass through the cylindrical axis of the fiber. The rays that cross the fiber axis as they propagate are called *meridional rays*. (In geometrical optics, any ray that lies in a plane containing the optical axis is a meridional ray; all other rays are called *skew rays*.)

Swiss physicist **Daniel Colladon** first demonstrated a light jet experiment in Geneva in 1841, but **Tyndall** was given credit for the idea—evidently, his demonstration in 1854 received more publicity. Nowadays, water/light shows can be found in every resort area (Figure 5.15).

A theoretical investigation of guided waves was not conducted until the publication of an analysis by **Peter Debye** in 1910. The use of guided waves was not practical until the idea of cladding a core glass of index n_2 by another glass, of index $n_1 < n_2$, was introduced in 1951. The guiding structures were suggested for use as endoscopes in medical diagnosis,

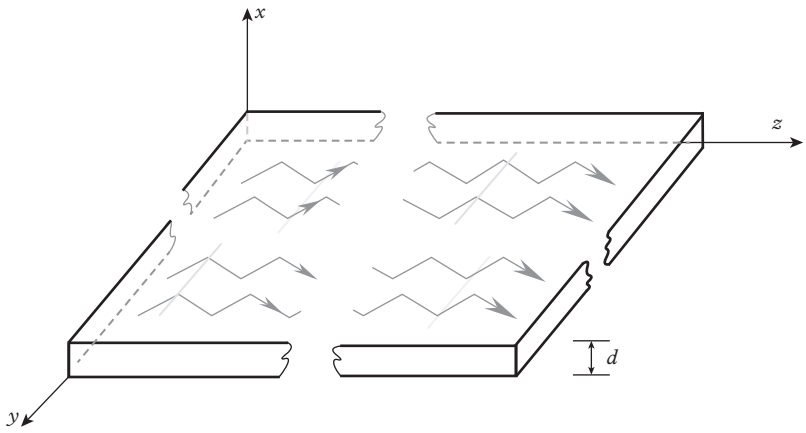

Figure 5.14 *Geometry of planar waveguide. Light is propagated along the z-direction.*

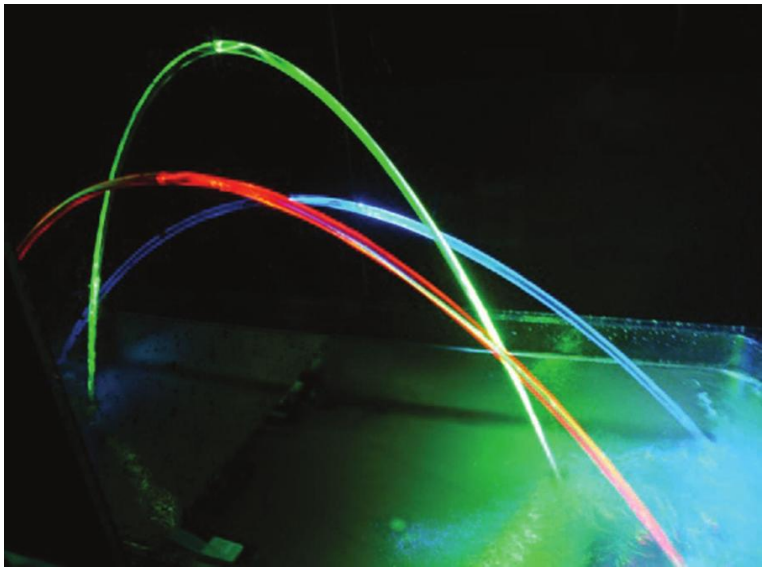

Figure 5.15 *Laser fountain. (By S forget at fr.wikipedia [CC BY 2.5], from Wikimedia Commons.)*

but this application did not trigger much interest in guided wave technology. Research in guided wave optics did not blossom into a full-scale research area until proposals were made in the mid 1960s for communications. The first fiber-optic link was installed by the Dorset (UK) police in 1975. Two years later, the first live telephone traffic through fiber optics occurred in Long Beach, California.

Consider a three-layer sandwich of dielectrics with indices $n_2 > n_3 > n_1$. When light coming from the region of index n_3 strikes the two interfaces, we can have the three possible outcomes shown schematically in Figure 5.16.

When θ_3 in Figure 5.16a is small and the rays meet the inequalities

$$0 \leq \theta_1 \leq \frac{\pi}{2}, \quad \theta_3 < \sin^{-1}\left(\frac{n_1}{n_3}\right), \quad \theta_2 < \sin^{-1}\left(\frac{n_1}{n_2}\right) m \tag{5.24}$$

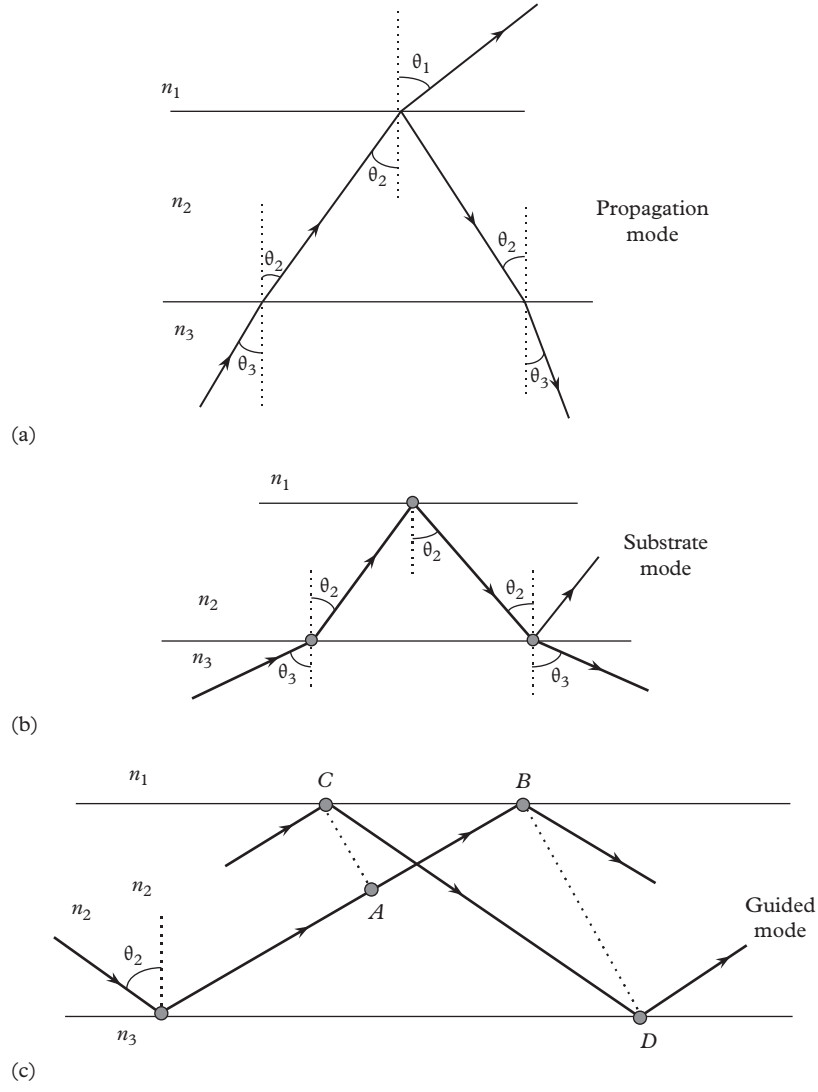

Figure 5.16 *(a) The rays shown here are called radiation modes, air modes, or propagation modes. They occur when the inequalities (5.24) are met. (b) The rays shown here are the substrate modes of a dielectric guide using the zigzag-wave or geometrical optical model of propagation. As in (a), these modes are propagation modes, but the rays do not enter the medium with index n_1. For these modes to exist, the inequalities (5.25) must be met. (c) The waveguide modes of a dielectric layer are illustrated using the zigzag-wave or geometrical optical model of propagation. The dotted lines AC and BD represent the wavefronts of a plane wave represented by the rays at two different positions during the propagation down the dielectric layer.*

the light is transmitted across the two interfaces, as shown in Figure 5.16(a). We will call rays that meet the inequalities (5.24) *radiation modes* or air modes, because medium 1 is often air. The discussions in Chapter 3 on reflection and refraction were descriptions of the behavior of radiation modes. If the thickness d of the dielectric layer is of the order of a wavelength, if the interfaces are very flat, or if the illuminating light wave has a high degree of coherence (see Chapter 8), then interference, discussed in Chapter 4, would be observed.

When θ_3 increases to a large enough value, θ_2 will exceed the critical angle for total reflection and light rays will not enter the region with index n_1; see Figure 5.16(b). For this condition to occur, θ_2 and θ_3 are limited by the inequalities

$$\sin^{-1}\left(\frac{n_1}{n_2}\right) < \theta_2 < \sin^{-1}\left(\frac{n_3}{n_2}\right), \quad \sin^{-1}\left(\frac{n_1}{n_3}\right) < \theta_3 < \frac{\pi}{2}. \tag{5.25}$$

We call rays that satisfy (5.25) *substrate modes*[4] because the medium in which they propagate, with index of refraction n_3, is the *substrate* or supporting medium for the dielectric layer with index n_2. We treated the waves associated with the rays obeying (5.25) in Chapter 3 during the discussion of total reflection.

Finally, it is possible to introduce a ray into the region of index n_2 so that the angle of incidence of the ray satisfies the inequality

$$\sin^{-1}\left(\frac{n_3}{n_2}\right) < \theta_2 < \frac{\pi}{2}. \tag{5.26}$$

These rays, called *waveguide modes*, are associated with waves trapped in the region of index n_2, which we will call the waveguide region or the guiding layer; see Figure 5.16(c). To obtain the guided wave modes of Figure 5.16(c), the incident angle θ_3 must exceed $\pi/2$. A waveguide mode cannot be excited by simply illuminating the guide surface. Figure 3.14 illustrates one method of successfully coupling energy into a guide. We will discuss another method of coupling once we have developed an understanding of propagation modes.

5.7.1 End Coupling

One technique for launching a waveguide mode is to couple the light into the polished end of the dielectric layer—along the z-direction and perpendicular to the (x, y) plane. This technique is called *end-fired coupling*.

As an example, we will consider a step-index waveguide and use geometrical optics to follow the light, introduced into a flat end surface of the guide, through the guide. Figure 5.17(a) shows the (x, y) plane of the step-index guide and its index-of-refraction profile, a step function; a fiber geometry is presented to allow discovery of the limits placed

[4] These modes are propagating waves and thus could also be called radiation modes.

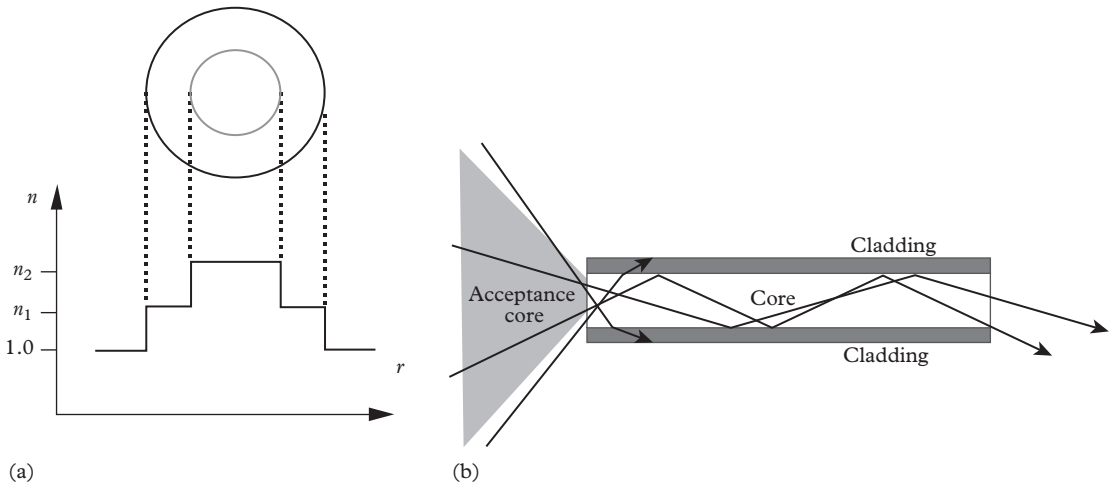

Figure 5.17 *(a) Step-index fiber. The fiber is shown end on and the index of refraction profile is displayed. (b) Limitation on incident angle for end-fired coupling.*

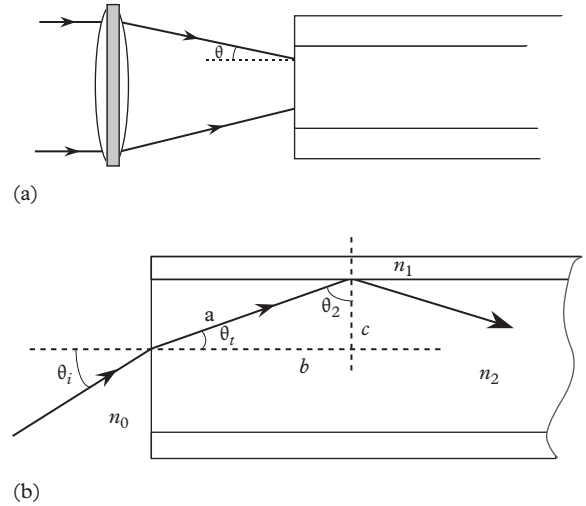

Figure 5.18 *(a) Edge-coupled guide. A lens is used to focus light onto the polished end of a guided wave structure. (b) Coordinates for determining the numerical aperture of a step-index optical guide.*

on the incident angle for end-fired coupling into a fiber. For a fiber, the high-index region at the center is called the core and the lower-index region surrounding the core is called the cladding; see Figure 5.17(b).

As shown in Figure 5.18(a), a lens is used to focus light onto the end face of the guide. The guide will accept rays that are incident at an angle θ that is less than a critical angle that we will denote by θ_{NA} and call the *acceptance angle*. The value of this maximum angle is obtained by using the fact that rays trapped in the guide must be incident on the core–cladding interface at an angle θ_2 that exceeds the critical angle for total reflection; see Figure 5.18(b). When this requirement is met, the light is trapped in the guide until it emerges from the other end.

The maximum incident angle θ_{NA} that will allow propagation as a guided wave can be obtained using the geometry in Figure 5.18(b). The angle θ_2 must exceed the critical angle:

$$\theta_2 \geq \theta_c = \sin^{-1} \frac{n_1}{n_2}.$$

The angle θ_2 can be written in terms of the sides of the triangle drawn in Figure 5.18(b):

$$a^2 = b^2 + c^2,$$

$$1 = \left(\frac{b}{a}\right)^2 + \left(\frac{c}{a}\right)^2,$$

$$\sin\theta_2 = \frac{b}{a},$$

$$\left(\frac{c}{a}\right)^2 = 1 - \left(\frac{b}{a}\right)^2 \leq 1 - \left(\frac{n_1}{n_2}\right)^2.$$

The sides of the triangle can also be related to the transmission angle θ_t at the front surface of the guide:

$$\frac{c}{a} = \sqrt{1 - \left(\frac{n_1}{n_2}\right)^2} = \sin\theta_t.$$

Snell's law relates the transmission angle to the angle of incidence on the fiber face:

$$\frac{n_2}{n_0} = \frac{\sin\theta_i}{\sin\theta_t}.$$

The acceptance angle can be written in terms of the above relations:

$$\sin\theta_i \leq \sin\theta_{\mathrm{NA}} = \frac{n_2}{n_0}\sqrt{1-\left(\frac{n_1}{n_2}\right)^2}.$$

We define the *numerical aperture* of the guide in terms of the acceptance angle as

$$\begin{aligned}\mathrm{NA} &= n_0 \sin\theta_{\mathrm{NA}} = n_2 \sin\theta_t \\ &= n_2\sqrt{1-\left(\frac{n_1}{n_2}\right)^2} \\ &= \sqrt{n_2^2 - n_1^2}. \end{aligned} \tag{5.27}$$

The numerical aperture is proportional to the largest incident angle that the guide can accept and emit into. The result just derived will apply to rays in a planar guide or to meridional rays in a fiber, but it must be modified for skew rays.

In addition to meridional rays, a fiber will allow the propagation of skew rays. As mentioned earlier, skew rays travel the length of the fiber without ever crossing its cylindrical axis. Figure 5.19 shows a skew ray from two perspectives.

Figure 5.19(a) is an end view of the fiber showing the skew ray propagating down the fiber without crossing its axis. The thicknesses of the arrows representing the rays indicate the depth of the rays propagating into the fiber—thinner arrows represent deeper rays. The angle between each pair of rays is 2φ, where φ is defined in Figure 5.19(b).

Figure 5.19(b) displays the geometry associated with the skew ray. The skew ray propagates in a plane that makes an angle φ with the plane containing the cylindrical axis of the fiber. The component of the ray propagating in the core parallel to the normal vector of the core–cladding interface is

$$k_t \cos\varphi \sin\theta_t.$$

The normal vector of the core–cladding interface is the radius vector from the cylindrical axis of the fiber to the point where the ray strikes the interface and, with the ray, establishes the plane of incidence. The component of the ray along the normal is given, in terms of the angle of incidence θ_2, as

$$k_t \cos\theta_2 = k_t\sqrt{1-\sin^2\theta_2}.$$

Assuming that θ_2 is equal to the critical angle for total reflection and using Snell's law to replace θ_t by θ_i, we have

$$(\cos\varphi)\frac{n_0}{n_2}\sin\theta_i = \sqrt{1-\left(\frac{n_1}{n_2}\right)^2}.$$

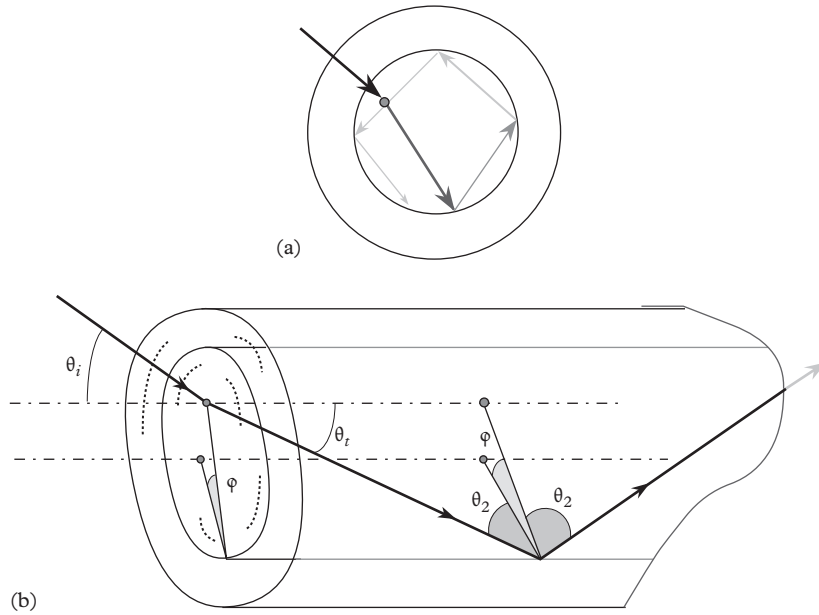

Figure 5.19 *Propagation of a skew ray in an optical fiber. The ray propagates in a helical path. (a) Propagation of a skew ray as viewed from the end of the fiber. As the ray progresses down the fiber, the arrows representing the rays decrease in thickness. (b) Geometry used to evaluate the numerical aperture for a skewed ray.*

We thus discover that the numerical aperture for a skew ray, propagating in the plane defined by φ, is given by

$$(\mathrm{NA})_s = \frac{\mathrm{NA}}{\cos\varphi},$$

where NA denotes the numerical aperture for a meridional ray given by (5.27). We see that the maximum acceptance angle of a meridional ray is the minimum acceptance angle for skew rays. The skew rays act to increase the light-gathering capability of a fiber.

As an example of the application of (5.27), assume $n_0 = 1$, $n_1 = 1.5$, and $n_2 = 1.53$. The critical angle is then

$$\theta_c = \sin^{-1}\left(\frac{n_1}{n_2}\right) = \sin^{-1}\left(\frac{1.5}{1.53}\right) = 78.6^\circ.$$

The numerical aperture is 0.303, which corresponds to a maximum incident angle of $\theta_{\mathrm{NA}} = 17.6^\circ$. If a skew ray is propagating in this fiber with $\varphi = 50^\circ$ then the maximum incident angle for this skew ray is 28.1°.

The symmetry associated with the propagation of a ray in an optical fiber predicts that the angle of the output ray from the fiber will be equal to the incident angle. Because a meridional ray is confined to a plane, it will always emerge at a position determined by the input ray. A skew ray, however, will exit a fiber at a position that is a function of the number of reflections it has undergone rather than being determined by the input ray. A skew ray will thus smooth the output distribution of light along a circumference of a circle of radius r, where r is the position of the input ray at the entrance to the fiber. An example of this smoothing is shown in

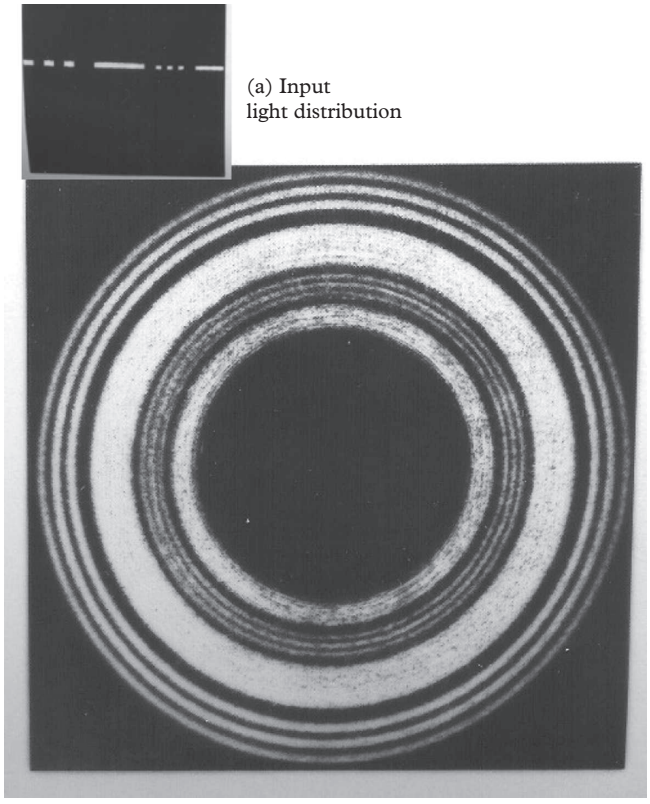

Figure 5.20 *(a) A set of slits form a one-dimensional pattern. This pattern is positioned at the fiber input with the rightmost edge of the pattern centered on the fiber axis. (b) The output of the multimode fiber with (a) as an input exhibits the intensity smoothing produced by skew rays. (Courtesy of A. Tia and A. Friesem [9].)*

Figure 5.20. In Figure 5.20(a), an array of slits is shown distributed along the radius of a fiber from the center (on the right of the figure) to the edge of the core (on the left). The light distribution upon exiting the fiber is shown in Figure 5.20(b).

5.7.2 Guided Modes

To analyze how the waveguide modes propagate in the waveguide region of index n_2, we use the geometry shown in Figure 5.16(c). We have developed all of the necessary theory to use the wave model for this problem, but we will instead use the more pictorial geometrical model. This ray model, sometimes called the *zigzag model* [10], will demonstrate the application of geometrical optics and, further, will develop an intuitive understanding of guided optics.

In free space, we proved (Chapter 2) that the electric and magnetic vectors are perpendicular to the propagation vector of the electromagnetic wave. It is customary to term such waves *transverse electromagnetic* (TEM) waves in guided wave theory. In Section 3.8, we found that for the case of total reflection, we no longer had transverse waves; therefore, we must modify the notation for the polarization of waves undergoing total reflection. The new notation defines *TE waves* as waves with a longitudinal component of the magnetic field

(these waves correspond closely to the E_N polarization for free-space waves) and *TM waves* as waves with a longitudinal component of the electric field. We will limit our discussion to TE waves, because the results are qualitatively the same for the two polarizations and the purpose of our discussion is to develop a qualitative understanding of guided waves.

Using Figure 5.21, we follow a plane wave propagating through a waveguide of index n_2 and thickness d. We have denoted the wavefronts associated with the rays, which are assumed planar, by dotted lines in Figure 5.21. One ray travels from C to D and undergoes two reflections, while a second ray goes from A to B and experiences no reflection. Since the wavefronts (dotted lines AC and BD in Figure 5.21) are surfaces of constant phase traveling in parallel directions, we must have the phase difference associated with the two propagation paths equal to a multiple of 2π.

The optical path lengths associated with the distances $\overline{CD}$ and $\overline{AB}$ can be determined using the triangles drawn in Figure 5.21. Triangle CDF of Figure 5.21 yields

$$\frac{d}{\overline{CD}} = \cos\theta_2.$$

Triangle ABC yields

$$\frac{\overline{AB}}{\overline{CB}} = \sin\theta_2.$$

Triangle CDE yields

$$\frac{\overline{CE}}{d} = \tan\theta_2.$$

Finally, triangle BDE yields

$$\frac{d}{\overline{BE}} = \tan\theta_2.$$

The distance along the guide axis is

$$\overline{\mathrm{CE}} = \overline{\mathrm{CB}} + \overline{\mathrm{BE}}.$$

Solving for $\overline{CB}$ and substituting for $\overline{CE}$ and $\overline{BE}$,

$$\overline{\mathrm{CB}} = d\left(\tan\theta_2 - \frac{1}{\tan\theta_2}\right).$$

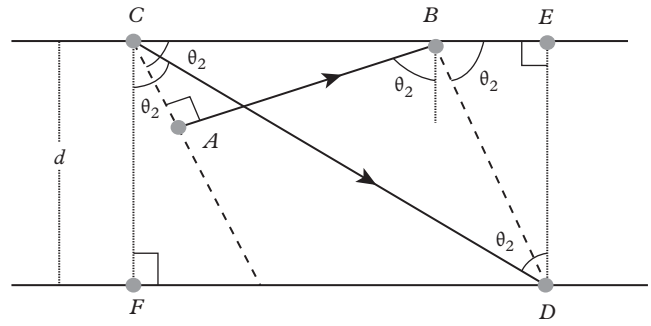

Figure 5.21 *Geometry for finding guided modes using the ray model of optics.*

The phase difference between the two paths is given by

$$n_2 k\left(\overline{\mathrm{CD}}-\overline{\mathrm{AB}}\right)+\delta_1+\delta_3,$$

where δ_1 and δ_3 are phase shifts due to total reflection, whose values can be obtained from (3.54). We require that the total phase difference be equal to an integer multiple of 2π:

$$n_2 k\left(\overline{\mathrm{CD}}-\overline{\mathrm{AB}}\right)+\delta_1+\delta_3 = m\cdot 2\pi, \tag{5.28}$$

$$\begin{aligned}
\frac{n_2 kd}{\cos\theta_2}-n_2 kd\sin\theta_2\left(\tan\theta_2-\frac{1}{\tan\theta_2}\right)+\delta_1+\delta_3 &= m\cdot 2\pi,\\
\frac{n_2 kd}{\cos\theta_2}\left(1-\sin^2\theta_2+\cos^2\theta_2\right)+\delta_1+\delta_3 &= m\cdot 2\pi,\\
\frac{n_2 kd}{\cos\theta_2}2\cos^2\theta_2+\delta_1+\delta_3 &= m\cdot 2\pi,\\
2n_2 kd\cos\theta_2+\delta_1+\delta_3 &= m\cdot 2\pi.
\end{aligned} \tag{5.29}$$

This relation describes how the propagation of the guided wave varies with wavelength and is called the *dispersion relation* for TE guided waves. We have neglected any effect on the plane waves arising from the finite size of the guide. It sounds a little strange, since we are working in a narrow waveguide, but this is an infinite plane wave result.

We see that θ_2 can only have certain values θ_m, determined by the integer values of m in (5.29). The rays associated with the discrete values of θ_m are the waveguide modes. Figure 5.22 displays a number of discrete modes propagating in a dielectric layer (xylene floating on a water surface). Each mode in Figure 5.22 can be characterized by the number of bounces it makes as it propagates through the layer.

Remember that for total reflection, the angle θ_2 must satisfy the inequality (5.26):

$$\sin\theta_m > \frac{n_3}{n_2}, \quad \text{or} \quad \cos\theta_m < \sqrt{1-\left(\frac{n_3}{n_2}\right)^2}.$$

This means that there is a maximum number of modes, $m_{\max}$, that can propagate in the guide. This maximum value is given by

$$m_{\max} \le \frac{2dn_2}{\lambda_0}\sqrt{1-\left(\frac{n_3}{n_2}\right)^2}+\frac{\delta_1+\delta_3}{2\pi}. \tag{5.30}$$

We define the quantity

$$V = kdn_2\sqrt{1-\left(\frac{n_3}{n_2}\right)^2} = kd\sqrt{n_2^2-n_3^2}, \tag{5.31}$$

called the *normalized film thickness* for the case of planar waveguides and the *normalized frequency* or simply the *V-number* for optical fibers. The inequality (5.30) can be written in terms of the V-number:

$$m_{\max} \le \frac{V}{\pi}+\frac{\delta_1+\delta_3}{2\pi}.$$

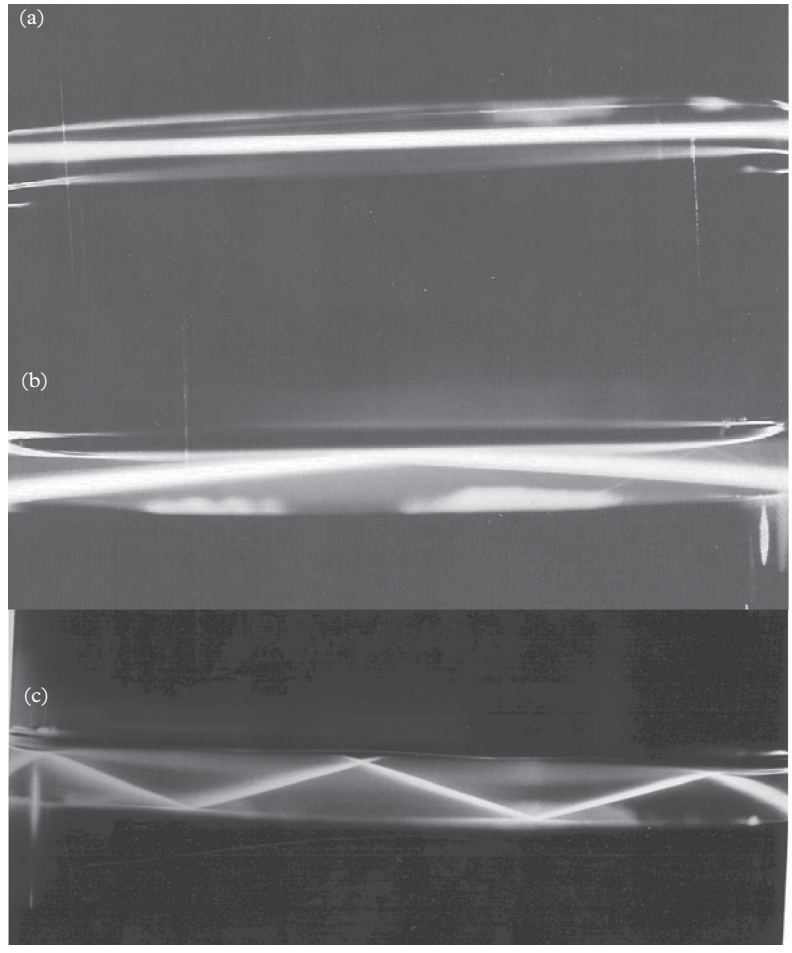

Figure 5.22 *Several modes are shown propagating in a guiding layer of xylene bounded above by air and below by water containing a dye.*

As an example of how the maximum number of modes and the normalized film thickness are calculated, assume that a waveguide 100 μm thick with an index $n_2 = 1.53$ is formed between a medium with index $n_1 = 1.0$ and a medium with index $n_3 = 1.5$. If the wavelength of the propagating light is 1 μm, the normalized film thickness is

$$V = \frac{2\pi}{1 \times 10^{-6}} \left(1 \times 10^{-4}\right) \sqrt{(1.53)^2 - (1.5)^2} = 189.4.$$

The maximum number of modes in this guide is

$$m_{\max} \leq \frac{189.4}{\pi} + 1 = 61.3,$$

yielding a maximum number of modes of about 60. We assume that the phase shift upon reflection should not exceed 180°.

We will discover in a moment [in (5.32) and (5.33)] that δ_1 and δ_3 are negative. Since m can only be a positive integer or zero, if $V < \delta_1 + \delta_3$, then no mode can propagate in the dielectric layer. This condition is called the *cutoff condition*, and the V-number where $2V_c = \delta_1 + \delta_3$ is defined as the cutoff value for the waveguide, V_c. We will return to this cutoff value of V in a moment.

Since the number of modes in a guide is a function of V, and $\delta_1 + \delta_3$ is limited in magnitude to be no larger than 2π, we can evaluate the contributions to the number of waveguide modes by the basic guide parameters from (5.31). The number of modes in the guide increases with increasing guide index n_2, decreasing substrate index n_3, increasing guide thickness, and decreasing wavelength.

We derived the functional forms of δ_1 and δ_3 during our discussion of total reflection, (3.54) and (3.55). It is these parameters that contain the effects of polarization. For the TE waves, we can rewrite (3.54) and (3.55) as

$$\delta_1 = -2\tan^{-1}\frac{\sqrt{\sin^2\theta_2 - \left(\frac{n_1}{n_2}\right)^2}}{\cos\theta_2}, \tag{5.32}$$

$$\delta_3 = -2\tan^{-1}\frac{\sqrt{\sin^2\theta_2 - \left(\frac{n_3}{n_2}\right)^2}}{\cos\theta_2}. \tag{5.33}$$

Substituting these relationships into (5.29) yields a transcendental equation that must be solved to determine the values of θ_2 associated with the waveguide modes. A graphical solution to this transcendental equation will be presented after the introduction of several new variables that are often used in the wave formalism of guided wave theory to describe the observed propagation in a guide. If we assume that the ray path is colinear with the propagation vector of the wave, then this notation can be incorporated into our ray theory.

5.7.3 Propagation Vector Formalism

The geometrical ray is parallel to the propagation vector **k**. Thus, there is a discrete set of propagation vectors associated with the set of rays predicted by (5.29). We can decompose any one of these propagation vectors into two components, as shown in Figure 5.23. To the external observer, the light associated with a particular waveguide mode appears to propagate through the guide with an effective propagation constant β, defined in Figure 5.23. The bounds on β for waveguide modes follow directly from (5.26):

$$kn_3 < \beta < kn_2.$$

We can use the effective propagation constant to define an *effective guide index of refraction*

$$N = \frac{\beta}{k}.$$

The limits on this effective index are

$$n_3 < N < n_2.$$

The effect of introducing the new terms β and κ in Figure 5.23 is to divide the wave in the guide into two components: a standing wave that exists between the two interfaces and

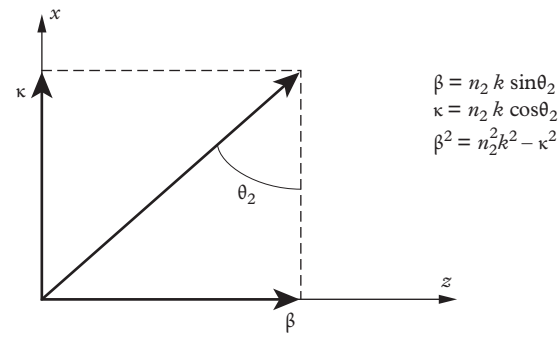

Figure 5.23 *Definition of the propagation constant of a guided wave.*

a wave propagating along the z-axis at a velocity ω/β. Using the newly defined variables, we may rewrite (5.32) and (5.33) as

$$\delta_{1,3} = -2\tan^{-1}\left[\frac{\sqrt{\beta^2 - (n_{1,3}k)^2}}{\kappa}\right]. \tag{5.34}$$

The radical in (5.34) is equal to the decay constant of an evanescent wave associated with total reflection, introduced in Chapter 3:

$$\sqrt{\beta^2 - n^2k^2} = kn\alpha = \gamma.$$

We introduce a decay constant for each of the guide boundaries:

$$\gamma_1^2 = (kn_1\alpha_1)^2 = \beta^2 - n_1^2k^2 = \left(n_2^2 - n_1^2\right)k^2 - \kappa^2, \tag{5.35a}$$

$$\gamma_3^2 = (kn_3\alpha_3)^2 = \beta^2 - n_3^2k^2 = \left(n_2^2 - n_3^2\right)k^2 - \kappa^2. \tag{5.35b}$$

Combining all of the new variables we have introduced, we may rewrite the dispersion relation (5.29) as

$$\kappa d - \tan^{-1}\left(\frac{\gamma_1}{\kappa}\right) - \tan^{-1}\left(\frac{\gamma_3}{\kappa}\right) = m\pi.$$

5.7.4 Solution for Asymmetric Guide

To solve the dispersion relation graphically, we first take the tangent of both sides of the dispersion equation to get

$$\tan(\kappa d - m\pi) = \tan\left[\tan^{-1}\left(\frac{\gamma_1}{\kappa}\right) + \tan^{-1}\left(\frac{\gamma_3}{\kappa}\right)\right].$$

We now apply the trigonometric identity

$$\tan(a \pm b) = \frac{\tan a \pm \tan b}{1 \mp \tan a \tan b}$$

to both sides of the equation, to give

$$\frac{\tan \kappa d - \tan m\pi}{1 + \tan \kappa d \tan m\pi} = \frac{\dfrac{\gamma_1}{\kappa} + \dfrac{\gamma_3}{\kappa}}{1 - \dfrac{\gamma_1 \gamma_3}{\kappa^2}},$$

and thus

$$\tan \kappa d = \frac{\kappa(\gamma_1 + \gamma_3)}{\kappa^2 - \gamma_1 \gamma_3}. \tag{5.36}$$

This is the mode equation for the TE waveguide modes and is the form of the dispersion relation usually encountered in the wave formalism of guided wave optics. We can solve this equation by plotting, in Figure 5.24, the functions $\tan \kappa d$ and

$$\mathrm{f}(\kappa d) = \frac{\kappa d(\gamma_1 d + \gamma_3 d)}{(\kappa d)^2 - (\gamma_1 d)(\gamma_3 d)}.$$

In Figure 5.24, the intersections of the $\mathrm{f}(\kappa d)$ curve with the various $\tan \kappa d$ curves are the solutions of (5.36). The value of κd at each intersection allows the calculation of the guided ray's incident angle for that mode:

$$\cos \theta_2 = \frac{(\kappa d)\lambda}{2\pi n_2 d}.$$

Table 5.1 lists the angle of incidence of a guided ray for the modes shown in Figure 5.24. It is important to note that the intersection of $\mathrm{f}(\kappa d)$ and $\tan \kappa d$ at the origin in Figure 5.24 is not a physically realizable solution.

The curve $\mathrm{f}(\kappa d)$ in Figure 5.24 does not extend without limit toward larger and larger values of κd, but rather has a maximum value of κd, its asymptote, beyond which one of the γ's becomes imaginary. From (5.35),

$$\gamma_1 \text{ becomes imaginary when } \left(n_2^2 - n_1^2\right)k^2 < \kappa^2,$$

$$\gamma_3 \text{ becomes imaginary when } \left(n_2^2 - n_3^2\right)k^2 < \kappa^2.$$

Our initial conditions assumed $n_3 > n_1$, so γ_3 will become imaginary first. The point of interest to us is when $\gamma_3 = 0$, i.e., just before γ_3 becomes imaginary. Physically, it is at this

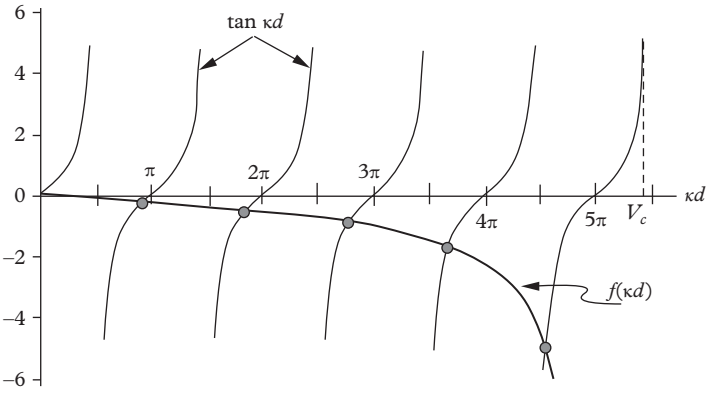

Figure 5.24 *The two sides of (5.37) are plotted as separate functions for $n_1 = 1.0$, $n_2 = 1.62$, and $n_3 = 1.515$ (the values for a sputtered glass waveguide), along with $d = 3$ μm and $\lambda = 0.63$ μm. The intersections of the curves are the solutions of (5.36). Table 5.1 lists the angle of incidence for the modes identified by the points of intersection. The cutoff value for the V-number is the asymptote of the $\mathrm{f}(\kappa d)$ curve.*

point that substrate modes are produced and the guided modes disappear. Remember that if $\gamma_3 = 0$, the evanescent wave extends infinitely far into the substrate because the penetration depth of the evanescent wave, $1/\gamma$, becomes infinite. At this point, θ_2 no longer meets the condition for total reflection at the boundary between media 2 and 3.

When $\gamma_3 = 0$,

$$\left(n_2^2 - n_3^2\right)k^2 = \kappa^2.$$

We take the square root and multiply both sides by the guide thickness:

$$kd\sqrt{n_2^2 - n_3^2} = \kappa d.$$

From (5.31),

$$V_c = \kappa d, \tag{5.37}$$

where V_c is the cutoff value of the normalized film thickness. For a given guide thickness d, there is a minimum wavelength that will propagate in the guide. This cutoff limit occurs for rays that have incident angles less than the critical angle.

By examining Figure 5.24, we see that not only is there a maximum κd beyond which f(κd) will not intersect tan κd, but also a minimum value of κd, namely, $\pi/2$, below which there are no solutions possible in an asymmetric waveguide, i.e., no guided mode can be supported. This means that the asymmetric guide can only support modes in a band of wavelengths established by $\pi/2 \leq \kappa d \leq V_c$. (The guide is said to act as a bandpass filter of frequency.)

5.7.5 Solution for Symmetric Guide

A symmetric guide will exhibit propagation characteristics that differ from those of an asymmetric guide. We rewriting (5.37) as

$$\tan V_c = \tan \kappa d = \frac{\gamma_1}{\kappa},$$

where we have used the fact that at cutoff, $\gamma_3 = 0$, and a propagating wave penetrates the interface. Using this relationship, we can obtain a new expression for the cutoff condition:

$$\tan V_c = \frac{\sqrt{\left(n_2^2 - n_1^2\right)k^2 - \kappa^2}}{\kappa} = \sqrt{\frac{n_3^2 - n_1^2}{n_2^2 - n_3^2}}. \tag{5.38}$$

Table 5.1 *Angle of incidence of a guided mode*

Mode	κd	q_2
0	0.9π	86.6°
1	1.8π	83.3°
3	3.7π	76.1°
4	4.55π	72.8°

This new expression for the cutoff condition leads to the conclusion that for a *symmetric guide*, where $n_1 = n_3$, there is no minimum value for κd, because V_c will equal zero. (The symmetric guide will act as a low-pass filter of frequency because there is a minimum propagating wavelength but no maximum wavelength, $0 \leq \kappa d \leq V_c$.) To understand this behavior, we will solve the dispersion equation for a symmetric guide.

Because the indices on either side of the guide are the same, (5.35a) and (5.35b) reduce to a single equation

$$\gamma^2 = \left(n_2^2 - n_3^2\right) k^2 - \kappa^2,$$

that is,

$$(\gamma d)^2 = V^2 - (\kappa d)^2, \tag{5.39a}$$

which is the equation of a circle. The dispersion relation for the symmetric guide is

$$\kappa d - m\pi = 2\tan^{-1}\left(\frac{\gamma d}{\kappa d}\right),$$

that is,

$$\gamma d = \kappa d \tan\left[\frac{1}{2}(\kappa d - m\pi)\right].$$

This dispersion relation can be expressed in two forms, depending on whether m is even or odd:

$$\gamma d = \begin{cases} \kappa d \tan\dfrac{\kappa d}{2}, & m \text{ even}, \\ -\kappa d \cot\dfrac{\kappa d}{2}, & m \text{ odd}. \end{cases} \tag{5.39b}$$

The TE modes are determined by simultaneous solution of (5.39a) and (5.39b). The graphical solutions for the even modes of a symmetric guide with properties similar to the asymmetric guide just discussed are shown in Figure 5.25. An intersection between (5.39a)

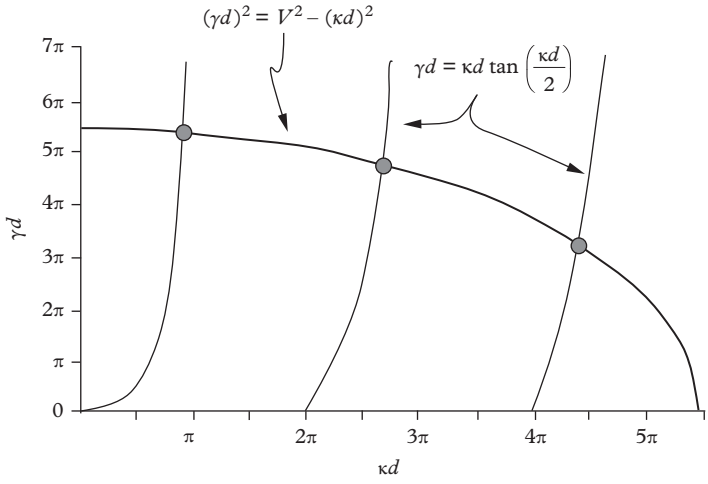

Figure 5.25 *The simultaneous solutions of (5.39a) and (5.39b) are plotted for $n_1 = n_3 = 1.515$ and $n_2 = 1.62$, along with $d = 3\ \mu m$ and $\lambda = 0.63\ \mu m$. The intersections of the curves are the solutions of (5.39a, b) for even modes. The lowest mode is never cut off for this symmetric guide.*

and (5.39b) at the origin is a physically realizable solution for a symmetric guide and results in a minimum κd of zero. It corresponds to $\theta_2 = \pi/2$, which is a ray propagating along the z-axis, parallel to the interfaces of the guide. The maximum κd, and thus the value of V_c, occurs at the value of κd where the circle intersects the abscissa.

5.7.6 Cutoff Condition

The term "cutoff"describes the inability of a waveguide to support a given propagation mode. The high-frequency cutoff value has been defined as $2V_c = \delta_1 + \delta_3$ based on the mathematical requirement that the mode number be a positive integer. The high-frequency cutoff condition has been given a more physical interpretation as the incident angle for which $\gamma_3 = 0$ and the evanescent field becomes a propagating field (since $n_3 > n_1$, γ_3 reaches zero before γ_1 and is thus the limiting parameter). When performing a graphical solution for the guided modes, we have found that an asymmetric guide of thickness d and with indices n_1, n_2, and n_3 has a low-frequency cutoff also. The asymmetric guide can only support guided waves for V-numbers larger than $\pi/2$. This means that an asymmetric guide cannot support guided modes for wavelengths

$$\lambda \geq 4d\sqrt{n_2^2 - n_3^2}.$$

In optical fibers, the propagation constants of the various TE modes are obtained by graphical solutions of equations involving Bessel functions rather than the tangent functions of (5.36); therefore, for fibers, the low-frequency cutoff condition is determined by the first zero of the Bessel function $\mathbf{J}_0(\kappa d)$, i.e., $2.405 \leq \kappa d \leq V_c$. In optical fibers, failure of total reflection is only one of the causes of cutoff [11].

The cutoff value of the V-number is given by (5.38). This relationship demonstrates that a symmetric guide has no maximum cutoff wavelength, as illustrated by the graphical solution for even modes of a symmetric guide. The physical origin of the existence of a low-frequency cutoff can be understood by considering the procedure used to analyze a waveguide through the use of Maxwell's equations.

To obtain wave solutions, we apply the boundary conditions introduced in Chapter 3 during the derivation of Fresnel's formula. In a symmetric guide, the boundary conditions in a plane normal to the guide interfaces would be the same at each interface. For an asymmetric guide, this would not be the case. For this reason, it is impossible for a plane wave to propagate through an asymmetric guide with its propagation vector parallel to the two interfaces. Such a wave can exist in a symmetric guide because the boundary conditions can be satisfied on the wavefront at both interfaces.

5.7.7 Coupling into Guided Wave Modes

Earlier, we mentioned that light could not be coupled into the guided modes of a waveguide by shining light onto the surface of the guide. We now have an understanding of guide modes, so we can examine the reasons behind the restriction on mode coupling. From the

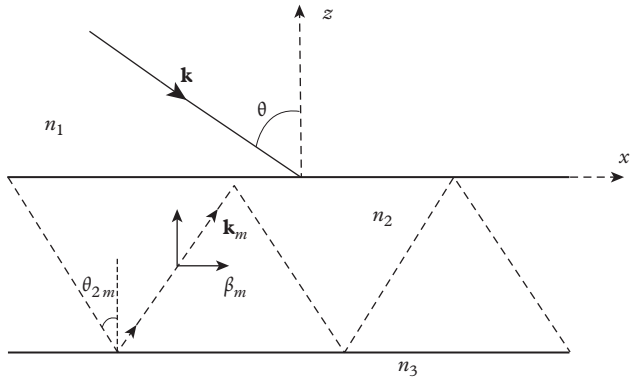

Figure 5.26 *Coupling geometry for radiation illuminating the wall of an optical guide.*

discussion of boundary conditions for Maxwell's equations in Chapter 3, we know that the tangential components of **E** and **H** must be continuous across a boundary. Using the geometry shown in Figure 5.26, we have the condition that

$$k_x = \frac{\omega}{c} n_1 \sin\theta \quad \text{must equal} \quad \beta_m = \frac{\omega}{c} n_2 \sin\theta_{2m}.$$

This can be viewed as a momentum conservation requirement. Snell's law allows us to relate the angle the illuminating wave makes on the guide surface, θ, to the angle that the guided mode makes with the boundary of the guide:

$$\sin\theta_{2m} = \frac{n_1}{n_2} \sin\theta < \frac{n_1}{n_2}.$$

The mode in the guide must meet the requirement for total reflection, $\theta_{2m} > \theta_c$, which implies that

$$\sin\theta_{2m} > \frac{n_1}{n_2}.$$

There is a conflict between the two conditions, making it impossible to couple energy into the guided mode!

5.7.7.1 Fiber Coupling

For fibers, end coupling is the most straightforward method to use. The telecommunication industry has developed a set of standard fiber couplers that allow easy changes in fiber connections to be made in the field. The most common connectors currently used are shown in Table 5.2. The fiber face is cleaved and polished after mounting in the coupler to provide a low-loss coupling between the fiber and an external optical component such as a lens or beam splitter. Typical insertion losses for each connector type are shown in Table 5.2.

Table 5.2 *Common fiber optic connectors*

Connector type	Image	Insertion loss (dB)	Characteristics
FC High-precision, ceramic ferrule connector equipped with an anti-rotation key	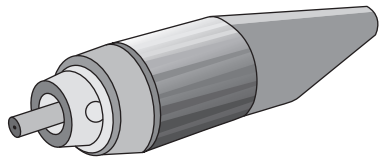	0.5–1.0	Prefered for single-mode fibers. Good mechanical isolation
ST Bayonet-style, keyed coupling mechanism, push and turn locking	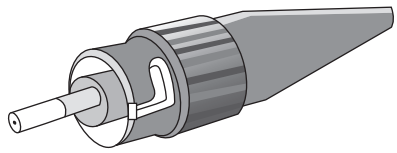	0.3	Good for field applications with multimode and single-mode fibers
SC Snap-in connector	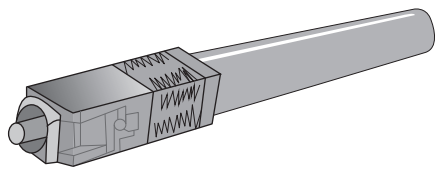	0.2–0.45	Push–pull design prevents fiber damage
LC Small-form-factor connector, half the size of the SC	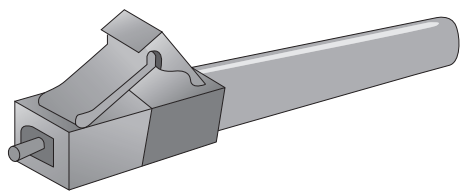	0.1–0.15	Very popular connector for single-mode fibers

5.7.7.2 Evanescent Wave Coupling

It is possible to couple to the guided mode by linking to the evanescent wave associated with the mode of the guide. Coupling is usually accomplished by placing two or more optical elements close together so that the evanescent field generated by one element overlaps the evanescent field associated with a propagating mode in the second element, thereby connecting (or coupling) the wave from one element to the next. The simplest technique applying this concept is prism coupling, where one optical element is a right-angle prism, with the incoming light wave totally reflecting from one of the prism's internal surfaces, and the second element is a planar waveguide (Figure 5.27).

To examine the prism coupling technique, we arrange for the light to strike a prism's base at an angle θ_p that would result in total reflection if the guide were not present. This means that the angle must exceed

$$\sin\theta_p > \frac{n_1}{n_p}.$$

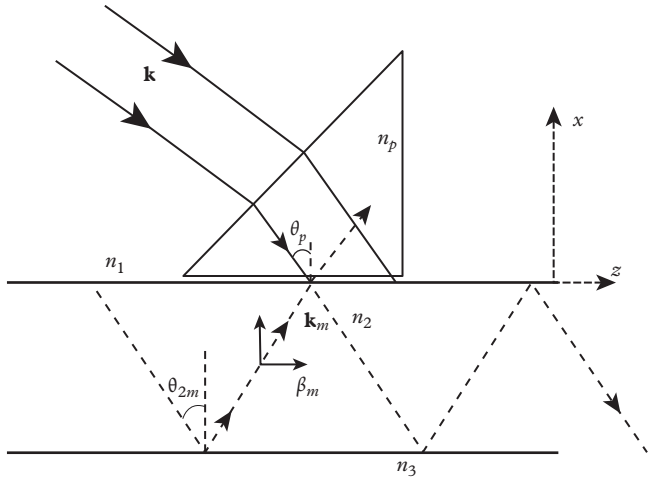

Figure 5.27 *Prism coupling into an optical guide.*

The z-component of the mth mode is given by

$$\beta_m = \frac{\omega}{c} n_2 \sin\theta_{2m}.$$

Using the requirement for total reflection, we find the lower limit on β:

$$\sin\theta_{2m} > \frac{n_1}{n_2}, \quad \text{which implies that} \quad \beta > \frac{\omega}{c} n_1.$$

We set the propagation constant in the prism, k_z, equal to β_m:

$$\beta_m = \frac{\omega}{c} n_p \sin\theta_p, \quad \text{implying that} \quad \frac{\omega}{c} n_p \sin\theta_p > \frac{\omega}{c} n_1.$$

We bring prism close to the guide to couple to the evanescent wave. All that is needed is for

$$\frac{n_2}{n_p} \sin\theta_{2m} = \sin\theta_p,$$

and so

$$\theta_{2m} > \theta_p,$$

which occurs when $n_p > n_2$: the prism can couple energy into the guide if its index is greater than the index of the guide.

5.8 Lagrangian Formulation of Optics

Because of the success of Fermat's principle in optics, the concept was extended to classical mechanics by Hamilton. The connection between geometrical optics and particle trajectories made by Hamilton brought him very close to the invention of quantum mechanics. He failed, however, to make the connection between wave optics and mechanics. Failure to make this connection should not be criticized—there were no experiments to suggest the need for such a connection.

5.8.1 Hamilton's Principle

The mathematical expression in classical mechanics equivalent to Fermat's principle is called *Hamilton's principle*. It states that the trajectory of a particle between times t_1 and t_2 is such that

$$\delta \int_{t_1}^{t_2} (T - V)\, dt = 0, \tag{5.40}$$

where T is the kinetic energy and V the potential energy of the particle, and the symbol δ indicates that the variation must be taken. The energy quantity

$$\mathcal{L} = T - V$$

is called the *Lagrangian* in classical mechanics.

If the forces acting on the particle are conservative, i.e., if the total energy $T + V$ is a constant during the motion, then Hamilton's principle leads to the equations of motion of the particle being of the form

$$\frac{d}{dt}\left(\frac{\partial \mathcal{L}}{\partial \dot{q}_k}\right) = \frac{\partial \mathcal{L}}{\partial q_k}. \tag{5.41}$$

This is called the Lagrangian equation; the q's are called generalized coordinates. In rectangular coordinates, $q_k \to (q_1, q_2, q_3) \to (x, y, z)$. For a simple pendulum, we would formulate the problem so that $q_k \to q_1 \to \theta$, where θ is the angle the pendulum makes with the vertical. In our shorthand notation,

$$\dot{q} = \frac{\partial q}{\partial t},$$

and

$$\frac{\partial \mathcal{L}}{\partial \dot{q}}$$

is a generalized momentum. For example, if $V = 0$, then

$$\mathcal{L} = \frac{mv^2}{2} = \frac{m\dot{x}^2}{2}$$

and

$$\frac{\partial \mathcal{L}}{\partial \dot{x}} = m\dot{x}.$$

Hamilton placed optics and classical mechanics into a common mathematical formalism. We will use that formalism to derive the equation of motion for a light ray and then use that equation to derive rectilinear propagation and the law of refraction.

In optics, we can write the path length of a ray as

$$ds = \sqrt{(dx)^2 + (dy)^2 + (dz)^2}$$

$$= dz\sqrt{1 + \left(\frac{dx}{dz}\right)^2 + \left(\frac{dy}{dz}\right)^2}.$$

Fermat's principle can be rewritten

$$\delta \int n\, ds = \delta \int n(x,y,z)\sqrt{1+\left(\frac{dx}{dz}\right)^2+\left(\frac{dy}{dz}\right)^2}\, dz = 0. \tag{5.42}$$

Comparing this with Hamilton's principle, we can define an optical Lagrangian

$$\mathcal{L} = n(x,y,z)\sqrt{1+\left(\frac{dx}{dz}\right)^2+\left(\frac{dy}{dz}\right)^2}, \tag{5.43}$$

where we are allowing z to play the same role in optics as time t does in classical mechanics.

The optical equations of motion are

$$\frac{d}{dz}\left(\frac{\partial \mathcal{L}}{\partial x'}\right) = \frac{\partial \mathcal{L}}{\partial x}, \qquad \frac{d}{dz}\left(\frac{\partial \mathcal{L}}{\partial y'}\right) = \frac{\partial \mathcal{L}}{\partial y}, \tag{5.44}$$

where

$$x' = \frac{dx}{dz} \qquad \text{and} \qquad y' = \frac{dy}{dz}.$$

We can substitute (5.43) into (5.44) to get the functional form of the optical equation of motion. For the x-component, where we assume that n is independent of x',

$$\frac{\partial \mathcal{L}}{\partial x'} = \frac{nx'}{\sqrt{1+x'^2+y'^2}}, \qquad \frac{\partial \mathcal{L}}{\partial x} = \sqrt{1+x'^2+y'^2}\,\frac{\partial n}{\partial x}.$$

The x-component of the equation of motion is thus

$$\frac{d}{dz}\left(\frac{nx'}{\sqrt{1+x'^2+y'^2}}\right) = \sqrt{1+x'^2+y'^2}\,\frac{\partial n}{\partial x}.$$

We may use the identity

$$\frac{d}{ds} = \frac{1}{\sqrt{1+x'^2+y'^2}}\,\frac{d}{dz}$$

to rewrite the equation of motion as

$$\frac{d}{ds}\left(n\frac{dx}{ds}\right) = \frac{\partial n}{\partial x}.$$

If we carry out the same procedure for the y- and z-components, we obtain the vector equation

$$\frac{d}{ds}\left(n\frac{d\mathbf{r}}{ds}\right) = \nabla n(x,y,z). \tag{5.45}$$

This is called the *ray equation*; the vector $\mathbf{r}$ represents the position of any point on the ray. The derivative $d\mathbf{r}/ds$ is the unit vector along the tangent to the ray; the ray need not be rectilinear.

5.8.2 Rectilinear Propagation

A very simple application of the ray equation (5.45) is to the calculation of the light trajectory in a homogeneous medium where the index of refraction is independent of position, $\nabla n = 0$:

$$\frac{d^2\mathbf{r}}{ds^2} = 0.$$

The solution of this equation is

$$\mathbf{r} = \mathbf{a}s + \mathbf{b},$$

which is the equation of a straight line. Thus, in a homogeneous medium, light rays travel in straight lines.

5.8.3 Law of Refraction

We can derive the law of refraction using the ray equation by assuming that the index of refraction is only a function of the x-coordinate, as shown in Figure 5.28. In the shaded region, the index changes in some unknown manner in the x-direction from n_1 to n_2, but there is no index variation in the z-direction. The z-component of the ray equation is, by analogy with (5.45),

$$\frac{d}{ds}\left(n\frac{dz}{ds}\right) = \frac{\partial n}{\partial z} = 0. \tag{5.46}$$

Integrating, we find

$$n\frac{dz}{ds} = \text{constant}.$$

From the geometry of Figure 5.28, we see that $dz/ds = \sin\theta$ (remember that ds is measured along the ray path), which leads to

$$n\sin\theta = \text{constant}. \tag{5.47}$$

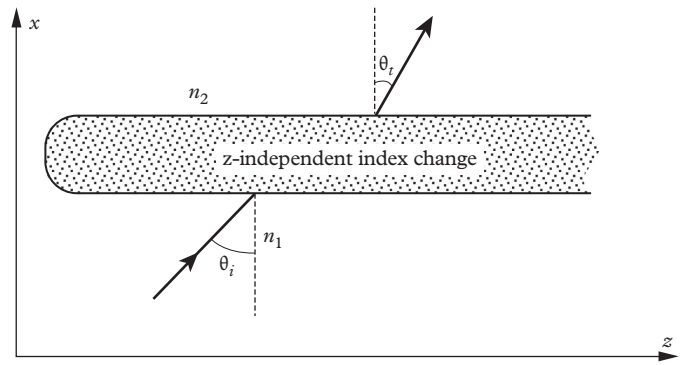

Figure 5.28 *Refraction by a boundary between two media with different indices of refraction.*

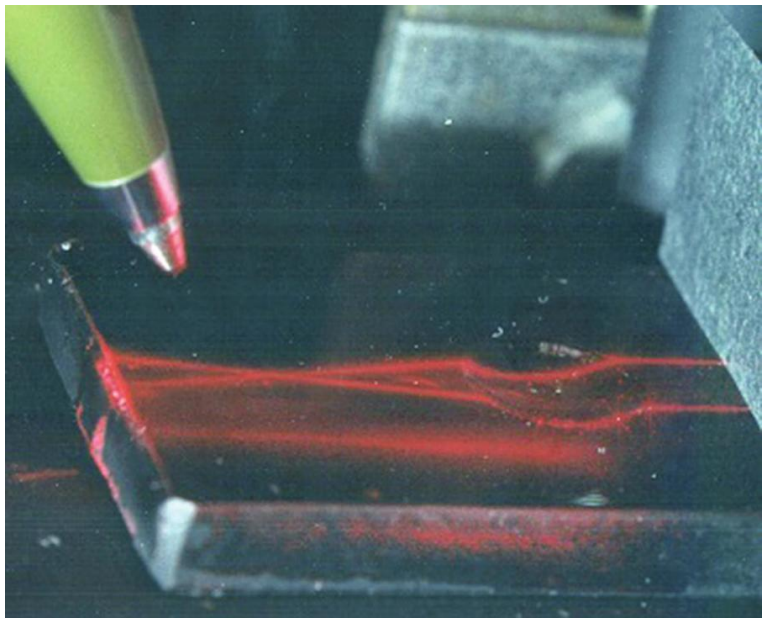

Figure 5.29 *A guided wave lens has been formed in a guiding layer. Two narrow beams of light from a HeNe laser propagate through the lens and are focused by the lens. In a "good" guiding structure, the two beams could not be seen. The guide shown here was intentionally created with a large amount of scattering to allow the photograph to be made. (Courtesy of Carl Verber.)*

Thus by assuming only that the index of refraction does not vary in the z-direction, we have obtained the law of refraction:

$$n_1 \sin\theta_i = n_2 \sin\theta_t.$$

An application of this result is seen in Figure 5.29, where a lens has been created in a guided wave structure. It was not necessary to control the detailed way the index changed—only that an index change occurred.

5.9 Propagation in a Graded-Index Optical Fiber

Generally, the ray equation (5.45) is difficult to solve. To reduce the complexity of the problem, the assumption is made that the light rays propagate in the general direction of the z-axis and those that travel at an angle to the z-axis depart by only small angles. This is another statement of the paraxial ray approximation and allows us to write $ds \approx dz$ (equivalent to the approximation $\sin\theta \approx \tan\theta$). This approximation results in the paraxial ray equation

$$\frac{d}{dz}\left(n\frac{d\mathbf{r}}{dz}\right) = \nabla n. \tag{5.48}$$

We will apply the paraxial approximation to evaluate the problem of an optical fiber whose index of refraction varies in the direction normal to, but not along, the axis of the fiber, i.e., the z-axis. Before applying the paraxial approximation, we will rewrite the general ray equation in cylindrical coordinates. While we could use rectangular coordinates in

this problem, it seems more appropriate to use cylindrical polar coordinates, which are the symmetry coordinates of the fiber. The z-axis of the coordinate system is aligned along the cylindrical axis of the fiber, and the cylindrical coordinates are related to the rectangular coordinates through the equations

$$\begin{aligned} r &= \sqrt{x^2 + y^2}, \\ \phi &= \tan^{-1}\frac{y}{x}, \\ z &= z. \end{aligned}$$

We must rewrite the partial derivatives, in x and y, of n in terms of the cylindrical coordinates:

$$\begin{aligned} \frac{\partial n}{\partial x} &= \frac{\partial n}{\partial r}\frac{\partial r}{\partial x} + \frac{\partial n}{\partial \phi}\frac{\partial \phi}{\partial x}, \\ &= \frac{\partial n}{\partial r}\cos\phi - \frac{\partial n}{\partial \phi}\frac{\sin\phi}{r}, \\ \frac{\partial n}{\partial y} &= \frac{\partial n}{\partial r}\frac{\partial r}{\partial y} + \frac{\partial n}{\partial \phi}\frac{\partial \phi}{\partial y}, \\ &= \frac{\partial n}{\partial r}\sin\phi + \frac{\partial n}{\partial \phi}\frac{\cos\phi}{r}. \end{aligned}$$

The derivatives of x and y with respect to s are

$$\begin{aligned} \frac{dx}{ds} &= \frac{dr}{ds}\cos\phi - r\frac{d\phi}{ds}\sin\phi, \\ \frac{dy}{ds} &= \frac{dr}{ds}\sin\phi + r\frac{d\phi}{ds}\cos\phi. \end{aligned}$$

With these newly formulated derivatives, we can multiply the x-component of the ray equation by x and the y-component by y, and then add, to generate the r-component of the ray equation:

$$\frac{d}{ds}\left(n\frac{dr}{ds}\right) - nr\left(\frac{d\phi}{ds}\right)^2 = \frac{\partial n}{\partial r}. \tag{5.49}$$

If we multiply the x-component of the ray equation by $-y$ and the y-component by x, and then add, we generate the ϕ-component of the ray equation:

$$\frac{d}{ds}\left(nr^2\frac{d\phi}{ds}\right) = \frac{\partial n}{\partial \phi}. \tag{5.50}$$

The z-component of the ray equation is

$$\frac{d}{ds}\left(n\frac{dz}{ds}\right) = 0.$$

Because the index of refraction is independent of the z-coordinate, we do not need to make the paraxial approximation to solve this equation; we need only perform the integration. After integration, we get a result analogous to (5.47):

$$n\frac{dz}{ds} = n\sin\theta = \frac{\beta}{k} = \text{constant}. \tag{5.51}$$

Not only is the index of refraction in this fiber independent of z, but it is also independent of ϕ, so that

$$\begin{aligned} \frac{d}{ds}\left(nr^2\frac{d\phi}{ds}\right) &= 0, \\ nr^2\frac{d\phi}{ds} &= \text{constant} = K_1. \end{aligned} \tag{5.52}$$

To proceed farther we must use the paraxial approximation. To apply the paraxial approximation, we must replace ds by dz in (5.49) and (5.52). The paraxial approximation requires that the variation of $n(r,\phi)$ with r be small, allowing us to replace $n(r,\phi)$ by a spatial average of the guide's index, $n_2 \approx \langle\langle n(r,\phi)\rangle\rangle$, where $\langle\langle \ldots \rangle\rangle$ denotes the spatial average. Using the spatial average, the ray equations become

$$\frac{d^2r}{dz^2} - r\left(\frac{d\phi}{dz}\right)^2 = \frac{1}{n_2}\frac{\partial n}{\partial r}, \tag{5.53}$$

$$r^2\frac{d\phi}{dz} = \frac{K_1}{n_2}. \tag{5.54}$$

We cannot obtain an exact solution for arbitrary refractive index profiles, so we will assume a parabolic-shaped profile (see Figure 5.30)

$$n(r) = n_2\left[1 - \left(\frac{r}{a}\right)^2\Delta\right], \qquad r < a, \tag{5.55}$$

where we have introduced the quantity Δ, which is defined as

$$\Delta = \frac{n_2^2 - n_1^2}{2n_2^2}.$$

In practice, the index of the cladding is almost the same as that of the core, resulting in an approximation for Δ of

$$\Delta = \frac{(n_2 - n_1)(n_2 + n_1)}{2n_2^2} \approx \frac{n_2 - n_1}{n_2}.$$

Equation (5.55) describes the variation in the index of refraction illustrated in Figure 5.30. The core of the fiber has an index of refraction that varies from n_2 to n_1 along the radius of the fiber from the center outward. At the boundary between the core and the cladding, the index of refraction is n_1 and remains constant throughout the cladding, as shown in Figure 5.30. The assumption that n_1 is constant throughout the cladding is not important for this problem because, as we will learn, the guided rays do not travel in the region $r > a$, and we can ignore completely any index variation in this region.

The derivative of the index along the fiber radius is

$$\frac{\partial n}{\partial r} = -2n_2\Delta\frac{r}{a^2}.$$

We can substitute this derivative into (5.53) along with (5.54), where we introduce a new constant $K_2 = K_1^2/n_2^2$ for brevity:

$$\frac{d^2r}{dz^2} - \frac{K_2^2}{r^3} = -\frac{2r\Delta}{a^2}. \tag{5.56}$$

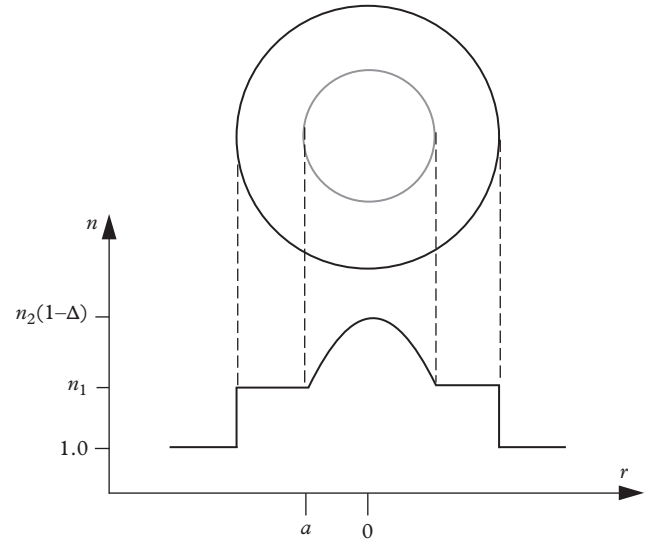

Figure 5.30 *Profile of the index of refraction in a graded-index optical fiber with a parabolic variation of the index with radius.*

The objective is to find a solution to (5.56) that will provide an equation for the ray's coordinates (r, ϕ) as a function of position z along the fiber. If we multiply both sides of (5.56) by dr/dz, we create the derivative

$$\frac{d}{dz}\left[\frac{1}{2}\left(\frac{dr}{dz}\right)^2 + \frac{r^2\Delta}{a^2} + \frac{K_2}{2r^2}\right] = 0.$$

This can be integrated to give

$$\frac{1}{2}\left(\frac{dr}{dz}\right)^2 + \frac{r^2\Delta}{a^2} + \frac{K_2}{2r^2} = K_3.$$

We may integrate a second time to get

$$z - Z_0 = \frac{a}{2\sqrt{2\Delta}} \sin^{-1}\left[\frac{4\Delta\left(\frac{r}{a}\right)^2 - 2K_3}{\sqrt{4K_3^2 - 8\Delta\left(\frac{K_2}{a^2}\right)}}\right], \tag{5.57}$$

where Z_0 is yet another constant of integration whose value is determined by the origin of the coordinate system.

This is the solution we sought, but its form is difficult to interpret. We can simplify the expression and make it easier to understand the physical significance of the result by introducing the variables

$$\Omega = \frac{\sqrt{2\Delta}}{a}, \qquad b^2 = K_2\left(\frac{\Omega}{K_3}\right)^2, \qquad A = \frac{\sqrt{K_3}}{\Omega}.$$

The r-coordinate of the ray's trajectory is

$$r(z) = A\sqrt{1 + \sqrt{1-b^2}\sin[2\Omega(z - Z_0)]}. \tag{5.58}$$

The ray's r-coordinate is shown by (5.49) to be a periodic function of the distance along the cylindrical axis of the fiber, oscillating between a maximum and a minimum value as we move along the z axis:

$$A\sqrt{1-\sqrt{1-b^2}} < r < A\sqrt{1+\sqrt{1-b^2}}\,. \tag{5.59}$$

Thus, the ray moves through the fiber constrained between the two extremes defined by (5.59). These extremes are called the *classical turning points* of the ray.

Figure 5.31 shows the propagation of a general ray in the core of a graded-index fiber. The radii r_1 and r_2 denote the locations of the maximum and minimum values in (5.59). By substituting (5.58) into (5.54) and integrating, we find the angular coordinate of the ray's trajectory to be

$$\phi = \phi_0 + \tan^{-1}\left\{\frac{\sqrt{1-b^2} + \tan[\Omega(z - Z_0)]}{b}\right\}. \tag{5.60}$$

To understand the trajectories of the rays as they move between the turning points, we will evaluate two limiting cases. The first occurs when we set the first integration constant from (5.54) equal to zero, i.e., $K_1 = 0$. This is equivalent to assuming that the azimuth angle ϕ is a constant and the ray is confined to a plane. Whenever $K_1 = 0$, we have $b = 0$, allowing the use of (5.60) to demonstrate that the azimuth angle is a constant,

$$\phi = \phi_0 + \frac{1}{2}\pi.$$

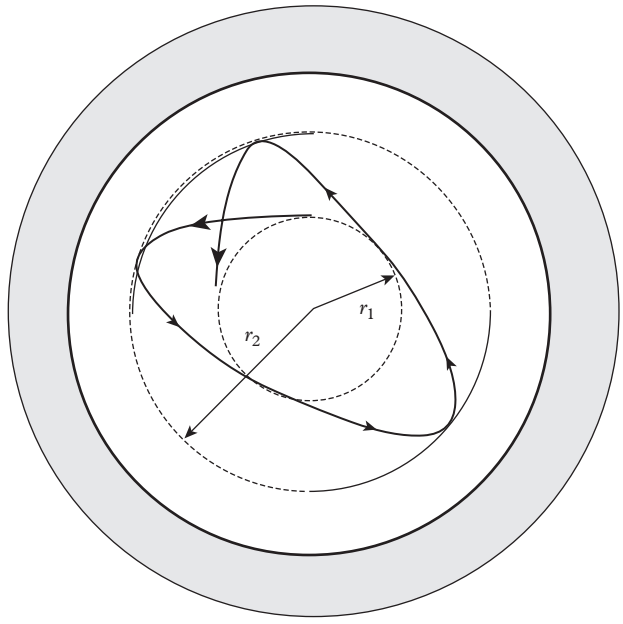

Figure 5.31 *Ray projection showing the path of a general ray in the core of a graded-index fiber. The path is contained between the classical turning points. The cladding is denoted by the shaded region.*

The inequality in (5.59) becomes

$$0 < r < a\sqrt{\frac{K_3}{\Delta}},$$

and the equation for $r(z)$, (5.58), becomes

$$r(z) = A\sqrt{\cos^2[\Omega(z-Z_0)] + \sin^2[\Omega(z-Z_0)] + 2\sin[\Omega(z-Z_0)]\cos[\Omega(z-Z_0)]},$$

$$= A\sqrt{2}\sin\left[\Omega(z-Z_0) + \frac{1}{4}\pi\right].$$

The ray is a meridional ray, confined to the meridional plane defined by ϕ. The ray moves in a sinusoidal trajectory, periodically crossing the symmetry axis (the z-axis) with a period of

$$\frac{1}{\Omega} = \frac{a}{\sqrt{\Delta}}.$$

Several trajectories of this type, each corresponding to a different mode, are shown in Figure 5.32(a). A small beam of light is shown propagating along a graded-index guide in Figure 5.32(b), demonstrating the sinusodial propagation path predicted by our result.

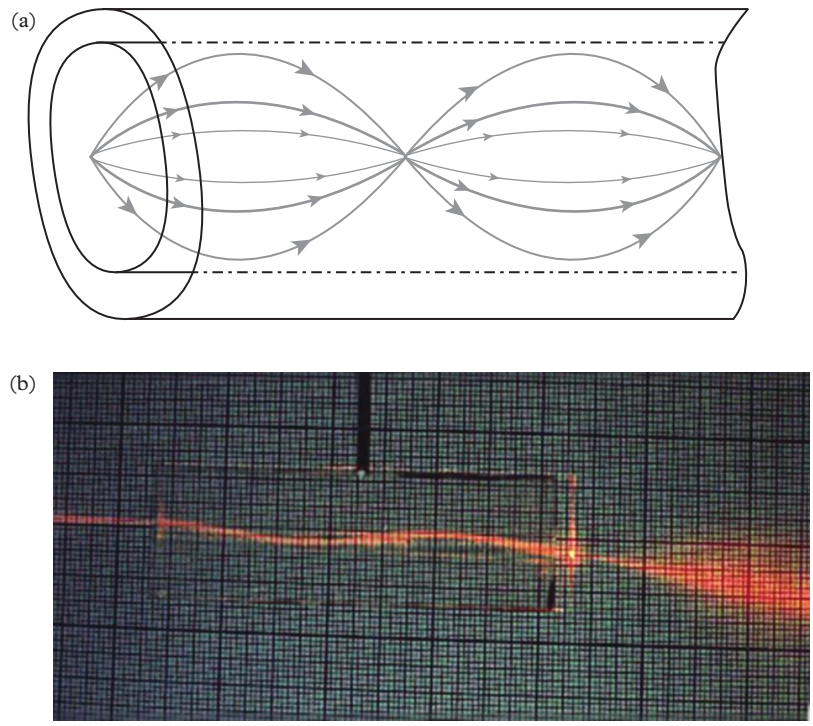

Figure 5.32 *(a) Meridional rays propagating in a graded-index fiber with a parabolic index profile. (b) Beam of light propagating along a graded-index guide. (Courtesy David Hamblen.)*

The graded-index guide shown in Figure 5.32(b) can be described by an *ABCD* matrix. To generate the *ABCD* matrix, it is better to return to (5.56), which is modified by the assumption that $K_1 = 0$ to read

$$\frac{d^2r}{dz^2} + \frac{2r\Delta}{a^2} = 0.$$

The solution of this differential equation is

$$r(z) = \frac{\gamma_0}{\Omega} \sin \Omega z + r_0 \cos \Omega z.$$

We have assumed that the fiber has its entrance face at $Z_0 = 0$ and that at that position the ray's parameters are r_0 and γ_0, where we have defined the ray's angle by

$$\gamma = \frac{dr}{dz}.$$

The *ABCD* matrix for the fiber is

$$\begin{bmatrix} \sin \Omega z & \frac{1}{\Omega} \cos \Omega z \\ -\Omega \cos \Omega z & \sin \Omega z \end{bmatrix}.$$

By adjusting the length of this type of fiber, we can construct what is called a SELFOC lens and use the fiber to focus, collimate, or image the meridional rays as shown in Figure 5.33.

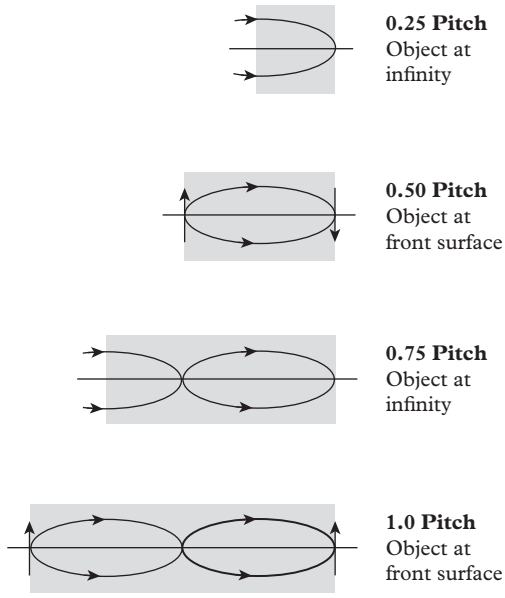

Figure 5.33 *Gradient index (GRIN) lenses. Commercially available lenses of this type are called SELFOC lenses [12]. (Image courtesy of Go!Foton, an exclusive licensee of SELFOC, SELFOC is a registered trademark of NSG Group.)*

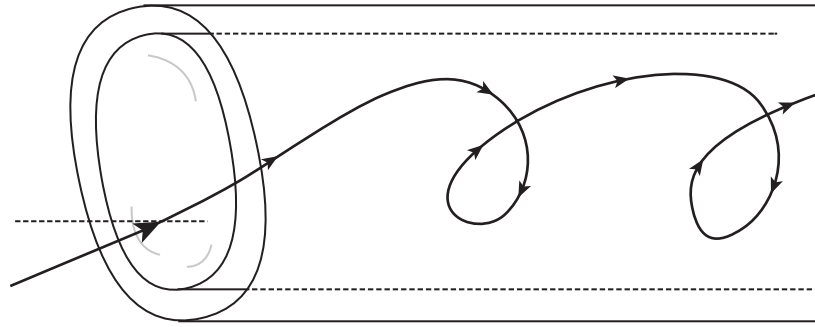

Figure 5.34 *Propagation of a skew ray in a graded-index fiber.*

A second limiting case occurs when $b = 1$. In this case, r is a constant, equal to

$$a\sqrt{\frac{K_3}{2\Delta}},$$

and the azimuth angle is a linear function of the z-coordinate:

$$\phi(z) = \phi_0 + \Omega(z - Z_0).$$

These are called helical rays, because they travel on a helical path about the z-axis a fixed distance A from the axis. A typical helical ray is shown in Figure 5.34.

A general ray has a trajectory that falls between these two limiting cases.

It is possible to attack the problem of a wave propagating in a fiber by using the same mathematical method used to treat an electron in a potential well. In quantum mechanics, we solve the Schrödinger equation of an electron:

$$\frac{d^2\Psi}{dx^2} + \frac{2m}{\hbar}(E - V)\Psi = 0.$$

In optics, we want to solve the Helmholtz equation of a wave:

$$\left(\nabla^2 + k^2 n_2^2\right)E = 0.$$

In a dielectric slab, where the index in the guide is uniform and

$$\frac{\partial^2 E}{\partial y^2} = 0, \qquad \frac{\partial^2 E}{\partial z^2} = -\beta^2 E,$$

the Helmholtz equation becomes

$$\frac{d^2E}{dx^2} + \left[\left(k^2 n_1^2 - \beta^2\right) - \left(k^2 n_1^2 - k^2 n_2^2\right)\right]E = 0.$$

The Schrödinger and Helmholtz equations have the same mathematical form. In quantum mechanics, we use the WKB (Wentzel–Kramers–Brillouin) method to solve the Schrödinger equation in the classical limit where the change of potential energy within the particle's wavelength (a de Broglie wavelength) is small compared with the kinetic energy [13]. In optics,we apply the same WKB method [14] to solve the Helmholtz equation in the geometrical optics limit when the index of refraction changes slowly over the distance of a wavelength.

The result of the application of the WKB method is a dispersion equation of the form

$$\int_0^{r_t} \sqrt{n^2(r)k_0^2 - \beta^2}\, dr = \delta_1 + \delta_3 + m\pi,$$

where $n(r)$ is the refractive index profile, which might have the form (5.55). The turning point r_t is the upper limit of the integration and is found by solving the equation

$$n_2^2(r)k_0^2 - \beta^2 = 0.$$

The dispersion equation can be used to perform an analysis, similar to the one carried out for planar guides, to determine the cutoff condition and an estimate of the number of modes in a fiber.

5.10 Summary

With the objective of demonstrating that geometrical optics is a special case of the wave theory, the wavelength was allowed to approach zero and the solution of the Helmholtz equation was evaluated. The solution was found to predict the motion of the normal to the phasefront of a wave. Geometrical optics was found to treat a light wave at a point as if it were a plane wave and to obtain the wave's propagation path by following the path of the normal to the plane at that point. No application of this result was made, but it was pointed out that the result led mathematically to a statement of Fermat's principle.

> *The time it takes a light ray to travel an optical path between any two points is a minimum; i.e., the optical path of a light ray between any two points is equal to the optical length of any other curve that joins these points and lies in a neighborhood of the proper path.*

The optical path length was defined as the distance light would travel in a vacuum during the time it traveled a distance ℓ in a medium with index n. Thus, the optical path length is

$$\Delta = n\ell.$$

Fermat's principle was used to derive the principle of reciprocity, the law of refraction and the law of reflection.

The law of refraction and the concept of rectilinear propagation were used to generate a matrix describing the propagation of light through an optical element. The resulting matrix equation is of the form

$$\begin{bmatrix} x' \\ \gamma' \end{bmatrix} = \begin{bmatrix} A & B \\ C & D \end{bmatrix} \begin{bmatrix} x \\ \gamma \end{bmatrix},$$

where x is the height above the optical axis of the ray upon entering the optical system and γ is the angle the ray makes with the optical axis. The primes denote the same parameters upon leaving the optical system.

The *ABCD* matrix was derived after making the paraxial approximation. This approximation assumes that the first terms of the expansions of the trigonometric functions are all that are needed to represent the functions, for example, $\sin\theta \approx \theta$.

Refraction at a spherical surface with radius of curvature R_1 separating two media with indices of refraction n_1 and n_2 was shown to be described by the matrix

$$\mathbf{R}_1 = \begin{bmatrix} 1 & 0 \\ \dfrac{n_1 - n_2}{n_2 R_1} & \dfrac{n_1}{n_2} \end{bmatrix}. \tag{5.61}$$

Propagation through a medium with index of refraction n_2 is described by the matrix

$$\mathbf{T} = \begin{bmatrix} 1 & d \\ 0 & 1 \end{bmatrix},$$

where d is the path length traveled by a ray in the medium.

The elements of the *ABCD* matrix for a complete lens was found by combining the refraction and transfer matrices.

$$A = 1 + \frac{d(n_1 - n_2)}{n_2 R_1}, \qquad B = \frac{dn_1}{n_2},$$

$$C = \frac{1}{n_3}\left[\frac{n_2 - n_3}{R_2} + \frac{n_1 - n_2}{R_1} + \frac{d(n_1 - n_2)(n_2 - n_3)}{n_2 R_1 R_2}\right], \qquad D = \frac{n_1}{n_3}\left[1 + \frac{d(n_2 - n_3)}{n_2 R_2}\right].$$

The relationships between these matrix elements and other more familiar representations of geometrical optics are obtained in Appendix 5A. In this chapter, the *ABCD* matrix was used to find the stability condition for a Fabry–Perot resonator. The stability condition establishes the requirements upon the mirror curvature R and separation d that result in the trapping of a light ray in a Fabry–Perot cavity. The result of the analysis was a stability condition of the form

$$0 \le \left(1 - \frac{d}{2f_1}\right)\left(1 - \frac{d}{2f_2}\right) \le 1,$$

where $f = R/2$ is the focal length of a mirror with spherical curvature R.

Geometrical optics was also used to determine some of the properties of guided waves. It was learned that light could be coupled into the end of an optical waveguide, but that there was a maximum acceptance angle for the light given by

$$\mathrm{NA} = \sqrt{n_2^2 - n_1^2}\,.$$

Rays, guided by the waveguide, propagate by undergoing total reflection. The angles of reflection can only assume discrete values determined by a dispersion equation. Several expressions for the dispersion equation were derived. The first,

$$2n_2 kd\cos\theta_2 + \delta_1 + \delta_3 = m \cdot 2\pi,$$

was derived by assuming that the ray was associated with an infinite plane wave whose phase front propagated through the guide without distortion. The second representation,

$$\tan\kappa d = \frac{\kappa(\gamma_1 + \gamma_3)}{\kappa^2 - \gamma_1\gamma_3},$$

was constructed by anticipating the results that would have been obtained if a wave analysis had been carried out.

The V-number of a waveguide was defined as

$$V = kd\sqrt{n_2^2 - n_3^2}.$$

The definition of the V-number can be used to determine the values of the physical parameters when cutoff occurs. The V-number also provides information about the maximum number of modes that can propagate in a guide.

5.11 Problems

5.1. What length plane mirror must you purchase for you to see your full height when it is mounted in a vertical position? Do not assume that you have eyes on the top of your head!

5.2. Prove that the reflected ray from a plane mirror turns through an angle 2θ when the mirror rotates through θ.

5.3. Consider a series of plane interfaces, all parallel. At the first, the index changes from n_0 to n_1; at the second from n_1 to n_2; at the mth from n_{m-1} to n_m, etc. If θ_m is the angle of refraction and θ_{m-1} is the angle of incidence at the mth interface, show that

$$n_0 \sin\theta_0 = n_m \sin\theta_m.$$

5.4. A fish appears to be 2 m below the surface of a pond ($n = 1.33$). What is its actual depth?

5.5. A collimated laser beam shines on a tank of water. Part reflects off the surface (beam A) and part reflects off the bottom and exits the water (beam B), as shown in Figure 5.35. Show that beams A and B are parallel.

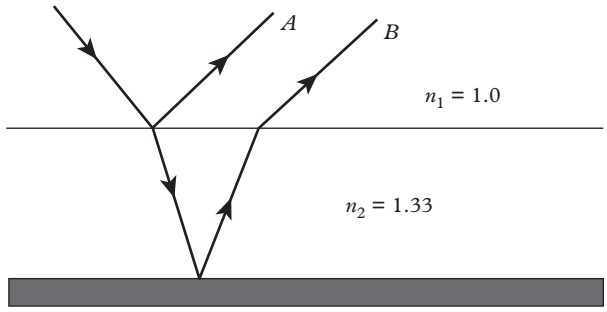

Figure 5.35 *Prove that beams A and B are parallel.*

5.6. The SELFOC fiber has a graded index of refraction given by

$$n^2(x, y, z) = n_0^2\left[1 - \alpha^2\left(x^2 + y^2\right)\right],$$

where n_0 and α are material constants. Find the path of a ray in the fiber without assuming a paraxial ray.

5.7. To analyze a Fabry–Perot cavity with mirrors of radii R_1 and R_2, we can replace the mirror with a set of lenses of focal lengths $f_1 = R_1/2$ and $f_2 = R_2/2$, alternately spaced by the cavity length. Rederive the *ABCD* matrix for this lens system. What effect does this *ABCD* matrix have on the stability condition (5.23)?

5.8. Assume that we have a step-index fiber with $n_2 = 1.6$ and $n_1 = 1.46$. Considering only meridional rays, what is the smallest value that the angle of incidence in the fiber, θ_2, can have? What is the numerical aperture when $d = 0.6\ \mu\text{m}$ and $\lambda = 1\ \mu\text{m}$?

5.9. Using the parameters in Problem 5.8, how many modes can propagate in the fiber? What happens if we increase d to 3 μm? If we increase λ to 1.3 μm?

5.10. What is the maximum radius that the fiber in Problem 5.8 can have if single-mode operation is desired?

5.11. Calculate the phase shifts, introduced on total reflection inside a plane guide, with $n_2 = 1.53$, $n_3 = 1.5$, and $n_1 = 1.0$. Assume that the angle of incidence $\theta_2 = 85°$.

5.12. Calculate the object–image matrix (see Appendix 5A) for the lens system shown in Figure 5.36, where the lens on the left has a focal length f_1 and the one on the right has a focal length$_2$. Prove that conjugate planes occur for $s = -f_1$ and $s' = f_2$. This latter matrix is sometimes called the focal plane matrix.

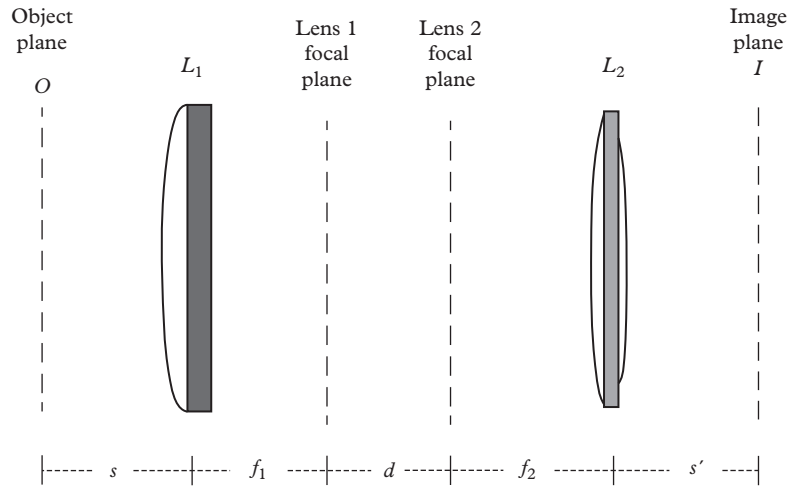

Figure 5.36 *General two-lens optical system.*

5.13. (a) Using the object–image matrix from Problem 5.12, calculate the positions of the cardinal points when $s = -f_1$ and $s' = f_2$. (b) What is the effective focal length of this optical system if the two lenses are in contact with each other?

5.14. Using the results of Problem 5.13, assume $f_1 = 2f_2$ and sketch the optical system, including the positions of the principal planes: (a) for a Huygens eyepiece,with $d = -1.5f_2$; (b) for an astronomical telescope, with $d = 0$; (c) for a compound microscope, with $d = 2f_2$. The condition $d < 0$ occurs when the distance between the two lenses is less than $f_1 + f_2$.

5.15. Using the results of Problem 5.12, assume $f_1 = -2f_2$ and sketch the optical system, including the positions of the principal planes: (a) for a Galilean telescope, with $d = 0$; (b) for a telephoto lens, with $d = -0.5f_2$.

5.16. Trace a ray through the prism shown in Figure 5.37. The angle between the initial and final rays is called the *angle of deviation*, denoted by δ in Figure 5.37. Derive an equation for the angle of deviation in terms of the apex angle α in Figure 5.37. Assume that the prism has an index of refraction n_2 and is in a medium of index n_1. What is the minimum angle of deviation? Prove that the angle of minimum deviation occurs when $\theta_i = \theta_e$.

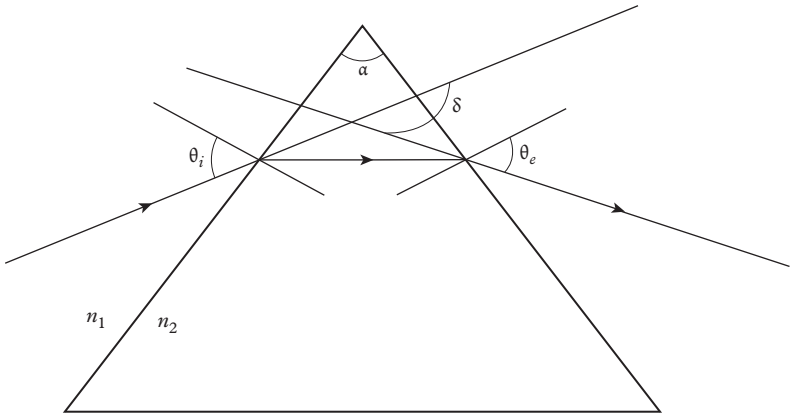

Figure 5.37 *Prism with apex angle equal to* α.

5.17. Represent the electric and magnetic fields of a light wave by

$$\tilde{\mathbf{E}} = E_0 e^{ik_0 \mathcal{S}}, \qquad \tilde{\mathbf{B}} = B_0 e^{ik_0 \mathcal{S}},$$

where $\mathcal{S}$ is the eikonal. Prove that the Poynting vector is proportional to $\nabla \mathcal{S}$.

5.18. Assume that a plane wave in incident normal to the polished end of a step-index fiber, shown in Figure 5.38. Derive an equation for the minimum radius to which a fiber can be bent before light is lost from the guided mode. Assume that the index of the core is 1.66 and the index of the cladding is 1.52. Using the equation just derived, what is the minimum radius?

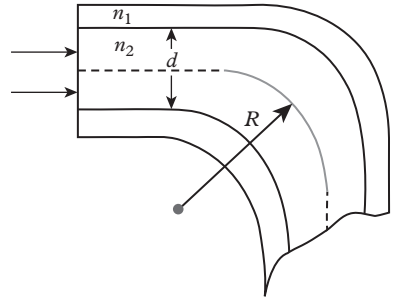

Figure 5.38 *Minimum radius for which guided waves can still exist.*

5.19. If a parallel beam of width W_1 is incident upon a prism such as that in Figure 5.39, find an equation that gives the width of the beam exiting the prism in terms of the incident angle and the apex angle α. Sir David Brewster, in 1835, first suggested the use

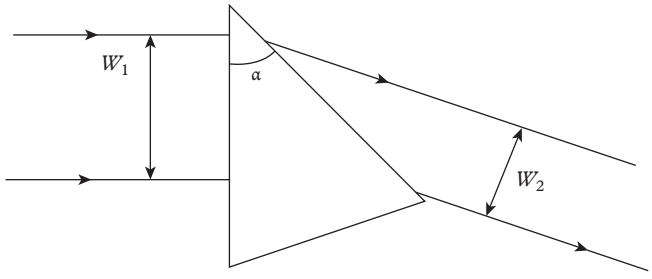

Figure 5.39 *A prism used to magnify or demagnify a parallel beam of light.*

of this type of magnification. Today, a component based upon this concept is found in the CinemaScope optical system. Can you guess why this optical component is used?

5.20. In Figure 5.40, the bottom trace shows the initiation of a laser diode pulse ($\lambda = 850$ nm) at the entrance of a step-index optical fiber, and the top trace shows the arrival of that pulse at the end of 1100 m of the fiber. Calculate the index of refraction of the core of the fiber. The scope time base is 1 μs/division. The core of the fiber is 100 μm and the cladding is 140 μm.

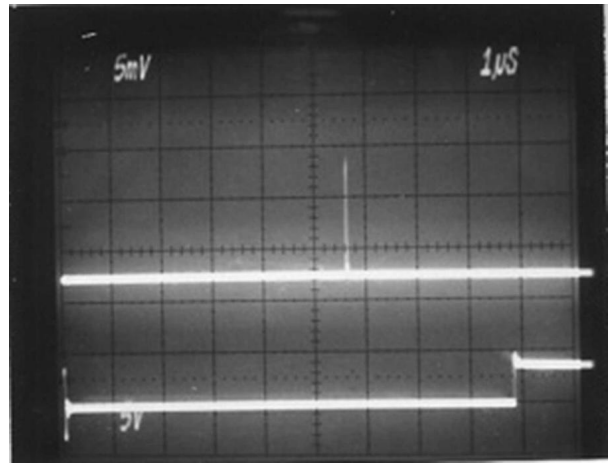

Figure 5.40 *An optical pulse propagating through 1100 m of optical fiber. The bottom trace indicates the initiation of the optical pulse at the start of the fiber, and the top trace indicates the arrival of the pulse at the end of the fiber. The timescale is 1 μs/division.*

REFERENCES

1. Feynman, R., R.B. Leighton, and M.L. Sands, *The Feynman Lectures on Physics*. Vol. II. 1964: Addison-Wesley, Chap. 19.
2. Conrady, A.E., *Applied Optics and Optical Design*. 1992: Dover. p. 855.
3. Smith, W.J., *Modern Lens Design*. 2004: McGraw-Hill. p. 631.
4. *Oslo*. 2008: Available from <http://www.lambdares.com/contact_us/oslo/>.
5. Nussbaum, A. and R.A. Phillips, *Contemporary Optics for Scientists and Engineers*. 1976: Prentice-Hall.
6. O'Shea, D.C., *Elements of Modern Optical Design*. 1985: Wiley.
7. Geary, J.M., *Introduction to Lens Design*. 2002: Willmann-Bell. 462.
8. Yariv, A., *Optical Electronics*. 3rd ed. 1985: Holt, Rinehart, and Winston. p. 552.
9. Levy, H. and F. Lessman, *Finite Difference Equations*. 1992: Dover. p. 278.
10. Friesem, A.A., U. Levy, and Y. Silberberg, *Parallel transmission of images through single optical fibers*. Proc. IEEE, 1983. **71**: p. 208–221.
11. Tien, P.K., *Light waves in thin film and integrated optics*. Appl. Opt., 1971. **10**: p. 2395.
12. Marcuse, D., *Cut off conditions in optical fibers*. J. Opt. Soc. Am., 1973. **63**: p. 1369–1371.
13. *Physics of the SELFOC Lens*. 2008: Nippon Sheet Glass Co., Ltd. of Japan.
14. Bohm, D., *Quantum Theory*. 1951: Prentice-Hall.
15. Cherin, A.E., *An Introduction to Optical Fibers*. 1983: McGraw-Hill.

Appendix 5A The *ABCD* Matrix

In Chapter 5 we derived the general form of the *ABCD* matrix and generated the matrix for two refracting surfaces. Now we would like to relate the elements of the *ABCD* matrix to some of the traditional parameters and equations of geometrical optics.

If the optical element is thin, we can assume $d \to 0$, and because most imaging systems will be used in air, we can also assume that $n_1 = n_3 = 1$. The system matrix (5.12) for the thin lens becomes

$$\mathbf{S} = \begin{bmatrix} 1 & 0 \\ (n_2 - 1)\left(\dfrac{1}{R_2} - \dfrac{1}{R_1}\right) & 1 \end{bmatrix}. \tag{5A.1}$$

For this case, the determinant of the system matrix is

$$\|\mathbf{S}\| = 1.$$

The lateral magnification is defined as $\beta = x_1'/x_1 = 1$. Because the elements of the *ABCD* matrix are $A = 1$ and $B = 0$, the values of the x-coordinate at the vertices V_1 and V_2 are unchanged by the system matrix. This is equivalent to saying that the front and back vertices of the thin lens define planes of unit magnification. The planes of unit magnification are important reference planes for both thick ($d \neq 0$) and thin ($d = 0$) lenses. We will introduce a technique for locating the planes of unit magnification for a thick lens later in this appendix.

The *ABCD* matrix for the general imaging condition can be shown to be equivalent to the more familiar thin-lens equation. To obtain the equivalence, we first apply the transfer matrix from the object point O in Figure 5A.1 to the lens, then apply the lens's system matrix, and finally use a second transfer matrix to reach the image point I:

$$\begin{bmatrix} 1 & s' \\ 0 & 1 \end{bmatrix} \begin{bmatrix} 1 & 0 \\ (n_2 - 1)\left(\dfrac{1}{R_2} - \dfrac{1}{R_1}\right) & 1 \end{bmatrix} \begin{bmatrix} 1 & -s \\ 0 & 1 \end{bmatrix} \begin{bmatrix} x_1 \\ \gamma \end{bmatrix} = \begin{bmatrix} x_1' \\ \gamma' \end{bmatrix}.$$

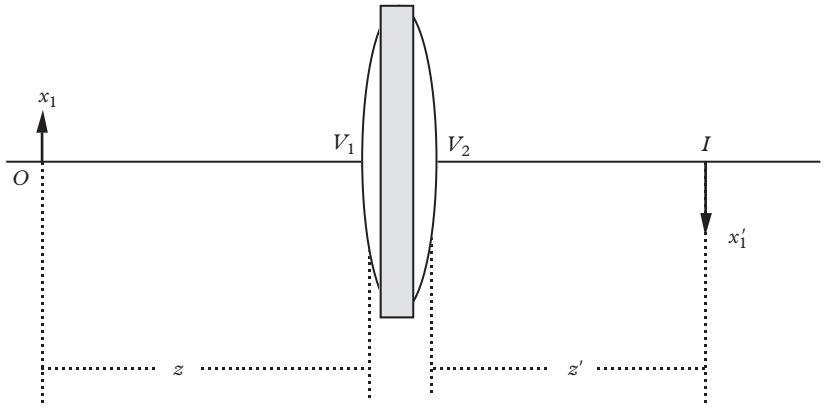

Figure 5A.1 *Thin-lens imaging system.*

A negative s is used in the propagation matrix for the region to the left of the lens because of the sign convention; s is a negative quantity, and the negative sign ensures that the propagation matrix contains a positive quantity for propagation from left to right. We then have

$$\begin{bmatrix} 1 + s'(n_2 - 1)\left(\frac{1}{R_2} - \frac{1}{R_1}\right) & s' - s - ss'(n_2 - 1)\left(\frac{1}{R_2} - \frac{1}{R_1}\right) \\ (n_2 - 1)\left(\frac{1}{R_2} - \frac{1}{R_1}\right) & 1 - s(n_2 - 1)\left(\frac{1}{R_2} - \frac{1}{R_1}\right) \end{bmatrix} \begin{bmatrix} x_1 \\ \gamma \end{bmatrix} = \begin{bmatrix} x_1' \\ \gamma' \end{bmatrix}.$$

This is called the object–image matrix, **O**.

5A.1 Thin-Lens Equation

If x_1' is an image of x_1, then all rays, regardless of their value of γ, must arrive at x_1' according to Fermat's principle. This means that x_1' is independent of γ, and we must have the object–image matrix element $B = 0$. This requirement, called the *imaging requirement*, leads to

$$s' - s - ss'(n_2 - 1)\left(\frac{1}{R_2} - \frac{1}{R_1}\right) = 0,$$

which can be rewritten in the form of the familiar *thin-lens equation*

$$\frac{1}{s'} - \frac{1}{s} = (n_2 - 1)\left(\frac{1}{R_1} - \frac{1}{R_2}\right). \tag{5A.2}$$

If we allow the indices of refraction in the object and image spaces to differ, then (5A.2) is modified to read

$$\frac{n_3}{s'} - \frac{n_1}{s} = \frac{n_2 - n_1}{R_1} - \frac{n_3 - n_2}{R_2}.$$

The elements $ABCD$ of the object–image matrix can be identified with some simple parameters of the thin lens. From our definition of the *lateral magnification* of the imaging system, we find that the element A of the object–image matrix is equal to the lateral magnification

$$\begin{aligned} \beta &= \frac{x_1'}{x_1} = A \\ &= 1 + s'(n_2 - 1)\left(\frac{1}{R_2} - \frac{1}{R_1}\right). \end{aligned} \tag{5A.3}$$

5A.2 Optical Invariant

The determinants of both the transfer matrix and the lens system matrix are equal to 1,

$$\|\mathbf{T}\| = \|\mathbf{S}\| = 1,$$

and therefore the object–image matrix also has unit determinant:

$$\|\mathbf{O}\| = \|\mathbf{T}\| \cdot \|\mathbf{S}\| \cdot \|\mathbf{T}\| = 1.$$

The determinant is equal to the product

$$\|\mathbf{O}\| = AD - BC = 1.$$

For the imaging condition, we must have $B = 0$, requiring that

$$\|\mathbf{O}\| = AD = 1.$$

If we now introduce the concept of *angular magnification* as

$$\beta_\gamma = \frac{\gamma'}{\gamma} = D = 1 - s(n_2 - 1)\left(\frac{1}{R_2} - \frac{1}{R_1}\right). \tag{5A.4}$$

This definition leads to the optical invariant of an optical system. Because the determinant is 1, the product of the lateral and angular magnification is

$$\|\mathbf{O}\| = \beta\beta_\gamma = 1,$$

which can be rewritten as

$$x_1'\gamma' = x_1\gamma$$

A more general form of this invariant can be obtained by recalling that when the index of refraction differs in the object and image space, then the object–image determinant is

$$\|\mathbf{O}\| = \beta\beta_\gamma = \frac{n_1}{n_3}.$$

The *optical invariant* is then

$$\mathcal{H} = n_1 x_1 \gamma = n_3 x_1' \gamma'. \tag{5A.5}$$

This relationship is also called the *Lagrange invariant* or *Smith–Helmholtz* equation. The invariant was derived using ray parameters from the object and image spaces. The relationship holds for any two conjugate planes of the optical system.

5A.3 Lensmaker's Equation

When the indices are the same in the object and image spaces, the object–image matrix simplifies to

$$\mathbf{O} = \begin{bmatrix} \beta & 0 \\ C & \dfrac{1}{\beta} \end{bmatrix}.$$

We still have one constant, C, that has not been identified with any simple property of a thin lens. We can easily show that C is related to the focal point of the lens.

When we put the object at infinity, the image point, located a distance f_2 from the lens vertex V_2, is defined as the *focal point* of the lens, F_2 (see Figure 5A.2):

$$\frac{1}{s'} = \frac{1}{f_2} = (n_2 - 1)\left(\frac{1}{R_1} - \frac{1}{R_2}\right). \tag{5A.6}$$

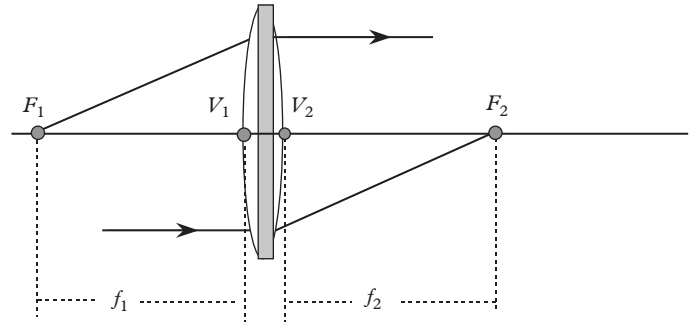

Figure 5A.2 *Definition of the focal points and focal planes of a lens.*

This relationship for the focal length is called the *lensmaker's equation*. From the lensmaker's equation, we discover that the same focal length (or power) can be obtained by using a variety of indices and lens curvatures. Comparing (5A.6) with the element C of the object–image matrix, we discover that $C = -1/f_2$; i.e., C is equal to the negative of the power of the lens, and the object–image matrix is further simplified

$$\mathbf{O} = \begin{bmatrix} \beta & 0 \\ -\dfrac{1}{f_2} & \dfrac{1}{\beta} \end{bmatrix}. \tag{5A.7}$$

5A.4 Gaussian Formalism

If we measure a distance equal to the focal distance f_2 from V_1 at the front of the lens, we locate a second focal point, F_1. If the index of refraction is the same on both sides of the lens, then the focal length, i.e., the distance from each focal point to its vertex, is $f_1 = f_2 = f$. Using the definition of the focal length given by (5A.6), we can rewrite (5A.2) as

$$\frac{1}{s'} - \frac{1}{s} = \frac{1}{f}. \tag{5A.8}$$

This is called the *Gaussian form* of the thin-lens equation. The sign of the focal length f used in (5A.8) is given by f_2 in (5A.6). If f_2 is positive, the lens is called a *positive lens*; it will focus a plane wave to a point located a distance f_2 from the lens vertex. If f_2 is negative, the lens is called a *negative lens*; it will cause a plane wave to diverge, as if it originated from a point located a distance $-f_2$ from the lens vertex.

5A.5 Newtonian Formalism

The pair of focal points, F_1 and F_2, is the first of three pairs of points called the *cardinal points* of the lens. The two focal points can be used to establish reference planes as replacements for the vertices of the lens. The object and image distances are then measured with respect to the focal planes. The lens equation (5A.8) is modified to reflect the new reference points by substituting

$$Z = s - f_1, \quad Z' = s' - f_2,$$

yielding the *Newtonian form* of the thin-lens equation:

$$ZZ' = -f_1 f_2. \tag{5A.9}$$

5A.6 Principal Planes

The thin lens results in a very simple *ABCD* matrix. It is possible to retain this simplicity for very complex optical systems by defining a pair of cardinal points, called the *principal points*, to replace the vertices V_1 and V_2 as reference points of the lens (see Figure 5A.3). These new principal points define planes of unit magnification, just as the vertices did, but they may not lie anywhere near the outer surfaces of the optical system. With these new reference points, the *ABCD* matrix for any complex lens assumes the simple form of the thin lens. These reference points are said to be *conjugate points* because the points are related through the optical system as an *object–image pair*.

We need to replace the *ABCD* system matrix for a thin lens defined using the vertices V_1 and V_2 by the more general *ABCD* system matrix referenced to the principal planes. The new matrix will describe the propagation of light from the principal point H_1 to the principal point H_2. By combining this new *ABCD* system matrix with transfer matrices from the object to H_1 and from H_2 to the image, an object–image matrix for any complex lens can be generated.

To create the new *ABCD* matrix, we begin by using a ray trace procedure similar to the one used in Chapter 5 to produce the system matrix. The system matrix is then combined with two transfer matrices that describe the ray propagation from H_1 through the optical system and onto H_2:

$$\mathbf{M} = \begin{bmatrix} 1 & h_2 \\ 0 & 1 \end{bmatrix} \begin{bmatrix} A & B \\ C & D \end{bmatrix} \begin{bmatrix} 1 & -h_1 \\ 0 & 1 \end{bmatrix}. \tag{5A.10}$$

Here, as with the thin-lens object–image-matrix, the propagation matrix for the region to the left of the lens contains a negative distance because of the sign convention selected for geometrical optics:

$$\mathbf{M} = \begin{bmatrix} A + h_2 C & B - h_1 A + h_2 (D - h_1 C) \\ C & D - h_1 C \end{bmatrix}. \tag{5A.11}$$

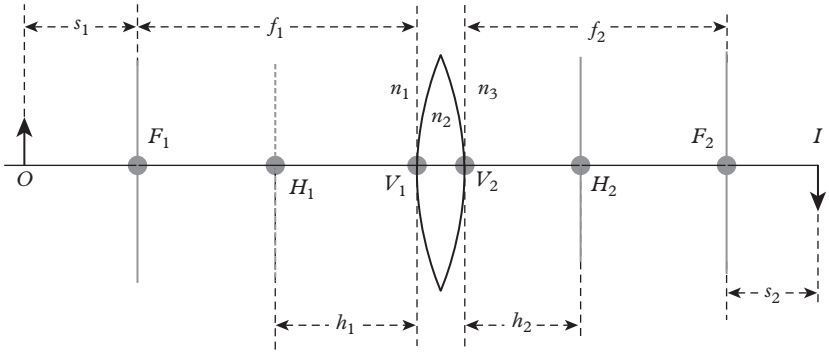

Figure 5A.3 *Principal points for a lens.*

The principal planes H_1 and H_2 located at h_1 and h_2, are equivalent to the thin-lens vertices, which requires that they be planes of unit magnification. Because the principal planes are planes of unit magnification,

$$M_{11} = 1.$$

We can therefore write

$$A + Ch_2 = 1,$$

$$h_2 = \frac{1-A}{C}.$$

Because the two planes are defined by conjugate points, the imaging condition must hold between them. This means that

$$M_{12} = 0.$$

Since

$$\|\mathbf{M}\| = \frac{n_1}{n_3},$$

we must have

$$M_{22} = \frac{n_1}{n_3},$$

$$D - Ch_1 = \frac{n_1}{n_3},$$

$$h_1 = \frac{D - \dfrac{n_1}{n_3}}{C}.$$

When $n_3 = n_1$, we have

$$h_1 = \frac{D-1}{C}.$$

We now have defined the location of the principal points with respect to the vertices of the lens vertices. For these equations to be meaningful, we must have $C \neq 0$ (it occurs in the denominator of h_1 and h_2). In (5A.6), we associated C with $-1/f$; here, C is equal to the reciprocal of the *effective focal length*, f_2, measured from the principal plane H_2, i.e.,

$$C = -\frac{1}{f_2}.$$

There is a special optical system for which $C = 0$; the *afocal system*. This optical system produces an image at infinity of an object located at infinity. Because an astronomical telescope performs this optical operation, an afocal system is often called a *telescopic system*. The object and the image are both located at infinity, and so it is more useful to specify the size of the object by the angle it subtends. We therefore use angular magnification (5A.4) as a measure of the performance of the telescopic system:

$$\beta_\gamma = \frac{\gamma'}{\gamma} = D.$$

5A.6.1 Nodal Points

The third set of cardinal points are called the *nodal points*, N_1 and N_2, and the pair of planes, normal to the optical axis, that contain these points are called *nodal planes*. The nodal points are defined as those points for which

$$\gamma' = \gamma,$$

or, equivalently, the points of unit angular magnification

$$\beta_\gamma = 1.$$

The image of an object will not move if the imaging lens is rotated a small amount about an axis passing through a nodal point perpendicular to the optical axis. Thus, it is quite easy to locate the nodal points of a lens experimentally. If the index of refraction on each side of an optical system is the same, $n_1 = n_3$, then the nodal points coincide with the principal points and we need only deal with four cardinal points.

The *ABCD* matrices for some common optical elements and media are shown in Figure 5A.4.

5A.7 Aperture Stop and Pupil

The finite size of an optical system limits the bundle of axial rays leaving the object point O on the optical axis of Figure 5A.5. The obstruction that limits the maximum angle γ_M of a ray from the object to the image is called the *aperture stop*. The rays that leave the object at angles nearly equal to γ_M are called marginal rays. In Figure 5A.5, we show a marginal ray leaving the object at γ_M and just skimming the aperture stop labeled A.

To locate the aperture stop is quite easy. In conventional ray tracing, we trace a single ray through the system, as illustrated in Figure 5A.6. We then calculate the ratio of aperture radius to ray height,

$$\left|\frac{r_j}{x_j}\right|.$$

The smallest ratio indicates the aperture stop. With the matrix technique, we create an *ABCD* matrix from the object O, on the optical axis, to each stop in the optical system, as

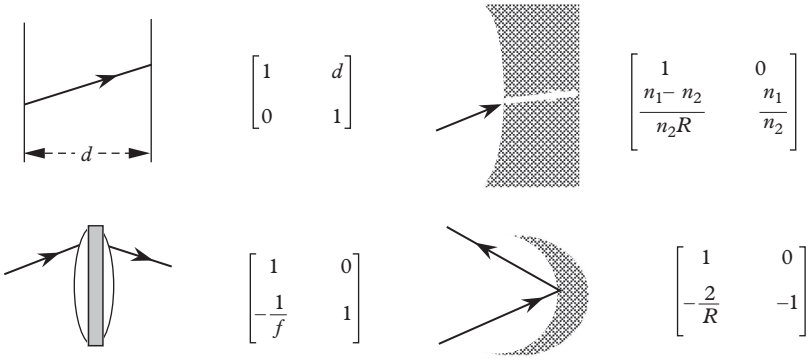
d
$\begin{bmatrix} 1 & d \\ 0 & 1 \end{bmatrix}$
$\begin{bmatrix} 1 & 0 \\ \frac{n_1 - n_2}{n_2 R} & \frac{n_1}{n_2} \end{bmatrix}$
$\begin{bmatrix} 1 & 0 \\ -\frac{1}{f} & 1 \end{bmatrix}$
$\begin{bmatrix} 1 & 0 \\ -\frac{2}{R} & -1 \end{bmatrix}$

Figure 5A.4 *The ABCD matrices for translation in a uniform medium and refraction at an interface. Also show are the ABCD matrices for a thin lens and a mirror.*

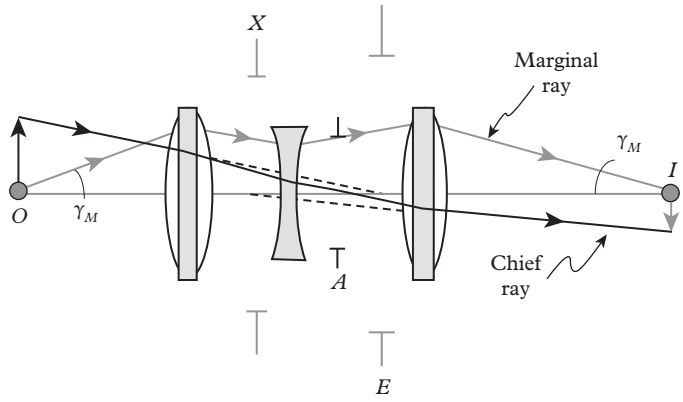

Figure 5A.5 *A complex lens system (Cooke triplet) containing a stop, A, that acts as the aperture stop for the lens. The rays that just skim pass the aperture stop are called marginal rays. Any ray that passes through the center of the aperture stop is called a principal ray. The image of the aperture stop as seen from the object is called the entrance pupil, labeled E in the figure. The image of the aperture stop as seen from the image is called the exit pupil, labeled X. Because the entrance and exit pupils are conjugates of the aperture stop, the principal ray will also pass through the center of these pupils, or, as in this figure, will appear to do so as indicated by the dotted lines.*

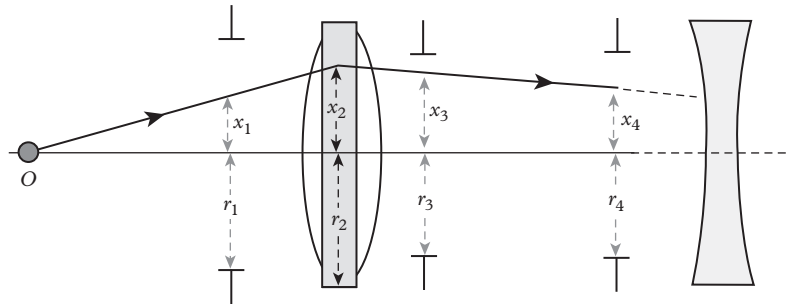

Figure 5A.6 *Geometry for finding aperture stop of an optical system.*

illustrated in Figure 5A.6. Because the object height is zero, the matrix equation for each ray height is then

$$\begin{bmatrix} x_j \\ \gamma_j \end{bmatrix} = \begin{bmatrix} A & B \\ C & D \end{bmatrix} \begin{bmatrix} 0 \\ \gamma \end{bmatrix}.$$

From this equation, the value of x_j in each aperture is given by

$$x_j = B\gamma.$$

If we set each x_j equal to the radius of the stop at that point, r_j, then the object angle for the marginal ray of that stop is

$$\gamma_j = \frac{r_j}{B}.$$

Thus, to find the aperture stop, we simply calculate the matrix element B for the optical elements to the left of each stop. The stop with the smallest ratio of stop radius to matrix element B is the aperture stop.

The maximum angle γ'_M determines the numerical aperture of the lens:

$$\text{NA} = n_3 \sin \gamma'_M, \tag{5A.12}$$

and the $f/\#$ of the lens

$$f/\# = \frac{1}{2\sin\gamma'_M}. \tag{5A.13}$$

The equation normally used to define and calculate $f/\#$ is a special case of (5A.13). If a plane wave fully illuminates the aperture of the optical system then γ'_M is given by

$$\gamma' = \frac{r_M}{f_2},$$

where f_2 is the effective focal length and r_M is the aperture radius. Applying the paraxial approximation allows us to write the normally encountered definition of $f/\#$:

$$f/\# = \frac{f_2}{D},$$

where D is the diameter of the aperture stop.

The image of the aperture stop formed by the optical system to its left, i.e., the image of the aperture stop as seen from the object position, is called the *entrance pupil*, and is labeled E in Figure 5A.5. The image of the aperture stop formed by the optical system to its right, i.e., the image of the aperture stop as seen from the image position, is called the *exit pupil*, and is labeled X in Figure 5A.5.

A ray passing through the center of the aperture stop is called a *principal ray*.[5] Because the entrance and exit pupils are conjugates (images) of the aperture stop, principal rays pass through the centers of these pupils also. In Figure 5A.5, the entrance and exit pupils are virtual images, and thus a principal ray appears to originate at the centers of these pupils.

Other stops exist in an optical system; they may be placed there to control aberrations, to act as lens mounts, or to reduce scattered light (glare stops). The stop that limits the maximum oblique principal ray that can propagate through the optical system is called the *field stop*. This stop will occur at an object or image plane and is therefore conjugate to the final image plane and limits the size of the image.

If a ray bundle is created by the principal ray and a marginal ray for an object point on the optical axis, we find that this size ray bundle cannot propagate through the system for object points located off the optical axis. Another way to state this fact is that oblique ray bundles will not fill the aperture stop. This means that the flux density that can pass from the object to the image is a function of the distance off the optical axis. This effect is called *vignetting*. Vignetting is not always a defect. Sometimes lens designers "hide" aberrations in the low-light region produced by vignetting. Also, vignetting may be used to emphasize part of the image or for artistic effect.

Appendix 5B Aberrations

A perfect optical system, from a geometrical optics point of view, is one that redirects all light rays from an object point through a single conjugate (image) point. For a real image, the wavefront associated with each of the rays leaving the optical system must be spherical, centered upon the image point. Fermat's principle states that the optical path length of each ray will be identical.

[5] Sometimes, the term *chief ray* is used in place of principal ray, although at other times, the term chief ray is reserved for the center ray of a ray bundle. Most of the time, the two rays are identical.

If the perfect optical system were a positive lens, then a plane wave incident upon the lens would be focused to a point. If we inspected the light distribution in planes on either side of the focal plane, we would expect to see uniformly illuminated disks of light that decreased in diameter as we approached focus and increased in diameter as we moved away from focus.

As we already know, light is a wave and geometrical optics is only an approximate theory. We expect to see a departure from the predictions of geometrical optics when dimensions are of the order of a wavelength. Small dimensions are found near the focal plane, and, as shown in Figure 5B.1, there is a departure from

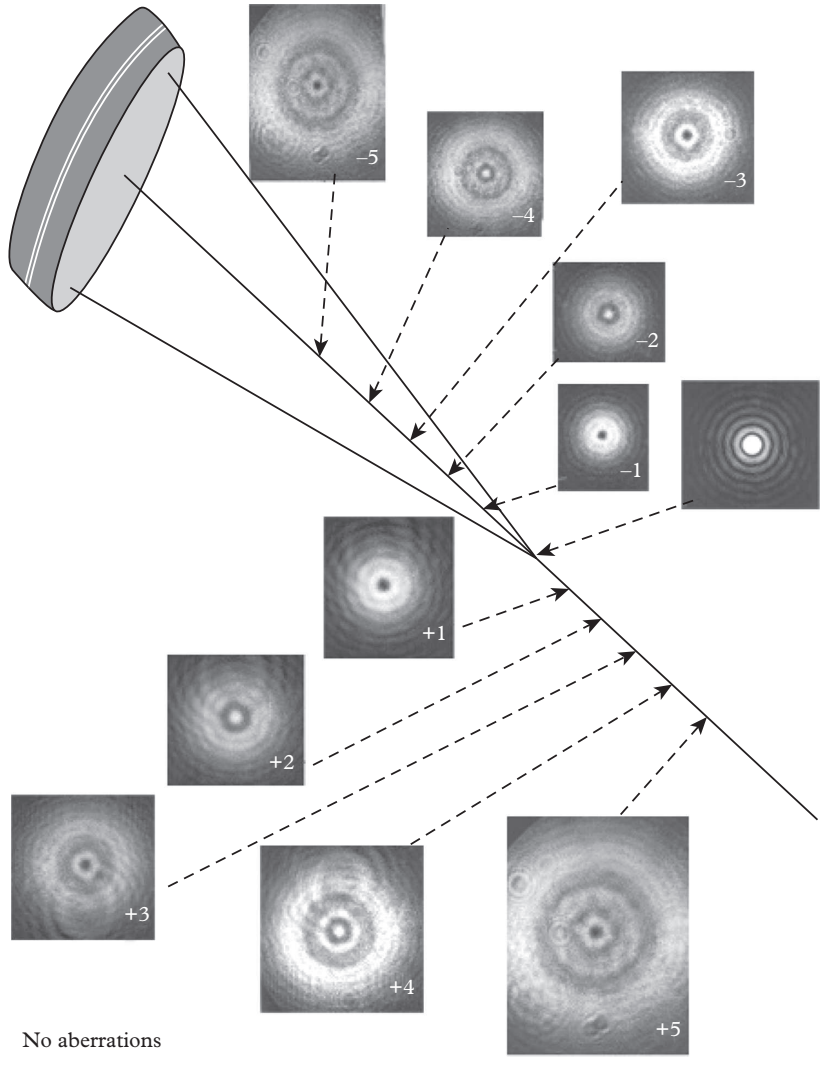

Figure 5B.1 *Light distributions found in planes normal to the optical axis and equally spaced along the optical axis of a nearly perfect lens. The planes were spaced about 1 mm apart and the focal length of the lens was about 500 mm. Notice that the images are symmetric about the focus.*

the predictions of geometric optics. The light distributions are quite complicated with the light intensity on the optical axis passing through zero periodically. We do however observe identical distributions in planes symmetrically positioned about the focal plane. These light distributions are due to diffractive effects, and a critical analysis of them has been made [1]. These diffractive effects will not be dealt with in this book. It was necessary to point out the effects, however, because they are an obvious component of the images we will present during our discussion of aberrations.

The objective of the lens designer is to produce an optical system that is perfect from the geometrical optics viewpoint, but he is usually prevented from doing so by cost. The most economical materials available to the lens designer are glasses with a uniform index of refraction. To form these materials into optical components, grinding and polishing techniques are used, again because of their economy. When two materials are placed in contact, separated only by some abrasive material, and moved with respect to one another in a great number of different relative positions, the points of contact between the materials will be worn away until the two surfaces form plane or spherical surfaces—touching at every point. Thus, the cheapest optical surface has a spherical shape (a plane is viewed as a spherical surface with an infinite radius of curvature).

Economy requires that the optical designer attempt to produce a perfect optical system using optical components with a uniform index of refraction and having spherical surfaces. Normally, these components will be axially centered and rotationally symmetric. Paraxial theory predicts the formation of a perfect image by these components. However, when the exact theory is used, we discover that a spherical component can only produce an imperfect image. The departure from the desired image is called aberration. The goal of the lens designer is to combine a number of spherical components in such a way as to reduce the aberrations.

The first aberration-corrected lenses were designed by **Chester Moor-Hall (1704–1771)** and **John Dollond (1706–1761)** around 1729 for use in astronomy. Much later, in 1840, **Josef Max Petzval (1807–1891)** designed a portrait camera lens. These designs were accomplished without the benefit of a formal theory. **Ludwig Philipp von Seidel (1821–1896)** established a rigorous theory of third-order aberrations in 1856. **Ernst Abbe (1840–1905)** developed and implemented the analytical methods of optical design.

Optimization techniques are used to guide the lens designer in reducing aberrations. The optimization techniques require a method of quantifying the departure from a perfect image. In this appendix, we will introduce the methods used to quantify aberrations. The approach measures the departure of the actual image, as predicted by application of the laws of refraction and reflection (called *finite ray tracing*), from the predictions of paraxial theory. Here, we will only discuss the differences between paraxial theory and the third-order approximation to the exact theory. The third-order approximation[6] to aberration theory leads to what are called *primary* aberrations.

There are two basic ways to characterize aberrations:

1. In terms of the departure of the wavefront from a spherical surface, called the reference sphere, and
2. The displacement of the ray-intercept from the paraxial image point.

To quantify these characterizations, a set of rays is followed through the optical system. To select those rays, the entrance pupil of the system is divided into an array of points

[6] In the United Kingdom, the aberrations we will discuss are viewed as the *first-order* corrections to the paraxial theory, while in the United States, they are viewed as the *third-order* corrections to the first-order theory.

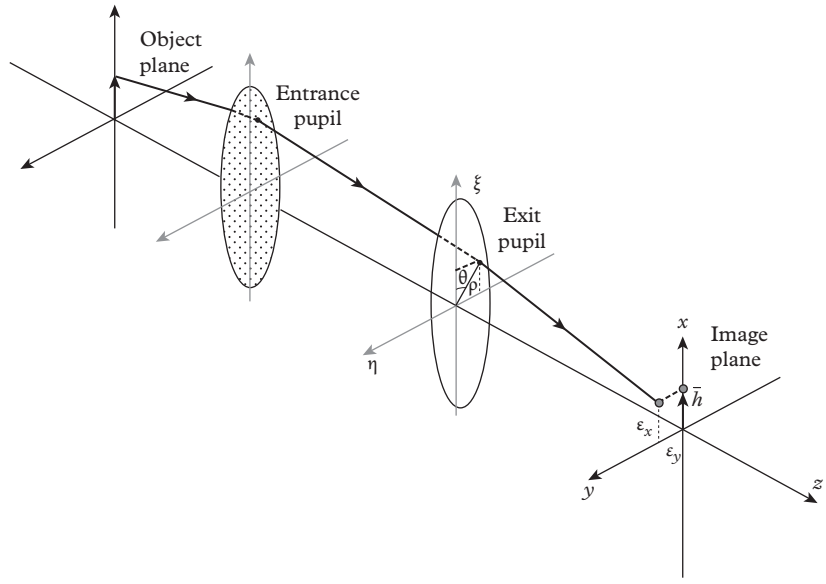

Figure 5B.2 *Coordinate system for aberration theory. The lenses in this optical system are not shown.*

(see Figure 5B.2), and rays are traced from the object to the entrance pupil, through the system to the exit pupil, and finally from the exit pupil to the image plane.

In Figure 5B.2, the various coordinate planes used in the following discussion are defined. The vector **h** defines the location of the Gaussian ray's intercept in the plane of interest, i.e., the ray point determined by paraxial theory; here, the point shown is the conjugate point of the object. The second point shown in the image plane is the point determined by finite ray tracing to be the actual image point. In the exit pupil, polar coordinates (ρ, θ), are used and the exit pupil is divided into *zones*. In the image plane, a rectangular coordinate system (ξ, η) is used. The aberrations are described in terms of rays propagating in two perpendicular planes: the *tangential* and *sagittal planes*.

The *tangential plane* is another name for the meridional plane and is defined as any plane containing the object point and the optical axis of the system (see Figure 5B.3). In our discussion, the tangential plane has always been the (x, z) plane. In the exit pupil of Figure 5B.2, it is defined as the (ξ, z) plane. All rays confined to this plane are called tangential rays.

The plane at right angles to the tangential plane and containing the principal ray is called the *sagittal plane* (see Figure 5B.3). The sagittal plane changes at each surface, but at the pupils and the aperture stop the sagittal plane is also the (η, z) plane. This is because the principal ray crosses the optical axis at these positions. It should be pointed out that the principal ray lies in both the tangential and sagittal planes–it is the only ray that does so.

5B.1 Wavefront Aberration Coefficients

One technique for characterizing aberrations was introduced by Hamilton while he was in his early twenties. This technique expresses the aberration of an optical system in terms of the departure of the geometrical wavefront from a spherical shape. Paraxial theory predicts that an optical system will image a point source into a point image. All rays from the point source will travel to the point image. The geometrical wavefront is constructed by generating

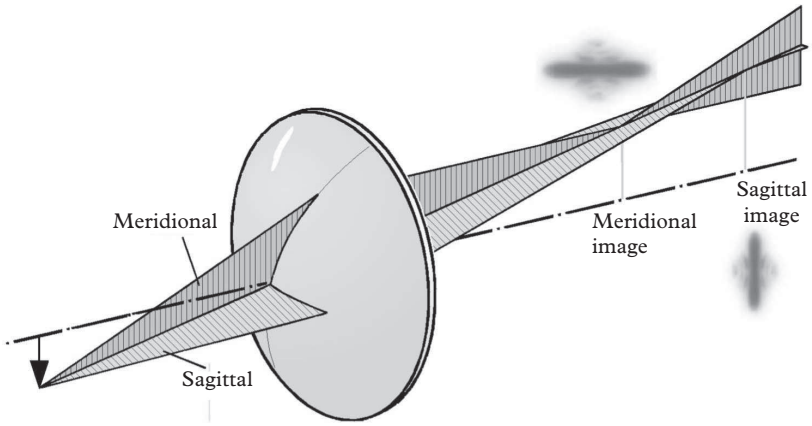

Figure 5B.3 *Definition of meridional or tangential plane and sagittal plane of a simple optical system. The focus due to astigmatism is also shown.*

the normal to each of the rays and is a sphere for a point image. This spherical surface, predicted by the paraxial theory, is called the reference sphere.

If we calculate the distance between the reference sphere $S(\xi, \eta, z)$ and the actual wavefront $\Sigma(\xi, \eta, z)$ in the exit pupil, we generate the wave aberration function Δ:

$$\Delta(\xi, \eta, z) = n_2[\Sigma(\xi, \eta, z) - S(\xi, \eta, z)]. \tag{5B.1}$$

This function defines the optical path difference between the two surfaces and is measured along the radius of the reference sphere.

We will not develop the theory, but simply state that we may find the wavefront surface, usually in the exit pupil, and then measure the departure of this surface from a reference sphere positioned around the image point. The departure at each ray is given as an optical path length and is a function of the image position **h** and the coordinates of the point in the exit pupil, specified by the vector ρ (see Figure 5B.4). Because the optical system is axially

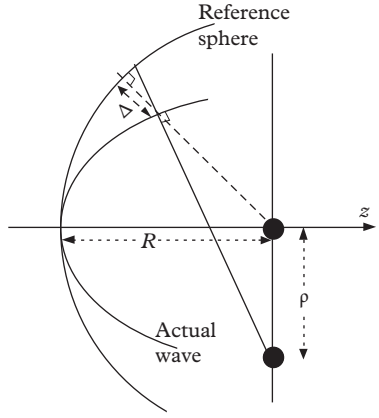

Figure 5B.4 *The reference sphere and actual wavefront are shown in the exit pupil of a lens. The optical path difference and the ray intercept in the image plane are also shown.*

symmetric, Δ must not change when we simultaneously rotate the vectors ρ and $\mathbf{h}$. This means that we should be able to describe the functional dependence of Δ in terms of scalar quantities. The simplest independent scalar relationships involving the variables are

$$\rho^2, \quad \rho \cdot \mathbf{h} = \rho h \cos\theta, \quad h^2.$$

If we expand Δ as a power series in the scalar variables, we obtain

$$\begin{aligned}\Delta(h^2, \rho^2, \rho h\cos\theta) = {} & \Delta_{000} \\ & + \Delta_{020}\rho^2 + \Delta_{111} h\rho\cos\theta \\ & + \Delta_{040}\rho^4 + \Delta_{131} h\rho^3\cos\theta + \Delta_{222} h^2\rho^2\cos^2\theta \\ & + \Delta_{220} h^2\rho^2 + \Delta_{311} h^3\rho\cos\theta. \end{aligned} \tag{5B.2}$$

The indices of the coefficients of the expansion, Δ_{ijk}, indicate the powers of each of the variables h, ρ, and $\cos\theta$. The constant term, Δ_{000}, must be zero because, by definition, the reference sphere and wavefront are in contact at the optical axis (see Figure 5B.4). The second and third terms are associated with a shift in the location of the Gaussian image, $\Delta_{020}\rho^2$, and a small change in the magnification of the image, $\Delta_{111} h\rho\cos\theta$. These terms do not affect image quality and thus are not really aberrations. The last five terms correspond to the lowest-order aberrations.

The wavefront aberration function (5B.2) can be used to determine the interference pattern that will be produced by the optical system in an interferometer such as the Twyman–Green interferometer (Figure 4.18b). The interferogram is represented by constructing contours of constant optical path difference (OPD).

5B.1.1 Optical Path Difference

Before computers, when ray tracing was a labor-intensive process it was convenient to have a single number to characterize aberration. One technique used to generate such a number was to set ρ and h equal to their maximum values; then the Δ_{ijk} are equal to the optical path difference contributions from each of the aberrations. The OPDs are usually quoted in terms of wavelength.

An optical system with an OPD of $\lambda/4$ is considered a perfect system from a geometrical optics point of view. This criterion is often called the *Rayleigh criterion*. (This is an approximate measure of imaging capability proposed by Lord Rayleigh in 1879. It is not the same thing as the Rayleigh limit to be discussed later.) A system that meets the Rayleigh criterion has its performance controlled by the wave properties of light and is called a *diffraction-limited system*. In such systems, it is necessary to use an additional criterion to specify their performance.

As we will see in Chapter 10, a diffraction-limited system produces as an image of a point, a small disk surrounded by a set of rings; see the paraxial focal plane in Figure 5B.1, where we see the ring pattern known as the Airy pattern. (We will give a mathematical description of this pattern in Chapter 10.) The fraction of energy contained in the central disk is used to characterize the performance of a nearly perfect, diffraction-limited system. The characterization is made through the use of the *Strehl ratio*, which is the ratio of light intensity at the peak of the diffraction

Table 5B.1 *Strehl ratio*

OPD	Fraction of the Rayleigh criterion	Intensity (%)	Strehl ratio
0	Perfect lens	84	1.0
1/16	1/4	83	0.988
1/8	1/2	80	0.952
1/4	1	68	0.8095

pattern of an aberrated image relative to the peak in a perfect image. A perfect lens, with an OPD of 0, should contain 84% of the energy in the central disk of the Airy pattern at paraxial focus. It is conventional to assume that a diffraction-limited lens has a Strehl ratio > 0.80. Table 5B.1 compares several measures of lens perfection.

5B.1.2 Transverse Ray Coefficients

To study the performance of a lens design, rays are traced through the optical system. These rays are then used to generate the wavefront and the wavefront aberration coefficients. Instead of obtaining the wavefront surface, we may instead use the rays to determine the miss distance of the ray from the paraxial image point in the image plane. The two approaches are equivalent; they simply represent a change of the reference plane where the aberration measurement is made. The use of the ray intercept is of more immediate interest to the designer, since it represents the effect of the aberration on the image.

As can be seen in Figure 5B.2, the ray intercept is represented by its coordinates ε_x and ε_y. In the image plane, the aberrations are specified by expanding ε_x and ε_y as power series in h, ρ and θ:

$$\varepsilon_x = \sigma_1 \rho^3 \cos\theta + \sigma_2 \rho^2 h(2 + \cos 2\theta) + (3\sigma_3 + \sigma_4)\rho h^2 \cos\theta + \sigma_5 h^3,$$

$$\varepsilon_y = \sigma_1 \rho^3 \sin\theta + \sigma_2 \rho^2 h \sin 2\theta + (\sigma_3 + \sigma_4)\rho h^2 \sin\theta. \tag{5B.3}$$

The coefficients of this expansion, σ_i, are called *the Seidel coefficients* (sometimes they are know as *third-order coefficients*). The two descriptions of aberrations are geometrically related, and the coefficients of the expansions (5B.2) and (5B.3) are simply related through paraxial ray trace parameters. We can obtain the intercepts by calculating the normal to the wave surface:

$$\varepsilon_x = -R\frac{\partial \Delta}{\partial x}, \qquad \varepsilon_y = -R\frac{\partial \Delta}{\partial y}. \tag{5B.4}$$

The normals yield the direction of the ray, and R is the distance from the exit pupil to the image plane, approximately equal to the radius of the reference sphere.

The third-order aberration coefficients can all be calculated from paraxial ray trace data by tracing two rays: a marginal and a principal ray [2]. We will examine qualitatively each of the terms in the expansions introduced above, but will make no attempt to calculate the coefficients of the expansion or develop a detailed theory of any of the aberrations. In modern computer-based lens design, these coefficients are calculated by the software,

but, because many rays are traced, a graphical representation of the image plane is used to evaluate the lens performance.

One of the aberrations, spherical aberration, can be considered alone because it is the only term in (5B.2) and (5B.3) that is independent of h. Therefore, on axis, it is the only aberration that is not identically zero. When we move off axis, all of the aberrations are present and it is difficult to independently analyze a single aberration with a simple optical system. Spherical aberration is also symmetric about the optical axis, so we can perform all ray tracing in the tangential plane. We will use ray tracing of a very simple optical system to study spherical aberration. We have not developed the formalism for tracing skew rays [3] and therefore can only provide a qualitative discussion of the off-axis aberrations. In this qualitative discussion, we will assume that only the aberration under discussion is present, and all other aberrations will be assumed to be zero.

5B.2 Spherical Aberrations

The first term in the two expansions introduced above is associated with *spherical aberration*:

$$\text{wave} \leftrightarrow \{\Delta_{040}\rho^4, \qquad \text{Seidel} \leftrightarrow \begin{cases}\sigma_1\rho^3\cos\theta, \\ \sigma_1\rho^3\sin\theta.\end{cases} \tag{5B.5}$$

The aberration depends upon the ray position in the exit pupil but is independent of the position in the image plane. To understand this aberration, we will present an example that illustrates spherical aberration and demonstrates the technique used by the lens designer to obtain a measure of the aberration. Our example will involve a single refracting surface. Such an analysis is not wasted, because each surface contributes to the total aberration of an optical system as if it were alone. The total aberration of a system is simply the sum of the contributions from all surfaces.

The example we wish to examine is the lens shown in Figure 5B.5(a). This is not a contrived lens but is often found in front of the photosensor of a sunlight-activated street or yard light. The lens found in a yard light usually has a lower index of refraction and therefore has a different length.

From the paraxial theory given in Chapter 5,

$$\begin{aligned} n_2\gamma'' &= n_1\gamma - x_1\frac{n_2 - n_1}{R}, \\ x_1 &= x_1'', \\ x_2'' &= x_1'' + 2R\gamma_2'', \\ \gamma'' &= \gamma_2''. \end{aligned}$$

We want the incoming ray to strike the optical axis at the back face of the lens, located a distance $2R$ from the front vertex

$$x_2'' = 0.$$

We assume the object is at infinity:

$$\gamma = 0.$$

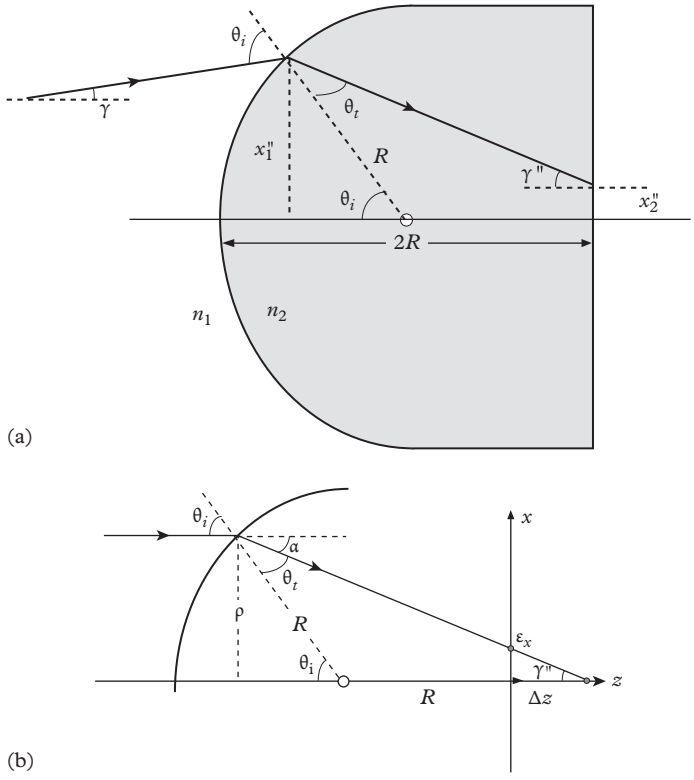

Figure 5B.5 *(a) Simple lens with only one refractive surface. (b) Geometry for finite lens trace of lens in (a).*

The index of refraction required to focus the plane wave from the object onto the back of the lens is obtained by solving the above equations for n_2:

$$x_1 = -2R\gamma'',$$

$$n_2\gamma'' = -\frac{x_1(n_2 - n_1)}{R},$$

$$n_2 = 2n_1.$$

If $n_1 = 1$ (the lens is located in air), then $n_2 = 2$.

The optical surface we are considering is spherical. Fermat's principle requires that the surface be Cartesian (see Figure 5.7). For an object at infinity, the required Cartesian surface is an ellipsoid with an eccentricity of 1/2. Because our surface is not the surface required, we should expect to encounter aberrations.

We will use Snell's law to perform a finite ray trace on this optical system and discover what aberrations exist in this lens. The geometry used in the ray trace is shown in Figure 5B.5(b).

The aperture stop is the diameter of the lens and the entrance and exit pupils are at the same location because there are no optical components to the left or right of the stop. The radius of the ray intercept in the exit pupil is

$$\rho = R\sin\theta_i.$$

Snell's law allows us to write the transmitted angle in terms of the incident angle:

$$\sin\theta_t = \frac{\sin\theta_i}{2}.$$

The angle the refracted ray makes with the optical axis is given by

$$\gamma'' = \alpha = \theta_i - \theta_t.$$

The law of sines allows us to calculate the z-axis intercept

$$\Delta z = \frac{R\sin\theta_i}{2\sin(\theta_i - \theta_t)} - R.$$

This is called the *longitudinal spherical aberration*. We see that the optical system will have a focus that varies with the height of the ray in the aperture, $R\sin\theta_i$. This variation is illustrated in Figure 5B.6, where the paths of a fan of rays through the lens were generated by a commercial lens design program. When spherical aberration causes the focal length to decrease with increasing zone radius, as it does in Figure 5B.6, the aberration is said to be *undercorrected*. When the marginal rays have a larger focal length than the paraxial rays, the aberration is said to be *overcorrected*.

We can plot the displacement of the ray intercept from the paraxial intercept along the z-direction as a function of the ray height (see Figure 5B.7). This agrees over the range height used with the longitudinal spherical aberration calculated by the lens design program and shown in Figure 5B.6.

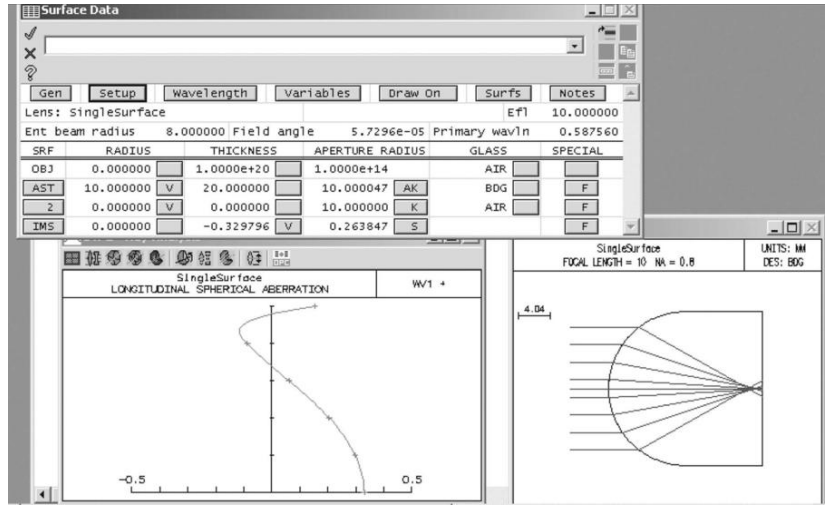

Figure 5B.6 *Commercial lens design program with the lens in Figure 5B.5(a) as the design lens.*

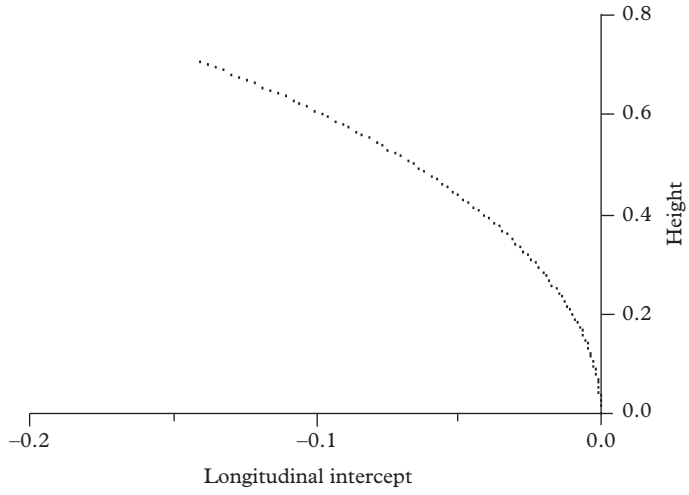

Figure 5B.7 *Longitudinal spherical aberration of a single spherical refracting surface. This is undercorrected spherical aberration.*

A set of images equivalent to those shown in Figure 5B.1 for a perfect optical system, but using an optical system with spherical aberration, are shown in Figure 5B.8. We observe here that rays through the outer zones focus nearer the lens than the paraxial rays, as predicted by Figure 5B.6. The images suggest that if we moved the focal plane inward from the paraxial plane toward the lens, then we could improve the image. This is called defocus and is used by lens designers to minimize the effects of aberrations. It does not, however, remove the aberrations; in fact, spherical aberration cannot be completely eliminated from a single spherical lens. The characterization of spherical aberration by the longitudinal displacement of the ray is not as useful to the lens designer as is the use of the image plane intercept ε_x, because it is more difficult to construct an optimization procedure with the longitudinal displacement.[7]

5B.2.1 Ray Intercept Plot

The image plane intercept ε_x is a measure of the *transverse spherical aberration* and can be calculated by using the simple trigonometric relationship suggested by Figure 5B.5(b):

$$\varepsilon_x = \Delta z \tan\gamma'' = R\left[\frac{\sin\theta_i}{2\cos(\theta_i - \theta_t)} - \tan(\theta_i - \theta_t)\right].$$

Because

$$\tan\gamma \propto \rho,$$

the ray intercept curve in Figure 5B.9 is a cubic function of the radial position in the exit pupil, ρ, as predicted by (5B.5). We find that as the aperture of the optical system increases, so does the spherical aberration, and more and more energy appears outside the paraxial focus. In Figure 5B.10, we have recorded the image of a point source in the paraxial focal plane for an optical system with increasing amounts of spherical aberration present. We increased the spherical aberration by increasing the aperture of the optical system. At first, diffraction dominates, and as the aperture size increases, the Airy disk decreases in size; see Chapter 10 for an explanation of this effect. Quickly, however, the spherical aberration dominates, and we see a spreading of energy in the paraxial focal plane.

[7] The difficulty with the longitudinal intercept is that it has a large range of possible values $(-\infty, \infty)$. This makes it hard to specify improvement criteria or to check for convergence. Skew rays may never intercept the optical axis. This means that separate code would have to be written to handle skew rays. With the transverse intercept, the range of values can be restricted, and a single code can handle skew and meridional rays by making measurements with respect to the principal rays.

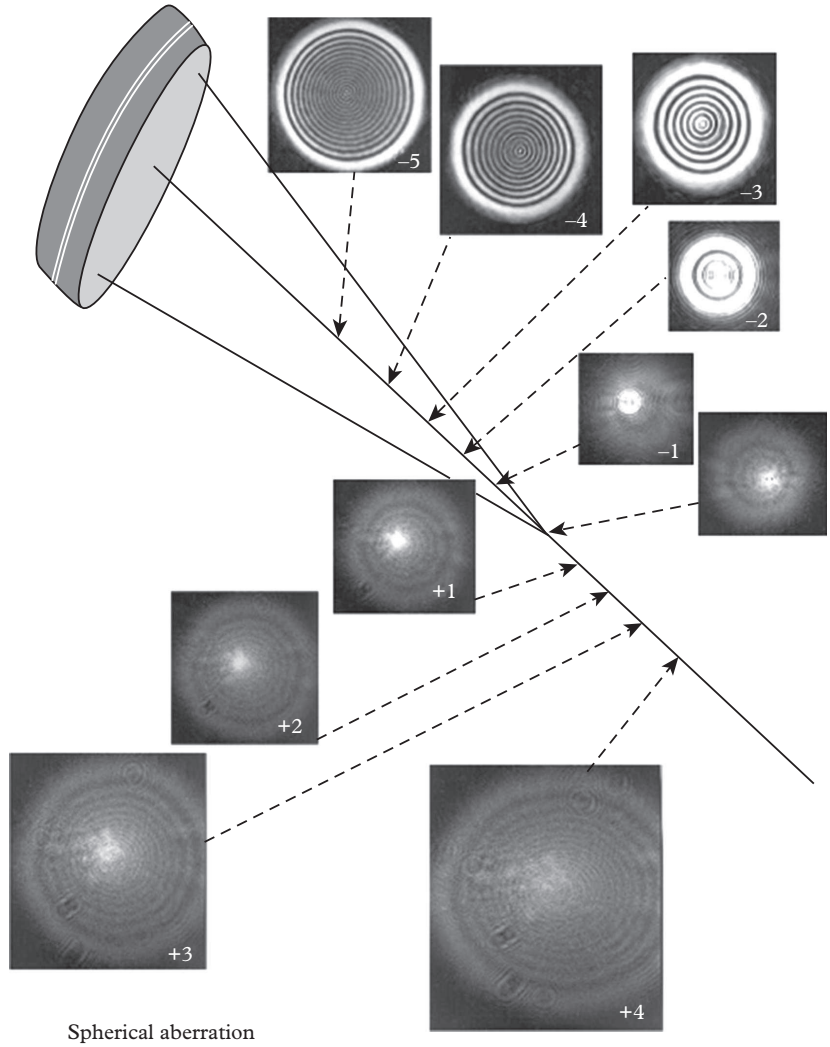

Figure 5B.8 *Images of a point source recorded in planes spaced equally on either side of the paraxial focal plane of an optical system with under corrected spherical aberration.*

5B.3 Coma

The first off–axis aberration we wish to discuss is called coma. It is associated with the terms

$$\text{wave} \leftrightarrow \{\Delta_{131}\rho^3 h\cos\theta\,, \qquad \text{Seidel} \leftrightarrow \begin{cases}\sigma_2\rho^2 h(2+\cos 2\theta),\\ \sigma_2\rho^2 h\sin 2\theta\end{cases} \tag{5B.6}$$

from (5B.2) and (5B.3). The image of a spot in the presence of coma is a comet shape (Figure 5B.11)–hence the name coma. The aberration is measured by measuring the distance between the ray intercept of the chief ray, the head of the comet, and a zonal ray in the comet tail. Physically, the magnification of the object rays passing through marginal zones differs from that of rays passing through zones near the optical axis.

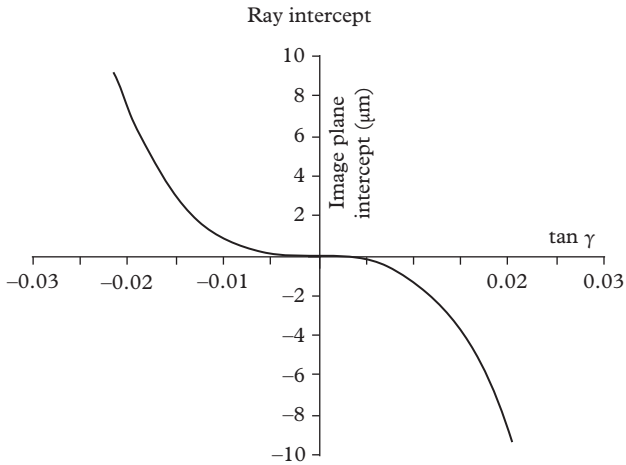

Figure 5B.9 *Ray intercept plot for a single spherical refracting surface.*

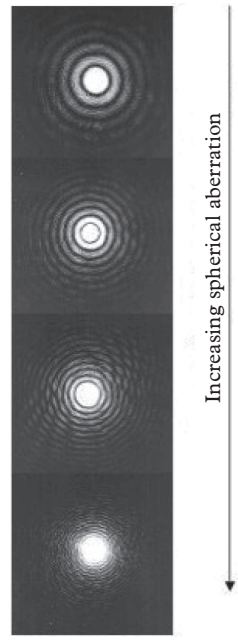

Figure 5B.10 *Images of a point source produced by an optical system with increasing amounts of spherical aberration.*

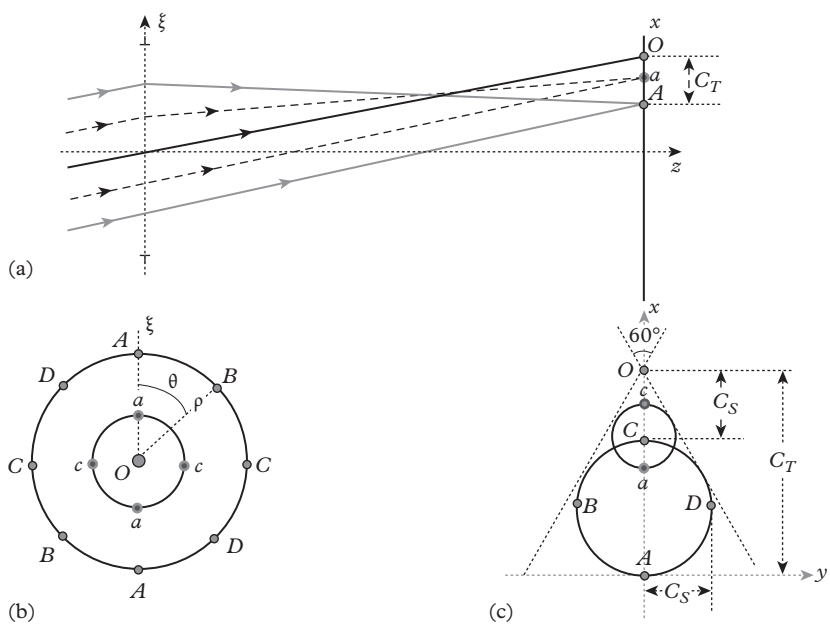

Figure 5B.11 *Coma is due to aperture zones having different magnification. (a) Off-axis rays are focused at different heights above the optical axis with these heights being proportional to the square of the zone radius; i.e., each aperture zone has a different magnification. (b) We select rays from two different zones in the exit pupil. (c) At the image plane, the tangential rays, A and a, focus at a distance C_T from the principal ray O, while the sagittal rays, C and c, focus a distance C_S from the principal ray. The envelope of the circular images created by rays passing through individual zones form a 60° wedge, which means that $C_T = 3C_S$.*

Table 5B.2 *Ray intercepts for coma*

Label	θ	Tangential	Sagittal
A	0°	$3\sigma_2^2\rho^2 h$	0
B	45°	$2\sigma_2^2\rho^2 h$	$\sigma_2^2\rho^2 h$
C	90°	$\sigma_2^2\rho^2 h$	0
D	135°	$2\sigma_2^2\rho^2 h$	$-\sigma_2^2\rho^2 h$
A	180°	$3\sigma_2^2\rho^2 h$	0

To describe the formation of the comet, we will follow several skew rays. To treat the skew rays, we decompose each ray into a sagittal component and a tangential component; the tangential component is shown in Figure 5B.11(a). Because of the change in magnification with ray height, rays passing through a marginal zone are focused at different heights above the optical axis than the chief ray, labeled O in Figure 5B.11. To generate the pattern formed by this aberration, assume that the image height h and the zone radius ρ are fixed. The fixed zone radius defines a large circle in the exit pupil shown in Figure 5B.11(b). The value of h defines the position of O in the image plane and scales the size of the comet. Table 5B.2 lists the ray intercepts in the sagittal and tangential planes for rays passing through the points labeled A, B, C, D, A. From Table 5B.2, we see that the coma is given by

$$C_T = 3\sigma_2^2\rho^2 h, \quad C_S = \sigma_2^2\rho^2 h. \tag{5B.7}$$

About 55% of the light falls in the region between O and C in Figure 5B.11, so the sagittal coma C_S is a useful measure of image quality.

5B.3.1 Optical Sine Theorem

An important relationship, discovered simultaneously in 1873 by Abbe and Helmholtz, is the *optical sine theorem*:

$$n_1 x_1 \sin\gamma_1 = n_3 x_3 \sin\gamma_3. \tag{5B.8}$$

It can be expressed in terms of the magnification of the optical system,

$$\beta = \frac{x_3}{x_1},$$

where the optical system is assumed to be in air, $n_1 = n_3 = 1$:

$$\beta = \frac{\sin\gamma_1}{\sin\gamma_3}.$$

Satisfying this *Abbe sine condition* is a necessary condition for no coma, and, if spherical aberration is absent, it is also a sufficient condition. Coma arises from a variation in the magnification with ray angle. By meeting the sine condition, i.e., by requiring the magnification of the optical system to be a constant for all ray angles, we remove comatic aberration.

Lens designers have developed a parameter to measure the departure from the sine condition, called *offense against sine condition (OSC)*. This term,

$$\text{OSC} = \frac{C_S}{h},$$

was developed to reduce the calculational load in lens design. With the advent of computers, its original rationale has disappeared, but lens designers continue to find it useful.

The optical sine theorem (5B.8) looks like a generalization of the Lagrange invariant (5A.5), but that is not completely true. The Lagrange invariant is true for all rays, but only for angles that satisfy the paraxial approximation. The optical sine theorem is true for all angles, but only for rays in the sagittal plane.

Because of the quadratic dependence of C_S on ρ, (5B.6), we would expect the ray intercept curve to be parabolic in shape. Figure 5B.12 shows a ray intercept curve for a Cooke triplet lens. In this lens design, coma is the dominant aberration, so the general shape of the curve is parabolic.

5B.3.2 Spot Diagram

Much can be learned from the general shape of the image of a point source. For this reason, a useful method of displaying aberrations is the *spot diagram*. To produce a spot diagram, a number of rays are traced through the optical system to the image plane. The intersection of these rays with the image plane is represented by small circles or squares. An example of spot diagrams produced for an optical system with coma is shown in Figure 5B.13.

Figure 5B.14 shows a set of images of a point source produced by an optical system with all off-axis aberrations other than coma minimized. The images were made with increasing amounts of coma. The modern view of an optical system utilizes the response of an optical system to a point object as the means of characterizing the system.[8] The value of the spot diagram and the images of a point source will be understood after studying Appendix 10B.

[8] The spot diagram is called the impulse response of the system, we will discuss this later.

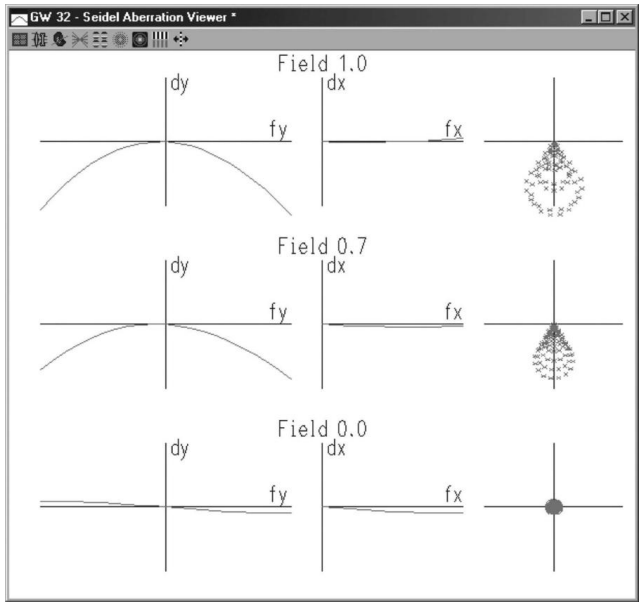

Figure 5B.12 *A ray intercept curve of a lens whose dominate aberration is coma. The spot diagrams show the amount of coma.*

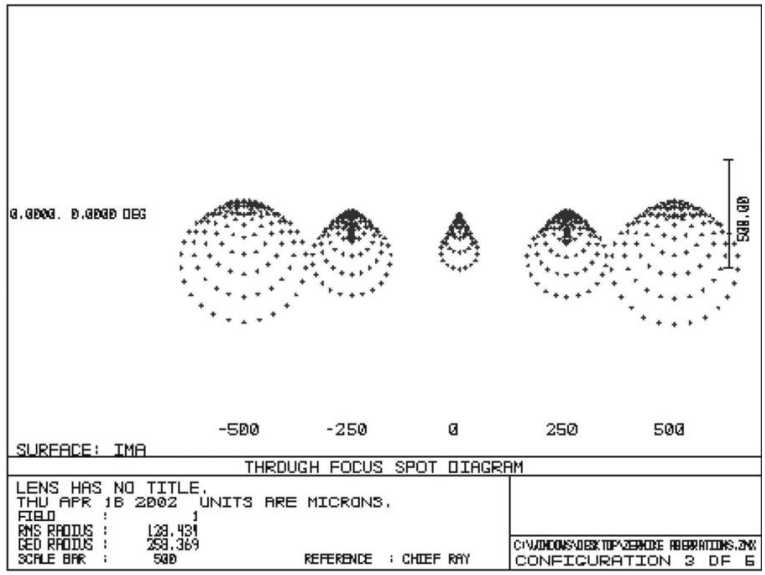

Figure 5B.13 *Spot diagrams of a lens moving through focus.*

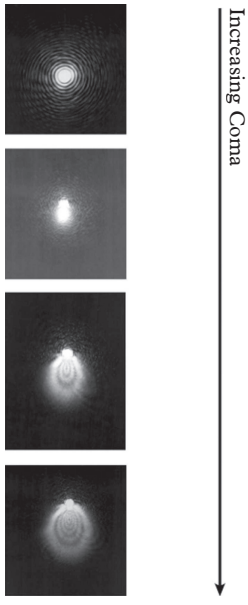

Figure 5B.14 *Images of a point source produced by an optical system with increasing amounts of coma.*

5B.4 Astigmatism

In the absence of all other aberrations, the tangential and sagittal rays from an off-axis point do not focus in the same plane. This behavior is predicted by the following terms from (5B.2) and (5B.3):

$$\text{wave} \leftrightarrow \{\Delta_{222}\rho^2 h^2 \cos^2\theta, \qquad \text{Seidel} \leftrightarrow \begin{cases} 3\sigma_3\rho h^2\cos\theta, \\ \sigma_3\rho h^2 \sin\theta. \end{cases} \tag{5B.9}$$

This aberration is due to the lens exhibiting different powers in the tangential and sagittal planes. If we look at the wavefront expansion term, we see that there is no aberration in the sagittal plane $\theta = \pi/2$, but there is a quadratic distortion of the wavefront in the tangential plane. The additional curvature brings the tangential component of the wave to a focus earlier than predicted by paraxial theory. A spherical lens with astigmatism behaves, for off-axis rays, as if a cylindrical lens were in contact with the spherical lens. Figure 5B.3 displays the focal properties of such a lens.

The rays in the tangential plane, $\theta = 0$, come to a focus in the tangential image plane, called the *tangential field.* The tangential field is defined by

$$\varepsilon_x = 0,$$
$$\varepsilon_y = \sigma_3\rho h^2.$$

The tangential rays continue on from the focus to form a line image of the point source, called the *sagittal focal line*. The sagittal focal line occurs where

$$\varepsilon_x = 3\sigma_3\rho h^2,$$
$$\varepsilon_y = 0.$$

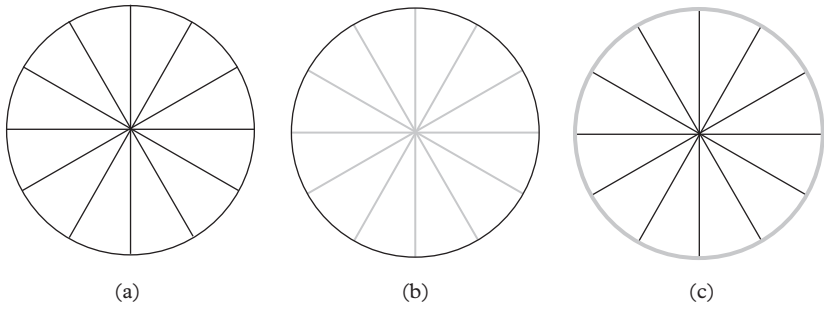

Figure 5B.15 *(a) Object to be imaged an optical system with astigmatism. (b) Image of wheel in tangential focal plane. (c) Image of wheel in sagittal focal plane.*

These relationships also define the plane where the rays in the sagittal plane $\theta = \pi/2$ come to a focus. This focal plane is called the sagittal image plane or the *sagittal field*. Before reaching their focal plane, the sagittal rays form a line image, called the *tangential focal line*. It is a little confusing when stated, but it is obvious from an examination of Figure 5B.3 that the sagittal focal line, which defines the sagittal field, lies in the tangential plane, and the tangential focal line, which defines the tangential field, lies in the sagittal plane.

Because of the axial symmetry of the optical systems, we know that the tangential plane represents an infinite number of planes about the optical axis over the angular range

$$0 \leq \theta \leq 2\pi.$$

If we place the wheel shown in Figure 5B.15(a) in the object plane of the optical system, then the image in the tangential field should have the appearance of Figure 5B.15(b). The name tangential now assumes some significance. The points along the circumference of the wheel are all associated with tangential rays and are in focus. The spokes of the wheel are normal to the circumference of the wheel and are associated with rays in the sagittal plane, which is defined as the plane normal to the tangential plane. All of the spokes are thus imaged in the sagittal field, as shown in Figure 5B.15(c).

An optical system with astigmatism produces two line images of a point source. Astigmatic images of a point source, recorded in the paraxial plane, are shown in Figure 5B.16.

A ray intercept curve is not as useful for astigmatism, because the curve only displays intercepts for rays in one plane. Instead of a ray intercept plot, the z-coordinates of the tangential and sagittal image points are plotted as functions of h. The z-coordinate is found by dividing the intercept value ε_x or ε_y by the tangent of the ray angle γ_3. The result is a pair of curves such as those shown in Figure 5B.17. The shift of the off-axis image point along the optical axis is called the *sagitta* or *sag* of the lens. The curves are parabolic in shape owing to the dependence upon h^2.

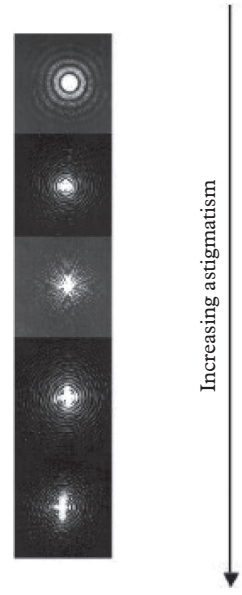

Figure 5B.16 *Images of a point source produced by an optical system with increasing amounts of astigmatism. The images were produced in the paraxial image plane.*

5B.5 Field Curvature

There is another aberration term with a functional form similar to the astigmatism aberration term:

$$\text{wave} \leftrightarrow \{\Delta_{220}\rho^2 h^2, \quad \text{Seidel} \leftrightarrow \begin{cases} \sigma_4 \rho h^2 \cos\theta, \\ \sigma_4 \rho h^2 \sin\theta. \end{cases} \tag{5B.10}$$

If we compare the wavefront expansion component associated with an image plane shift, $\Delta_{020}\rho^2$, with this wavefront aberration term, we discover that the aberration must be

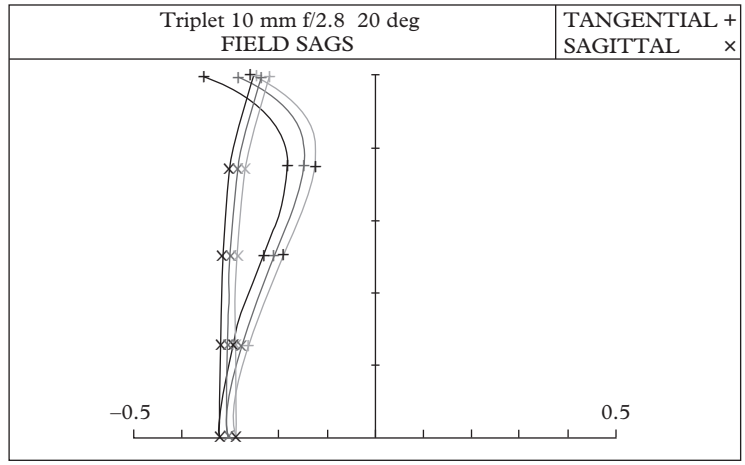

Figure 5B.17 *The field sags of a lens with astigmatism. The amounts of astigmatism for three different wavelengths are shown.*

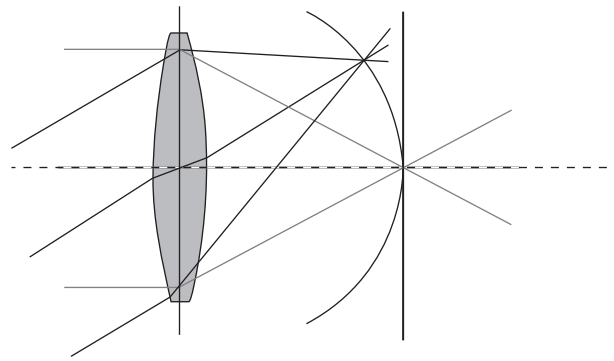

Figure 5B.18 *Field curvature. (By Ben FrantzDale (Own work) [CC-BY-SA-3.0 <http://creativecommons.org/licenses/by-sa/3.0> or GFDL <http://www.gnu.org/copyleft/fdl.html>], via Wikimedia Commons.)*

associated with an image plane shift that changes with image height as h^2; i.e., the term is associated with an image plane curvature that is parabolic. This aberration is called *field curvature* or *Petzval curvature* (Figure 5B.18).

The field curvature is measured in the same way as astigmatism, by the displacement along the optical axis of the image point as a function of the image height. If there is no astigmatism, this displacement, the sag, is given by the *Petzval sum*

$$\mathcal{H}^2 \sum_i \frac{1}{n_i f_i},$$

where $\mathcal{H}$ is the Lagrange invariant (5A.5).

Since the curvature is proportional to the sum of the powers of the optical elements, we must combine positive and negative lenses to reduce the field curvature. Often, a negative lens called a *field flattener* is placed at or near an image plane. It has little effect on image quality, but reduces the field curvature by reducing the Petzval sum.

5B.6 Distortion

The final aberration is associated with the terms

$$\text{wave} \leftrightarrow \{\Delta_{311}\rho h^3 \cos\theta\ , \qquad \text{Seidel} \leftrightarrow \begin{cases} \sigma_5 h^3, \\ 0. \end{cases} \tag{5B.11}$$

These terms are similar to the term involving a transverse displacement in focus, $\Delta_{111}h\rho\cos\theta$, introduced early in our discussion. Because it is associated with a change in image height, this shift can also be viewed as a change in magnification. The cubic dependence on h causes the magnification to increase with image height. This term thus leads to a variation in image scale over the image plane. The image in Figure 5B.19(a) displays barrel distortion.

Distortion is measured by measuring the fractional change in image position. A typical distortion plot is shown in Figure 5B.19(b) for barrel distortion.

Pincushion distortion is shown in Figure 5B.20. The distortion is easy to control because it is zero for optical systems symmetric about an aperture stop.

(a)

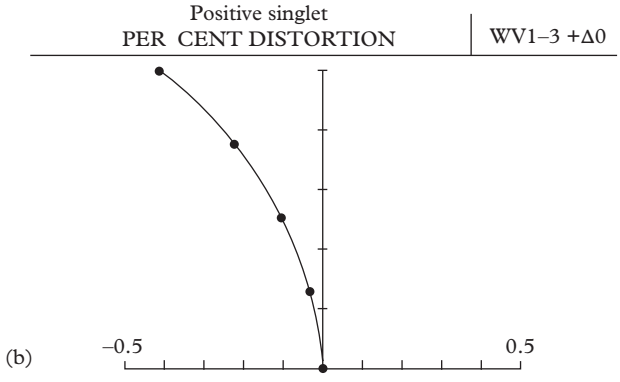

(b)

Figure 5B.19 *(a) This image displays barrel distortion, which is associated with negative distortion. (b) Distortion plot. (Image courtesy of Sean McHugh <http://www.cambridgeincolour.com/tutorials/lens-corrections.htm>.)*

(a)

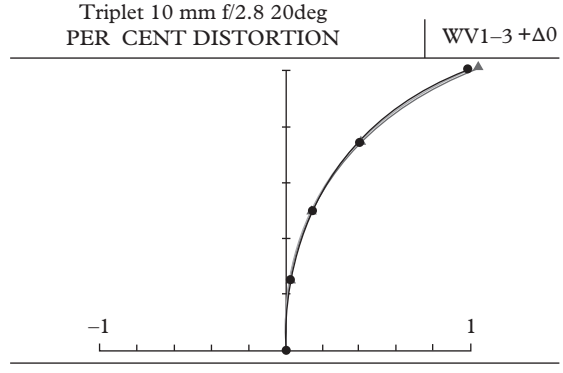

(b)

Figure 5B.20 *(a) Pincushion distortion can be seen as the edges of the walls curve outward at the top and bottom. Pincushion distortion is associated with positive distortion. (b) Distortion plot. (Image courtesy of Sean McHugh <http://www.cambridgeincolour.com/tutorials/lens-corrections.htm>.)*

5B.7 Aberration Reduction

Seldom do economic considerations allow one to design an optical system from scratch, minimizing aberrations and optimizing performance for the job to be done. What is usually done is to combine a number of off-the-shelf lenses to accomplish the desired operation. It is still possible to control the aberrations in these "store-bought" systems; to see how, we must introduce two new parameters [4]:

5B.7.1 Coddington Shape Factor

The Coddington shape factor is given by

$$\sigma = \frac{R_1 + R_2}{R_2 - R_1} = \frac{c_1 + c_2}{c_1 - c_2},$$
$$c_i = \frac{1}{R_i}.$$

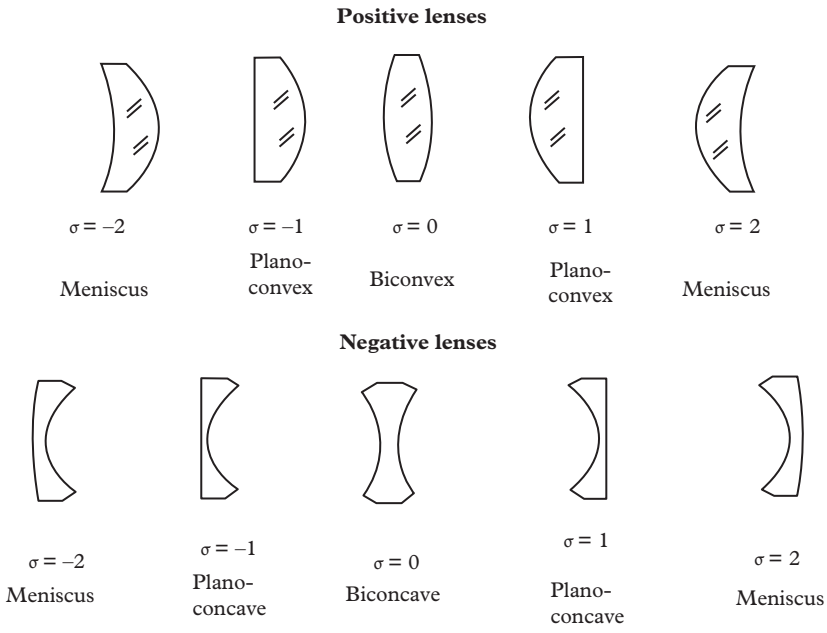

Figure 5B.21 *Coddington shape factors for a number of simple positive and negative lenses. All of the lenses have the same absolute value of power. The process of increasing or decreasing the shape factor is called bending.*

The shape factors for a number of lenses with the same absolute value of the focal length are shown in Figure 5B.21, where the positive and negative lenses each have the same power. The process of increasing or decreasing the Coddington shape factor is called *bending*. Bending is a basic tool of lens design.

5B.7.2 Coddington Position Factor

The Coddington position factor is given by

$$\pi = \frac{s' + s}{s' - s} = \frac{1 + \beta}{1 - \beta},$$

where β is the magnification. A collimating lens, with a point object at the front focal point, allowing the lens to produce a plane wave, has a position factor $\pi = +1$. A condensing lens, which focuses a plane wave to a point, has a position factor $\pi = -1$. A lens arranged to produce unit magnification, with the object positioned at $2f$ in front of the lens and the image at $2f$ behind the lens, has a position factor $\pi = 0$.

Third-order aberration theory allows coma and spherical aberration to be formulated in terms of these Coddington factors [4]. Plots of spherical aberration as a function of σ, with π as a parameter, are shown in Figure 5B.22.

The optimum shape factor for minimizing spherical aberration as a function of the position factor is

$$\sigma = \frac{2\left(n^2 - 1\right)}{n + 2}\pi.$$

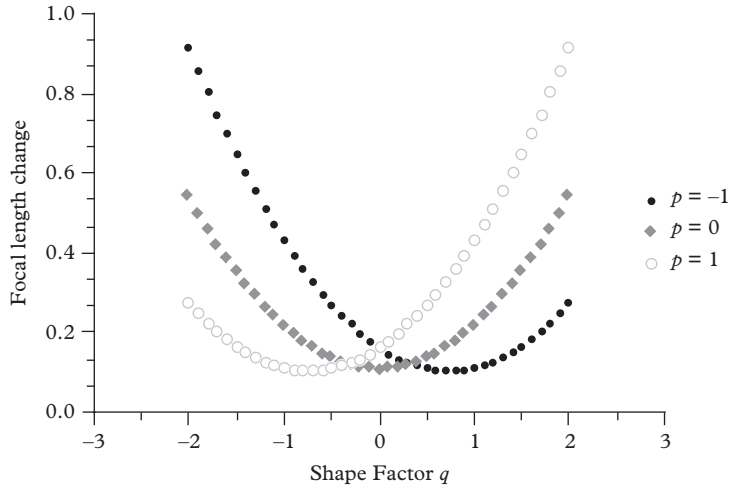

Figure 5B.22 *Longitudinal spherical aberration as a function of the Coddington shape factor for three values of the Coddington position factor.*

The minima obtained from this equation can be compared with those shown in Figure 5B.22.

For coma, third-order theory produces a linear relationship between the shape factor and the aberration. The position factor simply changes the curve's intercept. Coma is minimized whenever

$$\sigma = \frac{(2n+1)(n-1)}{n+1}\pi.$$

These results suggest that to minimize coma and spherical aberration, we need only purchase lenses with the shape factor dictated by the imaging job to be done. This is true—but we could quickly go broke trying to buy lenses for every new imaging configuration!

A solution to our problem is to perform *lens splitting*. The concept is shown in Figure 5B.23. Assume that in the laboratory we wish to transfer an image from one point to another, without a change in magnification. From the curves in Figure 5B.22, we would

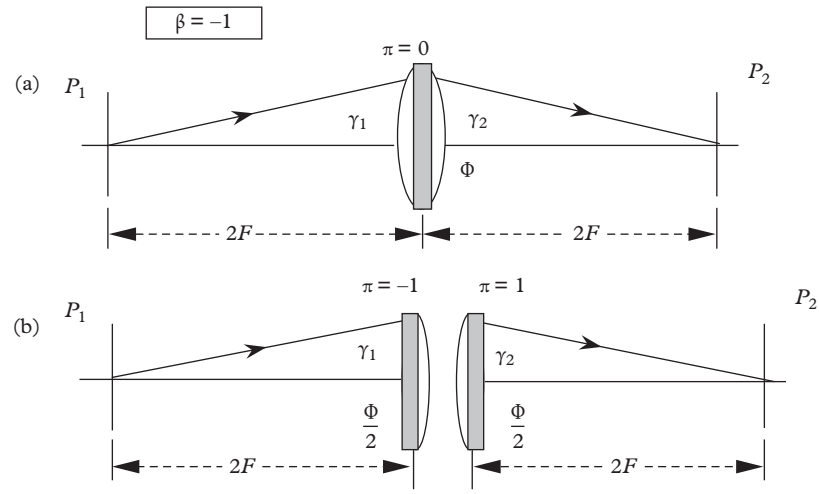

Figure 5B.23 *The use of lens splitting to reduce aberrations in a lens system.*

select a biconvex lens with a power to allow the transfer over the distance $4F$. If we split the lens into two lenses with half the power, we still accomplish the desired task.

No matter what magnification β we desire, we will benefit if we split a lens. We will add an additional restriction to the splitting procedure. We require the position parameter, after splitting, to be

$$|\pi| = 1.$$

By making this restriction, we reduce the number of lens shapes needed to only one, a planoconvex lens. This is because the minimum of that position parameter is, from Figure 5B.22, ± 0.8, which is close enough to 1 for most applications. With this added restriction, we find that the powers of the split lenses are given by

$$\Phi_1 = \frac{\beta\Phi}{\beta - 1}, \quad \Phi_2 = \frac{\Phi}{\beta - 1}.$$

The splitting procedure provides a number of benefits:

1. The relative apertures of the lenses have been reduced by a factor of 2. This reduces spherical aberration, coma, astigmatism, and curvature of field.
2. Spherical aberration and coma have been minimized by using the best lens shapes.
3. The numbers of lenses we must have in our stock has been reduced. Now we need purchase only planoconvex lenses.

REFERENCES

1. Born, M. and E. Wolf, *Principles of Optics*. 7th ed. 1999: Cambridge University Press.
2. Welford, W.T., *Aberrations of the Symmetrical Optical System*. 1974: Academic Press.
3. Nussbaum, A. and R.A. Phillips, *Contemporary Optics for Scientists and Engineers*. 1976: Prentice-Hall.
4. Klein, M.V. and T.E. Furtak, *Optics*. 2nd ed. 1986: Wiley.

6

Fourier Analysis

6.1 Introduction 214
6.2 Fourier Series 215
6.3 Periodic Square Wave 219
6.4 The Fourier Integral 222
6.5 Rectangular Pulse 225
6.6 Pulse Modulation Wave Trains 227
6.7 Dirac Delta Function 230
6.8 Replication and Sampling 234
6.9 Correlation 237
6.10 Convolution Integrals 239
6.11 Linear System Theory 242
6.12 Fourier Transforms in Two Dimensions 244
6.13 Summary 246
6.14 Problems 249
References 251
Appendix 6A: Fourier Transform Properties 252

6.1 Introduction

In the foregoing theoretical development of light, we have assumed that only one frequency of light was present. In nature, this never occurs, and therefore we need to expand our discussion to allow for multiple frequencies. We will introduce several mathematical techniques in this chapter that will help in handling multiple frequencies. The techniques we will discuss were developed by **Jean Baptiste Joseph, Baron de Fourier (1768–1830)**. (The technique was developed to aid Fourier in the solution of heat flow problems. His first paper on the subject was rejected because Lagrange did not believe the series would converge. In the eighteenth century, mathematicians did not consider it possible that a function could contain an infinite series of terms. The approach presented by Fourier required a major modification in the thinking of mathematicians. Fourier did not discover any of the principal results of the theory that bears his name. Dirichlet was one of the key contributors to the development of the theory, establishing some of the convergence criteria for the series.) The Fourier theory states that a Fourier series, a sum of sinusoidal functions, can be used to describe any periodic functions and that the Fourier transform, an integral transform, can be used to describe aperiodic functions [1].

Our discussions concerning light waves have also been limited to plane wavefronts. We will learn in later chapters that the Fourier theory, developed to handle multiple frequencies, can be used to describe an arbitrary wavefront in terms of combinations of plane waves. The mathematical techniques for handling multiple frequencies and arbitrary wavefronts, based on the Fourier theory, form the foundations of the modern approach to physical optics. Applications of the Fourier theory will be found in Chapter 8 in the discussions concerning coherence and in Chapter 10 in the discussions concerning diffraction.

The Fourier theory allows the representation of a function in terms of its frequency or of its temporal characteristics and to easily move between the two representations. The ability to move from a temporal to a frequency representation, and back, provided by the Fourier theory, allow the theory of optics to be developed using single frequencies and simple waveforms. The resultant theory can then be applied to more general waves through application of the Fourier series or transform.

In this chapter, we will first discuss the Fourier series for the representation of periodic functions and then introduce the Fourier transform, as an extension of the series, to handle aperiodic functions. The use of a Fourier series to describe a square wave is discussed, as is the use of a Fourier transform to describe a sinusoidal wave of finite duration.

The measurement process used to obtain information about continuous functions found in nature is accomplished by making discrete measurements (called samples) of the functions. The development of the Fourier theory presents the opportunity to justify the experimental approach, by examining the processes of replication and sampling. The opportunity to discuss this important concept is taken in this chapter, even though the theory will not be directly applied in this book.

In the mid 1940s, the concepts developed for electrical communication systems based on linear system theory, and dependent upon the use of the Fourier method, were introduced

Modern Optics. Second Edition. B. D. Guenther.

© B. D. Guenther 2015. Published in 2015 by Oxford University Press.

by **P.M. Duffieux** [2, 3] and **R.K. Luneberg** [4] for analysis of optical imaging systems. In this chapter, the concepts of impulse response (also called the Green's function) and convolution integrals are introduced, and their use in the description of a linear system operating on an arbitrary input is discussed. The linear system approach to optics will be associated with the Fresnel formulation of diffraction in Chapters 9 and 10. This approach to optics has resulted in the development of the application of optical signal processing (Appendix 10B) and has led to many of the advances in the area of medical imaging.

The mathematical concepts and examples in this chapter will often be presented without immediate association with the physical observations that require their use. The physical observations will be introduced in later chapters after the development of the mathematical tools.

6.2 Fourier Series

We wish to examine the use of a trigonometric expansion of sine and cosine functions called the Fourier series to describe periodic functions. The possibility of such an expansion was known to Euler, but it was not until the derivation and use of the expansion by Fourier that its usefulness was recognized.

The Fourier theorem as stated and proved by Dirichlet is as follows:

> *If a function $f(t)$ is periodic, has a finite number of points of ordinary discontinuity, and has a finite number of maxima and minima in the interval representing the period, then the function can be represented by a Fourier series*

$$f(t) = \frac{a_0}{2} + \sum_{\ell=1}^{\infty} a_\ell \cos \ell\omega t + \sum_{\ell=1}^{\infty} b_\ell \sin \ell\omega t. \tag{6.1}$$

The requirements on the function are all met by physically realizable functions.

We will not prove the theorem, but simply show that it is plausible by proving that the right-hand side of (6.1) is periodic. We have required the left-hand side, $f(t)$, to be periodic, i.e., $f(t) = f(t + T)$, where $T = 2\pi/\omega$. For the equality to hold, the right-hand side must also be periodic:

$$\frac{a_0}{2} + \sum_{\ell=1}^{\infty} a_\ell \cos \ell\omega t + \sum_{\ell=1}^{\infty} b_\ell \sin \ell\omega t = \frac{a_0}{2} + \sum_{\ell=1}^{\infty} a_\ell \cos \ell\omega(t + T) + \sum_{\ell=1}^{\infty} b_\ell \sin \ell\omega(t + T).$$

For all values of ℓ, we must have

$$a_\ell \cos \ell\omega t = a_\ell \cos(\ell\omega t + 2\pi\ell),$$
$$b_\ell \sin \ell\omega t = b_\ell \sin(\ell\omega t + 2\pi\ell),$$

which are true if ℓ is an integer.

Examination of (6.1) shows that the expansion is in terms of sine and cosine functions that are harmonics of the frequency $\omega = 2\pi/T$, where T is the period of the periodic function $f(t)$. Each harmonic ℓ of the fundamental frequency ω is multiplied by a coefficient, and the task of applying the Fourier theorem reduces to the problem of finding the coefficients a_ℓ and b_ℓ. The steps needed to derive the expressions for the coefficients are quite simple, as are the resulting equations for determining the coefficients. We will derive the expressions used to determine the coefficients of the harmonics making up the Fourier series and discuss two special cases that result in a short cut in applying the Fourier series to certain classes of functions.

6.2.1 DC Term

The coefficient associated with $\ell = 0$ is called the *DC term* because it is associated with zero frequency.[1] To determine the constant a_0, we integrate both sides of (6.1) with respect to time over one period ($-\pi/\omega < t < \pi/\omega$):

$$\int_{-\pi/\omega}^{\pi/\omega} f(t)\, dt = \int_{-\pi/\omega}^{\pi/\omega} \frac{a_0}{2}\, dt + \sum_{\ell=1}^{\infty} \int_{-\pi/\omega}^{\pi/\omega} a_\ell \cos \ell\omega t\, dt + \sum_{\ell=1}^{\infty} \int_{-\pi/\omega}^{\pi/\omega} b_\ell \sin \ell\omega t\, dt.$$

The integral of a sine or a cosine function over one period is zero, and thus

$$a_0 = \frac{\omega}{\pi} \int_{-\pi/\omega}^{\pi/\omega} f(t)dt. \tag{6.2}$$

We see that a_0 is the average value of $f(t)$ over one period. If $f(t)$ is symmetric about the abscissa, then $a_0 = 0$.

6.2.2 Cosine Series

To obtain the coefficients of the cosine series, a_ℓ, we multiply both sides of (6.1) by $\cos n\omega t$, where n represents a preselected harmonic of the series, and integrate:

$$\int_{-\pi/\omega}^{\pi/\omega} \mathrm{f}(t) \cos n\omega t\, dt = \int_{-\pi/\omega}^{\pi/\omega} \frac{a_0}{2} \cos n\omega t\, dt + \sum_{\ell=1}^{\infty} \int_{-\pi/\omega}^{\pi/\omega} a_\ell \cos \ell\omega t \cos n\omega t\, dt + \sum_{\ell=1}^{\infty} \int_{-\pi/\omega}^{\pi/\omega} b_\ell \sin \ell\omega t \cos n\omega t\, dt.$$

We now use the trigonometric identities

$$\cos(\ell\omega t)\cos(n\omega t) = \frac{1}{2}[\cos(\ell + n)\omega t + \cos(\ell - n)\omega t],$$
$$\sin(\ell\omega t)\cos(n\omega t) = \frac{1}{2}[\sin(\ell + n)\omega t + \sin(\ell - n)\omega t]$$

to evaluate the two summations. The first summation contains terms of the form

$$\int_{-\pi/\omega}^{\pi/\omega} a_\ell \cos \ell\omega t \cos n\omega t\, dt = \frac{1}{2} \int_{-\pi/\omega}^{\pi/\omega} a_\ell \cos(\ell + n)\omega t\, dt + \frac{1}{2} \int_{-\pi/\omega}^{\pi/\omega} a_\ell \cos(\ell - n)\omega t\, dt.$$

When $\ell \neq n$, both of the integrals are zero (see Problem 6.14). When $\ell = n$, the first integral is zero, but the second integral is $(\pi/\omega)a_n$. The second summation contains terms of the form

$$\int_{-\pi/\omega}^{\pi/\omega} a_\ell \sin \ell\omega t \cos n\omega t\, dt = \frac{1}{2} \int_{-\pi/\omega}^{\pi/\omega} a_\ell \sin(\ell + n)\omega t\, dt + \frac{1}{2} \int_{-\pi/\omega}^{\pi/\omega} a_\ell \sin(\ell - n)\omega t\, dt,$$

[1] There is no b_0 coefficient, because the sine of zero frequency is zero.

which are zero for all values of ℓ. (The fact that the integrals involving sines and cosines are zero except when $\ell = n$ defines a property of sinusoids known as orthogonality.) Therefore

$$\int_{-\pi/\omega}^{\pi/\omega} f(t)\cos n\omega t\, dt = \frac{1}{2}\int_{-\pi/\omega}^{\pi/\omega} a_n\, dt = \frac{\pi a_n}{\omega}.$$

The coefficients of the cosine series are obtained by using the integral

$$a_n = \frac{\omega}{\pi}\int_{-\pi/\omega}^{\pi/\omega} f(t)\cos n\omega t\, dt. \tag{6.3}$$

6.2.3 Sine Series

An integral similar to (6.3) can be derived for the coefficients b_ℓ of the sine series if we multiply both sides of (6.1) by $\sin n\omega t$ and make use of the identity

$$\sin(\ell\omega t)\cdot\sin(n\omega t) = \frac{1}{2}[\cos(\ell - n)\omega t - \cos(\ell + n)\omega t].$$

We find that the coefficients of the sine series are given by

$$b_n = \frac{\omega}{\pi}\int_{-\pi/\omega}^{\pi/\omega} f(t)\sin n\omega t\, dt. \tag{6.4}$$

The equations for the Fourier coefficients, (6.3) and (6.4), are sometimes called Euler's formulas, in recognition of Euler's early involvement with the expansion.

6.2.4 Even and Odd Functions

The sine and cosine series can individually be used to represent certain classes of functions. For example, suppose f is an even function,

$$f(t) = f(-t),$$

then $f(t)$ can be represented by a series of cosines (a_0 is included in this series as the coefficient of cos 0). This occurs because the integral over one period, about zero (from $-\pi/\omega$ to π/ω), of an even function is nonzero, but the integral of an odd function over the same interval is zero (see Problem 6.15). Using this fact, we can determine that (6.4) will be zero whenever $f(t)$ is an even function. [To understand why (6.4) is zero for an even function, remember that the sine is an odd function and that the product of an odd function and an even function is an odd function.]

If $f(t)$ is an odd function,

$$f(t) = -f(-t),$$

then it can be represented by a series of sine terms. If $f(t)$ is neither odd nor even [e.g., $f(t) = e^t$] then both the sine and cosine series are required.

6.2.5 Exponential Representation

The representation of the Fourier series given in (6.1) is convenient for analyzing real functions, but for extending our discussion to Fourier transforms, we will find it useful to express the Fourier series as an exponential series.

The first step in reformulating the Fourier series is to use the identities

$$\cos \ell\omega t = \frac{1}{2}(e^{i\ell\omega t} + e^{-i\ell\omega t}),$$
$$\sin \ell\omega t = -\frac{1}{2}i(e^{i\ell\omega t} - e^{-i\ell\omega t})$$

to rewrite (6.1) in complex notation as

$$f(t) = \frac{a_0}{2} + \frac{1}{2}\sum_{\ell=1}^{\infty}(a_\ell - ib_\ell)e^{i\ell\omega t} + \frac{1}{2}\sum_{\ell=1}^{\infty}(a_\ell + ib_\ell)e^{-i\ell\omega t}, \tag{6.5}$$

where the coefficients in the summations are given by

$$\alpha_{\mp\ell} = a_\ell \pm ib_\ell = \frac{\omega}{\pi}\int_{-\pi/\omega}^{\pi/\omega} f(t)(\cos \ell\omega t \pm i \sin \ell\omega t)\, dt,$$
$$= \frac{\omega}{\pi}\int_{-\pi/\omega}^{\pi/\omega} f(t)e^{\pm i\ell\omega t}\, dt.$$

This allows (6.5) to be rewritten as a summation over positive and negative values of ℓ:

$$f(t) = \sum_{\ell=-\infty}^{\infty} \alpha_\ell e^{i\ell\omega t}. \tag{6.6}$$

where

$$\alpha_\ell = \frac{\omega}{2\pi}\int_{-\pi/\omega}^{\pi/\omega} f(t)e^{-i\ell\omega t}\, dt. \tag{6.7}$$

We can establish some general properties of α_ℓ given by (6.7) by replacing t by $-t$:

$$\alpha_\ell = \frac{\omega}{2\pi}\int_{-\pi/\omega}^{\pi/\omega} f(-t)e^{i\ell\omega t}\, dt.$$

Since $f(-t) = f(t)$ for an even function and $f(-t) = -f(t)$ for an odd function, we can make the following statement about the coefficients:

$$\begin{aligned}
\alpha_\ell &= \alpha_{-\ell}, && f(t) \text{ even},\\
\alpha_\ell &= -\alpha_{-\ell}, && f(t) \text{ odd},\\
\alpha_\ell &\neq \alpha_{-\ell}, && f(t) \text{ neither odd nor even},\\
\alpha\text{'s complex}, && && f(t) \text{ neither odd nor even}.
\end{aligned}$$

6.3 Periodic Square Wave

As an example of how the Fourier series is applied, we will evaluate the function

$$f(t) = \begin{cases} 1, & -T/k \le t \le T/k, \\ 0, & T/k \le t \le T - T/k. \end{cases} \tag{6.8}$$

The graphical representation of (6.8), shown in Figure 6.1, consists of a periodic array of rectangular pulses called a square wave. The process of calculating the Fourier coefficients of the square wave is called *harmonic analysis.*

The coefficients of the Fourier series in exponential form are given by

$$\alpha_\ell = \frac{1}{T} \int_{-T/k}^{T/k} e^{-i\ell\omega t}\, dt.$$

For $\ell \neq 0$, we have

$$\alpha_\ell = -\frac{1}{2\pi\ell i}\left(e^{-i\ell(2\pi/k)} - e^{i\ell(2\pi/k)}\right) = \frac{2}{k}\,\frac{\sin(2\pi\ell/k)}{2\pi\ell/k}. \tag{6.9}$$

For α_0, the integral is

$$\alpha_0 = \frac{1}{T}\int_{-T/k}^{T/k} dt = \frac{1}{T}\left(\frac{T}{k} + \frac{T}{k}\right) = \frac{2}{k}. \tag{6.10}$$

As an example let $k = 4$. The Fourier series is given by

$$f(t) = \frac{1}{2} + 2\left(\frac{\cos\omega t}{\pi} - \frac{\cos 3\omega t}{3\pi} + \frac{\cos 5\omega t}{5\pi} - \cdots\right),$$

where we have combined the positive and negative exponents of (6.6) in order to express the expansion in terms of cosine functions. As you can see in Figure 6.1, the square wave defined by (6.8) is an even function; from our previous comments concerning even and odd functions, we are not surprised to find that the Fourier series is a cosine series.

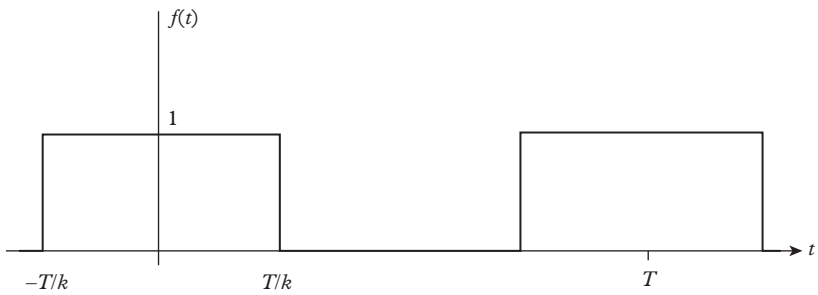

Figure 6.1 *Generalized square wave, where k is a constant. The duration of the square wave is inversely related to the size of k.*

One of the mathematical dividends provided by the Fourier series is that it can be used to evaluate infinite series. While it does not impact our study of optics, it is interesting to see an example of this application of Fourier series. We demonstrate this use of the Fourier series by evaluating the square wave at $t = 0$ in Figure 6.1 to obtain

$$f(0) = 1 = \frac{1}{2} + 2\left(\frac{1}{\pi} - \frac{1}{3\pi} + \frac{1}{5\pi} - \frac{1}{7\pi} + \cdots\right).$$

By rewriting this relationship, we obtain the sum of Gregory's series, a method of calculating π:

$$\frac{\pi}{4} = 1 - \frac{1}{3} + \frac{1}{5} - \frac{1}{7} + \cdots .$$

In Figure 6.2 we plot the Fourier series for f(t) with the series terminated at $\ell = 1, 3, 5,$ and 7. Each additional term adds another odd harmonic to the previous estimate of the function. As we include more and more terms, the series becomes a better approximation of the square wave we are attempting to represent.

Increasing the value of k in Figure 6.1 is equivalent to increasing the period of the square wave. If we think of each positive-going part of $f(t)$ in Figure 6.1 as a pulse, then the width of the pulse decreases as k increases, and the time between pulses increases. We can easily calculate the coefficients of the harmonics for three examples of square waves with $k = 4$, 8, and 16. The results of the calculation are shown in Table 6.1.

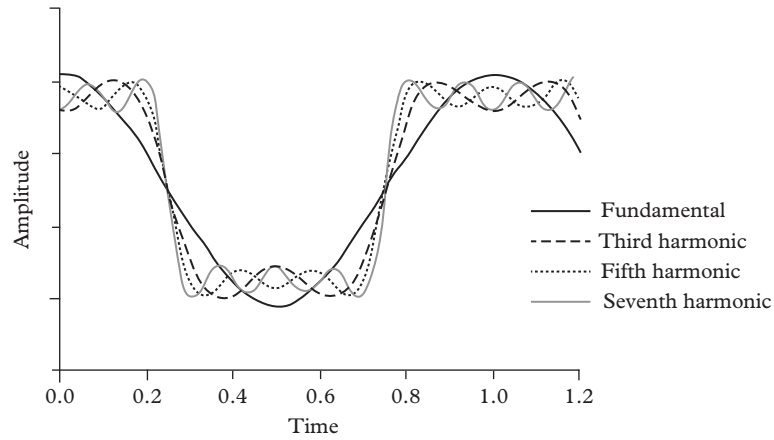

Figure 6.2 *The Fourier series approximation of a square wave with the series terminated after the fundamental, third, fifth, and seventh harmonics.*

Table 6.1 *Fourier coefficients for a square wave*

k	α_0	α_1	α_2	α_3	α_4	α_5	α_6	α_7	α_8
4	0.5	0.318	0	–0.106	0	0.064	0	–0.045	0
8	0.25	0.225	0.159	0.075	0	–0.045	–0.053	–0.032	0
16	0.125	0.122	0.113	0.098	0.080	0.059	0.038	0.017	0

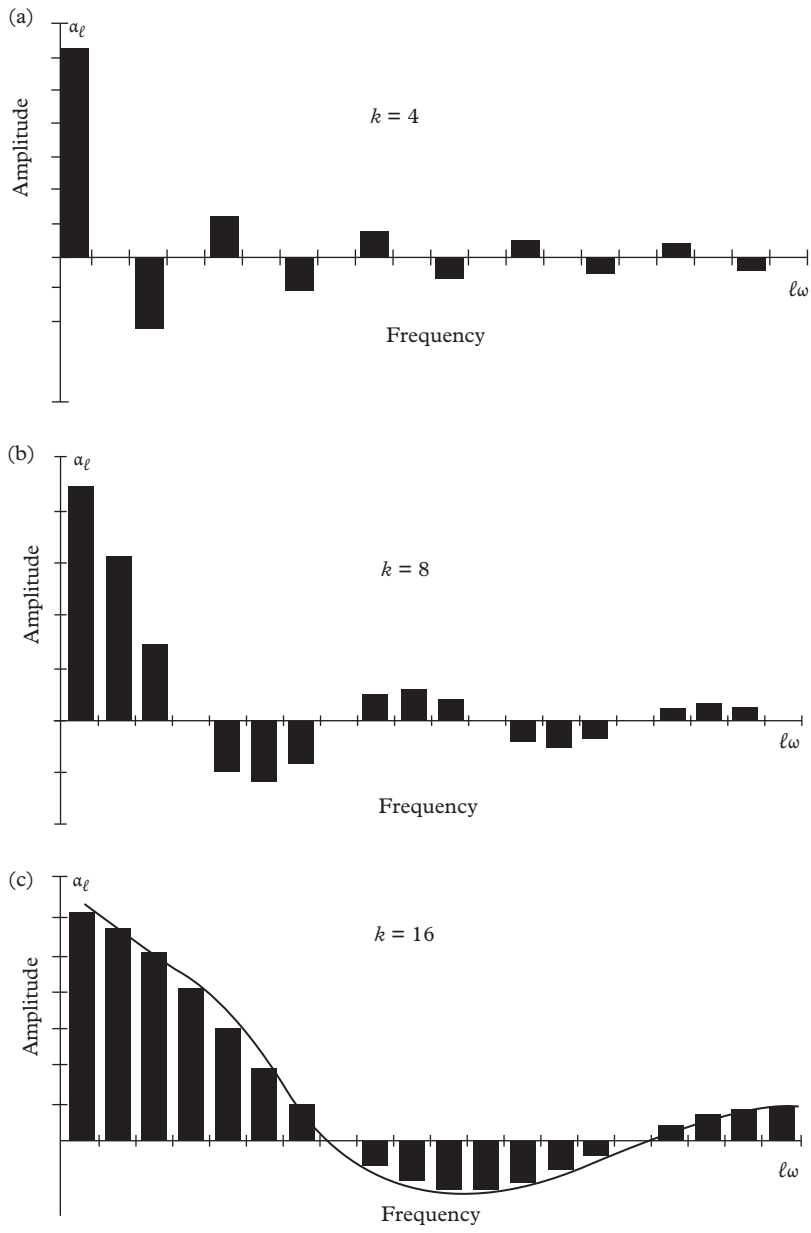

Figure 6.3 *Frequency spectrum of a square wave. (a) The coefficients of the Fourier series of a square wave of width T|2. (b) Coefficients of the Fourier series of a square wave of width T|4. (c) Coefficients of the Fourier series of a square wave of width T|8. The line traced over the histogram is only to aid the eye in seeing the general shape determined by the histogram.*

A convenient way of displaying these results is to plot the size of the coefficients α_ℓ as a function of $\ell\omega$. This plot is called the *frequency spectrum* and is shown in Figure 6.3. Each spectrum displays the coefficients, i.e., the amplitudes, of each of the harmonic waves in the Fourier series of a square wave with different values of k.

The discrete spectra in Figure 6.3 are symmetric about zero because $f(t)$ is symmetric. For this reason, we only display the positive values of ℓ, i.e., $\ell > 0$.

As we decrease the width of the square pulse, i.e., increase the value of k, there is the suggestion in Figure 6.3(c) that a smooth curve could be drawn through the α's. Upon examining the interval between zero frequency and the frequency of the first occurrence of a zero coefficient, we find that the number of coefficients contained in this interval increases as the width of the pulse decreases. If we measure the position of the first zero coefficient in terms of the harmonic ℓ associated with the zero, we see that the frequency $\ell\omega$ at which the zero occurs increases as the width of the pulse decreases. We will find this reciprocal relationship between frequency and time is a fundamental property of Fourier series and transforms and will be repeatedly encountered both in mathematics and optics.

6.4 The Fourier Integral

In the discussion of Fourier series, we have required that $f(t)$ be periodic. We now wish to expand the theory to handle aperiodic functions. We can apply a Fourier expansion to aperiodic functions by recognizing that a aperiodic function is really a periodic function whose period is infinite. Allowing the period of a periodic function to approach infinity is an extrapolation of the procedure used to generate Figure 6.3; i.e., k increases until the width of the pulse is an infinitesimal fraction of the period T. Since $\omega = 2\pi/T$, we have $\omega \to 0$ as $T \to \infty$, and in the limit as the fundamental frequency approaches zero, the summation over discrete harmonics of the fundamental frequency becomes a definite integral over a continuous distribution of frequencies.

In taking the limit, we first define the fundamental frequency as $\Delta\omega$ and rewrite (6.6) in terms of the frequency $\Delta\omega$:

$$f(t) = f\left(t + \frac{2\pi}{\Delta\omega}\right) = \frac{1}{2\pi}\sum_{\ell=-\infty}^{\infty}\left[\int_{-\pi/\Delta\omega}^{\pi/\Delta\omega} f(t)e^{-i\ell\Delta\omega t}dt\right]e^{i\ell\Delta\omega t}\Delta\omega. \tag{6.11}$$

The limit is now taken as $\Delta\omega \to 0$. The harmonics making up the distribution become infinitely close to one another, and, in the limit, we replace the discrete set of harmonics with a continuous function:

$$\lim_{\Delta\omega\to 0}(\ell\Delta\omega) = \omega.$$

Also, as the limit is taken, the period approaches infinity:

$$\lim_{\Delta\omega\to 0} T = \lim_{\Delta\omega\to 0}\left(\pm\frac{\pi}{\Delta\omega}\right) = \pm\infty.$$

Taking the limit of (6.11) gives

$$f(t) = \frac{1}{2\pi}\int_{-\infty}^{\infty}\int_{-\infty}^{\infty} f(\tau)e^{i\omega(t-\tau)}\,d\tau\,d\omega. \tag{6.12}$$

We define the function $F(\omega)$ as the *Fourier transform* of $f(t)$:

$$\mathcal{F}\{f(t)\} \equiv F(\omega) \equiv \int_{-\infty}^{\infty} f(\tau)e^{-i\omega\tau}\, d\tau. \tag{6.13}$$

The transformation from a temporal to a frequency representation given by (6.13) does not destroy information; thus, the inverse transform can also be defined by simply substituting the definition (6.13) into (6.12):

$$\mathcal{F}^{-1}\{F(\omega)\} = f(t) = \frac{1}{2\pi}\int_{-\infty}^{\infty} F(\omega)e^{i\omega t}\, d\omega. \tag{6.14}$$

[$f(t)$ and $F(\omega)$ are called a Fourier transform pair and will be denoted by lower and upper case letters.] The aperiodic function $f(t)$ is represented by an infinite number of sinusoidal functions with angular frequencies infinitely close together. $F(\omega)$ measures the spectral density, i.e., the fractional contribution of frequency ω to the representation of the function. The absolute value of $F(\omega)$ is called the spectrum of the function $f(t)$.

Slightly different definitions of the Fourier transform are found in the literature. Sometimes, the transform (6.13) and its inverse (6.14) are defined symmetrically as

$$\mathcal{F}\{f(t)\} = F(\omega) = \frac{1}{\sqrt{2\pi}}\int_{-\infty}^{\infty} f(\tau)e^{-i\omega\tau}\, d\tau,$$

$$\mathcal{F}^{-1}\{F(\omega)\} = f(t) = \frac{1}{\sqrt{2\pi}}\int_{-\infty}^{\infty} F(\omega)e^{i\omega t}\, d\omega.$$

Sometimes the constant factors

$$\frac{1}{\sqrt{2\pi}}$$

are absent and the integrals are expressed in terms of ν rather than $\omega(=2\pi\nu)$. Sometimes, the positive and negative exponentials in (6.13) and (6.14) are interchanged. The definition one selects is somewhat arbitrary.

We have written the relationships using time and frequency, but we could replace time by a space variable, say x. The transform or conjugate variable must have reciprocal units; thus, when a space variable is used, the conjugate units would be "distance" and its reciprocal, 1/"distance". The conjugate variable to the space variable is called *spatial frequency* and in optics is the propagation constant **k**. Another example of conjugate variables is the periodic lattice and the reciprocal lattice that are the members of a three-dimensional Fourier transform pair used in crystallography (see Figure 12.20).

6.4.1 Dirichlet Conditions

There are validity conditions, called Dirichlet conditions, placed on $f(t)$ for $F(\omega)$ to exist. These are the same conditions we placed of $f(t)$ for the Fourier series to exist. They state that $f(t)$ must

(a) be single-valued;

(b) have a finite number of maxima and minima in any finite interval;

(c) have a finite number of finite discontinuities but no infinite discontinuities in any finite interval;

(d) lead to a finite frequency spectrum,

$$\int_{-\infty}^{\infty} f(\tau)e^{-i\omega\tau}\, d\tau < \infty.$$

The approach we have used to obtain the Fourier transform would not be satisfactory to a mathematician. It would be more correct to consider the Fourier series as a special case of the Fourier transform. In this case, the validity conditions for the series follow naturally from a statement of the conditions for the transform.

These conditions are met by all physically occurring functions, but not by such useful functions as constants and periodic functions. Techniques involving the use of limits allow these useful functions to be included. The difficulty also disappears when the theory of generalized functions (distributions) is used [5]. (We will discuss an example of a generalized function, the Dirac delta function, later in this chapter.)

6.4.2 Evaluation of the Fourier Transform

It is not immediately obvious how the Fourier transform defined by (6.13) is to be calculated. By expressing the transform in terms of its real and imaginary components, we see that

$$F(\omega) = \int_{-\infty}^{\infty} f(\tau)\cos\omega\tau\, d\tau - i\int_{-\infty}^{\infty} f(\tau)\sin\omega\tau\, d\tau.$$

If $f(\tau)$ is a real function, then the Fourier transform can be obtained by calculating the *cosine transform*

$$\int_{-\infty}^{\infty} f(\tau)\cos\omega\tau\, d\tau \tag{6.15a}$$

and the *sine transform*

$$\int_{-\infty}^{\infty} f(\tau)\sin\omega\tau\, d\tau. \tag{6.15b}$$

The real function $f(t)$ can be written as the sum of an even and an odd function:

$$f(t) = f_e(t) + f_o(t),$$

where

$$\underbrace{f_e(t) = \frac{1}{2}[f(t) + f(-t)]}_{\text{even function}},$$

$$\underbrace{f_o(t) = \frac{1}{2}[f(t) - f(-t)]}_{\text{odd function}}.$$

If $f(\tau)$ is even, we need only calculate the cosine transform (6.15a). In general, the Fourier transform of a real function is a complex function

$$\mathcal{F}\{f(t)\} = F(\omega) = \underbrace{\int_{-\infty}^{\infty} f_e(t)\cos\omega t\ dt}_{F_e(\omega)} - i\underbrace{\int_{-\infty}^{\infty} f_o(t)\sin\omega t\ dt}_{F_o(\omega)}.$$

If $f(\tau)$ is complex, it can be expressed as $f(\tau) = \eta(\tau) + i\xi(\tau)$, and the Fourier transform is

$$F(\omega) = \int_{-\infty}^{\infty} \eta(\tau)\cos\omega\tau\ d\tau + \int_{-\infty}^{\infty} \xi(\tau)\sin\omega\tau\ d\tau - i\left[\int_{-\infty}^{\infty} \xi(\tau)\cos\omega\tau\ d\tau - \int_{-\infty}^{\infty} \eta(\tau)\sin\omega\tau\ d\tau\right],$$

To display the Fourier transform in general, we can use the exponential format,

$$F(\omega) = f(\omega)e^{-i\phi(\omega)},$$

and plot the amplitude spectrum $f(\omega)$ and the phase spectrum $\phi(\omega)$. As we have shown above, if $f(t)$ is real and even, then $\phi(\omega)$ is a constant and we can ignore it.

We will now examine three applications of Fourier transforms. Appendix 6A contains a few additional Fourier transform pairs along with some of the important properties of the Fourier transform.

6.5 Rectangular Pulse

To understand the Fourier transform, the transform of the real, even function

$$f(\tau) = \text{rect}(\tau) = \begin{cases} 1, & |\tau| \le \dfrac{1}{2}, \\ 0, & \text{all other } \tau \end{cases} \tag{6.16}$$

will be calculated. This function is a rectangular pulse (see Figure 6.4), and is the result of allowing $k \to \infty$ in the expression for a square wave, (6.8). (It might be easier to think of the process of obtaining the single pulse as one where we keep the pulse width constant and allow the period $T \to \infty$.) To calculate the Fourier transform, we use (6.15a), which reduces to

$$F(\omega) = \int_{-1/2}^{1/2} \cos\omega\tau\ d\tau = \frac{1}{\omega}\left[\sin\omega\tau\right]_{-1/2}^{1/2} = \frac{\sin\dfrac{1}{2}\omega}{\dfrac{1}{2}\omega}. \tag{6.17}$$

We interpret this equation as follows: cos ωt is a weighting function called the kernel. The shape and duration of the weighting function determine the time average of $f(t)$ calculated by (6.15a). In Figure 6.5, the cosine weighting function is plotted as a two-dimensional surface in ωt-space.

The function rect(t) slices the weighting function perpendicular to the ω-axis. The profile of each slice is modified by the cosine weighting function; the frequency of the weighting function is determined by the position of the slice on the ω-axis. The extent of the weighting function in the t-direction is determined by rect(t). The value of $F(\omega)$ at each frequency is the area under the cosine curve. Figure 6.5 displays a few representative points [6].

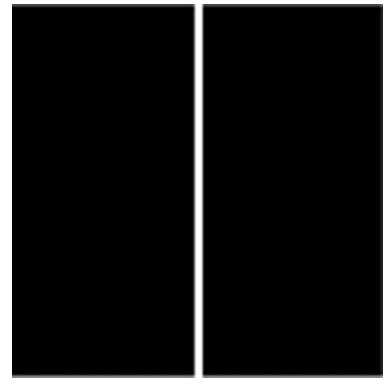

Figure 6.4 *Optical representation of* rect(τ) *defined in (6.16).*

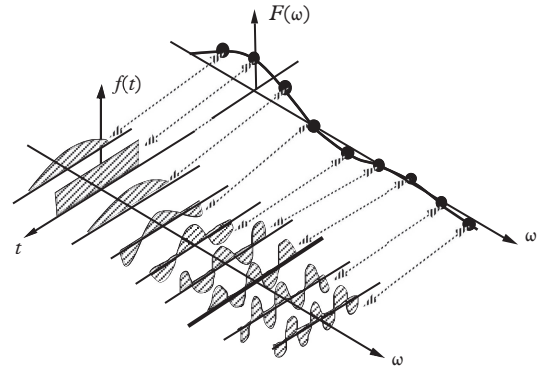

Figure 6.5 *Geometrical construction of the Fourier transform integral of a rectangular pulse. (Courtesy Jack D. Gaskill [6].)*

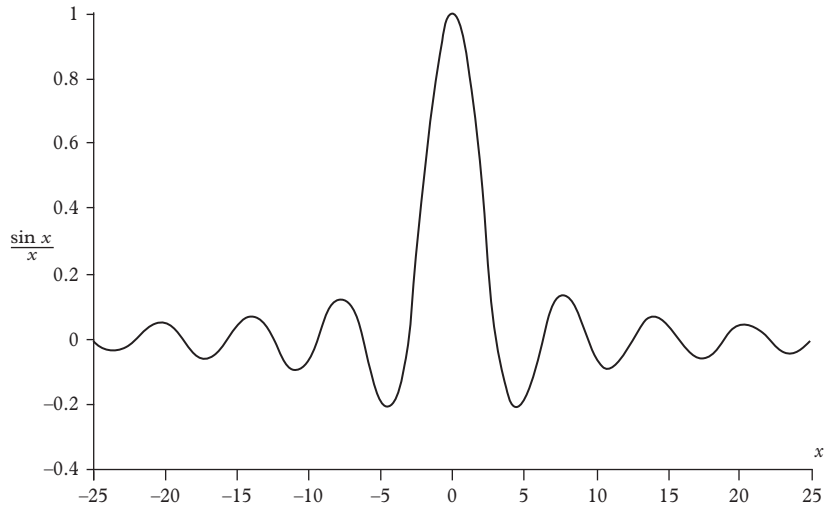

(a)

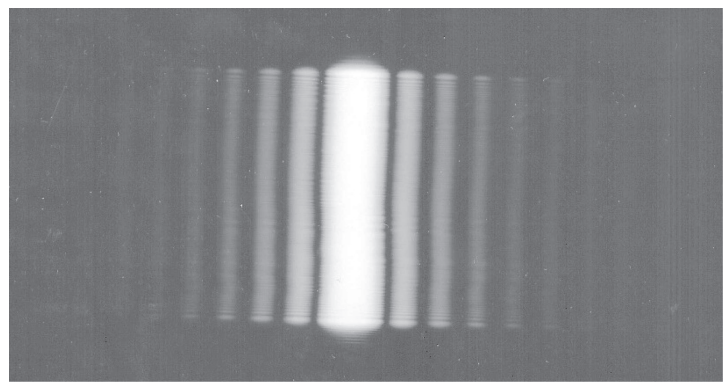

(b)

Figure 6.6 *(a) The sinc function* sinc $x = (\sin x)/x$. *(b) Optical representation of the* sinc *function.*

The Fourier transform of the rectangular pulse (6.16) is the continuous frequency spectrum shown in Figure 6.6 and is given by a function of the form

$$\operatorname{sinc} x = \frac{\sin x}{x}, \tag{6.18}$$

where x may represent ω or k, for example. This function is encountered so often it has been given its own name: the *sinc function*. It has zeroes whenever $x = n\pi$.

In the literature, the sinc function is sometimes defined as

$$\operatorname{sinc} x = \frac{\sin \pi x}{\pi x}.$$

The only advantage of this alternate definition is that the zeroes occur at integer values of x.

At $x = 0$, the sinc function takes on the indeterminate form 0/0, and we must apply L'Hôpital's rule to determine the value of the function:

$$\lim_{x \to 0} \frac{\dfrac{d}{dx}(\sin x)}{\dfrac{d}{dx}(x)} = \lim_{x \to 0} \cos x = 1.$$

Comparing a plot of (6.18) in Figure 6.6(a) with the envelope of the coefficients of the Fourier series in Figure 6.3(c), we find that they are equivalent. We can also compare (6.9) with (6.18) to see that (6.9) is a discrete representation of (6.18). Equation (6.9) is said to be a *sampled* version of (6.18).

6.6 Pulse Modulation Wave Trains

The Fourier transform provides us with a tool to evaluate any wave of finite duration. As an example, consider a wave of frequency ω_0 that is turned on at time $-t_1$ and off at time t_1 (see Figure 6.7). The wave shown in Figure 6.7 has its amplitude modulated by a rectangular pulse of width $2t_1$. Because the wave is symmetric about the time origin, we need only calculate the cosine transform

$$\begin{aligned} F(\omega) &= \int_{-t_1}^{t_1} A \cos \omega_0 \tau \cos \omega \tau \, d\tau, \\ &= \int_{-t_1}^{t_1} A[\cos(\omega_0 + \omega)\tau + \cos(\omega_0 - \omega)\tau] \, d\tau. \end{aligned}$$

The Fourier transform of the pulse-modulated wave contains two terms:

$$F(\omega) = 2A \left[\frac{\sin(\omega_0 + \omega)t_1}{\omega_0 + \omega} + \frac{\sin(\omega_0 - \omega)t_1}{\omega_0 - \omega} \right]. \tag{6.19}$$

The frequency spectrum given by (6.19) is shown in Figure 6.8. There are two identical frequency spectra, centered at ω_0 and $-\omega_0$, where ω_0 is called the *carrier frequency*. The small

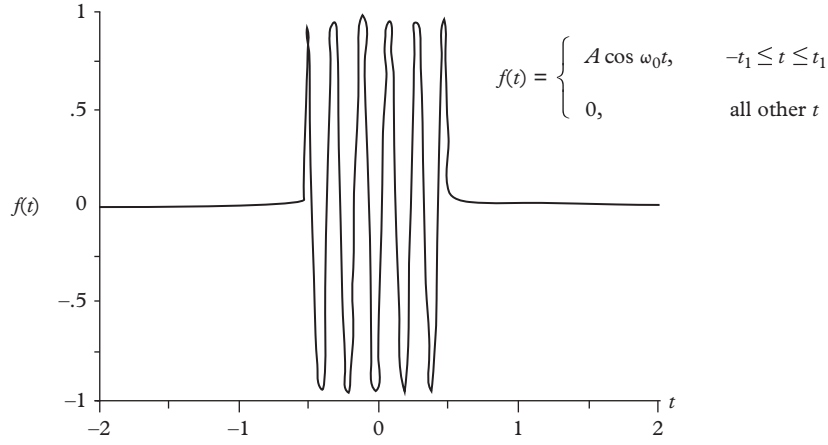

Figure 6.7 *A wave of frequency ω_0 whose amplitude is modulated by a rectangular pulse of duration $2t_1$.*

peaks to the sides of each large central peak are called *side lobes*. The first term in (6.19) is associated with the negative frequency distribution in Figure 6.8. It appears to contain redundant information, but we must retain the negative frequencies if we wish to recover the original signal. If the conjugate variables were x and k, the negative values of k would have physical significance, as we will see later in the discussion of diffraction.

The major contribution to $F(\omega)$ is generated by the central peak (in fact, the first side lobe's peak is only 21.7% of the center peak), and thus the spectrum can be evaluated without excessive error by considering only the central peak. The width of the central peak can be defined as twice the distance from the carrier frequency ω_0 to the frequency at which $F(\omega) = 0$. The frequency spectrum of the pulse-modulated wave, $F(\omega)$, is equal to zero when $\sin(\omega_0 - \omega)t_1 = 0$ and when $\omega_0 \neq \omega$. The zeroes occur when

$$\omega = \omega_0 \pm \frac{n\pi}{t_1}, \qquad n = 1, 2, \ldots.$$

The width of the central peak,

$$2\,(\omega_0 - \omega) = \frac{\pi}{t_1},$$

is inversely proportional to the pulse width t_1. Here we see a reciprocal relationship between conjugate variables similar to what we observed in the Fourier series of Figure 6.3.

As an example, suppose that $\omega_0 = 10^6$ Hz and $t_1 = 10$ μs: then the width of the frequency spectrum will be 600 kHz (from 700 kHz to 1.3 MHz). If the duration of the 1 MHz signal is 1 s, then the width of the spectral distribution will be about 6 Hz.

The Fourier spectra at two different values of pulse width, t_1, are shown in Figure 6.8. There are two ways to interpret the frequency spectra of Figure 6.8:

1. The classical viewpoint treats the frequency plot as a display of the actual frequencies contained in the pulse.
2. The quantum viewpoint treats the frequency plot as a display of the uncertainty in assigning a particular frequency to the pulse. Another way to state this viewpoint is that the frequency spectrum is the probability that a given frequency is present in the pulse.

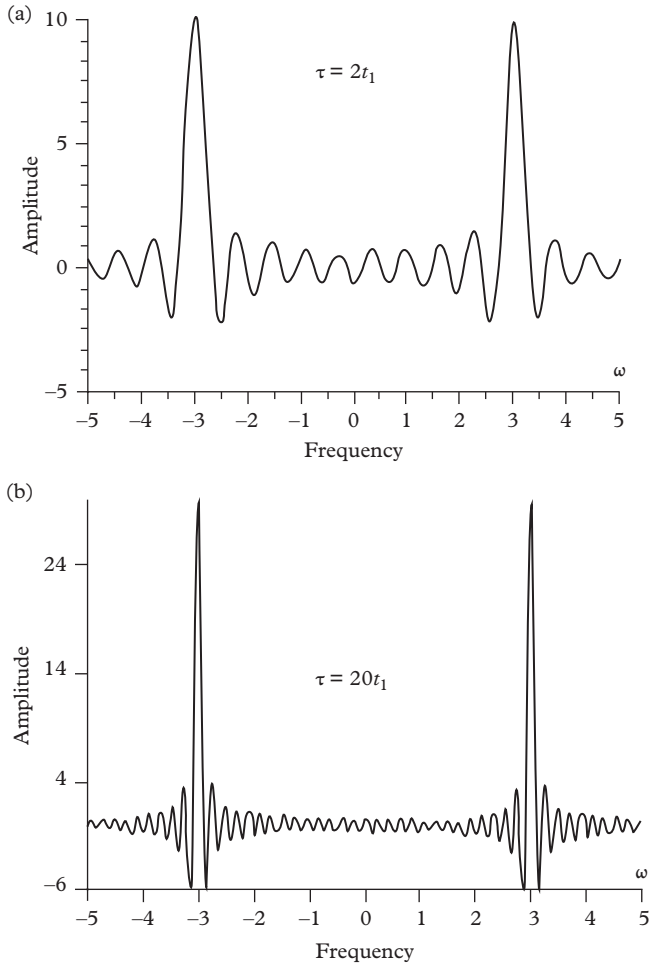

Figure 6.8 *Frequency spectra of pulses of width (a) $2t_1$ and (b) $20t_1$ and carrier frequency $\omega_o = 3$. Note that the wider pulse results in a narrower frequency spectrum.*

A second pulse shape that will be analyzed is a pulse with a Gaussian profile, as shown in Figure 6.9 and described mathematically by

$$f(t) = A\sqrt{\frac{\pi}{\alpha}}e^{-t^2/4\alpha}\cos\omega_0 t. \tag{6.20}$$

We can rewrite this real function using complex notation:

$$f(t) = \frac{A}{2}\sqrt{\frac{\pi}{\alpha}}e^{-t^2/4\alpha}(e^{i\omega_0 t} + e^{-i\omega_0 t}).$$

The Fourier transform of this Gaussian modulated wave is

$$F(\omega) = \frac{A}{2}\sqrt{\frac{\pi}{\alpha}}\left(\int_{-\infty}^{\infty} e^{-[\tau^2/4\alpha + i(\omega-\omega_0)\tau]}\,d\tau + \int_{-\infty}^{\infty} e^{-[\tau^2/4\alpha + i(\omega+\omega_0)\tau]}\,d\tau\right).$$

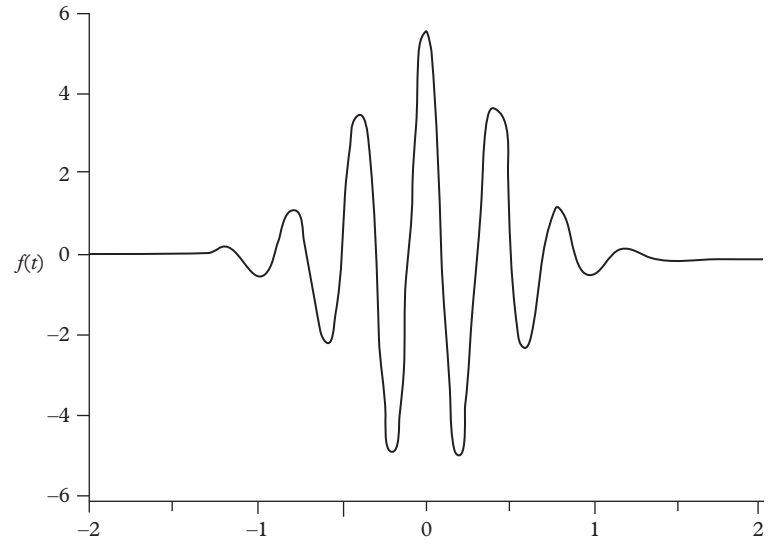

Figure 6.9 *A wave of frequency ω_0 whose amplitude is modulated by a Gaussian pulse.*

This integral can be solved by completing the squares in the exponents:

$$-\frac{\tau^2}{4\alpha} - i(\omega \pm \omega_0)\tau = -\alpha(\omega \pm \omega_0)^2 - \left[\frac{\tau^2}{4\alpha} + i(\omega \pm \omega_0)\tau - \alpha(\omega \pm \omega_0)^2\right],$$
$$= -\alpha(\omega \pm \omega_0)^2 - \left[\frac{\tau}{2\sqrt{\alpha}} + i\sqrt{\alpha}(\omega \pm \omega_0)\right]^2.$$

Now, by substituting

$$u_\pm^2 = \left[\frac{\tau}{2\sqrt{\alpha}} + i\sqrt{\alpha}(\omega \pm \omega_0)\right]^2, \quad du_\pm = \frac{1}{2\sqrt{\alpha}}\, d\tau,$$

we can solve the integrals to get

$$F(\omega) = A\pi\,(e^{-\alpha(\omega-\omega_0)^2} + e^{-\alpha(\omega+\omega_0)^2}).$$

The Fourier transform of a Gaussian is another Gaussian. The widths of the transform pair are conjugate variables and are thus inversely proportional to each other.

6.7 Dirac Delta Function

Consider the envelope of the two pulses we have just examined using Fourier transforms. We can widen the temporal pulse, and, as we do so, the frequency spectrum narrows until in the limit of a continuous-wave signal, only one frequency exists in frequency space. In this limit, the frequency spectrum becomes the *Dirac delta function* (sometimes called the unit impulse function). The Dirac delta function was the first generalized function to be defined and is the only one that we will discuss[2] [7]. **Paul Dirac (1902–1984)** introduced the delta function in his quantum textbook in 1958 [8].

[2] A generalized function is also called a singularity function, a functional, or a distribution.

The definition of the delta function usually encountered is as follows:

$$\delta(t - t_0) = 0, \qquad t \neq t_0; \tag{6.21}$$

i.e., the function is zero everywhere except at the point t_0. The integral of the delta function is

$$\int_{-\infty}^{\infty} \delta(t - t_0)\, dt = 1; \tag{6.22}$$

i.e., the delta function has a finite area contained beneath it.

A mathematically more precise definition of the delta function, based upon distribution theory, is obtained by using the *sifting property* of the delta function:

$$\int_{-\infty}^{\infty} f(t)\delta(t - t_0)\, dt = f(t_0). \tag{6.23}$$

A distribution is not an ordinary function, but rather it is a method of assigning a number to a function. The assignment is expressed formally by an integral of the form (6.23), where the delta function located at t_0 assigns the value $f(t_0)$ to the function $f(t)$. It should be emphasized that it is not the delta function itself but rather the assignment operation that is defined.

The Fourier transform of the delta function is easily obtained using (6.23):

$$D(\omega) = \int_{-\infty}^{\infty} \delta(t - t_0)e^{-i\omega t}\, dt = e^{-i\omega t_0}. \tag{6.24}$$

The function $D(\omega)$ has a constant amplitude but a phase that varies linearly with ω. If $t_0 = 0$, i.e., the delta function is centered at the origin $t = 0$, then the delta function is an even function and the Fourier transform is given by the cosine transform. The transform of the delta function located at the origin is a constant [$D(\omega) = \cos 0 = 1$].

A series of equally spaced delta functions, called the *Dirac series* or sometimes the *comb function* (Figure 6.10) is written

$$\text{comb}(t) = \sum_{n=-N}^{N} \delta(t - t_n), \tag{6.25}$$

where $t_n = nt_0$. It is useful because it performs a sampling operation on another function, as we will see in a moment. The Fourier transform of the comb function is

$$\mathcal{F}\{\text{comb}(t)\} = \text{COMB}(\omega) = \sum_{n=-N}^{N} e^{-\omega t_n}. \tag{6.26}$$

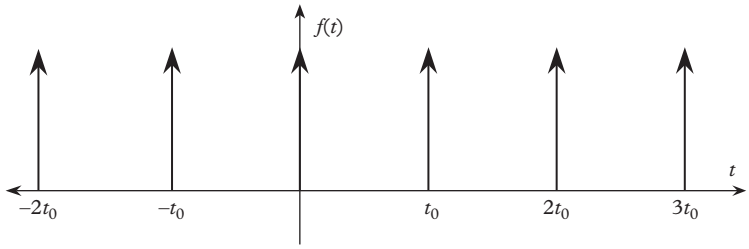

Figure 6.10 *The comb function consisting of delta functions spaced by* t_0.

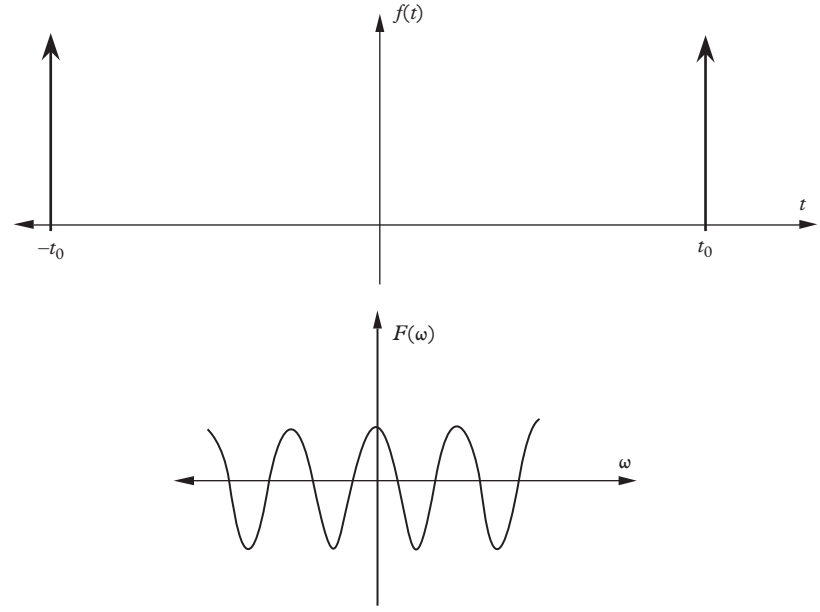

Figure 6.11 *The Fourier transform of two delta functions positioned at* $\pm t_0$ *is the cosine function with a frequency of* $1/t_0$.

If there are two delta functions at t_0 and $-t_0$ (Figure 6.11), then the Fourier transform is a cosine function of frequency $1/t_0$:

$$C(\omega) = e^{-i\omega t_0} + e^{i\omega t_0} = 2\cos\omega t_0,$$

as shown in the lower half of Figure 6.11.

For a series of $2N + 1$ delta functions equally spaced about the origin, the Fourier transform of their sum can be written as a geometric series:

$$\mathcal{F}\left\{\sum_{n=-N}^{N}\delta(t-nt_0)\right\} = \sum_{n=-N}^{N}\mathcal{F}\{\delta(t-nt_0)\} = \sum_{n=-N}^{N}e^{-i\omega nt_0}. \tag{6.27}$$

Since this is the sum of a geometric series, we can write

$$\begin{aligned}\mathcal{F}\left\{\sum_{n=-N}^{N}\delta(t-nt_0)\right\} &= \frac{e^{-iN\omega t_0}-1}{e^{-i\omega t_0}-1} + \frac{e^{iN\omega t_0}-1}{e^{i\omega t_0}-1} - 1\\ &= \frac{\cos(N-1)\omega t_0 - \cos N\omega t_0}{2\sin^2\left(\frac{1}{2}\omega t_0\right)}\\ &= \frac{\sin\left[\frac{1}{2}(2N+1)\omega t_0\right]}{\sin\left(\frac{1}{2}\omega t_0\right)}.\end{aligned} \tag{6.28}$$

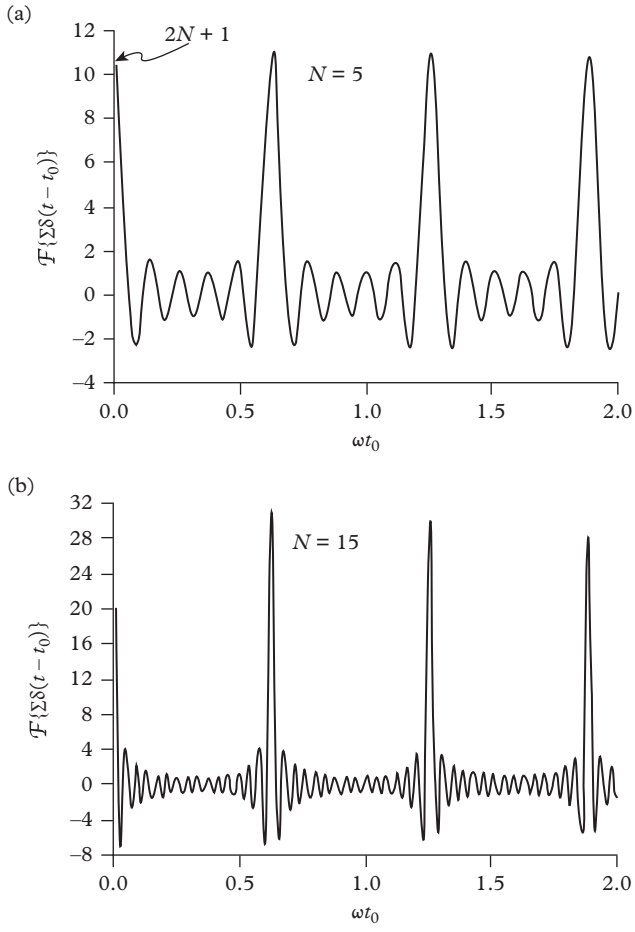

Figure 6.12 *(a) A plot of the Fourier transform of a set of $2N+1$ equally spaced delta functions where $N=10$. The maximum value of the Fourier transform is $2N+1$ and the first zero is inversely proportional to $2N+1$. (b) A plot of the Fourier transform of a set of $2N+1$ equally spaced delta functions where $N=20$. Note that the width of the primary peaks narrow as N increases.*

A plot of (6.28) is shown in Figure 6.12 for $N = 10$ and $N = 20$. As can be seen, (6.28) is a periodic function made up of large primary peaks surrounded by secondary peaks that decrease in amplitude as you move away from the primary peak. The amplitude of the primary peak is $2N + 1$, and the first zero (a measure of the width of the primary peak) is given by

$$\omega = \frac{n\pi}{(2N+1)t_0}.$$

In the limit as $N \to \infty$, Figure 6.12 suggests that (6.28) approaches a series of delta functions; this can be proved formally [9]. Thus, the Fourier transform of the comb function in the time domain, for $N \to \infty$, is a similar comb function in the frequency domain, as shown in Figure 6.13:

$$\mathcal{F}\left\{\sum_{n=-N}^{N}\delta(t-nt_0)\right\} = \frac{1}{t_0}\sum_{n=-\infty}^{\infty}\delta(\omega-n\omega_0).$$

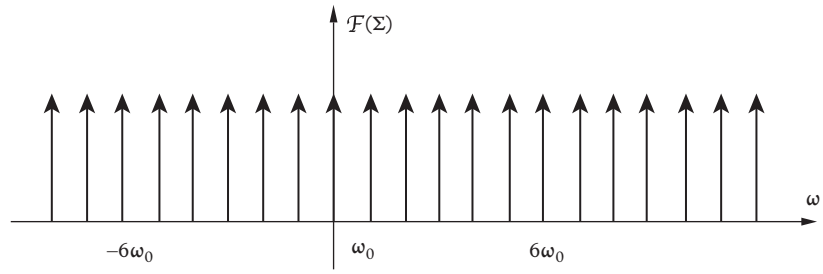

Figure 6.13 *The Fourier transform of the infinite comb function shown in Figure 6.9.*

In the limit as $N \to \infty$, the comb function becomes a periodic function, and the coefficients of the Fourier series of the periodic function can be shown to be equal to the values of the Fourier integral at $n\omega_0 = 2\pi n/t_0$, which are the location of the delta functions in the frequency domain (see Figure 6.13).

6.8 Replication and Sampling

A second approach to evaluating the spectral content of an aperiodic function is to assume that the function, over the interval of interest, is one period of a periodic function. In making this assumption, we treat the function as if it were replicated over all time; the period of the replication would be equal to the length of the interval of interest. We will look at an example of the application of this replication process and then treat the replication process formally. The result of the formal treatment will be the demonstration that the process of replication in the time domain results in a frequency spectrum consisting of discrete frequencies, a sampled version of the continuous frequency distribution that would be obtained by application of the Fourier transform. This result will justify the statement of an important theorem from communication theory that specifies the number of samples of a function that are needed to represent the function.

As an example of the application of replication, a Fourier series is used to represent a straight line over the interval $-1 \leq t \leq 1$. The details are left for Problem 6.8; here we will only display, in Figure 6.14, the first three terms of the series over the interval $-2 < x < 2$. In the interval of interest, the series approaches the straight line. Outside the interval, the fit is poor. The curve for the Fourier series (the gray curve) demonstrates that the function has been replicated.

To treat the replication process formally, assume we have a aperiodic function $g(t)$ defined over the interval $-t_0 < t < t_0$, such as the function, $g(t) = t$, shown in Figure 6.14. We replicate $g(t)$ $2N$ times, creating the function

$$g_N(t) = \sum_{n=-N}^{N} g(t - nt_0) \tag{6.29}$$

shown in Figure 6.15. We can use a property of a Fourier transform called *the shifting property*, (6A.5), to write

$$\mathcal{F}\{g_N(t)\} = \sum_{n=-N}^{N} G(\omega)e^{-in\omega t_0}. \tag{6.30}$$

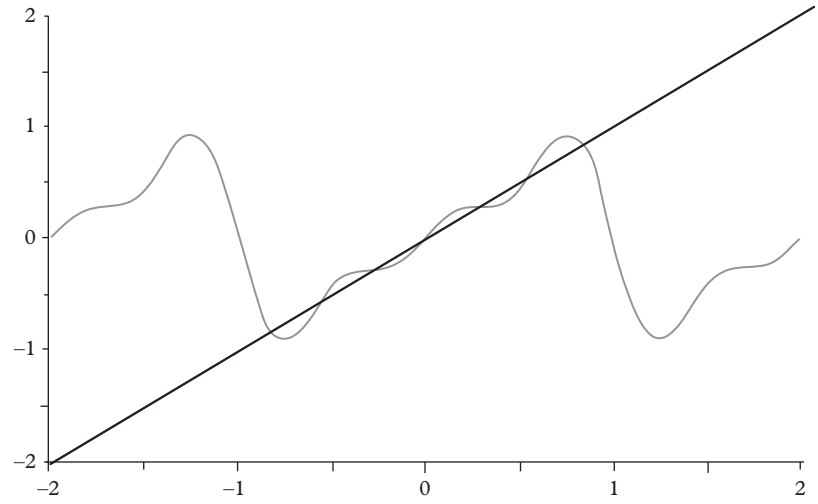

Figure 6.14 *Fourier series approximation of the function* $g(t) = t$ *over the interval* $-1 \le t \le 1$ *using the first three terms of the series. We display the interval* $-2 \le t \le 2$ *to show the failure of the approximation outside the desired interval.*

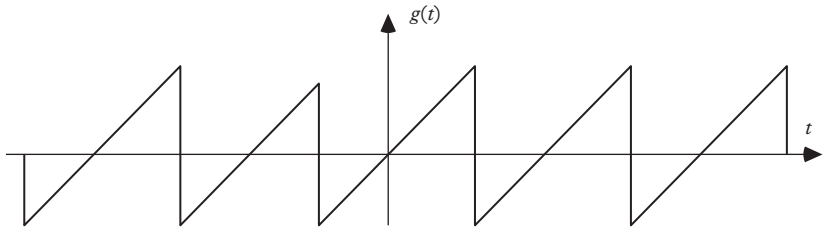

Figure 6.15 *Replication of the function shown in Figure 6.14.*

We have already found the sum of the geometric progression of this form in (6.27) and (6.28):

$$\mathcal{F}\{g_N(t)\} = G(\omega) \sum_{n=-N}^{N} e^{-in\omega t_0} = G(\omega) \frac{\sin\left[\frac{1}{2}\omega t_0(2N+1)\right]}{\sin\left(\frac{1}{2}\omega t_0\right)}.$$

This equation can be rewritten as a function centered on the point $\omega t_0 = 2\pi n$ and defined over the frequency region one half a period on either side of these points; i.e., we replace ω by $\omega \pm 2\pi n/t_0$:

$$\mathcal{F}\{g_N(t)\} \approx G(\omega) \frac{\sin\left[\left(\frac{1}{2}\omega t_0 - n\pi\right)(2N+1)\right]}{\sin\left(\frac{1}{2}\omega t_0 - n\pi\right)}.$$

As was mentioned earlier, in the limit as $N \to \infty$, this becomes a series of delta functions. We can use the definition $\omega_0 = 2\pi/t_0$ to write each delta function in terms of frequency:

$$\delta\left(\frac{1}{2}\omega t_0 - n\pi\right) = \frac{2}{t_0}\delta\left(\omega - \frac{2n\pi}{t_0}\right) = \frac{2}{t_0}\delta(\omega - n\omega_0).$$

When $\omega t_0 \neq 2\pi n$, then $\mathcal{F}\{g_N(t)\} = 0$. Because there is a periodic array of these delta functions (see Figure 6.13), the Fourier transform is an infinite sum:

$$\mathcal{F}\{g_N(t)\} = \frac{1}{t_0} \sum_{n=-\infty}^{\infty} G(\omega)\delta(\omega - n\omega_0). \tag{6.31}$$

We have shown mathematically what can be surmised by inspecting Figures 6.3 and 6.6(a). The frequency spectrum of a rectangular pulse is shown in Figure 6.6(a). If we replicate the rectangular pulse, we generate a square wave. The frequency spectrum of the square wave, shown in Figure 6.3, is a sampled version of Figure 6.6(a). By replication in the time domain, a function that is sampled in the frequency domain is obtained (the comb function, discussed in the previous section, performs the sampling).

The converse is also true. We could measure the spectrum in Figure 6.6(a) at discrete, equally spaced, frequency intervals and obtain the same spectrum shown in Figure 6.3. If we took the inverse transform of the discrete frequency samples, we would not get a square pulse, but instead would generate the function that led to Figure 6.3—namely, a periodic square wave whose period equals the original pulse width.

A natural question is how should $F(\omega)$ be sampled if the resulting periodic function is to truly represent the desired function over one period? The answer is called the *sampling theorem* and was developed by Claude Shannon to determine the amount of information that can be transmitted in a communication channel [10]. The sampling theorem states that if the Fourier transform $F(\omega)$ of the function $f(t)$ is zero above some cutoff frequency,

$$F(\omega) = 0, \qquad \omega > \omega_c,$$

then $f(t)$ is uniquely determined from its values measured at a set of times

$$t = nt_0 = n\frac{\pi}{\omega_c}.$$

Thus, at a minimum, *we must sample twice in one period of the highest frequency present in a waveform.*

Figure 6.16 *A commonly observed failure to properly sample spatial data resulted in moiré patterns as shown on the left. (By Serych at cs.wikipedia [Public domain], via Wikimedia Commons.)*

Experimentally, the sampling theorem is very important for both temporal and spatial signals. The normal procedure for measuring a temporal signal is to sample the signal at a number of points in a time interval. The sampled data are then plotted or put into a computer for data analysis. An example of the use of sampled temporal data is found in digital audio recordings. These recordings are made by sampling the audio signal and storing the sampled data in digital form. According to sampling theory, if frequencies above a certain value are unimportant (20 kHz for human hearing), then samples need only be taken at a temporal spacing of $t_0 = 1/(2\nu)$: 25 μs for audio signals. (The actual sampling frequency used in digital audio recording is 44.1 kHz, corresponding to a temporal sampling of 22.7 μs. The frequency used is slightly higher than required, in order to be compatible with television signals.) In early television, a commonly observed failure to properly sample spatial data resulted in moiré patterns when the TV scan lines conflicted with patterns in clothing (see Figure 6.16). Digital cameras can exhibit similar moiré effects.

6.9 Correlation

We often find it necessary to compare functions. With light, we compare two waves by interfering them. Where the two waves are similar, we see a bright illumination, and when they are dissimilar, we see a reduced illumination. We will show an example of this type of comparison after discussing the methodology. The method for calculating the similarity of two functions is called the *correlation integral* and the resulting function is called the *correlation function* $h(\tau)$. If we wish to compare $a(t)$ and $b(t)$, where $a(t)$ and $b(t)$ are different functions, we create the integral called the *cross-correlation function*

$$h(\tau) = a(t) \oplus b(t) = \int_{-\infty}^{\infty} a(t)b^*(t-\tau)\, dt. \tag{6.32}$$

If $a(t)$ and $b(t)$ are the same function, then the correlation integral is called the *autocorrelation function*. It is useful to normalize correlation functions by dividing by the root mean square average of the two functions $a(t)$ and $b(t)$, to allow comparison with other correlations. The normalized correlation function is

$$h(\tau) = a(t) \oplus b(t) = \frac{\displaystyle\int_{-\infty}^{\infty} a(t)b^*(t-\tau)\, dt}{\left[\displaystyle\int_{-\infty}^{\infty} a(t)a^*(t)\, dt\right]^{1/2}\left[\displaystyle\int_{-\infty}^{\infty} b(t)b^*(t)\, dt\right]^{1/2}}. \tag{6.33}$$

If $a(t)$ and $b(t)$ were light waves, the integrals in the denominator would be the average intensity of each wave—hence, the name *average energy* is usually associated with these integrals.

To develop a physical intuition about the correlation function, we will calculate the autocorrelation function of $A(t)$, a square pulse, defined as

$$A(t) = \begin{cases} A, & -t_0 \le t \le t_0, \\ 0, & \text{all other } t. \end{cases}$$

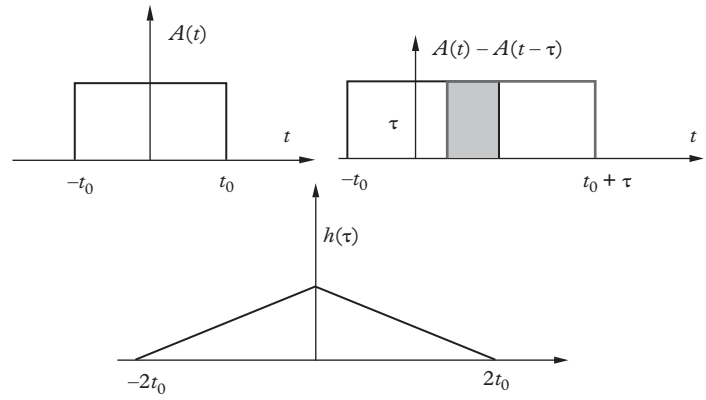

Figure 6.17 *The autocorrelation function of $A(t)$, $h(\tau)$, can be generatedif we simply slide one realization of $A(t)$ over another copy and record the overlapping area, shown here as the shaded area.*

We will use this example to discover that

- the autocorrelation function is always an even function;
- $h(0)$ of the autocorrelation function is the average energy of the function.

Figure 6.17 displays the function $A(t)$, a graphical construction to obtain the correlation value for $t = \tau$, and the normalized autocorrelation function. To calculate the correlation function graphically, we simply slide one function across the second; measuring the overlapping area for each displacement τ. The autocorrelation function at τ is the overlap area of the function and its clone, the area shaded in Figure 6.17. For $A(t)$, the area of overlap equals the area of the two pulses, $A \cdot 2t_0 + A \cdot 2t_0$, minus the area of each pulse not overlapped, $A\tau + A\tau$. The area is thus

$$4At_0 - 2A\tau.$$

We divide by the area of the pulses to normalize, yielding

$$h(\tau) = \begin{cases} 1 - \dfrac{|\tau|}{2t_0}, & |\tau| \leq 2t_0, \\ 0, & |\tau| > 2t_0. \end{cases}$$

If we plot $h(\tau)$, we obtain a triangle whose base is twice the width of the pulse; this is the autocorrelation of the square pulse $A(t)$.

A negative shift of $A(t)$ with respect to its clone (leftward shift in Figure 6.17) is equivalent to a positive shift between the two functions. Mathematically, the use of a negative shift to generate the autocorrelation function is written as

$$h(-\tau) = \int_{-\infty}^{\infty} A(t)A(t + \tau)\, dt.$$

Let $t + \tau = \gamma$ and $dt = d\gamma$; the correlation integral can then be rewritten as

$$h(-\tau) = \int_{-\infty}^{\infty} A(\gamma - \tau)A(\gamma)\, d\gamma = h(\tau).$$

This means that the autocorrelation is always an even function.

The maximum value of the autocorrelation occurs when the two identical functions are aligned and $\tau = 0$, where the autocorrelation is given by

$$h(0) = \int_{-\infty}^{\infty} [A(t)]^2 \, dt.$$

This integral is equal to the average energy of $A(t)$.

If the two functions are identical but one leads the other by a time Γ, then the maximum value of what should now be called a cross correlation occurs at $\tau = \Gamma$. As an example of this property, we will calculate the cross-correlation function of two periodic functions with the same period but different epoch angles:

$$a(t) = A\cos(\omega_0 t + \theta),$$
$$b(t) = B\cos(\omega_0 t + \phi).$$

The cross-correlation function is

$$h(\tau) = \frac{AB}{2}\cos(\omega_0 \tau + \theta - \phi).$$

The peak of this correlation function is periodic and the location of the maximum allows the determination of the relative phase difference between $a(t)$ and $b(t)$, i.e., how much $a(t)$ leads or lags $b(t)$. This result is the mathematical representation of an optical interference experiment.

In summary, the peak value of a correlation function as well as the value of the relative displacement τ measures the degree of similarity and the relative temporal position of the functions.

One of the properties of the Fourier transform is that the correlation integral is given by the Fourier transform of the product of the Fourier transforms of the two functions

$$h(\tau) = a(t) \oplus b(t) = \mathcal{F}\{A(\omega)B^*(\omega)\}. \tag{6.34}$$

6.10 Convolution Integrals

Another class of integrals we will find useful are *convolution integrals*

$$g(t) = a(t) \otimes b(t) = \int_{-\infty}^{\infty} a(t)b(\tau - t) \, dt. \tag{6.35}$$

In German, this integral is called the *Faltung* or folding integral because the function $b(t)$ is folded over the ordinate before the integral is performed. The weighting function $b(\tau - t)$, called the convolution kernel, can be thought of as a window that moves in time and through which we observe the function $a(t)$. The convolution is the time average of the temporal function $a(t)$ viewed through this window.

The convolution function is easily confused with the correlation function (6.33), but they are not the same. In general, the correlation operation does not commute,

$$a(t) \oplus b(t) \neq b(t) \oplus a(t),$$

while the convolution does (see Appendix 6A),

$$a(t) \otimes b(t) = b(t) \otimes a(t).$$

There is a simple relationship between the convolution and correlation functions:

$$a(t) \oplus b(t) = a(t) \otimes b^*(-t). \tag{6.36}$$

We see that the correlation and convolution functions are identical if the weighting function $b(t)$ is a real, even function. If we look back at (6.12), we can now recognize it as a convolution integral.

We will evaluate the convolution of the two functions in Figures 6.18(a, b). Figures 6.18(c, d) display graphically the evaluation of the integral. The convolution and correlation for the two functions shown in Figures 6.18(a, b) are listed in Table 6.2. The differences between the convolution and correlation for these two functions are not large, even though the functions are not symmetric about the origin; Problem 6.9 involves two functions that produce larger differences in the correlation and convolution. Figure 6.19 displays a plot of the convolution and correlation functions for our example.

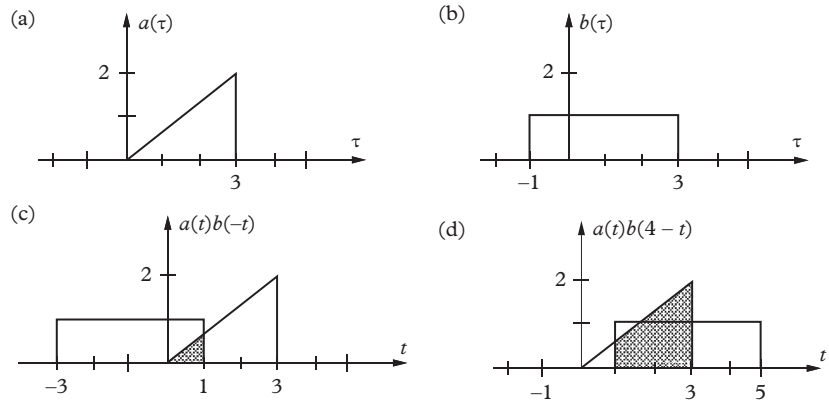

Figure 6.18 *The calculation of the convolution integral involving the functions shown in (a) and (b) is obtained by the operation shown in (c) and (d). We reflect $b(t)$ through the ordinate and then slide the reflected $b(t)$ over $a(t)$ as we did for the correlation function.*

Table 6.2 *Comparison of correlation and convolution*

Correlation $h(\tau)$		Convolution $g(\tau)$	
0	$\tau < -3$	0	$\tau < -1$
$\frac{1}{3}(\tau+3)^2$	$-3 < \tau < 0$	$\frac{1}{3}(\tau+3)^2$	$-1 < \tau < 2$
3	$0 < \tau < 1$	3	$2 < \tau < 3$
$3-\frac{1}{3}(\tau-1)^2$	$1 < \tau < 4$	$3-\frac{1}{3}(\tau-1)^2$	$3 < \tau < 6$
0	$\tau > 4$	0	$\tau > 6$

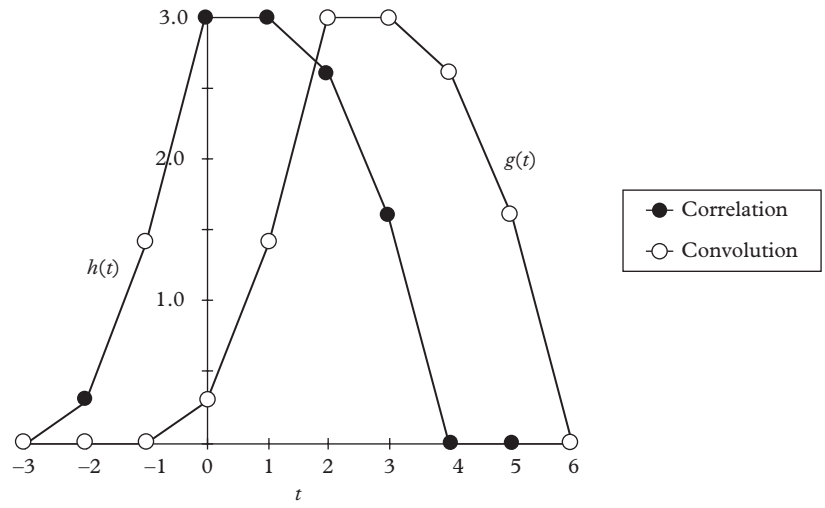

Figure 6.19 *Convolution and correlation functions for the two functions shown in Figure 6.18.*

Note that the convolution operation is a smoothing operation, i.e., sharp peaks are rounded and steep slopes are reduced. Because of the smoothing process, the convolution is often referred to as a filtering operation. The amount of smoothing depends upon the nature of the two functions. For example, if we replaced $b(t)$ in the above example with a delta function, then the convolution of $a(t)$ with $\delta(t)$ would be

$$a(t) \otimes \delta(t) = \int_{-\infty}^{\infty} a(t)\delta(\tau - t)\, dt = a(\tau). \tag{6.37}$$

Thus, the convolution of an arbitrary function $a(t)$ with a delta function reproduces the value of the function $a(t)$ at the delta function position. If we move the delta function over $a(t)$, the convolution function produced is identical to the original function. If the function $b(t)$ is allowed to change from the delta function to a rectangular pulse of increasing width, then the resulting convolution becomes an increasingly smoothed version of $a(t)$. The amount of smoothing is directly proportional to the width of the rectangular pulse.

The two functions in Figures 6.18(a, b) are called functions with compact support. This means that both are identically zero outside some finite interval. For functions with compact support, the width of the convolution is equal to the sum of the widths of the two functions being convolved. Figures 6.18 and 6.19 verify this statement. For functions that do not have compact support, the relationship between the widths is only approximate.

A Fourier transform property allows us to write the Fourier transform of the convolution as the product of the Fourier transforms of the two functions involved in the convolution:

$$\mathcal{F}\{a(t) \otimes b(t)\} = \mathcal{F}\left\{\int_{-\infty}^{\infty} a(t)b(\tau - t)\, dt\right\} = A(\omega)B(\omega). \tag{6.38}$$

6.11 Linear System Theory

Why are we interested in the convolution? It is an important function in the theory of linear systems, and we will find it useful to treat optical systems as linear systems. We use an operational definition to define a linear system; then we use the operational definition to prove that we can characterize a linear system by determining its response to a delta function input. The output of the linear system to an arbitrary input function will be shown to be the convolution of the input function and the delta function response.

To define linear systems, assume that the system is a black box that may contain an optical, electrical, or mechanical system. The black box uniquely maps any input onto an output, but not necessarily in a one-to-one manner. We will represent the operation of the black box by a mathematical operator $\mathcal{T}$ that maps the input function $f(t)$ onto the output function $g(t)$:

$$\mathcal{T}\{f_1(t)\} \to g_1(t), \quad \mathcal{T}\{f_2(t)\} \to g_2(t).$$

- The box (system) has the property of *homogeneity* if

  $$\mathcal{T}\{af_1(t)\} \to ag_1(t).$$

  where a is independent of t.
- It has the property of *linearity* if it obeys the principle of superposition

  $$\mathcal{T}\{af_1(t) + bf_2(t)\} \to ag_1(t) + bg_2(t),$$

  where a and b are independent of t.
- It has the property of *stationarity*, or is *shift-invariant*, if

  $$\mathcal{T}\{f_1(t - t_0)\} \to g_1(t - t_0).$$

  where t_0 is a constant.

If the black box is linear and stationary (invariant), then we will be able to develop a number of useful relationships between the input and output of the system that form the foundation of linear system theory. The relationships are based on the principle of superposition, which allows the decomposition of a complex input into a linear combination of simple functions. Theory allows the calculation of the effect of the linear system on these simple functions. The modified versions of the simple functions are then recombined to form the response to the complex input.

The simple functions selected for characterization of a system are the eigenfunctions of the linear, invariant system. These eigenfunctions are exponentials of the form $e^{i\omega t}$. The linear system modifies the phase and amplitude of the eigenfunctions but the eigenfunctions retain their form; i.e., if $f(t) + ig(t)$ is an eigenfunction of the linear system, then the output will be $c_1 f(t) + ic_2 g(t)$. The constants c_1 and c_2 are called eigenvalues of the system. The problem of finding the output of a linear system given a complex input is therefore reduced to a problem of properly decomposing the input into a set of eigenfunctions and then modifying and recombining these eigenfunctions into the output function.

To prove that the exponential $e^{i\omega t}$ is an eigenfunction, we denote the operation of the system on the exponential by

$$\mathcal{T}\{e^{i\omega t}\} = e(t).$$

Since the system is invariant,

$$e(t + t_1) = \mathcal{T}\{e^{i\omega(t+t_1)}\} = \mathcal{T}\{e^{i\omega t}e^{i\omega t_1}\}.$$

Because the system is homogeneous, this can be written

$$\mathcal{T}\{e^{i\omega(t+t_1)}\} = \mathcal{T}\{e^{i\omega t}\}e^{i\omega t_1} = e^{i\omega t_1}e(t).$$

At $t = 0$, we have

$$e(t + t_1)|_{t=0} = e(t_1) = e(0)e^{i\omega t_1},$$

but t_1 is arbitrary, so we can replace t_1 by t and rewrite this result as

$$e(t) = e(0)e^{i\omega t}.$$

The multiplier of the exponent, $e(0)$, is a constant, possibly complex, demonstrating that the exponential is an eigenfunction.

When we put an impulse function (a delta function) into the input of the linear system, we obtain

$$\mathcal{T}\{\delta(t)\} \Rightarrow s(t),$$

where $s(t)$ is called the *impulse response* [in mathematics, $s(t)$ is called the *Green's function*, and in optics, it is called the *point spread function*]. Because of the assumed properties of linearity and stationarity,

$$\mathcal{T}\{f(t_1)\delta(t-t_1) + f(t_2)\delta(t-t_2)\} \rightarrow f(t_1)s(t-t_1) + f(t_2)s(t-t_2),$$

where $f(t_1)$ and $f(t_2)$ are eigenfunctions of the linear operator $\mathcal{T}$. For a large set of impulse responses,

$$\mathcal{T}\left\{\sum_{n=1}^{N} f(t_n)\delta(t-t_n)\right\} \rightarrow \sum_{n=1}^{N} f(t_n)s(t-t_n). \tag{6.39}$$

We can extrapolate the result given by (6.39) to a continuous distribution by using the sifting property of the delta function,

$$f(t_1) = \int f(t')\delta(t'-t_1)\,dt',$$

to decompose the input function

$$\mathcal{T}\left\{\int f(t')\delta(t-t')\,dt'\right\}.$$

We now use the linearity of the system and the fact that $f(t')$ is an eigenfunction of $\boldsymbol{\mathcal{T}}$ to write

$$\mathcal{T}\left\{\int f(t')\delta(t-t')\,dt'\right\} \rightarrow \int f(t')\mathcal{T}\{\delta(t-t')\}\,dt' \rightarrow \int f(t')s(t-t')\,dt'.$$

The integral

$$\int f(t')s(t-t')\ dt' \tag{6.40}$$

is a convolution integral (sometimes, this integral is called the superposition integral, and the result just obtained explains why). Our result demonstrates the fact that a linear system is completely characterized by its response to an impulse. To obtain the output from a linear system for a complex input, we need only convolve the input with the impulse response of the system.

The Fourier transform of $s(t)$ is $S(\omega)$ and is called the *transfer function frequency response*. The frequency spectrum of the system's output is the product of the input spectrum (the Fourier transform of the input function) and the transfer function: $S(\omega)F(\omega)$. The output of the system is the Fourier transform of this product, as stated mathematically by (6.38).

Another interpretation of the impulse response $s(t)$ emphasizes its role as a weighting function in the convolution integral (6.40). The impulse response can be viewed as a measure of the ability of the system to remember past events. This is in keeping with the earlier interpretation of the weighting function as a window through which a time average is performed. The window determines how much of the past history of the function can be seen when the time average is performed.

6.12 Fourier Transforms in Two Dimensions

We have limited our discussion to one-dimensional temporal functions, but in optics, we will need to perform transforms of functions with two spatial coordinates. We can define a two-dimensional Fourier transform by making a simple extension of the one-dimensional definition (6.13):

$$F(\xi,\eta) = \int_{-\infty}^{\infty}\int f(x,y)e^{-i(\xi x+\eta y)}\ dxdy.$$

If $f(x,y)$ is separable in x and y, we can write

$$\begin{aligned} F(\xi,\eta) &= \int_{-\infty}^{\infty}\int f(x)g(y)e^{-i\xi x}e^{-i\eta y}\ dx\,dy \\ &= \int_{-\infty}^{\infty} f(x)e^{-i\xi x}\ dx \int_{-\infty}^{\infty} g(y)e^{-i\eta y}\ dy. \qquad (6.41) \\ &= F(\xi)G(\eta) \qquad (6.42) \end{aligned}$$

For separable functions, our previous discussions are easily extended to two dimensions; however, performing the integration of the two-dimensional transform can become very difficult if the function is not separable.

In optics, most of the functions we wish to consider have circular symmetry, and it is appropriate to make a change of variables to polar format:

$$\begin{aligned} x &= r\cos\theta, \quad & y &= r\sin\theta, \\ \xi &= \rho\cos\Theta, \quad & \eta &= \rho\sin\Theta. \end{aligned}$$

In polar coordinates, the circularly symmetric function is not only separable but, because it has circular symmetry, it is also independent of θ; thus,

$$f(x,y) \to f(r,\theta) = f(r)g(\theta) = f(r),$$
$$\mathcal{F}\{f(r,\theta)\} = F(\rho,\Theta) = F(\rho).$$

We have

$$F(\rho,\Theta) = \int_0^{2\pi} d\theta \int_0^{\infty} f(r) e^{-i\rho r(\cos\theta\cos\Theta+\sin\theta\sin\Theta)}\, r\, dr$$
$$= \int_0^{\infty} f(r) r\, dr \int_0^{2\pi} e^{-i\rho r\cos(\theta-\Theta)}\, d\theta. \tag{6.43}$$

The second integral belongs to a class of functions called Bessel functions,[3] defined by the integral

$$J_n(x) = \frac{1}{2\pi}\int_{-\pi}^{\pi} e^{i(x\sin\theta - n\theta)}\, d\theta,$$

or, equivalently,

$$J_n(x) = \frac{1}{\pi}\int_0^{\pi} \cos(n\theta - x\sin\theta) d\theta.$$

The integral in (6.43) corresponds to the $n = 0$, zeroth-order, Bessel function. Using this definition, we can write (6.43) as

$$F(\rho) = \int_0^{\infty} f(r) J_0(r\rho) r\, dr. \tag{6.44}$$

This transform is called the Fourier–Bessel transform or the *Hankel zeroth-order transform*. We now apply (6.44) to a simple circular symmetric function, sometimes called the *top-hat* function:

$$f(x,y) = \begin{cases} 1, & \sqrt{x^2+y^2} \le 1, \\ 0, & \text{all other } x,y \end{cases}$$
$$= f(r,\theta) = f(r) = \begin{cases} 1, & r \le 1, \\ 0, & \text{all other } r. \end{cases}$$

The transform of the top-hat function is

$$F(\rho) = \int_0^1 J_0(r\rho) r\, dr.$$

We use the identity

$$xJ_1(x) = \int_0^x \alpha J_0(\alpha)\, d\alpha,$$

[3] In mathematics, Bessel functions arise as a special case of Sturm-Liouville boundary value problems and are encountered when symmetry requires the use of cylindrical coordinates. An approximate way to view the Bessel function at large values of x is as a damped simple harmonic function.

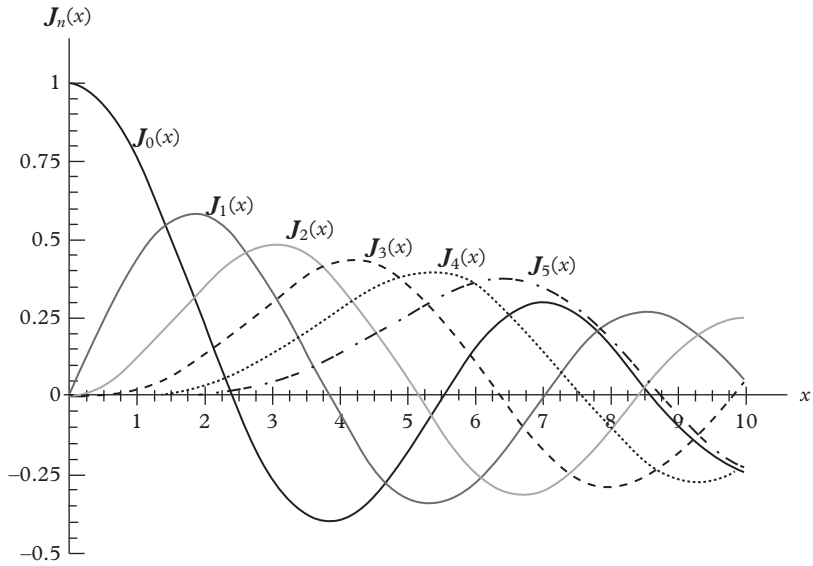

Figure 6.20 *Bessel functions of the first kind.*

to obtain

$$F(\rho) = \frac{J_1(\rho)}{\rho}. \tag{6.45}$$

The Bessel functions are important in optics because most optical systems have circular symmetry. A whole family of Bessel functions exists (see Figure 6.20), and, as in the case of sines and cosines, they may be calculated using a series expansion. The series expansion is

$$J_n(\rho) = \sum_{k=0}^{\infty} \frac{(-1)^k \rho^{n+2k}}{2^{n+2k} k!(n+k)!}. \tag{6.46}$$

The values of Bessel functions have been tabulated and are found in most collections of mathematical tables. We will discuss the Bessel function of order 1 when we discuss diffraction by a circular aperture.

6.13 Summary

In this chapter, we have introduced a number of mathematical tools that will be needed to interpret the optical observations presented in later chapters.

Fourier Series To describe a periodic function $f(t)$, the series

$$f(t) = \frac{a_0}{2} + \sum_{\ell=1}^{\infty} a_\ell \cos \ell\omega t + \sum_{\ell=1}^{\infty} b_\ell \sin \ell\omega t$$

can be used. The coefficients of the two summations are obtained from the integrals

$$a_n = \frac{\omega}{\pi} \int_{-\pi/\omega}^{\pi/\omega} f(t) \cos n\omega t \, dt,$$

$$b_n = \frac{\omega}{\pi} \int_{-\pi/\omega}^{\pi/\omega} f(t) \sin n\omega t \, dt.$$

Fourier Transform An aperiodic function can be represented by the integral

$$\mathcal{F}\{f(t)\} = F(\omega) = \int_{-\infty}^{\infty} f(\tau) e^{-i\omega\tau} \, d\tau,$$

which transforms $f(t)$ from a temporal representation to the frequency representation $F(\omega)$. The inverse transform can also be performed:

$$\mathcal{F}^{-1}\{F(\omega)\} = f(t) = \frac{1}{2\pi} \int_{-\infty}^{\infty} F(\omega) e^{j\omega\tau} d\omega.$$

Correlation The correlation function is a useful integral for comparing the similarity between two functions:

$$h(\tau) = a(t) \oplus b(t) = \int_{-\infty}^{\infty} a(t) b^*(t - \tau) \, dt.$$

It can be though of as the calculation of the area of overlap of two functions as one of the functions slides over the other. We suggested that optical interference was related to this mathematical function.

The Fourier transform provides another way of calculating the correlation function. The Fourier transform of the correlation function is the product of the Fourier transforms of the two functions to be correlated:

$$h(\tau) = a(t) \oplus b(t) = \mathcal{F}\{A(\omega) B^*(\omega)\}.$$

Convolution A second integral, of use in linear system theory, is the convolution integral. It is sometimes called the smoothing operation because if the function $a(t)$ has any sharp peaks, they will be rounded, or if $a(t)$ has any steep slopes, they will be reduced. The amount of smoothing depends upon the nature of $a(t)$ and $b(t)$. The convolution integral of $a(t)$ and $b(t)$ is defined as

$$g(\tau) = a(t) \otimes b(t) = \int_{-\infty}^{\infty} a(t) b(\tau - t) \, dt.$$

As was the case with the correlation, the Fourier transform can be used in the calculation of the convolution. The Fourier transform of the convolution is the product of the Fourier transforms of the two functions to be convolved:

$$\mathcal{F}\{a(t) \otimes b(t)\} = A(\omega) B(\omega).$$

Linear Systems In the discussion of linear systems, the delta function is found to be useful in the description of the response of a linear system. The delta function is defined by the integral

$$\int_{-\infty}^{\infty} f(t)\delta(t-t_0)\,dt = f(t_0).$$

If the delta function is the input function to the linear system, then the output is $s(t)$, the impulse response of the linear system. The impulse response can be used in the convolution integral to predict the output of the linear system for an arbitrary input $f(t)$:

$$\int f(t')\delta(t-t')\,dt'.$$

Again, the Fourier transform can be used to calculate this information. The Fourier transform of the impulse response is called the transfer function of the linear system, $S(\omega)$. If $F(\omega)$ is the frequency spectrum (Fourier transform) of the input function $f(t)$, then the output frequency spectrum of the linear system is given by $S(\omega)F(\omega)$.

Two-Dimensional Fourier Transforms If the two-dimensional function under study, $h(x, y)$, is separable in its dependence on the spatial coordinates, $h(x, y) = f(x)g(y)$, then the two-dimensional Fourier transform is

$$F(x,\eta) = \int_{-\infty}^{\infty} f(x)e^{-i\xi x}\,dx \int_{-\infty}^{\infty} g(y)e^{-i\eta y}\,dy.$$

For circularly symmetric functions

$$f(x, y) \to f(r, \theta) = f(r)g(\theta) = f(r),$$

the Fourier transform is

$$\mathcal{F}\{f(r,\theta)\} = F(\rho, \Theta) = F(\rho),$$

and is given by the Hankel transform

$$\mathcal{F}(\rho) = \int_0^{\infty} f(r)\boldsymbol{J}_0(r\rho)r\,dr.$$

Sampling Theorem The sampling theorem states that if the Fourier transform $F(\omega)$ of the function $f(t)$ is zero above some cutoff frequency,

$$F(\omega) = 0, \qquad \omega > \omega_c,$$

then $f(t)$ is uniquely determined by the values of $f(t)$ measured at a set of times calculated using the formula

$$t = nt_0 = n\frac{\pi}{\omega_c}.$$

This means that we must take two sample points in every period t_0, where $1/t_0$ is the highest frequency contained in the function $f(t)$.

6.14 Problems

6.1. Prove the linearity theorem of Fourier transforms:

$$\begin{aligned}\mathcal{F}\{ag(x) + bh(x)\} &= a\mathcal{F}\{g(x)\} + b\mathcal{F}\{h(x)\} \\ &= aG(k) + bH(k),\end{aligned}$$

where

$$\mathcal{F}\{g(x)\} = \int_{-\infty}^{\infty} g(x)e^{-ikx}\,dx = G(k).$$

6.2. Prove the similarity theorem of Fourier transforms:
If

$$\mathcal{F}\{g(x)\} = G(k),$$

then

$$\mathcal{F}\{g(ax)\} = \frac{1}{|a|}G\left(\frac{k}{a}\right).$$

6.3. Prove the shift theorem of Fourier transforms:
If

$$\mathcal{F}\{g(x)\} = G(k),$$

then

$$\mathcal{F}\{g(x-a)\} = G(k)e^{-ika}.$$

6.4. Prove the convolution theorem of Fourier transforms:
If

$$\mathcal{F}\{g(x)\} = G(k)$$

and

$$\mathcal{F}\{h(x)\} = H(k),$$

then

$$\mathcal{F}\left\{\int_{-\infty}^{\infty} g(\xi)h(x-\xi)\,d\xi\right\} = G(k)H(k).$$

6.5. Prove the autocorrelation theorem of Fourier transforms:

$$\mathcal{F}\left\{\int_{-\infty}^{\infty} g(\xi)g^*(\xi-x)\,d\xi\right\} = |G(k)|^2.$$

6.6. Find the Fourier series for the function $f(x) = x^2$ over the range $-a \le x \le a$.

6.7. Find the Fourier series representation of the periodic function

$$f(t) = \begin{cases} 1, & 0 < t < \dfrac{1}{2}T, \\ -1, & \dfrac{1}{2}T < t < T. \end{cases}$$

6.8. Find the Fourier transform of

$$f(x) = \begin{cases} e^{-ax}, & x > 0, \\ 0, & x < 0. \end{cases}$$

6.9. Compare the convolution and correlation of the following two functions:

$$a(t) = \begin{cases} 1, & 0 \le t \le 1, \\ 0, & 0 > t > 1, \end{cases}$$

$$b(t) = \begin{cases} \delta(t) - e^{-t}, & t \ge 0, \\ 0, & t < 0. \end{cases}$$

6.10. We can perform repeated convolutions, and, as we do, the final convolution will tend toward a Gaussian function. To demonstrate this fact, calculate the convolutions of

$$f_n(t) = \begin{cases} 1, & |\tau| \le \tau_n, \\ 0, & \text{all other } t \end{cases}$$

for

$$\tau_1 = 1, \quad \tau_2 = 2, \quad \tau_3 = \frac{1}{2}, \quad \tau_4 = \frac{3}{2}.$$

Plot the results for each convolution,

$$f_1 \otimes f_2, \quad f_1 \otimes f_2 \otimes f_3, \quad \text{and} \quad f_1 \otimes f_2 \otimes f_3 \otimes f_4.$$

6.11. Assume that the function

$$f(t) = \begin{cases} t, & -1 \le t \le 1, \\ 0, & \text{all other } t \end{cases}$$

is periodic and find the Fourier series over the interval $-1 < t < 1$.

6.12. Evaluate the infinite series derived in Problem 6.11 when $t = \pi/3$.

6.13. Using the results of Problem 6.11, write a computer program to verify Figure 6.13.

6.14. Show that

$$\int_{-\pi/\omega}^{\pi/\omega} \cos[(m-n)\omega t]\, dt = 0,$$

unless $m = n$.

6.15. Show that

$$\int_{-\pi/\omega}^{\pi/\omega} f(t)\,dt = \begin{cases} 0, & f(t) = -f(-t), \\ \text{nonzero}, & f(t) = f(-t). \end{cases}$$

6.16. Assume that the Fourier transform of $f(t)$ is $F(\omega)$. What is the Fourier transform of $f(t + t') + f(t - t')$?

6.17. Assume that the Fourier transform of $f(t)$ is $F(\omega)$. What is the Fourier transform of $f(t)\sin[(\omega'/2)t]$?

6.18. Prove that the Dirac delta function is the unit operator for convolutions just as 0 is for addition and 1is for multiplication.

6.19. Find the Fourier transform of the function

$$f(t) = \begin{cases} 1 + \cos\omega_0 t, & -\dfrac{1}{2}T \le t \le \dfrac{1}{2}T, \\ 0, & \text{all other } t. \end{cases}$$

6.20. Use the shifting property of the Fourier transform, (6A.5), to rewrite (6.29) in the form shown in (6.30).

6.21. Use (6.34) to find the Fourier transform of

$$f(t) = \begin{cases} 1 - \dfrac{|t|}{2t_0}, & |t| \le 2t_0, \\ 0, & |t| > 2t_0. \end{cases}$$

REFERENCES

1. James, J.F., *A Student's Guide to Fourier Transforms*. 2nd ed. 2004: Cambridge University Press.
2. Duffieux, P.M., *L'Integral de Fourier et ses Applications å L'Optique*. 1946: Faculté des Sciences, Besançon.
3. Duffieux, P.M., *The Fourier Integral and its Applications to Optics*. 2nd ed. 1983: Wiley.
4. Luneberg, R.K., *The Mathematical Theory of Optics*. 1964: University of California Press.
5. Cochran, W.T., et al., *What Is the Fast Fourier Transform?* Proc. IEEE, 1967. 55: p. 1664–1674.
6. Gaskill, J.D., *Linear Systems, Fourier Transforms and Optics*. 1978: Wiley.
7. Lighthill, M.J., *Introduction to Fourier Analysis and Generalized Functions*. 1964: Cambridge University Press.
8. Dirac, P., *Principles of Quantum Mechanics*. 4th ed. 1958: Clarendon Press.
9. Papoulis, A., *The Fourier Integral and its Applications*. 1962: McGraw-Hill.
10. Shannon, C.E. and W. Weaver, *The Mathematical Theory of Communications*. 1963: University of Illinois Press.

Appendix 6A Fourier Transform Properties

Some of the important properties of the Fourier transform are given here. Their proofs are left to the reader as problems. We use the following definitions:

$$F(\omega) = \mathcal{F}\{f(t)\} = \int_{-\infty}^{\infty} f(\tau)e^{-i\omega\tau}\, d\tau, \tag{6A.1}$$

$$G(\omega) = \mathcal{F}\{g(t)\} = \int_{-\infty}^{\infty} g(\tau)e^{-i\omega\tau}\, d\tau. \tag{6A.2}$$

We also let a and b be constants.

6A.1 Linearity

$$\mathcal{F}\{af(t) + bg(t)\} = aF(\omega) + bG(\omega). \tag{6A.3}$$

6A.2 Scaling

$$\mathcal{F}\{f(at)\} = \frac{1}{|a|}F\left(\frac{\omega}{a}\right). \tag{6A.4}$$

6A.3 Shifting

$$\mathcal{F}\{f(t-t_0)\} = e^{-i\omega t_0}F(\omega). \tag{6A.5}$$

6A.4 Conjugation

$$\mathcal{F}\{f^*(t)\} = F^*(-\omega). \tag{6A.6}$$

6A.5 Differentiation

$$\mathcal{F}\left\{\frac{d^n f(t)}{dt^n}\right\} = (i\omega)^n F(\omega). \tag{6A.7}$$

6A.6 Convolution

$$\mathcal{F}\left\{\int_{-\infty}^{\infty} f(\tau)g(t-\tau)\, d\tau\right\} = F(\omega)G(\omega). \tag{6A.8}$$

6A.7 Parseval's Theorem

$$\int_{-\infty}^{\infty} f(t)g^*(t)\, dt = \int_{-\infty}^{\infty} F(\omega)G(\omega)\, d\omega. \tag{6A.9}$$

6A.8 Correlation

$$\mathcal{F}\left\{\int_{-\infty}^{\infty} f(t)g^*(t-\tau)\, dt\right\} = F(\omega)G^*(\omega). \tag{6A.10}$$

6A.9 Common Fourier Transform Pairs

A few common Fourier transform pairs are listed here. Some of these have been derived in Chapter 6 and others are the subject of end-of-chapter problems. See [1] for a more complete listing as well as more details on the subject of Fourier transforms.

$f(t)$	$F(\omega)$	
$\begin{cases} 1, & -t_0 \le t \le t_0, \\ 0, & \text{all other } t \end{cases}$	$\dfrac{\sin \omega t_0}{\omega t_0}$	(6A.11)
$\begin{cases} 1 - \left\lvert \dfrac{t}{t_0} \right\rvert, & -t_0 \le t \le t_0, \\ 0, & \text{all other } t \end{cases}$	$\text{sinc}^2 \omega t_0$	(6A.12)
e^{-t}	$\dfrac{1}{1+\omega^2}$	(6A.13)
$\text{comb}(t)$	$\text{comb}(\omega)$	(6A.14)

6A.10 Convolution Properties

- **Commutativity**

$$f(x) \otimes g(x) = g(x) \otimes f(x). \tag{6A.15}$$

- **Distributivity**

$$[af(x) + bg(x)] \otimes w(x) = a[f(x) \otimes w(x)] + b[g(x) \otimes w(x)]. \tag{6A.16}$$

- **Associativity**

$$[f(x) \otimes g(x)] \otimes w(x) = f(x) \otimes [g(x) \otimes w(x)]. \tag{6A.17}$$

- **Identity**

$$f(x) \otimes \delta(x) = f(x). \tag{6A.18}$$

- **Shift invariance**

$$f(x - x_0) \otimes g(x) = f(x) \otimes g(x - x_0). \tag{6A.19}$$

REFERENCE

1. Papoulis, A., *The Fourier Integral and its Applications*. 1962: McGraw-Hill.

7

Dispersion

7.1 Introduction 254
7.2 Stiff Strings 256
7.3 Group Velocity 258
7.4 Dispersion of Guided Waves 264
7.5 Material Dispersion 266
7.6 Plasmons and Polaritons 283
7.7 Lorenz–Lorentz Law 287
7.8 Signal Velocity, Superluminal Propagation 289
7.9 Summary 293
7.10 Problems 295
References 298
Appendix 7A: Chromatic Aberrations 298

7.1 Introduction

In the derivation of the propagation equation from Maxwell's equations, the material constants σ, μ, and ε were assumed independent of frequency. The measured material constants, σ, μ, and ε are compared for dielectrics in Table 7.1 and for metals in Table 7.2. The measurements were made near DC (usually around 60 Hz) and at visible light frequencies (usually at the sodium D line). The dielectrics listed in Table 7.1 do not show the agreement between the index n and the dielectric constant $\sqrt{\varepsilon/\varepsilon_0}$ displayed in a similar list in Table 2.2.

Table 7.1 *Static dielectric constant and index of refraction*

Dielectric material	n (yellow light)	$\sqrt{\varepsilon/\varepsilon_0}$ (static)
CH_3OH (methanol)	1.34	5.7
C_2H_3OH (ethanol)	1.36	5.0
Water	1.33	9.0
Fused silica	1.458	1.94
NaCl	1.50	2.37

Table 7.2 *Conductivity and optical attenuation*

Metal	n	$n\kappa$	$n^2\kappa$	$c^2\mu\sigma/\omega$
Sodium	0.044	2.42	0.213	867
Silver	0.2	3.44	1.38	2564
Cadmium	1.130	5.01	11.3	490
Aluminum	1.44	5.23	15.1	1335
Gold	0.47	2.83	2.7	1546
Copper	0.62	2.57	3.19	2228
Nickel	1.58	3.42	10.8	520
Lead	2.01	3.48	14	192
Iron	1.51	1.63	4.9	415

Modern Optics. Second Edition. B. D. Guenther.

© B. D. Guenther 2015. Published in 2015 by Oxford University Press.

In the discussion of propagation in a conducting medium (Chapter 2), we found from (2.61) that

$$2n^2\kappa = c^2\frac{\mu\sigma}{\omega}.$$

This equality is not supported by the experimentally obtained values in Table 7.2. The disagreement is obvious on comparing the last two columns of Table 7.2.

The disagreement between measurements made at low frequencies and those at visible frequencies develops because the electrons and nuclei cannot respond instantaneously to an applied electromagnetic field at visible frequencies. The result of the sluggish response of atoms and molecules to light waves is *dispersion*, i.e., the variation of the index of refraction with frequency. A proper treatment of the subject requires the use of quantum mechanics, but we can obtain an equation of the same form by using a classical model of a molecule. The classical model is useful in visualizing the optical response of materials, but it cannot be used to calculate experimentally observable parameters.

In this chapter, the propagation of a wave on a stiff string will be discussed to develop a familiarity with waves displaying frequency-dependent propagation parameters. Having demonstrated that such waves can exist, using this simple model, the effect of dispersion on the propagation of two closely spaced frequencies will be discussed. It will be shown that the two waves, propagating at slightly different velocities, will alternately undergo constructive and destructive interference, exhibiting the phenomena of beats. The results derived for two frequencies will then be extended to a Gaussian distribution of frequencies, and a discussion of phase and group velocities of a wave will be presented.

To explain the origin of material dispersion, a simple classical model will be developed. The model will first treat a system of charges that do not interact. The complexity of the theory will be increased by adding an unspecified force between two charges so that they experience a restoring force when acted upon by an electromagnetic field. The final addition to the theory will allow pairs of charges to interact. The objective is to obtain an equation for the dielectric constant (or, equivalently, the index of refraction) from each model. The resulting theory will explain the origin of a complex dielectric constant and the observation of resonant absorption. The theory derived is quite simplistic, but, in general, is supported when compared with optical experiments.

The dispersion theory predicts that the index of refraction will decrease with wavelength except in the region of a resonant absorption, where it will increase with wavelength. The increase of the index of refraction with increasing wavelength is called *anomalous dispersion*.

Anomalous dispersion can yield both a phase and a group velocity greater than the speed of light. The final topic of this chapter will be the theory developed to explain this apparent contradiction with the theory of relativity.

The first observations of dispersion were recorded by **Marcus (1648)** and **Grimaldi (1665)**. Newton attempted to explain his observations of dispersion, using a glass prism, by his particle model, but was not successful. **Augustin Louis Cauchy (1789–1857)**, the French mathematician famous for his contributions to calculus and complex variables, derived the dispersion relationship that bears his name,

$$n = a + \frac{b}{\lambda^2} + \frac{d}{\lambda^4} + \frac{f}{\lambda^6} + \ldots,$$

using the mechanistic concept of an elastic solid. Later observations of anomalous dispersion by **P. Le Roux (1832–1907)** pointed out the limited applicability of Cauchy's equation.

Maxwell suggested that atoms and molecules may act as oscillators and possess natural frequencies, but he did not follow up his idea. **Sellmeier (1871)** independently used the idea of natural resonances to derive the Sellmeier relation,

$$n^2 = 1 + \frac{a\lambda^2}{\lambda^2 - \lambda_0^2},$$

to explain simple cases of anomalous dispersion.

A more rigorous classical theory was derived first by **Paul Karl Ludwig Drude (1863–1906)** and **W. Voigt (1850–1919)**. The theory was extended to its present form by **Hendrik Antoon Lorentz (1853–1928)**, a Dutch physicist who shared the Nobel Prize with Zeeman for the study of the effects of magnetism on light. Before we look at the theory of Lorentz, we will examine a string model that includes dispersion.

7.2 Stiff Strings

The simple wave equation discussed in Chapter 1 for a wave on a string assumed that a pulse could propagate along the string without changing shape. The discussion of Fourier transforms in Chapter 6 leads us to view this pulse as a distribution of frequencies. If the pulse shape does not change, we are essentially stating that the frequency distribution must not change in either amplitude or in relative phase as the wave propagates along the string. All of the frequencies must propagate at the same velocity if they are to retain the same relative phase. Thus, our discussion of waves in Chapter 1 was limited to nondispersive waves. We can prove that this is true by substituting a harmonic wave into the wave equation. This will allow the derivation of the *dispersion equation*. The dispersion equation relates the phase velocity of a wave to its frequency and propagation constant for the medium modeled by the wave equation.

The wave equation is given by (1.6) as

$$\frac{\partial^2 f}{\partial x^2} - \left(\frac{1}{c^2}\right)\frac{\partial^2 f}{\partial t^2} = 0.$$

Using (1.22) and (1.23) to rewrite the simple wave equation, we obtain

$$(-ik)^2 f = \left(\frac{i\omega}{c}\right)^2 f,$$

leading to the dispersion equation

$$c^2 = \left(\frac{\omega}{k}\right)^2 \tag{7.1}$$

For the simple wave equation and a harmonic wave, we find that the phase velocity ω/k is a constant; i.e., the medium is nondispersive and all frequencies travel at the same velocity.

We now will introduce a model of wave propagation that includes dispersion. The model selected has additional interest in that it has a frequency region for which no wave can propagate and only evanescent waves exist. The simple model used in Chapter 1 for propagation of a wave on a string did not recognize any force other than the tension in the string. A real guitar string is stiff and tends to coil up when it is not strung. We will extend the string model to recognize that the string is stiff. Rather than introduce a force dependent upon

the length of the string, as might be the case for a real guitar string, we will assume that the vibrating string experiences a restoring force proportional only to the string's displacement, i.e., a simple elastic resorting force. The wave equation for this stiff string is

$$\frac{\partial^2 f}{\partial x^2} - sf = \frac{1}{c^2}\frac{\partial^2 f}{\partial t^2}, \tag{7.2}$$

where s is the force constant. (In quantum mechanics, this equation is called the Klein–Gordon equation.) On substituting a harmonic wave into (7.2), we obtain

$$(-ik)^2 f - sf = \left(\frac{i\omega}{c}\right)^2 f,$$

leading to the dispersion equation

$$\frac{\omega}{k} = c\sqrt{1 + \frac{s}{k^2}}. \tag{7.3}$$

The wave equation is now dispersive; the phase velocity ω/k depends upon k, i.e., upon the wavelength. Figure 7.1 shows a plot of the two dispersion equations, (7.1) and (7.3).

The stiff string has a minimum, or cutoff, frequency

$$\omega_c = c\sqrt{s}$$

below which there are no propagating constants associated with the frequencies. We can discover the significance of the cutoff frequency by examining (7.3). Below ω_c, the propagation constant k is imaginary:

$$\tilde{k} = \frac{i}{c}\sqrt{\omega_c^2 - \omega^2}, \qquad \omega_c > \omega. \tag{7.4}$$

The significance of a complex propagation constant was discovered in Chapter 1 during the study of the propagation of a wave in a medium with loss. Here, we have a different issue—the propagation constant has no real component. To discover the significance of a purely imaginary propagation constant, we define

$$\tilde{k} = -i\kappa$$

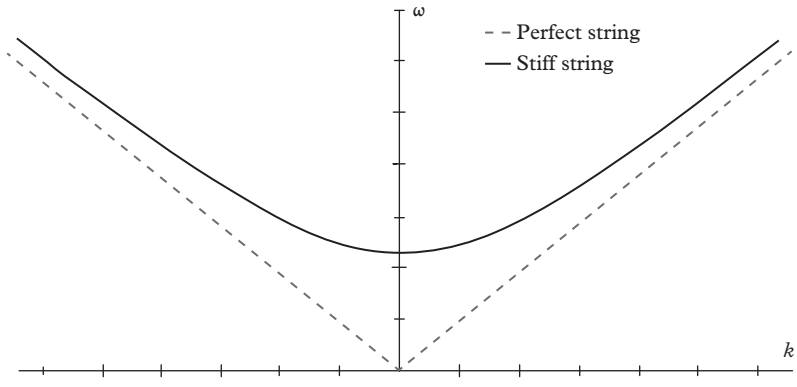

Figure 7.1 *Dispersion curve for a nondispersive wave (the perfect string) and a dispersive wave (the stiff string). There is a range of frequencies $\omega < \omega_c = c\sqrt{s}$ for which there are no real values of k for the stiff string.*

and replace k in the complex representation of the one-dimensional wave by $-i\kappa$. The result is

$$f(x,t) = Ae^{i(\omega t + i\kappa x + \phi)} = Ae^{-\kappa x}e^{i(\omega t + \phi)}. \tag{7.5}$$

The actual wave is the real part of (7.5):

$$f(x,t) = Ae^{-\kappa x}\cos(\omega t + \phi).$$

This is a nonpropagating, evanescent wave with an amplitude that decreases exponentially with increasing values of x. Thus, if the propagation constant is purely imaginary, a wave cannot propagate in the medium.

By attaching a perfect string to a stiff string, total reflection could be observed at the connection point when the wave propagating in the perfect string was incident onto the connection point and had a frequency below the cutoff frequency of the stiff string. If the stiff string consisted of a short segment joined at either end by perfect strings, then the wave propagating in the first perfect string toward the stiff string segment could tunnel through the barrier imposed by the stiff string segment and continue propagating, at a reduced amplitude, along the second perfect string.

7.3 Group Velocity

In Section 7.2, we stated that when a distribution of frequencies, needed to describe a pulse shape, propagated at different velocities, the shape of the pulse, described by the distribution, would change as it propagated. Fourier theory will here be used to prove that statement.

We will first evaluate the propagation of two waves with slightly different frequencies. We will add the two waves to obtain, as the resultant wave, an amplitude-modulated wave. We will use this wave to define the group velocity associated with the propagation of the amplitude modulation. The procedure will then be extended, first to the addition of $2n$ waves and finally to a continuous Gaussian distribution of frequencies. Through the description of combining waves, first for a few discrete frequencies and then for a continuous distribution of frequencies, we will demonstrate how an arbitrary waveform can be produced—an immediate application of the Fourier theory of Chapter 6.

The initial analysis will be in terms of the temporal properties of the wave, because it can easily be related to the material of Chapter 6. After having developed an understanding of the temporal properties, the discussion will be extended to an evaluation of the spatial properties of the wave. The details of the mathematics will not be emphasized, but rather the emphasis will be on the development of a qualitative understanding of the effect of dispersion on the shape of the propagating pulse.

Assume two co-propagating waves of equal amplitude but different frequencies and propagating constants,

$$\omega_1 = \omega + \Delta\omega, \quad k_1 = k + \Delta k,$$
$$\omega_2 = \omega - \Delta\omega, \quad k_2 = k - \Delta k.$$

The resulting wave is obtained by simple algebraic addition of the two waves:

$$\begin{aligned} f(x,t) &= A\cos(\omega_1 t - k_1 x) + A\cos(\omega_2 t - k_2 x) \\ &= A\cos[(\omega t - kx) + (\Delta\omega t - \Delta k x)] + A\cos[(\omega t - kx) - (\Delta\omega t - \Delta k x)]. \end{aligned}$$

Using the trigonometric identity

$$\cos(\alpha \pm \beta) = \cos\alpha\cos\beta - \sin\alpha\sin\beta,$$

the resultant wave becomes

$$f(x,t) = 2A\cos(\Delta\omega t - \Delta k x)\cos(\omega t - kx).$$

This wave is shown in Figure 7.2.

Because the two waves are at slightly different frequencies, their relative phase difference is a function of time. The time-dependent phase results in the two waves alternately adding constructively and destructively, creating an amplitude modulation that is a periodic series of maxima due to constructive interference. We will call these maxima *groups*.

The modulation is on a carrier wave of frequency

$$\omega = \frac{1}{2}(\omega_1 + \omega_2)$$

and propagation constant k traveling at a velocity

$$v = \frac{\omega}{k}. \tag{7.6}$$

This velocity we recognize as the phase velocity (1.14).

The amplitude modulation of the carrier wave is a wave of frequency $\Delta\omega$, called the *beat frequency*, and propagation constant Δk propagating at a velocity

$$u = \frac{\Delta\omega}{\Delta k}. \tag{7.7}$$

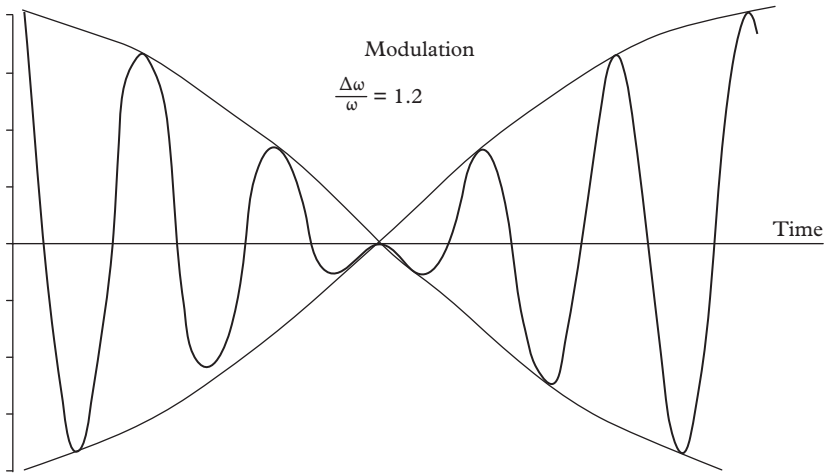

Figure 7.2 *A traveling wave group with a ratio of the carrier frequency to the modulation frequency of 1.2. We could also identify this wave as an amplitude-modulated wave or as an example of beating between two frequencies. All of these descriptions are equivalent.*

This velocity is called the *group velocity*. In a nondispersive medium, the group and phase velocities are identical.

The simple example of the addition of two harmonic waves of different frequencies can now be extended to $2n$ waves. If the waves are uniformly distributed from frequency ω to frequency $2n\omega$, the temporal behavior of the wave is found to be

$$f(0,t) = \frac{m(0,t)}{2}\left(e^{i\omega_0 t} + e^{-i\omega_0 t}\right). \tag{7.8}$$

As an example, the result of adding $2n = 16$ waves of frequency $m\omega$, where $1 \le m \le 16$, is shown in Figure 7.3. The carrier's frequency is $\omega_0 = n\omega = 8\omega$, and the modulation envelope is proportional to

$$m(0,t) \propto \cos^4\left(\frac{1}{2}\omega t\right).$$

We can use the Fourier series to describe $f(0, t)$ of (7.8):

$$\begin{aligned}\alpha_\ell &= \frac{\omega'}{4\pi}\int_{-\infty}^{\infty} m(0,t)(e^{in\omega t} + e^{-in\omega t})e^{-i\ell\omega t}\,dt \\ &= \frac{\omega'}{4\pi}\left[\int_{-\infty}^{\infty} m(0,t)e^{-i(\ell-n)\omega t}\,dt + \int_{-\infty}^{\infty} m(0,t)e^{-i(\ell+n)\omega t}\,dt\right],\end{aligned} \tag{7.9}$$

where ω' is the average modulation frequency. The spectrum of the modulated wave consists of two copies of the spectrum of $m(0, t)$, one centered a distance $n\omega$ above and one centered a distance $-n\omega$ below zero frequency.

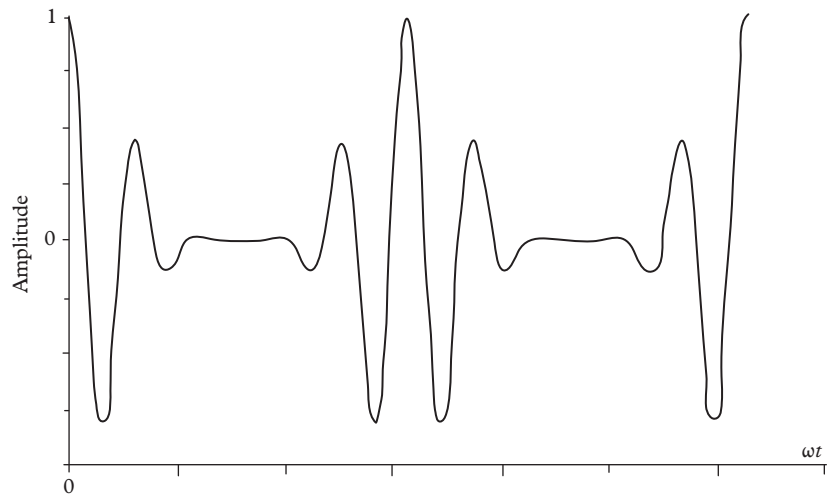

Figure 7.3 *The resultant waveform given by (7.8) when n = 8. In this plot, the frequencies were distributed equally about* ω_0*, each separated by* $0.1\ \omega_0$.

The modulated waves used as examples have all involved periodic amplitude modulation. This procedure can be extended to a nonperiodic modulation; an example is found in Chapter 6. The modulation envelope $m(0, t)$ is equal to (6.16), and the waveform $f(0, t)$ is shown in Figure 6.6. The frequency spectrum for the pulse modulation, shown in Figure 6.8, exhibits the same characteristics seen in (7.9), i.e., two copies of the spectrum of $m(0, t)$ centered on the carrier frequency and the negative carrier frequency.

While the temporal behavior of these waves is interesting, the objective of this discussion is to learn what happens spatially to a complicated waveform as it propagates in a dispersive medium. The waveform can be analyzed as a harmonic carrier wave modulated in both space and time by a modulation function $m(x, t)$. To see the effects of dispersion on the spatial properties of the modulation, the modulation must be described as a function of the propagation constant rather than frequency.

By analogy to (6.14), and the discussion of the temporal properties of a modulated wave, a modulated wave can be described using the x-coordinate and the propagation constant k as follows:

$$f(x, t) = \int M(k) e^{i(\omega t - kx)}\, dk, \tag{7.10}$$

where $M(k)$ is the Fourier transform of $m(x, 0)$, the spatial dependence of the modulation. The dispersion equation can be used to eliminate ω from (7.10), allowing the modulated wave to be written in terms of a harmonic carrier wave with a spatially dependent modulation. The resulting expression will be used to follow a Gaussian wave through a medium with a simple dispersion relation.

The dispersion equation for the propagation medium can be written as a Taylor series, treating k as the independent variable:

$$\omega(k) = \omega_0 + \left(\frac{d\omega}{dk}\right)_{k=k_0} (k - k_0) + \left(\frac{d^2\omega}{dk^2}\right)_{k=k_0} (k - k_0)^2 + \cdots .$$

This expansion of the dispersion relation can be used to rewrite (7.10) as

$$f(x, t) = e^{i(\omega_0 t - k_0 x)} \int M(k) e^{i(k-k_0)(ut-x)} e^{i(k-k_0)^2 wt}\, dk, \tag{7.11}$$

where we have made use of the following definitions to simplify the expression:

$$u = \left(\frac{d\omega}{dk}\right)_{k_0}, \quad w = \left(\frac{d^2\omega}{dk^2}\right)_{k_0} .$$

These definitions are not arbitrarily selected, if $w = 0$, then the surface of constant phase, $ut - x$, propagates with velocity

$$u = \left(\frac{d\omega}{dk}\right)_{k_0} .$$

Thus, u is the group velocity, agreeing with the definition used for two waves of different frequencies, (7.7). To display the relationship between group and phase velocities in terms of spatial parameters, the definition of group velocity is rewritten as

$$u = v - \lambda\left(\frac{dv}{d\lambda}\right). \tag{7.12}$$

To obtain a physical interpretation of (7.11), a Gaussian wave (6.20),

$$f(x,t) = A\sqrt{\frac{\pi}{\alpha}}e^{-x^2/4\alpha}\cos(\omega_0 t - k_0 x),$$

will be followed as it propagates through a dispersive medium. In Chapter 6, the Fourier transform of a Gaussian wave from a temporal to a frequency representation was derived. By analogy, the Fourier transform from a spatial representation (x-variable) to a spatial frequency representation (k-variable) is

$$\begin{aligned} M(k) &= \int_{-\infty}^{\infty} f(x,0)e^{-ikx}\,dx \\ &= A\pi\left(e^{-\alpha(k-k_0)^2} + e^{-\alpha(k+k_0)^2}\right). \end{aligned}$$

We will neglect the component $e^{-\alpha(k+k_0)^2}$ and only follow the positive spatial frequency components.

Inserting the spatial transform into (7.11) yields

$$f(x,t) = A\pi e^{i(\omega_0 t - k_0 x)}\int_{-\infty}^{\infty} e^{i(ut-x)(k-k_0)}e^{-i(\alpha - iwt)(k-k_0)^2}\,d(k-k_0).$$

To perform this integration, we observe that the integral is of the form

$$\int e^{ax-bx^2}\,dx = \sqrt{\frac{\pi}{b}}e^{a^2/4b},$$

where

$$a = i(ut-x), \quad b = \alpha - iwt.$$

We can therefore write

$$f(x,t) = A\pi e^{i(\omega_0 t - k_0 x)}\sqrt{\frac{\pi}{\alpha - iwt}}\ \exp\left[-\frac{(ut-x)^2}{4(\alpha - iwt)}\right].$$

The argument of the second exponential function contains a complex quantity in the denominator that needs to be removed to allow the separation of the real and imaginary parts of the waveform:

$$f(x,t) = A\sqrt{\frac{\pi^3(\alpha + iwt)}{\alpha^2 + (wt)^2}}\ \exp\left[-\frac{(ut-x)^2(\alpha + iwt)}{4(\alpha^2 + w^2t^2)}\right]e^{i(\omega_0 t - k_0 x)}.$$

The imaginary part of this function is a phase term that varies slowly with time and is not of interest in a discussion of the shape of the waveform. The real part of the function describes the envelope of the waveform, which is a Gaussian.

If $w = 0$, then the medium is nondispersive, and

$$f(x,t) = A\sqrt{\frac{\pi^3}{\alpha}}e^{-(ut-x)^2/4\alpha}\cos(\omega_0 t - k_0 x).$$

This is a Gaussian pulse moving at velocity u. The half-width $\sqrt{\alpha}$ of the Gaussian pulse is independent of time; the pulse retains its Gaussian shape and its width is unchanged as it propagates in the nondispersive media. This is the propagation character assumed for the pulse in Chapter 1.

If $w \neq 0$, then the width of the Gaussian pulse is

$$\sqrt{\frac{\alpha^2 + w^2 t^2}{\alpha}}.$$

This width increases with time. If the medium has a large enough dispersion, the pulse will deform rapidly and the concept of a group, propagating with a group velocity u, will lose its physical significance.

To further evaluate the propagation of the Gaussian pulse, we will assume that the dispersion is given by

$$\omega(k) = \omega_p\left(1 + \frac{a^2k^2}{2}\right), \tag{7.13}$$

where ω_p is a constant with units of frequency and a is a constant with units of length. The two parameters from the Taylor expansion of the dispersion relation are

$$u = \omega_p a^2 k_0, \quad w = \omega_p a^2.$$

If the pulse has propagated in the dispersive medium a long distance, i.e., if the time is large, the width of the Gaussian pulse is

$$\sqrt{\alpha + \frac{(\omega_p a^2 t)^2}{\alpha}} \approx \frac{\omega_p a^2 t}{\sqrt{\alpha}}.$$

The width changes faster for a narrow pulse (small α) than for a broad pulse.

Using an assumed dispersion relationship, we have demonstrated that the effect on a light pulse by a dispersive medium is a spatial broadening of the pulse as it propagates. An analogous derivation can be used to demonstrate that there will also be a temporal broadening of a pulse as it propagates.

The dispersive medium does not respond in the same way to all frequencies. As we try to propagate narrower and narrower pulses through a dispersive medium, Fourier theory states that the medium must pass a wider and wider range of frequencies (Figure 6.7 displays the spectral content of pulses differing in width by a factor of 10.) In Section 7.5, a model will be formulated to describe the response of a dispersive medium based on a treatment of molecules as classical oscillators driven by electromagnetic radiation. On a microscopic scale, the oscillators absorb and reradiate the electromagnetic wave, and this process modifies the propagation velocity of the wave. The oscillators have resonant frequencies associated with the binding forces in the molecules. Near and below resonance, the oscillators absorb and reemit radiation, while far above the resonant frequency, the oscillator

will not absorb energy from the radiation. The absorption and reemission process slows the propagation of the low-frequency components. The wider the range of frequencies contained in a pulse, the more noticeable is the failure of the oscillators to respond to the high-frequency components. This failure is exhibited by a rapid loss of the high-frequency components and a resulting broadening of the pulse. The high frequencies—those far above the oscillator resonances—are lost because they run away from the lower frequencies.

7.4 Dispersion of Guided Waves

Dispersion, through a broadening of pulses as they propagate, causes distortion and reduces the allowable data rates in optical fiber communication. Because of its importance, we will briefly review the sources of dispersion in fibers. This topic is interesting because dispersion in fibers can be due to processes other than the response of molecules to light.

The effects on the propagation of light that are due to the wavelength dependence of the refractive index are called *material* (or *chromatic*) *dispersion*. Material dispersion will be treated in Section 7.5 by a classical model based on interaction of light and molecules. Material dispersion in silica-based optical fibers is negligible at wavelengths around 1.3 μm. Most applications, requiring high data rates, attempt to take advantage of this fact by proper choice of materials in fiber construction and proper choice of light sources.

A smaller chromatic dispersion, called *waveguide dispersion*, is observed in a guide with a gradient index of refraction; it is also called *profile dispersion*. The propagation in the cladding is faster than that in the core because the index of the cladding is lower. This means the longer wavelengths move faster than the shorter wavelengths. The dispersion is specified as ps/km.

Polarization mode dispersion has several origins: stress birefringence set up in the fiber due to micro-bends or geometric asymmetry due to slightly elliptical cores. We will introduce stress birefringence when we discuss birefringence with reference to Figure 14.15.

The final source of dispersion in a guided wave is called *multimode dispersion* (some prefer to call this *distortion*). If a light pulse introduced into a guide excites several modes, then the energy in each mode will appear to travel at a different velocity, and the modes will arrive at the end of the fiber at different times. If we retain the geometrical view of guided waves used in Chapter 5, we see that the physical reason that the modes appear to travel at different velocities is that rays associated with each mode travel different optical path lengths (see Figure 7.4).

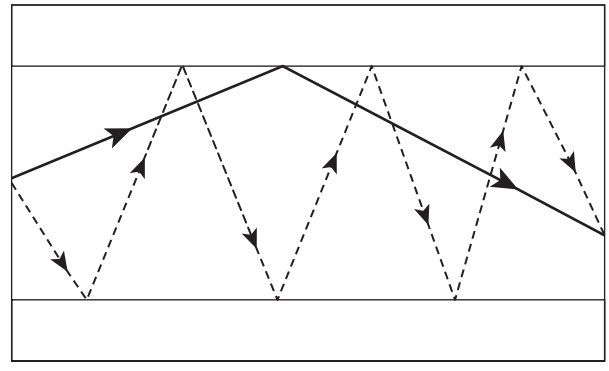

Figure 7.4 *Two guide wave modes propagating in an optical guide. The different path lengths show the origin of multimode dispersion in optical guides.*

A simple relation can be derived for a fiber if skew rays are ignored. For meridional rays, an optical fiber can be viewed as a symmetric guide with a velocity of propagation given by ω/β, where

$$\beta = kn_2 \sin\theta_2.$$

The limits on θ_2 for guided waves are given by (5.26). Using the two limits of θ_2, we find the maximum difference in propagation time for a fiber of length L is

$$\Delta t = \frac{Ln_2}{c}\left(\frac{1}{\sin\theta_c} - \frac{1}{\sin\frac{1}{2}\pi}\right) = L\,\frac{n_2(n_2 - n_1)}{n_1 c}. \tag{7.14}$$

If we code information as pulses and propagate the pulses down the fiber, we must not have any overlapping pulses. Let the pulse width at the start of the fiber be τ, and let the pulse width after propagating along the fiber be $\tau + \Delta t$. The minimum pulse spacing that can be used is thus Δt. Energy would be wasted if the pulse width exceeded Δt, so we also set the pulse width at Δt. We saw in Chapter 6 that we need two samples for the highest frequency transmitted; thus, the maximum bandwidth of the fiber is

$$B = \omega_c \propto \frac{1}{2\Delta t}$$

Multimode dispersion is the major difference between the various classes of optical fibers. The allowable communication bandwidth of a fiber shown in Table 7.3 indicates the effect of multimode dispersion.

Multimode dispersion in graded index fibers is lower than that in step index fibers because rays traveling at small angles relative to the fiber axis travel almost exclusively in the high-index region of the fiber and therefore at slow propagation speeds. Rays traveling at large angles travel in the low-index region and have high propagation velocities. The gradient in the index of refraction partially compensates for the difference in geometrical path lengths by modifying the optical path lengths of the various rays. Single-mode fibers only transmit one mode, and thus multimode dispersion does not exist.

Table 7.3 *Optical fiber bandwidth*

Fiber type	Bandwidth
Multimode, step-index	20 MHz·km
Multimode, graded-index	1 GHz·km
Single-mode, step-index	100 GHz·km

7.5 Material Dispersion

While the data presented in Tables 7.1 and Table 7.2 demonstrated that the electromagnetic properties of materials were dependent on frequency, we still have no way to estimate that dependence. We saw that a relationship for dispersion was needed to calculate the effect of dispersion on the shape of a light pulse. A model could provide such a relationship and provide an understanding of such optical properties as the origin of color and the reflectivity of metals. The model we will develop, based upon the treatment of molecules as classical oscillators, will provide all of these benefits. Rather than develop one all-inclusive model whose properties might be difficult to interpret, we will develop three models of increasing complexity. We will identify the physical significance of the results of each of the models as we complete its development. The models will have the general behavior sketched in Figure 7.5.

We assume that the medium in which the wave is propagating is made up of classical molecules consisting of positive and negative charges of magnitude q. If we expose a material composed of these molecules to a plane harmonic wave $\tilde{\mathbf{E}} = \mathbf{E}e^{i\omega t}$, then the field inside the material will be due to the following:

1. The applied field

$$\tilde{\mathbf{E}} = \mathbf{E}e^{i\omega t}.$$

2. A contribution from molecules with a net charge. These are called free charges and their density ρ is used in Maxwell's equation

$$\nabla \cdot \mathbf{D} = \rho.$$

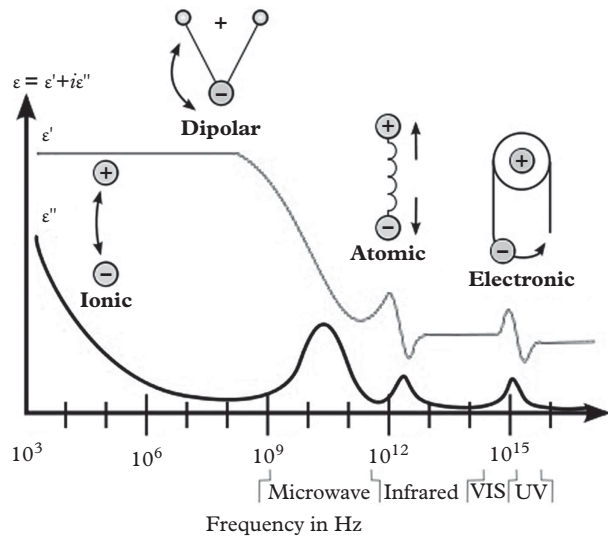

Figure 7.5 *An illustration of the frequency response of various dielectric mechanisms in terms of the real and imaginary parts of the permittivity. (By Archimerged at en.wikipedia [Attribution], from Wikimedia Commons and Kenneth A. Mauritz. Image used with the consent of Professor Kenneth A. Mauritz.)*

We will assume $\rho = 0$, i.e., that there are equal numbers of positive and negative charges in the material.

3. A contribution arising from the induced dipole created when the positive and negative charges are separated by the applied field (we will ignore the added complication of polar molecules that have permanent as well as induced dipole moments). The result of separating the positive and negative charges is an electric dipole moment

$$\mathbf{p} = \sum_i q_i \mathbf{r}_i - \sum_j q_j \mathbf{r}_j,$$

where the sum over i is over the positive charges multiplied by their displacement $\mathbf{r}$ relative to the center of mass and the sum over j is over the negative charges multiplied by their displacement.

To take this contribution due to "bound charge" into account, we sum over all the electric dipole moments $\mathbf{p}$, in a microscopically large volume with respect to the elemental charge and a macroscopically small volume ΔV with respect to the illuminating wavelength. The resulting vector $\mathbf{P}$ is called the polarization vector:

$$\mathbf{P} = \frac{1}{\Delta V} \sum_i \mathbf{p}_i. \tag{7.15}$$

We use the electric displacement to describe this internal field:

$$\mathbf{D} = \varepsilon \tilde{\mathbf{E}} = \varepsilon_0 \tilde{\mathbf{E}} + \mathbf{P}. \tag{7.16}$$

To keep the mathematics simple, we will assume a one-dimensional problem, with each molecule containing one positive and one negative charge of equal magnitude. This allows us to define the electric dipole moment as

$$\mathbf{p} = \sum_i q_i \mathbf{r}_i - \sum_j q_j \mathbf{r}_j = q(x_+ + x_-) = qx.$$

We will also assume that the initial velocity is equal to zero and the initial position of the charges is the equilibrium position.

7.5.1 Conductive Gas

If the negative charges, of mass m, are not bound to the positive charges and the positive charges are too heavy to respond to the light field, then the equation of motion is simply

$$F = ma = m\frac{d^2x}{dt^2} = qEe^{i\omega t}, \tag{7.17}$$

where the only force experienced by the charges is assumed to be the applied light wave. The solution of (7.17) is

$$x = -\frac{qEe^{i\omega t}}{m\omega^2}, \tag{7.18}$$

which gives the displacement of the charges due to the light wave.

Using the separation between the positive and negative charges obtained from the solution to the equation of motion (7.18), the polarization for the medium is

$$P = Nqx = -\frac{Nq^2E}{m\omega^2}, \tag{7.19}$$

where N is the number density (m^{-3}) of the charges. Using this polarization in (7.16), we obtain

$$\varepsilon E = \varepsilon_0 E - \frac{Nq^2E}{m\omega^2}.$$

We now have an equation for the dielectric constant, or equivalently the index of refraction, of the material

$$\frac{\varepsilon}{\varepsilon_0} = n^2 = 1 - \frac{Nq^2}{\varepsilon_0 m\omega^2}. \tag{7.20}$$

7.5.1.1 Plasma Frequency

We define the *plasma frequency*

$$\omega_p = \sqrt{\frac{Nq^2}{\varepsilon_0 m}}. \tag{7.21}$$

The plasma frequency is the natural frequency of the collective motion of the charges. The charges move much like a liquid. To understand the origin of the plasma frequency, consider a cloud of electrons confined to move in one dimension by a very large magnetic field—like beads on a string. The Coulomb repulsion between the electrons causes each electron to assume an equilibrium position between its neighbors. If one of the electrons is displaced from its equilibrium position, it will begin to oscillate. The neighboring electrons will experience perturbing forces due to the oscillating electron. In a short time, the initial displacement of a single electron will cause the whole cloud to oscillate. The frequency of this collective oscillation is the plasma frequency.

In terms of the plasma frequency, the index of refraction is

$$n^2 = 1 - \frac{\omega_p^2}{\omega^2}. \tag{7.22}$$

From this simple equation, originally derived by Drude in 1900, we can describe the optical behavior of electrons in metals. The conduction electrons in a metal are not restrained (at least to first order) by the metal's core ions, and therefore our model applies. Better agreement is obtained, however, if collisions of the electrons with other particles are included by the addition of a damping term,

$$-\gamma \frac{dx}{dt},$$

to the equation of motion. (This damping term is a function of the charge's velocity because the damping should depend inversely on the time between collisions.) The theory is also appropriate for the description of plasmas, as long as they are not too dense.

Equation (7.22) can be rewritten in the form of a dispersion relation

$$\omega = \omega_p \sqrt{1 + \left(\frac{c}{\omega_p}\right)^2 k^2}$$
$$\approx \omega_p \left[1 + \frac{1}{2}\left(\frac{c}{\omega_p}\right)^2 k^2\right],$$

which is identical to (7.13) if $a = c/\omega_p$. Thus, the dispersion relationship assumed during the discussion of pulse propagation is one appropriate for the description of an electromagnetic wave propagating in a plasma.

When $\omega < \omega_p$, (7.22) is negative and the index of refraction is imaginary:

$$\tilde{n} = \frac{\sqrt{\omega^2 - \omega_p^2}}{\omega} = i\frac{\sqrt{\omega_p^2 - \omega^2}}{\omega} = in\kappa.$$

In this situation, a wave incident on the medium would be completely reflected, as we found out in Chapter 3 by calculating the reflectivity

$$R = \frac{(\tilde{n} - 1)(\tilde{n}^* - 1)}{(\tilde{n} + 1)(\tilde{n}^* + 1)} = 1.$$

Experimental verification of this result is found in Figure 3.15.

As a verification of the qualitative agreement of this theory with experiment, the plasma frequency ω_p will be calculated for some materials. We continue to make the realistic assumption that the nucleus (positive charge) is massive and only the electrons (negative charge) respond to the high frequency ω. (This is not a necessary assumption, since m could be the reduced mass and q the effective charge.) The assumption allows the use of the fundamental constants associated with electrons to calculate the plasma frequency:

$$q = 1.6 \times 10^{-19}\ \text{C},$$
$$\varepsilon_0 = 8.85 \times 10^{-12}\ \text{C}^2 \cdot \text{s}^2/(\text{kg} \cdot m^2),$$
$$m = 9.11 \times 10^{-31}\text{kg},$$
$$\omega_p = \sqrt{\frac{N(1.6 \times 10^{-19})^2}{(8.85 \times 10^{-12})(9.11 \times 10^{-31})}} = \sqrt{N(3.175 \times 10^3)}\,.$$

1. For a gas at room temperature and a pressure of 2.5 Torr, $N = 10^{23}\,\text{m}^{-3}$, $\omega_p = 1.78 \times 10^{13}$ rad/s and $\nu_p = 2.84 \times 10^{12}$ Hz. For $\omega > \omega_p$, n is real; thus, from this result, we would expect to find most gases at low pressure to be transparent to visible light.
2. In the ionosphere (the Earth's atmosphere at altitudes above 70 km; see Figure 7.6), $N = 10^{11}\ \text{m}^{-3}$, $\omega_p = 1.78 \times 10^7$ rad/s, and $\nu_p = 2.84$ MHz, resulting in the prediction that the ionosphere should reflect frequencies below about 3 MHz. This result agrees with the experience of amateur radio operators, who know that the E-layer (100–200 km) reflects frequencies around 3 MHz. The higher-altitude F-layers (200–400 km) reflect higher frequencies and the lower-altitude D-layers (50–100 km) reflect lower frequencies, as they should if ω_p is proportional to the number density of charged particles.

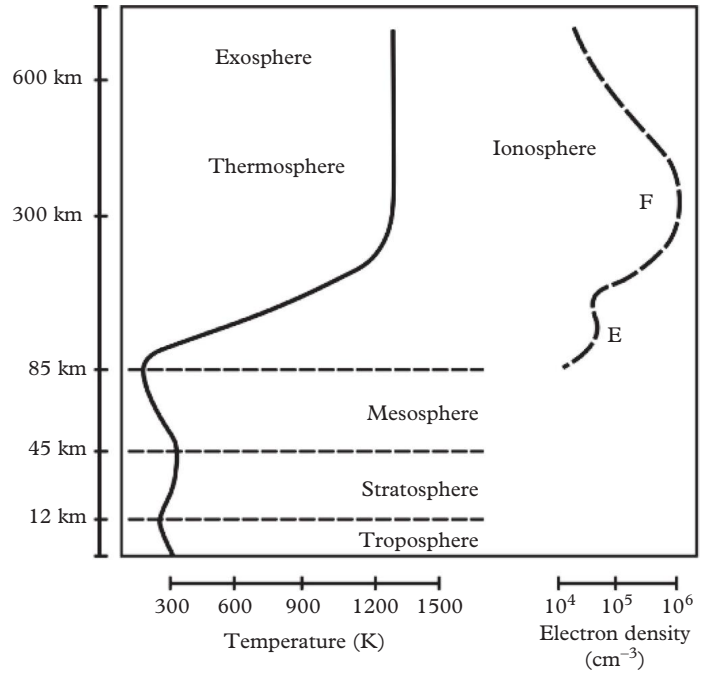

Figure 7.6 *Temperature and electron density in the ionosphere. (<http://en.wikipedia.org/wiki/Ionosphere#mediaviewer/File:Atmosphere_with_Ionosphere.svg>.)*

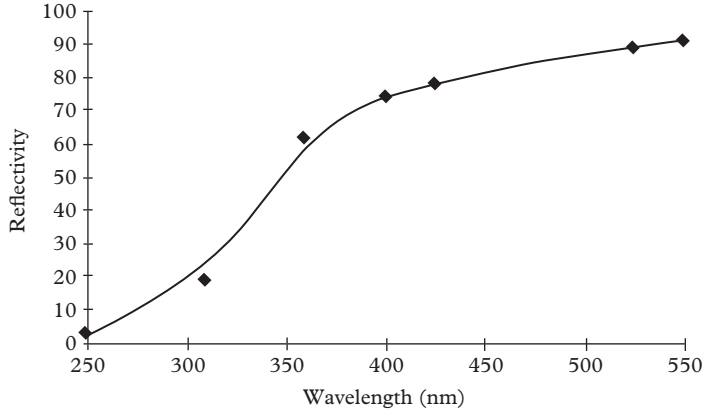

Figure 7.7 *Reflectivity of potassium as a function of wavelength near the transition associated with the plasma frequency. (Ives, H.E. and H.B. Briggs,* The Optical Constants of Potassium. *J. Opt Soc. Am, 1936. 26: p. 238.)*

3. In a metal, $N \approx 2.5 \times 10^{28}$ m^{-3}, $\omega_p = 8.91 \times 10^{15}$ rad/s, $\nu_p = 1.42 \times 10^{15}$ Hz. This plasma frequency yields a plasma wavelength $\lambda_p = 212$ nm. Experimentally, the plasma wavelength is observed to be $\lambda_p = 210$ nm for Na. From the result for sodium, we would expect a metal like potassium to exhibit high reflectivity in the visible and infrared but to be transparent in the ultraviolet. As shown in Figure 7.7, potassium is relatively transparent below 310 nm but reflective above 400 nm.

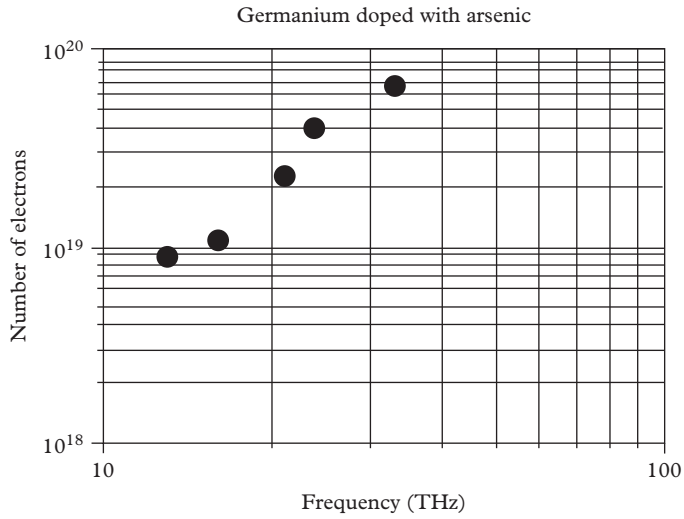

Figure 7.8 *Plasma frequency as a function of carrier concentration. (Pankove, J.I.,* Properties of Heavily Doped Germanium, *in* Progress in Semiconductors, *A.F. Gibson and R.E. Burgess, Editors. 1965, Heywood. p. 67.)*

4. The number of free charges in a semiconductor can be modified by changing the impurity doping. The change in plasma frequency with doping is shown in Figure 7.8, where the plasma frequency of germanium is plotted as a function of concentration of arsenic.

7.5.2 Molecular Gas

If the charges in the molecules are bound by some internal force that acts to bring them back to their equilibrium position, then we must modify the equation of motion (7.17) by the addition of a restoring force $F(x)$:

$$m\frac{d^2x}{dt^2} = -F(x). \tag{7.23}$$

(This equation describes the harmonic oscillator and only the highlights of its solution will be given here.) The exact form of the restoring force need not be known; we only require that the displacement from equilibrium be small so we can write the force as the first nonzero term in a Taylor series; i.e., we define the spring constant

$$\left[\frac{\partial F}{\partial x}\right]_{x=0} = s.$$

By approximating the restoring force with the first term of a Taylor series expansion, we can rewrite (7.23) as the equation of motion of a harmonic oscillator:

$$m\frac{d^2x}{dt^2} + sx = 0. \tag{7.24}$$

The solution of (7.24) is

$$x = x_0 e^{i\omega_0 t}, \tag{7.25}$$

where

$$\omega_0^2 = \frac{s}{m}.$$

We would have a more realistic model if we included a damping term linearly proportional to the velocity:

$$\frac{b}{m}\frac{dx}{dt} = \gamma\frac{dx}{dt},$$

modifying (7.24) to read

$$\frac{d^2x}{dt^2} + \gamma\frac{dx}{dt} + \omega_0^2 x = 0. \tag{7.26}$$

We will assume $\gamma \ll \omega_0$, which will allow the solution of this equation to be written as

$$x = x_0 e^{-(\gamma/2)t} e^{i\omega_0 t}. \tag{7.27}$$

If we illuminate the molecule with light of frequency ω, then we must add a driving term to (7.26):

$$\frac{d^2x}{dt^2} + \gamma\frac{dx}{xt} + \omega_0^2 x = \frac{q}{m}\tilde{E}. \tag{7.28}$$

Rather than solve the equation for x, we will replace x by the polarization using the definition of the latter:

$$P = Nqx, \tag{7.29}$$

where the number density is N molecules per unit volume. Substituting the polarization in (7.28) gives

$$\frac{d^2P}{dt^2} + \gamma\frac{dP}{dt} + \omega_0^2 P = \frac{Nq^2}{m}\tilde{E}.$$

We assume that the polarization P and the electric field have the same frequency but may have a different phase. The applied field and the induced polarization are thus

$$\tilde{E} = E_0 e^{i\omega t}, \quad P = \chi E_0 e^{i\omega t},$$

where χ is a complex constant. We can use the relations

$$\frac{dP}{dt} = i\omega P, \quad \frac{d^2P}{dt^2} = -\omega^2 P$$

to reformulate the equation of motion as (this formulation is sometimes called Drude's formula)

$$\chi(-\omega^2 + i\gamma\omega + \omega_0^2) = \frac{Nq^2}{m}.$$

The assumption about the form of P allows

$$\varepsilon\tilde{E} = \varepsilon_0\tilde{E} + P$$

to be rewritten as

$$\varepsilon = \varepsilon_0 + \frac{P}{\tilde{E}} = \varepsilon_0 + \chi.$$

Drude's formula can be substituted into this equation to yield

$$\varepsilon = \varepsilon_0 + \chi = \varepsilon_0 + \frac{Nq^2/m}{\omega_0^2 - \omega^2 + i\gamma\omega}.$$

We continue with the assumption that $\mu \approx \mu_0$, so $n^2 = \varepsilon/\varepsilon_0$ and

$$\frac{\varepsilon - \varepsilon_0}{\varepsilon_0} = n^2 - 1 = \frac{Nq^2/m\varepsilon_0}{\omega_0^2 - \omega^2 + i\gamma\omega}. \tag{7.30}$$

Using the definition of the plasma frequency,

$$n^2 - 1 = \frac{\omega_p^2}{\omega_0^2 - \omega^2 + i\gamma\omega}. \tag{7.31}$$

To separate the real and imaginary parts of the index of refraction, we use the assumption that the material is a dilute gas, so $n \approx 1$:

$$n^2 - 1 = (n+1)(n-1) \approx 2(n-1).$$

An equivalent approach is to assume

$$\frac{Nq^2/m\varepsilon_0}{\omega_0^2 - \omega^2 + i\gamma\omega} < 1$$

and use the approximation that

$$\sqrt{1+\delta} \approx 1 + \frac{1}{2}\delta.$$

This second approach corresponds, physically, to the assumption that the number of molecules, N, is small, or equivalently, that $\omega_0^2 - \omega^2$ is large. Either approximation leads to

$$n = 1 + \frac{\frac{1}{2}\omega_p^2(\omega_0^2 - \omega^2)}{(\omega_0^2 - \omega^2)^2 + \gamma^2\omega^2}, \tag{7.32}$$

$$n\kappa = \frac{\frac{1}{2}\omega_p^2\omega\gamma}{(\omega_0^2 - \omega^2)^2 + \gamma^2\omega^2}. \tag{7.33}$$

When

$$\omega_0^2 \gg \omega^2,$$

we can neglect ω^2, and (7.32) becomes

$$n \approx 1 + \frac{\omega_p^2}{2\omega_0^2} = \text{constant}. \tag{7.34}$$

Since we are assuming $\omega \approx 0$, (7.33) yields $n\kappa = 0$. For frequencies well below the resonant frequency of the oscillator, the index of refraction is real and independent of the frequency. There is no dispersion in this frequency region. As an example, in argon gas, $n = 1.000516$ for all frequencies below 1 MHz.

As ω approaches ω_0 from below, $\omega_0^2 - \omega^2$ decreases. We assume that ω is far enough from ω_0 so that $\omega_0 - \omega > \gamma$. (The physical significance of this limit can be found in Figure 7.10, where we see the assumption means that the applied frequency must be outside the curve labeled "absorption.") These limits lead to the conclusion that

$$\omega_0^2 - \omega^2 = (\omega_0 + \omega)(\omega_0 - \omega) > \omega_0(\omega_0 - \omega) > \gamma\omega_0 > \gamma\omega,$$
$$(\gamma\omega)^2 < (\gamma\omega_0)^2 < (\omega_0^2 - \omega^2)^2.$$

We can therefore neglect $(\gamma\omega)^2$ and rewrite (7.32) and (7.33) as

$$n = 1 + \frac{\omega_p^2}{2(\omega_0^2 - \omega^2)}, \tag{7.35}$$

$$n\kappa = \frac{\omega_p^2 \omega\gamma}{2(\omega_0^2 - \omega^2)^2},$$

$$= (n-1)\frac{\omega\gamma}{\omega_0^2 - \omega^2}. \tag{7.36}$$

As ω nears ω_0, we find from (7.35) that n increases with increasing frequency. This is called *normal dispersion*. We also find from (7.36) that $n\kappa \ll |n-1|$, and we may consider the index to be real if $\omega_0^2 - \omega^2 > \omega\gamma$.

Examples of the behavior predicted by (7.35) can be found among the inert gases. We can fit (7.35) to experimental data for the index of refraction of argon over the wavelength region from 240 to 600 nm, shown in Figure 7.9 as points. The smooth curve is predicted by (7.35), where we let ω_p and ω_0 be adjustable parameters. The equation of the smooth curve shown in Figure 7.9 is given by

$$n - 1 = \frac{19.732 \times 10^{28}}{7.0876 \times 10^{32} - \omega^2}.$$

The numerator in this equation is proportional to the square of the plasma frequency, which is equal to

$$\omega_p^2 = \frac{19.732 \times 10^{28}}{2} \text{ rad}^2/\text{s}^2,$$
$$\omega_p = 4.4 \times 10^{14} \text{ rad/s}.$$

The plasma wavelength $\lambda = 4.2$ μm. If the charged particles are assumed to be electrons, the number density can be obtained from the plasma frequency as

$$N = \frac{\omega_p^2}{3.175 \times 10^3} = 3.1 \times 10^{25} \text{m}^{-3},$$

which is roughly the density of a gas at 1 atm pressure, corresponding to the experimental conditions associated with the data.

The equation for the index predicts a static dielectric constant $n = 1.000278$; the measured DC value is 1.000516. The resonant frequency ω_0 in the equation corresponds to a wavelength of 71 nm—the atomic spectral data does not support this result. While the other constants correspond to realistic values, the classical theory is not able to predict the correct resonant frequency. To make an accurate prediction, we need the quantum theory.

When $\omega \approx \omega_0$, ω can be replaced by ω_0 in (7.32) and (7.33) except where the difference $\omega_0^2 - \omega^2$ occurs. This difference can be approximated by

$$\omega_0^2 - \omega^2 = (\omega_0 + \omega)(\omega_0 - \omega) \approx 2\omega_0(\omega_0 - \omega),$$

allowing (7.32) and (7.33) to be rewritten as

$$n = 1 + \frac{\omega_p^2 \dfrac{\omega_0 - \omega}{4\omega_0}}{(\omega_0 - \omega)^2 + \left(\dfrac{1}{2}\gamma\right)^2}, \tag{7.37}$$

$$n\kappa = \frac{\dfrac{\omega_p^2 \gamma}{8\omega_0}}{(\omega_0 - \omega)^2 + \left(\dfrac{1}{2}\gamma\right)^2}. \tag{7.38}$$

The previous approximation concerning $\omega\gamma$ is no longer correct, and we retain the damping term in (7.37) and (7.38).

The parameters obtained by fitting (7.35) to the experimental data in Figure 7.9 cannot be immediately applied to this new approximate result of our model. Near the resonance, these parameters lead to $n \gg 1$ and

$$\omega_p > \omega_0^2 - \omega^2 + i\gamma\omega,$$

in contradiction to the previous assumption that

$$\frac{Nq^2/m\varepsilon_0}{\omega_0^2 - \omega^2 + i\gamma\omega} = \frac{\omega_p^2}{\omega_0^2 - \omega^2 + i\gamma\omega} < 1.$$

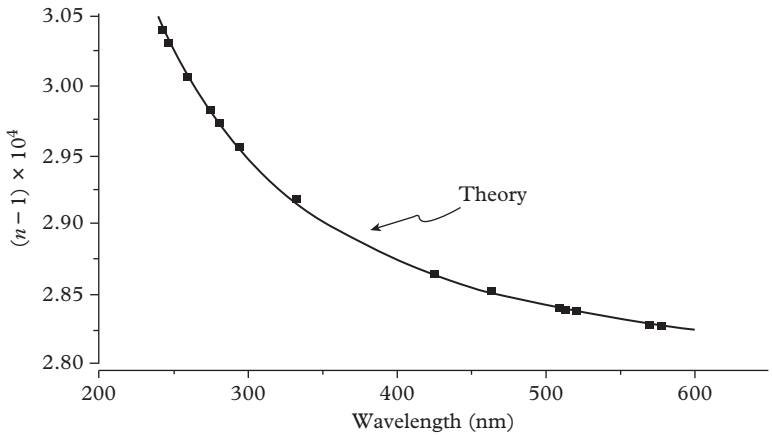

Figure 7.9 *Dispersion in argon in the visible region of the spectrum. (Korff, S.A.,* Optical dispersion. *Rev. Mod. Phys, 1932. 4: p. 471–503.)*

We need only make one modification to the parameters to remove this contradiction. The number density can be reduced to $N = 10^{23}$ m^{-3}, corresponding to a gas pressure of about 2 Torr. This assumption about the number density will lower the plasma frequency to

$$\omega_p = 1.27 \times 10^{13} \text{ rad/s}.$$

With the new plasma frequency, the assumption stated above is correct, and the other parameters from Figure 7.9 can be used to obtain the curves shown in Figure 7.10. As we stated before, the classical model does not correctly predict the details near a resonance, but the general behavior shown in Figure 7.10 is what is observed experimentally. This agreement with experiment is obtained by introducing into the model parameters obtained from experiments made far from the resonance condition.

The curve labeled "absorption" in Figure 7.10 is a plot of $n\kappa$ using (7.38). The curve can be described mathematically by a Lorentzian function. The curve is often called the absorption line or the resonance line in the literature. It is easy to show that its maximum occurs at ω_0 and that its width is γ.

As the resonant condition is approached from longer wavelength, the index curve in Figure 7.10, plotted using (7.37), increases; this is called normal dispersion. Within γ of the resonant frequency ω_0, the index n decreases from its maximum to its minimum value. This region is called the region of anomalous dispersion because the index decreases with increasing frequency. The occurrence of anomalous dispersion can be demonstrated by evaluating n at three points:

$$\begin{aligned} \omega_0 - \omega &= \frac{1}{2}\gamma \quad &\Rightarrow \quad & n = 1 + \frac{\omega_p^2}{4\omega_0\gamma}, \\ \omega_0 - \omega &= 0 \quad &\Rightarrow \quad & n = 1, \\ \omega_0 - \omega &= -\frac{1}{2}\gamma \quad &\Rightarrow \quad & n = 1 - \frac{\omega_p^2}{4\omega_0\gamma}. \end{aligned}$$

At wavelengths shorter than the resonant wavelength, the index is less than 1, but approaches the value of 1 as the wavelength decreases.

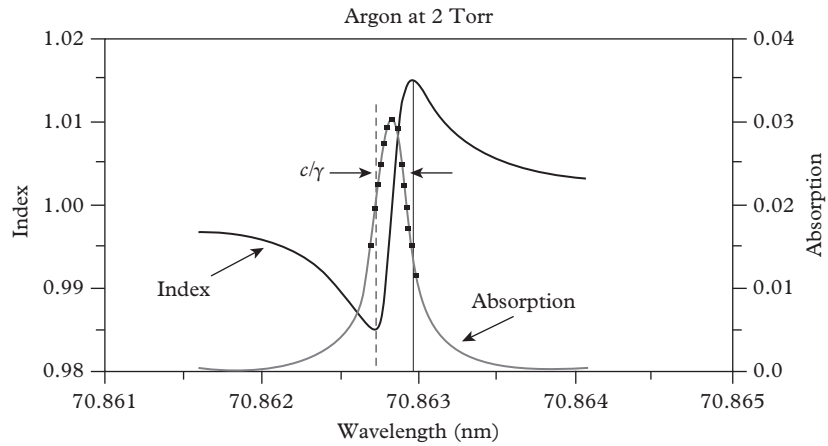

Figure 7.10 *A plot of the index (7.37), shown by the dark curve, and nκ, (7.38), shown by the gray curve, calculated using the parameters used to calculate the curve shown in Figure 7.9 modified to apply to a pressure of 2 Torr. Note that the abscissa is in wavelength rather than frequency.*

Finally, when $\omega \gg \omega_0$, we return to (7.31) to obtain a result identical to (7.22) modified by the addition of a damping term:

$$n \approx 1 - \frac{\omega_p^2}{\omega^2 - i\gamma\omega}.$$

The second term on the right-hand side of this equation will approach zero as the frequency ω becomes much larger than ω_p. Therefore, for very high frequencies (short wavelengths), the index will approach 1 from values less than 1, and the medium will appears to the wave as if it were a vacuum. This behavior can be seen in Figure 7.24, where the index of refraction for aluminum is plotted. For wavelengths below the plasma frequency, the index of refraction of aluminum is less than 1 and approaches the value of 1 as the wavelength decreases.

If absorption, such as that shown in Figure 7.10, occurs in the visible region of the spectrum, then the material will be colored. Resonant frequencies occurring in the ultraviolet and visible regions of the spectrum are due to the electrons in atoms and molecules. The vibrations of the atoms making up a molecule result in resonances in the infrared. Molecules can also rotate, and resonances associated with reorientation of molecules are found throughout the far infrared and into the microwave regions of the spectrum. In each of these wavelength regions, the data suggest that a number of oscillators with different spring constants s_j exist. In order to model a material containing a collection of resonances, the assumption is made that a fraction f_j of the oscillators in a material will have resonant frequency ω_j and loss term γ_j. With this assumption, (7.31) is modified to read

$$n^2 - 1 = \omega_p^2 \sum_{j=1}^{n} \frac{f_j}{\omega_j^2 - \omega^2 + i\gamma_j\omega},$$

where f_j is called the *oscillator strength.*

7.5.3 Dense Dielectric

In our treatment of dispersion, we have neglected the fact that the electric dipoles induced by the applied field will interact through the long-range field produced by one dipole at the site of another. One would think that it would be impossible to take into account the modification of the applied field at the molecule due to its many neighbors, but this is not the case. Lorentz solved the problem by noting that

1. Molecules have a minimum separation that is twice the molecular radius.
2. The distribution of the neighboring molecules can be treated as isotropic for a large number of materials.
3. The molecular dimensions are small compared the wavelength of light, so the electric field variables can be treated as constants with respect to spatial variables, and propagation times can be ignored.

Using these assumptions, Lorentz derived what is now called the Lorentz field, $\mathbf{E}_L = \mathbf{E} + a\mathbf{P}$, where $\mathbf{E}$ is the applied field. For nonpolar dielectrics with certain symmetries such as cubic, $a = 1/(3\varepsilon_0)$ [the derivation of this result can be found in a number of solid state physics books (e.g., [1]) and will not be given here.] We will assume this value for a in our discussion:

$$\mathbf{E}_L = \mathbf{E} + \frac{\mathbf{P}}{3\varepsilon_0}. \tag{7.39}$$

Much of what we earlier derived can be modified to apply to a dense medium by using the Lorentz field in place of the applied field. The modified one-dimensional equation of motion is

$$\frac{d^2P}{dt^2} + \gamma\frac{dP}{dt} + \omega_0^2 P = \frac{Nq^2}{m}\left(E + \frac{P}{3\varepsilon_0}\right)$$

and the dielectric constant is

$$\varepsilon = \varepsilon_0 + \frac{\dfrac{Nq^2}{m}}{\omega_0^2 - \omega^2 - \dfrac{Nq^2}{3\varepsilon_0 m} + i\gamma\omega}. \tag{7.40}$$

The index of refraction is

$$n^2 = 1 + \frac{\omega_p^2}{\omega_0^2 - \dfrac{1}{3}\omega_p^2 - \omega^2 + i\gamma\omega}. \tag{7.41}$$

This equation can be put into the same mathematical form as (7.31), derived for a dilute dielectric medium, by defining a new resonant frequency

$$\omega_m^2 = \omega_0^2 - \frac{1}{3}\omega_p^2.$$

The effect of having a dense medium, i.e., a medium where the individual charges are allowed to interact, is simply to lower the resonant frequency from that of a free molecule. In quantum mechanics, this shift in resonant frequency is called *renormalization*. Physically, the shift can be understood by noting that the neighboring molecules will be oscillating together. The electric field from the neighbors acts against the restoring force of the oscillator, reducing the effective "spring constant" s. The difference between ω_m and ω_0 leads to the Clausius–Mossotti relation (7.51)(see Section 7.7) by solving (7.40) for ω_p^2.

Figure 7.11 shows the variation in the index of refraction for a solid, the semiconductor gallium phosphide (GaP). The region of the spectrum over which a material exhibits

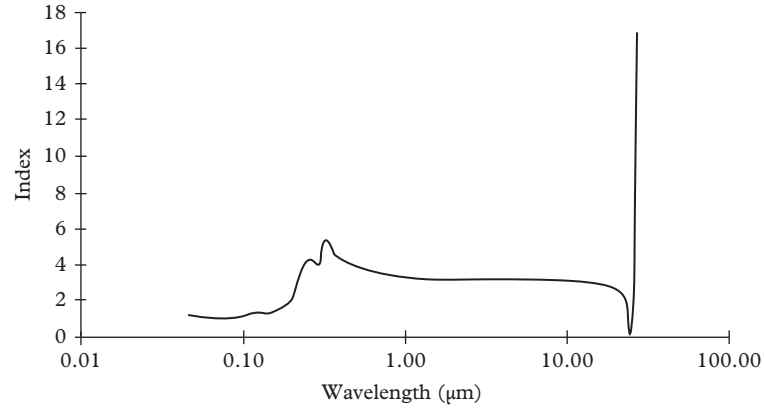

Figure 7.11 *Real part of the index of refraction of GaP.*

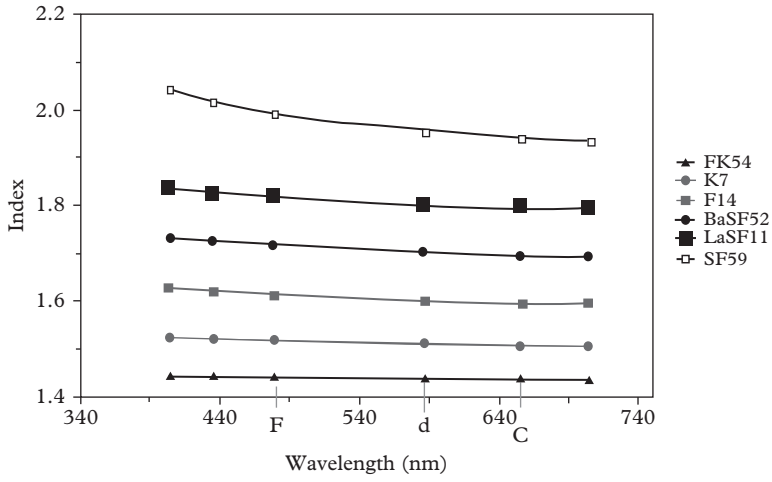

Figure 7.12 *Index of refraction as a function of wavelength for some optical glasses [2]. The materials were selected to show the range of indexes available for visible optics. Outside of the visible region, there are few indices available to the optical designer. The wavelengths labeled C, d, and F are Fraunhofer lines used to characterize the dispersion in optical glasses (see Appendix 7A).*

low absorption and high transmission is the region in which the material can serve as an optical material. The useful wavelength span of any optical material is limited on the low- and high-frequency ends by an increase in absorption. The spectrum of GaP contains the general characteristics of all optical materials. It is transparent between 600 nm and 4.5 μm, with strong absorption in the visible and far-infrared regions, making it a useful infrared optical material. Because of the availability of ultraviolet and infrared data on GaP, we will look at it in some detail. All optical materials will exhibit the same general behavior regardless of their useful range of wavelengths. For example, Figure 7.12 displays the index of refraction for a number of optical glasses. (The labels C, d, and F on the wavelength axis of Figure 7.12 denote the Fraunhofer solar spectrum lines used by optical designers to characterize dispersion in glass; see Appendix 7A.) In the visible region, the optical glasses shown in Figure 7.12 exhibit the same type of dispersion as is exhibited by GaP in the near infrared, i.e., a smooth, nearly linear curve with a negative slope. On either side of the low-absorption region, strong absorptions will appear. For example, a nearby resonance in the ultraviolet is the origin of the rise in the index of SF59 glass at short wavelengths.

In Figure 7.13, the visible and ultraviolet region of the spectrum shown in Figure 7.11 is expanded. If the small variations are ignored, then the index does show anomalous dispersion in the region of maximum absorption and we do see the index approaching the value of 1 at short wavelengths (high frequencies). However, the curve is a large departure from Figure 7.9. This departure is due to a failure of the simple classical model. The allowable electronic energies, in a solid, fall into bands (Figure 7.14), and this band structure is not adequately modeled by a simple harmonic oscillator. Evidence of the band structure can be obtained from the imaginary component of the index. For energies below the energy difference between the conduction band and the valence band very little absorption is observed. At the frequency corresponding to the energy gap between these two bands, a rapid rise in absorption is observed. In Figure 7.13, the rise starts at about 450 nm.

This rapid increase in absorption below 450 nm is due to the light wave exciting electrons from the valence band of the GaP into the conduction band (see Figure 7.14).

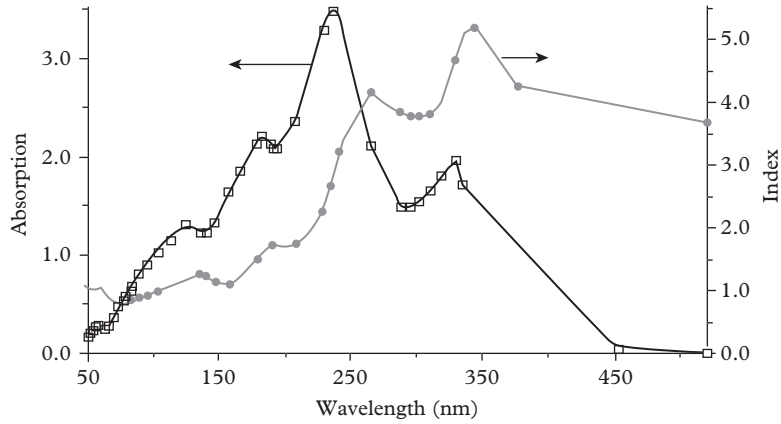

Figure 7.13 *Complex index of refraction of GaP.*

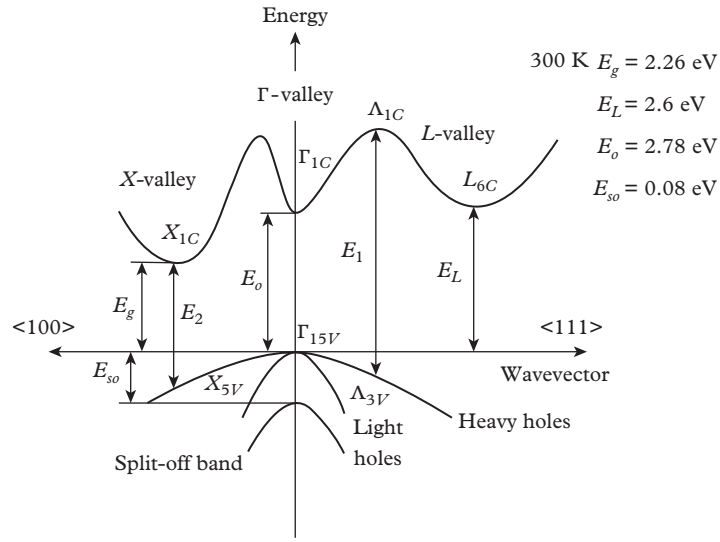

Figure 7.14 *Band structure of GaP.*

For this to happen, the frequency of the light must exceed the bandgap frequency of GaP, which occurs at 2.26 eV. The conversion between energy and wavelength is given by

$$E(\text{eV}) = \frac{1239}{\lambda(\text{nm})}.$$

(Details of how to interpret the absorption spectrum of a semiconductor can be found in [3].)

The band structure shown in Figure 7.14 for GaP is the dispersion curve for the propagation of electrons (viewed as waves) in a solid. A free electron has a simple parabolic dispersion curve, as shown in Figure 7.15(a). If the electron is moving in a small periodic

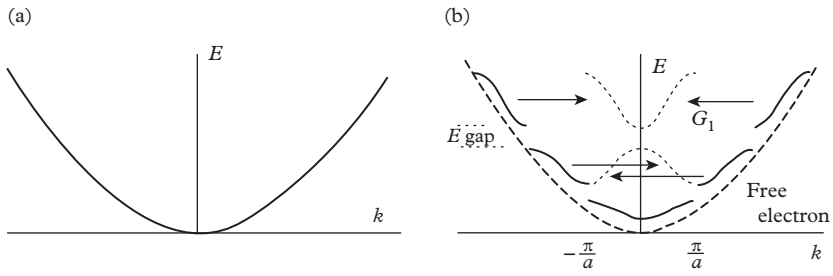

Figure 7.15 *(a) Dispersion for free electron. (b) Bandgaps in a periodic potential due to Bragg scattering.*

potential, modeling the movement of an electron in a crystalline solid, the dispersion curve displays bandgaps, as shown in Figure 7.15(b). This is quite a departure from the behavior predicted by the simple oscillator theory we have been using. We will discuss structures that exhibit a similar dispersion bandgap property for light in Chapter 12.

All optical materials have strong absorptions at short wavelengths. Insulators such as the glasses used in visible optics, shown in Figure 7.12, have much larger bandgaps than GaP, usually greater than three times the energy in electron volts. Because of the large bandgap, insulators exhibit a rapid rise in absorption at a much shorter wavelength than GaP. The index of refraction of the glass SF59 in Figure 7.12 displays the expected rapid rise at short wavelengths.

Optical materials also exhibit absorption bands in the infrared, and GaP is no exception. In Figure 7.16, we expand the infrared region of the spectrum shown in Figure 7.11 to display both the real and imaginary components of the index of refraction. The structure of this resonance is different from the structure of the ultraviolet resonance. For the infrared resonance, the model leading to (7.40) applies. The charges making up the oscillator associated with this resonance are the Ga and P atoms in the solid. As can be seen from Figure 7.16, the optical behavior of a solid is complicated, even when the model applies; there is no way to produce a simple expression for n and $n\kappa$ from (7.40).

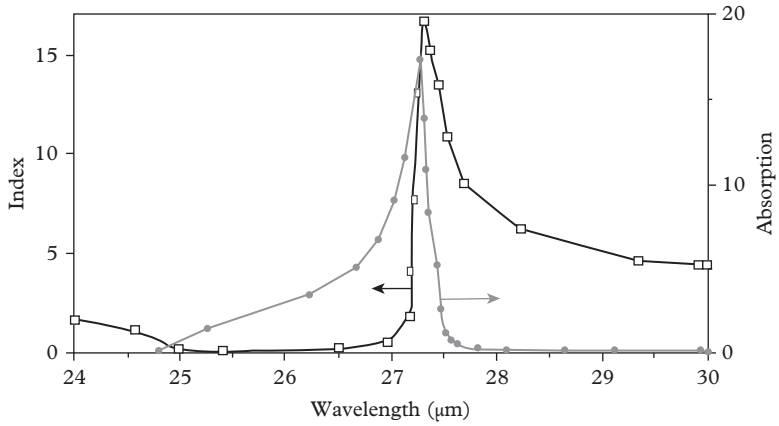

Figure 7.16 *The complex index of refraction of GaP in the infrared.*

Rather than work with the complicated functions obtained for n and $n\kappa$ that would describe the curves in Figure 7.16, the dielectric constant is used to characterize the material:

$$\begin{aligned}\varepsilon' = \mathcal{R}e\{\varepsilon\} &= n^2(1-\kappa^2)\\ &= 1 + \omega_p^2\left[\frac{\omega_m^2-\omega^2}{(\omega_m^2-\omega^2)^2+\gamma^2\omega^2}\right]\\ &= c^2\mu\varepsilon, \end{aligned} \tag{7.42}$$

$$\begin{aligned}\varepsilon'' = Im\{\varepsilon\} &= 2n^2\kappa\\ &= \omega_p^2\left[\frac{\gamma\omega}{(\omega_m^2-\omega^2)^2+\gamma^2\omega^2}\right]\\ &= \frac{c^2\mu\sigma}{\omega}. \end{aligned} \tag{7.43}$$

The functional forms of the real and imaginary parts of the dielectric constant are the same as were obtained for n and $n\kappa$ by assuming a dilute medium.

The similarity between the dielectric constant results of (7.42) and (7.43) and the index results for a dilute medium, given by (7.37) and (7.38), can be demonstrated by making a normalized plot of (7.42) and (7.43). The universal plot is generated by first defining the following normalized parameters:

$$a^2 = \left(\frac{\omega_p}{\omega_m}\right)^2, \quad g = \frac{\gamma}{\omega_m},$$

$$x = \frac{\omega^2-\omega_m^2}{\omega_m^2}, \quad y = \frac{n^2(1-\kappa^2)}{a^2}, \quad z = \frac{2n^2\kappa}{a^2}.$$

Substituting into (7.42) yields a general function for the real part of the dielectric constant,

$$y = \frac{1}{a^2} - \frac{x}{x^2+g^2(1+x)},$$

and substituting into (7.43) yields a general function for the imaginary part of the dielectric constant,

$$z = \frac{g\sqrt{1+x}}{x^2+g^2(1+x)}.$$

Figure 7.17 shows plots of $y(x)$ and $z(x)$.

We have implicitly assumed that only one resonant frequency is present. Normally, however, many resonances are present. If each resonance is very narrow, i.e., if γ is small, then the multiple resonant frequencies can be treated independently of each other, according to the theory just developed. However, if γ is large for some resonant frequency, then that frequency will affect its neighboring resonances. To incorporate the effects of nearby strong absorptions, an average index of refraction, $\langle n\rangle$, can be introduced, where $\langle n\rangle$ is experimentally determined. This is done to generate an experimentally based dispersion relation

$$y = \frac{\langle n\rangle}{a^2} - \frac{x}{x^2+g^2(1+x)}.$$

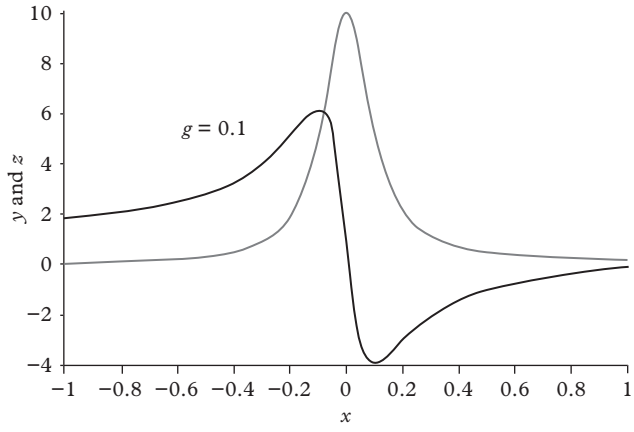

Figure 7.17 *Normalized plots of the real (dark curve) and imaginary (light curve) parts of the dielectric constant.*

7.5.4 Metals

The results derived for the dielectric constant of a solid can be applied to a metal and are consistent with the results we obtained for an electron gas. In a metal, the conduction electrons are not bound tightly to the core metal ions; therefore, for these electrons, the resonant frequency can be neglected, $\omega_0 \ll \omega$. Not all electrons are free; for those electrons that are bound, the resonant frequency ω_0 is used (within a metal, $\mathbf{E}$, rather than $\mathbf{E}+\mathbf{P}/(3\varepsilon_0)$, is the proper internal field.) Using this information, (7.42) and (7.43) can be rewritten as

$$c^2\mu\varepsilon \approx \frac{\varepsilon}{\varepsilon_0} = 1 - \frac{\omega_p^2}{\omega^2+\gamma^2} + \omega_p^2\left[\frac{\omega_0^2-\omega^2}{(\omega_0^2-\omega^2)^2+\gamma^2\omega^2}\right], \tag{7.44}$$

$$\frac{c^2\mu\sigma}{\omega} \approx \frac{\sigma}{\varepsilon_0\omega} = \frac{\omega_p^2\gamma}{\omega(\omega^2+\gamma^2)} + \omega_p^2\left[\frac{\gamma\omega}{(\omega_0^2-\omega^2)^2+\gamma^2\omega^2}\right]. \tag{7.45}$$

From (7.44) and (7.45), we see that

$$\mathcal{R}e\{\varepsilon(\omega)\} \approx 1 - \left(\frac{\omega_p}{\omega}\right)^2. \tag{7.46a}$$

$$\mathcal{I}m\{\varepsilon(\omega)\} \approx \frac{\omega_p^2\gamma}{\omega^3} \approx \frac{\sigma}{\omega\varepsilon_0}. \tag{7.46b}$$

The bound electrons lead to the color of some metals such as gold and copper. If we neglect the effect of the bound electrons, we discover that this result is in agreement with the analysis of the dispersion of free charges made earlier.

7.6 Plasmons and Polaritons

The electrons in a metal are free to move as a cloud about the positive charged atoms. The electron cloud has a collective plasma frequency (7.21) that is a material resonance determined by the number of electrons. The plasma frequency determines when the metal transitions from a strong reflector to a transparent material (see Figures 7.8 and 7.9).

At low frequencies, metals are strongly absorbing, and the absorption is characterized by the skin depth. When the incident frequency exceeds the plasma frequency, the waves propagate in the metal. At the plasma frequency, a longitudinal mode is created in the electron gas. Associated with the propagation of this mode are quantum particles called plasmons (more descriptively, bulk plasmons). They occur when $\varepsilon = 0$ in (7.46). ε becomes negative when $\omega^2 \leq \omega_p^2$. Since $n = \sqrt{\varepsilon/\varepsilon_0}$, the index becomes imaginary and the material reflects all the incident light; see (3.56) and Figure 3.15. This cutoff is used in the design of energy-saving window coatings (low-E windows), which are designed to transmit visible wavelengths but reflect infrared wavelengths. To get the cutoff in the infrared, a highly doped semiconductor such as indium tin oxide is used for the coating.

At the boundary between a dielectric and the metal, transverse electromagnetic surface modes called surface plasmons (or, better, surface plasmon polaritons) exist. They are generated when the applied frequency is given by $\omega_{\text{SP}}^2 = \omega_p^2/2$ and $\varepsilon = -1$. We can indicate the relative values of these newly defined resonances by plotting their values on the dispersion curves of Figure 7.17; see Figure 7.18.

In Chapter 3 [see (3.7)], we applied Maxwell's boundary conditions to determine how much light is reflected from an interface. We have the requirement that the tangential components of **E**, (3.19), and the tangential components of **H**, (3.25), must be continuous. We can follow the same procedure here to look at a wave polarized in the plane of incidence:

$$\frac{k_{dz}}{n_d^2} = \frac{k_{mz}}{n_m^2} \tag{7.47a}$$

Across the boundary,

$$k_x = k_{xd} = k_{xm},$$

$$k_{dz}^2 + k_x^2 = n_d^2 k_0^2,$$

$$k_{dz} = -i\sqrt{k_x^2 - n_d^2 k_0^2}, \quad k_x^2 > n_d^2 k^2. \tag{7.47b}$$

$$k_{zm} = i\sqrt{k_x^2 - n_m^2 k_2}, \quad k_x^2 > n_m^2 k^2. \tag{7.47c}$$

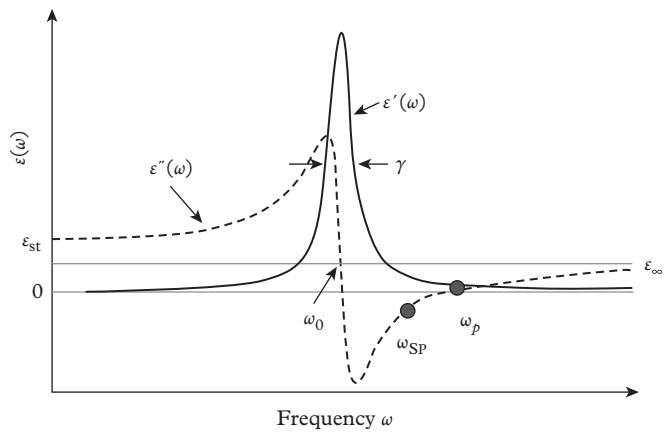

Figure 7.18 *Dielectric constant with plasma frequency and surface plasmon frequency identified.*

This means that the dielectric constant ε must change sign across the boundary. As we discovered in Chapter 3 with total reflection, the imaginary k results in a nonpropagating wave whose amplitude falls exponentially perpendicular to the boundary. If we use (7.47b, c) in (7.47a), we obtain an expression for the surface plasmon wavevector k_x:

$$k_x = k_{\mathrm{SP}} = \frac{2\pi}{\lambda}\sqrt{\frac{n_d^2 n_m^2}{n_d^2 + n_m^2}} = k_0\sqrt{\frac{n_d^2 n_m^2}{n_d^2 + n_m^2}}, \quad k_0 = \frac{\omega}{c}. \tag{7.48}$$

Note that the wavevector of the surface plasmon is larger than the free-space wavevector. This means that the effective wavelength is reduced, resulting in a compression of the area occupied by the wave.

If ε_d is real (a dielectric) and ε_m is complex (a metal),

$$\varepsilon_d = n_d^2, \quad \varepsilon_m = \varepsilon_m' + i\varepsilon_m'',$$
$$k_{\mathrm{SP}} = k_{\mathrm{SP}}' + ik_{\mathrm{SP}}''.$$

Akin to the skin depth and similar to what we did for total reflection, we can calculate the propagation length of the surface plasmon:

$$\delta_{\mathrm{SP}} = \frac{1}{2k_{\mathrm{SP}}''} = \frac{c}{\omega}\left(\frac{\varepsilon_m' + \varepsilon_d}{\varepsilon_m'\varepsilon_d}\right)^{3/2}\frac{\varepsilon_m'^2}{\varepsilon_m''}. \tag{7.49}$$

Figure 7.19 provides an indication of how the surface plasmon propagation length varies with wavelength for different metals. In silver, the propagation distance in the visible is from 10 to 100 μm. The losses are high at high frequencies, when (7.46a) applies, and acceptable at low frequencies, when (7.46b) applies. The frequency at which the transition between acceptable and unacceptable losses occurs is given by $\omega = \gamma$ and is about 5–10 THz

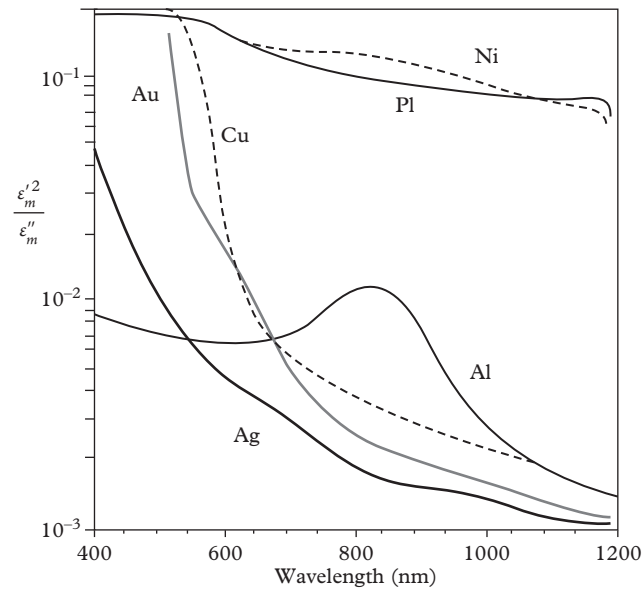

Figure 7.19 *Ratio of real to imaginary dielectric constant in metals.*

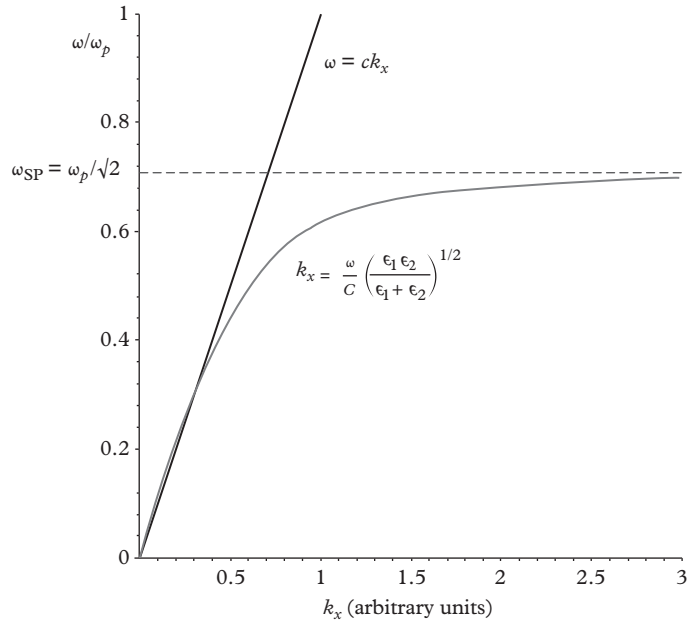

Figure 7.20 *The dispersion of a surface plasmon is shown by the curve. The free-space dispersion is given by the straight line (7.1).*

Table 7.4 *Optical attenuation for optoelectronic devices*

Guide type	Attenuation	Scale
Silicon ridge guide	<0.1 dB/mm	$\lambda/2$
Metal strip guide	>0.5 dB/mm	λ
Metal–insulator–metal (MIM) slot guide	>500 dB/mm	$\lambda/10$

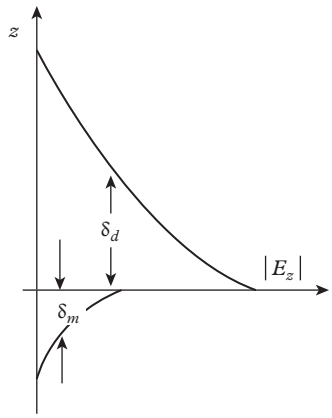

Figure 7.21 *Field of a surface plasmon, decaying exponentially downward into the metal and upward into the dielectric. Propagation occurs along the surface.*

($\lambda = 30 - 60$ μm). Physically, high frequency is when displacement current density dominates, and low frequency is when conduction current dominates.

We can see from Figure 7.20 that at low values of k_x, the surface plasmon acts like a photon, but at large values, the plasmon is localized as is indicated by (7.48). This localization is the reason for the recent interest in surface plasmons. The enthusiasm for reducing the size of optical integrated systems through the use of this localization has masked the negative aspects of optical losses in metals. Table 7.4 shows loss and confinement for some typical waveguides used in integrated electro-optical circuits. A number of paths to efficient plasmonic-based optical systems have been taken, but none has yet proved successful [4].

Just as we saw for coupling of radiation into an optical guide, we cannot couple into a plasmon mode by shining light onto the surface of the metal. The field of the surface plasmon is evanescent perpendicular to the interface, decays exponentially into the metal and dielectric at different proportions as shown in Figure 7.21, and propagates along the boundary between the metal and dielectric. To couple into the evanescent wave, we must use a momentum matching technique as we discussed for guided optical waves in Figures 3.13

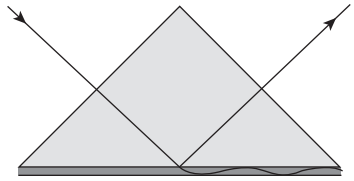

(a)

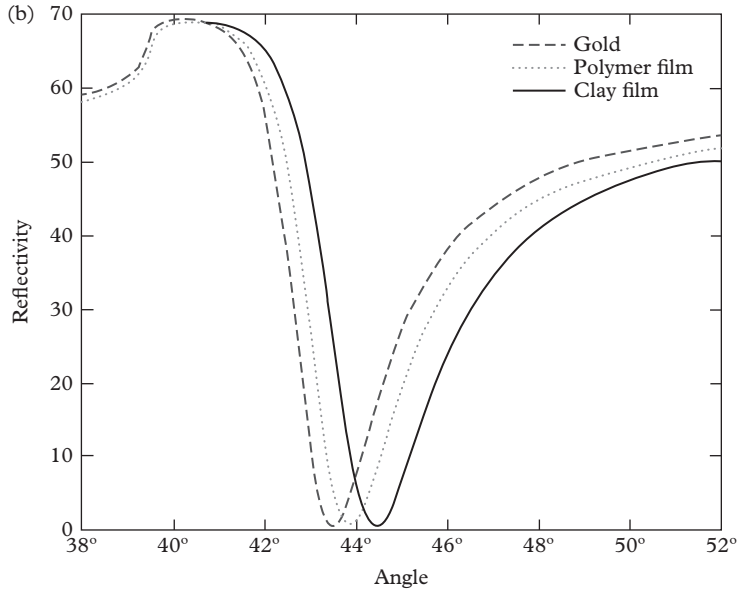

Figure 7.22 *(a) The Otto configuration of SPR measurement derived from Figure 5.27. The bottom film is gold. ("Otto-schema" by Tomio—at en.wikipedia—Transferred from en.wikipedia. Licensed under Creative Commons Attribution-Share Alike 3.0 via Wikimedia Commons; <http://commons.wikimedia.org/wiki/File:Otto-schema.png#mediaviewer/File:Otto-schema.png>.) (b) Surface plasmon resonance shifts measured using the device shown in (a). The reflected energy is recorded as a function of angle as nanofilms self-assemble on 38 nm gold film. ("SPR-adsorption-data" by Tomio Haraszti—at en.wikipedia—Transferred from en.wikipedia. Licensed under Creative Commons Attribution-Share Alike 3.0 via Wikimedia Commons; <http://commons.wikimedia.org/wiki/File:SPR-adsorption-data.png#mediaviewer/File:SPR-adsorption-data.png>.)*

and 5.27. Experimentally, we see the creation of the surface plasmon by monitoring the reflected light as a function of angle as in Figure 7.22(b), using the optical configuration in Figure 7.22(a) (derived from Figure 5.27). The shift in the minimum in reflectivity in the presence of a film on gold in Figure 7.22 indicates two of the major applications of plasmonics, namely, the detection of chemical contamination with enhanced sensitivity due to surface-enhanced Raman scattering and the biochemical determination of the concentration of protein films.

7.7 Lorenz–Lorentz Law

If we have a transparent substance, where the index of refraction is real, and we can neglect the damping constant γ, we find

$$\frac{1}{\rho}\left(\frac{n^2-1}{n^2+2}\right) = \text{constant}, \tag{7.50}$$

where ρ is the density. (Remember that the density is proportional to the number density N.) In this form, (7.50) is called the *Lorenz–Lorentz law*. (For a gas, $n \approx 1$ and the Lorenz–Lorentz law can be rewritten as

$$\frac{n-1}{\rho} = \text{constant},$$

which is sometimes called the *law of Gladstone and Dale*.)

The constant in (7.50) is called the *atomic refractivity*. For molecular gases and liquids with a molecular weight M, (7.50) is modified to read

$$\left(\frac{n^2-1}{n^2+2}\right)\frac{M}{\rho} = \text{constant},$$

where the constant is now called the *molar refractivity*. From this result, we can obtain an equation that allows the calculation of the index of refraction of a mixture of noninteracting substances by using the index of refraction of each of the components of the mixture. For a mixture of N materials that do not interact,

$$\left(\frac{n^2-1}{n^2+2}\right)\frac{W}{\rho} = \sum_{j=1}^{N}\left(\frac{n_j^2-1}{n_j^2+2}\right)\frac{W_j}{\rho_j},$$

where W is the weight of the mixture and W_j is the weight of the jth component of the mixture. By dividing through by W, the weight fraction of each component can be used in the summation on the right.

In the limit as we approach very low frequencies, the Lorenz–Lorentz equation is written in terms of the dielectric constant:

$$\frac{1}{\rho}\left(\frac{\dfrac{\varepsilon}{\varepsilon_0}-1}{\dfrac{\varepsilon}{\varepsilon_0}+2}\right) = \text{constant} \tag{7.51}$$

and is called the *Clausius–Mossotti relation*. The constant in (7.51) is called the *molar polarization*. If (7.50) and (7.51) are correct, we should be able to use the index of refraction of a gas at a given wavelength to predict the dielectric constant of a liquid at that same wavelength. For nonpolar molecules in the visible region, we can use the relations to an accuracy of a few percent (see Table 7.5 for the molar refractivities of a few simple molecules).

Table 7.5 *Molecular refractivity*

Material	n		Molar refractivity	
	Liquid	Gas	Liquid	Gas
O_2	1.221	1.000271	2.00	2.01
HCl	1.245	1.000447	6.88	6.62
H_2O	1.334	1.000244	3.71	3.70
CS_2	1.628	1.00147	21.33	21.78

The Clausius–Mossotti equation fails to predict the molar refractivity of polar liquids or gases (e.g., water). The cause of the failure has as its origin the failure of the Lorentz theory to include permanent dipole moments. In the treatment by Lorentz, he assumed that all of the dipole moments were parallel, aligned by the field that induced them. Permanent dipole moments would be oriented at random [1].

We use (7.41) to rewrite (7.50) as

$$\frac{n^2-1}{n^2+2} = \frac{\frac{1}{3}\omega_p^2}{\omega_m^2 - \omega^2 + i\gamma\omega}. \tag{7.52}$$

Up to now, we have assumed that the solid contains N identical oscillators. If we instead suppose that a molecule contains several types of oscillators, we may write, as we did for a molecular gas,

$$\frac{n^2-1}{n^2+2} = \frac{1}{3}\omega_p^2 \sum_j \frac{f_j}{\omega_j^2 - \omega^2 + i\gamma_j\omega}. \tag{7.53}$$

Drude called the quantity f_j the number of dispersion electrons per atom. **Wolfgang Pauli (1900–1958)** gave f_j its present name of oscillator strength. Quantum mechanics leads to an expression equivalent to (7.53). However, the oscillator strengths f_j are not introduced in an ad hoc fashion as we have; instead, they are found to be proportional to intramolecular dipole transition probabilities, i.e., the probability that a transition between two quantum levels will take place and a single photon produced. The frequencies ω_j are those associated with transitions between pairs of quantum states, and the damping term γ_j is found to be proportional to $1/\tau$, where τ is the lifetime of the upper quantum state, i.e., the one at the higher energy.

7.8 Signal Velocity, Superluminal Propagation

The definitions of phase velocity

$$v = \frac{\omega}{k}$$

and group velocity

$$u = \frac{d\omega}{dk} = v - \lambda \frac{dv}{d\lambda}$$

lead to an unusual result in the region of anomalous dispersion. The wave velocity decreases with increasing wavelength; i.e.,

$$\frac{dv}{d\lambda} < 0.$$

Because this derivative is negative, the group velocity must be greater than the phase velocity, $u > v$. On the high-frequency side of the absorption peak (see Figure 7.11), the index of refraction is less than 1, which implies that $v > c$. Therefore, we are led to the conclusion that the group velocity is greater than the velocity of light. This result is in contradiction to a

basic premise of the theory of relativity. The dilemma posed by this result was raised during the years immediately following Einstein's publication of the special theory of relativity as a demonstration that the basic assumption of Einstein was in error.

The apparent conflict between the propagation velocity of light near a resonant absorption and the Theory of Relativity was resolved by **Sommerfeld** [5] and **Brillouin** [6]. The original papers and a detailed discussion of the topic can be found in the book by Brillouin [7] on the subject of wave propagation. We will not perform the derivation of the theories here, but will rather discuss the conclusions that can be drawn from the theory.

The conclusions of the theory developed by Sommerfeld and Brillouin are as follows:

1. No signal can propagate faster than the speed of light in a vacuum.
2. The leading edge of a pulse propagating in a dispersive medium travels at the vacuum velocity of light. This component of the pulse, called the *Sommerfeld precursor*, has a small amplitude that grows from zero to a maximum and then decays back to zero. The frequencies associated with the precursor are very high at its front edge but decrease behind the pulse front. The frequencies are not a function of the incident wave but rather a function of the plasma frequency of the medium and the distance traveled,

$$\frac{\omega_p^2 z_0}{c},$$

   where z_0 is the distance propagated.
3. Later in the pulse's temporal evolution, a second precursor, the *Brillouin precursor*, arrives. The amplitude and frequency of this precursor grow and then decay. The frequency of this precursor is not equal to that of the incident wave or that of the first precursor. The second precursor is much lower in frequency than the first precursor, and the difference in frequency between the two precursors increases with propagation distance.
4. The main part of the pulse finally arrives, and the wave assumes the "steady-state" values dictated by the incident wave. The time needed to reach this final state is associated with the signal velocity in the medium, which is limited by the theory of relativity to a value no higher than the velocity of light.

Figure 7.23 displays the general shape of this propagating pulse, with the time of arrival plotted from left to right.

The classical model of dispersion can provide a qualitative understanding of the propagation of light. As light propagates in a dispersive medium, some of it is absorbed and

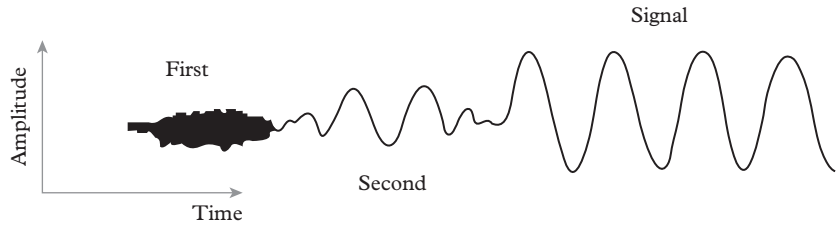

Figure 7.23 *The first and second precursors and the signal are shown here with time of arrival increasing to the right. The origin and thus the front edge of the pulse are on the left.*

reradiated by the electrons in the medium. Because of inertia of the oscillators, the reradiated energy is out of phase with the incident wave. It is this lag in the reradiated energy that results in a slower propagation velocity.

To describe the shape of the leading edge of the propagating wave, we must use a number of frequencies. A number of very high frequencies will be needed if the front of the wave is very steep. The free and bound electrons will not follow these very high frequencies, because of inertia. Thus, the very high frequencies will pass through the medium without seeing the electrons, i.e., as if they were propagating in a vacuum. The waves associated with the highest frequencies make up the first precursor (see Figure 7.23) and travel at the velocity of light in a vacuum.

Verification that very high frequencies propagate through a medium as if it were a vacuum can be obtained from the index of refraction of materials at very high frequencies (very short wavelengths). Figure 7.24 shows the index of refraction of aluminum, which at very short wavelengths is approximately equal to 1.

The second precursor, and the final arrival of the signal component of the pulse, can also be understood in a qualitative manner as the variation in the response of the classical oscillators to the Fourier components making up the pulse.

The concept of precursors developed by Sommerfeld and Brillouin seemed to settle the issue of propagation of light beyond the speed of light, called *superluminal propagation*. Because the conditions of anomalous dispersion occur in the presence of strong absorption, observation of superluminal propagation was not likely, so the debate faded.

With the discovery of the laser, it became possible to overcome the absorption and observe superluminal propagation [8, 9]. Theoretical and experimental papers quickly appeared [10]. It would take us too far afield to explore this subject in detail, but we can consider what, if anything, is propagating at the group velocity.

By proper selection of the waves contributing to the group shown in Figure 7.2, we can generate a variety of both positive and negative group velocities. Table 7.6 displays values calculated using

$$f(x,t) = 2A\cos(\Delta\omega t - \Delta kx)\cos(\omega t - kx)$$

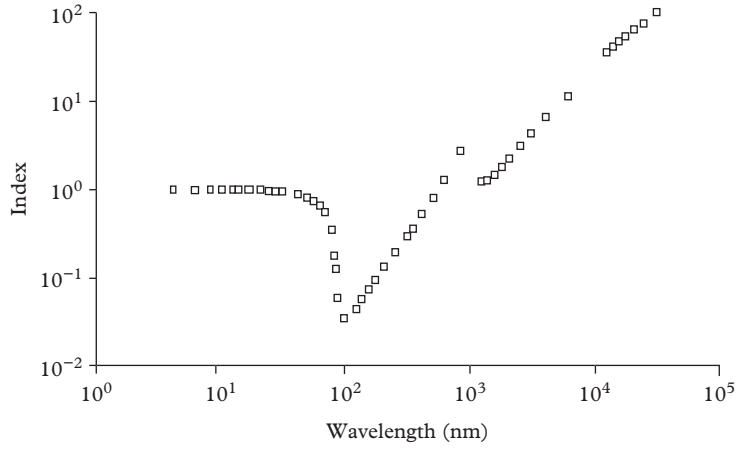

Figure 7.24 *Index of refraction of aluminum from soft X-ray wavelengths to submillimeter wavelengths.*

Table 7.6 *Composition of wave group in Figure 7.2*

Wave	ω (rad/s)	k (rad/m)	$\Delta\omega$ (rad/s)	Δk (rad/m)	v_p (m/s)	v_g (m/s)
1	2	2			1	
2	8	2.2			3.6	
Group	5	2.1	–3	–0.1		30

that might lead to Figure 7.2. The group is traveling from left to right in Figure 7.2 at about ten times the velocity of the individual waves creating the group. The waves that interfere constructively to create the peak in the group at the far right of Figure 7.2 entered the figure at a much earlier time. Any signal placed on either wave 1 or 2 would not travel across the figure at the group velocity. To further emphasize that any information that we wish to carry with the waves does not travel at the group velocity, consider what happens if we interchange the values of k for waves 1 and 2. Now the group propagates backward across the figure.

We have discussed this behavior using only the mathematical wave theory and have not associated it with any physical theory. If the waves used in the example above were light waves, we see that we have not obtained a prediction of superluminal propagation. Group

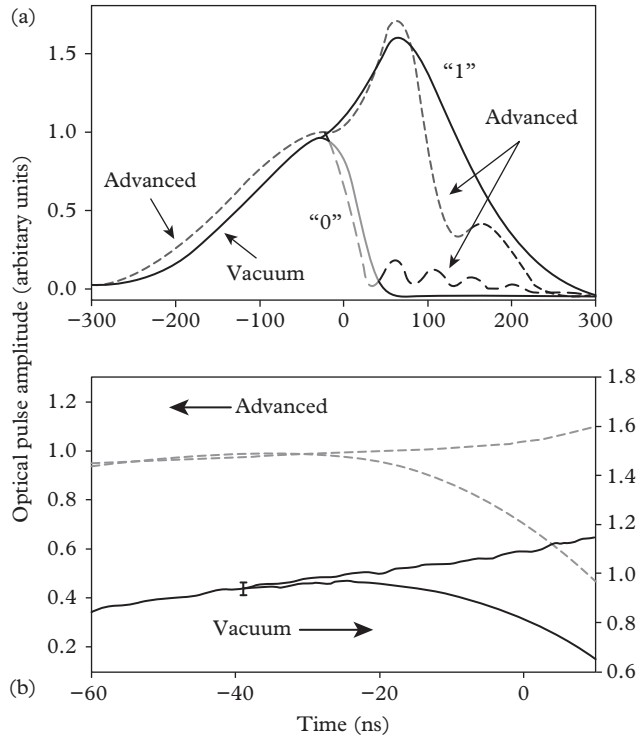

Figure 7.25 *Propagation of a digital signal in a region exhibiting superluminal propagation. (a) Transmission of a "0" and "1" through a superluminal region (solid line) and the vacuum (dashed line). Each curve is the average of 50 pulses. (b) Magnified view of the two pulses (offset for clarity). It can be seen from (a) that the leading edge of the superluminal pulse arrives earlier than the leading edge of the vacuum pulse, but that is not the case for the signals. (Reprinted by permission from Macmillan Publishers Ltd: Letters to Nature 425(16 October): p. 695–697, Copyright 2003.)*

velocities that exceed the phase velocities are simply a consequence of classical interference between the pulse's frequency components. A review of this subject is available [11] and provides a good source of references on the topic of superluminal propagation.

Relativity states that "objects" do not propagate faster than the speed of light. To do so would violate causality, i.e., the wave would be detected before it was produced. For electromagnetic waves, Sommerfeld suggested that the causality limitation should be placed on a signal and defined a signal as *"... nothing until a certain moment in time, then, for instance, a series of regular sine waves, which stop after a certain time or which continues indefinitely"* [7].

A recent experiment has been performed that demonstrated that the propagation speed of information in a region exhibiting superluminal propagation travels below the speed of light [12]. A wave was coded with the digits "0" and "1" and propagated through a cell that was exhibiting superluminal propagation. Figure 7.25 displays the fact that even though superluminal propagation is observed in the gas cell of the experiment, the information on the light pulse does not exceed the speed of light in a vacuum.

7.9 Summary

The original model used in Chapter 1 to discuss wave propagation was based upon the assumption that the wave would propagate without change. This assumption is equivalent to assuming that all frequencies propagate at the same velocity. We found that if a wave model allowed a frequency-dependent wave velocity, i.e., dispersion, a pulse would change shape as it propagated. By assuming a functional form for the relationship between the phase velocity and the wavelength, we were able to demonstrate that a pulse would increase in both temporal and spatial breadth as it propagated.

It was necessary to introduce a new velocity to describe the propagation of a pulse in a dispersive medium. This velocity was called the group velocity

$$u = \frac{d\omega}{dk}.$$

A wave of a single frequency would propagate at the phase velocity

$$v = \frac{\omega}{k},$$

and a wave made up of a group of frequencies would travel at the group velocity

$$u = v - \lambda \frac{dv}{d\lambda}.$$

A model was developed to explain dispersion in an optical material based upon a classical harmonic oscillator. The model was used to calculate the index of refraction for three cases.

Plasma A neutral gas of unbound charges has no resonant frequency. The index of refraction of a neutral gas or a plasma was found to be given by

$$n^2 = 1 - \frac{\omega_p^2}{\omega^2},$$

where the plasma frequency is defined as

$$\omega_p = \sqrt{\frac{Nq^2}{\varepsilon_0 m}}.$$

If a loss term is included in the model for a conductive gas, then the index of refraction is complex. The real component of the index is

$$n^2(1-\kappa^2) = 1 - \frac{\omega_p^2}{\omega^2+\gamma^2}$$

and the imaginary component is

$$2n^2\kappa = \frac{\omega_p^2\gamma}{\omega(\omega^2+\gamma^2)}.$$

Molecular gas By assuming a collection of noninteracting harmonic oscillators, the index of refraction for a gas was calculated to be

$$n^2 = 1 + \frac{\omega_p^2}{\omega_0^2-\omega^2+i\gamma\omega}.$$

To compare this result with experiment, the real and imaginary parts of the index were separated by assuming that the gas was dilute. The real part of the index could then be written

$$n = 1 + \frac{\frac{1}{2}\omega_p^2(\omega_0^2-\omega^2)}{(\omega_0^2-\omega^2)^2+\gamma^2\omega^2}.$$

The imaginary part of the complex index of refraction of a dilute gas was found to be

$$n\kappa = \frac{\frac{1}{2}\omega_p^2\omega\gamma}{(\omega_0^2-\omega^2)^2+\gamma^2\omega^2}.$$

Dense dielectric The final case evaluated allowed the individual oscillators to interact. The interaction lowered the resonant frequency from that of a noninteracting oscillator to

$$\omega_m^2 = \omega_0^2 - \frac{1}{3}\omega_p^2.$$

The expression for the index of refraction could no longer be separated easily into its real and imaginary components. Instead, the expression for the dielectric constant was used to describe the dispersion. The real part of the dielectric constant was found to be

$$\mathcal{R}e\{\varepsilon\} = 1 + \omega_p^2\left[\frac{\omega_m^2-\omega^2}{(\omega_m^2-\omega^2)^2+\gamma^2\omega^2}\right]$$

and the imaginary part to be

$$Im\{\varepsilon\} = \omega_p^2\left[\frac{\gamma\omega}{(\omega_m^2-\omega^2)^2+\gamma^2\omega^2}\right].$$

For a transparent, nonpolar material, which has only a real dielectric constant, the index of refraction was shown to obey the Lorenz–Lorentz law

$$\left(\frac{n^2-1}{n^2+2}\right)\frac{M}{\rho} = \text{constant}.$$

This relationship allows the use of the index of refraction of a gas to predict the dielectric constant of a liquid.

Surface plasmon At the interface between a metal and a dielectric, a surface wave can be generated. Its propagation constant is

$$k_x = k_{\mathrm{SP}} = \frac{2\pi}{\lambda}\sqrt{\frac{n_d^2 n_m^2}{n_d^2 + n_m^2}} = k_0\sqrt{\frac{n_d^2 n_m^2}{n_d^2 + n_m^2}}, \quad k_0 = \frac{\omega}{c},$$

with a propagation length

$$\delta_{\mathrm{SP}} = \frac{1}{2k''_{\mathrm{SP}}} = \frac{c}{\omega}\left(\frac{\varepsilon'_m + \varepsilon_d}{\varepsilon'_m \varepsilon_d}\right)^{3/2}\frac{\varepsilon'^2_m}{\varepsilon''_m}.$$

Optical precursor The final topic covered in this chapter concerned the propagation of a pulse of light through a dispersive medium. For a carrier frequency of the pulse in the region of anomalous dispersion, the resultant group velocity seemed to contradict the postulate that information cannot be transmitted faster than the speed of light. We learned that the leading edge of a pulse travels no faster than the speed of light, and the information or signal velocity is always limited to a value that does not exceed this velocity.

7.10 Problems

7.1. In the ionosphere, the lowest layer (called the D layer) has an electron density that reaches its maximum of $N \approx 10^9$ m^{-3} at midday and rapidly disappears after sunset. The highest layer (called the F_2 layer) has a density of 10^{12} m^{-3}. What are the plasma frequencies of these two layers? How does the behavior of the D layer affect radio transmission?

7.2. At a wavelength $\lambda = 589.3$ nm, the index of N_2 at standard temperature and pressure (STP) is $n = 1.000297$ and the index of liquid nitrogen at –196°C is $n = 1.205$. The gas density $\rho = 1.251 \times 10^{-3}$ g/m^3 and the liquid density $\rho = 0.808$ g/m^3. Use these data to see how well the Lorenz–Lorentz equation agrees with experiment.

7.3. Calculate the indices of refraction for acetone and ether in the gas phase at STP using the indices from the liquids:

Material	ρ (g/cm^3)	n
Acetone	0.7899	1.3588
Ethyl Ether	0.7138	1.3526

Compare with the observed values of 1.00108 for acetone and 1.00152 for ether. (*Hint:* Remember from chemistry that the volume occupied by one molecular weight of a gas is 22.4 liters.)

7.4. Derive the Clausius–Mossotti equation (7.51) using the equation

$$\varepsilon = \varepsilon_0 + \frac{\varepsilon_0 \omega_p^2}{\omega_0^2 - \frac{1}{3}\omega_p^2 - \omega^2 - i\gamma\omega}.$$

7.5. In the case of normal dispersion in the visible region, in optical materials with the nearest absorption in the ultraviolet, the index of refraction can be approximated by Cauchy's equation

$$n = A + \frac{B}{\lambda^2} + \frac{C}{\lambda^4}.$$

Derive Cauchy's equation from (7.32).

7.6. The following measurements were made for air:

λ (m)	$n-1$
6.563×10^{-7}	2.916×10^{-4}
5.184×10^{-7}	2.940×10^{-4}
4.308×10^{-7}	2.966×10^{-4}
3.441×10^{-7}	3.016×10^{-4}
2.948×10^{-7}	3.065×10^{-4}

Fit Cauchy's equation to these data, using only the first two terms of the Cauchy equation.

7.7. From the equation for $n\kappa$,

$$n\kappa = \frac{\omega\gamma\omega_p^2/2}{(\omega_0^2-\omega^2)^2+\gamma^2\omega^2},$$

find the relationship between the width of the absorption peak at half-maximum and γ. What about n? (*Hint:* Use the equations for a molecular gas.)

7.8. From the equations for the real component of the dielectric constant for a dense dielectric,

$$\varepsilon = 1 + \frac{\omega_p^2(\omega_0^2-\omega^2)}{(\omega_0^2-\omega^2)^2+\gamma^2\omega^2},$$

find the maximum, minimum, and width.

7.9. If we have a step-index fiber with a numerical aperture of 0.16, $n_2 = 1.45$ and a core diameter of 90 μm, how much intermodal dispersion should we expect?

7.10. Calculate the group velocity of light at a wavelength of 500 nm when the index of refraction is given by

$$n = 1.577 + \frac{1.78\times10^{-14}}{\lambda^2}.$$

7.11. The experimentally derived dispersion relation for hydrogen in the wavelength range $0.4\ \mu\text{m} < \lambda < 9\ \mu\text{m}$ is

$$n^2 - 1 = 2.721\times10^{-4} + \frac{2.11\times10^{-18}}{\lambda^2}.$$

Using the results of Problem 7.5, find the resonant frequency.

7.12. Find the group velocity for a radio wave propagating in the ionosphere. The dispersion of the phase velocity is

$$v = \sqrt{c^2 + b^2\lambda^2}.$$

7.13. Write a computer program to generate the plots shown in Figure 7.17. Vary the constant g, which corresponds to the loss term, and see what effect it has on the shape of the curves.

7.14. Starting with (7.45), show that the DC conductivity of a metal is given by

$$\sigma_0 = \frac{Nq^2}{m\gamma}.$$

7.15. Derive Sellmeier's equation

$$n^2 = 1 + \frac{a\lambda^2}{\lambda^2 - \lambda_0^2},$$

using (7.31) as the starting point. Under what conditions will Sellmeier's equation reduce to Cauchy's equation?

7.16. The following data have been gathered for the index of refraction of water–ethanol mixtures:

Weight fraction of ethanol	ρ	n
0.0000	0.998	1.337
0.2075	0.97	1.3508
0.4089	0.939	1.3616
0.5998	0.899	1.367
0.7999	0.854	1.3693
1.000	0.805	1.3676

Use these data to evaluate the Lorenz–Lorentz law.

7.17. Derive (7.12) from the definition of the group velocity,

$$u = \frac{d\omega}{dk}.$$

7.18. Find the radii of curvature for a cemented achromatic double with a focal length of 10 cm using BK7 as the crown and SF6 as the flint. Assume that the crown is equiconvex (the radii of curvature of both surfaces are the same) and set one curvature of the flint equal to the crown so that they can be glued together.

7.19. Redesign the lens in Problem 7.18, but now make the flint an equiconvex lens.

7.20. Redesign the lens in Problem 7.18 using SK4 as the crown and F4 as the flint.

REFERENCES

1. Kittel, C., *Introduction to Solid State Physics*. 7th ed. 1995: Wiley.
2. *Schott Optical Glass Catalog*. 2007: Schott North America.
3. Pankove, J.I., *Optical Processes in Semiconductors*. 1975: Dover.
4. Khurgin, J.B and G. Sun, *Practicality of compensating the loss in the plasmonic waveguides using semiconductor gain medium*. Appl. Phys. Lett., 2012. **100**: 011105.
5. Sommerfeld, A., *Über die fortpflanzung des lichtes in disperdierenden medien*. Ann. Phys, 1914. **44**: p. 177.
6. Brillouin, L., *Über die Fortpflanzung des Licht in disperdierenden Medien*. Ann. Phys., 1914. **44**: p. 203.
7. Brillouin, L., *Wave Propagation and Group Velocity*. 1960: Academic Press.
8. Wang, L.J., A. Kuzmich, and A. Dogarlu, *Gain-assisted superluminal light propagation*. Nature, 2000. **406**: p. 277–279.
9. Jeong, H., A.M.C. Dawes, and D.J. Gauthier, *Direct observation of optical precursors in a region of anomalous dispersion*. Phys. Rev. Lett., 2006. **96**: 143901.
10. Recami, E., *Superluminal motions? A bird's-eye view of the experimental situation*. Found. Phys., 2001. **31**: p. 1119–1135.
11. Maiorino, J.E. and W.A. Rodrigues. *What is superluminal wave motion?* Sci. Tech. Mag., **2**(4): p. 167; <http://www.ime.unicamp.br/rel_pesq/1999/rp59-99.html>.
12. Stenner, M.D., D.J. Gauthier, and M.A. Nelfeld, *The speed of information in a "fast-light" optical medium*. Nature, 2003. **425**: p. 695–697.

Appendix 7A Chromatic Aberrations

Dispersion in optical glasses, illustrated in Figure 7.12, produces wavelength-dependent optical properties. Refraction displays a wavelength dependence that leads to the dispersion of white light into individual colors by a prism as shown in Figure 7A.1.

The wavelength dependence of refraction produces a modification in the performance of a lens called *primary chromatic aberration* (Figure 7A.2). Chromatic aberration is a result of a variation in the focal length or, equivalently, the power of a lens

$$\frac{1}{f} = \Phi = (n-1)\left(\frac{1}{R_1} - \frac{1}{R_2}\right),$$

$$\delta\Phi = \delta n\left(\frac{1}{R_1} - \frac{1}{R_2}\right) = \frac{\delta n}{n_i - 1}\Phi = \frac{\Phi}{v_i}, \tag{7A.1}$$

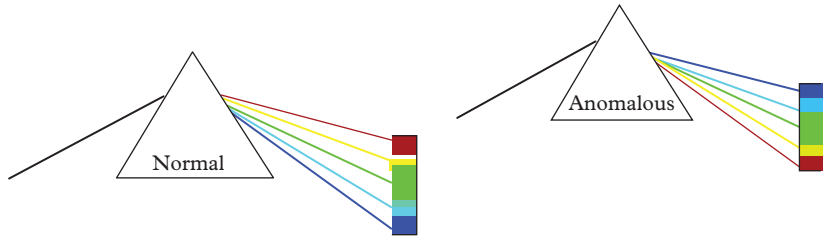

Figure 7A.1 *Effects on refraction of normal and anomalous dispersion.*

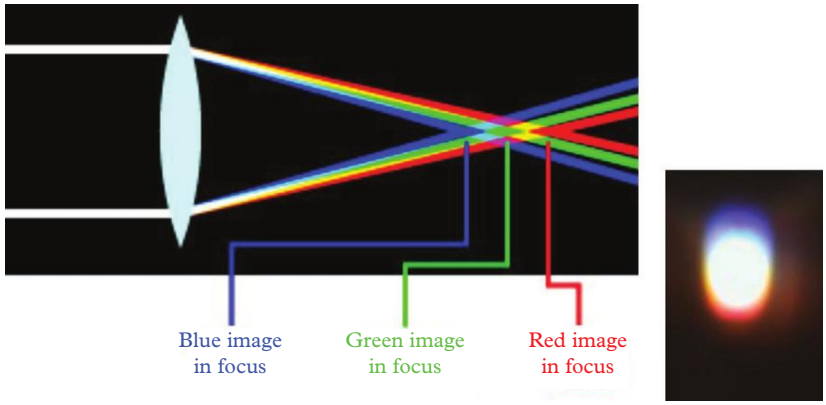

Figure 7A.2 *On the left is longitudinal chromatic aberration with the blue focus occurring first and the red focus occurring last. On the right is an image of the best focus displaying lateral chromatic aberration, with blue light appearing on the top of the image and red light on the bottom.*

Table 7A.1 *Standard wavelengths*

Fraunhofer designation	Wavelength (nm)	Element
r	706.5188	He
C	656.2725	H
C′	643.8469	Cd
D_1	589.5923	Na
D_2	588.9953	Na
d	587.5618	He
e	546.0740	Hg
F	486.1327	H
F′	479.9914	Cd
g	435.8343	Hg
h	404.6561	Hg

where v_i is the *Abbe value* of the glass. (In the optics literature, the Abbe value is also known as the *V-number*, the *constringence*, or the *reciprocal dispersive power*.) The change in the focal length is called *longitudinal chromatic aberration* or *longitudinal color*. The magnification of a lens also changes with wavelength. This change is called *lateral chromatic aberration* or *lateral color*.

The dispersion properties of glasses are measured at standard wavelengths (see Table 7A.1). These wavelengths are prominent lines in the solar spectrum that were labeled with letters by Joseph von Fraunhofer. These letter labels are used in all discussions of dispersion in the visible region of the spectrum.

The Abbe value, defined in (7A.1), is used to characterize the dispersion of a particular glass. Its definition suggests an infinitesimal change, but in practice it is defined as

$$v_d = \frac{n_d - 1}{n_F - n_C}. \tag{7A.2}$$

The numerator $n_d - 1$ is called the *refractivity* and the denominator $n_F - n_C$ is called the *partial dispersion*. The partial dispersion spans the visible spectrum, with the refractivity positioned roughly in the center.

Glasses are grouped into two types: *crown* and *flint*. A very long time ago, the crowns were window glass composed of soda, lime, and silica. The glass was formed by blowing a globe and whirling it into a disk (Figure 7A.3). The appearance of the disk led to the name crown. Flint glass was composed of alkalis, lead oxide, and silica and was used for cut-glass tableware. It was first produce by George Ravenscroft under commission to the trade organization entitled the *Worshipful Company of Spectacle Makers of London* (who are still functioning in London).

Today, the adjectives crown and flint separate glasses into low-dispersion, low-index crowns that fulfill the inequalities

$$n_d > 1.60, \qquad v_d > 50,$$
$$n_d < 1.60, \qquad v_d > 55$$

and high-dispersion, high-index flints, that do not fulfill these inequalities.

Glass types are identified by an alphanumeric such as BK7 and a numerical index such as 517642. The letter B indicates a borosilicate and the letter K indicates a crown-type glass.

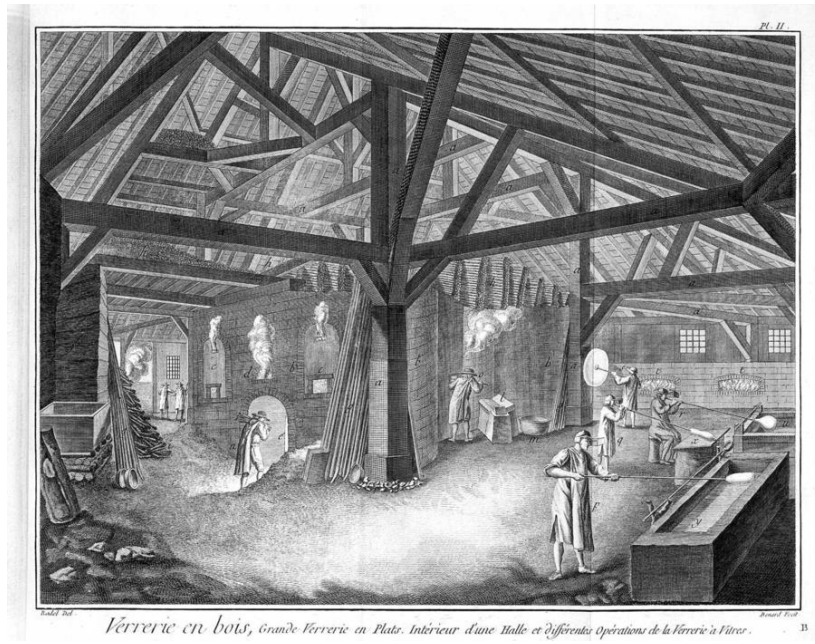

Figure 7A.3 *Manufacturing method of Crown Glass. This technique was replaced by cast and rolled glass by about the 1660s. (By Diderot Encyclopedia [Public domain], via Wikimedia Commons.)*

The numerical index provides much more information about the glass type, but is not easy to remember. The first three digits are the refractivity of the glass, in this case

$$n_d - 1 = (1.51680 - 1) \times 10^3 \approx 517,$$

and the last three digits are the Abbe number, in this case

$$\nu_d = (64.17) \times 10 \approx 642.$$

A lens where $\delta\Phi = 0$ is called an achromat. From (7A.1), we see that a single lens cannot be an achromat unless it has zero power.

We can combine several lenses to approach an achromat. In the solution of Problem 5.13, it was discovered that the focal length of two lenses in contact is given by

$$\frac{1}{f} = \frac{1}{f_1} + \frac{1}{f_2}, \tag{7A.3}$$

where f_1 and f_2 are the focal lengths of the individual lenses. In terms of the power of a lens, this result is written

$$\Phi = \Phi_1 + \Phi_2. \tag{7A.4}$$

The variation in the power of the lens pair with wavelength is given by

$$d\Phi = \delta\Phi_1 + \delta\Phi_2 = \frac{\Phi_1}{\nu_{d1}} + \frac{\Phi_2}{\nu_{d2}}. \tag{7A.5}$$

Newton believed that all glasses exhibited the same dispersion, making it impossible to produce an achromat. His belief led him to invent the reflecting telescope. A lawyer and amateur astronomer, Chester Moor Hall, proved Newton wrong by discovering that crown and flint glass could be combined into a doublet with no chromatic aberration. He attempted to keep his discovery secret by using different London lensmakers to produce the two components of his doublet. Unfortunately, both lensmakers were swamped with work and subcontracted the job to the same individual, John Dollond. Dollond recognized the purpose of the two lenses and applied for a patent on the idea (Figure 7A.4). The court awarded Dollond the patent, even though Moor Hall was the inventor. The judge ruled that the person who made an invention public for the general good deserved the patent.

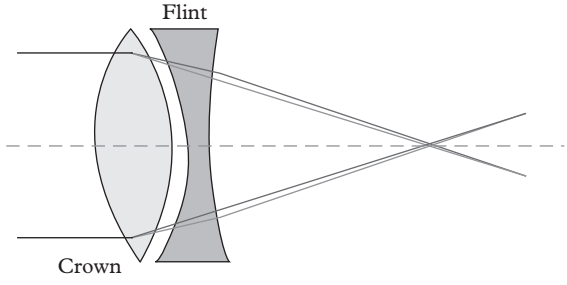

Figure 7A.4 *Dolland's telescope objective. This design differed from the one produced by Hall by interchanging the crown and flint. The design was more rugged than Hall's design and easier to manufacture. (Guenther, B.D.,* Chromatic aberrations. *Optics and Photonics News, 1999. (10): p. 15–18.)*

By proper choice of optical glasses, we can keep the power required by (7A.4) constant while reducing the variation in the power predicted by (7A.5) to zero:

$$d\Phi = 0,$$
$$\frac{\Phi_1}{\nu_{d1}} = -\frac{\Phi_2}{\nu_{d2}}, \tag{7A.6}$$

We can solve (7A.6) for the focal lengths to obtain

$$-\frac{f_1}{f_2} = \frac{\nu_{d2}}{\nu_{d1}}. \tag{7A.7}$$

Because all optical glasses have normal dispersion (see Figure 7.12), the Abbe value must be positive (a diffractive optical element has a negative Abbe value). Equation (7A.7) therefore implies that an achromat must be a combination of a positive and a negative lens.

Simultaneous solution of (7A.3) and (7A.6) yields

$$\Phi_1 = \frac{\nu_{d1}}{\nu_{d1} - \nu_{d2}}\,\Phi, \quad \Phi_2 = \frac{\nu_{d2}}{\nu_{d2} - \nu_{d1}}\,\Phi. \tag{7A.8}$$

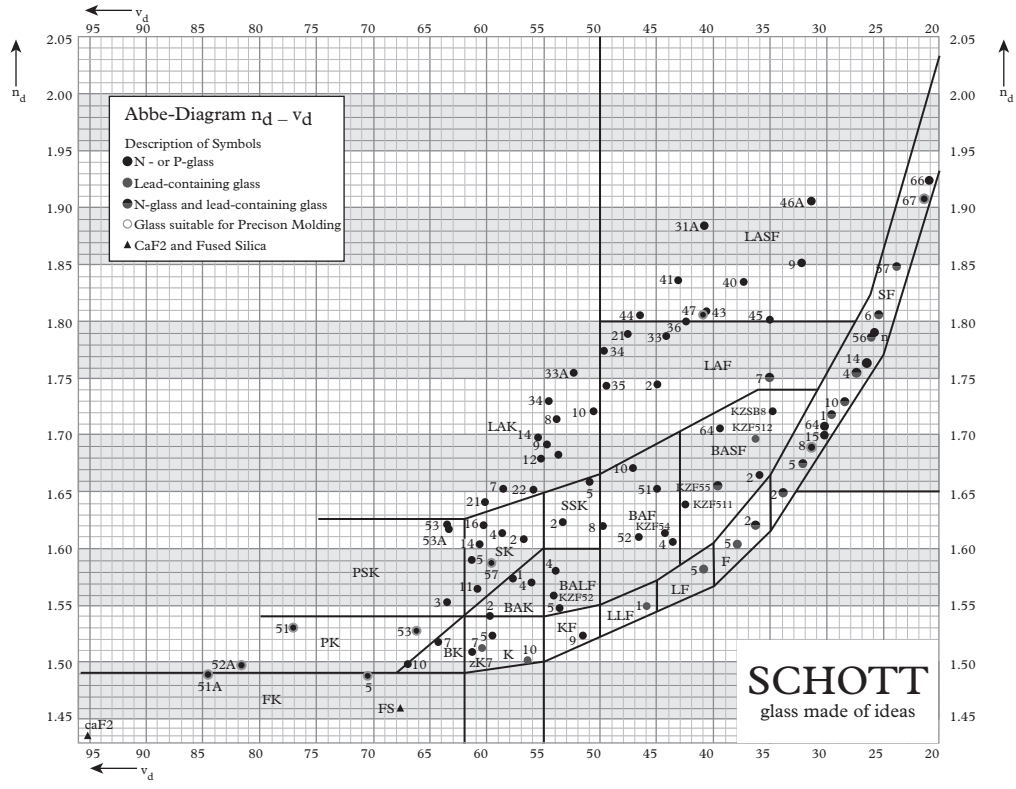

Figure 7A.5 *Abbe diagram produced by Schott Glass of North America.*

Table 7A.2 *Optical glasses*

Glass type	n_d	v_d	$n_F - n_C$	n_C
BK1 510635	1.51009	63.46	0.008038	1.50763
BK7 517642	1.51680	64.17	0.008054	1.51432
SK4 613586	1.61272	58.63	0.010451	1.60954
F2 62036	1.62004	36.37	0.017050	1.61503
F4 617366	1.61659	36.63	0.016834	1.61164
SF6 805254	1.80518	25.43	0.031660	1.79609

We see that the powers of the two lenses making up the achromat are inversely proportional to the difference in the Abbe values, Δv, of their glasses. High-power, short-focal-length lenses are more expensive and have a smaller maximum aperture and larger aberrations than low-power lenses. For this reason, glasses that yield $\Delta v > 20$ are usually selected in an achromat design. The properties of commercial glasses are shown in the Abbe Diagram in Figure 7A.5. A sample of optical glasses found in the Schott Optical Glass Catalog (No. 3111) are listed in Table 7A.2.

Assume we wish to construct an achromatic doublet using BK7 as the crown component and F4 as the flint component. From (7A.8) and the data in Table 7A.2, we have

$$\Phi_1 = \frac{64.17}{64.17 - 36.63}\Phi = 2.33\Phi,$$

$$\Phi_2 = \frac{36.63}{36.63 - 64.17} = -1.33\Phi.$$

The power of the achromat is 43% of the power of the crown element, and the power of the flint is 57% of that of the crown. We see that the positive element overshoots the desired

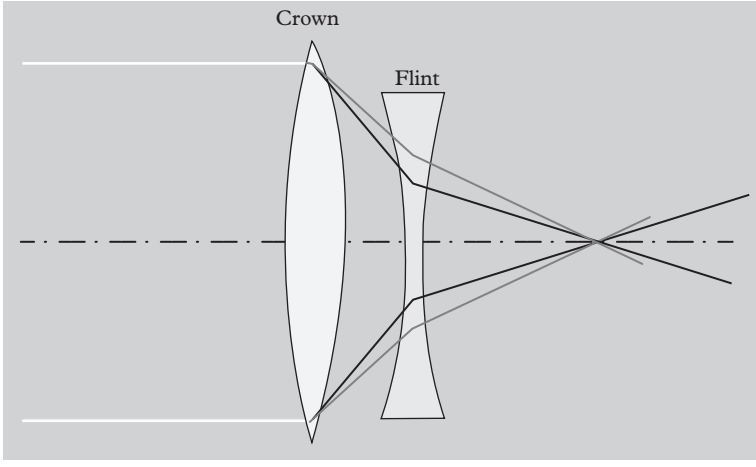

Figure 7A.6 *Achromat produced using the procedure outlined in the text.*

power and that the overshoot is subtracted out by the negative element. Along with the reduction in power, there is a cancellation of the dispersion effects for two wavelengths.

The method of producing an achromat just described ensures that the focal length of the doublet is the same at two wavelengths, C and F light. At other wavelengths, this is not the case. The chromatic aberration still present is called the secondary spectrum. If we wish to make the focal length the same at C, F, and d light, then we must make the variation in power equal to zero. In the expression,

$$\delta\Phi_{d,C} = (n_{1d} - n_{1C})\frac{\Phi_1}{n_{1d} - 1} + (n_{2d} - n_{2C})\frac{\Phi_2}{n_{2d} - 1}$$

$$= \left[\frac{n_{1d} - n_{1C}}{n_{1F} - n_{1C}}\right]\frac{\Phi_1}{v_{1d}} + \left[\frac{n_{2d} - n_{2C}}{n_{2F} - n_{2C}}\right]\frac{\Phi_2}{v_{2d}}, \tag{7A.9}$$

the fractions in square brackets are called *relative partial dispersions*. Only if the partial dispersions of the two glasses are equal can we reduce the secondary spectrum by achromatizing the lens at three wavelengths. Abbe was the first to note that if the relative partial

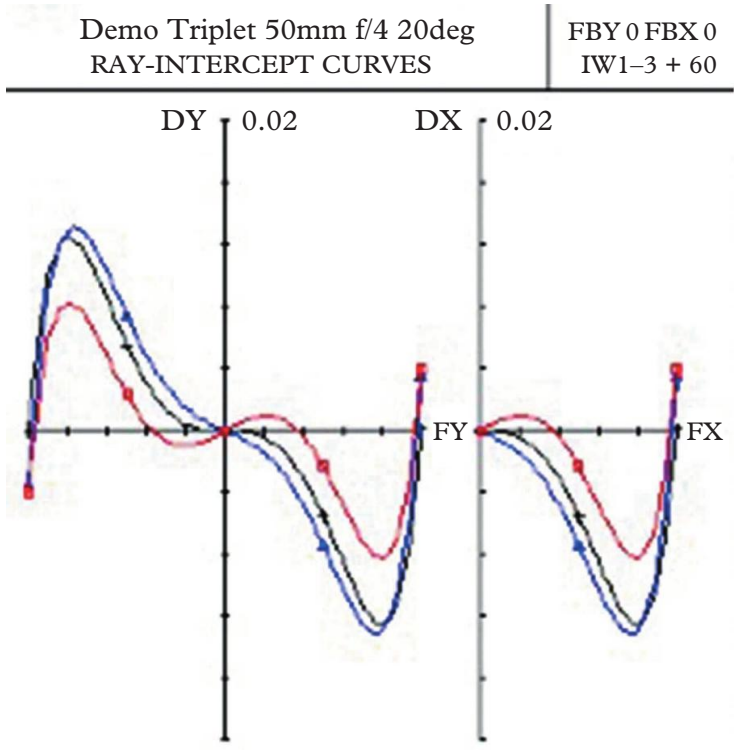

Figure 7A.7 *Ray-intercept curve for a Cooke triplet for three wavelengths.*

dispersion is plotted versus v_d for various optical glasses, a nearly linear relation is observed between the two parameters. This means that we cannot meet the condition for reduced secondary spectrum and also fulfill the requirement that the Abbe values for the two glasses have a large difference. It is for this reason that it is impossible to reduce chromatic aberration below that obtained by the simple calculations above.

Figure 7A.6 shows an achromat produced using the procedure outlined above.

Wavelength-dependent variations of the aberrations introduced in Appendix 5B also occur. To display these wavelength dependences, ray-intercept curves are generated for three wavelengths as illustrated in Figure 7A.7.

8

Coherence

8.1 Introduction 306
8.2 Photoelectric Mixing 307
8.3 Interference Spectroscopy 310
8.4 Fourier Transform Spectroscopy 312
8.5 Fringe Contrast and Coherence 316
8.6 Temporal Coherence Time 318
8.7 Autocorrelation Function 320
8.8 Spatial Coherence 323
8.9 Spatial Coherence Length 329
8.10 Stellar Interferometer 330
8.11 Intensity Interferometry 332
8.12 Summary 335
8.13 Problems 338
References 340

8.1 Introduction

Everyday experience suggests that the observation of interference must be subject to very restrictive conditions. The intensity distribution from a number of light sources is uniform, with no evidence of the fringe patterns discussed in Chapter 4. When interference is observed, it is usually associated with small dimensions; for example, two slits separated by only a few millimeters, or thin films much less than a millimeter thick, are required to produce interference fringes in natural light. The need for small dimensions is not, however, associated with the wavelength of light. When laser illumination is used, interference is quite easy to produce. In fact, interference is a major noise source in images produced with laser illumination (see Appendix 10B for a brief discussion of the generation of a random interference pattern called speckle noise). The ability to observe interference is associated with a property of a wave called coherence. In this chapter, the measurement of coherence will be discussed. (An excellent review of coherence from the point of view of interference is found in [1].)

The terms coherent and incoherent were introduced in Chapter 4 in association with the presence or absence of interference. Two waves were said to be coherent if the interference term

$$\langle \mathbf{E}_1 \cdot \mathbf{E}_2 \rangle = \sqrt{I_1 I_2} \cos \delta$$

was nonzero within the region occupied by both $\mathbf{E}_1$ and $\mathbf{E}_2$. Simply restated, the two waves are coherent if $\mathbf{E}_1$ and $\mathbf{E}_2$ have a constant phase relation δ. The measurement of the property of coherence is thus a comparison of the relative phase of two light waves or two samples of the same wave. The comparison can be made in terms of the waves' temporal or spatial dependence, making coherence a function of both space and time. In this chapter, we will treat the temporal and spatial dependence separately.

The mathematical implementation of a comparison of two quantities is the correlation operation. We will develop the connection between coherence theory and correlation and discuss the experimental techniques that duplicate the correlation operation. We will discover that a temporal correlation of a wave with itself can be performed using a Michelson interferometer and that a spatial correlation can be performed using Young's two-slit configuration.

Interference of waves of different frequencies will be analyzed using the amplitude-modulated wave, derived in Chapter 7 by the addition of two waves of different frequencies. An association will be established between the beat frequency of an amplitude-modulated wave and coherence that will demonstrate the need for a quantified measurement of coherence. The connection between the concepts of modulation and interference led **A.T. Forrester** to develop the idea of photoelectric mixing, which is now the basis of a number of applications, including light-beating spectroscopy [2].

The Michelson interferometer's operation will be examined when the input wave contains two frequencies. The conclusions of this examination will then be extended to a continuous distribution of frequencies. The output intensity will be associated with the

Modern Optics. Second Edition. B. D. Guenther.

© B. D. Guenther 2015. Published in 2015 by Oxford University Press.

measurement of coherence, and a coherence function will be defined. The coherence function will be calculated for a typical spectral distribution found in emission or absorption spectroscopy. This example will demonstrate one of the important applications of coherence theory—Fourier transform spectroscopy.

A recent imaging modality, optical coherence tomography (OCT) [3] utilizes the temporal coherence of a superluminous diode to generate high-spatial-resolution images for medical applications, especially in ophthalmology. We will discuss how this technique uses a partially coherent source and interferometry to provide a noninvasive, high-resolution, two- or three-dimensional microscope image.

Fourier theory provides a connection between the spectral analysis view of the coherence function and the concept of correlation that will be formally established in this chapter. The correlation viewpoint will be used to discuss spatial coherence. The spatial coherence of a line source will be calculated to demonstrate the application of the concept of spatial coherence. The theoretical analysis of a line source will aid in understanding the use of Michelson's stellar interferometer to measure the spatial extent of a star.

Stellar interferometry has been extended to allow the utilization of intensity interferometry. A brief discussion of this application will conclude the chapter.

One of the first experiments on coherence was conduced by **Émile Verdet (1824–1866)**, who measured the spatial coherence length of an extended light source in 1865. Michelson expanded the work of Verdet during the 1890s by connecting the source distribution and the source's spectral content with the visibility of interference fringes. Coherence was successfully treated classically by **Frits Zernike (1885–1966)** [4], with **H.H. Hopkins** [5] placing Zernike's ideas into an easier-to-understand framework.

A key event in the development of coherence theory was the introduction of a new interferometric technique by **Robert Hanbury Brown (1916–2002)** and the derivation of a theoretical basis for the technique by **Richard Q. Twiss (1920–2005)**. The technique involved intensity correlation between signals collected at two points in space. It could be explained quite easily by classical theory, but seemed to contradict quantum theory. The contradiction led to a vigorous controversy during the early 1960s that was resolved by **R.J. Glauber**, who placed the quantum theory of coherence on a firm theoretical foundation and received the 2005 Nobel Prize in Physics for his effort.

A detailed review of both classical and quantum theories of coherence can be found in several books on the subject [6, 7].

8.2 Photoelectric Mixing

In Chapter 7, two harmonic waves of different frequencies, but equal amplitudes, were added together to produce a resultant, harmonic, carrier wave with a frequency equal to the average of the frequencies of the two waves. The carrier wave's amplitude was found to be modulated by a harmonic wave whose frequency equaled the beat frequency, i.e., one-half of the difference between the frequencies of the two primary waves. In this section, we will calculate the intensity of the amplitude-modulated wave at an arbitrary point in space. We will compare this result with the intensity produced by interference between two waves of equal frequency. The result of this comparison will allow us to establish under what conditions waves of different frequencies will interfere.

Assume initially that we have two one-dimensional waves of identical amplitudes but different frequencies. The ith wave is

$$E_i(x,t) = E_0 \cos(\omega_i t - k_i x + \phi_i), \qquad i = 1, 2. \tag{8.1}$$

In Chapter 7, we added two such waves and obtained a resultant amplitude-modulated wave of the form

$$E(x,t) = 2E_0 \cos(\omega t - kx)\cos(\Delta\omega t - \Delta kx),$$

where

$$\Delta\omega = \frac{\omega_2 - \omega_1}{2}$$

is the beat frequency between the two waves. Because the time average of the Poynting vector is the quantity measured, the time average of E^2 must be found. This is accomplished by using (2.23) to obtain the intensity given by (2.23):

$$I(x) = |\langle \mathbf{S} \rangle| \propto \langle |\mathbf{E}|^2 \rangle = 4E_0^2 \langle \cos^2(\omega t - kx) \rangle \langle \cos^2(\Delta\omega t - \Delta kx) \rangle. \tag{8.2}$$

We wish to compare this intensity distribution with the intensity distribution obtained in Chapter 4 for the interference between two waves, (4.11),

$$I(x) = |\langle \mathbf{S} \rangle| \propto \langle |\mathbf{E}_1|^2 \rangle + \langle |\mathbf{E}_2|^2 \rangle + 2\langle |\mathbf{E}_1 \cdot \mathbf{E}_2| \rangle.$$

When the two waves are of identical frequency, the intensity distribution given by this relationship was found to be

$$\frac{I}{I_0} = 2 + 2\cos\delta$$

where, from (2.24),

$$I_0 = \langle S \rangle \propto \frac{1}{T} \int_{t_0}^{t_0+T} E_i^2 \, dt \propto \frac{|E_0|^2}{2}$$

and T is the measurement period.

Performing the temporal average of $\cos^2(\omega t - kx)$ in (8.2) yields

$$\frac{I(x)}{I_0} = 4\langle \cos^2(\Delta\omega t - \Delta kx) \rangle, \tag{8.3}$$

where the assumption that $\omega T \gg 1$ is used, as in Chapter 2, to simplify the temporal average (ω is, at optical frequencies, $\approx 10^{14}$ Hz).
The temporal average of (8.3) yields two terms:

$$\frac{I(x)}{I_0} = 2 + \frac{2}{\Delta\omega T}\{\cos[\Delta\omega(2t_0 + T) - 2\Delta kx] \sin \Delta\omega T\}. \tag{8.4}$$

If $\Delta\omega T \gg 1$, then the resultant intensity, at the position x, is equal to the sum of the intensities of the individual waves

$$I \propto \langle E^2 \rangle = \langle E_1^2 \rangle + \langle E_2^2 \rangle = |E_0|^2 \propto 2I_0.$$

If a detector with a 100 kHz bandwidth, T$\approx 10^{-5}$, is used to measure the intensity and the beat frequency is $\Delta\omega > 10^6$, or, in terms of the wavelength, $\Delta\lambda \approx 10^{-4}$ nm, then the

time–bandwidth product $\Delta\omega T \approx 10$. Under this condition, a 10% error is made when the second term in (8.4) is neglected. When the second term can be neglected, the source is said to be incoherent.

This result can be extended to the addition of N waves at N different frequencies. When the assumption that $\Delta\omega T \gg 1$ holds, the resultant intensity is given by the sum of N individual intensities:

$$\langle E^2 \rangle = \sum_{i=1}^{N} \langle E_i^2 \rangle.$$

Real sources contain a continuous distribution of frequencies. For an incoherent source with an intensity distribution $I(\omega)$, the observed intensity is given by an integral over the frequency distribution of the intensity of the source:

$$I_0 \propto \langle E^2 \rangle = \int_{\omega_1}^{\omega_2} I(\omega)\, d\omega, \tag{8.5}$$

where $\omega_2 - \omega_1$ is the frequency bandwidth of the detector or the source, whichever is smaller. Any source for which the beat frequency is not observable because of the detector's frequency response is describes by (8.5).

If $\Delta\omega T < 1$, so that $\sin \Delta\omega T \approx \Delta\omega T$, then (8.4) can be written

$$\frac{I}{I_0} = 2 + 2\cos[\Delta\omega(2t_0 + T) - 2\Delta kx].$$

Because the detector's response time will allow observation of the beat frequency, the wave is now considered coherent. To obtain the resultant intensity for coherent waves, we must add amplitudes of the individual waves before calculating the intensity. (Since we know that interference can occur, we need to develop some measure that will tell us if $\omega_2 - \omega_1$ is small enough to allow interference to be measured.)

The view of interference as a function of a detector's response time led Forrester to conduct an experiment to demonstrate the production of beats from light waves. This first demonstration of photoelectric mixing, in 1955, involved two light waves with discrete frequencies separated by about 10 GHz.[1] Later, the concept of photoelectric mixing was extended: first, to beating between the frequency components of a continuous distribution of light, and, later, to beating between light produced by two different lasers. The former type of mixing, usually called *homodyne*, is associated with the application of light-beating spectroscopy, and the second type, usually called *heterodyne*, is associated with the application of laser radar.

If the beat frequency is small enough, we may neglect it, to obtain, from (8.4),

$$\frac{I}{I_0} = 2 + 2\cos(2\Delta kx) = 2 + 2\cos\delta,$$

which is identical to the result obtained in Chapter 4 during the analysis of interference between two waves of equal amplitude and frequency.

We have demonstrated that interference between waves of different frequencies is possible if the difference in frequency between the waves is sufficiently "small," but we have not quantified "small." If we can do this, we will have a measure of the coherence of light. As the first step in developing that measure, we will look at the response of a Michelson interferometer to waves of different frequencies.

[1] In the derivation presented here, the wave's amplitude E_0 has been assumed constant, but in the original experiment by Forrester, this was not the case. The noise introduced by the temporal variations of the amplitude made the experimental observation of beats very difficult.

8.3 Interference Spectroscopy

The Michelson interferometer (Figure 4.17) can be used to obtain a characterization of the coherence of a wave. To discover the origin of this characterization, we will calculate the form of the interference produced by a Michelson interferometer when the input wave contains two frequencies. The results of this analysis will then be extended to a continuous distribution of frequencies. We will assume that the detector cannot respond to the beat frequencies produced on the detector surface by the two waves. Because of this assumption, the output intensity of the interferometer is obtained by adding the intensities associated with each frequency contained in the input. We will find that measurement of the interferometer's output intensity, as we move one mirror, will generate information about the spectral content of the source.

We will begin the analysis by assuming that the light wave incident upon the Michelson interferometer contains two monochromatic (single-frequency) waves of frequencies ω_1 and ω_2 with intensities I_1 and I_2. Because the beat frequency $(\omega_2 - \omega_1)/2$ is too high to be detected, the output intensity of the interferometer is calculated by adding the intensities associated with the interference pattern created by each frequency. Each frequency will produce an interference pattern at the detector whose intensity is given by (4.31). We add the two intensities:

$$\begin{aligned} I_d &= I_{d1} + I_{d2} \\ &= I_1 + I_2 + I_1 \cos \omega_1 \tau + I_2 \cos \omega_2 \tau \\ &= I_0(1 + \gamma). \end{aligned} \tag{8.6}$$

Just as in (4.31), the resultant intensity contains a constant term

$$I_0 = I_1 + I_2$$

and an oscillating term

$$I_0 \gamma(\tau).$$

For the current example of two frequencies, the normalized oscillating term is

$$\gamma(\tau) = \frac{I_1}{I_0} \cos \omega_1 \tau + \frac{I_2}{I_0} \cos \omega_2 \tau.$$

If the two arms of the Michelson interferometer are the same length, we have $\tau = 0$, and γ takes its maximum value

$$\gamma(\tau) = \frac{I_1 + I_2}{I_0} = 1.$$

The minimum value that γ can have is zero. Whenever $\gamma = 0$, there is no interference, and the resultant intensity is

$$I_d = I_1 + I_2 = I_0.$$

An example of the output intensity of the interferometer is given in Figure 8.1 for three representative values of γ. The intensities plotted in Figure 8.1 are measured on axis as one mirror is moved to vary d.

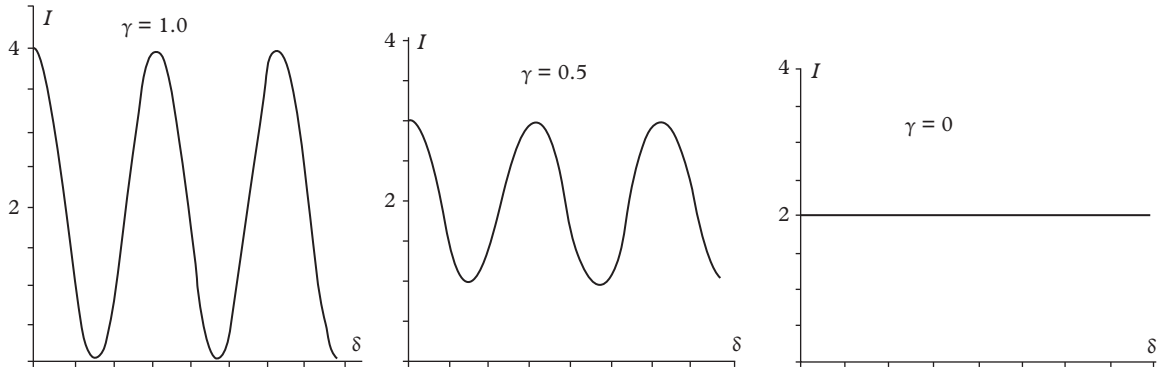

Figure 8.1 *The intensity output of a Michelson interferometer as a function of mirror spacing for three values of the degree-of-coherence function.*

By measuring γ, we can measure the separation between the two wavelengths present in the source illumination. To see how this measurement is accomplished, first note that the two wavelengths of the source can prevent the observation of interference. The loss of interference fringes is due to a filling in of the minimum-intensity fringe associated with one frequency by the maximum-intensity fringe of another frequency. The loss of visible fringes occurs when

$$\gamma(\tau) = \frac{I_1}{I_0}\cos\omega_1\tau + \frac{I_2}{I_0}\cos\omega_2\tau = 0.$$

If

$$I_1 = I_2 = \frac{1}{2}I_0,$$

then the function $\gamma(\tau)$ for the two frequencies can be rewritten as

$$\gamma(\tau) = \cos\left(\frac{\omega_1 + \omega_2}{2}\right)\tau \cos\left(\frac{\omega_1 - \omega_2}{2}\right)\tau,$$

which equals zero whenever

$$\frac{\omega_2 - \omega_1}{2}\tau = \pi(\nu_2 - \nu_1)\tau = \frac{\pi}{2},$$

$$\delta\nu = \frac{1}{2\tau}.$$

Physically, γ is zero when the maximum intensity of the fringe associated with one frequency occurs at the same mirror separation as the minimum intensity of the fringe associated with the second frequency.

We now have a technique for measuring the separation, in wavelength, of two monochromatic sources. We begin by adjusting the two arms of a Michelson interferometer so that they have equal optical path lengths. Light from the two monochromatic sources is combined and introduced into the interferometer. A detector monitors the central fringe at the output of the interferometer as one mirror is moved, increasing d [see Figure 8.2(a) in Section 8.4]. When the difference in optical path length of the two arms becomes large,

the output intensity will no longer vary as d changes ($\gamma = 0$). The value of d where the variation in intensity ceases can be used to calculate the wavelength separation between the two sources:

$$\Delta\nu = \frac{c}{4d}.$$

The spectral resolving power needed to discriminate between two wavelengths, or frequencies, is defined as

$$\mathcal{R} = \left|\frac{\lambda_a}{\delta\lambda}\right| = \left|\frac{\nu_a}{\Delta\nu}\right|,$$

where

$$\lambda_a = \frac{\lambda_1 + \lambda_2}{2}$$

is the average wavelength and

$$\delta\lambda = \lambda_2 - \lambda_1$$

is the resolvable wavelength separation. The maximum resolving power of a Michelson interferometer is given by

$$\mathcal{R}_{\max} = 2\nu_a\tau_{\max} = \frac{2d_{\max}}{\lambda/2}.$$

The length

$$d_{\max} = \frac{c\tau_{\max}}{2},$$

is the maximum displacement, measured from the position of zero optical path difference, that can be obtained with the Michelson interferometer.

Naturally occurring sources contain a distribution of frequencies; therefore, the theory must be expanded to include a continuous distribution of frequencies.

8.4 Fourier Transform Spectroscopy

We can extend the theory for interference produced by a source with two frequencies, to a continuous distribution of frequencies. This extension will demonstrate that the coherence function of a light source can be measured using a Michelson interferometer. We will also learn that by taking the Fourier transform of the measured coherence function, we can obtain the spectral distribution of a light source [see Figure 8.2(b)]. We will use a commonly occurring spectral distribution to learn how to measure the coherence function.

The resultant intensity at the output of a Michelson interferometer for a source with a continuous spectral distribution of intensity $I(\omega)$ is obtained by analogy with the two-frequency result. The form of the resultant intensity, as was the case for (8.6), is given by

$$I_d(\tau) = \int_0^\infty I(\omega)(1 + \cos\omega\tau)d\omega. \tag{8.7}$$

This integral contains a sum of constant and oscillatory terms. The constant term is

$$I_0 = \int_0^\infty I(\omega)d\omega$$

and the oscillatory term is

$$\int_0^\infty I(\omega) \cos \omega\tau \; d\omega.$$

By defining a normalized intensity distribution of frequencies called the *spectral distribution function* or the *power spectrum* of the light source,

$$P(\omega) = \frac{I(\omega)}{\int_0^\infty I(\omega) \; d\omega} = \frac{I(\omega)}{I_0}, \tag{8.8}$$

the oscillating term can be written in a form independent of the incident intensity:

$$\gamma(\tau) = \int_0^\infty P(\omega) \cos \omega\tau \; d\omega. \tag{8.9}$$

The oscillatory function (8.9), called the *degree of coherence*, is the cosine transform of $P(\omega)$.[2]

As was the case for two frequencies, if the two arms of the Michelson interferometer are the same length, $\tau = 0$, and we have the maximum value for γ:

$$\gamma(0) = \int_0^\infty P(\omega) \; d\omega = 1.$$

If there is no interference, then the resultant intensity (8.7) is obtained by integrating over $I(\omega)$. We know from (8.8) that $I(\omega)$ equals the fraction of light contained in the interval between ω and $\omega + d\omega$, $P(\omega)$, multiplied by the total intensity I_0. The integrand is therefore the spectral intensity distribution. Performing the integration over this function produces a resultant intensity that equals the incident intensity:

$$I_d(\tau) = \int_0^\infty I(\omega) d\omega = \int_0^\infty I_0 P(\omega) d\omega = I_0.$$

We see that for $\gamma = 0$, the output intensity of the interferometer is a constant, independent of the difference in length between the two interferometer arms, $d = \tau c/2$. For this condition, the wave is said to be incoherent. We find that the degree of coherence $\gamma(\tau)$ has a total range of values $0 \leq |\gamma(\tau)| \leq 1$.

Because γ describes the interference part of the intensity distribution of the Michelson interferometer, it is the quantitative measure we seek. Our discussion suggests that we should be able to measure the coherence function of any light source with the Michelson interferometer. From (8.9), we infer that by taking the Fourier transform of the measured coherence function, the spectral distribution of a light source can be recovered. Michelson used this procedure to determine the shape of a number of spectral emission lines, such as the hydrogen line at $\lambda = 656.3$ nm. The approach developed by Michelson was ignored for many years because the Fabry–Perot interferometer was much easier to use. Now, with the availability of small computers and the fast Fourier transform algorithm, the technique is very popular in the far-infrared and terahertz regions of the spectrum.

A typical output from a Michelson interferometer might look like Figure 8.2(a). The big spike is the fringe at $\tau = 0$ called the white light fringe. Upon examining Figure 8.2(a), it is not clear what quantity associated with this output should be measured to obtain the

[2] Here, the degree of coherence is shown as the real part of the Fourier transform of $P(\omega)$. We would expect in general to find $\gamma(\tau)$ to be a complex function.

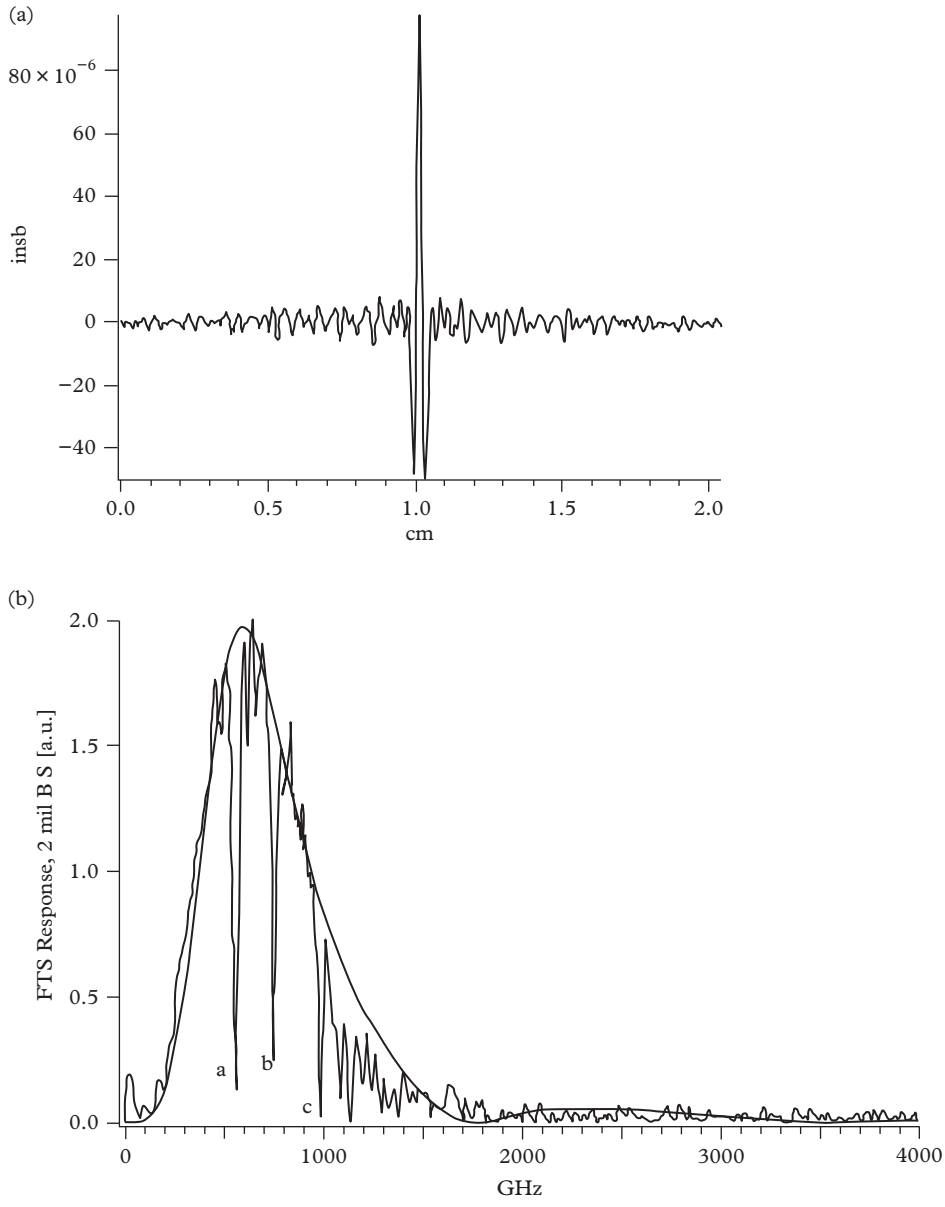

Figure 8.2 *(a) Interferogram from a Michelson interferometer. (b) Transform of the interferogram in (a). The dips labeled a–c are absorption dips due to rotational spectral lines of water vapor in the atmosphere.*

coherence function. We will calculate the output of a Michelson interferometer for a commonly occurring spectral distribution to discover the form of the degree of coherence. In performing this calculation, we will discover the parameter that must be measured to obtain the degree of coherence.

8.4.1 Gaussian Spectral Distribution

We will calculate the coherence function of an atomic emission line from a gas at low pressure. The spectral distribution of this line is Gaussian rather than the Lorentzian shape of Figure 7.10. The physical origin of this spectral distribution is the atomic motion in the gas.

When an atom or a molecule in a low-pressure gas emits radiation, a sharp quasi-monochromatic line at frequency ν_0 is emitted *in the atom's rest frame*. If the atom is moving at a relative velocity v toward or away from the viewer, then the observer will see a frequency

$$\nu = \nu_0 \left(1 \pm \frac{v}{c}\right). \tag{8.10}$$

This effect is called the *Doppler effect* after **Christian Doppler (1803–1853)**, who explained the frequency shift for sound waves in 1842. The explanation of the effect is quite simple. As the source of light moves toward the observer, the wave crests emitted at times t_0 and $t_0 + \Delta t$ are closer to each other because the source has moved forward. More wave crests arrive, in unit time, at the observer, owing to the motion, and the frequency measured by the observer is higher than if the source were at rest. [**Armand H.L. Fizeau (1819–1896)** made the first correct application of the Doppler effect to starlight and showed how it could be used to measure stellar velocities.]

If the molecules are in thermal equilibrium, classical statistical mechanics states that they will have a Maxwellian velocity distribution. The spectral distribution function resulting from the motion of the molecules in thermal equilibrium has the form

$$P(\omega) = \sqrt{\pi}\,\tau_d e^{-(\omega-\omega_0)^2(\tau_d/2)^2}. \tag{8.11}$$

This is a Gaussian line centered at the frequency ω_0 with a width

$$\Delta\omega = \frac{1}{\tau_d}.$$

From the kinetic theory of gases, the dependence of the linewidth on the physical properties of the gas can be obtained as

$$\tau_d^2 = \frac{c^2 m}{8\omega_0^2 kT}.$$

(The Lorentzian spectral distribution of Figure 7.10 is observed if the duration of the oscillations is shorter than the time τ_δ; see Problem 8.1. We associate the interruption of the oscillations with atomic collisions. Thus, a Lorentzian distribution is said to be pressure-broadened, while the Gaussian distribution is said to be thermally broadened.)

The Gaussian spectral distribution (8.11) for atomic or molecular emission from a low-pressure gas, can be used to calculate $\gamma(\tau)$ by calculating the Fourier transform of $P(\omega)$. $P(\omega)$ has the same form as the transform of (6.20). We can therefore immediately write

$$\gamma(\tau) = e^{-(\tau/\tau_d)^2} \cos\omega_0\tau \tag{8.12}$$

$$= \vartheta(\tau) \cos\omega_0\tau. \tag{8.13}$$

The degree of coherence is made up of a rapidly varying term $\cos\omega_0\tau$ and a slowly varying term $\vartheta(\tau)$, which modulates the amplitude of the rapidly varying term (see Figure 8.3). When $\tau \ll \tau_d$, only the rapidly varying component

$$\gamma(\tau) \approx \cos\omega_0\tau$$

is important. This rapidly varying term, equivalent to (4.31), describes the fringes expected for a monochromatic wave. When τ is of the order of τ_d, then the effects of the finite frequency spread, associated with (8.11), can be observed in the slowly varying term

$$\vartheta(\tau) \approx e^{-(\tau/\tau_d)^2}.$$

The combined terms in (8.13) are due to the fact that the spectral distribution (8.11) is centered about ω_0. If the center of the spectral distribution were shifted to zero from ω_0, then $\vartheta(\tau)$ would equal the Fourier transform of the shifted function.

8.5 Fringe Contrast and Coherence

The slowly varying function $\vartheta(\tau)$ discussed above is quite easy to measure. [Remember from (4.30) that $\tau = 2d/c$, where d is the difference in length of the two arms of the Michelson interferometer; thus, we have no trouble accessing all values of τ.] We will show that it is equivalent to a parameter defined as the fringe contrast by Michelson.

If we illuminate the Michelson interferometer with light from a Doppler-broadened transition, described by (8.11), then the intensity output of the interferometer, as the mirror in one arm is moved, will be

$$I_d(\tau) = I_1 + I_2 + 2\sqrt{I_1 I_2}\,\vartheta(\tau)\cos\omega_0\tau. \tag{8.14}$$

We define a parameter, called the *fringe visibility*, by the equation

$$\mathcal{V} = \frac{I_{\max} - I_{\min}}{I_{\max} + I_{\min}}. \tag{8.15}$$

The maximum intensity observed at the output of the Michelson interferometer is

$$I_{\max} = I_1 + I_2 + 2\sqrt{I_1 I_2}\,\vartheta(\tau)$$

and the minimum intensity is

$$I_{\min} = I_1 + I_2 - 2\sqrt{I_1 I_2}\,\vartheta(\tau).$$

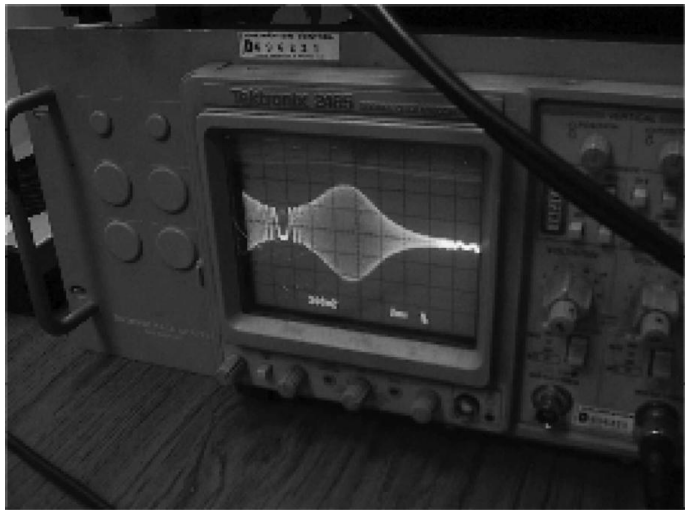

Figure 8.3 *Coherence function of a superluminous diode from an OCT spectrometer.*

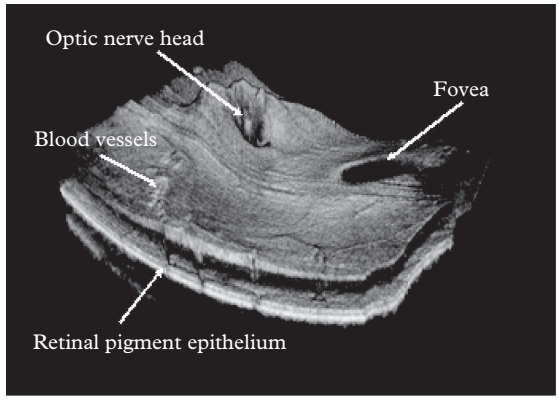

Figure 8.4 *Retina of the human eye [8]. (Professor Joseph Izatt, Fitzpatrick Institute for Photonics, Duke University.)*

The fringe visibility is thus

$$\mathcal{V} = \frac{2\sqrt{I_1 I_2}}{I_1 + I_2}\,\vartheta(\tau). \tag{8.16}$$

If $I_1 = I_2$, then $\mathcal{V} = \vartheta(\tau)$; the visibility of the fringes is equal to the degree of coherence.[3] We now have an experimental method of obtaining the coherence of a light source that is a general result and not limited to the Gaussian distribution used in the example.

If we know the coherence function, then the measurement of the fringe visibility can be used to determine d. For example, the optical coherence tomography technique uses a superluminous diode of know linewidth (as large as 100 nm) (see Figure 8.3) to measure d with resolution better than 10 μm. The amplitude of the coherence function can then be used to determine the z-coordinate of backscattered radiation from biological tissue such as the retina of the human eye, shown in Figure 8.4.

[3] If we used complex-valued field distributions, then $\vartheta(\tau)$ would be complex and the fringe visibility would be equal to the real part of $\vartheta(\tau)$.

8.6 Temporal Coherence Time

The arms of the Michelson interferometer act as delay lines, allowing light waves that were generated at different times to interfere. Because the interfering light waves differ in their time origin, the coherence measured by the Michelson interferometer is called *temporal coherence*.

The degree of coherence function completely characterizes the temporal coherence of a source, but is too complicated for general use. We need a simple parameter that can be used to specify the amount of coherence present in a light source. The parameter used to characterize temporal coherence will be a characteristic time, called the *coherence time*; it specifies the duration of time that a source maintains its phase.

The wave groups shown in Figures 7.2 and 7.3 were created by the addition of a number of waves of different frequencies. The temporal duration of a group is equal to the time that the different source frequencies, contributing to the group, remain in a fixed phase relationship and can therefore be interpreted as the coherence time of the source. To calculate the group duration, and thus the coherence time, we find the time between zeroes in the amplitude modulation, at a fixed position in space:

$$\begin{aligned}(\Delta\omega t_2 - \Delta k x_1) - (\Delta\omega t_1 - \Delta k x_1) &= \Delta\omega(t_2 - t_1) \\ &= (2m+1)\frac{\pi}{2} - (2m-1)\frac{\pi}{2}.\end{aligned}$$

We find that the coherence time is equal to

$$\tau_c = t_2 - t_1 = \frac{\pi}{\Delta\omega}.$$

In this section, a more formal approach will be used to obtain the coherence time. We will discover that the coherence time for a Gaussian spectral distribution is proportional to the reciprocal of the spectral width of the source, $\tau_c \propto 1/\Delta\omega$, agreeing with the simple definition of coherence time that has just been introduced. The reciprocal relationship between coherence time and spectral linewidth should not be much of a surprise; it has already been demonstrated that the spectral distribution and the coherence function are a Fourier transform pair.

One characterization of a well-behaved function such as γ^2 would be the root mean square width of the function:

$$\tau_c^2 = \frac{\displaystyle\int_{-\infty}^{\infty} (\tau - \langle\tau\rangle)^2 \gamma^2(\tau)\, d\tau}{\displaystyle\int_{-\infty}^{\infty} \gamma^2(\tau)\, d\tau}. \tag{8.17}$$

The average value of τ is zero since $\gamma^2(\tau)$ is an even function, and thus (8.17) can be rewritten as

$$\tau_c^2 = \frac{\displaystyle\int_{-\infty}^{\infty} \tau^2 \gamma^2(\tau)\, d\tau}{\displaystyle\int_{-\infty}^{\infty} \gamma^2(\tau)\, d\tau}. \tag{8.18}$$

Another equally adequate definition of the coherence time, used extensively in the coherence theory literature, can be obtained by approaching coherence theory from a statistical point of view. By treating the lack of interference as arising from intensity fluctuations, the definition of the coherence time becomes

$$\tau_c = 4 \int_0^\infty \gamma^2(\tau) d\tau \tag{8.19}$$

[Coherence will be associated with amplitude fluctuations in Section 8.7, but a detailed treatment that included a discussion of intensity fluctuations and a derivation of (8.19) would take us too far astray. The interested reader can find a discussion of this subject in the literature [6].]

We will apply the definition given in (8.19) to find the coherence time for a Doppler-broadened line with a spectral distribution given by (8.11) and a degree of coherence (or a coherence function) given by (8.12). Using (8.12), the coherence time can be quickly calculated:

$$\begin{aligned}
\tau_c &= 4 \int_0^\infty \cos^2(\omega_0 \tau)\, e^{-2(\tau/\tau_d)^2}\, d\tau \\
&= 2 \int_0^\infty e^{-2(\tau/\tau_d)^2}\, d\tau + 2 \int_0^\infty \cos(2\omega_0 \tau)\, e^{-2(\tau/\tau_d)^2}\, d\tau \\
&= \tau_d \sqrt{\frac{\pi}{2}}\, (1 + e^{-(\omega_0 \tau_d)^2/2}).
\end{aligned}$$

The squared frequency ω_0^2 is a very large number (somewhere around 10^{28} for visible light), and thus the second term in the equation for τ_c is very small and may be neglected. By neglecting the second term, the coherence time becomes

$$\tau_c \approx \tau_d \sqrt{\frac{\pi}{2}}\,.$$

The line width of the Gaussian line is $\Delta\omega \propto 1/\tau_c$, and thus $\tau_c \propto 1/\Delta\omega$, agreeing with the earlier result. In fact, it is easy to show that for a Gaussian line, $\tau_c\, \Delta\omega > 1/4\pi$. We have proved that very narrow spectral lines are very coherent, as we expected at the beginning of the analysis.

If the wave were frozen in time, the interference could be thought of as occurring between the wave at two different positions, in space, along the direction of propagation. For this reason, temporal coherence is also called *longitudinal coherence.* Using this spatial concept of temporal coherence, the coherence time is equivalent to a *coherence length* through the relationship

$$\ell_\ell = c\tau_c = \frac{c}{\Delta\omega}. \tag{8.20}$$

In a Michelson interferometer, the coherence length is equal to twice the difference in optical path length between the arms of the interferometer, measured at the position when the fringe visibility goes to zero. Applying the concept of coherence length to the wave group discussion above leads to a view of the coherence length as the spatial extent of a wave group, frozen in time.

We can also express ℓ_ℓ in terms of wavelength:

$$\frac{\Delta\nu}{\nu} = \frac{|\Delta\lambda|}{\lambda},$$

$$\ell_\ell = \frac{\lambda^2}{\Delta\lambda}. \tag{8.21}$$

For a sodium lamp, $\lambda \approx 500$ nm and $\Delta\lambda = 0.1$ nm (see Table 5B.2 for the wavelengths of the two visible lines produced by a sodium lamp), which gives $\ell_\ell \approx 2$ mm. For lasers, typical values of ℓ_ℓ are 10 m for a 1 mW HeNe laser and 4 cm for an argon laser. Larger coherence lengths can be produced in the visible region of the spectrum, but only with effort. Laser sources with coherence lengths of the order of kilometers can be produced in the infrared. This is a result of the fact that changes in dimensions due to thermal expansion and vibration are a small fraction of a wavelength at infrared wavelengths, making it easier to stabilize an infrared laser.

8.7 Autocorrelation Function

Another way to view the loss of interference fringes in a Michelson interferometer is as a result of the random fluctuations in time of the light wave's amplitude and/or phase. Up to now, all waves have been assumed to have amplitudes A and phases $\omega t - kx + \phi$ that were independent of time. By approaching interference in terms of fluctuating phases and amplitudes, we find that interference can be associated with the mathematical operation of correlation. Using this mathematical formalism, the coherence function can be shown to be equal to the autocorrelation of a wave. From this viewpoint, the concept of coherence is seen to be a statement concerning the similarity of two waves. We will discover that this mathematical view of correlation is consistent with the view of coherence in terms of beat frequencies or in terms of the Fourier transform of the power spectrum.

The complex representation of the light wave is

$$\tilde{E}(t) = A(t)e^{i[\omega_0 t + \phi(t)]},$$

where we are allowed to suppress the spatial dependence by the experimental configuration of a Michelson interferometer. The wave in one arm of the interferometer occurred at time t and the wave in the other arm occurred at the earlier time $t - \tau$, where $\tau = 2d/c$. The amplitudes in the two arms are added, and the detected interference signal is the temporal average of the resultant wave:

$$I_d = \frac{1}{T}\int_{t_0 - T/2}^{t_0 + T/2} \left[\tilde{E}(t) + \tilde{E}(t-\tau)\right]\left[\tilde{E}(t) + \tilde{E}(t-\tau)\right]^* dt.$$

After performing the multiplication in the integrand, we can separate the products into three temporal averages:

$$I_d = \frac{1}{T}\int_{t_0-T/2}^{t_0+T/2} \tilde{E}(t)\tilde{E}^*(t)\,dt + \frac{1}{T}\int_{t_0-T/2}^{t_0+T/2} \tilde{E}(t-\tau)\tilde{E}^*(t-\tau)\,dt + \frac{1}{T}\int_{t_0-T/2}^{t_0+T/2} \left[\tilde{E}^*(t)\tilde{E}(t-\tau) + \tilde{E}(t)\tilde{E}^*(t-\tau)\right] dt. \tag{8.22}$$

The first two integrals in (8.22) are individually equal to the intensity in one of the interferometer's arms; here, we will assume that they are each equal to I_0. The third integral contains all the interference effects. If we assume that the statistics are stationary, i.e., independent of the origin of time, then the intensity output of the interferometer is

$$I_d = 2I_0 + \frac{2}{T}\int_{t_0-T/2}^{t_0+T/2} \tilde{E}(t)\tilde{E}^*(t-\tau)\,dt = 2I_0[1+\gamma(\tau)]. \tag{8.23}$$

This is of the same form as (8.6). Equating like terms, we see that

$$\gamma(\tau) = \frac{\langle \tilde{E}(t)\tilde{E}^*(t-\tau)\rangle}{\langle \tilde{E}(t)^2\rangle} = \frac{\displaystyle\int_{t_0-T/2}^{t_0+T/2} \tilde{E}(t)\tilde{E}^*(t-\tau)\,dt}{\displaystyle\int_{t_0-T/2}^{t_0+T/2} \tilde{E}(t)\tilde{E}^*(t)\,dt}. \tag{8.24}$$

Comparing (8.24) with (6.32) and assuming that T is so large that the integral is independent of t_0, i.e., in the limit as $T \to \infty$, we find that the degree of coherence is now defined in terms of the normalized autocorrelation function. The assumption that T is very large is equivalent to the earlier assumption that the detector could not record the beat frequency.

In general, the intensities in the two arms of the interferometer would not be equal, and we would define the degree of coherence in terms of the cross correlation of the two waves:

$$\gamma_{12}(\tau) = \frac{\displaystyle\int_{-\infty}^{\infty} \tilde{E}_1(t)\tilde{E}_2^*(t-\tau)\,dt}{\left[\displaystyle\int_{-\infty}^{\infty} \tilde{E}_1(t)\tilde{E}_1^*(t)\,dt\right]^{1/2}\left[\displaystyle\int_{-\infty}^{\infty} \tilde{E}_2(t)\tilde{E}_2^*(t)\,dt\right]^{1/2}} = \frac{\langle \tilde{E}_1(t)\tilde{E}_2^*(t-\tau)\rangle}{\sqrt{\langle \tilde{E}_1(t)\tilde{E}_1^*(t)\rangle}\sqrt{\langle \tilde{E}_2(t)\tilde{E}_2^*(t)\rangle}}. \tag{8.25}$$

[We have been somewhat sloppy in our notation in letting $\gamma(\tau)$ represent a real function sometimes and a complex function other times. We are only interested in $\mathcal{R}e\{\gamma(\tau)\}$ and as always expect the reader to take the necessary care in manipulating the function when complex notation is used.]

We now have two definitions for $\gamma(\tau)$:

(1) the Fourier transform of the power spectrum, (8.9);
(2) a correlation between two samples of the wave, (8.25).

For the two definitions to be equivalent, we must assume that the beats are unobservable. We have made this assumption by interpreting (8.24) as a correlation operation; thus, we can write

$$\frac{\langle \tilde{E}(t)\tilde{E}^*(t-\tau)\rangle}{\langle \tilde{E}(t)^2\rangle} = \frac{\int_{-\infty}^{\infty} I(\omega)e^{-i\omega\tau}\, d\omega}{\int_{-\infty}^{\infty} I(\omega)\, d\omega}. \tag{8.26}$$

The equivalence between the two representations stated in (8.26) is based on the *Wiener–Khintchine theorem*. To prove this theorem would take us too far from optics [9], but it should be noted that the key assumption for the proof of the theorem is based on the absence of interference between different frequencies. This is equivalent to stating that T is long, $T \to \infty$, and that the beats between the two frequencies cannot be observed. The key value of this theorem is that it applies to functions that do not have a Fourier transform, i.e., are not square-integrable.

We can examine (7.24) in terms of a general light field:

$$\begin{aligned}\tilde{E}(t)\tilde{E}^*(t-\tau) &= A(t)A(t-\tau)e^{i[\omega_0(t-t+\tau)+\phi(t)-\phi(t-\tau)]} \\ &= A(t)A(t-\tau)e^{i[\omega_0\tau+\phi(t)-\phi(t-\tau)]}.\end{aligned} \tag{8.27}$$

Only the real part of the coherence function is of interest:

$$\begin{aligned}\gamma(\tau) &= \frac{\int_{-\infty}^{\infty} A(t)A(t-\tau)\cos[\omega_0\tau+\phi(t)-\phi(t-\tau)]dt}{\int_{-\infty}^{\infty} A(t)^2\, dt} \\ &= \frac{\langle A(t)A(t-\tau)\cos[\omega_0\tau+\phi(t)-\phi(t-\tau)]\rangle}{\langle A(t)^2\rangle}.\end{aligned} \tag{8.28}$$

This relationship states that the interference pattern, represented by $\gamma(\tau)$, is, for small fluctuations, a function of $\cos\omega_0\tau$. For signals where $A(t)$ is a constant, a condition obtainable with a laser, the result is in agreement with (8.3). The phase difference $\Delta\phi = \phi(t)-\phi(t-\tau)$, in this case, would be interpreted as arising from random frequency variations about a mean frequency.

8.8 Spatial Coherence

Temporal coherence is associated with the wave's properties along the direction of propagation. A second type of coherence can be defined that is associated with the wave's properties transverse to the direction of propagation. If the wave is a perfect plane wave, then there is a uniform phase in a plane perpendicular to the direction of propagation. The phase may exhibit fluctuations, but all points in the plane will have identical fluctuations. The perfect plane wave is said to be *spatially coherent*. The temporal coherence is associated with the frequency distribution of the source, while the spatial coherence is associated with a distribution of propagation vectors **k** associated with the wave, i.e., with a departure of the wave from the ideal plane wave. We will see in our later discussion of diffraction that complete spatial coherence is as difficult to obtain as complete temporal coherence.

The theoretical development of this concept is identical to the development just completed for temporal coherence. By a simple redefinition of the retardation time τ and a generalization of the degree-of-coherence function, we will demonstrate that the same equations apply to the two classes of coherence. This is because the two forms of coherence are not different. We separate the two types only to increase our ability to understand coherence.

In our discussion, Young's two-slit experiment, as displayed in Figure 8.5, will play the same role as Michelson's interferometer did in the discussion of temporal coherence. The intensity at point P in Figure 8.5 is, from (4.11),

$$\langle \mathbf{E}^2 \rangle = \left\langle \mathbf{E}_1^2 \left(t + \frac{d_1}{c} + \frac{r_1}{c} \right) \right\rangle + \left\langle \mathbf{E}_2^2 \left(t + \frac{d_2}{c} + \frac{r_2}{c} \right) \right\rangle + 2 \left\langle \mathbf{E}_1 \left(t + \frac{d_1}{c} + \frac{r_1}{c} \right) \mathbf{E}_2 \left(t + \frac{d_2}{c} + \frac{r_2}{c} \right) \right\rangle,$$

where

$$t + \frac{d_1}{c} + \frac{r_1}{c}$$

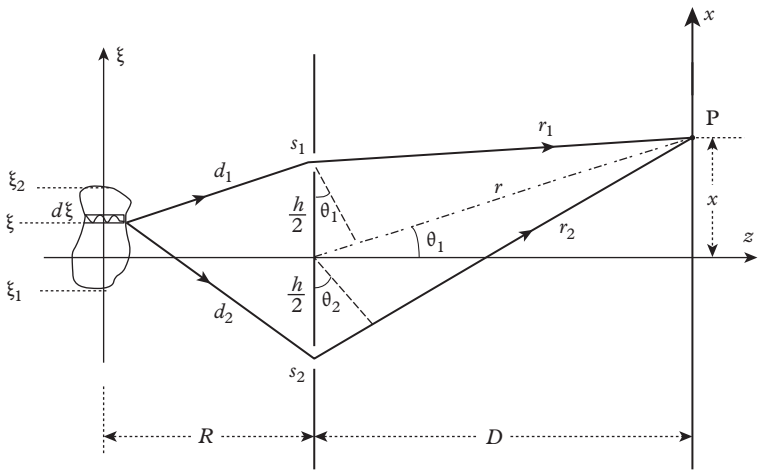

Figure 8.5 *Young's two-slit experiment with an extended source.*

is the time for light to travel from the source to point P by way of slit 1 and

$$t' = t + \frac{d_2}{c} + \frac{r_2}{c}$$

is the time to travel from the source to point P by way of slit 2. The phase difference associated with propagation from the source to the slits is given by

$$\Delta\varphi = \frac{d_2 - d_1}{c}$$

and the difference in propagation time from the two slits to point P is

$$\tau = \frac{r_2 - r_1}{c}.$$

In terms of these newly defined parameters, the intensity at point P is

$$\langle E^2 \rangle = \langle E_1^2(t' - \Delta\varphi - \tau) \rangle + \langle E_2^2(t') \rangle + 2 \langle E_1(t' - \Delta\varphi - \tau) E_2(t') \rangle.$$

The difference in propagation time in Young's two-slit experiment, τ, is equivalent to the retardation time used in temporal coherence. They both temporally define the waves that are to undergo interference. The retardation time associated with temporal coherence was defined in terms of the Michelson interferometer,

$$\tau = \frac{2d}{c},$$

where d is the difference in length of the two arms of the interferometer. The retardation time is redefined for spatial coherence in terms of the parameters associated with Young's two-slit experiment:

$$\tau = \frac{r_2 - r_1}{c}.$$

All of the equations developed for temporal coherence can be utilized in spatial coherence theory by using this new retardation time.

A new quantity, the *mutual coherence function* $\Gamma_{12}(\tau)$ can now be defined:

$$\begin{aligned} \Gamma_{12}(\tau) &= \langle \mathbf{E}_1(t' - \Delta\varphi - \tau) \mathbf{E}_2(t') \rangle \\ &= \frac{1}{2T} \int_{-T}^{T} \mathbf{E}_1(t' - \Delta\varphi - \tau) \mathbf{E}_2(t')\, dt'. \end{aligned}$$

This function is a correlation integral. The two waves that are compared are samples of the wavefront taken by slits 1 and 2. The intensities passing through each of the two slits can be expressed in terms of the mutual coherence function. They are the values of what are now the autocorrelation functions $\Gamma_{11}(0)$ and $\Gamma_{22}(0)$ at $\tau = 0$

$$\Gamma_{11}(0) = \langle \mathbf{E}_1^2 \rangle, \quad \Gamma_{22}(0) = \langle \mathbf{E}_2^2 \rangle.$$

The normalized version of $\Gamma_{12}(\tau)$ is the degree of spatial coherence,

$$\gamma_{12}(\tau) = \frac{\langle \mathbf{E}_1(t) \mathbf{E}_2(t - \tau) \rangle}{\sqrt{\langle \mathbf{E}_1(t)^2 \rangle} \sqrt{\langle \mathbf{E}_2(t)^2 \rangle}}, \tag{8.29}$$

or, in terms of the Γ notation,

$$\gamma_{12}(\tau) = \frac{\Gamma_{12}(\tau)}{\sqrt{\Gamma_{11}(0)\Gamma_{22}(0)}}.$$

In general, $\gamma_{12}(\tau)$ is a complex function of the form

$$\gamma_{12}(\tau) = |\gamma_{12}(\tau)|e^{i\delta_{12}(\tau)},$$

where the real part of this relation is identical to (8.13). The intensity at point P is produced by interference between the waves from slits 1 and 2 is given by

$$I_P = I_1 + I_2 + 2\sqrt{I_1 I_2}\,|\gamma_{12}(\tau)|\,\cos\delta_{12}(\tau),$$

which is identical to our result (4.12) in Chapter 4, except for $|\gamma_{12}(\tau)|$. It is obvious from this expression that the coherence function $\gamma_{12}(\tau)$ reduces the fringe visibility when the degree of coherence is less than 1. The degree of coherence $\gamma_{12}(\tau)$ is a function of $r_2 - r_1$ and thus describes how the visibility of the interference fringes vary as the observation point P is moved over the observation plane.

8.8.1 A Line Source

While the identical formalism of spatial coherence and temporal coherence makes it easy to develop coherence theory, it does not help in obtaining physical insight into the theory. We will expand our physical understanding of spatial coherence theory by performing a very simple experiment. We will examine Young's two-slit experiment, shown in Figure 8.5, following the discussion of Chapter 4; however, the experiment will be modified by the addition of a source of finite size. We will calculate the appearance of Young's fringes due to the source size and shape. The result will anticipate findings to be obtained in the discussion of diffraction—that spatial coherence limits the region in space over which Young's interference fringes can be observed.

We will assume that the source is a line source lying along the ξ-axis and extending from ξ_1 to ξ_2, where $\xi_2 - \xi_1 = s$ is the source's length. Initially, we will consider only an element of size $d\xi$ located at a position ξ above the optical axis. The derivation we carried out in Chapter 4 now has an added complication: we must evaluate the phase change

$$\Delta\phi = \Phi_2 - \phi_1,$$

which here is

$$\Delta\phi = \frac{d_2 - d_1}{c}.$$

The optical path difference from the source to P, by way of the two slits, is

$$\Delta = n[(d_2 + r_2) - (d_1 + r_1)]. \tag{8.30}$$

(We will assume $n = 1$ in this discussion.) In Chapter 4, we derived the relationship

$$c\tau = r_2 - r_1 = \frac{xh}{D}.$$

We now wish to perform an equivalent derivation for

$$d_2 - d_1 = c\Delta\phi,$$

using Figure 8.5. The distances from the source to the two slits are given by

$$d_1^2 = R^2 + \left(\frac{h}{2} - \xi\right)^2, \quad d_2^2 = R^2 + \left(\frac{h}{2} + \xi\right)^2. \tag{8.31}$$

The difference between these two equations is

$$\begin{aligned} d_2^2 - d_1^2 &= R^2 + \frac{h^2}{4} + h\xi + \xi^2 - R^2 - \frac{h^2}{4} + h\xi - \xi^2 \\ &= 2h\xi, \end{aligned}$$

which can be written as the product of the sum and difference of the two distances:

$$(d_2 - d_1)(d_2 + d_1) = 2h\xi.$$

Since the distance from the source to the slit plane, R, is large and the slit spacing is very small compared with this distance, $R \gg h$, we may write $d_1 \approx d_2 \approx R$. Using this approximation, the path difference from the source to the two slits is

$$d_2 - d_1 \approx \frac{h\xi}{R}. \tag{8.32}$$

From (4.12), we know that the intensity at P for a point source is

$$I_P = I_1 + I_2 + 2\sqrt{I_1 I_2}\cos\delta,$$

where, from (4.16),

$$\delta = k\Delta = \frac{kh\xi}{R} + \frac{khx}{D}. \tag{8.33}$$

We will assume that the total light reaching P from each pinhole, illuminated by $d\xi$, is the same:

$$dI_1 = dI_2 = I_0 P(\xi)\ d\xi,$$

where $P(\xi)$ is the normalized spatial intensity distribution across the source. For this problem, the intensity distribution is that of a line of length $\xi_2 - \xi_1 = s$:

$$P(\xi) = \begin{cases} 1, & \xi_2 \geq \xi \geq \xi_1, \\ 0, & \text{all other } \xi. \end{cases} \tag{8.34}$$

The intensity at point P from the source element $d\xi$ is

$$dI_P = 2(1 + \cos\delta) I_0 P(\xi) d\xi. \tag{8.35}$$

To obtain the total intensity at point P, we must integrate (8.35) over the source:

$$I_P = 2I_0 \int P(\xi)(1 + \cos\delta)d\xi.$$

By analogy with (8.9), the degree of spatial coherence must be

$$\gamma = \int P(\xi)\cos\delta \; d\xi \tag{8.36}$$

$$= \int_{\xi_1}^{\xi_2} P(\xi)\cos\left(\frac{kh\xi}{R} + \frac{khx}{D}\right) d\xi. \tag{8.37}$$

Using a trigonometric identity, we can write

$$\gamma = \cos\left(\frac{khx}{D}\right)\int P(\xi)\,\cos\left(\frac{kh\xi}{R}\right)d\xi - \sin\left(\frac{khx}{D}\right)\int P(\xi)\,\sin\left(\frac{kh\xi}{R}\right)\,d\xi. \tag{8.38}$$

The two terms of (8.38) are the cosine and sine transforms of $P(\xi)$. As was the case for temporal coherence, where the degree of coherence is the Fourier transform of the spectral distribution of the light source, here the spatial coherence is the Fourier transform of the spatial distribution of the light source.

8.8.2 van Cittert–Zernike Theorem

The fact that the spatial coherence is the Fourier transform of the spatial distribution of the light source is a manifestation of the *van Cittert–Zernike Theorem*. More precisely, the van Cittert–Zernike theorem states that [10]

The complex degree of coherence is equal to the diffraction pattern of an aperture of the same size and shape as the source and illuminated by a spherical wave whose amplitude distribution is proportional to the intensity distribution across the source.

Diffraction theory will be applied to Young's two-slit experiment in Chapter 10 to obtain a result identical to (8.38) [see (10.31)].

If the source is centered on the optical axis of the experiment (the z-axis), then, because $\sin(kh\xi/R)$ is odd, the second integral in (8.38) is zero and the problem simplifies to the calculation of an integral identical in form to (6.17). The coherence function for this source is

$$\gamma = s\,\frac{\sin(khs/2R)}{khs/2R}\cos(khx/D). \tag{8.39}$$

A computer simulation of the interference pattern that would be observed with the line source is shown in Figure 8.6. In Figure 8.6(a), the source size was held constant and the pinhole spacing h was varied, as one might do in the measurement of the spatial coherence of a source. In Figure 8.6(b), the pinhole spacing was held constant and the source size was varied, demonstrating the importance of source size in the observation of interference fringes.

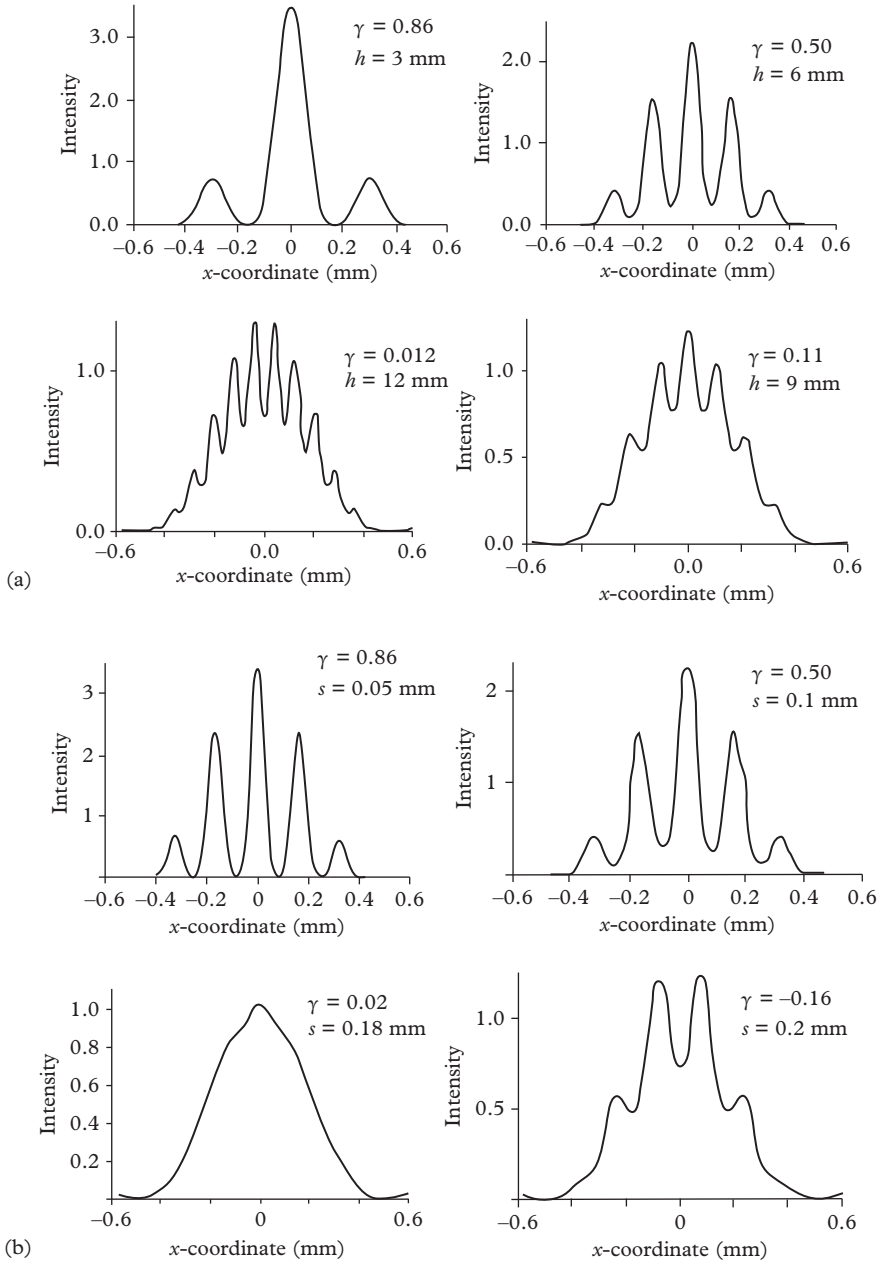

Figure 8.6 *(a) Interference pattern from two pinholes with a fixed source size. A finite source was used, and the pinhole spacing h was varied over a factor of four. The degree of coherence is* sinc *x and is the cause of the fringe visibility dropping to zero and then increasing. The overall shape of the pattern is due to diffraction. (b) The interference pattern for two pinholes with a fixed pinhole spacing. The source size was varied by a factor of four. The upper left interference patterns in (a) and (b) are identical.*

8.9 Spatial Coherence Length

The operational definition of the longitudinal coherence length equated it to the difference in length between the two arms of the Michelson interferometer when the fringe visibility became zero. A *transverse coherence length* ℓ_t, can be defined in an analogous way, in terms of Young's two-slit experiment. It represents a distance, in a plane normal to the direction of propagation, over which the phases at two points remain correlated and equals the slit separation for which the interference fringes disappear.

The transverse coherence length can be defined in terms of the spatial extent of the light source. To derive the relationship between source size and transverse coherence length, we use the geometry of Figure 8.5. The distance between bright bands on the plane containing point P was derived in Chapter 4, and an outline of that derivation is repeated here. The optical path change in going from one bright band to the next is

$$k(\Delta_1 - \Delta_2) = 2\pi.$$

From the geometry of Figure 8.5, the path change is

$$\frac{h\xi}{R} - \frac{h\xi}{R} + \frac{hx_1}{D} - \frac{hx_2}{D} = \lambda.$$

The spacing between the bright bands is therefore

$$x_1 - x_2 = \frac{\lambda D}{h},$$

which agrees with (4.17).

The magnitude of the fringe spacing is independent of the source position ξ. However, if the source position, ξ is changed, the position of the fringes moves, as can be seen by taking the variation of (8.33) at constant phase δ:

$$\frac{\delta\xi}{R} = -\frac{\delta x}{D}, \tag{8.40}$$

where δx is the distance a band moves when the source is moved a distance $\delta\xi$ (the minus sign means that the fringes move up if the source is moved down). If there are two sets of fringes created by two points on a source located at ξ_1 and ξ_2, then the fringe visibility is destroyed when a bright band due to the light from ξ_1 falls on a dark band produced by ξ_2. This cancellation of fringe visibility occurs when $\delta x = \lambda D/2h$, which corresponds to a source displacement of

$$\delta\xi = -R\frac{\lambda}{2h}. \tag{8.41}$$

Equation (8.41) allows the calculation of the maximum source size that can produce interference fringes at the observation point, a distance R away, when the Young's slit spacing is equal to h. A source larger than this value will not produce a fringe pattern in Young's experiment, but rather will produce uniform illumination on the observation plane. The maximum source size that can produce interference may be described as an angular width $\Delta\theta$, using the fact that $\delta\xi \ll R$:

$$\frac{\delta\xi}{R} = \tan\frac{\Delta\theta}{2} \approx \sin\frac{\Delta\theta}{2} \approx \frac{\Delta\theta}{2}.$$

The value of h calculated using (8.41) is equal to the transverse coherent length ℓ_t, because that slit spacing is associated with a fringe visibility of zero. The source size associated with the transverse coherence length is called the *coherent source size*

$$\Delta\theta = \frac{\lambda}{h} = \frac{\lambda}{\ell_t}. \tag{8.42}$$

To get some idea of the magnitude of ℓ_t, assume the source is $\xi = 1.2$ mm wide and is $R = 2$ m from the slits; then,

$$\Delta\theta = \frac{\delta\xi}{R} = \frac{1.2}{2 \times 10^3} = 6 \times 10^{-4} \text{ rad}.$$

If $\lambda = 600$ nm, then the slits cannot be separated by more than 1 mm if interference is to be observed using this source, i.e., $\ell_t = 1$ mm. The Sun produces an ℓ_t of the order of 1/20 mm. This coherence length is smaller than the resolution of the eye and explains why interference fringes are not normally observed.

8.10 Stellar Interferometer

Michelson made use of the concepts of spatial coherence and coherent source size to measure the angular dimensions associated with stellar objects. His stellar interferometer [Figure 8.7(b)] looks a great deal like Young's two-slit experiment but the scale is a good deal larger—the two input mirrors of his device were over 6 m apart. With the geometry of Figure 8.5, (8.33) becomes

$$\delta = kh_1\Delta\theta + kh_2\frac{x}{D}.$$

If we assume that the light intensities gathered by the two input mirrors are equal, then, at the fringe plane of Figure 8.7(a), the intensity pattern will be given by

$$\begin{aligned} I_P &= 2I_0(1 + \cos\delta) \\ &= 2I_0\left[1 + \cos(kh_1\Delta\theta)\cos\left(kh_2\frac{x}{D}\right) - \sin(kh_1\Delta\theta)\sin\left(kh_2\frac{x}{D}\right)\right]. \end{aligned}$$

The angular extent of the source, $\Delta\theta$, is assumed small compared with the dimensions of the experiment, allowing the intensity distribution to be approximated by

$$I_P \approx 2I_0\left[2 - kh_1\Delta\theta\sin\left(kh_2\frac{x}{D}\right)\right].$$

The fringe spacing at the fringe plane of Figure 8.7(a) is determined by the separation h_2 of the two slits in the screen at the front of the lens and is calculated using (4.17). The two input mirrors sample the incoming wavefront at two points a distance h_1 apart and determine the contrast of the fringes. The observed fringe patterns will have an appearance similar to those in Figure 8.6(b).

Michelson proved the validity of the interferometric technique by measuring the diameters of Jupiter's moons, which have an angular extent of 1 arcsecond and are thus resolvable with conventional imaging techniques. Having done this, Michelson then applied the technique to the measurement of the separation of binary stars and the angular diameters of single stars. One of the largest stars measured was Betelgeuse, with an angular diameter of 0.047 arcsecond. The spatial coherence length ℓ_t of this star is of the order of several meters.

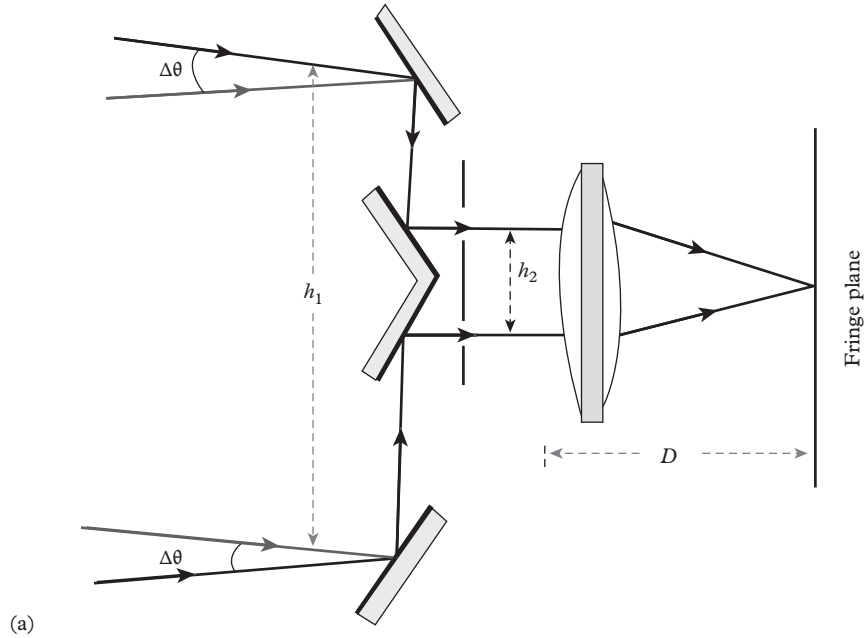

(a)

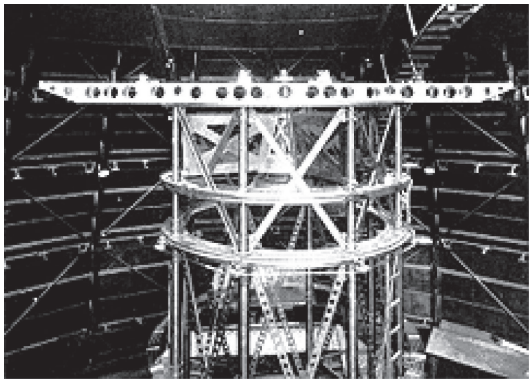

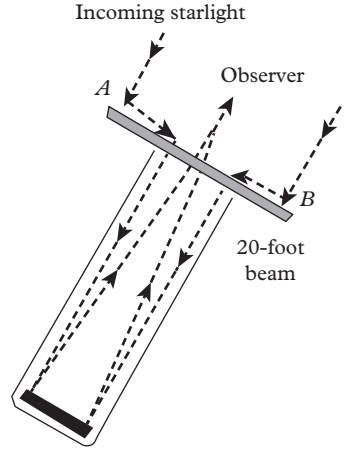

(b)

Figure 8.7 *Michelson stellar interferometer. (a) Schematic representation of the interferometer. The distance h_1 is adjusted until the fringes on the fringe plane disappear. The separation h_2 of the two apertures at the front of the lens establish the fringe spacing according to the theory developed in Chapter 4. The mirror spacing h_1 determines the fringe visibility because it determines the distance between samples of the wavefront. (b) The 20-foot Michelson interferometer for measuring stellar diameters, attached to the upper end of the skeleton tube of the 100-inch Hooker telescope on Mount Wilson near Pasadena, California. This instrument is now on display at the Rose Center of the American Museum of Natural History in New York.*

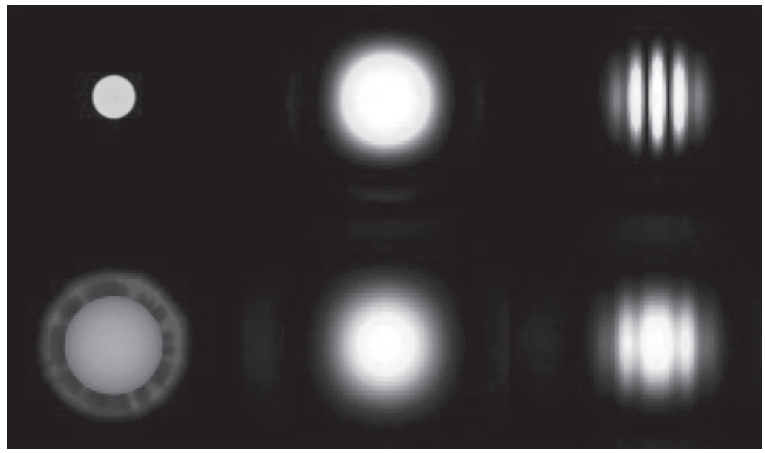

Figure 8.8 *The power of a stellar interferometer (right column) over a conventional telescope (center column) to distinguish between a large (bottom left) and a small star (top left). (Open source from European Southern Observatory <http://www.eso.org>.)*

At $\lambda = 600$ nm, fringes produced by a single wavelength from Betelgeuse disappeared for $h_1 = 2.63$ cm. This yields an angular diameter for Betelgeuse of 0.047 arcsecond:

$$\Delta\theta = \frac{\lambda}{\ell_t} = \frac{6 \times 10^{-7}}{2.63}$$

$$= \begin{cases} 2.28 \times 10^{-7} \text{ rad} \\ 1.31 \times 10^{-5} \text{ deg} \\ 0.047 \text{ arcsec.} \end{cases}$$

Images seen by the astronomer with an interferometer and with a conventional telescope are compared in Figure 8.8.

8.11 Intensity Interferometry

The Michelson stellar interferometer is very sensitive to vibrations and to fluctuations in the relative phase of the two wave samples, due to propagation through the atmosphere. These disturbances prevent the use of an interferometer with a value of h_1 larger than about 5 or 6 m. Another technique, developed by **R. Hanbury Brown** and **Richard Q. Twiss** [11] and involving the measurement of intensity from two detectors spaced a distance h apart is not sensitive to vibrations or atmospheric distortions. Dimensions associated with this type of interferometer exceed 300 m.

The theory behind the technique is based upon the assumption that the fluctuations in the outputs of two detectors must be correlated if the amplitudes of the two waves are correlated. Justification for this assumption can be obtained by squaring (8.25):

$$|\gamma_{12}(\tau, h)|^2 = \frac{\left|\langle \tilde{E}_1(t)\tilde{E}_2^*(t-\tau)\rangle\right|^2}{\langle I_1\rangle\langle I_2\rangle} \geq \frac{\langle I_1(t)I_2(t-\tau)\rangle}{\langle I_1\rangle\langle I_2\rangle},$$

where the subscript $i = 1$ or 2 corresponds to the detector position r_i. We can see that at least a lower bound for the degree of coherence can be obtained by measuring the intensity

correlation. For a classical thermal source, an exact relationship can be derived [11] using statistical arguments:

$$\frac{\langle I_1(t)I_2(t-\tau)\rangle}{\langle I_1\rangle\langle I_2\rangle} = 1 + \frac{1}{2}\,|\,\gamma_{12}(\tau,h)\,|^2. \tag{8.43}$$

(A thermal source is one for which the amplitude and phase fluctuations obey Gaussian statistics; i.e., if we plot the number of occurrences of an amplitude versus the amplitude, then the resultant distribution is Gaussian.)

The variance of the measured intensity is defined as

$$\delta I = I - \langle I\rangle.$$

The correlation of the variances measured by two detectors located at r_1 and r_2 can be written as

$$\begin{aligned}\langle \delta I_1(t)\delta I_2(t-\tau)\rangle &= \langle [I_1(t) - \langle I_1\rangle][I_2(t-\tau) - \langle I_2\rangle]\rangle \\ &= \langle I_1(t)I_2(t-\tau\rangle - \langle I_1\rangle\langle I_2\rangle.\end{aligned} \tag{8.44}$$

Using (8.43) in (8.44) and drawing upon a basic result of coherence theory, called the *reduction property* of the degree of coherence [9]

$$\gamma_{12}(\tau,h) = \gamma(\tau)\gamma_{12}(0,h), \tag{8.45}$$

we can rewrite the correlation of the variances of the intensities as

$$\langle \delta I_1(t)\delta I_2(t-\tau)\rangle = \frac{\langle I_1\rangle\,\langle I_2\rangle}{2}\;|\gamma(\tau)|^2\,|\gamma_{12}(0,h)|^2\,. \tag{8.46}$$

This result states that by measuring the fluctuations of the light intensity at two points in space, the degree of coherence can be measured.

To carry out the coherence measurement, the Michelson stellar interferometer of Figure 8.7 is replaced by two detectors spaced a distance h apart, as shown in Figure 8.9. Amplifiers, following the detectors, remove the time-invariant components $\langle I_1\rangle$ and $\langle I_2\rangle$ by high-pass filtering. The signal from one detector is delayed, electronically, by a time τ

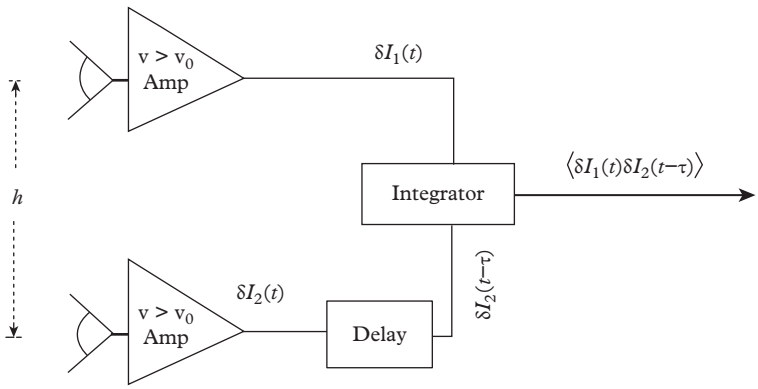

Figure 8.9 *Hanbury Brown–Twiss interferometer for radio astronomy.*

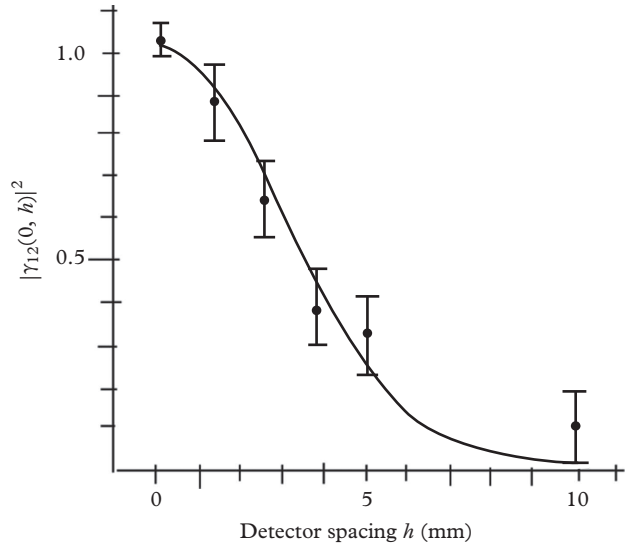

Figure 8.10 *Experimental data and theoretical curve for the Hanbury Brown–Twiss experiment [12].*

with respect to the other signal, and an electronic integrator performs a time average of the product of the delayed output of one detector with the prompt output of the second detector.

To prove the validity of the technique at visible wavelengths, Hanbury Brown and Twiss measured $|\gamma_{12}(0, h)|^2$ for a mercury arc lamp. Figure 8.10 displays a solid curve predicted by theory on which are plotted points obtained by experimental measurements.

The difference between the intensity interferometer and the Michelson interferometer is that the Hanbury Brown–Twiss intensity interferometer measures the square of the modulus of the complex degree of coherence, while the Michelson interferometer also measures the phase.

The Hanbury Brown–Twiss experiments introduced a great deal of controversy into the optics community during the late 1950s and early 1960s. From a quantum viewpoint, the basic assumption that the two detectors receive a correlated signal suggests that photons must arrive at the detectors in pairs. Since stars are thermal sources, this seemed absurd to many physicists. If photons are emitted at random at the source, how could they arrive in pairs at the detectors?

The apparent conflict is a manifestation of the wave–particle duality of light. When we make certain types of measurements on light, such interference measurements, light appears to be a wave. For other types of measurements, such as the low-light-level images of Figure 8.11, the particle nature of light is evident.

Intensity interferometry seems to emphasize the particle nature of light because it records the simultaneous arrival of pairs of photons. The result of the measurement, however, seems to require an interpretation based on the wave nature of light. The two detectors appear to sample portions of a wavefront associated with a wave that originated at a point on the source and diverges toward the detector. The solution to the conflict was to allow the

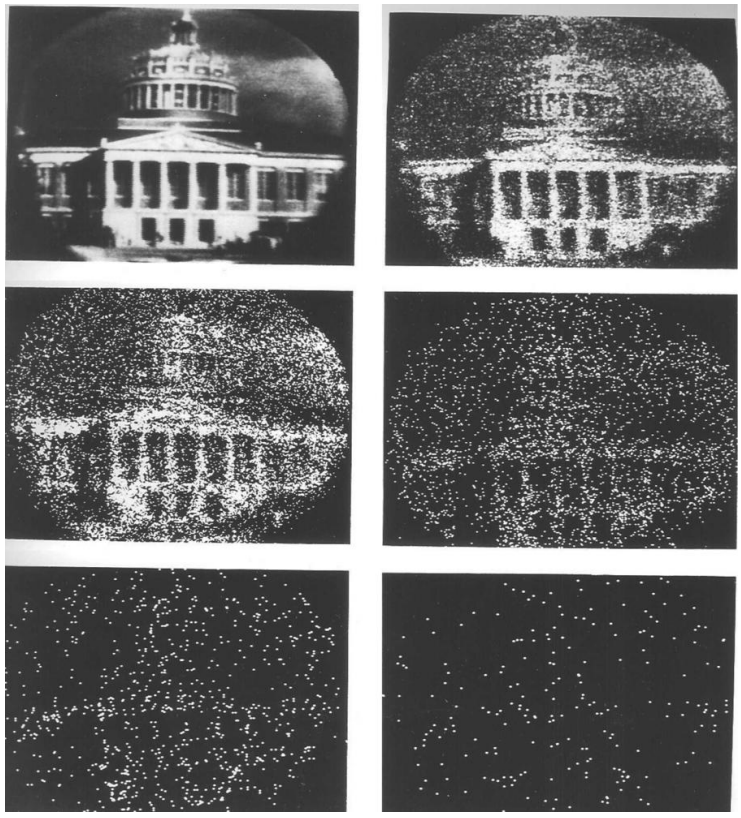

Figure 8.11 *In these low-light-level images, a bright spot in the display shows the arrival position of a single photon measured by the detector. The numbers of photons used to record the images, from the upper right to the lower left, were* 10^7, 64×10^3, 16×10^3, 4×10^3, 10^3, *and 250. (G. M. Morris,* Image correlation at low light levels: a computer simulation. *Appl. Opt., 1984.* **23***: p. 3152–4159.)*

original emitted photon to disappear and new photons to reform during propagation. The wavefunction associated with the photons would predict periodic increases in the probability of detection in a manner similar to the disappearance and reformation of a classical wave group (Figure 7.3).

Many people were reluctant to accept the concept of a photon that did not retain its identity throughout the propagation of light, from emission to absorption. Purcell showed that a quantitative explanation of the observed correlation could be given based on the quantum statistical behavior of photons. Hanbury Brown and Twiss conducted a number of experiments that verified their approach and overcame the objections of other scientists. R.J. Glauber later developed the quantum theory of optical coherence, which gave a firm quantum theoretical basis for the experimental results of Hanbury Brown and Twiss [13].

8.12 Summary

The intensity at a point in space, due to two waves of frequencies ω_1 and ω_2 was calculated. It was found that if $\Delta\omega T \gg 1$, where T is the response time of the detector and $\Delta\omega = \omega_2 - \omega_1$, then the intensity of the resultant wave is obtained by adding the intensities

of the individual waves. This result was generalized to N waves:

$$\langle \mathbf{E}^2 \rangle = \sum_{i=1}^{N} \langle \mathbf{E}_i^2 \rangle.$$

If $\Delta\omega T < 1$, then the intensity of the resultant wave is obtained by first adding the amplitudes of the individual waves and then calculating the intensity.

The Michelson interferometer can be used to interfere a wave sample with a sample of the wave delayed by a time $\tau = 2d/c$, where d is the difference between the lengths of the two arms of the interferometer. By varying d, the wavelength content of a source can be measured. The resolution that can be obtained by the Michelson interferometer is given by

$$\mathcal{R}_{\max} = 2\nu_a \tau = \frac{2d_{\max}}{\lambda/2},$$

where $d_{\max}$ is the maximum optical path difference that can be produced with the interferometer.

The temporal degree of coherence characterizes the ability of a wave from the source to interfere with a sample of the wave produced at an earlier time τ. The degree of coherence is a complex function of the form

$$\gamma(\tau) = |\gamma(\tau)| e^{i\delta(\tau)},$$

whose absolute value $|\gamma(\tau)| \leq 1$. The interference intensity observed when the source is described by a coherence $\gamma(\tau)$ is

$$I_P = I_1 + I_2 + 2\sqrt{I_1 I_2}\ |\gamma(\tau)| \cos\delta(\tau).$$

A source with a continuous distribution of frequencies is characterized by its power spectrum

$$P(\omega) = \frac{I(\omega)}{\displaystyle\int_0^\infty I(\omega)\ d\omega} = \frac{I(\omega)}{I_0}.$$

The temporal degree of coherence associated with the source is obtained by calculating the Fourier transform of its power spectrum:

$$\gamma(\tau) = \int_0^\infty P(\omega) \cos\omega\tau\ d\omega.$$

To measure the degree of coherence, the fringe visibility

$$\mathcal{V} = \frac{I_{\max} - I_{\min}}{I_{\max} + I_{\min}}$$

of the interference pattern produced by the Michelson interferometer is measured as a function of d. The temporal degree of coherence is then

$$\gamma(\tau) = \mathcal{V}\, \frac{I_1 + I_2}{2\sqrt{I_1 I_2}} \cos\omega_0\tau.$$

where I_1 and I_2 are the average intensities in the two arms of the interferometer; the two intensities are normally made equal.

To characterize a source's temporal coherence, a characteristic time, called the coherence time, is defined as

$$\tau_c = 4 \int_0^\infty \gamma(\tau)^2 \, d\tau .$$

This coherence time can be used to define a longitudinal coherence length

$$\begin{aligned} \ell_\ell &= c\tau_c \\ &= \frac{c}{\Delta\omega} \\ &= \frac{\lambda^2}{\Delta\lambda}. \end{aligned}$$

This length corresponds to the difference in length between the two arms of the interferometer when the fringe visibility drops to a value determined by the spectral distribution of the source. If the power spectrum were Gaussian, then the fringe visibility would have dropped to one-half of its maximum value; if the power spectrum were Lorentzian, then the fringe visibility would have dropped to $1/e$ of the maximum value.

The degree of coherence can be defined in terms of a correlation operation. For temporal coherence, the two waves used in the correlation operation are different temporal samples of the same wave; thus, the coherence function is an autocorrelation operation. This approach views coherence as a measure of the size of the amplitude and phase fluctuations occurring in the source. The resultant degree of coherence is identical to the one obtained by calculating the Fourier transform of the power spectrum:

$$\frac{\left\langle \tilde{E}(t)\tilde{E}^*(t-\tau)\right\rangle}{\left\langle \tilde{E}(t)^2\right\rangle} = \frac{\displaystyle\int_{-\infty}^{\infty} I(\omega)e^{-i\omega\tau} \, d\omega}{\displaystyle\int_{-\infty}^{\infty} I(\omega) \, d\omega}.$$

Coherence is a function not only of time but also of the spatial coordinates. The spatial degree of coherence is a correlation of two samples of a wavefront, obtained at two different positions in space, r_1 and r_2. The mathematical formalism used for spatial coherence is the same as that used for temporal coherence if the temporal parameter is redefined as

$$\tau = \frac{r_2 - r_1}{c}.$$

The spatial degree of coherence in terms of this newly defined temporal parameter is given by the cross correlation

$$\begin{aligned} \gamma_{12}(\tau) &= \frac{\displaystyle\int_{-\infty}^{\infty} \tilde{E}_1(t)\tilde{E}_2^*(t-\tau) \, dt}{\left[\displaystyle\int_{-\infty}^{\infty} \tilde{E}_1(t)\tilde{E}_1^*(t) \, dt\right]^{1/2} \left[\displaystyle\int_{-\infty}^{\infty} \tilde{E}_2(t)\tilde{E}_2^*(t) \, dt\right]^{1/2}} \\ &= \frac{\left\langle \tilde{E}_1(t)\tilde{E}_2^*(t-\tau)\right\rangle}{\sqrt{\left\langle \tilde{E}_1(t)\tilde{E}_1^*(t)\right\rangle}\sqrt{\left\langle \tilde{E}_2(t)\tilde{E}_2^*(t)\right\rangle}}. \end{aligned}$$

It is also, in general, a complex function:

$$\gamma_{12}(\tau) = |\gamma_{12}(\tau)|e^{i\delta_{12}(\tau)}.$$

The interference that would now be produced using Young's two slit experiment can be written in terms of the degree of coherence:

$$I_P = I_1 + I_2 + 2\sqrt{I_1 I_2}\,|\gamma_{12}(\tau)|\cos\delta_{12}(\tau),$$

where I_1 and I_2 are the intensities passing through slits 1 and 2, respectively.

The size and the shape of a source determine the spatial degree of coherence. For a line source of length s, the degree of coherence is

$$\gamma = s\,\frac{\sin(khs/2R)}{khs/2R}\,\cos(khx/D).$$

As was done for temporal coherence, a spatial or transverse coherence length can be defined. This transverse coherence length is given by

$$\Delta\theta = \frac{\lambda}{\ell_t},$$

where $\Delta\theta$ is the angular extent of a coherent source. When the actual source exceeds this dimension, then $\Delta\theta$ is said to be the size of a coherent patch on the source.

The degree of coherence of a source can also be obtained by measuring the correlation of the intensity fluctuations in light from the source:

$$\langle \delta I_1(t)\delta I_2(t-\tau)\rangle = \frac{\langle I_1\rangle\langle I_2\rangle}{2}\,|\gamma(\tau)|^2\,|\gamma_{12}(0,h)|^2.$$

8.13 Problems

8.1. Calculate the power spectrum of a damped wave

$$f(t) = \begin{cases} Ae^{-(at-i\omega t)}, & t \geq 0, \\ 0, & t < 0. \end{cases}$$

8.2. Calculate the degree of coherence $\gamma(\tau)$ for the damped wave train in Problem 8.1.

8.3. What is the line width in nanometers and in hertz of light from a laser with a 10 km coherence length? The mean wavelength is 632.8 nm.

8.4. A 1 mm diameter pinhole 2 m from a double slit is illuminated by light with λ = 589 nm. What is the maximum slit spacing for which interference fringes are visible?

8.5. A ^{189}Hg low-pressure isotope lamp emits a line at λ = 546.078 nm with a bandwidth $\Delta\nu$ = 1000 MHz. What are the coherence length and coherence time?

8.6. A Michelson interferometer is illuminated by red cadmium light with a mean wavelength of 643.847 nm and a linewidth of 0.0013 nm. The mirror is initially set so that the two arms have equal length, and then one mirror is moved until the fringes disappear (the fringe visibility goes to zero). How far must the mirror be moved?

8.7. Assume a Michelson interferometer is illuminated by two wavelengths λ_1 and λ_2 (say a Na doublet). As one mirror is moved, the fringe visibility periodically goes

from maximum to minimum. Obtain a relationship between the mirror displacement Δd between two low-fringe-visibility conditions and the separation of the two wavelengths $\Delta\lambda = \lambda_2 - \lambda_1$.

8.8. In a gas at high pressure, the atoms experience frequent collisions. The collisions interrupt the radiation process, and the resulting line shape is Lorentzian:

$$I(\omega) = \frac{A}{(\omega - \omega_0)^2 + b^2}.$$

Calculate the degree of coherence.

8.9. The emission from sodium is predominantly the two Fraunhofer D-lines. In a low-pressure gas discharge, these two lines, centered at 589 and 589.6 nm, are Gaussian in shape and the intensity of the second is 80% of the first:

$$I(\omega) = A(e^{-[(\omega-\omega_0+b)/a]^2} + 0.8e^{-[(\omega-\omega_0-b)/a]^2}).$$

Calculate the degree of coherence and identify the origin of the various terms.

8.10. The laser transition in a HeNe laser has a Gaussian line shape. The Fabry–Perot cavity, which produces feedback for oscillation, will support oscillations at three different longitudinal modes under this Gaussian line (see Figure 8.12). We can represent this system by

$$I(\omega) = A_1\delta(\omega - \omega_0) + 0.5A_1\delta(\omega - \omega_0 - a) + 0.5A_1\delta(\omega - \omega_0 + a),$$

where we have assumed the longitudinal modes are delta functions. Calculate the degree of coherence.

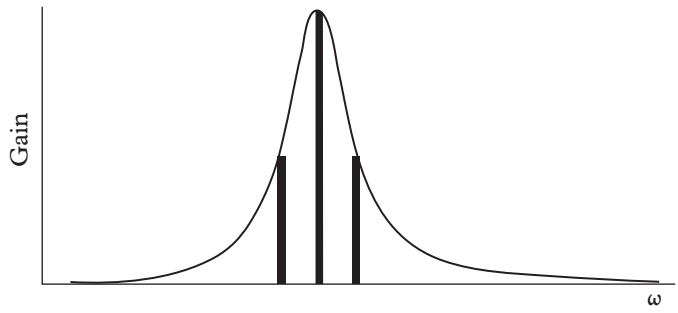

Figure 8.12 *Laser cavity modes for Problem 8.10.*

8.11. Write a computer program that will reproduce Figure 8.4. Explore the effects of varying γ. Produce several curves for which the intensities from the pinholes differ.

8.12. If a monochromatic light wave with $\lambda = 488$ nm is chopped at a frequency of 40 MHz, what is the bandwidth (in nm) of the light pulses?

8.13. We stated that the transverse coherence length of the Sun was 1/20 mm. Assuming that $\lambda \approx 600$ nm, what is the apparent angular diameter of the Sun?

8.14. A grating monochromator with a linear dispersion

$$\frac{\Delta x}{\Delta\lambda} = \frac{1\text{ mm}}{2\text{ nm}}$$

and an exit slit of 0.2 mm produces a light wave at $\lambda = 500$ nm. What is the temporal coherence length of the light exiting the slit?

8.15. Michelson's stellar interferometer had a slit spacing of 6 m. At $\lambda = 500$ nm, what is the smallest angular diameter it could measure?

8.16. A source emits radiation at two wavelengths, 589 and 589.6 nm. If this radiation illuminates two narrow slits separated by a distance $2d$ and the interference fringes are viewed a distance of 100 cm from the slits, what is the visibility of the fringes in the region of the 20th fringe maximum?

8.17. Show that the superposition of three waves at frequencies ω, $\omega+\omega_0$, and $\omega-\omega_0$ results in an amplitude-modulated wave given by

$$E = E_0(1 + A\cos\omega_0 t)\cos\omega t.$$

8.18. A multilayer bandpass filter has a center wavelength of 632.8 nm and a bandwidth of 0.1 nm. What is the coherence length of the light that is transmitted by this filter?

8.19. A local fm station operates at a frequency of 91.5 MHz and its carrier frequency has a short-term stability of 5 parts in 10^8. What is the temporal coherence length of this source?

8.20. In the chapter, it was stated that the spatial coherence length of the sun was 1/20 mm. Assume a wavelength of 500 nm and calculate the angular size of the sun in degrees.

REFERENCES

1. Paul, H., *Interference between independent photons*. Rev. Mod. Phys, 1986. **58**: p. 209–231.
2. Cummins, H., Editor, *Photon Correlation and Light Beating Spectroscopy*. 1974, Springer.
3. Brexinski, M.E., *Optical Coherence Tomography*. 2006: Academic Press.
4. Zernike, F., *The concept of degree of coherence and its application to optical problems*. Physica, 1938. **5**: p. 785.
5. Hopkins, H.H., *On the diffraction theory of optical images*. Proc. R. Soc. Lond., 1953. **A217**: p. 408.
6. Mandel, L. and E. Wolf, *Optical Coherence and Quantum Optics*. 1995: Cambridge University Press.
7. Marathay, A.S., *Elements of Optical Coherence Theory*. 1982: Wiley.
8. Radhakrishnan, S., et al., *Real-time optical coherence tomography of the anterior segment at 1310 nm*. Arch. Ophthalmol., 2001. **119**: p. 1179–1185.
9. Klein, M.V. and T.E. Furtak, *Optics*. 2nd ed. 1986: Wiley.
10. Born, M. and E. Wolf, *Principles of Optics*. 7th ed. 1999: Cambridge University Press.
11. Brown, R.H. and R.Q. Twiss, *A new type of interferometer for use in radio astronomy*. Phil. Mag., 1954. **45**: p. 663.
12. Brown, R.H. and R.Q. Twiss, *Interferometry of the intensity fluctuations in light, II. An experimental test of the theory for partially coherent light*. Proc. R. Soc. Lond., 1957. **A243**: p. 291.
13. Klauder, J.R. and E.C.G. Sudarshan, *Fundamentals of Quantum Optics*. 2006: Dover.

Diffraction and Gaussian Beams

9

9.1 Introduction 341
9.2 Huygens' Principle 343
9.3 Fresnel Formulation 347
9.4 The Obliquity Factor 350
9.5 Gaussian Beams 356
9.6 Higher-Order Gaussian Modes and Bessel Beams 363
9.7 Beam Propagation 365
9.8 Summary 372
9.9 Problems 373
References 375
Appendix 9A: Fresnel–Kirchhoff Diffraction 375
Appendix 9B: Rayleigh–Sommerfeld Formula 381

9.1 Introduction

Geometrical optics does a reasonable job of describing the propagation of light in free space unless that light encounters an obstacle. Geometrical optics predicts that the obstacle would cast a sharp shadow. On one side of the shadow's edge would be a bright uniform light distribution, due to the incident light, and on the other side there would be darkness. Close examination of an actual shadow edge reveals, however, dark fringes in the bright region and bright fringes in the dark region. This departure from the predictions of geometrical optics was given the name *diffraction* by **Francesco Maria Grimaldi (1613–1663)**.

There is no substantive difference between diffraction and interference. The separation between the two subjects is historical in origin and is retained for pedagogical reasons. Interference may be associated with the intentional formation of two or more light waves that are analyzed in their region of overlap according to the procedures outlined in previous chapters. Diffraction may be associated with the obstruction of a single wave, by either a transparent or an opaque obstacle, resulting in the obstruction casting shadows (or forming light beams) that are larger than the size predicted by geometrical optics. This distinction between interference and diffraction is, however, rather fuzzy and arbitrary.

A rigorous diffraction theory is based on Maxwell's equations and the boundary conditions associated with the obstacle [1]. The boundary conditions are used to calculate a field scattered by the obstacle. The origins of this scattered field are currents induced in the obstacle by the incident field. The scattered field is allowed to interfere with the incident field to produce a resultant diffracted field. The application of the rigorous theory is very difficult and for most problems, an approximate scalar theory is used.

The approximate scalar theory is based on *Huygens' principle* **(Christiaan Huygens, 1629–1695)**, which states that

> *Each point on a wavefront can be treated as a source of a spherical wavelet called a* ***secondary wavelet*** *or a* ***Huygens wavelet****. The envelope of these wavelets, at some later time, is constructed by finding the tangent to the wavelets. The envelope is assumed to be the new position of the wavefront.*

Rather than simply using the wavelets to construct an envelope, the scalar theory assumes that the Huygens wavelets interfere to produce a new wavefront.

Application of the scalar theory results in an integral called the *Huygens–Fresnel integral*. The traditional interpretation given to this integral is that it is the sum of a group of Huygens wavelets. The modern interpretation of the integral is in terms of linear system theory.

Free space is viewed, by modern theory, as a linear system, and the incident wave is the input to this linear system. The Huygens wavelet is interpreted as the impulse response of free space, and the Huygens–Fresnel integral is a convolution of the incident wave with the impulse response of free space.

Modern Optics. Second Edition. B. D. Guenther.

© B. D. Guenther 2015. Published in 2015 by Oxford University Press.

Approximate analytic solutions of the Huygens–Fresnel integral are usually obtained through the use of two approximations. In both approximations, all dimensions are assumed to be large with respect to a wavelength. In one approximation, the viewing position is assumed to be far from the obstruction; the resulting diffraction is called *Fraunhofer diffraction* and will be discussed in Chapter 10. The second approximation, which leads to *Fresnel diffraction*, assumes that the observation point is near the obstruction. This approximation, which is the more difficult mathematically, will be discussed in Chapter 11.

In this chapter, a simple derivation of the Huygens–Fresnel integral will be given based on an application of Huygens' principle and on the addition of waves to calculate an interference field. The derivation will be more descriptive and intuitive than formal. A more rigorous mathematical treatment of scalar diffraction theory, due to **Gustav Kirchhoff** and **Arnold Johannes Wilhelm Sommerfeld (1868–1951)**, will be given in Appendices 9A, and 9B.

In this chapter Huygens' principle will be justified by demonstrating that it can be used to derive the laws of reflection and refraction. Having justified the use of this principle, we will apply it to diffraction by assuming two pinholes act as sources for Huygens' wavelets. The interference between these two sources is a generalization of the discussion of Young's interference experiment which is used as justification for the addition of the Huygens' wavelets. The addition of the Huygens' wavelets will be extended to N wavelets and then to a continuous distribution of Huygens sources. The use of a continuous distribution leads to the Huygens-Fresnel integral for diffraction.

When using Huygens' principle, a problem arises with the spherical wavelet produced by each Huygens source. Part of the spherical wavelet propagates backward and results in an envelope propagating toward the light source, but such a wave is not observed in nature. Huygens neglected this problem. Fresnel required the existence of an *obliquity factor* to cancel the backward wavelet but was unable to derive its functional form. When Kirchhoff placed the theory of diffraction on a firm mathematical foundation, the obliquity factor was generated quite naturally in the derivation. In the intuitive derivation of the Huygens–Fresnel integral given in this chapter, we will present an argument for treating the obliquity factor as a constant at optical wavelengths. We will then derive the constant value it must be assigned.

A quite modern approach to the subject of diffraction is to look for solutions of the differential equation describing the optical system. In this chapter, the optical system to be treated will be free space. The differential equation to be solved is the Helmholtz equation. A particular solution will be shown to be a *Gaussian wave*, i.e., a wave whose intensity distribution, transverse to the propagation direction, is a Gaussian function. We will discover that the Gaussian wave can be characterized by a *beam waist* (the diameter of the beam of light at the half-power points of the Gaussian distribution) and the *radius of curvature* of the wave's phase front.

The Gaussian beam parameters will be related to geometrical optics by showing how a Gaussian beam can be traced through an optical system. The technique will then be used to trace light through a thin lens and a Fabry–Perot cavity. We will conclude by using the connection between Gaussian waves and the *ABCD* matrix to begin the analysis of a commercial laser cavity.

The first reference to diffraction appears in the notebooks of **Leonardo De Vinci (1452–1519)**, but a description was not published until the works of Grimaldi appeared, posthumously. Grimaldi conducted a number of experiments involving narrow light beams grazing small obstacles. Newton repeated many of Grimaldi's experiments but dropped the subject when he found that he could not explain the observations in terms of his particle

model. Both Grimaldi and Newton conducted their experiments in the hope of determining the nature of light, but both seemed to retreat from their observations of wavelike behavior.

Young attempted to treat diffraction in terms of interference of light reflected from an edge but was convinced by Fresnel that the approach was wrong. Scientists have returned to Young's concept of diffraction, and it is now an active research topic [2].

To explain diffraction, Fresnel adapted a technique developed by Huygens for the explanation of birefringence. Fresnel enhanced Huygens' theorem by assuming interference between wavelets and was thereby able to explain diffraction from straight edges and apertures.

Fresnel was a civil engineer who pursued optics as a hobby, after a long day of road construction. Fresnel was also active politically, supporting Napoleon at an inopportune time. His detention by the police for his political views gave Fresnel time to conduct very high quality observations of diffraction. Fresnel submitted the theory, based on his observations, to the Paris Academy in competition for a prize in 1818. **Siméon Denis Poisson (1781–1840)**, one of the judges, presented an argument, as a *reductio ad absurdum*, to prove the theory was incorrect.

Poisson pointed out that a natural consequence of Fresnel's theory was the appearance of a bright spot at the center of the shadow of a circular object. **François Jean Dominique Arago (1786–1853)**, also a judge, conducted an immediate experiment and verified the presence of what is now know as Poisson's spot. As you might expect, Fresnel won the prize. (Arago and Poisson had been unaware that **Joseph-Nicolas Delisle**, a French astronomer, had observed the spot in 1715.)

The theory developed by Fresnel was placed on a firm mathematical basis by Kirchhoff in 1882. The theory as developed by Kirchhoff had problems, associated with the boundary conditions. Sommerfeld avoided these problems by treating the case of an aperture or edge in a perfectly conducting thin screen and was the first to obtain a rigorous solution for the diffraction of light waves from a conducting obstruction (in 1894). Smythe extended this result to a vector formulation in 1947.

9.2 Huygens' Principle

To discover how a wave propagates through an aperture, we must solve the vector wave equation obtained from Maxwell's equations in combination with the boundary conditions associated with the aperture. This is a very difficult mathematical problem, and we will be forced to discuss only approximate solutions. The approximate solutions we will evaluate are based on the application of Huygens' principle to the propagation problem.

Huygens said that each point on a wavefront (i.e., a surface of constant phase) could be regarded as a source for a secondary wavelet in the form of a spherical wave (Figure 9.1). The envelope of the secondary wavelets gives the wavefront at some later time. We will follow the lead of Huygens and ignore the problems associated with the backward-propagating part of the wavelets.

Before applying Huygens' principle to the study of diffraction, we will demonstrate the utility of the principle and learn how to implement it. This will be accomplished by rederiving the laws of reflection and refraction using Huygens' principle. Figure 9.2 shows the geometry to be used in the derivation. We assume in Figure 9.2 that a plane wave is incident upon the interface between a region of index n_1 and a region of index n_2. A wavefront of the incident wave, at a time before $t = 0$, is shown as AB. When the leading portion of this wavefront, point A, strikes the interface, at point O, we set our clock to $t = 0$. Huygens' principle

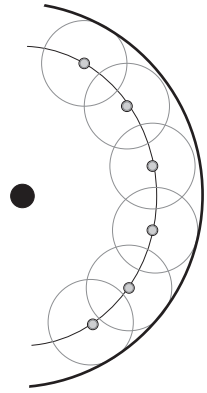

Figure 9.1 *Huygens wavelet shown in gray and the resulting new propagating wavefront.*

says that we should treat point O as a source of a wavelet. It is a point source, so it will radiate a spherical wavelet that, in region 1, will have a radius $v_1 t$, at time t, where $v_1 = c/n_1$. The time t is selected to be equal to the time for point B to reach point P. (The wavefront of the Huygens' wavelet generated by point O is shown by the large gray semicircle in Figure 9.2.) If the interface were not there, the wavefront at time t would be the plane formed by the line connecting points P and P' and denoted by PP'.

The interface is present, and thus the Huygens' wavelet in the second medium is a spherical wavelet of radius $v_2 t$, shown as the small semicircle below the interface in Figure 9.2. The wavefront of the transmitted wave in the second medium is therefore PP_2 after time t. A portion of the incident wave is reflected by the interface, and, after time t, the wavefront of the reflected wave is PP_1.

The geometry of the problem is now established and can be used to demonstrate rectilinear propagation of light and prove the laws of reflection and refraction. To reduce confusion, each portion of Figure 9.2 will be redrawn in enlarged form, as it is discussed.

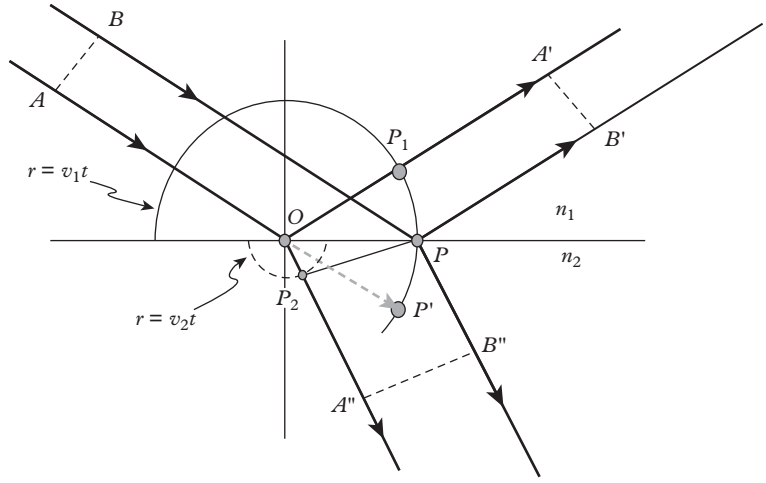

Figure 9.2 *The geometry of reflection and refraction using Huygens' principle to construct the wavefronts.*

9.2.1 Rectilinear Propagation

In Figure 9.3, we highlight the arriving wave. At $t = 0$, the incident wavefront AB is at position OO'. In time t, O' travels to P, and, from Huygens' principle, a secondary wavelet forms a sphere of radius $v_1 t$, centered on point O. From the triangles OPO',

$$\overline{O'P} = v_1 t = \overline{OP} \sin\theta_i. \tag{9.1}$$

If region 2 were not present, the spherical wavelet would establish that the distance

$$\overline{OP'} = v_1 t.$$

This means that the two distances $O'P$ and OP' are identical:

$$\overline{O'P} = \overline{OP'}.$$

This equality states that the wavefront PP' is parallel to OO', and the application of Huygens' principle leads to rectilinear propagation.

9.2.2 Law of Reflection

In Figure 9.4, we highlight the reflected wave. Huygens' principle establishes that PP_1 is the plane of the reflected wave at time t; thus, from the triangle OP_1P,

$$\overline{OP_1} = v_1 t = \overline{OP} \sin\theta_i'. \tag{9.2}$$

From (9.1) and (9.2), we obtain

$$\sin\theta_i' = \frac{\overline{OP_1}}{\overline{OP}} = \frac{v_1 t}{\overline{OP}} = \sin\theta_i, \tag{9.3}$$

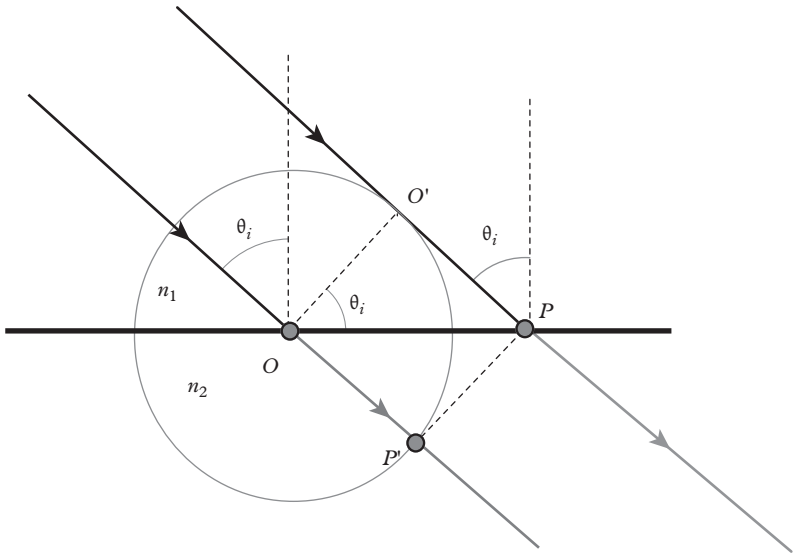

Figure 9.3 *The incident wave from Figure 9.2. The wave with wavefront PP′ does not exist. It would be present only if the interface were not there.*

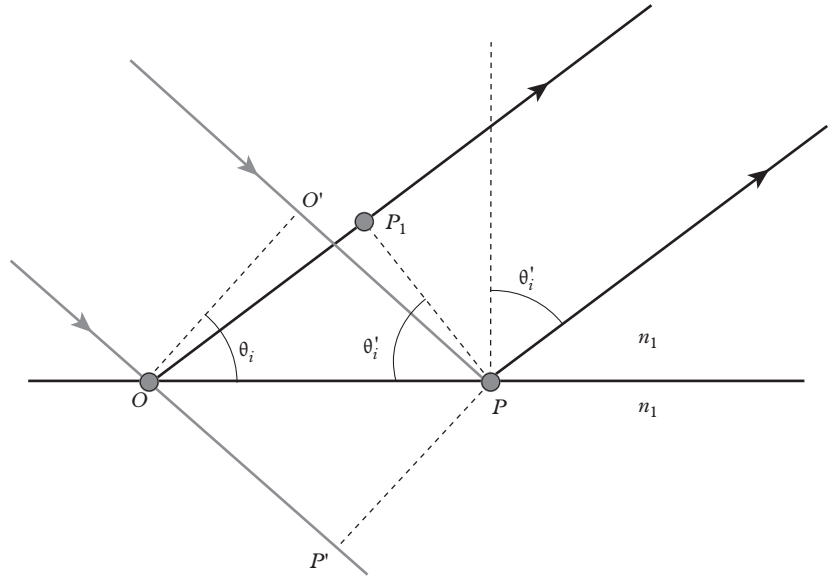

Figure 9.4 *The reflected wave using Huygens' principle.*

which is the law of reflection. We now see that Figure 9.4 is distorted (simply to aid in the discussion). Lines OP_1 and $O'P$ must be the same length, and O' and P_1 fall on top of one another.

9.2.3 Snell's Law

The transmitted wave is highlighted in Figure 9.5. The geometry of this figure will allow the derivation of Snell's law. In medium 2, Huygens' principle states that point O will act as a source of a spherical wave of radius $v_2 t$, where $v_2 = c/n_2$. From Figure 9.5, triangle OPP_2,

$$v_2 t = \overline{OP_2} = \overline{OP} \sin\theta_t. \tag{9.4}$$

From Figure 9.2, we have

$$\overline{OP} = \frac{v_1 t}{\sin\theta_i}.$$

Substituting into (9.4), we obtain

$$v_1 \sin\theta_t = v_2 \sin\theta_i.$$

Using $v_1 = c/n_1$ and $v_2 = c/n_2$, we obtain Snell's law:

$$n_1 \sin\theta_i = n_2 \sin\theta_t.$$

We have been able to demonstrate rectilinear propagation of light and prove the laws of reflection and refraction with Huygens' principle. This gives us some confidence in using this principle to derive the properties of diffraction.

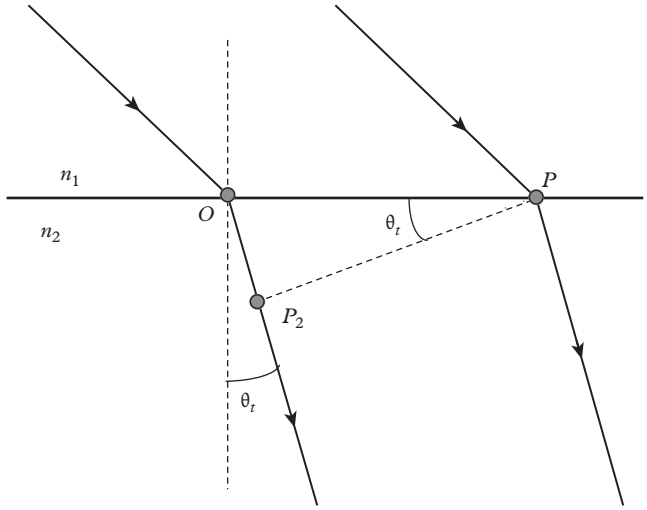

Figure 9.5 *The refracted wave from Figure 9.1 using Huygens' principle.*

9.3 Fresnel Formulation

Fresnel used Huygens' principle as a foundation for his theoretical explanation of diffraction, but it was not until the theoretical derivations by Kirchhoff that the theory of diffraction was placed on a firm mathematical foundation. The formal derivation of the diffraction integral developed by Kirchhoff is found in Appendix 9A. In this section, we will use a descriptive approach to obtain the Huygens–Fresnel integral of diffraction.

To apply Huygens' principle to the propagation of light through an aperture of arbitrary shape, we need to develop a mathematical description of the field from an array of Huygens sources filling the aperture. We will begin by obtaining the field from a pinhole that is illuminated by a wave

$$\tilde{\mathbf{E}}_i(\mathbf{r}, t) = \tilde{\mathbf{E}}_i(\mathbf{r})e^{i\omega t}.$$

The theory of interference provides the rules for combining the fields from two pinholes and allows the generalization of the result to N pinholes. Finally, by letting the area of each pinhole approach an infinitesimal value, we will construct an arbitrary aperture of infinitesimal pinholes. The result will be the Huygens–Fresnel integral.

We know that the wave obtained after propagation through an aperture must be a solution of the wave equation

$$\nabla^2\tilde{\mathbf{E}} = \mu\varepsilon\frac{\partial^2\tilde{\mathbf{E}}}{\partial t^2}.$$

We will be interested only in the spatial variation of the wave, so we need only look for solutions of the Helmholtz equation

$$\left(\nabla^2 + k^2\right)\tilde{\mathbf{E}} = 0.$$

The problem is further simplified by replacing this vector equation with a scalar equation

$$\left(\nabla^2 + k^2\right)\tilde{E}(x, y, z) = 0.$$

This replacement is proper for those cases where $\hat{\mathbf{n}}E(x,y,z)$ (where $\hat{\mathbf{n}}$ is a unit vector) is a solution of the vector Helmholtz equation. In general, we cannot substitute $\hat{\mathbf{n}}E$ for the electric field $\mathbf{E}$ because of Maxwell's equation

$$\nabla \cdot \mathbf{E} = 0.$$

Rather than working with the magnitude of the electric field, we should use the scalar amplitude of the vector potential [3]. We will neglect this complication and assume that the scalar E is a single component of the vector field $\mathbf{E}$. A complete solution would involve a scalar solution for each component of $\mathbf{E}$.

The pinhole is illuminated by a plane wave

$$\tilde{\mathbf{E}}_i(\mathbf{r}, t) = \tilde{\mathbf{E}}_i(\mathbf{r})e^{i\omega t}.$$

The wave that leaves the pinhole will be a spherical wave that is written in complex notation as

$$\tilde{E}(\mathbf{r})e^{i\omega t} = A\,\frac{e^{-i\delta}e^{-i\mathbf{k}\cdot\mathbf{r}}}{r}\,e^{i\omega t}.$$

The complex amplitude

$$\tilde{E}(\mathbf{r}) = A\,\frac{e^{-i\delta}e^{-i\mathbf{k}\cdot\mathbf{r}}}{r} \tag{9.5}$$

is a solution of the Helmholtz equation. The prescription for adding waves developed for interference can be applied to the problem of calculating the field at P_0 in Figure 9.6 from two pinholes: one at P_1, located a distance $\mathbf{r}_{01} = |\mathbf{r}_0 - \mathbf{r}_1|$ from P_0, and one at P_2, located a distance $\mathbf{r}_{02} = |\mathbf{r}_0 - \mathbf{r}_2|$ from P_0.

The two pinholes are a generalization of Young's interference experiment with the field at P_0, given by the superposition of the wavelets emitted from P_1 and P_2:

$$\tilde{E}(\mathbf{r}_0) = \frac{A_1}{r_{01}}\,e^{-i\mathbf{k}\cdot\mathbf{r}_{01}} + \frac{A_2}{r_{02}}\,e^{-i\mathbf{k}\cdot\mathbf{r}_{02}}. \tag{9.6}$$

We have incorporated the phases δ_1 and δ_2 into the constants A_1 and A_2 to simplify the equations.

The light emitted from the pinholes is due to a wave E_i, incident onto the screen from the left. The units of E_i are per unit area so to obtain the amount of light passing through

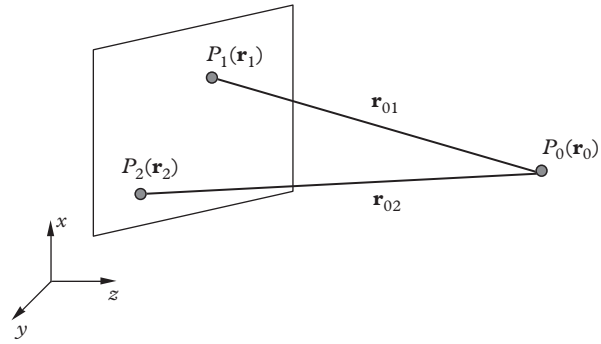

Figure 9.6 *Geometry for application of Huygens' principle to two pinholes.*

the pinholes, we must multiply E_i by the areas of the pinholes. If $\Delta\sigma_1$ and $\Delta\sigma_2$ are the areas of the two pinholes, then

$$A_1 \propto \tilde{E}_i(\mathbf{r}_1)\Delta\sigma_1, \quad A_2 \propto \tilde{E}_i(\mathbf{r}_2)\Delta\sigma_2,$$
$$\tilde{E}(\mathbf{r}_0) = C_1 \frac{\tilde{E}_i(\mathbf{r}_1)}{r_{01}} e^{-i\mathbf{k}\cdot\mathbf{r}_{01}} \Delta\sigma_1 + C_2 \frac{\tilde{E}_i(\mathbf{r}_2)}{r_{02}} e^{-i\mathbf{k}\cdot\mathbf{r}_{02}} \Delta\sigma_2, \tag{9.7}$$

where C_i are constants of proportionality. The constant C_i will depend on the angle that $\mathbf{r}_{0i}$ makes with the normal to $\Delta\sigma_i$. This geometrical dependence arises from the fact that the apparent area of the pinhole decreases as the observation angle approaches 90°.

We can generalize (9.7) to N pinholes:

$$\tilde{E}(\mathbf{r}_0) = \sum_{j=1}^{N} C_j \frac{\tilde{E}_i(\mathbf{r}_j)}{r_{0j}} e^{-i\mathbf{k}\cdot\mathbf{r}_{0j}} \Delta\sigma_j. \tag{9.8}$$

The pinhole diameter is assumed small compared with the distances to the viewing position but large compared with a wavelength. In the limit as $\Delta\sigma_j$ goes to zero, the pinhole becomes a Huygens source. By letting N become large, we can fill the aperture with these infinitesimal Huygens sources and convert the summation to an integral.

It is in this way that we obtain the complex amplitude at the point P_0 from a wave exiting an aperture by integrating over the area of the aperture. We replace $\mathbf{r}_{0j}$ in (9.8) by $\mathbf{R}$, the position of the infinitesimal Huygens source of area dS measured with respect to the observation point P_0. We also replace $\mathbf{r}_j$ by $\mathbf{r}$, the position of the infinitesimal area dS with respect to the origin of the coordinate system. The discrete summation (9.8) becomes an integral

$$\tilde{E}(\mathbf{r}_0) = \iint_A C(\mathbf{r}) \frac{\tilde{E}_i(\mathbf{r})}{R} e^{-i\mathbf{k}\cdot\mathbf{R}}\, dS. \tag{9.9}$$

This is the *Fresnel integral.* The geometry associated with (9.9) is shown in Figure 9.7, where the aperture is denoted by Σ_0, the observation point by P_0, and an arbitrary point in the aperture by P_1.

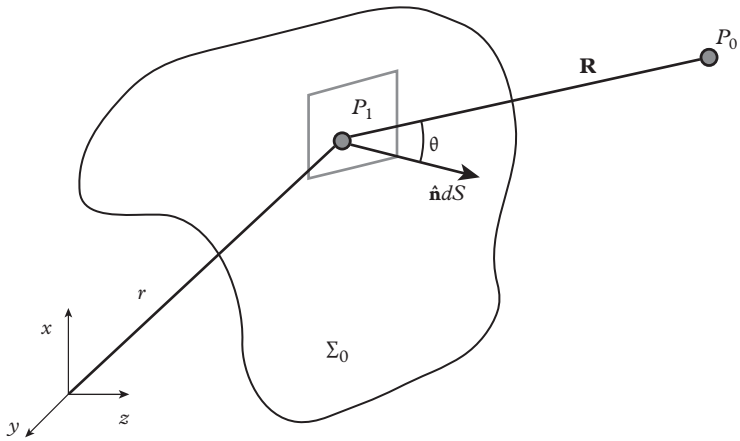

Figure 9.7 *The geometry for calculating the field at P_0 using (9.9).*

The constant $C(\mathbf{r})$ depends upon θ, the angle between $\hat{\mathbf{n}}$, the unit vector normal to the aperture, and $\mathbf{R}$, shown in Figure 9.7. We will treat $C(\mathbf{r})$ as a constant that we may remove from the integrand. Before continuing, we must digress to justify the assumption that the angular dependence of $C(\mathbf{r})$ can be ignored.

9.4 The Obliquity Factor

The parameter $C(\mathbf{r})$ in (9.9) is called the *obliquity factor*. In Appendix 9A, the obliquity factor is shown to have an angular dependence given by

$$\frac{\cos(\hat{\mathbf{n}}, \mathbf{R}) - \cos(\hat{\mathbf{n}}, \mathbf{r}_{21})}{2},$$

which includes the geometrical effect of the incident wave arriving at the aperture, at an angle with respect to the normal to the aperture. The source is located at a position $\mathbf{r}_{21}$ with respect to the aperture, and the effective area that it illuminates is a function of the angle between $\mathbf{r}_{21}$ and the aperture normal $\hat{\mathbf{n}}$.

If the source is at infinity, then the incident wave can be treated as a plane wave, incident normal to the aperture, and we may simplify the angular dependence of the obliquity factor to

$$\frac{1 + \cos\theta}{2},$$

where θ is the angle between the normal to the aperture and the vector $\mathbf{R}$. This is the configuration shown in Figure 9.7. The obliquity factor provides an explanation of why it is possible to ignore the backward-propagating wave that occurs in application of Huygens' principle. For the backward wave, $\theta = \pi$, and the obliquity factor is zero.

The obliquity factor causes the amplitude per unit area, of the incident and transmitted light, to decrease as the viewing angle increases. This is a result of a decrease in the effective aperture area with viewing angle. In this chapter, the obliquity factor is introduced in an ad hoc fashion, but in Appendices A and B, the obliquity factor is generated by the formal theory.

The obliquity factor increases the difficulty of working with the Fresnel integral, and it is to our benefit to be able to treat it as a constant. If we neglect its angular contribution, we need to justify the approximation. Our justification will be based upon the resolving power of an optical system operating at visible wavelengths.

Assume we are attempting to resolve two stars that produce plane waves at the aperture of a telescope with an aperture diameter a (Figure 9.8). The wavefronts from the two stars make an angle ψ with respect to each other (Figure 9.8):

$$\tan\psi \approx \psi = \frac{\Delta x}{a}. \tag{9.10}$$

The smallest angle ψ that can be measured is determined by the smallest length Δx that can be measured. We know we can measure a fraction of wavelength with an interferometer,

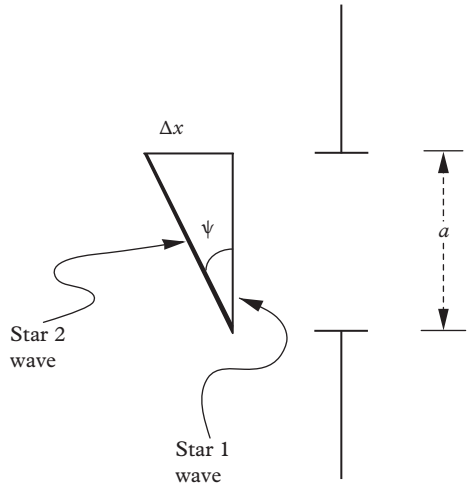

Figure 9.8 *Wavefronts from two stars arriving at our telescope.*

but, without an interferometer, we can only count the crests of the waves, leading to the assumption that $\Delta x \geq \lambda$; i.e., we can measure a length no smaller than λ. This reasoning leads to the assumption that the smallest angle we can measure is

$$\psi \geq \frac{\lambda}{a}. \tag{9.11}$$

The resolution limit established by the above reasoning places a limit on the minimum separation that can be produced at the back focal plane of the telescope. We will demonstrate in Chapter 10 (for now it must be accepted on faith) that the minimum distance on the focal plane between the images of stars 1 and 2 is given by

$$d = f\psi. \tag{9.12}$$

From (9.11),

$$d = \frac{\lambda f}{a}.$$

The resolution limit of the telescope, to be derived in Appendix 10B, can also be expressed in terms of the cone angle produced when the incident plane wave is focused on the back focal plane of the lens. From the geometry of Figure 9.9, the cone angle is given by

$$\tan\theta = \frac{a}{2f},$$

The separation between the two stars at the back focal plane of the lens is thus

$$d = \frac{\lambda}{2\tan\theta}. \tag{9.13}$$

This equation will establish the maximum value of θ to be encountered in a conventional optical system. We need a reasonable value for the minimum d we are capable of measuring, in order to find the maximum value of θ that will be encountered. We will assume that the minimum d is 3λ—this is four times the resolution of a typical photographic film at visible wavelengths and even farther above the performance of a consumer-grade digital camera.

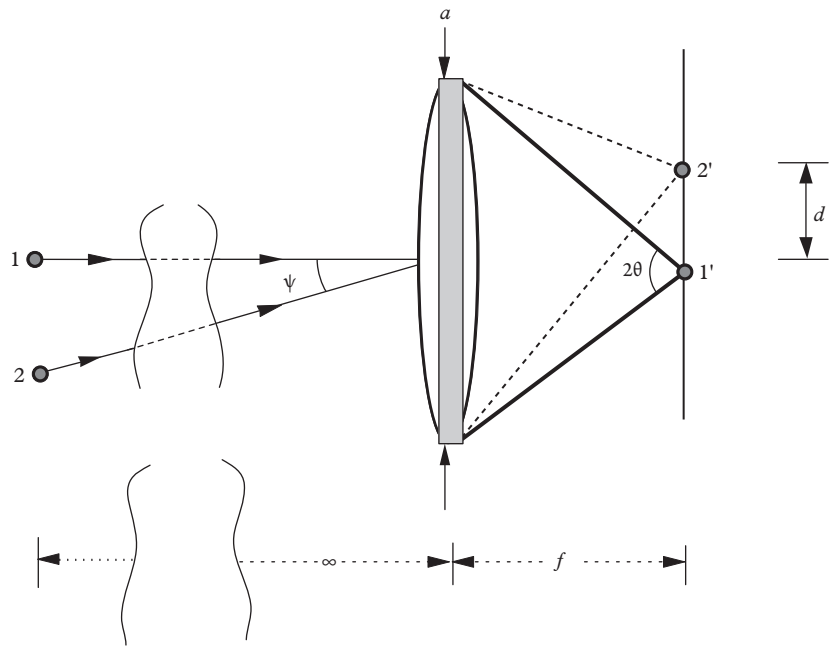

Figure 9.9 *Telescope resolution.*

With this value for d in (9.13), the largest obliquity angle that should be encountered in a visible imaging system is

$$\tan\theta = \frac{\lambda}{2d} = \frac{\lambda}{6\lambda} = \frac{1}{6} = 0.167,$$

$$\theta = 9.5^\circ \approx 10^\circ.$$

(If we had assumed that the smallest value of d were equal to λ, then $\theta = 26.6^\circ$.) We can now make an estimate of a reasonable upper bound on the variation in the obliquity factor over the range of angles that will be encountered in a visible optical system. At $\theta = 0^\circ, (1 + \cos\theta)/2 = 1$. At $\theta = 10^\circ, \cos\theta = 0.985$ and $(1 + \cos\theta)/2 = 0.992$. The obliquity factor has only changed by 0.8% over the angular variation of 0° to 10°; thus, in most situations encountered in visible optics, we are safe in treating the factor as a constant and removing it from the integrand.

The obliquity factor undergoes a 10% change when θ varies from 0° to about 40°; therefore, the obliquity factor cannot safely be treated as a constant in any optical system that involves angles larger than 40°. This can occur in optical systems designed for wavelengths longer than visible wavelengths. (Additional comments about the variation of the obliquity factor are found in Chapter 11.)

While we have shown that it is safe to ignore the variability of C, we have still not assigned a value to the obliquity factor. To find the proper value for C, we will compare the result obtained using (9.9) with the result predicted using geometrical optics.

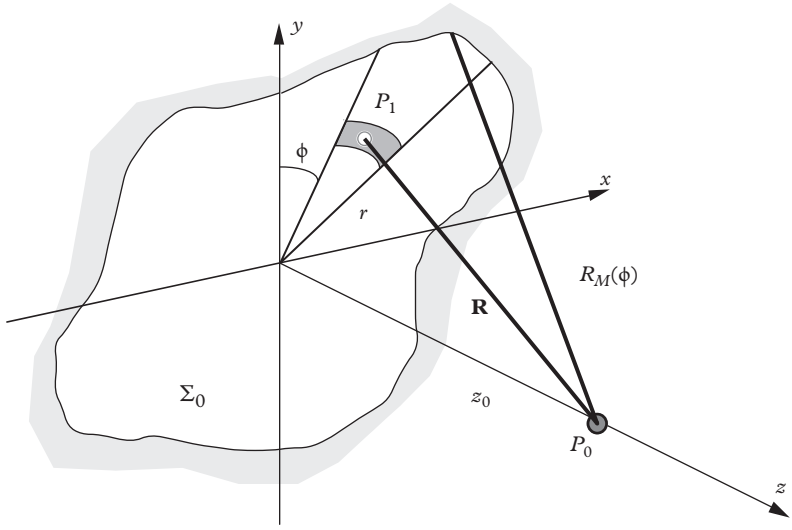

Figure 9.10 *Geometry for evaluating the constant in the Fresnel integral.*

We illuminate the aperture Σ_0 in Figure 9.10 with a plane wave of amplitude α, traveling parallel to the z-axis. Geometrical optics predicts a field at P_0, on the z-axis, a distance z_0 from the aperture, given by

$$\tilde{E}_{\text{geom}} = \alpha e^{-ikz_0}. \tag{9.14}$$

The area of the infinitesimal at P_1 (the Huygens source) is

$$dS = r\, dr\, d\phi.$$

The obliquity factor is assumed to be a constant, C, that can be removed from under the integral. The incident wave is a plane wave whose value at $z = 0$ is $E(r) = \alpha$. Using these parameters, the Fresnel integral (9.9) can be written as

$$\tilde{E}(z_0) = C\alpha \iint \frac{e^{-i\mathbf{k}\cdot\mathbf{R}}}{R}\, r\, dr\, d\phi. \tag{9.15}$$

The distance from the Huygens source to the observation point is

$$z_0^2 + r^2 = R^2,$$

where z_0 is a constant equal to the distance from the observation point to the aperture plane. The variable of integration can be written in terms of R:

$$r\, dr = R\, dR.$$

The limits of integration over the aperture extend from $R = z_0$ to the maximum value of $R = R_m(\phi)$:

$$\tilde{E}(z_0) = C\alpha \int_0^{2\pi} \int_{z_0}^{R_m(\phi)} e^{-ikR}\, dR\, d\phi. \tag{9.16}$$

The integration over R can now be carried out, to yield

$$\tilde{E}(z_0) = \frac{C\alpha}{ik}\, e^{-ikz_0} \int_0^{2\pi} d\phi - \frac{C\alpha}{ik} \int_0^{2\pi} e^{-ikR_m(\phi)}\, d\phi. \tag{9.17}$$

The first integration in (9.17) is easy to perform. The second integral cannot be calculated, because we are performing the evaluation of the Fresnel integral for a general aperture and the functional form of $R_m(\phi)$ is not known. However, the physical significance of the second integral can be obtained. The first term in (9.17) is the amplitude due to geometrical optics. The second term may be interpreted as the sum of the waves diffracted by the boundary of the aperture. An equivalent statement is that the second term represents the interference of the waves scattered from the aperture's boundary. As we mentioned earlier, this interpretation of diffraction was first suggested by Young.

The aperture is irregular in shape, at least on the scale of a wavelength, and thus kR_m will vary by many multiples of 2π as we integrate around the aperture. For this reason, we should be able to assume that the integral is near zero and ignore its value in (9.17) if we confine our attention to the light distribution on the z-axis. After neglecting the second term, we are left with only the geometrical optics component of (9.17):

$$\tilde{\mathbf{E}}(z_0) = \frac{2\pi C}{ik}\alpha e^{-ikz_0}. \tag{9.18}$$

For (9.18) to agree with the prediction of geometrical optics, (9.14), the constant C must be equal to

$$C = \frac{ik}{2\pi} = \frac{i}{\lambda}. \tag{9.19}$$

Using this result in (9.17), we obtain

$$\tilde{E}(z_0) = \alpha\, e^{-ikz_0} - \frac{1}{2\pi} \int_0^{2\pi} \alpha\, e^{-ikR_m(\phi)}\, d\phi.$$

The Huygens–Fresnel integral can be written, using the value for C just derived, as

$$\tilde{E}(\mathbf{r}_0) = \frac{i}{\lambda} \iint_\Sigma \frac{\tilde{E}_i(\mathbf{r})}{R}\, e^{-i\mathbf{k}\cdot\mathbf{R}}\, dS. \tag{9.20}$$

The Huygens–Fresnel integral can be interpreted in two equivalent ways. The classical interpretation views

$$\frac{i}{\lambda}\,\frac{e^{-i\mathbf{k}\cdot\mathbf{R}}}{R}$$

as a Huygens wavelet. This spherical wave of unit amplitude, when multiplied by the value of the incident wave $E_i(\mathbf{r})$ at a point $\mathbf{r}$ in space yields the Huygens wavelet radiated by that point. The integral (9.20) adds all of the interfering wavelets together, to produce the resultant wave.

A more modern interpretation of the Huygens–Fresnel integral is to view it as a convolution integral. Considering free space as a linear system, one finds that the result of

propagation can be calculated by convolving the incident (input) wave with the impulse response of free space,

$$\frac{i}{\lambda}\frac{e^{-i\mathbf{k}\cdot\mathbf{R}}}{R}.$$

9.4.1 Approximate Solutions of the Huygens–Fresnel integral

The job of calculating diffraction has only begun with the derivation of the Huygens–Fresnel integral (9.20). In general, an analytic expression for the integral cannot be found because of the difficulty of performing the integration over R in Figure 9.10. Two approximations that we can make to obtain analytic expressions for the Huygens–Fresnel integral will be discussed in Chapters 10 and 11.

Rigorous solutions exist for only a few idealized obstructions. To allow discussion of the general properties of diffraction, it is necessary to use approximate solutions. Let us look for an approximate solution of the one-dimensional Huygens–Fresnel integral

$$\int \frac{\tilde{E}_i(\mathbf{r})}{R} e^{-i\mathbf{k}\cdot\mathbf{R}}\, dx.$$

For this diffraction component to contribute to the field at point P in Figure 9.11, the phase of the exponent must not vary over 2π when the integration is performed over the aperture shown in Figure 9.11; i.e.,

$$\Delta = \mathbf{k}\cdot\left(\mathbf{R}_1 - \mathbf{R}_1' + \mathbf{R}_2 - \mathbf{R}_2'\right) < 2\pi.$$

From the geometry of Figure 9.11, the two paths from the source S to the observation point P_0 are

$$R_1 + R_2 = \sqrt{z_1^2 + (x_1 + b)^2} + \sqrt{z_2^2 + (x_2 + b)^2},$$

$$R_1' + R_2' = \sqrt{z_1^2 + x_1^2} + \sqrt{z_2^2 + x_2^2}.$$

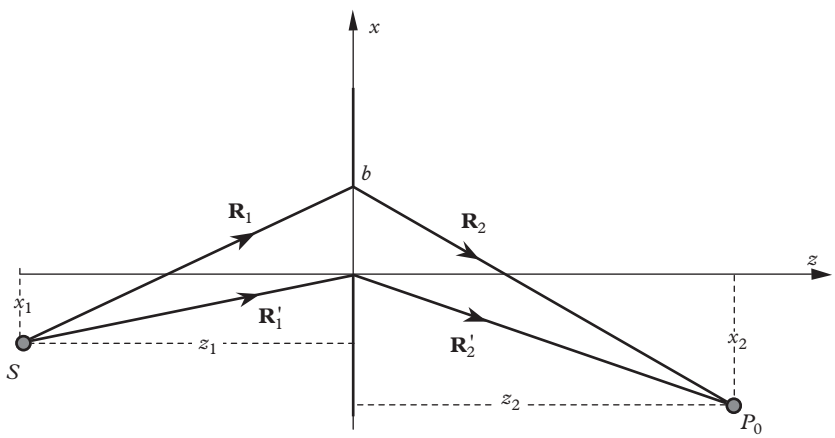

Figure 9.11 *One-dimensional slit used to establish the Fraunhofer and Fresnel approximations.*

By assuming that the aperture, of width b, is small compared with the distances z_1 and z_2, the difference between these distances, Δ, can be rewritten as an expansion in terms of b (details of the expansion will be given in Chapter 10):

$$\Delta \approx k\left(\frac{x_1}{z_1}+\frac{x_2}{z_2}\right)b+\frac{k}{2}\left(\frac{1}{z_1}+\frac{1}{z_2}\right)b^2+\cdots. \tag{9.21}$$

If we assume that the second term of this expansion is small, i.e.,

$$\frac{k}{2}\left(\frac{1}{z_1}+\frac{1}{z_2}\right)b^2 \ll 2\pi,$$

$$\frac{b^2}{2}\left(\frac{1}{z_1}+\frac{1}{z_2}\right) < \lambda,$$

then we may treat the variation of the phase across the aperture as if it were linear. Physically, this means that all waves in the aperture are assumed to be plane waves. The diffraction predicted by the theory based on this assumption is called *Fraunhofer diffraction* and is the subject of Chapter 10.[1]

Appendices 9A and 9B contain a formal derivation of the Huygens–Fresnel integral. The details contained in these derivations are not required to understand diffraction, but will provide a more formal derivation of the diffraction integral for the reader not satisfied with the intuitive approach taken above.

9.5 Gaussian Beams

We have just introduced a view of diffraction that treats the propagation of light using an integral method, as modifications made on an input beam. A second approach to describing the paraxial propagation of light is to develop the differential equation of the optical system. The output of the system is then obtained, given the input wave, from the solutions of the differential equation. The differential equation that must be satisfied to determine the spatial behavior of a wave in free space is the Helmholtz equation.

We will find that if we make the paraxial approximation, then solutions of the Helmholtz equation with Gaussian amplitude distributions are obtained. We will show that the waves described by these particular solutions can be characterized by two simple parameters. These parameters are the beam waist and the radius of curvature of the phasefront of the wave. The *beam waist* is defined as the half-width at an amplitude equal to $1/e$ of the maximum amplitude of the wave, transverse to the propagation direction. The *radius of curvature* describes the radius of curvature of the phase front of the wave, as measured from the position of minimum beam waist.

The mathematical manipulations required to obtain the characteristic parameters of a Gaussian wave are long, but not complicated. The results are worth the effort in that they allow the inclusion of diffraction in the analysis of complicated optical systems [4]. The transverse amplitude distribution of optical beams from lasers have Gaussian amplitude distributions, as do the propagation modes of some optical fibers and the cavity modes of Fabry–Perot resonators with spherical mirrors.

To derive the characteristics of a Gaussian wave, we use the paraxial approximation. A plane wave is assumed to be propagating nearly parallel to the z-direction, allowing it to be described by a scalar wave of the form

$$\tilde{E}(r) = \Psi(x,y,z)\, e^{-ikz}, \tag{9.22}$$

i.e., the wave does not propagate in the x- or y-direction.

[1] Retention of the first two terms of (9.1) leads to Fresnel diffraction, the subject of Chapter 11.

We will substitute this general wave into the Helmholtz equation to produce the scalar, paraxial, wave equation that must be solved:

$$\left(\frac{\partial^2\Psi}{\partial x^2}+\frac{\partial^2\Psi}{\partial y^2}+\frac{\partial^2\Psi}{\partial z^2}\right)e^{-ikz}+k^2\Psi e^{-ikz}-2ik\frac{\partial\Psi}{\partial z}e^{-ikz}-k^2\Psi e^{-ikz}=0. \tag{9.23}$$

The assumption that Ψ changes very slowly with z (linearly with z will do it) allows $\partial^2\Psi/\partial z^2$ to be ignored. The resulting scalar wave equation,

$$\frac{\partial^2\Psi}{\partial x^2}+\frac{\partial^2\Psi}{\partial y^2}-2ik\frac{\partial\Psi}{\partial z}=0, \tag{9.24}$$

is called the *paraxial wave equation*. This equation and its solutions lead to a description that can be shown to be equivalent to the Fresnel description of diffraction [3].

We assume that the solution of (9.23) has the form

$$\Psi=e^{-iQ(z)(x^2+y^2)}\,e^{-iP(z)}. \tag{9.25}$$

We assume that (9.25) is a solution of (9.24), and this assumption will impose requirements on P and Q. By proper specification of $P(z)$ and $Q(z)$, (9.25) will assume a Gaussian form. We will discover that $Q(z)$ must be a complex variable associated with the reciprocal of the Gaussian width and that $P(z)$ must contain information on the phase of the wave.

By the selection of (9.25) as the solution of (9.24), we have implicitly assumed that the transverse dependence of the wave is only a function of x^2+y^2. The assumption results in the simplest Gaussian wave solutions, i.e., waves that have circular symmetry [3].

We first determine the derivatives of (9.25), to be substituted into (9.24):

$$\begin{aligned}\frac{\partial^2\Psi}{\partial x^2}&=-4x^2Q^2\Psi-2iQ\Psi,\\ \frac{\partial^2\Psi}{\partial y^2}&=-4y^2Q^2\Psi-2iQ\Psi,\\ \frac{\partial\Psi}{\partial z}&=-i\frac{\partial P}{\partial z}\Psi-i\left(x^2+y^2\right)\frac{\partial Q}{\partial z}\Psi.\end{aligned} \tag{9.26}$$

Substituting (9.26) into (9.24) results in an expression that will yield the required forms of $P(z)$ and $Q(z)$

$$-4(x^2+y^2)Q^2-4iQ-2k\frac{\partial P}{\partial z}-2k\left(x^2+y^2\right)\frac{\partial Q}{\partial z}=0. \tag{9.27}$$

Since (9.27) must hold for all values of x and y, we may equate the coefficients of the different powers of x and y to zero:

$$k\frac{\partial P}{\partial z}+2iQ=0, \tag{9.28a}$$

$$2Q^2+k\frac{\partial Q}{\partial z}=0. \tag{9.28b}$$

[Equation (9.28b) is called Riccati's equation [5].]

We make a change of variables:

$$q = \frac{k}{2Q}. \tag{9.29}$$

In a moment, q will be identified as the desired Gaussian width of the amplitude distribution of the wave. Using the new variable, we may write

$$\frac{\partial q}{\partial z} = -\frac{k}{2Q^2}\frac{\partial Q}{\partial z}.$$

We can use this new variable to rewrite (9.28a, b) as

$$\frac{\partial q}{\partial z} = 1, \tag{9.30}$$

$$\frac{\partial P}{\partial z} = \frac{-i}{q}. \tag{9.31}$$

Equation (9.30) integrates to give

$$q = \tilde{q}_0 + z, \tag{9.32}$$

where we have chosen the constant of integration $\tilde{q}_0$ to be purely imaginary. By moving $\tilde{q}_0$ off the real axis, we remove the singularity that would occur in $\partial Q/\partial z$ if $q_0 = -z_0$. Requiring q to be complex also makes it possible to interpret (9.25) as a wave with a Gaussian amplitude distribution.

If q is known in one plane, we can calculate q in a plane, a distance z away, by using (9.32). This solution of the paraxial wave equation provides a capability similar to that provided by Huygens' principle. The determination of new properties of a wave can be made using the old properties of the wave.

The derived form of q, (9.32), can be substituted into (9.31),

$$\frac{\partial P}{\partial z} = \frac{-i}{\tilde{q}_0 + z},$$

to obtain the function $P(z)$:

$$P(z) = -i \ln\left(1 + \frac{z}{\tilde{q}_0}\right). \tag{9.33}$$

The results obtained for $P(z)$ and $1/Q(z)$ can now be substituted into (9.25) to produce the wave solution of the paraxial Helmholtz equation:

$$\Psi = \exp\left\{-i\left[-i \ln\left(1 + \frac{z}{\tilde{q}_0}\right) + \frac{k}{2(\tilde{q}_0 + z)}\left(x^2 + y^2\right)\right]\right\}. \tag{9.34}$$

Since $\tilde{q}_0$, is imaginary it is possible to make the substitution

$$\ln\left(1 + \frac{z}{\tilde{q}_0}\right) = \ln\left(1 - \frac{iz}{q_0}\right),$$

where q_0 is now a real quantity. The identity

$$\ln(x \pm iy) = \ln\sqrt{x^2 + y^2} \pm i \tan^{-1}\left(\frac{y}{x}\right)$$

can now be used to obtain a new formulation of (9.34):

$$\Psi = \frac{1}{\sqrt{1 + \left(\frac{z}{q_0}\right)^2}} \exp\left[-\frac{kq_0\left(x^2 + y^2\right)}{2\left(z^2 + q_0^2\right)}\right] \exp\left[i\tan^{-1}\left(\frac{z}{q_0}\right) - \frac{ikz\left(x^2 + y^2\right)}{2\left(z^2 + q_0^2\right)}\right]. \quad (9.35)$$

Evaluating (9.35) at $z = 0$ allows the identification of the physical significance of the amplitude of Ψ. At $z = 0$, (9.35) reduces to

$$\Psi_0 = e^{-k\left(x^2+y^2\right)/2q_0}. \quad (9.36)$$

This is a Gaussian function, as we can see by comparing it with a Gaussian spatial amplitude distribution, given by

$$E = E_0 e^{-\left(x^2+y^2\right)/w^2},$$

and plotted in Figure 9.12. The comparison demonstrates that Ψ can be interpreted as a wave, whose transverse amplitude distribution is a Gaussian.

The parameter w of the Gaussian distribution is the half-width of the Gaussian function measured at the point where the amplitude is $1/e$ of its maximum value (see Figure 9.12). We define $w = w_0$ as the minimum half-width of the Gaussian function. Comparing the Gaussian function with the equation for Ψ_0 produces the definition of a minimum width for the Gaussian wave, the *minimum beam waist*, in terms of q_0:

$$w_0^2 \equiv \frac{2q_0}{k}. \quad (9.37)$$

The minimum beam waist occurs when $z = 0$; thus the minimum beam diameter establishes the origin of the coordinate system. The real-valued constant

$$q_0 \equiv \frac{kw_0^2}{2} = \frac{\pi w_0^2}{\lambda} \quad (9.38)$$

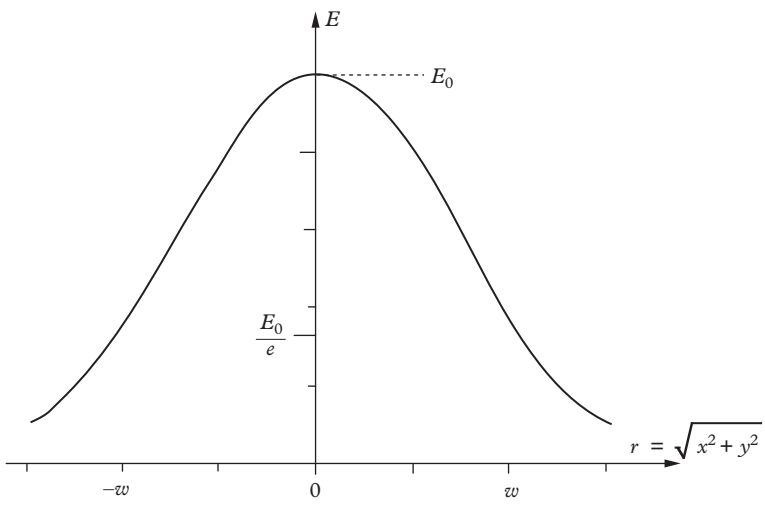

Figure 9.12 *Gaussian wave of width w and height* E_0.

is often called the *confocal parameter* (its significance will be identified in a moment). The complex constant of integration

$$\tilde{q}_0 = iq_0,$$

introduced in (9.32), can now be interpreted as the minimum value of the *complex size parameter* of a Gaussian wave:

$$\tilde{q}_0 = \frac{i\pi w_0^2}{\lambda}. \tag{9.39}$$

This analysis allows the association of the complex function q with the physical variables of the beam. With this association, the physical interpretation of (9.32) is that as z increases, the beam variables evolve. The minimum value of the parameter is the minimum beam waist w_0, and its position is established as the origin of the coordinate system. The value of q at a distance z from the beam waist is obtained from (9.32):

$$\tilde{q} = \tilde{q}_0 + z = z + \frac{i\pi w_0^2}{\lambda}.$$

Using the definition of q_0 given in (9.38), we can write (9.35) as

$$\Psi = \frac{1}{\sqrt{1 + \left(\dfrac{\lambda z}{\pi w_0^2}\right)^2}} \exp\left\{ - \frac{x^2 + y^2}{w_0^2 \left[1 + \left(\dfrac{\lambda z}{\pi w_0^2} \right)^2 \right]} \right\}$$

$$\times \exp\left\{ i \tan^{-1}\left(\frac{\lambda z}{\pi w_0^2} \right) - \frac{i\pi (x^2 + y^2)}{\lambda z \left[1 + \left(\dfrac{\pi w_0^2}{\lambda z} \right)^2 \right]} \right\}. \tag{9.40}$$

We began our analysis by assuming a paraxial wave, i.e., that the wave must propagate in a direction that is nearly parallel with the z-axis. Examination of that assumption will allow us to assign physical significance to the quantities contained in (9.40). We allow the wave of interest to be a spherical wave, propagating away from the origin, with a wavefront of radius of curvature $R(z)$ a distance z from the origin as shown in Figure 9.13. The assumption of a paraxial wave implies that this spherical wave can be approximated by a *paraxial spherical wave* of the form

$$\begin{aligned} \frac{1}{R} e^{-ikR} &= \frac{1}{R} e^{-ik\sqrt{z^2 + x^2 + y^2}} \\ &\approx \frac{1}{R} e^{-ikz} e^{-ik\left(x^2 + y^2\right)/2z}, \end{aligned}$$

where were have assumed that $z^2 \gg x^2 + y^2$. The paraxial assumption is that $z \approx R$, so

$$\frac{1}{R} e^{-ikR} \approx \frac{1}{z} e^{-ikz}\, e^{-ik\left(x^2 + y^2\right)/2R}.$$

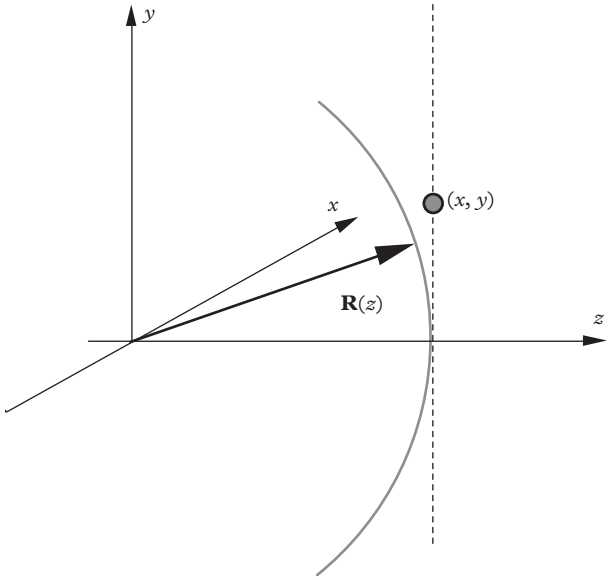

Figure 9.13 *Propagation of a spherical wave. If point (x, y) is not too far from the z-axis, we may approximate this wave by a nearly plane wave called a paraxial spherical wave.*

All of the terms in the equation for a Gaussian wave, (9.40), can now be given a physical interpretation. Upon examining (9.40), we find that it can be written in the same form as the paraxial spherical wave if we define the radius of curvature of the wavefront as

$$\frac{k}{2R} = \frac{\pi}{\lambda z\left[1 + \left(\frac{\pi w_0^2}{\lambda z}\right)^2\right]}.$$

The radius of curvature of the phasefront of a paraxial spherical waved escribed by (9.40) is therefore determined by the function

$$R(z) = z\left[1 + \left(\frac{\pi w_0^2}{\lambda z}\right)^2\right]. \tag{9.41}$$

At large values of z, $R \approx z$. The sign convention is such that the beam shown in Figure 9.13 has a positive radius of curvature.[2]

There is an extra phase term in (9.40):

$$\phi(z) = \tan^{-1}\left(\frac{\lambda z}{\pi w_0^2}\right). \tag{9.42}$$

$\phi(z)$ as defined by (9.42) is the phase difference between an ideal plane wave, shown by the dotted line through the point (x, y) in Figure 9.13, and the "nearly plane" spherical wave of this theory. This phase shift is called the Gouy phase shift. When you pass through focus (from $-\infty$ to ∞), this phase shift equals π.

[2] This convention is consistent with the sign convention for the radius of curvature of optical surfaces, defined in Chapter 5. The radius of curvature of an optical surface is measured from the surface to the center of curvature. Here, the coordinate origin is at the beam waist, so the radius is measured, in the opposite sense, from the center of curvature to the phase front.

The first exponent in (9.40) describes the amplitude distribution across the wave. It has the same functional form as a Gaussian distribution with a beam width, sometimes called the beam's *spot size*, given by

$$w(z)^2 = w_0^2 \left[1 + \left(\frac{\lambda z}{\pi w_0^2} \right)^2 \right]. \tag{9.43}$$

The curve created by connecting the $1/e$ points of the transverse amplitude of the Gaussian beam along its propagation path is described by (9.43). The curve is a hyperbola along the wave's propagation path. At large z, the asymptotic representation of (9.43) is a straight line, the geometric ray,

$$w(z) = \left(\frac{\lambda}{\pi w_0} \right) z,$$

originating at the origin and propagating in the positive z-direction. The ray is inclined with respect to the z-axis at the *diffraction angle*

$$\theta = \frac{\lambda}{\pi w_0}. \tag{9.44}$$

We will discover in Chapter 10 that the Fresnel formalism also yields (9.44).

The physical interpretation given to (9.44) is that diffraction causes a wave of diameter $2w_0$ to spread by an amount

$$\frac{2Z\lambda}{\pi w_0}$$

after propagating a distance Z. The larger the value of the beam waist w_0, the less the beam will spread due to diffraction. This is why a megaphone works for a cheerleader. The megaphone changes the effective aperture producing sound from the small diameter of a human mouth, about 50 mm, to a much larger diameter, something over 30 cm. The propagation properties of laser beams are closely modeled by (9.44). For this reason, lasers are often characterized by their *divergence angle*, which is equal to the diffraction angle.

The diffraction angle can be used to calculate the beam diameter at a distance z from the beam waist:

$$w(z)^2 = w_0^2 + \theta^2 z^2. \tag{9.45}$$

Figure 9.14 schematically represents the propagation of a Gaussian beam. The dark lines are the hyperbola given by (9.43), and the dashed straight lines are asymptotes of the hyperbola, i.e., the geometric rays, inclined at an angle θ, calculated from (9.44).

The significance of the confocal parameter can be identified by examining (9.43). When the definition of the confocal parameter (9.38) is substituted into (9.43), the resulting equation,

$$w(z)^2 = w_0^2 \left[1 + \left(\frac{z}{q_0} \right)^2 \right],$$

demonstrates that the confocal parameter, also called the *Rayleigh range*, is the propagation distance z over which the wave's width increases, from w_0 to $\sqrt{2}w_0$, or, stated another way,

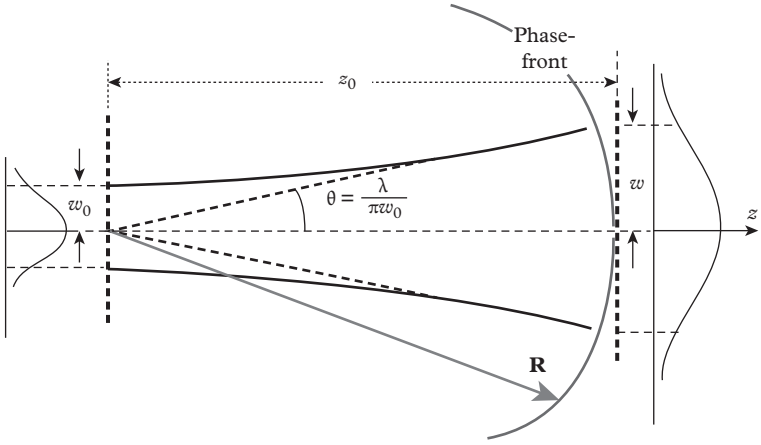

Figure 9.14 *Propagation of a Gaussian wave from its beam waist to the far field.*

it is the distance over which the area of the beam's cross section doubles. The confocal parameter characterizes a Gaussian beam's convergent or divergent properties. To emphasize the connection with the divergence of the beam, we rewrite the Rayleigh range using (9.38) and (9.44) as

$$q_0 = \frac{w_0}{\theta} = \frac{\pi w_0^2}{\lambda}.$$

Using the newly defined parameters, (9.40) can be written as

$$\Psi = \underbrace{\left[\frac{w_0}{w(z)}\right] e^{-\left(x^2+y^2\right)/w(z)^2}}_{\text{amplitude}} \underbrace{e^{-ik\left(x^2+y^2\right)/2R(z)}}_{\substack{\text{paraxialwave}\\ \text{profile}}} \underbrace{e^{-i\phi(z)}}_{\text{phase}}. \tag{9.46}$$

9.6 Higher-Order Gaussian Modes and Bessel Beams

The Gaussian wave described by (9.46) has the property that its cross section is everywhere given by the same function, a Gaussian. There are other solutions to (9.23) with this property. These additional solutions arise when the transverse amplitude distribution is not constrained to have circular symmetry. The complete collection of a particular set of solutions form a complete orthogonal set called the *modes of propagation*. We will not explore the higher-order modes but simply give examples of two classes of higher-order modes, namely Hermite–Gaussian waves and Laguerre–Gaussian waves.

9.6.1 Hermite–Gaussian Waves

If the symmetry is rectangular, the additional solutions are Hermite–Gaussian functions (Figure 9.15):

$$U_{m,n}^{\mathrm{HG}}(x,y,z) = C_{mn}^{\mathrm{HG}} \frac{1}{w} e^{-ik\left(x^2+y^2\right)/2R} e^{-\left(x^2+y^2\right)/w^2} e^{-i(m+n+1)\phi} H_m\left(\frac{x\sqrt{2}}{w}\right) H_n\left(\frac{y\sqrt{2}}{w}\right),$$

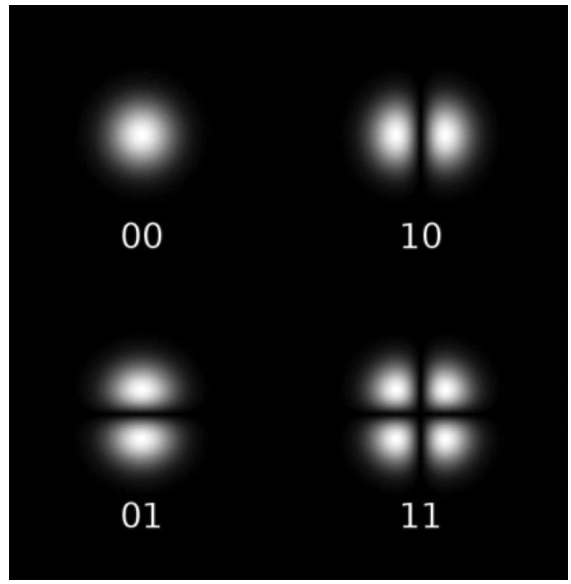

Figure 9.15 *Hermite–Gaussian modes, (m,n). (DrBob at en.wikipedia.)*

where

$$H_m(u) = (-1)^m e^{u^2} \frac{d^m}{du^m}\left(e^{-u^2}\right),$$

$$C_{mn}^{\mathrm{HG}} = \left(\frac{2}{\pi\, n!m!}\right)^{1/2} 2^{-N/2}.$$

9.6.2 Laguerre–Gaussian Waves

If the beam has rotational symmetry along the propagation direction, the additional solutions are Laguerre–Gaussian functions (Figure 9.16):

$$U_{l,m}^{\mathrm{LG}}(r,\theta,z) = C_{lm}^{\mathrm{LG}} \frac{1}{w} e^{-ikr^2/2R} e^{-r^2/w^2} e^{-(l+m+1)\phi} e^{-i(l-m)\theta} (-1)^{\min(l,m)} \left(\frac{r\sqrt{2}}{w}\right)^{l-m} L_{\min(l,m)}^{(l-m)}\left(\frac{2r^2}{w^2}\right),$$

where

$$L_n^{(m)}(u) = \frac{u^{-m}e^u}{n!}\frac{d^n}{du^n}\left(u^{m+n}e^{-u}\right),$$

$$C_{lm}^{\mathrm{LG}} = \left(\frac{2}{\pi\, l!m!}\right)^{1/2} \min(l,m)!\,.$$

Laguerre–Gaussian waves have found use as optical tweezers.

9.6.3 Bessel Beams

In circular cylindrical coordinates, the solution to the Helmholtz equation are beams with a transverse beam profile given by Bessel functions [6]. There is some controversy about the

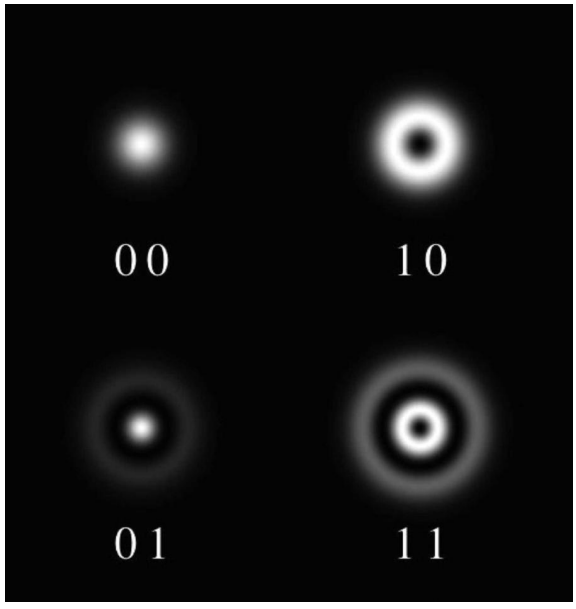

Figure 9.16 *First four Laguerre–Gaussian modes, (n,m). (Ziofil at Wikimedia.org.)*

ability to actually create a true Bessel beam, but quasi-Bessel beams can be created whose central maxima exhibit resistance to diffraction spreading during propagation, which makes them useful as optical tweezers. An ideal Bessel beam is given by

$$E(r,\theta,z) = A_0 e^{ik_z z} J_n(k_r r) e^{\pm in\theta}$$

(Figure 9.17). See Figures 6.20 and 12A.1 for the first five Bessel functions of the first kind, J_n. The propagation vector is

$$k = \sqrt{k_z^2 + k_r^2} = \frac{2\pi}{\lambda}.$$

The Fourier transform of the Bessel beam is a ring. The power in the beam is equally distributed among all of the rings. All of the higher-order modes have zero energy on axis.

The Bessel beam cannot create a true trap, but it can be used for long distance optical guiding.

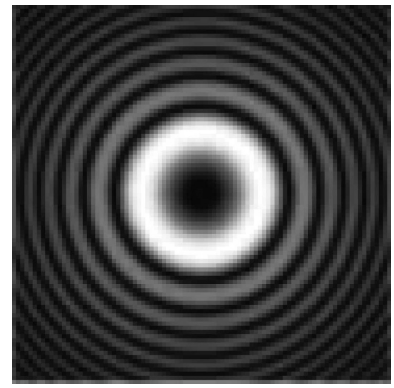

Figure 9.17 *Bessel beam associated with the Bessel function J_1. This is the Fourier transform (far-field pattern) of the zeroth-order beam. (McGloin, D. and K. Dholakia,* Bessel beams: diffraction in a new light. *Contemp. Phys., 2005.* ***46****: p. 15–28.)*

9.7 Beam Propagation

If we divide $R(z)$ by $w(z)$, we can use the result to obtain expressions for w_0 and z in terms of R and w:

$$w_0^2 = \frac{w^2}{\left[1 + \left(\frac{\pi w^2}{\lambda R}\right)^2\right]}, \tag{9.47}$$

$$z = \frac{R}{\left[1 + \left(\frac{\lambda R}{\pi w^2}\right)^2\right]}. \tag{9.48}$$

We see from (9.47) that at the minimum beam waist, the phase front of the Gaussian wave is a plane, i.e., $R = \infty$. These equations can be used to locate the beam waist of any Gaussian wave. To obtain the parameters of a wave at any point along its propagation path, the *ABCD* law can be used, as we will learn in the next subsection.

9.7.1 The *ABCD* Law

We will establish a relationship between the Gaussian beam parameters just introduced and geometrical optics that will allow the calculation of Gaussian beam parameters after the wave has passed through an optical system. We first discover how the radius of curvature of a Gaussian wavefront is changed by a thin lens. We will learn that the radius of curvature and the complex beam parameter are governed by the same propagation equations. This finding will allow the construction of an *ABCD* law for a Gaussian wave.

In Chapter 5, we found the *ABCD* matrix, which relates the input and output parameters of an optical system, using the paraxial approximation

$$\begin{bmatrix} x_2 \\ \gamma_2 \end{bmatrix} = \begin{bmatrix} A & B \\ C & D \end{bmatrix} \begin{bmatrix} x_1 \\ \gamma_1 \end{bmatrix},$$

$$x_2 = Ax_1 + B\gamma_1, \quad \gamma_2 = Cx_1 + D\gamma_1.$$

The variable x_1 is the coordinate position, above the optical (z-)axis, of the ray entering the optical system, x_2 is the coordinate position of the ray leaving the system, and the γ's are the ray slopes. The ray slope for a Gaussian wave of radius R shown in Figure 9.18 is

$$\gamma = \frac{dx}{dz} = \tan\gamma \approx \frac{x}{R}, \tag{9.49}$$

so

$$R = \frac{x}{\gamma}. \tag{9.50}$$

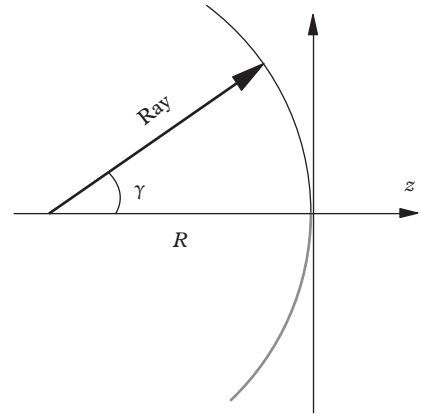

Figure 9.18 *Geometry for a Gaussian wave in geometrical optics.*

The radius of curvature of the Gaussian wave leaving the optical system described by the *ABCD* matrix is given by

$$\begin{aligned} R_2 &= \frac{x_2}{\gamma_2} \\ &= \frac{\gamma_1\left(A\dfrac{x_1}{\gamma_1}+B\right)}{\gamma_1\left(C\dfrac{x_1}{\gamma_1}+D\right)} \\ &= \frac{AR_1+B}{CR_1+D}, \end{aligned} \tag{9.51}$$

where R_1 is the radius of curvature of the Gaussian wave entering the optical system.

To determine the radius of curvature of the phasefront of a Gaussian wave after it has passed through a simple lens, we substitute into (9.51) the *ABCD* matrix from Figure 5A.4:

$$R_2 = \frac{R_1}{-\dfrac{R_1}{f}+1},$$

$$\frac{1}{R_2} = \frac{1-\dfrac{R_1}{f}}{R_1} = \frac{1}{R_1}-\frac{1}{f}. \tag{9.52}$$

When the Gaussian wave is propagating through free space, we use the *ABCD* matrix (5.12) to obtain the radius of curvature of the phasefront, R_2, after the wave has propagated a distance d:

$$R_2 = R_1 + d. \tag{9.53}$$

The Gaussian wave's complex size parameter q provides a concise description of the propagation of a Gaussian beam through an optical system, and it extends easily to higher-order modes. In fact, the higher-order modes have the same w, R, and q as the fundamental mode we are discussing; only the phase ϕ is different. For a Gaussian wave propagating through free space, from the beam waist to a position z, the complex size parameter is

$$\tilde{q}_1 = \tilde{q}_0 + z.$$

If we propagate from z to $z + d$, the q-parameter becomes

$$\tilde{q}_2 = \tilde{q}_1 + d. \tag{9.54}$$

The complex size parameter obeys the same rule as the radius of curvature for a wave propagating in free space.

To analyze the effects of a simple lens on a Gaussian wave, recall that the complex size parameter q can be written as

$$\frac{1}{\tilde{q}} = \frac{1}{z+\dfrac{i\pi w_0^2}{\lambda}} = \frac{z-\dfrac{i\pi w_0^2}{\lambda}}{z^2+\left(\dfrac{\pi w_0^2}{\lambda}\right)^2}.$$

Using (9.41) and (9.43), we can rewrite this as

$$\frac{1}{\tilde{q}} = \frac{1}{R} - \frac{i\lambda}{\pi w^2}. \tag{9.55}$$

For a thin lens, the spot size w is the same at the front and back surfaces of the lens (remember from Appendix 5A that the front and back vertices of a thin lens define planes of unit magnification), and thus $w_2 = w_1$. The beam radius of curvature should change according to (9.52), allowing us to write (9.55) as

$$\begin{aligned}\frac{1}{\tilde{q}_2} &= \frac{1}{R_2} - \frac{i\lambda}{\pi w_2^2} \\ &= \left(\frac{1}{R_1} - \frac{1}{f}\right) - \frac{i\lambda}{\pi w_1^2}.\end{aligned} \tag{9.56}$$

Rearranging the terms yields

$$\frac{1}{\tilde{q}_2} = \frac{1}{\tilde{q}_1} - \frac{1}{f}. \tag{9.57}$$

Comparing (9.52) and (9.57) again leads us to the conclusion that the complex beam parameter q plays a role corresponding to that played by the radius of curvature R of a spherical wave. This should not surprise us, because (9.55) defines the real part of $1/q$ as being equal to $1/R$. We can rename q as the *complex curvature* of a Gaussian wave.

Because of the formal equivalence between q and R, (9.51) can be used to write

$$\tilde{q}_2 = \frac{A\tilde{q}_1 + B}{C\tilde{q}_1 + D}. \tag{9.58}$$

Equation (9.58) allows a Gaussian beam to be traced through any optical system. Several examples of the application of (9.58) will show the usefulness of this result.

9.7.2 Thin Lens

As the first example of the use of (9.58), a Gaussian beam will be followed through a thin lens. Assume that a plane wave uniformly illuminates a lens of diameter D. Because it is a plane wave, $R_1 = \infty$, and because the aperture of the lens is uniformly illuminated, $w = D/2$. The q-parameter at the left surface of the lens is given by

$$\frac{1}{\tilde{q}_1} = 0 - \frac{4i\lambda}{\pi D^2}.$$

The *ABCD* matrix for a thin lens can be obtained from Figure 5A.4 and can be used to calculate the q-parameter, after the beam has passed through the lens:

$$\tilde{q}_2 = \frac{\tilde{q}_1}{1 - \dfrac{\tilde{q}_1}{f}},$$

$$\frac{1}{\tilde{q}_2} = -\frac{1}{f} - \frac{i\lambda}{\pi\,(D/2)^2}.$$

After passing through the thin lens, the beam waist remains the same size, $w = D/2$, but the radius of curvature of the phase front becomes

$$R_2 = -f;$$

i.e., the beam is now converging with the center of curvature of the wavefront on the right of the wavefront.

To find the location of the minimum beam waist, we use (9.48):

$$z = \frac{-f}{1 + \left(\dfrac{4\lambda f}{\pi D^2}\right)^2} \approx -f.$$

The minus sign signifies that the current position is to the left of the minimum beam waist; i.e., the minimum beam waist lies to the right of the lens, a distance f from the lens. The size of the minimum beam waist is given by (9.47):

$$w_0^2 = \frac{D^2/4}{1 + \left(\dfrac{\pi D^2}{4\lambda f}\right)^2} \approx \frac{4\lambda^2 f^2}{D^2}.$$

The conclusion of this analysis is that parallel light filling the aperture of a thin lens is brought to a focus at the back focal plane of the lens. Diffraction by the aperture of the lens prevents the beam from being focused to a spot smaller than the minimum beam waist. The focal spot size is inversely proportional to the lens aperture and linearly proportional to the focal length of the lens.

9.7.3 Fabry–Perot Resonator

The stability condition of a Fabry–Perot resonator, derived in Chapter 5, can be obtained using (9.58). For a mode to be stable, we require that the q-parameter, at any arbitrary reference plane, must reproduce itself after a round trip in the cavity; i.e.,

$$\tilde{q} = \frac{A\tilde{q} + B}{C\tilde{q} + D},$$

where A, B, C, and D are the elements of the $ABCD$ matrix for the Fabry–Perot resonator—the matrix elements for a reference plane located at mirror 1 of Figure 5.13 are given in (5.13). The equation may be solved for $1/q$ to obtain

$$\frac{1}{\tilde{q}} = \frac{(D-A) \pm \sqrt{(D-A)^2 + 4BC}}{2B}.$$

The $ABCD$ determinant for the resonator must equal 1 because the index of refraction is a constant in the resonator, i.e., $AD - BC = 1$. This allows the equation for $1/q$ to be simplified:

$$\frac{1}{\tilde{q}} = \frac{D-A}{2B} \pm \frac{i\sqrt{1 - (D+A)^2/4}}{B}.$$

This equation is in the standard form of the q-parameter. The real part of the equation for the q-parameter can be extracted to discover the radius of curvature of the Gaussian wave in the Fabry–Perot resonator:

$$R = \frac{2B}{D-A}.$$

To ensure that the q-parameter is complex, we require that

$$\left|\frac{D+A}{2}\right| < 1.$$

This is the same stability condition derived using geometrical optics, (5.19).

In Chapter 5, (5.14), we calculated the *ABCD* matrix for a ray whose round trip left it at the surface of mirror 1 in Figure 5.12. Using this *ABCD* matrix, we will find that the radius of curvature of the stable Gaussian wave is equal to the radius of curvature of mirror 1:

$$R = \frac{4d\left(1-\frac{d}{R_2}\right)}{\left(1-\frac{2d}{R_2}\right)-1+\frac{4d}{R_1}+\frac{2d}{R_2}\left(1-\frac{2d}{R_1}\right)} = R_1.$$

If the *ABCD* matrix for a wave ending at mirror 2 were used to calculate R, then we would discover that at that mirror, the radius of curvature of a reproducing Gaussian wave would be $R = R_2$.

We are led to the conclusion that if a stable, reproducing, Gaussian wave exists in a Fabry–Perot resonator, then the radii of curvature of the mirrors making up the resonator match the wave's wavefront curvature. Figure 9.19 shows a typical Gaussian wave. This wave would be a mode of a Fabry–Perot resonator if the mirrors of the resonator were positioned so that their curvature matched the wavefront curvature, shown by the gray lines in Figure 9.19. The mirror's diameter would be selected so that it intercepted say 99% of the beam at that location on the optical axis.

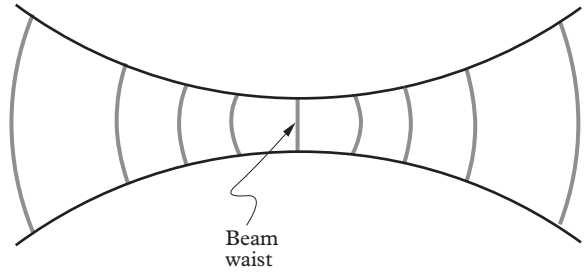

Figure 9.19 *The beam waist occurs at the point where the radius of curvature of the phase is infinite.*

9.7.4 Laser Cavity

As a final example, we will analyze a commercial HeNe laser designed to operate at $\lambda = 632.8$ nm. The optical layout of the laser cavity is shown in Figure 9.20. We will derive the *ABCD* matrix for this design but will leave the details of the calculation to the reader (see Problem 9.4).

Inside the laser cavity, the phase front curvature of the Gaussian wave must match the curvature of the mirrors in the cavity. This means that at the plane mirror, on the left of Figure 9.19, the radius of curvature is infinite. From (9.47), we see that the beam waist always occurs at the point where the radius of curvature is infinite (see Figure 9.19). We will make all of our measurements from the beam waist, which we now know to be at the plane mirror. The second mirror is a lens whose concave surface has a reflective dielectric coating. At mirror 2, $z = 0.7$ m and $R = 2$ m. We use (9.41) to find the size of the beam waist w_0, from which we can calculate the complex beam parameter q_1.

Light leaves the laser cavity through the lens, whose concave surface serves as one of the Fabry–Perot mirrors. To locate the beam waist and find its size outside the cavity, we must calculate the *ABCD* matrix. From left to right in Figure 9.20, we have the following matrices (see Figure 5A.4 for the proper matrix formulas):

1. Propagation in the laser cavity from mirror 1 to mirror 2; we assume the index of refraction in the cavity is $n_1 = 1.0$:

$$\begin{bmatrix} 1 & 0.7 \\ 0 & 1 \end{bmatrix}.$$

2. Refraction at the surface of mirror 2; we assume the index of refraction of the lens, which also serves as mirror surface 2, is $n_2 = 1.5$:

$$\begin{bmatrix} 1 & 0 \\ \dfrac{n_2 - n_1}{n_2 R_2} & \dfrac{n_1}{n_2} \end{bmatrix}.$$

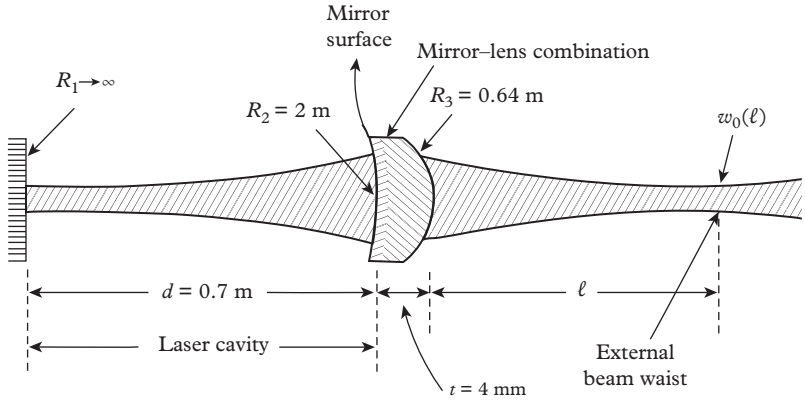

Figure 9.20 *HeNe laser cavity design.*

3. Propagation of light through the glass between the surfaces of mirror 2; the mirror thickness $t = 4$ mm:

$$\begin{bmatrix} 1 & \dfrac{t}{n_2} \\ 0 & 1 \end{bmatrix}.$$

4. Refraction at the back surface of mirror 2; we assume the index of refraction outside the laser is $n_1 = 1$:

$$\begin{bmatrix} 1 & 0 \\ \dfrac{n_1 - n_2}{n_1 R_3} & \dfrac{n_2}{n_1} \end{bmatrix}.$$

5. Propagation to the beam waist outside the laser cavity; this matrix contains the quantity of interest, d:

$$\begin{bmatrix} 1 & d \\ 0 & 1 \end{bmatrix}.$$

The *ABCD* matrix for the system is obtained by multiplying all of the above matrices. The resultant matrix is then used in (9.58) to find q_2. The beam waist found outside the laser cavity is a minimum beam waist, so, at the minimum waist, $R(z) = \infty$. This means that q_2 must be completely imaginary:

$$\tilde{q}_2 = -\frac{i\lambda}{\pi w_0^2}.$$

9.8 Summary

Huygens' principle state that the wavefront of a propagating wave can be obtained by treating all of the points on a wavefront, at an earlier time, as sources of spherical waves called Huygens wavelets. Fresnel was able to describe diffraction by assuming that the new wavefront should be determined by allowing the Huygens wavelets to interfere. The result of Fresnel's theory is the Huygens–Fresnel integral

$$\tilde{E}(\mathbf{r}_0) = \frac{i}{\lambda} \iint_{\Sigma} \frac{\tilde{E}_i(\mathbf{r})}{R} e^{-i\mathbf{k}\cdot\mathbf{R}}\, dS,$$

where $E_i(\mathbf{r})$ is the wave incident on the aperture, denoted by Σ. R is the distance from a point in the aperture to the observation point located at position $\mathbf{r}_0$. The integral is an area integral taken over the aperture Σ.

In this approach to diffraction, free space is assumed to be a linear system with an impulse response given by

$$\frac{i}{\lambda} \frac{e^{-i\mathbf{k}\cdot\mathbf{R}}}{R}.$$

The Huygens–Fresnel integral is interpreted as a convolution of the impulse response with the input wave.

A second approach to diffraction is often used when the light wave's transverse amplitude distribution is Gaussian. The Gaussian wave is characterized by its width

$$w(z)^2 = w_0^2 \left[1 + \left(\frac{z}{q_0}\right)^2\right]$$

and the radius of curvature of its wavefront

$$R(z) = z\left[1 + \left(\frac{q_0}{z}\right)^2\right],$$

where

$$q_0 = \frac{\pi w_0^2}{\lambda},$$

the parameter w_0, is the minimum beam width (or waist), and z is the distance from the minimum beam waist to the observation point.

Given the beam waist w and the radius of curvature R at any point, the minimum beam waist and its location can be found by using

$$w_0^2 = \frac{w^2}{\left[1 + \left(\frac{\pi w^2}{\lambda R}\right)^2\right]},$$

$$z = \frac{R}{\left[1 + \left(\frac{\lambda R}{\pi w^2}\right)^2\right]}.$$

The *ABCD* matrix, introduced in Chapter 5, can be used to trace the behavior of a Gaussian wave as it propagates through an optical system. The Gaussian wave at any point z is characterized by a q-parameter,

$$\frac{1}{\tilde{q}(z)} = \frac{1}{R(z)} - \frac{i\lambda}{\pi w(z)^2}.$$

The q-parameter after the wave has propagated through an optical system is given by

$$\tilde{q}_2 = \frac{A\tilde{q}_1 + B}{C\tilde{q}_1 + D},$$

where A, B, C, and D are the elements of the *ABCD* matrix.

9.9 Problems

9.1. Calculate the *ABCD* matrix for a ray that has made a round trip in the Fabry–Perot resonator of Figure 5.12 ending at mirror 2. Find the radius of curvature of the Gaussian wave at this reference plane.

9.2. Find the location of the beam waist, relative to mirror 1, in the Fabry–Perot resonator of Figure 5.12.

9.3. A Fabry–Perot resonator has a spherical front mirror of radius 2ℓ and a plane back mirror. It is illuminated by a Gaussian beam with a waist w_0 at $z = 0$. The resonator's front mirror is located at $z = 3\ell$, its back mirror at $z = 4\ell$. A lens of focal length f at $z = 2\ell$ couples the Gaussian beam into the resonator. What values should f and w_0 have so that the beam will match the resonator's fundamental mode.

9.4. Complete the details of the calculation for the laser cavity design started in the chapter. You will find a second beam waist, the image of the first, outside the cavity. Can you think of any reasons the optical designer placed this waist outside the cavity?

9.5. Find the value of z at which the radius of curvature of the phase of a Gaussian wave is a minimum. What Gaussian parameter can be used to specify this position?

9.6. What is the beam waist of a HeNe laser ($\lambda = 632.8$ nm) with a beam divergence of 0.7 mrad? What is the Rayleigh range q_0?

9.7. Use the object image matrix to show that

$$q_2 = \frac{\left(1 - \frac{z_2}{f}\right) q_1 + \left(z_1 + z_2 - \frac{z_1 z_2}{f}\right)}{\left(1 - \frac{z_1}{f}\right) - \frac{q_1}{f}}, \tag{9.59}$$

where q_1 is the beam parameter in the object plane of a positive thin lens and q_2 is the beam parameter in the conjugate (image) plane. [*Hint:* Use (9.32) to follow the beam from the first waist to the lens and from the lens to the second waist. Use (9.58) to obtain the effect of the lens. Use (9.55) at each waist to relate the complex size parameter to the Gaussian parameters of radius of curvature and spot size.]

9.8. Assume the beam waist w_{01}, of a Gaussian beam is located a distance z_1 from a positive lens of focal length f. (a) Show that there will be a new beam waist w_{02}, located at a distance

$$z_2 = f + \frac{(z_1 - f) f^2}{(z_1 - f)^2 + q_0^2} \tag{9.60}$$

from the lens. (b) Also show that the beam waist will be given by

$$w_{02}^2 = \frac{f^2}{(z_1 - f)^2 + q_0^2} w_{01}^2. \tag{9.61}$$

[*Hint:* Remember that at a Gaussian beam's waist, $R = \infty$.]

9.9. Find approximate expressions for (9.60) and (9.61) when $z_1, f \ll q_0$.

9.10. We wish to focus the HeNe laser described in Problem 9.6 using a lens with a focal length of 100 mm. Using (9.60), find the beam waist and position when $z_1 \ll q_0$.

9.11. Find approximate expressions for (9.60) and (9.61) when $z_1 \gg q_0, f$.

9.12. Assume that in the object plane of Problem 9.7 there is a beam waist of w_{01} and in the image plane there is a new beam waist of w_{02}. Show that

$$\frac{z_1 - f}{z_2 - f} = \frac{w_{01}^2}{w_{02}^2}. \tag{9.62}$$

9.13. Find the beam waist for an argon laser cavity with two concave mirrors with radii of 3 and 1.5 m, separated by 1 m. Assume the operating wavelength is 488 nm. Prove that this is a stable configuration.

9.14. Calculate the Rayleigh range and the beam divergence of the laser in Problem 9.13.

9.15. We wish to couple energy from an argon laser (λ = 488 nm), with a beam waist of 350 μm, into a single-mode fiber. The mode's beam waist is 2 μm. What are the separations between the laser waist and the fiber face if as a lens we use a 10× microscope objective? *Note:* the focal length of a microscope objective is given by

$$f = \frac{160 \text{ mm}}{\text{power}}.$$

9.16. We wish to relocate the position of a beam waist but not change its size. The lens that performs this operation is called a *relay lens*. Derive a relationship for the distance between the two waist locations, $z_1 + z_2$, and the focal length of the lens. Remember that $w_{01} = w_{02}$.

9.17. We would like to move the beam waist of a HeNe laser (λ = 632.8 nm, with a beam divergence of 0.7 mrad, to a new location with a relay lens of focal length 1.65 m. How far apart are the two beam waists? How does this agree with the predictions of the thin-lens equation? What happens if we try to use a shorter-focal-length lens?

9.18. We wish to use a 1 m relay lens to move the beam waist of a dye laser to a new position. The dye laser is operating at a wavelength of 600 nm with a beam divergence of 1 mrad. How far apart are the two waists?

REFERENCES

1. Born, M. and E. Wolf, *Principles of Optics*. 7th ed. 1999: Cambridge University Press.
2. Rubinowicz, A., *The Miyamoto–Wolf diffraction wave*, in *Progress in Optics*, E. Wolf, Editor. 1965, North-Holland. p. 192–240.
3. Haus, H.A., *Waves and Fields in Optoelectronics*. 1983: Prentice Hall.
4. Yariv, A., *Optical Electronics*. 3rd ed. 1985: Holt, Rinehart, and Winston.
5. Ince, E.L., *Ordinary Differential Equations*. 1956: Dover.
6. McGloin, D. and K. Dholakia, *Bessel beams: diffraction in a new light*. Contemp. Phys., 2005. **46**: p. 15–28.

Appendix 9A Fresnel–Kirchhoff Diffraction

Kirchhoff, in 1887, developed a rigorous theory of diffraction that demonstrated that the results of Fresnel and Huygens could be obtained from the wave equation. His scalar theory was based on the elastic theory of light, but can be reformulated into a vector theory [1]. We will be using Green's theorem

$$\iint_S \left(\varphi \nabla\Psi \cdot \hat{\mathbf{n}} - \Psi \nabla\varphi \cdot \hat{\mathbf{n}}\right) dS = \iiint_V \left(\varphi \nabla^2\Psi - \Psi \nabla^2\varphi\right) dV \tag{9A.1}$$

to formally develop the Kirchhoff theory of diffraction. The surface and volume differentials in this equation are shown in Table 9A.1.

Given an incident wave φ, we wish to calculate the optical wave at point P_0 in Figure 9A.1, located at $\mathbf{r}_0$, in terms of the wave's value on a surface S that we construct

Table 9A.1 *Surface and volume differentials*

Differential	Coordinate system		
	Rectangular	Cylindrical	Spherical
dS	$dx\ dy$	$r\,d\theta\ dz$	$r^2 \sin\theta\ d\theta\ d\varphi$
dV	$dx\ dy\ dz$	$r\ dr\ d\theta\ dz$	$r^2\ sin\ \theta\ dr\ d\theta\ d\varphi$

about the observation point. To obtain a solution to the wave equation at the point P_0, we select as a Green's function a unit-amplitude spherical wave, expanding about the point at $\mathbf{r}_0$, denoted by Ψ, and then apply Green's theorem. At an observation point $\mathbf{r}_1$, the Green's function is given by

$$\Psi(\mathbf{r}_1) = \frac{e^{-i\mathbf{k}\cdot\mathbf{r}_{01}}}{r_{01}}, \tag{9A.2}$$

where

$$r_{01} = |\mathbf{r}_{01}| = |\mathbf{r}_1 - \mathbf{r}_0|$$

is the distance from the source of the Green's function, at $\mathbf{r}_0$, to the observation position, at $\mathbf{r}_1$.

Green's theorem requires that there be no sources (singularities) inside the surface S. This requirement is met by constructing a small spherical surface S_ε, of radius ε, about $\mathbf{r}_0$, excluding the singularity at $\mathbf{r}_0$ from the volume of interest, shown in gray in Figure 9A.1. The surface integration that must be performed in Green's theorem is over the surface $S' = S + S_\varepsilon$.

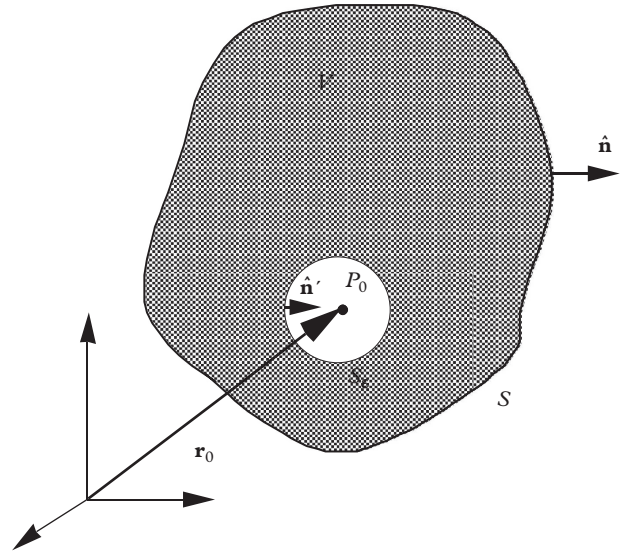

Figure 9A.1 *Region of integration for solution of the Kirchhoff diffraction integral.*

Within the volume enclosed by S', the Green's function Ψ and the incident wave φ satisfy the scalar Helmholtz equation, so the volume integral can be written as

$$\iiint_V \left(\Psi\nabla^2\varphi - \varphi\nabla^2\Psi\right) dV = -\iiint_V \left(\Psi\varphi k^2 - \varphi\Psi k^2\right) dV. \tag{9A.3}$$

The right-hand side of (9A.3) is identically equal to zero. This fact and the vector identities

$$\nabla\Psi \cdot \hat{\mathbf{n}} = \frac{\partial\Psi}{\partial n}, \quad \nabla\varphi \cdot \hat{\mathbf{n}} = \frac{\partial\varphi}{\partial n} \tag{9A.4}$$

lead to a simplified statement of Green's theorem:

$$\iint_{S'} \left(\Psi\frac{\partial\varphi}{\partial n} - \varphi\frac{\partial\Psi}{\partial n}\right) dS = 0. \tag{9A.5}$$

Because the integral over the two surfaces S and S_ε, is equal to zero, the integral over S must equal the negative of the integral over S_ε:

$$-\iint_{S_\varepsilon} \left(\Psi\frac{\partial\varphi}{\partial n} - \varphi\frac{\partial\Psi}{\partial n}\right) dS = \iint_{S} \left(\Psi\frac{\partial\varphi}{\partial n} - \varphi\frac{\partial\Psi}{\partial n}\right) dS. \tag{9A.6}$$

To perform the surface integrals, we must evaluate the Green's function on the surface S'. We therefore select $\mathbf{r}_1$, the vector defining the observation point, to be on either of the two surfaces that make up S'. The derivative $\partial\Psi/\partial n$ to be evaluated is

$$\begin{aligned}\frac{\partial\Psi}{\partial n} &= \frac{\partial\Psi}{\partial r}\frac{\partial r}{\partial n} \\ &= \left(-ik\frac{e^{-i\mathbf{k}\cdot\mathbf{r}_{01}}}{r_{01}} - \frac{e^{-i\mathbf{k}\cdot\mathbf{r}_{01}}}{r_{01}^2}\right)\cos\left(\hat{\mathbf{n}}, \mathbf{r}_{01}\right),\end{aligned} \tag{9A.7}$$

where $\cos(\hat{\mathbf{n}}, \mathbf{r}_{01})$ is the cosine of the angle between the outward normal $\hat{\mathbf{n}}$ and the vector $\mathbf{r}_{01}$, the vector between points P_0 and P_1.[3] In particular, if $\mathbf{r}_1$ were on S_ε, then

$$\cos\left(\hat{\mathbf{n}}, \mathbf{r}_{01}\right) = -1,$$

$$\Psi(\mathbf{r}_1) = \frac{e^{-ik\varepsilon}}{\varepsilon},$$

$$\frac{\partial\Psi(\mathbf{r}_1)}{\partial n} = \left(\frac{1}{\varepsilon} + ik\right)\frac{e^{-ik\varepsilon}}{\varepsilon},$$

where ε is the radius of the small sphere around the point P_0.

We now use these results to rewrite the two integrals in (9A.6). The integral over the surface S_ε is

$$\iint_{S_\varepsilon} \left(\Psi\frac{\partial\varphi}{\partial n} - \varphi\frac{\partial\Psi}{\partial n}\right) ds = \iint_{S_\varepsilon} \left[\frac{\partial\varphi}{\partial n}\frac{e^{-ik\varepsilon}}{\varepsilon} - \varphi\frac{e^{-ik\varepsilon}}{\varepsilon}\left(\frac{1}{\varepsilon} + ik\right)\right]\varepsilon^2 \sin\theta\, d\theta\, d\phi. \tag{9A.8}$$

[3] Note from Figure 9A.1 that the outward normal on S_ε is inward—toward P_0, while the normal on S is outward—away from P_0.

The integral over the surface S is

$$\iint_S \left[\frac{e^{-i\mathbf{k}\cdot\mathbf{r}_{01}}}{r_{01}} \frac{\partial \varphi}{\partial n} - \varphi \frac{\partial}{\partial n} \left(\frac{e^{-i\mathbf{k}\cdot\mathbf{r}_{01}}}{r_{01}} \right) \right] r^2 \sin\theta \, d\theta \, d\phi. \tag{9A.9}$$

The omitted volume contained within the surface S_ε is allowed to shrink to zero by taking the limit as $\varepsilon \to 0$. Equation (9A.8), but not (9A.9), will be affected by taking the limit. The first and last terms on the right-hand side of (9A.8) go to zero as $\varepsilon \to 0$ because they contain $\varepsilon e^{-ik\varepsilon}$. The second term on the right-hand side of (9A.8) contains $e^{-ik\varepsilon}$, which goes to 1 as $\varepsilon \to 0$. Therefore, in the limit as $\varepsilon \to 0$, (9A.6) becomes

$$\varphi(\mathbf{r}_0) = \frac{1}{4\pi} \iint_S \left[\frac{e^{-i\mathbf{k}\cdot\mathbf{r}_{01}}}{r_{01}} \frac{\partial \varphi}{\partial n} - \varphi \frac{\partial}{\partial n} \left(\frac{e^{-i\mathbf{k}\cdot\mathbf{r}_{01}}}{r_{01}} \right) \right] dS. \tag{9A.10}$$

which is sometimes called the *integral theorem of Kirchhoff*. We can apply this result to the problem of diffraction by an aperture in an infinite opaque screen, if the surface of integration is carefully selected.

Assume that a source at P_2 in Figure 9A.2 produces a spherical wave that is incident on an infinite, opaque screen from the left. To find the field at P_0 in Figure 9A.2, we apply (9A.10) to the surface $S_1 + S_2 + \Sigma$, where S_1 is a plane surface adjacent to the screen, Σ is that portion of S_1 in the aperture, and S_2 is a large spherical surface, of radius R, centered on P_0 (see Figure 9A.2). As R increases, Ψ and φ will decrease as $1/R$. However, the area of integration increases as R^2, so the $1/R$ fall-off is not a sufficient reason for neglecting the contribution of the integration over S_2.

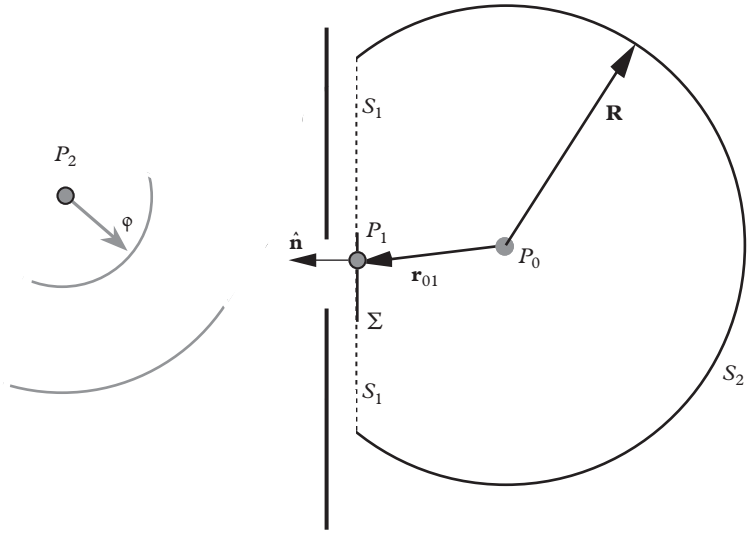

Figure 9A.2 *Integration surface for diffraction calculation. P_2 is the source and P_0 is the point at which the field is to be calculated.*

On the surface S_2, the Green's function and its derivative are

$$\Psi = \frac{e^{-ikR}}{R}, \tag{9A.11}$$

$$\frac{\partial \Psi}{\partial n} = \left(-ik - \frac{1}{R}\right) \frac{e^{-ikR}}{R} \approx -ik\Psi, \tag{9A.12}$$

where the approximate equality is for large R. Thus, the integral over S_2 for large R is

$$\iint_{S_2} \left[\Psi \frac{\partial \varphi}{\partial n} + \varphi(ik\Psi)\right] dS = \iint_{S_2} \Psi \left(\frac{\partial \varphi}{\partial n} + ik\varphi\right) R^2 \sin\theta \, d\theta \, d\phi. \tag{9A.13}$$

The quantity $R\Psi = e^{-i\mathbf{k}\cdot\mathbf{R}}$ is finite as $R \to \infty$, so, for the integral to vanish, we must have

$$\lim_{R\to\infty} R\left(\frac{\partial \varphi}{\partial n} + ik\varphi\right) = 0. \tag{9A.14}$$

This requirement is called the *Sommerfeld radiation condition* and is satisfied if $\varphi \to 0$ as fast as $1/R$ (e.g., a spherical wave). Since the illumination of the screen will be a spherical wave, or at least a linear combination of spherical waves, we should expect the integral over S_2 to make no contribution (it is exactly zero).

Another way to ensure that the surface S_2 makes no contributionis to assume that the light turns on at time t_0. At a later time t, when we desire to know the field at P_0, the radius of S_2 is $R > c(t - t_0)$, which means, physically, that the light has not had time to reach S_2. In this situation, there can be no contribution from S_2. This is not a perfect solution, because the wave can no longer be considered monochromatic.

We should expect the major contribution in the integral over S_1 to come from the portion of the surface in the aperture, Σ. We make the following assumptions about the incident wave φ (these assumptions are known as *St Venant's hypothesis* or *Kirchhoff's boundary conditions*).

1. We assume that, in the aperture, φ and $\partial\varphi/\partial n$ have the values they would have if the screen were absent.
2. On the portion of S_1 not in the aperture, φ and $\partial\varphi/\partial n$ are identically zero.

The Kirchhoff boundary conditions allow the screen to be neglected, greatly simplifying the problem and yielding very accurate results (as long as polarization is not important). However, mathematically, the assumptions are incorrect [2]. The two boundary conditions imply that the field is zero everywhere behind the screen, except in the aperture, which makes Ψ and $\partial\Psi/\partial n$ discontinuous on the boundary of the aperture. Another problem with the boundary conditions is that Ψ and $\partial\Psi/\partial n$ are known only if the problem has already been solved. We must make assumptions about the values of Ψ and $\partial\Psi/\partial n$, resulting in only approximate solutions of the diffraction problem.

Even with the problems concerning the boundary conditions, if the aperture is large with respect to a wavelength, and we do not get too close to the aperture, the theory does

work. Sommerfeld removed some of the problems created by the boundary conditions; see Appendix 9B.

As a result of the above discussion, the surface integral (9A.10 is only performed over the surface Σ in the aperture. The evaluation of the Green's function on this surface can be simplified by noting that normally $r_{01} \gg \lambda$, i.e., $k \gg 1/r_{01}$, and thus, on Σ,

$$\frac{\partial \Psi}{\partial n} = \cos\left(\hat{\mathbf{n}}, \mathbf{r}_{01}\right)\left(-ik - \frac{1}{r_{01}}\right)\frac{e^{-i\mathbf{k}\cdot\mathbf{r}_{01}}}{r_{01}}$$

$$\approx -ik\cos\left(\hat{\mathbf{n}}, \mathbf{r}_{01}\right)\frac{e^{-i\mathbf{k}\cdot\mathbf{r}_{01}}}{r_{01}}. \tag{9A.15}$$

Substituting this approximate evaluation of the derivative into (9A.8) yields

$$\varphi(\mathbf{r}_0) = \frac{1}{4\pi}\iint_{\Sigma}\frac{e^{-i\mathbf{k}\cdot\mathbf{r}_{01}}}{r_{01}}\left[\frac{\partial \varphi}{\partial n} + ik\varphi\cos\left(\hat{\mathbf{n}}, \mathbf{r}_{01}\right)\right]dS. \tag{9A.16}$$

The source of the incident wave is a point source located at P_2, with a position vector $\mathbf{r}_2$ measured with respect to the coordinate system and a distance $|\mathbf{r}_{21}|$ away from P_1, a point in the aperture (see Figure 9A.3). The incident wave is therefore a spherical wave

$$\varphi(\mathbf{r}_{21}) = A\frac{e^{-i\mathbf{k}\cdot\mathbf{r}_{21}}}{r_{21}}, \tag{9A.17}$$

which fills the aperture. Here also, we will assume that $r_{21} \gg \lambda$, so the derivative of the incident wave assumes the same form as (9A.15). Equation (9A.16) can now be written

$$\varphi(\mathbf{r}_0) = \frac{iA}{\lambda}\iint_{\Sigma}\frac{e^{-i\mathbf{k}\cdot(\mathbf{r}_{21}+\mathbf{r}_{01})}}{r_{21}r_{01}}\left[\frac{\cos\left(\hat{\mathbf{n}}, \mathbf{r}_{01}\right) - \cos\left(\hat{\mathbf{n}}, \mathbf{r}_{21}\right)}{2}\right]dS. \tag{9A.18}$$

This relationship is called the *Fresnel–Kirchhoff diffraction formula.* It is symmetric with respect to r_{01} and r_{21}, making the problem identical when the source and measurement points are interchanged.

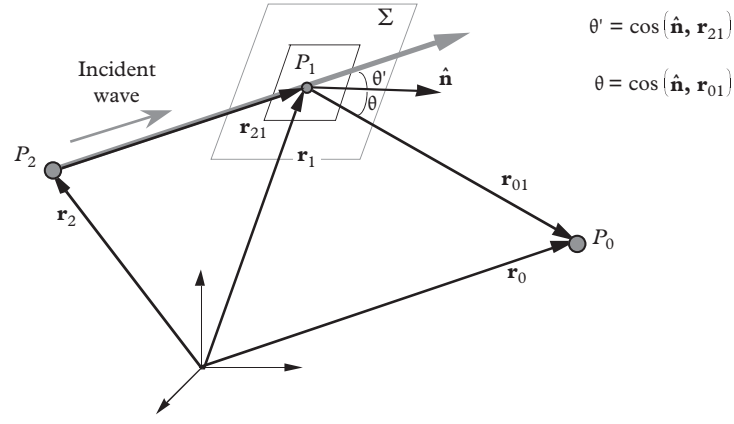

Figure 9A.3 *Geometry for the Fresnel–Kirchhoff diffraction formula.*

A physical understanding of this equation can be obtained if it is rewritten as

$$\varphi(\mathbf{r}_0) = \iint_{\Sigma} \Phi(\mathbf{r}_{21}) \frac{e^{-i\mathbf{k}\cdot\mathbf{r}_{01}}}{r_{01}} \, dS, \tag{9A.19}$$

where the integrand contains

$$\Phi(\mathbf{r}_{21}) = \frac{i}{\lambda}\left(A\frac{e^{-i\mathbf{k}\cdot\mathbf{r}_{21}}}{r_{21}}\right)\left[\frac{\cos\left(\hat{\mathbf{n}},\mathbf{r}_{01}\right) - \cos\left(\hat{\mathbf{n}},\mathbf{r}_{21}\right)}{2}\right]. \tag{9A.20}$$

The field at P_0 is due to the sum of an infinite number of secondary Huygens sources in the aperture Σ. The secondary sources are point sources radiating spherical waves of the form

$$\Phi(\mathbf{r}_{21})\frac{e^{-i\mathbf{k}\cdot\mathbf{r}_{01}}}{r_{01}},$$

with amplitude $\Phi(\mathrm{r}_{21})$ defined in (9A.20). The obliquity factor

$$\frac{1}{2}\left[\cos\left(\hat{\mathbf{n}},\mathbf{r}_{01}\right) - \cos\left(\hat{\mathbf{n}},\mathbf{r}_{21}\right)\right]$$

causes the secondary sources to have a forward-directed radiation pattern. The imaginary constant i causes the wavelets from each of these secondary sources to be phase-shifted with respect to the incident wave. This is the Gouy phase shift we mentioned in Chapter 9 and agrees with the notation used in Chapter 9 if the substitution $r_{01} = R$ is made.

REFERENCES

1. Wangsness, R.K., *Electromagnetic Fields*. 2nd ed. 1986: Wiley.
2. Sommerfeld, A., *Optics (Lectures on Theoretical Physics. Vol. 4)*. 1964: Academic Press.

Appendix 9B Rayleigh–Sommerfeld Formula

A number of problems are associated with the Kirchhoff formulation of scalar diffraction theory [1]. Sommerfeld corrected the problem associated with the boundary conditions by selecting a different Green's function for the solution of the wave equation. Here, we will introduce two possible Green's functions and show the consequence of selecting each of them.

The modification that must be made to the Kirchhoff theorem (9A.8) concerns the assumption about the Green's function Ψ. Instead of assuming that the wave Ψ is due to a single point source (9A.2), we assume that there are two point sources, one at P_0 and one at P_0' (see Figure 9B.1), with the source at P_0' positioned to be the mirror image of the source at P_0 on the opposite side of the screen; thus,

$$r_{01} = r_{01}', \quad \cos\left(\hat{\mathbf{n}},\mathbf{r}_{01}\right) = -\cos\left(\hat{\mathbf{n}},\mathbf{r}_{01}'\right).$$

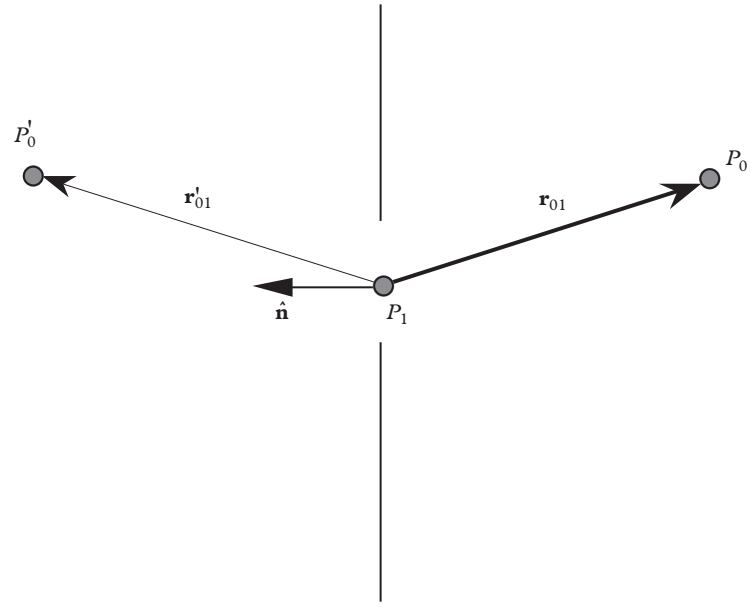

Figure 9B.1 *Geometry for the Sommerfeld derivation.*

Evaluating the new wave, denoted by Ψ', and its derivative in the aperture yields

$$\Psi' = \frac{e^{-i\mathbf{k}\cdot\mathbf{r}_{01}}}{r_{01}} - \frac{e^{-i\mathbf{k}\cdot\mathbf{r}'_{01}}}{r'_{01}}, \tag{9B.1}$$

$$\frac{\partial \Psi'}{\partial n} = \cos\left(\hat{\mathbf{n}}, \mathbf{r}_{01}\right)\left(-ik - \frac{1}{r_{01}}\right)\frac{e^{-i\mathbf{k}\cdot\mathbf{r}_{01}}}{r_{01}}$$

$$-\cos\left(\hat{\mathbf{n}}, \mathbf{r}'_{01}\right)\left(-ik - \frac{1}{r'_{01}}\right)\frac{e^{-i\mathbf{k}\cdot\mathbf{r}'_{01}}}{r'_{01}}. \tag{9B.2}$$

Because the point P_0' is the mirror image of P_0, the values of (9B.1) and (9B.2) at any point P_1 in the aperture are

$$\Psi'\big|_{P_1} = 0,$$

$$\left.\frac{\partial \Psi'}{\partial n}\right|_{P_1} = 2\cos\left(\hat{\mathbf{n}}, \mathbf{r}_{01}\right)\left(-ik - \frac{1}{r_{01}}\right)\frac{e^{-i\mathbf{k}\cdot\mathbf{r}_{01}}}{r_{01}}.$$

Another possible Green's function that could be used is

$$\Psi' = \frac{e^{-i\mathbf{k}\cdot\mathbf{r}_{01}}}{r_{01}} + \frac{e^{-i\mathbf{k}\cdot\mathbf{r}'_{01}}}{r'_{01}}. \tag{9B.3}$$

With this Green's function, we have, in the aperture,

$$\left.\frac{\partial \Psi'}{\partial n}\right|_{P_1} = 0.$$

If we replace the simple point source wave function that was used for a Green's function in Appendix 9A with either (9B.1) or (9B.3), i.e., a double point source, we obtain the *Sommerfeld integral*

$$\varphi(\mathbf{r}_0) = \frac{i}{\lambda} \iint_{\Sigma} \varphi(\mathbf{r}_1) \frac{e^{-i\mathbf{k}\cdot\mathbf{r}_{01}}}{r_{01}} \cos\left(\hat{\mathbf{n}}, \mathbf{r}_{01}\right) dS, \tag{9B.4}$$

where the assumption has been made that $r_{01} \gg \lambda$. The only difference between the Sommerfeld integral (9B.4) and (9A.18) is in the obliquity factor.

Kirchhoff's boundary conditions are now applied to either φ for (9B.1) or $\partial\varphi/\partial n$ for (9B.3). Since we no longer need to specify boundary conditions for both φ and $\partial\varphi/\partial n$, the inconsistencies of the Kirchhoff theory are removed. The assumption that the value of φ in the aperture is the same as would be obtained in the absences of the screen is still a questionable assumption, however.

REFERENCE

1. Sommerfeld, A., *Optics (Lectures on Theoretical Physics. Vol. 4)*. 1964: Academic Press.

10 Fraunhofer Diffraction

10.1 Introduction 384
10.2 Fraunhofer Diffraction 385
10.3 Fourier Transforms via a Lens 388
10.4 Plane Wave Representation 391
10.5 Diffraction by a Rectangular Aperture 392
10.6 Diffraction by a Circular Aperture 394
10.7 Array Theorem 398
10.8 *N* Rectangular Slits 401
10.9 Summary 411
10.10 Problems 413
References 416
Appendix 10A: Abbe Theory and Optical Processing 417
Appendix 10B: Imaging 442

10.1 Introduction

The job of calculating diffraction has only begun with the derivation of the Huygens–Fresnel integral (9.20). We outlined in Chapter 9 the approach to generate a one-dimensional approximate solution by treating the variation of the phase across the aperture as if it were linear. Physically, this means that all waves in the aperture are assumed to be plane waves. The diffraction predicted by the theory based on this assumption is called *Fraunhofer diffraction* and is the subject of this chapter.

Since diffraction and interference are actually the same physical process, we expect the observation of diffraction to be a strong function of the coherence of the illumination. With incoherent sources, geometrical optics is usually all that is needed to predict the performance of an optical system, and diffraction can be ignored. With light sources having a large degree of spatial coherence, it is impossible to neglect diffraction in any analysis. Even though diffraction produced by most common light sources and objects is a small effect, it is possible to observe diffraction without special equipment. By viewing a light source through a slit formed by two fingers that are nearly touching, fringes can be observed.

Fraunhofer diffraction is used by photographers and television cameramen to provide artistic highlights in an image containing small light sources. They accomplish this by placing a screen in front of the camera lens. Light from point sources in the field of view is diffracted by the screen and produces "stars" in the image. The stars are the Fraunhofer diffraction patterns of the screen, produced by each point source. By observing mercury or sodium streetlight, a few hundred meters away, through a sheer curtain, a Fraunhofer diffraction pattern of the fabric weave can easily be observed.

Joseph von Fraunhofer (1787–1826) developed, in 1823, the theory to be discussed in this chapter. (It is interesting that Fraunhofer started out as a lens grinder and before he died at the age of 39 had become an owner of an optical company and a professor at the University of Munich.) The approach to Fraunhofer diffraction to be taken here is based on a novel interpretation given to the theory, in 1873, by **Ernst Abbe (1840–1905)**. In not too clear a fashion, Abbe described Fraunhofer diffraction as a decomposition of a spatial distribution of light into a series of plane waves. Abbe's objective was the explanation of resolution in high-power microscopes. His theory described image resolution in terms of the spatial frequencies contained in the plane wave decomposition. The first application based upon Abbe's interpretation of Fraunhofer diffraction was the phase contrast microscope invented by **Frits Zernike** in 1935.

The view of the Fraunhofer theory to be taken in this chapter is a modern extension of Abbe's theory, based upon linear system theory. Linear system theory uses an impulse response function (called the Green's function in mathematics and the point spread function in optics), convolved with an input function, to generate the output function of the linear system. The initial stimulus for the use of linear system theory in optics began with the publication of a book, in French, by **P. M. Duffieux** [1]. Several books in English have been written to introduce this approach to optics [2, 3].

Modern Optics. Second Edition. B. D. Guenther.

© B. D. Guenther 2015. Published in 2015 by Oxford University Press.

By applying the approximation discussed in Chapter 9 to the Huygens–Fresnel integral, the fundamental equation of Fraunhofer diffraction will be derived. We will discover that the integral used to calculate Fraunhofer diffraction is mathematically identical to the Fourier transform integral. Because we have already developed the tools needed to evaluate Fourier transforms, we will find it quite easy to obtain Fraunhofer diffraction from rectangular and circular apertures. We will derive a theorem from Fourier transform theory, called the array theorem, that will allow the diffraction associated with Young's two-slit experiment to be calculated. The array theorem will also allow the analysis of an important optical component, the diffraction grating.

We will demonstrate, using an intuitive argument, that a lens generates a Fraunhofer diffraction pattern in its back focal plane. The Fourier transform relationship between the amplitude distribution function in the front focal plane of a lens and the Fraunhofer diffraction pattern in the back focal plane is the basis of Abbe's theory of a microscope. In Appendix 10A, we view a lens as an analog computer that calculates the Fourier transform and allows us to understand the phase contrast microscope, aperture apodization, and optical pattern recognition.

The theory of coherent and incoherent imaging systems will be discussed in Appendix 10B, where resolution limits of imaging systems will be established. A unique noise that limits the resolving capability of coherent optical systems will be introduced.

10.2 Fraunhofer Diffraction

In this section, we will derive the equation describing Fraunhofer diffraction. We will assume the source of light is at infinity, $z_1 = \infty$ in Figure 9.11, so that the aperture Σ is illuminated by a plane wave, traveling parallel to the z-axis. We then derive an approximate expression, analogous to (9.21), for the position vector $\mathbf{R}$ in Figure 10.1. We obtain an approximate expression for the position vector of the observation point P_0 relative to the aperture, by assuming the aperture size to be small compared with the distance to the observation point. Using this approximate expression, and the paraxial approximation, we are able to formulate the Huygens–Fresnel integral as a two-dimensional Fourier transform.

In Fraunhofer diffraction, we require that the source of light and the observation point P_0 be far from the aperture so that the incident and diffracted waves can be approximated by

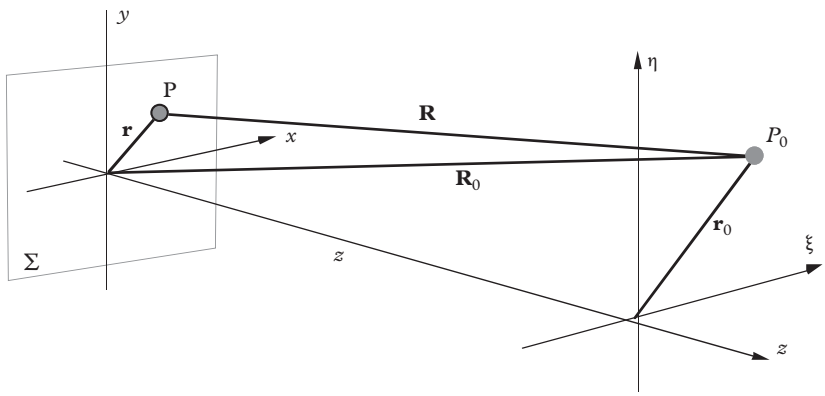

Figure 10.1 *Geometry for Fraunhofer diffraction.*

plane waves. A consequence of this requirement is that the entire waveform passing through the aperture contributes to the observed diffraction. We will see in Chapter 11 that, for Fresnel diffraction, this is not the case.

The geometry to be used in this derivation is shown in Figure 10.1. The wave incident on the aperture Σ is a plane wave of amplitude α, and the objective of the calculation is to find the departure of the transmitted wave from its geometrical optics path. The calculation will provide the light distribution transmitted by the aperture as a function of the angle the light is deflected from the incident direction. We assume that diffraction makes only a small perturbation on the predictions of geometrical optics. The deflection angles encountered in this derivation are therefore small and we will be able to use the paraxial approximation.

The distance from a point P in the aperture to the observation point P_0 (Figure 10.1) is

$$R^2 = (x - \xi)^2 + (y - \eta)^2 + Z^2. \tag{10.1}$$

From Figure 10.1, we see R_0 is the distance from the center of the screen to the observation point P_0:

$$R_0^2 = \xi^2 + \eta^2 + Z^2. \tag{10.2}$$

The difference between these two vectors is

$$\begin{aligned} R_0^2 - R^2 &= \xi^2 + \eta^2 + Z^2 - Z^2 - \left(x^2 - 2x\xi + \xi^2\right) - \left(y^2 - 2y\eta + \eta^2\right) \\ &= 2\,(x\xi + y\eta) - \left(x^2 + y^2\right). \end{aligned} \tag{10.3}$$

We can rewrite the difference between the two vectors as

$$R_0^2 - R^2 = (R_0 - R)(R_0 + R). \tag{10.4}$$

Using (10.3), we can write an equation for the position of point P in the aperture in terms of (10.4):

$$\begin{aligned} r = R_0 - R &= \frac{R_0^2 - R^2}{R_0 + R} \\ &= \left[2\,(x\xi + y\eta) - \left(x^2 + y^2\right)\right] \frac{1}{R_0 + R}. \end{aligned}$$

The reciprocal of $R_0 + R$ can be written as

$$\begin{aligned} \frac{1}{R_0 + R} &= \frac{1}{2R_0 + R - R_0} \\ &= \frac{1}{2R_0} \left(1 + \frac{R - R_0}{2R_0}\right)^{-1}. \end{aligned} \tag{10.5}$$

Now using (10.5),

$$R_0 - R = \left(\frac{x\xi + y\eta}{R_0} - \frac{x^2 + y^2}{2R_0}\right) \left(1 - \frac{R_0 - R}{2R_0}\right)^{-1}.$$

If the diffraction integral is to have a finite (nonzero) value, then

$$k\,|R_0 - R| \ll kR_0.$$

This requirement ensures that all the Huygens' wavelets produced over the half of the aperture from the center out to the position r will have similar phases and will interfere to produce a nonzero amplitude at P_0. The requirement that the phase changes be small can be written as

$$\frac{1}{1-\dfrac{R_0-R}{2R_0}}=\frac{1}{1-\dfrac{r}{2R_0}}\approx 1.$$

The approximation is equivalent to assuming that the aperture is small.

By making the approximation on (9.20), we obtain the diffraction integral

$$\tilde{E}_P=\frac{i\alpha e^{-i\mathbf{k}\cdot\mathbf{R}_0}}{\lambda R_0}\iint_{\Sigma} f(x,y)\exp\left[+ik\left(\frac{x\xi+y\eta}{R_0}-\frac{x^2+y^2}{2R_0}\right)\right]dx\,dy. \tag{10.6}$$

The change in the amplitude of the wave due to the change in R, as we move away from the z-axis, is neglected, allowing R in the denominator of the Huygens–Fresnel integral to be replaced by R_0 and moved outside of the integral. We have introduced a complex transmission function $f(x, y)$, to allow a very general aperture to be treated. If the aperture function described the variation in absorption of the aperture as a function of position, as would be produced by a photographic negative, then $f(x, y)$ would be a real function. If the aperture function described the variation in transmission of a biological sample, it might be entirely imaginary.

The argument of the exponent in (10.6) is

$$ik\left(\frac{x\xi+y\eta}{R_0}-\frac{x^2+y^2}{2R_0}\right)=i2\pi\left(\frac{x\xi+y\eta}{\lambda R_0}-\frac{x^2+y^2}{2\lambda R_0}\right). \tag{10.7}$$

If the observation point P_0 is far from the screen, we can neglect the second term and treat the phase variation across the aperture as a linear function of position. This is equivalent to assuming that the diffracted wave is a collection of plane waves. Mathematically, the second term in (10.7) can be neglected if

$$\frac{x^2+y^2}{2\lambda R_0}\ll 2\pi. \tag{10.8}$$

This is called the *far-field approximation*.

The first term in (10.7) contains the direction cosines

$$L=\frac{\xi}{R_0},\quad M=\frac{\eta}{R_0}. \tag{10.9}$$

These cosines can remain finite even in the far field. As the unit of measure at the aperture screen, we use the illuminating wavelength, which allows the aperture coordinates to be defined as

$$X=\frac{x}{\lambda},\quad Y=\frac{y}{\lambda}. \tag{10.10}$$

We can rewrite (10.6) by using the approximation allowed by (10.8) and the definitions (10.9) and (10.10):

$$\tilde{E}_P(L,M)=\frac{i\alpha e^{-i\mathbf{k}\cdot\mathbf{R}_0}}{\lambda R_0}\iint_{\Sigma} f(X,Y)e^{+i2\pi(LX+MY)}\,dX\,dY. \tag{10.11}$$

In this form, the integral may not be recognizable, but, by defining two spatial frequencies, we can obtain a familiar form. The spatial frequencies in the x- and y-directions are defined as

$$\omega_x = kL = -\frac{2\pi\xi}{\lambda R_0}, \quad \omega_y = kM = -\frac{2\pi\eta}{\lambda R_0}. \tag{10.12}$$

We define the spatial frequencies with a negative sign to allow equations involving spatial frequencies to have the same form as those involving temporal frequencies. The negative sign is required because ωt and $\mathbf{k}\cdot\mathbf{r}$ appear in the phase of the wave with opposite signs. Rather than use a negative spatial frequency, we could have redefined the Fourier transform using a positive exponential for spatial transforms.

We equate the spatial frequencies to coordinate positions in the observation plane by applying the paraxial approximation; this makes the mapping from the aperture to the observation plane easy to interpret. With the variables defined in (10.12), the integral becomes

$$\tilde{E}_P(\omega_x, \omega_y) = \frac{i\alpha e^{-i\mathbf{k}\cdot\mathbf{R}_0}}{\lambda R_0} \iint_\Sigma f(x,y) e^{-i(\omega_x x + \omega_y y)}\, dx\, dy. \tag{10.13}$$

The Fraunhofer diffraction field $\tilde{E}_P$ is equal to the two-dimensional Fourier transform of the aperture's transmission function.

To summarize, by assuming that the illumination is a plane wave and that the observation position is in the "far field," the diffraction of an aperture is found to be given by the Fourier transform of the function describing the amplitude transmission of the aperture. The resulting Fraunhofer diffraction spectrum has an angular distribution $\tilde{E}_P(L, M)$ that is equal to the spatial frequency spectrum of the diffracting screen. The amplitude transmission of the aperture, $f(x, y)$, may thus be interpreted as the superposition of mutually coherent plane waves leaving the diffracting screen in directions given by (L, M).

10.3 Fourier Transforms via a Lens

A numerical estimate of the far-field distance can be obtained by first restating (10.8) in one dimension:

$$\frac{x^2}{4\pi\lambda} \ll R_0.$$

For an illumination wavelength of $\lambda = 6 \times 10^{-7}$ m and an aperture width of 2.5 cm, the location of the far-field observation point must exceed $R_0 \gg 1600$ m. This demonstrates why this requirement is called the far-field condition. It is not necessary to go to such distances to observe Fraunhofer diffraction, as we will show in this section.

If we place a point source in the focal plane of a positive lens, the image of the point source occurs at infinity. The inverse is also true—the image of a source at infinity is found in

the focal plane of the lens. Because the focal plane and a plane at infinity are conjugate planes, it seems plausible that a lens would form an image of the far-field diffraction pattern in its focal plane. To support our supposition that the lens would create the Fraunhofer diffraction pattern in its focal plane, we will examine how a lens transforms a plane wave. We will demonstrate that the transformation is equivalent to a Fourier transform.

It is possible to demonstrate that the angle of arrival of a plane wave is mapped onto a unique spatial position in the back focal plane of a lens. This demonstration can be accomplished by the use of geometrical optics. We will be able to show that a lens with an off-axis point source in its front focal plane will produce a plane wave traveling at an angle to the optical axis of the lens.

In Appendix 5A, we defined the back and front focal planes [(5A.6) and Figure 5A.2] as the image planes of objects at infinity. This means that a lens will produce a plane wave if a source is located in one of the focal planes. The *ABCD* matrix can be used to demonstrate this fact. We use Figure 5A.4 to create the *ABCD* matrix for a light ray propagating from the front to the back focal plane of a simple lens:

$$\begin{bmatrix} x' \\ \gamma' \end{bmatrix} = \begin{bmatrix} 1 & f \\ 0 & 1 \end{bmatrix} \begin{bmatrix} 1 & 0 \\ -\frac{1}{f} & 0 \end{bmatrix} \begin{bmatrix} 1 & f \\ 0 & 1 \end{bmatrix} \begin{bmatrix} x_0 \\ \gamma \end{bmatrix}$$

$$= \begin{bmatrix} 0 & f \\ -\frac{1}{f} & 0 \end{bmatrix} \begin{bmatrix} x_0 \\ \gamma \end{bmatrix},$$

From this, we discover that

$$\gamma' = -\frac{x_0}{f}.$$

Thus, a source located in the front focal plane of the lens at a position x_0 above the optical axis will generate a plane wave, which makes an angle $\gamma' = -x_0/f$ with the optical axis, in the back focal plane. In Figure 10.2, we show that the plane wave will be traveling downward at an angle γ', as predicted by the negative sign.

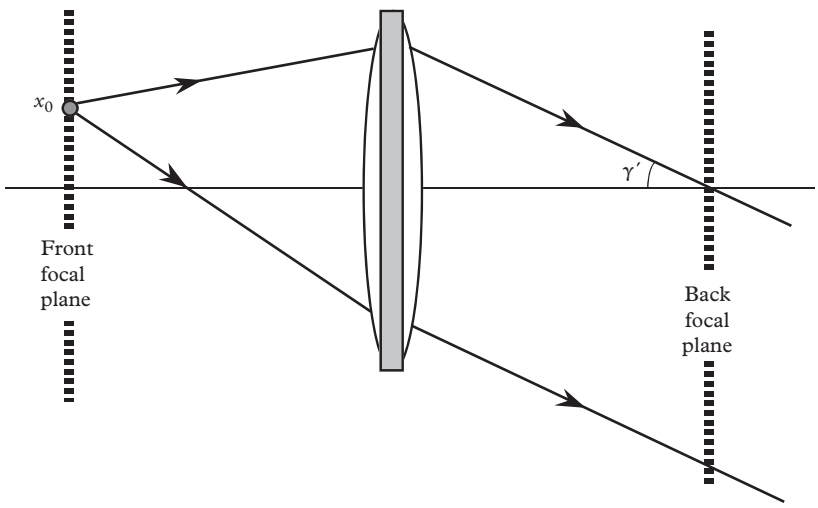

Figure 10.2 *Connection between the direction of a plane wave and the position of a spot in the focal plane.*

The result for a single point source, shown in Figure 10.2, agrees with the Fourier transform calculated in Chapter 6, (6.24), for a single delta function. The Fourier transform of a delta function located at the origin, $\delta(x)$, is a constant. In the optical analog, the delta function represents a point source located on the optical axis. The resulting Fourier transform, produced by the lens, corresponds to a plane wave propagating parallel to the optical axis. When the delta function is moved off-axis, the shifting property of a Fourier transform, (6A.5), can be applied to yield a constant with a varying phase $e^{-i\omega_x x}$. The shifted delta function $\delta(x - x_0)$ corresponds to the point source located off-axis, at position x_0, in Figure 10.2, and the constant with a linearly varying phase corresponds to the plane wave propagating at an angle $\gamma' = \omega_x$ to the optical axis.

If a lens is added to Young's two-slit experiment to collect the light from the two slits, then the light distribution in the back focal plane of the lens is the Fourier transform of the light distribution at the front focal plane.

Suppose that two slits are placed in the front focal plane of a lens. A wave illuminating the slits is polarized along the y-axis and propagating in the (x, z) plane. The light from the two slits that overlaps in the back focal plane will produce interference. The light distribution should be given by (4.12), with the phase angle δ being given by (4.16). To see that this is the case, consider that the two slits will act, in one dimension, as two point sources. The lens transforms light from the two slits into two plane waves propagating at angles γ_1 and γ_2, with respect to the z-axis. We can write the phase difference between the two plane waves as

$$g_2 - h_2 = kz(\cos\gamma_1 - \cos\gamma_2) + kx(\sin\gamma_1 - \sin\gamma_2).$$

From Figure 4.9, we have

$$\gamma_1 = \frac{h}{2f}, \quad \gamma_2 = -\frac{h}{2f},$$

so that

$$g_2 - h_2 = 2kx\sin\left(\frac{h}{2f}\right) \approx \frac{kxh}{f}, \tag{10.14}$$

which agrees with (4.16) if we replace the distance D between the slit and observation plane by the focal plane of the lens. The conclusion we can draw from this analysis is that the intensity distribution in the back focal plane of the lens, with two equally spaced slits in the front focal plane, is proportional to

$$\cos^2\left(\frac{kxh}{2f}\right).$$

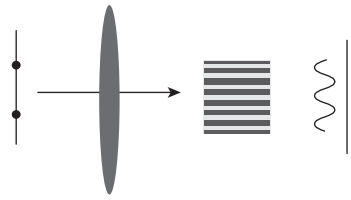

Figure 10.3 *Fourier transform of two point sources.*

The two slits can be viewed as an experimental representation of two delta functions, see Figure 10.3:

$$\delta\left(x - \frac{h}{2}\right) \quad \text{and} \quad \delta\left(x + \frac{h}{2}\right).$$

In Chapter 6, the Fourier transform of N delta functions was calculated, (6.28), and was shown to equal a cosine function for $N = 2$. For the two slits, the experimental observation is equivalent to the formal mathematical treatment. We have again demonstrated that a Fourier transform relationship exists between the amplitude distribution in the front focal plane of the lens and the amplitude distribution in the back focal plane. It seems reasonable to extend

the results for two point sources to N sources. A larger leap in reasoning is needed to extend this result to a continuous distribution, but it seems to be a reasonable extension.

We therefore conclude that a lens will generate, in its back focal plane, the Fraunhofer diffraction pattern (or, equivalently, the Fourier transform) of the amplitude distribution in its front focal plane.

It should be noted that a second lens will take the positive mapping of spatial frequency onto coordinate position in the focal plane and convert it into negative-going plane waves. Therefore, two lenses perform two Fourier transforms, yielding the original function. The recovered function, however, is displayed in a coordinate system that is the negative of the original coordinate system; i.e., x $\Rightarrow -x$ and y $\Rightarrow -y$.

10.4 Plane Wave Representation

We have demonstrated that the Fraunhofer diffraction pattern of an aperture is calculated by performing a spatial Fourier transform of the aperture's amplitude transmission function. We proved that the point at x_0, in the front focal plane of the lens in Figure 10.2, produces a plane wave propagating at an angle γ' to the optical axis. We extended this concept to two sources and can expand it to a large number of points allowing us to conclude that the Fraunhofer diffraction pattern is equal to the interference pattern produced by a collection of plane waves.

Because of the reciprocal relationship between a function and its Fourier transform, we should be able to treat the plane waves that form the diffraction pattern as a unique representation of the aperture. This view is equivalent to the one taken of a temporal wave packet as a frequency distribution of sine and cosine functions (Figures 10.6, 10.7, and 10.8).

We can define an aperture as a collection of plane waves, distributed over a group of propagating directions. In this section, we will demonstrate that this representation is possible by showing that the spatial distribution of a wave is obtained by integrating over a distribution of plane waves. The integral will have the form of the inverse Fourier transform.

We saw in our discussion of Fourier transforms, Figures 10.6 and 10.7, that a wave of finite temporal duration cannot be represented by a single frequency but instead required a distribution of frequencies. We now conclude that a beam of light, with a finite width, cannot be represented by a single plane wave but instead will need a distribution of plane waves. Consider a nearly plane wave traveling in the x,z plane with $\mathbf{k} \cdot \mathbf{r} = k_x x + k_z z$. The wave propagating with a wave vector between

$$k_x - \frac{dk_x}{2} < k_x < k_x + \frac{dk_x}{2}$$

is

$$d\tilde{E} = A(k_x) e^{j(\omega t - \mathbf{k}\cdot\mathbf{r})}\, dk_x. \tag{10.15}$$

The amplitude A is allowed to be a function of k_x that is zero beyond some limit.

The resultant wave (using the principle of superposition and treating the plane waves as coherent waves) is given by the integral of (10.15). The mean direction of the resultant

wave is along the z-direction, but it is spread over angles corresponding to a range of wave vectors defined by the inequality

$$-\Delta \leq k_x \leq \Delta.$$

We will consider the wave evaluated at $t = 0$ to remove all temporal dependence of the wave:

$$\tilde{E}(x) = \int_{-\Delta}^{\Delta} A(k_x) e^{-ik_x x}\, dk_x. \tag{10.16}$$

Since $A(k_x) = 0$ for values of k_x outside the range $\pm\Delta$, we can extend the limits to $\pm\infty$. If we multiply the integral by $1/2\pi$ we have the inverse Fourier transform (6.14), with x corresponding to t and $-k_x$ to ω. We have demonstrated that a distribution of plane waves yields a resultant wave, with a bounded spatial extent, given by the inverse Fourier transform (10.16). The result supports the premise that an aperture can be described in terms of a distribution of plane waves.

10.5 Diffraction by a Rectangular Aperture

We will now use Fourier transform theory to calculate the Fraunhofer diffraction pattern from a rectangular slit and will point out the reciprocal relationship between the size of the diffraction pattern and the size of the aperture.

Consider a rectangular aperture with a transmission function given by

$$f(x,y) = \begin{cases} 1, & |x| \leq x_0, \quad |y| \leq y_0, \\ 0, & \text{all other } x \text{ and } y. \end{cases}$$

Because the aperture is two-dimensional, we need to apply a two-dimensional Fourier transform (6.41). The amplitude transmission function is separable, in x and y, so we may use (6.41) and write the diffraction amplitude distribution from a rectangular slit illuminated by a plane wave of amplitude α as

$$\tilde{E}_P = \frac{i\alpha}{\lambda R_0} e^{-i\mathbf{k}\cdot\mathbf{R}_0} \int_{-x_0}^{x_0} f(x) e^{-i\omega_x x}\, dx \int_{-y_0}^{y_0} f(y) e^{-i\omega_y y}\, dy. \tag{10.17}$$

Since both $f(x)$ and $f(y)$ are defined as symmetric functions, we need only calculate the cosine transforms (6.15a):

$$\tilde{E}_P = i\, \frac{4x_0 y_0 \alpha}{\lambda R_0} e^{-i\mathbf{k}\cdot\mathbf{R}_0} \frac{\sin \omega_x x_0}{\omega_x x_0} \frac{\sin \omega_y y_0}{\omega_y y_0}. \tag{10.18}$$

The intensity distribution of the Fraunhofer diffraction produced by the rectangular aperture is

$$I_P = I_0 \frac{\sin^2 \omega_x x_0}{(\omega_x x_0)^2} \frac{\sin^2 \omega_y y_0}{(\omega_y y_0)^2}, \tag{10.19}$$

where the spatial frequencies are defined as

$$\omega_x = -\frac{2\pi \sin\theta_x}{\lambda} = -\frac{2\pi\xi}{\lambda R_0},$$

$$\omega_y = -\frac{2\pi \sin\theta_y}{\lambda} = -\frac{2\pi\eta}{\lambda R_0}.$$

The maximum intensities in the x- and y-directions occur at

$$\omega_x x_0 = \omega_y y_0 = 0.$$

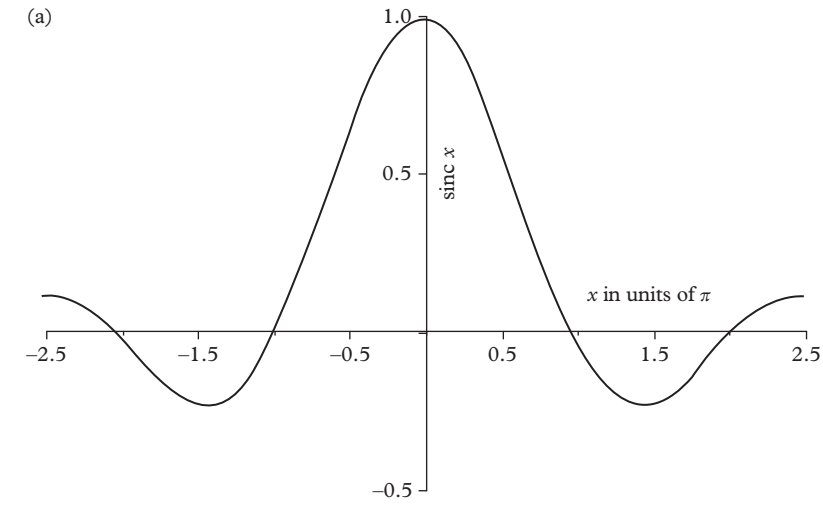

(b)

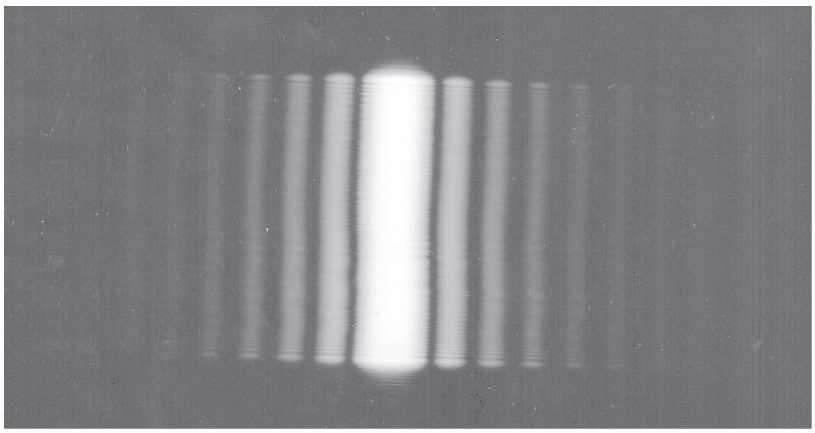

Figure 10.4 *(a) Calculation of diffraction from a rectangular slit. This sinc function describes the light wave's amplitude that would exist in both the x- and y-directions. (b) Experimentally generated Fraunhofer diffraction pattern from a rectangular aperture. You can see fringes near the top and bottom because the slit is not infinite in one dimension.*

Remembering that the area of this rectangular aperture is defined as $A = 4x_0y_0$, we may write the maximum intensity as

$$I_0 = \left(\frac{i4x_0y_0\alpha e^{-i\mathbf{k}\cdot\mathbf{R}_0}}{\lambda R_0} \right)^2 = \frac{A^2\alpha^2}{\lambda^2 R_0^2}.$$

The minima of this function occur when $\omega_x x_0 = n\pi$ or when $\omega_y y_0 = m\pi$. The location of the zeroes can be specified as a dimension in the observation plane or, using the paraxial approximation, in terms of an angle:

$$\sin\theta_x \approx \theta_x \approx \frac{\xi}{R_0} = \frac{n\lambda}{2x_0},$$

$$\sin\theta_y \approx \theta_y \approx \frac{\eta}{R_0} = \frac{m\lambda}{2y_0}.$$

The dimensions of the diffraction pattern are characterized by the location of the first zero, i.e., when $n = m = 1$, and are given by the observation plane coordinates ξ and η. The dimensions of the diffraction pattern are inversely proportional to the dimensions of the aperture. As the aperture dimension expands, the width of the diffraction pattern decreases until, in the limit of an infinitely wide aperture, the diffraction pattern becomes a delta function.

If a lens is used to display the diffraction pattern, then R_0 is replaced by the focal length of the lens, f, in all of the equations. If the aperture of the lens is very large, we can consider a plane wave incident upon it as infinitely wide. For this plane wave, the lens would produce a focal spot in its back focal plane that approximated a delta function—the diffraction pattern of an infinite plane wave.

Figure 10.4(a) is a theoretical plot of the diffraction pattern from a rectangular slit. Figure 10.4(b) is an experimentally obtained Fraunhofer diffraction pattern.

10.6 Diffraction by a Circular Aperture

From the discussion of two-dimensional transforms in Chapter 6, we can immediately obtain the diffraction pattern from a circular aperture of diameter a by using the transform (6.44). A second procedure will be used here to obtain the diffraction pattern. The cylindrical geometry shown in Figure 10.5 is used to convert the Huygens–Fresnel integral from rectangular to cylindrical coordinates. To transform to the new coordinate system, we make use of the following equations: at the aperture plane,

$$x = s\cos\varphi, \qquad y = s\sin\varphi,$$

$$f(x,y) = f(s,\varphi), \quad dx\,dy = s\,ds\,d\varphi; \tag{10.20}$$

at the observation plane,

$$\xi = \rho\cos\theta, \quad \eta = \rho\sin\theta. \tag{10.21}$$

In the new, cylindrical, coordinate system at the observation plane, the spatial frequencies are written as

$$\omega_x = -\frac{k\xi}{R_0} = -\frac{k\rho}{R_0}\cos\theta,$$

$$\omega_y = -\frac{k\eta}{R_0} = -\frac{k\rho}{R_0}\sin\theta. \tag{10.22}$$

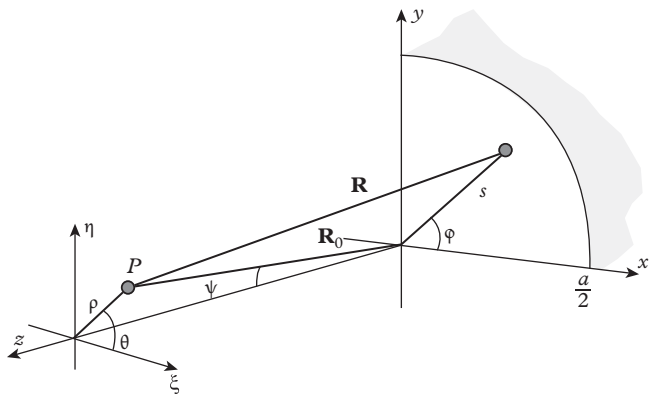

Figure 10.5 *Geometry for diffraction from a circular aperture.*

From Figure 10.5, we see that the observation point P can be defined in terms of the angle ψ, where

$$\sin\psi = \frac{\rho}{R_0}.$$

This allows an angular representation for the size of the diffraction pattern if it is desired.

Using (10.20) and (10.22), we may write

$$\begin{aligned}\omega_x x + \omega_y y &= -\frac{ks\rho}{R_0}(\cos\theta\cos\varphi + \sin\theta\sin\varphi)\\ &= -\frac{ks\rho}{R_0}\cos(\theta-\varphi).\end{aligned} \tag{10.23}$$

The Huygens–Fresnel integral can now be written in terms of cylindrical coordinates as

$$\tilde{E}_P = \frac{i\alpha}{\lambda R_0}e^{-i\mathbf{k}\cdot\mathbf{R}_0}\int_0^{a/2}\int_0^{2\pi} f(s,\varphi)\exp\left[-ik\frac{s\rho}{R_0}\cos(\theta-\varphi)\right]s\,ds\,d\varphi. \tag{10.24}$$

We can demonstrate the use of (10.24) by using it to calculate the diffraction amplitude from a clear aperture of diameter a, defined by the equation

$$f(s,\varphi) = \begin{cases} 1, & s \le \frac{1}{2}a, \text{ all } \varphi,\\ 0, & s > \frac{1}{2}a.\end{cases}$$

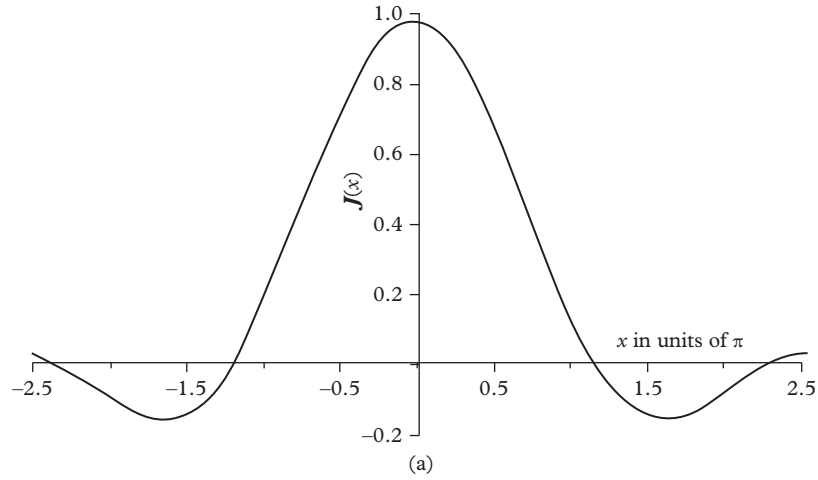

(a)

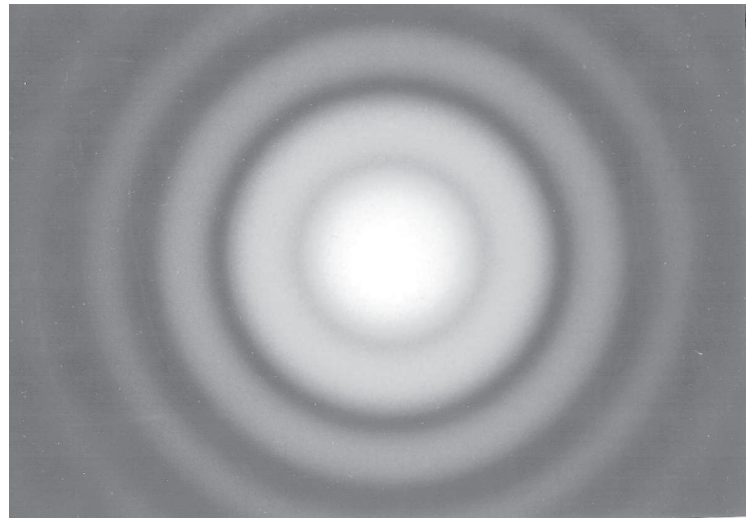

(b)

Figure 10.6 *(a) Diffraction amplitude from a circular aperture. The observed light distribution is constructed by rotating this Bessel function around the optical axis. (b) Experimentally obtained Fraunhofer diffraction pattern from a circular aperture.*

The symmetry of this problem is such that $f(s, \varphi) = f(s)$, which makes (10.24) identical to (6.44). We may therefore use (6.45) to write the diffraction pattern amplitude

$$\tilde{E}_P = \frac{i\alpha}{\lambda} e^{-i\mathbf{k}\cdot\mathbf{R}_0} \left[\frac{\pi a}{k\rho} J_1\left(\frac{ka\rho}{2R_0}\right) \right]. \tag{10.25}$$

A plot of the function in the square brackets is given in Figure 10.6(a).

If we define

$$u = \frac{ka\rho}{2R_0},$$

then the spatial distribution of intensity in the diffraction pattern can be written in a form known as the *Airy formula*, named after the British astronomer **George Biddell Airy (1801–1892)**:

$$I = I_0 \left[\frac{2J_1(u)}{u} \right]^2, \tag{10.26}$$

where we have defined

$$I_0 = \left(\frac{\alpha A}{\lambda R_0} \right)^2,$$

and $A = \pi (a/2)^2$ is the area of the aperture. The intensity pattern described by (10.26) and shown in Figure 10.6(b) is called the Airy pattern. The intensity at $u = 0$ in (10.26) is the same as was obtained for a rectangular aperture of the same area, (10.19), because, in the limit,

$$\lim_{u \to 0} \left[\frac{2J_1(u)}{u} \right] = 1.$$

At first glance, Figures 10.4(a) and 10.6(a) seem to have the same functional form, but a close examination of the locations of the zeroes of the two functions reveals the difference. Figure 10.7 displays the two functions on the same graph. The first few zeroes of the sinc function occur at $\pi, 2\pi, 3\pi, 4\pi, \ldots$ and the first few zeroes of the Airy function are $1.22\pi, 2.233\pi, 3.238\pi, \ldots$.

The location of the first zero is used to characterize the size of the diffraction pattern. The circular area defined by the first zero of (10.26) is called the *Airy disk*. The Airy disk, formed by a lens of diameter a uniformly illuminated by a plane wave, is obtained by solving

$$u = \frac{ka\rho}{2f} = \frac{\pi\, a\rho}{\lambda f} = 1.22\pi$$

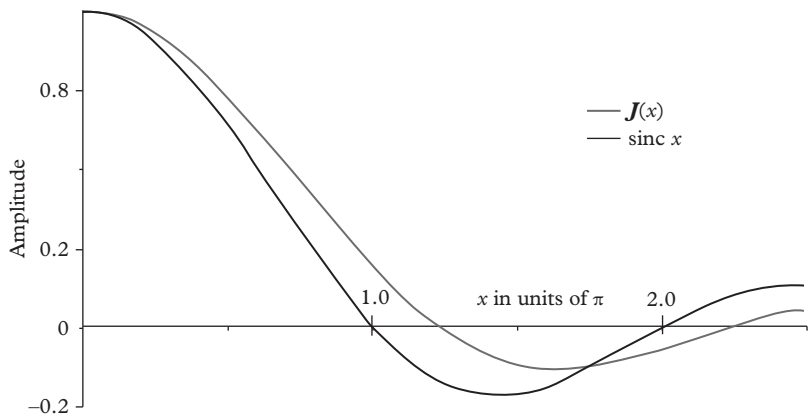

Figure 10.7 *Comparison of the amplitude distributions of the diffraction patterns for rectangular and circular apertures.*

for ρ. The diameter of the Airy disk, 2ρ, which we will denote by w, is given by

$$2\rho = w = \frac{2.44\lambda f}{a}.$$

This is in agreement with the result from Chapter 9, obtained by using the Gaussian wave formalism of diffraction. In Chapter 9, we found that the minimum beam waist produced, in the back focal plane of a lens uniformly illuminated by a plane wave, is

$$w_0 \approx \frac{2\lambda f}{a}.$$

The mathematical description of the amplitude distribution in the two spots is different, causing the constants in the two formulas to differ, but the dependence on the experimental parameters is the same.

For the Airy pattern, 84% of the total area is contained in the Airy disk, and 91% of the light is contained within the circle bounded by the second minimum at 2.233π. The intensities in the secondary maxima of the diffraction pattern of a rectangular aperture are much larger than that in the Airy pattern of a circular aperture. The peak intensities, relative to the central maximum, of the first three secondary maxima of a rectangular aperture are 4.7%, 1.6%, and 0.8%, respectively. For a circular aperture, the same quantities are 1.7%, 0.04%, and 0.02%, respectively.

To get a feeling for the sizes associated with the Airy disk, we can calculate the size produced on the retina when the pupil is uniformly illuminated. The eye's aperture in daylight is 2.2 mm and the distance to the retina is 20 mm. For green light with a wavelength $\lambda = 550$ nm, the Airy disk is given by

$$\frac{r}{d} = 1.22\frac{\lambda}{d},$$

$$2r = \frac{2(1.22)\left(550 \times 10^{-9}\right)\left(20 \times 10^{-3}\right)}{2.2 \times 10^{-3}}$$

$$= 0.01 \text{ mm} = 10\ \mu\text{m}.$$

10.7 Array Theorem

There is an elegant mathematical technique for handling multiple apertures, called the array theorem. The theorem is based on the convolution integral discussed in Chapter 6, (6.35). The theorem uses the fact that the Fourier transform of a convolution of two functions is the product of the Fourier transforms of the individual functions, (6.38). We will prove the theorem for one dimension, where the functions represent slit apertures. The results can be extended to two dimensions in a straightforward way.

Assume that we have a collection of identical apertures, shown on the right of Figure 10.8. If one of the apertures is located at the origin of the aperture plane, its transmission function is $\psi(x)$. The transmission function of an aperture located at a point x_n

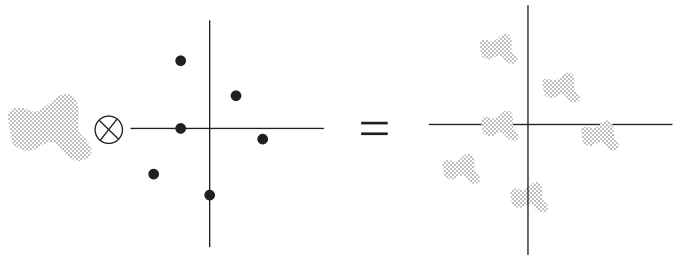

Figure 10.8 *The convolution of an aperture with an array of delta functions will produce an array of identical apertures, each located at the position of one of the delta functions.*

can be written in terms of a generalized aperture function $\psi(x-\alpha)$ by the use of the sifting property of the delta function:

$$\psi(x-x_n) = \int \psi(x-\alpha)\delta(\alpha-x_n)\,d\alpha. \tag{10.27}$$

This convolution integral will allow the application of the convolution theorem to complete the derivation of the array theorem.

Equation (10.27) can be recognized as the convolution integral if we redefine the terms

$$t = \alpha - x_n, \quad dt = d\alpha,$$

$$\psi(x-x_n) = \int \psi(x-x_n-t)\delta(t)\,dt.$$

By defining $x - x_n = \tau$, we may rewrite the integral in the same form as the convolution integral (6.35).

The aperture transmission function representing an array of apertures will be the sum of the distributions of the individual apertures, represented graphically in Figure 10.8 and mathematically by the summation

$$\Psi(x) = \sum_{n=1}^{N} \psi(x-x_n).$$

The Fraunhofer diffraction from this array is the Fourier transform of $\Psi(x)$:

$$\Phi(\omega_x) = \int_{-\infty}^{\infty} \Psi(x)e^{-i\omega_x x}\,dx.$$

From (6A.3), we can write

$$\Phi(\omega_x) = \sum_{n=1}^{N} \int_{-\infty}^{\infty} \psi(x-x_n)e^{-i\omega_x x}\,dx.$$

We now make use of the fact that $\psi(x-x_n)$ can be expressed in terms of a convolution integral. The Fourier transform of $\psi(x-x_n)$ is, from the convolution theorem (6A.8), the product of the Fourier transforms of the individual functions that makeup the convolution:

$$\Phi(\omega_x) = \sum_{n=1}^{N} \mathcal{F}\{\psi(x-\alpha)\}\mathcal{F}\{\delta(x-x_n)\}$$

$$= \mathcal{F}\{\psi(x-\alpha)\}\sum_{n=1}^{N} \mathcal{F}\{\delta(x-x_n)\}.$$

Applying (6A.3) again gives

$$\Phi(\omega_x) = \mathcal{F}\{\psi(x-\alpha)\}\mathcal{F}\left\{\sum_{n=1}^{N} \delta(x-x_n)\right\}. \tag{10.28}$$

The first transform in (10.28) is the diffraction pattern of an individual aperture. The second transform is the diffraction pattern produced by a set of point sources with the same spatial distribution as the array of identical apertures; we will call this second transform the array function. In one dimension, the array function is the comb function, whose Fourier transform has been calculated, (6.27).

To summarize, the array theorem states that the diffraction pattern of an array of similar apertures is given by the product of the diffraction pattern from a single aperture and the diffraction (or interference) pattern of an identically distributed array of point sources.

Figure 10.9 is a physical realization of the array theorem. Figure 10.9(b) is the diffraction pattern of a random array of circular apertures shown in Figure 10.9(a). The overall diffraction pattern is an Airy pattern due to diffraction by an individual circular aperture. The intensity distribution in the Airy disk is a random distribution of intensity maxima and

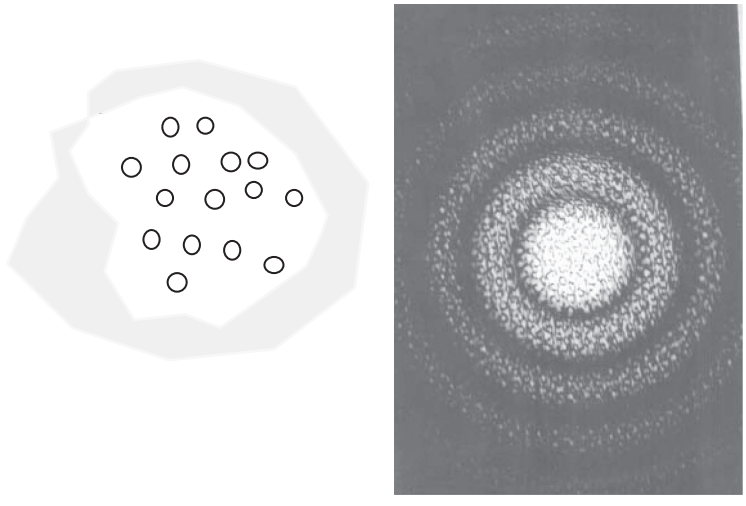

(a) (b)

Figure 10.9 *A random array of circular apertures as shown in (a) produces the Fraunhofer diffraction pattern shown in (b). As predicted by the array theorem, the overall diffraction pattern (the shape factor) is the Airy pattern of a circular aperture, while the intensity distribution in the Airy disk (the grating factor) is due to the interference between the waves from the random array of apertures. The speckled intensity pattern produced by the interference is called speckle noise. We will make some additional comments about this type of noise in Appendix 10B.*

minima. This "speckled" distribution is called speckle noise and is due to interference between the waves from the random array of circular apertures. We will mention speckle noise again in Appendix 10B.

10.8 *N* Rectangular Slits

An array of N identical apertures is called a *diffraction grating* in optics. The Fraunhofer diffraction patterns produced by such an array have two important properties: a number of very narrow beams are produced by the array, and the beam position is a function of the wavelength of illumination of the apertures and the relative phase of the waves radiated by each of the apertures.

Because of these properties, arrays of diffracting apertures have been used in a number of applications. At radio frequencies, arrays of dipole antennas are used to both radiate and receive signals in radar and radio astronomy systems. One advantage offered by diffracting arrays at radio frequencies is that the beam produced by the array can be electrically steered by adjusting the relative phase of the individual dipoles.

An optical realization of a two-element array of radiators is Young's two-slit experiment, while a realization of a two-element array of receivers is Michelson's stellar interferometer. Two optical implementations of arrays, containing more diffracting elements, are diffraction grating and holograms. In nature, periodic arrays of diffracting elements are the origin of the colors observed on some invertebrates; see Chapter 12.

Many solids are naturally arranged in three-dimensional arrays of atoms or molecules that act as diffraction gratings when illuminated by X-ray wavelengths. The resulting Fraunhofer diffraction patterns are used to analyze the ordered structure of the solids.

The array theorem can be used to calculate the diffraction pattern from a linear array of N slits each of width a and separation d. The aperture function of a single slit is

$$\psi(x,y) = \begin{cases} 1, & |x| \le \tfrac{1}{2}a, \quad |y| \le y_0, \\ 0, & \text{all other } x \text{ and } y. \end{cases}$$

The Fraunhofer diffraction pattern of this aperture has already been calculated and is given by (10.18):

$$\mathcal{F}\{\psi(x,y)\} = K\,\frac{\sin\alpha}{\alpha},$$

where the constant K and the variable α are

$$K = \frac{i2ay_0\alpha}{\lambda R_0}\, e^{-i\mathbf{k}\cdot\mathbf{R}_0}\, \frac{\sin\omega_y y_0}{\omega_y y_0},$$

$$\alpha = \frac{ka}{2}\,\sin\theta_x.$$

The array function is the comb function (6.25):

$$A(x) = \sum_{n=1}^{N} \delta(x - x_n), \qquad \text{where } x_n = (n-1)d.$$

The Fourier transform of the comb function is given by (6.28):

$$\mathcal{F}\{A(x)\} = \frac{\sin N\beta}{\sin \beta},$$

$$\beta = \frac{kd}{2} \sin\theta_x.$$

The Fraunhofer diffraction pattern's intensity distribution in the x-direction is thus given by

$$I_\theta = I_0 \underbrace{\frac{\sin^2 \alpha}{\alpha^2}}_{\substack{\text{shape} \\ \text{factor}}} \underbrace{\frac{\sin^2 N\beta}{\sin^2 \beta}}_{\substack{\text{grating} \\ \text{factor}}}. \tag{10.29}$$

We have combined the variation in intensity in the y-direction into the constant I_0 because we assume that the intensity variation in the x-direction will be measured at a constant value of y.

In Figure 10.9, the shape factor is the Airy pattern. The second factor arises from the interference between light from different slits; it is called the *grating factor*. In Figure 10.9, the grating factor is a random function. The fine detail in the spatial light distribution of the diffraction pattern is described by the grating factor arising from the coarse detail in the diffracting object. The coarse, overall light distribution in the diffraction pattern is described by the shape factor arising from the fine detail in the diffracting object.

10.8.1 Young's Double Slit

The array theorem makes the analysis of Young's two-slit experiment a trivial exercise. The application of the array theorem will combine the effects of diffraction with the interference effects discussed in Chapter 4 and will demonstrate that the interference between the two slits arises naturally from an application of diffraction theory. The result of this analysis will support a previous assertion that interference describes the same physical process as diffraction and that the division of the two subjects is an arbitrary one.

In Chapter 4, we discussed interference in Young's two-slit experiment without considering diffraction from the slits. However, we did assume that diffraction would spread the light from each slit, causing the two waves to overlap. By using the results from the array theorem (10.29) with $N = 2$, the effects of diffraction can be included explicitly in the theoretical explanation of Young's experiment.

The intensity of the diffraction pattern from two slits is obtained from (10.29) by setting $N = 2$:

$$I_\theta = I_0 \frac{\sin^2 \alpha}{\alpha^2} \cos^2 \beta. \tag{10.30}$$

The sinc function describes the energy distribution of the overall diffraction pattern, while the cosine function describes the energy distribution created by interference between the light waves from the two slits. Physically, α is a measure of the phase difference between points in one slit, and β is a measure of the phase difference between similar points in the two slits. Zeroes in the diffraction intensity occur whenever $\alpha = n\pi$ or whenever $\beta = (2n+1)\pi/2$. Figure 10.10 shows the interference maxima, from the grating factor, under the central

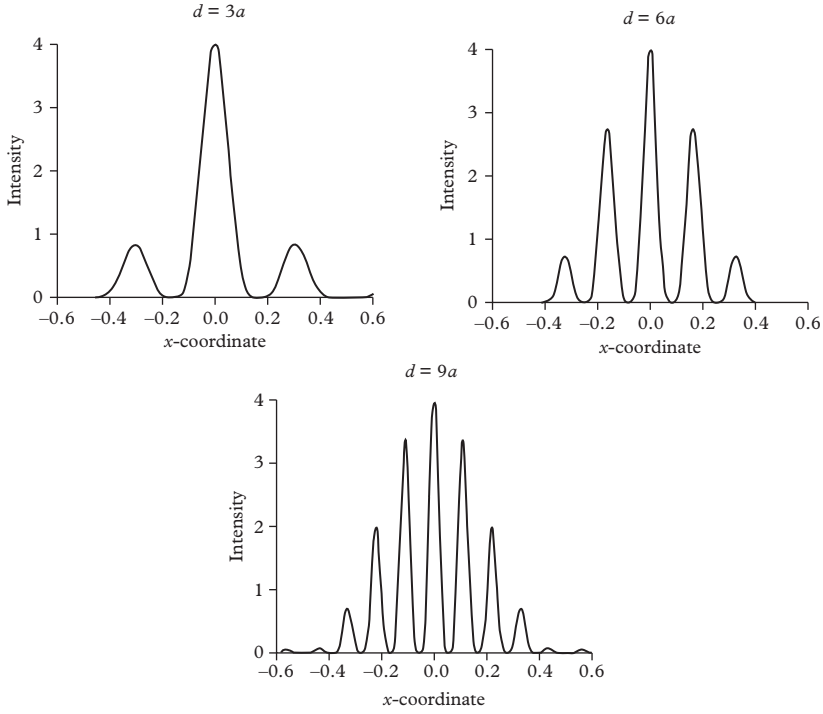

Figure 10.10 *The number of interference fringes beneath the main diffraction peak of a rectangular aperture.*

maximum, described by the shape factor. The number of interference maxima appearing within the central diffraction maximum is given by (see Problem 10.1)

$$\frac{2d}{a} - 1.$$

The diffraction patterns for three values of the ratio d/a are shown in Figure 10.10.

A physical interpretation of (10.29) can be identified in Figure 10.11, where the first factor generates the diffraction associated with a single slit; it is called the *shape factor*. Sharp lines around the central white maxima is due to interference from six slits.

Figure 10.11 *White light diffraction from six slits.*

10.8.2 The Diffraction Grating

In this section, we will use the array theorem to derive the diffraction intensity distribution of a large number of identical apertures. We will discover that the positions of the principal maxima are a function of the illuminating wavelength. This functional relationship has led to the application of diffraction gratings to wavelength measurements.

The diffraction grating normally used for wavelength measurements is not composed of a large number of diffracting apertures but rather a large number of reflecting grooves cut in a surface such as gold or aluminum. The theory to be derived also applies to these reflection gratings, but a modification must be made to the theory because the shape of the grooves in the reflection grating controls the fraction of light diffracted into a principal maximum.

A grating whose groove shape has been controlled to enhance the energy contained in a particular principal maximum is called a *blazed grating*. The use of special groove shapes is equivalent to the modification of the phase in an antenna array at radio frequencies.

The construction of a large number of diffracting elements into an optical device for measuring wavelength was first suggested by **David Rittenhouse**, an American astronomer, in 1785, but the idea was ignored until Fraunhofer reinvented the concept in 1819. Fraunhofer's first gratings were fine wires spaced by wrapping them in the threads of two parallel threaded shafts. He later made gratings by cutting (*ruling*) grooves in gold films deposited on the surface of glass. **H. A. Rowland** made a number of well-designed ruling machines that allowed the production of large area gratings. Following a suggestion by Lord Rayleigh, **Robert Williams Wood (1868–1955)** developed the capability to control the shape of the grooves.

If N is allowed to assume values much larger than 2, the appearance of the interference fringes, predicted by the grating factor, changes from a simple sinusoidal variation to a set of narrow maxima, called principal maxima, surrounded by much smaller secondary maxima, as shown in Figure 10.12 for $N = 2$, 3, 4, 5, and 6. To understand the images in Figure 10.12, we must interpret the predictions of (10.29) when N is large. Whenever $N\beta = m\pi$, where $m = 0, 1, 2, \ldots$, the numerator of the second factor in (10.29) will be zero, leading to an intensity that is zero, $I_\theta = 0$. The denominator of the second factor in (10.29) is zero when $\beta = \lambda\pi$, $\lambda = 0, 1, 2, \ldots$ If both conditions occur at the same time, the ratio of m and N is equal to an integer, $m/N = \ell$, and an indeterminate value for the intensity, $I_\theta = 0/0$ is obtained. For this situation, we must apply l'Hôpital's rule:

$$\lim_{\beta \to \ell\pi} \frac{\sin N\beta}{\sin \beta} = \lim_{\beta \to \ell\pi} \frac{N \cos N\beta}{\cos \beta} = N.$$

L'Hôpital's rule predicts that whenever

$$\beta = \frac{m}{N}\pi,$$

where m/N is an integer, a principal maximum in the intensity will occur with a value given by

$$I_{\theta P} = N^2 I_0 \frac{\sin^2 \alpha}{\alpha^2}. \tag{10.31}$$

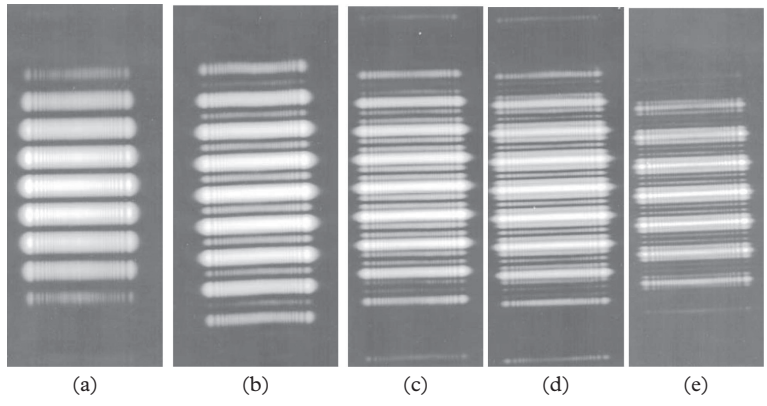

Figure 10.12 *Diffraction patterns from N slits, each identical to the one used to produce Figure 10.4(b): (a) N = 2; (b) N = 3; (c) N = 4; (d) N = 5; (e) N = 6.*

Secondary maxima, much weaker than the principal maxima, occur when

$$\beta = \left(\frac{2m+1}{2N}\right)\pi, \qquad m = 1, 2 \ldots . \tag{10.32}$$

[When $m = 0$, m/N is an integer, and thus the first value that m can have in (10.32) is $m = 1$.] The intensity of each secondary maximum is given by

$$\begin{aligned} I_{\theta S} &= I_0 \frac{\sin^2\alpha}{\alpha^2} \frac{\sin^2 N\beta}{\sin^2\beta} \\ &= I_0 \frac{\sin^2\alpha}{\alpha^2} \left[\frac{\sin^2\left(\frac{2m+1}{2}\right)\pi}{\sin^2\left(\frac{2m+1}{2N}\right)\pi}\right] \\ &= I_0 \frac{\sin^2\alpha}{\alpha^2} \left[\frac{1}{\sin\left(\frac{2m+1}{2N}\right)\pi}\right]^2 . \end{aligned}$$

The quantity $(2m + 1)/2N$ is small owing to the size of N, allowing the small-angle approximation to be made:

$$I_{\theta S} \approx I_0 \frac{\sin^2\alpha}{\alpha^2} \left[\frac{2N}{\pi(2m+1)}\right]^2 . \tag{10.33}$$

The ratio of the intensity of a secondary maximum and a principal maximum is given by

$$\frac{I_{\theta S}}{I_{\theta P}} = \left[\frac{2}{\pi(2m+1)}\right]^2 .$$

The strongest secondary maximum occurs for $m = 1$ and, for large N, has an intensity that is about 4.5% of the intensity of the neighboring principal maximum.

The positions of principal maxima occurs at angles specified by the *grating formula*

$$\begin{aligned} \beta = \ell\pi &= \frac{m}{N}\pi \\ &= \frac{kd\sin\theta}{2} \\ &= \frac{\pi\, d\sin\theta}{\lambda} . \end{aligned} \tag{10.34}$$

The angular positions of the principal maxima are thus

$$\sin\theta_x = \frac{m\lambda}{Nd},$$

where m is called the *interference order*; see Figure 10.13. [We will encounter this same equation later in the analysis of holography, (12.13), and the acousto-optic effect, (14.62). It is called the *Bragg equation*, derived by father and son: William Henry and William Lawrence Bragg.]

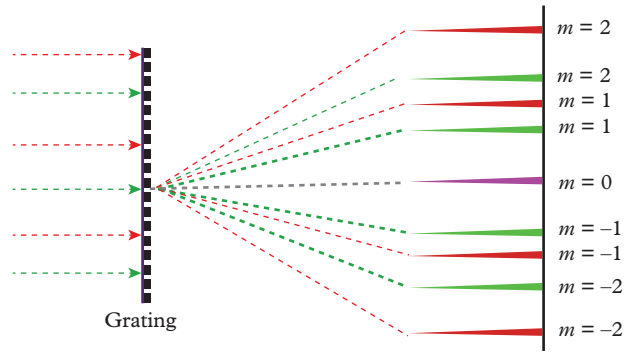

Figure 10.13 *Interference orders of transmission grating: ±2 orders showing a red and a green line.*

The model we have used to obtain this result is based on a periodic array of identical apertures. The transmission function of this array would be a periodic square wave. If, for the moment, we treat the grating as infinite in size, we discover that the principal maxima in the diffraction pattern correspond to the terms of the Fourier series describing the square wave transmission function (see Figure 6.3).

The zeroth order, $m = 0$, corresponds to the a_0 term in the Fourier series and has an intensity proportional to the spatially averaged transmission of the grating. Because of its equivalence to the temporal average of a time varying signal, the zeroth-order principal maximum is often called the *DC term*.

The first-order ($m = 1$) principal maximum corresponds to the fundamental spatial frequency of the grating, and the higher orders correspond to the harmonics of this frequency.

The DC term provides no information about the wavelength of the illumination. Information about the wavelength of the illuminating light can only be obtained by measuring the angular positions of the first- or a higher-order principal maximum (see Figure 10.13).

The fact that the grating is finite in size causes each of the principal maxima to have an angular width that limits the resolution with which the illuminating wavelength can be measured. To calculate the resolving power of the grating, we first determine the angular width of a principal maximum. This is accomplished by measuring the angular change in the position of the principal maximum when β changes from $\beta = \lambda\pi = m\pi/N$ to $\beta = (m + 1)\pi/N$, i.e., $\Delta\beta = \pi/N$. Using the definition

$$\beta = \frac{kd \sin\theta}{2}$$

we have

$$\Delta\beta = \frac{\pi\, d \cos\theta\, \Delta\theta}{\lambda}.$$

The angular width is then

$$\Delta\theta = \frac{\lambda}{Nd \cos\theta}. \tag{10.35}$$

The derivative of the grating formula gives

$$\Delta\lambda = \frac{d}{\ell}\cos\theta\,\Delta\theta,$$

$$\Delta\theta = \frac{\ell\Delta\lambda}{d\cos\theta}.$$

Equating this result to (10.35) yields

$$\frac{\ell\Delta\lambda}{d\cos\theta} = \frac{\lambda}{Nd\cos\theta}.$$

The resolving power of a grating is therefore

$$\frac{\lambda}{\Delta\lambda} = N\ell. \tag{10.36}$$

The improvement in resolving power with increasing N can be seen in Figure 10.14. A grating 2 inches wide and containing 15 000 grooves per inch would have a resolving power in second order ($\ell = 2$) of 6×10^4. At a wavelength of 600 nm, this grating could resolve two waves differing in wavelength by 0.01 nm.

The dependence of the principal maxima on N and d can be seen by comparing the curves shown in Figure 10.14. The separation of the principal maxima is displayed as a function of $\sin\theta$. The angular separation of principal maxima can be converted to a linear dimension by assuming a distance R from the grating to the observation plane. In Figure 10.14(d), a distance of 2 m was assumed. Grating spectrometers are classified by the distance R used in their design. The larger the value of R, the easier it is to resolve wavelength differences. For example, a 1 m spectrometer is a higher-resolution instrument than a 1/4 m spectrometer.

The diffraction grating is limited by overlapping orders (see Figure 10.15), as was the Fabry–Perot interferometer discussed in Chapter 4. If two wavelengths, λ and $\lambda + \Delta\lambda$, have successive orders that are coincident, then $(m+1)\lambda = m(\lambda+\Delta\lambda)$. The minimum wavelength difference for which this occurs is defined as the free spectral range of the diffraction grating:

$$(\Delta\lambda)_{\mathrm{SR}} = \frac{\lambda}{m}.$$

This result is identical to the result obtained for the Fabry–Perot interferometer, (4.54).

We have been discussing amplitude transmission gratings. Such gratings are of poor utility because they waste light. The light loss is from a number of sources:

1. Light is diffracted simultaneously into both positive and negative orders (the positive and negative frequencies of the Fourier transform), see Figure 10.13. The negative diffraction orders contain redundant information and waste light.
2. In an amplitude transmission grating, light is thrown away because of the opaque portions of the slit array.

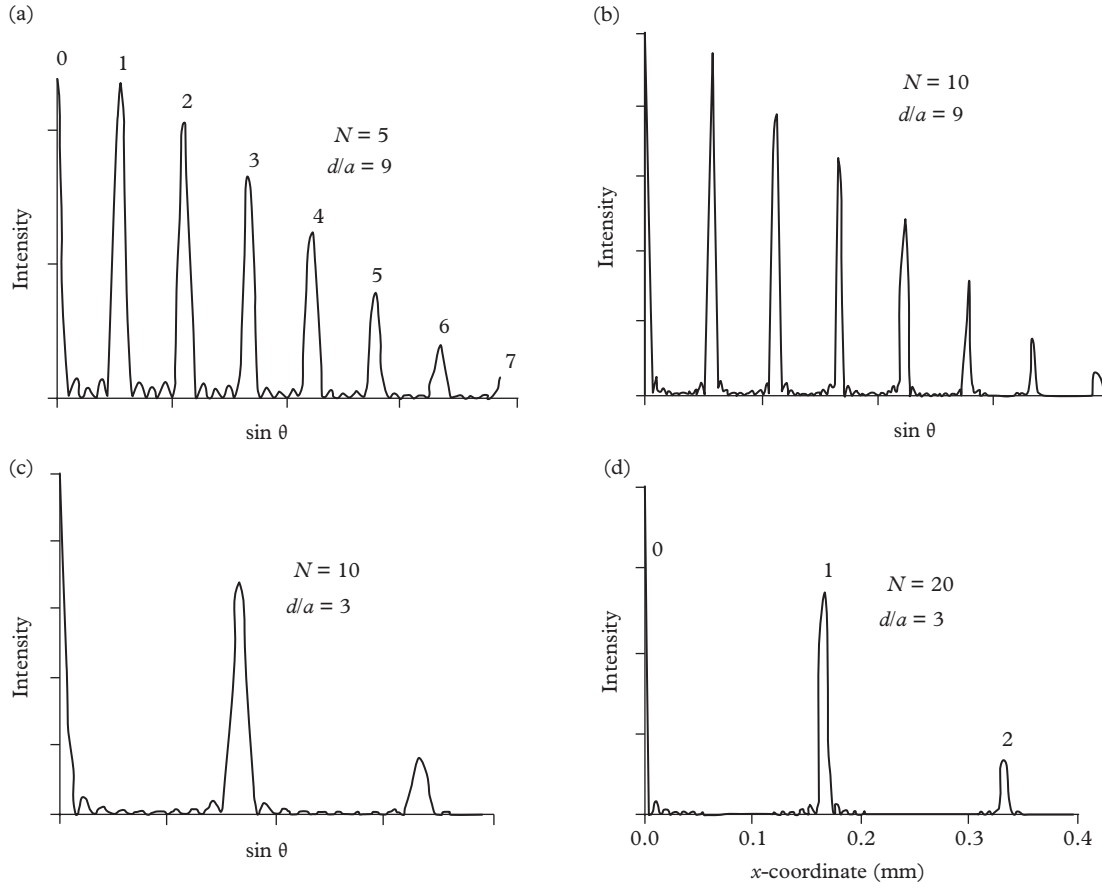

Figure 10.14 *Decrease in the width of the principal maxima of a transmission grating with increasing number of slits. The various principal maxima are called orders, numbering from zero, at the origin, out to as large as 7 in this example. Also shown is the effect of different ratios d/a on the number of visible orders. Note that plot (d) has its abscissa in mm, assuming an observation distance of 2 m from the grating.*

3. The width of an aperture leads to a shape factor,

$$\text{sinc}^2\alpha = \frac{\sin^2\alpha}{\alpha^2},$$

for a rectangular aperture, which modulates the grating factor and causes the amplitude of the orders to rapidly decrease. This can be observed in Figure 10.14(c, d), for $d/a = 3$, where the second order is very weak. Because of the loss in intensity at higher orders, only the first few orders ($\ell = 1, 2,$ or 3) are useful. The shape factor also causes a decrease in diffracted light intensity with increasing wavelength for higher-order principal maxima.

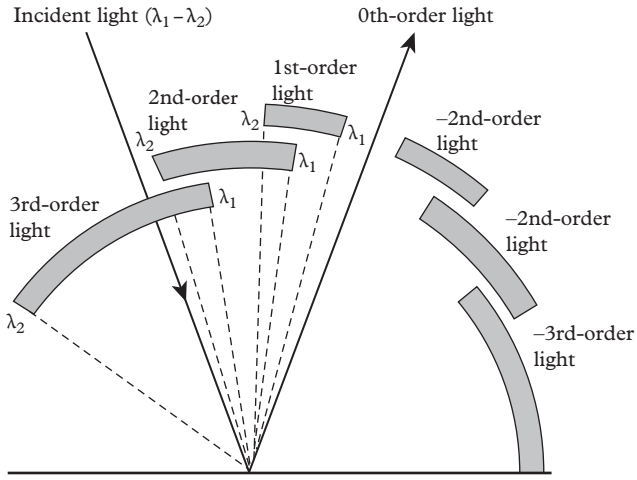

Figure 10.15 *Free spectral range of a grating.*

4. The location of the maximum in the diffracted light, i.e., the angular position for which the shape factor is a maximum, coincides with the location of the principal maximum due to the zeroth-order interference. This zeroth-order maximum is independent of wavelength and is not of much use.

One solution to the problems created by transmission gratings would be the use of a grating that modified only the phase of the transmitted wave. Such gratings would operate using the same physical processes as a microwave phased array antenna, where the location of the maximum of the shape factor is controlled by adding a constant phase shift to each antenna element. The construction of an optical transmission phase grating with a uniform phase variation across the aperture of the grating is very difficult. For this reason, a second approach, based on the use of reflection gratings, is the practical solution to the problems listed above.

By tilting the reflecting surface of each groove of a reflection grating (Figure 10.16), the position of the shape factor maximum can be controlled. The first, third, and fourth problems are eliminated because the shape factor maximum is moved from the optical axis out to some angle with respect to the axis. The use of reflection gratings also removes the second problem, because all of the incident light is reflected by the grating.

Robert Wood, in 1910, developed a technique for producing grooves of a desired shape in a reflective grating. Gratings with grooves shaped to enhance their performance at a particular wavelength are said to be *blazed* for that wavelength. The physical properties on which blazed gratings are based can be understood by using Figure 10.16. The shape of the grooves is controlled so that the groove walls can be treated as an array of mirror surfaces. The normal to each of the groove faces makes an angle θ_B with the normal to the grating surface. We can measure the angle of incidence and the angle of diffraction with respect to the grating normal or with respect to the groove normal, as shown in Figure 10.16. From Figure 10.16, we can write a relationship between the angles:

$$\theta_i = \varphi_i - \theta_B, \quad -\theta_d = -\varphi_d + \theta_B.$$

(The sign convention here is in accord with the one used in geometrical optics: positive angles are those measured in a counterclockwise rotation from the normal to the surface.

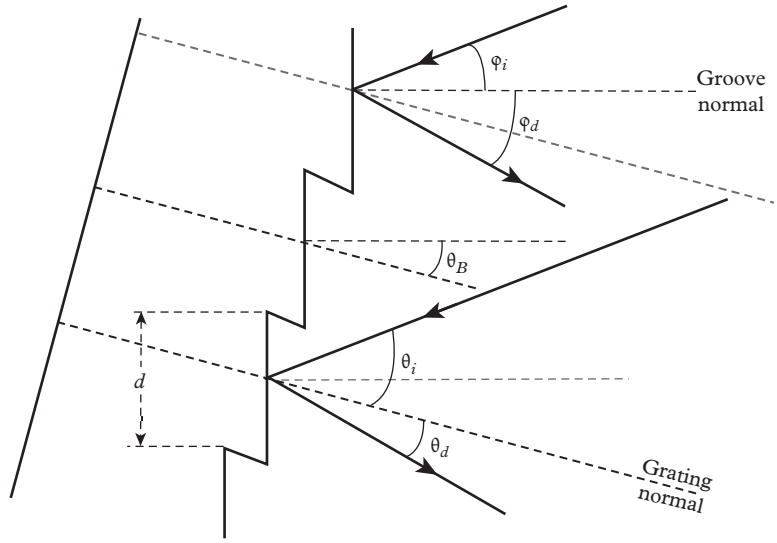

Figure 10.16 *Geometry for a blazed reflection grating.*

Therefore, θ_B is a negative angle.) The blaze angle provides an extra degree of freedom that will allow independent adjustment of the angular location of the principal maxima of the grating factor and the zeroth-order single-aperture diffraction maximum. To see how this is accomplished, we must first determine the effect of off-axis illumination of a diffraction grating.

In the discussion of spatial coherence, we mentioned briefly the effect of an off-axis source on the interference pattern produced by two slits. We saw in (8.33) that the interference pattern is shifted by off-axis illumination. Off-axis illumination is easy to incorporate into the equation for the diffraction intensity from an array. To include the effect of an off-axis source, the phase of the illuminating wave is modified by changing the incident illumination from a plane wave of amplitude E traveling parallel to the optical axis to a plane wave with the same amplitude traveling at an angle θ_i to the optical axis:

$$\tilde{E}e^{-ikx\sin\theta_i}.$$

(Because we are interested only in the effects in a plane normal to the direction of propagation, we ignore the phase associated with propagation along the z-direction, $kz\cos\theta_i$.) The off-axis illumination results in a modification of the parameter for single-aperture diffraction from

$$\alpha = \frac{ka}{2}\sin\theta_d$$

to

$$\alpha = \frac{ka}{2}(\sin\theta_i + \sin\theta_d) \tag{10.37}$$

and in a modification of the parameter for multiple-aperture interference from

$$\beta = \frac{kd}{2}\sin\theta_d$$

to

$$\beta = \frac{kd}{2}(\sin\theta_i + \sin\theta_d) \tag{10.38}$$

where we have relabeled θ_x in the equations for α and β as θ_d, the angle the diffracted light makes with the grating normal.

The zeroth-order single-aperture diffraction peak occurs when $\alpha = 0$. If we measure the angles with respect to the groove face, this occurs when

$$\alpha = \frac{ka}{2}(\sin\varphi_i + \sin\varphi_d) = 0.$$

The angles are therefore related by

$$\sin\varphi_i = -\sin\varphi_d,$$
$$\varphi_i = -\varphi_d.$$

We see that the single-aperture diffraction maximum (the shape factor maximum) occurs at the same angle that reflection from the groove faces occurs. We can write this result in terms of the angles measured with respect to the grating normal:

$$\theta_i = -(\theta_d + 2\theta_B)\,. \tag{10.39}$$

The blaze condition requires the single-aperture diffraction maximum to occur at the ℓth principal maximum, for wavelength λ_B. At that position,

$$\ell\pi = \frac{2\pi d}{\lambda_B}(\sin\theta_i + \sin\theta_d),$$
$$\ell\lambda_B = 2d\sin\frac{1}{2}(\theta_i + \theta_d)\cos\frac{1}{2}(\theta_i - \theta_d).$$

For the special geometrical configuration called the *Littrow condition* (Figure 10.17), where $\theta_i = \theta_d$, we find that (10.39) leads to the equation

$$\ell\lambda_B = 2d\sin\theta_B.$$

A moment's thought will reveal that the physical significance of the blaze condition in the Littrow configuration is that the groove face must be normal to the incident wave, so $\theta_d = \theta_B$. By adjusting the blaze angle, the single-aperture diffraction peak can be positioned on any order of the interference pattern. Typical blaze angles are between 15° and 30°, but gratings are made with larger blaze angles.

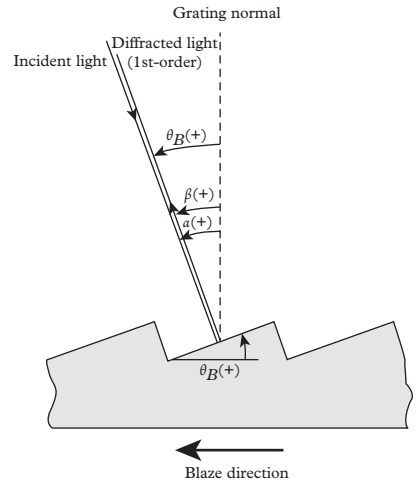

Figure 10.17 *Littrow condition for a grating where the incoming beam and the diffracted beam are parallel to the groove normal. This is a condition that maximizes the efficiency of a blaze grating.*

10.9 Summary

An approximate formulation of the Huygens–Fresnel diffraction integral was obtained by assuming that the distance from the diffracting obstruction, R_0, to the observation point was large enough to fulfill the "far-field" condition

$$R_0 \gg \frac{r^2}{4\pi\lambda},$$

where r is the dimension of the obstruction. Diffraction meeting this condition is called Fraunhofer diffraction and is described by the integral

$$\tilde{E}_P(\omega_x, \omega_y) = \frac{i\alpha e^{-i\mathbf{k}\cdot\mathbf{R}_0}}{\lambda R_0} \iint_{\Sigma} f(x,y) e^{-i(\omega_x x + \omega_y y)}\, dx\, dy.$$

This is a two-dimensional spatial Fourier transform of the aperture transmission function $f(x, y)$, with spatial frequencies defined by

$$\omega_x = -\frac{2\pi\xi}{\lambda R_0},\ \omega_y = \frac{2\pi\eta}{\lambda R_0},$$

We discovered that a lens would produce in its back focal plane the Fraunhofer diffraction pattern of an object in its front focal plane. Thus, a lens can be thought of as a Fourier transform operator. The above equations apply to a lens if we replace R_0 by the focal length of the lens. The negative signs used in these definitions allow an identical mathematical formalism for spatial frequencies and temporal frequencies.

The Fraunhofer diffraction patterns for two simple but important apertures were calculated.

Rectangular slit The amplitude transmission function was assumed to be

$$f(x,y) = \begin{cases} 1, & |x| \le x_0,\ \ |y| \le y_0, \\ 0, & \text{all other } x \text{ and } y. \end{cases}$$

The intensity of the diffracted light was found to be given by

$$I_P = I_0 \frac{\sin^2 \omega_x x_0}{(\omega_x x_0)^2} \frac{\sin^2 \omega_y y_0}{(\omega_y y_0)^2},$$

where the spatial frequencies can also be defined in terms of angles:

$$\omega_x = -\frac{2\pi\xi}{\lambda R_0} = \frac{2\pi \sin\theta_x}{\lambda},$$

$$\omega_y = -\frac{2\pi\eta}{\lambda R_0} = \frac{2\pi \sin\theta_y}{\lambda}.$$

Circular aperture Here,

$$f(s,\varphi) = \begin{cases} 1, & s \le \frac{1}{2}a, \ \text{ all } \varphi, \\ 0, & s > \frac{1}{2}a. \end{cases}$$

The intensity of the diffracted wave is

$$I_P = \left(\frac{\alpha A}{\lambda R_0}\right)^2 \left[\frac{2J_1(u)}{u}\right]^2,$$

where $A = \pi(a/2)^2$ is the area of the aperture and the argument of the Bessel function is

$$u = \frac{ka\rho}{2R_0}.$$

The array theorem was used to find the diffraction patterns from an array of N identical apertures. The intensity distribution of the diffraction pattern was found to be

$$I_\theta = I_0 \frac{\sin^2 \alpha}{\alpha^2} \frac{\sin^2 N\beta}{\sin^2 \beta},$$

where the variable α is defined as

$$\alpha = \frac{ka}{2} \sin\theta_x$$

and a is the x-dimension of a single aperture. The variable β is defined as

$$\beta = \frac{kd}{2} \sin\theta_x,$$

where d is the separation, in the x direction, of the individual apertures.

Diffraction grating The model of an array of N identical apertures was used to describe the operation of a diffraction grating. The diffraction pattern of a grating contains a set of principal maxima with intensity given by

$$I_{\theta P} = N^2 I_0 \frac{\sin^2 \alpha}{\alpha^2}.$$

The grating equation

$$\beta = \frac{\pi d \sin\theta}{\lambda}$$

was solved to give the Bragg equation,

$$\sin\theta_x = \frac{m\lambda}{Nd}.$$

This specifies the angular position of each of the principal maxima produced in the diffraction pattern. The resolution of the diffraction grating was found to depend upon the size of the grating, as shown by the equation for the resolving power:

$$\mathcal{R} = \frac{\lambda}{\Delta\lambda} = \ell N.$$

10.10 Problems

10.1. In a double-slit Fraunhofer diffraction experiment, missing orders occur at those values of $\sin\theta$ that simultaneously satisfy the condition for interference maxima and the condition for diffraction minima. Show that this leads to the condition d/a = integer, where a is the slit width and d is the distance between slits. Derive the approximate relation $d\sin\theta = m\lambda$ as the condition for interference maxima.

10.2. Using the results of Problem 10.1, show that the number of interference maxima under the central diffraction maximum of the double-slit diffraction pattern is given by $2d/a - 1$, where a is the slit width and d is the distance between slits. What is the physical significance of noninteger values of d/a?

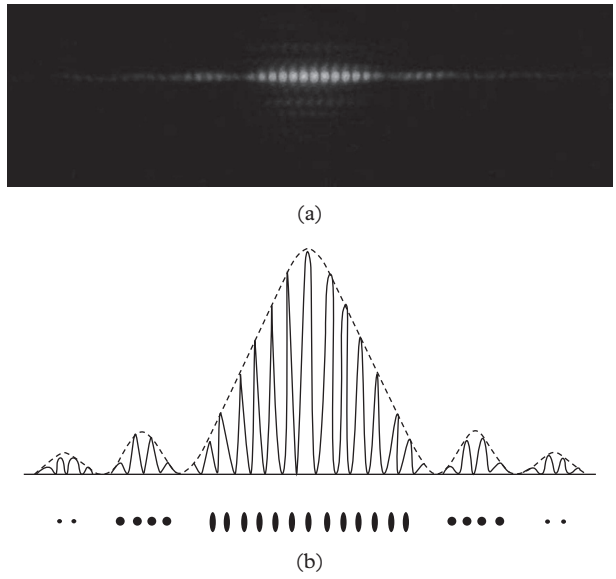

Figure 10.18 *Fraunhofer diffraction pattern from a double slit. (a) The diffraction pattern formed by a double slit illuminated by a laser with wavelength 650 nm. (By Jordgette (Own work) [CC BY-SA 3.0 via Wikimedia Commons] <http://en.wikipedia.org/wiki/Double-slit_experiment#/media/File:Single_slit_and_double_slit2.jpg>.) (b) Plot of the intensity profile of the image in (a). Use the information gathered from measurements of this pattern in Problem 10.3 to determine the width and spacing of the slits.*

10.3. The Fraunhofer pattern of a double slit under $\lambda = 650$ nm illumination appears at the back focal plane of a 80 cm focal length lens. Using measurements taken from Figure 10.18, calculate the width and spacing of the slits.

10.4. How many lines must be ruled on a transmission grating so that it will just resolve the sodium doublet (589.592 and 588.995 nm) in the first-order spectrum?

10.5. Is there any limit to the number of principal maxima in the far-field pattern of an N-slit array (see Figure 10.19)? Explain the answer.

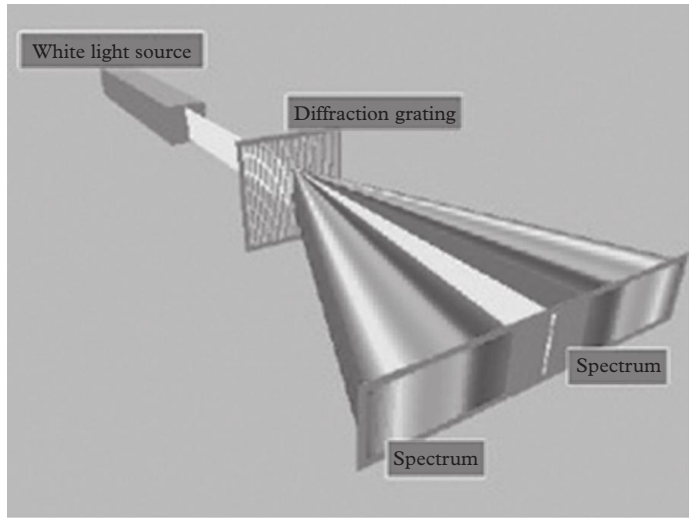

Figure 10.19 *Diffraction by a grating.*

10.6. A grating is ruled at 1000 lines/mm. How wide must it be in order to resolve the spectral content of an HeNe laser (λ = 632.8 nm)? The frequency content of the HeNe laser consists of three very narrow emission lines: one at 632.8 nm, with two others spaced 450 MHz on either side of the 632.8 nm line. Would there be a better instrument to resolve this spectrum?

10.7. Monochromatic radiation is incident normal to a grating surface from a narrow slit so that the principal maxima appear as thin bright bands. Show that the width $\Delta\theta$ of each band is inversely proportional to the width of the grating. See Figure 10.20.

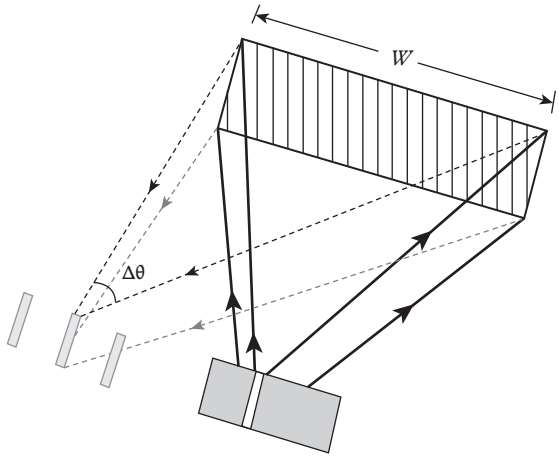

Figure 10.20 *Geometry for Problem 10.7.*

10.8. Formulate a rough estimate of the extent of the Airy disk at visible wavelengths for a lens in terms of its f-number (the ratio of its focal length to its diameter).

10.9. A point source of yellow light (λ = 589 nm) is viewed through a piece of light closely woven material 30 m from the observer. A square array of bright points separated by 30 cm is observed. What is the number of threads per meter in the material?

10.10. What does an increase in wavelength do to a Fraunhofer diffraction pattern?

10.11. What happens when we increase the focal length of the lens used to produce Fraunhofer diffraction?

10.12. The transmission function of a slit is given by

$$f(x) = \begin{cases} \dfrac{a-|x|}{a}, & -a < x < a, \\ 0, & \text{all other } x. \end{cases}$$

Calculate the diffraction pattern. Calculate the peak intensity in the sidebands and compare it with the intensity observed in the sidebands produced by a uniformly illuminated slit. Intentional modification of the transmission function of an aperture is called apodization (see Appendix 10A).

10.13. Calculate the diffraction pattern of an apodized slit for which the transmission function is

$$f(x) = \frac{1}{a}\sqrt{\frac{2}{\pi}}\, e^{-2(x/a)^2}.$$

Comment on the sidebands of this diffraction pattern.

10.14. Prove that the secondary maxima of a single-slit diffraction pattern occur when $\alpha = \tan\alpha$.

10.15. What diameter telescope aperture is needed to resolve a double star with a separation of 10^8 km if the star is located 10 light-years from the earth? (Assume $\lambda = 500$ nm.)

10.16. A single-slit Fraunhofer diffraction pattern is formed using white light. For what wavelength does the second minimum coincide with the third minimum produced by a wavelength of $\lambda = 400$ nm?

10.17. A rectangular horizontal hole 0.25 mm high and 1.0 mm wide is illuminated by a plane wave from an argon laser ($\lambda = 488$ nm). A lens of focal length 2.5 m forms a diffraction pattern in its back focal plane. What is the size of the central maximum?

10.18. A collimated beam ($\lambda = 600$ nm) is incident normally onto a 1.2 cm diameter, 50 cm focal length converging lens. What is the size of the Airy disk?

10.19. From the Rayleigh criterion (see Appendix 10B), what would be the smallest angular separation between two equally bright stars that could be resolved by the 200-inch Hale telescope? Assume $\lambda = 550$ nm.

10.20. Explain why the first minimum of

$$\tilde{E}_a(\xi) = \frac{2\pi}{b}\left[\frac{\cos\frac{1}{2}\xi b}{(\pi/b)^2 - \xi^2}\right]$$

does not occur when $\xi = \pi/b$. What is the value of $\tilde{E}_a$ at $\xi = \pi/b$?

10.21. Under what conditions does the integral

$$\tilde{E}_P = \frac{i\alpha}{\lambda R_0}\, e^{-i\mathbf{k}\cdot\mathbf{R}_0} \int_{-x_0}^{x_0} f(x)\, e^{i\omega_x x}\, dx$$

yields the same result as the integral

$$\tilde{E}_P = \frac{i\alpha}{\lambda R_0}\, e^{-i\mathbf{k}\cdot\mathbf{R}_0} \int_{-x_0}^{x_0} f(x)\, e^{-i\omega_x x}\, dx.$$

REFERENCES

1. Duffieux, P.M., *The Fourier Integral and its Applications to Optics*. 2nd ed. 1983: Wiley.
2. Goodman, J., *Introduction to Fourier Optics*. 3rd ed. 2004: Roberts.
3. O'Neil, E.L., *Introduction to Statistical Optics*. 2004: Dover.

Appendix 10A Abbe Theory and Optical Processing

10A.1 Introduction

In 1871, while developing a theory of the microscope for Karl Zeiss, **Ernst Abbe (1840–1905)** introduced a view of coherent imaging that has led to the field of optics called *optical signal processing*. Abbe's theory assumes that the object to be imaged can be decomposed into a number of elemental gratings, each of which diffracts light at an angle that is a function of the grating's period and orientation. The diffracted light beams are plane waves that are focused by the imaging lens to diffraction patterns of light in the back focal plane of the lens. The shapes of the diffraction patterns are determined by the aperture of the imaging lens. The diffraction patterns act as sources of waves that propagate from the focal plane to the image plane, where they interfere to produce the image.

In 1896, Rayleigh developed a similar approach to coherent imaging that assumes that the object can be treated as a large number of point sources. The lens produces a diffraction pattern in the image plane for each of the points. The shape of the diffraction pattern is determined by the lens aperture. The diffraction patterns interfere at the image plane to produce an image. In the following discussion, only Abbe's theory will be treated.

Once Abbe's theory of imaging has been developed, a few applications to the field of signal processing will be discussed, all based on the premise of Abbe's theory that the Fourier transform of the object is present in the back focal plane of an imaging lens. The applications to be discussed modify the Fourier transform of an object by changing

(1) its amplitude distribution;

(2) its phase distribution;

(3) both the phase and the amplitude of the transform.

The objective of two of the applications is to modify the image produced by the optical system; thus, they could be called image processing applications. The objective of the third application is to recognize and locate a particular object in the field of view of the optical system; thus, it could be called a pattern recognition application.

We will assume that the light is both temporally and spatially coherent. The demands on temporal coherence made by the theory are much less stringent than the demands on spatial coherence. We will mention the different coherence requirements during the development of the theory.

10A.2 Abbe's Theory of Imaging

A simple lens, shown in Figure 10A.1, is used to image an extended object. The extended object is located a distance $-S$ to the left of the lens and the image of the object is located a distance S' to the right of the lens.

The Huygens–Fresnel integral can be used to determine the electric field distribution at the back focal plane of the lens. The field distribution is

$$\mathcal{P}(\xi) = \alpha\sqrt{\frac{i}{\lambda f}}\, e^{-ik(f-S)} \exp\left[-ik\left(\frac{\xi}{f}\right)^2\left(\frac{f+S}{2}\right)\right] \int_{-a/2}^{a/2} f(x_s) e^{ikx_s\xi/f}\, dx_s, \qquad (10A.1)$$

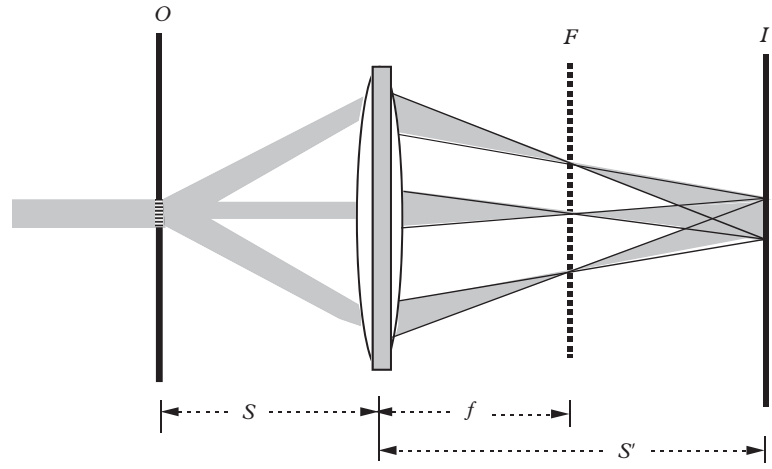

Figure 10A.1 *Abbe's theory of imaging.*

where the limits of integration are established by the size of the object. The result of this is that the lens's transmission function will be neglected in the analysis. We will assume that no light is produced outside the boundary of the object, which will allow us to let the limits go to infinity. Using the definition (10.13), we can write

$$\mathcal{P}(\omega_x) = \alpha\sqrt{\frac{i}{\lambda f}}\, e^{-ik(f-S)} e^{-i\omega_x^2(f+S)/2} \int_{-\infty}^{\infty} f(x_s) e^{-i\omega_x x_s}\, dx_s. \tag{10A.2}$$

Equation (10A.2) demonstrates that the back focal plane of the lens contains the Fourier transform of the object. This is one of the two basic ideas contained in Abbe's theory. We decompose the light from the object into a set of plane waves that are focused to Airy disks (we will assume the limiting aperture is circular) in the back focal plane of the lens. The location of an Airy disk in the focal plane, as we saw in Chapter 10, is a function of the angle the plane wave makes with the optical axis.

An equivalent view of this first step in the imaging process is that the object is made up of a number of sinusoidal gratings, each with a different period and amplitude. Each grating diffracts light into a plane wave, at an angle that is a function of the period and orientation of the grating. The plane waves produced by each grating are then focused to a set of Airy disks by the lens. Figure 10A.1 illustrates the imaging process when the object is a simple sinusoidal grating.

The second fundamental idea contained in Abbe's theory is that each Airy disk in the back focal plane of the lens acts as a source, producing a spherical wave. These spherical waves interfere at the image plane to produce the image of the object. We will not write out the Huygens–Fresnel integral for this second step, but instead refer the interested reader to the book by Klein [1].

To understand the ideas contained in Abbe's theory and to see how they might be applied, it is useful to replace the simple lens of Figure 10A.1 with a pair of lenses, as in Figure 10A.2. There are three lenses in Figure 10A.2, but the first is present only to produce a plane wave to illuminate the object. For this reason, we will ignore this lens in our discussion. We will assume for this discussion that both lenses in the two-lens system shown in Figure 10A.2 have the same focal length, making the magnification of the system unity,

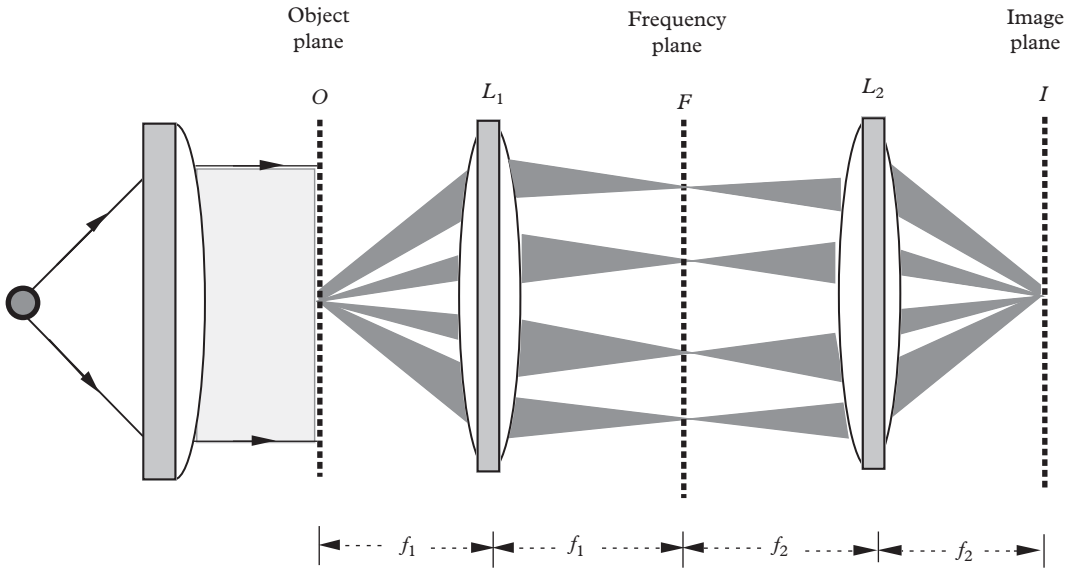

Figure 10A.2 *Two-lens imaging system. The first lens is to produce a plane wave that illuminates the object. Here, the object is assumed to be a transparency.*

$\beta = 1$ (see Problem 5.12). The object plane for the two-lens system is the front focal plane of lens L_1 and the image plane, which contains an inverted replica of the object, is the back focal plane of lens L_2.

We will follow, in a stepwise fashion, the light as it propagates from the object to the image plane in Figure 10A.2. The lens L_1 produces a Fourier transform of the object in plane F, the back focal plane of L_1, designated as the *frequency plane*. The light distribution in the frequency plane acts as the source for lens L_2, which produces the Fourier transform of the frequency plane at plane I. Thus, the field distribution in plane I is the Fourier transform of the Fourier transform of the object. This light distribution is the image of the object.

A logical question to ask is what would happen to the image of the object if we modified the light distribution in the frequency plane F. To answer this question, we will examine a simple sinusoidal grating with amplitude $d \leq 1$ and of finite extent in the object plane O of Figure 10A.2 [see (10B.11)]:

$$f(x,y) = \begin{cases} \frac{1}{2} + \frac{1}{2} d \cos \omega_0 x, & |x| \leq \frac{1}{2}\ell, \quad |y| \leq \frac{1}{2}\ell, \\ 0, & \text{all other } x \text{ and } y. \end{cases} \tag{10A.3}$$

The multiplicative factor d is know as the *amplitude modulation* of the grating. Because in optics we measure intensity rather than amplitude, it is more useful to define object *contrast*

$$C = \frac{I_{\max} - I_{\min}}{I_{\max} + I_{\min}}.$$

For the object (10A.3), the contrast is

$$C = \frac{2d}{1 + d^2} \approx 2d.$$

We will have more to say about contrast in Appendix 10B.

The source must have a spatial coherence length larger that the width and height of the aperture, defined by the grating. If the source meets the spatial coherence requirement, the amplitude distribution in plane F of Figure 10A.2 will be

$$\tilde{E}(x_0, y_0) = \frac{i\ell^2}{2\lambda f} e^{-2ikf} \operatorname{sinc}\left(\frac{\ell y_0}{\lambda f}\right) \times \left(\operatorname{sinc}\left(\frac{\ell x_0}{\lambda f}\right) + \frac{d}{2}\left\{\operatorname{sinc}\left[\frac{\ell}{\lambda f}\left(x_0 + \frac{\omega_0 f}{k}\right)\right] + \operatorname{sinc}\left[\frac{\ell}{\lambda f}\left(x_0 - \frac{\omega_0 f}{k}\right)\right]\right\}\right). \tag{10A.4}$$

The intensity distribution in plane F is

$$I(x_0, y_0) = \left(\frac{\ell^2}{2\lambda f}\right)^2 \operatorname{sinc}^2\left(\frac{\ell y_0}{\lambda f}\right) \times \left\{\operatorname{sinc}^2\left(\frac{\ell x_0}{\lambda f}\right) + \frac{d^2}{4}\operatorname{sinc}^2\left[\frac{\ell}{\lambda f}\left(x_0 + \frac{\omega_0 f}{k}\right)\right] + \frac{d^2}{4}\operatorname{sinc}^2\left[\frac{\ell}{\lambda f}\left(x_0 - \frac{\omega_0 f}{k}\right)\right]\right\}. \tag{10A.5}$$

A schematic representation of the process described by (10A.5) is shown in Figure 10A.3. The distribution described by (10A.5) is the origin of the graphical display in Figure 10A.1,

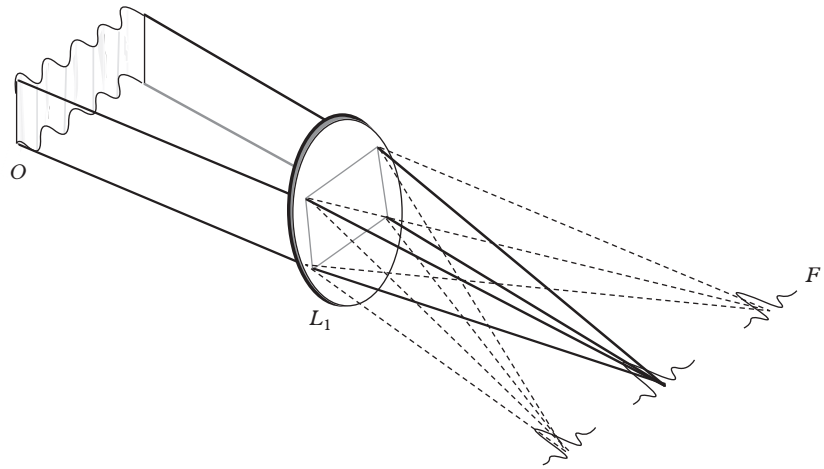

Figure 10A.3 *Fraunhofer diffraction pattern produced by a sinusoidal grating of finite size.*

where an object diffraction pattern, located in plane F of the lens, is shown to consist of a light spot on the optical axis and a spot above and a spot below the optical axis.

The multiplier of the quantity in braces on the right-hand side of (10A.5),

$$\text{sinc}^2\left(\frac{\ell y_0}{\lambda f}\right),$$

gives the diffraction intensity distribution in the y-direction due to the aperture dimension of the grating in the y-direction. The first term within the braces of (10A.5),

$$\text{sinc}^2\left(\frac{\ell x_0}{\lambda f}\right),$$

is the diffraction intensity due to the aperture dimension of the grating in the x-direction. The product of these two terms gives the intensity distribution on the optical axis. This intensity distribution is often called the *DC component* or the *zeroth order*. It corresponds to the zeroth-order principal maximum of a grating and equals the spatial average over the aperture of the transmission function of the grating.

The sinusoidal transmission variation of the grating produces two additional side patterns (called the *first-order components*) or spatial sidebands, located a distance $\omega_0 f/k$ on either side of the DC component,

$$\text{sinc}^2\left[\frac{\ell}{\lambda f}\left(x_0 \pm \frac{\omega_0 f}{k}\right)\right].$$

The intensity distribution of each of these spots is identical to the distribution of the DC spot and is determined by the shape of the grating aperture.

If the grating were not sinusoidal but instead represented by a periodic square wave, then the resulting diffraction pattern would consist of a large number of sinc functions as shown in Figure 10A.4. This behavior is consistent with the interpretation of the diffraction pattern as a Fourier transform or, for an infinite grating, a Fourier series. The Fourier series of the sinusoidal grating has only one term, but the Fourier series of a square wave would be an infinite series of terms involving harmonics of the fundamental frequency of the square wave; see (6.9).

The maximum amplitude transmission in the object plane occurs when the amplitude transmission function, $\cos \omega_0 x$, is a maximum; the separation between each maximum is equal to the period of the cosine function:

$$E'(\omega_x) = A(\omega_x)e^{\pm i\pi/2} + i\Phi(\omega_x) = \pm i[A(\omega_x) \pm \Phi(\omega_x)].$$

We will denote by Δx the *resolution* of the object. The periodic variations in transmission, associated with the grating structure, result in large-scale variations in the frequency plane, namely, the three sinc functions in (10A.5). The large-scale variations in the object plane, dictated by the rectangular aperture that limits the grating, result in small-scale variations in the frequency plane, namely, the sinc distribution at each spatial frequency.

The size of a diffraction pattern will change with the wavelength. If the temporal coherence of the source is small and a frequency spectrum of light is present, then the diffraction pattern formed by light at the blue end of the spectrum is smaller than the pattern formed by light at the red end, causing the sidebands for each wavelength to occur at different positions. Figure 10A.5(a) shows the Fourier transform of a nested set of triangles, illuminated

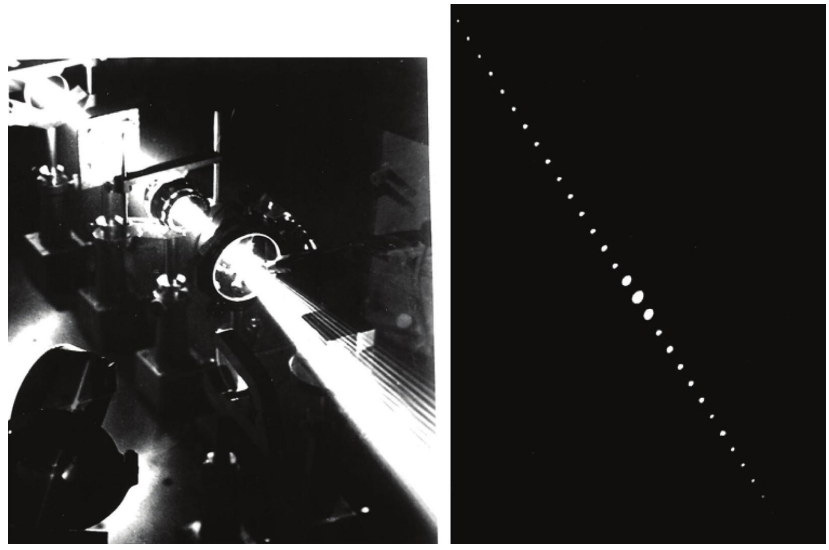

(a) (b)

Figure 10A.4 *A Ronchi ruling is a periodic array of opaque lines separated by clear regions of the same width. The transmission function of the Ronchi ruling is a square wave. The Fourier transform of a square wave is a set of harmonic functions. The diffraction pattern of the Ronchi ruling should thus be a set of bright spots whose intensity corresponds to the coefficients of the harmonic functions of the Fourier transform. In (a), we see the formation of the spots of light by the lens. If a screen is placed so it intercepts the beams of light seen in (a), then the image (b) is observed in the back focal plane.*

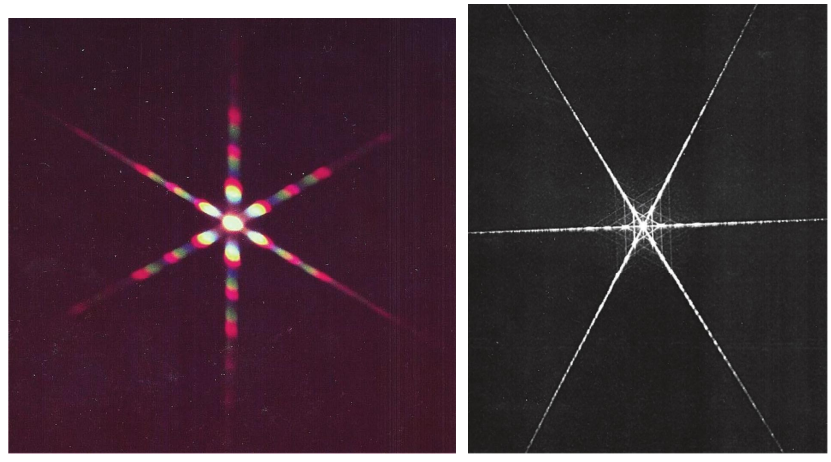

(a) (b)

Figure 10A.5 *The Fraunhofer diffraction pattern produced by a nested set of triangles that form three sets of gratings oriented at 120° with respect to each other. (a) The illuminating light was spatially coherent (small point source) white light. The spots are very broad owing to the spread in wavelengths of the source. (b) The illuminating light producing this diffraction pattern contained only a single wavelength. (Nested triangles courtesy N. George.)*

by a temporally incoherent light source. The spread in wavelengths present in the white light used to create Figure 10A.5(a) causes the spots of light in the photograph to appear much larger than would be predicted by the size of the set of triangles. Figure 10A.5(b) shows an identical Fraunhofer diffraction pattern of the nested set of triangles obtained using a single wavelength of light. Comparison of the spots of light in Figures 10A.5(a) and (b) shows the effect of temporal coherence on the spots that make up the diffraction pattern.

We can establish the wavelength spread that would destroy the diffraction pattern observed in Figure 10A.4(a) by assuming that the sinc functions for the two extremes in wavelength, λ_1 and λ_2, are separated by the width of the sinc function of λ_1, see Figure 10A.6. With this assumption, the allowable spread in wavelength is

$$\frac{\Delta\lambda}{\lambda} = \frac{\lambda_1 - \lambda_2}{\lambda_1} = \frac{4\pi^2}{\ell\omega_0} = \frac{2\pi\,\Delta x}{\ell}. \tag{10A.6}$$

This result states that as the resolution in the object increases (i.e., as the value of Δx decreases) or as the size of the object, ℓ, increases, the temporal coherence of the source must increase if the diffraction pattern is still to be observed.

Suppose an aperture is placed in plane F of Figure 10A.2 with its symmetry axis aligned with the optical axis of the system. If the size of the aperture, D, is too small to allow the two sidebands of (10A.5) to pass on to plane I, then we will not see the sinusoidal grating at the image plane. Stated mathematically, if

$$D < \frac{2\omega_0 f}{k} + \frac{2\pi\lambda f}{\ell} = \frac{2f\lambda}{\Delta x} + \frac{2\pi\lambda f}{\ell},$$

then the optical system cannot resolve the grating. If D is less than this dimension, then the light distribution in the image plane is a constant, equal to the Fourier transform of

$$\operatorname{sinc}\left(\frac{\ell y_0}{\lambda f}\right)\operatorname{sinc}\left(\frac{\ell x_0}{\lambda f}\right).$$

Any aperture less than the above dimension, but larger than a minimum dimension of

$$D = \frac{2\pi\lambda f}{\ell},$$

yields an image that is a uniform light distribution over a rectangle the size of the grating. If a small aperture, equal to the minimum dimension, could be moved up or down in the frequency plane so that it allowed either of the sidebands to pass, we would find minimal change in the appearance of the image plane. Because each of the three components is a simple sinc function, the light distribution in plane I, when any one of the three components is allowed to pass, is the image of the rectangular aperture with uniform illumination, i.e., a plane wave with limited extent. If the zeroth order is passed through, the plane wave will propagate parallel to the z-axis, while if a sideband is passed through, the plane wave will propagate at an angle with respect to the z-axis.

By neglecting the effect of a finite-sized grating, the minimum diameter required to resolve a grating with resolution Δx can be simplified to

$$D = \frac{2f\lambda}{\Delta x}. \tag{10A.7}$$

This result should be compared with the diameter of an optical system needed to produce a Gaussian beam waist w, calculated in Chapter 9:

$$D = \frac{2\lambda f}{w}.$$

The minimum resolution of an optical system is associated with the minimum spot size that the optical system can produce.

Rayleigh postulated a criterion for resolution, the *Rayleigh criterion* (see Figure 10A.6):

For an imaging system with a circular aperture, *two Airy functions in the image plane can be just resolved if the central maximum of one function falls on the first zero of the other function.*

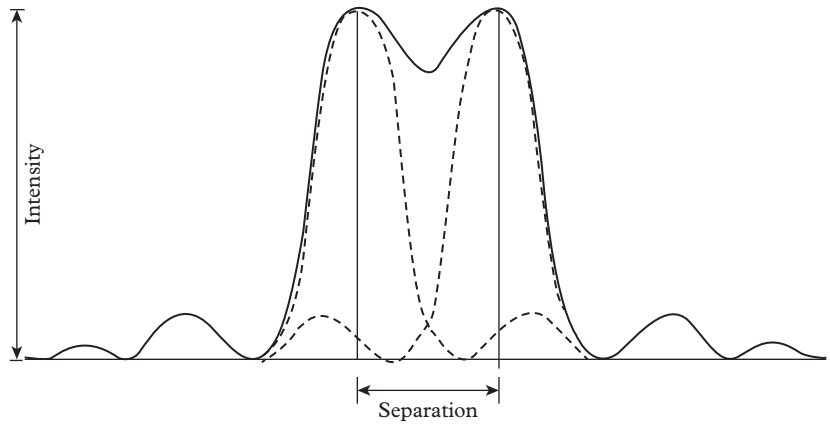

Figure 10A.6 *The resolution of two circular sources based on the Rayleigh criterion.*

This postulated criterion is in agreement with the relationship between resolution and beam waist established by the theories developed here. (The Rayleigh criterion is discussed in more detail in Appendix 10B.)

We now set the size of the aperture in plane F equal to the value

$$D = \frac{f\lambda}{\Delta x} + \frac{2\pi\lambda f}{\ell}$$

and move its symmetry axis above the optical axis, so that only the zeroth order and one sideband are allowed to pass through to the image plane. This configuration reduces the number of diffraction patterns in the frequency plane to two. The two diffraction patterns—sinc functions in the example we are considering—act as point sources. The transition from the frequency plane to the image plane is equivalent to Young's experiment.

In the image plane, light from the two sources will interfere to produce a sinusoidal interference pattern. From (4.17) the period of this interference pattern is

$$T = \frac{\lambda D}{h},$$

yielding a spatial frequency of the sinusoidal interference pattern equal to

$$\omega = \frac{2\pi}{T} = \frac{kh}{D}.$$

In the example we are considering, the distance to the observation plane is given by $D = f$ and the point source separation is

$$h = \frac{\omega_0 f}{k}.$$

Thus, the spatial frequency of the interference pattern is ω_0, the frequency of the input object.

The peak intensities of the two sources in plane F are

$$I_1 = \left(\frac{\ell^2}{2\lambda f}\right)^2, \quad I_2 = \left(\frac{\ell^2}{2\lambda f}\right)^2 \frac{d^2}{4}.$$

From (4.12) we can write the intensity distribution in the image plane I as

$$I = \frac{\ell^2}{2\lambda f}\left[\left(1 + \frac{d^2}{4}\right) + d\cos\omega_0 x\right]. \tag{10A.8}$$

From our definition of the contrast (or modulation) of the object above, $C_0 = d$, the contrast of the image is given by

$$C_I = \frac{d}{1 + (d/2)^2}.$$

The image of the object retains the object's spatial frequency content, but at a reduced contrast.

If we neglect the term associated with the size of the grating, we find that the aperture diameter required to resolve the grating is half the size of the aperture needed to pass both sidebands. (This is equivalent to single-sideband transmission in communication theory.) If the noise associated with the object is small enough to allow detection of the image at the reduced contrast, then the aperture (or, equivalently, the spatial bandwidth) of the imaging system can be reduced by one-half with no loss in resolution.

Instead of displacing the aperture in the frequency plane, above the optical axis, we could illuminate the object with a plane wave incident from below the optical axis at an angle γ (see Figure 10A.7):

$$\gamma = \frac{x_0}{f} = \frac{\omega_0}{2k} = \frac{\lambda}{2\Delta x}.$$

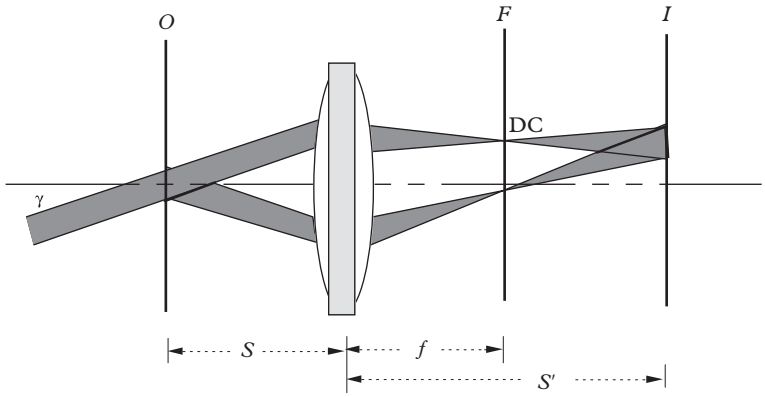

Figure 10A.7 *Off-axis illumination allows an aperture to provide the same resolution as an aperture twice its size operating with illumination parallel to the optical axis.*

The off-axis illumination causes the diffraction pattern in the frequency plane to move upward, half the distance between the DC component and the first-order sideband:

$$x_0 = \frac{\omega_0 f}{2k}.$$

For the off-axis illumination, shown in Figure 10A.7, an aperture of size

$$D_\theta = \frac{f\lambda}{\Delta x},$$

centered upon the optical axis, will pass the DC component and the first-order sideband. We therefore find that by illuminating the object at an angle with respect to the optical axis, the imaging system is able to resolve the object grating with an aperture only one-half the size needed to resolve the same grating with illumination incident normal to the grating.

Figure 10A.8(a) illustrates a microscope designed to operate with oblique illumination. Figures 10A.8(b) and (c) show images of an etched metal surface under normal and oblique illumination, respectively.

If the DC is prevented from passing through the system by placing a ring aperture in plane F of Figure 10A.2, then we again simulate Young's experiment. Now, however, the spacing of the two interfering sources is

$$h = \frac{2\omega_0 f}{k}.$$

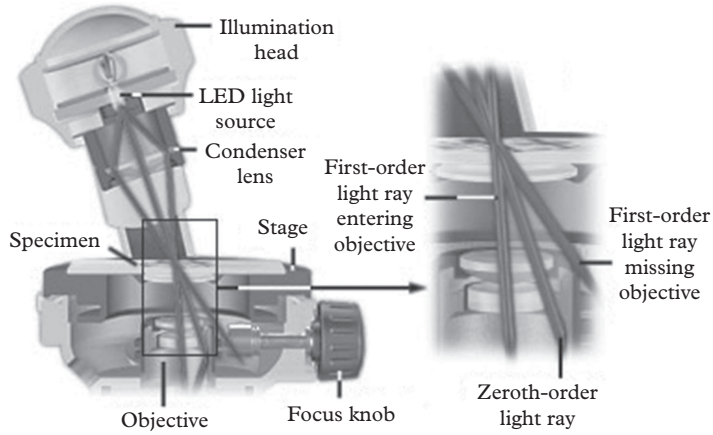

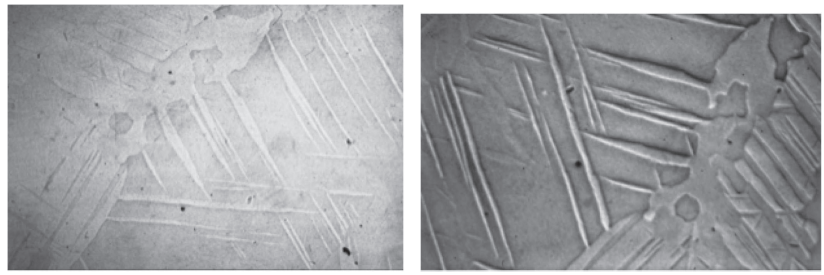

Figure 10A.8 *(a) Optical design of an obliquely illuminated microscope. (b, c) Comparison of images of an etched metal surface: in (b) conventional (brightfield) illumination; (c) oblique illumination. (Provided by H. K. D. H. Bhadeshia; <http://www.msm.cam.ac.uk/phase-trans/abstracts/optical.html>.)*

The spatial frequency of the interference pattern for this case is

$$\omega = \frac{kh}{f} = 2\omega_0.$$

The spatial frequency is twice the object's spatial frequency, and the contrast of the image is $C_I = d/2$, one-half of the object's contrast. This is the appearance of false detail described first by Abbe.

The origin of the false detail we have discovered is quite easy to understand mathematically. The original object has an amplitude transmission that is a sinusoidal amplitude variation with a bias term added, as shown on the left of Figure 10A.9(a). When the DC and sidebands are retained, then the image, which is detected as the square of the amplitude at plane *I*, is a function with the same period as the object, as shown on the right of Figure 10A.9(a). The detected image has the same spatial period as the original object. If the DC component is removed in the frequency plane, then, at the image plane, the spatial variation of the amplitude of the image is the waveform shown on the left of Figure 10A.9(b). The intensity distribution of the image, shown on the right of Figure 10A.9(b), has twice the spatial period as the original object.

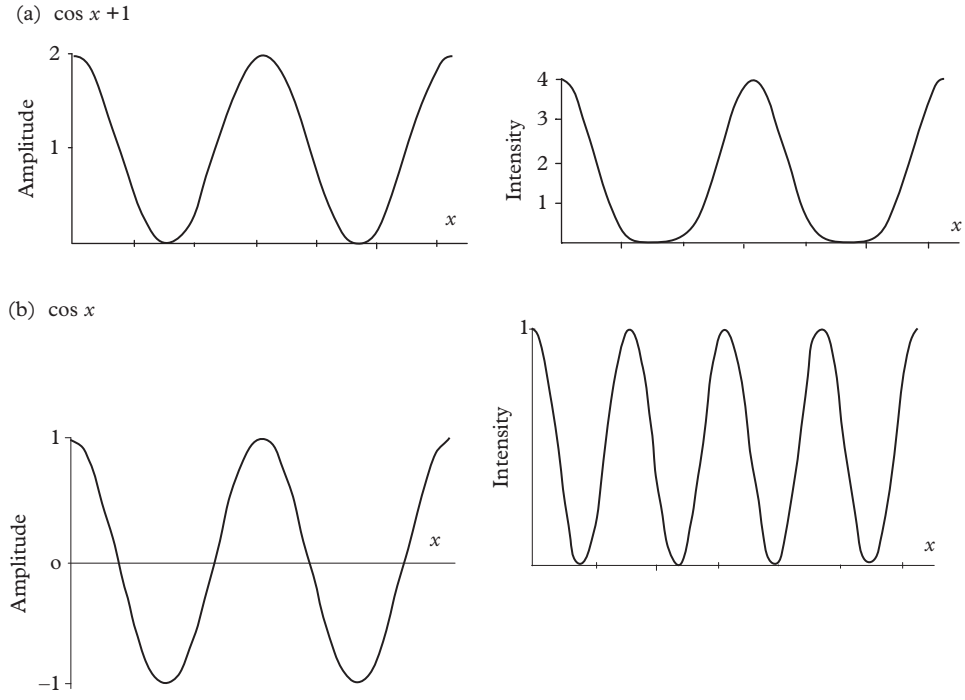

Figure 10A.9 *(a) The amplitude and intensity of a sinusoidal spatial variation with a bias term added. (b) The amplitude distribution of a sinusoidal grating with no bias term. The false resolution can be seen in the plot of the intensity shown on the right of the figure.*

The ideas of Abbe were not well received, particularly the statement that false detail could appear in an image. A. B. Porter was able to construct experiments, without the objectionable components of Abbe's experiments, that demonstrated Abbe's conclusions. Today, a number of applications utilize Abbe's theory and demonstrate its accuracy. As we will see in our discussion, Abbe's concepts allow the methods of signal processing, used in communication theory, for one-dimensional signals, to be applied to two-dimensional signals, such as images.

The intensity distribution found in the frequency plane reflects the symmetry of the object, as can be seen in Figure 10A.10. In Figure 10A.10(a), the diffraction pattern of an equilateral triangle is shown. This pattern should be compared with that shown in Figure 10A.10(b), produced by a scalene triangle. It is possible to use the diffraction patterns produced by different areas of a complex scene to rapidly sort aerial images, as illustrated by the images shown in Figure 10A.11. Of particular interest are the diffraction patterns produced by surface waves on the ocean. From the orientation and scale of these diffraction patterns, the wave pattern can be analyzed.

10A.3 Amplitude Spatial Filtering

A more complicated object than the sinusoidal one we have considered would contain many more frequencies, but the analysis just completed would still apply. An aperture, in the frequency plane, would restrict the maximum frequency that could pass through the imaging system, limiting the resolution of the resulting image. Using the terminology of communication theory, the aperture would act as a *low-pass filter*. An example of low-pass spatial filtering of an image is shown in Figure 10A.12. In Figure 10A.12(a), a resolution test target and an enlargement of a small section of the target are shown at the top. The imaging

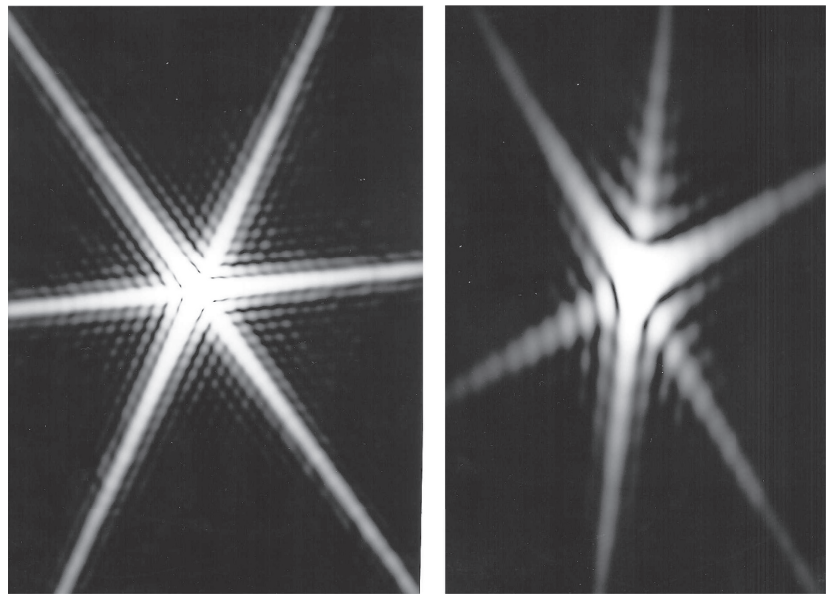

(a) (b)

Figure 10A.10 *Diffraction patterns produced by (a) an equilateral triangle and (b) a scalene triangle. Both diffraction patterns have the threefold symmetry of a triangle, but there is a reduction in the symmetry of the pattern from the scalene triangle.*

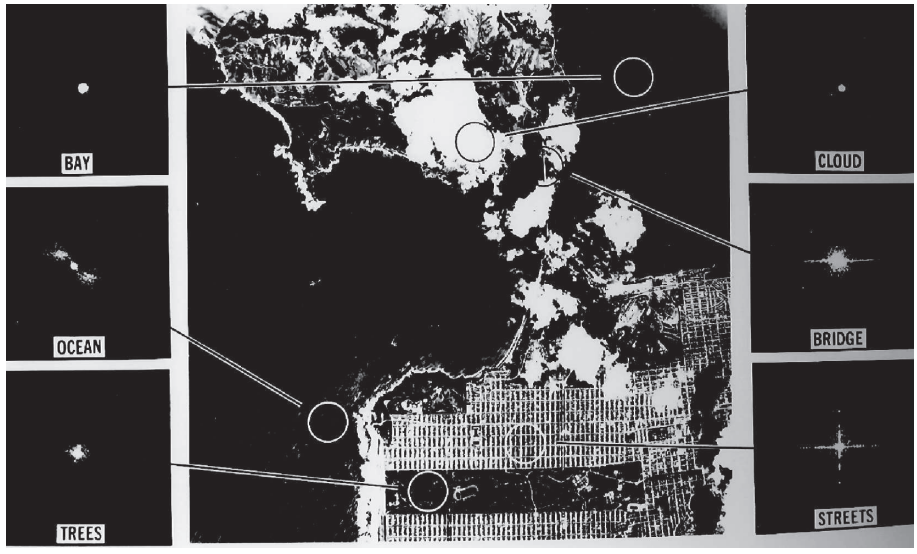

Figure 10A.11 *The images to the right and left are Fraunhofer diffraction patterns taken of small areas of the photograph in the center. The symmetry and extent of the diffraction patterns can be used to recognize geographical classes in the photograph. For example, the diffraction pattern of the ocean can be used to analyze the wave structure on the ocean surface. (Courtesy of Robert Leighty, U.S. Army Engineering Topographic Laboratory.)*

system, as constructed, had no problem resolving 10 lines/mm. In fact, the spatial bandpass of the imaging system was 63 lines/mm. The pictures in Figure 10A.12(b) are identical to those in (a), but now the imaging system has a circular aperture, centered on the optical axis, in the frequency plane, which reduces the spatial bandwidth of the imaging system from 63 to 6 lines/mm by blocking the passage of the high spatial frequencies. After the reduction in spatial bandwidth, the imaging system can just resolve the 6 lines/mm pattern.

A disk-shaped obstruction placed on the optical axis would act as *a high-pass* filter, preventing low spatial frequencies from contributing to the image. High-pass filtering with such an obstruction is shown in Figure 10A.13. With no obstructions in the frequency plane, the imaging system had a spatial bandwidth of 63 lines/mm, as shown in Figure 10A.13(a). With a disk centered on the optical axis, in the frequency plane, the spatial bandwidth of the imaging system is reduced, by restricting its low-spatial-frequency response. Three different spatial bandwidths are shown in Figures 10A.13(b–d). The low-frequency bars are eliminated by the high-pass filter, but their edges are still observable. In image processing, this is called *edge enhancement*. The high spatial frequencies needed to describe the rapidly changing transmission at the edge of an object are allowed to pass through the system; the slowly varying transmission from the bulk of the object, described by low spatial frequencies, is stopped by the disk.

A frequent application of amplitude spatial filtering is the use of a simple circular aperture to smooth the output beam of a laser. The fundamental (TEM_{00}) mode of a laser, using a conventional Fabry–Perot resonator as the cavity, is a Gaussian wave with amplitude

$$E = Ae^{-(x^2+y^2)/\rho^2},$$

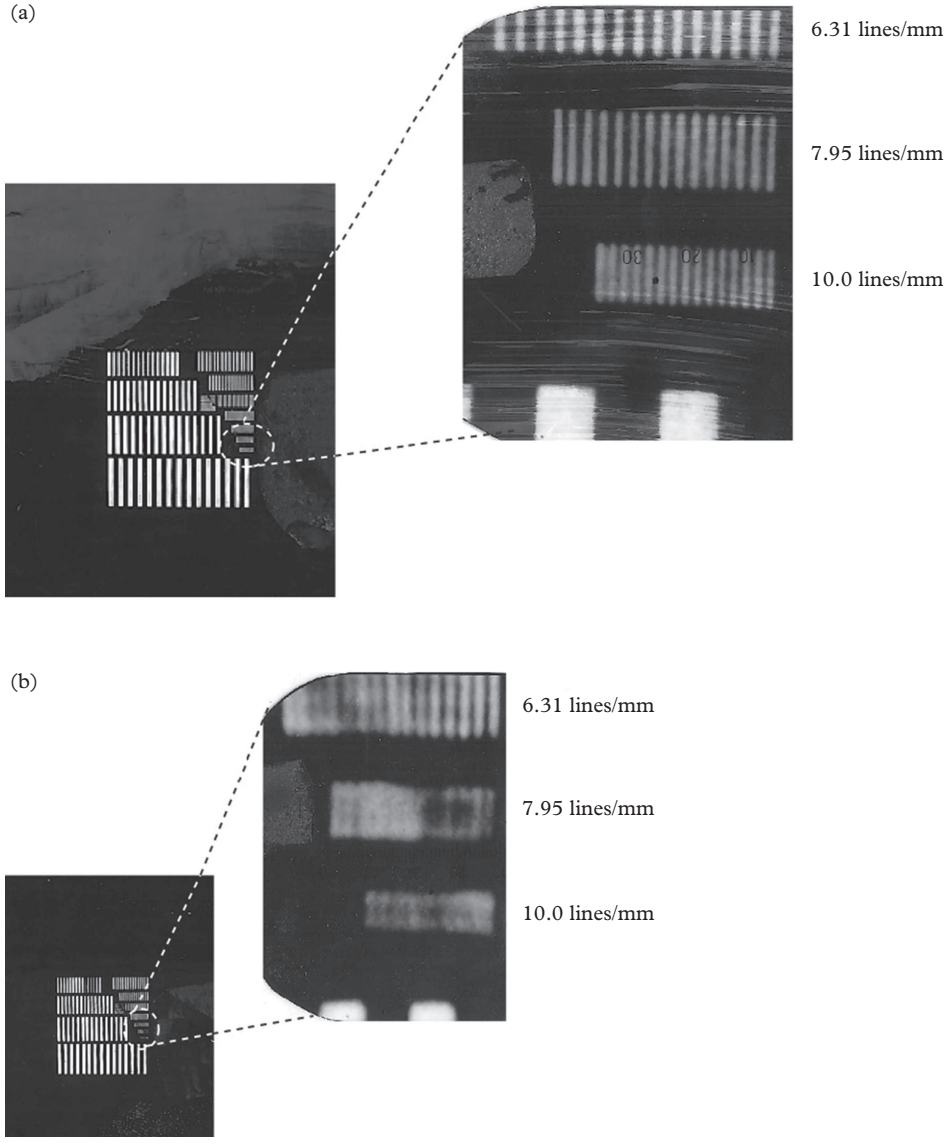

Figure 10A.12 *(a) Resolution chart imaged by a optical system with a maximum spatial frequency of 63 lines/mm. (b) Optical low-pass filtering performed by introducing a circular aperture in the frequency plane of an imaging system similar to the one shown in Figure 10A.2. The resolution of the optical system has been reduced by a factor of about 10. Now, we can just resolve 6.3 lines/mm.*

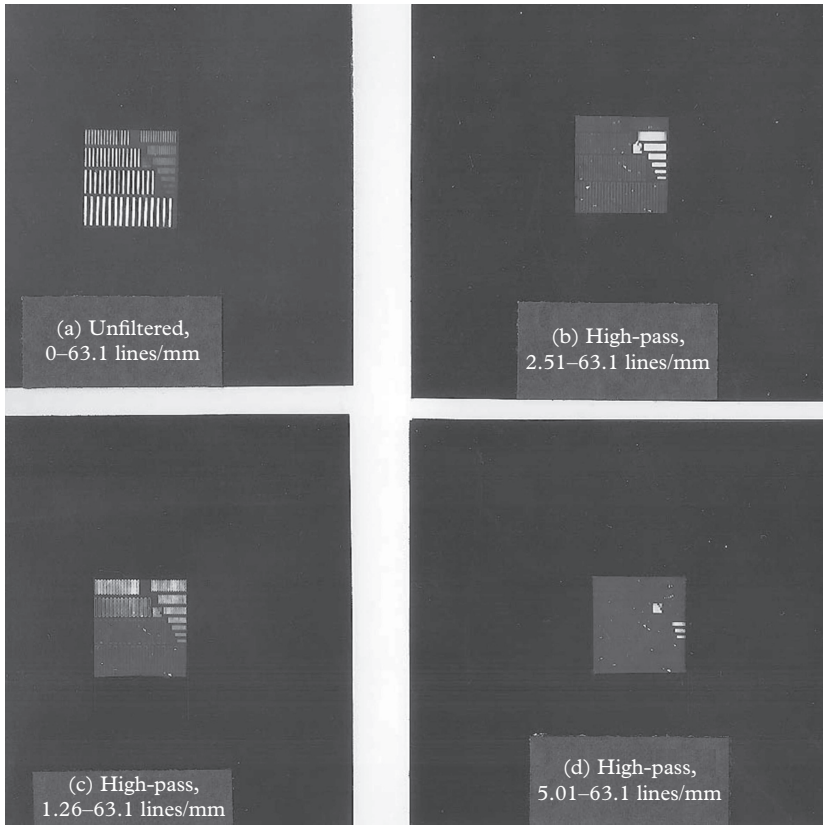

Figure 10A.13 *(a) Unfiltered high-resolution image identical to that in Figure 10A.12(a). Optical high-pass spatial filtering was accomplished by placing a disk in the frequency plane of the imaging system shown in Figure 10A.2. (b–d) Images produced after placing three unique disks in the frequency plane with diameters in the ratio of 1:2:4.*

where A and ρ are the wave constants that were defined in Chapter 9; see (9.46). The Fourier transform of the Gaussian wave is

$$\mathcal{F}\{E\} = A\pi\rho^2 e^{-\pi^2\rho^2\left(\xi^2+\eta^2\right)}.$$

This result assumes an ideal beam; however, the laser beam departs from this simple theoretical function because of imperfections in the laser. We can treat the departures from the ideal beam by adding a correction to the laser's light field: $E_r = E + \Delta E$. The fluctuations described by ΔE will create spatial frequencies at much higher values than $1/\rho$. If we place in the back focal plane of a lens, of focal length f, an aperture with a diameter of approximately $\lambda f/\rho$, then we can eliminate the fluctuations at high spatial frequencies and generate an ideal beam.

A typical experimental arrangement used to produce a plane wave is shown in Figure 10A.14. A laser beam strikes a microscope objective from the left. The wave is focused down to a spot by the microscope objective, and a pinhole is positioned so that it allows only the DC component to pass on to a second lens. As shown schematically in Figure 10A.14, the beam's wavefront departs from a plane wave, but the pinhole removes the higher spatial frequencies contained in the initial beam to produce a final beam with a

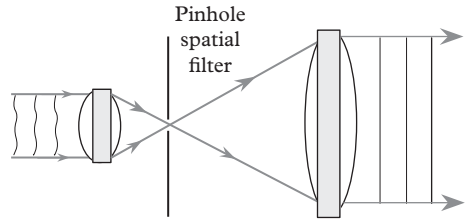

Figure 10A.14 *Spatial filter to produce a plane wave. A laser beam strikes a microscope objective from the left. The beam's wavefront departs from a plane wave. The wave is focused down to a spot by the microscope objective, and a pinhole is positioned to allow only the DC component to pass on to a second lens. Often, the focal length of the second lens is selected to produce a larger-diameter beam of light.*

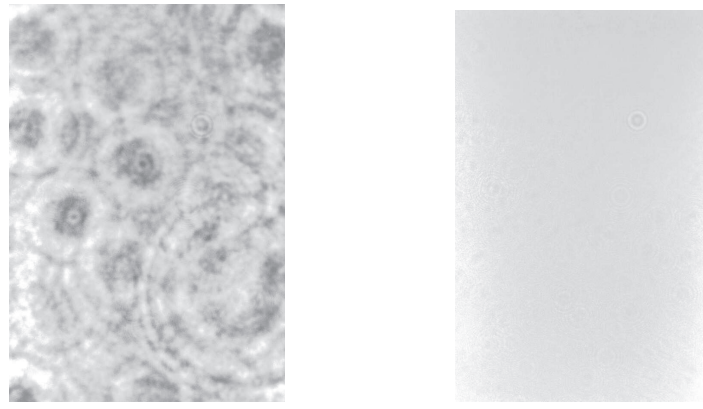

Figure 10A.15 *Laser beam (a) before and (b) after spatial filtering.*

plane wavefront. Figure 10A.15 shows an image of a beam before (a) and after (b) spatial filtering. In order to magnify the diameter of the beam, the focal length of the second lens is usually much larger than the microscope objective.

10A.4 Apodization

The amplitude distribution of a wave after passing through an aperture, has not only a central maximum but also a number of secondary maxima, called sidelobes in radio-frequency antenna design. It is desirable, when operating an imaging system near its diffraction-limited resolution, to reduce the sidelobes. This can be done by a process known as *apodization* (the term is derived from the Greek word meaning foot). Apodization has as its objective the removal of the secondary diffraction maxima produced by an aperture with sharp boundaries.

We have just discussed modifying a beam by removing spatial frequencies with an opaque screen in the spatial frequency plane. By modifying the edge of the diffracting aperture, the secondary maxima contained in the Fraunhofer diffraction pattern can also be modified. A simple example will make this application of spatial filtering clear.

Assume that the aperture of the optical system is a simple slit and ignore the y-dependence:

$$f(x) = \begin{cases} 1, & -\frac{1}{2}b \le x \le \frac{1}{2}b, \\ 0, & \text{all other } x. \end{cases}$$

The Fraunhofer diffraction pattern produced by this aperture is equal to the Fourier transform of the aperture:

$$F(\omega_x) = \int_{-b/2}^{b/2} e^{-i\omega_x x}\, dx$$

$$= \frac{b \sin(\omega_x b/2)}{\omega_x b/2}.$$

This result is identical to that obtained in Chapter 10, see (10.18). We now apodize the aperture by changing its transmission function to a cosine function:

$$f(x) = \begin{cases} \cos\dfrac{\pi x}{b}, & -\dfrac{1}{2}b \le x \le \dfrac{1}{2}b, \\ 0, & \text{all other } x. \end{cases}$$

The Fraunhofer diffraction pattern produced by this aperture is

$$F_a(\omega_x) = \int_{-b/2}^{b/2} \cos\left(\frac{\pi x}{b}\right) e^{-i\omega_x x}\, dx$$

$$= \cos(\omega_x b/2)\, \left(\frac{1}{\omega_x + \pi/b} - \frac{1}{\omega_x - \pi/b}\right).$$

The apodization smoothes the edge of the aperture from a discontinuous change in transmission to a continuous change. The result of apodization is a diffraction amplitude given by

$$F_a(\omega_x) = \frac{2\pi}{b}\left[\frac{\cos(\omega_x b/2)}{(\pi/b)^2 - \omega_x}\right].$$

Comparing the amplitudes of the diffraction patterns for these two slit functions, we find that the amplitude on the optical axis is given by $E_a(0) = 2b/\pi$ and $E(0) = b$. Apodization has reduced the intensity on the optical axis of the apodized aperture to 41% of the intensity of the slit aperture.

If the widths of the central peaks of the diffraction patterns are compared, we find that the apodized central maximum is broader. The first minimum in the diffraction from a slit occurs when $\omega_x = \pi/b$. The first minimum in the diffraction pattern of the apodized aperture occurs when $\omega_x = 3\pi/b$. The central spot in the diffraction pattern from the apodized aperture is wider than the central spot produced by the slit.

From the analysis so far, the advantage provided by apodization is not clear. The advantage becomes apparent when the intensities in the sidelobes of the diffraction patterns are compared. The first secondary maximum in the diffraction pattern for the apodized aperture occurs when $\omega_x b/2 = 2\pi$. The amplitude of the diffraction wave at this secondary maximum is $2b/15\pi$. The ratio of the secondary maximum intensity to the on axis intensity for the apodized pattern, is

$$\left[\frac{F_a(4\pi/b)}{F_a(0)}\right]^2 = \left(\frac{2b/15\pi}{2b/\pi}\right)^2 = 0.0044.$$

When we calculate the same intensity ratio for the diffraction pattern from a rectangular aperture, we obtain 0.047.

The advantage of apodization is now clear. The relative intensity of the first secondary maximum in the diffraction pattern of the apodized aperture is a factor of ten smaller than that found in the diffraction pattern of the rectangular aperture. A comparison of the two diffraction patterns is shown in Figure 10A.16. The improvement in sidelobe intensity has come at the expense of on-axis intensity and central beam width. In photography, apodization is used to produce the aesthetic quality of blur about the subject of the photograph called bokeh.

10A.5 Phase Filtering

With a coherent optical system, both the phase and amplitude of the light wave are available. Several applications in the field of optical processing utilize spatial filtering operations to observe the phase changes experienced by a light wave.

The *dark-ground illumination* microscopy technique uses a circular obstruction to prevent the DC component from propagating past the frequency plane. (The circular obstruction is sometimes called a *DC stop* because it is used to remove the DC component of the diffraction field.) The image generated is an edge-enhanced image. The large bars in Figure 10A.13 are examples of edge-enhanced images. This technique permits the observation of objects that are transparent but scatter a small amount of light. The scattered light is at high spatial frequencies and misses the DC stop; the majority of the light, which is unscattered, is removed from the image by the obstruction.

A second phase filtering technique, called the *Schlieren method* [2], replaces the circular obstruction of the dark-ground technique by a knife edge that interrupts all spatial frequencies on one side of the DC component. This technique produces an intensity distribution that is proportional to the phase change produced by the object. The Schlieren method is used in aerodynamics to measure density changes associated with airflow.

A special case of the Schlieren method, the *Foucault knife-edge test*, is used to evaluate lens and mirrors. This technique brings a knife edge into the DC spot in the back focal plane of an optical component under test (see Figure 10A.17). Aberrations in the optical system

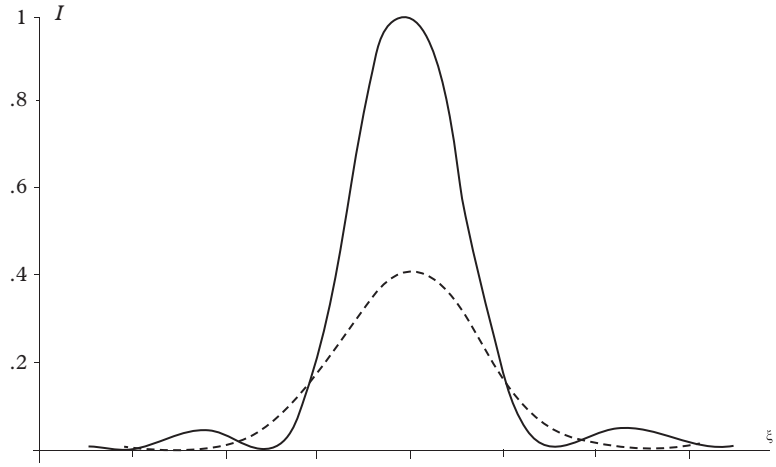

Figure 10A.16 *Diffraction patterns for a slit (solid curve) and for a slit apodized by a cosine function (dashed curve).*

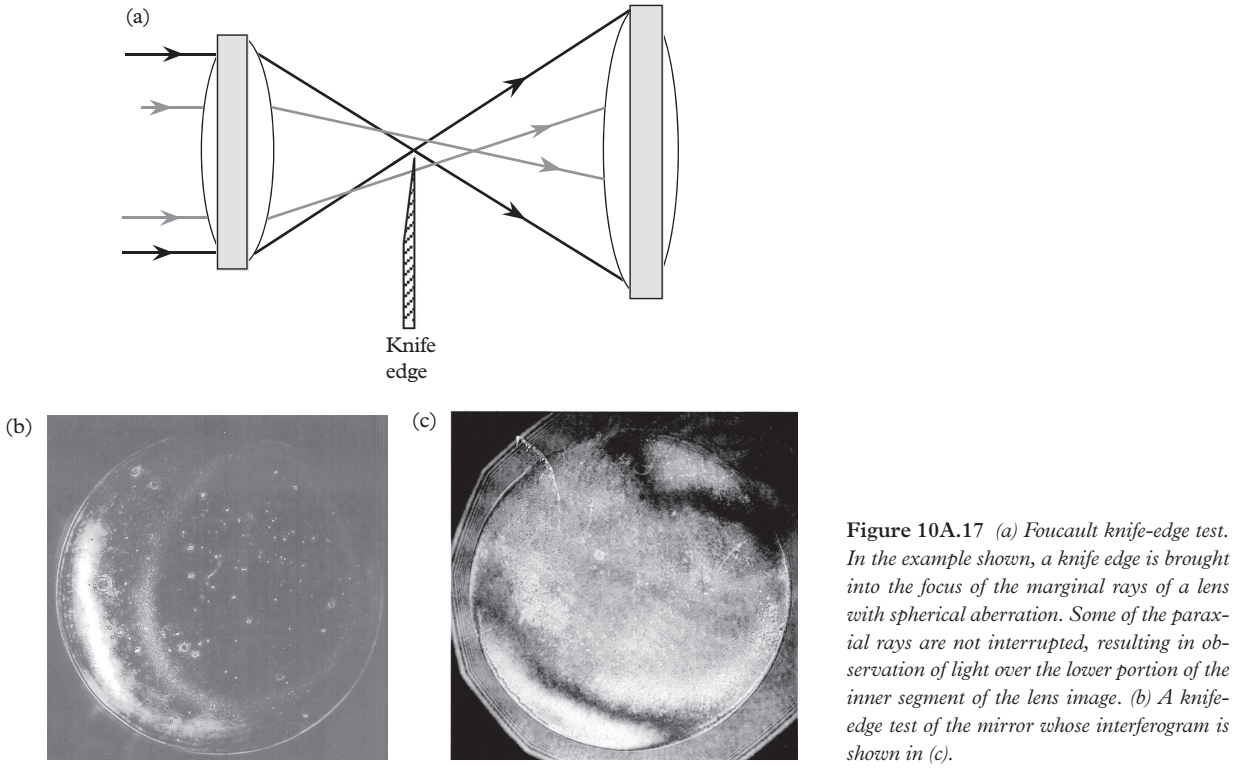

Figure 10A.17 *(a) Foucault knife-edge test. In the example shown, a knife edge is brought into the focus of the marginal rays of a lens with spherical aberration. Some of the paraxial rays are not interrupted, resulting in observation of light over the lower portion of the inner segment of the lens image. (b) A knife-edge test of the mirror whose interferogram is shown in (c).*

will cause the light from different portions of the optical element to be focused at different positions along the optical axis (see Appendix 5B). The portion of the lens producing these rays can be identified by interrupting light at different positions along the optical axis.

The above two processing schemes are special cases of amplitude filtering. There is also a processing technique that operates only upon the phase of the light wave. This technique was developed by **Fritz Zernike (1888–1966)** to generate images of microscopic organisms. Zernike received the Nobel Prize for this invention, called the *phase contrast microscope* (Figure 10A.18). This microscope is now used extensively in the study of biological specimens.

Rather than removing the DC spot in the frequency plane, Zernike shifted the phase of this portion of the spatial frequency spectrum by $\pi/2$ (a quarter wave) relative to the phase of the rest of the spatial spectrum. The technique allows the observation of transparent objects that absorb very little light, by converting phase changes introduced by the transparent object into intensity changes. The conversion from spatial phase variations to equivalent variations in the intensity is accomplished by placing a transparent plate in the frequency plane of the optical system with a quarter-wave coating placed over the low- frequency portion of the spatial spectrum.

To understand the Zernike phase contrast microscope, assume that the object absorbs no light but rather has a transmission function that is a spatial modulation of only the phase:

$$f(x) = e^{i\phi(x)}.$$

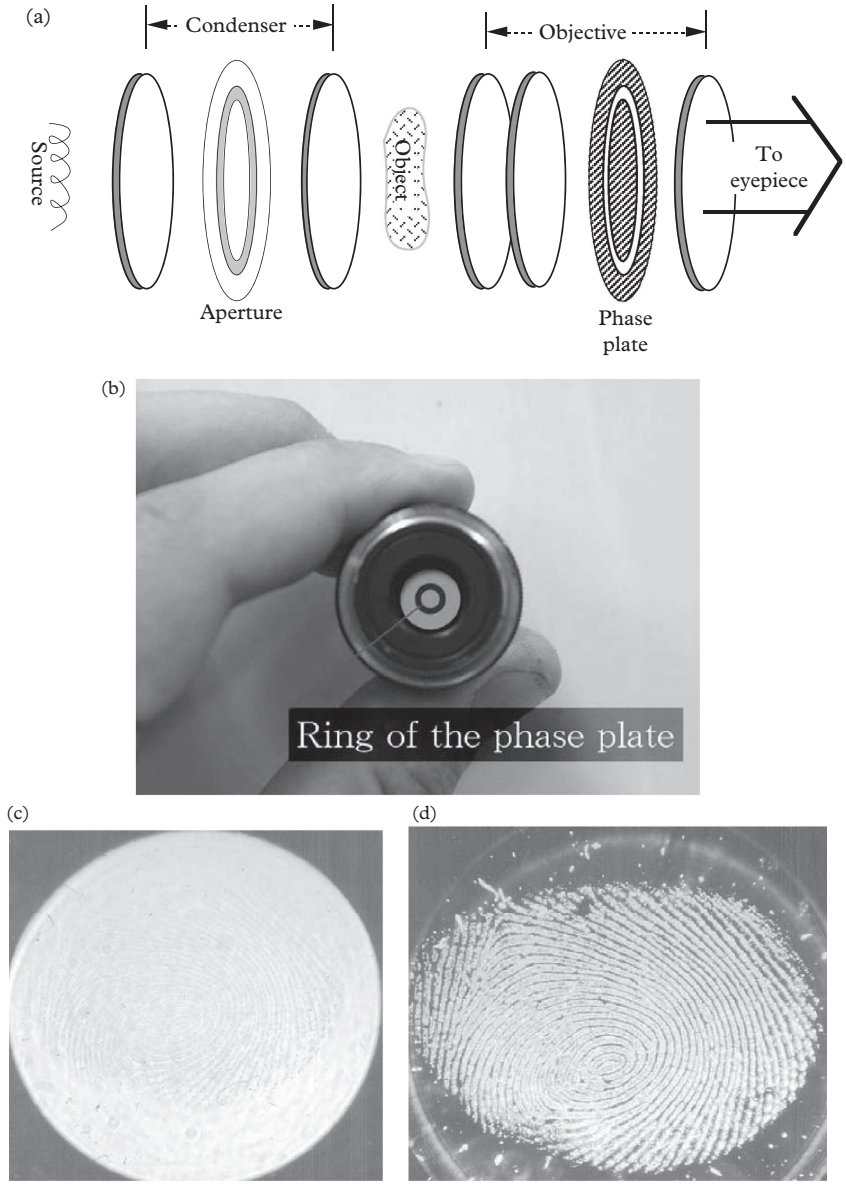

Figure 10A.18 *(a) Phase contrast microscope. The aperture is focused on the phase plate (b). Low spatial frequencies are given a quarter-wave phase shift relative to higher spatial frequencies. (c) Conventional image of a fingerprint produced by skin oils. (d) Fingerprint from (c) viewed through a phase contrast microscope.*

We will also assume that the index of refraction is very nearly that of its surroundings. For a living organism in water, this approximation is very good and allows the exponent to be approximated by the first two terms of its power series:

$$f(x) \approx 1 + \phi(x).$$

The Fourier transform of this transmission function is of the form

$$E(\omega_x) = \int_{-\infty}^{\infty} [1 + i\phi(x)]e^{-i\omega_x x}\, dx$$

$$= \mathcal{F}\{1\} + \mathcal{F}\{\phi(x)\} = A(\omega_x) + i\Phi(\omega_x).$$

The functions $A(\omega)$ and $\Phi(\omega)$ have a relative phase difference of 90°, as indicated by the multiplicative factor i.[1] We will demonstrate that if the relative phase of the two functions can be retarded or advanced, then it is possible to produce an image of the phase object.

We construct a spatial filter that modifies only the phase of the light, by the deposition of a quarter-wave dielectric layer on an optically flat plate. By using a flat plate of transparent material, that is made thicker near the optical axis, we can shift the phase of the low spatial frequencies by more than that of the high spatial frequencies. This phase plate is placed in the F plane of Figure 10A.2, which represents a microscope when the appropriate values for f_1 and f_2 are selected.

$A(\omega)$ is the diffraction pattern of the entire aperture, and, because there is no amplitude modulation in the aperture, it is nonzero only near $\omega = 0$; i.e., $A(\omega)$ contains only low spatial frequencies. The phase plate will modify only the phase of $A(\omega)$, because of the limited extent of the dielectric layer. The diffraction pattern, modified by the phase plate, is

$$E'(\omega_x) = A(\omega_x)e^{\pm i\pi/2} + i\Phi(\omega_x) = \pm i[A(\omega_x) \pm \Phi(\omega_x)].$$

[The positive and negative signs allow the use of a quarter-wave layer in the DC region of the spectrum (a positive phase plate) or a quarter-wave layer in the high-frequency region of the spatial spectrum (a negative phase plate) to obtain the relative phase shift.]

The image at plane I of Figure 10A.2 is the inverse transform of the phase-modified signal. The inverse transform is given by $f' = \pm i(1 \pm \phi)$ and has an intensity distribution (neglecting ϕ^2) given by $1 \pm \phi(x)$. To the degree that the approximation of small spatial phase variation is correct, the phase filter provides an image whose variation in intensity is directly proportional to the variation in phase in the object.

The actual optical design is slightly more complicated than implied by the above discussion. To increase the amount of available light and to increase the depth of field, which will eliminate the confusion of out-of-focus images, a source in the form of an annular ring is used. With an annular source, the phase plate must have a quarter-wave layer in the form of a ring; see Figure 10A.18(b).

10A.6 Phase and Amplitude Filter

We have repeatedly used the fact that a lens can generate the complex representation of the Fourier transform $G(\omega_x, \omega_y)$ of a function $g(x, y)$ to perform simple signal processing operations on $g(x, y)$. The operations that have been discussed are limited by the complexity of the filter placed in the frequency plane. To perform more complicated operations, filters that operate on both the amplitude and phase of the input function are needed. One useful complex operation that can be performed with a complex filter is the correlation of two functions. By storing the complex representation $G(\omega_x, \omega_y)$ in the frequency plane of the lens, a convolution operation can be performed between $g(x, y)$ and any other function, say $f(x, y)$. The calculation of the convolution is accomplished by multiplying Fourier transforms, according to (6A.10), and generating the Fourier transform of the product.

[1] Recall that $e^{\pm i\pi/2} = \pm i$.

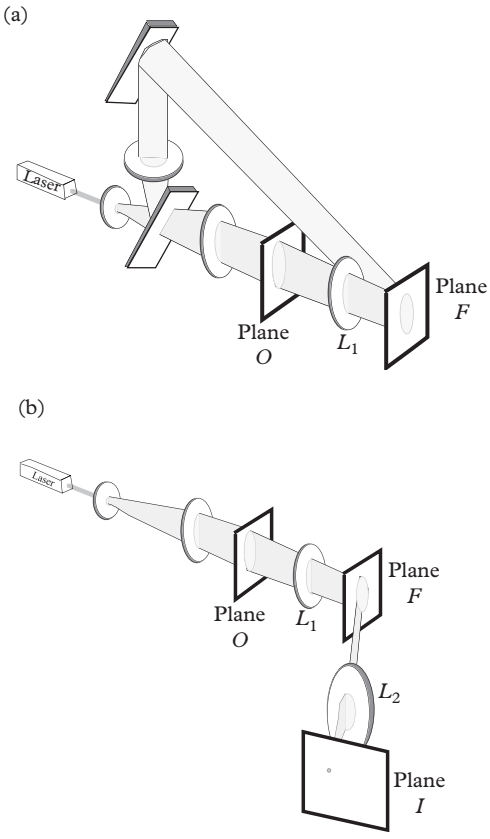

Figure 10A.19 *(a) Storage of the phase and amplitude of the Fourier transform of the input function $g(x, y)$ is accomplished by interfering the Fourier transform with a reference beam and recording the interference pattern. (b) Optical configuration used to calculate the correlation and convolution of pairs of two-dimensional functions.*

Optically, a lens configuration similar to the one shown in Figure 10A.2 will perform the convolution operation.

Initially, the function $g(x, y)$ is placed in the front focal plane of lens L_1, labeled plane O, and its Fourier transform is stored in the frequency plane F; see Figure 10A.19(a), where the labels identify the optical components of Figure 10A.2. The function $g(x, y)$ in plane O is then replace by a new function $f(x, y)$, and its Fourier transform is projected onto the stored representation of $G(\omega_x, \omega_y)$ by L_1, as shown in Figure 10A.19(b). The light transmitted through the complex filter in the frequency plane F is the product of $G(\omega_x, \omega_y)$ and $\mathcal{F}(\omega_x, \omega_y)$. Lens L_2, behind the frequency plane, generates the Fourier transform of the product and in plane I is a light distribution representing the convolution of f and g.

The technique used for storing the complex filter $G(\omega_x, \omega_y)$ shown in Figure 10A.19(a) was developed by **Anthony VanderLugt**. (The first successful experiments were on December 7, 1962.) The phase and amplitude of the complex transform are stored as an amplitude transmittance variation, produced by an interferometric technique to be discussed in Appendix 12B. The technique allows the storage of not only the complex function $G(\omega_x, \omega_y)$ but also its complex conjugate $G^*(\omega_x, \omega_y)$. The presence of the complex conjugate means that the correlation function of $f(x, y)$ and $g(x, y)$ may also be generated, using the configuration displayed in Figure 10A.19(b).

The calculation of the correlation between the functions g and f can be demonstrated both mathematically and experimentally by an appropriate choice of f and g. The family of Gaussian functions introduced in Chapter 9 is a good choice for the demonstration of optical correlation. The Fourier transform of any of the Gaussian functions yields the function itself; thus, the mathematical performance of the correlation operation is very simple.

Experimentally, this class of functions are easy to produce because they form the resonant modes of a Fabry–Perot resonator. By properly adjusting a Fabry-Perot resonator, a function $g(x, y)$ can be produced and made to fall on plane O of Figure 10A.19(a). In the example to be described here, the simplest Gaussian wave, a Gaussian function, is used as $g(x, y)$.

After the reference $G^*(\omega_x, \omega_y)$ has been stored, a generalized output of the Fabry–Perot is made to fall on plane O of Figure 10A.19(b). The two-dimensional intensity distributions of the various modes produced by the Fabry–Perot are shown in Figure 10A.20(b–e).

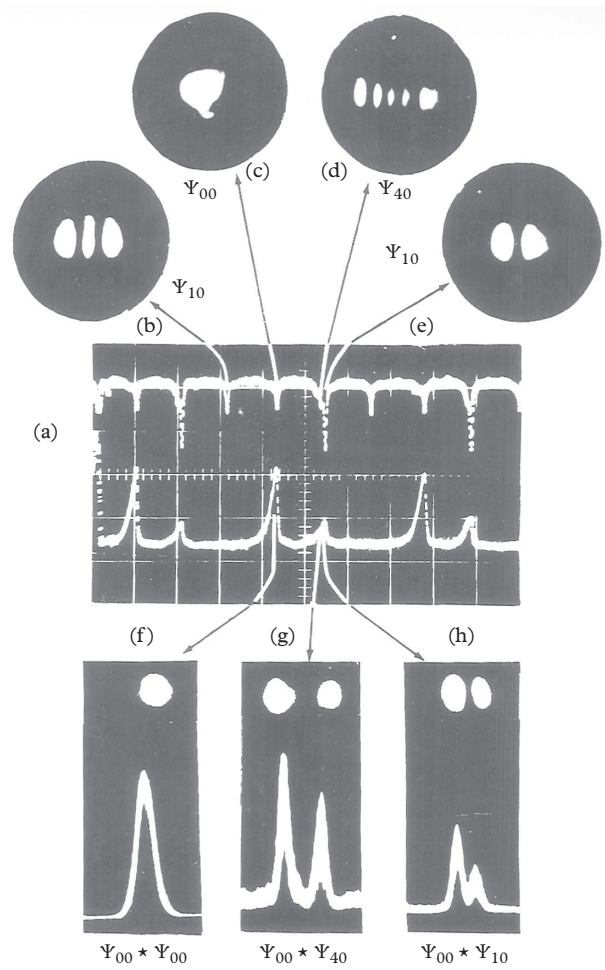

Figure 10A.20 *Pattern recognition using an optical processor. Here, the ability to store a recording of the Fourier transform of a function and then correlate that function with a number of similar functions is demonstrated. (a) Transmission of a Fabry–Perot interferometer, recorded on axis, as the mirror separation is changed. The interferometer was aligned so that a number of transverse Gaussian modes were present. The spatial intensity distributions of these modes are identified in (b)–(e). A filter was recorded of the fundamental Gaussian mode (c), the Gaussian wave discussed in Chapter 9. The autocorrelation of this function is shown in (f) and the cross correlations with two other spatial modes are shown in (g) and (h). Figure 10A.21 displays the theoretical calculation of the correlation functions.*

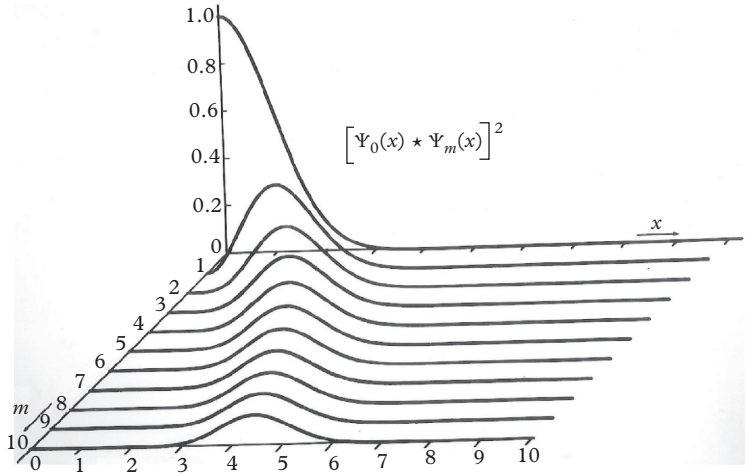

Figure 10A.21 *The spatial modes used in the experiment shown in Figure 10A.20 can be represented by a set of analytic functions and those functions used to calculate the correlation functions. The theoretical correlation functions associated with the experiment of Figure 10A.20 are shown here. The calculation represents the intensity distribution from the center of plane I out along the x-axis. The curves labeled 0, 4, and 1 should be compared with the images in Figure 10A.20(f), (g), and (h), respectively.*

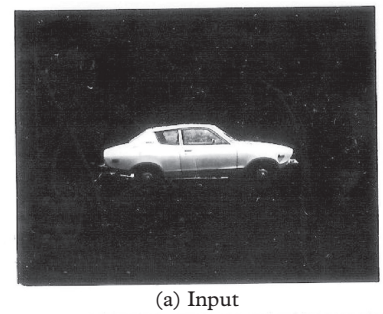

(a) Input

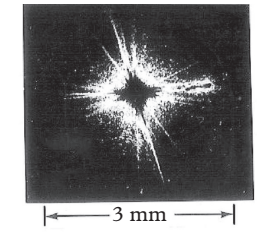

(b) Matched filter

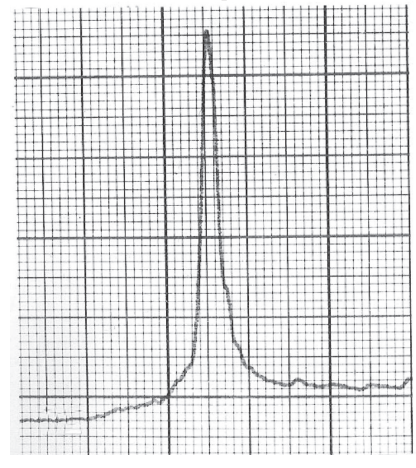

(c) He–Ne laser correlation

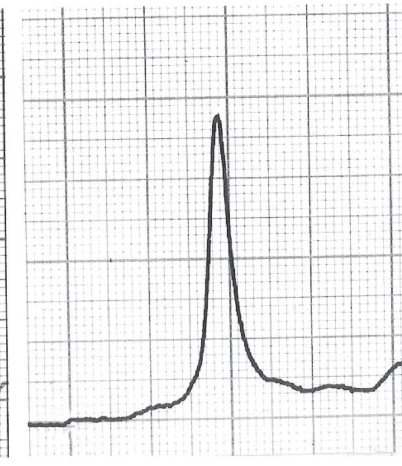

(d) Diode laser correlation

Figure 10A.22 *(a) Image used in the optical system of Figure 10A.19. (b) Image of the recording made in plane F of Figure 10A.19(a). (c, d) Intensity scans through the correlation function in plane I of Figure 10A.19(b). The two traces were made with different laser sources, with no effect on the correlation function.*

The top trace in Figure 10A.20(a) displays the transmission of the Fabry–Perot on axis, as the mirror separation is changed. The various modes are identified with the peaks in transmitted intensity. The transmitted intensity, on the optical axis, at plane *I* is shown by the bottom trace in Figure 10A.20(a).

Of greater interest are the two-dimensional intensity distributions recorded in plane *I*. These are the correlation functions generated by the optical system and can be compared to the calculated correlation functions shown in Figure 10A.21. The calculated functions show the intensity distribution measured, in plane *I*, outward from the optical axis. Below each recording of the intensity distribution in plane *I* shown in Figure 10A.20 is an intensity scan across this plane. The agreement between these scan lines and the calculated correlation functions, labeled 0, 1, and 4, is excellent.

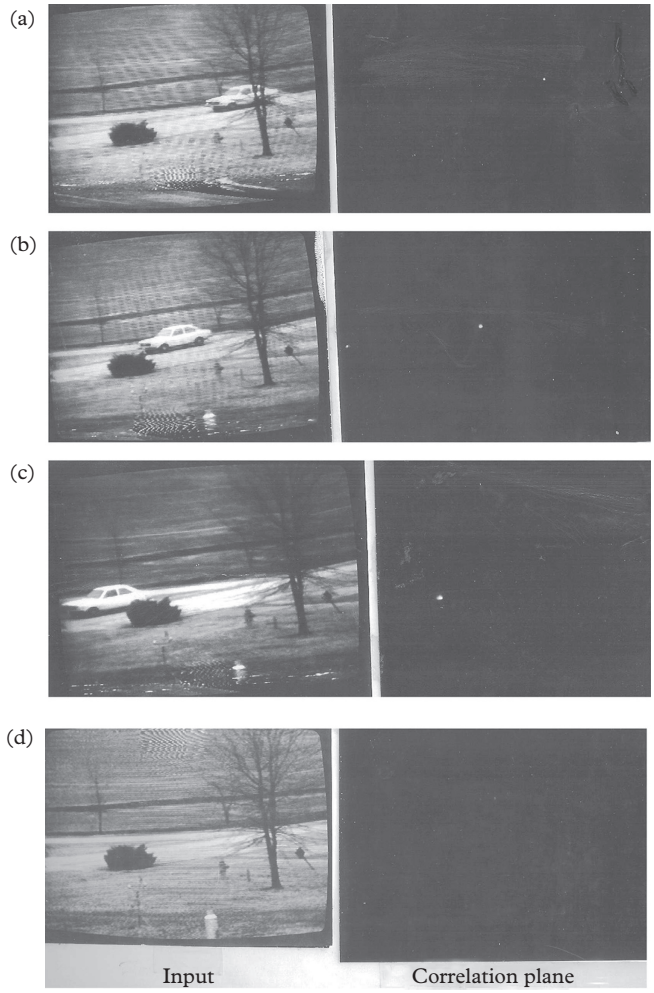

Figure 10A.23 *The reference filter shown in Figure 10A.22 is placed in plane F of the optical processor shown in Figure 10A.19(b). A videotape of a car driving down a road is played into plane O, and the spatial intensity distribution seen in plane I is recorded. The left column shows several frames from the videotape (the herringbone structure seen on the images results when the videotape is stopped to allow the recording of the picture). The image in the second column is the equivalent frame recorded at plane I. Note the bright spot of light in the correlation plane that identifies the car and its input scene location.*

The correlation operation compares two signals and generates a measure of the similarity of the two functions. This is why the correlation operation can be used for the complex pattern recognition task of identifying and tracking a car. The Fourier transform of the car, shown in Figure 10A.22, is stored in plane F of Figure 10A.19(b) as $G(\omega_x, \omega_y)$, and the images shown in the left column of Figure 10A.23 are the functions $f(x, y)$ displayed in plane O. The light distribution in plane I is shown in the right column of Figure 10A.23. A bright spot of light occurs at the same location in plane I as the car does in plane O, and as the car moves through the object field, the spot of light moves through the correlation field in plane I.

REFERENCES

1. Klein, M.V. and T.E. Furtak, *Optics*. 2nd ed. 1986: Wiley.
2. Settles, G.S., *Schlieren and Shadowgraph Techniques: Visualizing Phenomena in Transparent Media*. 2 ed. 2001: Springer-Verlag.

Appendix 10B Imaging

10B.1 Introduction

One of the most important applications of optics is the task of imaging. The theory of image formation developed independently from diffraction, but as the capability to image improved, it became necessary to consider the limitations imposed upon imaging by diffraction. Most imaging tasks encountered in our daily experience involve incoherent images, so we will examine incoherent illumination first. The approach we will take is based upon communication theory [1].

We will theoretically develop a one-dimensional model of an incoherent imaging system and use the model to discuss two criteria that have been used to characterize the imaging capability of an optical system.

The optical system will be treated as a linear system, characterized by its impulse response or by the Fourier transform of the impulse response. The convolution theorem will be used to show that the impulse response of the optical system modifies the intensity variations found in the object, creating an image that is an inexact reproduction of the object.

We will show that the incoherent imaging system is linear in intensity, while a coherent imaging system is linear in field amplitude. We will discover that the criterion for resolution must be applied with care to a coherent system. When properly applied, we will find that the resolution criterion requires a coherent optical system to have a larger aperture than an incoherent system to produce equivalent imaging capability.

We will end with a look at future efforts in computational optics. The incorporation of CCD and CMOS detector arrays in modern photography allows the capture of digital imagery that can be optically coded images. These coded images can be computationally decoded to produce new images. Coded aperture imaging was initially applied in astronomy and X-ray imaging to boost image quality [2]. For example, a pinhole pattern was coupled with the mathematical operation reversing the effects of convolution to recover an image [3]. Now, the research community is expanding the concept to lens-based coded apertures [4] and micro-optical coded lens arrays [5, 6] to increase optical performance. We will examine a simple example of the use of aperture coding.

10B.2 Incoherent Imaging

An optical system utilizing incoherent illumination can be considered to be linear in intensity. The impulse response used to describe this linear system is found by calculating the absolute value squared of the amplitude impulse response. The amplitude impulse response is obtained using the Huygens–Fresnel integral (9.20) to follow the propagation of light from a point source, through an optical system, to the image plane. This procedure can be used to demonstrate that the impulse response of an imaging system is the Fourier transform of its aperture function.

Linear system theory states that an optical system with an amplitude impulse response $\mathcal{R}(x)$ and an input wave $\tilde{E}_O(x,t)$ has a scalar wave output of

$$\tilde{E}_I(x,t) = \int_{-\infty}^{\infty} \tilde{E}_O(\xi,t)\mathcal{R}(x-\xi)\,d\xi,$$

where the subscripts O and I represent object and image waves. We will restrict the discussion to one dimension. [In this appendix, we will use the spatial coordinate ξ rather than the spatial frequency ω_x in our discussions, since the coordinate is directly related to the image. The results we derive can easily be extended to two dimensions. For example, if the aperture of the optical system had a rectangular shape, then $\mathcal{R}(x,y)$ would be given by (10.18), and if the aperture had a circular shape, then $\mathcal{R}(r)$ would be given by (10.25).]

The time average of the square of the amplitude of the output wave is the measured quantity. This intensity function is proportional to

$$\langle \tilde{E}_I(x,t)\tilde{E}_I^*(x,t)\rangle = \left\langle \int_{-\infty}^{\infty} \tilde{E}_O(\xi,t)\mathcal{R}(x-\xi)\,d\xi \right\rangle \left\langle \int_{-\infty}^{\infty} \tilde{E}_O^*(\xi',t)\,\mathcal{R}^*(x-\xi')\,d\xi' \right\rangle.$$

The impulse response of the linear system is independent of time, and thus we may remove it, and its complex conjugate, from the time averages:

$$\langle \tilde{E}_I(x,t)\tilde{E}_I^*(x,t)\rangle = \int_{-\infty}^{\infty}\int \langle \tilde{E}_O(\xi,t)\tilde{E}_O^*(\xi',t)\rangle\,\mathcal{R}(x-\xi)\mathcal{R}^*(x-\xi')d\xi\,d\xi'.$$

The time average in the integral can be identified as the unnormalized mutual coherence function introduced in Chapter 8, (8.29). (In making the connection with the mutual coherence function, we implicitly assume that the light is temporally coherent.)

For spatially incoherent light, it can be shown, using coherence theory, that

$$\langle \tilde{E}_O(\xi,t)\tilde{E}_O^*(\xi',t)\rangle = I_O(\xi)\delta(\xi-\xi'),$$

which is a statement of the fact that all points on a spatially incoherent source are uncorrelated. (The correlation function is a delta function and is zero as soon as we move away from the source point.) Using this identity relation, the integration over ξ' can quickly be performed. The result of the integration states that the output image of the optical system is the convolution of the input intensity with the square of the system's amplitude impulse response. The square of the amplitude impulse response is physically equal to the Fraunhofer diffraction intensity pattern of the system's aperture.

10B.2.1 Resolution Criteria

Some sort of criterion is needed to specify how well an incoherent imaging system performs. Historically, the first criterion used was to specify how well an imaging system could resolve two point objects. We will derive the criterion for an optical system with a rectangular aperture, allowing the use of a one-dimensional theory. The result for a two-dimensional system with a circular aperture will be stated but not derived.

Assume that the aperture of the one-dimensional system, shown in Figure 10B.1, is a slit of width $2a$. The system's impulse response is, from (10.19),

$$\mathcal{R}(\xi)\mathcal{R}^*(\xi) = s(\xi) = \frac{I_d(\xi)}{I_0}$$

$$= \frac{\sin^2 \dfrac{k\xi a}{S'}}{\left(\dfrac{k\xi a}{S'}\right)^2} = \text{sinc}^2 \frac{k\xi a}{S'}. \tag{10B.1}$$

From Figure 10B.1, the source distribution consists of two incoherent point sources, A and B, located, equally spaced about the optical axis, a distance $2b$ apart:

$$I(x) = I_0[\delta(x-b) + \delta(x+b)]. \tag{10B.2a}$$

This distribution is imaged onto the image points A' and B', whose locations, at positions

$$\beta = \pm\frac{bS'}{S},$$

are found by using geometrical optics, (5A.3). In the image plane, geometrical optics predicts a light distribution of

$$I(x') = I_0[\delta(x'-\beta) + \delta(x'+\beta)]. \tag{10B.2b}$$

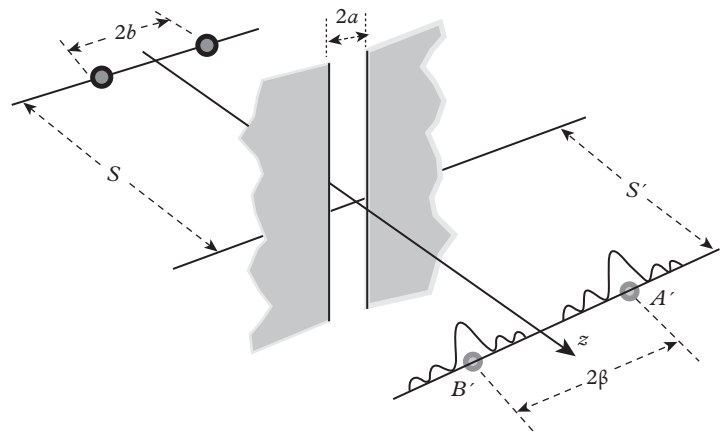

Figure 10B.1 *Geometry for imaging points A and B onto the positions A′ and B′ using an imaging system with a rectangular aperture.*

The image intensity is obtained by convolving (10B.1) with (10B.2b):

$$I(\xi) = \int_{-\infty}^{\infty} I_0[\delta(x' + \beta) + \delta(x' - \beta)] \operatorname{sinc}^2\left[\frac{ka}{S'}(x' - \xi)\right] dx'$$

$$= I_0\left\{\operatorname{sinc}^2\left[\frac{ka}{S'}(\xi + \beta)\right] + \operatorname{sinc}^2\left[\frac{ka}{S'}(\xi - \beta)\right]\right\},$$

We wish to discover the minimum value of b for which we can just resolve image points A' and B'. One criterion that can be applied is the Rayleigh criterion, restated here from Appendix 10A as follows:

> *Two image points A' and B' in the image plane can be just resolved if the central diffraction maximum of one image falls on the first diffraction pattern zero of the second image.*

The location of the central maximum and the first diffraction zero are obtained from

$$\frac{ka}{S'}(\xi - \beta) = 0, \quad \frac{ka}{S'}(\xi + \beta) = \pi.$$

Arranging the central maximum of image A' to fall on the first minimum of image B' results in

$$2\beta = \frac{\lambda S'}{2a}.$$

This resolution criterion is equivalent to the resolution condition derived in Appendix 10A, using Abbe's theory, (10A.7),

$$\Delta x = \frac{2\lambda f}{D},$$

and is also equivalent to the result obtained in Chapter 9 using Gaussian wave theory for an optical system's minimum beam waist

$$w = \frac{2\lambda f}{D}.$$

From the geometrical optics relationship between b and β, the minimum object separation that can be resolved in the image plane is given by

$$2b = \frac{\lambda S}{2a}. \tag{10B.3a}$$

The resolution criterion is usually stated in terms of the angular extent of the object,

$$\sin\Psi \approx \tan\Psi = \frac{2b}{S},$$

and thus the minimum angular extent of an object that can just be resolved by the optical system is

$$\sin\Psi \approx \frac{\lambda}{2a}. \tag{10B.3b}$$

If we used a circular aperture of radius a, then the resolution criterion would be

$$\sin \Psi = 1.22 \frac{\lambda}{2a}.$$

To generate a feeling for the magnitude of this criterion, we will apply it to a common resolution problem. How far away can we resolve car headlights? We will assume they are spaced 1.5 m apart, restrict the wavelength to 550 nm, and assume the pupil of the eye is dilated to 5 mm. Applying the Rayleigh criterion,

$$\begin{aligned} \theta_R &= 1.22 \frac{\lambda}{d} \\ &= \frac{(1.22)(550 \times 10^{-9})}{5 \times 10^{-3}} \\ &= 1.34 \times 10^{-4} \text{ rad}. \end{aligned}$$

The distance from the eye to the car is

$$\begin{aligned} R &= \frac{1.5}{\theta_R} \\ &= \frac{1.5}{1.34 \times 10^{-4}} \\ &= 11.2 \text{ km}. \end{aligned}$$

The Rayleigh criterion is not a law but rather is a rule of thumb. For that reason, other criteria can be used; one of the most popular is the *Sparrow criterion*:

> *Two image points A' and B' in the image plane can be just resolved if the intensity is a constant as we move from image point A' to point B' in the image plane.*

Mathematically, the Sparrow criterion is stated in terms of the second spatial derivative of the intensity:

$$\left[\frac{\partial^2 I(\xi)}{\partial \xi^2} \right]_{\xi = 0} = 0. \tag{10B.4}$$

We have evaluated the second derivative at the origin because we assume that, as in Figure 10B.1, the two objects and their images are separated by equal distances on either side of the optical axis. The second derivative is obtained by using the relations

$$\frac{\partial}{\partial x} \left(\frac{\sin^2 x}{x^2} \right) = \frac{x^2 \sin 2x - 2x \sin^2 x}{x^4},$$

$$\begin{aligned} \frac{\partial^2}{\partial x^2} \left(\frac{\sin^2 x}{x^2} \right) &= \frac{2x^2 \cos 2x - 2x \sin 2x}{x^4} - \frac{2x^3 \sin 2x - 6x^2 \sin^2 x}{x^6} \\ &= \frac{2 \cos 2x}{x^2} - \frac{4 \sin 2x}{x^3} + \frac{6 \sin^2 x}{x^4}. \end{aligned}$$

We also make use of the fact that the sinc function is an even function, sinc x = sinc($-x$):

$$\frac{\partial^2 I(\xi)}{\partial \xi^2} = \cos\frac{2ka\beta}{S'} - \frac{S'}{2ka\beta}\sin\frac{2ka\beta}{S'} + 3\left(\frac{S'}{2ka\beta}\right)^2 \sin^2\frac{ka\beta}{S'} = 0.$$

This equation can be solved to yield

$$\sin\Psi = \frac{2.606\lambda}{\pi 2a} = 0.83\,\frac{\lambda}{2a}. \tag{10B.5}$$

For a circular aperture, the Sparrow criterion becomes

$$\sin\Psi = \frac{2.976\lambda}{\pi 2a} = 0.95\,\frac{\lambda}{2a}. \tag{10B.6}$$

Figure 10B.2 shows the Rayleigh and Sparrow criteria for a slit aperture and incoherent illumination.

The Rayleigh and Sparrow criteria are too restrictive for general imagery, and attempting to treat a general image as a continuous distribution of point sources is too cumbersome, and often intractable, because of the convolution integral. Instead, another approach, based on linear system theory, is used. We move to spatial frequency space, via the Fourier transform, and describe the linear optical system in terms of its spatial frequency response. The imaging process is described in terms of the convolution integral. The most straightforward implementation of this would describe the imaging process by convolving the object with the impulse response of the optical system. It is usually much easier, however, to utilize the convolution theorem (6A.8) and write the Fourier transform of the convolution as the product of the Fourier transform of the object function with the Fourier transform of the impulse response.

10B.2.2 Optical Transfer Function

The Fourier transform of the impulse response of an optical system is called *the optical transfer function* (**OTF**). It draws its name from the analogy that can be formed between optical and electronic systems. In a linear electronic system, a sinusoidal input wave will result in

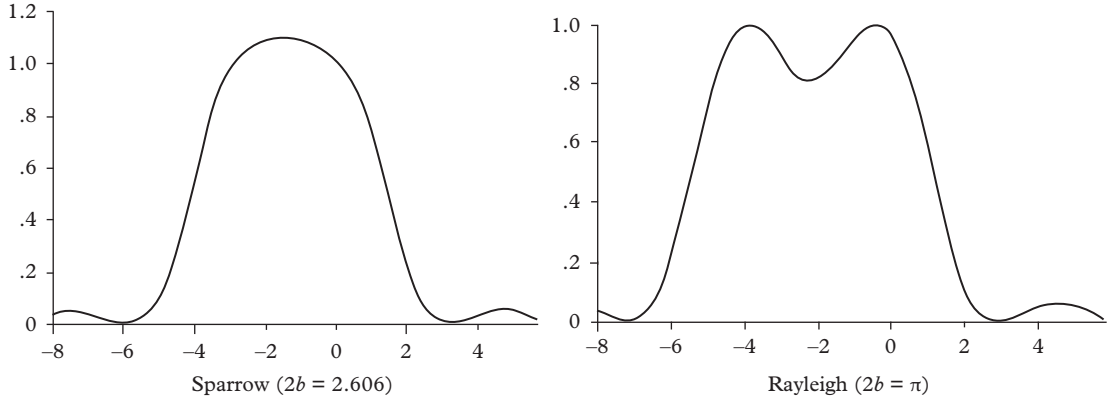

Figure 10B.2 *The Rayleigh (10B.3b) and Sparrow (10B.5) criteria for a slit aperture and incoherent illumination.*

a sinusoidal output wave, with an amplitude and phase modified by the transfer function of the electronic system. We will demonstrate, by using the one-dimensional model of an imaging system, that the **OTF** of an optical system similarly modifies the contrast of a simple sinusoidal object. It will become apparent that an imaging system can be characterized by the modification it produces on a distribution of single-spatial-frequency objects.

For the imaging system in Figure 10B.1, the Fourier transform of the impulse response is

$$\tilde{S}(\omega_x) = \mathcal{F}\{s(x)\} = \int_{-\infty}^{\infty} \operatorname{sinc}^2\left(\frac{kax}{S'}\right) e^{-i\omega_x x}\, dx. \tag{10B.7}$$

This unnormalized transfer function can be evaluated using a mathematical trick, which will also provide another interpretation of the **OTF**. The integrand of (10B.7) is the product of two sinc functions,

$$\left[\operatorname{sinc}\left(\frac{kax}{S'}\right)\right]\left[\operatorname{sinc}\left(\frac{kax}{S'}\right)\right]^*.$$

From (6.17), we find that a sinc function can be viewed as the Fourier transform of a rectangular function:

$$\mathcal{F}\left\{\operatorname{sinc}\left(\frac{kax}{S'}\right)\right\} = \operatorname{rect}(x).$$

Because of the relationship between the Fourier transform of a correlation and the product of the Fourier transforms of the correlated functions, (6A.10), the integral (10B.7) can now be viewed as the correlation of two identical rectangular functions. The rectangular function is equal to the aperture function of the imaging system. Thus, the **OTF** of the one-dimensional model of an imaging system is equal to the autocorrelation of the aperture function of the system.

Using the result displayed in Figure 6.17 for the autocorrelation of a rectangular function, we can write (10B.7) as a triangular function:

$$\tilde{S}(\omega_x) = \begin{cases} 2a\left(1 - \dfrac{S'}{2ak}\omega\right), & |\omega_x| \le \dfrac{2ak}{S'}, \\ 0, & \text{all other } \omega. \end{cases} \tag{10B.8}$$

The normalized transfer function is defined as

$$\tau(\omega_x) = \frac{\tilde{S}(\omega_x)}{\tilde{S}(0)} = \begin{cases} 1 - \dfrac{S'}{2ak}\omega, & |\omega_x| \le \dfrac{2ak}{S'}, \\ 0, & \text{all other } \omega, \end{cases} \tag{10B.9}$$

and is shown in Figure 10B.3.

The result obtained for the simple one-dimensional model can be extended to two dimensions, allowing the **OTF** for any imaging system to be generated by calculating the autocorrelation of the aperture function of the imaging system. The behavior of the transfer function shown in Figure 10B.3 exhibits the general behavior of all imaging systems. We can obtain the properties of a typical imaging system by assuming a two-dimensional, circularly symmetric aperture. We replace S' by the focal length of the optical system and use the definition that the f-number, $f/\#$, of the optical system is [see (5A.13)]

$$f/\# = \frac{f}{2a}, \tag{10B.10}$$

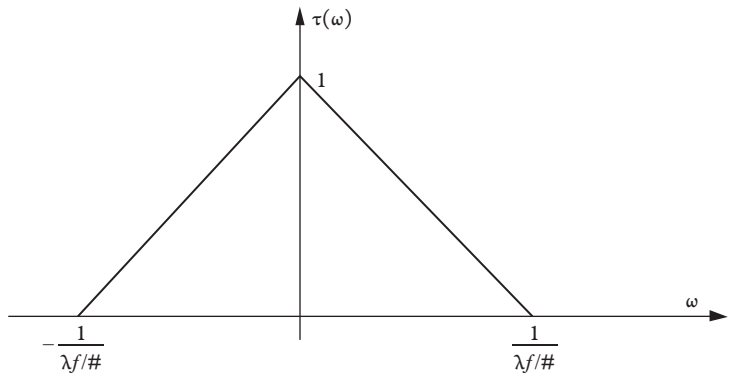

Figure 10B.3 *Incoherent transfer function for a rectangular aperture.*

where a is now the radius of the aperture of the system. With these replacements, Figure 10B.3 demonstrates that spatial frequencies beyond $1/\lambda f\#$ are not imaged by an incoherent imaging system.

The **OTF** of an optical system is consistent with other views of the imaging process. It is zero for frequencies greater than

$$\omega_{\max} = \frac{D}{\lambda f},$$

where D is the system's aperture diameter and f is its focal length, and therefore no frequencies higher than $\omega_{\max}$ can pass through the system. From (10A.7), we can rewrite this cutoff frequency as

$$\omega_{\max} = \frac{2}{\Delta x}.$$

The maximum spatial frequency that an optical system will pass is inversely proportional to the resolution of the system. The factor of two in the relationship is consistent with the sampling theorem, which requires two samples at the highest frequency needed to accurately represent a signal.

To find the physical interpretation that should be associated with the **OTF** in Figure 10B.3, we evaluate the response of the optical system to a simple sinusoidal intensity distribution

$$I_O(x) = 1 + d\cos\omega_0 x. \tag{10B.11}$$

In electronics, the constant d is called the modulation of the signal; in optics, we define it as the *contrast* of the object, and, as defined in Appendix 10A, it is given by

$$C_O(\omega_0) = \frac{I_{\max} - I_{\min}}{I_{\max} + I_{\min}} = d. \tag{10B.12}$$

We expect the contrast to exhibit a dependence on the spatial frequency, and we emphasize that functional dependence in (10B.12) by writing $C_O(\omega_0)$.

The intensity distribution of the image is

$$I_I(x) = \int_{-\infty}^{\infty} (1 + d\cos\omega_0\xi)s(x-\xi)\,d\xi = \mathcal{F}\{\mathcal{F}\{I_O(x)\}\mathcal{F}\{s(x)\}\}.$$

Using the results from (6.24) and (6.26), we can write the spatial frequency spectrum of the object as

$$\mathcal{F}\{I_O(x)\} = \delta(\omega) + \frac{1}{2}d[\delta(\omega-\omega_0) + \delta(\omega+\omega_0)].$$

If we multiply this function by the transfer function shown in Figure 10B.3 and perform the inverse transform, we obtain the image intensity

$$I_I(x) = 1 + \tau(\omega_0)d\cos\omega_0 x.$$

The final image has its contrast reduced by

$$\tau(\omega_0) = 1 - \frac{S'\omega_0}{2ka}.$$

This result is generally true, as we will demonstrate by using a general transfer function with the sinusoidal object's frequency spectrum.

10B.2.3 Modulation Transfer Function

We assume that the impulse response of the imaging system is $s(x)$ and the optical transfer function is $S(\omega)$. In general, it is a complex function of the form

$$\tilde{S}(\omega_0) = \left|\tilde{S}(\omega_0)\right| e^{i\phi(\omega_0)},$$

where $\left|\tilde{S}(\omega_0)\right|$ is the modulus of the transfer function and $\phi(\omega_w)$ is the phase. The image intensity is then

$$\begin{aligned} I_I(x) &= \int \left\{\delta(\omega) + \frac{1}{2}d\left[\delta(\omega-\omega_0) + \delta(\omega+\omega_0)\right]\right\}\tilde{S}(\omega)e^{-i\omega x}\,d\omega \\ &= \tilde{S}(0) + \frac{1}{2}d\left[\tilde{S}(\omega_0)e^{i\omega_0 x} + \tilde{S}(-\omega_0)e^{-i\omega_0 x}\right]. \end{aligned}$$

The impulse response of an incoherent system, $s(x)$, is always a real function because it equals the square of the amplitude impulse response. From the discussions in Chapter 6, the Fourier transform of a real function is of the form

$$\tilde{S}(\omega) = K[\cos\omega - i\sin\omega].$$

We can therefore write

$$\tilde{S}(-\omega) = \tilde{S}^*(\omega)$$

and

$$\begin{aligned} I_I(x) &= \tilde{S}(0) + d\mathcal{R}e\left\{\tilde{S}(\omega_0)e^{i\omega_0 x}\right\} \\ &= \tilde{S}(0)\left[1 + d\frac{\left|\tilde{S}(\omega_0)\right|}{\tilde{S}(0)}\cos(\omega_0 x + \phi)\right]. \end{aligned} \tag{10B.13}$$

The use of the **OTF** to obtain an image of a simple sinusoidal function demonstrates that the image contrast is equal to the object contrast, modified by the modulus of the transfer function. Because d is called the modulation in electronics, the modifier of d is called *the modulation transfer function* (**MTF**) in optics. The image contrast of an optical system is thus

$$C_I(\omega_0) = C_O(\omega_0)\frac{|\tilde{S}(\omega_0)|}{\tilde{S}(0)}$$
$$= C_O(\omega_0)\tau(\omega_0), \tag{10B.14}$$

where $\tau(\omega_0)$ is the **MTF**.

This relationship suggests a method for measuring the **MTF**. The contrast in the image is measured using different spatial frequencies as object functions (see Figure 10B.4) An example of the **MTF** for the human eye is shown in Figure 10B.5. Note that it differs from man-made imaging systems in that it has a maximum response frequency that is not at DC. Man-made imaging systems usually have an **MTF** that is a monotonically decreasing function of spatial frequency as shown in Figure 10B.3.

10B.3 Coherent Imaging

The same one-dimensional model of an imaging system (Figure 10B.1) will be used to evaluate coherent imaging. An added complication exists for coherent imaging systems. Not only do we have the intensity images of A and B, as in the incoherent case, but now we also have a light distribution due to interference between sources A and B. In Chapter 8, we discovered, during the discussion of spatial coherence, that the intensity at some observation point, due to two point sources, is given by

$$I_P = I_1 + I_2 + 2\sqrt{I_1 I_2}\,|\gamma_{12}|\cos\delta_{12}.$$

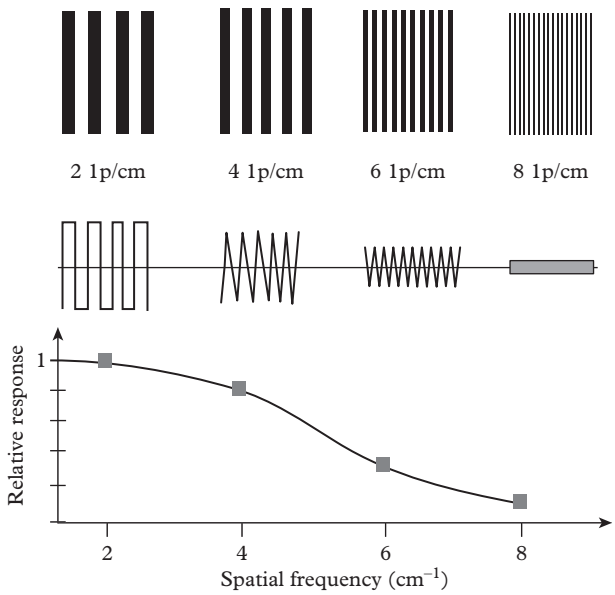

Figure 10B.4 *Determination of the modulation transfer function.*

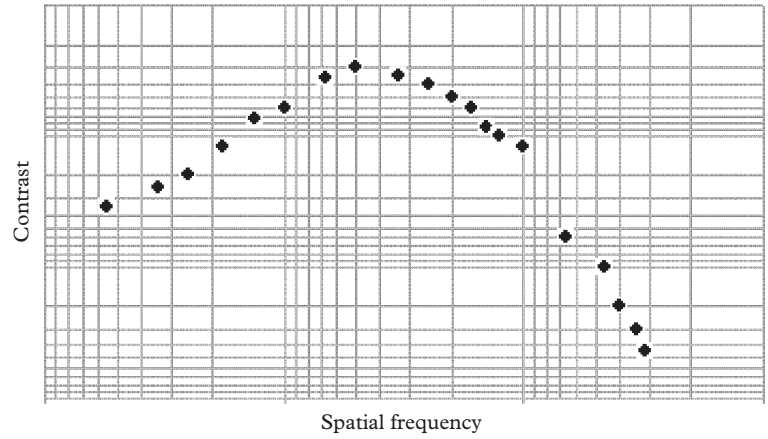

Figure 10B.5 *The modulation transfer function for the human eye.*

Using this result, we can write, as we did for the incoherent case, the intensity distribution due to the imaging system in Figure 10B.1:

$$I_I(\xi) = 4a^2 I_0 \left\{ \operatorname{sinc}^2 \left[\frac{ka}{S'}(\xi - \beta) \right] + \operatorname{sinc}^2 \left[\frac{ka}{S'}(\xi + \beta) \right] \right.$$
$$\left. + 2\gamma_{AB} \operatorname{sinc} \left[\frac{ka}{S'}(\xi - \beta) \right] \operatorname{sinc} \left[\frac{ka}{S'}(\xi + \beta) \right] \right\}. \tag{10B.15}$$

For complete coherence, the spatial coherence function is $\gamma_{AB} = 1$ and the image intensity is

$$I_I(\xi) = 4a^2 I_O \left\{ \operatorname{sinc} \left[\frac{ka}{S'}(\xi - \beta) \right] + \operatorname{sinc} \left[\frac{ka}{S'}(\xi + \beta) \right] \right\}^2 .$$

This implies that for coherent imaging,

$$I_I(x) = \left[\int_{-\infty}^{\infty} E(\xi, t) \mathcal{R}(x - \xi) d\xi \right]^2 . \tag{10B.16}$$

The coherent system is linear in amplitude rather than intensity, as was the case for the incoherent system.

The Rayleigh criterion is inappropriate for coherent imaging. Figure 10B.6 displays the images of A and B separated by a distance equal to the Rayleigh criterion. The images A' and B' are not resolved when the objects A and B are in phase, but are easily resolved when A and B are out of phase.

Unlike the Rayleigh criterion, the Sparrow criterion can be used to obtain a minimum resolution for coherent imaging. We simply set the second derivative of (10B.15) with respect to ξ equal to zero to obtain the minimum angular resolution:

$$\sin \Psi = \frac{4.164}{ka} = 1.33 \frac{\lambda}{2a} \tag{10B.17}$$

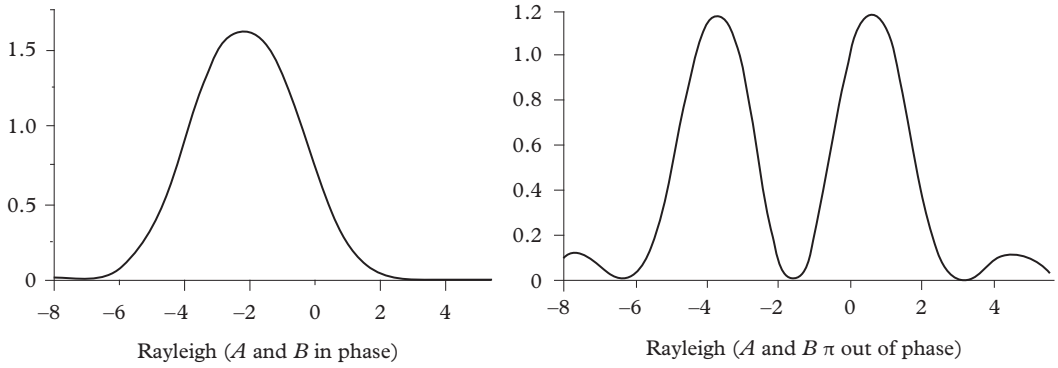

Figure 10B.6 *Application of the Rayleigh criterion with coherent sources A and B in Figure 10B.1. The relative phase of the two sources determines whether resolution is possible, making this criterion useless for a coherent system.*

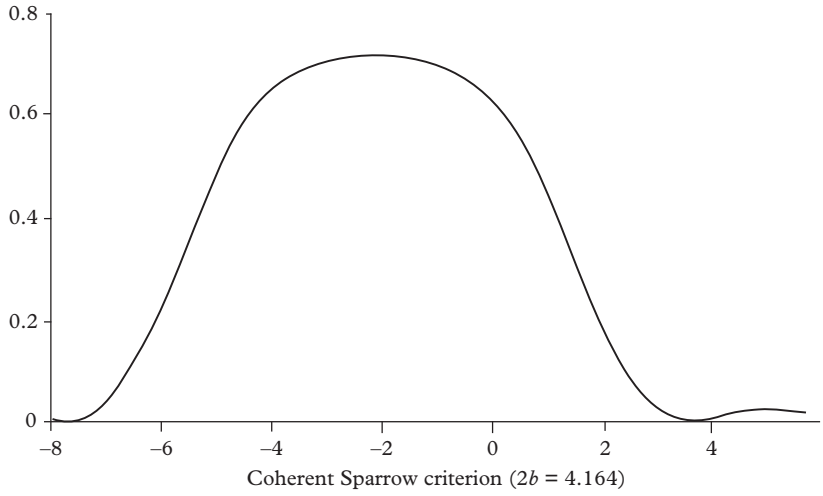

Figure 10B.7 *Resolution of two coherent sources in phase using the Sparrow criterion. If the sources are out of phase, the discrimination between the two sources is better, as shown in Figure 10B.6.*

for a slit of width $2a$ and

$$\sin \Psi = \frac{4.60}{ka} = 1.46 \frac{\lambda}{2a} \tag{10B.18}$$

for a circular aperture of radius a. Figure 10B.7 shows the image of two in-phase coherent point sources separated by a distance equal to the Sparrow criterion.

Comparing (10B.17) and (10B.18) with (10B.5) and (10B.6), we see that the incoherent resolution for point objects is better than the coherent resolution. Figure 10B.8 displays images of a standard resolution chart with the spatial frequencies associated with the various bars identified in the figure. Coherent images are shown for imaging systems with two different apertures. Below each coherent image is shown an incoherent image with the same resolution. The incoherent image could be obtained with an aperture of about one-half of the size of the aperture needed to produce the coherent image with the same resolution. These images of a standard resolution chart support the statement that the resolution of a coherent imaging system is less than the resolution of an incoherent system.

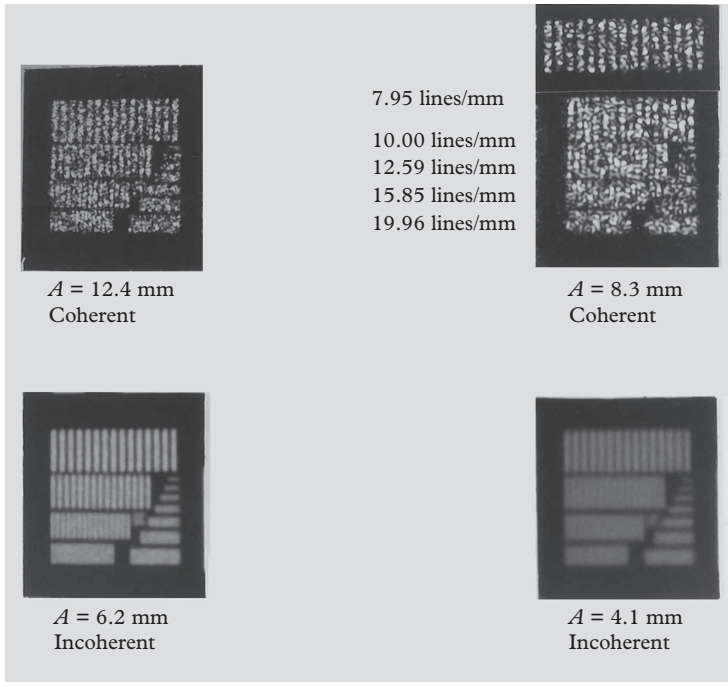

Figure 10B.8 *Images of a standard resolution chart containing rows of high-contrast bars at different spatial frequencies. The top images were made using coherent light at apertures of 12 and 8 mm. The lower images were made with incoherent light at apertures of half the diameter used in the upper images, i.e., 6 and 4 mm. The smallest spatial frequency that can be detected in the coherent images is about the same as in the incoherent images. To produce the same resolution, the coherent system required an aperture twice the size required by the incoherent optical system. (Courtesy C.R. Christensen.)*

Another effect that reduces the resolution of a coherent system is speckle noise. Coherent light that travels different optical path lengths will interfere and produce an image with an intensity variation called speckle. The intensity variations depend upon the atmospheric path and/or the surface roughness of the object. The speckle noise is often completely random, and can be smoothed only by averaging statistically independent samples of the image.

Figure 10B.9 shows a test pattern consisting of a matrix of disks. The diameters of the disks in each row are identical, but the diameters decrease by a factor of two as we move down from row to row. The disks in each column have the same contrast, but the contrast decreases from left to right. (This test pattern was developed by A. Rose for the evaluation of television systems.) The image at the lower right of the figure, labeled $N = 1$, is immersed in speckle noise, while the other images are created by recording multiple exposures (N denotes the number of exposures) of statistically independent images. The images contributing to the multiple exposed recordings differed only in their speckle noise. The intensity averaging produced by the multiple exposures increase the signal-to-noise ratio in the images, allowing small disks of lower contrast to be detected when N is large.

We introduced a transfer function for the incoherent imaging case. By analogy, we could define an amplitude transfer function for a coherent imaging system by applying the convolution theorem to (10B.16). If we followed through the mathematical development, we would discover that the amplitude transfer function is the Fourier transform of the amplitude impulse response. The maximum spatial frequency that can be imaged by a coherent system is therefore one-half of the maximum spatial frequency imaged by the incoherent system. This result agrees with the images displayed in Figure 10B.8. The contrast for a coherent imaging system does not decrease monotonically, as it does for an incoherent imaging system, but instead remains equal to 1 up to the frequency cutoff. The coherent transfer function of a rectangular aperture is shown in Figure 10B.10.

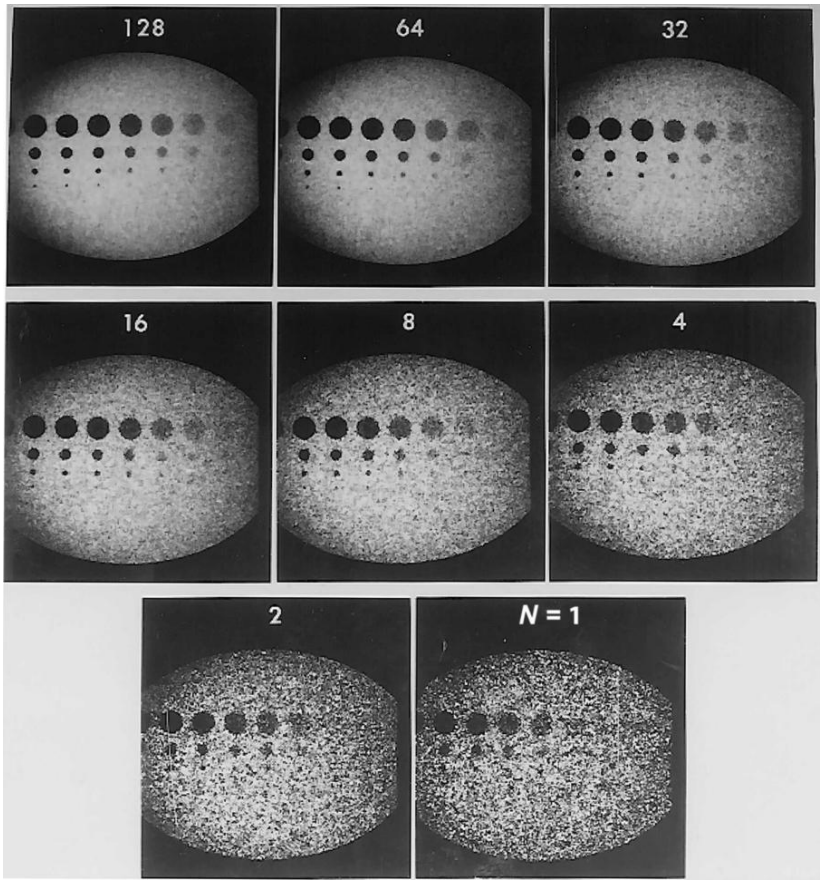

Figure 10B.9 *Images of a resolution chart developed by A. Rose have been produced using coherent light. The contrast decreases from left to right along each row, and the size of the disks decreases from top to bottom along each column. The value of N shown on the images is equal to the number of exposures of the object made to produce the image. The noise, most apparent in the images with low N, is called speckle and is a coherent noise that limits the imaging performance of a coherent optical system. The noise is due to interference between waves that have traveled over slightly different optical paths from the object to the image. The same speckle noise is observable in Figures 10B.8 and 10.9. The speckle can be reduced by statistically averaging a number of independent samples of the noise field, as was done in the multiple exposures shown here.*

10B.4 Computational Imaging

In computational imaging, digital samples of the light distribution are collected, and a digital computer modifies the samples to produce some desired performance such as increased depth of field, increased field of view, or spectral information. A digital computer is used to replace parts of the optical system or to perform operations that are not possible with conventional optics [7].

To see how a computational imaging system might work, let us assume that we want to record an image of a scene that contains four pixels with intensity values

$$2\ 4\ 6\ 8$$

We will assume that the optical system is similar to the one shown in Figure 10B.1 but with four objects rather than only two to image. To resolve the image, we will need an aperture that will resolve each pixel as derived from Figure 10B.1:

$$2\beta = \frac{\lambda S'}{2a}.$$

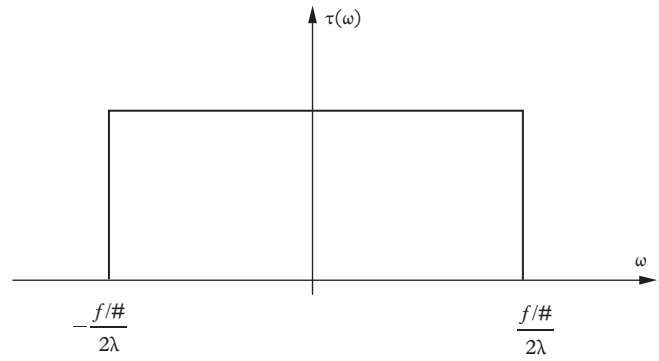

Figure 10B.10 *Coherent transfer function for a rectangular aperture.*

Because of design constraints, the only aperture we can use is a factor of four smaller than this requirement. We will not see the individual values of the pixels on our detector, but instead see the sum of the values; i.e., the image will be a single value, "20". We can recover the original resolution by coding the larger aperture with four spatial filters (Table 10B.1). We could take four readings and change the aperture code for each reading, or we could stack the filters vertically in the slit of Figure 10B.1. The result would be four detectors arranged vertically to measure the integrated intensity through each mask. The set of masks represent the mathematical construct called a Hadamard[2] matrix [8]:

$$\mathcal{H} = \begin{bmatrix} 1 & 1 & 1 & 1 \\ 1 & 1 & 0 & 0 \\ 1 & 0 & 1 & 0 \\ 1 & 0 & 0 & 1 \end{bmatrix}.$$

With the Hadamard matrix representation, the imaging process becomes

$$I = \mathcal{H}\mathcal{O} = \begin{bmatrix} 1 & 1 & 1 & 1 \\ 1 & 1 & 0 & 0 \\ 1 & 0 & 1 & 0 \\ 1 & 0 & 0 & 1 \end{bmatrix} \begin{bmatrix} 2 \\ 4 \\ 6 \\ 8 \end{bmatrix} = \begin{bmatrix} 20 \\ 6 \\ 8 \\ 10 \end{bmatrix}.$$

Table 10B.1 *Computational image design*

Detector reading*	Mask configuration
$[1\ 1\ 1\ 1] \cdot [2\ 4\ 6\ 8]^T = 20$	□□□□
$[1\ 1\ 0\ 0] \cdot [2\ 4\ 6\ 8]^T = 6$	□□■■
$[1\ 0\ 1\ 0] \cdot [2\ 4\ 6\ 8]^T = 8$	□■□■
$[1\ 0\ 0\ 1] \cdot [2\ 4\ 6\ 8]^T = 10$	□■■□

*The transpose of a row matrix is a column matrix.

[2] A Hadamard matrix is

$$\mathcal{H}_2 = \begin{bmatrix} 1 & 1 \\ 1 & -1 \end{bmatrix}, (\mathcal{H})_N = \begin{bmatrix} \mathcal{H}_{2N-1} & \mathcal{H}_{2N-1} \\ \mathcal{H}_{2N-1} & -\mathcal{H}_{2N-1} \end{bmatrix}.$$

We can recover the actual object from our unresolved image data by multiplying the recorded data by the inverse of the Hadamard matrix:

$$\mathcal{O} = \mathcal{H}^{-1} I = \begin{bmatrix} -\frac{1}{2} & \frac{1}{2} & \frac{1}{2} & \frac{1}{2} \\ \frac{1}{2} & \frac{1}{2} & -\frac{1}{2} & -\frac{1}{2} \\ \frac{1}{2} & -\frac{1}{2} & \frac{1}{2} & -\frac{1}{2} \\ \frac{1}{2} & -\frac{1}{2} & -\frac{1}{2} & \frac{1}{2} \end{bmatrix} \begin{bmatrix} 20 \\ 6 \\ 8 \\ 10 \end{bmatrix} = \begin{bmatrix} 2 \\ 4 \\ 6 \\ 8 \end{bmatrix}.$$

This combination of computer and optical system to obtain a desired performance can be used in two dimensions. Figure 10B.11 shows a mask that might be used for a 4×4

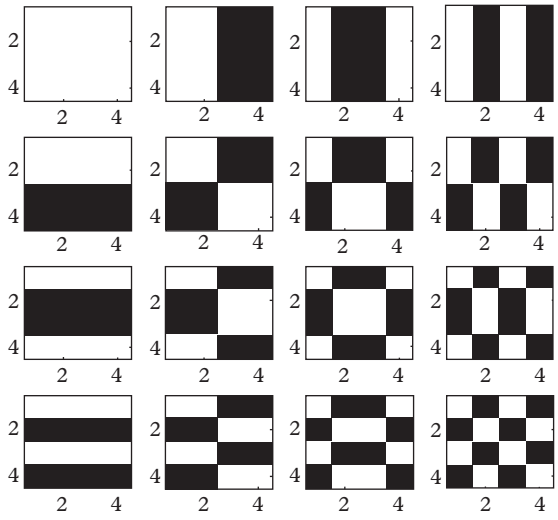

Figure 10B.11 *A Hadamard matrix of order 4. (Portnoy, A.D.,* Coded Measurement for Imaging and Spectroscopy. *2009: PhD Dissertation, Department of Electrical and Computer Engineering, Duke University, Durham, NC.)*

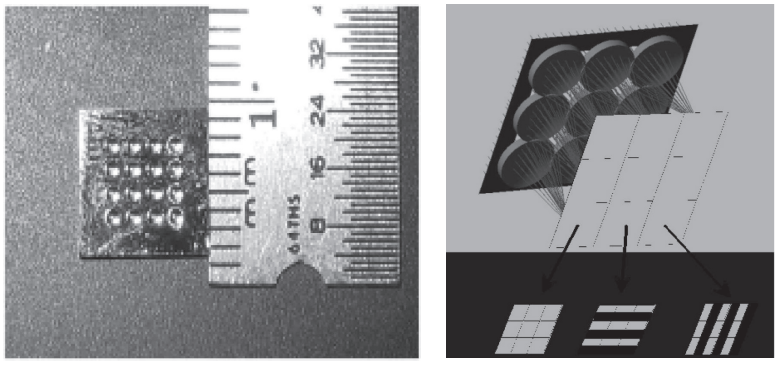

(a) (b)

Figure 10B.12 *(a) A4 × 4 micro-optical array. (b) Coupling of a micro-optical array to Hadamard masks.*

microlens assembly like the one shown in Figure 10B.12(a). Hadamard masks can be coupled to a micro-array as shown in Figure 10B.12(b).

REFERENCES

1. Reynolds, G.O., et al., *New Physical Optics Notebook: Tutorials in Fourier Optics*. 1989: SPIE–International Society for Optical Engineers.
2. Ables, J.G., *Fourier Transform Photography: A New Method for X-ray Astronomy.* Proc. Astron. Soc. Australia, 1968. **1**: p. 172.
3. Brown, C., *Multiplex imaging with multiple-pinhole cameras.* J. Appl. Phys., 1974. **45**: p. 1806.
4. Cathey, W.T. and E.R. Dowski, *New paradigm for imaging systems*. Appl. Opt., 2002. **41**: p. 6080–6092.
5. Tanida, J., et al., *Thin observation module by bound optics (TOMBO): concept and experimental verification*. Appl. Opt., 2001. **40**: p. 1806–1813.
6. Portnoy, A.D., et al., *Multichannel sampling schemes for optical imaging systems.* Appl. Opt., 2008. **47**: p. 76–85.
7. Mait, J.N., R. Athale, and J. van der Gracht, *Evolutionary paths in imaging and recent trends*. Opt. Express, 2003. **11**: p. 2093–2101.
8. Yarlagadda, R.K. and J.E. Hershey, *Hadamard Matrix Analysis and Synthesis: With Applications to Communications and Signal/Image Processing*. 1997: Springer.

Fresnel Diffraction

11

11.1 Introduction 459
11.2 Fresnel Approximation 460
11.3 Rectangular Apertures 464
11.4 Fresnel Zones 469
11.5 Circular Aperture 477
11.6 Opaque Screen 479
11.7 Zone Plate 481
11.8 Pinhole Camera 484
11.9 Fermat's Principle 485
11.10 Comparison of Techniques 486
11.11 Summary 487
11.12 Problems 488
References 489
Appendix 11A: Babinet's Principle 490
Appendix 11B: Fresnel Integral Solutions 493

11.1 Introduction

In the first approximate solution to the Huygens–Fresnel integral, presented in Chapter 10, it was assumed that the phase of the wavefront in the aperture was a linear function of the aperture coordinates. This assumption led to Fraunhofer diffraction theory. We now return to the Huygens–Fresnel integral to discuss another approximate solution of the integral. This approximate solution, called *Fresnel diffraction*, assumes that the phase of the wavefront in the aperture has a quadratic dependence upon the aperture coordinates. The curvature of the wavefront increases the mathematical difficulty of the diffraction problem over that of Fraunhofer diffraction. We will discover that, in contrast to Fraunhofer diffraction, only a portion of the wave in the aperture contributes to Fresnel diffraction. That portion of the aperture that contributes to the diffraction amplitude lies near the line connecting the source and observation point, which means that, as with Fraunhofer diffraction, we are limiting our considerations to small departures from geometrical optics.

We will reformulate the Huygens–Fresnel integral

$$\int \frac{\tilde{E}_i}{R} e^{-i\mathbf{k}\cdot\mathbf{R}}\, dx$$

using the approximation derived in Chapter 9, (9.21):

$$\Delta \approx k\left(\frac{x_1}{z_1} + \frac{x_2}{z_2}\right)b + \frac{k}{2}\left(\frac{1}{z_1} + \frac{1}{z_2}\right)b^2 + \cdots .$$

In this chapter, we will retain both terms of the expansion. For those apertures whose transmission functions can be separated into two independent one-dimensional functions of the aperture coordinates, i.e., $h(x, y) = f(x)g(y)$, the integral, with the quadratic approximation, can be separated into two integrals, called Fresnel integrals.

The Fresnel integrals have been evaluated numerically, and a table of these integrals (to be found in Appendix 11B) will be used to calculate the Fresnel diffraction from a straight edge. A plot of the Fresnel integrals, called the Cornu spiral (also to be found in Appendix 11B), can be used to obtain a graphical solution of Fresnel diffraction. The graphical technique will be demonstrated by obtaining diffraction from a straight edge and comparing the results with the solution obtained using the tabulated data.

Fresnel developed a technique for the solution of the Huygens–Fresnel integral based upon a geometrical construction called Fresnel zones. The Fresnel zone approach provides a unique insight into the diffraction process and can provide a partial description of Fresnel diffraction from circularly symmetric objects. The concept of Fresnel zones will be used to discuss diffraction from a circular aperture and a disk and to obtain additional insight into Fermat's principle.

In Appendix 11A, a mathematical theorem called Babinet's principle, will be discussed. The theorem connects the diffraction patterns from similar diffracting objects such as a

Modern Optics. Second Edition. B. D. Guenther.
© B. D. Guenther 2015. Published in 2015 by Oxford University Press.

circular aperture and a disk. This theorem provides a useful tool for calculating diffraction. The application of the theorem will be demonstrated by recalculating diffraction by a circular disk using the Fresnel diffraction from a circular aperture.

The fact that Fraunhofer diffraction is an integral part of the theory of imaging makes Fraunhofer diffraction a more important topic than Fresnel diffraction. Because there are fewer applications of Fresnel diffraction, only two applications based upon the Fresnel zone approach will be discussed.

11.2 Fresnel Approximation

In Fraunhofer diffraction, the phase of the wave in the aperture is assumed to vary linearly across the aperture. This would occur if, for example, a plane wave were incident upon the aperture at an angle with respect to the optical axis. In Fresnel diffraction, we replace the assumption of a linear phase variation with a quadratic phase variation. This is equivalent to assuming that a spherical wave of amplitude α from a point source at position (x_s, y_s, Z') illuminates the aperture (see Figure 11.1). We found the relation that is needed for solution of this diffraction problem in Appendix 9A. Here, we will continue to treat the obliquity factor as a constant and rewrite (9A.18) as

$$\tilde{E}_P = \frac{i\alpha}{\lambda} \iint_{\Sigma} f(x,y) \frac{e^{-i\mathbf{k}\cdot(\mathbf{R}+\mathbf{R}')}}{RR'} \, dx\, dy. \tag{11.1}$$

In our discussion of the Huygens–Fresnel integral in Chapter 9, we pointed out that the integral is nonzero only when the phase of the integrand is stationary. For Fresnel diffraction, we can ensure that the phase is nearly constant if R does not differ appreciably from Z, or R' from Z'. This is equivalent to stating that only the wave in the aperture, around a point **S**, called the *stationary point*, will contribute to E_p. Physically, only light propagating over paths nearly equal to the path predicted by geometrical optics (obtained from Fermat's principle) will contribute to E_p. The stationary point **S** is the point in the aperture plane where the line connecting the source and observation positions intersects the plane.

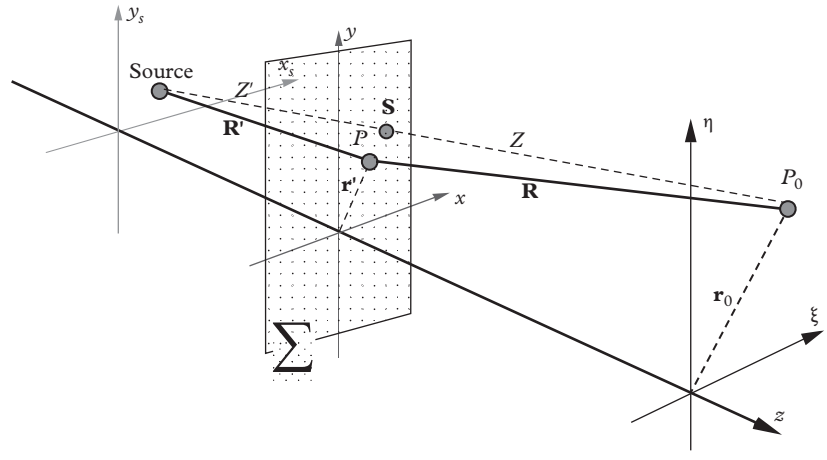

Figure 11.1 *Geometry for Fresnel diffraction.*

The geometry of Figure 11.1 allows the distances R and R' to be written as

$$\begin{aligned} R^2 &= (x-\xi)^2 + (y-\eta)^2 + Z^2, \\ R'^2 &= (x_s-x)^2 + (y_s-y)^2 + Z'^2. \end{aligned} \tag{11.2}$$

The same procedure used in Chapter 10 to obtain (10.5) could be used here to find an approximate expression for R and R'. We will apply instead the binomial expansion of a square root,

$$\sqrt{1+b} = 1 + \frac{b}{2} - \frac{b^2}{8} + \ldots, \tag{11.3}$$

to obtain R and R'. In the Fresnel approximation, the first two terms of the binomial expansion (11.3) are retained:

$$R \approx Z + \frac{(x-\xi)^2 + (y-\eta)^2}{2Z}, \tag{11.4a}$$

$$R' \approx Z' + \frac{(x_s-x)^2 + (y_s-y)^2}{2Z'}. \tag{11.4b}$$

In the denominator of (11.1), R is replaced by Z and R' by Z'. (By making this replacement, we are implicitly assuming that the amplitudes of the spherical waves are not modified by the differences in propagation distances over the area of integration. This is a reasonable approximation because the two propagation distances are within a few hundred wavelengths of each other.) In the exponent, we must use (11.4), because the phase changes by a large fraction of a wavelength as we move from point to point in the aperture. This procedure differs from that used in Chapter 10 for Fraunhofer diffraction only in the fact that here we will retain the quadratic terms of the binomial expansion:

$$R + R' \approx Z + Z' + \left[\frac{(x-\xi)^2}{2Z} + \frac{(x_s-x)^2}{2Z'}\right] + \left[\frac{(y-\eta)^2}{2Z} + \frac{(y_s-y)^2}{2Z'}\right].$$

The integral obtained using these terms is quite complicated, because it assumes that the source wave and the diffracted wave are both spherical.

A less complicated expression for the Huygens–Fresnel integral would be obtained if the wave incident on the aperture were a plane wave. The Huygens–Fresnel integral

$$\tilde{E}_P = \frac{i\alpha}{\lambda} \iint_{\Sigma} f(x,y)\, \frac{e^{-i\mathbf{k}\cdot\mathbf{R}}}{R}\, dx\, dy$$

would be rewritten, using the approximate expression for R given by (11.4),

$$\tilde{E}_P = \frac{i\alpha}{\lambda}\, \frac{e^{-ikZ}}{Z} \iint_{\Sigma} f(x,y) \exp\left\{-\frac{ik}{2Z}\left[(x-\xi)^2 + (y-\eta)^2\right]\right\} dx\, dy. \tag{11.5}$$

The physical interpretation of this equation states that when a plane wave illuminates the obstruction, the field at point P is a spherical wave, originating at the aperture, a distance Z away from P:

$$\frac{e^{-ikZ}}{Z}.$$

The amplitude and phase of this spherical wave are modified by an integral, with a quadratic phase dependent on the obstruction's spatial coordinates.

By defining three new parameters,

$$\rho = \frac{ZZ'}{Z+Z'}, \qquad \text{or} \qquad \frac{1}{\rho} = \frac{1}{Z} + \frac{1}{Z'}, \tag{11.6a}$$

$$x_0 = \frac{Z'\xi + Zx_s}{Z+Z'}, \tag{11.6b}$$

$$y_0 = \frac{Z'\eta + Zy_s}{Z+Z'}, \tag{11.6c}$$

the more general expression for Fresnel diffraction of a spherical wave can be placed in the same format as the expression obtained for an incident plane wave.

The parameters x_0 and y_0 are the coordinates, in the aperture plane, of the stationary point **S**, which lies on a line joining the source and the observation point. To illustrate the derivation of the stationary point's coordinates, the x-coordinate will be obtained, using the geometry in Figure 11.2. We have

$$\tan\theta = \frac{\xi - x_s}{Z+Z'} \qquad \text{and} \qquad \tan\theta = \frac{x_0 - x_s}{Z'}.$$

If we equate the two relations and solve for x_0, we obtain (11.6).

The parameters in (11.6) {can be used to express, after some manipulation, the spatial dependence of the phase in the integrand of (11.1):

$$R + R' = Z + Z' + \frac{(\xi - x_s)^2 + (\eta - y_s)^2}{2(Z+Z')} + \left[\frac{(x-x_0)^2 + (y-y_0)^2}{2\rho}\right].$$

A further simplification to the Fresnel diffraction integral can be made by obtaining an expression for the distance D between the source and the observation point. We will demonstrate the derivation, in one dimension, by using Figure 11.2. The total distance from the source position x_s to the observation position ξ in Figure 11.2 is

$$\sqrt{(Z+Z')^2 + (\xi - x_s)^2} \approx Z + Z' + \frac{(\xi - x_s)^2}{2(Z+Z')}.$$

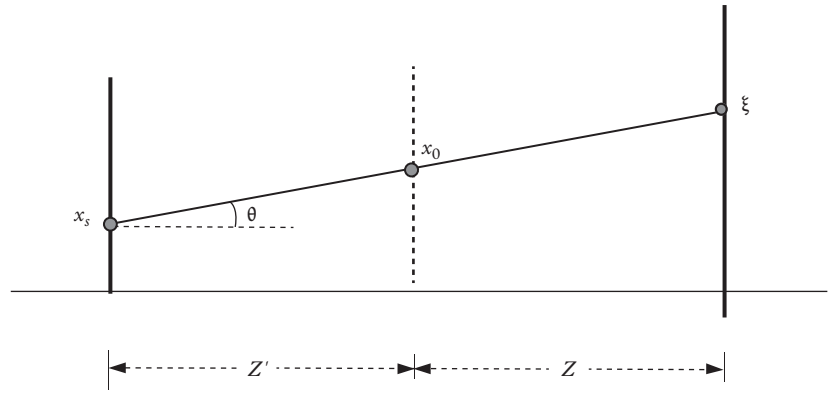

Figure 11.2 *Geometry for evaluation of parameters used in equation for Fresnel diffraction.*

If this one-dimensional calculation is extended to two dimensions, the distance between the source and the observation point can be defined as

$$D = Z + Z' + \frac{(\xi - x_s)^2 + (\eta - y_s)^2}{2(Z + Z')}. \tag{11.7}$$

We use this definition of D to also write

$$\frac{1}{ZZ'} = \frac{Z + Z'}{ZZ'} \frac{1}{Z + Z'} \approx \frac{1}{\rho D}.$$

Using the parameters we have just defined, we may rewrite (11.1) as

$$\tilde{E}_P = \frac{i\alpha}{\lambda \rho D} e^{-ikD} \iint f(x, y) \exp\left\{-\frac{ik}{2\rho}\left[(x - x_0)^2 + (y - y_0)^2\right]\right\} dx\, dy. \tag{11.8}$$

By introducing the variables x_0, y_0, ρ, and D, the physical significance of the general expression of the Huygens–Fresnel integral can be understood. At point P, a spherical wave

$$\frac{e^{-ikD}}{D},$$

originating at the source, a distance D away, is observed. This wave would be observed if no obstruction were present. Because of the obstruction, the amplitude and phase of the spherical wave are modified by the integral in (11.8). The modification of the spherical wave made by the integral is called Fresnel diffraction.

Equation (11.8) can be shown to be equivalent to (11.5) by taking the limit as the source is moved to infinity:

$$\lim_{Z' \to \infty} \rho = Z, \quad \lim_{Z' \to \infty} x_0 = \xi, \quad \lim_{Z' \to \infty} y_0 = \eta.$$

The spherical wave, containing the variable Z', becomes a plane wave as Z' approaches infinity:

$$\lim_{Z' \to \infty} \frac{\alpha e^{-ikD}}{\rho D} = \lim_{Z' \to \infty} \left(\frac{e^{-ikZ}}{Z} \frac{\alpha e^{-ikZ'}}{Z'} \right) = \frac{\alpha e^{-ikZ}}{Z}.$$

Mathematically, (11.8) is an application of the method of *stationary phase*, a technique developed in 1887 by Lord Kelvin to calculate the form of a boat's wake. The integration is nonzero only in the region of the critical point we have labeled **S**. Physically, the light distribution at the observation point is due to wavelets from the region around **S**. The phase variations of light coming from other regions in the aperture are so rapid that the value of the integral over those spatial coordinates is zero.

The calculation of the integral for Fresnel diffraction is more complicated than for Fraunhofer diffraction because, when the observation point is moved, we must perform the integration over a new region in the aperture.

11.3 Rectangular Apertures

If the aperture function $f(x, y)$ is separable in the spatial coordinates of the aperture, then we can rewrite (11.8) as

$$\tilde{E}_P = \frac{i\alpha}{\lambda\rho D} e^{-ikD} \int_{-\infty}^{\infty} f(x) e^{-ig(x)}\, dx \int_{-\infty}^{\infty} f(y) e^{-ig(y)}\, dy,$$

$$\tilde{E}_P = A[C(x) - iS(x)][C(y) - iS(y)].$$

The spherical wave from the source is represented by

$$A = \frac{i\alpha}{2D} e^{-ikD}.$$

If we treat the aperture function as a simple constant, then C and S are integrals of the form

$$C(x) = \int_{x_1}^{x_2} \cos[g(x)]\, dx, \tag{11.9a}$$

$$S(x) = \int_{x_1}^{x_2} \sin[g(x)]\, dx. \tag{11.9b}$$

The integrals $C(x)$ and $S(x)$ have been evaluated numerically and can be found in the table of Fresnel integrals in Appendix 11B. More complete listings can be found in collections of mathematical tables [1,2]. To use the tabulated values for the integrals, (11.9) must be written in the general form

$$C(w) = \int_0^w \cos\left(\frac{1}{2}\pi u^2\right) du, \tag{11.10}$$

$$S(w) = \int_0^w \sin\left(\frac{1}{2}\pi u^2\right) du. \tag{11.11}$$

$C(w)$ and $S(w)$ are plotted in Figure 11.3. The variable u in these integrals is an aperture coordinate, measured relative to the stationary point **S** in units of $\sqrt{\lambda\rho/2}$:

$$u = \sqrt{\frac{2}{\lambda\rho}}\,(x - x_0) \qquad \text{or} \qquad u = \sqrt{\frac{2}{\lambda\rho}}\,(y - y_0). \tag{11.12}$$

The parameter w in (11.10), (11.11), and Figure 11.3 specifies the location of the aperture edge relative to the stationary point **S**. It is calculated with (11.12).

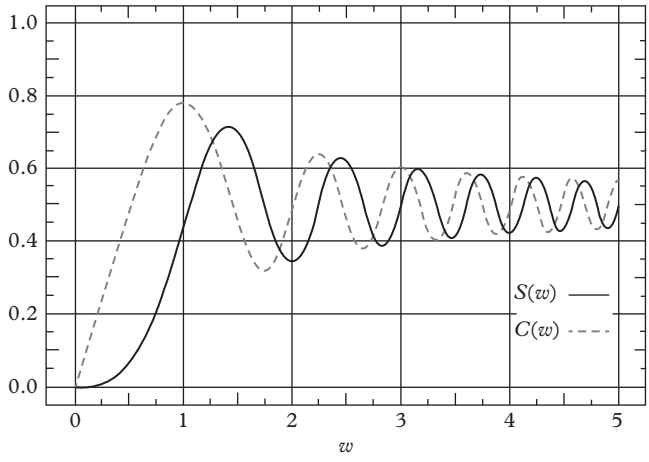

Figure 11.3 *Normalized Fresnel integrals (11.10) and (11.11).*

An example will clarify the method of calculating the parameter w for use in evaluating the Fresnel integrals. Assume the diffracting aperture is a rectangular aperture, defined as

$$f(x,y) = \begin{cases} 1, & x_1 \le x \le x_2, y_1 \le y \le y_2, \\ 0, & \text{all other } x \text{ and } y. \end{cases}$$

The upper edge of the aperture is

$$w_{x_2} = \sqrt{\frac{2}{\lambda\rho}}\,(x_2 - x_0)$$

and its right edge is

$$w_{y_2} = \sqrt{\frac{2}{\lambda\rho}}\,(y_2 - y_0).$$

When the observation point is moved, the coordinates x_0 and y_0 of **S** change, and the origin of the aperture's coordinate system moves. New values for the w's must therefore be calculated for each observation point.

The values from the Fresnel integral table are used to calculate the light wave amplitude E_P and intensity I_P:

$$I_P = A^2 \left\{ \left[C\left(w_{x_2}\right) - C\left(w_{x_1}\right) \right]^2 + \left[S\left(w_{x_2}\right) - S\left(w_{x_1}\right) \right]^2 \right\} \times \left\{ \left[C\left(w_{y_2}\right) - C\left(w_{y_1}\right) \right]^2 + \left[S\left(w_{y_2}\right) - S\left(w_{y_1}\right) \right]^2 \right\}. \tag{11.13}$$

The calculation of the two integrals is simplified because the integrals are odd functions,

$$C(-w) = -C(w), \quad S(-w) = -S(w).$$

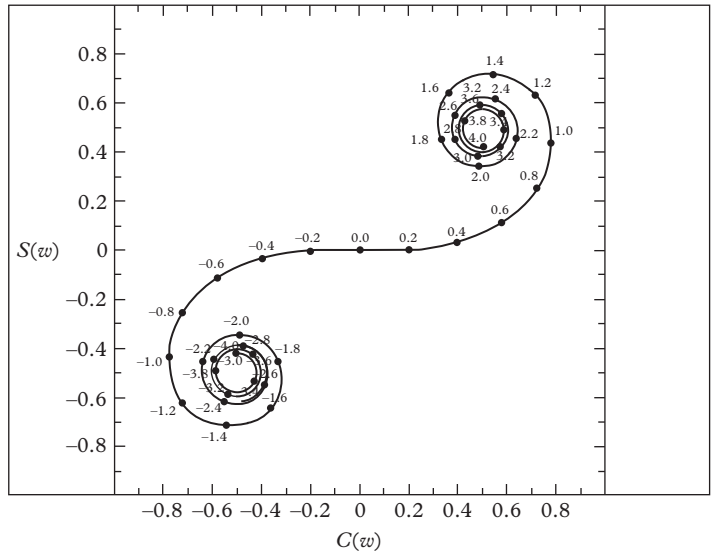

Figure 11.4 *Cornu spiral obtained by plotting the values for C(w) versus S(w) from the table of Fresnel integrals in Appendix 11B. The numbers indicated along the arc of the spiral are values of w.*

This is evident in the plot of $C(w)$ versus $S(w)$ in Figure 11.4. This plot is called the Cornu spiral in honor of **Marie Alfred Cornu (1841–1902)**, who was the first to use this plot for graphical evaluation of the Fresnel integrals. [The vertical axis of Figure 11.4 must be multiplied by $-i$ if the plot is to represent the complex amplitude of (11.8). A more accurate plot of the Cornu spiral can be found in Appendix 11B.]

To use the Cornu spiral, the limits w_1 and w_2 of the aperture are located along the arc of the spiral. The length of the straight-line segment drawn from w_1 to w_2 gives the magnitude of the integral. For example, if there were no aperture present, then, for the x-dimension, $w_1 = -\infty$ and $w_2 = \infty$. The length of the line segment from the point (–1/2,–1/2) to (1/2,1/2) would be the value of E_P, i.e., $\sqrt{2}$. An identical value is obtained for the y-dimension, so that

$$\tilde{E}_P = 2A = \frac{\alpha e^{-ikD}}{D}.$$

This is the spherical wave that would be seen when no aperture was present.

An example will clarify the use of the Cornu spiral and the table of Fresnel integrals. Assume that the obstruction is an infinitely long straight edge, reducing the problem to one dimension. The straight edge is assumed to block the negative half-plane with its edge located at $x_1 = 0$. The other limit to be used in (11.9) is $x_2 = \infty$; i.e., the straight edge is treated as an infinitely wide slit with one edge located at infinity. Figure 11.5 shows the geometry of the problem. A set of observation points $P_1, \ldots, P_5$ on the observation screen are selected. The origin of the coordinate system in the aperture plane is relocated to a new position (given by the position of **S**) when a new observation point is selected. The value of w_1, the position of the edge with respect to **S**, must be recalculated using (11.12) for each observation point. The distance from the origin to the straight edge, w_1, is positive for P_1 and P_2, zero for P_3, and negative for P_4 and P_5.

Figure 11.6 shows the geometrical method used to calculate the intensity values at each of the observation points in Figure 11.5 using the Cornu spiral. The numbers labeling the straight-line segments in Figure 11.6 are associated with the labels of the observation points P_i in Figure 11.5.

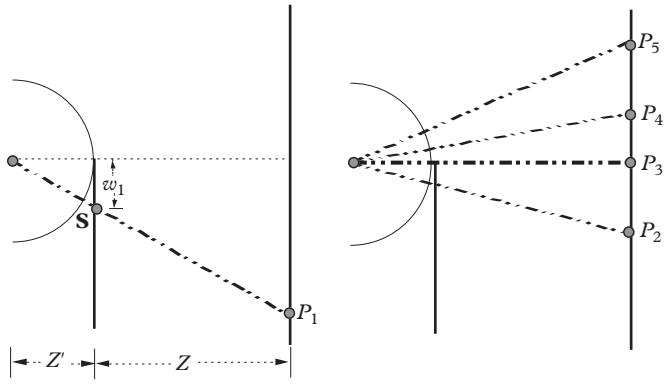

Figure 11.5 *Geometry of diffraction from a straight edge.*

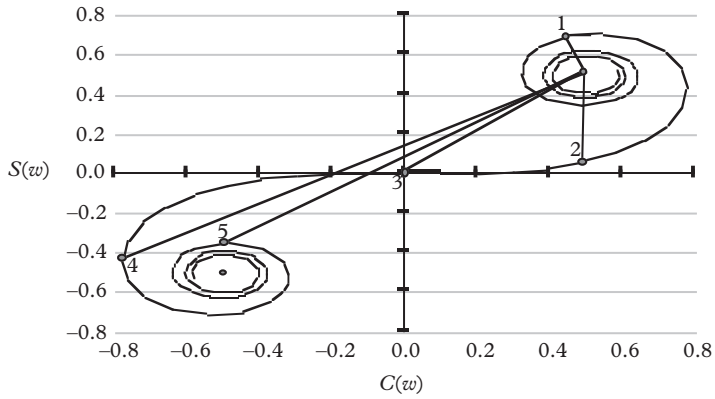

Figure 11.6 *Use of the Cornu spiral to solve problem of diffraction around a straight edge.*

To obtain an accurate calculation of Fresnel diffraction from a straight edge, the table of Fresnel integrals in Appendix 11B must be used. Before the calculation can proceed, (11.13) must be modified to apply to the geometry of this problem:

$$I_P = I_0 \left\{ \left[\frac{1}{2} - C(w_1) \right]^2 + \left[\frac{1}{2} - S(w_1) \right]^2 \right\},$$

where $I_0 = 2A^2$. Table 11.1 shows the values extracted from the table of Fresnel integrals and used in the modified version of (11.13) to find the relative intensity at various observation points.

The result obtained by using either method for calculating the light distribution in the observation plane, due to the straight edge in Figure 11.5, is plotted in Figure 11.7. The relative intensities at the observation points depicted in Figure 11.5 are labeled on the diffraction curve of Figure 11.7.

An experimentally obtained Fresnel diffraction pattern from a straight edge, along one side of a large rectangular aperture, is shown in Figure 11.8.

The same procedure can be used to calculate the light distribution of a slit of finite width. The only modification that must be made to the straight-edge calculation in order to treat a slit is the recalculation of w_2 for each observation point. The calculation of w_2 is accomplished by using the same procedure used to calculate w_1, in the straight edge

Table 11.1 *Fresnel integrals for a straight edge*

w_1	$C(w_1)$	$S(w_1)$	I_P/I_0	Point in Figure 11.5
∞	0.5	0.5	0	
2.0	0.4882	0.3434	0.01	
1.5	0.4453	0.6975	0.021	P_1
1.0	0.7799	0.4383	0.04	
0.5	0.4923	0.0647	0.09	P_2
0	0	0	0.25	P_3
–0.5	–0.4923	–0.0647	0.65	
–1.0	–0.7799	–0.4383	1.26	P_4
–1.2	–0.7154	–0.6234	1.37	
–1.5	–0.4453	–0.6975	1.16	
–2.0	–0.4882	–0.3434	0.84	P_5
–2.5	–0.4574	–0.6192	1.08	
$-\infty$	–0.5	–0.5	1.0	

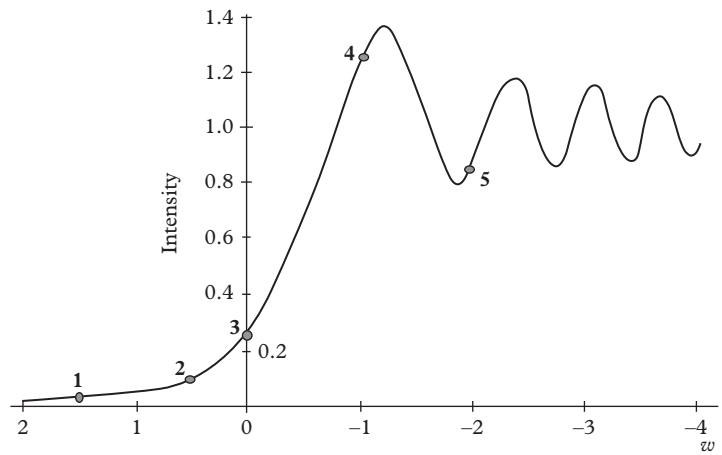

Figure 11.7 *Light distribution around a straight edge with its edge located at w = 0.*

problem. For Fresnel diffraction from a slit, the arc length on the Cornu spiral $s = w_2 - w_1$ is a constant, proportional to the slit width $x_2 - x_1$:

$$
\begin{aligned}
s &= w_2 - w_1 \\
&= \sqrt{\frac{2}{\lambda\rho}}\,[(x_2 - x_0) - (x_1 - x_0)] \\
&= \sqrt{\frac{2}{\lambda\rho}}\,(x_2 - x_1).
\end{aligned}
$$

The position of the center of this arc segment moves because the location of the center of the aperture, relative to **S**, changes with the observation position. The position of the center of the arc is given by

$$\frac{w_2 + w_1}{2} = \frac{1}{2}\sqrt{\frac{2}{\lambda\rho}}\,[(x_2 - x_0) + (x_1 - x_0)]$$

$$= \sqrt{\frac{2}{\lambda\rho}}\left[\left(\frac{x_2 + x_1}{2}\right) - x_0\right].$$

The square of the length of the chord spanning the arc gives the intensity of light at the observation point. Fresnel diffraction from a rectangular aperture is shown in Figure 11.9. The aperture is not infinite in length; fringes on the right and left side of the images are due to the edges of the aperture in the y-dimension.

We are forced to stop the development of general solutions to Fresnel diffraction at this point. The calculations of apertures that are more complex than simple rectangular apertures, with uniform amplitude transmission functions, are very demanding and are best left to the specialist. These calculations usually require numerical evaluation of (11.8). The reader can get an idea of the next degree of difficulty in diffraction problems by referring to Born and Wolf [3], where examples are given of the use of Fresnel diffraction to calculate the optical fields near the focal planes of optical systems, including systems with aberrations.

We will now develop a semiquantitative method for visualizing Fresnel diffraction that is particularly useful for predicting diffraction by a circular aperture. This method uses the concept of Fresnel zones.

Figure 11.8 *Fresnel diffraction pattern from a large rectangular aperture produced by illuminating the aperture with a plane wave from a HeNe laser. One edge of the aperture produces the fringe pattern calculated in Figures 11.6 and 11.7. The fringes produced by the second edge of the aperture extend into the shadow region of the first slit, as can be seen by close examination of the image.*

11.4 Fresnel Zones

Fresnel used the geometrical construction now called the Fresnel zone to evaluate the Huygens–Fresnel integral. The Fresnel zone is a mathematical construct serving the role of a Huygens source in the description of wave propagation. Assume that at time t, a spherical wavefront from a source at P_1 has a radius R'. To determine the field at the observation point P_0 due to this wavefront, a set of concentric spheres of radii Z, $Z + \lambda/2$, $Z+2\lambda/2, \ldots, Z+j\lambda/2, \ldots$ are constructed, where Z is the distance from the wavefront to the observation point on the line connecting P_1 and P_0 (see Figure 11.10). These spheres divide the wavefront into a number of zones $\zeta_1, \zeta_2, \ldots, \zeta_j \ldots$, called *Fresnel zones*, or *half-period zones*.

We treat each zone as a circular aperture illuminated from the left by a spherical wave of the form

$$\tilde{E}_j(\mathbf{R}') = \frac{Ae^{-i\mathbf{k}\cdot\mathbf{R}'}}{R'} = \frac{Ae^{-ikR'}}{R'},$$

where R' is the radius of the spherical wave. The field at P_0 due to the jth zone is obtained by using (9.9):

$$\tilde{E}_j(P_0) = \frac{A}{R'}\,e^{-i\mathbf{k}\cdot\mathbf{R}'} \iint_{\zeta_j} C(\varphi)\frac{e^{-i\mathbf{k}\cdot\mathbf{R}}}{R}\,dS. \tag{11.14}$$

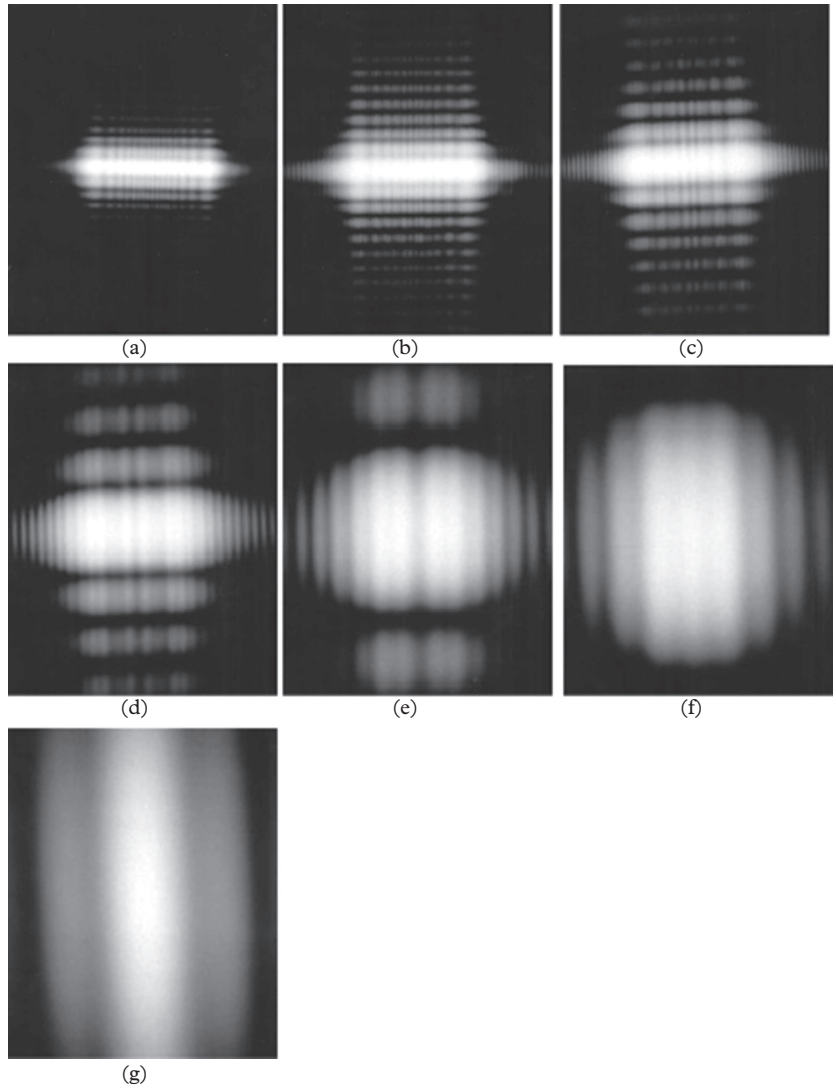

Figure 11.9 *Fresnel diffraction from a rectangular aperture, recorded at a number of distances from the aperture. The distances were selected by calculating the number of zones that would exist in the short dimension if the aperture were circular. The zones match the number of zones used in Figure 11.19: (a) 5, (b) 4, (c) 3, (d) 2, (e) 1, (f) 1/2, and (g) 1/3 zones present in the aperture. In (a), the light distribution is roughly the shape of the aperture, while in (g), the shape is determined by the far-field theory of Chapter 10 (i.e., the light distribution size is inversely proportional to the dimension of the slit).*

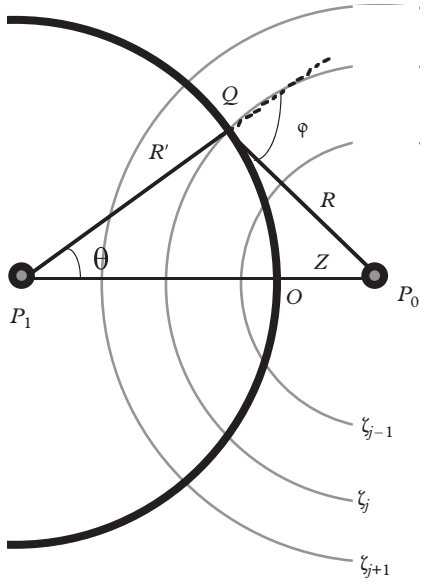

Figure 11.10 *Construction of Fresnel zones for a spherical wave.*

For the integration over the *j*th zone, the surface element is

$$dS = R'^2 \sin\theta \, d\theta \, d\phi. \tag{11.15}$$

The limits of integration extend over the range

$$Z + (j-1)\frac{\lambda}{2} \leq R \leq Z + j\frac{\lambda}{2}.$$

The variable of integration is R; thus, a relationship between R' and R must be found. This is accomplished by using the geometrical construction shown in Figure 11.10.

A perpendicular is drawn from the point Q on the spherical wave to the line connecting P_1 and P_0 (see Figure 11.11). In the notation of this chapter, the distance from the source to the observation point is $Z' + Z$, and the distance from the source to the plane of the zone is the radius of the incident spherical wave, $Z' = R'$. The distance from P_1 to P_0 can be written

$$x_1 + x_2 = R' + Z.$$

The distance from the observation point to the zone is

$$\begin{aligned} R^2 = x_2^2 + y^2 &= [(R' + Z) - x_1]^2 + (R' \sin\theta)^2 \\ &= R'^2 + (R' + Z)^2 - 2R'(R' + Z)\cos\theta. \end{aligned}$$

The derivative of this expression yields

$$R\,dR = R'(R' + Z)\sin\theta \, d\theta. \tag{11.16}$$

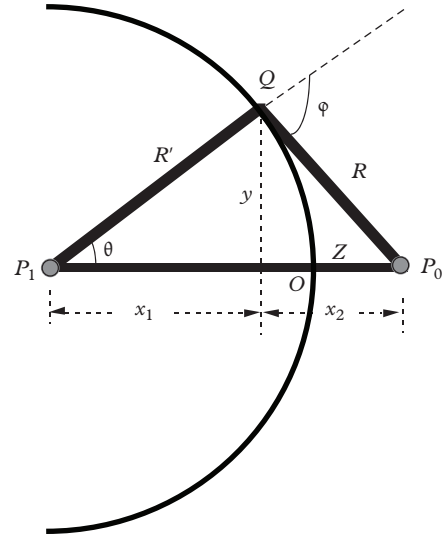

Figure 11.11 *Geometry for finding R.*

Substituting (11.16) into (11.15) gives

$$dS = \frac{R'}{R' + Z} R\, dR\, d\phi. \tag{11.17}$$

The integration over ϕ is accomplished by rotating the surface element about the P_1P_0 axis. After integrating over ϕ between the limits of 0 and 2π, we obtain

$$\tilde{E}_j(P_0) = \frac{2\pi A}{R' + Z} e^{-i\mathbf{k}\cdot\mathbf{R}'} \int_{Z+(j-1)\lambda/2}^{Z+j\lambda/2} e^{-i\mathbf{k}\cdot\mathbf{R}} C(\varphi)\, dR. \tag{11.18}$$

We assume that $R', Z \gg \lambda$ so that the obliquity factor is a constant over a single zone, i.e., $C(\varphi) = C_j$. To demonstrate that this assumption is reasonable, a list of obliquity factors for the first 12 zones is shown in Table 11.2. The parameters used to calculate these factors were $Z = 1$ m and $\lambda = 500$ nm. As can be seen in Table 11.2, the obliquity factor only changes by 2 parts in 10^{-7} across one zone. Applying the assumption that the obliquity factor is constant over a zone allows the integral in (11.18) to be calculated:

$$\tilde{E}_j(P_0) = \frac{2\pi i C_j A}{k(R' + Z)} e^{-ik(R'+Z)} e^{-ikj\lambda/2} \left(1 - e^{-ik\lambda/2}\right). \tag{11.19}$$

Using the identity $k\lambda = 2\pi$ and the definition for the distance between the source and observation point, $D = R' + Z$, (11.19) can be simplified to

$$\tilde{E}_j(P_0) = 2i\lambda(-1)^j \frac{C_j A}{D} e^{-ikD}. \tag{11.20}$$

Not only is the obliquity factor C_j constant over a single zone, but it is a very slowly varying parameter of j, as shown in Figure 11.12, where the obliquity factor can be seen

Table 11.2 *Obliquity factor*

Zone	Angle	Obliquity
0	0	1.0
1	0.057295768	0.99999975
2	0.081028435	0.9999995
3	0.099239139	0.99999925
4	0.114591464	0.999999
5	0.128117124	0.99999875
6	0.140345249	0.9999985
7	0.151590163	0.99999825
8	0.162056667	0.9999980
9	0.171887016	0.99999775
10	0.181184786	0.9999975
11	0.190028167	0.99999725
12	0.198477906	0.999997

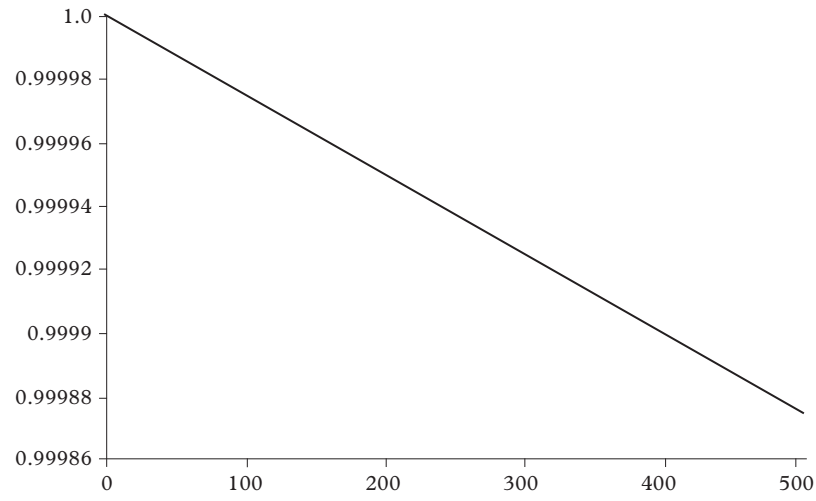

Figure 11.12 *Obliquity factor as a function of zone number. In this example, Z = 1 m and the wavelength is 500 nm.*

to change by less than 2 parts in 10^4 when j changes by 500. We are therefore justified in treating the absolute value of (11.20) as constant as j varies over a large range of values.

The physical reasons for the behavior predicted by (11.20) are quite easy to understand. The distance from P_0 to a zone changes by only $\lambda/2$ as we move from zone to zone and the area of a zone is almost a constant, independent of zone number; thus, the amplitudes of the Huygens wavelets from each zone should be approximately equal. The alternation in

sign from zone to zone is due to the phase change of the light wave from adjacent zones because the propagation path for adjacent zones differs by $\lambda/2$.

To find the total field strength at P_0 due to N zones, the collection of Huygens wavelets are added:

$$E(P_0) = \sum_{j=1}^{N} \tilde{E}_j(P_0)$$

$$= \frac{2i\lambda A}{D} e^{-ikD} \sum_{j=1}^{N} (-1)^j C_j. \tag{11.21}$$

To evaluate the sum, its elements are regrouped and rewritten as

$$-\sum_{j=1}^{N} (-1)^j C_j = \frac{C_1}{2} + \left(\frac{C_1}{2} - C_2 + \frac{C_3}{2}\right) + \left(\frac{C_3}{2} - C_4 + \frac{C_5}{2}\right) + \cdots .$$

Because the C's are very slowly varying functions of j, even out to 500 zones, as shown in Figure 11.12, we are justified in setting the quantities in parentheses equal to zero. With this approximation, the summation can be set equal to one of two values, depending upon whether there are an even or odd number of terms in the summation:

$$-\sum_{j=1}^{N} (-1)^j C_j = \begin{cases} \frac{1}{2}(C_1 + C_N), & N \text{ odd}, \\ \frac{1}{2}(C_1 - C_N), & N \text{ even}. \end{cases}$$

For very large N, the obliquity factor approaches zero, $C_N \to 0$, as demonstrated in Figure 11.13. Thus, the theory has led to the conclusion that the total field produced by an unobstructed wave is equal to one-half the contribution from the first Fresnel zone, i.e., $E = E_1/2$. Stating this in a slightly different way, we see that a surprising result has been obtained—the contribution from the first Fresnel zone is twice the amplitude of the unobstructed wave!

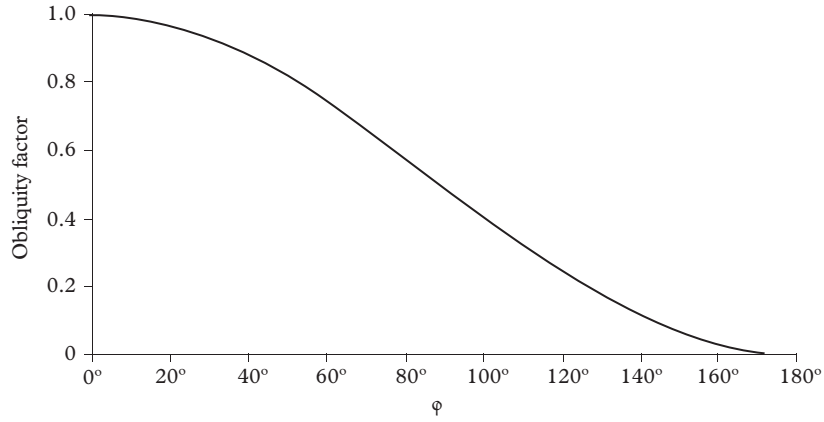

Figure 11.13 *The obliquity factor as a function of the angle defined in Figure 11.9.*

The zone construction can be used to analyze the effect of the obstruction of all or part of a zone. For example, by constructing a circular aperture with a diameter equal to the diameter of the first Fresnel zone, we have just demonstrated that it is possible to produce intensity at the point P_0 equal to four times the intensity that would be observed if no aperture were present. To analyze the effects of a smaller aperture, we subdivide a half-period zone into a number of subzones such that there is a constant phase difference between each subzone. To add the waves from each of the subzones, the vector approach introduced in Chapter 4 (see Figure 4.2) will be used. The individual vectors form a curve known as the *vibrational curve*. Figure 11.14(a) shows the vibrational curve produced by the addition of waves from nine subzones of the first Fresnel zone. The vibrational curve in Figure 11.14(b) is an arc with the appearance of a half-circle. The radius of curvature of the arc is defined as

$$\frac{\Delta s}{\Delta \alpha} = \rho,$$

where s and α are defined as the arc length between two subzones and the phase difference between two subzones, respectively. [See Figure 11.16(b) for a geometrical representation of these parameters.] If the radius of curvature of the arc were calculated, we would discover that it is a constant, except for the contribution of the obliquity factor:

$$\rho = \frac{\lambda R'}{R' + Z} C(\varphi).$$

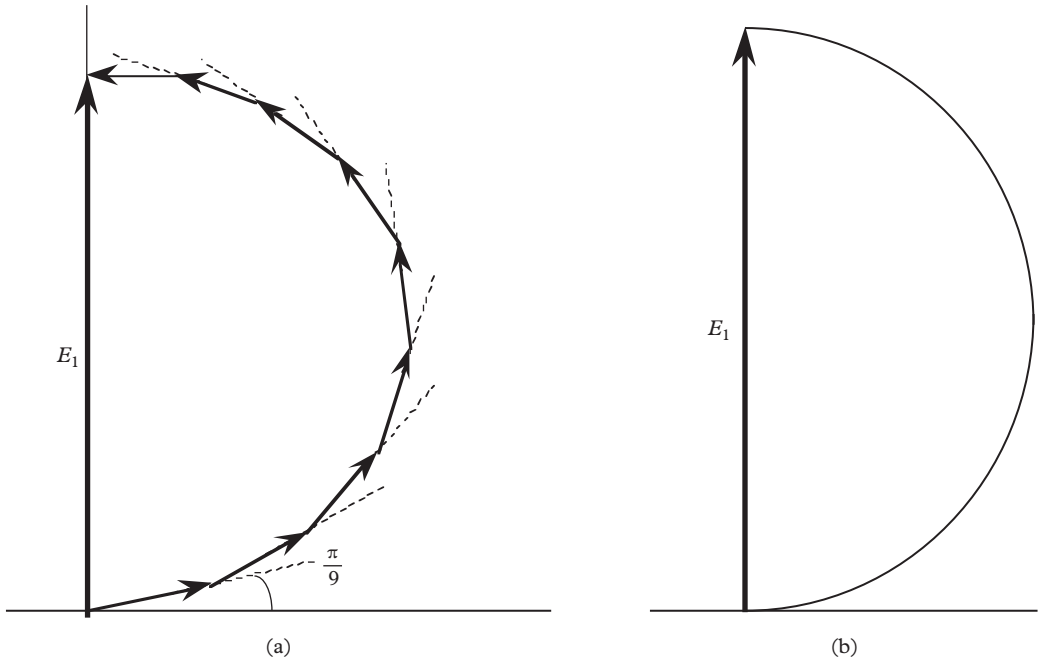

Figure 11.14 *(a) Vector addition of waves from nine subzones from the first Fresnel zone. (b) Vector addition of waves from an infinite number of subzones from the first Fresnel zone.*

Because the obliquity factor for a single zone is assumed constant, the radius of curvature of the vibrational curve is constant over a single zone. If we let the number of subzones approach infinity [Figure 11.14(b)], the vibrational curve becomes a semicircle whose chord is equal to the wavelet produced by zone one, i.e., E_1. If we subdivide additional zones and add the subzone contributions, we create other half-circles whose radii decrease at the same rate as the obliquity factor. The vibrational curve for the total wave is a spiral, constructed of semicircles that converge to a point halfway between the ends of the first half-circle. The length of the vector from the start to the end of the spiral is $E = E_1/2$, as we derived above.

To appreciate the utility of the vibrational curve, we will use the spiral just described to evaluate the Fresnel diffraction due to a circular aperture and a circular disk.

11.4.1 Incident Plane Wave

The Fresnel zones have been defined as spherical rings constructed upon a spherical wave. By replacing the incident spherical wave with a plane wave, the problem can be greatly simplified. With an incident plane wave, the zone is defined on a plane, removing the need for solid geometry. The use of an incident plane wave does not, however, reduce the physical insight provided by the zone construction.

Plane wave Fresnel zones consist of a set of concentric rings, constructed by drawing circles of radius R_j (see Figure 11.15). The nth plane wave Fresnel zone, shown in Figure 11.15, has a radius of

$$\begin{aligned} r_n^2 &= R_n^2 - Z^2 \\ &= \left(Z + \frac{n\lambda}{2}\right)^2 - Z^2 = nZ\lambda + \left(\frac{n\lambda}{2}\right)^2. \end{aligned} \tag{11.22}$$

For small values of n, the nth zone has a radius

$$r_n \approx \sqrt{nZ\lambda}. \tag{11.23}$$

In the discussion of Fresnel zones, when it is necessary to calculate the area of a zone, it will be assumed that the incident wave is a plane wave. This assumption will reduce the mathematical complexity of the examples.

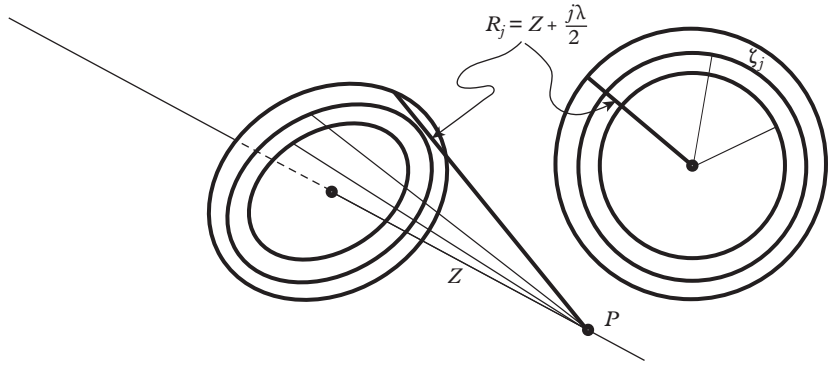

Figure 11.15 *Construction of Fresnel zones for a plane wave.*

11.5 Circular Aperture

The vector addition technique, described in Figure 11.14, can be used to evaluate Fresnel diffraction at a point P_0 from a circular aperture and yields the intensity distribution along the axis of symmetry of the circular aperture. The zone concept will also allow a qualitative description of the light distribution normal to this axis.

To develop a quantitative estimate of the intensity at an observation point on the axis of symmetry of the circular aperture, we construct a spiral (Figure 11.16) to represent the Fresnel zones of a spherical wave incident on the aperture. The point B on the spiral shown in Figure 11.16(a) corresponds to the portion of the spherical wave unobstructed by the screen. The length of the chord AB represents the amplitude of the light wave at the observation point P_0. As the diameter of the aperture increases, B moves along the spiral, in a counterclockwise fashion, away from A. AB first reaches a maximum when B reaches the point labeled A_1 in Figure 11.16; the aperture has then uncovered the first Fresnel zone. At this point, the amplitude is twice what it would be with no obstruction! Four times the intensity!

If the aperture diameter continues to increase, B reaches the point labeled A_2 in Figure 11.16, and the amplitude is very nearly zero; two zones are now exposed in the aperture. Further maxima occur when an odd number of zones are exposed in the aperture and further minima when an even number of zones are exposed. Figure 11.17 shows an aperture containing four exposed Fresnel zones. The amplitude at the observation point would correspond to the chord drawn from A to A_4 in Figure 11.16.

The aperture diameter can be fixed and the observation point P_0 can move along or perpendicular to the axis of symmetry of the circular aperture. As P_0 is moved away from the aperture, along the symmetry axis, i.e., as Z increases, the radius of the Fresnel zones increases without limit. [See (11.23) to calculate the zone radius for an incident plane wave.] If Z is large enough, the aperture radius a will be smaller than the radius of the first zone:

$$Z_{\max} = \frac{a^2}{\lambda}. \tag{11.24}$$

For values of Z that exceed (11.24), Fraunhofer diffraction will be observed. At $Z_{\max}$, the light intensity is a maximum, given by the chord length from A to A_1 in Figure 11.16. If $\lambda = 500$ nm and $a = 0.5$ mm, then this maximum occurs when $Z = 0.5$ m.

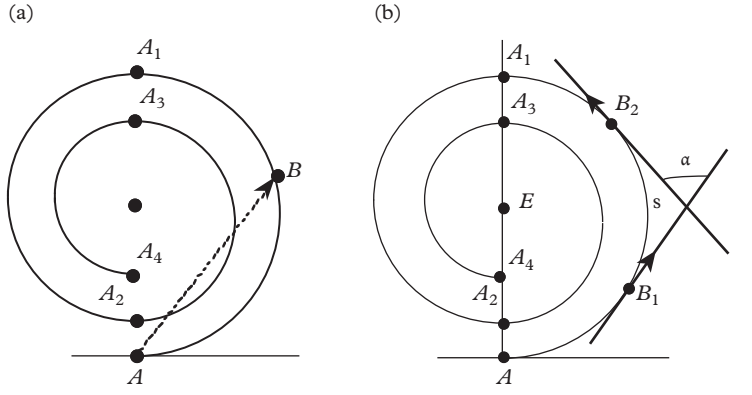

Figure 11.16 *(a) Vibrational curve for determining Fresnel diffraction from a circular aperture. The changes in diameter of the half-circles making up the spiral have been greatly exaggerated for easy visualization. The actual changes are those displayed in Figure 11.12. (b) B_1 and B_2 are two points on the incident wave surface, distances R_1 and R_2 from the observation point. The arc length s is the arithmetic sum of the amplitude of the wavelets from B_1 and B_2. The phase difference between the wavelets from B_1 and B_2 is α.*

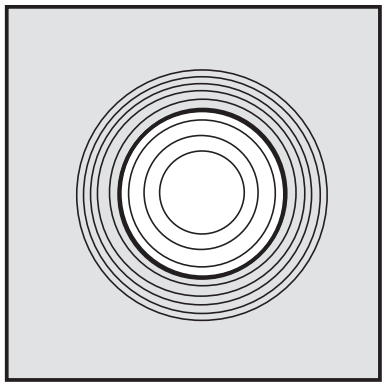

Figure 11.17 *Aperture with four Fresnel zones exposed.*

If we start at Z_{max} and move toward the aperture along the axis, Z will be decreasing in value, and a point will be reached when the intensity on axis becomes a minimum. The value of Z where the first minimum in intensity is observed is equal to

$$Z_{min} = \frac{a^2}{2\lambda}.$$

In Figure 11.16, the chord would extend from A to A_2.

As the observation point P_0 is moved along the axis toward the aperture, and Z assumes values less than Z_{min}, point B in Figure 11.16 spirals inward, toward the center of the spiral, and the intensity cycles through maximum and minimum values. The cycling of the intensity as the observation point moves toward the aperture will not continue indefinitely. At some point, the field on the axis must approach the field observed without the aperture. It is easy to demonstrate that the theory predicts this behavior, by calculating the distance between maximum and minimum values of intensity.

11.5.1 Intensity near the Aperture

We can derive an expression for the distance between the maximum and minimum intensities along the symmetry axis of the circular aperture. We will demonstrate that this distance decreases as the observation point approaches the aperture until the distance between maxima is equal to a wavelength. Once that position has been reached, the on-axis intensity can be treated as constant.

Using the geometry of Figure 11.15,

$$R_n^2 = Z^2 + a^2,$$

where a is the aperture radius. We define the distance

$$q_n = R_n - Z$$

as the increase in distance from the wavefront to the observation point if we move out from the center of the wavefront to the nth zone. The change in q as we move between two adjacent zones is $\Delta q = \lambda/2$. Since

$$R_n^2 = (q_n + Z)^2,$$

we may write

$$(q_n + Z)^2 = Z^2 + a^2.$$

Differentiating this equation yields

$$\begin{aligned} \Delta Z &= -\frac{q_n + Z}{q_n}\Delta q \\ &= -\frac{R_n}{R_n - Z}\Delta q \\ &= -\frac{R_n}{R_n - Z}\,\frac{\lambda}{2}. \end{aligned} \tag{11.25}$$

When the observation point is very near the aperture, and Z is not very large compared with the aperture radius a, then $Z \approx R_n \approx a$. We have already stated that

$$R_n^2 - Z^2 = (R_n - Z)(R_n + Z) = a^2,$$

so

$$R_n - Z \approx \frac{R_n}{2}.$$

Substituting this result into (11.25) demonstrates that ΔZ is of the order of a wavelength. Thus, when the observation point gets close to the aperture, the cycles between intensity maxima, occur over a distance equal to a wavelength. The intensity changes are then unobservable and the on-axis intensity is a constant. Figure 11.20 in Section 11.5.2 displays experimental data supporting this result on axis.

11.5.2 Off-Axis Intensity

We can also determine in a qualitative way the light distribution perpendicular to the axis of a circular aperture using Fresnel zones. Assume that a plane wave is incident upon a circular aperture of radius a and that the observation point is located a distance

$$Z = \frac{a^2}{4\lambda}$$

away from the aperture. There are four Fresnel zones in the aperture at this observation point, and the light intensity on axis is very nearly zero (see Figure 11.17). As the observation point is moved off axis to the left, the fourth zone becomes partially obstructed and the fifth zone begins to appear (see Figure 11.18). Since the negative contribution to the amplitude is decreasing, and the positive contribution is increasing, the light intensity increases as the observation point moves off-axis. In moving off-axis, successive zones appear and disappear in the aperture, and a set of maxima and minima are observed in the plane perpendicular to the symmetry axis. Because of the cylindrical symmetry of the aperture, lines of constant intensity will be circles about the axis.

If the observation point is moved far off axis (Figure 11.19), the central zone becomes obscured, the contributions from the many exposed partial zones cancel one another, and the intensity falls to zero. If we pick any of the images in Figure 11.20, we see bright rings supporting this result.

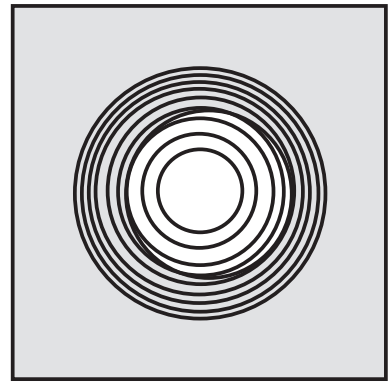

Figure 11.18 *The Fresnel zones in the aperture of Figure 11.17 as the observation point moves to the left.*

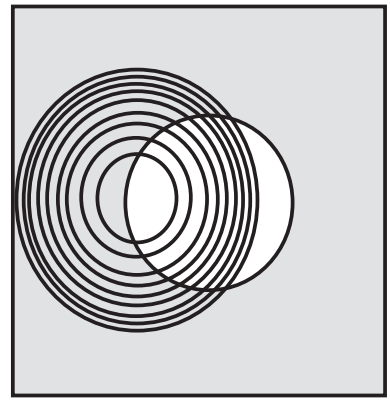

Figure 11.19 *The Fresnel zones exposed just as we move into the geometrical shadow region.*

11.6 Opaque Screen

If the screen containing a circular aperture of radius a is replaced by an opaque disk of radius a, then the intensity distribution on the symmetry axis behind the disk is found to be equal to the value that would be observed with no disk present. This prediction was first derived by Poisson, with the aim of demonstrating that wave theory was incorrect; however, experimental observation supported the prediction and verified the theory. We will develop a qualitative derivation of this prediction here, and a quantitative description will be given in Appendix 11A using Babinet's principle.

We construct a spiral, shown in Figure 11.21, similar to the one for the circular aperture in Figure 11.16. Point B on the spiral represents the edge of the disk. The portion of the

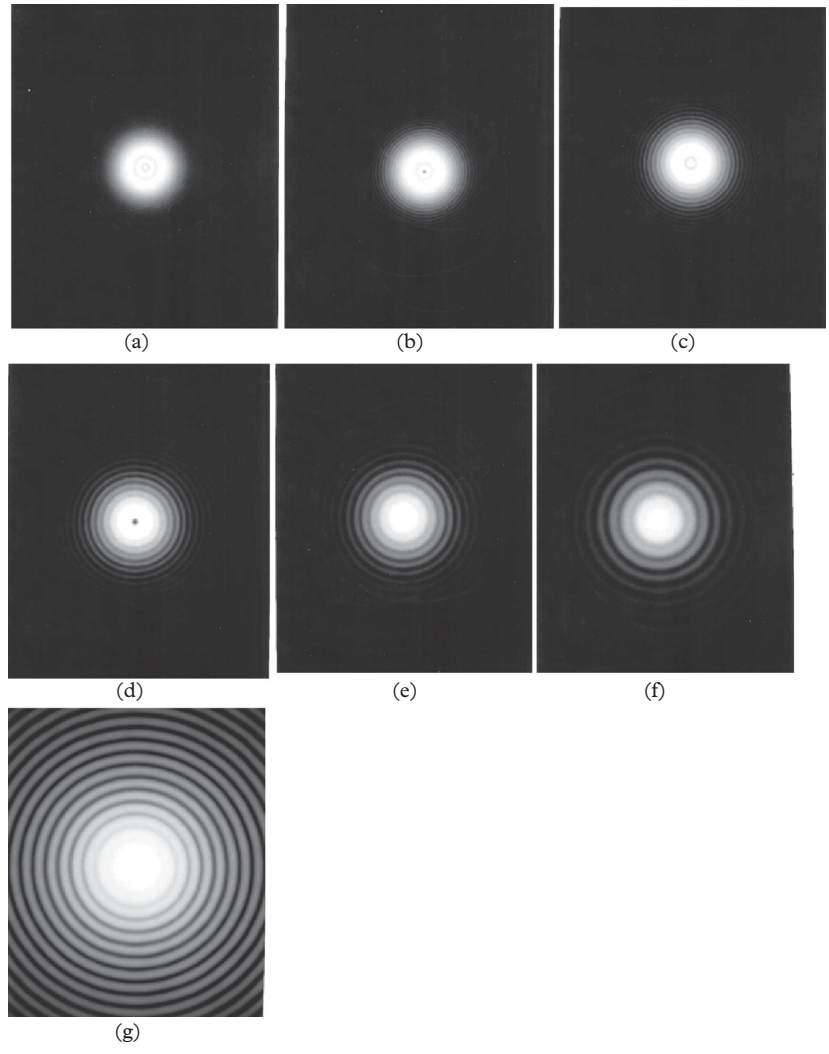

Figure 11.20 *Fresnel diffraction from a circular aperture measured at positions from the aperture corresponding to (a) 5, (b) 4, (c) 3, (d) 2, (e) 1, (f) 1/2, and (g) 1/3 zones present in the aperture.*

spiral from A to B does not contribute, because that portion of the wave is covered by the disk, and the zones associated with that portion of the wave cannot be seen from the observation point. The amplitude at P_0 is the length of the chord from B to Z shown in Figure 11.20. If the observation point moves toward the disk, then B moves along the spiral toward Z. There is always intensity on axis for this configuration, although it slowly decreases until it reaches zero when the observation point is on the disk, which corresponds to point B reaching point Z on the spiral. There are no maxima or minima observed as the disk diameter a increases or as the observation distance changes. If the observation point is moved perpendicular to the symmetry axis, a set of concentric bright rings are observed. The origin of these bright rings, shown in Figures 11.22(a) and (b) for circular and rectangular

symmetry, respectively, can be explained using Fresnel zones, in a manner similar to that used to explain the bright rings observed in a Fresnel diffraction pattern from a circular aperture.

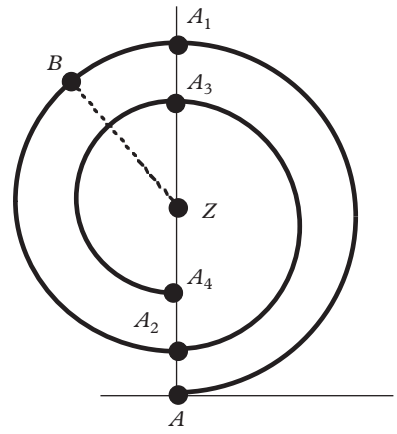

Figure 11.21 *Vibrational curve for an opaque disk.*

11.7 Zone Plate

In the construction of Fresnel zones, each zone was assumed to produce a Huygens wavelet, out of phase with the wavelets produced by its nearest neighbors. If every other zone were blocked, then there would be no negative contributions to (11.21). The intensity on axis would be equal to the square of the sum of the amplitudes produced by the in-phase zones—exceeding the intensity of the incident wave. An optical component made by the obstruction of either the odd or the even zones could therefore be used to concentrate the energy in a light wave.

We will use the geometry shown in Figure 11.23 to determine how to construct an aperture that would block every other Fresnel zone. We will neglect the curvature of the wavefront, shown by the dotted line in Figure 11.23. By ignoring the wavefront curvature, we introduce aberrations into any optical component designed with this theory.

The radius of an arbitrary zone is given by y and can be found using the Pythagorean theorem:

$$y^2 = R'^2 - Z'^2, \quad y^2 = R^2 - Z^2.$$

The difference in path length from the center of the wavefront to the point Q, a height y above the optical axis, can be obtained from these two equations:

$$R' - Z' = \frac{y^2}{R' + Z'}, \quad R - Z = \frac{y^2}{R + Z}.$$

We will assume that $R' \approx Z'$ and $R \approx Z$, allowing these equations to be rewritten as

$$R' - Z' \approx \frac{y^2}{2Z'}, \quad R - Z \approx \frac{y^2}{2Z}.$$

When $y = r_0$, the radius of the nth Fresnel zone, then the difference in propagation paths for a light ray propagating from the source to the edge of the opening and then to point P_0

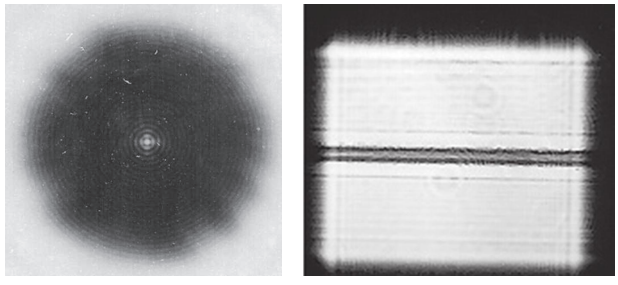

(a) (b)

Figure 11.22 *Poisson's spot observed in the shadow of a ball bearing (a) and a thin wire (b) illuminated by a plane wave from a HeNe laser.*

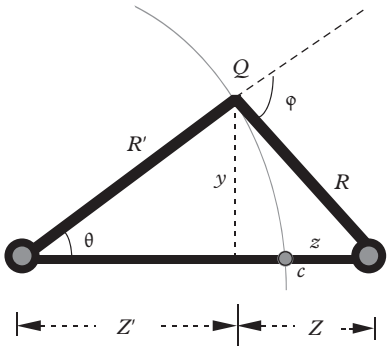

Figure 11.23 *Geometry for the design of a zone plate.*

and a light ray propagating from the source P_1 to P_0 along the axis is given by

$$(R' + R) - (Z' + Z) = \pm\frac{n\lambda}{2}.$$

By constructing an obstruction in the shape of a ring with a minimum radius given by $y = r_1$, we prevent the out-of-phase light wave from reaching the observation point. The opaque ring will block the out-of-phase light rays as long as its radius satisfies the equation

$$\pm\frac{\lambda}{r_1^2} = \frac{1}{Z'} + \frac{1}{Z}. \tag{11.26}$$

Equation (11.26) can be generalized to allow the calculation of the radius of a ring that will block a preselected zone, given the source and observation positions:

$$\pm\frac{n\lambda}{r_n^2} = \frac{1}{Z'} + \frac{1}{Z}.$$

The boundaries of the opaque zones used to block out-of-phase wavelets are seen to increase as the square root of the integers. An array of opaque rings constructed according to this prescription is called a *zone plate* (see Figure 11.24).

(a)

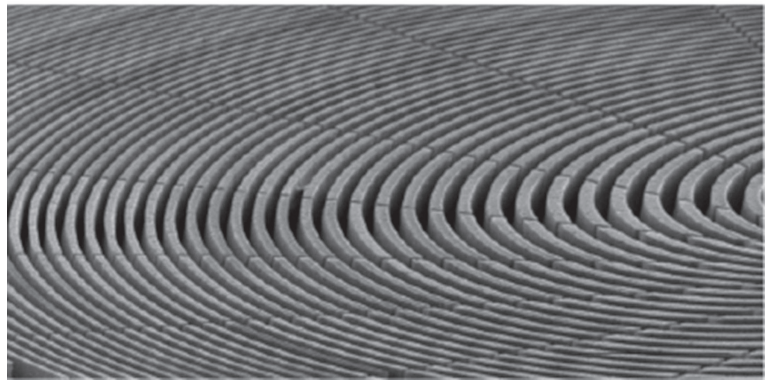

(b)

Figure 11.24 *(a) Calculated amplitude zone plate with alternate opaque zones. (b) Phase zone plate produced using X-ray lithography. (Reprinted by permission from Macmillan Publishers Ltd: Nature Communications (Chang, C. and A. Sakdinawat, Ultra-high aspect ratio high-resolution nanofabrication for hard X-ray diffractive optics. Nature Communications, 2014. 5), Copyright 2014.)*

By comparing (11.26) with (5A.8), we see that a zone plate with zone radii constructed according to the rule just derived will perform like a lens of focal length

$$f = \pm\frac{r_1^2}{\lambda}. \tag{11.27}$$

The zone plate's operation is based upon diffraction, while a lens' operation is based upon the law of refraction. For this reason, the performance of a zone plate is different than that of a conventional lens.

The zone plate shown in Figure 11.25 will act as both a positive and negative lens. What we originally called the source can now be labeled the object point *O*, and what we called the observation point can now be labeled the image point *I*. The light passing through the zone plate is diffracted into two paths, labeled *C* and *D* in Figure 11.25. The light waves labeled *C* converge to a real image point *I*. For these waves, the zone plate performs the role of a positive lens with a focal length given by the positive value of (11.27). The light waves labeled *D* appear to originate from the virtual image point labeled *I*. For these waves, the zone plate performs the role of a negative lens with a focal length given by the negative value of (11.27).

The zone plate will not have a single focus, as is the case for a refractive optical element, but rather will have multiple foci. As we move toward the zone plate, from the first focus, given by (11.27), the effective Fresnel zones will decrease in diameter. The zone plate will no longer obstruct out-of-phase Fresnel zones, and the light intensity on the axis will decrease. However, additional maxima of the on-axis intensity will be observed at values of *Z* for which the first zone plate opening contains an odd number of zones. These positions can also be labeled as foci of the zone plate; however, the intensity at each of these foci will be less than the intensity at the primary focus.

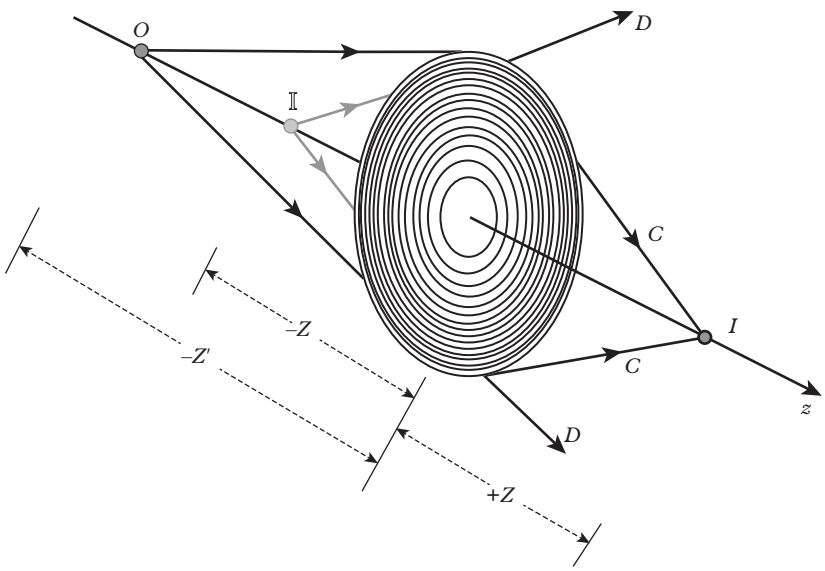

Figure 11.25 *A zone plate acts as if it were both a positive and a negative lens.*

Lord Rayleigh suggested that an improvement of the zone plate design would result if, instead of blocking every other zone, the phase of alternate zones were shifted by 180°. The resulting zone plate, called a *phase-reversal zone plate* [Figure 11.24(b)], would utilize the incident light more efficiently. R.W. Wood was the first to make such a zone plate. A zone plate in the microwave region of the spectrum can be constructed using polyethylene with an index of refraction of 2.25 at 33 GHz. A 9 mm thick sheet of this plastic is about one wavelength thick. By cutting circular slots of radii given by (11.27) into a 9 mm sheet of polyethylene, an efficient millimeter-wave Fresnel zone plate can be constructed. (Holography and X-ray lithography [4] provide a method of constructing phase-reversal zone plates at shorter wavelengths.)

The resolving power of a zone plate is a function of the number of zones contained in the plate. When this number exceeds 200, the zone plate's resolution approaches that of a lens [5].

11.8 Pinhole Camera

A special case of the Fresnel zone plate is a simple aperture of radius r_1. Only the central zone will exist in this aperture, and an image of an object will be generated in a plane whose position is determined by (11.26). An aperture designed using (11.26) produces images for a single object/image distance and a single wavelength, but the performance of the device is tolerant of variations of these parameters. The single-Fresnel-zone pinhole is very small compared with the other dimensions of the camera. If we use geometrical optics to analyze the camera's performance, we find that the pinhole's size prevents more than one ray from an object point from reaching the image plane. For this reason, we expect to observe only a small amount of image blurring. Figure 11.26 contains an image recorded using such an

Figure 11.26 *Photograph produced with a pinhole camera. This was a timed exposure, and the wind moved the flowers.*

aperture. The aperture generates acceptable, although still blurry, images over a wide range of wavelengths and object distances.

An aperture containing a single Fresnel zone is called a *pinhole camera* and is quite easy to construct [6]. The camera used to produce Figure 11.26 was made of cardboard and had nominal dimensions of 35 mm × 35 mm × 45 mm. It was sized to use with 126 film cartridges. The pinhole was about 500 μm in diameter, but the size is not critical. The pinhole can be produced in aluminum foil using a straight pin.

From Figure 11.26, we can see several properties of a pinhole camera:

1. There is no linear distortion: observe the tree trunks in all parts of the field.
2. The depth of field is large: near and far objects are in focus.
3. Long exposure times are required: the flowers moved in the breeze during this exposure, resulting in their image being blurred.

The geometrical optics view of a pinhole camera is not adequate. The modulation transfer function approach discussed in Appendix 10B is a more correct approach for the analysis of the imaging properties of the pinhole. When this approach is taken, one finds that the pinhole diameter given by (11.27) is too large [7]. The proper focal length suggested by a detailed analysis is

$$f = \frac{r_1^2}{3.8\lambda}.$$

The pinhole constructed according to this formula covers about nine-tenths of the first Fresnel zone. The modification of (11.27) is a result of balancing the aberrations due to the neglect of wavefront curvature against the resolving power due to the aperture size.

11.9 Fermat's Principle

The Fresnel zone construction provides physical insight into the interpretation given to Fermat's principle in Chapter 5. Fermat's principle states that if the optical path length of a light ray is varied in a neighborhood about the "true" path, there is no change in path length. By constructing a set of Fresnel zones about the optical path of a light ray, we can discover the size of the neighborhood.

The rules for constructing a Fresnel zone require that all rays passing through a given Fresnel zone have the same optical path length. The true path will pass through the center of the first Fresnel zone constructed on the actual wavefront. The neighborhood must be the area of the first Fresnel zone, since it is over this area that the optical path length does not change. Figure 11.27(a) shows the neighborhood about the true optical path as a crosshatched region equal to the first Fresnel zone.

In Chapter 5, we stated that light waves did not travel over "wrong" paths, because the phase differences for those waves that travel over the "wrong" paths are such that they destructively interfere. By moving the neighborhood defined in the previous paragraph to a region displaced from the "true" optical path, we can use the zone construction to see that this statement is correct.

In Figure 11.27(b), the neighborhood is constructed about a ray that is improper according to Fermat's principle. We see that this region of space would contribute no energy at the observation point, because of destructive interference between the large number of partial zones contained in the neighborhood.

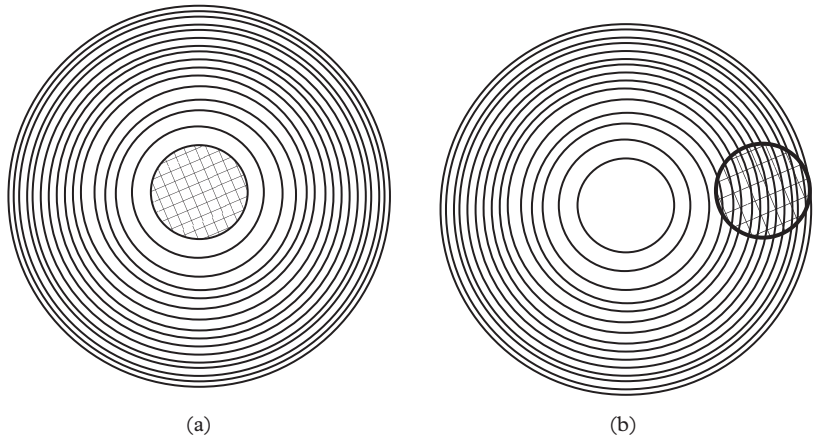

Figure 11.27 *(a) A set of Fresnel zones have been constructed about the optical path taken by some light ray. If the optical path of the ray is varied over the crosshatched area shown in the figure, then the optical path length does not change. This crosshatched area is equal to the first Fresnel zone and is described as the neighborhood of the light ray. (b) The neighborhood defined in (a) is moved so that it surrounds an incorrect optical path for a light ray. We see that this region of space would contribute no wave amplitude at the observation point, because of the destructive interference between the large number of partial zones contained in the neighborhood.*

11.10 Comparison of Techniques

The technique of zones introduced in this chapter to obtain information about Fresnel diffraction from a circular aperture can also be applied to rectangular apertures. The vibrational curve produced using rectangular zones has a radius of curvature α that is a quadratic function of the arc length s. The equation for the vibrational curve is

$$\alpha = Ks^2,$$

where K is a constant of proportionality [8]. This is the equation for a Cornu spiral. Thus, the vibrational curve generated by applying the Fresnel zone construction to apertures of rectangular symmetry is the same Cornu spiral that was obtained by direct solution of the Huygens–Fresnel integral. It is comforting to see that the two approaches lead to the same result.

A vibrational curve equivalent to the Cornu spiral could be constructed for Fraunhofer diffraction. The equation describing such a vibrational curve is

$$\alpha = \frac{\lambda}{2\pi \sin\theta},$$

where

$$\sin\theta = \frac{\xi}{R_0}.$$

The radius is constant; i.e., the vibrational curve is a circle. Such a construction is not nearly as useful for understanding Fraunhofer diffraction as the equivalent construction is for understanding Fresnel diffraction.

All of the techniques introduced in the study of diffraction could be applied generally, but are not, because each technique provides some unique physical insight to aid in understanding a particular diffraction problem.

11.11 Summary

The Huygens–Fresnel integral was reformulated in this chapter by approximating the distances from a point in the aperture to the observation point and to the source, respectively:

$$R \approx Z + \frac{(x-\xi)^2 + (y-\eta)^2}{2Z},$$

$$R' \approx Z' + \frac{(x_s-x)^2 + (y_s-y)^2}{2Z'}.$$

The physical interpretation of this approximation is that the wavefront of the diffracted light is spherical. The integral resulting from the approximation describes Fresnel diffraction:

$$\tilde{E}_P = \frac{i\alpha}{\lambda\rho D} e^{-ikD} \iint f(x,y) \exp\left\{-\frac{ik}{2\rho}\left[(x-x_0)^2 + (y-y_0)^2\right]\right\} dx\, dy.$$

The variables in this expression are defined as follows. D, the distance from the source to the observation point, is

$$D = Z + Z' + \frac{(\xi - x_s)^2 + (\eta - y_s)^2}{2(Z+Z')}.$$

ρ, the effective radius of curvature for the diffracted wave, is

$$\rho = \frac{ZZ'}{Z+Z'}, \qquad \text{or} \qquad \frac{1}{\rho} = \frac{1}{Z} + \frac{1}{Z'}.$$

The diffracted wave is assumed to be only a slightly modified version of the original spherical wave. Finally, the coordinates of the stationary point about which the integration is performed are

$$x_0 = \frac{Z'\xi + Zx_s}{Z+Z'},$$

$$y_0 = \frac{Z'\eta + Zy_s}{Z+Z'}.$$

Fresnel integrals In general, the Fresnel diffraction integral can only be evaluated numerically. For a simple aperture with rectangular symmetry, the integral can be written as

$$\tilde{E}_P = \frac{i\alpha}{2D} e^{-ikD}[C(x) - iS(x)][C(y) - iS(y)],$$

where the Fresnel integrals C and S are defined as

$$C(w) = \int_0^w \cos\left(\frac{1}{2}\pi u^2\right) du,$$

$$S(w) = \int_0^w \sin\left(\frac{1}{2}\pi u^2\right) du.$$

The variable w is the coordinate of the aperture edge and is calculated using the equation for the dummy variable u:

$$u = \sqrt{\frac{2}{\lambda\rho}}\,(x - x_0) \qquad \text{or} \qquad u = \sqrt{\frac{2}{\lambda\rho}}\,(y - y_0).$$

By plotting $C(w)$ versus $S(w)$, a graphical representation called the Cornu spiral (see Appendix 11B) is obtained that can be used to calculate the light distribution due to Fresnel diffraction. If this graphical solution is not of sufficient accuracy, then tables of the two Fresnel integrals are used (see Appendix 11B).

Fresnel zones The most useful concept introduced in this chapter is the geometrical construction called the Fresnel zone. For incident plane waves, the radius of the nth Fresnel zone is given approximately by

$$r_n = \sqrt{nZ\lambda}.$$

When the diameter of the zone for $n = 1$ exceeds the diameter of the aperture, Fraunhofer diffraction is observed. When the converse is true, Fresnel diffraction is observed. The distance at which Fresnel diffraction gives way to Fraunhofer diffraction is given by the Rayleigh range introduced in Chapter 9.

Using the concept of Fresnel zones, a semi quantitative evaluation of Fresnel diffraction from obstructions with circular symmetry can be obtained. However, a more important benefit gained from using the concept of Fresnel zones is the intuitive understanding of light propagation that can be developed.

11.12 Problems

11.1. Use the table of Fresnel integrals to calculate the points $w = +1.5$, $w = -1.7$, and $w = -1.3$ in the diffraction pattern of a straight edge.

11.2. A HeNe laser ($\lambda = 632.8$ nm) produces a plane wave, which passes through a lens of focal length 25 cm. A 0.5 mm diameter straight wire is oriented vertically in the beam, 225 cm from the lens, and the Fresnel pattern is observed 3 m from the wire. Use the Cornu spiral to find the intensity (in terms of incident intensity I_0) on axis.

11.3. A point source ($\lambda = 500$ nm) is placed 1 m from an aperture consisting of a 1 mm radius hole with an opaque disc 0.5 mm radius at its center. The observation point is 1 m away. What is the intensity with the aperture present, compared with the intensity without the aperture?

11.4. A plane wave from a HeNe laser ($\lambda = 632.8$ nm) impinges normally on a circular aperture of radius 0.795 mm. What is the intensity 2 m from the hole, in terms of the incident intensity?

11.5. A plane wave ($\lambda = 500$ nm) is normally incident on a 1 cm diameter hole. How many Fresnel zones are visible when the aperture is viewed from a position on axis, 0.5 m away?

11.6. The innermost zone of a zone plate has a diameter of 0.4 mm. What are the focal length and the first subsidiary focal length when it is illuminated by a plane wave with $\lambda = 441.6$ nm?

11.7. A 3 mm circular aperture is illuminated by $\lambda = 500$ nm plane waves. What are the locations of the first three maxima and minima along the optical axis?

11.8. A plane wave with a wavelength of $\lambda = 500$ nm is incident normal to a square hole, 4 mm on a side. The square hole is oriented with its sides parallel to the *x*- and *y*-axes. What is the intensity, relative to the incident intensity, 0.1 mm from the optical axis along the positive *y*-axis, 4 m from the hole?

11.9. A plane monochromatic wave ($\lambda = 488$ nm) is incident normal to an opaque screen containing an aperture. The aperture is an annulus of radii 1 mm and 1.414 mm. What is the amplitude of the electric field on axis 2.05 m away from the screen in terms of the incident field E_0?

11.10. A plane wave ($\lambda = 500$ nm) of intensity I_0 is normally incident on a square aperture, 2 mm on a side. What is the intensity 4 m from the screen and 0.1 mm below the optical axis (–*x*-direction) and 0.1 mm to the right (–*y*-direction)?

11.11. Calculate the distance between intensity maxima on the axis of symmetry of a circular aperture using (11A.6). Compare the result with the distance predicted using Fresnel zones, (11.25).

11.12. A plane monochromatic wave ($\lambda = 488$ nm) is incident normal to an opaque screen containing an aperture. The aperture is an opaque ring with an outer radius of 1.414 mm and an inner radius of 1 mm. What is the amplitude of the electric field on axis 2.05 m away from the screen in terms of the incident field E_0?

11.13. Using (10B.7), find an expression for the resolution of a zone plate in terms of the number of zones and the maximum zone radius.

11.14. What is the longitudinal chromatic aberration of a pinhole camera with a pinhole diameter of 100 μm? Use C and F light in making the calculation.

11.15. A HeNe laser ($\lambda = 632.8$ nm) produces a plane wave, which is incident on a 0.5 mm diameter straight wire oriented vertically, in the beam. Use the Cornu spiral to find the Fresnel pattern on axis 3 m from the wire in terms of the incident intensity I_0. Make a plot similar to Figure 11.7.

11.16. An Argon laser of wavelength $\lambda = 488$ nm is focused to a point 50 cm in front of a pair of slits. The slits are each 1 mm wide and are spaced 0.5 mm apart. Use the Cornu spiral to generate a plot of the Fresnel diffraction pattern a distance 50 cm behind the slits. Plot a graph of the relative intensity versus w over the range $-2.0 \leq w \leq 2.0$.

REFERENCES

1. Abramowitz, M. and I.A. Stegun, *Handbook of Mathematical Functions*. 1972: Dover.
2. Olver, F.W.J., D.W. Lozier, R.F. Boisvert, and C.W. Clark, Editors, *NIST Handbook of Mathmatical Functions*. 2010: NIST and Cambridge University Press. Online version: *NIST Digital Library of Mathematical Functions*; <http://dlmf.nist.gov/>.
3. Born, M. and E. Wolf, *Principles of Optics*. 7th ed. 1999: Cambridge University Press.
4. Vladimirsky, Y., et al., *Demagnification in proximity x-ray lithography and extensibility to 25 nm by optimizing Fresnel diffraction*. J. Phys. D: Appl. Phys., 1999. **32**: p. L114–L118.
5. Stegliani, D.J., R. Mittra, and R.G. Semonin, *Resolving power of a zone plate*. J. Opt. Soc. Am., 1967. **57**: p. 610–613.
6. *How to Make and Use a Pinhole Camera*; <http://www.kodak.com/ek/US/en/Pinhole_Camera.htm>.
7. Sayanagi, I., *Pinhole imagery*. J. Opt Soc. Am, 1967. **57**: p. 1091–1099.
8. Rossi, B., *Optics*. 1957: Addison-Wesley.

Appendix 11A Babinet's Principle

In the development of the theory of diffraction, we saw that the diffraction field is due to a surface integral, but no restrictions were imposed on the choice of the surface over which the integration must be performed. This fact leads to a very useful property called *Babinet's principle*, first stated by **Jacques Babinet** (**1794–1872**) in 1837 for scalar waves. We will discuss only the scalar Babinet's principle; discussion of the rigorous vector formulation can be found in a number of books on electromagnetic theory (e.g., [1]).

To introduce Babinet's principle, we label a plane separating the source S and observation point P as Σ. If no obstructions are present, then a surface integration over Σ yields the light distribution at P. If we place an opaque screen in this plane with a clear aperture Σ_1, then the field at P is given by integrating over only Σ_1; contributions from Σ outside of Σ_1 are zero.

We may define a screen Σ_2 as *complementary* to Σ_1 if the screen is constructed by replacing the transparent regions of Σ, i.e., Σ_1, by opaque surfaces and the opaque regions of Σ by clear apertures. Figure 11A.1 shows two complementary screens, where the shaded region indicates an opaque surface.

The surface integral over Σ generates the field E in the absence of any screen. If screen Σ_1 is present, then the diffraction field is E_1, obtained by integrating over Σ_1. According to Babinet's principle, the diffraction field due to screen Σ_2 must be

$$\tilde{E}_2 = \tilde{E} - \tilde{E}_1.$$

We will look at examples of the application of the principle for both Fraunhofer and Fresnel diffraction.

11A.1 Fraunhofer Diffraction

Assume that $a(x)$ is the amplitude transmission of an aperture in a screen, $b(x)$ is the amplitude transmission function of the complementary screen, and g is the amplitude of the wave when no screen is present. The Fourier transforms of the amplitude transmission functions

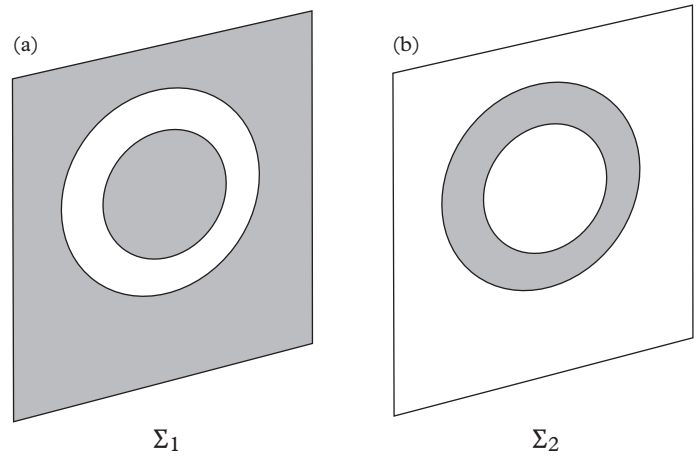

Figure 11A.1 *The unshaded regions in (a) and (b) show an aperture* Σ_1 *and its complement* Σ_2*, respectively.*

of the two apertures are equal to the Fraunhofer diffraction patterns that will be generated by the two apertures:

$$A(k) = \int_{-\infty}^{\infty} a(x)e^{-ikx}\,dx,$$

$$B(k) = \int_{-\infty}^{\infty} b(x)e^{-ikx}\,dx.$$

With no aperture present, the far-field amplitude is

$$G(k) = g\int_{-\infty}^{\infty} e^{-ikx}\,dx.$$

Babinet's principle states that

$$B(x) = G - A(x)$$

must be the diffraction field of the complementary aperture. We may rewrite this equation for the diffraction field as

$$B(k) = G\delta(k) + A(k)e^{i\pi}. \tag{11A.1}$$

The first term in the Fraunhofer diffraction field (11A.1) is located at the origin of the observation plane and is proportional to the amplitude of the unobstructed wave. The second term i is identical to the Fraunhofer diffraction pattern of the original aperture, except for a constant phase. Thus, the Fraunhofer diffraction from the two complementary apertures is equal, except for a constant phase and the bias term at the origin. Physically, this means that the diffraction intensity distributions of complementary apertures will be identical, but their brightnesses will differ!

11A.2 Fresnel Diffraction

We can calculate the Fresnel diffraction from an opaque disk by applying Babinet's principle to the diffraction pattern calculated for a circular aperture. The discussion of Fresnel diffraction from a circular aperture in Chapter 11 was only qualitative, so we will first derive a quantitative expression for Fresnel diffraction, on axis, from a circular aperture.

We assume that a circular aperture of radius a is illuminated by a point source a distance Z' from the aperture. We observe the transmitted wave at the point P, located a distance Z from the aperture (see Figure 11A.2). The Fresnel diffraction integral (11.8) must be expressed in cylindrical coordinates. Before doing so, the parameters of the integral are simplified to fit the geometry of Figure 11A.2. Both the observation point and source are located on the axis of symmetry of the aperture, which lies along the z-axis of a cylindrical coordinate system, and thus

$$x_0 = y_0 = \xi = \eta = 0, \quad D = Z' + Z.$$

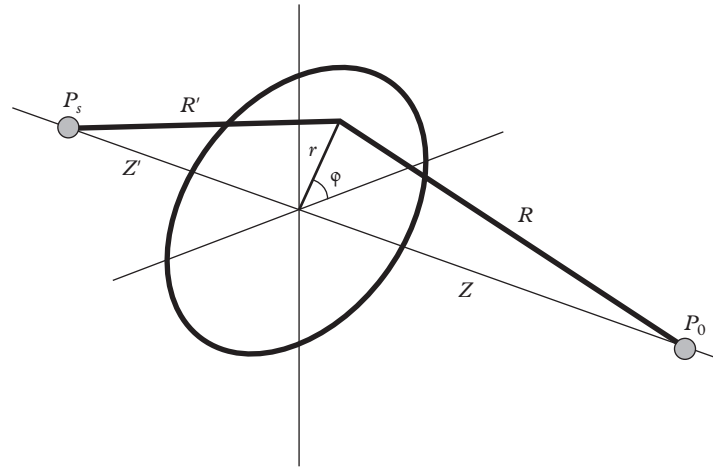

Figure 11A.2 *Geometry for analysis of Fresnel diffraction of circular aperture.*

The approximation for the distance from the source and observation point to the aperture yields

$$R + R' \approx Z + Z' + \frac{r^2}{2\rho} = D + \frac{r^2}{2\rho}, \tag{11A.2}$$

where $r^2 = x^2 + y^2$. The cylindrical coordinate version of (11.8) is then

$$\tilde{E}_P = \frac{i\alpha}{\lambda\rho D} e^{-ikD} \int_0^a \int_0^{2\pi} f(r,\varphi) e^{-i\,kr^2/2\rho}\, r\, dr\, d\varphi. \tag{11A.3}$$

We assume that the transmission function of the aperture is a constant, $f(r,\varphi) = 1$, to make the integral as simple as possible. After performing the integration over the angle φ, (11A.3) can be rewritten as

$$\tilde{E}_{Pa} = \frac{i\alpha\pi}{D} e^{-ikD} \int_0^{a^2/\rho\lambda} e^{-i\pi r^2/\rho\lambda}\, d\left(r^2/\rho\lambda\right). \tag{11A.4}$$

Performing the integration in (11A.4) results in the Fresnel diffraction amplitude

$$\tilde{E}_{Pa} = \frac{\alpha}{D} e^{-ikD} \left(1 - e^{-i\pi a^2/\rho\lambda}\right). \tag{11A.5}$$

The intensity of the diffraction field is

$$\begin{aligned} I_{Pa} &= 2I_0 \left(1 - \cos\frac{\pi a^2}{\rho\lambda}\right) \\ &= 4I_0 \sin^2 \frac{\pi a^2}{2\rho\lambda}. \end{aligned} \tag{11A.6}$$

Equation (11A.6) predicts a sinusoidal variation in intensity as the observation point moves toward the aperture. The separation between maxima in intensity predicted by this result is equivalent to the separation in intensity maxima predicted by (11.25); see Problem 11.11.

Babinet's principle can now be used to evaluate Fresnel diffraction by an opaque disk the same size as the circular aperture, i.e., of radius a. The field for the disk is obtained by subtracting the field diffracted by a circular aperture from the field of an unobstructed spherical wave, E_P:

$$\begin{aligned}\tilde{E}_{Pd} &= \tilde{E}_P - \tilde{E}_{Pa} \\ &= \frac{\alpha}{D} e^{-ikD} - \tilde{E}_{Pa} \\ &= \frac{\alpha}{D} e^{-ikD} e^{-i\pi a^2/\rho\lambda}. \end{aligned} \tag{11A.7}$$

The intensity is

$$I_{Pd} = I_0.$$

The result of the application of Babinet's principle is the conclusion that, at the center of the geometrical shadow cast by the disk, there is a bright spot with the same intensity as would exist if no disk were present. This is Poisson's spot (Figure 11A.3). The intensity of this spot is independent of the choice of observation point. This result agrees with the findings in Chapter 11, obtained by using the Fresnel zone construction.

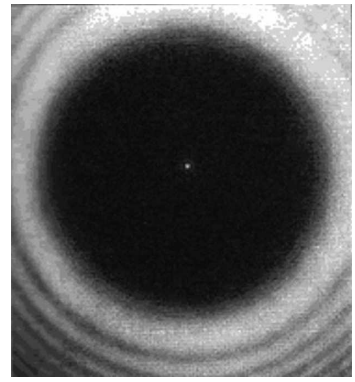

Figure 11A.3 *Poisson's spot.*

REFERENCE

1. Wangsness, R.K., *Electromagnetic Fields*. 2nd ed. 1986: Wiley.

Appendix 11B Fresnel Integral Solutions

11B.1 Table of Fresnel Integrals

w	$C(w)$	$S(w)$	w	$C(w)$	$S(w)$	w	$C(w)$	$S(w)$
0	0	0	3.6	0.588	0.4923	6.2	0.4676	0.5398
0.1	0.1	0.0005	3.7	0.542	0.575	6.25	0.4493	0.4954
0.2	0.1999	0.0042	3.8	0.4481	0.5656	6.3	0.476	0.4555
0.3	0.2994	0.0141	3.9	0.4223	0.4752	6.35	0.524	0.456
0.4	0.3975	0.0334	4	0.4984	0.4204	6.4	0.5496	0.4965
0.5	0.4923	0.0647	4.1	0.5738	0.4758	6.45	0.5292	0.5398
0.6	0.5811	0.1105	4.2	0.5418	0.5633	6.5	0.4816	0.5454
0.7	0.6597	0.1721	4.3	0.4494	0.554	6.55	0.452	0.5078

continued

w	$C(w)$	$S(w)$	w	$C(w)$	$S(w)$	w	$C(w)$	$S(w)$
0.8	0.723	0.2493	4.4	0.4383	0.4622	6.6	0.469	0.4631
0.9	0.7648	0.3398	4.5	0.5261	0.4342	6.65	0.5161	0.4549
1	0.7799	0.4383	4.6	0.5673	0.5162	6.7	0.5467	0.4915
1.1	0.7638	0.5365	4.7	0.4914	0.5672	6.75	0.5302	0.5362
1.2	0.7154	0.6234	4.8	0.4338	0.4968	6.8	0.4831	0.5436
1.3	0.6386	0.6863	4.9	0.5002	0.435	6.85	0.4539	0.506
1.4	0.5431	0.7135	5	0.5637	0.4992	6.9	0.4732	0.4624
1.5	0.4453	0.6975	5.1	0.4998	0.5624	6.95	0.5207	0.4591
1.6	0.3655	0.6389	5.2	0.4389	0.4969	7	0.5455	0.4997
1.7	0.3238	0.5492	5.25	0.461	0.4536	7.05	0.4733	0.536
1.8	0.3336	0.4508	5.3	0.5078	0.4405	7.1	0.4887	0.4572
1.9	0.3944	0.3734	5.35	0.549	0.4662	7.15	0.5393	0.5199
2	0.4882	0.3434	5.4	0.5573	0.514	7.25	0.4601	0.5161
2.1	0.5815	0.3743	5.45	0.5269	0.5519	7.35	0.516	0.4607
2.2	0.6363	0.4557	5.5	0.4784	0.5537	7.45	0.5156	0.5389
2.3	0.6266	0.5531	5.55	0.4456	0.5181	7.55	0.4628	0.482
2.4	0.555	0.6197	5.6	0.4517	0.47	7.65	0.5395	0.4896
2.5	0.4574	0.6192	5.65	0.4926	0.4441	7.75	0.476	0.5323
2.6	0.389	0.55	5.7	0.5385	0.4595	7.85	0.4998	0.4602
2.7	0.3925	0.4529	5.75	0.5551	0.5049	7.95	0.5228	0.532
2.8	0.4675	0.3915	5.8	0.5298	0.5461	8.05	0.4638	0.4859
2.9	0.5624	0.4101	5.85	0.4819	0.5513	8.15	0.5378	0.4932
3	0.6058	0.4963	5.9	0.4486	0.5163	8.25	0.4709	0.5243
3.1	0.5616	0.5818	5.95	0.4566	0.4688	8.35	0.5142	0.4653
3.2	0.4664	0.5933	6	0.4995	0.447	∞	0.5	0.5
3.3	0.4058	0.5192	6.05	0.5424	0.4689			
3.4	0.4385	0.4296	6.1	0.5495	0.5165			
3.5	0.5326	0.4152	6.15	0.5146	0.5496			

11B.2 Cornu Spiral

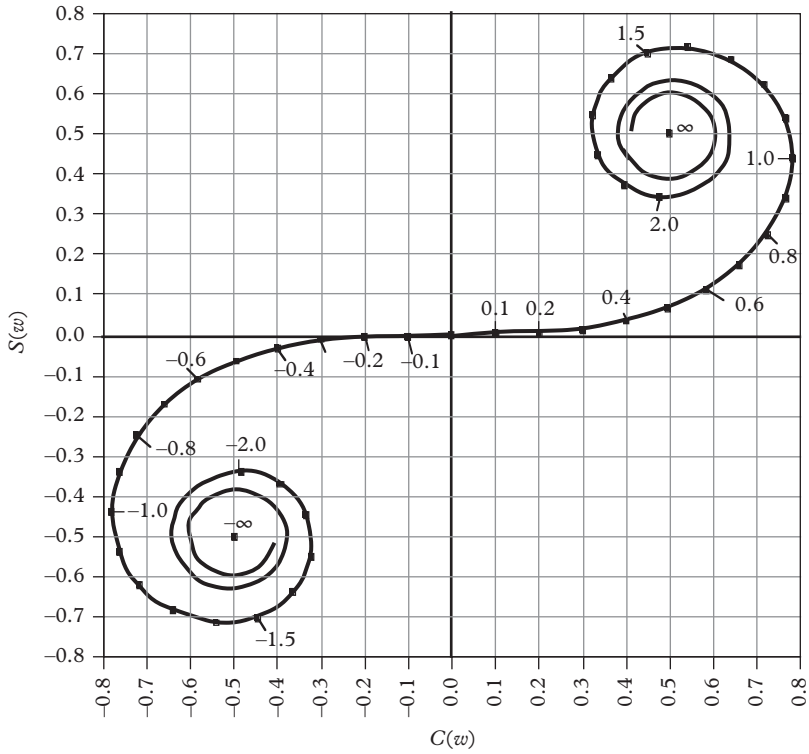

12 Periodic Index of Refraction

12.1 Introduction 496
12.2 Holography 497
12.3 Holographic Recording 502
12.4 Off-Axis Holography 505
12.5 Spatial Spectrum of Off-Axis Holograms 508
12.6 Classification of Holograms 511
12.7 Diffraction Efficiency 512
12.8 Holography and Zone Plates 513
12.9 Resolution Requirements 517
12.10 Coherence Requirements 519
12.11 Photonic Crystals 522
12.12 The Bloch (or Floquet) Theorem 524
12.13 Multilayer Photonic Crystal 526
12.14 Numerical Techniques 529
12.15 Two-Dimensional Periodic Structure 530
12.16 Three-Dimensional Periodic Structure 533
12.17 Fabrication Defects 533
12.18 Natural Photonic Crystals 533
12.19 Summary 533
12.20 Problems 536
References 539
Appendix 12A: Phase Holograms 540
Appendix 12B: VanderLugt Filter 543

12.1 Introduction

We have so far viewed diffraction as a limiting property of light that prevents us from reaching the potential predicted by geometrical optics. We will discover in this chapter that diffraction can be used as a tool to increase the performance of optical systems. Two theoretical approaches have been taken to evaluate the performance of diffractive systems, each based on periodic index of refraction materials: holography [1] and photonic structures [2]. Holography approaches the use of diffraction by using optical waves to generate an index-modulated diffractive structure and pays very little attention to the actual structure generated. The theory of photonic structures considers simple one-, two-, and three-dimensional modulations of the index of refraction of a material and then calculates the propagation of light through the resulting structure.

Dennis Gabor coined the word hologram from the Greek word *holos*, meaning whole, because the recording of the interference pattern contains all of the information of an image field. Gabor invented holography in 1948 [3] with the objective of improving the image quality of the electron microscope.[1] The method of implementing the concept had some serious performance problems. Holography did not prove to be useful to electron microscopy and did not attract much interest until the demonstration of the laser in 1960. The laser allowed the use of the off-axis recording technique developed by **Emmett N. Leith** and **Juris Upatnieks** [4–6]. The off-axis recording geometry made it possible to produce bright, sharp, three-dimensional images. Both the artistic and scientific communities were stimulated to exploit this technology.

In condensed matter physics, the ability to develop electronic devices is based on our understanding of how charge carriers move within the lattice that forms the crystal structure of the material. Electrons propagate as waves, and if the waves meet certain criteria, they can travel through the periodic potential created by the atoms and molecules that make up the material. Importantly, however, the structure can prohibit the propagation of certain waves, creating gaps in the allowable electron energy through interference, as we was mentioned in Chapter 7 (see Figure 7.15). The theory was developed by **Felix Bloch (1905–1983)** in his 1928 thesis [7]. Bloch showed that the quantum wavefunction of an electron in a periodic potential, $\Phi(\mathbf{r}) = \Phi(\mathbf{r} + \mathbf{\Lambda})$, consists of the product of a plane wave envelope $e^{\omega t - \mathbf{k}\cdot\mathbf{r}}$ and a periodic function (periodic Bloch function) $\mathbf{E}_\mathbf{k}(\mathbf{r})$, which has the same periodicity $\mathbf{\Lambda}$ as the potential $\mathbf{E}_\mathbf{k}(\mathbf{r}) = \mathbf{E}_\mathbf{k}(\mathbf{r} + \mathbf{\Lambda})$. The Bloch wave description applies to any wave-like phenomenon, for example, the propagation of an electromagnetic wave in a periodic dielectric. The dispersion curves for electrons and photons in a one-dimensional system are shown in Figure 12.1.

In 1987, almost simultaneously, **Eli Yablonovitch** [8] and **Sajeev John** [9] began efforts to utilize the analogy between the propagation of electromagnetic waves in periodic dielectric structures and electrons in crystals. Their objectives differed. Yablonovitch was interested in controlling spontaneous emission through the use of bandgaps. John was

[1] Gabor's Nobel Lecture contains a very readable review of the early history of holography.

Modern Optics. Second Edition. B. D. Guenther.
© B. D. Guenther 2015. Published in 2015 by Oxford University Press.

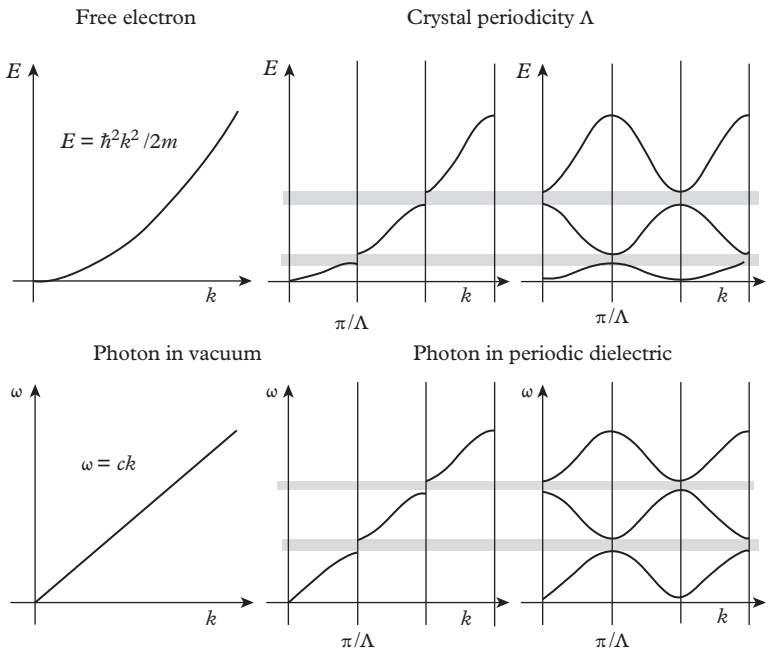

Figure 12.1 *The dispersion curves on the left are for propagation in a uniform medium. The gray bands in the dispersion plots on the right indicate bandgaps for electron and photon propagation in periodic one-dimensional structures. Dispersion in a periodic medium is indicated in the second plot to the right, with each of the periodic zones indicated by vertical lines. The plot on the far right of the figure is called the reduced zone representation and is created by reflecting the regions of the dispersion curves outside the first period into the first period.*

interested in using light to observe Anderson localization [10].[2] Optical functionality well beyond these two concepts has been demonstrated, as we will point out in this chapter.

This is not the first time we have found a use for periodic index structures. In Appendix 4A, we considered the construction of dielectric layers with different indices of refraction to generated a desired reflectivity or transmissivity through interference. We examined the properties of a multilayer stack made up of alternating layers of indices n_1 and n_2, but we paid little attention to the fact that the layers formed a periodic structure, and we emphasized interference rather than diffraction. We will use the same type of structure to discuss one-dimensional photonic structures after first examining holography.

12.2 Holography

All detectors of optical radiation respond to the intensity of the incident radiation, but the measurement of intensity does not uniquely determine the optical field. For example, assume two light signals exist, with the time average of the spatial amplitude distribution in the x-direction given by $\cos x$ and $|\cos x|$, as shown on the left of Figure 12.2(a). The measured intensity distributions of these two signals are identical, as shown on the right of Figure 12.2(a).

The inability of a detector to characterize the optical field occurs in all spectral regions and complicates the measurement process. For example, if both the amplitude and phase of a diffracted X-ray pattern could be measured, then a crystal structure could be determined by a simple Fourier transformation of the scattered field.

An interferometric technique can be used to overcome the shortcoming of optical detectors. By the coherent addition of a uniform background (a bias) to the signal that we

[2] In addition to bandgaps effecting the propagation of electrons in crystalline solids, P. W. Anderson predicted that errors in the periodicity of a crystal would result in electronic localization, but electron–electron interactions and electron–phonon scattering prevented the observation. John looked to electromagnetic radiation propagating in a periodic index medium as the ideal structure in which to observe localization.

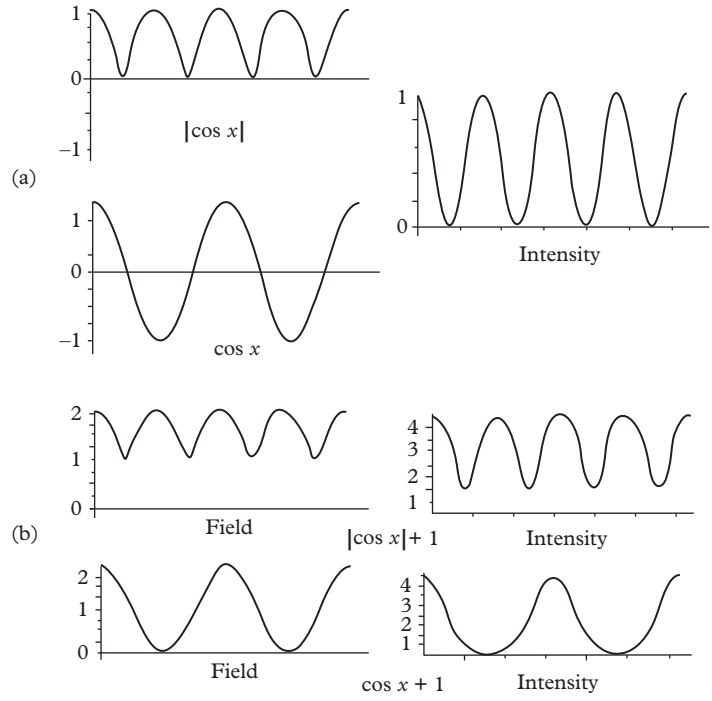

Figure 12.2 *(a) Spatial distribution of two possible optical fields and the detected spatial intensity distribution. With no bias term, the two fields yield the same intensity distribution. (b) The two spatial field distributions from (a) with a bias added are shown on the left. On the right are the detected intensity distributions.*

wish to record, the difference between $\cos x$ and $|\cos x|$ can be detected, as shown in Figure 12.2(b). The coherent addition of two light fields produces an interference pattern whose recording is called a *hologram*. *Holography*, the study of the production and application of holograms, differs from the study of interference only in the complexity of the waves that are allowed to interfere and the geometry of the interference experiments.

A hologram is capable of producing a three-dimensional image of any object. Three-dimensional images produced by holograms have been used for advertising, educational, technical, and artistic displays. Two examples of such applications are shown in Figure 12.3.

A typical arrangement used to make a hologram is shown in Figure 12.4. A light wave is divided into two mutually coherent waves. One wave, called the *reference wave*, illuminates the recording medium; the reference wave provides the bias needed for recording both the amplitude and phase of the signal wave. The second coherent wave illuminates the object of interest, and the light scattered from the object creates the *signal wave*. The signal and reference waves interfere at the hologram plane, and a light-sensitive medium records the spatial intensity distribution of the interference.

Later, the recorded fringes can be illuminated by a reproduction of the reference wave, called the *reconstruction wave*. The recorded interference pattern diffracts the reconstruction wave into an *image wave*. If an observer looks through the recording, we call the recording a *transmission hologram*, and the observer will see a three-dimensional image of the original object, created by the image wave. In Figure 12.5, showing a rickshaw and the letters "U of M" (i.e., University of Michigan), the basic properties of a hologram are displayed. A comparison of Figures 12.5(a) and (b) demonstrates that the image produced by the

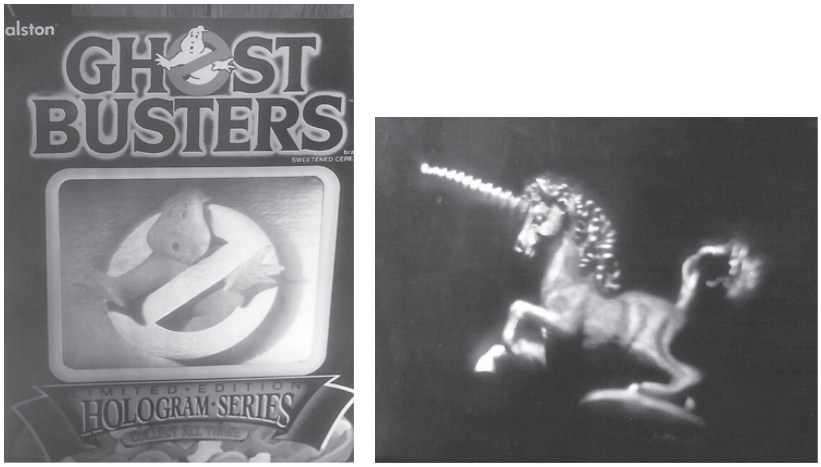

(a) (b)

Figure 12.3 *(a) A hologram used to help sell a box of cereal. (b) An artistic display hologram.*

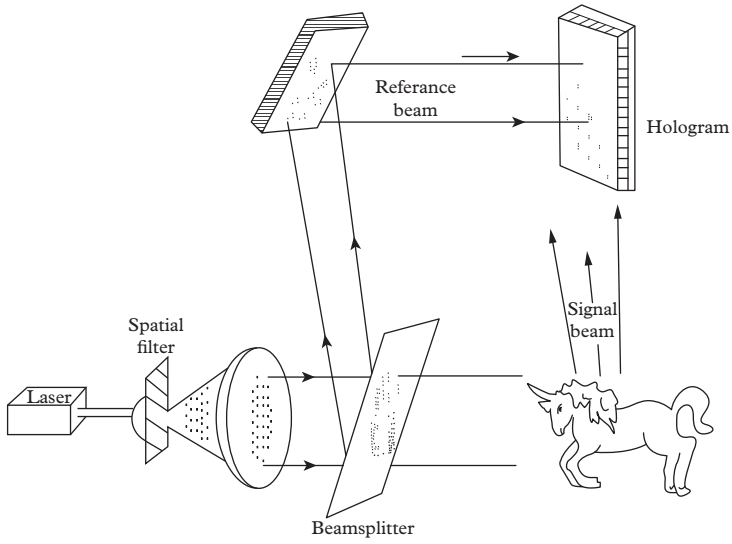

Figure 12.4 *Experimental arrangement for recording a hologram of a three-dimensional object.*

hologram has a large depth of field. Figure 12.5(c) demonstrates, by the obstruction of the word "of", that the holographic image displays parallax; i.e., we can look around near-field objects.

The three-dimensional image is so striking that it is easy to forget that a hologram has applications other than display. A number of the applications of holography [11] are actually more important to technology than displays.

Holograms of large volumes of air containing microscopic particles can be recorded and later examined in detail to measure the particle size distributions. These distributions are of interest in such diverse fields as meteorology (in the study of fog formation), biology (in

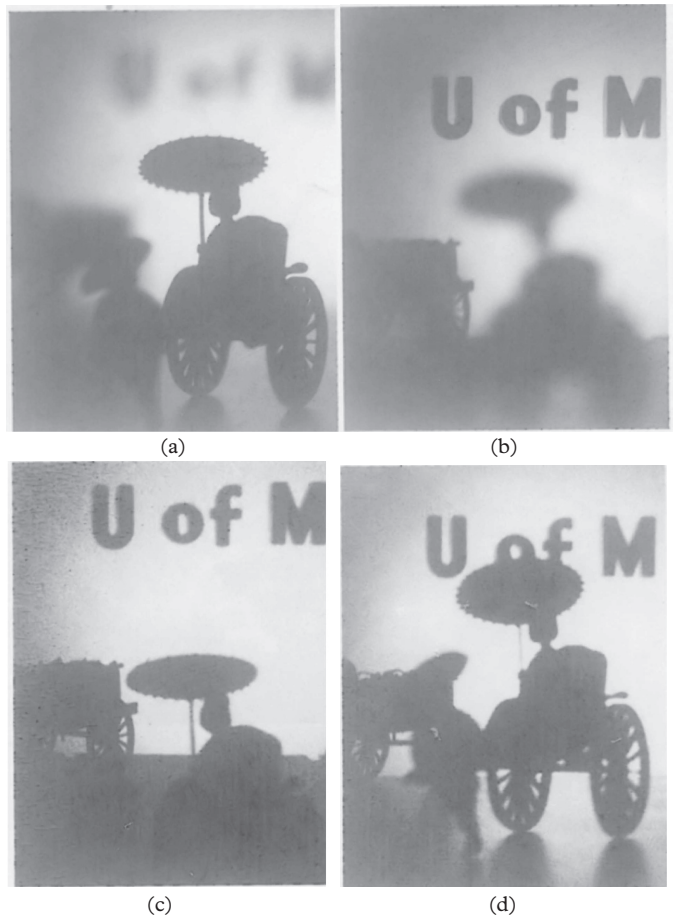

Figure 12.5 *These photographs of an early hologram display the three-dimensional properties of the holographic image. The depth contained in the images is demonstrated by focusing the camera first on the foreground (a) and then the background (b). The parallax associated with a three-dimensional image can be seen by comparing images (c) and (d). (Courtesy J. Upatniek.)*

the study of marine plankton), and elementary particle physics (in the analysis of bubble chamber tracks).

The recorded interference pattern created by the reference and signal waves forms a periodic index modulation that acts as a diffracting structure. If the two interfering waves are simple plane waves, the diffracting structure is a holographic grating with the same appearance as a ruled grating. If photoresist is used as the recording medium, exposure and development will produce a relief image of the interference pattern; by proper alignment, the relief pattern produced is triangular in shape, producing a blazed grating. If the relief image is coated with a metal layer, a reflection grating is produced. Holographic gratings offer several advantages over ruled gratings. Holography is a low-cost method of producing not only plane gratings but also gratings on curved shapes, gratings with curved grooves, and three-dimensional (volume) gratings. Gratings produced holographically are free from both periodic and random errors in the grating period, defects normally found in ruled gratings. Holographic gratings are not only used for wavelength measurement; specially designed gratings are used as optical scanners in supermarkets, copy machines, and printers.

The hologram can be viewed as an optical component that transforms the reconstruction wave into the signal wave. If the reconstruction wave were a plane wave and the signal wave were a spherical wave, then the hologram would perform the same transformation performed by a simple lens. This type of hologram, called a *holographic optical element (HOE)*, has been used in a number of specialized optical applications, for example, the "heads-up" displays that project important instrument readings into the forward field of view of an aircraft pilot. Such displays can also be found in a number of modern automobiles.

Because holography is an extension of interference, it is not surprising to find a large number of applications of holography in interferometry. Holography allows the study of nontransparent objects, a capability not available to conventional interferometry. Holography also provides interferometry with the capability of comparing a stored wavefront with a wave produced at a different location or at a different time. For example, in nondestructive testing, a hologram can be made of a component, and later that same component can be modified by the application of stress, induced by, for example, pressure or temperature. By making a double exposure or by viewing the component through a previously exposed and developed hologram, the result of the applied stress can be measured.

Other interferometric applications utilizing holography can be found in medical and dental research, in aerodynamics, in plasma diagnostics, and in the measurement of the amplitude and phase of vibrating objects.

A number of other applications of holography have been suggested but have yet to be extensively implemented. One such application is holographic information storage, either as an alternate implementation of a conventional memory or as an associative memory. (An associative memory allows the recovery of data without complete knowledge of its location.) Another suggested application is the use of holography to record the amplitude and phase of Fourier transforms, for use in optical correlators and convolvers, as discussed in Chapter 10. A brief discussion of the theory of the latter type of hologram is contained in Appendix 12B. In the future, the use of four-wave mixing, discussed in Chapter 15, will allow the use of a dynamic holographic device.

In this chapter, we will attempt to develop an intuitive understanding of holography by developing a theory based on point objects. Our first examination of holography will treat the recording and reconstruction of interference patterns, using collinearly propagating reference and signal waves. The recording will be assumed to be an amplitude recording; the use of phase recording will be briefly discussed in Appendix 12A. In the discussion of holography, we will ignore effects of hologram thickness. A more detailed analysis of holography can be found in the literature [12].

We will demonstrate that the hologram of collinearly propagating reference and signal waves can produce the amplitude and phase of the signal wave when illuminated by the proper reconstruction wave. We will find that a number of unwanted waves are also present when this configuration is used. By allowing the reference wave to propagate at an angle with respect to the signal wave, we will find that the unwanted waves can be spatially separated from the desired signal wave. Initially, Fourier transforms are used to analyze the *off-axis holograms* recorded using noncollinearly propagating waves.

An intuitive understanding of off-axis holograms can be developed by viewing the hologram as a large number of Fresnel zone lenses. We will develop a theory around this view based on a hologram recording of the interference between a spherical signal wave and a plane reference wave.

The simple model developed here allows specifications to be placed upon the recording material. We will discover that the properties of a hologram make unique demands upon the recording material. These demands exceed the requirements of ordinary photography.

Coherence requirements must be addressed in any process based upon interference, and holography is no exception. We will discuss the coherence requirements that are placed upon the light waves used in holography. One of the most interesting results of our brief analysis is that the coherence of the reconstruction wave affects the resolution of images produced by a hologram.

12.3 Holographic Recording

We will demonstrate that the holographic technique can be used to record, using a conventional intensity recording, the amplitude and phase of a wave. More importantly, we will demonstrate that it is possible to use the recording to regenerate either of the recorded waves. For this demonstration, we will examine the recording and playback of a hologram, without regard to the wave's propagation direction. We will do this by assuming that all of the waves propagate in a collinear fashion. In Section 12.4, we will consider the more general, and more useful, situation where the waves propagate at an angle with respect to each other.

Assume that the signal wave can be represented by the complex amplitude

$$a(x,y) = a_0(x,y)e^{-i\phi(x,y)} \tag{12.1}$$

and the reference wave by the complex amplitude

$$A(x,y) = A_0(x,y)e^{-i\Psi(x,y)}. \tag{12.2}$$

The theory of interference from Chapter 4, (4.12), gives the resultant intensity

$$\begin{aligned} I(x,y) &= AA^* + aa^* + A^*a + Aa^*, \\ &= |A(x,y)|^2 + |a(x,y)|^2 + 2A_0a_0\cos\delta, \\ \delta(x,y) &= \Psi(x,y) - \phi(x,y). \end{aligned} \tag{12.3}$$

If the two waves were spherical waves produced by point sources, then the interference fringes described by (12.3) would appear as the dark lines shown in Figure 12.6. We will assume that the recording medium is located in a plane normal to the line, parallel to the z-axis, connecting the two sources. In this situation, all of waves in the problem are collinearly propagating between the two sources.

A number of methods exist for recording the intensity in (12.3). Conventional photographic film records the fringes as variations in the absorption of the light transmitted through the film. For obvious reasons, this is called an *absorption hologram*. The silver in the developed absorption hologram can be replaced, through a process called *bleaching*, by a transparent compound with an index of refraction different than the film's gelatin base; the result is a *phase hologram*. In this type of hologram, the phase of the reconstruction phase is modified at each spatial position on the hologram by an amount proportional to the intensity of the interference pattern at that position. It is also possible to produce phase holograms directly in certain photopolymers or in gelatin sensitized with ammonium dichromate. Finally, the thickness of the recording medium can be varied to produce a phase hologram. Thermoplastic films and photoresist have been used to accomplish the required surface deformation. We will limit our discussion to amplitude recording to simplify

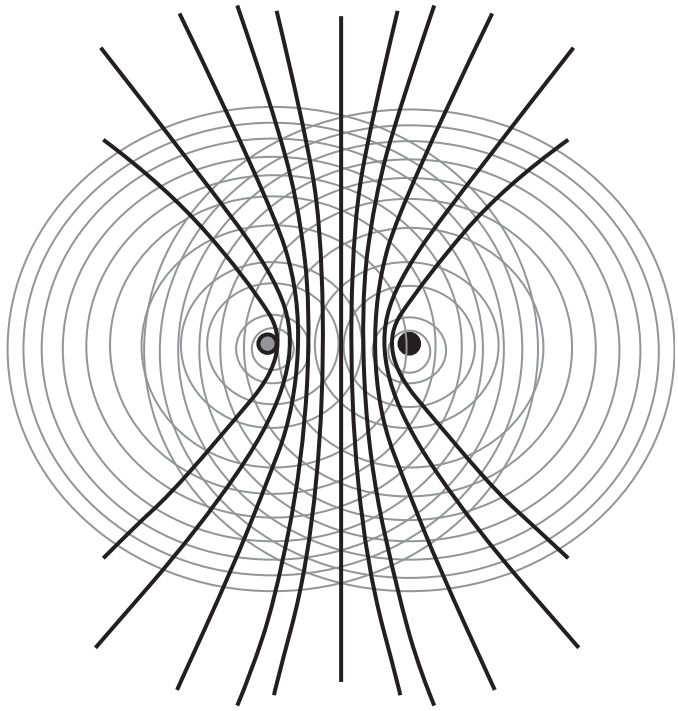

Figure 12.6 *Interference fringes produced by two point sources are shown by the dark lines in this drawing. The light lines represent the wavefronts produced by the two point sources. The point sources are the two dark spots.*

the mathematical representation. The hologram recorded will therefore have a transmission given by

$$t_h(x, y) = t_0 + \beta(A^* a + A a^*). \tag{12.4}$$

Whatever medium is used, we require that after development, the recording medium must linearly map the intensity of the interference pattern incident during the recording into a complex amplitude transmitted by the medium. The recording we have produced is then illuminated by a reconstruction (playback) wave $B(x, y)$. The transmitted reconstruction beam is given by

$$B(x, y)t_h(x, y) = t_0 B + \beta A^* B a + \beta A B a^*. \tag{12.5}$$

If the reconstruction wave is identical to the reference wave, $B = A$, then the second term of (12.5) is

$$\beta |A|^2 \, a(x, y),$$

and the original signal wave a is reproduced by the transmitted reconstruction beam. If the reconstruction wave is the conjugate of the reference wave, $B = A^*$, then the third term is

$$\beta |A|^2 \, a^*(x, y),$$

and the conjugate of the original signal beam, a^*, is produced. Either of these terms will produce a useable duplication of the original signal wave's amplitude and phase.

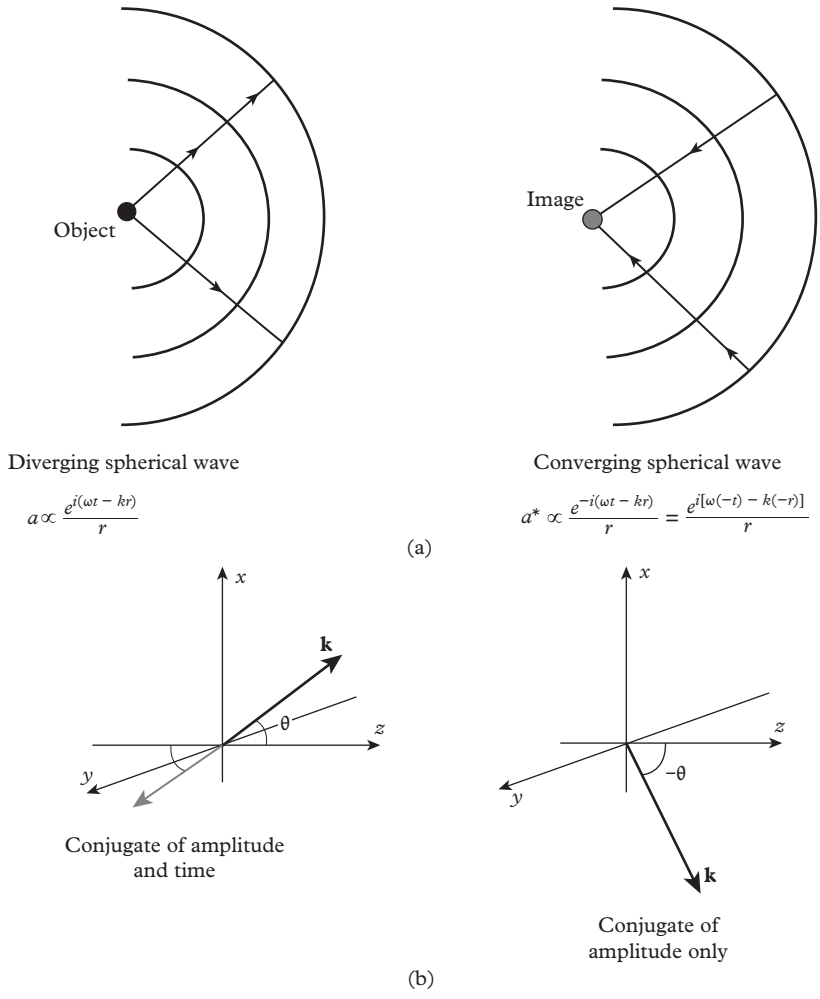

Figure 12.7 *(a) A spherical wave and its conjugate. The conjugate wave is identical to the original wave but propagates backward in time, (–t), and in the opposite direction, (–k). (b) The wavevector of a plane wave is shown in black on the left. The conjugate wave when both temporal and spatial characteristics of a wave must be considered is shown on the left as a shaded vector. The conjugate wave when only the complex amplitude of a wave must be considered is shown on the right as a black vector.*

To understand the meaning of the conjugate of a wave, consider a diverging spherical wave generated by a point source, displayed graphically on the left of Figure 12.7(a) by the wave labeled a. The conjugate of a, i.e., a^*, is identical to a, but is propagating backward in time (the time reversal of a) and backward in space. The conjugate wave is shown graphically on the right of Figure 12.7(a) as a wave converging toward a point.

The terms in (12.5) can now be interpreted by first assuming that a is a diverging spherical wave. The first term in (12.5) is equal to the average amplitude transmission of the developed film. The second term can be interpreted as containing the original diverging spherical wave a when B is identical to A. The transmitted wave appears to originate from a nonexistent point source; thus, a virtual image of the original point source has been reconstructed. The third term of (12.5) can be interpreted as a wave converging toward a point when B is equal to A^*. For this case, a real image of the original point source has been reconstructed.

In holography, the complex amplitude of the signal wave is stored in the hologram in the form of an interference pattern; all information concerning the temporal character of the wave is lost. If the recording medium is thin, then the information about the phase of the wave along the propagation direction is also lost. To first order then, a thin hologram only records information about the phase of the signal wave transverse to the propagation direction. Because the propagation information is lost, upon reconstruction, the transmitted wave assumes the propagation properties of the reconstruction wave. When it is appropriate to ignore the hologram thickness, a second type of conjugate wave, the space-conjugate wave, can be defined in terms of the complex amplitude of the wave. On the left of Figure 12.7(b), the wavevector of a plane wave propagating in the (x, z) plane is shown in black.

We assume the hologram is positioned normal to the z-axis. The wave stored in the hologram is given by

$$a = a_0 e^{-i\mathbf{k}\cdot\mathbf{r}} \approx a_0 e^{-ikx\sin\theta}.$$

When both the temporal and spatial characters of the wave are considered, the previous interpretation of the conjugate wave yields a wave with the wavevector shown as a shaded vector on the left of Figure 12.7(b). If only the stored amplitude of the wave is considered, the space conjugate wave would have the wavevector shown on the right of Figure 12.7(b). The mathematical representation of the space-conjugate wave is

$$\begin{aligned} a^* &= a_0^* e^{+ikx\sin\theta} \\ &= a_0^* e^{-ik(-x)\sin\theta}. \end{aligned}$$

12.4 Off-Axis Holography

We have just demonstrated, through (12.5), that by recording the interference pattern produced by a signal and a reference waveform, the signal waveform can be reconstructed later. The reconstruction is accomplished by using a "reconstruction" waveform identical to the original reference waveform. However, two unwanted signals must be separated from the desired signal waveform. The unwanted and desired signals are separated by the use of noncollinear waveforms. This off-axis technique seems to be a trivial modification of the collinear holographic method introduced by Gabor; however, it was over 10 years after the original papers by Gabor before Leith and Upatnieks introduced the off-axis technique.

To understand the off-axis technique, and to obtain information about how the off-axis angle affects the properties of the hologram, we will use Young's two-slit experiment as a model. The necessary equations have been derived in previous chapters. Here, we need only make the proper physical interpretation of the mathematics to understand the operation of an off-axis hologram.

12.4.1 Recording

The experimental arrangement that corresponds to the mathematical model is shown in Figure 12.8. Two slits of infinitesimal width in the x-direction and infinite width in the y-dimension are located at the front focal plane of the lens: slit 1 at position x_1 and slit 2

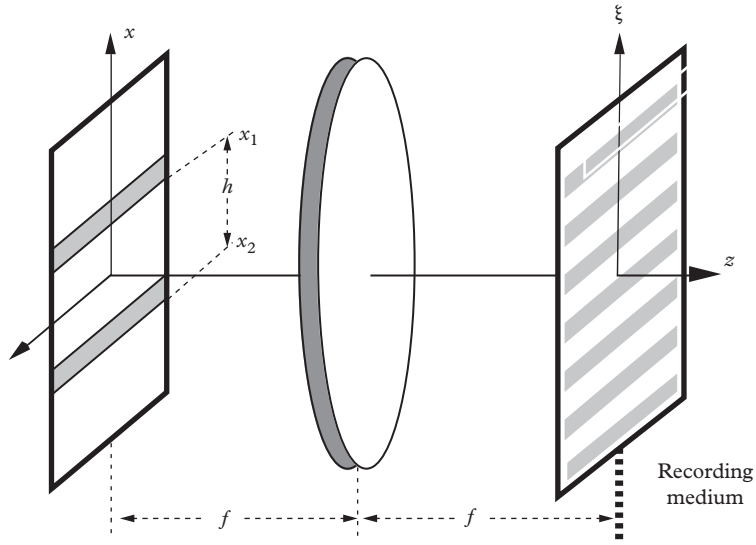

Figure 12.8 *Geometry of off-axis holography. The two slits and the lens produce two plane waves arriving at the recording medium at angles of θ_1 and θ_2 with respect to the normal of the recording medium, where $\theta_i = x_i/f$.*

at position $-x_2$, measured from the optical axis of the lens—the z-axis. These slits act as sources for two spherical waves, the signal and reference waves, that arrive at the recording medium, placed in the back focal plane of the lens, as plane waves propagating at angles

$$\theta_1 = -\frac{x_1}{f}, \quad \theta_2 = \frac{x_2}{f}$$

with respect to the optical axis. A magnified view of the recording medium is shown in Figure 12.9. The interference pattern that will be recorded is seen in Figure 12.9 to extend throughout the recording medium. The fringes are parallel to the bisector of the angle $\theta_1 + \theta_2$ between the signal and reference waves.

The mathematical description of the interference pattern produced in the back focal plane of the lens in Figure 12.8 is equal to the Fraunhofer diffraction pattern produced by the two slits and is given by (10.30):

$$I_D = I_0 \frac{\sin^2 \alpha}{\alpha^2} \cos^2 \beta_h.$$

Because we have assumed that the widths of the slits are infinitesimal, we may assume that $\operatorname{sinc} \alpha \approx 1$. The fringe pattern to be recorded in the hologram positioned in the back focal plane of the lens is therefore a simple sinusoidal intensity distribution given by

$$\begin{aligned} I_D &= I_0 \cos^2 \beta_h \\ &= \frac{I_0}{2}(1 + \cos 2\beta_h), \end{aligned} \tag{12.6}$$

where

$$\begin{aligned} \beta_h &= \frac{k(x_1 + x_2)}{2} \frac{\xi}{f} \\ &= \frac{\pi h \xi}{\lambda f}. \end{aligned}$$

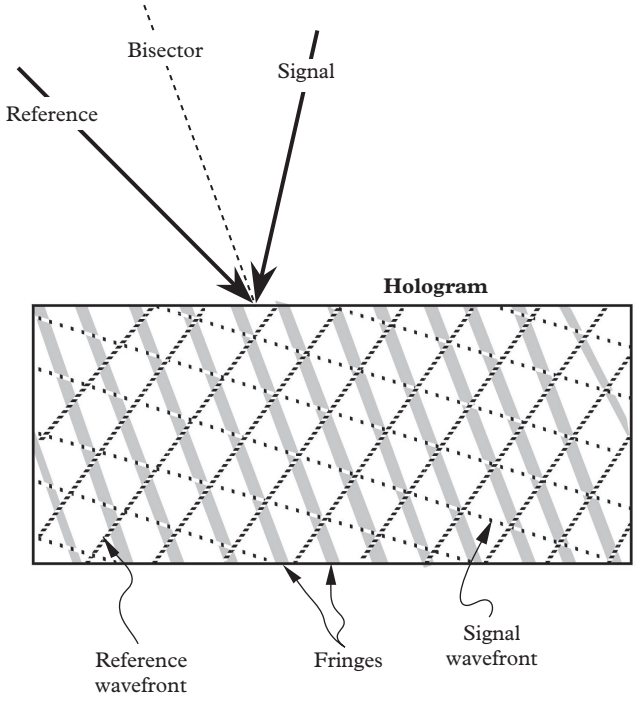

Figure 12.9 *Fringes produced by the interference of the signal and reference waves are shown here by the gray areas in the holographic recording medium. The wavefronts of the two waves are shown by the two types of dotted lines. The fringes are parallel to the bisector of the angle between the two waves. If the bisector of the angle is parallel to the normal to the surface of the recording medium, then the fringes will also be normal to the surface. If the reference and signal waves enter from opposite sides of the medium, then the fringes will be parallel to the surface of the medium.*

12.4.2 Development

After recording the interference fringes in the (x, y) plane and developing the recorded intensity distribution, the transmission coefficient of the hologram is given by

$$\begin{aligned} t_H &= t_0(1 + d_H \cos 2\beta_h) \\ &= t_0 + \frac{t_0 d_H}{2}(e^{-i2\beta_h} + e^{i2\beta_h}), \end{aligned} \tag{12.7}$$

where

$$t_0 = \frac{\beta' I_0 \tau_e}{2}.$$

Here, $\beta'\tau_e$ contains the information about how the exposure and development occurs. An additional factor d_H, the contrast, has been added to this equation. The contrast allows the inclusion of the visibility of the interference fringes into the equation for the recording of the interference pattern from the two slits. (It should be noted, however, that a contrast less than 1 may result not only from a fringe visibility that is less than 1 but also from a nonlinear recording process,)

12.4.3 Reconstruction

The developed hologram is placed in the front focal plane of the lens and illuminated with a plane wave of amplitude B, as shown in Figure 12.10. The light transmitted by the hologram

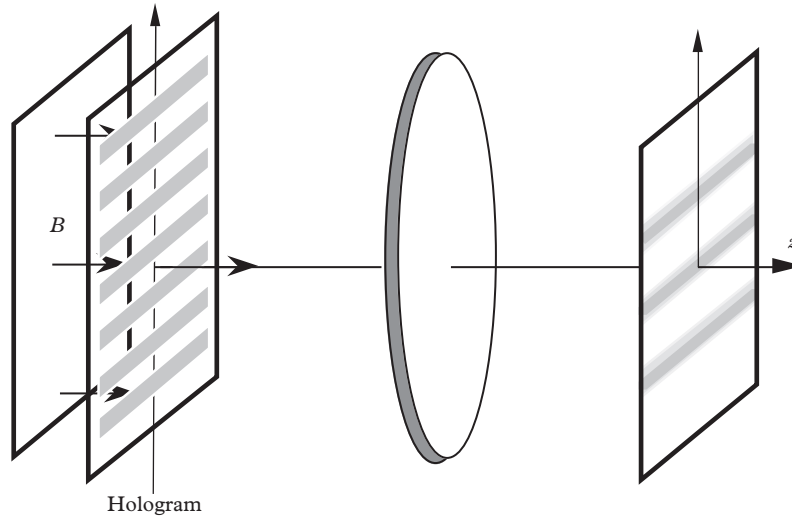

Figure 12.10 *Reconstruction of the hologram. By looking at the Fraunhofer diffraction produced by the hologram, the requirements for recording a signal can be obtained.*

is diffracted by the transmission given by (12.7) into three plane waves that are focused onto the back focal plane of the lens. The mathematical description of the diffraction pattern is given by (10A.4):

$$\tilde{E}_H(\xi) = Bt_0[\text{sinc}\xi + d_H \,\text{sinc}(\xi + x_2) + d_H \,\text{sinc}(\xi - x_1)].$$

The hologram produces a sinc function on axis that is the diffraction pattern due to the finite size of the hologram. The hologram also produces a real image of slit 2 at a distance x_2 above the optical axis and a real, inverted image of slit 2 at a distance $-x_1$ below the optical axis, as shown in Figure 12.10. Each image is a sinc function because of the finite size of the hologram.

Two real images are generated because the reconstruction wave B does not reproduce the reference wave. The origin of these two images can be discovered by decomposing the complex amplitude of the reconstruction wave B into two components: B_1, parallel to the propagation direction of the plane wave associated with slit 1, and B_2, the space conjugate of B_1 (i.e., $B_2 = B_1^*$). The wave reconstructed by B_1 creates the real image of slit 2, and the wave reconstructed by B_2 produces an inverted real image of slit 2, the conjugate image.

12.5 Spatial Spectrum of Off-Axis Holograms

The result just obtained can be generalized to describe a hologram of an arbitrary signal, by assuming that the signal wave is produced by a distribution of point sources located about the position $-x_2$. The hologram would contain a distribution of sinusoidal gratings oriented at different angles with respect to the hologram's surface normal. The distribution of gratings would diffract the reconstruction wave into a large number of plane waves, which would be focused by the lens in Figure 12.10 to an array of real image points, duplicating the distribution of point sources in the original object.

To simplify the discussion, assume that the slit producing the reference wave is located a distance $x_1 = |x_2|$ above the optical axis and the object is located a distance x_2 below the optical axis. The geometry of the slit experiment, except for this slight modification in distances, is as shown in Figure 12.8. The reference wave at the recording plane (which we here define as $z = 0$ to suppress the z-dependence) is

$$A = A_0 e^{-ik_x x},$$

and the signal wave is

$$a = a_0 e^{ik_x x},$$

where the component of the propagation vector along the x-direction is

$$k_x = \frac{2\pi \sin \frac{1}{2}\theta}{\lambda}.$$

The complex variable a contains the spatial information about the object that creates the signal wave. After exposure and development, (12.4) yields a film with a transmission coefficient

$$t_H(x,y) = \beta\left(A_0 A_0^* + a_0 a_0^* + A_0^* a_0 e^{i2k_x x} + A_0 a_0^* e^{-i2k_x x}\right), \tag{12.8}$$

where the elements of the bias term

$$t_0 = \beta\left(A_0 A_0^* + a_0 a_0^*\right)$$

have been shown for this discussion. The hologram with this transmission coefficient is reconstructed using the geometry of Figure 12.10. The Fourier transform of the jth term of (12.8) ($j = 1, \ldots, 4$) is defined as

$$G_j(\omega_x) = \mathcal{F}\left\{t_{Hj}\right\} = \int_{-\infty}^{\infty} t_{Hj}(x) e^{-i\omega_x x}\, dx,$$

where $t_{Hj}(x)$ represents the jth term of (12.8).

The first term is

$$G_1 = \mathcal{F}\left\{\beta A_0^2\right\} = \beta A_0^2 \delta(\omega_x).$$

This term is associated with the diffraction pattern created by the limiting aperture of the hologram. Its magnitude is determined by the intensity of the reference beam. Here it is a delta function because we are assuming that the hologram is infinite in size.

The second term is found by applying the correlation theorem (6A.10):

$$G_2 = \beta \mathcal{F}\left\{|a|^2\right\} = \beta \int_{-\infty}^{\infty} G_a(\xi) G_a^*(\xi - \omega_x)\, d\xi, \tag{12.9}$$

where G_a is the Fourier transform of the signal beam. The wave associated with (12.9) is created by the interference between the various point-scatterers that make up the object. This term was not present in the hologram of two slits, because we assumed that the slits had infinitesimal widths.

From the shift theorem (6A.5),

$$G_3 = \beta\mathcal{F}\{A_0^* a_0 e^{i2k_x x}\} = \beta A_0^* G_a(\omega_x - 2k_x), \tag{12.10}$$

$$G_4 = \beta\mathcal{F}\{A_0 a_0^* e^{-i2k_x x}\} = \beta A_0 G_a(\omega_x + 2k_x). \tag{12.11}$$

For the purpose of illustration, we will assume that G_a, the Fourier transform of the signal, is a rectangle of width $2k_w$; i.e., the signal is a sinc function. With this assumption, (12.9) becomes a triangular function. The total spatial spectrum of the hologram will appear as shown in Figure 12.11.

The frequency spectrum displayed in Figure 12.11 provides a method for determining the minimum allowable angle between the reference and signal waves that is needed to separate the various diffracted waves produced by the hologram. We ensure this separation by making the angle between the signal and reference beam greater than

$$\theta_{\min} = \sin^{-1}\left(\frac{3k_w\lambda}{2\pi}\right). \tag{12.12}$$

This angle ensures that $2k_x \geq 3k_w$ and allows the signal wave to be separated from the other terms by simply propagating some distance.

If the smallest object spacing of interest in the signal is 0.1 mm (which is about the minimum resolution of the unaided eye when viewing an object 0.1 m away and corresponds to a spatial frequency of 10 lines/mm), we have $k_w = 2\pi \times 10^4$ lines/m. For an object with this spatial frequency content, $\theta_{\min}$ must be greater than 1.1° if the illumination is at a wavelength of λ = 633 nm. Of course, this angle neglects the constraint created by the finite size of the hologram. The reference and signal beams would have to propagate 260 cm before they no longer overlapped if this offset angle was used to record a 5 cm diameter hologram.

An arbitrarily large offset angle may not be possible, because the offset angle determines the resolving capability needed by the recording medium. If we record a hologram using the minimum offset angle, then the maximum spatial frequency that the hologram must record is $4k_w$, which is four times the maximum spatial frequency in the signal.

Nonlinear recording will produce additional terms that diffract at larger angles and will generally not overlap the desired signal. For this reason, we can use a signal wave with an amplitude that is comparable to the amplitude of the reference wave and still recover the signal wave.

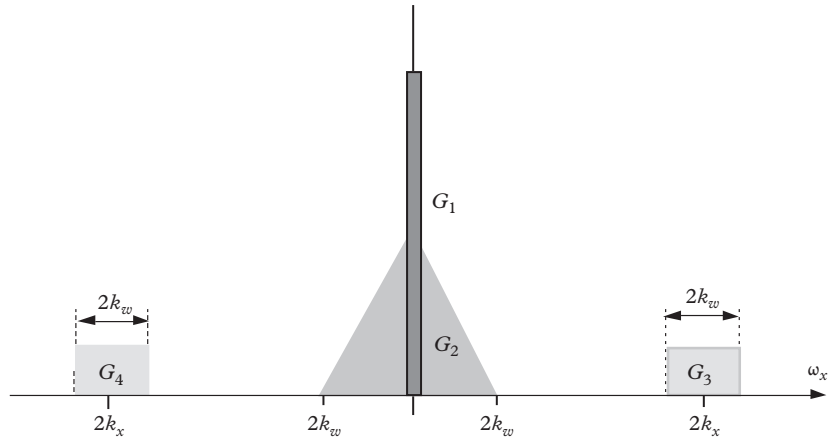

Figure 12.11 *Spatial frequency spectrum of the holographic recording described by the transmission function in (12.5).*

12.6 Classification of Holograms

Holograms can be classified by the size of the angle between the reference and signal waves. If the angle is small, then the hologram's thickness can be neglected and the grating equation can be used to describe the performance of the hologram. Figure 12.12(a) shows a section through a thin absorption hologram.

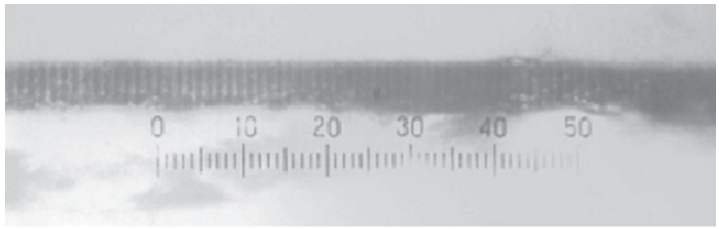

(a)

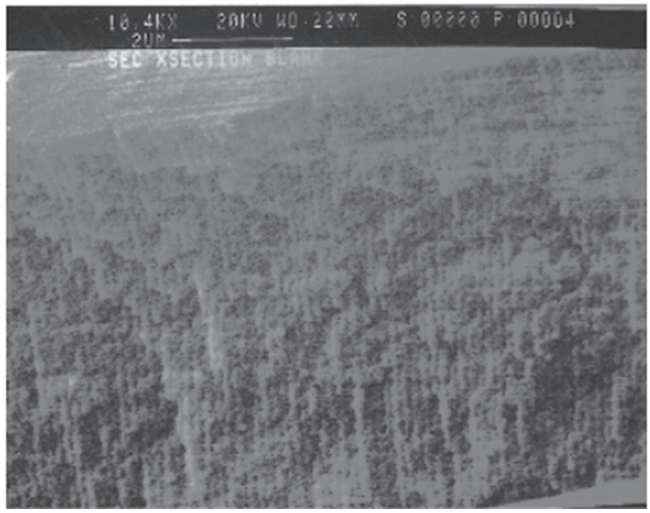

(b)

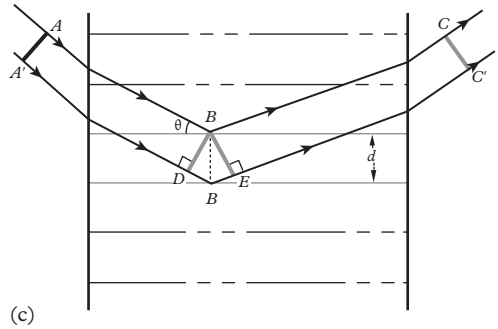

(c)

Figure 12.12 *(a) Cross section of the developed gelatin of an absorption hologram exposed to two interfering plane waves. The bright lines are layers of silver produced by bright interference bands. (Bendall, C.R., B.D. Guenther, and R. L. Hartman,* Technique for obtaining a photomicrograph of a cross section of photographic emulsion. *Appl. Opt., 1972. 11: p. 1653.) (b) Cross section of a thick phase hologram. The fringes in this photopolymer are voids separated by polymer. The general appearance is that of a photonic crystal. (Stone, T., N. George, and B.D. Guenther,* Index variation and scattering in a holographic medium, *in* Holographic Optics II: Principles and Applications, *G.M. Morris, Editor. 1989: SPIE.) (c) Geometry for Bragg diffraction.*

If the angle is large, then the hologram is classified as thick [see the phase grating in Figure 12.12(b)], and its performance is described by Bragg's law, which we will derive using Figure 12.12(c). The horizontal lines in Figure 12.12(c) represent the location of the fringe maxima in a thick hologram. In photographic film, these lines would be deposits of silver, and in the phase material shown in Figure 12.12(b), they indicate a change in index of refraction.

In Figure 12.12(c), a parallel beam of light with wavefront AA' is incident on the fringe maxima in the hologram at an angle θ. If the light reflected from the silver atoms in the two adjacent fringe maxima is to be in phase, so that a plane wave with wavefront CC' exits the hologram, then

$$\overline{DB'} + \overline{B'E} = n\lambda.$$

From the geometry of Figure 12.12(c),

$$\overline{DB'} = \overline{B'E} = d\sin\theta.$$

Reflections of waves propagating parallel to the plane wave AA' by other, equally spaced, parallel fringe planes create plane waves parallel to the plane wave CC'. These waves constructively interfere, producing a maximum in the light diffracted by the fringe system. Bragg's law gives the angle θ for which this maximum in diffracted light occurs:

$$2d\sin\theta = n\lambda. \tag{12.13}$$

12.7 Diffraction Efficiency

A hologram is recorded so that at a later time the signal wave can be reproduced. An important characteristic of a hologram is the fraction of energy diffracted from the reconstruction wave into the signal wave. The parameter used to characterize this energy fraction is called the *diffraction efficiency* of the hologram:

$$\eta = \frac{I_D}{I_0} = \frac{(\beta BA^* a)^2}{|B|^2}, \tag{12.14}$$

where B is the light amplitude of the reconstruction wave. The most useful hologram is normally one with a large diffraction efficiency.[3]

To measure the diffraction efficiency of a particular recording material, two plane waves A_0 and a_0 are used as the reference and signal waves. The measurement of η is then not confused by the spatial variation in the signal beam. In this section, we will relate the diffraction efficiency to the interference pattern produced by two plane waves. The resulting equation can be used to establish a maximum diffraction efficiency for thin holograms.

The diffraction efficiency η depends upon the visibility of the fringes produced during the recording process. To display the dependence explicitly, we use the definition of the fringe visibility

$$V = \frac{I_{\max} - I_{\min}}{I_{\max} + I_{\min}}.$$

The maximum and minimum intensities during interference are

$$I_{\max} = A_0^2 + a_0^2 + 2A_0 a_0, \quad I_{\min} = A_0^2 + a_0^2 - 2A_0 a_0,$$

[3] A hologram's diffraction efficiency may be designed to be less than the maximum possible because of the desired application. For example, a hologram used to produce copies should have a diffraction efficiency around 50%.

and the visibility becomes

$$V = \frac{2A_0 a_0}{A_0^2 + a_0^2}.$$

We also make use of the fact that the hologram's amplitude transmission coefficient is linearly related to the exposure energy used to generate the hologram and is given by

$$t_0 = \beta' \mathcal{E}_0 = \beta' \tau_e \left(A_0^2 + a_0^2\right) = \beta \left(A_0^2 + a_0^2\right).$$

We can now write the diffraction efficiency as an explicit function of the fringe visibility:

$$\eta = \left(\frac{\beta' \mathcal{E}_0 V}{2}\right)^2. \tag{12.15}$$

In the holographic literature, the ratio of the intensities of the two beams, A_0^2 and a_0^2, is usually called the *K-ratio*,

$$\mathcal{K} = \frac{A_0^2}{a_0^2}.$$

We see that the maximum efficiency is obtained when $V = 1$, i.e., when $A_0 = a_0$ and the K-ratio is 1.

It would appear that any diffraction efficiency desired could be obtained by proper selection of the exposure energy. Real materials, however, depart from the simple relationship (12.7) because the recording medium departs from a linear relationship between t_0 and $\mathcal{E}_0$. In particular, the recording material saturates above some exposure energy, preventing the hologram from exceeding a maximum diffraction efficiency.

The maximum diffraction efficiency η that can be exhibited by a thin hologram can be estimated by assuming that the hologram is produced by the interference of two plane waves. The hologram's transmission coefficient is given by (12.7), which can be used to calculate the diffraction efficiency. If the hologram is illuminated by a reconstruction wave of amplitude B, then the maximum light amplitude transmitted by the hologram is $t_0 B(1+d_H)$, and the light diffracted into one order is $t_0 B d_H/2$, yielding a diffraction efficiency

$$\eta = \left[\frac{t_0 B d_H}{2 t_0 B(1 + d_H)}\right]^2$$

$$= \left[\frac{1}{2(1 + 1/d_H)}\right]^2.$$

The maximum fringe contrast that can be produced occurs when $d_H = 1$ and is equal to $\eta \leq 6.25\%$. Other types of holograms exhibit higher diffraction efficiencies (see Appendix 12A).

12.8 Holography and Zone Plates

An intuitive feel for the performance of a hologram can be obtained by developing a theoretical description of a hologram produced by a point source, which generates both the reference wave and, in an indirect fashion, the signal wave. One portion of the wave from this point source is scattered by a single point object and then interferes with the primary

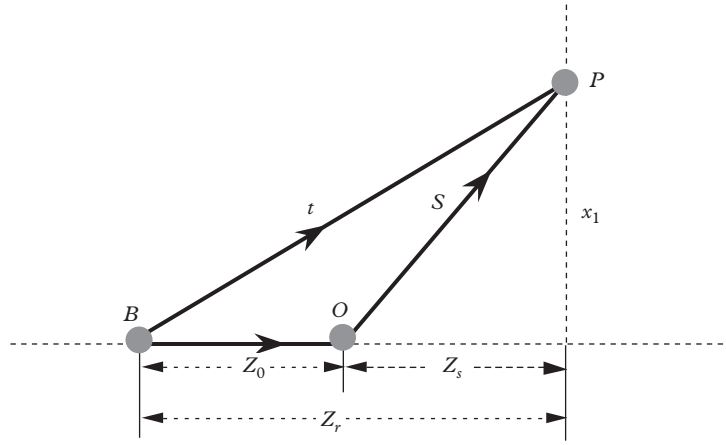

Figure 12.13 *Geometry for the interference of two in-line point sources. The interference pattern can be recorded to produce a zone plate.*

portion of the wave to generate the hologram. Figure 12.13 displays the geometry for this simple configuration. Upon calculating the resultant interference pattern, we will find that the hologram produced by this interference pattern acts like a simple zone plate.

The concept of a hologram as a zone plate can be extended to an arbitrary object, viewed as a set of point scatterers. The hologram of the object, a recording of the fringes resulting from the interference between each scattering point and the reference beam, can be viewed as a set of overlapping zone plates. The image produced by the hologram is a set of image points, conjugate to the set of object points, created by the zone plates.

Consider a single point source at position B, a distance Z_r from the recording plane in Figure 12.13, and one point scatterer at position O, a distance Z_s from the recording plane. Light reaches point P, in the recording plane, from the source at B, a distance t away, and from the scattering object, point O, a distance s from P. The light scattered by O is produced by the source at B; therefore, the phase difference between light waves that have traversed the two different paths, along t and along Z_0 plus s, is given by

$$\begin{aligned}\delta &= kt - k(Z_0 + s)\\ &= k(t + Z_s - Z_r - s).\end{aligned}$$

The geometrical optics sign convention that we selected in Chapter 5 will be applied here. The coordinate system is positioned so that the x-plane, containing P, is at the origin. An approximate expression for the phase difference δ is obtained by using the binomial expansion:

$$\begin{aligned}\delta &\approx k\left(Z_s - Z_r + Z_r + \frac{x_1^2}{2Z_r}Z_s - \frac{x_1^2}{2Z_s}\right),\\ &\approx \frac{kx_1^2}{2}\left(\frac{1}{Z_r} - \frac{1}{Z_s}\right).\end{aligned}$$

The bright bands of the interference fringes are separated by a distance Δx associated with a phase change $\Delta\delta = 2\pi n$. The first bright fringe, at $n = 0$, is on the z-axis and the second bright band, $n = 1$, is located at $\Delta x = x_1$, leading to the result

$$2\pi = \frac{2\pi}{\lambda}\frac{x_1^2}{2}\left(\frac{1}{Z_r} - \frac{1}{Z_s}\right),$$

which gives

$$\frac{\lambda}{x_1^2} = \frac{1}{Z_r} - \frac{1}{Z_s}. \tag{12.16}$$

This equation is identical to (11.26), derived for a zone plate. [Note that in (11.26), we must use $Z = -Z_s$ to meet the requirements of the sign convention.]

If the field from the source has amplitude A and the scattered field has amplitude a, then the intensity at P is

$$\begin{aligned} I &= |A|^2 + |a|^2 + 2Aa\cos\delta \\ &= \left(|A|^2 + |a|^2\right)\left\{1 + 2V\cos\left[\frac{kx_1^2}{2}\left(\frac{1}{Z_r} - \frac{1}{Z_s}\right)\right]\right\}. \end{aligned} \tag{12.17}$$

We define the focal length f of the zone plate described by (12.17) by

$$\frac{1}{f} = \frac{1}{Z_r} - \frac{1}{Z_s}.$$

Using this definition in the expression for the transmission function of the recorded intensity distribution, we obtain

$$t(x) = t_0 + 2\beta V\cos\frac{\pi x_1^2}{\lambda f}.$$

This is the transmission function of a sinusoidal zone plate.

The field distribution produced by any zone plate along the optical axis of the plate (here the z-axis) can be calculated by using the transmission function $t(r, \varphi)$ of the zone plate in the cylindrical coordinate version of the Fresnel diffraction integral, (11A.3). Because the zone plate is circularly symmetric, (11A.3) becomes

$$\tilde{E}_P = \frac{ik\alpha}{\rho D}\, e^{-ikD} \int_0^{x_{\max}} t(x) e^{-ikx^2/2\rho}\, x\, dx.$$

By a change of variables, we may write

$$\tilde{E}_P = \frac{ik\alpha}{D}\, e^{-ikD} \int_0^{u_{\max}} t(u) e^{-iku}\, du,$$

where

$$u_{\max} = \frac{x_{\max}^2}{2\rho}, \quad \frac{1}{\rho} = \frac{1}{Z_s} + \frac{1}{Z_r}, \quad D = Z_s + Z_r.$$

This integral can be identified as a Fourier transform, (6.13). Thus, the light distribution along the optical axis of the zone plate is equal to the Fourier transform of the radial transmission function of the zone plate. The Fourier transform of the sinusoidal zone plate, mathematically identical to (12.7), leads to two intensity maxima, and thus two foci.

$$\frac{1}{f_\pm} = \mp\frac{\lambda_2}{x_1^2}. \tag{12.18}$$

If we allowed the recording process to be nonlinear, additional higher-order foci would appear. The binary zone plate discussed in Chapter 11 has a radial transmission function that is a square wave of varying frequency (called a chirped grating because the frequency increases with increasing x). The Fourier transform of this radial transmission function would have an infinite number of components. The binary zone plate thus produces an infinite number of foci.

We have introduced into (12.18) a second wavelength, λ_2, the reconstruction wavelength, which we allow to be different from the recording wavelength λ_1. The radius of the first zone is given by (12.16). Substituting the expression for the radius of the first zone, x_1, into (12.18) yields

$$\frac{1}{f_{\pm}} = \mp \frac{\lambda_2}{\lambda_1} \left(\frac{1}{Z_r} - \frac{1}{Z_s} \right), \tag{12.19}$$

where f_+ represents the focal length of a positive lens and f_- the focal length of a negative lens. Equation (12.19) describes the imaging property of the hologram and suggests that the magnification of the hologram could be modified by reconstructing the image at a longer wavelength than that used to record the hologram.

The hologram we record, using the configuration shown in Figure 12.13, behaves simultaneously as a positive and a negative lens (see Figure 11.24). From this Fresnel zone viewpoint of holography, we find, as we did in (12.5), that the hologram produces two images, a real image at Z_s and a virtual image at $-Z_s$, which must be separated.

A more complicated object would contain a collection of point scatterers, and we assume the hologram would consist of a summation of zone plates, one for each scatterer. Each of these zone plates acts independently of the others to produce a field; all of the fields add to produce the image. The use of a zone plate to interpret the behavior of a hologram is useful, but it is flawed because it neglects the interference between the waves from each point scatterer and considers only the interference between the individual scattered waves and the reference wave.

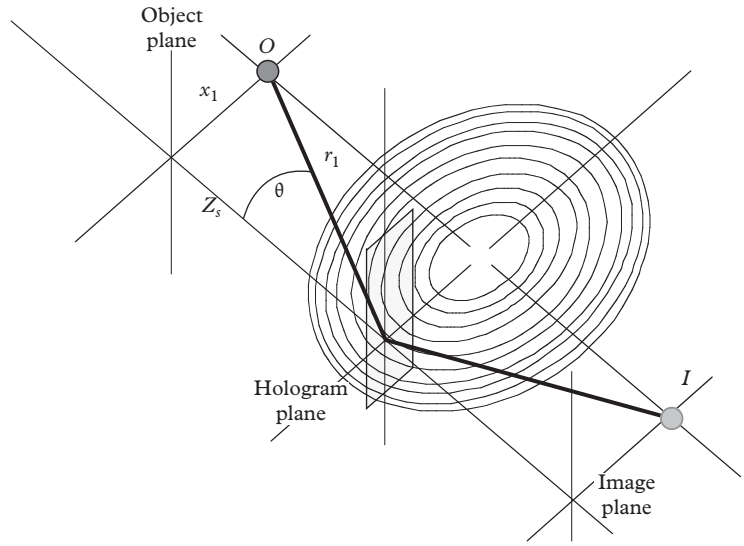

Figure 12.14 *Fresnel zone picture of an off-axis hologram. Point O is the object during recording and the virtual image during playback. Point I is the real image during playback. The reference and reconstruction beams are assumed to be plane waves.*

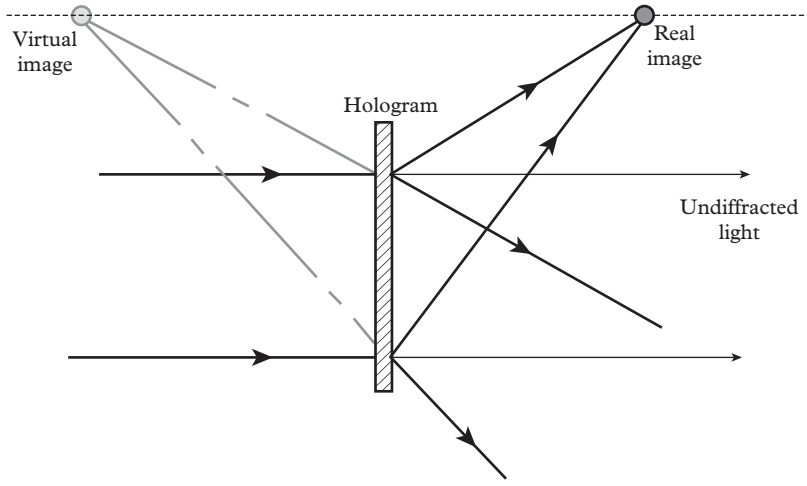

Figure 12.15 *The real and virtual images of an off-axis hologram.*

The spatial frequency of the fringes producing the zone plate can be defined as

$$\frac{1}{2\pi}\frac{\partial\delta}{\partial x} = \frac{kx}{2\pi}\left(\frac{1}{Z_r} - \frac{1}{Z_s}\right) = \frac{x}{\lambda f}.$$

As with a normal zone plate, the fringe frequency increases linearly with increasing x. At some point $x_{\max}$, the photosensitive material can no longer record the fringes—we will exceed the resolving capability of the medium. This $x_{\max}$ defines the limiting aperture of the hologram.

When we move our recording medium off axis, we obtain an interference pattern as shown in Figure 12.14, where we assume for illustrative purposes that the reference beam is a plane wave. The rectangle in Figure 12.14 is assumed to be the recording medium. We see that the object O and the real image I would lie on the optical axis of the zone plate. The various waves produced by the developed hologram are shown schematically in Figure 12.15. From this view of a hologram, we discover that we can separate the two images of the hologram if we offset the reference so that the central Fresnel zone is not recorded.

12.9 Resolution Requirements

To find the resolution requirements imposed on a holographic recording medium, we need to define three angles, shown in Figure 12.16. The object subtends an angle θ_O at the recording surface, and the recording surface subtends an angle θ_R at the object. These angles are defined so that they are the largest angles that will be encountered. In this simple analysis, we will assume the reference wave is a plane wave propagating in a direction normal to the hologram. The largest angle encountered at the recording plane, between the reference wave and a wave from the object is θ_T. The half-angle, $\theta_T/2$, is shown on the right of Figure 12.16. Interference between the wave propagating at θ_T and the reference wave will

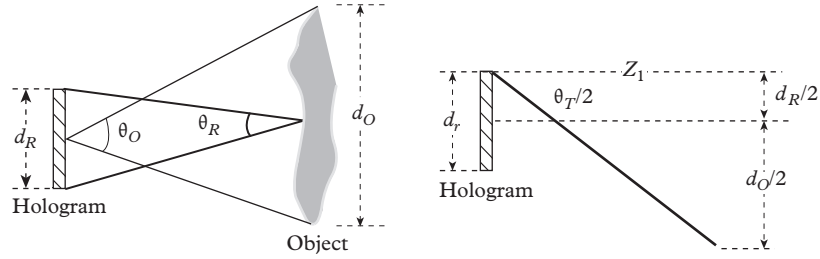

Figure 12.16 *Geometrical definition of angular bandwidth of holographic recording.*

create the highest spatial frequency that must be recorded; this maximum spatial frequency is given by

$$k^T = \frac{2\pi \sin(\theta_T/2)}{\lambda}.$$

The spatial frequency bandwidth is defined as

$$k_w = 2k^T = \frac{4\pi}{\lambda}\sin(\theta_T/2). \tag{12.20}$$

The geometry of Figure 12.16 can be used to relate the three angles just defined:

$$\tan(\theta_T/2) = \frac{1}{Z}\left(\frac{d_O}{2} + \frac{d_R}{2}\right) = \tan(\theta_O/2) + \tan(\theta_R/2). \tag{12.21}$$

By using the object angle θ_O, we can calculate the maximum value of the object's spatial bandwidth:

$$k_W^O = \frac{4\pi}{\lambda}\sin(\theta_O/2).$$

Similarly the recording's maximum spatial bandwidth can be calculated using the hologram angle θ_R:

$$k_W^R = \frac{4\pi}{\lambda}\sin(\theta_R/2).$$

Using these limiting definitions of spatial bandwidth, we may write (12.21) as

$$\frac{k_W^T}{\cos(\theta_T/2)} = \frac{k_W^O}{\cos(\theta_O/2)} + \frac{k_W^R}{\cos(\theta_R/2)}.$$

From the definitions of the three angles, we know that $\theta_T > \theta_R$ or θ_O, leading to the inequality

$$k_W^T \leq k_W^O + k_W^R. \tag{12.22}$$

If the object to be recorded is much larger than the hologram, we may neglect the hologram's spatial bandwidth. For example suppose the vibrations of a guitar face are to be studied. The standard photographic plate is 4 in. × 5 in. At a distance of 0.9 m from the guitar, the hologram subtends an angle of approximately 16° at the guitar. The guitar, which is

0.5 m long, subtends an angle of 60°. The sine of the half-angle of the object is $\sin 30° = 1/2$ and $k_W^T \leq 2\pi/\lambda$. For green light, $\lambda = 500$ nm, and the required spatial bandwidth becomes

$$\frac{k_W^T}{2\pi} \leq 2000 \text{ lines/mm}.$$

This spatial bandwidth requirement means that the recording medium must record detail beyond the resolution capability of conventional photographic film by a factor of 20. High-resolution spectroscopic plates are capable of recording the required resolution of 5×10^{-4} mm, as are a variety of photopolymers.

The resolution requirement is due to the wide field of view recorded by the hologram. If the field of view of the hologram were limited to that covered by the fovea region of the human eye, 2°, then the spatial bandwidth the hologram must record would only be 70 lines/mm.

12.10 Coherence Requirements

Hopefully, after the discussion of interference and coherence in Chapter 8, no-one will be surprised that the source needed to produce a hologram must be both spatially and temporally coherent. It may be a surprise, however, to learn that the reconstruction wave must also be coherent if maximum resolution of the image is to be obtained. After briefly examining the coherence requirements placed on the recording light by the special geometries associated with holography, we will examine the coherence requirements for reconstruction of a holographic image.

12.10.1 Temporal Coherence

Recording an off-axis hologram places demands on the temporal coherence of the recording source. Consider the typical layouts of Figure 12.17. The reference ray, at the top of the off-axis hologram, has traveled $\ell = a \sin \alpha_r$ farther than the reference ray, at the bottom of the

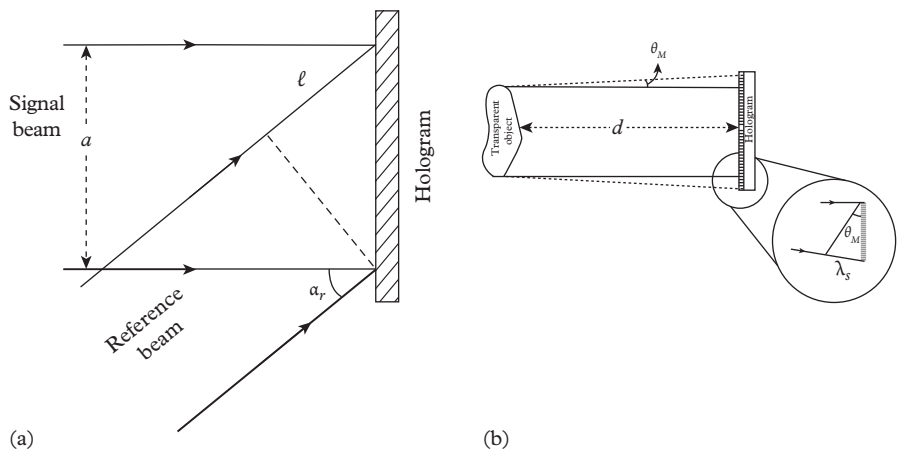

Figure 12.17 *Recording geometry for (a) an off-axis hologram and (b) an in-line hologram.*

hologram. If we adjust the paths of the signal and reference beams so that they are in phase at the center of the hologram, the recording source must have sufficient temporal coherence so that its longitudinal coherence length exceeds $\ell_R = \ell/2$. If this condition is met, fringes will be produced across the hologram. The information content of the signal places additional demands on the temporal coherence of the source used to record the hologram. For ease of visualization, consider the case when the object is a transparency [Figure 12.17(b)]. The transverse coherence length of the reconstruction source establishes the minimum resolvable image dimension. The highest spatial frequency in the object diffracts the signal beam at an angle θ_M. This portion of the signal travels a distance

$$\ell_s = \frac{d}{\cos\theta_M} - d.$$

This is a longer distance than that traveled by the undiffracted signal beam. Thus, to record the spatial information in the signal beam requires a longitudinal coherence length in excess of ℓ_s. The requirements on coherence made by the off-axis reference beam and the information content of the signal beam, demand a recording source with a longitudinal coherence length

$$\ell_\ell > \ell_R + \ell_s.$$

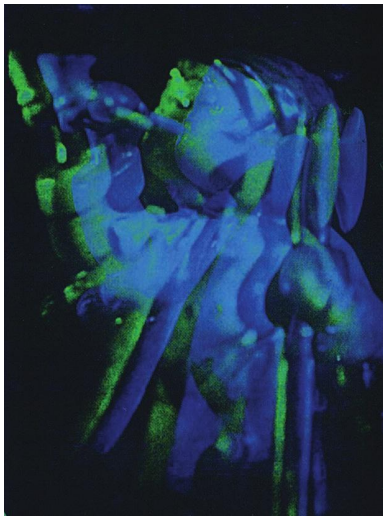

Figure 12.18 *A hologram of a ceramic statue reconstructed at three discrete wavelengths. (Hologram courtesy of N. George.)*

To generate a feeling for the effects of temporal coherence, we can examine Figure 12.18, which displays a hologram reconstructed using three discrete wavelengths. The color image can be used to observe the dependence of the image coordinates on wavelength. As can be seen in Figure 12.18, the size and position of the reconstruction depends on the wavelength. A spread in the reconstruction source's wavelength will produce a blur of the image.

Moving the object close to the unexposed hologram can reduce the required spatial coherence. We may use a lens to project an image of the object we wish to record onto the hologram plane. Now the depth of the image will determine the required coherence of the reconstruction source. In Figure 12.19, the object used in this hologram was the real image of another hologram with its midline falling on the surface of the recording media. The reference beam illuminated the recording medium from the opposite direction of the image beam. The resulting hologram is played back here using sunlight.

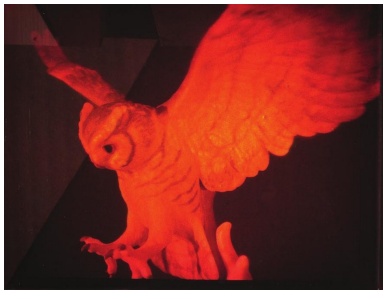

Figure 12.19 *Reducing the coherence demands on the reconstruction beam.*

12.10.2 Spatial Coherence

The requirements on the spatial coherence of the reference and reconstruction waves can be calculated by obtaining the point spread function of a hologram. In this approach, the hologram is treated as a linear system. The impulse response of the linear system is found by calculating the image produced by a hologram, generated by a point source. The point source acts as the impulse and the point spread function is the impulse response function. This general treatment cannot be carried to completion, so we will use a geometrical analysis of a source of finite dimension and one emitting several wavelengths, to obtain a statement of the coherence requirements.

The hologram to be evaluated is a Fourier transform hologram. Fourier transform holograms are discussed in Appendix 12B; here, we will give the briefest of details so that we may immediately see the effects of spatial coherence on image resolution.

The object light distribution at the hologram plane, shown in Figure 12.20, is

$$O(\xi) = \mathcal{F}\{a(x)\}. \tag{12.23a}$$

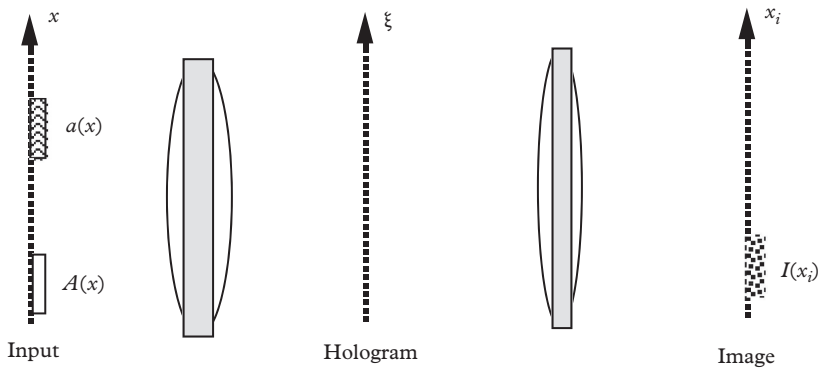

Figure 12.20 *Geometry for producing a Fourier transform hologram.*

The reference light distribution at the hologram plane is

$$R(\xi) = \mathcal{F}\{A(x)\}. \tag{12.23b}$$

After exposure and development, we obtain a hologram that we illuminate with a reconstruction wave. The light distribution of the reconstruction, or playback, wave at the hologram is

$$P(\xi) = \mathcal{F}\{B(x)\}. \tag{12.24}$$

The light transmitted by the hologram is imaged at the back focal plane of a second lens, labeled the image plane in Figure 12.20. We will only follow the image wave to this plane; its amplitude distribution in the image plane is

$$I(x_i) = \mathcal{F}\{POR^*\}. \tag{12.25}$$

The point spread function of the hologram can be calculated by assuming the object is a point source, located at position x_0 in the front focal plane of the first lens; i.e.,

$$a(x) = \delta(x - x_0).$$

The Fourier transform of a delta function is, from (6.24),

$$O(\xi) = \mathcal{F}\{\delta(x - x_0)\} = e^{-i(k/f)\xi x_0}.$$

We can now use the rule for conjugation of a Fourier transform, (6A.6), and the shifting property of a Fourier transform, (6A.5), to write

$$I(x_i) = \mathcal{F}\{\mathcal{F}\{B(x)\}\mathcal{F}\{A^*(x - x_0)\}\}. \tag{12.26}$$

From the correlation theorem (6A.10), we see that the amplitude point spread function of the hologram is the correlation of the spatial distribution of the reference and reconstruction sources.

12.11 Photonic Crystals

In the previous discussions about light waves, we assumed that the medium through which the light propagated was homogeneous and isotropic. In those cases, we could relate the electromagnetic field vectors **E** and **B** to the electric displacement **D** and the magnetic vector **H** through the scalar quantities ε (dielectric constant) and μ (magnetic permeability). We will continue to assume that the material is isotropic with regard to the magnetic field, so that μ remains a scalar, but we will now assume that the dielectric properties can vary periodically with position. The impact of discarding the assumption of isotropic electrical properties is the need to use tensor relationships between **E** and **D**, because the electric field **E** will in general not be parallel to **D**. In this chapter, we will limit our attention to periodic variations of infinite extent. In the remaining chapters, we will allow the electrical properties to assume more complicated variations with respect to position.

12.11.1 Maxwell's Equations for Sinusoidal ε

We will continue to make the assumption that the medium is nonconducting and that there are no currents or charges present. Maxwell's equations as given by (2.6) no longer apply, because the dielectric constant ε is no longer independent of the coordinate derivatives. We continue to assume that $\mu \approx \mu_0$, so **H** and **B** satisfy identical equations. The modified equations are

$$\nabla \cdot \mathbf{B} = 0, \qquad \nabla \cdot \mathbf{D} = 0,$$

$$\nabla \times \mathbf{H} = \frac{\partial \mathbf{D}}{\partial t}, \quad \nabla \times \mathbf{E} = -\frac{\partial \mathbf{B}}{\partial t} \tag{12.27}$$

We will interpret Maxwell's equations, as we did in Chapter 2, by the use of plane waves

$$\mathbf{E} = \mathbf{E}_0 e^{i(\omega t - \mathbf{k}\cdot\mathbf{r} + \phi)}, \quad \mathbf{D} = \mathbf{D}_0 e^{i(\omega t - \mathbf{k}\cdot\mathbf{r} + \phi)},$$

$$\mathbf{B} = \mathbf{B}_0 e^{i(\omega t - \mathbf{k}\cdot\mathbf{r} + \phi)}, \quad \mathbf{B} = \mu_0 \mathbf{H}.$$

Substituting the plane wave solutions into the second pair of equations in (12.27) using (2.13) and (2.14) yields

$$\nabla \times \mathbf{E} = -\frac{\partial \mathbf{B}}{\partial t} = -i\omega \mathbf{B} = -i\omega\mu_0 \mathbf{H} = -\frac{i\omega}{c^2 \varepsilon_0}\mathbf{H},$$

$$\nabla \times \mathbf{H} = \frac{\partial \mathbf{D}}{\partial t} = \varepsilon(\mathbf{r})\frac{\partial \mathbf{E}}{\partial t} = i\omega\varepsilon(\mathbf{r})\mathbf{E}.$$

If we take the curl of the second of these equations as we did in Chapter 2 to determine the propagation properties, we obtain

$$\nabla \times \left[\frac{\varepsilon_0}{\varepsilon(\mathbf{r})}\nabla \times \mathbf{H}\right] = \nabla \times (i\omega \mathbf{E}) = \frac{\omega^2}{c^2}\mathbf{H}. \tag{12.28}$$

The curl of the first equation yields

$$\nabla \times \nabla \times \mathbf{E} = -\frac{i\omega}{c^2 \varepsilon_0}(\nabla \times \mathbf{H}) = \frac{\omega^2 \varepsilon(\mathbf{r})}{c^2 \varepsilon_0}\mathbf{E},$$

$$\frac{\varepsilon_0}{\varepsilon(\mathbf{r})}(\nabla \times \nabla \times \mathbf{E}) = \frac{\omega^2}{c^2}\mathbf{E}. \tag{12.29}$$

We can generate a similar equation for **D**:

$$\nabla \times \nabla \times \frac{\varepsilon_0}{\varepsilon}\mathbf{D} = \frac{\omega^2}{c^2}\mathbf{D}. \tag{12.30}$$

We saw in Chapter 2 that we only need calculate one of the fields, with the others being obtained using equations derived from Maxwell's equations—we selected the electric field. We will assume a geometry such as that shown in Figure 12.21, a multilayer dielectric stack whose interferometric response we investigated in Appendix 4A. We also assume that the periodicity extends to infinity in the z-direction. Using the vector calculus rules from Appendix 2A, we can write (12.29) in terms of the individual vector components:

$$\frac{\varepsilon_0}{\varepsilon}\left(-\frac{\partial^2 E_x}{\partial y^2} - \frac{\partial^2 E_x}{\partial z^2} + \frac{\partial^2 E_y}{\partial x \partial y} + \frac{\partial^2 E_z}{\partial x \partial z}\right) = \left(\frac{\omega}{c}\right)^2 E_x,$$

$$\frac{\varepsilon_0}{\varepsilon}\left(-\frac{\partial^2 E_y}{\partial x^2} - \frac{\partial^2 E_y}{\partial z^2} + \frac{\partial^2 E_z}{\partial y \partial z} + \frac{\partial^2 E_x}{\partial x \partial y}\right) = \left(\frac{\omega}{c}\right)^2 E_y,$$

$$\frac{\varepsilon_0}{\varepsilon}\left(-\frac{\partial^2 E_z}{\partial x^2} - \frac{\partial^2 E_z}{\partial y^2} + \frac{\partial^2 E_x}{\partial x \partial z} + \frac{\partial^2 E_y}{\partial y \partial z}\right) = \left(\frac{\omega}{c}\right)^2 E_z.$$

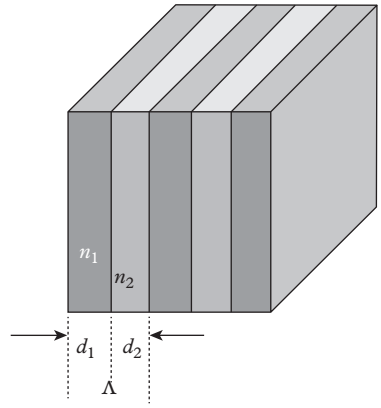

Figure 12.21 *One-dimensional photonic crystal identical to a multilayer dielectric mirror as discussed in Appendix 4A.*

We will assume as we first did in Chapter 4 that the light wave is linearly polarized in the y-direction and is propagating in the z-direction. This reduces the number of equations to one:

$$\frac{\varepsilon_0}{\varepsilon}\left(-\frac{\partial^2 E_y}{\partial x^2} - \frac{\partial^2 E_y}{\partial z^2}\right) = \left(\frac{\omega}{c}\right)^2 E_y \tag{12.31}$$

We can expand the E field in a Fourier expansion using complex notation:

$$E_y = \sum_{\ell} \alpha_{\ell y} e^{-i[(2\pi\ell/\Lambda)z + k_z z]},$$

and, since the dielectric is periodic, there is a similar Fourier expansion of the reciprocal of the dielectric function:

$$\frac{\varepsilon_0}{\varepsilon} = \sum_{m} \beta_m e^{-iz(2\pi m/\Lambda)},$$

where Λ is the spatial period of the index modulation (see Figure 12.21). If we substitute the Fourier expansions into (12.29), we obtain

$$\sum_m \sum_\ell \left(\frac{2\pi\ell}{\Lambda} + k_z\right)^2 \alpha_\ell \beta_m e^{-i(2\pi\ell/\Lambda)z} e^{-i(2\pi m/\Lambda)z} e^{-ik_z z} = \frac{\omega^2}{c^2} \sum_\ell \alpha_{\ell y} e^{-i(2\pi\ell/\Lambda)z} e^{-ik_z z}.$$

In Chapter 6, we multiplied the Fourier series by a sine or cosine function to determine the value of the coefficient. Here, because we are using complex notation, we will multiply both sides of the equation by $e^{i(2\pi n/\Lambda)z}$ and integrate both sides over $-\Lambda/2 \le z \le \Lambda/2$. The only nonzero terms occur when $\ell = n$, leaving us with the expression

$$\sum_n \left(\frac{2\pi n}{\Lambda} + k_z\right)^2 \alpha_n \beta_{m-n} = \frac{\omega^2}{c^2} \alpha_{ny}.$$

To solve this matrix equation, we would truncate m and n to finite values, symmetrically about zero, and diagonalize the resulting matrix using standard numerical techniques. The accuracy is determined by the number of terms in n and m that we retain.

12.12 The Bloch (or Floquet) Theorem

If we turn to the magnetic field (12.28), we can use techniques developed in solid state physics to solve the problem by using symmetry properties of the photonic structure. For the multilayer structure, we can obtain an analytic result. For the theorist, (12.28) has greater appeal because it contains the Hermitian operator

$$\left[\nabla \times \frac{1}{\varepsilon} \times \nabla \times\right]$$

whenever ε is real and because we treat μ as an isotropic constant, avoiding the need for tensors. This means that the eigenstate solutions $\mathbf{H}$, with the same eigenfrequencies $(\omega/c)^2$, are orthogonal and the eigenfrequencies are real.[4] Equation (12.28),

$$\left[\nabla \times \frac{\varepsilon_0}{\varepsilon(\mathbf{r})} \nabla \times\right] \mathbf{H} = \frac{\omega^2}{c^2} \mathbf{H},$$

has the same mathematical form as the quantum mechanical scalar equation developed to explain electron propagation through solids by Bloch [7, 13]. Bloch expanded to three dimensions the solution of a one-dimensional wave equation obtained independently by Floquet [14] using wave equations developed by Hill and Mathieu.

$$\left[-\frac{\hbar^2}{2m}\nabla^2 + \mathcal{V}(\mathbf{r})\right] \Psi(\mathbf{r}) = U\Psi(\mathbf{r}), \tag{12.32}$$

where $\mathcal{V}(\mathbf{r}) = \mathcal{V}(\mathbf{r} + \mathbf{\Lambda})$ is a periodic potential function with a period $\mathbf{\Lambda}$ and U is the energy. Both (12.28) and (12.32) are Hermitian eigenproblems.

For the one-dimensional multilayer shown in Figure 12.21, the symmetry operation of the structure is translation. Because of the translational symmetry in the multilayer, the normal modes will be eigenfunctions of the translation operator T that shifts the solutions by one period, $Tf(x) = f(x + \Lambda)$. Instead of trying to solve the wave equation directly, we will determine the eigenfunctions of the translation operator. Notice that any function of the form

$$f(z) = e^{iKz}\boldsymbol{\mathcal{U}}(z), \quad \text{with } \boldsymbol{\mathcal{U}}(z) = \boldsymbol{\mathcal{U}}(z + \Lambda),$$

is an eigenfunction of the translation operator with eigenvalue $e^{iK\Lambda}$:

$$Tf(z) = e^{iK(z+\Lambda)}\boldsymbol{\mathcal{U}}(z + \Lambda) = e^{iK\Lambda}f(z). \tag{12.33}$$

$K_n = 2\pi n/\Lambda$ is called the Bloch wave constant associated with frequency ω_n. If $\boldsymbol{\mathcal{U}}(z)$ is a simple sinusoid, then there will be only one value of ω. A more complex function will require more harmonics, as we saw in Chapter 6.

The solutions of equations (12.28) and (12.32) differ in several important ways:

1. Electrons are fermions and photons are bosons.
2. Equation (12.28) is a vector equation, while (12.32) is a scalar equation.
3. There are only real positive eigenvalues for (12.28), while (12.32) can have negative eigenvalues.

[4] The mathematical definition of a Hermitian function $f(x)$ is that its complex conjugate is equal to the function with a change in sign of the variable: $f^*(x) = f(-x)$.

The propagation of electromagnetic waves in a one-dimensional periodic index of refraction was first modeled by Lord Rayleigh [15]. In 1977, an analytic solution for a one-dimensional photonic structure was derived [16], which we will outline below. Two- and three-dimensional structures could not be solved analytically, but were addressed numerically in 1987 [8, 9].

We will explore the impact on the propagation of light in a material with spatially periodic electrical properties along the z-direction and isotropic magnetic properties. We will generate solutions of the equation for the magnetic field by using Bloch's theorem, which says if $\varepsilon(z) = \varepsilon(z + \Lambda)$, then the solution of (12.28) has the form

$$\mathbf{H} = e^{i(\mathbf{K}\cdot\mathbf{r}-\omega t)}\boldsymbol{\mathcal{H}}, \tag{12.34}$$

where

$$\boldsymbol{\mathcal{H}}(z) = \boldsymbol{\mathcal{H}}(z + \Lambda) = \sum_{n=0}^{\infty} \mathbf{a}_n \exp[i(k + nK)z]$$

is a periodic function with period Λ that can be decomposed into a Fourier series. If we substitute (12.34) into (12.28), we find that the periodic function is given by

$$(\nabla \times i\mathbf{k}) \times \frac{1}{\varepsilon}(\nabla + i\mathbf{k}) \times \boldsymbol{\mathcal{H}} = \left(\frac{\omega}{c}\right)^2 \boldsymbol{\mathcal{H}}.$$

Because $\boldsymbol{\mathcal{H}}$ is periodic, we need only discuss its behavior over the "unit cell" of its periodicity.[5] This also allows us to assign a wavevector to the periodicity K given by $2\pi/\Lambda$, and our solution needs to be stated only over the interval $-K_z/\Lambda \le K_z \le K_z/\Lambda$. This interval is called the first Brillouin zone. The Brillouin zone is a primitive unit cell of the periodic lattice described in spatial reciprocal space (see Figure 12.22). It is useful because the Bloch wave can be completely characterized by determining its behavior in a single Brillouin zone.

The periodic eigenfunctions have a well-defined frequency and form a complete set that can be used to describe any wave. The eigenfunction is specified by the K_n that appears in the expression for the eigenvalue ω_n. It turns out that the physical interpretation of K_n is nearly the same as that of the wavenumber k of harmonic waves. To obtain an expression for K_n, we need to solve (12.33) for K_n. We can rewrite (12.33) as a matrix equation

$$\left(\mathbf{T} - e^{iK_n\Lambda}\mathbf{I}_m\right)f(z) = 0,$$

[5] A unit cell is the simplest repeating unit of a periodic structure.

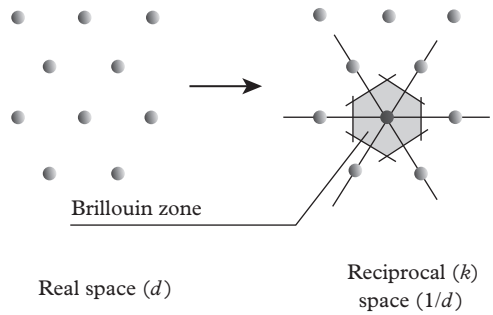

Figure 12.22 *Real space with a periodic structure and the spatial reciprocal space showing the Brillouin zone.*

where $\mathbf{T}$ is an $m \times m$ square matrix and $\mathbf{I}$ is the identity matrix. For any 2×2 matrix

$$\mathbf{T} = \begin{bmatrix} A & B \\ C & D \end{bmatrix},$$

the characteristic equation of $\mathbf{T}$ can be written as

$$\begin{vmatrix} A - e^{iK_n\Lambda} & B \\ C & D - e^{iK_n\Lambda} \end{vmatrix} = e^{i2K_n\Lambda} - (A + D)e^{iK_n\Lambda} + AD - BC = 0.$$

$A + D = \text{tr}(\mathbf{T})$ is the trace of the matrix $\mathbf{T}$ and $AD - BC = \det(\mathbf{T})$ is the determinant of $\mathbf{T}$. Because $\mathbf{T}$ is periodic, the unit cell translation matrix connects two regions with identical index of refraction, and we have $AD - BC = 1$. Using this shorthand notation, we have to solve the following equation to obtain the eigenvalues of (12.33):

$$e^{i2K\Lambda} - \text{tr}(\mathbf{T})e^{iK\Lambda} + \det(\mathbf{T}) = e^{i2K\Lambda} - \text{tr}(\mathbf{T})e^{iK\Lambda} + 1 = 0.$$

The solution of this equation is

$$\cos K_n\Lambda = \frac{1}{2}(A + D),$$

that is,

$$K = \frac{1}{\Lambda}\cos^{-1}\left[\frac{1}{2}(A + D)\right].$$

As we pointed out in (7.5), in our discussion of total reflection, when K has a complex component, there is no propagation in the direction where K is complex. Let us assume that K is in the (x, z) plane and the z-component of k is complex:

$$\mathbf{k} \to (k_x, 0, ik_z),$$

$$E \propto e^{-i\mathbf{k}_t\cdot\mathbf{r}} = e^{-i(k_x x + ik_z z)},$$

$$\mathbf{k}\cdot\mathbf{r} = k(x\sin\theta + z\cos\theta), \quad \text{where } k_z \text{ is imaginary},$$

$$E \propto e^{-i\mathbf{k}\cdot\mathbf{r}} = e^{-ik(x\sin\theta + z\cos\theta)},$$

$$E = \mathcal{R}e\left\{\underbrace{e^{-k_z z}}_{\text{attenuation}} \quad \underbrace{e^{-ik_x x}}_{x\text{-propagation}}\right\} = e^{-kz\cos\theta}\cos(kx\sin\theta).$$

If $\frac{1}{2}(A + D) \leq 1$, then K_n is real, and the frequency bands are allowed. If $\frac{1}{2}(A + D) > 1$, then K_n is imaginary, and we have bandgaps and propagation will not be allowed.

12.13 Multilayer Photonic Crystal

In Appendix 4A, we constructed the translation operator for a unit cell by applying the boundary conditions of Maxwell's equations to calculate the propagation of light through a series of dielectric layers. To construct the matrix $\mathbf{T}$ for our current problem, we simply use (4A.14) and (4A.15) to generate the transfer matrix for the unit cell:

$$\mathbf{T} = \mathbf{I}_1\mathbf{T}_1\mathbf{I}_2\mathbf{T}_2.$$

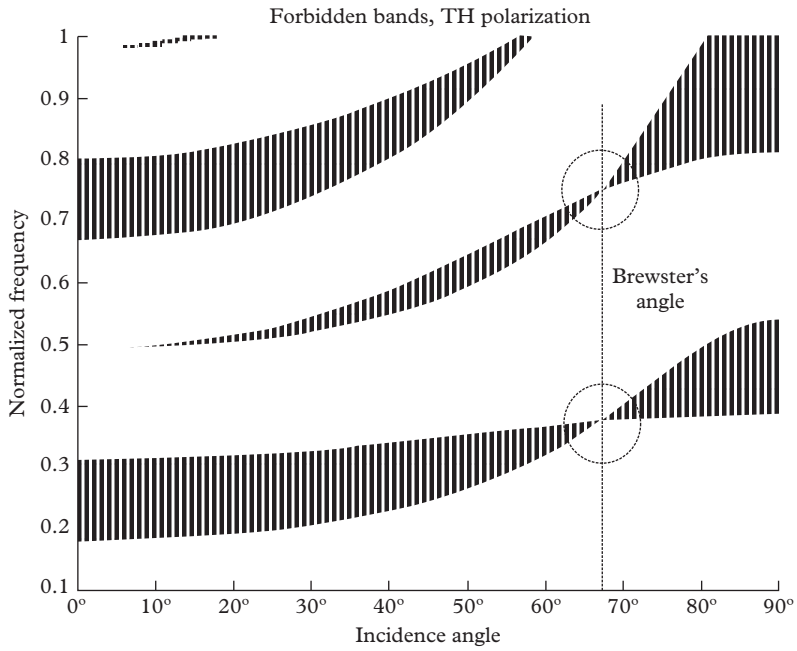

Figure 12.23 *Dispersion relation for a one-dimensional TH photonic crystal. The shadedareas are bandgaps and the white areas are allowed for a dielectric stack with index $n_1 = 1.45$ (SiO_2) and $n_2 = 3.45$ (Si). If there were bandgaps for all values of K, then we would have a complete bandgap. One-dimensional photonic structures do not have a complete bandgap. For this in-plane polarization, we see that at Brewster's angle (indicated by the circles), there are no reflections and thus no bandgap [17].*

Using the matrix from Appendix 4A, we can create the band structure for both polarizations for layers of silicon and silicon dioxide in the multilayer shown in Figure 12.21. Figure 12.23 shows the band structure for polarization in the plane of incidence (TH) and Figure 12.24 the band structure for polarization normal to the plane of incidence (TE). In both figures, the bandgaps are indicated by shading. Notice that at the edge of the bandgap, the slope of the dispersion curve flattens out, meaning that the group velocity decreases to zero at the band edge. This is of use in laser design and other applications where extended interactions with the optical field are desired.

12.13.1 Photonic Crystal Defect

As in semiconductor physics, we introduce a defect into the crystal to control the propagation of the wave. The defect introduced into the multilayer dielectric of Figure 12.21 is a break in the periodicity of the crystal as shown in Figure 12.25. In the multilayer structure, the multilayers form mirrors on either side of the defect, creating a Fabry–Perot cavity. The presence of the space creates a transmission peak in the stop band of the mirror pair: the optical transmittance of the multilayer structure without a defect is shown in Figure 12.26(a) and that of the structure with a defect in Figure 12.26(b).

The analytic solution for the one-dimensional photonic structure was carried out in hopes of being able to use these multilayers to design improved optical fibers that would provide performance similar to the TE_{01} low-loss mode in a metal circular waveguide. Of particular interest was the creation of hollow fibers to distribute infrared radiation in medical applications; there are no materials that are transparent enough to provide low-loss infrared fiber transmission. The problem with the multilayer design is the difficulty in finding materials that provide a high index contrast, mechanical stability, compatible thermal expansion,

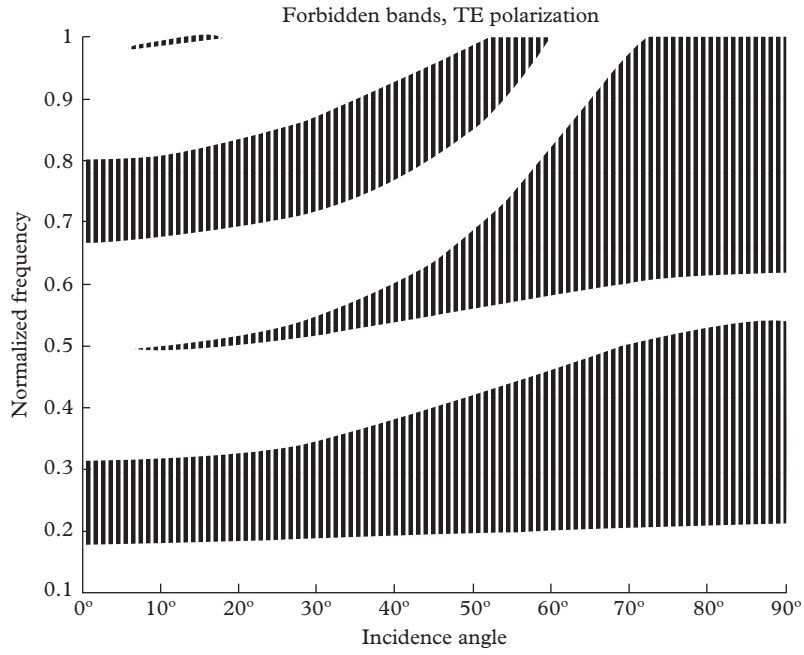

Figure 12.24 *Dispersion relation for a one-dimensional TE photonic crystal. The shaded areas are bandgaps and the white areas are allowed for a dielectric stack with index n_1 = 1.45 (SiO_2) and n_2 = 3.45 (Si) [17].*

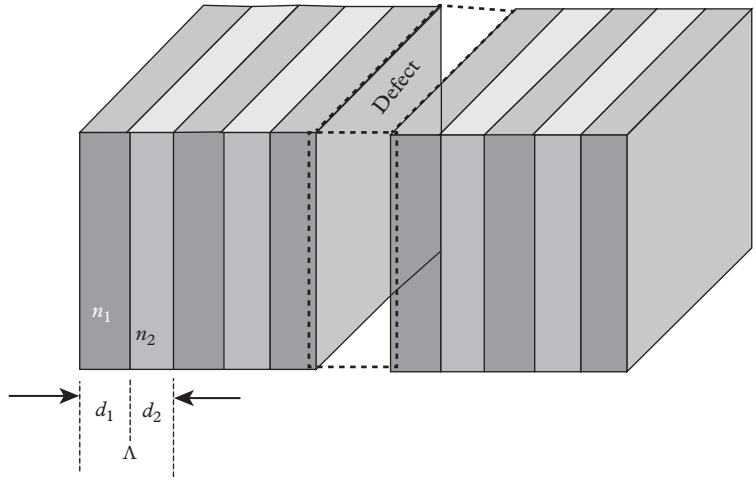

Figure 12.25 *A defect in a one-dimensional photonic crystal acts as a Fabry–Perot cavity. In Chapter 4, Fig 4.21, we calculated the spectrum expected. Figure 12.26(b) shows the spectrum obtained experimentally.*

and low optical absorption. Figure 12.27 shows one solution to the material problems, but before this was accomplished, a unique design approach was found to be superior to the multilayer approach. We will discuss this approach when we consider two-dimensional photonic crystals.

We seem to have gained little in capability with this new approach to multilayer design; however, we uncover the real benefit and new capabilities when we move to two- and photonic crystals. In these higher dimensions of periodic structures, we can

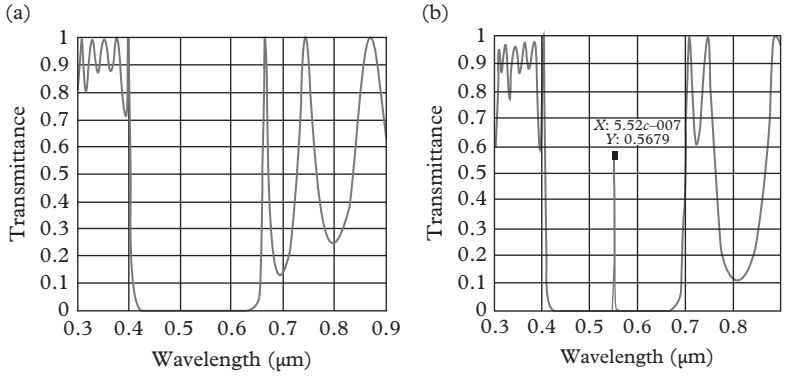

Figure 12.26 *Optical transmittance for a photonic crystal of Si:SiO_2: (a) without a defect; (b) with a defect (a single layer of $BaTiO_3$:SiO_2). (Wilson, K.S.J. and V. Revathy,* Investigation of photonic band gap in Si-Based one-dimensional photonic crystal. *Opt. Photonics J., 2013. 3: p. 365–368.)*

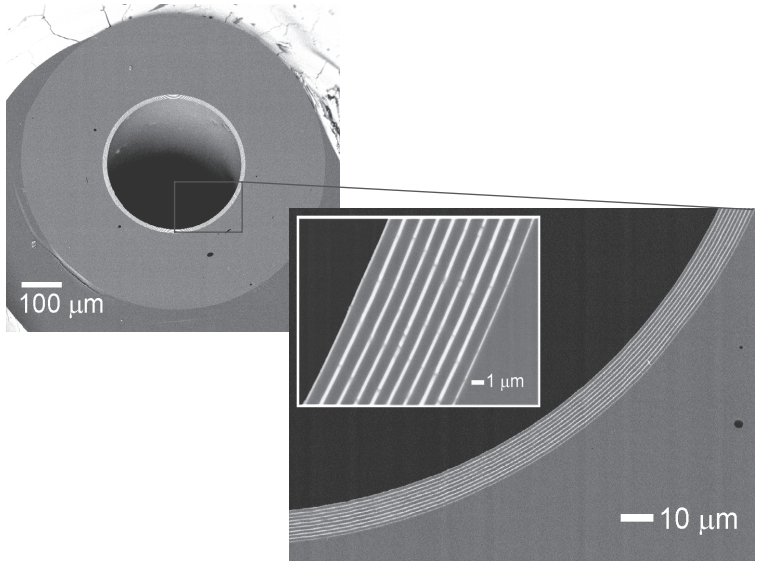

Figure 12.27 *A hollow-core multilayer fiber to transmit 3.5 μm radiation. (Reprinted by permission from Macmillan Publishers Ltd: Nature (Nature, 2002.* ***420****: p. 651–653), copyright 2002.)*

produce complete bandgaps and exploit a number of applications. As we pointed out previously, we must use numerical techniques to solve propagation in two- and three-dimensional systems. We will first present an overview of the various methods and then look at these systems.

12.14 Numerical Techniques

In the study of photonic structures, there are three general problem types:

- frequency-domain eigenproblems for the calculation of the band structure;
- frequency-domain responses to find the fields at a given frequency;
- time-domain simulations to calculate the propagation of fields in the structures.

Our main interest is the generation of the band structure. We were able to obtain an analytic solution for one dimension, but for two and three dimensions we must solve the partial differential equations using numerical techniques.

There are a variety of methods that can result in erroneous results and should be avoided, these include methods that only work for low index contrast or that assume the problem can be reduced to a scalar wave equation. There are precise techniques available that have been proven by experimental confirmation. These techniques reduce the infinite number of unknowns to a finite number of discretized unknowns. The following techniques are available:

- *Finite differences:* Form a grid over the region of interest whose crossings are given values of the unknown function.
- *Finite elements:* Use geometrical elements rather than crossing points and again define the unknown on these elements.
- *Spectral methods:* Expand the unknown function using an orthonormal set of basis functions. The typical expansion uses the Fourier series and is called the plane wave method [18]. The number of terms retained in the expansion determines the accuracy of the solution, as we mentioned in our one-dimensional calculation.
- *Boundary element methods:* Discretize the unknowns using any one of the above techniques, but only at the boundaries between what are assumed to be homogeneous regions. The homogeneous regions are treated analytically.

There are commercial and open source software packages available using the above techniques. There are several open source software packages that use the plane wave method [19–21]. For those who would like to write their own software, the plane wave method is discussed in detail by Danner [18].

12.15 Two-Dimensional Periodic Structure

The chief issue with two- and three-dimensional structures is how to fabricate them [22]. An arrangement of hollow tubes in a triangular pattern provides a useful two-dimensional structure [23] that is relatively easy to manufacture (see Figure 12.28). Fibers produced by

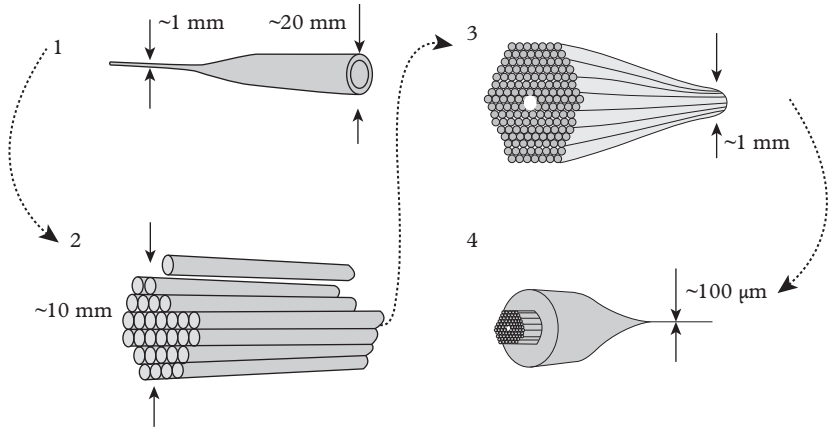

Figure 12.28 *Construction of hollow-core photonic crystal fiber. Staring with a 20 mm glass tube, capillary tubes are pulled and stacked to create a triangular array of tubes around a solid core. This is pulled down to a 1 mm preform that is coated with glass and pulled down to 100 μm. Air pressure is used when surface tension is not sufficient to prevent collapse of the microtubes. (Benabid, F.* Hollow-core photonic bandgap fibre: new light guidance for new science and technology. *Phil. Trans. R. Soc. A, 2006. 364: p. 3439–3462 by permission of the Royal Society.)*

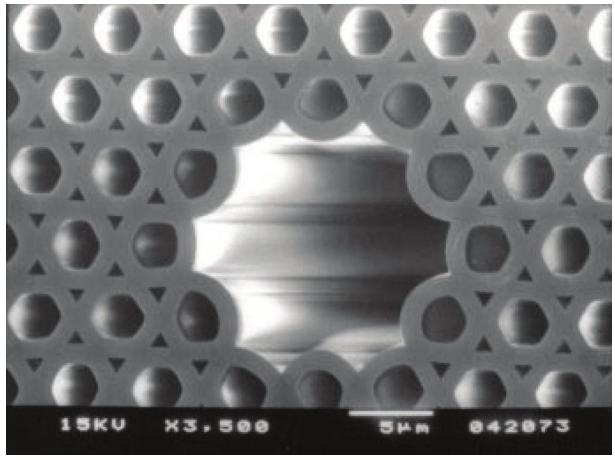

Figure 12.29 *Scanning electron micrograph of the first hollow-core PCF, drawn at the University of Bath. (Russell, P.,* Photonic crystal fibers. *Science, 2003.* ***299****: p. 358–362. Courtesy Philip Russell.)*

the construction technique outlined in Figure 12.28 are able to guide diffraction-free light beams. Such hollow-core photonic crystal fibers (PCFs) (see Figure 12.29) have found the following commercial uses:

- low-loss transmission of infrared signals for communications;
- transmission of high-energy laser radiation for surgery and materials processing;
- dispersion compensation;
- fiber lasers;
- nonlinear optical devices;
- sensing applications [24].

Commercial hollow-core fibers have large continuous bandwidths, only a small number of core modes, zero dispersion at the design wavelength, and very little nonlinearity or bending loss. It was hoped that the transmission loss in hollow-core fibers would be less than in current communication fibers (about 0.2 db/km). However, scattering from surface defects introduced during pulling of the fiber has limited attenuation in hollow core PCFs to just over 1 db/km.

Electrochemical fabrication techniques can be used to produce a two-dimensional photonic crystal surface. The general pattern shown in Figure 12.30 was produced using lithography, and the holes were etched using optically controlled electrochemical techniques.

Lithographic fabrication techniques have also been used to successfully produce two-dimensional photonic crystals on surfaces. Surface modification of an LED light source using two-dimensional photonic crystals can enhance the light extraction efficiency of the LED by preventing total reflection of the internally generated light (see Figure 12.31). An example of a commercial LED incorporating photonic crystal technology is the C4 LED, which is used in some high-end flashlights.

A similar surface modification technique is currently under study to improve the efficiency of thin solar cells (see Figure 12.32). A second fabrication technique, which has been used below 10 nm, is nanoimprint lithography, which causes mechanical deformation of a resist that is UV-cured. This technique has been validated for 22 nm manufacturing and been used successfully in the manufacture of surface photonic structures.

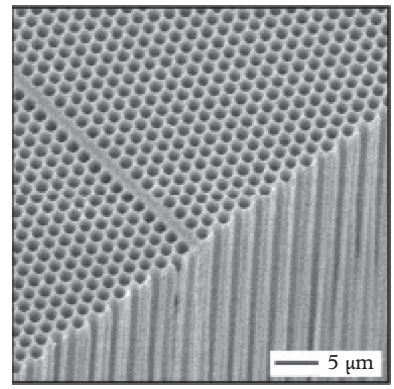

Figure 12.30 *Silicon two-dimensional photonic crystal with a line defect. The tubes are 100 μm tall and their spacing is 1.5 μm. (Birner, A., et al.,* Silicon-based photonic crystals. *Adv. Mater., 2001.* ***13****: p. 377–388* *© IOP Publishing. Reproduced by permission of IOP Publishing. All rights reserved.)*

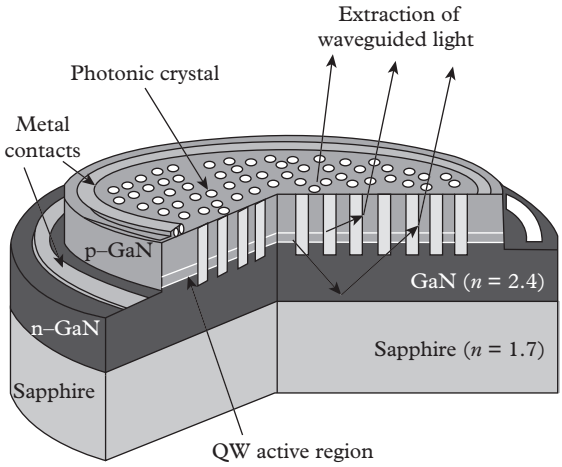

Figure 12.31 *Indium gallium nitride LED with a photonic crystal to enhance the extracted light. (Barton, D.L. and A.J. Fischer,* Photonic crystals improve LED efficiency. *2014: SPIE Newsroom. Courtesy A. J. Fischer, Sandia National Laboratories.)*

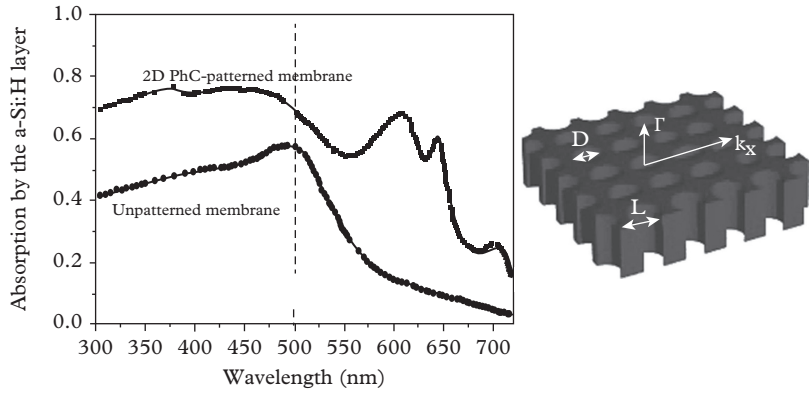

Figure 12.32 *Enhanced absorption of a thin film of amorphous silicon with and without a two-dimensional photonic crystal surface pattern. (*Light harvesting by planar photonic crystals in solar cells: the case of amorphous silicon, *Guillaume Gomard et al. 2012 J. Opt. 14 024011.)*

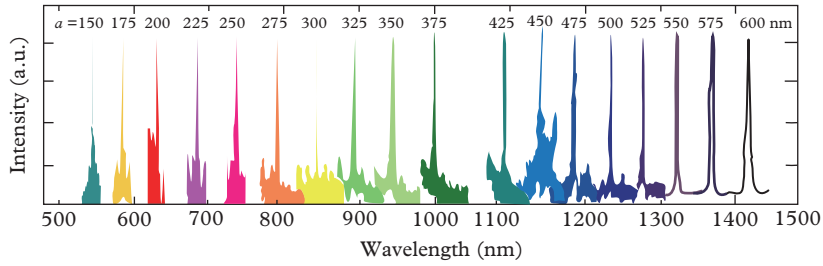

Figure 12.33 *Measured resonant spectra of individual SiC-based nanocavities made of three missing holes in a two-dimensional SiC photonic crystal slab structure with a triangular lattice of air holes and a lattice-constant spacing Δa of 25 nm. A supercontinuum white light source was used to probe the coupled cavities. (Reprinted with permission from Appl. Phys. Lett.* **99**, *201102 (2011). Copyright 2011, AIP Publishing LLC.)*

A point defect in a two-dimensional structure produces an optical cavity that can exhibit Q as high as 4.6×10^6. These high-Q cavities have been used for experimental demonstrations of spontaneous emission suppression, enhancement, and strong coupling. Figure 12.33 shows the frequency response of a string of these coupled cavities.

12.16 Three-Dimensional Periodic Structure

The first three-dimensional photonic crystal to be demonstrated operated at 13 GHz [25] (Figure 12.34), and a microwave application of this crystal as a substrate for a planar antenna a short time later [26] stimulated interest in developing methods of creating photonic structures at optical wavelengths. At 13 GHz, the periodic structure was created by drilling holes in a dielectric material, but creating a similar structure for visible wavelengths is much harder. To control 1 μm wavelength light, feature size control of the order of 100 nm is needed. The attempt to develop this fabrication capability is called nanophotonics. Both top-down (lithography and etching) and bottom-up (e.g., self-assembly) approaches have been tried, and the winner has yet to be decided.

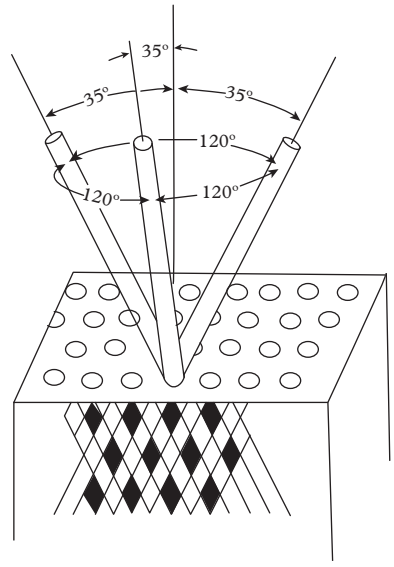

Figure 12.34 *The first three-dimensional photonic structure, with a complete bandgap at 13 GHz. (Yablonovitch, E.,* Photonic band-gap structures. *J. Opt. Soc. Am. B, 1993. 10: p. 283–295.)*

12.17 Fabrication Defects

The bandgap in the photonic structure depends on the index contrast, the lattice symmetry, and the filing factor (the fraction of low-index surface in the unit cell). Defects in these parameters can occur accidently or intentionally. Nanometer and subnanometer precision is difficult to achieve, even with state-of-the art fabrication methods. It is very difficult to introduce desired defects without error, and once constructed there are no practical ways to alter or correct the fabricated structure.

Fabrication with electron beams or X-rays uses techniques developed in the semiconductor electronics industry to build photonic crystals one layer at a time. Figure 12.35 shows an electron micrograph of a "woodpile" structure created by electron lithography. Speed and cost required to produce the structures are limiting factors with these techniques.

Self-assembly is troubled by the occurrence of random defects. Colloidal self-assembly utilizes sedimentation of micro or nanospheres into face-centered cubic (fcc) lattices. The resulting structure, called synthetic opal, is used as a mold into which a semiconductor material may infiltrate. After this process is complete, the mold is removed, leaving a lattice of air-filled spheres surrounded by a high-dielectric medium. Altogether, this process is quick, efficient, and cheap, but the assemblies are riddled with unintended defects.

Holographic interferometric techniques can produce large-area, defect-free photonic crystals, but it is difficult to obtain large index modulation.

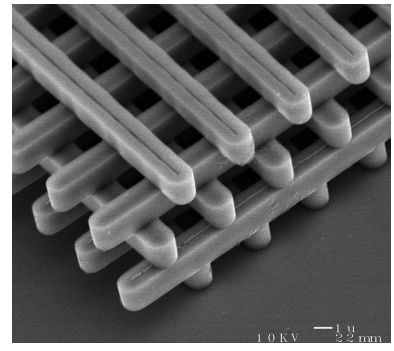

Figure 12.35 *Electron micrograph of a "woodpile" or "Lincoln log" structure [27]. (Courtesy Sandia National Laboratories.)*

12.18 Natural Photonic Crystals

While nature has created a number of examples of photonic structures as shown in Figures 12.36–12.38, these structures do not meet the accuracy requirements for our applications.

12.19 Summary

Holography By recording the fringe pattern produced by two coherent waves, a hologram can be produced with an amplitude transmission function given by

$$t_h(x, y) = t_0 + \beta(A^* a + A a^*).$$

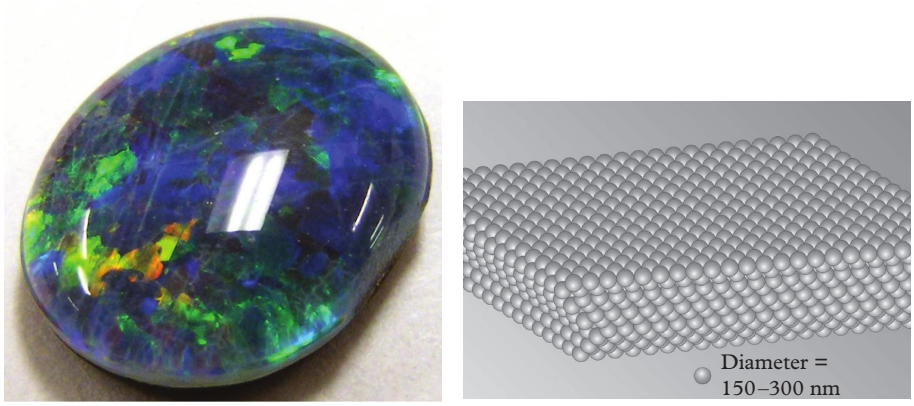

Figure 12.36 *(a) Australian black opal. This is the most valuable of the opals. The darkness comes from trace amounts of carbon and iron oxide. (b) The colors come from photonic structures made up of spheres of silicon dioxide. ("Opal molecular structure2" by Dpulitzer—Own work. Licensed under Creative Commons Attribution—Share Alike 3.0 via Wikimedia Commons.)*

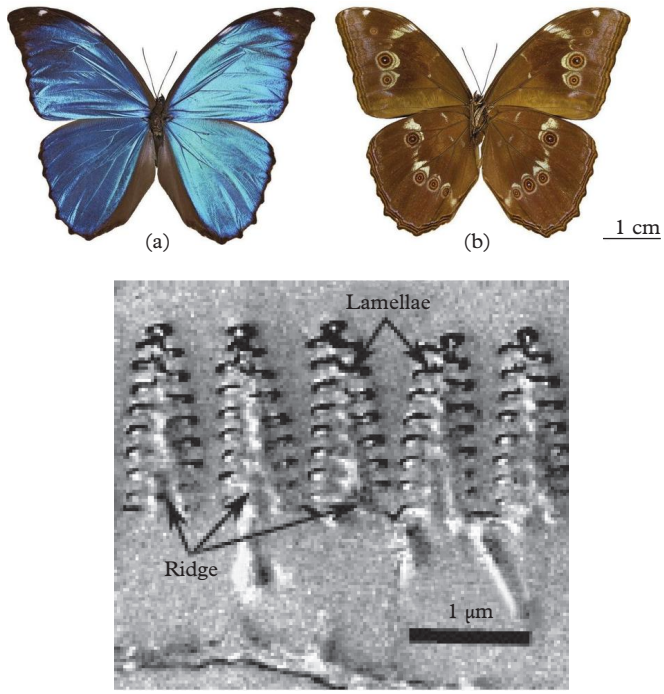

Figure 12.37 *Blue morpho butterfly (*Morpho menelaus*): (a) the upper surfaces of the wings are blue owing to the presence of photonic structures, while (b) the undersides are brown. (*"Morpho menelaus huebneri *MHNT Male" by Didier Descouens—Own work via Wikimedia Commons.) (c) Magnification of the upper wing surface: this transmission electron micrograph shows the "Christmas tree" structure responsible for the blue iridescence. (Siddique, R.H., S. Diewald, J. Leuthold, and H. Hölscher,* Theoretical and experimental analysis of the structural pattern responsible for the iridescence of *Morpho* butterflies. *Opt. Express, 2013.* ***21****: p. 14351–14361.)*

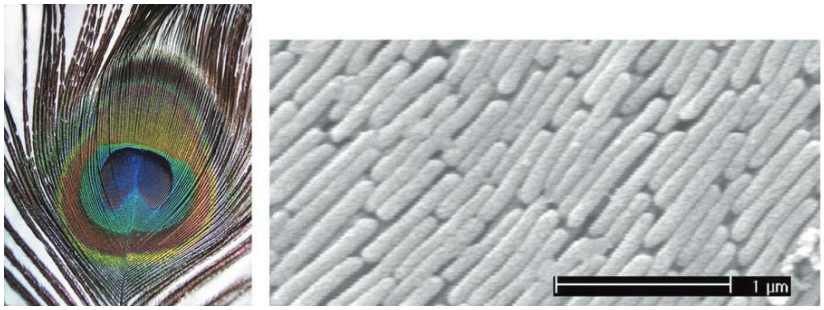

(a) (b)

Figure 12.38 *(a) Feather of a male Indian peafowl (*Pavo cristatus*). (I, Beyond silence, via Wikimedia Commons.) (b) Longitudinal cross section of the green barbule. A change in just the dimensions of the structures creates the other colors. (*Coloration strategies in peacock feathers, *PNAS, vol. 100, no. 22. Jian Zi, et al., 12576–12578, Copyright (2003) National Academy of Sciences, U.S.A.)*

If the hologram is illuminated by a wave of amplitude B, then the wave transmitted by the hologram will have an amplitude given by

$$B(x,y)t_h(x,y) = t_0B + \beta A^*Ba + \beta ABa^*.$$

The transmitted wave contains a reproduction of the complex amplitudes of both waves. The wave we wish to reproduce is identified as the signal wave and its complex amplitude is denoted by a.

The wave transmitted by the hologram contains not only the desired signal wave but also a number of unwanted waves. To separate the signal wave from these unwanted waves, we produce the hologram by illuminating the recording medium with a signal wave and a reference wave, which propagate at an angle with respect to each other. The minimum angle between the reference and signal waves that will allow an uncluttered reproduction of the signal wave is given by

$$\theta_{\min} = \sin^{-1}\left(\frac{3k_w\lambda}{2\pi}\right),$$

where k_w is the spatial frequency bandwidth of the signal wave.

The fraction of the reconstruction wave that is diffracted into the signal wave by the hologram is called the diffraction efficiency of the hologram:

$$\eta = \frac{(\beta BA^*a)^2}{|B|^2}.$$

The diffraction efficiency is a function of the exposure energy $\mathcal{E}_0$ and the visibility V of the interference fringes:

$$\eta = \left(\frac{\beta'\mathcal{E}_0V}{2}\right)^2.$$

The fringe visibility is determined by the relative amplitudes of the signal and reference waves, called the K-ratio,

$$K = \frac{A_0^2}{a_0^2}.$$

A hologram can be viewed as a collection of Fresnel zone plates. The focal length of a zone plate created by interfering the waves from two point sources is given by

$$\frac{1}{f_{\pm}} = \mp\left(\frac{1}{Z_r} - \frac{1}{Z_s}\right).$$

The reconstruction of the zone plate is described by the equation

$$\frac{1}{f_{\pm}} = \mp\frac{\lambda_2}{\lambda_1}\left(\frac{1}{Z_c} - \frac{1}{Z_i}\right),$$

where λ_1 is the recording wavelength, λ_2 is the reconstruction wavelength, Z_c is the position of the reconstruction source, and Z_i is the position of the image of the signal wave source.

Photonic crystals To calculate the propagation of the electromagnetic wave in a material with a periodic index of refraction, we must solve either

$$\nabla \times \left[\frac{1}{\varepsilon(\mathbf{r})}\nabla \times \mathbf{H}\right] = \frac{\omega^2}{c^2\varepsilon_0}\mathbf{H}$$

or

$$\frac{1}{\varepsilon(\mathbf{r})}(\nabla \times \nabla \times \mathbf{E}) = \frac{\omega^2}{c^2\varepsilon_0}\mathbf{E}.$$

Equation (12.28) is the better choice, because it allows us to use Bloch's theorem: if $\varepsilon(z) = \varepsilon(z + \Lambda)$, then the solution of (12.28) has the form

$$\mathbf{H} = e^{i(\mathbf{K}\cdot\mathbf{r}-\omega t)}\boldsymbol{\mathcal{H}},$$

where

$$\boldsymbol{\mathcal{H}}(z) = \boldsymbol{\mathcal{H}}(z + \Lambda) = \sum_{n=0}^{\infty}\mathbf{a}_n \exp[i(k + nK)z]$$

is a periodic function with period Λ.

12.20 Problems

12.1. Assume that the reference and signal positions are 100 mm apart and are both 100 m from the recording medium. If the wavelength is 632.8 nm, what is the minimum resolution the recording medium must have? What type of hologram will be created?

12.2. Assume a hologram is made with a plane wave of wavelength $\lambda = 632.8$ nm and a signal of the same wavelength located 1 m from the recording plane. If the hologram is reconstructed with a plane wave of wavelength $\lambda = 488$ nm, where is the virtual image located?

12.3. A holographic diffraction grating with 1000 lines/mm is to be constructed using plane waves from a HeNe laser of wavelength $\lambda = 632.8$ nm. What is the angle between the waves? Draw the experimental configuration.

12.4. Kodak Tri-X photographic film has a maximum resolution of about 50 lines/mm. What is the maximum angle between the reference and signal waves for this film if we use $\lambda = 441.6$ nm? What if we use $\lambda = 632.8$ nm?

12.5. Using a wavelength of 514.5 nm, a hologram is recorded with the reference point source located at (–0.5 m, –1 m) and the signal located at (0.5 m, –0.5 m). After development, the hologram is illuminated by a reconstruction wave of $\lambda = 488$ nm located at (–0.5 m, –0.5 m). What are the lateral and longitudinal magnifications? Where are the real and virtual images?

12.6. Where are the images in Problem 12.5 if the developed hologram is enlarged by 10% during processing?

12.7. We wish to record a hologram 10 cm on a side with a resolution of 0.01 mm using an argon laser with a wavelength $\lambda = 488$ nm. What is the minimum angle between the signal and reference beams if the recording and viewing distance must be 20 cm?

12.8. A zone plate is created on a photographic film using two point sources, one 20 cm and the other 50 cm from the recording film. If the recording and playback wavelengths are both 632.8 nm, what is the focal length of the zone plate?

12.9. If the recording film used in Problem 12.8 can record 2000 lines/mm, what size zone plate can be recorded?

12.10. We wish to record a hologram of an automobile that is 18 ft × 4 ft. The hologram will be recorded on an 8 in. × 10 in. glass plate using 488 nm radiation from an argon laser. How far from the car should we locate the film plate if the film can record 2500 lines/mm?

12.11. Calculate the magnification and find the location of the images for a hologram made with a reference beam located at (15, –200) and a signal at (0, –100). [In these problems, the coordinates are presented as (x, z).] The reconstruction wave is a plane wave arriving at the hologram at an angle of –30° to the hologram normal. Assume that there is no change in dimensions of the hologram during processing and that the wavelengths used for construction and reconstruction are the same.

12.12. Calculate the magnification and find the location of the images for a hologram made at a wavelength of 514.5 nm with a reference beam located at (0, –200) and a signal at (5, –100). The reconstruction wave of wavelength 488 nm has coordinates of (0, –190). Assume that the hologram swelled by 5% during processing.

12.13. Calculate the magnification and find the location of the images for a hologram made at a wavelength of 514.5 nm with a reference beam located at (–20, –200) and a signal at (15, –200). The reconstruction wave of wavelength 488 nm has coordinates of (–20, –200). Assume that the hologram swelled by 5% during processing.

12.14. Calculate the values of A, B, C, and D for the transfer matrix for the unit cell of a multilayer photonic one-dimensional crystal,

$$\mathbf{T} = \begin{bmatrix} A & B \\ C & D \end{bmatrix},$$

using (4A.14) and (4A.15).

12.15. Calculate the magnification and find the location of the images for a hologram made at a wavelength of 488 nm with a reference beam located at (0, –200) and a signal at (15, –200). The reconstruction wave of wavelength 488 nm has coordinates

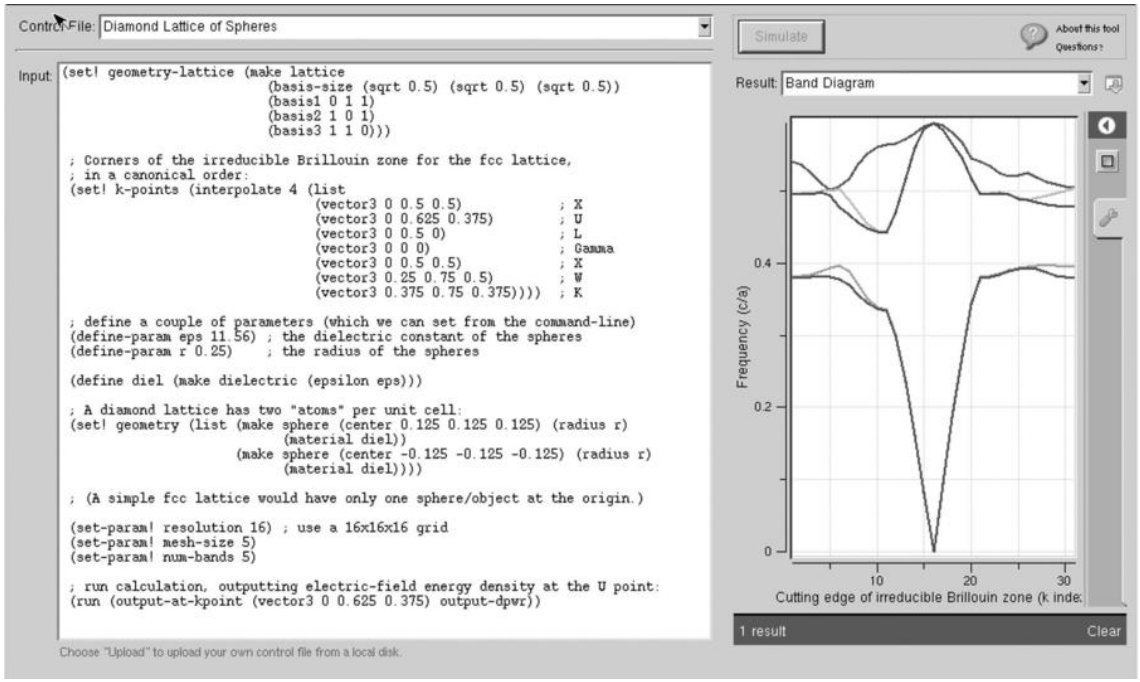
Control File: Diamond Lattice of Spheres
Simulate
About this tool
Questions?
Input:
(set! geometry-lattice (make lattice
(basis-size (sqrt 0.5) (sqrt 0.5) (sqrt 0.5))
(basis1 0 1 1)
(basis2 1 0 1)
(basis3 1 1 0)))
; Corners of the irreducible Brillouin zone for the fcc lattice,
; in a canonical order:
(set! k-points (interpolate 4 (list
(vector3 0 0.5 0.5) ; X
(vector3 0 0.625 0.375) ; U
(vector3 0 0.5 0) ; L
(vector3 0 0 0) ; Gamma
(vector3 0 0.5 0.5) ; X
(vector3 0.25 0.75 0.5) ; W
(vector3 0.375 0.75 0.375)))) ; K
; define a couple of parameters (which we can set from the command-line)
(define-param eps 11.56) ; the dielectric constant of the spheres
(define-param r 0.25) ; the radius of the spheres
(define diel (make dielectric (epsilon eps)))
; A diamond lattice has two "atoms" per unit cell:
(set! geometry (list (make sphere (center 0.125 0.125 0.125) (radius r)
(material diel))
(make sphere (center -0.125 -0.125 -0.125) (radius r)
(material diel))))
; (A simple fcc lattice would have only one sphere/object at the origin.)
(set-param! resolution 16) ; use a 16x16x16 grid
(set-param! mesh-size 5)
(set-param! num-bands 5)
; run calculation, outputting electric-field energy density at the U point:
(run (output-at-kpoint (vector3 0 0.625 0.375) output-dpwr))
Choose "Upload" to upload your own control file from a local disk.
Result: Band Diagram
Frequency (c/a)
0.4
0.2
0
10
20
30
Cutting edge of irreducible Brillouin zone (k inde
1 result
Clear

Figure 12.39 *Band structure simulation using MIT Photonic Bands software on nanoHUB. (Carlos Montalvo; Jing Ouyang; Minghao Qi (2015), "MIT Photonic Bands," <https://nanohub.org/resources/MPB>. (DOI: 10.4231/D3Q23R16X).)*

$(0, -\infty)$. Assume that no changes in dimension occurred during processing. How should this hologram be viewed?

12.16. A recording medium is placed at the origin of a coordinate system in the (x, y) plane and normal to the z-axis. The reference wave's propagation vector is

$$k\left(\sin\theta_r\,\hat{\mathbf{i}} + \cos\theta_r\,\hat{\mathbf{k}}\right).$$

The signal wave's propagation vector is

$$k\left(-\sin\theta_s\,\hat{\mathbf{i}} + \cos\theta_s\,\hat{\mathbf{k}}\right).$$

Derive an expression for the fringe spacing along the x- and z-directions. *Hint:* This is a generalization of Problem 4.17.

12.17. Using the arrangement described in Problem 12.16, find the fringe spacing along the bisector of the angle between the signal and reference waves, $\theta_r + \theta_s$. Assume that the bisector makes an angle φ with respect to the z-axis.

12.18. Using the arrangement described in Problem 12.16, find the fringe spacing along the normal to the bisector of the angle between the signal and reference waves.

12.19. We have constructed a hologram of an object 10 cm long. We used a lens to image the object at the hologram plate so that the reconstruction appears to be centered

at the hologram. What is the transverse coherence length needed to reconstruct the hologram with an image blur less than 100 μm?

12.20. We wish to use sunlight and a filter centered at 500 nm with a spectral width of 50 nm to display a hologram. The hologram was made with a reference angle of 30°. What is the maximum depth we can expect to see in the hologram if we require an image blur of 100 μm?

12.21. To calculate the band structure of a photonic crystal, we must turn to the use of numerical methods. Software to carry out the calculations can be found at http://ab-initio.mit.edu/wiki/index.php/MPB_download
The software can run on most Unix-like operating systems, but may require additional software packages. Another approach is to run the program on nanoHUB: https://nanohub.org/tools/mpb/
Simply click "Launch Tool." Select the Control File from the dropdown box at the top of the page. Figure 12.39 shows the result of running the Control File "Diamond Lattice of Spheres." The result shown is the band diagram. A number of other plots can be generated. The parameters entered in the Control File can be changed and the simulation rerun to see the impact. The student should explore photonic crystals via this free simulation resource.

REFERENCES

1. Collier, R.J., C.B. Burckhardt, and L.H. Lin, *Optical Holography*. 1971: Academic Press.
2. Joannopoulos, J.D., et al., *Photonic Crystals: Molding the Flow of Light*. 2nd ed. 2008: Princeton University Press.
3. Gabor, D., *Holography, 1948–1971*. Proc. IEEE, 1972. **60**: p. 655–668.
4. Leith, E.N. and J. Upatnieks, *Reconsructed wavefronts and communication theory.* J. Opt. Soc. Am., 1962. **52**: p. 1123.
5. Leith, E.N. and J. Upatnieks, *Wavefront reconstruction with continuous-tone objects*. J. Opt Soc. Am, 1963. **53**: p. 1377–1381.
6. Leith, E.N. and J. Upatnieks, *Wavefront reconstruction with continuous-tone transparencies*. J. Opt Soc. Am, 1963. **53**: p. 522.
7. Bloch, F., *Über die Quantenmechanik der Elektronen in Kristallgittern*. Z. Phys., 1928. **52**: p. 555–600.
8. Yablonovitch, E., *Inhibited spontaneous emission in solid state physics and electronics*. Phys. Rev. Lett., 1987. **58**: p. 2059–2061.
9. John, S., *Strong localization of photons in certain disordered dielectric superlattices*. Phys. Rev. Lett., 1987. **58**: p. 2486–2489.
10. Anderson, P.W., *Absence of diffusion in certain random lattices.* Phys. Rev., 1958. **109**: p. 1492–1505.
11. Hariharan, P., *Optical Holography: Principles, Techniques and Applications*. 2nd ed.1996: Cambridge University Press.
12. Collier, R.J., C.B. Burckhardt, and L.H. Lin, *Optical Holography*. 1971: Academic Press.
13. Kittel, C., *Introduction to Solid State Physics*. 7th ed. 1995: Wiley.
14. Floquet, M.G., *Équations différentielles linéaires, àcoefficients périodiques.* Ann. Sci. ENS, 1883. **12**: p. 48–44.

15. Rayleigh, J.W.S., *On the remarkable phenomenon of crystalline reflexion described by Prof. Stokes*. Phil. Mag., 1886. **26**: p. 256–265.
16. Yeh, P., A. Yariv, and C.-S. Hong, *Electromagnetic propagation in periodic stratified media. I. General theory*. J. Opt. Soc. Am., 1977. **67**: p. 423–438.
17. Cazimir-Gabriel, B., *One-Dimensional Photonic Crystal Dispersion Relations*. 2008: Mathworks; <http://www.mathworks.com/matlabcentral/fileexchange/21810-one-dimensional-photonic-crystal-dispersion-relations/>
18. Danner, A.J., *An Introduction to the Plane Wave Expansion Method for Calculating Photonic Crystal Band Diagrams*. 2011: University of Illinois at Urbana-Champaign; <http://www.ece.nus.edu.sg/stfpage/eleadj/planewave.htm>.
19. Guo, S., *Plane Wave Expansion Method For Photonic Band Gap Calculation Using MATLAB®. Manual Version 1.00*. Department of Electrical and Computer Engineering, Old Dominion University, Norfolk, VA; <http://www.phys.ubbcluj.ro/~emil.vinteler/nanofotonica/PWM/pwmmanual_Guo.pdf>.
20. *Modul2: Plane Wave Method* (based on Aaron Danner, *An introduction to the plane wave expansion method for calculating photonic crystal band diagrams*); <http://www.phys.ubbcluj.ro/~emil.vinteler/nanofotonica/PWM/Modul2_PWM.pdf>.
21. MIT Photonic-Bands (MPB) Package <http://ab-initio.mit.edu/wiki/index.php/MIT_Photonic_Bands>.
22. Bowden, C.M., J.P. Dowling, and H.O. Everitt, Editors, *Development and applications of materials exhibiting photonic band gaps*. J. Opt. Soc. Am. B, 1993. **10**: p. 280.
23. Birks, T.A., et al., *Full 2-D photonic bandgaps in silica/air structures*. Electron. Lett., 1995. **31**: p. 1941–1943.
24. Pinto, A.M.R. and M. Lopez-Amo, *Photonic crystal fibers for sensing applications*. J. Sensors, 2012. **2012**: p. 21.
25. Yablonovitch, E. and T.J. Gmitter, *Photonic band structure: the face-centered-cubic case*. Phys. Rev. Lett., 1989. **63**: p. 1950–1953.
26. Brown, E.R., C.D. Parker, and E. Yablonovitch, *Radiation properties of a planar antenna on a photonic-crystal substrate*. J. Opt Soc. Am. B, 1993. **10**: p. 404–407.
27. Maka, T., et al., *Three dimensional photonic crystals in the visible regime*. Prog. Electromagn. Res. (PIER), 2003. **41**: p. 307–335.

Appendix 12A Phase Holograms

In the discussion of holography in Chapter 12, the holographic recording was always assumed to be an amplitude recording. We now wish to indicate briefly the properties of a hologram produced by phase recording. In this type of recording, the amplitude transmission coefficient of the developed hologram will be assumed to be constant, independent of spatial position, and the phase change produced by the developed hologram will depend linearly on the exposure energy.

The signal wave will be represented by

$$a(x) = a_0 e^{i\varphi(x)}, \tag{12A.1}$$

and the reference wave will be assumed to be a plane wave

$$A(x) = A_0 e^{ikx}, \tag{12A.2}$$

where

$$k = \frac{2\pi}{\lambda} \sin\theta_r.$$

We assume that the recording material will linearly record the spatial variation of the exposure energy $\mathcal{E}(x)$ as a spatial phase variation given by

$$\Phi(x) = \beta \mathcal{E}(x).$$

After exposure and development, the transmission coefficient of the hologram will be

$$t_h(x) = t_0 e^{i\beta a_0^2} e^{i\beta A_0^2} e^{2i\beta a_0 A_0 \cos(\varphi - kx)}. \tag{12A.3}$$

To simplify the equation, we define an average complex transmission coefficient of the developed hologram as

$$\tilde{t}_c = t_0 e^{i\beta a_0^2} e^{i\beta A_0^2}.$$

We also define the phase change due to the amplitude variation of the interference pattern as

$$\Gamma = 2\beta a_0 A_0,$$

and the spatial variation of the phase due to the phase variation of the interference pattern as

$$\psi = \varphi - kx.$$

Using these newly defined parameters, the transmission coefficient of the hologram becomes

$$\begin{aligned} t_h(x) &= \tilde{t}_c e^{i\Gamma \cos\psi} \\ &= \tilde{t}_c [\cos(\Gamma \cos\psi) + i \sin(\Gamma \cos\psi)]. \end{aligned} \tag{12A.4}$$

The sine and cosine functions in (12A.4) can be expressed as series of Bessel functions (see relations (9.1.44) and (9.1.45) in [1]):

$$\cos(\Gamma \cos\psi) = J_0(\Gamma) + 2\sum_{n=1}^{\infty} (-1)^n J_{2n}(\Gamma) \cos(2n\psi), \tag{12A.5}$$

$$\sin(\Gamma \cos\psi) = 2\sum_{n=0}^{\infty} (-1)^{n+2} J_{2n+1}(\Gamma) \cos[(2n+1)\psi]. \tag{12A.6}$$

Equation (12A.4) can be expressed in terms of (12A.5) and (12A.6):

$$\begin{aligned} t_h(x) = \tilde{t}_c \Bigg\{ & J_0(\Gamma) + 2\sum_{n=1}^{\infty} (-1)^n J_{2n}(\Gamma) \cos(2n\psi) \\ & + 2i \sum_{n=0}^{\infty} (-1)^{n+2} J_{2n+1}(\Gamma) \cos[(2n+1)\psi] \Bigg\}. \end{aligned}$$

We see that a large number of diffraction orders, one for each value of n, will be reconstructed by the thin phase hologram. This is in contrast to the presence of only two diffraction orders in a linearly recorded amplitude hologram [see (12.5)]. The amplitude of

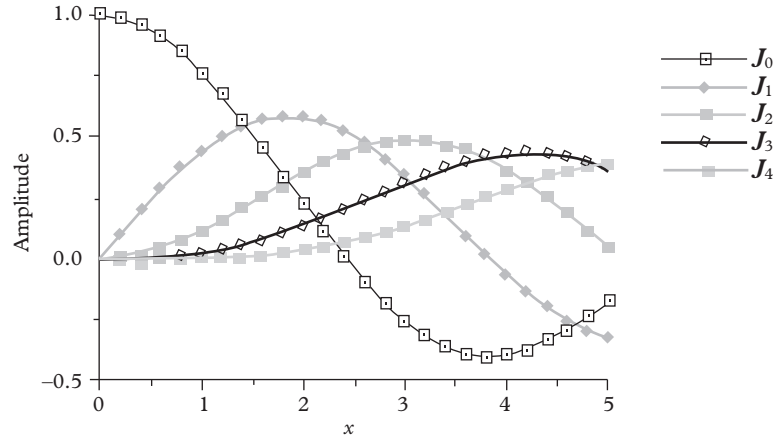

Figure 12A.1 *Amplitudes of the first five Bessel functions of the first kind.*

the nth diffracted order is proportional to the nth-order Bessel function J_n. Figure 12A.1 displays the amplitude variations of the first five Bessel functions.

We will limit our attention to the $n = 0$ term, corresponding to the first diffracted order. The hologram's transmission coefficient associated with the first diffracted order is denoted by t_{h0}:

$$\begin{aligned} t_{h0}(x) &= 2i\tilde{t}_c J_1(\Gamma)\cos\psi \\ &= i\tilde{t}_c J_1(\Gamma)\left(e^{i(\varphi-kx)} + e^{-i(\varphi-kx)}\right). \end{aligned} \tag{12A.7}$$

If we illuminate the exposed hologram with a duplicate of the reference wave, then the first diffracted order of the reconstruction wave is

$$\begin{aligned} Bt_{h0}(x) &= A_0 e^{ikx}\tilde{t}_c e^{i\pi/2} J_1(\Gamma)\left(e^{i(\varphi-kx)} + e^{-i(\varphi-kx)}\right) \\ &= A_0 t_0 e^{i\left(\beta a_0^2 + \beta A_0^2 + \pi/2\right)} J_1(\Gamma)\left(e^{i\varphi} + e^{-i(\varphi-2kx)}\right). \end{aligned} \tag{12A.8}$$

This wave does not appear to be a reasonable reproduction of the original signal beam. However, if $a_0 \ll A_0$, then we can replace $J_1(\Gamma)$ with the first term of its series expansion

$$J_1(2x) = x - \frac{x^3}{2} + \frac{x^5}{2^2 \cdot 3} - \ldots .$$

Using the definition of Γ, we can approximate the first-order Bessel function by

$$J_1(\Gamma) \approx \beta a_0 A_0,$$

whenever the signal beam is small relative to the reference beam. This enables us to write an expression for the virtual image wave,

$$A_0^2 \beta t_0 e^{i(\beta a_0^2 + \beta A_0^2 + \pi/2)}\left\{a_0 e^{i\varphi}\right\}. \tag{12A.9}$$

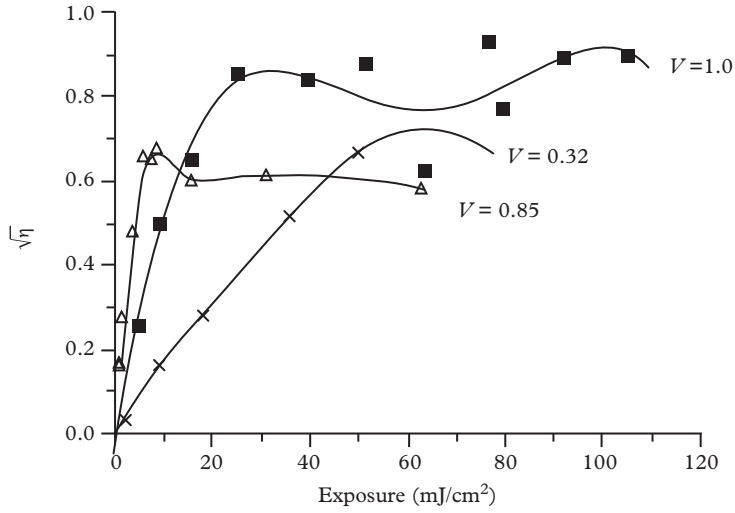

Figure 12A.2 *Diffraction efficiency versus exposure energy for several values of the fringe visibility V. The material is a phase recording using a photopolymer.*

The term in braces is the original signal wave. The intensity distribution of the diffracted wave reproduces the signal wave's intensity distribution, and the diffracted wave is within a constant phase factor of the original signal wave.

The maximum transmissivity of the phase recording is $(A_0\tau_0)^2$, and the maximum intensity diffracted into the first order is given by the maximum value of $(J_1)^2$ multiplied by $(A_0\tau_0)^2$, which is $(0.582)^2(A_0\tau_0)^2 = 0.339(A_0\tau_0)^2$. The maximum diffraction efficiency of a thin phase hologram is therefore 33.9%.

The amplitude holograms we discussed in Chapter 12 and the thin phase holograms we have just discussed have marginally useful diffraction efficiencies. If we could do no better, holography would be of limited utility. However, thick phase holograms have a maximum diffraction efficiency of 100% and simple holographic optical elements have approached this theoretical diffraction efficiency (see Figure 12A.2).

REFERENCE

1. Abramowitz, M. and I.A. Stegun, *Handbook of Mathematical Functions*. 1964: National Bureau of Standards.

Appendix 12B VanderLugt Filter

As discussed in Appendix 10A, the calculation of a correlation or a convolution integral can be accomplished by recording the amplitude and phase of a Fourier transform. From the theoretical development made in Chapter 12, it is apparent that this type of recording is a Fourier transform hologram. A. VanderLugt, in 1963, was the first to introduce the use of a Fourier transform hologram for pattern recognition operations, and the hologram is often called a *VanderLugt filter*. The technique works because both the phase and amplitude of the Fourier transform are recorded in the hologram.

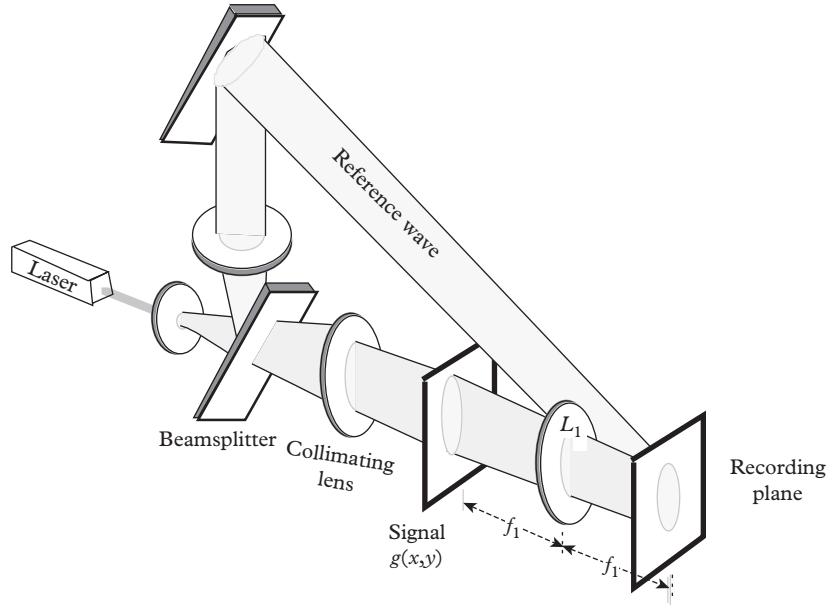

Figure 12B.1 *Geometry for recording a Fourier transform hologram.*

To construct a VanderLugt filter, we place a function $g(x, y)$, which we will call the reference function, in the front focal plane of lens L_1, a distance f_1 from L_1, as shown in Figure 12B.1. The Fourier transform $G(p, q)$ of $g(x, y)$ appears in the back focal plane of L_1 (the transform plane), a distance f_1 behind L_1. We add a reference plane wave $R(p, q)$ coherently to $G(p, q)$ at the transform plane—the recording plane of the hologram. For simplicity, we will limit the analysis to one dimension, with the dimension in the signal plane represented by x and that in the recording plane by p. The reference wave, of amplitude R_0, is incident at an angle θ to the transform plane—this angle is the hologram's offset angle:

$$R(p) = R_0 e^{ikp\sin\theta}. \tag{12B.1}$$

The amplitude distribution of the interference pattern in the transform plane,

$$\begin{aligned}\tilde{E}(p) &= R_0 e^{ikp\sin\theta} + \sqrt{\frac{-i}{\lambda f_1}} \int_{-\infty}^{\infty} g(x) e^{i(k/f_1)px}\, dx \\ &= R(p) + G(p),\end{aligned} \tag{12B.2}$$

is recorded on photosensitive material. The exposure is made using an exposure time τ_e such that the average exposure energy $|R_0|^2\tau_e$ creates an amplitude transmission coefficient t_0, centered in the linear portion of the amplitude transmission coefficient curve of the developed hologram.

The amplitude transmission coefficient of the developed hologram is

$$t_h = t_0 + \beta|G(p)|^2 + \beta R_0 G(p) e^{-ikp\sin\theta} + \beta R_0 G^*(p) e^{ikp\sin\theta}. \tag{12B.3}$$

No provision has been made in (12B.3) for dimensional changes in the hologram due to processing. Also, it is implicitly assumed here that the entire Fourier transform can be linearly recorded by the recording medium—we will show that it is not in Figure 12B.4.

The recording is illuminated with a reconstruction wave obtained by replacing $g(x, y)$ by a new function $f(x, y)$ in the front focal plane of L_1. After passing through L_1, the reconstruction field at the hologram is described by the Fourier transform of $f(x, y)$,

$$F(p) = \sqrt{\frac{-i}{\lambda f_1}} \int_{-\infty}^{\infty} f(x') e^{i(k/f_1)px'}\, dx'. \tag{12B.4}$$

The hologram diffracts $F(p)$ into four component waves:

$$\begin{aligned}\Psi(p) =& t_0 F(p) + \beta |G(p)|^2 F(p) \\ &+ \beta R_0 G(p) F(p) e^{-ikp\sin\theta} \\ &+ \beta R_0 G^*(p) F(p) e^{ikp\sin\theta}.\end{aligned} \tag{12B.5}$$

The various terms of this diffracted field can be associated with the wave directions shown in Figure 12B.2. The first two terms,

$$t_0 F(p) + \beta\, |G(p)|^2\, F(p),$$

propagate along the optical axis of lens L_1 and are not of interest here. The third term, propagating at an angle $-\theta$ to the optical axis, is labeled "Convolution" in Figure 12B.2. The fourth term, propagating at an angle θ to the optical axis, is labeled "Correlation" in Figure 12B.2. We will restrict our attention to the fourth term of (12B.5).

A lens L_2 of focal length f_2 is positioned with its optical axis at an angle θ with respect to the optical axis of L_1 so that it collects all of the fourth term of (12B.5), as shown in Figure 12B.3. At the front focal plane of L_2, the fourth term of (12B.5) can be written

$$\Psi_4(p) = \frac{\beta R_0}{\lambda f_1} e^{ikp\sin\theta} \int_{-\infty}^{\infty} f(x') e^{i(k/f_1)px'}\, dx' \int_{-\infty}^{\infty} g^*(x) e^{-i(k/f_1)px}\, dx \tag{12B.6}$$

$$= \frac{\beta R_0}{\lambda f_1} e^{ikp\sin\theta} \int_{-\infty}^{\infty}\int_{-\infty}^{\infty} f(x') g^*(x) e^{i(k/f_1)p(x'-x)}\, dx'\, dx\,. \tag{12B.7}$$

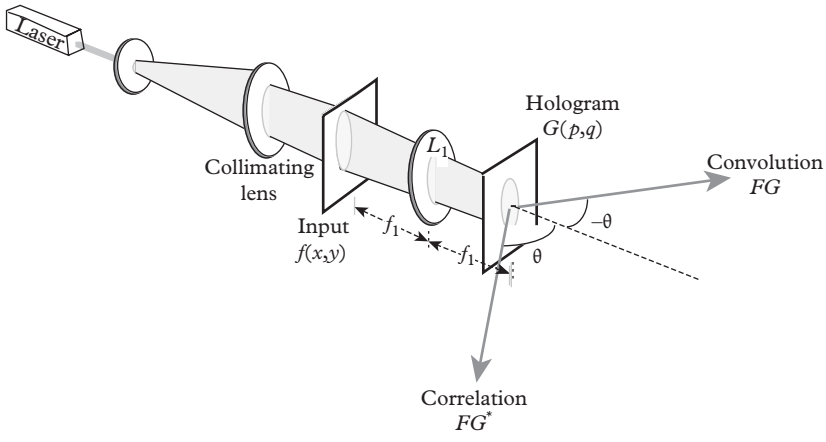

Figure 12B.2 *The waves reconstructed by the Fourier transform hologram when illuminated by the reconstruction wave, f(x,y).*

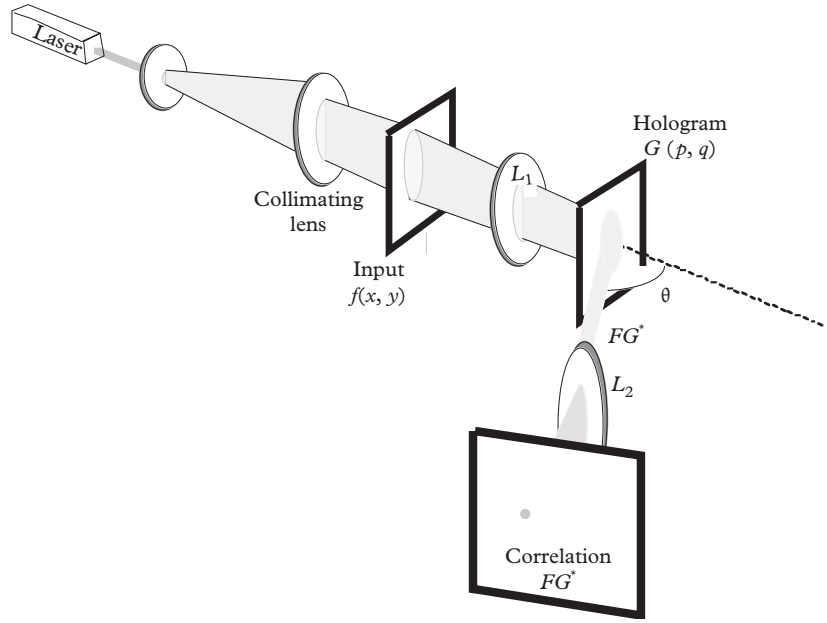

Figure 12B.3 *Geometry for reconstruction of a Fourier transform hologram in a correlation configuration.*

The second lens L_2 forms the Fourier transform of (12B.7) in its back focal plane a distance f_2 from L_2 (the coordinate in the back focal plane of L_2 is represented by ξ):

$$R(\xi) = \sqrt{\frac{-i}{\lambda f_2}} \int_{-\infty}^{\infty} \Psi_4(p) e^{i(k/f_2)p\xi}\, dp. \tag{12B.8}$$

To simplify the mathematical manipulation, we assume that the focal lengths of L_1 and L_2 are the same: $f_1 = f_2 = f$. The field in the back focal plane of L_2, labeled "Correlation" in Figure 12B.3, is obtained by substituting (12B.7) into (12B.8):

$$R(\xi) = \frac{\beta R_0}{\lambda f} \sqrt{\frac{-i}{\lambda f}} \int_{-\infty}^{\infty}\int_{-\infty}^{\infty}\int_{-\infty}^{\infty} g^*(x) f(x') e^{i(k/f)p(x'-x+\xi+f\sin\theta)}\, dx\, dx'\, dp. \tag{12B.9}$$

The sifting property of the delta function, (6.23), simplifies (12B.9) to

$$\begin{aligned} R(\xi) &= \frac{\beta R_0}{\lambda f} \sqrt{\frac{-i}{\lambda f}}\, 2\pi \int_{-\infty}^{\infty}\int_{-\infty}^{\infty} g^*(x) f(x') \delta\left(\frac{k}{f}(x' - x + \xi + f\sin\theta)\right) dx\, dx' \\ &= \beta R_0 \sqrt{\frac{-i}{\lambda f}} \int_{-\infty}^{\infty} g^*(x) f(x - \xi - f\sin\theta)\, dx. \end{aligned} \tag{12B.10}$$

Equation (12B.10) can be identified as the correlation of the input function $f(x, y)$ and the function $g(x, y)$.

An operational interpretation of (12B.10) can be obtained by assuming that $f(x, y)$ is identical to $g(x, y)$. The Fourier transform of f, which is now $G(p, q)$, is used as the reconstruction wave for the hologram stored in the back focal plane of L_1. From our knowledge of holograms, we know that if one of the two waves used to record a hologram is used as the reconstruction wave, then the second recording wave will be reproduced. Here $G(p, q)$ is to be used as the reconstruction wave, and thus the hologram will form, through diffraction, a wave identical to the reference wave $R(p)$ when it is illuminated with $G(p, q)$. The reference wave, a plane wave, is focused by L_2 to a spot in the correlation plane. The occurrence of a spot of light in the correlation plane will thus indicate that $g(x, y)$ is at the input of the optical system shown in Figure 12B.3.

An argument identical to that leading to (12B.10) can be used to demonstrate that the third term of (12B.5),

$$\Psi_3(p) = \beta R_0 G(p) e^{-ikp \sin\theta},$$

can be used to generate the convolution of $f(x)$ and $g(x)$. To do so, we need only position a lens with its optical axis aligned along the direction $-\theta$ shown in Figure 12B.2.

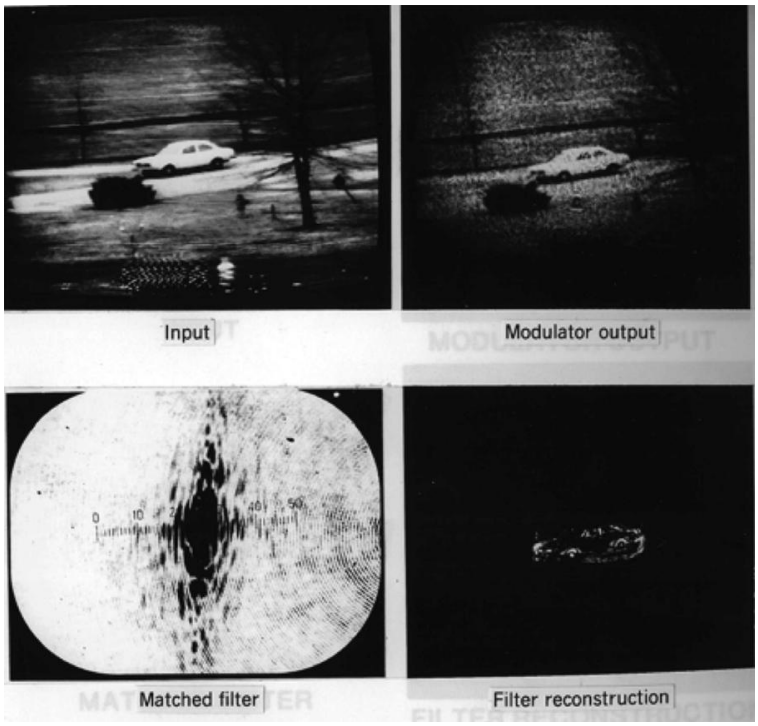

Figure 12B.5 *In the upper left is the image used in the optical system of Figure 12B.1, labeled "Input." The upper right image is the image at the signal plane of Figure 12B.1, labeled "Modulator output." The lower left image, labeled "Matched filter," is a magnified image of the Fourier transform hologram. The lower right image, labeled "Filter reconstruction," is the reconstructed image generated by the Fourier transform hologram when exposed to a plane wave.*

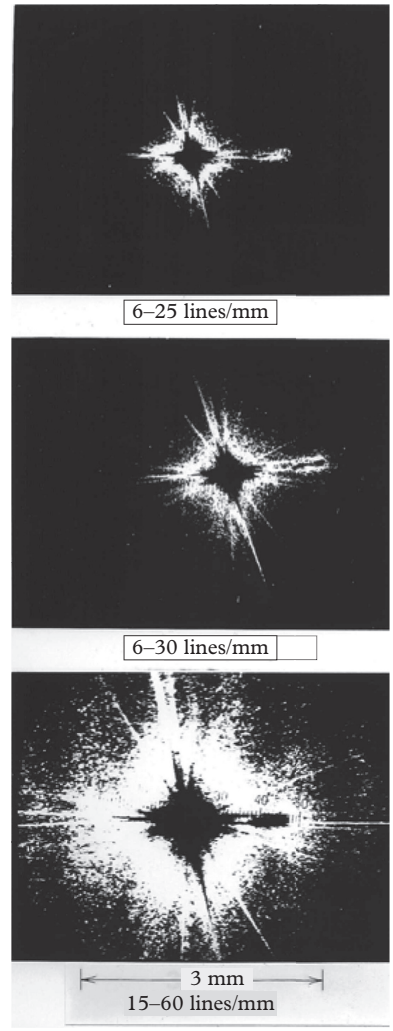

Figure 12B.4 *Three Fourier transform holograms at identical magnifications. The bright region in the three images is due to light diffracted by the holograms. The exposure time and the reference wave intensity were adjusted to produce band-limited Fourier transform holograms that would operate over different spatial frequency regions.*

The convolution will then be formed in the back focal plane of the lens, by the diffracted wave described by $\Psi_3(p)$.

The range of amplitudes in the Fourier transform of most signals exceeds the dynamic range of holographic recording media. For this reason, the hologram recorded in the configuration shown in Figure 12B.1 does not reproduce the entire Fourier transform of the reference object. Instead, a "band-limited" version of the Fourier transform is recorded; i.e., the recorded hologram only reproduces a limited number of spatial frequencies of the object. Very low spatial frequencies have a very large amplitude and overexpose the recording medium, while very high spatial frequencies have very small amplitudes and underexpose the recording medium. If we look at the light diffracted by a typical Fourier transform hologram, (Figure 12B.4), we find that only a limited range of spatial frequencies contribute to the diffracted light. Control of the exposure time and the reference wave amplitude can be used to select the spatial frequency bandwidth of the Fourier transform recorded in the hologram. This technique was used to generate the Fourier transform holograms of different bandwidths shown in Figure 12B.4.

If a Fourier transform hologram of limited bandwidth is reconstructed using a duplicate of the original reference wave, the original signal is not reproduced, but instead a rather fuzzy, edge-enhanced version of the original object is obtained (see Figure 12B.5). In Figure 12B.5, an automobile, labeled "Input," is used as the original object. The appearance of the object at the signal plane of Figure 12B.1 is labeled "Modulator output." A photograph of the Fourier transform hologram is labeled "Matched filter." When the matched filter is placed in the optical system of Figure 12B.1 and illuminated by only the reference wave, the image labeled "Filter reconstruction" is observed when a lens is used to collect the light propagating along the optical axis of lens L_1.

Anisotropy

13

13.1 Introduction

When a physical property of a material varies with direction, the material is said to be *anisotropic*. A non-optical example of an anisotropic property is the mechanical strength of wood. Along the grain direction, the strength of wood is much lower than it is across the grain. We have just treated materials with periodic variation in index of refraction. Now we will remove the requirement of periodicity and evaluate the propagation of light in optical anisotropic materials.

Optical anisotropic materials have an index of refraction that varies with the propagation direction in the material. These materials are said to be *birefringent*. When an object is viewed through a birefringent material, two images of the object are observed that move relative to one another as the birefringent material is rotated. The first recorded observation of this behavior was made in 1669 by **Erasmus Bartholinus (1625–1692)** with calcite, a naturally occurring mineral (calcite, the mineral $CaCO_3$, is called Iceland spar in older textbooks). Bartholinus believed that the observed behavior was a special case of refraction and therefore called the effect *double refraction*.[1]

Bartholinus' observation led Huygens, in 1690, to describe birefringence using his construction technique we discussed in Chapter 9. Huygens assumed that a point on the object produced two wavelets in the calcite: a spherical wave, called the *ordinary wave*, which obeyed Snell's law, and an ellipsoidal wave, called the *extraordinary wave*, which did not obey Snell's law. Huygens found that the light that passed through calcite could be extinguished by passing it through a second, properly oriented, calcite crystal, but he was unable to explain the origin of his observations.

Newton developed an explanation of the observations of birefringence based upon his particle theory of light. He believed that birefringence and rectilinear propagation were the important obstacles to the acceptance of a wave theory of light. One reason for Newton's failure to associate birefringence with wave behavior was the inability to envision a transverse, polarized wave. During Newton's time, all waves were assumed to be longitudinal.

In 1808, **Etienne Louis Malus (1775–1812)** accidentally observed, while watching a sunset reflected from the windows across the street from his apartment, that the two images of the sun produced by a piece of calcite would alternately dim and brighten as the calcite was rotated. He coined the word *polarization* for the observed property of light, relating the orientation of the preferred direction of the light to the Earth's poles. Malus defined the plane of polarization of the reflected light as the plane of incidence. This was an arbitrary definition made with no knowledge of electromagnetic theory; in fact, Malus' view of light was based upon Newton's particle theory. The definition of the plane of polarization used by Malus is orthogonal to the current definition of polarization in terms of the electric field. Many authors use the term *plane of vibration* for the plane containing the electric field to differentiate the modern definition from the one made by Malus.

13.1 Introduction 549
13.2 Dichroic Polarizers 551
13.3 Reflection Polarizers 554
13.4 Polarization by Birefringence 559
13.5 Optical Indicatrix 564
13.6 Fresnel's Equation 568
13.7 Retarder 572
13.8 Mueller Calculus 575
13.9 Jones Calculus 577
13.10 Optical Activity 578
13.11 Summary 585
13.12 Problems 586
References 588
Appendix 13A: Tensors 588
Appendix 13B: Poynting Vector in an Anisotropic Dielectric 592
Appendix 13C: Normal Surfaces 595
Appendix 13D: Ray Surfaces 599

[1] Refringence is an archaic synonym of refraction. The derivative, birefringence, remains the common descriptor for double refraction.

Modern Optics. Second Edition. B. D. Guenther.

© B. D. Guenther 2015. Published in 2015 by Oxford University Press.

The present concept of polarization had to await the suggestion by Young, in 1817, that light propagated as a transverse wave. Fresnel claimed to have made the association of light and transverse waves prior to Young, but even if he did not, he did construct a formal theory of the concept in 1824. The final step in understanding the polarization properties of light came with the introduction of Maxwell's theory.

We introduced the concept and description of polarized light in Chapter 2. Here, we wish to explore methods for the production and control of polarized light. There are materials, called *dichroic*, whose absorption constant varies with polarization. The anisotropic absorption properties can be used to detect the polarization of a wave or to produce a wave of a desired polarization. The use of the selective reflection of a single polarization at Brewster's angle can also be used to manipulate the polarization of waves.

Of most interest is the application of the observation of Malus that the two images produced by a birefringent material are orthogonally polarized. In fact, the prime objective in this presentation of polarization is to introduce birefringent materials and discuss their properties. We will find in later chapters that birefringence is useful not only for the manipulation of polarized light, but also in the design of optical modulators and in the use of nonlinear optics for harmonic generation.

The mathematics needed to describe birefringence relies on the use of tensors. Some of the properties of tensors and a geometrical construct used to aid in the interpretation of symmetric second-rank tensors are presented in Appendix 13A. The nonzero components of the tensors are determined by the symmetry of the birefringent crystals. The nonzero elements of second-order tensors are presented for each of the crystal symmetry classes in Appendix 13A.

The first encounter with a tensor is in relating the **E** and **D** fields in an anisotropic medium through the constitutive relationship. We discover that if the anisotropic material has no loss mechanism, then a second-order symmetric tensor, represented by a graphical construct in the shape of an ellipsoid, describes the relationship between **E** and **D**.

The need for a tensor relationship between **E** and **D** is because in an anisotropic material the two vectors are no longer parallel to one another. In fact, we will demonstrate in this chapter that the electric field is no longer perpendicular to the propagation vector **k**, and the Poynting vector is no longer parallel to the propagation vector. However, Maxwell's equations require that **D** and **k** be perpendicular to each other, and the definition of the Poynting vector requires that **E** and **S** be perpendicular to each other.

Because each of the two pairs of vectors, $\mathbf{E} \perp \mathbf{S}$ and $\mathbf{D} \perp \mathbf{k}$, are orthogonal, it is possible to formulate two descriptions of propagation in an anisotropic material. The descriptions are based on a coordinate system established by **D** and **k** or by **E** and **S**. We will use the former formulation in this chapter, but will provide a discussion of the latter in Appendix 13B. (The multiple descriptions of anisotropy, and the geometrical constructions associated with the descriptions, cause a great deal of confusion. To help avoid this, only one geometrical construction will be presented in this chapter. All other constructions are discussed in separate appendices.)

In this chapter, the ellipsoid called the optical indicatrix, describing **E** in terms of **D**, will be introduced and its use in determining **E**, **k**, and **S**, given **D**, will be demonstrated. The reciprocal formulation based on the tensor describing **D** in terms of **E** is presented in Appendix 13B.

Maxwell's equations are used to discuss the propagation of plane waves in an anisotropic material. The nonzero scalar product, $\mathbf{E} \cdot \mathbf{k} \neq 0$, leads to an equation called Fresnel's equation. The solution of this equation yields two indices of refraction for each possible propagation vector. The two indices are associated with two mutually orthogonal

displacement vectors **D**, each orthogonal to the propagation vector **k**. This association allows the construction of an optical component called a retarder. A retarder can be used to rotate the direction of linear polarization or to convert linearly polarized light into elliptically polarized light.

The operation of a polarizer or a retarder can be described using the Mueller or the Jones matrices. The matrices for the most common components are given and examples of their use are presented.

To complete the discussion of anisotropic materials, a description of optically active materials is presented. The effects of an optically active material on light are described by assigning different indices of refraction for right circularly and left circularly polarized light.

Two additional constructions are used in the discussion of wave propagation in an anisotropic material. They have been placed in the appendices to reduce the confusion these additional geometrical surfaces create. A construction based on the two indices of refraction associated with each propagation vector, called a *normal surface*, is discussed in Appendix 13C. (The Fermi surface used in the study of electron transport in solids is a normal surface for electron motion when electrons are treated as waves.)

A construction similar to the normal surface, called the *ray surface*, is discussed in Appendix 13D. It is constructed using the two ray velocities associated with each possible direction of the Poynting vector. The normal surface is of use if quantitative information about the propagation of a wave is desired, and the ray surface is of use in the application of Huygens' principal for a qualitative picture of light propagation.

13.2 Dichroic Polarizers

In a *dichroic polarizer*, one component of polarization is absorbed more than its transverse partner. Anisotropic absorption occurs in nature and can be engineered by man, both on the molecular and on the laboratory scale.

13.2.1 Crystals

When the optical absorption in a crystal depends upon the direction of propagation in the crystal and upon the state of polarization, the crystal is said to exhibit *dichroism*. The dichroic property is due to a complex index of refraction that depends upon crystallographic direction. The effect was first observed by **Jean Baptiste Biot (1774–1862)** in 1815. Examples of naturally occurring dichroic materials are tourmaline (Figure 13.1) and herapathite (iodosulfate of quinine) in the visible and pyrolytic graphite in the infrared. By present-day standards, dichroic materials make poor polarizers, but some dichroic crystals have been studied as possible optical storage materials and as laser hosts. These crystals also make interesting gemstones because the color of the crystals can vary with the viewing angle.

Figure 13.1 *This tourmaline gemstone is a good example of dichroic behavior. (Arpingstone (Adrian Pingstone)—Own work licensed under public domain via Wikimedia Commons.)*

The term *dichroic* also means two-color and is used to describe the change in color with concentration of dye solutions, to label a filter that transmits and reflects different colors, or to label a filter that transmits two colors. In mineralogy, the term *pleochroism*, meaning many colors, is used to describe crystals that absorb light differently in different crystallographic directions.

13.2.2 Wire Grids

We can construct a dichroic polarizer by stringing a set of wires as shown in Figure 13.2. Heinrich Hertz invented this type of polarizer in 1888 to study the properties of microwaves. Our first thought would be that Figure 13.2 is drawn improperly because the transmitted polarization is perpendicular to the openings between the wires. Our intuition is wrong: the grid attenuates $\mathbf{E}_v$ because $\mathbf{E}_v$ induces currents in the wires and the resistance of the wires dissipates the energy provided by the wave. The grid performs badly if the wires are thick ($\mathbf{E}_h$ is then attenuated), the spaces between the wires are large ($\mathbf{E}_v$ can leak through the grid), or the wires have a high resistivity.

The wire grid polarizer has been shown to operate over a large range of angles of incidence, from 0° to 45°, and over a large wavelength region. The long-wavelength limit of this polarizer is set by absorption in the supporting substrate, if any, and the short-wavelength limit is established by the grid spacing. The minimum operating wavelength of a wire grid polarizer is equal to twice the grid spacing.

13.2.3 Polaroid Sheet

"H-sheet" Polaroid is the most popular and familiar dichroic polarizer. This type of polarizer was invented in 1928 by **Edwin Herbert Land (1909–1991)** while he was a 19-year-old undergraduate student. Long-chain polymeric molecules that make up polyvinyl alcohol are aligned by stretching sheets of the plastic. After stretching, the polyvinyl plastic is cemented to a rigid base such as cellulose acetate to prevent relaxation to the original alignment. Iodine is then diffused into the polyvinyl alcohol layer, where the iodine atoms affix themselves along the polymer molecule. The electrons from the iodine are free to move along the polymer chain. A moment's thought reveals that the Polaroid film is a molecular analog of the wire grid. The first version of Polaroid film (called J-sheet) was a sheet of nitrocellulose with microscopic herapathite crystals imbedded in the plastic. The J-sheet was later replaced by the more achromatic H-sheet. A number of different grades of H-sheet were manufactured and are still available. There is also a K-sheet that has good temperature and humidity

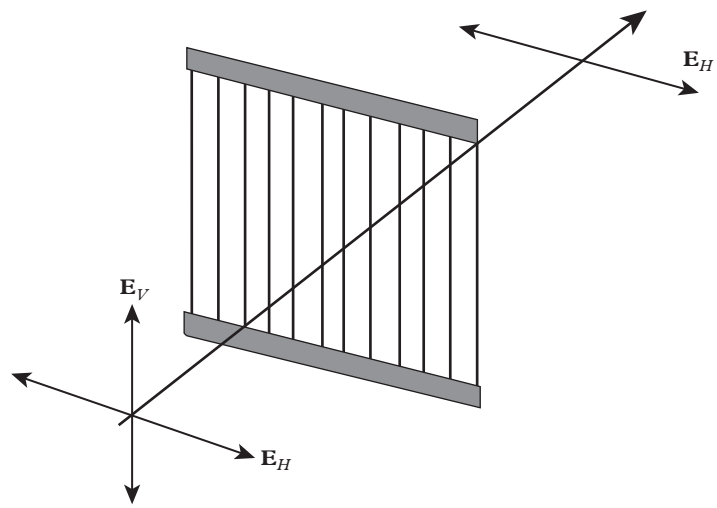

Figure 13.2 *Wire grid polarizer.*

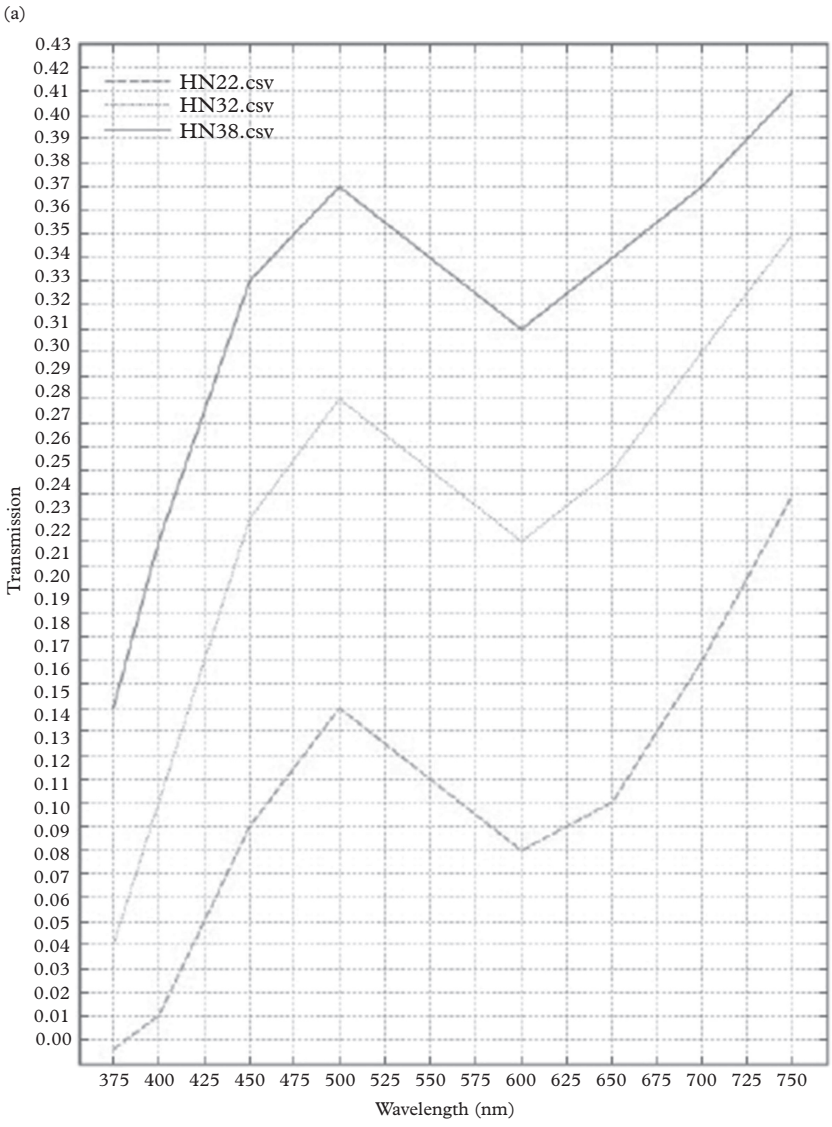

Figure 13.3 *(a) Transmission of light polarized parallel to the polarizer axis for different grades of H-sheet polarizer film. (b) Transmission of H-sheet film with the light's plane of polarization normal to the axis of the polarizer film.*

characteristics. The performances of three types of H-sheet as functions of wavelength are shown in Figure 13.3.

The quality of a polarizer is measured by the ratio of the maximum transmission of the polarizer to the minimum transmission, the *extinction ratio*, as shown in Figure 13.3. Examples of the extinction ratio for a few types of polarizers are listed in Table 13.1.

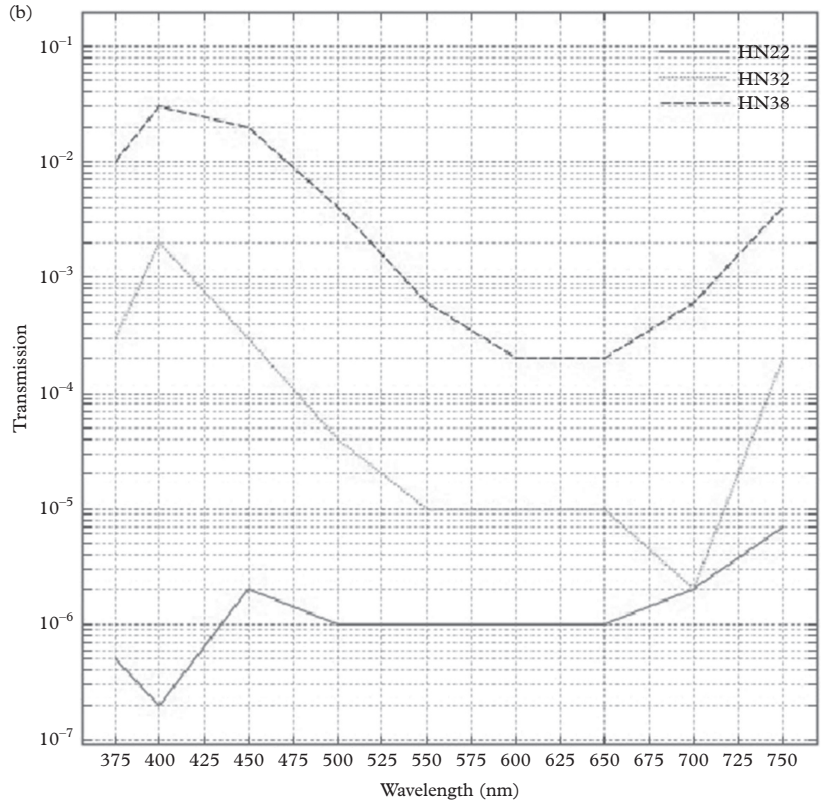

Figure 13.3 *(continued)*

Table 13.1 *Extinction ratios of polarizers*

Material	Extinction ratio
Polaroid	$10^{-3} - 10^{-5}$
Tourmaline	10^{-2}
Wire grid	$10^{-2} - 10^{-3}$
Calcite	10^{-7}
4-plate reflection:	
$n = 2.46$	10^{-2}
$n = 4.0$	10^{-4}

13.3 Reflection Polarizers

The Fresnel equations describing the reflection of light from an interface (see Chapter 3) depend upon the polarization of the incident light. Polarizers can be designed using this polarization-dependent reflectivity.

13.3.1 Brewster's Angle Polarizers

During our discussion of the Fresnel equations for reflection (Chapter 3), we found that at the Brewster's angle, the reflected wave is polarized perpendicular to the plane of incidence. A device based upon the polarization of a wave reflected from a stack of dielectric plates was invented by Arago in 1812. The polarization of light by a stack of thin glass plates is shown in Figure 13.4.

Polarizers that use reflected light have two drawbacks. The light beam is deviated through a large angle, and the polarizer becomes quite long when other reflectors are added to redirect the deviated beam. To overcome the drawbacks of the reflective device, a transmissive Brewster's angle polarizer is used. The transmitted beam is partially polarized by virtue of the fact that some of the light polarized perpendicular to the plane of incidence has been removed through reflection. This is indicated schematically in Figure 13.4(a). By assembling a stack of glass plates and transmitting light through the stack, the degree of polarization of the transmitted beam can be increased.

To demonstration polarization by a stack of glass plates, the experimental arrangement shown in Figure 13.4(b) was assembled. The word "TRANSMISSION" is positioned behind a stack of very thin glass plates (microscope cover slips) and the word "REFLECTION" is placed in the foreground of the stack. In this configuration, we see a mirror image of "REFLECTION" from the front surfaces of the glass plates and "TRANSMISSION" through the stack of plates. A photograph of the actual experiment is shown in Figure 13.4(c). The two images can be seen, but there is no indication of the polarization properties of the two images. A rectangular shaped H-sheet Polaroid polarizer with its axis of polarization oriented along its long dimension is placed in the foreground in Figure 13.4(d) and (e). In Figure 13.4(d), the polarizer has its axis oriented normal to the plane of incidence. The word "TRANSMISSION"cannot be seen, but "REFLECTION"is visible. In Figure 13.4(e), the polarizer is oriented with its axis in the plane of incidence. Here, "TRANSMISSION" can be seen through the plates, but no reflection of "REFLECTION" can be seen.

Any nonmetallic, smooth object can act as a Brewster's angle polarizer, but carefully designed reflection polarizers (see Figure 13.5) tend to be bulky and expensive. The fraction of polarized light produced is often too low, and there is too much leakage of the unwanted polarization. The utilization of the reflection polarizer, with the exception of lasers, is limited to the infrared and ultraviolet, where it is often the only option.

The polarized output of lasers is a result of surfaces oriented at Brewster's angle in the laser cavity to reduce reflective loss due to the surfaces. The polarization that is not reflected, because of Brewster's law, has very low loss and thus is preferentially amplified by the gain medium in the laser.

13.3.2 Interference Polarizers

If a transmission polarizer is needed over a limited wavelength range, then it can be constructed using multilayer dielectric coatings. The approach makes use of the theory of multilayer reflector design introduced in Appendix 4A. Here, we will examine the design philosophy using a single dielectric layer, as displayed in Figure 13.6(a).

The reflection coefficients, for the electric field parallel to the plane of incidence, from the two interfaces are equated and the thickness of the dielectric layer is adjusted to ensure destructive interference between the waves reflected from the two interfaces. The result of this design procedure is a dielectric mirror that reflects only the normal component of polarization.

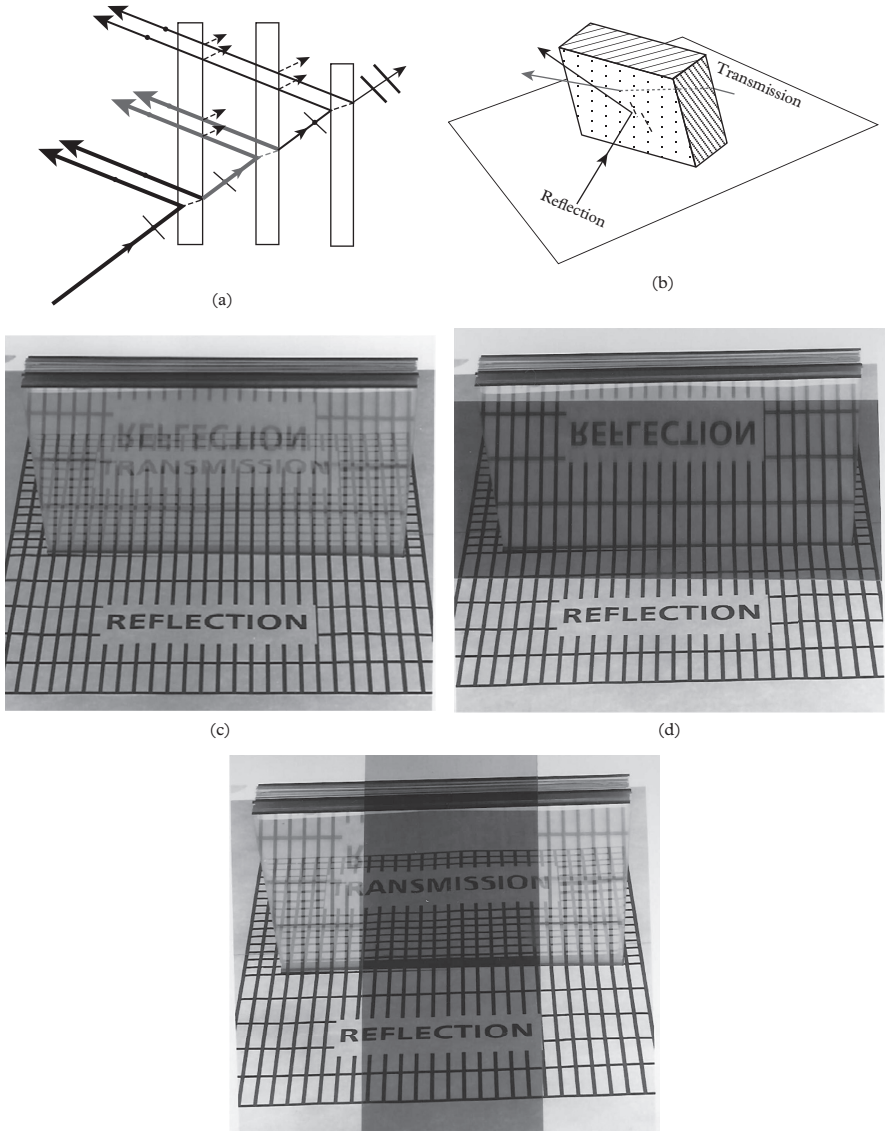

Figure 13.4 *Polarization of light by a stack of glass plates. (a) Schematic display of the operation of a stack of glass plates that use Brewster's angle to polarize light. To demonstrate polarization by a stack of glass plates, the experimental arrangement shown in (b) was assembled. The word "TRANSMISSION" is positioned behind a stack of very thin glass plates and the word "REFLECTION" is placed in the foreground of the stack. In this configuration, we see a mirror image of "REFLECTION" from the front surfaces of the glass plates and "TRANSMISSION" through the stack of plates. A photograph of the actual experiment is shown in (c). The two images can be seen, but because the light is unpolarized, there is no indication of the polarization properties of the two images. An H-sheet Polaroid polarizer with its axis of polarization oriented along its long dimension is placed in the foreground in (d) and (e). In (d,) the polarizer has its axis oriented normal to the plane of incidence. The word "TRANSMISSION"cannot be seen, but "REFLECTION" is visible. In (e), the polarizer is oriented with its axis in the plane of incidence. Here, "TRANSMISSION" can be seen through the plates, but no reflection of "REFLECTION" can be seen.*

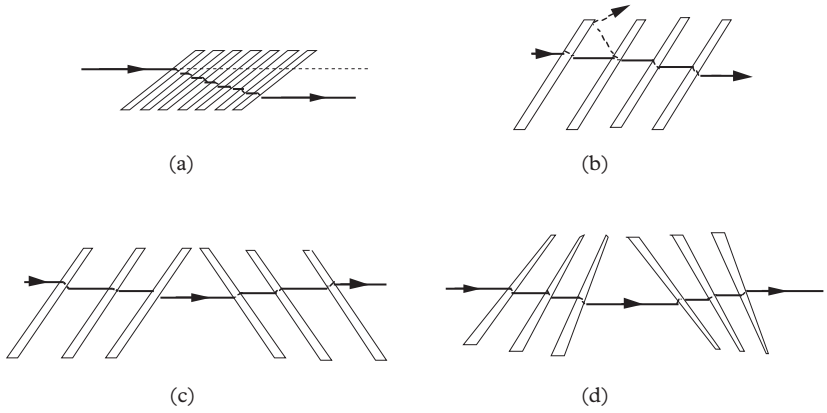

Figure 13.5 *In Figure 13.4, we implied that a reflection polarizer would look much like (a). However, a number of modifications must be made if the polarizer is to function properly. (b) A design that allows the escape of unwanted reflected light by increasing the spacing of the plates. (c) A design to keep the transmitted light on the optical axis. (d) A carefully designed polarizer with wedged plates so that multiple reflections can be removed with apertures and the transmitted beam remains on the optical axis.*

The reflectivity of the dielectric layer in Figure 13.6(a) can be calculated using (4.40):

$$R = 1 - T = \frac{r_1^2 + r_2^2 + 2r_1 r_2 \cos 2\delta}{1 + r_1^2 r_2^2 + 2r_1 r_2 \cos 2\delta},$$

where we have replaced the single reflection coefficient of (4.40) with the two reflection coefficients needed in Figure 13.6(a), i.e., $r^2 = r_1 r_2$. Following the prescription just outlined, the phase from (4.34) is set equal to an odd multiple of π:

$$\delta = (2m + 1)\pi = \frac{4\pi n_1 d \cos\theta_{t1}}{\lambda},$$

establishing the required film thickness as

$$d = \frac{(2m + 1)\lambda}{4n_1 \cos\theta_{t1}}.$$

The reflection coefficients for the parallel polarization components from the two interfaces are set equal to each other:

$$\frac{\tan(\theta_i - \theta_{t1})}{\tan(\theta_i + \theta_{t1})} = \frac{\tan(\theta_{t1} - \theta_{t2})}{\tan(\theta_{t1} + \theta_{t2})}.$$

This equality ensures complete cancellation of the parallel component of polarization. After applying these design rules, the reflectivity of the normal component of polarization from the dielectric layer is

$$R = \frac{(n_1^2 - 1)\sin^2\theta_i - \cos\theta_i \sqrt{n_2^2 - \sin^2\theta_i}}{(n_1^2 - 1)\sin^2\theta_i + \cos\theta_i \sqrt{n_2^2 - \sin^2\theta_i}}.$$

Interference polarizers are used in laser systems when the incident radiation will strike the dielectric layer at an angle. The polarizing beamsplitter is a popular example of this design; see Figure 13.6(b). The radiation is incident on the dielectric layer at an angle of 45°. The wave transmitted by the layer is polarized with its electric vector in the plane of incidence, while the reflected wave has its electric vector normal to the plane of incidence.

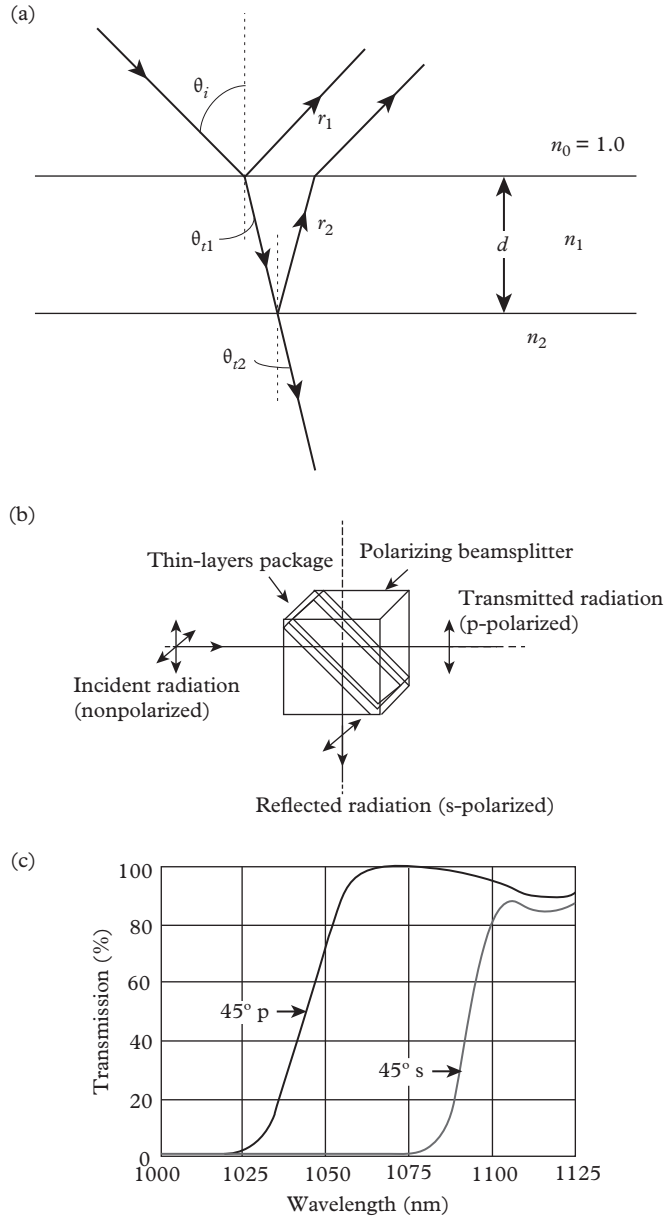

Figure 13.6 *(a) Use of interference from a dielectric layer to produce a reflective polarizer. If we design the polarizer to work at 45°, the reflected and transmitted beams are separated by 90° and orthogonally polarized, just like a cube beamsplitter, (b). (c) Wavelength sensitivity of a thin film polarizer.*

13.4 Polarization by Birefringence

In crystals with cubic symmetry, the propagation properties of light are isotropic, there is a single index of refraction, and the crystal behaves optically like a noncrystalline material such as glass (at least to first order). All other classes of crystals are optically anisotropic. The index of refraction (and naturally the dielectric constant) depends on the direction of propagation of the light, relative to the crystal axes. We must use tensor calculus (see Appendix 13A) to discuss propagation of light in these materials. In general, to analyze the propagation of light in an anisotropic medium, the wave is divided into two waves with orthogonal polarizations (the polarization direction in the medium will be denoted by the direction of the displacement **D**). The two waves, with orthogonal polarizations $\mathbf{D}_1$ and $\mathbf{D}_2$, will not have the same propagation vector and will exhibit double refraction. There are, however, special directions in an anisotropic crystal for which both polarizations have the same propagation velocity. These special directions are called *optical axes*, and their mathematical definition will be given at the end of Section 13.5. If there is only one direction for which the two orthogonal polarizations have the same propagation velocity, the crystal is called *uniaxial*. If two such directions exist, the crystal is called *biaxial*. Examples of uniaxial and biaxial crystals are listed in Tables 13.2 and 13.3, respectively.

The physical origins of birefringence can be understood by modifying the classical model of dispersion introduced in Chapter 7. The single spring constant used in the model (7.24) can be replaced by three spring constants—one for each of the coordinate directions. Application of the procedure used in Chapter 7 to this modified model leads to three indices of refraction for the material, i.e., a biaxial crystal (Table 13.3). If the spring constants are equal in two coordinate directions, then the model predicts two indices of refraction, i.e., a uniaxial crystal (Table 13.2). If a different damping term for each coordinate direction is included in the model (7.26), then the result is a complex index of refraction that has directional dependence. This model would describe pleochroism (Figure 13.1).

To help understand the physical origin of the different coupling constants, consider the unit cell of the uniaxial crystal calcite, shown in Figure 13.7. A crystal of calcite is made up of

Table 13.2 *Uniaxial crystals*

Mineral	Index of refraction (Na-D)	
	n_o	n_e
Ice (H_2O)	1.309	1.313
Sellaite (MgF_2)	1.378	1.390
Quartz	1.54424	1.55335
Wurtzite (ZnS)	2.356	2.378
Rutile (TiO_2)	2.616	2.903
Cinnabar (HgS)	2.854	3.201
Calcite ($CaCO_3$)	1.658	1.486
Tourmaline	1.669	1.638
Sapphire	1.7681	1.7599

Table 13.3 *Biaxial crystals*

Mineral	Index of refraction		
	n_α	n_β	n_γ
Tridymite	1.469	1.47	1.473
Mica (muscovite)	1.5601	1.5936	1.5977
Turquoise	1.61	1.62	1.65
Topaz	1.619	1.62	1.627
Sulfur	1.95	2.043	2.240
Borax	1.447	1.47	1.472
Lanthanite	1.52	1.587	1.613
Stibnite (Sb_2S_3)	3.194	4.303	4.46

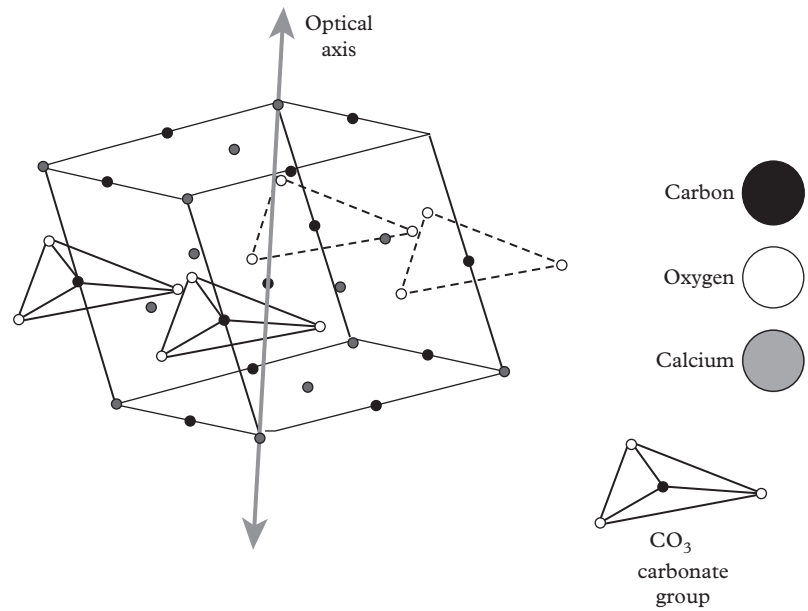

Figure 13.7 *The unit cell of calcite. Only four of the carbonate groups that make up the unit cell are shown in their entirety; the other groups are represented by the carbon atoms at their centers.*

a three-dimensional array of these unit cells. Each carbon atom in the crystal lies at the center of an imaginary equilateral triangle with oxygen atoms at each corner. The direction normal to the planes containing these triangles is the optical axis of calcite. From the arrangement of atoms, it seems reasonable to assume that the binding energy in the planes containing the oxygen atoms is different from the binding energy normal to these planes. When light is incident on a crystal of calcite parallel to the optical axis, shown in Figure 13.7, the electric displacement of the light wave lies in the same plane as the oxygen atoms. The electric

polarization induced by the electric field is the same for all polarization directions in this case, and the resulting index of diffraction would be independent of polarization direction.

When a light wave is incident on the calcite crystal normal to the optical axis, the electric polarization induced by the light wave's electric field, in the plane of the oxygen atoms, is different from the polarization induced by the electric field normal to that plane, resulting in two indices of refraction.

A light wave propagating in an arbitrary direction through this crystal can be decomposed into two waves, with orthogonal polarizations, propagating at different velocities. Any wave whose electric displacement lies in the plane of the oxygen atoms, and thus perpendicular to the optical axis, obeys Snell's law. For this polarization orientation, the propagation velocity is isotropic and the wave is called an *ordinary wave*. Any other wave, with its electric displacement at an angle to the plane containing the oxygen atoms, has an anisotropic propagation velocity and does not obey Snell's law. This wave is called an *extraordinary wave* (see Figure 13.9).

The electrons can move quite easily in the planes containing the oxygen atoms, so the spring constant for these atoms is small relative to the direction normal to the planes. In the direction normal to the oxygen planes, the electrons experience strong binding forces. For this reason, the propagation velocity in the direction of the optical axis, the ordinary wave's velocity, is less than the propagation velocity normal to that direction. The index of refraction associated with the ordinary wave is thus greater than the index associated with the extraordinary wave, $n_o > n_e$. Crystals with this property are called *negative* uniaxial crystals ($n_e - n_o < 0$). The polarization direction for the ordinary wave of a negative uniaxial crystal is called the *slow axis*. The polarization direction (the direction of **D**) for the wave that has the higher propagation velocity is called the *fast axis*. For the opposite case ($n_e - n_o > 0$), we have a *positive* uniaxial crystal. For this class, the fast axis is the direction of the ordinary wave.

In general, when an unpolarized beam of light is incident normal to the surface of a plane parallel plate of a uniaxial crystal, there will be two beams emerge from the back side of the crystal as is shown in Figure 13.8. The ordinary wave, labeled *O* in Figure 13.8, is polarized with its displacement vector **D** normal to the plane containing the optical axis. The extraordinary wave, labeled *E* in Figure 13.8, is polarized with its displacement vector in the plane containing the optical axis. The two waves indicated in Figure 13.8(a) produce two images with perpendicular polarizations as shown in Figure 13.8(b). One class of polarizers are designed to utilize the spatial separation of the two beams shown in Figure 13.8 to select a desired polarization direction.

Polarizers are constructed using a uniaxial material. The simplest design utilizes the naturally occurring birefringent crystal calcite and a set of "stops" to remove either of the two beams (see Figure 13.9). Because the separation of the two waves is small (only 6.2° in calcite), this technique can only be used with very narrow beams.

The Wollaston and Rochon polarizers increase the separation of the two beams over that obtainable with a single crystal by using two single crystals, usually quartz, cut and polished into two prisms (see Figure 13.10). The Rochon polarizer has an entrance prism with its optical axis oriented perpendicular to the incident face of the polarizer, in the plane of Figure 13.10, and a second, exit, prism, glued to the first with its optical axis perpendicular to the first prism's axis, perpendicular to the plane of Figure 13.10. The light wave whose polarization is perpendicular to the second prism's axis, and in the plane of Figure 13.10, sees no index discontinuity at the interface between the two prisms because the wave also has its polarization perpendicular to the optical axis of the first prism. For this reason, the ordinary wave is not deviated by the Rochon polarizer. The extraordinary wave of the second prism, with its polarization parallel to the optical axis, however, is an ordinary wave in the first prism. It sees a discontinuous change in the index of $n_e - n_o$ as it crosses the

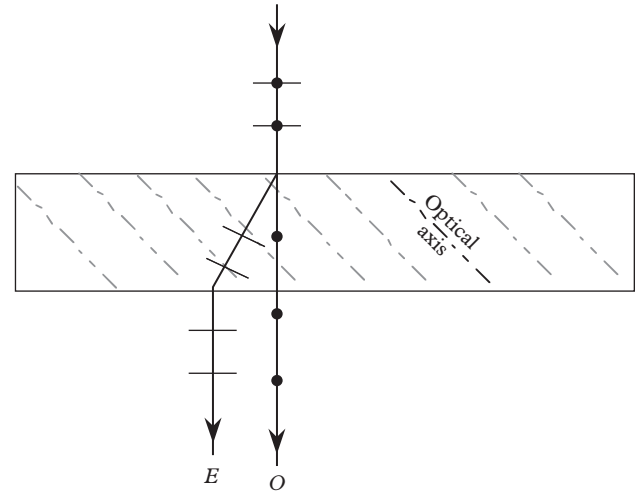

(a)

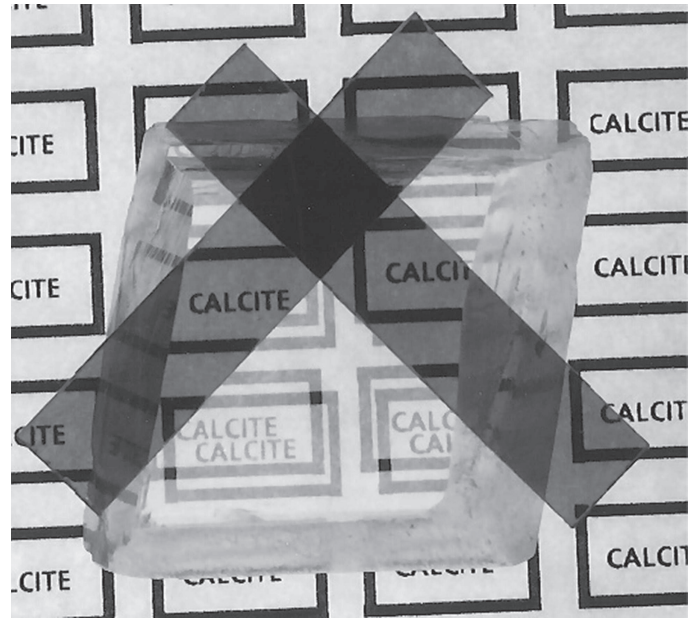

(b)

Figure 13.8 *(a) Uniaxial crystal showing the failure of the extraordinary wave to obey Snell's law. The lines in the crystal indicate the direction called the optical axis. (b) The birefringence shown in (a) results in a double image. The polarizations of the two images are orthogonal. The two polarizers at 90° have their polarization axis along the long dimension of the sheet.*

boundary between the two prisms. The prism angle θ and the difference between the extraordinary and ordinary indices determine the angle φ between the E and O beams. The Wollaston polarizer produces twice the deviation as the Rochon polarizer by causing both the ordinary and extraordinary waves to see the same discontinuous change in the index. This occurs because the extraordinary and ordinary waves interchange roles in the two

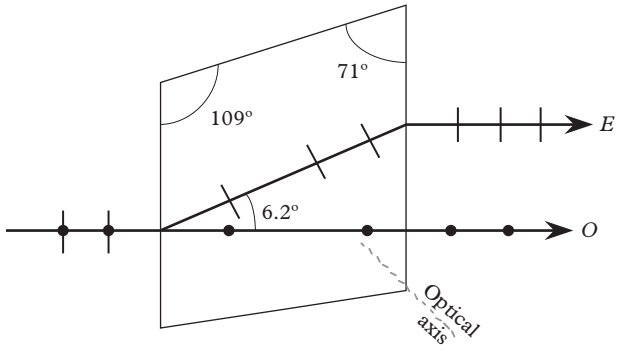

Figure 13.9 *Separation of the extraordinary (upper beam) and ordinary (lower beam) waves in calcite. The dotted line labeled "Optical axis" indicates the direction of the optical axis. The rhombohedron shown is the naturally occurring form of a single crystal of calcite.*

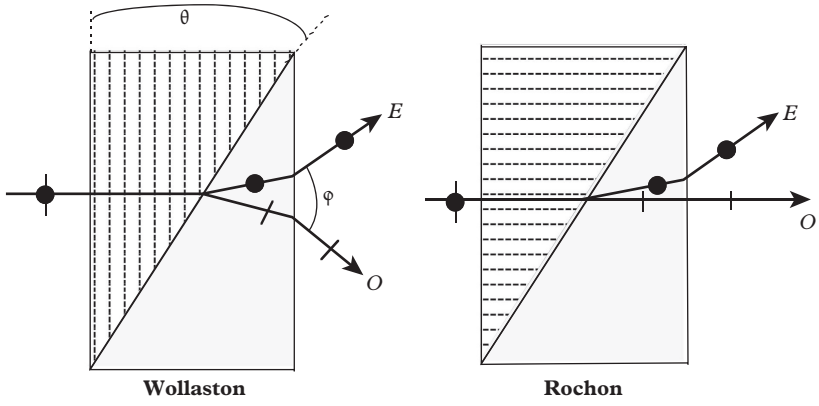

Figure 13.10 *Two polarizers designed to increase the separation of the extraordinary and ordinary waves. The entrance prism on both polarizers has its ordinary wave polarized out of the paper. The second prism has its ordinary wave polarized in the plane of the paper. The lines and dots used to shade the two prisms indicate the direction of the optical axis.*

prisms. The advantage of the Rochon prism is that it keeps the ordinary wave on the optical axis.

Another method of separating the two orthogonal polarizations in a birefringent crystal is the use of total internal reflection to deflect one beam toward an absorber, (see Figure 13.11). The Nicol prism, named after **William Nicol (1768–1857)**, was the first of this type of polarizer. A calcite crystal is cut into two prisms and polished to obtain the angles shown in Figure 13.11. The two prisms are then glued together with cement called Canada balsam (the resin of the balsam fir tree, with an index of 1.55). The cement used to assemble the two prisms is selected so that the ordinary wave experiences total internal reflection at the glue joint but the extraordinary wave passes through the polarizer. (Just as is the case with an optical fiber, which depends upon total internal reflection, the Nicol polarizer will operate only with rays arriving within a cone whose angle, called the acceptance angle, is 24°. The acceptance angle of this type of polarizer is determined by the difference between the critical angle of the ordinary and extraordinary rays.) The cement restricts the wavelength range of the polarizer, so designs were developed that eliminated the cement.

The Glan–Foucault is a more modern polarizer design (see Figure 13.12), based on the same principal as the Nicol. Its advantages are that it replaces glue with air at the interface of total internal reflection, and the incident and exit faces are perpendicular to the light wave. The acceptance angle of this polarizer is only 7°, but it will operate from 0.23 to 5.0 μm.

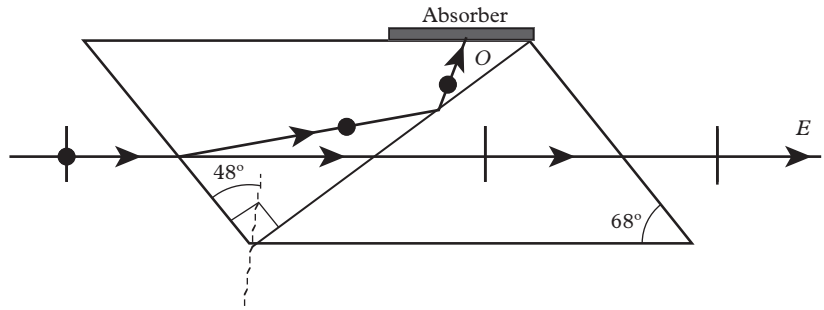

Figure 13.11 *The geometry of a Nicol prism polarizer. The direction of the optical axis is indicated by the dotted line.*

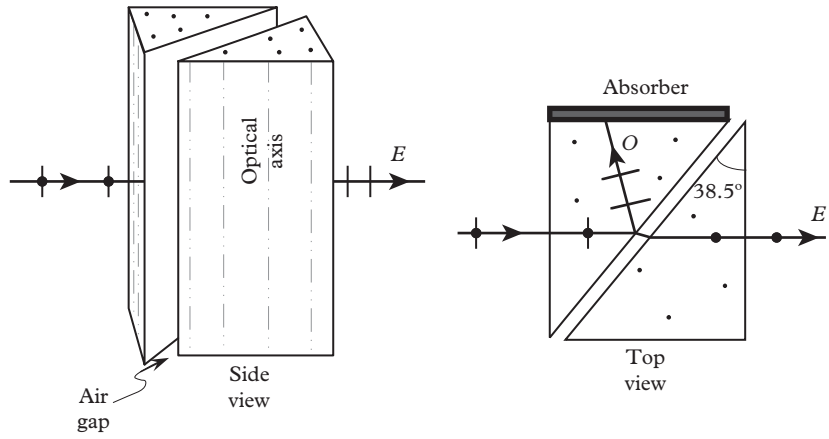

Figure 13.12 *Two views of the Glan–Foucault polarizer showing its operation. The parallel lines indicate the direction of the optical axis.*

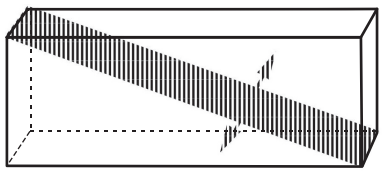

Figure 13.13 *A Feussner polarizer [1]. The optical axis of the birefringent material is normal to the slab of material, as shown by the arrows.*

The Glan–Taylor prism, a popular design, has the advantage over the Glan–Foucault because the angle of incidence at the gap is reasonably close to Brewster's angle, giving it better transmission. If the two prisms of the Glan–Foucault polarizer are cemented together, the name is changed to Glan–Thompson polarizer. This design modification increases the field of view to 30°, but it cannot be used in the ultraviolet.

One of the problems in constructing polarizers using birefringent material is finding or growing a birefringent crystal of a size and optical quality to be useful. One polarizer design uses isotropic prisms with a thin plate of birefringent material sandwiched between them (see Figure 13.13). The two prisms are made of a glass with an index equal to the higher index of the birefringent material. If the birefringent material is calcite, then the ordinary ray is transmitted. The optical axis can be oriented normal to the slab (Feussner polarizer [1]) or parallel to the entrance face (Bertrand type).[2]

13.5 Optical Indicatrix

In the previous discussions about light waves, we assumed that the medium through which the light propagated was homogeneous and isotropic. In those cases, we could relate the electromagnetic field vectors **E** and **B** to the electric displacement **D** and the magnetic vector **H** through the scalar quantities ε (dielectric constant) and μ (magnetic permeability).

[2] Polarizers in optics are like beakers in chemistry—even a slight modification of a design results in a new device bearing the designer's name.

We will continue to assume that the material is isotropic with regard to the magnetic field, so that μ remains a scalar, but we will now assume that the dielectric properties can vary with direction. The impact of discarding the assumption of isotropic electrical properties is the need to use tensor relationships between **E** and **D**, because the electric field **E** will in general not be parallel to **D**.

The complexity of the tensor can be reduced if there are no losses in the medium. We will show that this assumption also allows the use of a geometrical construction to aid in understanding the properties of the anisotropic medium. This geometrical construction, called the optical indicatrix, demonstrates the origin of two propagation velocities in the anisotropic material and can be used to determine **E**, **k**, and **S** from the specification of **D**.

The simple relationship between **D** and **E** that we have used up to now must be replaced by the more general equations

$$\begin{aligned} D_x &= \varepsilon_{xx}E_x + \varepsilon_{xy}E_y + \varepsilon_{xz}E_z, \\ D_y &= \varepsilon_{yx}E_x + \varepsilon_{yy}E_y + \varepsilon_{yz}E_z, \\ D_z &= \varepsilon_{zx}E_x + \varepsilon_{zy}E_y + \varepsilon_{zz}E_z, \end{aligned} \tag{13.1a}$$

or, in more compact notation,

$$D_i = \sum_{j=1}^{3} \varepsilon_{ij}E_j. \tag{13.1b}$$

In many books, the Einstein summation convention is used when writing tensor equations such as (13.1). According to this convention, repeated indices are summed over and the summation symbol is suppressed, so that, for example, (13.1b) is written as

$$D_i = \varepsilon_{ij}E_j.$$

We will not use this notation.

The ε_{ij} are the components of a tensor of second rank. In general, there would be nine such components, but energy considerations reduce the number of independent elements in the dielectric tensor to six or less. To prove this statement, we must make several assumptions:

1. The energy of the electromagnetic field that we used in Chapter 2 for an isotropic medium, (2.21), is valid for an anisotropic medium.
2. The energy flux (Poynting vector) that we used in Chapter 2 for an isotropic medium, (2.22), is valid for an anisotropic medium.
3. There is no energy loss in the medium.

The Poynting vector (2.22) is used to obtain the unit energy flow into a unit volume:

$$\nabla \cdot \mathbf{S} = \nabla \cdot (\mathbf{E} \times \mathbf{H}). \tag{13.2}$$

We use the identity (2A.13) to rewrite (13.2) as

$$\begin{aligned}\nabla \cdot \mathbf{S} &= \mathbf{E} \cdot \left(\frac{\partial \mathbf{D}}{\partial t}\right) + \mathbf{H} \cdot \left(\frac{\partial \mathbf{H}}{\partial t}\right) \\ &= \left(\sum_{k=1}^{3}\sum_{j=1}^{3} E_k \varepsilon_{kj} \frac{\partial E_j}{\partial t}\right) + \mathbf{H} \cdot \frac{\partial \mathbf{H}}{\partial t},\end{aligned} \tag{13.3}$$

where we assume that the components of the dielectric tensor are independent of time.

We are only interested in the electric energy flux, which is the first term of (13.3). The steady-state value of the electric energy flux is obtained by applying (2.26), to give

$$\langle \nabla \cdot \mathbf{S} \rangle_E = \frac{1}{2}\left(\sum_{j=1}^{3} E_j \sum_{k=1}^{3} \varepsilon_{jk}^* \frac{\partial E_k^*}{\partial t} + \sum_{j=1}^{3} E_j^* \sum_{k=1}^{3} \varepsilon_{jk} \frac{\partial E_k}{\partial t}\right). \tag{13.4}$$

Using (2.14), we can rewrite (13.4) as

$$\langle \nabla \cdot \mathbf{S} \rangle_E = \frac{i\omega}{2} \sum_{j=1}^{3} E_j \sum_{k=1}^{3} E_k^* \left(\varepsilon_{kj} - \varepsilon_{jk}^*\right). \tag{13.5}$$

We now use the third assumption, that the medium is a lossless one, which means that (13.5) will be equal to zero; i.e., there is no change in energy flow through the medium. This results in the requirement that $\varepsilon_{jk}^* = \varepsilon_{kj}$. Thus, the dielectric tensor ε must be Hermitian (as a reminder, this means that the element in the ith row and jth column is equal to the complex conjugate of the element in the jth row and ith column for all indices i and j).

We will treat the dielectric tensor as real, resulting in the requirement that the tensor ε_{ij} must be symmetric (a matrix that has only real entries is Hermitian if and only if it is a symmetric matrix.) The assumption of a lossless medium reduces the maximum number of tensor components that must be considered to six. A further reduction in the number of components, to three, can be made by a proper choice of the coordinate system. In the properly oriented coordinate system (with coordinate axes parallel to the *principal dielectric axes*), the nonzero tensor components are called the *principal dielectric constants*. As discussed in Appendix 13A, by assuming a lossless medium, we can use a geometrical surface to aid in understanding the properties of the tensor. The geometrical surface used to represent a second-order symmetric dielectric tensor is called the *optical indicatrix*.

Starting with the equation for the electric energy density, (2.21),

$$2U_E = \mathbf{D} \cdot \mathbf{E},$$

we select as the coordinate system the principal dielectric axes, allowing us write

$$D_x = \varepsilon_x E_x, \quad D_y = \varepsilon_y E_y, \quad D_z = \varepsilon_z E_z.$$

In this coordinate system, we may rewrite the energy density equation as

$$\frac{D_x^2}{2U_E\varepsilon_x} + \frac{D_y^2}{2U_E\varepsilon_y} + \frac{D_z^2}{2U_E\varepsilon_z} = 1. \tag{13.6}$$

This is the equation of an ellipsoid, (13A.5), whose semi-axes are equal to the square roots of the principal dielectric constants, or, equivalently, the principal indices of refraction. This ellipsoid (see Figure 13A.1) is called the optical indicatrix.

The study of anisotropy is confusing because different names are used to indicate the optical indicatrix. Some of these are listed in Table 13.4. A second confusing aspect is that the optical indicatrix is not the only surface used in the description of optical anisotropy. The first step in reading the optical anisotropy literature is to determine what surface the author is discussing. Other surfaces used in the discussion of optical anisotropy are introduced in the appendices.

Table 13.4 *Names for the optical indicatrix*

Index ellipsoid
Optical indicatrix
Reciprocal ellipsoid
Poinsot ellipsoid
Ellipsoid of wave normals

The ellipsoid defined by (13.6) is not a representative of the dielectric tensor but of its reciprocal, called the *impermeability tensor* $\ni_{ij}$ and defined by the relation

$$E_i = \sum_{j=1}^{3} \ni_{ij} D_j.$$

The dielectric tensor is discussed in Appendix 13B; see (13B.4).

The optical indicatrix can be used to determine **E**, **k**, and **S**, given **D**. The geometrical construction shown in Figure 13.14 will demonstrate the method used to determine these parameters. Assume that **D** is known and represented by the vector from O to P, where P is a point on the ellipsoid in Figure 13.14. Construct first a surface, tangent to the ellipsoid at P, with a normal $\hat{\mathbf{n}}$; then construct the line OQ to be parallel to the surface normal $\hat{\mathbf{n}}$ at P. The point Q is in the plane tangent to P (see Figure 13.14). The magnitude of **E** is given by $1/OQ$, where $\overline{OQ}$ is the distance from the origin to the plane tangent to P. The direction of **E** is parallel to $\hat{\mathbf{n}}$, and the direction of the Poynting vector **S** is parallel to the line $\overline{PQ}$ in Figure 13.14.

If the propagation vector **k** of a wave is known, we can determine **D** and **E**. This is accomplished by constructing a plane through the origin, normal to **k** (see Figure 13.15). The curve formed by the intersection of the ellipsoid and the plane perpendicular to **k** is an ellipse. The principal semi-axes of the ellipse are proportional to the indices of refraction n_1 and n_2 (or, equivalently, to the reciprocals of the phase velocities):

$$n_1 = \frac{c}{v_{p1}}, \quad n_2 = \frac{c}{v_{p2}}.$$

The directions of the principal semi-axes coincide with $\mathbf{D}_1$ and $\mathbf{D}_2$, which are the two orthogonal polarizations for the wave, with wavevector **k**.

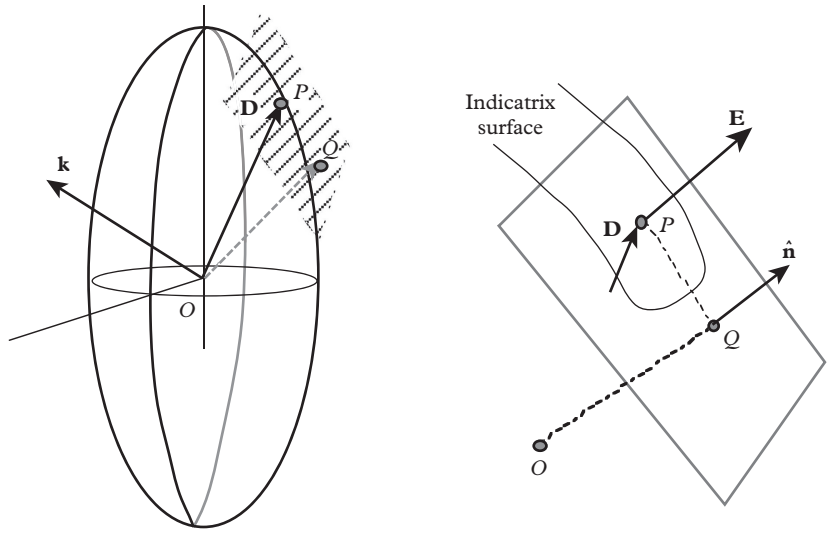

Figure 13.14 *Use of the optical indicatrix to find the electric field given* **D**.

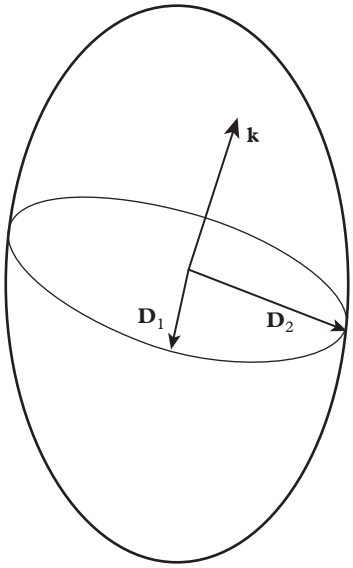

Figure 13.15 *Determination of* **D** *given the propagation vector* **k**.

For certain directions of **k**, the plane normal to **k** will cut the ellipsoid to form an intersecting curve that is a circle. These special directions mathematically define the *optical axes* (of the wave normals) of the crystal introduced at the beginning of Section 13.4. If there is only one such direction, the crystal is uniaxial. The maximum number of directions that can be found is two. Crystals with two optical axes are biaxial.

13.6 Fresnel's Equation

In this section, we will examine the propagation of a plane wave in an electrically anisotropic medium; we continue to assume that all of the media under consideration are magnetically isotopic, so $\mathbf{B} = \mu_0\mathbf{H}$. The analysis will parallel the one in Chapter 2 for an isotropic medium. We will discover that **D** remains perpendicular to **k** but that **E** no longer is perpendicular to **k**. The nonzero scalar product between **E** and **k** produces an equation, called Fresnel's equation, that predicts that the medium will have two indices of refraction associated with two electric displacement vectors. We conclude the section by proving that the two displacement vectors are mutually orthogonal.

We will proceed as we did in Chapter 12, making the assumption that the medium is nonconducting and that there are no currents or charges present. If we allowed a conductive medium, the analysis would also apply to dichroic materials. We will not treat ε as periodic as we did in Chapter 12, but instead allow it to be a general function of space. Substituting plane waves into Maxwell's equations

$$\nabla \cdot \mathbf{B} = 0, \qquad \nabla \cdot \mathbf{D} = 0,$$

$$\nabla \times \mathbf{H} = \frac{\partial \mathbf{D}}{\partial t}, \quad \nabla \times \mathbf{E} = -\frac{\partial \mathbf{B}}{\partial t} \tag{13.7}$$

yields the following information.

13.6.1 Transverse Waves

Substituting the plane wave solutions into the first pair of Maxwell's equations, $\nabla \cdot \mathbf{B} = 0$ and $\nabla \cdot \mathbf{D} = 0$, yields, for the electric field,

$$\nabla \cdot \mathbf{D} = -i\mathbf{k} \cdot \mathbf{D} = 0.$$

D remains perpendicular to **k**, but this no longer implies that **E** is perpendicular to **k**. For the magnetic field,

$$\nabla \cdot \mathbf{B} = \mu \nabla \cdot \mathbf{H} = -i\mathbf{k} \cdot \mathbf{H} = 0.$$

Since we continue to assume that the material is magnetically isotropic, we still find that both **B** and **H** are perpendicular to **k**.

13.6.2 Interdependence of D and H

Continuing to examine Maxwell's equations, we substitute the plane wave equations into the second pair of equations, $\nabla \times \mathbf{H} = \partial \mathbf{D}/\partial t$ and $\nabla \times \mathbf{E} = -\partial \mathbf{B}/\partial t$, to give

$$i\mathbf{k} \times \mathbf{H} = -i\omega \mathbf{D}, \quad i\mathbf{k} \times \mathbf{E} = i\omega \mathbf{B} = i\omega \mu_0 \mathbf{H}.$$

The plane wave solutions of Maxwell's equations require that **H** be perpendicular to both **k** and **D**, and **H** must be perpendicular to both **k** and **E**.

13.6.3 Fresnel's Equation

The fact that **E** may not be perpendicular to **k** requires that we now depart from the analysis that was followed in Chapter 2, to discover the significance of the nonzero scalar product,

$$\mathbf{k} \cdot \mathbf{E} \neq 0.$$

To find what this dot product is equal to, we use Maxwell's equation to write

$$\mathbf{k} \times \mathbf{E} = \omega \mu_0 \mathbf{H},$$

and then the cross produce of this equation with **k** yields

$$\mathbf{k} \times (\mathbf{k} \times \mathbf{E}) = \omega \mu_0 \mathbf{k} \times \mathbf{H} = \omega \mu_0 (-\omega \mathbf{D}).$$

We can rewrite this equation by using the vector identity (2A.3):

$$\mathbf{k}(\mathbf{k} \cdot \mathbf{E}) - \mathbf{E}(\mathbf{k} \cdot \mathbf{k}) = -\omega^2 \mu_0 \mathbf{D}. \tag{13.8}$$

The propagation constant is given by

$$k^2 = \left(\frac{n\omega}{c}\right)^2.$$

This allows (13.8) to be rewritten to yield an expression for the dot product $\mathbf{k} \cdot \mathbf{E}$:

$$\frac{\mathbf{k}}{k^2}(\mathbf{k} \cdot \mathbf{E}) = \mathbf{E} - \frac{c^2 \mu_0}{n^2} \mathbf{D}. \tag{13.9}$$

D and **E** must satisfy (13.9) if they are to satisfy Maxwell's equations.

To allow a physical interpretation of, (13.9) we evaluate the components of this vector equation along the three principal directions. The *j*th component of the vector equation is

$$\frac{k_j}{k^2}(\mathbf{k}\cdot\mathbf{E}) = \left(1 - \frac{c^2\mu_0\varepsilon_j}{n^2}\right)E_j, \tag{13.10}$$

where the ε_j are the principal dielectric constants. By multiplying both sides of the *j*th component by k_j, we obtain an eigenvalue equation:

$$\frac{k_j^2}{k^2\left(1 - \dfrac{\varepsilon_j}{n^2\varepsilon_0}\right)}(\mathbf{k}\cdot\mathbf{E}) = k_j E_j, \tag{13.11}$$

where we have made the substitution $c^2 = (\mu_0\varepsilon_0)^{-1}$. Adding the three component equations of (13.11) together yields a new expression of the vector equation (13.9):

$$(\mathbf{k}\cdot\mathbf{E})\sum_{j=1}^{3}\frac{k_j^2}{k^2\left(1 - \dfrac{\varepsilon_j}{n^2\varepsilon_0}\right)} = \mathbf{k}\cdot\mathbf{E}.$$

If $\mathbf{k}\cdot\mathbf{E} \neq 0$, as we implied might be the case, then we may divide both sides of the equation by the scalar product. We also divide both sides by n^2 to obtain

$$\sum_{j=1}^{3}\frac{k_j^2}{k^2\left(n^2 - \dfrac{\varepsilon_j}{\varepsilon_0}\right)} = \frac{1}{n^2}. \tag{13.12}$$

A new parameter, which we will call *the principal refractive index*, is defined as

$$n_j^2 = \frac{\varepsilon_j}{\varepsilon_0}. \tag{13.13}$$

Using the new definition, we can write (13.12) in the form called *Fresnel's equation of wave normals*:

$$\sum_{j=1}^{3}\frac{k_j^2}{k^2\left(n^2 - n_j^2\right)} = \frac{1}{n^2}. \tag{13.14}$$

This equation allows the calculation of the index of refraction for an arbitrary propagation direction. It appears to be cubic in n^2, but is actually only quadratic in n^2, with two positive roots, n_1^2 and n_2^2. This is due to the fact that

$$\sum_{j=1}^{3}\frac{k_j^2}{k^2} = 1.$$

Fresnel's equation (13.14) states that for any propagation direction **k**, there are, in general, two values of the refractive index: n_1 and n_2. If the solutions of (13.14) are substituted into (13.10), two values of the electric field, $\mathbf{E}_1$ and $\mathbf{E}_2$, are obtained for the selected propagation direction. Finally, the two solutions for the electric field corresponding to n_1 and n_2 can be substituted into (13.9) to yield two values for the electric displacement, $\mathbf{D}_1$ and $\mathbf{D}_2$.

The two electric displacement vectors $\mathbf{D}_1$ and $\mathbf{D}_2$ associated with a selected propagation vector are perpendicular to one another, as will be demonstrated below. These vectors specify the polarizations of two light waves, propagating at two different velocities, given by n_1 and n_2, in the anisotropic material. From Maxwell's equations, we have generated a theoretical explanation of the birefringent observations in any optically anisotropic material.

We can demonstrate that the two electric displacement vectors are orthogonal by first decomposing $\mathbf{E}$ into components parallel ($\mathbf{E}_\parallel$) and perpendicular ($\mathbf{E}_\perp$) to $\mathbf{k}$:

$$\mathbf{E}_\parallel = \frac{\mathbf{k}}{k^2}(\mathbf{k}\cdot\mathbf{E}), \quad \mathbf{E}_\perp = \mathbf{E} - \frac{\mathbf{k}}{k^2}(\mathbf{k}\cdot\mathbf{E}). \tag{13.15}$$

By rewriting (13.9), we discover a relationship between $\mathbf{D}$ and $\mathbf{E}_\perp$:

$$\mathbf{D} = \frac{k^2}{\mu_0\omega^2}\left[\mathbf{E} - \frac{\mathbf{k}}{k^2}(\mathbf{k}\cdot\mathbf{E})\right] = \frac{n^2}{\mu_0 c^2}\mathbf{E}_\perp. \tag{13.16}$$

Since we have two indices of refraction, (13.16) produces two equations:

$$\mathbf{D}_1 = \frac{n_1^2}{\mu_0 c^2}\mathbf{E}_{1\perp}, \quad \mathbf{D}_2 = \frac{n_2^2}{\mu_0 c^2}\mathbf{E}_{2\perp}. \tag{13.17}$$

To evaluate the scalar product $\mathbf{D}_1 \cdot \mathbf{D}_2$, we first evaluate the scalar product

$$\mathbf{E}_2 \cdot \mathbf{D}_1 = \sum_{i=1}^{3} E_{2i} D_{1i} = \sum_{i=1}^{3}\sum_{j=1}^{3} E_{2i}\varepsilon_{ij} E_{1j}.$$

Since the dielectric tensor must be symmetric, the scalar product between $\mathbf{E}$ and $\mathbf{D}$ is identical for either index of refraction:

$$\sum_{i=1}^{3}\sum_{j=1}^{3} E_{2i}\varepsilon_{ij}E_{1j} = \sum_{j=1}^{3}\sum_{i=1}^{3} E_{1j}\varepsilon_{ji}E_{2i} = \sum_{j=1}^{3} E_{1j}D_{2j},$$

and we may write

$$\mathbf{E}_2 \cdot \mathbf{D}_1 = \mathbf{E}_1 \cdot \mathbf{D}_2. \tag{13.18}$$

The electric field can be written as the sum of the components parallel and perpendicular to $\mathbf{k}$:

$$\left(\mathbf{E}_{2\perp} + \mathbf{E}_{2\parallel}\right)\cdot\mathbf{D}_1 = \left(\mathbf{E}_{1\perp} + \mathbf{E}_{1\parallel}\right)\cdot\mathbf{D}_2.$$

From the definition (13.15), we known that $\mathbf{E}_{i\parallel}\cdot\mathbf{E}_{j\perp} = 0$ for all i and j. We combine this fact with (13.17) to write

$$\left(n_1^2 - n_2^2\right)(\mathbf{E}_{2\perp}\cdot\mathbf{E}_{1\perp}) = 0.$$

If $n_1^2 \neq n_2^2$, then $\mathbf{E}_{2\perp}\cdot\mathbf{E}_{1\perp} = 0$, and (13.17) allows us to write

$$\mathbf{D}_1\cdot\mathbf{D}_2 = \frac{n_1^2 n_2^2}{\left(\mu_0 c^2\right)^2}(\mathbf{E}_{1\perp}\cdot\mathbf{E}_{2\perp}) = 0. \tag{13.19}$$

When $n_1^2 = n_2^2$, the directions of $\mathbf{D}_1$ and $\mathbf{D}_2$ are arbitrary, but it is convenient to choose them to also be perpendicular.

13.7 Retarder

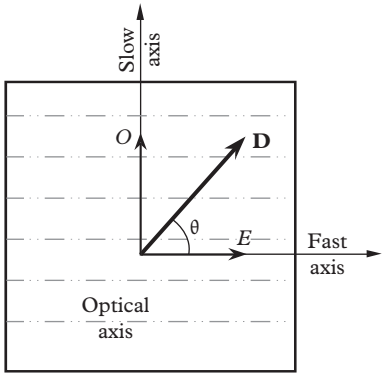

Figure 13.16 *A linearly polarized wave is incident on a negative uniaxial crystal cut so that its face is parallel to the optical axis.*

Retarders modify the polarization of an incident wave by changing the relative phase of two orthogonally polarized waves that form the incident wave. Either birefringence or reflection can be used to produce the desired phase change.

To understand how birefringent retarders operate, and to learn how they are constructed, we will examine a uniaxial, birefringent plate, cut with the optical axis parallel to the plate's face. In Figure 13.16, we show a linearly polarized wave incident on such a crystal with the electric displacement **D** making an angle θ with the optical axis. Any polarized wave can be decomposed into two linearly polarized waves with orthogonal polarization directions. These waves are the ordinary and extraordinary waves in the birefringent crystal. In this geometry, the ordinary and extraordinary waves propagate parallel to one another but at different velocities. The different propagation velocities cause the component of polarization parallel to the slow axis (vertical in Figure 13.16) to lag the component parallel to the fast axis.

The birefringent plate modifies the polarization of the incident light because of the different propagation velocities, characterized by the two indices n_o and n_e. If the retarder plate has thickness d, then the optical path difference between the two orthogonally polarized waves is

$$N\lambda = \pm(n_e - n_o). \tag{13.20}$$

N is called the *retardation* and is expressed in fractions of a wavelength. For example, $N = 1/4$ corresponds to a quarter-wave retardation.

The phase difference between the two orthogonally polarized waves, generated by propagating through the retarder plate, is simply 2π times the retardation:

$$\delta = 2\pi N = \pm\frac{2\pi d(n_e - n_o)}{\lambda}. \tag{13.21}$$

This phase is used to determine the polarization after propagation through the retarder plate, using (2.33).

If the displacement **D** of the linearly polarized light is incident on the birefringent plate, with the direction of polarization parallel to either the fast or slow axis of the plate, the plate will not modify the polarization. In all other orientations, the plate will modify the polarization of the incident light because of the phase difference between the polarization components parallel to the fast and slow axes.

13.7.1 Quarter-Wave Plate

If the plate's thickness results in (13.21) having a value of $\delta = \pi/2$, then a phase retardation equivalent to a shift of one-quarter of a sinusoidal wave is generated between the ordinary and extraordinary waves, and the plate is called a *quarter-wave plate*, $N = 1/4$. Mica or quartz are normally used for retarders because it is easy to produce plates of the desired thickness. In quartz, a plate 13.7 μm thick produces a quarter-wave phase retardation, while in mica, the quarter-wave thickness is 22.3 μm at $\lambda = 500$ nm.

Mica is actually biaxial, with the angle between the two optic axes varying between 0° and 42°. The mica selected for retarders has a biaxial angle near 0°. Mica can be cleaved into very thin plates, by virtue of its crystal structure, and this ease overrides any complication introduced by the small departure from uniaxial

behavior. The cleavage planes that allow mica to be formed into thin plates are not parallel to either optic axis. For the crystal orientation with the faces of the retarder determined by the cleavage planes, the ordinary and extraordinary indices are $n_o = n_\gamma$ and $n_e = n_\beta$ (see Table 13.3).

If linearly polarized light is incident on a quarter-wave plate such that $\theta = 45°$ in Figure 13.17(a), then the linear polarization is converted to circularly polarized light (see Chapter 2). If elliptically polarized light is incident on a quarter-wave plate, the elliptically polarized light will be converted to linearly polarized light when the slow and fast axes of the quarter-wave plate coincide with the major and minor axes of the elliptically polarized light.

If the plate's thickness results in (13.21) having a value of $\delta = \pi$, then the plate is called a *half-wave plate*; see Figure 13.17(b). The half-wave plate changes the orientation of the polarization, but does not change its form. For example, suppose in Figure 13.17 that **D** represents the polarization of an incident plane wave, or the major axis of an incident elliptically polarized wave; then the emerging wave will have **D** oriented at an angle of $-\theta$ with respect to the optical axis. The half-wave plate will have rotated the polarization through an angle of 2θ.

13.7.2 Compensator

Because the desired phase retardation produced by a wave plate occurs only at the design wavelength, the plate will be too thick for shorter wavelengths and too thin for longer wavelengths. It is useful to have a component with a continuously variable phase retardation for use at any wavelength. Such a device, called a *compensator*, will allow the measurement of an unknown retardation by comparison with the known retardation of the compensator.

One way to produce continuously varying phase retardation is to construct a wedge using a birefringent material—the upper wedge shown in Figure 13.18(a) would meet this

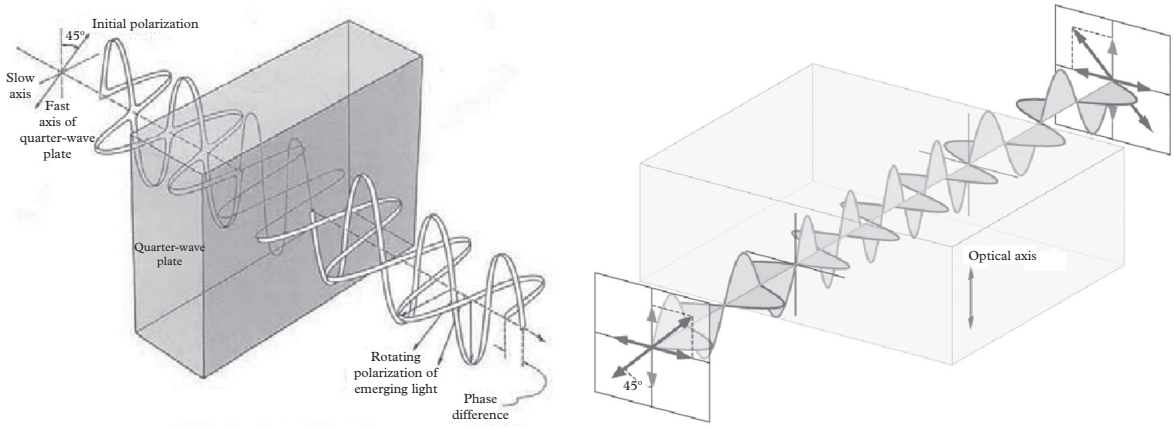

Figure 13.17 *(a) Quarter-wave plate. (b) Half-wave plate.*

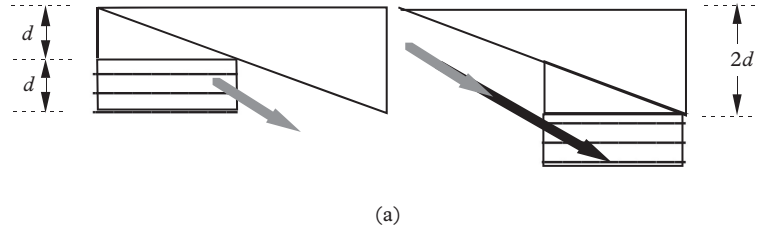

(a)

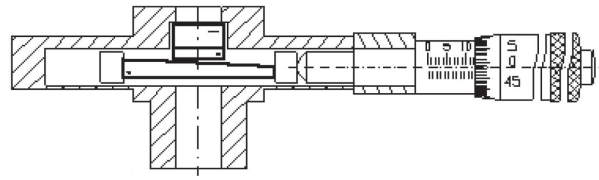

(b)

Figure 13.18 *Soleil–Babinet compensator. (a) The optical design. On the left is the configuration of the compensator that produces no retardation. On the right, the maximum retardation is produced. (b) A commercial compensator design. The compensator is designed to produce a uniform retardation across the aperture of the device, which is the width of the small sliding component.*

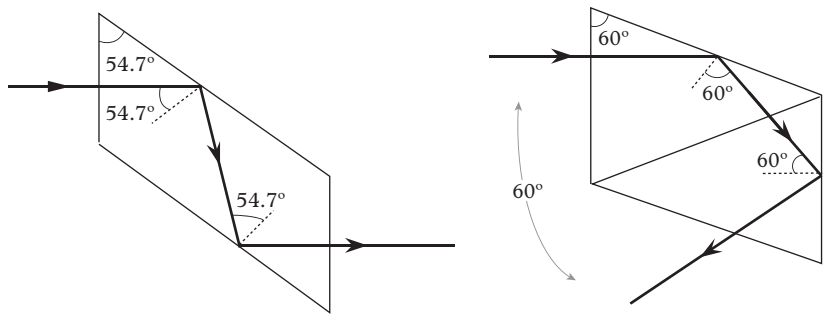

Fresnel **Mooney**

(a)

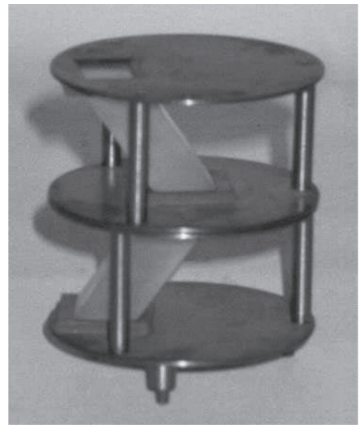

(b)

Figure 13.19 *(a) Two types of rhomb retarder design. (b) A double rhomb retarder from the U.S. Military Academy. The double rhomb removes the displacement of the optical axis.*

requirement. The simple wedge is not too useful, because it cannot produce zero phase retardation. If two wedges are used, with the slow axis of one normal to the slow axis of the other, then by moving one wedge relative to the other, a continuous variation of phase retardation can be produced. This design is called a *Babinet compensator.*

The *Soleil–Babinet compensator*, shown in Figure 13.18, produces the same phase retardation as the Babinet compensator, but over a wide aperture. The aperture of the compensator is determined by the small wedge and plate at the bottom of Figure 13.18(a). When the small wedge is positioned as shown at the left of Figure 13.18(a), the phase shift produced by the rectangular plate is exactly canceled by the two overlapping wedges, producing zero retardation. When the small wedge is positioned to the extreme right of the large wedge, as shown on the right of Figure 13.18(a), the two wedges produce a phase retardation equal to twice the negative of the phase retardation of the rectangular plate. This design can produce as much as two waves of retardation.

13.7.3 Rhomb

The rhomb-type retarder is a popular substitute when the strong wavelength dependence of the birefringent phase shifter design is a problem. The rhombs derive their phase retardation from the phase change introduced by total internal reflection [see (3.54), (3.55), and Figure 3.15]. Figure 13.19 shows two typical examples from a large number of rhomb designs. All of the designs require that the rhomb be constructed of homogeneous, isotropic material.

13.8 Mueller Calculus

Soleillet discovered, in 1929, that an optical device performed a linear transformation on the input wave, and, in 1942, Perrin put this fact into a matrix formalism:

$$\boldsymbol{\mathcal{S}}_1 = \boldsymbol{\mathcal{M}}\boldsymbol{\mathcal{S}}_0. \tag{13.22}$$

Mueller used experimentally derived 4×4 matrices, $\boldsymbol{\mathcal{M}}$ in (13.22), to describe the effect of an optical device on a light wave's polarization. The matrices are based upon an assumed linear relationship between the incident and transmitted beams, which is the usual case. (We will examine nonlinear behavior later.)

The analysis of the effect of a number of polarizers and retarders is made easier by the use of the Mueller–Stokes matrix calculus coupled with the use of the Stokes vectors (2.42).

The $\boldsymbol{\mathcal{S}}$ in (13.22) are column matrices whose elements are the Stokes parameters:

$$\boldsymbol{\mathcal{S}} = \begin{bmatrix} s_0 \\ s_1 \\ s_2 \\ s_3 \end{bmatrix}. \tag{13.23}$$

A few optical devices and their Mueller matrices are listed in Tables 13.5 and 13.6.

The Mueller matrix contains 16 parameters, but there are only 7 independent parameters. The matrix contains no information about absolute phase, but it handles partially polarized and unpolarized light without modification.

Table 13.5 *Mueller matrices for polarizers*

Linear

Transmission axis

Horizontal	Vertical
$\frac{1}{2}\begin{bmatrix} 1 & 1 & 0 & 0 \\ 1 & 1 & 0 & 0 \\ 0 & 0 & 0 & 0 \\ 0 & 0 & 0 & 0 \end{bmatrix}$	$\frac{1}{2}\begin{bmatrix} 1 & -1 & 0 & 0 \\ -1 & 1 & 0 & 0 \\ 0 & 0 & 0 & 0 \\ 0 & 0 & 0 & 0 \end{bmatrix}$
45°	–45°
$\frac{1}{2}\begin{bmatrix} 1 & 0 & 1 & 0 \\ 0 & 0 & 0 & 0 \\ 1 & 0 & 1 & 0 \\ 0 & 0 & 0 & 0 \end{bmatrix}$	$\frac{1}{2}\begin{bmatrix} 1 & 0 & -1 & 0 \\ 0 & 0 & 0 & 0 \\ -1 & 0 & 1 & 0 \\ 0 & 0 & 0 & 0 \end{bmatrix}$

Circular

Right	Left
$\frac{1}{2}\begin{bmatrix} 1 & 0 & 0 & 1 \\ 0 & 0 & 0 & 0 \\ 0 & 0 & 0 & 0 \\ 1 & 0 & 0 & 1 \end{bmatrix}$	$\frac{1}{2}\begin{bmatrix} 1 & 0 & 0 & -1 \\ 0 & 0 & 0 & 0 \\ 0 & 0 & 0 & 0 \\ -1 & 0 & 0 & 1 \end{bmatrix}$

Table 13.6 *Mueller matrices for retarders*

Quarter-wave plate

Fast axis

Horizontal	Vertical
$\begin{bmatrix} 1 & 0 & 0 & 0 \\ 0 & 1 & 0 & 0 \\ 0 & 0 & 0 & 1 \\ 0 & 0 & -1 & 0 \end{bmatrix}$	$\begin{bmatrix} 1 & 0 & 0 & 0 \\ 0 & 1 & 0 & 0 \\ 0 & 0 & 0 & -1 \\ 0 & 0 & 1 & 0 \end{bmatrix}$
45°	–45°
$\begin{bmatrix} 1 & 0 & 0 & 0 \\ 0 & 0 & 0 & -1 \\ 0 & 0 & 1 & 0 \\ 0 & 1 & 0 & 0 \end{bmatrix}$	$\begin{bmatrix} 1 & 0 & 0 & 0 \\ 0 & 0 & 0 & 1 \\ 0 & 0 & 1 & 0 \\ 0 & -1 & 0 & 0 \end{bmatrix}$

Half-wave plate

0° or 90°	±45°
$\begin{bmatrix} 1 & 0 & 0 & 0 \\ 0 & 1 & 0 & 0 \\ 0 & 0 & -1 & 0 \\ 0 & 0 & 0 & -1 \end{bmatrix}$	$\begin{bmatrix} 1 & 0 & 0 & 0 \\ 0 & -1 & 0 & 0 \\ 0 & 0 & 1 & 0 \\ 0 & 0 & 0 & -1 \end{bmatrix}$

13.9 Jones Calculus

The Jones calculus [2] is complementary to the Mueller calculus and operates on the Jones vector (2.46) in a manner similar to the way the Mueller matrix operates on the Stokes vector. The Jones matrix contains eight independent parameters with no redundancy, making the Jones calculus simpler than the Mueller calculus. However, the Jones calculus only applies to polarized light. It can be extended, using the density matrix formalism, mentioned in Chapter 2, to allow manipulation of unpolarized light, but with a loss of simplicity. The matrix equation for Jones calculus is

$$\mathbf{E}_{\text{out}} = \boldsymbol{\Omega}\mathbf{E}_{\text{in}}. \tag{13.24}$$

A few optical devices and their Jones matrices $\boldsymbol{\Omega}$ are listed in Tables 13.7 and 13.8.

Table 13.7 *Jones matrices for polarizers*

Linear				
	Transmission axis			
	Horizontal	Vertical	45°	–45°
	$\begin{bmatrix} 1 & 0 \\ 0 & 0 \end{bmatrix}$	$\begin{bmatrix} 0 & 0 \\ 0 & 1 \end{bmatrix}$	$\frac{1}{2}\begin{bmatrix} 1 & 1 \\ 1 & 1 \end{bmatrix}$	$\frac{1}{2}\begin{bmatrix} 1 & -1 \\ -1 & 1 \end{bmatrix}$
Circular				
	Right		Left	
	$\frac{1}{2}\begin{bmatrix} 1 & -i \\ i & 1 \end{bmatrix}$		$\frac{1}{2}\begin{bmatrix} 1 & i \\ -i & 1 \end{bmatrix}$	

Table 13.8 *Jones matrices for retarders*

Quarter-wave plate		
	Fast axis	
	Horizontal	Vertical
	$\begin{bmatrix} e^{i\pi/4} & 0 \\ 0 & e^{-i\pi/4} \end{bmatrix}$	$\begin{bmatrix} e^{-i\pi/4} & 0 \\ 0 & e^{i\pi/4} \end{bmatrix}$
	45°	–45°
	$\frac{1}{2}\begin{bmatrix} 1 & i \\ i & 1 \end{bmatrix}$	$\frac{1}{2}\begin{bmatrix} 1 & -i \\ -i & 1 \end{bmatrix}$
Half-wave plate		
	0° or 90°	±45°
	$\begin{bmatrix} 1 & 0 \\ 1 & -1 \end{bmatrix}$	$\begin{bmatrix} 0 & 1 \\ 1 & 0 \end{bmatrix}$

For every matrix in Jones calculus, there is a matrix in Mueller calculus, but the converse is not true. For example, it is possible to construct a depolarizer by using a thick piece of opal glass in the visible or by using gold-covered sandpaper in the infrared. Such a device can be described in Mueller calculus, but there is no corresponding matrix in Jones calculus.

13.10 Optical Activity

Arago observed in 1811 that the direction of polarization was rotated when plane-polarized light was propagated through quartz, parallel to the optical axis of the quartz. **Jean Baptiste Biot (1774–1862)**, in 1815, extended Arago's observations and discovered that the continuous rotation of the plane of polarization occurred in gases and liquids, as well as in crystalline material. (During the experiment that led to the first observation of rotation in a gas, Biot set a church on fire!) Materials that rotate the plane of polarization are said to be *optically active*. It is sometimes known as *natural rotation* to distinguish it from magnetic rotation (the Faraday effect), which we will discuss later.

Biot observed that if one looked at a light source through optically active materials, such materials could be grouped into two classes: those that rotated the polarization to the left—*levorotatory*—and those that rotated it to the right—*dextrorotatory*. (In chemistry, anything that can exhibit a "handedness" is said to be *chiral*, and atoms that differ only in the direction they rotate polarized light are said to differ in their *chirality*.) **Louis Pasteur (1822–1895)**, in 1848, demonstrated that molecules that differ only in their chirality are mirror images of each other.

Fresnel developed the first theoretical description of optical activity by first demonstrating, experimentally, that linearly polarized light can be decomposed into right- and left-circularly polarized waves (see Figure 2.9). He then developed an explanation of optical rotation by assuming that the two circularly polarized components of a linearly polarized wave propagated at different velocities. Fresnel suggested that the observed optical activity might be due to "a helical arrangement of molecules of the medium."

Later investigations have confirmed Fresnel's postulated cause of optical activity, a good example being crystalline quartz. The right-hand form of quartz is shown in Figure 13.20. By following along the Si—O bond from silicon atom to silicon atom (A→B→C→A in Figure 13.20), a right-handed spiral is traced out—this path is shown in Figure 13.20 by the dark arrows. If the silicon atoms are projected onto a plane, they form the vertices of an equilateral triangle, shown on the right of Figure 13.20. To aid in visualizing the helical path, a shaded version of the triangle is shown at each of four planes in the quartz unit cell.

Two classical models have been developed to explain optical activity [3]. One model is based upon the interaction of the electromagnetic wave with charges confined to a helical path as illustrated in Figure 13.21. This model approximates the behavior of charge carriers in quartz and in many optically active molecules. Maxwell's equations will allow us to visualize how the helical conductor causes rotation. Consider a molecule in which the electrons are constrained to move along the helical path shown in Figure 13.21. Suppose plane-polarized light is incident upon the molecule such that the oscillating magnetic field is parallel to the helix axis. According to (2.3), the changing magnetic field creates an oscillating electric field that is perpendicular to the electric field of the incident light:

$$\nabla \times \mathbf{E} = -\frac{\partial \mathbf{B}}{\partial t}.$$

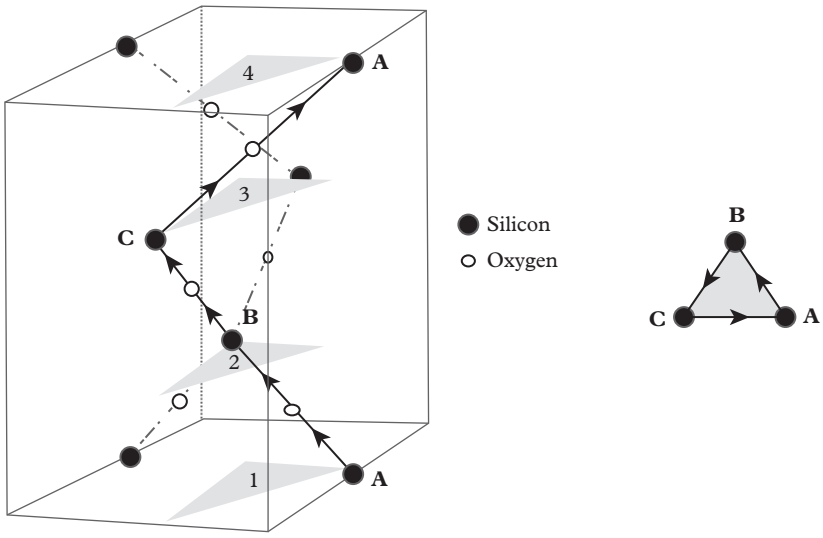

Figure 13.20 *Crystal structure of quartz.*

The cross product guarantees that the induced field is perpendicular to the incident field. Since the incident and induced fields are in phase, they can be combined by vector addition, leading to a resultant electric field that is rotated relative to the incident field. The same argument holds for the magnetic field induced by the alternating electric displacement of the light, (2.4).

A second classical model treats the interaction of an electromagnetic wave with two coupled harmonic oscillators that lie in separate planes. The two-oscillator model approximates the behavior of tetrahedrally bonded atoms, such as the molecule shown in Figure 13.22. The coupled oscillator model is equivalent to the helical model, but proof of this fact will not be given here.

The unique property possessed by optically active molecules is that a mirror image of the molecule exists. For example, the molecule and its mirror image shown in Figure 13.22 will lose their separate identity, and their optical activity, if any two of the bonded atoms are identical. For example, if the fluorine atom is replaced by a hydrogen, then the mirror image does not exist because the same image can be generated by a simple rotation about the normal to the plane of the figure.

Classical and quantum mechanical models predict that there will be both an electric ($\boldsymbol{\mu}$) and a magnetic ($\mathbf{m}$) dipole moment induced in an optically active molecule by the incident radiation. The rotation strength is given by

$$R = Im\{\boldsymbol{\mu} \cdot \mathbf{m}\},$$

where complex notation is required to allow inclusion of the difference in phase between the two dipoles. In symmetric molecules, the two dipoles are always perpendicular, and so $R = 0$, but this is not the case for asymmetric molecules.

We have previously ignored any possible spatial dependence of $\mathbf{D}$ on $\mathbf{E}$, but now we must include, at least to first order, the dependence of the space derivatives of $\mathbf{E}$ to explain the magnetic contribution, see (2.6c). Drude demonstrated that the inclusion of the spatial variation of the electric field led to the prediction of optical activity by Maxwell's equations.

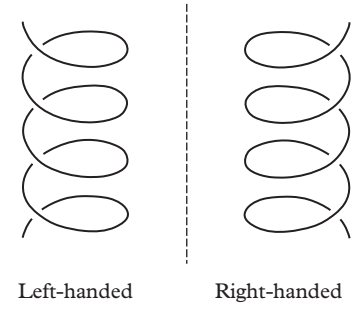

Figure 13.21 *Helical conductors with right and left handedness.*

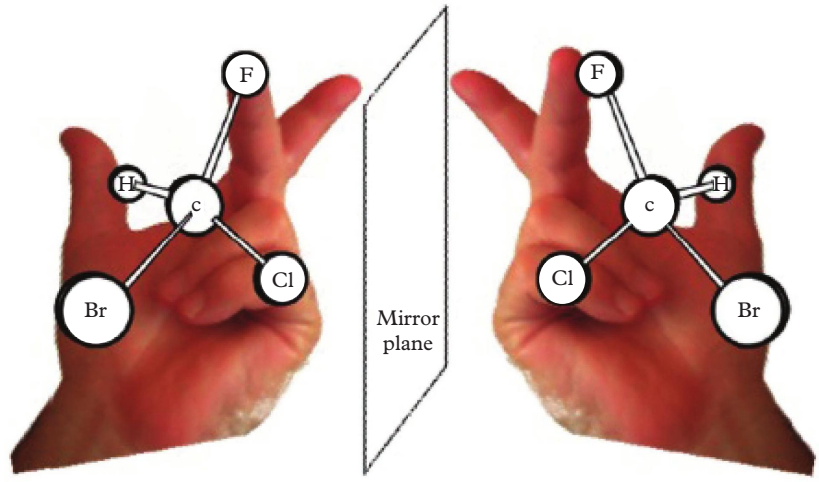

Figure 13.22 *The molecular structure on the left is the simplest optically active molecule. The mirror image of this tetrahedral molecule, shown on the right, is a unique molecule that cannot be reproduced by rotation of the molecule on the left. If any two of the atoms on this tetrahedral bonded molecule are the same, then the molecule is no longer dissymmetric and it is not optically active.*

The result of Drude's theory yielded a prediction of wavelength dependence of optical activity given by

$$\theta \propto R\frac{\lambda_0^2}{\lambda^2-\lambda_0^2},$$

where θ is the angle through which the plane of polarization is rotated.

Adding the dependence of $\mathbf{D}$ on $\nabla\cdot\mathbf{E}$ requires that we replace the real dielectric tensor we have been using by a complex tensor

$$\tilde{\varepsilon}^0 = \varepsilon + i\gamma.$$

We have to add an imaginary term because the space derivatives of

$$\mathbf{E} = \mathbf{E}_0 e^{i(\omega t - kx)}$$

yield terms involving i. We will continue to assume that the medium is lossless, so the requirement placed on the dielectric tensor by (13.6) is

$$\varepsilon_{jk} + i\gamma_{jk} = \varepsilon_{kj} - i\gamma_{kj}. \tag{13.25}$$

The real part of the dielectric tensor continues to be a symmetric tensor; however, the imaginary part must be an antisymmetric tensor. It is interesting to note that a lossless anisotropic medium can have a complex dielectric constant, whereas a lossless isotropic medium must have a real dielectric constant. (If loss were included, this theory would also describe *circular dichroism*: the observation of a difference in absorption of the right- and left-circularly polarized light waves.)

The constitutive relations must be rewritten, but how? There are at least three forms of constitutive relations, each with their supporters. One that seems to be free from issues with the boundary conditions is

$$\frac{1}{\varepsilon_0} D_i = \varepsilon_{ij} E_j + \gamma_{ijk} \frac{\partial}{\partial x_j} E_k,$$
$$\frac{1}{\mu_0} B_i = \mu_{ij} H_j + \xi_{ijk} \frac{\partial}{\partial x_j} H_k. \tag{13.26}$$

Conservation of energy requires that $\varepsilon_{ij} = \varepsilon_{ji}$ and $\gamma_{ijk} = -\gamma_{kij}$, and thus $\gamma_{ijk} = \beta_{ijk}\gamma_{ij}$. We can now write the constitutive relation for **D** as

$$\frac{1}{\varepsilon_0} \mathbf{D} = \varepsilon \cdot \mathbf{E} + (\gamma \cdot \nabla) \times \mathbf{E}. \tag{13.27}$$

We may always replace an antisymmetric tensor by a vector $\boldsymbol{\gamma}$ with components

$$\gamma_1 = \gamma_{23} = -\gamma_{32}, \quad \gamma_2 = \gamma_{31} = -\gamma_{13}, \quad \gamma_3 = \gamma_{12} = -\gamma_{21}.$$

The microscopic analogue of the constitutive relations (13.27) and the one for **B** can be used to calculate the induced electric and magnetic dipole moments.

By using (13.27) in place of (13.1), we will be able to describe optical activity. A formal derivation of the theory would demonstrate that, except for differences in second order in $\boldsymbol{\gamma}$, the normal surfaces and ray surfaces of an optically active crystal agree with those of an nonactive, birefringent crystal (see Appendices 13C and 13D). While the surfaces have the same appearance, their interpretation must be modified.

If we have a positive uniaxial crystal that does not exhibit optical activity, the index surfaces consist of a sphere and a inscribed prolate spheroid [see (13C.6) and (13C.7)]. The radius from the center to any point on either sheet gives the index of refraction for one of the two orthogonal linearly polarized waves. The two sheets touch at two points, and the line between those two points defines the direction of the optical axis.

Consider now the positive uniaxial crystal, quartz, which is also optically active. The second-order effects of optical activity result in two propagation velocities in the direction of the optical axis; i.e., the two normal surfaces no longer touch (see Figure 13.23). (In Figure 13.23, we have exaggerated the separation, which is actually only 0.6% of the sphere's radius normal to the optical axis and 4.5×10^{-5} of the sphere's radius along the optical axis.) In addition to the appearance of two indices of refractions along the optical axis, the polarizations associated with those indices are no longer linear but are now right- and left-circular. Thus, along the optical axis of quartz, the normal surfaces give the index of refraction for right- and left-circular polarized light. Normal to the optical axis, the normal surfaces are as they are in a nonactive material; i.e., they give the index of refraction for the two orthogonal linearly polarized light waves. In between these two extreme conditions, the two polarizations that are represented by the two normal surfaces are right- and left-elliptically polarized light.

To follow a plane-polarized wave as it propagates through an optically active material, we assume that at the surface of the optically active material, $z = 0$, we have a vertically polarized beam. Using the Jones vector notation (2.42),

$$\frac{E_0}{2} \begin{bmatrix} 0 \\ \sqrt{2} \end{bmatrix} e^{i\omega t},$$

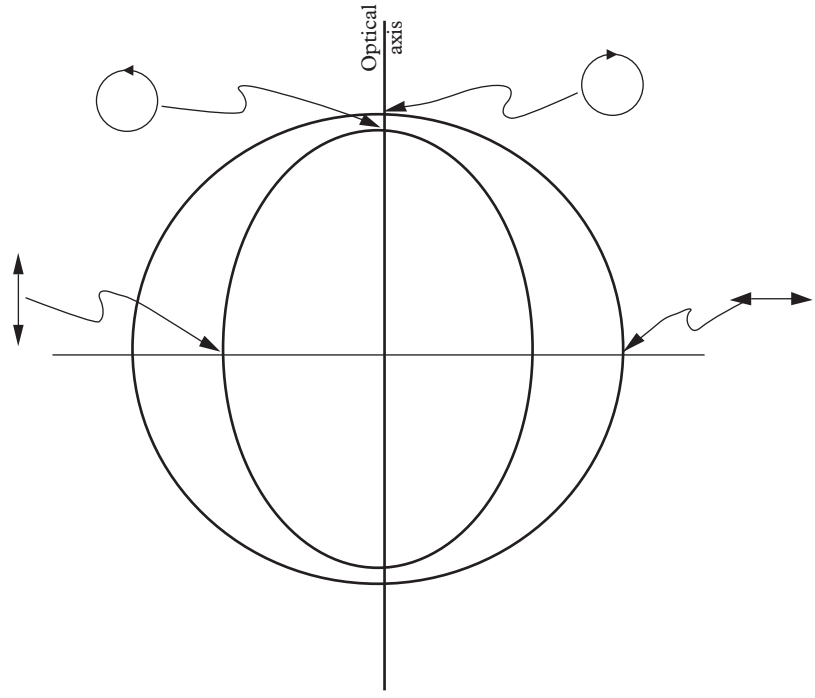

Figure 13.23 *A very schematic representation of the normal surfaces of quartz. Also shown are the states of polarization that propagate in two directions in the crystal. The difference in the two normal sheets has been exaggerated for illustrative purposes.*

we decompose the plane-polarized wave in the optically active material into a right- and a left-circularly polarized component, as in (2.36) and (2.37). The wave traveling in the positive z-direction is

$$\frac{E_0}{2\sqrt{2}}\begin{bmatrix}-i\\1\end{bmatrix}e^{i(\omega t-kz)}+\frac{E_0}{2\sqrt{2}}\begin{bmatrix}i\\1\end{bmatrix}e^{i(\omega t-kz)}. \tag{13.28}$$

After traveling through a thickness d of a crystal of index of refraction n, the phase of light, relative to the initial wave, at the surface $z = 0$ is

$$nkd=\frac{2\pi}{\lambda}nd.$$

We assume that the right-circularly polarized wave sees an index of refraction n_+ and the left-circularly polarized waves sees n_-. Upon leaving the optically active material, the wave is

$$\frac{E_0}{2\sqrt{2}}\begin{bmatrix}-i\\1\end{bmatrix}e^{i(\omega t-n_+kz)}+\frac{E_0}{2\sqrt{2}}\begin{bmatrix}i\\1\end{bmatrix}e^{i(\omega t-n_-kz)}. \tag{13.29}$$

This can be rewritten

$$\frac{E_0}{2\sqrt{2}}e^{i[\omega t-(n_++n_-)kd/2]}\left(\begin{bmatrix}-i\\1\end{bmatrix}e^{i(n_--n_+)kd/2}+\begin{bmatrix}i\\1\end{bmatrix}e^{i(n_+-n_-)kd/2}\right). \tag{13.30}$$

To interpret the physical meaning of (13.30), we simplify the equation by defining

$$\psi = (n_+ + n_-)kd/2, \quad \theta = (n_- - n_+)kd/2.$$

With these definitions, we can write (13.30) as

$$\frac{E_0}{\sqrt{2}} e^{i(\omega t - \psi)} \left(\begin{bmatrix} 0 \\ 1 \end{bmatrix} \frac{e^{i\theta} + e^{-i\theta}}{2} + \begin{bmatrix} 1 \\ 0 \end{bmatrix} \frac{e^{i\theta} - e^{-i\theta}}{2i} \right),$$

that is,

$$\frac{E_0}{\sqrt{2}} e^{i(\omega t - \psi)} \left(\begin{bmatrix} 0 \\ 1 \end{bmatrix} \cos\theta + \begin{bmatrix} 1 \\ 0 \end{bmatrix} \sin\theta \right). \tag{13.31}$$

The expression (13.31) describes a plane-polarized wave with the polarization direction at an angle

$$\theta = \frac{\pi d}{\lambda}(n_- - n_+). \tag{13.32}$$

The incident plane-polarized wave has had its plane of polarization rotated through an angle θ proportional to the length of path traversed in the substance. If $n_- > n_+$, then the right-circularly polarized wave travels faster than the left, and the material is called dextrorotatory. For the opposite case, the material is called levorotatory.

For most crystals, $n_- - n_+$ is of the order of 10^{-4} or less. For quartz, the index difference is 7.1×10^{-5} at 589.3 nm; thus, a 1 mm thick plate of quartz cut normal to the optical axis rotates a linearly polarized wave through an angle of 21.7°. The angle through which the plane of polarization is rotated for a 1 mm thick crystal is defined as the *specific rotation* (or *rotatory power*),

$$\beta = \frac{\theta}{1 \text{ mm}}.$$

The specific rotations for a few solids can be found in Table 13.9.

We see from (13.32) that the specific rotation of any material has an explicit wavelength dependence of $1/\lambda$. For quartz, the index difference $n_- - n_+$ also varies inversely with wavelength, so that the specific rotation of quartz should vary as $1/\lambda^2$. Throughout most of the visible region of the spectrum, the specific rotation of quartz can described by an equation of the same form as Cauchy's equation (see Figure 13.24), which is in agreement with the prediction of Drude's theory.

As Biot discovered, optical activity is also exhibited by fluids. A fluid is isotropic in the sense that the molecules are randomly oriented throughout. The observed optical activity is attributed to molecules with no center of symmetry and no plane of symmetry. The molecules are randomly oriented in a fluid, but they still produce optically activity because the preferred direction of rotation associated with each molecule is independent of orientation. To aid in visualizing this property, think of a box of screws—they remain right-handed, no matter what orientation they have in the box.

The vector $\boldsymbol{\gamma}$ for a liquid or gas reduces to a scalar, and the two indices have the forms

$$n_+ = \sqrt{\varepsilon} + \frac{\gamma}{\sqrt{\varepsilon}}, \tag{13.33}$$

$$n_- = \sqrt{\varepsilon} - \frac{\gamma}{\sqrt{\varepsilon}}. \tag{13.34}$$

Table 13.9 *Specific rotations of some solids*

Material	Specific rotation β (deg/mm)
HgS	+32.5
Lead hyposulfate	+5.5
Potassium hyposulfate	+8.4
Quartz	+21.684
$NaBrO_3$	+2.8
$NaClO_3$	+3.13

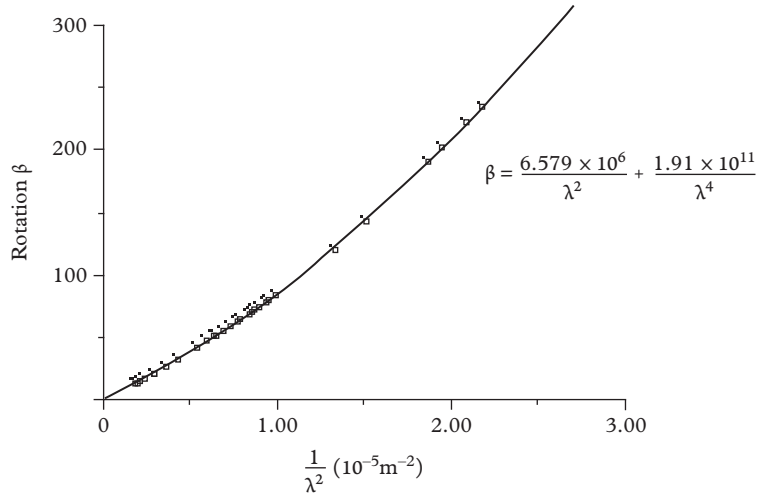

Figure 13.24 *Frequency dependence of the specific rotation of quartz.*

Table 13.10 *Specific rotations of some liquids*

Material	Specific rotation β (deg/dm)
Amyl alcohol	–5.7
Camphor	+70.33
Menthol	–49.7
Nicotine	–162
Turpentine	–37

If an optically active compound is dissolved in an inactive solvent, then the rotation is nearly proportional to the amount of the compound dissolved; for this reason the specific rotation is defined for 1 g of solute in 1 cm^3 of solution. The specific rotation of a liquid is smaller than for a crystal, so it is usually defined for a 10 cm = 1 dm path length rather than a 1 mm path length. If the concentration of the solution is m g/cm^3, then the rotation of the plane of polarization, θ, produced by a solution of an optically active material is

$$\theta = \beta \frac{md}{10}.$$

Table 13.11 *Specific rotations of some solutions*

Substance	Solvent	Specific rotation β (deg/dm)
Camphor	Alcohol	+54.4
Camphor	Benzene	+56
Camphor	Ether	+57
Galactose	Water	+83.9
d-Glucose (dextrose)	Water	+52.5
l-Glucose	Water	–51.4
Lactose	Water	+52.4
Maltose	Water	+138.48
Nicotine	Water	–77
Nicotine	Benzene	–164
Sucrose	Water	+66.412

For a pure liquid, m is replaced by the density of the liquid. The specific rotations of a few pure liquids and typical solutions are listed in Tables 13.10 and 13.11.

13.11 Summary

A number of methods for the control of the polarization of light were presented in this chapter:

1. **Absorption:** Dichroic polarizers absorb one polarization to a greater extent than the orthogonal polarization. When the two orthogonal polarizations are right- and left-circular, then the phenomena is called circular dichroism.
2. **Reflection:** The Fresnel equations for reflection are different for light polarized parallel and light polarized normal to the plane of incidence. At Brewster's angle

$$\theta_B = \tan^{-1} \frac{n_t}{n_i},$$

only the polarization normal to the plane of incidence is reflected. This fact can be used to produce a linearly polarized wave.
3. **Interference:** By using the design rules for a multilayer filter, a stack of dielectric layers can be produced that will selectively reflect a desired polarization. The unwanted polarization will be reflected from the interfaces of the multilayer stack and will destructively interfere.
4. **Birefringence:** In an anisotropic crystal, one polarization has an isotropic propagation velocity and obeys Snell's law; the wave associated with this polarization is called the ordinary wave. The orthogonal polarization has an anisotropic propagation velocity and does not obey Snell's law. The departure from Snell's law can be used to separate the two polarized waves. Once separated, one of the two polarizations can be removed by using a stop or by using total internal reflection. Birefringence of the two orthogonal circularly polarized waves leads to optical activity. An optically active material rotates the plane of polarization of a linearly polarized wave through an angle

$$\theta = \frac{\pi d}{\lambda}(n_- - n_+),$$

where d is the thickness of the optically active medium, n_+ is the index of refraction for a right-circularly polarized wave, and n_- is the index of refraction for a left-circularly polarized wave.

These physical processes can be used to construct a number of optical devices that can be used to manipulate a light wave's polarization. The operation of the devices can be described by Mueller matrices, which multiply a wave's Stokes vector to produce the Stokes vector of the final wave. A similar set of matrices, called Jones matrices, exist for use with Jones vectors. The following polarization devices were discussed in this chapter:

1. **Polarizer:** This device will only transmit one polarization. If it is a linear polarizer, then it will transmit the component of the polarization parallel to its axis. A circular polarizer will transmit either a right- or a left-circularly polarized wave.

2. **Retarder:** This device converts one form of polarization into another. It does so because the two orthogonal polarizations travel at different velocities. After passing through the retarder, there is a phase difference between the two polarizations given by

$$\delta = \pm \frac{2\pi d(n_e - n_o)}{\lambda},$$

where n_e and n_o are the indices of refraction of the extraordinary and ordinary waves, respectively. If the thickness d of the retarder produces a phase shift of $\pi/2$, then the retarder is called a quarter-wave plate and linearly polarized light is converted to circularly polarized light. If d is such that a phase shift $\delta = \pi$ is produced, then the retarder is called a half-wave plate and linearly polarized light has its plane of polarization rotated by an angle of 2θ, where θ is the angle between the plane of polarization of the wave and the optical axis of the retarder.

3. **Compensator:** This is a retarder that will produce a variable phase shift.

To describe the propagation of electromagnetic waves in an anisotropic medium, we must use a dielectric tensor. We demonstrated that if the medium is lossless, then the tensor is symmetric. The properties of the tensor can be understood by using a geometrical construct defined by the equation

$$\frac{D_x^2}{2U_E\varepsilon_x} + \frac{D_y^2}{2U_E\varepsilon_y} + \frac{D_z^2}{2U_E\varepsilon_z} = 1.$$

This equation describes an ellipsoid called the optical indicatrix. The indicatrix can be used to determine **E**, **k**, and **S**, given **D**.

There are two indices of refraction in a birefringent material. Their values, in the propagation direction specified by **k**, can be obtained using Fresnel's equation,

$$\sum_{j=1}^{3} \frac{k_j^2}{k^2(n^2 - n_j^2)} = \frac{1}{n^2}.$$

13.12 Problems

13.1. Discuss the reasoning behind the statement that wire polarizers should have a low resistivity for optimum performance.

13.2. Prove that Fresnel's equation,

$$\sum_{j=1}^{3} \frac{k_j^2}{k^2(n^2 - n_j^2)} = \frac{1}{n^2},$$

is a quadratic equation.

13.3. Calculate the maximum index of refraction that the cement in a Nicol prism can have.

13.4. Derive equation (13C.1).

13.5. The mirrors shown in Figure 13.25 can be used to rotate the polarization of an incident linearly polarized wave through 2θ when the mirrors are rotated through an angle θ about an axis parallel to the incident wave and passing through the centers of the two faces of the prism. Describe how this rotator works. Find an equation that relates the maximum aperture of this device to the prism's angle and the distance from the tip of the prism to the top mirror. What does the result say about the angle of the prism?

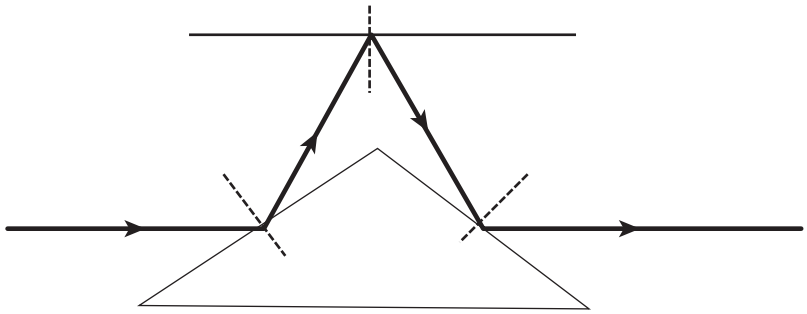

Figure 13.25 *A "K-mirror,".*

13.6. What is the effect of stacking two linear half-wave retarders in series with the fast axis of one at 0° and the second at $\theta = 45°$? Use the Mueller calculus to obtain your result.

13.7. Explain why the dielectric tensor of a loss-free isotropic medium must be a real function.

13.8. Assume a uniaxial crystal with $n_1 = n_2 = n_o$, $n_3 = n_e$, and a wave propagating in the (x, z) plane at an angle θ with respect to the z-axis (optical axis). Write the vector expressions for a unit vector in the direction of wave propagation and for **D** and **E**.

13.9. Show that for a uniaxial crystal, the Poynting vector **S** for the extraordinary wave makes an angle ϕ with respect to the wavevector **k** (see Figure 13B.1), where ϕ is given by

$$\cos\phi = \frac{n_0^2 \cos^2\theta + n_e^2 \sin^2\theta}{\sqrt{n_0^4 \cos^2\theta + n_e^4 \sin^2\theta}}. \tag{13.35}$$

This is called *Poynting vector walkoff.*

13.10. Show that the Poynting vector walkoff angle is also given by

$$\tan\phi = \frac{\sin\theta\cos\theta\,(n_o^2 - n_e^2)}{n_e^2\cos^2\theta + n_o^2\sin^2\theta}. \tag{13.36}$$

13.11. A 1 mm diameter beam of light of wavelength $\lambda = 589.3$ nm travels through a 1 cm thick calcite crystal at an angle of 32° with respect to the optical axis. How far apart will the extraordinary and ordinary beams be upon exit from the crystal?

13.12. A 10 cm long cylinder contains a 20% solution of maltose. If the observed rotation of linearly polarized light after passing through the solution is 28.8°, what is the specific rotation of maltose?

13.13. A solution of camphor in alcohol in a 20 cm long cylinder rotates linearly polarized light 33°. The specific rotation of camphor is 54°. What is the concentration of camphor in the solution?

13.14. Elliptically polarized light with a Jones vector

$$\begin{bmatrix} 3 \\ i \end{bmatrix}$$

passes through a quarter-wave plate oriented with its fast axis vertical. What is the Jones vector for the light after passing through the quarter-wave plate?

13.15. Use the Jones calculus to describe the effect of a right-circular polarizer on vertically polarized light.

13.16. Describe the polarization of a wave, initially unpolarized, after passing through a linear polarizer and then a half-wave plate. What happens if we reverse the order of the two components?

13.17. Light is incident on eight glass plates of index $n = 1.75$, at Brewster's angle. What is the percent polarization of the transmitted light?

13.18. A plate of quartz 0.5 mm thick has its faces parallel to the optical axis. What is the phase difference between the ordinary and extraordinary waves after passing through the plate for $\lambda = 589$ nm? For $\lambda = 1$ μm?

13.19. Using the Mueller calculus, describe the effect of a linear polarizer and a quarter-wave plate on an unpolarized wave. What happens if the order of the two components is reversed?

13.20. Why do most polarizers using birefringent materials contain two prisms?

REFERENCES

1. Sleeman, P.R., *Dr. Feussner's new polarizing prism*. Sci. Am. Suppl., 1884. No. 441.
2. Jones, R.C., *A new calculus for the treatment of optical systems*. J. Opt. Soc. Am., 1941. **31**: p. 488.
3. Kauzmann, W., *Quantum Chemistry: An Introduction*. 1957: Academic Press.

Appendix 13A Tensors

In this appendix, we will define a tensor. A geometrical construction of use in determining the properties of a symmetric second-order tensor will be discussed. Second-order symmetric tensors for each of the crystal symmetry classes will also be presented.

A tensor is an abstract mathematical object that has specific components in every coordinate system and undergoes a well-defined transformation when the coordinate system undergoes a transformation, say a rotation. We will define below several tensors that are of use in optics.

13A.1 Scalars

A scalars is a quantity that is not connected with direction (e.g., charge). We can completely specify the value of a scalar by assigning it a single number. A scalar is a tensor of rank zero.

13A.2 Vectors

A vectors is a quantity that must be defined with reference to a direction (e.g., the electric field). To specify a vector's value at a point, we must give both its magnitude and direction, or, equivalently, we may specify the vector's components along three mutually perpendicular directions:

$$\mathbf{E} = (E_1, E_2, E_3).$$

A vector is a tensor of rank one.

13A.3 Second-Rank Tensors

A tensor of second rank relates two general vectors. If we wish to relate displacement **D** and electric field **E**, we introduce the dielectric tensor ε such that

$$D_i = \sum_{j=1}^{3} \varepsilon_{ij} E_j. \tag{13A.1}$$

The constants ε_{ij} are the components of the tensor $\boldsymbol{\varepsilon}$ and can be given the following physical meaning. Suppose the electric field is in the x-direction:

$$\mathbf{E} = (E_1, 0, 0).$$

Then **D** has components, according to (13A.1), along all three axes:

$$\mathbf{D} = (\varepsilon_{11} E_1, \varepsilon_{21} E_1, \varepsilon_{31} E_1).$$

The component ε_{21} gives the component of **D** in the y-direction due to the electric field in the x-direction.

In matrix notation, (13A.1) is written

$$[D_1 \quad D_2 \quad D_3] = \begin{bmatrix} \varepsilon_{11} & \varepsilon_{12} & \varepsilon_{13} \\ \varepsilon_{21} & \varepsilon_{22} & \varepsilon_{23} \\ \varepsilon_{31} & \varepsilon_{32} & \varepsilon_{33} \end{bmatrix} \begin{bmatrix} E_1 \\ E_2 \\ E_3 \end{bmatrix}. \tag{13A.2}$$

The 3×3 matrix of ε's is a tensor of the second rank, denoted by ε. In general, there are nine components in a second-rank tensor.

13A.4 Higher-Rank Tensors

A tensor of third rank relates a vector **A** to two vectors **B** and **C**. In general, each component of **A** will depend on all the components of **B** and **C**:

$$A_i = \sum_{j=1}^{3} \sum_{k=1}^{3} S_{ijk} B_j C_k.$$

The S_{ijk} are components of a third-rank tensor. In general, an Nth-rank tensor relates one vector to $N - 1$ other vectors.

13A.5 Coordinate Transformations

The components of the tensor will change if a coordinate transformation is made. In fact, the way in which a tensor changes under a coordinate transformation is part of its definition. The transformation from one rectangular coordinate system to another is defined by the equation

$$x_i' = \sum_{j=1}^{3} \gamma_{ij} x_j.$$

To transform a second-rank tensor between the two coordinate systems defined by this transformation, we use the equation

$$\varepsilon_{ij}' = \sum_{k=1}^{3} \sum_{\ell=1}^{3} \gamma_{ik} \gamma_{j\ell} \varepsilon_{k\ell}. \tag{13A.3}$$

Third-rank tensors transform according to the equation

$$S_{ijk}' = \sum_{\ell=1}^{3} \sum_{m=1}^{3} \sum_{n=1}^{3} \gamma_{i\ell} \gamma_{jm} \gamma_{kn} S_{\ell mn}.$$

The physical property that the tensor represents—in the example of a second-rank tensor the dielectric constant—should be uniquely defined by the tensor, independent of the coordinate system. The tensor selected to represent the physical property is the simplest matrix that can be constructed.

If the tensor is symmetric, i.e., if $\varepsilon_{kj} = \varepsilon_{jk}$, then, by proper choice of the coordinate system, we can write the tensor as a diagonal matrix, reducing the number of constants from six to three. The three elements of the diagonal tensor are called the principal elements of the tensor and are the quantities used to characterize the physical property described by the tensor.

13A.6 Geometrical Representation

Our understanding of symmetrical tensors of second rank can be aided by the use of a geometric construction. In its most general form, (13A.1) is a second-degree equation, which, for an arbitrary set of unit vectors, can be written

$$\sum_{i=1}^{3} \sum_{j=1}^{3} S_{ij} x_i x_j = 1.$$

If the tensor is symmetric, $S_{ij} = S_{ji}$, then the second-degree equation can be written in expanded form as

$$S_{11} x_1^2 + S_{22} x_2^2 + S_{33} x_3^2 + 2(S_{23} x_2 x_3 + S_{31} x_3 x_1 + S_{12} x_1 x_2) = 1. \tag{13A.4}$$

This is the general equation of a quadric (a second-degree surface or conicoid). The surface described by this equation may be an ellipsoid or a hyperboloid (see Figure 13A.1).

The coefficients S_{ij} of (13A.4) transform according to the same equation as the components of a symmetric tensor of second rank, (13A.3), and thus we can say that **S** is a tensor.

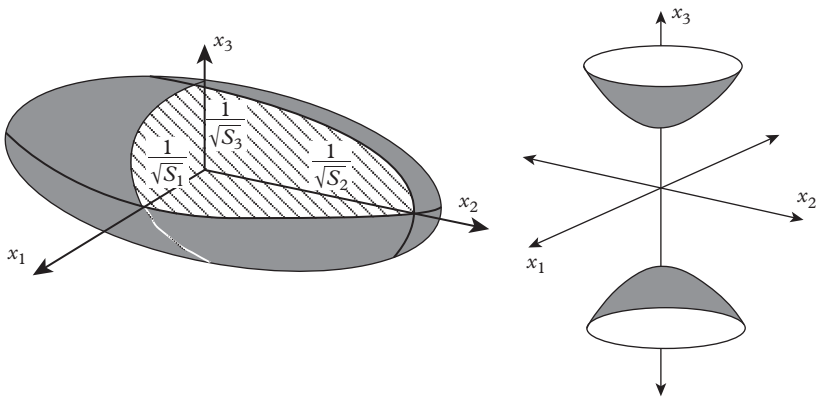

Figure 13A.1 *The quadric surface described by (13A.4). (a) An ellipsoid. (b) A hyperboloid of two sheets.*

The surfaces in Figure 13A.1 are aligned with the principal axes; therefore, the equation for the surfaces shown has the simplified form

$$S_1 x_1^2 + S_2 x_2^2 + S_3 x_3^2 = 1. \tag{13A.5}$$

The standard equation of the quadric is

$$\frac{x^2}{a^2} + \frac{y^2}{b^2} + \frac{z^2}{c^2} = 1. \tag{13A.6}$$

Comparing (13A.5) with (13A.6), we see that the semi-axes of the ellipsoid in Figure 13A.1 are equal to the principal elements of the tensor **S**:

$$a = \frac{1}{\sqrt{S_1}}, \quad b = \frac{1}{\sqrt{S_2}}, \quad c = \frac{1}{\sqrt{S_3}}.$$

The major use of the geometrical representation in Figure 13.1 is in providing an understanding of how symmetric tensors of second rank change with coordinate transformations.

If the symmetrical tensor **S** is referred to an arbitrary set of axes, then six independent components (S_{11}, S_{22}, S_{33}, S_{23}, S_{31}, and S_{12}) are needed to describe the surface. Naturally, we would try, when possible, to refer the tensor to its principal axes, the surface's symmetry axes, so that only the three principal components are needed.

13A.7 Crystal Symmetry

Another way in which the number of required components of a tensor are reduced is when the environment requires that the tensor obey certain symmetry operations. For example, the dielectric constant of a crystal must mirror the symmetry exhibited by the crystal. The crystallographic symmetry classes can be divided into three groups according to the number of symmetry axes present in the crystal. The groups, and the crystal classes that are members of these groups, are listed in Table 13A.1.

Table 13A.1 *Crystal symmetries*

Group	Quadric surface	Orientation of quadric	Crystal class	Tensor	Number of coefficients	Optical type
Three equivalent orthogonal directions	Sphere	Unimportant	Cubic, three 4-fold symmetry axes	$\begin{bmatrix} S & 0 & 0 \\ 0 & S & 0 \\ 0 & 0 & S \end{bmatrix}$	1	Isotropic
Two equivalent orthogonal directions in a plane normal to crystal's symmetry axis	Spheroid	One principal axis parallel to crystal's symmetry axis	Trigonal, one 3-fold symmetry axis	$\begin{bmatrix} S_1 & 0 & 0 \\ 0 & S_1 & 0 \\ 0 & 0 & S_2 \end{bmatrix}$	2	Uniaxial
			Tetragonal, one 4-fold symmetry axis			
			Hexagonal, one 6-fold symmetry axis			
No equivalent directions	General quadric	Not specified	Triclinic, no symmetry (at most a center of symmetry)	$\begin{bmatrix} S_{11} & S_{12} & S_{31} \\ S_{12} & S_{22} & S_{23} \\ S_{31} & S_{23} & S_{33} \end{bmatrix}$	6	Biaxial
		Principal axis parallel to crystal's symmetry axis	Monoclinic, one 2-fold symmetry axis	$\begin{bmatrix} S_1 & 0 & S_{31} \\ 0 & S_2 & 0 \\ S_{31} & 0 & S_3 \end{bmatrix}$	4	
		Principal axes aligned with crystal's symmetry axes	Orthorhombic, three perpendicular 2-fold symmetry axes	$\begin{bmatrix} S_1 & 0 & 0 \\ 0 & S_2 & 0 \\ 0 & 0 & S_3 \end{bmatrix}$	3	

Appendix 13B Poynting Vector in an Anisotropic Dielectric

The ray of geometrical optics was defined in Chapter 5, (5.4), as a unit vector $\hat{\mathbf{s}}$ normal to the wavefront and (see Problem 5.17) parallel to the Poynting vector **S**, i.e., parallel to the direction of energy flow. The theory of Chapter 13 is not suitable for use with geometrical optics or Huygens' principle, because it does not follow the flow of energy in the crystal but rather tracks the progress of **k** and the transverse displacement **D**. A suitable theory of propagation for use with geometrical optics must be built around the vectors **E** and **S**

rather than **D** and **k**. The theory follows a development parallel to the theory presented in Chapter 13; therefore, the results will be presented here in summary form.

We can determine **E** in terms of **D** in a manner analogous to (13.16) by using the following definitions. The unit vector in the direction of energy flow is

$$\hat{\mathbf{s}} = \frac{\mathbf{S}}{|\mathbf{S}|}$$

and the ray, or energy, index of refraction is defined as

$$n_r = \frac{c}{v_r}, \tag{13B.1a}$$

where v_r is called the *ray velocity*

$$\mathbf{v}_r = \frac{\mathbf{S}}{U}. \tag{13B.1b}$$

This velocity, parallel to the Poynting vector, is related to the velocity of the phase front of a wave through the relation

$$v_p = v_r \frac{\hat{\mathbf{s}} \cdot \mathbf{k}}{k} = v_r \cos\phi.$$

The relationship that yields **E** in terms of **D** is

$$\mathbf{E} = \frac{\mu_0 c^2}{n_r^2}[\mathbf{D} - \hat{\mathbf{s}}(\hat{\mathbf{s}} \cdot \mathbf{D})]. \tag{13B.2}$$

In Figure 13B.1, the various vectors associated with an electromagnetic wave propagating in an anisotropic medium are displayed. The Poynting vector (2.22) is perpendicular to

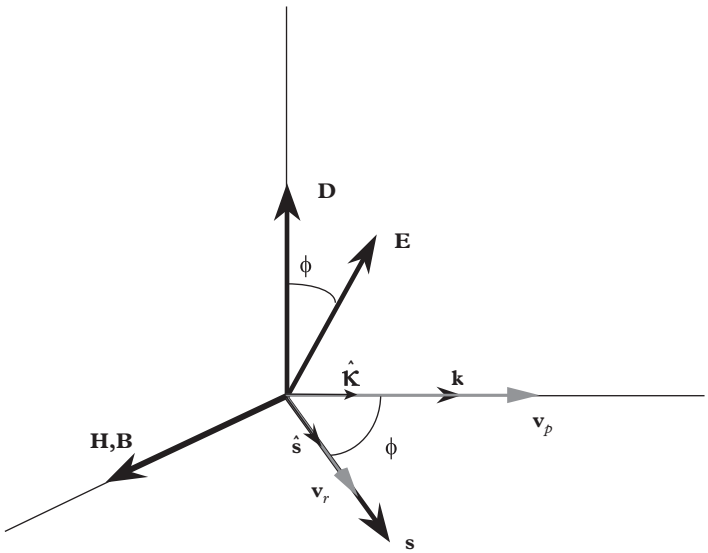

Figure 13B.1 *Relationship between the various vectors used in the discussion of the propagation of light in an anisotropic medium.*

both **E** and **H**, and, because **H** is normal to the plane formed by **D**, **E**, and **k**, the Poynting vector **S** will also be in that plane. However, unlike the case of propagation in an isotropic medium, (2.23), **S** is not parallel to **k**.

A Fresnel equation, equivalent to (13.14) but based upon the electric field representation of a wave, can be derived [1] using an approach similar to the one used to obtain (13.14). The resulting equation is called the *ray equation*:

$$\sum_{j=1}^{3} \frac{s_j^2}{v_r^2 - v_j^2} = \frac{1}{v_r^2}. \tag{13B.3}$$

Because (13B.3) is quadratic in v_r^2, there are two roots, v_{r1}^2 and v_{r2}^2, corresponding to two ray velocities. The *principal velocities* used in the ray equation,

$$v_j^2 = \frac{\varepsilon_0}{\varepsilon_j},$$

are not components of a wave velocity but rather material constants.

13B.1 Ray Ellipsoid

If in the equation for the electric energy density,

$$2U_E = \mathbf{D} \cdot \mathbf{E},$$

the electric field representation is used instead of the electric displacement, then (13.6) is replaced by

$$\varepsilon_x \frac{E_x^2}{2U_E} + \varepsilon_y \frac{E_y^2}{2U_E} + \varepsilon_z \frac{E_z^2}{2U_E} = 1. \tag{13B.4}$$

This equation describes an ellipsoid representing the dielectric tensor and called the *ray* or *Fresnel ellipsoid*. It has semi-axes that are proportional to the ray velocities (13B.1b) rather than to the index, as was the case for the optical indicatrix used in Chapter 13.

A plane cutting through this ellipsoid and passing through the origin, normal to $\hat{\mathbf{s}}$ (the unit vector parallel to the Poynting vector **S**), forms an ellipse at the intersection with the ellipsoid. The semi-axes of the ellipse have lengths proportional to the two ray velocities and directions parallel to $\mathbf{E}_1$ and $\mathbf{E}_2$.

Given the direction of **E**, we can find the direction of **D** using a construction equivalent to the one shown in Figure 13.14. In this construction, the normals to the planes that cut the ellipsoid at circular cross sections define the directions of the *optic ray axes* (or *biradials*). The optical ray axes are not in the same direction as the optical axes introduced in Chapter 13.

REFERENCE

1. Longhurst, R.S., *Geometrical and Physical Optics*. 3rd ed. 1974: Longman.

Appendix 13C Normal Surfaces

A geometrical construction called the *normal surface* or the *index surface* is quite helpful in understanding wave propagation in an anisotropic medium. Normal surfaces are constructed by plotting, in the direction of **k**, two vectors of lengths n_1 and n_2. The loci of the tips of all such vectors form the normal surfaces (see Figure 13C.1).

To determine the form of the normal surfaces, both sides of Fresnel's equation (13.14) are multiplied by n^2/k^2. The unit vector components $\kappa_i = k_i/k$ associated with the propagation vector are then defined, yielding the equation

$$\kappa_1^2 n_1^2 (n^2 - n_2^2)(n^2 - n_3^2) + \kappa_2^2 n_2^2 (n^2 - n_1^2)(n^2 - n_3^2) + \kappa_3^2 n_3^2 (n^2 - n_1^2)(n^2 - n_2^2) = 0. \quad (13C.1)$$

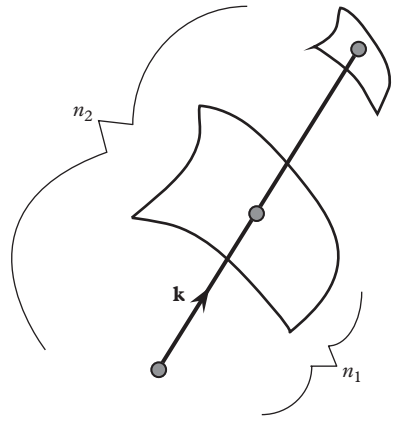

Figure 13C.1 *Construction of normal surfaces.*

13C.1 Biaxial Crystal

For a biaxial crystal, we retain the three indices of refraction in (13C.1). To visualize the shape of the surfaces described by (13C.1) for a biaxial crystal, we look at a cross section of the volume enclosed by (13C.1) by assuming that $\hat{\kappa} = (0, \kappa_y, \kappa_z)$:

$$(n^2 - n_1^2)[\kappa_2^2 n_2^2 (n^2 - n_3^2) + \kappa_3^2 n_3^2 (n^2 - n_2^2)] = 0. \quad (13C.2)$$

The solutions of (13C.2) are

$$n^2 = n_1^2, \quad (13C.3)$$

$$\frac{1}{n^2} = \frac{\kappa_2^2}{n_3^2} + \frac{\kappa_3^2}{n_2^2}. \quad (13C.4)$$

As can be seen from (13C.3), the index n_1 is independent of the direction of propagation in the (y, z) plane. The normal surface associated with this index is a circle, in this plane. Equation (13C.4) is the equation of an ellipse, and if we assume that $n_1 < n_2 < n_3$, the ellipse encloses a circle of radius n_1.

For a biaxial crystal, the cross sections of the normal surfaces in all three coordinate planes can be constructed using the procedure just outlined for the (y, z) plane. With some artistic license, the cross sections of the normal surfaces are displayed in Figure 13C.2; the differences between the indices have been exaggerated. The points of intersection of the two surfaces, labeled A in Figure 13C.2(b), define the optical axes for the normal surfaces. There are two optical axes for a biaxial crystal. The two polarizations have the same refractive index when **k** is parallel to the direction defined by a line passing from A through the origin.

13C.2 Uniaxial Crystal

To calculate the surfaces for a uniaxial crystal, we set $n_1 = n_2 = n_o$ and $n_3 = n_e$ in (13C.1), yielding

$$\kappa_1^2 n_o^2 (n^2 - n_o^2)(n^2 - n_e^2) + \kappa_2^2 n_o^2 (n^2 - n_o^2)(n^2 - n_e^2) + \kappa_3^2 n_e^2 (n^2 - n_o^2)^2 = 0. \quad (13C.5)$$

Because the propagation in the (x, y) plane is independent of direction $(n_1 = n_2 = n_o)$, we need only determine the two-dimensional normal surfaces in the (x, z) plane. Assume that a wave is propagating in the (x, z) plane, at an angle θ with respect to the z-axis,

$$\hat{\kappa} = (\sin\theta, 0, \cos\theta).$$

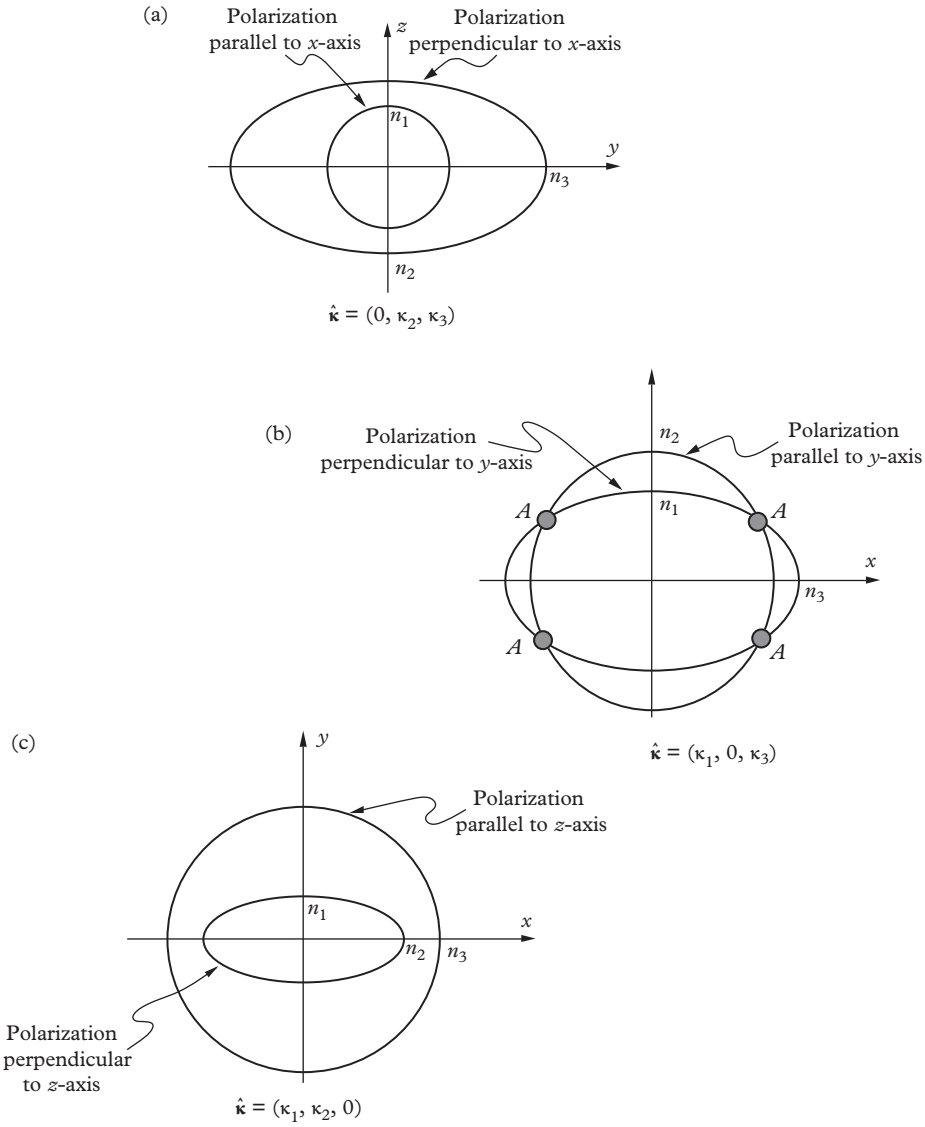

Figure 13C.2 *Cuts through the normal surfaces for a biaxial crystal in (a) the (y, z) plane; (b) the (x, z) plane; (c) the(x, y) plane.*

We may now rewrite (13C.5) as

$$(n^2 - n_o^2)[n_o^2(n^2 - n_e^2)\sin^2\theta + n_e^2(n^2 - n_o^2)\cos^2\theta] = 0.$$

Solutions of this equation are

$$n = n_o^2, \tag{13C.6}$$

$$\frac{1}{n^2} = \frac{\sin^2\theta}{n_e^2} + \frac{\cos^2\theta}{n_o^2}. \tag{13C.7}$$

The surfaces described by (13C.6) and (13C.7) are a circle and an ellipse. The points of intersection of the circle and ellipse define a single optical axis for a uniaxial crystal.

13C.3 Refraction in Crystals

We have derived Snell's law for light crossing a boundary from one isotropic medium to another by a number of techniques; here, we introduce yet another approach. The objective of this derivation is to derive what happens when light crosses the boundary between an isotropic and an anisotropic material.

We assume that a plane wave is incident from the isotropic medium onto a planar boundary at an incident angle of θ_i with respect to the normal of the boundary. We will require, as the boundary condition, that the phase of the plane wave not change as the boundary is crossed. The incident and transmitted waves are

$$\mathbf{E}_i = \mathbf{E}_0 e^{i(\omega t - \mathbf{k}\cdot\mathbf{r})}, \quad \mathbf{E}_t = \mathbf{E}_0 e^{i(\omega t - \mathbf{k}'\cdot\mathbf{r})},$$

and the boundary condition is

$$\omega t - \mathbf{k}\cdot\mathbf{r} = \omega t - \mathbf{k}'\cdot\mathbf{r}. \tag{13C.8}$$

A unit vector $\hat{\boldsymbol{\kappa}}$ is defined in the propagation direction,

$$\mathbf{k} = \frac{n\omega}{c}\hat{\boldsymbol{\kappa}}, \tag{13C.9}$$

where n is the index of the medium. To simplify the derivation, we will assume that the index of refraction of the first, isotropic, medium is 1, leading to the boundary condition

$$\mathbf{r}\cdot(n\hat{\boldsymbol{\kappa}}' - \hat{\boldsymbol{\kappa}}) = 0. \tag{13C.10}$$

The surface of the boundary is positioned at $z = 0$, with its normal parallel to the z-axis, and the vector $\mathbf{r}$ lies in the (x, y) plane. From (13C.10), we find that for this geometry, the vector $n\hat{\boldsymbol{\kappa}}' - \hat{\boldsymbol{\kappa}}$ must be normal to the surface.

A geometrical construction involving the index surfaces can be used to determine the allowed values for $\hat{\boldsymbol{\kappa}}'$ and $\hat{\boldsymbol{\kappa}}$ (see Figure 13C.3).[3] First select a point O on the boundary and construct the two index surfaces centered on O. From O, construct the unit vector $\hat{\boldsymbol{\kappa}}$. The only vectors that meet the condition (13C.10) are those of length OQ' or OQ'' that terminate on the two index surfaces labeled n' and n''. Each incident wave will undergo double refraction and generate two refracted waves $n'\hat{\boldsymbol{\kappa}}'$ and $n''\hat{\boldsymbol{\kappa}}''$.

[3] We will use the term "index surface" here to prevent confusion with the normal to a surface.

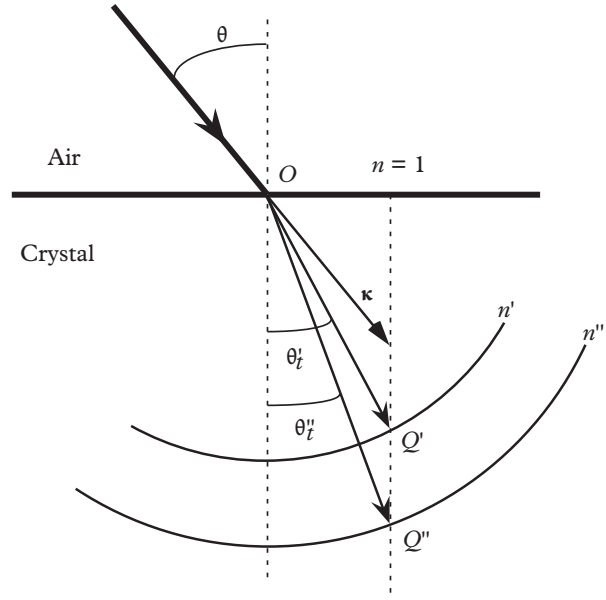

Figure 13C.3 *Reflection at the boundary of an anisotropic medium.*

Since we know that the frequency is unchanged across the boundary at $z = 0$, we can rewrite (13C.8) as

$$\mathbf{r} \cdot \hat{\boldsymbol{\kappa}} = \mathbf{r} \cdot n' \hat{\boldsymbol{\kappa}}' = \mathbf{r} \cdot n'' \hat{\boldsymbol{\kappa}}'', \tag{13C.11a}$$

$$x\kappa_x + y\kappa_y = n'(x\kappa'_x + y\kappa'_y) = n''(x\kappa''_x + y\kappa''_y). \tag{13C.11b}$$

This equation must be obeyed for all x and y, and thus

$$\frac{\kappa'_x}{\kappa_x} = \frac{\kappa'_y}{\kappa_y} = \frac{\kappa''_x}{\kappa_x} = \frac{\kappa''_y}{\kappa_y}.$$

From these relationships, we learn that the propagation vectors of the two transmitted waves must lie in the plane of incidence and that θ'_t and θ''_t, shown in Figure 13C.3, are given by

$$\frac{\sin\theta_i}{\sin\theta'_t} = n', \quad \frac{\sin\theta_i}{\sin\theta''_t} = n''. \tag{13C.12}$$

The velocity of propagation is independent of direction for the spherical index surface (the ordinary wave), with index of refraction n'. For the orthogonal polarization, the index n'' is a function of direction, given by (13C.7) for a uniaxial crystal. Snell's law is no longer obeyed, and the simple relationship must be replaced.

Appendix 13D Ray Surfaces

A useful construction that allows ray tracing in an anisotropic material is called the *ray surface*. It is based upon the theoretical evaluation of wave propagation formulated around the orthogonal vectors **E** and **S**. In this appendix, we will see how the ray surfaces can be used along with Huygens' principle to follow the propagation of a ray in an anisotropic material.

In the same way that normal surfaces were generated in Appendix 13C, we can generate ray surfaces. The procedure generates two surfaces by plotting, in the direction of $\hat{\mathbf{s}}$ (the unit vector parallel to the Poynting vector **S**), the two ray velocities associated with that direction. Either of the surfaces, ray or normal, can be used to produce the other.

To generate the ray surfaces, we proceed as we did in Appendix 13C for the normal surfaces. Starting with (13B.3), a general equation for the ray surfaces can be generated:

$$s_1^2 v_1^2 (v_r^2 - v_2^2)(v_r^2 - v_3^2) + s_2^2 v_2^2 (v_r^2 - v_1^2)(v_r^2 - v_3^2) + s_3^2 v_3^2 (v_r^2 - v_1^2)(v_r^2 - v_2^2) = 0. \tag{13D.1}$$

This equation has the same form as (13C.1) for the normal surfaces.

To determine the shape of the ray surfaces a procedure parallel to the one used in Appendix 13C is followed. The ray surfaces appear identical to the normal surfaces, but they are not.

To demonstrate that the normal and ray surfaces are different, we will examine the cross section of the ray surfaces in the (x, z) plane:

$$\hat{\mathbf{s}} = (s_1, 0, s_3),$$
$$s_1^2 v_1^2 (v_r^2 - v_2^2)(v_r^2 - v_3^2) + s_3^2 v_3^2 (v_r^2 - v_1^2)(v_r^2 - v_2^2) = 0.$$

One of the ray surfaces is described by the equation

$$v_r^2 = v_2^2, \tag{13D.2}$$

and the second surface is described by

$$\frac{s_1^2}{v_3^2} + \frac{s_3^2}{v_1^2} = \frac{1}{v_r^2}. \tag{13D.3}$$

To display the ray surface, we assume that $v_1 > v_2 > v_3$. The ray surfaces just calculated for the (x, z) plane are shown in Figure 13D.1. The points labeled B define the directions in which there is only one ray velocity. An optical axis is defined as the direction for which there is only one phase velocity, but the ray velocity is not normal to the phasefront and thus is not parallel to the phase velocity. Thus, the directions determined by the points labeled B in Figure 13D.1 are not parallel to the optical axes.

The ray surface has the physical significance of being the locus of all points reached in unit time by a wave disturbance starting from a point source at the origin. Thus, the ray surface can be used with Huygens' principle to generate the ray path taken in an anisotropic medium. Figure 13D.2 displays how one would find the direction of the transmitted rays in a uniaxial crystal using the ray surfaces. At time $t = 0$, the wavefront AA' reaches point O. At time t_1, point P' of the wavefront reaches point P. During the time t_1, two waves can be assumed to have radiated out from point O according to Huygens' principle. The ordinary ray surface would be a circle of radius PP'/n_o. The extraordinary ray surface would be an

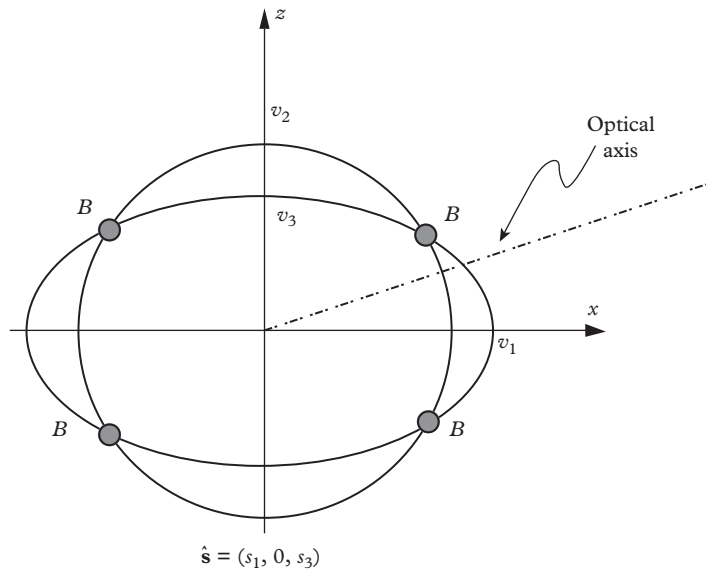

Figure 13D.1 *Ray surface cross section for a uniaxial crystal. Note that the optical axis is not in the same direction as the direction for a single ray velocity.*

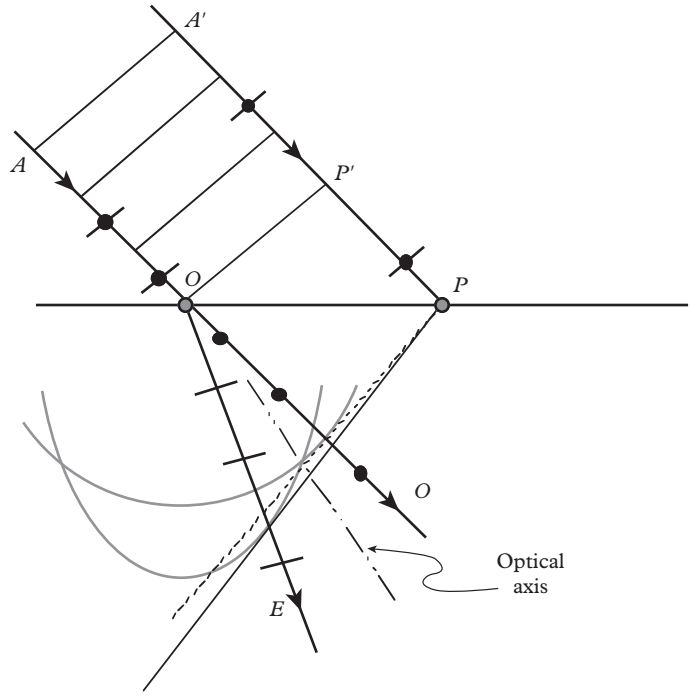

Figure 13D.2 *Use of Huygens' principle in an anisotropic crystal.*

ellipse with major axis PP'/n_e. The refracted rays are the normals to planes from point P, tangent to the two ray surfaces. The direction of **D** is indicated on the two rays.

The ray geometry view of anisotropy is useful for qualitative discussions of double refraction, but for quantitative work, the index geometry used in Appendix 13C is more convenient. It is for this reason that we find an equivalent approach to the normal surfaces in other problems of wave propagation in anisotropic materials. For example, in solid state physics, the Fermi surface (an index surface) is used in the study of propagation of electrons in solids.

14 Optical Modulation

14.1 Introduction 602
14.2 Electro-optic Effect 604
14.3 Electro-optic Indicatrix 606
14.4 Amplitude Modulation 612
14.5 Modulator Design 621
14.6 Magneto-optic Effect 623
14.7 Photoelastic Effect 630
14.8 Acousto-optics 634
14.9 Summary 646
14.10 Problems 648
References 649
Appendix 14A: Pockels and Kerr Tensors 649
Appendix 14B: Phenomenological Acousto-optic Theory 653
Appendix 14C: Acoustic Figure of Merit 662

14.1 Introduction

Many applications incorporating optics require the capability of temporally modifying the amplitude, phase, direction, or frequency of the light wave. For example, in fiber-optic communications, the amplitude of a light wave is encoded with a desired signal, and the wave's frequency is adjusted to allow multiplexing of a number of signals. In information storage (e.g., compact disks), a light wave's intensity is encoded with an audio signal that is then recorded by modifying the reflective properties of the disk. In printing and photocopying, a laser source's intensity is encoded with information while the beam is scanned over a photosensitive medium. Finally, for entertainment and displays, such as laser light shows, a number of laser beams are rapidly scanned over a display screen in artistic patterns.

When a light wave has one of its parameters modified with respect to time, it is said to be *modulated*, and the device accomplishing this modification is called a *modulator*. Modulation may be accomplished by modifying the intensity of the light source, as is done, for example, by varying the current in semiconductor injection lasers. The intensity or the direction of a wave can be modulated by mechanical means through the use of a simple shutter, a chopper (a disk with apertures cut in its circumference), or a moving optical component such as a mirror, a hologram, or a microelectromechanical structure (MEMS) as shown in Figure 14.1. Finally, modifying the medium through which it propagates can modulate an optical wave.

In this chapter, we will examine in detail the use of an electric, magnetic, or stress field to modify the optical properties of a medium. The application of one of these disturbances

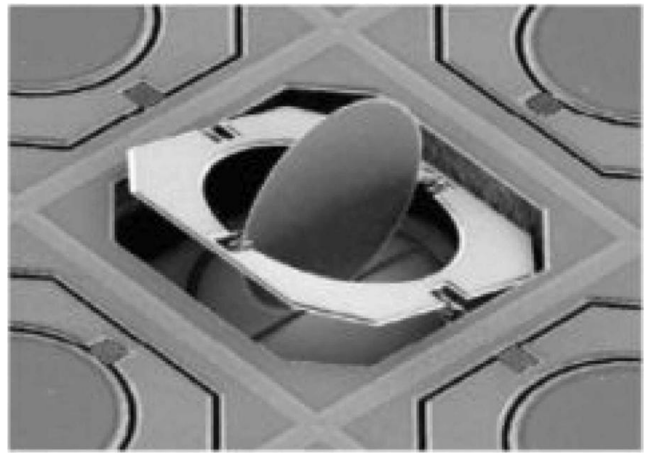

Figure 14.1 *A single element of a MEMS mirror array. (Courtesy of Jungsang Kim, Duke University.)*

Modern Optics. Second Edition. B. D. Guenther.

© B. D. Guenther 2015. Published in 2015 by Oxford University Press.

to the medium produces an anisotropy that requires a tensor description. The nonzero elements of the various tensors needed in this chapter are listed in Appendix 14A.

The application of an electric field causes the electrons, ions, and permanent dipoles, if they exist, to reorient, inducing an electric polarization. The induced polarization produces an anisotropy that creates a birefringence. The field-dependent birefringence modifies the optical polarization of a light wave propagating through the medium. The theory describing the birefringence induced by an electric field will be developed based on changes in the optical indicatrix induced by the field. The theory will assume that the change in index of refraction with applied field is small and can be described by a series expansion in powers of the applied electric field. The applied field contains both the optical field and an AC electric field. In this chapter, we will assume that the optical field is small and will neglect it.[1]

In materials with a center of symmetry, only even powers of the AC electric field are found in the description of the index change. A very simple theory will be used to derive the quadratic dependence of the index of refraction. In materials without a center of symmetry, the quadratic field dependence of the index of refraction is overshadowed by linear field dependence. A brief analysis will be made to demonstrate the modifications to the optical indicatrix that arise from this linear field dependence.

Both the linear and the quadratic electric field effects induce a birefringence in the material. The induced birefringence results in an electric-field-dependent phase difference between two orthogonally polarized waves propagating in the material. If a polarized wave is incident upon the material, the polarization of the wave exiting the material will be modified by an amount proportional to the electric field. The technique used to convert the modification of the polarization to an intensity modulation will be described and its implementation in the design of an electro-optic modulator will be discussed.

To describe the modification of optical properties of a material by a magnetic field, we will add a static magnetic field to the molecular model introduced in Chapter 7. The magnetic field induces microscopic currents. The induced currents lead to an equation for the index of refraction that predicts different propagation velocities for right- and left-circularly polarized waves. The propagation velocities will be shown to depend upon the "handedness" of the circularly polarized light, relative to the circulating currents.

Application of a stress to a material modifies the optical properties of the material by producing an anisotropy in the density of the material. The spatial density variation produces a birefringence in the material that can be treated in terms of a distortion of the optical indicatrix. The stress-induced birefringence modifies the polarization of a light wave as it propagates through the material. By observing the modification of polarized light by the material under stress, a measurement of the size and location of the stress can be obtained.

A time-varying stress can be regarded as an acoustic wave. The theory used to explain light modulation by an acoustic wave is based upon scattering theory. The scattering process modifies the direction and frequency of the light wave, and the modification can be predicted through the use of the laws of conservation of energy and of momentum. The uses of an acousto-optic modulator as a beam deflector and as a frequency modulator are discussed in light of the predictions of the scattering theory.

In Appendix 14B, a phenomenological theory of the acousto-optic process will be given, based on the change in index of refraction produced by the density modulation created by a sound wave. In Appendix 14C, a figure of merit is defined that can be used to evaluate the performance of an acousto-optic device.

Michael Faraday made the first observation of externally modified optical properties, in 1845. Faraday observed that an achiral (not chiral) material could rotate the orientation of the plane of polarization of a light wave if a strong magnetic field was applied to the

[1] In Chapter 15, we will discuss the physical behavior of materials in the presence of large optical fields.

material, parallel to the light's propagation direction. This effect is now called the *Faraday* or *magneto-optic effect*.

In 1876, **John Kerr (1824–1907)** observed that optically isotropic materials exhibited uniaxial, birefringent behavior when placed in an electric field. This effect, called the *Kerr effect*, has a quadratic dependence on the applied electric field. A very simple theory will be presented that gives the proper wavelength dependence. The theory will be used to design an optical shutter.

Another electro-optic effect, first observed by **Wilhelm Conrad Röntgen** in quartz, is the linear electro-optic effect, called the *Pockels effect*.[2] This electro-optic effect varies linearly with the applied field.

In 1901, Kerr observed a second optical effect due to a magnetic field perpendicular to the optical propagation direction. The effect, observed in fluids, caused the material to exhibit a birefringence with a quadratic dependence on the magnetic field. This effect was discovered in 1907, by **Aimé Auguste Cotton (1869–1951)** and **Henri Mouton (1869–1935)** and thus is associated with their names.

Brewster discovered in 1816 that an applied mechanical stress could modify the optical properties of a material. This behavior is known as *mechanical birefringence*, *photoelasticity*, or *stress birefringence*. In 1921, Brillouin, who developed a theory treating the compression waves of sound as a grating and describing the interaction of light and sound in terms of diffraction, suggested the interaction's usefulness in optical modulation. Debye and Sears, and, independently, Lucas and Biquard, observed the diffraction of light by sound waves in 1932.

14.2 Electro-optic Effect

In Chapter 7, a linear relationship between the applied electric field and the material field, (7.16), was adequate to describe the behavior of light propagating in a medium. The linear theory could be used because the only field under consideration was a small optical field. In this chapter, we will continue to assume that the optical field is quite small, but will assume that a second, larger, time-dependent electric field, the modulation field, is also present. The modulation field increases the total applied electric field to a value sufficient to produce nonlinear behavior. The nonlinear behavior can be modeled by modifying the linear theory using a series expansion of the internal field in terms of powers of the applied field.

The modulation field introduces a preferred direction, creating anisotropic behavior in the material under study. The dielectric constant generated by the model will therefore be a tensor, which will be shown to be symmetric if there are no losses in the material. An ellipsoid, similar to the one introduced in Chapter 13, can be used to describe the properties of the symmetric tensor. In this section, we will present the basic tensor equation for $1/n^2$ and simplify the equation by assuming that the applied light field is small. The resulting equation will be a function of only the modulation field.

We assume that two applied fields, at frequencies ω_1, the modulation frequency, and ω_2, an optical frequency, are imposed on the optical material. The amplitude of the modulation field is assumed to be much larger than that of the light field, $E_1 \gg E_2$. The applied fields produce a small change in the index of refraction of the material, so we may expand,

$$\frac{1}{n^2} = \wp = \frac{\varepsilon_0}{\varepsilon},$$

[2] Because Friedrich Carl Alwin Pockels (1865–1913) studied the effect extensively, it bears his name.

the impermeability tensor, in a power series in the total applied field:

$$\mathfrak{I}_{ik} = \frac{\varepsilon_0}{\varepsilon_{ik}} = \mathfrak{I}_{ik}^0 + \sum_{j=1}^{3} r_{ikj} E_j^{\omega} + \sum_{j=1}^{3}\sum_{m=1}^{3} \rho_{ikjm} E_j^{\omega} E_m^{\omega} + \ldots, \tag{14.1}$$

where

$$\varepsilon_{ik}^0 = \frac{\varepsilon_0}{\mathfrak{I}_{ik}^0}$$

is the zero-field dielectric constant. The term linear in the electric field describes the Pockels effect, and the constants r_{ijk} are the *linear electro-optic coefficients* or *Pockels coefficients*. The term displaying a quadratic dependence on the electric field describes the Kerr effect, and the constants ρ_{ijkm} are the *quadratic electro-optic coefficients* or *Kerr coefficients*. The definition of the Pockels and Kerr constants in terms of the reciprocal dielectric tensor allows the use of the index ellipsoid in the discussion of the electro-optic behavior of a crystal.

The applied field is made up of the optical and modulation fields:

$$\mathbf{E}^{\omega} = \mathbf{E}^{\omega_1} \cos\omega_1 t + \mathbf{E}^{\omega_2} \cos\omega_2 t. \tag{14.2}$$

where we have hidden any spatial variation of the applied field in the amplitude. Using this applied field, we may rewrite (14.1) as

$$\begin{aligned}\mathfrak{I}_{ik} = {} & \mathfrak{I}_{ik}^0 + \sum_{j=1}^{3} r_{ikj}(E_j^{\omega_1} \cos\omega_1 t + E_j^{\omega_2} \cos\omega_2 t) \\ & + \sum_{j=1}^{3}\sum_{m=1}^{3} \frac{\rho_{ikjm}}{2}[(E_j^{\omega_1} E_m^{\omega_1} + E_j^{\omega_2} E_m^{\omega_2}) + E_j^{\omega_1} E_m^{\omega_1} \cos 2\omega_1 t + E_j^{\omega_2} E_m^{\omega_2} \cos 2\omega_2 t] \\ & + \sum_{j=1}^{3}\sum_{m=1}^{3} \frac{\rho_{ikjm}}{2}(E_j^{\omega_1} E_m^{\omega_2} + E_j^{\omega_2} E_m^{\omega_1})[\cos(\omega_1 + \omega_2)t + \cos(\omega_1 - \omega_2)t].\end{aligned} \tag{14.3}$$

Each component of (14.3) is a function of the fundamental frequencies, their harmonics, or the sum and difference frequencies. In its most general form, we know from Chapter 13 that (14.3) must be a tensor. We will divide $\mathfrak{I}$ into a set of tensors associated with each of these frequencies

$$\mathfrak{I} = \mathfrak{I}^{\,0} + \mathfrak{I}^{\,\omega_1} \cos\omega_1 t + \mathfrak{I}^{\,\omega_2} \cos\omega_2 t + \mathfrak{I}^{\,2\omega_1 t} \cos 2\omega_1 t + \cdots.$$

Each tensor can be represented by an ellipsoid, as was done in Chapter 13 for naturally occurring birefringence. Each ellipsoid will have its own orientation, allowable planes of polarization, etc.

In this chapter, we will assume that the electric field associated with ω_1 is much larger than the optical field, $E^{\omega_1} \gg E^{\omega_2}$, which will allow terms containing ω_2 to be ignored. By neglecting terms involving the optical field, we can write (14.1) as a function of only the modulation field:

$$\mathfrak{I}_{ik} = \mathfrak{I}_{ik}^0 + \sum_{j=1}^{3} r_{ikj} E_j \cos\omega t + \sum_{j=1}^{3}\sum_{m=1}^{3} \rho_{ikjm} E_j E_m (2\cos^2\omega t) + \cdots, \tag{14.4}$$

where we have suppressed the superscript ω_1. In the remainder of this chapter, the reader should remember that the applied field will only refer to the modulating field.

The coefficients of the two tensors, r_{ijk} and ρ_{ikjm}, are determined by the material's symmetry. Appendix 14A gives the nonzero coefficients for the 32 crystal point groups that are optically distinguishable.

A *center of symmetry*, or *inversion center*, exists at a point if there is no change in the atomic arrangement when each atom, a vector **r** away from the point, is replaced by one **–r** away. If a material has a center of symmetry, then reversing the field **E** should not change any physical property. Consider the one-dimensional case where we assume that the application of a field E to a material produces a change in the index of refraction of $\Delta n_1 = rE$, where r is a constant characterizing the linear electro-optic effect. If we reverse the applied field E, then $\Delta n_2 = -rE$. However, if the material has inversion symmetry, then $\Delta n_1 = \Delta n_2$, which implies $r = -r$. This can only be true for $r = 0$. Therefore, materials with inversion symmetry (e.g., liquids) will not exhibit a Pockels effect. The electro-optic effect displayed by these materials is the Kerr effect. In materials with no inversion symmetry, the Kerr effect will be masked by the larger Pockels effect.

The derivation of the electro-optic properties of materials used in this chapter is based upon an expansion of the impermeability tensor in terms of the electric field. An equivalent description, based upon the material's dielectric polarization, can be made and is often encountered in the literature. The constants in the polarization-based expansion are called the *polarization-optic coefficients* and have a simple relationship to the electro-optic coefficients that will be discussed here. The mathematical formalism associated with the dielectric polarization is identical to this presentation, and the two descriptions can be interchanged. The similarities between the two descriptions make it unnecessary to discuss the polarization formalism.

14.3 Electro-optic Indicatrix

14.3.1 Pockels Effect

In materials without a center of symmetry, the dominant interaction is the Pockels effect. The objective of the discussion in this section is to obtain an expression for the index of refraction change produced, through the Pockels effect, by the application of a modulation field to the material. We will discuss later in this chapter how this index change can be used to produce amplitude modulation of a light wave.

The Pockels effect exhibits dispersion associated with a number of different physical processes. In the simple theory presented here, we will ignore dispersion. A brief discussion of the various physical processes leading to dispersion will explain why it may be neglected.

All crystals that exhibit the linear electro-optic effect are also *piezoelectric*; i.e., the application of an electric field will produce macroscopic deformations of the material—strains. In fact, the Pockels tensor and the piezoelectric tensor have identical symmetries. The strains produced by the piezoelectric effect will modify the indices of refraction, producing a second interaction affecting the optical properties of the material, known as the *photoelastic effect* (or the *strain-optic effect*). We can ignore the complications introduced by the feedback from the photoelastic effect if we clamp the crystal or if the modulation frequency is above

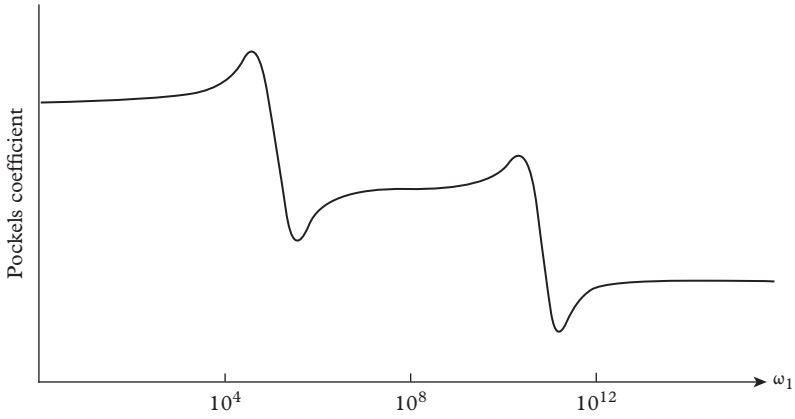

Figure 14.2 *Dispersion curve for the Pockels coefficient for an idealized material. Only one mechanical resonance at about 1 MHz is shown. No electronic resonances are displayed.*

the frequency of the fundamental mechanical resonance of the solid; typically, mechanical resonances lie below 1 MHz.

Between 1 and 100 MHz, at harmonics of the mechanical resonance, the photoelastic effect can again become important, but above 100 MHz, the crystal can no longer undergo macroscopic deformation. Above 1 THz, electron motion is the only contribution to the linear electro-optic effect. Between 10 GHz and 1 THz, both atomic and electronic motions contribute to the field-induced polarization. In Figure 14.2, an idealized dispersion curve for the Pockels coefficient is displayed. We select an optical frequency ω_2 of the order of 10^{15} Hz and restrict the range of modulation frequencies ω_1 to between 1 MHz and 10 GHz. By limiting the frequencies of the applied electric fields to these ranges and staying away from harmonics of the fundamental mechanical resonance, we eliminate the need to consider dispersion effects.

Some values of Pockels coefficients for electro-optic materials used as optical modulators are shown in Table 14.1.

When an electric field is applied to a crystal, the general equation for the indicatrix can be obtained from (13A.4):

$$\sum_{i=1}^{3}\sum_{j=1}^{3}\sum_{k=1}^{3}\sum_{m=1}^{3}\left(\mathfrak{s}_{ij}+r_{ijk}E_k+\rho_{ijkm}E_kE_m\right)x_jx_i=1, \tag{14.5}$$

where the time dependence of the electric field is not shown explicitly. The material is assumed to have no center of symmetry, so only the linear electro-optic effect is observable; i.e., $\rho_{ijkm} \ll r_{ijk}$.

We define a coordinate system with the wavevector along x_3 and the applied field along x_1, as shown in Figure 14.3. The indicatrix cross section, taken through $x_3 = 0$, is described by the equation

$$\left(\frac{1}{n_1^2}+r_{11}E_1\right)x_1^2+\left(\frac{1}{n_2^2}+r_{21}E_1\right)x_2^2+2r_{61}E_1x_1x_2=0. \tag{14.6}$$

We have used the definition $1/\mathfrak{s}=\varepsilon/\varepsilon_0=n^2$ and are neglecting any simplification that may result owing to crystal symmetry.

Table 14.1 *Pockels coefficients*

Material	Crystal class	n	r (10^{-12} m/V)
$BaTiO_2$	4*mm*	$n_1 = 2.480$ $n_3 = 2.426$	$r_{33} = 28$ $r_{13} = 8$ $r_{51} = 820$
$KNbO_3$	*mm*2	$n_1 = 2.279$ $n_2 = 2.329$ $n_3 = 2.167$	$r_{33} = 25$ $r_{13} = 10$
$LiNbO_3$	3*m*	$n_1 = 2.272$ $n_3 = 2.187$	$r_{33} = 30.8$ $r_{51} = 30.8$ $r_{13} = 30.8$ $r_{22} = 30.8$
ZnS	6*mm*	$n_o = 2.135$	$r_{33} = 1.8$ $r_{13} = 0.9$
$Bi_{12}SiO_{20}$	23	$n_o = 2.54$	$r_{41} = 5.0$
GaAs	$\bar{4}3m$	$n_o = 3.6$	$r_{41} = -1.5$
Quartz	32	$n_o = 1.544$ $n_e = 1.553$	$r_{41} = 1.4$ $r_{11} = 0.59$

For the moment, we will ignore the term containing r_{61}. The effect on (14.6) of the term involving $r_{11}E_1$ is to modify the index of refraction along the x_1 axis:

$$\frac{1}{(n_1 + \Delta n_1)^2} = \frac{1}{n_1^2} + r_{11}E_1. \tag{14.7}$$

Using the geometrical representation of the tensor, the dimension of the indicatrix along x_1 is changed by the applied field. Since $\Delta n_1 \ll n_1$ (Δn is of the order of 10^{-4} for fields below 20 kV/cm), we can use the binomial expansion to write

$$\frac{1}{(n_1 + \Delta n_1)^2} \approx \frac{1}{n_1^2} - \frac{2\Delta n_1}{n_1^3} = \frac{1}{n_1^2} + r_{11}E_1.$$

The change in index due to the field is obtained by equating equivalent terms:

$$\Delta n_1 \approx -\frac{n_1^3 r_{11} E_1}{2}. \tag{14.8}$$

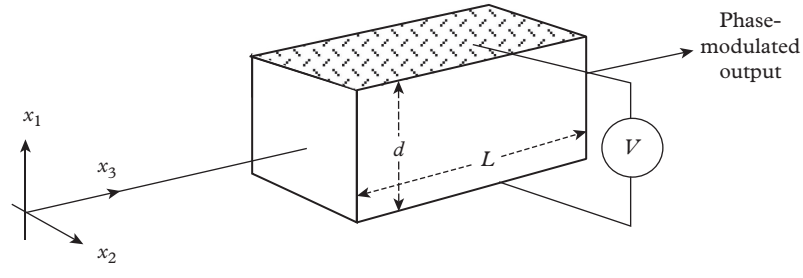

Figure 14.3 *Geometry of electro-optic analysis.*

Using the same reasoning for the x_2 direction,

$$\Delta n_2 \approx -\frac{n_2^3 r_{21} E_1}{2}. \tag{14.9}$$

A polarized light wave propagating along the x_3 direction can be described by two linearly polarized waves: one with its electric field along the x_2 direction and the other with its electric field along the x_1 direction:

$$E(x_2) = A_2 e^{i(\omega t - k_0 n_2 x_3)}, \quad E(x_1) = A_1 e^{i(\omega t - k_0 n_1 x_3)}, \tag{14.10}$$

where k_0 is the magnitude of the wavevector in free space. The relative phases of the two orthogonal polarization components depend upon n_i ($i = 1$ or 2). After traveling a distance L in the x_3 direction in the crystal, the change in phase of the two polarization components in (14.10) is

$$\begin{aligned} -k_0 L[n_2 - (n_2 + \Delta n_2)] &= -\frac{k_0 n_2^3 r_{21} E_1 L}{2}, \\ -k_0 L[n_1 - (n_1 + \Delta n_1)] &= -\frac{k_0 n_1^3 r_{11} E_1 L}{2}. \end{aligned} \tag{14.11}$$

If the applied field E_1 varies sinusoidally with time, then the relative phase between the two polarizations will also vary sinusoidally and phase modulation will occur. In Section 14.4, we will describe how this phase modulation can be converted into amplitude modulation.

We now return to (14.6) to consider the previously ignored third term,

$$2r_{61} E_1 x_1 x_2.$$

The effect of this term on the elliptical cross section of the indicatrix described by (14.6) is to rotate the axes of the ellipse through an angle α (see Figure 14.4), where α is given by

$$\tan 2\alpha = \frac{2r_{61} E_1}{\dfrac{1}{n_1^2} - \dfrac{1}{n_2^2} + (r_{11} - r_{21}) E_1}. \tag{14.12}$$

The angle α is small if the natural birefringence of the crystal, $n_1 - n_2$, is large. Any change in n_1 and n_2 due to rotation is a second-order effect and can be neglected. However, we cannot

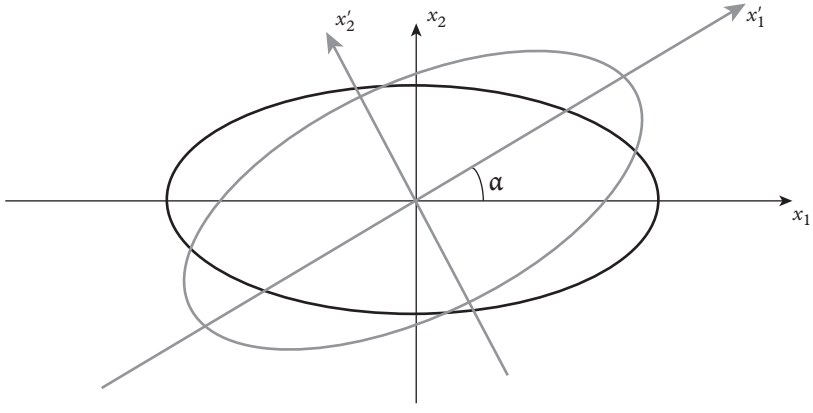

Figure 14.4 *Rotation of indicatrix cross section by the applied electric field.*

simply ignore the effect of $r_{61}E_1$, because the index of refraction for a wave polarized along the direction 45° to x_1 and x_2 (denoted by n') will vary linearly with a change in E_1:

$$\Delta n' = \frac{n'^3 r_{61} E_1}{2}. \tag{14.13}$$

To eliminate the complication introduced by the third term in (14.6), a coordinate transformation is found that eliminates all cross products $x_i x_j$. We will see how this step is accomplished a little later.

14.3.2 Kerr Effect

When a material has inversion symmetry, the Pockels effect will be absent and the observable electro-optic effect will be the Kerr effect. The Kerr effect was the first electro-optic process to find application, owing to the fact it was easy to obtain a modulator material with good optical properties. A liquid or a glass can be used as a modulator material, and, because natural birefringence is absent, a modulator constructed with these isotropic materials can handle a diverging or converging beam of light. The drawback of this effect is the large electric fields that must be used and the fact that the modulation is dependent upon the square of the applied electric field. Today, because of the availability of large strain-free transparent crystals, the Pockels modulator has replaced the Kerr device in many applications.

In this section, we will derive a relationship for the change in index of refraction due to the quadratic electro-optic effect. The theory presented here is a phenomenological theory that cannot be used for predictive purposes. However, it does provide some justification for the wavelength dependence of the Kerr constant that is observed in liquids.

One type of material with inversion symmetry is an isotropic material such as a fluid. The field-free dielectric constant of an isotropic material is a scalar, so (14.4) must be rewritten as

$$\mathfrak{e}_{ik} = \mathfrak{e}^0 + \sum_{j=1}^{3}\sum_{m=1}^{3} \rho_{ikjm} E_j E_m. \tag{14.14}$$

From Table 14A.3 in Appendix 14A, the nonzero coefficients of the Kerr tensor for an isotropic medium can be used to write (14.14) in matrix form:

$$\begin{bmatrix} \mathfrak{e}_{11} \\ \mathfrak{e}_{12} \\ \mathfrak{e}_{13} \\ \mathfrak{e}_{14} \\ \mathfrak{e}_{15} \\ \mathfrak{e}_{16} \end{bmatrix} = \begin{bmatrix} \mathfrak{e}^0 \\ \mathfrak{e}^0 \\ \mathfrak{e}^0 \\ 0 \\ 0 \\ 0 \end{bmatrix} + \begin{bmatrix} \rho_{11} & \rho_{12} & \rho_{12} & 0 & 0 & 0 \\ \rho_{12} & \rho_{11} & \rho_{12} & 0 & 0 & 0 \\ \rho_{12} & \rho_{12} & \rho_{11} & 0 & 0 & 0 \\ 0 & 0 & 0 & \rho_{11}-\rho_{12} & 0 & 0 \\ 0 & 0 & 0 & 0 & \rho_{11}-\rho_{12} & 0 \\ 0 & 0 & 0 & 0 & 0 & \rho_{11}-\rho_{12} \end{bmatrix} \begin{bmatrix} E_1^2 \\ E_2^2 \\ E_3^2 \\ E_2E_3 \\ E_3E_1 \\ E_1E_2 \end{bmatrix}$$

$$= \mathfrak{e}^0 + \begin{bmatrix} \rho_{11}E_1^2 + \rho_{12}E_2^2 + \rho_{12}E_3^2 \\ \rho_{12}E_1^2 + \rho_{11}E_2^2 + \rho_{12}E_3^2 \\ \rho_{12}E_1^2 + \rho_{12}E_2^2 + \rho_{11}E_3^2 \\ (\rho_{11}-\rho_{12})E_2E_3 \\ (\rho_{11}-\rho_{12})E_3E_1 \\ (\rho_{11}-\rho_{12})E_1E_2 \end{bmatrix}.$$

By orienting the coordinate system along the principal axes [see (13A.5)], we can make all terms in the tensor zero except for the principal elements, which, as we see in the above matrix, are all equal:

$$\rho_{11} = \rho_{22} = \rho_{33} = \rho.$$

We orient the applied electric field along the z-axis, reducing (14.14) to three equations. The first of these equations yields the index of refraction parallel to the electric field:

$$\mathfrak{I}_{\parallel} = \mathfrak{I}^0 + \rho E^2 = \frac{1}{n_e^2}. \tag{14.15}$$

The second and third equations are identical and represent the index of refraction normal to the electric field:

$$\mathfrak{I}_{\perp} = \mathfrak{I}^0 = \frac{1}{n_0^2}. \tag{14.16}$$

Thus, in the presence of an applied electric field, the isotropic material behaves like a uniaxial crystal with an optical axis parallel to the electric field. The change from the field-free index of refraction n_0 to n_e is small, allowing the use of the binomial expansion to give

$$\begin{aligned}\frac{1}{n_e^2} &= \frac{1}{(n_0 + \Delta n_0)^2} \\ &= \frac{1}{n_0^2} - \frac{2\Delta n_0}{n_0^3} \\ &= \frac{1}{n_0^2} + \rho E^2.\end{aligned}$$

Experimentally, it has been determined that the index difference between the ordinary and extraordinary indices due to the induced birefringence is

$$\Delta n = \mathcal{K} E^2 \lambda,$$

where $\mathcal{K}$ is called the *Kerr constant*. This index difference produces a phase difference between two orthogonally polarized waves of

$$\begin{aligned}\Gamma &= 2\pi \frac{\Delta n L}{\lambda} \\ &= 2\pi \mathcal{K} E^2 L.\end{aligned}$$

From the above derivation, the relative phase difference between the ordinary and extraordinary waves produced by the Kerr effect is

$$\begin{aligned}\Gamma &= k_0(n_e - n_0)L \\ &= k_0(n_0 + \Delta n_0 - n_0)L \\ &= \frac{2\pi}{\lambda}\Delta n_0 L \\ &= \frac{\pi}{\lambda} n_0^3 \rho E^2 L.\end{aligned} \tag{14.17}$$

Table 14.2 *Kerr coefficient and half-wave voltage*

Type	Material	$\mathcal{K}$(esu)[a]	$V_{\lambda/2}$ (kV)	
			3.2 × 5 cm cell	0.3 × 0.1 cm cell
Liquid	Nitrobenzene	33.0×10^{-6}	52.8	6.7
	o-Dichlorobenzene	4.6	142	18.1
	Acrylonitrile	7.8	109	13.7
	Benzonitrile	12.1	87.3	11
	Acetonitrile	4.7	140	17
Gas	CO_2 (STP)	2.5×10^{-11}		7700
Solid	Glass (typical)	9.0×10^{-9}		406

[a]To convert from esu to MKS units, divide by 9×10^6. The Kerr coefficient then has units of m/V^2.

Equating this result to the experimentally determined relationship yields a Kerr constant that is given by

$$\mathcal{K} = \frac{n_0^3 \rho}{2\lambda}.$$

A molecular theory of the Kerr effect in fluids also predicts the λ^{-1} dependence [1].

We can define a *half-wave voltage* as the voltage that when applied to a Kerr cell with thickness d and length L gives $\Gamma = \pi$:

$$V_{\lambda/2} = \frac{d}{\sqrt{2\mathcal{K}L}}. \tag{14.18}$$

The Kerr effect parameters for some liquids used in Kerr modulators are listed in Table 14.2. The half-wave voltages for Kerr cells of two different dimensions are also listed.

14.4 Amplitude Modulation

We saw from (14.11) and (14.17) that the output wave of an electro-optic crystal is phase modulated by the applied electric field. Intensity modulation of the light wave is of more general use; therefore, we wish to convert the phase modulation of the transmitted wave to an amplitude modulation. To do this, we use the experimental arrangement shown in Figure 14.5.

We first produce linearly polarized light by passing the incident light wave through a linear polarizer (see Figure 14.5). The polarizer is orientated so that its polarization axis makes an angle ϕ, with the x_1 axis. (Recall from Chapter 13 that the polarization axis of a linear polarizer is defined as the direction parallel to the electric field of a linearly polarized wave when the transmission of that wave through the polarizer is a maximum.) The next step is to pass the polarized light through the modulator and at the same time apply an electric field to the modulator, parallel to the x_1 axis. Upon leaving the modulator, the wave passes through a second linear polarizer, called an *analyzer* to differentiate it from the first polarizer.

The modulator performs the role of a dynamic optical retarder and converts the linearly polarized wave into an elliptically polarized wave. The analyzer transmits one component

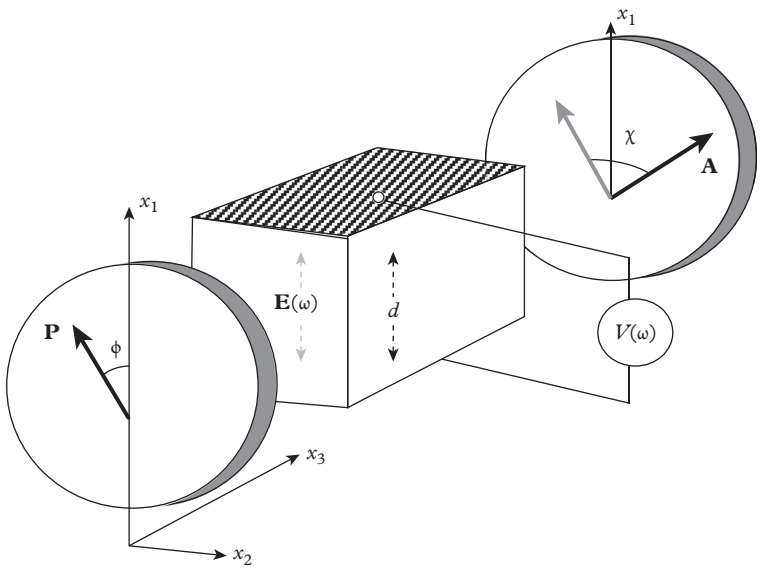

Figure 14.5 *Use of a polarizer and analyzer to convert phase modulation to amplitude modulation. The polarizer is the disk in the foreground of the picture and the analyzer is the disk in the background. The parallelepiped represents the electro-optic modulator. The electric field is applied parallel to the x_1 axis and light propagates along the x_3 axis. The vectors labeled* **P** *and* **A** *indicate the orientation of the electric field of a linearly polarized light wave when transmission through the polarizer is a maximum.*

of the elliptically polarized light. In this section, we will derive an equation for the intensity of the light transmitted by the analyzer as a function of the voltage applied to the modulator.

To analyze the total optical system, we will use the coordinate system shown in Figure 14.5 and redrawn in Figure 14.6. The applied electric field establishes a unique direction in the crystal along the x_1 axis. We will derive the phase difference between a wave polarized with its **D** vector parallel to the x_1 axis and one with its **D** vector polarized parallel to the x_2 axis, perpendicular to x_1. The incident wave is propagating along the x_3 axis. The initial polarizer is oriented such that the polarization axis makes an angle ϕ with respect to $\mathbf{D}_1$. The direction of the polarization axis is labeled $O\mathbf{P}$ in Figure 14.6. The analyzer, at the exit of the modulator crystal, is oriented such that its polarization axis, $O\mathbf{A}$ in Figure 14.6, makes an angle χ with respect to $O\mathbf{P}$. After passing through the polarizer, the light incident on the crystal has an amplitude component parallel to $\mathbf{D}_1$ given by $\mathcal{A}\cos\phi$ and in the $\mathbf{D}_2$ direction given by $\mathcal{A}\sin\phi$, where $\mathcal{A}$ is the wave amplitude after propagating through the polarizer.

After propagating through the crystal, the light is incident on the analyzer, which only transmits those components of polarization parallel to $O\mathbf{A}$. The component along $O\mathbf{A}$ due to $\mathbf{D}_1$ is

$$A\cos\phi\cos(\phi-\chi) \tag{14.19a}$$

and the component due to $\mathbf{D}_2$ is

$$A\sin\phi\sin(\phi-\chi), \tag{14.19b}$$

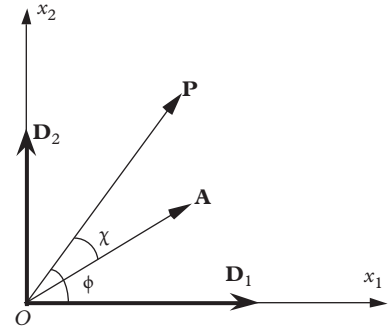

Figure 14.6 *Geometry associated with an electro-optic modulator.*

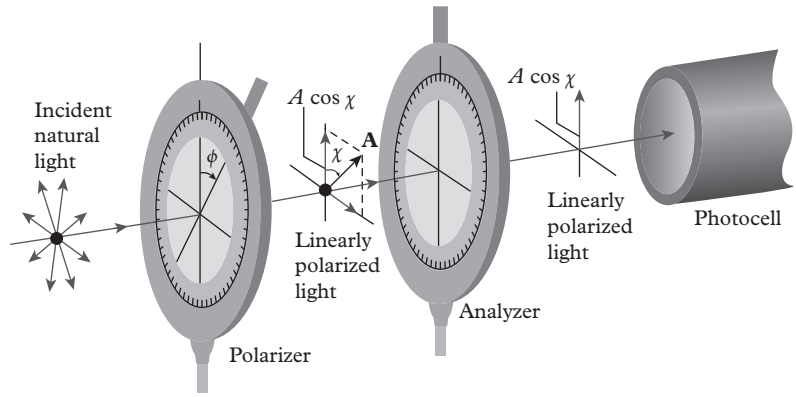

Figure 14.7 *Polarizer/analyzer pair described by (14.22).*

where A is the amplitude of the wave after propagating through the electro-optic crystal. We can write the phase difference between the components of $\mathbf{D}_1$ and $\mathbf{D}_2$ as we did in (14.11):

$$\begin{aligned}\Gamma &= k_0 L[(n_1 + \Delta n_1) - (n_2 + \Delta n_2)] \\ &= k_0 L[(n_1 - n_2) + (\Delta n_1 - \Delta n_2)].\end{aligned} \tag{14.20}$$

The components of $\mathbf{D}_1$ and $\mathbf{D}_2$ along the direction $O\mathbf{A}$ interfere coherently and yield, according to (4.13), an intensity

$$I = A^2 \left\{\cos^2\phi \cos^2(\phi - \chi) + \sin^2\phi \sin^2(\phi - \chi) + 2\cos\phi \sin\phi \, [\cos(\phi - \chi)\sin(\phi - \chi)\cos\Gamma]\right\}.$$

We use the identity $\cos\Gamma = 1 - 2\sin^2(\Gamma/2)$ to simplify the equation for the intensity:

$$I = A^2 \left[\cos^2\chi - \sin 2\phi \sin 2(\phi - \chi) \sin^2\frac{\Gamma}{2}\right]. \tag{14.21}$$

Three limiting cases of (14.21) exist:

(a) The electro-optic crystal is not present, as shown in Figure 14.7, so $\Gamma = 0$:

$$I = A^2 \cos^2\chi \tag{14.22}$$

(see Table 14.3). This equation is known as *Malus' law.* When $\chi = \pi/2$, the polarizers are said to be *crossed*, and no light propagates through the polarizer/analyzer pair. When $\chi = 0$, the polarizers are said to be *parallel*, and the maximum amount of light is transmitted by the pair.

(b) The analyzer and polarizer are aligned so that their axes are parallel ($\chi = 0$) and $\Gamma \neq 0$. For the condition of parallel polarizers, the transmitted intensity is

$$I_{\parallel} = A^2 \left(1 - \sin^2 2\phi \sin^2\frac{\Gamma}{2}\right). \tag{14.23}$$

(c) The analyzer and polarizer are aligned perpendicularly ($\chi = \pi/2$) and $\Gamma \neq 0$. For the condition of crossed polarizers, the transmitted intensity is

$$I_{\perp} = A^2 \sin^2 2\phi \sin^2\frac{\Gamma}{2}. \tag{14.24}$$

Table 14.3 *Transmission through polarizer/analyzer pair using (14.22)*

$I/I0$	$\cos\chi$	χ
$\frac{1}{2}$	0.707	45°
$\frac{1}{4}$	0.5	60°
$\frac{1}{8}$	0.354	69.3°

The intensity $I_\parallel$ is the complement of $I_\perp$. The maximum of $I_\parallel$ (minimum of $I_\perp$) occurs whenever $\phi = 0, \pi/2, \pi, \ldots$. The angle ϕ assumes these values whenever the polarizer is aligned parallel to $\mathbf{D}_1$ or $\mathbf{D}_2$. With the polarizer in these orientations, no light modulation takes place.

The minimum of $I_\parallel$ (maximum of $I_\perp$) occurs when

$$\sin 2\phi = \pm 1,$$
$$\phi = \frac{\pi}{4}, \frac{3\pi}{4}, \frac{5\pi}{4}, \ldots.$$

This orientation corresponds to the polarization axis aligned at a 45° angle with respect to the electric field direction. When the polarizer is in this orientation,

$$I_{\parallel \min} = A^2 \left(1 - \sin^2 \frac{\Gamma}{2}\right)$$
$$= A^2 \cos^2 \frac{\Gamma}{2}, \tag{14.25a}$$
$$I_{\perp \max} = A^2 \sin^2 \frac{\Gamma}{2}. \tag{14.25b}$$

These equations can be given a physical interpretation if we use (14.11) or (14.17) for the phase difference produced by the field-induced birefringence.

14.4.1 Kerr Modulation

If the parallelepiped in Figure 14.5 contains a Kerr medium, then the device shown in Figure 14.5 is called a Kerr cell. We can calculate the light intensity transmitted by the device as a function of the applied voltage V by replacing the phase difference Γ in (14.25) with that given in (14.17):

$$\Gamma = \frac{\pi}{\lambda} n_0^3 \rho E^2 L$$
$$= 2\pi E^2 \mathcal{K} L$$
$$= 2\pi \left(\frac{V}{d}\right)^2 \mathcal{K} L.$$

Using (14.18), we can write the phase difference as a function of the half-wave voltage of the Kerr cell:

$$\Gamma = \pi \left(\frac{V}{V_{\lambda/2}}\right)^2.$$

With this relationship for the phase difference, we can rewrite (14.25b) as

$$I_{\perp \max} = A^2 \sin^2 \left[\frac{\pi}{2} \left(\frac{V}{V_{\lambda/2}}\right)^2\right]. \tag{14.26}$$

The output intensity of the Kerr cell has the functional form shown in Figure 14.8. For comparison, the graph also displays the output intensity of a Pockels cell. The equation for the Pockels cell curve will be derived next.

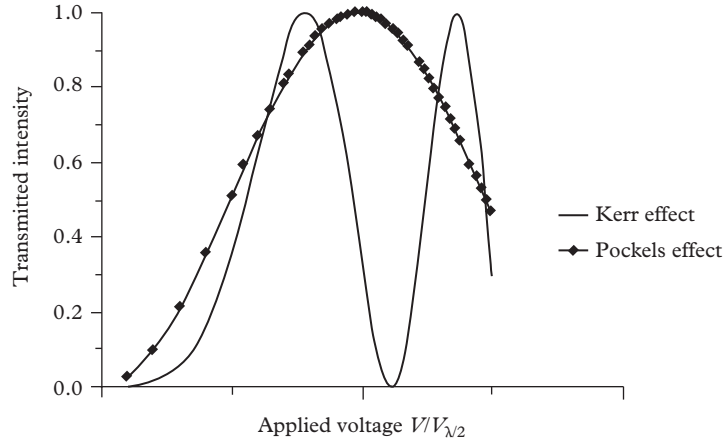

Figure 14.8 *The intensity transmitted through the optical system shown in Figure 14.5. Curves for idealized Kerr and Pockels media are shown. The linearity of the two effects should be compared between zero and the first intensity maximum.*

14.4.2 Pockels Modulation

If the parallelepiped in Figure 14.5 contains a material that exhibits the Pockels effect, then we need to use (14.20) in (14.25). By using the trigonometric identities

$$\cos(a+b) = \cos a \cos b - \sin a \sin b,$$
$$\sin(a+b) = \sin a \cos b + \cos a \sin b,$$

we can express the sinusoidal functions of the phase difference Γ in terms of the index modulation:

$$\cos\frac{\Gamma}{2} = \cos\left[\frac{k_0 L}{2}(n_1 - n_2)\right]\cos\left[\frac{k_0 L}{2}(\Delta n_1 - \Delta n_2)\right] - \sin\left[\frac{k_0 L}{2}(n_1 - n_2)\right]\sin\left[\frac{k_0 L}{2}(\Delta n_1 - \Delta n_2)\right],$$

$$\sin\frac{\Gamma}{2} = \sin\left[\frac{k_0 L}{2}(n_1 - n_2)\right]\cos\left[\frac{k_0 L}{2}(\Delta n_1 - \Delta n_2)\right] + \cos\left[\frac{k_0 L}{2}(n_1 - n_2)\right]\sin\left[\frac{k_0 L}{2}(\Delta n_1 - \Delta n_2)\right].$$

The expressions for the index modulation, Δn_1 and Δn_2, are found in (14.8) and (14.9). The contribution from $n_1 - n_2$ may be used by the experimenter to control the functional form of the intensity output of the Pockels cell.

This result for Pockels modulation is much more complicated than the result for Kerr modulation. Kerr modulation is simple because the field-free material is isotropic and the addition of an electric field creates an optically uniaxial material. The Pockels material may be birefringent in the field-free condition, and the application of a field to a birefringent material will produce in general a biaxial medium. The added complexity introduced by possible biaxial behavior means that more effort is required to understand the physical significance of the Pockels modulation result.

Several special cases will aid in interpretation of the results we have just derived for the Pockels effect modulator. Assume initially that the applied electric field is such that $\Delta n_1 = \Delta n_2$. This could occur when a time-varying electric field passes through zero. Whenever $\Delta n_1 = \Delta n_2$, we have

$$\cos^2 \frac{\Gamma}{2} = \cos^2 \left[\frac{k_0 L}{2} (n_1 - n_2) \right], \quad \sin^2 \frac{\Gamma}{2} = \sin^2 \frac{k_0 L}{2} (n_1 - n_2).$$

The field-free material produces a phase difference equivalent to that produced by a retarder plate, (13.21):

$$\frac{k_0 L}{2} (n_1 - n_2) = \pi N,$$

where N is the retardation defined in (13.20). We will examine the modulation produced by the Pockels effect for three different retardations of the field-free material.

(a) **Full-wave retardation:**

$$N = 1, \ 2, \ \ldots .$$

The intensity transmitted by the optical system shown in Figure 14.5 is

$$I_{\parallel \min} = A^2 \cos^2 \left[\frac{k_0 L}{4} (n_2^3 r_{21} - n_1^3 r_{11}) E_1 \right], \tag{14.27a}$$

$$I_{\perp \max} = A^2 \sin^2 \left[\frac{k_0 L}{4} (n_2^3 r_{21} - n_1^3 r_{11}) E_1 \right]. \tag{14.27b}$$

The geometry of Figure 14.5 allows the electric field to be written in terms of the applied voltage, $E_1 = V/d$, so that (14.27b) becomes

$$I_{\perp \max} = A^2 \sin^2 \left[\frac{k_0 L}{4d} (n_2^3 r_{21} - n_1^3 r_{11}) \, V \right]. \tag{14.28}$$

The intensity variation in (14.28) is the curve labeled "Pockels effect" in Figure 14.8. It describes the transmission of the optical system in Figure 14.5 when the polarizers are crossed.

(b) **Half-wave retardation:**

$$N = \frac{1}{2}, \ \frac{3}{2}, \ \ldots .$$

The transmitted intensity is

$$I_{\parallel \min} = A^2 \sin^2 \left[\frac{k_0 L}{4} (n_2^3 r_{21} - n_1^3 r_{11}) E_1 \right], \tag{14.29a}$$

$$I_{\perp \max} = A^2 \cos^2 \left[\frac{k_0 L}{4} (n_2^3 r_{21} - n_1^3 r_{11}) E_1 \right]. \tag{14.29b}$$

If the field-free retardation is a half-wave, then the transmitted intensity is the compliment of the full-wave retardation case. When the polarizer and analyzer are parallel, the transmitted intensity for half-wave retardation is identical to (14.28).

(c) **Quarter-wave retardation:**

$$N = \frac{1}{4}, \frac{3}{4}, \ldots .$$

For this field-free condition, the amplitude transmission of the optical system shown in Figure 14.5 is

$$\left.\begin{matrix}\sqrt{I_{\perp\max}} \\ \sqrt{I_{\parallel\min}}\end{matrix}\right\} = \frac{E}{\sqrt{2}}\left\{\cos\left[\frac{k_0 L}{4}(n_2^3 r_{21} - n_1^3 r_{11})E_1\right] \pm \sin\left[\frac{k_0 L}{4}(n_2^3 r_{21} - n_1^3 r_{11})E_1\right]\right\},$$

and the intensity transmitted by the system is given by

$$\left.\begin{matrix}I_{\perp\max} \\ I_{\parallel\min}\end{matrix}\right\} = \frac{A^2}{2}\left\{1 \pm \sin\left[\frac{k_0 L}{2}(n_2^3 r_{21} - n_1^3 r_{11})E_1\right]\right\}. \tag{14.30}$$

The transmitted intensity predicted by (14.30) is shown in Figure 14.9.

The quantity

$$\frac{k_0 L}{2}(n_1 - n_2)$$

is called the *modulation bias* of the modulation system. Any bias can be selected, even ones we have not considered, but normally a bias of $\pi/4$ is the most useful. The straight line drawn

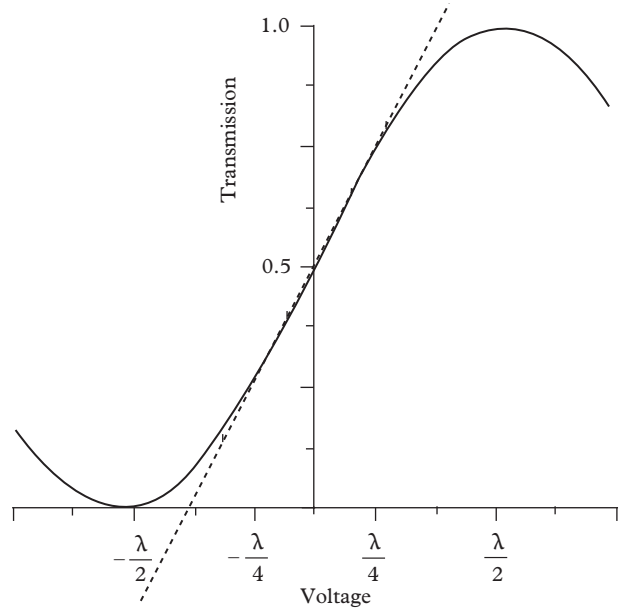

Figure 14.9 *Transmission of Pockels cell as predicted by (14.30). A straight line has been drawn through the curve to demonstrate the ability to generate an intensity transmission that varies linearly with modulation voltage.*

on the plot of (14.30) in Figure 14.9 displays the reason for the selection of a quarter-wave bias. With this bias, the output intensity of the Pockels cell is proportional to the applied modulation voltage, if the applied voltage swing is not too large.

If the bias is positioned at the 50% transmission point in Figure 14.9, then linear modulation of the light intensity can be obtained. Equation (14.30) gives the modulated intensity. The sine term is

$$\sin(\Gamma\cos\psi) = 2\sum_{n=0}^{\infty}(-1)^{n+1}J_{2n+1}(\Gamma)\cos[(2n+1)\psi],$$

$$\Gamma \to \frac{k_0 L E_0}{2}(n_2^3 r_{21} - n_1^3 r_{11}), \quad \psi \to \omega_n t,$$

$$I(t) = \frac{A^2}{2}[1 + 2J_1(\Gamma)\cos\omega_m t + \text{odd harmonics}],$$

and the distortion from linearity is proportional to the ratio of Bessel functions. For example, if a sine wave modulation voltage creates a transmissivity variation between 12.5% and 87.5% of the transmission maximum, then the frequency of the modulated light wave will contain less than 3% of higher harmonics of the modulation frequency.

The bias may be controlled by three methods:

1. If the modulation crystal is birefringent in zero field, then the length of the modulation crystal can be selected to satisfy the equation

$$L = \frac{\lambda N}{n_1 - n_2}. \tag{14.31}$$

2. A second method of obtaining the bias is through the application to the electro-optic crystal of a DC electric potential, along with the AC modulation field. Figure 14.10 displays the use of a DC bias voltage, in addition to the AC modulation voltage, to position the modulation on the most linear region of the transmission curve.
3. The third method of producing a bias in an electro-optic modulator is the use of an optical retarder between the polarizer and analyzer (see Figure 14.11). This method of bias application converts the linearly polarized input wave into a circularly polarized wave, through the use of a quarter-wave plate with its fast axis oriented at 45° to the plane of polarization. The circularly polarized light is converted into elliptically polarized light by the modulator. The analyzer then transmits the component of the elliptically polarized wave parallel to its axis.

The Jones calculus can be used to describe the electro-optic modulator in the same way as it can be used to describe static polarizing components. If δ is the retardation bias and Γ is the phase shift introduced by the electro-optic modulator, then the Jones matrix is

$$\begin{bmatrix} e^{i\delta/2} & 0 \\ 0 & e^{-i(\delta+\Gamma)/2} \end{bmatrix}. \tag{14.32}$$

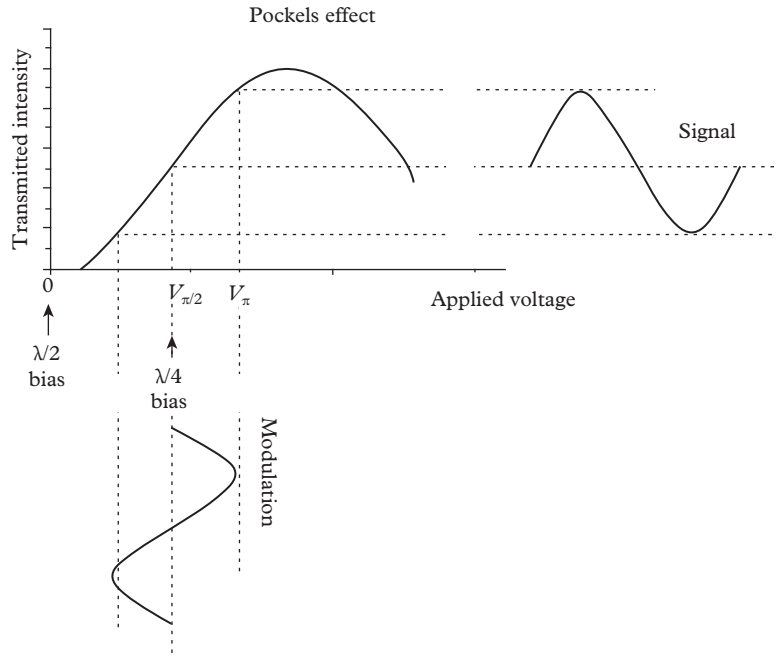

Figure 14.10 *DC field bias of an electro-optic modulator to produce an intensity modulation that is a linear representation of the modulation voltage.*

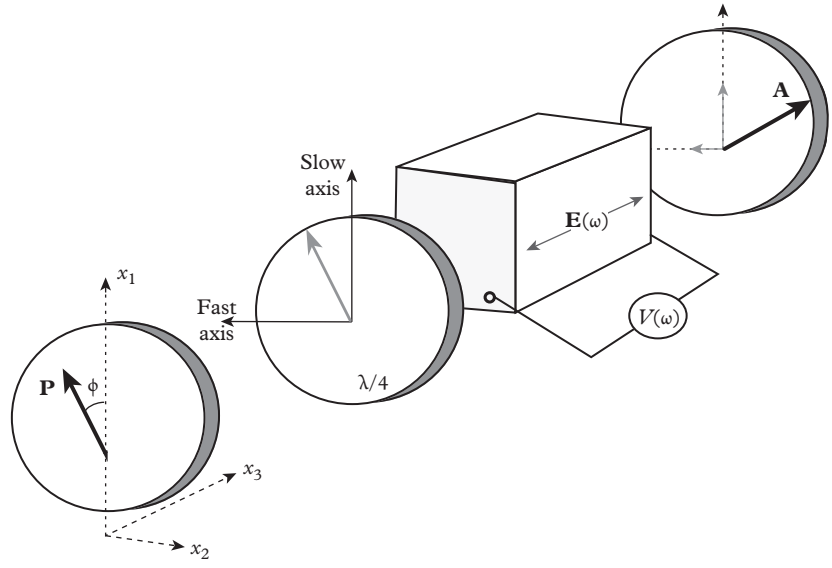

Figure 14.11 *The use of a quarter-wave retarder to adjust the modulation bias of an electro-optic modulator.*

14.5 Modulator Design

In this section, and in the problems at the end of the chapter, we will discuss the design of two types of electro-optic modulators. The Kerr modulator will be designed using nitrobenzene as the Kerr liquid. The Pockels modulator will use one of the most popular crystal types: the $\bar{4}2m$ symmetry group. (Discussions of crystal structure, a definition of the 32 crystal point groups, and a list of their symmetries can be found in most introductory solid state physics books [2].)

14.5.1 Kerr Modulator

A typical Kerr modulator contains the components shown in Figure 14.5. The polarizer is oriented with its axis at 45° with respect to the applied electric field, $\phi = 45°$. The analyzer and polarizer are crossed, $\chi = 90°$. Equation (14.26) give the transmitted intensity for this geometry. The Kerr medium that fills the parallelepiped is nitrobenzene, selected because of its large Kerr coefficient (see Table 14.2). The dimensions of the parallelepiped are selected as $L = 3$ cm, $d = 2$ cm, which allows the calculation of a half-wave voltage using (14.18):

$$V_{\lambda/2} = \frac{2 \times 10^{-2}}{\sqrt{2\left(\frac{33 \times 10^{-6}}{9 \times 10^{6}}\right)(3 \times 10^{-2})}} = 55.2 \text{ kV}.$$

The transmissivity of this Kerr modulator is given by

$$\mathcal{T} = \frac{I_{\perp \max}}{A^2} = \sin^2\left(\frac{V^2}{1.73 \times 10^{9}}\right).$$

The transmitted light intensity can be switched from zero to a maximum value by the application of 52.2 kV to the Kerr modulator. The transmitted intensity is not a linear function of the applied voltage; thus, the Kerr modulator is not an attractive device when complex signals are to be used. The device can operate as an effective shutter and has been used in this role to measure the speed of light and as a *Q*-spoiler in laser cavities.

14.5.2 Pockels Modulator

The popularity of the $\bar{4}2m$ symmetry group as a Pockels material is due in part to the fact that it is one of only two classes (the other being $\bar{4}3m$) for which the electro-optic effect is

Table 14.4 *Parameters of Pockels modulator*

	10^{-12} m/V		$\lambda = 550$ nm		
Type	r_{41}	r_{63}	n_o	n_e	T_C (K)
KDP (KH_2PO_4)	8.77	9.7	1.51	1.47	122
KD*P[a]	8.8	24.3	1.508	1.468	221
ADP($NH_4H_2PO_4$)	24.5	8.5	1.527	1.481	148

[a]The notation KD*P represents a KDP crystal with the hydrogen atoms replaced by deuterium atoms.

not complicated by unwanted birefringence or optical activity. Several members of the $\bar{4}2m$ symmetry group are listed in Table 14.4. The crystals listed in Table 14.4 are water-soluble and fragile, but can be handled without too much difficulty. In the absence of an applied field, these crystals are uniaxial, as can be inferred from the pair of indices in the table. The temperature T_C listed in Table 14.4 is the Curie temperature, below which KDP and KD*P become ferroelectric and ADP becomes antiferroelectric. If the temperature of the crystal is allowed to approach the Curie temperature, the electro-optic effect becomes very large,

$$r \propto \frac{1}{T - T_C},$$

but unfortunately so does the dielectric loss.

The first step we must take in developing design equations for these crystals is to obtain, from Appendix 14A, the nonzero elements of the Pockels tensor used to write the equation of the ellipsoid (see Problem 14.2). We will simplify this equation by assuming the external electric field lies along the z-axis, which is chosen to be the principal axis for the extraordinary index of refraction. (In crystallography, this axis is called the c-axis.)

In the absence of an external electric field, the principal axes of the indicatrix are aligned along the crystallographic axes. Upon the application of the external field, the indicatrix will rotate as shown in Figure 14.4. The resulting indicatrix equation will have cross terms, as did (14.6). To eliminate the cross terms, the tensor matrix must be rediagonalized; i.e., we must find a new, rotated coordinate system that will eliminate the cross term involving $x_1 x_2$ (see Problem 14.3). In the new coordinate system, the equation for the indicatrix is

$$\left(\frac{1}{n_0^2} + r_{63}E_3\right)x_1^2 + \left(\frac{1}{n_0^2} - r_{63}E_3\right)x_2^2 + \frac{x_3^2}{n_e^2} = 1. \tag{14.33}$$

Using the binomial expansion, as was done in the derivation of (14.8) and (14.9), we obtain the relationships between the index change and the applied electric field (see Problem 14.4). The equations for the index change induced by the applied electric field can be used to obtain the phase modulation created by the electro-optic effect, once the propagation direction of the light wave is specified.

14.5.3 Longitudinal Modulator

If the incident light wave propagates in a direction parallel to the applied electric field, along x_3 in Figure 14.11, we have a *longitudinal electro-optic modulator.* To propagate a light wave along the electric field, the electrodes producing the field must be transparent, or ring-shaped electrodes must be used. The phase change produced by this design is

$$\Gamma = k_0 L(n_0^3 r_{63} E_3). \tag{14.34}$$

This phase change may be substituted into the Jones matrix (14.32) to determine the polarization properties of the longitudinal modulator.

In this modulator design, the electric field is related to the applied voltage by $V = LE_3$. In terms of the applied voltage, the phase change produced by the Pockels cell is

$$\Gamma = \frac{2\pi V}{\lambda} n_0^3 r_{63}. \tag{14.35}$$

We see from (14.35) that the phase change produced by the longitudinal modulator is independent of the modulator dimensions.

We can define a half-wave voltage for the longitudinal modulator, as we did in (14.8) for the Kerr cell. This parameter, denoted by V_π to distinguish it from the Kerr half-wave voltage, equals the voltage that must be applied to the Pockels modulator to produce a phase change of one half-wave. The half-wave voltage of the longitudinal modulator is a characteristic of the Pockels material (see Table 14.5) and is independent of crystal dimensions:

$$V_\pi = \frac{\lambda}{2n_0^3 r_{63}}. \tag{14.36}$$

The geometrical orientation of the Pockels material in the longitudinal modulator discussed here is such that the light wave propagates along the optical axis of the crystal. (A crystal cut in the geometry of this example is called a 0° z-cut crystal.) In this orientation, $n_1 = n_2 = n_o$, so we cannot produce a bias by adjusting the length of the electro-optic material. We may produce a bias by the addition of a quarter wave plate (see Figure 14.11) or by the less desirable addition of a DC voltage to the modulation signal.[3]

Table 14.5 *Half-wave voltage for longitudinal modulator*

Type	V_π (kV) (λ = 546 nm)
KDP (KH_2PO_4)	7.5
KD*P	2.9
ADP ($NH_4H_2PO_4$)	9.2
$LiNbO_3$	4.0
$LiTaO_3$	2.7

14.5.4 Transverse Modulator

When the light propagates transverse to the direction of the applied electric field, say along x_2 in Figure 14.5, the modulator is called a *transverse electro-optic modulator*. This type of modulator is easier to construct, because transparent electrodes of the longitudinal modulator are not needed. We adjust the orientation of the modulator so that the direction of polarization of the incident wave, relative to the electric field, is $\phi = 45°$ and the electric field is along the x_3 axis. (A crystal cut to operate in this geometry is called a 45° z-cut configuration.) The retardation produced by the modulation field is

$$\Gamma = \frac{2\pi}{\lambda}(n_o - n_e)L - \frac{2\pi n_o^3 r_{63}}{\lambda}\left(\frac{VL}{d}\right). \tag{14.37}$$

Because the light wave is propagating normal to the optical axis of the Pockels material, this design allows the application of an optical bias through a proper choice of crystal dimensions. We can define a half-wave voltage for this design in terms of the half-wave voltage of (14.36):

$$V_\pi^t = \frac{2V_\pi}{L/d}.$$

The retardation is not independent of crystal dimensions, as it was in the longitudinal modulator design, but this can be used to our advantage. By selecting a large L/d ratio, the drive voltage requirements can be reduced below those required for a longitudinal modulator. The ordinary and extraordinary waves will travel different paths (this is called Poynting vector walkoff; see Problem 13.9) owing to the natural birefringence, and the use of a large L/d ratio will enhance the separation of the two waves, degrading the modulator's performance and preventing us from obtaining an arbitrarily large reduction in drive voltage.

14.6 Magneto-optic Effect

When linearly polarized light propagates through a medium parallel to an externally applied magnetic field, the plane of polarization will be rotated, as if the material were optically

[3] Electrical loss in the dielectric Pockels material introduces heating when a DC voltage bias is used. This heating can produce an unstable modulator because the electro-optic properties are a strong function of the temperature owing to the ferroelectric behavior of Pockels materials.

active; this is called the *Faraday effect*. The behavior of an optically inactive material in a magnetic field resembles the optical properties of a naturally active isotropic material, with one important exception: natural optical activity depends on the direction of propagation of the light, while the Faraday effect depends upon the direction of the magnetic field but *not* upon the direction of propagation of the light.

Because of their similarity, we could analyze the magneto-optic effect as we did natural optical activity, by introducing an antisymmetric tensor of rank two, or, equivalently, the *gyration vector* **g**. This formalism would allow a relationship, equivalent to (13.26), to be written for a component of the displacement:

$$D_j = \sum_{k=1}^{3} \varepsilon_{jk} E_k + i(\mathbf{E} \times \mathbf{g})_j. \tag{14.38}$$

The medium described by (14.38) is said to be *gyrotropic* [3]. To first order,

$$\mathbf{g} = \varepsilon_0 \chi^{(m)} \mathbf{H}$$

where $\chi^{(m)}$ is the magneto-optic susceptibility.

We will use a different mathematical formalism, one that is based on the classical dispersion model of Chapter 7. To explain the magnetic-field-induced optical activity, we will modify the classical dispersion model to include an externally applied magnetic field, parallel to the propagation direction. The incident linearly polarized light wave is decomposed into a right- and a left-circularly polarized wave. The rotating electric field associated with the light wave causes the electrons in the material to move in circular orbits in the plane transverse to the magnetic field, the (x, y) plane. The magnetic field exerts a radial force on the moving electrons that modifies the spring constant used in the dispersion model—increasing it for counterclockwise rotation and decreasing it for clockwise rotation about the **B** field. The modified spring constants lead to two resonant frequencies.

In a vapor, such as sodium, in the absence of a **B** field, there are certain resonant frequencies at which absorption takes place (in the classical theory developed in Chapter 7, there would be one frequency ω_0, which is a reminder for us not to put too much confidence in the classical theory). **Pieter Zeeman (1865–1943)**, in 1896, discovered that when a magnetic field is present, what had been a single absorption frequency splits into a number of absorption frequencies. The classical theory we will develop here predicts that an isotropic three-dimensional oscillator's resonant frequency will split into three frequencies. Two new frequencies associated with motion normal to the magnetic field, are observed (see Figure 14.12). The absorption lines associated with these new frequencies absorb right- or left-circularly polarized light. The unmodified, zero-field, frequency, associated with motion parallel to the magnetic field, is still present, but its absorption properties have been modified. It now absorbs linearly polarized light.

The classical theory explains the experimentally observed *normal Zeeman effect*. There are, however, some resonant absorptions that split into a number of new frequencies whose magnetic field behavior, and polarization properties, can only be explained by quantum theory [4]. This behavior is called the *anomalous Zeeman effect*. We will ignore the failure of the classical theory to explain the anomalous Zeeman effect and use the theory to explain the Faraday effect. The classical theory will demonstrate the close relationship between the Faraday effect and the Zeeman effect. The result will provide a useful visualization of the physical processes related to the Faraday effect.

A vector relationship will be necessary, because the addition of a magnetic field makes it impossible to treat the problem in one dimension. Starting with the equation of motion

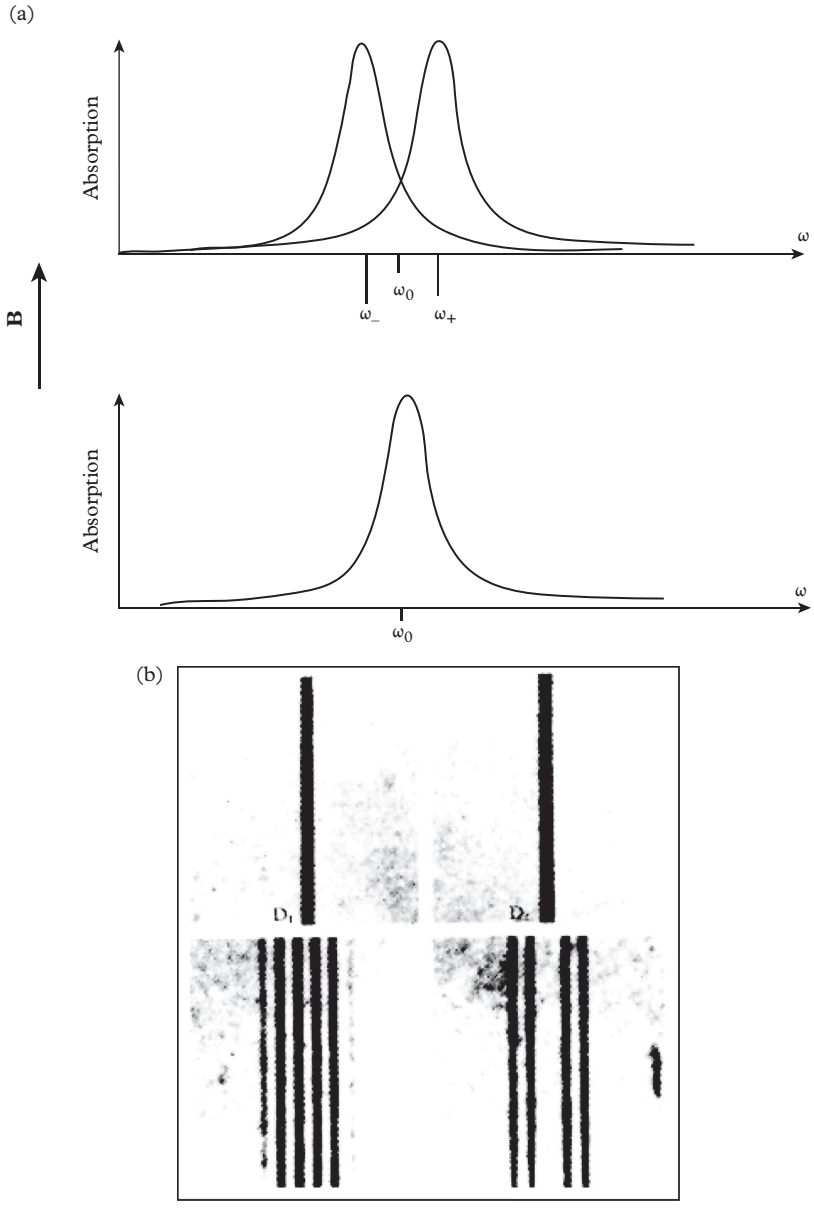

Figure 14.12 *(a) The Zeeman effect. When the material with the resonant absorption shown in the lower plot is placed in a magnetic field, the absorption splits into two absorptions. The displacement of the two new frequencies from the original frequency is a function of the applied magnetic field. (b) A photograph of the anomalous Zeeman Effect made by Zeeman in 1897. (Public Domain, <http://commons.wikimedia.org/wiki/File:ZeemanEffect.GIF>.)*

of bound charges in a noninteracting gas, (7.26), and adding to the electromagnetic field present a large magnetic field **B**, we obtain the modified equation of motion for the model:

$$\frac{d^2\mathbf{r}}{dt^2} + \omega_0^2\mathbf{r} = -\frac{e}{m}\left(\mathbf{E} + \frac{d\mathbf{r}}{dt} \times \mathbf{B}\right). \tag{14.39}$$

We assume that the magnetic field's frequency is much less than optical frequencies, so we may ignore its time dependence. We will continue to ignore the magnetic field associated with the light wave; see (2.33).

The coordinate system selected is oriented such that the magnetic field **B** lies in the positive z-direction and the light wave propagates along this same direction. For this geometry, the equation of motion reduces to the following two equations:

$$\frac{d^2x}{dt^2} + \frac{e}{m}B_z\frac{dy}{dt} + \omega_0^2 x = -\frac{e}{m}E_x, \tag{14.40}$$

$$\frac{d^2y}{dt^2} - \frac{e}{m}B_z\frac{dx}{dt} + \omega_0^2 y = -\frac{e}{m}E_y. \tag{14.41}$$

If we multiply (14.41) by $\pm i$ and add the result to (14.40), we obtain an equation of circular motion:

$$\frac{d^2\mathcal{R}_\pm}{dt^2} \mp \frac{e}{m}iB_z\frac{d\mathcal{R}_\pm}{dt} + \omega_0^2\mathcal{R}_\pm = -\frac{e}{m}E_\pm. \tag{14.42}$$

We now have a one-dimensional equation, with $\mathcal{R}_\pm = x \pm iy$ equal to the coordinate for a charge moving in a circular orbit in the (x, y) plane, and $E_\pm = E_x \pm iE$ equal to the electric field for a circularly polarized wave. The optical wave is assumed to be monochromatic, with a frequency ω.

At the surface of the magneto-optic material, which we select to be $z = 0$, the incident wave is linearly polarized:

$$E_x = E_0 \cos\omega t, \quad E_y = 0.$$

In the material, we describe the wave using a circular polarization representation,

$$E_\pm = E_0 e^{i(\omega t - k_\pm z)}.$$

The polarization induced by this electric field can be written with the help of (7.29):

$$P_\pm = P_x \pm iP_y = Ne(x \pm iy) = Ne\mathcal{R}_\pm. \tag{14.43}$$

As in Chapter 7, we assume that the induced polarization is of the same form as the applied optical field,

$$P_\pm = NeCE_\pm = NeC' e^{i(\omega t - k_\pm z)},$$

so the spatial coordinate can be written

$$\mathcal{R}_\pm = C' e^{i(\omega t - k_\pm z)}.$$

Substituting the assumed solution and its derivatives into (14.42) yields

$$-\omega^2 \mathcal{R}_\pm \pm \frac{e}{m} B_z \omega \mathcal{R}_\pm + \omega_0^2 \mathcal{R}_\pm = -\frac{e}{m} E_\pm,$$

$$\mathcal{R}_\pm = \frac{\frac{e}{m} E_x}{(\omega_0^2 - \omega^2) \pm \frac{e}{m} B_z \omega}. \tag{14.44}$$

Substituting (14.44) into (14.43) yields

$$P_\pm = \frac{N \frac{e^2}{m} E_\pm}{(\omega_0^2 - \omega^2) \pm \frac{e}{m} B_z \omega}. \tag{14.45}$$

We define the *Larmor precession frequency* [named after **Joseph Larmor (1857–1942)**] as

$$\omega_L = \frac{e}{2m} B_z. \tag{14.46}$$

The Larmor frequency is much smaller than the applied field's frequency ω or the resonant frequency ω_0, both of which are optical frequencies, of the order of 10^{14} Hz. For an electron in a magnetic field of 0.1 T,

$$\nu_L = \frac{\omega_L}{2\pi} = 1.4 \text{ GHz}.$$

We can write

$$(\omega_0 \pm \omega_L)^2 = \omega_0^2 \left[1 \pm 2 \frac{\omega_L}{\omega_0} + \left(\frac{\omega_L}{\omega_0} \right)^2 \right]$$

The small relative size of ω_L means that the term involving ω_L^2 can be neglected:

$$(\omega_0 \pm \omega_L)^2 \approx \omega_0^2 \left(1 \pm 2 \frac{\omega_L}{\omega_0} \right)$$

The fact that $\omega_L \ll \omega, \omega_0$ allows a replacement of $\omega\omega_L$ by $\omega_0\omega_L$. The denominator of (14.45) can now be rewritten as

$$\omega_0^2 - \omega^2 \pm 2\omega_L \omega \approx (\omega_0 \pm \omega_L)^2 - \omega^2.$$

We now see that the magnetic field splits the resonant frequency into two new frequencies, located above and below the field-free resonance by a distance equal to the Larmor frequency.

Using the same procedure used to obtain (7.30), we obtain the index of refraction of the magneto-optic material:

$$n_\pm^2 = 1 + \frac{\omega_p^2}{(\omega_0 \pm \omega_L)^2 - \omega^2}. \tag{14.47}$$

This equation describes the Faraday effect and demonstrates that the magnetic field creates unequal propagation velocities for left- and right-circularly polarized light.

When linearly polarized light passes through the Faraday medium, we can use this theory if we decompose the linear polarization into right- and left-circularly polarized components. Equation (14.47) states that the two circular polarizations travel at different velocities. After passing through a length L of the material, a linearly polarized wave will have the direction of its electric field rotated through an angle θ from its orientation at the entrance to the material. The angle θ can be calculated using (13.32):

$$\theta = \frac{\pi L}{\lambda_0}(n_- - n_+) = \frac{\omega L}{c}(n_- - n_+).$$

Because ω_L is much smaller than ω_0, the index difference $n_- - n_+$ predicted by (14.47) is small and we can use the approximation

$$n_-^2 - n_+^2 \approx 2n_0(n_- - n_+)$$

to write

$$\theta = \frac{\omega\omega_p^2 L}{cn_0}\left[\frac{2\omega_0\omega_L}{(\omega_0^2 + \omega_L^2 - \omega^2)^2 - 4\omega_0^2\omega_L^2}\right]. \tag{14.48}$$

A schematic representation of the prediction of this classical model is shown in Figure 14.13. The resonant absorption curve from Figure 14.12(a) exhibits the normal Zeeman effect and splits into two resonances that absorb circularly polarized light. The dispersion curves associated with these two resonances, shown in Figure 14.13, are used to calculate the Faraday rotation according to (14.48).

The equation for the angle of rotation generated by the classical model agrees with the empirically determined relationship[4]

$$\theta = \mathcal{V}LH. \tag{14.49}$$

[4] Equation (14.49) applies when the magnetic field is generated by an electrical current. However, in experiments, a permanent magnet is often used, and the corresponding relationship is written in terms of B rather than H: $\theta = \mathcal{V}LB$. The units of Verdet's constant differ in the two situations [rad/A for a current-generated field and rad/(T·m) for a permanent-magnet field].

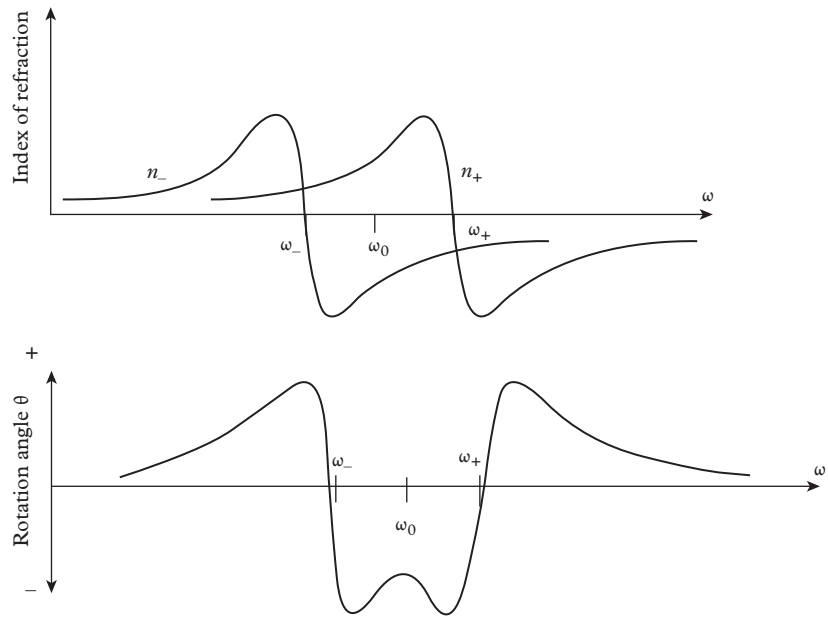

Figure 14.13 *Schematic representation of how Faraday rotation behaves as a function of frequency. The absorption resonance of Figure 14.10(a) is the origin of the dispersion shown here.*

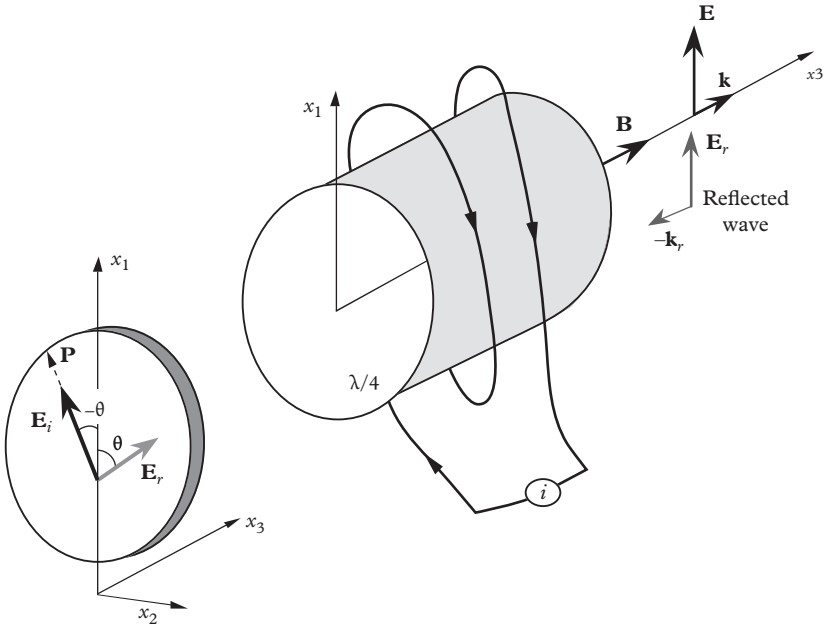

Figure 14.14 *An isolator based upon the Faraday effect. The wave initially encounters a polarizer that establishes the direction of the linearly polarized wave incident upon the Faraday rotator. A magnetic field is applied to the rotator, and the polarization is rotated through the angle θ so that it is now parallel to the x_1 axis. Any of the waves reflected back to the isolator is again rotated through an angle θ, and arrives at the polarizer at an angle of 2θ with respect to the polarizer's axis. By proper choice of the* **B** *field, we can make θ = 45°.*

Verdet's constant $\mathcal{V}$ is positive when the direction of the electric field of a linearly polarized wave is rotated clockwise, measured when looking along the direction of the field **H**. (The polarization rotates in the same direction as the flow of the current producing the magnetic field.) The very simple theory presented here agrees with experiment, which has demonstrated that, away from absorption bands, Verdet's constant falls to zero with increasing wavelength. Some typical Verdet's constants are shown in Table 14.6.

A light modulator could be designed using the Faraday effect, but it would have a limited modulation frequency range because it is very difficult to modulate a magnetic field at high frequencies. The major application of the Faraday effect is as an *isolator*, i.e., a device that allows an electromagnetic wave to propagate in only one direction. It makes use of the fact that the angle of rotation is the same for light propagating parallel and antiparallel to the applied magnetic field. A Faraday isolator is displayed in Figure 14.14. The initial polarizer determines the polarization angle of the incident light wave. It is normally adjusted so that it makes an angle of 45° with respect to the x_1 axis. The **B** field, of magnitude B_z, applied to the Faraday rotator is such that the electric field of the wave is rotated through 45°. Any reflected wave that propagates back through the Faraday rotator is rotated through an additional 45°. This reflected wave arrives at the polarizer with its electric field oriented 90° to the polarizer's axis and is not transmitted.

Table 14.6 *Verdet's constants*

Material	$\mathcal{V}$ [rad/(T·m)][a] at λ = 589 nm
H_2O	1.175
Crown glass	1.346
Flint glass	2.691
MOS-4 glass	73
NaCl	3.230
Quartz	1.489
$Tb_3Ga_5O_{12}$[b]	–134

[a]Verdet's constant is often given in the literature in Gaussian units, which can be converted to MKS units as follows. When the magnetic field is generated by an electric current, the Gaussian units are $1\,\text{arcmin}/(\text{Oe}\cdot\text{cm}) = 2.094 \times 10^{-2}\,\text{deg/A} = 3.655 \times 10^{-4}\,\text{rad/A}$. When the field is provided by a permanent magnet, the Gaussian units are $1\,\text{deg}/(\text{G}\cdot\text{cm}) = 10^6\,\text{deg}/(\text{T}\cdot\text{m}) = 1.745 \times 10^4\,\text{rad}/(\text{T}\cdot\text{m})$.

[b]This is terbium gallium garnet, a common commercial Faraday rotator, as is MOS-4 glass.

14.6.1 Cotton–Mouton and Voigt Effects

Several other magnetic effects are observed in materials, but they have little technological importance. The *Cotton–Mouton effect* is the magnetic analog of the Kerr effect in that it depends on the square of the applied field (a magnetic field for the

Table 14.7 *Cotton–Mouton coefficients*

Material	C (Oe^{-2} cm^{-1})[a] at $\lambda = 589$ nm
Acetone	37.6×10^{-13}
Benzene	7.5×10^{-13}
Chloroform	-65.8×10^{-13}
CS_2	-4.0×10^{-13}

[a]These units are those normally found in the literature. To convert from Oe^{-2} cm^{-1} to MKS units, we multiply by $(4\pi)^2 \times 10^{-4}$ to obtain $(A/m)^{-2}$ m^{-1}. When we can assume that $\mu = \mu_0$, we can multiply by 10^{10} to allow the use of tesla for the magnetic field.

Cotton–Mouton effect). A birefringence is observed in the presence of a magnetic field if the light waves are propagating in a direction normal to the applied magnetic field. The birefringence is interpreted as due to difference in propagation velocities of two waves. One wave, with **D** parallel to the external magnetic field **H**, has an index of refraction represented by $n_\parallel$; the second wave, with **D** perpendicular to the magnetic field, has an index of refraction represented by $n_\perp$.

The phase shift that is produced when the two orthogonally polarized waves propagate perpendicular to the applied magnetic field through a distance d in the material is given by

$$\delta = \frac{n_\parallel - n_\perp}{\lambda} d = CdH^2.$$

Table 14.7 lists some typical values for the Cotton–Mouton coefficient C.

A similar magneto-optic effect observed in gases, near resonant absorptions, is called the *Voigt effect*. The Cotton–Mouton and Voigt effects are too small to have found any practical application (the Faraday effect is approximately 10^3 times greater than the Cotton–Mouton effect, and the Voigt effect is about 10^3 times smaller than the Cotton–Mouton effect). We will not discuss them further.

14.7 Photoelastic Effect

An isotropic material can become anisotropic when subject to an applied stress or an induced strain, through an elasto-optic interaction know as *stress birefringence*, or the *photoelastic effect*. Brewster first observed the photoelastic effect in 1815 and H. Mueller published a microscopic theory of the effect in 1935 [5, 6].

The photoelastic effect reduces the performance of optical components and devices by introducing phase distortions. These distortions can arise from stresses produced by improper mounting or by unequal thermal expansion of the mounts and components. Another source of distortion is strain that has been frozen into the optical component during manufacture. When possible, optical materials with a small photoelastic effect are used to reduce these unwanted distortions.

There are applications that utilize the elasto-optic interaction, and the materials used in these applications are selected for their large photoelastic effect. In this section, we will discuss, very briefly, one such application:the use of stress birefringence in the analysis of mechanical structures under load. The purpose of introducing this application is to demonstrate that the optical indicatrix can be used in the analysis of the photoelastic effect. Later, a completely different approach will be used, to develop an important application of the photoelastic effect, involving acoustic waves.

As was the case for the electro-optic effect, the change in the index of refraction can be visualized as a change in the size, shape, and orientation of the indicatrix. As was done for the electro-optic effect in (14.1), the impermeability tensor, in the presence of stress, can be written as

$$\eta_{ik} = \eta_{ik}^0 + \sum_{j=1}^{3} \sum_{m=1}^{3} q_{ijkm} \mathcal{T}_{jm}. \tag{14.50}$$

$\mathcal{T}$ is a symmetric second-rank tensor; its diagonal terms are the normal components and the off-diagonal terms the shear components of stress. The typical sign convention treats compressive stress as negative. The q_{ikjm} are the coefficients of a fourth-rank tensor called the *stress–optic tensor* and are of order of magnitude 10^2 mm/N. There are 81 terms in this

tensor, but because $\mathcal{T}$ and $\mathfrak{s}$ are symmetric, we have $q_{ikjm} = q_{ikmj}$ and $q_{ikjm} = q_{kijm}$. This reduces the number of independent terms to 36. Symmetry arguments reduce the number of required indices of q to two, as was the case for the electro-optic effect:

$$\begin{bmatrix} \mathfrak{s}_1 \\ \mathfrak{s}_2 \\ \mathfrak{s}_3 \\ \mathfrak{s}_4 \\ \mathfrak{s}_5 \\ \mathfrak{s}_6 \end{bmatrix} = \begin{bmatrix} \mathfrak{s}_1^0 \\ \mathfrak{s}_2^0 \\ \mathfrak{s}_3^0 \\ \mathfrak{s}_4^0 \\ \mathfrak{s}_5^0 \\ \mathfrak{s}_6^0 \end{bmatrix} + \begin{bmatrix} q_{11} & q_{12} & q_{13} & q_{14} & q_{15} & q_{16} \\ q_{21} & q_{22} & q_{23} & q_{24} & q_{25} & q_{26} \\ q_{31} & q_{32} & q_{33} & q_{34} & q_{35} & q_{36} \\ q_{41} & q_{42} & q_{43} & q_{44} & q_{45} & q_{46} \\ q_{51} & q_{52} & q_{53} & q_{54} & q_{55} & q_{56} \\ q_{61} & q_{62} & q_{63} & q_{64} & q_{65} & q_{66} \end{bmatrix} \begin{bmatrix} \mathcal{T}_1 \\ \mathcal{T}_2 \\ \mathcal{T}_3 \\ \mathcal{T}_4 \\ \mathcal{T}_5 \\ \mathcal{T}_6 \end{bmatrix}. \tag{14.51}$$

Associating a change in the index of refraction with an internal strain provides an equivalent formulation of the elasto-optic interaction:

$$\mathfrak{s}_{ik} = \mathfrak{s}_{ik}^0 + \sum_{j=1}^{3} \sum_{m=1}^{3} p_{ijkm} S_{jm}. \tag{14.52}$$

The S_{jm} in (14.52) are the components of the strain tensor. The diagonal components are tensile or stretching strains and the off-diagonal components are shear. The *strain–optic* tensor components p_{ijkm} are dimensionless numbers, and, as with the stress–optic components, symmetry arguments reduce the number of required indices to two. Table 14.8 lists some typical values of strain–optic components. The strain–optic components p_{ikjm} and the stress–optic components q_{ikjm} are linearly related, through the elastic stiffness constants $c_{mnk\ell}$:

$$p_{ijk\ell} = \sum_{m=1}^{3} \sum_{n=1}^{3} q_{ijmn} c_{mnk\ell}. \tag{14.53}$$

Reversing the applied stress, or the induced strain, results in a change from tension to compression and in general produces a change in the index of refraction. This means that, unlike the electro-optic effect, the photoelastic effect can be observed in a centrosymmetric crystal and in an isotropic material such as a glass or a liquid.

From the strain formalism, the origin of the photoelastic effect is associated with a change in the density of the medium. As we demonstrated in Chapter 7, (7.46), a change in the density of a material will result in a change in the index of refraction:

$$\frac{n^2 - 1}{n^2 + 2} \propto \rho. \tag{14.54}$$

However, this result cannot be simply applied to predict the elasto-optic properties of a material. The index of refraction is also modified through a change in the polarizability, induced by the strain. The change in polarizability is not an important effect in liquids, but, in solids, the molecular polarizability normally decreases under compression, counteracting the modification produced by the density.

Another complication in predicting the elasto-optic properties of a material occurs when the material is piezoelectric. There is a coupling between the electro-optic and photoelastic terms through the piezoelectric effect in noncentrosymmetric crystals. An applied strain produces an electric field, via the piezoelectric effect; the electric field generated by the strain modifies the index of refraction through the electro-optic effect. The index change produced by the piezoelectric coupling can either add to or subtract from the photoelastic effect.

Table 14.8 Strain–optic components

Isotropic	p_{11}	p_{12}
Fused silica	0.121	0.27
Water	0.31	0.31
Polystyrene	0.3	0.31

Cubic	p_{11}	p_{12}	p_{14}
GaAs	–0.165	–0.14	–0.072
Ge	0.27	0.235	0.125
LiF	0.02	0.128	–0.064
NaCl	0.11	0.153	–0.01

Trigonal	p_{11}	p_{12}	p_{13}	p_{14}	p_{31}	p_{33}	p_{41}	p_{44}
Ruby	–0.23	–0.03	0.02	0.0	–0.04	–0.2	0.01	–0.1
$LiNbO_3$	–0.02	0.08	0.13	–0.08	0.17	0.07	–0.15	0.12

Tetragonal	p_{11}	p_{12}	p_{13}	p_{31}	p_{33}	p_{44}	p_{66}
KDP	0.254	0.230	0.233	0.221	0.212	—	–0.0552
TeO_2	0.0074	0.187	0.34	0.09	0.24	–0.17	–0.046

We will neglect these complications by examining the effects of an applied stress on an isotropic material. Without the stress, the optical indicatrix is a sphere and there is only one index of refraction. With a stress applied, the material will become birefringent. Appendix 14A can be used to determine the nonzero elements of the **q** tensor, because the Kerr matrix has the same nonzero terms as the matrix **q**. For an isotropic material, (14.51) becomes

$$\begin{bmatrix} \eta_1 \\ \eta_2 \\ \eta_3 \\ \eta_4 \\ \eta_5 \\ \eta_6 \end{bmatrix} = \begin{bmatrix} \eta^0 \\ \eta^0 \\ \eta^0 \\ 0 \\ 0 \\ 0 \end{bmatrix} + \begin{bmatrix} q_{11} & q_{12} & q_{12} & 0 & 0 & 0 \\ q_{12} & q_{11} & q_{12} & 0 & 0 & 0 \\ q_{12} & q_{12} & q_{11} & 0 & 0 & 0 \\ 0 & 0 & 0 & q_{11}-q_{12} & 0 & 0 \\ 0 & 0 & 0 & 0 & q_{11}-q_{12} & 0 \\ 0 & 0 & 0 & 0 & 0 & q_{11}-q_{12} \end{bmatrix} \begin{bmatrix} \mathcal{T}_1 \\ \mathcal{T}_2 \\ \mathcal{T}_3 \\ \mathcal{T}_4 \\ \mathcal{T}_5 \\ \mathcal{T}_6 \end{bmatrix}.$$

The proper choice of coordinate system can simplify this equation. Assume that the elasto-optic material is a parallelepiped of isotropic plastic [see Figure 14.15(a)]. Compression $\boldsymbol{\mathcal{T}}$ is applied in the x_1 direction and light propagates through the plastic in the x_3 direction. From the tensor equation, the principal axes of the new ellipsoid are aligned with the applied stress and are equal to

$$\frac{1}{n_1^2} = \frac{1}{\eta_1} = \frac{1}{n_0^2} + \mathcal{T}_1 q_{11}, \tag{14.55a}$$

$$\frac{1}{n_2^2} = \frac{1}{\eta_2} = \frac{1}{\eta^0} = \frac{1}{n_0^2}, \tag{14.55b}$$

$$\frac{1}{n_3^2} = \frac{1}{\eta_3} = \frac{1}{\eta^0} = \frac{1}{n_0^2}. \tag{14.55c}$$

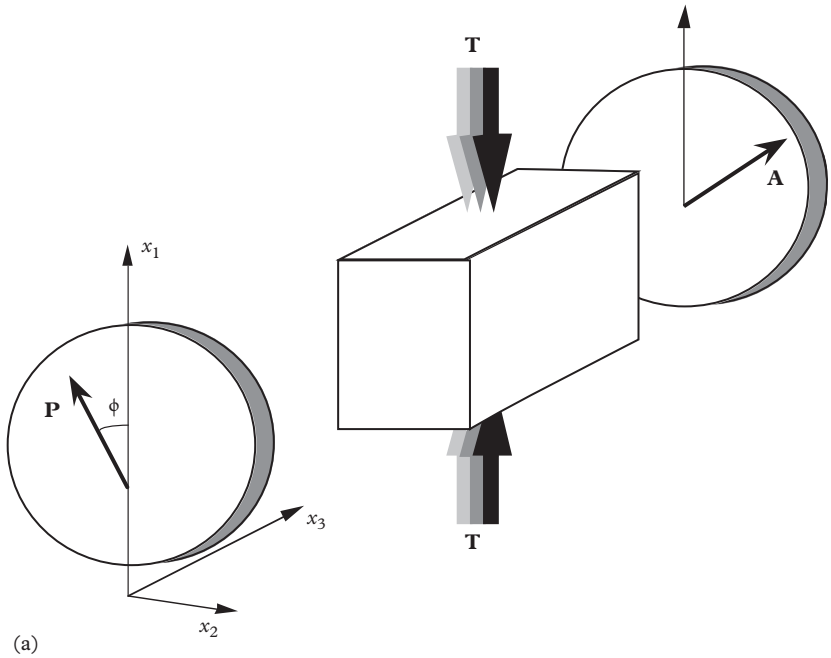

(a)

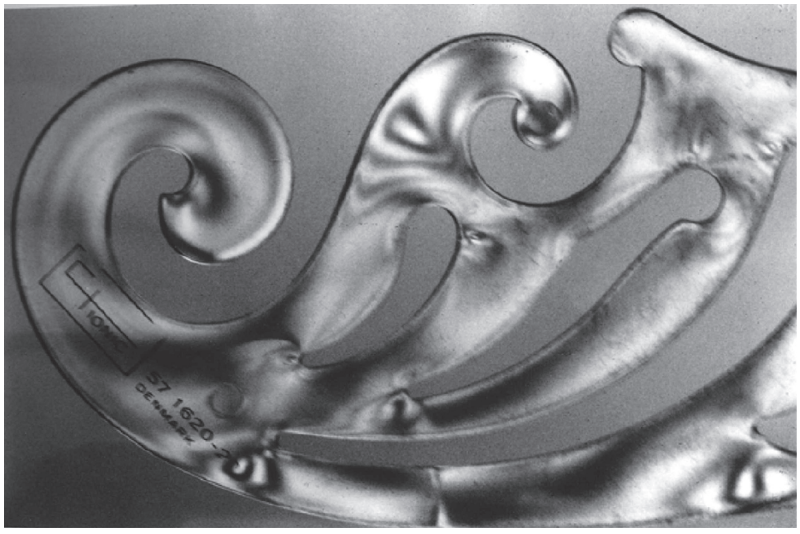

(b)

Figure 14.15 *(a) A compressive stress is applied to an isotropic material located between two crossed polarizers. The stress produces a birefringence, and the light transmitted by the system is a function of the applied stress. (b) In the manufacture of plastic French curves, components of stress are locked in the plastic. Here is shown a French curve, illuminated with polarized light and viewed through a polarizer oriented with its axis normal to the axis of polarization of the illumination. Sunlight, Rayleigh-scattered through 90° by the atmosphere, is polarized and was used to illuminate the French curve.*

The formerly isotropic material now has the indicatrix of a positive uniaxial crystal. In Figure 14.15(a), the material is illuminated by linearly polarized light, with the light wave's electric field oriented at 45° to the applied stress. This wave can be decomposed into two orthogonally polarized waves, polarized parallel to x_1 and x_2. The component of polarization along the x_1 axis and the component along the x_2 axis will travel at different velocities. The difference in phase between the two waves is given by

$$\Gamma = k_0 L(n_1 - n_2).$$

We may use (14.55) to write

$$\frac{1}{n_1^2} - \frac{1}{n_2^2} = q_{11}\mathcal{T}_1. \tag{14.56}$$

The stress does not produce a large change in the index of refraction, which allows the following approximation to be made:

$$\frac{1}{n_1^2} - \frac{1}{n_2^2} \approx \frac{2(n_2 - n_1)}{n^3}.$$

With this approximation, the phase difference for the two polarizations propagating through the stressed plastic is

$$\Gamma = \frac{\pi L}{\lambda_0} n^3 q_{11}\mathcal{T}_1. \tag{14.57}$$

The intensity transmitted by the crossed polarizers in Figure 14.15(a), after having passed through the stressed plastic, is given by (14.25b):

$$I = A^2 \sin^2\left(\frac{\pi L n^3}{2\lambda_0} q_{11}\mathcal{T}_1\right).$$

In monochromatic light, the contours of equal intensity, observed through the crossed polarizers, represent contours of equal stress. We have treated the easy problem of a single stress, lying in a predetermined direction. Usually, the direction of the stress will not be known, but can be determined by rotating the crossed polarizers. The size of the stress can be determined from the order of the fringes or, if white light is used, by their color.

14.8 Acousto-optics

If the strain in a medium is time-dependent, then we can treat the strain as a pressure wave or, equivalently, an acoustic wave, of wavelength Λ and frequency F, traveling at a velocity v:

$$\frac{\Omega}{\kappa} = \frac{\Lambda}{2\pi} 2\pi F = v.$$

Brillouin theoretically predicted the acousto-optic interaction in 1921. Concurrent verification of Brillouin's theory was made in 1932 by two pairs of investigators: by **P. Debye** and **F.W. Sears** and by **R. Lucas** and **P. Biquard**. A number of theoretical models have been developed for describing the acousto-optic interaction. [These mathematical models may also be used in describing holography (Chapter 12) and phase conjugation (Chapter 15).]

1. It is possible to treat acousto-optic diffraction as a parametric process in which the optic and acoustic waves are mixed via the elasto-optic effect. A *parametric process* occurs when an oscillator of frequency ω_0, described by the equation of motion

$$\frac{d^2y}{dt^2} + \gamma \frac{dy}{dt} + \omega_0^2 y = 0,$$

has one of its *parameters*, e.g., the spring constant, modulated by a frequency ω_P, the *pump frequency*. A typical equation of motion for a parametric oscillator is

$$\frac{d^2y}{dt^2} + \gamma \frac{dy}{dt} + (\omega_0^2 + \alpha \sin \omega_P t)y = 0.$$

When ω_P meets the proper conditions, the oscillations at ω_0 grow, using energy from the source of the pump frequency. A simple example of a parametric oscillator is a child's swing. The amplitude of the swing's excursions grows as the child "pumps" the swing, by modulating the length of the swing, twice each cycle. In the acousto-optic interaction, the pump wave is the incident light wave. The *signal wave*, which grows at the expense of the pump wave, has a frequency $\omega_P - \Omega$, where Ω is the acoustic wave's angular frequency. The acoustic wave is called the *idler wave* in the terminology of parametric processes. This model does not provide any unique insight into the acousto-optic effect, so we will not develop its formalism.

2. A second model is based on a phenomenological theory that assumes the induced polarization is proportional to the product of the electric field and the acoustic strain. This is equivalent to assuming that the dielectric constant has the same functional form as the density modulation produced by the acoustic wave. This formalism, known as coupled wave theory, will be discussed in Appendix 14B.
3. The third approach uses the formalism of scattering theory—treating light waves as photons and sound waves as particles called phonons. We will use this approach to discuss two limiting descriptions of acousto-optic scattering—Bragg scattering and Raman–Nath scattering.

We will conclude this section with a discussion of some applications that are based upon the Bragg scattering condition—the only type of acousto-optic scattering that has found extensive technological application.

The scattering model of the acousto-optic effect is based upon a quantum mechanical view of the interaction. Light, of frequency ω, and wavelength λ, is treated as a collection of particles, called *photons*, with energy

$$U_L = \hbar\omega$$

and momentum

$$p_L = \hbar k_L = \frac{h}{\lambda}.$$

The acoustic signal, of frequency Ω and wavelength Λ, is also treated as a collection of particles, called *phonons*, with energy

$$U_S = \hbar\Omega$$

and momentum

$$p_S = \hbar\kappa = \frac{h}{\Lambda}.$$

Two types of inelastic scattering processes can take place:

1. *Absorption:* An incident photon, of energy $\hbar\omega_i$, can collide with a phonon, of energy $\hbar\Omega$. The phonon is destroyed, and a photon, of energy $\hbar\omega_d$, leaves the scattering site.
2. *Emission:* A photon, of energy $\hbar\omega_i$, enters the scattering site, and a phonon, of energy $\hbar\Omega$, and a photon, of energy $\hbar\omega_d$, leave the scattering site.

The solution of a scattering problem requires the application of conservation of momentum and energy. Both types of three-particle inelastic scattering processes can use the same momentum conservation diagram by changing the direction of the phonon momentum $\boldsymbol{\kappa}$ (see Figure 14.16).

The energy conservation equations for emission and absorption are

$$\omega_i = \Omega + \omega_d, \quad \omega_i + \Omega = \omega_d. \tag{14.58}$$

The frequency of the scattered radiation is up- or down-shifted by the acoustic frequency. [Classically, the frequency shift associated with acousto-optic scattering can be viewed as a Doppler shift [see (8.10)] of the light wave reflected from the high-density region of the acoustic wave, traveling toward or receding from, the incident light wave.]

Quantum mechanics states that the probability of the absorption of a phonon is proportional to N and the probability of emission of a phonon is proportional to $N + 1$, where N is the number of phonons in a given mode. If these are thermal phonons, i.e., phonons that exist because of lattice vibrations of the material at a temperature T, then the number of phonons with energy $\hbar\Omega$ is

$$N = \frac{1}{e^{\hbar\Omega/kT} - 1}. \tag{14.59}$$

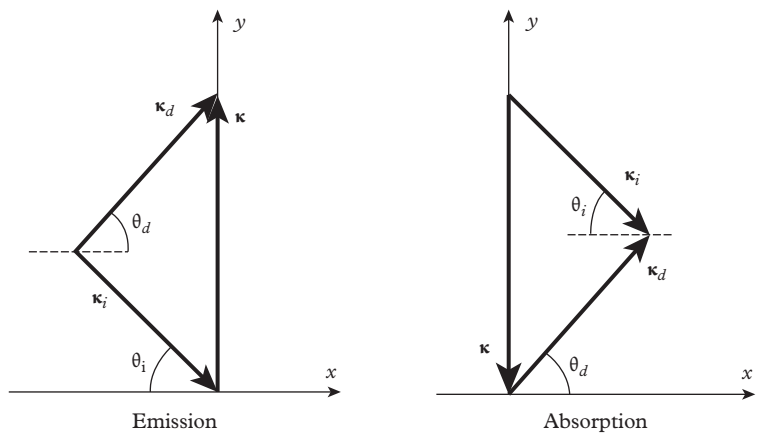

Figure 14.16 *Momentum conservation diagram for the scattering of light from acoustic waves. Subscript i denotes the incident wave parameters and subscript d the diffracted wave parameters.*

If T is room temperature (300 K) and Ω is a microwave frequency (10^9 Hz), then the approximation

$$N \approx \frac{kT}{\hbar\Omega} >> 1,$$

is an accurate one and the emission and absorption processes can be treated as equally probable.

From Figure 14.16, the x-components of the momentum vectors are

$$k_i \cos\theta_i = k_d \cos\theta_d \tag{14.60}$$

for both emission and absorption processes. The y-components for phonon absorption are

$$-k_i \sin\theta_i + \kappa = k_d \sin\theta_d$$

and those for phonon emission are

$$-k_i \sin\theta_i = -\kappa + k_d \sin\theta_d. \tag{14.61}$$

In this simple theory, we assume that the material is isotropic, so the velocity of the scattered light wave is identical to that of the incident wave.

14.8.1 Bragg Scattering

Since $\Omega \ll \omega$, we can, to first order, neglect the frequency shift predicted by (14.58) and assume that $\omega_i \approx \omega_d$. [This assumption, which treats the sound wave as stationary, is a reasonable approximation because the sound wave moves an infinitesimal amount during the passage of a light wave (see Problem 14.13)]. The momenta of the incident and scattered waves have identical magnitudes, $|k_i| = |k_d|$ because we neglect the frequency shift of the light wave caused by the inelastic scattering event. The solution of (14.61) can now be written as

$$\sin\theta_B = \frac{\kappa}{2k_i}. \tag{14.62}$$

This is Bragg's law, as given by (12.13), and describes diffraction of the light waves by the grating created from the wavefronts of the acoustic wave. The incident wavevector in the scattering calculation is defined in the scattering medium, but usually the wavevector is described in terms of its vacuum properties. If the material is isotropic, and the sides of the material are parallel to the direction of sound propagation, we can demonstrate (Problem 14.11) that it is not necessary to modify (14.62), because, in this case, the equation is independent of the index of refraction of the material.

A possible physical realization of Bragg diffraction is shown in Figure 14.17. The lines forming the grating in Figure 14.17 represent the regions of high density produced by the sound wave. For an acoustic frequency of 500 MHz and a sound speed of 6×10^3 m/s (the value for fused silica), the acoustic wavelength is

$$\Lambda = \frac{6 \times 10^3}{5 \times 10^8} = 1.2 \times 10^{-5} \text{ m}.$$

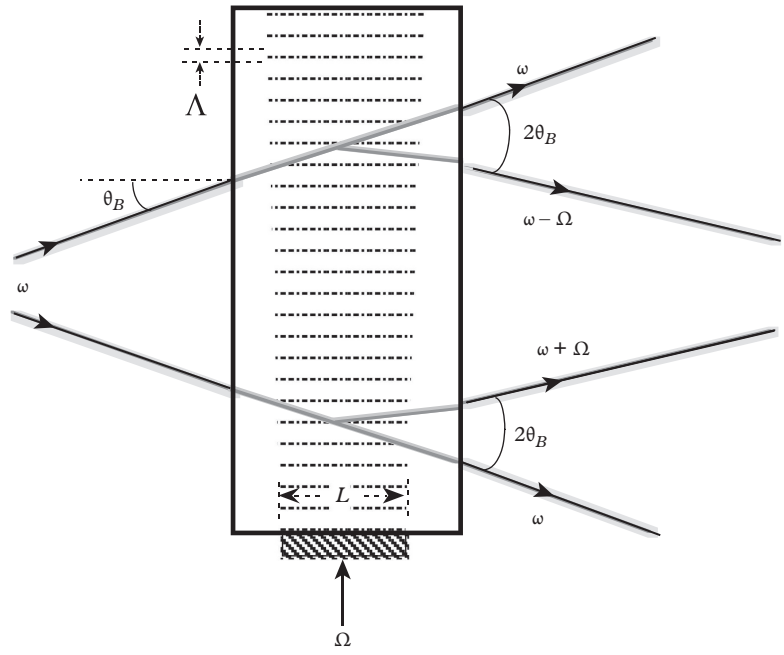

Figure 14.17 *Bragg scattering of an optical wave from an acoustic wave.*

If the illuminating wavelength $\lambda = 632.8$ nm, then (14.62) predicts a Bragg angle of

$$\theta_B = \sin^{-1}\left[\frac{6.238 \times 10^{-7}}{2(1.46)(1.2 \times 10^{-5})}\right] = 1.02°.$$

As will be shown in Appendix 14B, (14B.21), with sufficient acoustic power, all of the incident light can be diffracted into the Bragg angle.

14.8.2 Raman–Nath Scattering

A second limiting condition is approached when the width of the acoustic wavefront is decreased. [**C.V. Raman (1888–1970)** and his student, **N.S. Nagendra Nath** carried out the first analysis of this type of scattering.] It is through the analysis of this limiting condition that the scattering model provides a unique insight into the acousto-optic process. If the width of the sound wave, L, is decreased, diffraction will cause the wave to spread; see (10.17). Additional plane waves of sound are needed in the Fourier transform description of the more rapidly spreading wave. In the analysis, we will assume that a finite Fourier series is adequate to describe the sound beam. We will assume that as the width L of the beam is decreased, we need only add pairs of terms to the Fourier series to continue to describe the beam.

The first effect of decreasing L is that the pair of propagation vectors, $\boldsymbol{\kappa}_1$ and $\boldsymbol{\kappa}_{-1}$, must be added to the fundamental, $\boldsymbol{\kappa}_0$, to describe the sound wave. When a photon is scattered from this acoustic disturbance, the propagation vectors $(\mathbf{k}_d)_1$ and $(\mathbf{k}_d)_{-1}$ both satisfy the momentum conservation requirement. A further decrease in L results in $\boldsymbol{\kappa}_2$ and $\boldsymbol{\kappa}_{-2}$ appearing at reasonable amplitudes in the Fourier series. This increase in the number of propagation

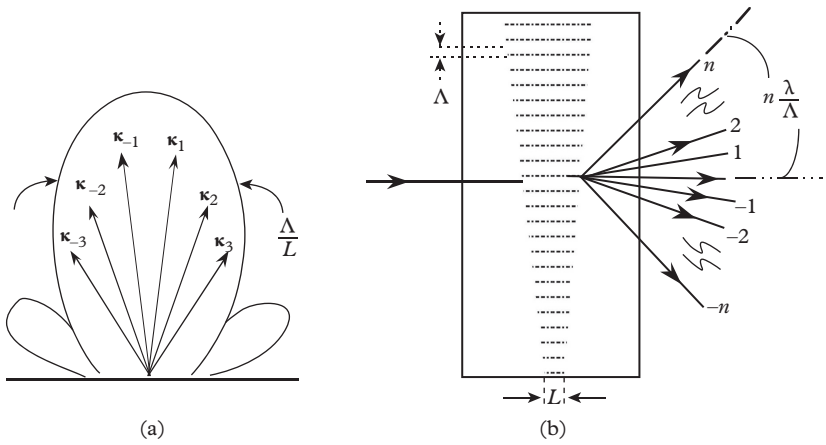

Figure 14.18 *Raman–Nath scattering. (a) Increase in propagation vectors due to diffraction of the acoustic wave. (b) Increase in number of diffracted orders of light.*

vectors $\boldsymbol{\kappa}_{\pm j}$ continues as L decreases. A schematic portrayal of the acoustic wave and its propagation vectors is shown in Figures 14.18(a) and 14B.2.

For each additional sound propagation vector needed to describe the sound beam, another light propagation vector is able to satisfy the momentum conservation condition. Reducing the width of the acoustic beam results in an increase in the number of diffracted waves produced by the acousto-optic interaction; see Figure 14.18(b). This scattering process resulting in a large number of diffracted orders is called *Raman–Nath scattering* and occurs for any grating whose thickness can be ignored. To meet the energy conservation condition, the nth diffracted order is Doppler-shifted in frequency by $n\Omega$.

The extent to which we can expect to observe a large number of diffracted orders is determined by the ratio of the angular width of the sound beam, Λ/L, to the separation between diffracted orders, λ/Λ. Historically, the quantity

$$Q = \frac{\kappa^2 L}{n k_{0i}} = \frac{2\pi}{n}\frac{\lambda_0}{\Lambda}\frac{L}{\Lambda}, \tag{14.63}$$

which contains this ratio, is used to define the Bragg ($Q > 1$) and Raman–Nath ($Q < 1$) regions. If the acoustic wavelength is 1.2×10^{-5} m and the illuminating wavelength is 623.8 nm, then $Q = (1.86 \times 10^4)L$. An acoustic beam wider than 0.1 mm would operate in the Bragg region. [The same quantity is used in holography to define thick ($Q > 10$) and thin ($Q < 10$) holograms. When Q is applied to holography, Λ is redefined as the fringe spacing and L as the hologram's thickness.]

Bragg scattering results in a more efficient light modulator because all of the light energy is contained in one diffracted beam. For this reason, most acousto-optic applications utilize the Bragg effect. The acousto-optic modulator excels over an electro-optic modulator in its capabilities to modify the frequency and direction of light waves. We will look at several applications of acoustic Bragg scattering that utilize the benefits provided by the acousto-optic device.

14.8.3 Acousto-optic Modulator

Any device that modifies the frequency of a wave is called a *frequency modulator*, or *fm modulator*, and is characterized by its bandwidth, i.e., the frequency range over which it can operate. An acousto-optic modulator shifts the frequency of the diffracted light by an amount equal to the acoustic frequency and therefore can be used as an fm modulator. The bandwidth of an acousto-optic light modulator is determined by the angular spread over which one can satisfy the Bragg condition (14.62). Usually, a large frequency bandwidth is needed to maximize the amount of information carried by the light wave; however, sometimes only a single frequency shift is required, for example, the generation of the local oscillator frequency for laser radar. We will determine the parameters affecting the operating bandwidth of an acousto-optic modulator by determining the angular bandwidth allowed by Bragg scattering. The analysis will demonstrate the technique for optimization of the acousto-optic cell as a frequency modulator.

The Bragg condition can be rewritten in terms of the acoustic frequency and velocity:

$$\sin\theta_B = \frac{\lambda F_m}{2v},$$

where v is the acoustic velocity and F_m is the modulation frequency. The derivative of this equation yields the angular spread created by a distribution of acoustic frequencies:

$$\cos\theta\ \Delta\theta = \frac{\lambda}{2v}\Delta F_m.$$

The maximum spread in acoustic frequencies defines the modulation bandwidth

$$\Delta F_m = \left(\frac{2v\cos\theta}{\lambda}\right)\Delta\theta. \tag{14.64}$$

The angle of incidence must change by $\Delta\theta$ in order to satisfy the Bragg condition when the acoustic frequency changes by ΔF. An alternate interpretation of (14.64) is that a wide instantaneous bandwidth is associated with a diverging beam, i.e., a large distribution of propagation vectors.

An increase in the bandwidth of the acousto-optic cell is accomplished by increasing the diffraction spreading of a finite-dimensioned optical or acoustic wave. Assume that we have an optical beam of width w, whose diffraction spread in the acousto-optic material is

$$\delta\theta = \frac{\lambda}{w},$$

and an acoustic beam of width L, with a diffraction spread of

$$\delta\Phi = \frac{\Lambda}{L}.$$

We will evaluate the effects of modifying the diffraction spread of the acoustic and/or light wave by the use of the momentum conservation diagrams in Figures 14.19 and 14.20. These diagrams are constructed through the use of a circle of radius equal to the magnitude of the incident optical wavevector k_i. Because we will neglect the frequency shift of the diffracted wave, the circle defines the lengths of both the incident and diffracted wavevectors.

If we assume $\delta\Phi \gg \delta\theta$, i.e., that the acoustic beam is narrow and the optical beam is wide, we obtain the conservation of momentum diagram shown in Figure 14.19. There will

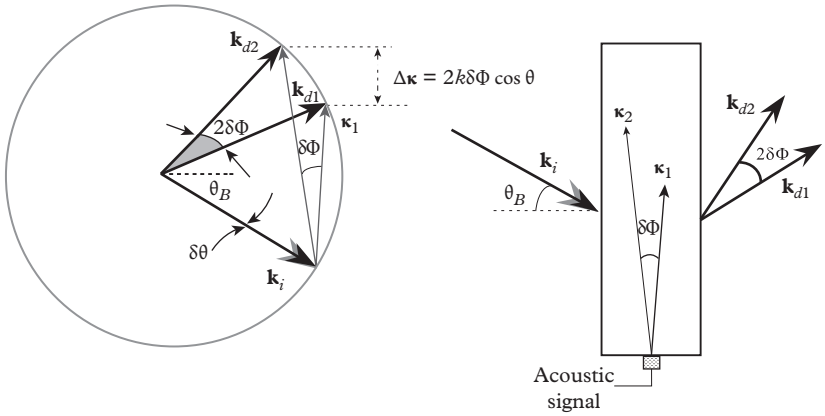

Figure 14.19 *Momentum conservation diagram for an acousto-optic modulator where the acoustic beam divergence dominates. A modulator with this property would be a good beam deflector.*

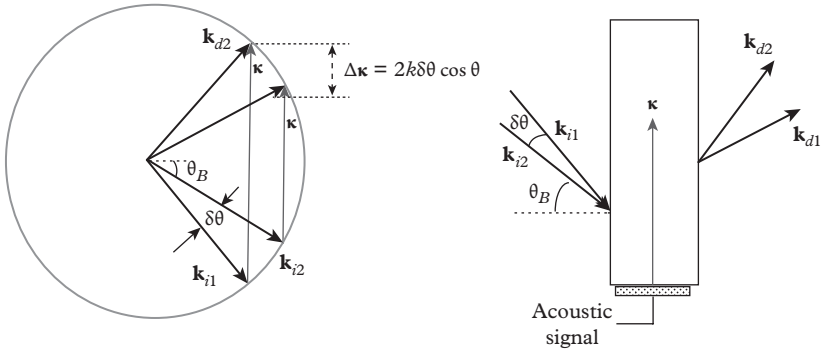

Figure 14.20 *Momentum diagram for the design of a frequency modulator using acousto-optics. Here we are assuming a very small spread in the acoustic beam, so all of the* $\boldsymbol{\kappa}$*'s are parallel.*

be a range of values of $\boldsymbol{\kappa}$, falling within $\delta\Phi$, whose vectors fall on the circle of Figure 14.19 and thus satisfy the Bragg condition. The apparent frequency bandwidth of this device is determined by the acoustic spread $\delta\Phi$ and is given by

$$\Delta F = \frac{2v\cos\theta_B}{L}\left(\frac{\Lambda}{\lambda}\right). \tag{14.65}$$

Not all of this apparent bandwidth, however, is available as a frequency-modulated signal. The acoustic waves diffract light into different directions, as is shown by $\mathbf{k}_{d1}$ and $\mathbf{k}_{d2}$ in Figure 14.19. Only light that is both frequency-shifted and collinear in direction can be used for fm modulation; thus, the frequency bandwidth is actually limited to the optical beam spread $\delta\theta$. If acoustic beam diffraction dominates, part of the acoustic energy is wasted.

If we assume that $\delta\theta \gg \delta\Phi$ (Figure 14.20), a broad, well-collimated, acoustic beam is used, with a narrow, diverging or converging, optical beam. Separate propagation vectors of the optical beam fall on the circle of Figure 14.20 and satisfy the Bragg condition for different acoustic frequencies. The spread in the optical beam provides an apparent frequency bandwidth of

$$\Delta F = \frac{2v\cos\theta}{w}. \tag{14.66}$$

Here also, the light is diffracted into a range of angles, and the entire bandwidth is not usable. The available bandwidth is determined by the acoustic beam's divergence, and the light at larger diverging angles is wasted.

The most efficient design matches the light's divergence to the acoustic beam's divergence: $\delta\theta = \delta\Phi$. The optimum design of a frequency modulator is thus given by

$$\frac{\lambda}{w} = \frac{\Lambda}{L},$$

and the modulation bandwidth can be calculated using either (14.65) or (14.64). With this design, no optical or acoustic energy is wasted.

From (14.66), we learn that a large bandwidth can be obtained by decreasing the width of the light beam; however, there is a minimum modulation frequency, F_{min}, which is determined by the beamwidth of the light wave. The minimum modulation frequency occurs when one wavelength of sound, Λ_{min}, is contained in the light beam:

$$\Lambda_{\text{min}} = \frac{2\pi v}{\Omega_{\text{min}}} = w\cos\theta.$$

(This limit is a bit too liberal, because it does not meet the sampling theorem requirement. A more useful minimum frequency is established by requiring three sound waves to be contained within the light beam.) Lower modulation frequencies cannot be resolved by the light beam, because only a portion of the density variation associated with the sound wave will be contained in the beam.

The material selected for an acousto-optic frequency modulator should have a large speed of sound if a large bandwidth is desired. Acousto-optic properties of a number of important materials are given in Table 14.9. For example, the velocity of propagation for a longitudinal wave in TeO_2 is 4.26 km/s; by using a beam focused to a width of 50 μm, the bandwidth of the modulator will be 170 MHz. In $LiNbO_3$, with the same optical parameters but a sound velocity of 6.6 km/s, the bandwidth will be 264 MHz. (A third method of expanding the bandwidth of an acousto-optic modulator uses an array of acoustic transducers. By adjusting the relative phase of the elements of the array, the acoustic beam direction is adjusted to ensure that the Bragg condition is met.)

Figures 14.19 and 14.20 assume that the medium isisotropic. If the acousto-optic diffraction occurs in a anisotropic (birefringent) medium, it is possible to construct an

Table 14.9 *Acousto-optic material properties*

Material	ρ (g/cm^3)	v_s (km/s)	n	Attenuation (dB/μs) at 500 MHz
Water	1.0	1.5	1.33	0.6
Fused silica	2.2	5.97	1.46	1.8
$LiNbO_3$	4.7	6.6	2.25	0.03
$PbMoO_4$	6.95	3.66	2.3	1.2
TeO_2	5.99	4.26 (long)	2.27	1.0
		0.617 (shear)[a]		

[a]An acoustic shear wave is a transverse acoustic wave.

acousto-optic tunable filter (AOTF) [7]. The resolution (bandpass) of a typical filter of this type ranges from several nanometers to tens of nanometers for the visible and near-infrared spectral regions, approximately one-thirtieth the value for ordinary Bragg diffraction.

14.8.4 Spectrum Analyzer

The Bragg equation (14.42) states that each frequency in an acoustic wave will be diffracted, through the elasto-optic interaction, into a unique angle. This reduces the effectiveness of an acousto-optic device used as a frequency modulator. However, what was a handicap is an advantage in a spectrum analyzer, where the objective is to measure the spectral content of the acoustic signal. The design goal of an fm modulator is to reduce the angular spread of the diffracted light, but the design goal of a spectrum analyzer is to maximize the angular spread to increase the accuracy of the analyzer. Figure 14.21 shows the optical system that performs the role of a spectrum analyzer. In the optical spectrum analyzer shown in Figure 14.21, a plane wave of light is incident on an acousto-optic modulator. The acoustic wave is generated by applying an electrical signal $f(t)$ to a piezoelectric transducer. The acoustic wave produced diffracts the light wave, via the elasto-optic interaction. The Fraunhofer diffraction pattern produced by the acousto-optic interaction appears at the back focal plane of the lens labeled "Fourier lens."

Figure 14.21 shows two typical diffraction patterns. The pattern in Figure 14.21(c) is produced when $f(t)$ consists of a simple sine wave at a frequency of 435 MHz. The pattern in Figure 14.14(b) is produced when $f(t)$ equals the sum of six sinusoidal waves, at six distinct frequencies. If a linear detector array is positioned in the plane where these diffraction patterns were recorded, it will measure the frequency content of $f(t)$. If you pick off one of the scattered beams, you can measure any modulation signal that might be contained on that tone.

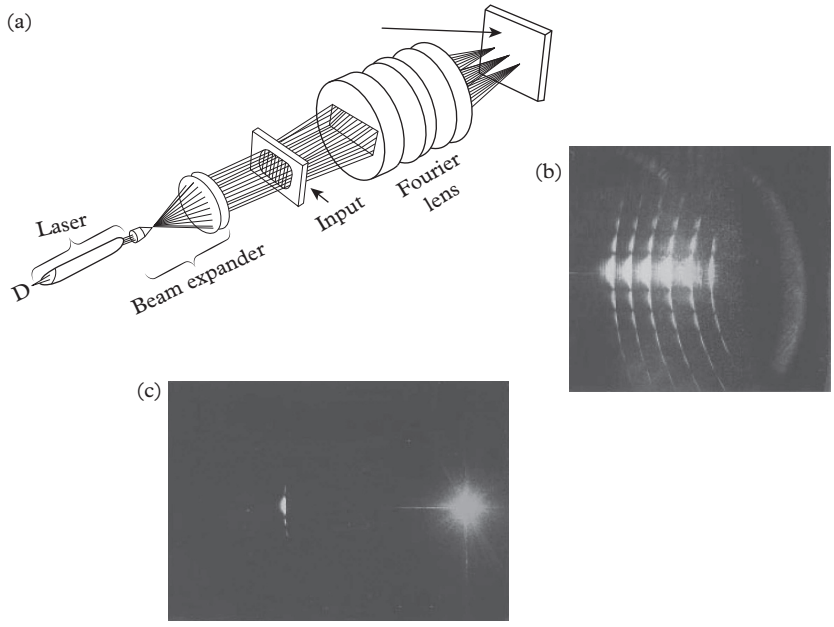

Figure 14.21 *(a) An optical spectrum analyzer. An electric signal is applied to a piezoelectric transducer that converts the electrical signal to an acoustic signal. A parallel beam of light is diffracted by the acoustic signal, and the diffraction pattern produced appears in the back focal plane of the transform lens. (b) The spectrum produced when $f(t)$ contains six pure tones. (c) The optical signal produced when a single tone is in the acousto-optic modulator. These photographs were intentionally overexposed to demonstrate that our theory has neglected other types of scattering processes. The engineer who wishes to use the acousto-optic effect in a spectrum analyzer must take all scattering processes into account, because the undesired scattered light will limit the dynamic range of the analyzer. (Courtesy A. VanderLugt.)*

14.8.5 Acousto-optic Beam Deflector

A second application that seeks to maximize the deflection angle change for a given frequency change is the acousto-optic beam deflector. The acousto-optic modulator can quite naturally be used as a deflection or scanning device, and a number of applications are based upon the ability to change the direction of the beam without modifying its intensity. If we rewrite (14.64), we obtain an equation for the change in a light beam's direction as a function of the change in the sound frequency:

$$\Delta\theta = \left(\frac{\lambda}{2v\cos\theta_B}\right)\Delta F.$$

By changing the frequency of the acoustic wave, the diffracted light beam can be redirected. A deflected light beam can address two independent diffraction angles in space, if they are spaced by more than the diffraction spread of the beam. Stated another way, the positions addressed by the diffracted light beam are unique if Rayleigh's criterion for resolution is met (Appendix 10B). In the optimum design of a beam deflector, it is therefore necessary for the diffraction spread of the acoustic beam, $\delta\Phi$, to be much larger than the diffraction spread of the optical beam (Figure 14.19). In this way, the positions addressed by the scanned light beam are determined by the diffraction spread of the light beam, $\delta\theta$, which is determined by the size of the incident light wave. If we divide the maximum deflection angle, $2\Delta\theta$, by the diffraction spread, we obtain the total number of resolvable positions that can be addressed by a beam deflector:

$$\begin{aligned} N &= \frac{2\Delta\theta}{\delta\theta} \\ &= \frac{w}{v\cos\theta_B}\Delta F. \end{aligned} \tag{14.67}$$

(This number also represents the total number of unique frequencies that can be measured by a spectrum analyzer.)To obtain a large value for N, the acousto-optic material should have a small acoustic propagation velocity. The modulator should also be very long, so that the optical beam size w can be large.

A second measure of a deflector's performance is the speed with which each resolvable position can be addressed. The maximum rate at which the frequency can be changed is limited by the time required for a sound wave to move across the light beam,

$$\tau = \frac{w}{v\cos\theta_B}.$$

(The acoustic wave at the old frequency must clear from the modulator before we are assured that the diffracted light beam is pointing in a new direction.). We are now faced with a trade-off that must be made. For the deflector to address a large number of spots, we wish w to be large, but to address the spots rapidly, we wish w to be small.

In recognition of the trade-off that must be made, a figure of merit for a deflector is defined to equal the number of separate positions that can be addressed in unit time:

$$\frac{N}{\tau} = \left(\frac{w}{v\cos\theta_B}\Delta F\right)\left(\frac{v\cos\theta_B}{w}\right) = \Delta F. \tag{14.68}$$

The quantity

$$N = \tau \Delta F,$$

called the *time–bandwidth product,* is a fundamental measure of the information-handling capability of any system.

In an imaging system, the equivalent measure of information throughput is called the *space–bandwidth* product. It is equal to the total number of pixels in an image, where a *pixel* is the smallest resolvable point in the image. In one dimension, a pixel would equal Δx, the resolution of the optical system. If the maximum image size were $x_{\max}$, then the space–bandwidth product would be

$$N = \frac{x_{\max}}{\Delta x}.$$

Equation (10A.7) gives the resolution of an imaging system:

$$\Delta x = \frac{\lambda f}{D} = \frac{\lambda f}{2a},$$

where f is the focal length of the optical system and D is its aperture diameter. From the geometrical optics definition of a ray angle γ (see Figure 5.9), we can rewrite this relationship as

$$\Delta x = \frac{\lambda}{2\gamma},$$

so the space–bandwidth product can be written

$$N = \frac{2x_{\max}\gamma}{\lambda}.$$

As the final step, recall the definition of the optical invariant, (5A.5):

$$\mathcal{H} = nx\gamma.$$

We see immediately that the space–bandwidth product of an imaging system is proportional to the optical invariant:

$$N = \frac{2}{n\lambda}\mathcal{H}.$$

We find that classical geometrical optics supports our modern view of an optical system as a linear system. The total information throughput is a constant proportional to the optical invariant.

One application of a beam deflector is the scanning of an image for electronic transmission or of a photosensitive material to produce an image in reception. In such an application, the time bandwidth of the scanner must match the space bandwidth of the image, and this requires a large value for N. As an example, consider an acousto-optic modulator made of TeO_2 using a slow shear wave; the propagation velocity is 0.617 km/s. If the optical beamwidth is 25 mm and the bandwidth is 50 MHz, then the number of addressable positions is 2026. The beam direction cannot be changed in a time shorter than 32 μs. This performance would be adequate for facsimile transmission applications or for a high-resolution spectrum analyzer.

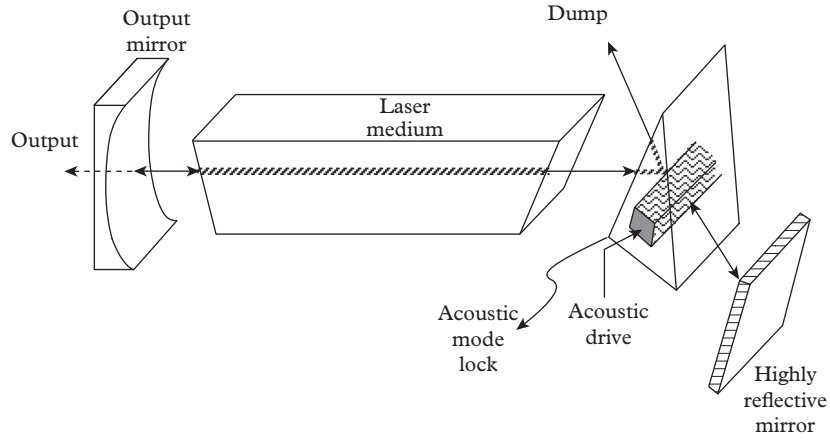

Figure 14.22 *The use of an acousto-optic transducer in a laser cavity. In the mode-locking application shown here, the acoustic wave turns the laser off by diffracting part of the energy out of the laser cavity. This loss is removed by turning off the acoustic energy.*

Another application of a beam deflector is the rapid diffraction of a light beam out of a laser cavity, as shown in Figure 14.22. In such an application, the value of N is not important, but τ should be very small. An acousto-optic beam deflector used for rapidly switching a light beam out of a laser cavity fulfills the role of a Q-switch, a cavity dumper, or a mode-locker. The details of the design will be ignored here, and only a general description of the role of the acousto-optic device will be given. In the design shown in Figure 14.22, the laser operates normally without an acoustic signal present. The laser oscillations are established between the output mirror and the highly reflective back mirror; the prism performs the role of a frequency selector by refracting only one wavelength onto the back mirror. When an acoustic wave is launched in the prism, part of the light energy, labeled "Dump" in Figure 14.22, is diffracted out of the cavity. This increases the loss in the cavity, and the laser turns off. By interrupting the laser action at the proper times, high-power narrow pulses can be generated.

As an example of an acousto-optic mode-locker, an acousto-optic beam deflector can be constructed of fused silica. The sound velocity is 6 km/s, the bandwidth is 40 MHz, and the width of the optical beam is 4 mm. The total number of addressable positions is 27, but now $\tau = 0.7\ \mu$s.

14.9 Summary

In this chapter, the linear and quadratic electro-optic effects were found to modify the index of refraction in a material and produce birefringent behavior. This behavior creates an electrically controllable retardation that can be used to produce intensity-modulated light. If the electro-optic material is placed between crossed polarizers, the light transmitted through the polarizers is given by

$$\frac{I}{I_0} = \sin^2 \frac{\Gamma}{2},$$

where the phase change Γ is a function of the applied electric field.

For the quadratic electro-optic effect,

$$\begin{aligned}\Gamma &= 2\pi \mathcal{K} E^2 L \\ &= \frac{\pi}{\lambda} n_0^3 \rho E^2 L \\ &= \frac{1}{2}\left(\frac{V}{V_{\lambda/2}}\right)^2,\end{aligned}$$

where

$$V_{\lambda/2} = \frac{d}{\sqrt{2\mathcal{K}L}}$$

is the voltage that must be applied across the electro-optic material, of thickness d and length L, to create a half-wave retardation. The parameter $\mathcal{K}$ is called the Kerr constant.

For the linear electro-optic effect, two possible modulator designs were analyzed:

1. The longitudinal modulator produces a phase change given by

$$\begin{aligned}\Gamma &= \frac{2\pi V}{\lambda} n^3 r \\ &= \pi \frac{V}{V_\pi},\end{aligned}$$

   where the voltage needed to create a half-wave retardation,

$$V_\pi = \frac{\lambda}{2n^3 r},$$

   is independent of the dimensions of the modulator.

2. The transverse modulator produces a phase change given by

$$\Gamma = \frac{\pi n^3 r}{\lambda}\left(\frac{VL}{d}\right).$$

   The half-wave retardation voltage for the transverse modulator is

$$V_\pi^t = \frac{2V_\pi}{L/d}.$$

A material placed in a magnetic field will exhibit a magneto-optic effect called the Faraday effect. This interaction causes the material to become optically active. A linearly polarized wave is rotated through an angle given by

$$\theta = \mathcal{V} L H,$$

where H is the applied magnetic field and $\mathcal{V}$ is called Verdet's constant.

Several magneto- and electro-optic effects were discussed in this chapter. A comparison of the size of each of the interactions Table 14.10.

A strain field will also create birefringent behavior in a normally isotropic material. A time-dependent strain field is called an acoustic field, even when the frequency exceeds

Table 14.10 *Order-of-magnitude estimates of electro- and magneto-optic effects*

Effect	Field	Magnitude
Pockels	E	10^{-12}
Kerr	E^2	10^{-19}
Faraday	H	10^{-14}
Cotton–Mouton	H^2	10^{-25}
Voigt	H^2	10^{-28}

the range of human hearing. The acoustic wave will diffract a light wave into an angle given by the Bragg equation

$$\sin\theta_B = \frac{\lambda}{2\Lambda}.$$

The frequency of the diffracted light is shifted, by the acoustic frequency, from the incident wave's frequency. The Bragg scattering condition only applies to an acoustic wave whose wavefront is wide relative to the acoustic wavelength. For waves that are narrow, a more complicated scattering condition called Raman–Nath scattering occurs. For Raman–Nath scattering, a number of diffracted orders are visible.

14.10 Problems

14.1. Derive the equation giving the change in the index of refraction produced by the linear electro-optic effect, (14.13).

14.2. Write the equation of the electro-optic indicatrix for a crystal belonging to the $\bar{4}2m$ symmetry group.

14.3. Assume that the indices of refraction for a uniaxial crystal belonging to point group $\bar{4}2m$ are $n_1 = n_2 = n_o$ and $n_3 = n_e$. Also assume that an external electric field is applied along the z-axis (label it E_3). Use these assumptions to modify the equation written in Problem 14.2 and then find the coordinate transformation needed to put this equation into the form (14.33).

14.4. Using (14.33), derive the index change produced by the electric field applied along the z-axis.

14.5. Derive the equation for the phase change produced by a longitudinal electro-optic modulator using the Pockels effect, (14.34).

14.6. Derive the equation for the phase change produced by a transverse electro-optic modulator using the Pockels effect, (14.37).

14.7. For a Pockels modulator, calculate the half-wave voltage for KDP and ADP for $\lambda = 500$ nm.

14.8. If we select the transverse electro-optic modulator design, what is the applied voltage needed to obtain a phase shift of π in KDP and ADP, assuming a crystal thickness $d = 1$ mm? What is the length needed to give a $\pi/4$ bias?

14.9. Calculate the value of the Larmor precession frequency for a magnetic field of 1 T.

14.10. What colors would signify large values of stress if we used white light to observe stress in a plastic model? (The use of photoelastic models is an important tool in architectural research.)

14.11. Show that Bragg's equation (14B.19) is independent of the index of refraction of the material if the material is isotropic and the sides of the material are parallel to the direction of sound propagation.

14.12. Assume that anacoustic system has a center frequency of 200 MHz and a bandwidth of 100 MHz. What should the diameters of the light and the acoustic beams beto address 25 positions?

14.13. The sound velocity in glass is 3 km/s. If the sound wave is 1 cm wide, how far does the sound wave move during the passage of a light wave across the width of the sound wave? The index of refraction of the glass is $n = 1.5$.

14.14. Lithium niobate, a member of the $3m$ point group, is a popular material for electro-optic modulators. Calculate the indicatrix for this material with the electric field along the z-direction.

14.15. Using the indicatrix produced in Problem 14.14, find the index change as a function of applied field in lithium niobate. Assume the light wave is propagating in the x-direction and find the phase shift as a function of applied voltage.

14.16. GaAs is a cubic material belonging to the $\bar{4}3m$ point group that is used as an electro-optic modulator in the infrared. Calculate the indicatrix for this material with the electric field along the z-direction.

14.17. Using the indicatrix produced in Problem 14.16, find the index change as a function of applied field in GaAs. Assume the light wave is propagating in the z-direction and find the phase shift as a function of applied voltage. What is the phase shift if the light is propagating in the x-direction?

14.18. If 1 W of acoustic energy is sent into a TeO_2 crystal as an acoustic shear wave, what change in the index of refraction is produced? Assume that the sound beam is round, with a diameter of 1 cm.

14.19. What is the size of the magnetic field required to rotate the polarization of light by $\pi/2$ in zinc sulfide?

REFERENCES

1. Odishaw, E.U. and H. Condon, *Handbook of Physics*. 2nd ed. 1967: McGraw-Hill.
2. Kittel, C., *Introduction to Solid State Physics*. 7th ed. 1995: Wiley.
3. Landau, L.D., L.P. Pitaevskii, and E.M. Lifshitz, *Electrodynamics of Continuous Media*. 2nd ed. (*Course of Theoretical Physics*. Vol. 8). 1984: Butterworth-Heinemann.
4. Grant, R.F., *Introduction to Modern Optics*. 2nd ed. 1989: Dover.
5. Brewster, D., *On the laws which regulate the polarisation of light by reflexion from transparent bodies*. Phil. Trans. R. Soc. Lond., 1815. **105**: p. 125–159.
6. Mueller, H., Phys. Rev., 1935. **47**: p. 947.
7. Harris, S.E. and R.W. Wallace, *Acousto-optic tunable filter*. J. Opt. Soc. Am., 1969. **59**: p. 744–747.

Appendix 14A Pockels and Kerr Tensors

In Chapter 14, we demonstrated that for a lossless crystal,

$$\mathfrak{I}^0_{ik} = \mathfrak{I}^0_{ki} .$$

We can use a similar argument to demonstrate that

$$r_{ikj} = r_{kij},$$
$$\rho_{ikjm} = \rho_{kijm} = \rho_{ikmj}.$$

This reduces the number of independent coefficients for the Pockels tensor to 18 and for the Kerr tensor to 36. Because of this symmetry requirement, we can reduce the number of subscripts by replacing *ik* by a single subscript and *jm* by a single subscript in the following manner:

$$\begin{aligned} 11 &\rightarrow 1, & 23 &\rightarrow 4,\\ 22 &\rightarrow 2, & 31 &\rightarrow 5,\\ 33 &\rightarrow 3, & 12 &\rightarrow 6. \end{aligned}$$

With this new notation, (14.1) can be rewritten in matrix notation as

$$\begin{bmatrix} \Im_{11}-\Im_1^0 \\ \Im_{22}-\Im_2^0 \\ \Im_{33}-\Im_3^0 \\ \Im_{23} \\ \Im_{31} \\ \Im_{12} \end{bmatrix} = \begin{bmatrix} r_{11} & r_{12} & r_{13} \\ r_{21} & r_{22} & r_{23} \\ r_{31} & r_{32} & r_{33} \\ r_{41} & r_{42} & r_{43} \\ r_{51} & r_{52} & r_{53} \\ r_{61} & r_{62} & r_{63} \end{bmatrix} \begin{bmatrix} E_1 \\ E_2 \\ E_3 \end{bmatrix} + \begin{bmatrix} \rho_{11} & \rho_{12} & \rho_{13} & \rho_{14} & \rho_{15} & \rho_{16} \\ \rho_{21} & \rho_{22} & \rho_{23} & \rho_{24} & \rho_{25} & \rho_{26} \\ \rho_{31} & \rho_{32} & \rho_{33} & \rho_{34} & \rho_{35} & \rho_{36} \\ \rho_{41} & \rho_{42} & \rho_{43} & \rho_{44} & \rho_{45} & \rho_{46} \\ \rho_{51} & \rho_{52} & \rho_{53} & \rho_{54} & \rho_{55} & \rho_{56} \\ \rho_{61} & \rho_{62} & \rho_{63} & \rho_{64} & \rho_{65} & \rho_{66} \end{bmatrix} \begin{bmatrix} E_1^2 \\ E_2^2 \\ E_3^2 \\ E_2E_3 \\ E_3E_1 \\ E_1E_2 \end{bmatrix}. \tag{14A.1}$$

The material's symmetry reduces the number of nonzero coefficients in (14A.1).

Table 14A.1 lists the point groups [1] that do not exhibit a Pockels effect.

Table 14A.1 *Crystal groups with no Pockels effect*

System		Group
Triclinic		$\bar{1}$
Monoclinic		$2/m$
Orthorhombic		mmm
Tetragonal	$4/m$	$4/mmm$
Trigonal	$\bar{3}$	$\bar{3}m$
Hexagonal	$6/m$	$6/mmm$
Cubic	$m3$	$432 \quad 3m$
Isotropic		—

Table 14A.2 displays the nonzero terms for each of the point groups without inversion symmetry. Table 14A.2 applies to the Pockels tensor, the second-order susceptibility tensor **d**, which is discussed in Chapter 15, and the piezoelectric tensor, which we will not discuss. Table 14A.3 displays the nonzero tensor elements for the Kerr and photoelastic tensors. Three of the fourth-rank tensors appear slightly more complicated than they actually are. For the trigonal and hexagonal systems,

$$\rho_{66} = \rho_{11} - \rho_{12}.$$

For the trigonal system, the Kerr tensor has

$$\rho_{16} = 2\rho_{62}, \quad \rho_{46} = 2\rho_{52}, \quad \rho_{56} = 2\rho_{41}.$$

For the hexagonal system, the Kerr tensor has

$$\rho_{61} = 2\rho_{26}.$$

The photoelastic tensors for these systems differ from the electro-optic tensors in that the elements just identified differ by a factor of two. Thus, for the trigonal and hexagonal systems,

$$p_{66} = \frac{1}{2}(p_{11} - p_{12})s.$$

For the trigonal system,

$$p_{16} = p_{62}, \quad p_{46} = p_{52}, \quad p_{56} = p_{41}.$$

For the hexagonal system,

$$p_{61} = p_{26}.$$

Table 14A.2 *Pockels and second-order susceptibility tensors*

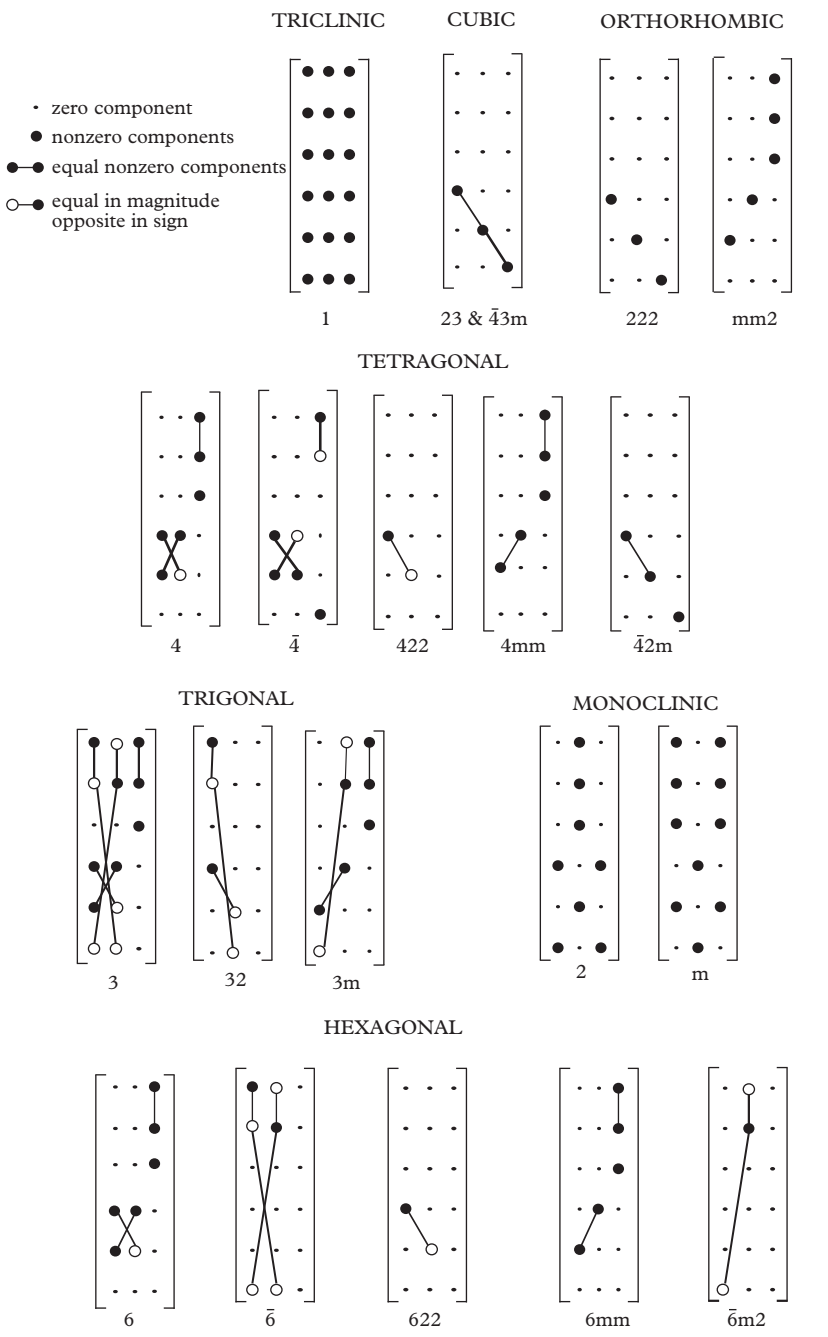

Table 14A.3 *Kerr and photoelastic tensors.*

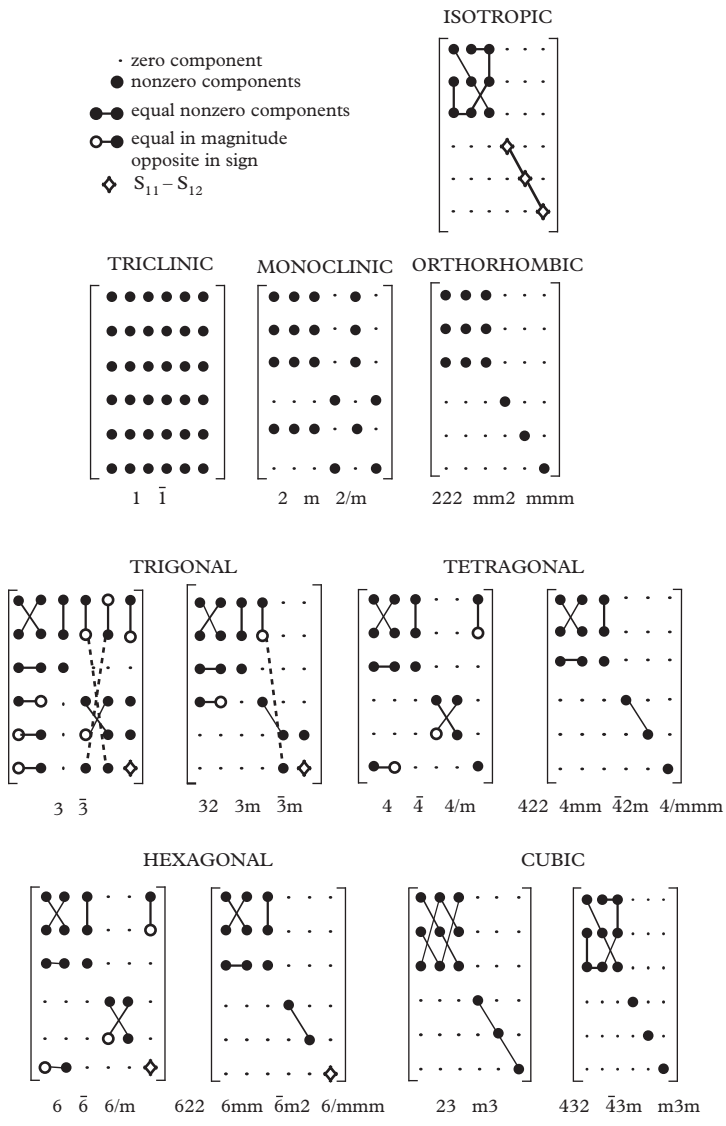

REFERENCE

1. Ashcroft, N.W. and N.D. Mermin, *Solid State Physics*. 1976: Saunders.

Appendix 14B Phenomenological Acousto-optic Theory

An acoustic wave is a pressure wave that modulates the number density of the atoms of the medium:

$$N(\mathbf{r},\mathbf{t}) = N_0[1 + \Delta\cos(\Omega t - \boldsymbol{\kappa}\cdot\mathbf{r})], \tag{14B.1}$$

where the acoustic wave variables are, as defined in Chapter 14,

$$\frac{\Omega}{\kappa} = \frac{\Lambda}{2\pi}2\pi F = v. \tag{14B.2}$$

We assume the dielectric constant has the same form as (14B.1),

$$\varepsilon = \varepsilon' + \varepsilon_1\cos(\Omega t - \boldsymbol{\kappa}\cdot\mathbf{r}), \tag{14B.3}$$

or, in terms of the index of refraction,

$$\frac{1}{n^2} = \frac{1}{n_0^2} + \frac{1}{n_1^2}\cos(\Omega t - \boldsymbol{\kappa}\cdot\mathbf{r}).$$

Since the dielectric constant is now a function of space and time, we must rederive the propagation properties of a wave from Maxwell's equations. Taking the curl of (2.3) and using (2A.12), as was done in Chapter 2, produces

$$-\nabla^2\mathrm{E} + \nabla(\nabla\cdot\mathbf{E}) = -\mu\frac{\partial^2\mathbf{D}}{\partial t^2}.$$

We can find the divergence of **E** by first writing the divergence of **D**,

$$\nabla\cdot\mathbf{D} = \varepsilon\nabla\cdot\mathbf{E} + \mathbf{E}\cdot\nabla\varepsilon = 0,$$

where ε is no longer independent of the spatial coordinates. Solving for the divergence of **E** yields

$$\begin{aligned}\nabla\cdot\mathbf{E} &= -\frac{1}{\varepsilon}\mathbf{E}\cdot\nabla\varepsilon \\ &= -\mathbf{E}\cdot\nabla\ln\varepsilon.\end{aligned} \tag{14B.4}$$

The wave equation that describes propagation of light in a medium modulated by an acoustic wave becomes

$$\nabla^2\mathbf{E} + \nabla(\mathbf{E}\cdot\nabla\ln\varepsilon) = \mu\frac{\partial^2}{\partial t^2}(\varepsilon\mathbf{E}). \tag{14B.5}$$

If we assume **E** is a superposition of plane waves, of wavelength λ/n in the medium, and we use the time- and-space dependent equation for ε, we find that $\boldsymbol{\nabla}(\mathbf{E}\cdot\boldsymbol{\nabla}\ln\varepsilon)$ is of the order

$$\mathcal{O}(\nabla(\mathbf{E}\cdot\nabla\ln\varepsilon)) = \varepsilon_1\frac{\lambda}{\Lambda}\nabla^2\mathbf{E}.$$

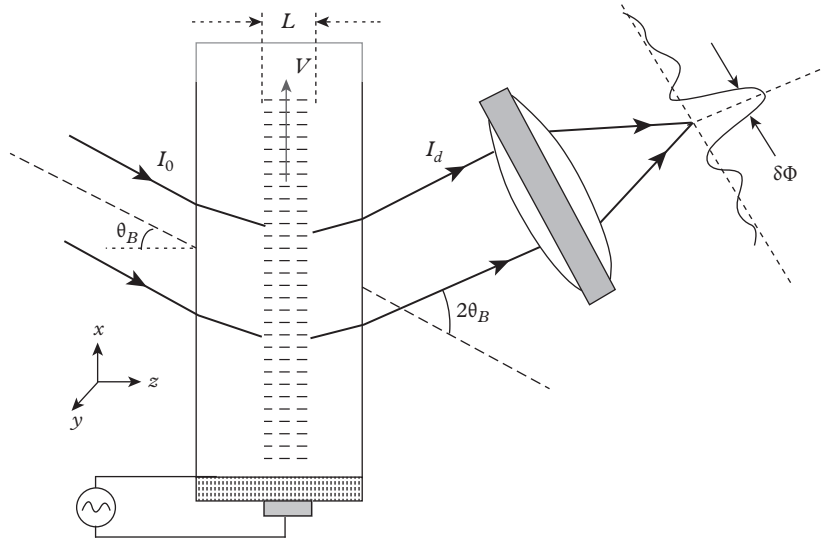

Figure 14B.1 *Geometry for an acousto-optic experiment. We assume that the device is infinitely wide in the y-direction.*

Since $\mathcal{O}(\lambda/\Lambda) = 10^{-2}$, we may normally neglect that term and write the wave equation as

$$\nabla^2 \mathbf{E} = \mu \frac{\partial^2}{\partial t^2}(\varepsilon \mathbf{E}). \tag{14B.6}$$

We will use the acousto-optic experiment shown in Figure 14B.1. The sound is traveling in the x-direction. It occupies the region, in the z-direction, of $-L/2 \le z \le L/2$. Light is incident on the sound column at an angle θ with respect to the z-axis and is represented by

$$\tilde{\mathbf{E}} = \mathbf{E}_0 e^{i(\omega t + kx \sin\theta - kz\cos\theta)}. \tag{14B.7}$$

After passing through the sound field, the electric field is modulated by the periodicity of the sound field. To describe the periodic disturbance of the light's wavefront, we expand the wave in a Fourier series:

$$\tilde{\mathbf{E}} = \sum_{\ell=-\infty}^{\infty} V_\ell(z) e^{i[(\omega+\Omega\ell)t + (k\sin\theta - \ell\kappa)x - kz\cos\theta]}. \tag{14B.8}$$

Equation (14B.8) represents an expansion of $\mathbf{E}$ in terms of plane waves. The index ℓ labels the ℓth Fraunhofer diffraction order or the ℓth spatial frequency needed to describe the wavefront.

The quantum mechanical formalism, used in the scattering model of acousto-optics, views the ℓth term of the expansion as a plane wave originating from the destruction or creation of ℓ phonons by the incident light beam.

The frequency of the ℓth order in (14B.8) is $\omega + \ell\Omega$. This frequency shift is the Doppler shift produced by the reflection of the light wave from a moving acoustic wavefront.

The x-component of the wavevector for the ℓth order is

$$\begin{aligned} k_{\ell x} &= k\sin\theta - \ell\kappa \\ &= -k_\ell \sin\phi_\ell . \end{aligned}$$

(In Figure 14B.1, the special case of Bragg scattering, where $\phi_\ell = 2\theta_B$, is shown). The ℓth wavevector has a magnitude given by

$$\begin{aligned} k_\ell &= \frac{\omega_\ell}{c} \\ &= \frac{\omega + \ell\Omega}{c}, \end{aligned}$$

and the angular deflection ϕ_ℓ of the ℓth wavevector is

$$\begin{aligned} \sin\phi_\ell &= \frac{c(\ell\kappa - k\sin\theta)}{\omega + \ell\Omega} \\ &= \frac{\ell\dfrac{\kappa}{k} - \sin\theta}{1 + \ell\dfrac{\Omega}{\omega}} \\ &\approx \ell\frac{\lambda}{\Lambda} - \sin\theta. \end{aligned} \tag{14B.9}$$

For a given λ, the angular deflection ϕ_ℓ of the ℓth order decreases with increasing Λ. If Λ is sufficiently large, diffraction of the light by the sound waves will not be observed. In Chapter 14, the lower limit on observation of acousto-optic diffraction was established by requiring an acoustic wavelength no longer than the width of the optical beam. Here, the limit is established by the requirement that the diffracted and undiffracted beams not overlap.

We substitute (14B.8) into (14B.6), neglecting terms in d^2V_ℓ/dz^2. The second derivative is neglected because, in this approximation, each diffracted plane wave changes slowly with z. Once the substitutions $\omega = kc$ and $\Omega = \kappa v$ have been made, the facts that $\Omega/\omega \ll 1$ and $v/c \ll 1$ are used to produce an equation describing the behavior of the amplitudes of the diffracted plane waves:

$$\frac{\partial V_\ell(z)}{\partial z} + i\beta_\ell V_\ell(z) + \xi[V_{\ell+1}(z) - V_{\ell-1}(z)] = 0, \tag{14B.10}$$

where

$$\beta_\ell = -\frac{\kappa\ell}{\cos\theta}\left(\sin\theta - \frac{\ell\kappa}{2k}\right) \tag{14B.11}$$

and

$$\begin{aligned} \xi &= \frac{1}{4}\left(\frac{\varepsilon_1}{\varepsilon'}\right)\frac{k}{\cos\theta} \\ &= \frac{1}{4}\left(\frac{n_0}{n_1}\right)^2\frac{k}{\cos\theta}. \end{aligned} \tag{14B.12}$$

The physical significance of the two parameters β_ℓ and ξ, will become apparent later in the analysis.

The general solution of the set of coupled equations (14B.10), is very difficult. Normally, the problem is considered in two limits. In the first limit, we assume that $V_{\ell+1} \ll V_\ell$. This approximation results in a theory that describes Bragg scattering. In the second limit, we assume

$$\frac{\beta_\ell V_\ell(z)}{\xi} = 0, \tag{14B.13}$$

which occurs when $\kappa \to 0$, as is apparent by examining (14B.11). This approximation describes Raman–Nath scattering.

14B.1 Bragg Region

The Bragg scattering equation is obtained by solving (14B.10) under the assumption that $V_{\ell+1} \ll V_\ell$. In the derivation, we will only consider terms of the Fourier series for which $\ell \geq 0$. (This assumption limits the theory to a description of light upshifted in frequency by acousto-optic scattering. The resulting theory can be used for light downshifted in frequency by replacing ℓ by $-\ell$.) The initial condition selected for this discussion assumes that before encountering the sound wave, only the fundamental frequency of the Fourier series is present, i.e., for $z < -L/2$, only $V_0 \neq 0$. These assumptions modify (14B.10), reducing it to a simple differential equation

$$\frac{\partial V_\ell}{\partial z} + i\beta_\ell V_\ell = \xi V_{\ell-1}. \tag{14B.14}$$

The solution of this equation is

$$V_\ell = e^{-i\beta_\ell z} \int_{-\infty}^{\infty} \xi V_{\ell-1} e^{i\beta_\ell z'}\, dz'. \tag{14B.15}$$

The physical significance of the parameter ξ can be deciphered by first obtaining an expression for the change in index of refraction produced by the acoustic wave. From (14B.3), we can write the difference between the maximum and minimum values of the dielectric constant produced by the acoustic wave:

$$\varepsilon_{\max} - \varepsilon_{\min} = \left.\frac{1}{n^2}\right|_{\max} - \left.\frac{1}{n^2}\right|_{\min} = \frac{2}{n_1^2}.$$

We define the difference between the index of refraction at its maximum and minimum values as

$$\Delta n = n_{\max} - n_{\min},$$

where

$$\left.\frac{1}{n^2}\right|_{\max} = \frac{1}{n_{\min}^2}, \quad \left.\frac{1}{n^2}\right|_{\min} = \frac{1}{n_{\max}^2},$$

The peak-to-peak dielectric constant variation produced by the acoustic wave is approximately equal to

$$\varepsilon_{\max} - \varepsilon_{\min} \approx \frac{2\Delta n}{n_0^3}.$$

The index change produce by the acoustic wave is therefore

$$\Delta n = \frac{n_0^3}{n_1^2}.$$

The parameter ξ, as defined in (14B.12) can now be seen to be proportional to the index change produced by the acoustic wave. Rewriting (14B.12) in terms of the index change yields

$$\xi = \frac{1}{4}\left(\frac{\Delta n}{n_0}\right)\frac{k}{\cos\theta}. \tag{14B.16}$$

If we treat the sound wave as a plane wave with a uniform amplitude across its wavefront, then over the acoustic beamwidth of $-L/2 \le z \le L/2$, Δn must be constant. Since ξ is proportional to the index change, it must be a nonzero constant over the acoustic beamwidth and zero outside of the beam.

If we limit our consideration to the case when $\ell = 1$, (14B.15) can be greatly simplified. The initial assumption of this model that $V_{\ell+1} \ll V_\ell$ now becomes $V_1 \ll V_0$. This assumption is equivalent to assuming that very little energy will be diffracted out of the incident light wave by the sound wave. This small-scattering assumption allows V_0 to be treated as a constant in (14B.15).

The fact that very little energy is diffracted by the acoustic wave means that Δn is small, and any departure of the sound wave from a plane wave will be negligible. This allows us to treat ξ as a constant and remove it from the integral in (14B.15). We can now rewrite (14B.15) as

$$V_1 = e^{-i\beta_1 z}\xi V_0 \int_{-L/2}^{L/2} e^{i\beta_1 z'}\, dz'.$$

This integral can be recognized as the Fourier transform of the rect(x) function, (6.17), and is a sinc function:

$$V_1(z) = \xi V_0 L \frac{\sin(\beta_1 L/2)}{\beta_1 L/2}\, e^{-i\beta_1 z}. \tag{14B.17}$$

The sinc function is large only when its argument is approximately zero, so we may write the approximate equation to find the condition for $(V_1)_{\max}$:

$$\beta_1 = -\frac{\kappa}{\cos\theta}\left(\sin\theta - \frac{\kappa}{2k}\right) \approx 0. \tag{14B.18}$$

The requirement that (14B.18) be zero can be rewritten as

$$\sin\theta_B = \frac{\kappa}{2k}. \tag{14B.19}$$

This condition is equivalent to the Bragg equation, where θ is denoted by θ_B to emphasize its unique character [see (12.13) and (14.62)].

The fraction of light diffracted at the Bragg angle θ_B is a measure of the diffraction efficiency (12.14) of the Bragg process. The fraction of energy found in the diffracted beam is

$$\frac{I_1}{I_0} = \frac{V_1 V_1^*}{V_0 V_0^*}$$
$$= \xi^2 L^2 \frac{\sin^2(\beta_1 L/2)}{(\beta_1 L/2)^2}. \tag{14B.20}$$

The diffracted intensity distribution predicted by (14B.20) is sketched in Figure 14B.1. The maximum intensity occurs at the Bragg angle, for which $\beta_1 = 0$:

$$\left(\frac{I_1}{I_0}\right)_{\max} = (\xi L)^2$$
$$= \left(\frac{\Delta n L}{4\cos\theta}\frac{k}{n_0}\right)^2.$$

The diffraction efficiency η is defined as this maximum value,

$$\eta = \left(\frac{I_1}{I_0}\right)_{\max} = \xi^2 L^2.$$

The diffraction efficiency obtained by assuming a small index modulation is only an approximate relationship for η. It is based upon the assumption that only a small amount of the incident energy is diffracted out of the incident beam. In a more complete theory,

$$\eta = \sin^2(\xi L).$$

The index change produced by an acoustic wave can be expressed in terms of the acoustic wave's parameters [see (14C.5)]. The diffraction efficiency can then be written in terms of the acoustic parameters:

$$\eta = \frac{\pi}{(\lambda n_0)^2 \cos^2\theta}\frac{P_{\text{ac}} p^2 n_0^6}{\rho v^3}, \tag{14B.21}$$

where we have assumed that the area of the acoustic wave is $\pi L^2/4$. For example, assume 1 W of acoustic power is applied to a TeO_2 crystal as a slow shear wave. The acoustic parameters are

$$P_{\text{ac}} = 1 \text{ W}, \quad p = 0.09,$$
$$v_s = 0.617 \text{ km / s}, \quad \rho = 5.99 \text{ g / cm}^3,$$

and the optical parameters are

$$n_0 = 2.27, \quad \lambda = 632.8 \text{ nm}.$$

From (14B.21), the diffraction efficiency is 12%. (The value for the photoelastic constant was obtained using the figure of merit $\mathcal{M}_2$ from Table 14C.1.)

In the Bragg approximation, the diffracted wave amplitudes V_ℓ decrease so rapidly that only V_1 is important. The theory just developed describes the scattering of light from sound wavefronts moving toward the light beam. The diffracted beam, corresponding to the $\ell = 1$ term in (14B.10), is Doppler-shifted upward in frequency and is called the +1 order. As was

mentioned earlier, to treat the case of scattering from a sound wave moving away from the incident light, the diffracted beam is represented by the negative index, $\lambda = -1$ in (14B.10) and is called the −1 order. This order is Doppler-shifted downward in frequency by the sound frequency Ω.

In summary:

1. The Bragg angle can be expressed as the reciprocal of the sound wavelength because the Bragg angle is quite small. From (14B.19),

$$\theta \propto \frac{2\pi}{\Lambda} = \frac{\Omega}{v}. \tag{14B.22}$$

   A reasonable estimate of the Bragg angle is obtained, therefore, from the ratio of the elastic wave's frequency to its velocity. This relationship demonstrates explicitly that the diffraction angle can be changed by changing the acoustic frequency as discussed in Chapter 14. An additional application of (14B.22) is the use of Bragg scattering to measure the elastic properties of a material.

2. The intensity of the diffracted light is proportional to the square of the index change produced by the acoustic wave. In Appendix 14C, the square of the index change is shown to be proportional to the acoustic intensity:

$$I_1 \propto \frac{P_{\text{ac}}}{A}.$$

   The relationship between diffracted energy and acoustic energy permits the modulation of the diffracted beam by amplitude modulation of the sound wave.

3. The frequency shift of the diffracted light, appearing in (14B.8), can be used to produce frequency-modulated light.

14B.2 Raman–Nath Region

Another limiting condition can be used to solve (14B.10). Rather than assuming that the amplitudes of the Fourier series rapidly decrease, $V_\ell \ll V_{\ell-1}$, we define a new parameter,

$$\chi = 2\xi z,$$

a simple rescaling of the z-coordinate, and rewrite (14B.10) in terms of this new parameter:

$$2\frac{\partial V_\ell(\chi)}{\partial \chi} + V_{\ell+1}(\chi) - V_{\ell-1}(\chi) = \left(-\frac{\ell\beta_\ell}{\xi}\right) V_\ell(\chi). \tag{14B.23}$$

Since $\mathcal{O}(\kappa/k) = \mathcal{O}(\lambda/\Lambda) = 10^{-2}$, we can assume that

$$\frac{\beta_\ell}{\xi} = \frac{4\kappa\ell}{k}\left(\frac{\varepsilon'}{\varepsilon_1}\right)\left(\sin\theta - \frac{\ell\kappa}{2k}\right) \ll 1. \tag{14B.24}$$

This assumption is correct in the limit as $\kappa \to 0$ for a given value of $\varepsilon'/\varepsilon_1$. If the elastic wave amplitude increases, then $\varepsilon'/\varepsilon_1$ decreases, under the assumption that κ is fixed. Thus, this approximation is expected to be applicable when light is diffracted by large-amplitude

(large ε_2), low-frequency (small $\Omega = \nu\kappa$) elastic waves. Using the assumption stated in (14B.24), we set

$$\frac{i\beta_\ell V_\ell(\chi)}{\xi} = 0, \tag{14B.25}$$

allowing us to rewrite (14B.23) as a recursion relation:

$$2\frac{\partial V_\ell}{\partial \chi} + V_{\ell+1}(\chi) - V_{\ell-1}(\chi) = 0. \tag{14B.26}$$

This recursion relation is satisfied by the Bessel functions of integral order.

We assume, as an initial condition, that before interaction of the light wave with the acoustic wave, only the fundamental component of the Fourier series is present; i.e., only $V_0 \neq 0$ when $z = -L/2$. The acoustic wave is assumed to be a plane wave, so that the parameter ξ is a nonzero constant over the region $-L/2 \leq z \leq L/2$ and zero outside this region. The intensity distribution for the first-order diffracted wave is given by

$$\frac{I_1}{I_0} = J_1^2\left(\frac{\Delta nkL}{n_0 2\cos\theta}\right). \tag{14B.27}$$

The intensity distribution of the ℓth order is described by the ℓth Bessel function J_ℓ. The total diffracted field is described by a series of Bessel functions, mathematically identical to

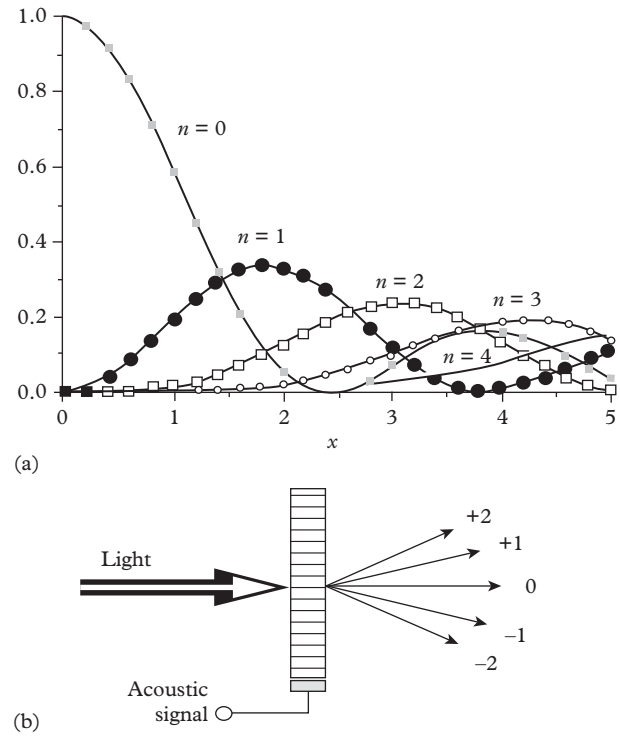

Figure 14B.2 *(a)Intensities of light scattered by an acoustic wave in the Raman–Nath regime. (b) Schematic of scattering process leading to the light patterns shown in Figure 14B.3.*

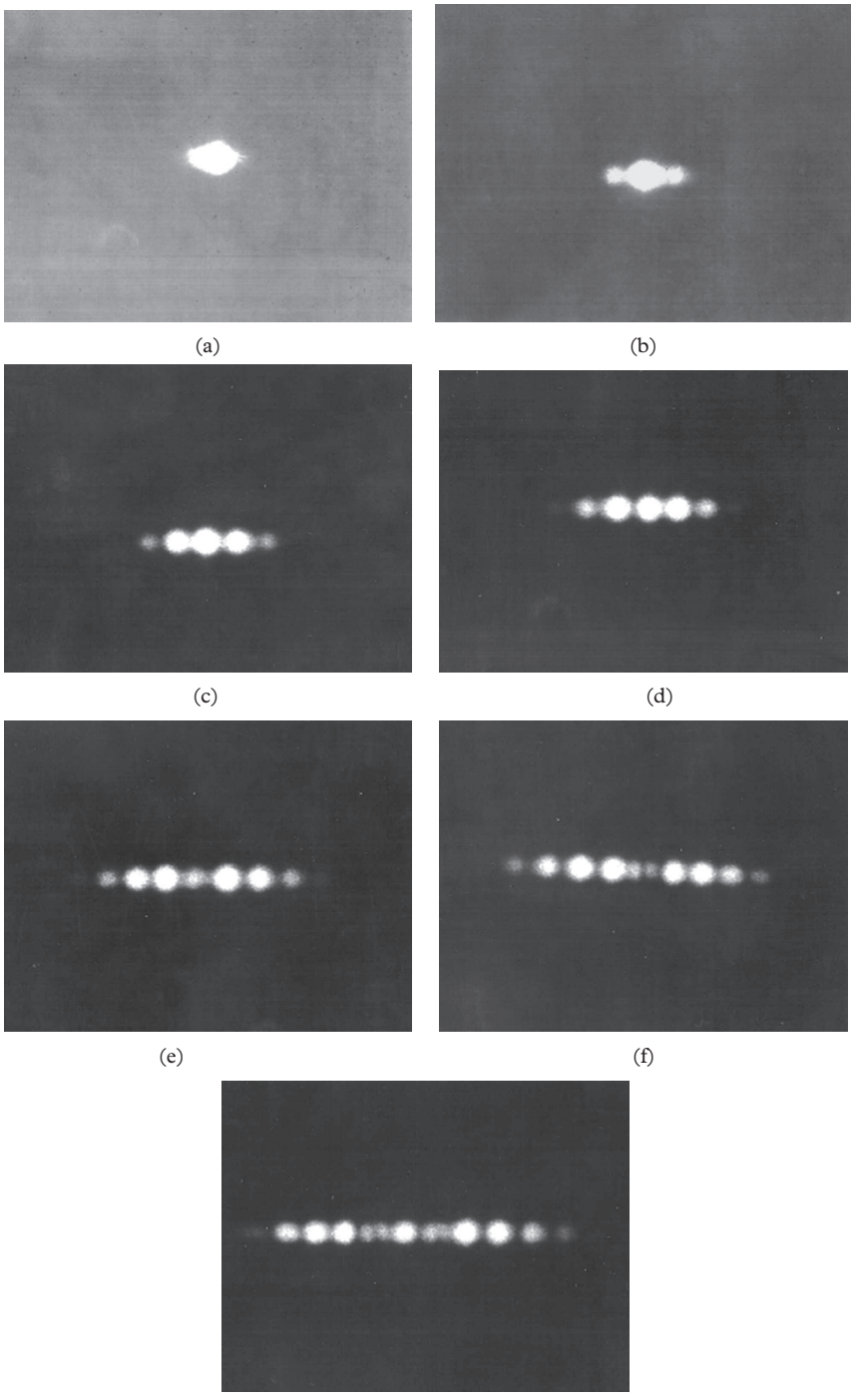

Figure 14B.3 *Experimentally obtained acousto-optic diffraction signals explained by the Raman–Nath theory. The value of x in Figure 14B.2(a) increases from (a) through (g), with* $x \approx 2.4$ *in (f) and 4.0 in (g). (Courtesy Eric Mazur.)*

the series obtained in Appendix 12A for a thin phase hologram. The intensity distribution predicted by (14B.27) is shown in Figure 14B.2 for the first five Bessel functions. This regime is sometimes called the *Lucas–Bequard* or *Debye–Sears* region.

Because each diffracted order is described by a Bessel function of that order, the maximum intensity of the first-order diffraction peak occurs when J_1 is a maximum, i.e., when the argument of J_1 is equal to 1.8. All of the light is diffracted out of the incident beam when the argument is equal to the first zero of the zeroth-order Bessel function, i.e.,

$$\frac{\Delta nkL}{n_0 2\cos\theta} = 2.4. \tag{14B.28}$$

Figure 14B.3 shows the intensity pattern of light scattered by an acoustic beam under conditions for Raman–Nath scattering. The acoustic energy, and therefore Δn, was increased to produce the pictures (a) through (g). It is easy to see that the energy in the incident beam is diffracted into the spatial sidebands as the acoustic energy is increased. At an acoustic energy that corresponds to the index modulation given by (14B.28), the intensity in the undiffracted beam, at the center of the pattern, goes to zero. The acoustic energy was increased further until, at higher acoustic modulation, in (g), the first-order diffracted intensity goes to zero.

Appendix 14C Acoustic Figure of Merit

In the acousto-optic literature, a number of figures of merit are used to characterize acousto-optic materials. To understand the reasoning that leads to these figures of merit, we will derive one of the most common.

We begin by assuming that the medium is isotropic so that we can use a scalar strain and an average photoelastic constant. The result of these assumptions is that the change in index due to strain is given by

$$\Delta\left(\frac{1}{n^2}\right) = pS, \tag{14C.1}$$

or, by using the approximation used to obtain (14.57), we can write

$$\Delta n = \frac{pn^3}{2}S. \tag{14C.2}$$

The energy density in a strained medium is

$$\frac{1}{2}SS^*\rho v^2 = \frac{1}{2}S^2\rho v^2, \tag{14C.3}$$

where v is the velocity of the pressure (sound) wave and ρ is the material's density. The power in an acoustic wave is the energy density (14C.3) multiplied by the volume occupied by the wave:

$$P_{\text{ac}} = (Av)\left(\frac{1}{2}S^2\rho v^2\right),$$

where A is the area of the sound wavefront, v is the velocity and Av is the volume containing the sound wave. Solving this equation for the strain yields

$$S = \sqrt{\frac{2P_{\text{ac}}}{A\rho v^3}}. \tag{14C.4}$$

Table 14C.1 *Acousto-optic figures of merit*

	$\mathcal{M}_1$	$\mathcal{M}_2$	$\mathcal{M}_3$
		(10^{-15} s^3/kg)	
Fused silica	1.0	1.51	1.0
Water	6.1	160	24
$LiNbO_3$	8.3	6.95	7.5
$PbMO_4$	15.3	35.8	24.9
TeO_2 (longitudinal)	18.5	34.4	25.6
TeO_2 (shear)	8.8	793	85

This equation can be used in (14C.2) to calculate the index change produced by the sound wave:

$$\Delta n = \sqrt{\frac{P_{ac} p^2 n^6}{A\rho v^3}}. \tag{14C.5}$$

The optical phase retardation of a light wave propagating across the sound wave is

$$\begin{aligned}\Gamma &= \frac{2\pi L}{\lambda}\Delta n \\ &= \frac{2\pi L}{\lambda}\sqrt{\frac{P_{ac} p^2 n^6}{A\rho v^3}}.\end{aligned} \tag{14C.6}$$

If the sound beam is round, with diameter L, then the beam's cross-sectional area $A = 4\pi L^2/4$, giving a phase retardation of

$$\Gamma = 4\sqrt{P_{ac}\frac{\pi\, p^2 n^6}{\lambda^2 \rho v^3}}.$$

The best material for an acousto-optic modulator is the one that produces the largest phase change Γ of a light wave with the smallest sound power. The figure of merit that indicates a material's ability to perform this modulation is given by

$$\mathcal{M}_2 = \frac{n^6 p^2}{\rho v^3}. \tag{14C.7}$$

Some typical values for this figure of merit are shown in Table 14C.1 along with two other figures of merit, $\mathcal{M}_1$ and $\mathcal{M}_3$. These figures of merit are referenced to fused silica.

The other two figures of merit listed in Table 14C.1 have been developed to discriminate between materials in applications where device geometries introduce additional constraints. These additional figures of merit are defined as

$$\mathcal{M}_1 = \frac{n^7 p^2}{\rho v}, \quad \mathcal{M}_3 = \frac{n^7 p^2}{\rho v^2}.$$

All of these figures of merit neglect two important physical properties: acoustic and optical absorption. The two absorption coefficients reduce the efficiency of any modulator.

15 Nonlinear Optics

15.1 Introduction 664
15.2 Nonlinear Polarization 667
15.3 Nonlinear Optical Coefficient 670
15.4 Symmetry Properties 671
15.5 Wave Propagation in a Nonlinear Medium 673
15.6 Conservation of Energy 676
15.7 Conservation of Momentum 677
15.8 Second-Harmonic Generation 682
15.9 Methods of Phase Matching 684
15.10 Phase Conjugation 693
15.11 Summary 698
15.12 Problems 701
References 702
Appendix 15A: Nonlinear Optical Medium 703
Appendix 15B: Miller's Rule 710
Appendix 15C: Nonlinear Polarization in the 32 Point Group 711

15.1 Introduction

Nonlinear processes are involved in the detection of light and in all the light-modulating devices discussed in Chapter 14. Before 1960, these nonlinear processes were the exception, and conventional optical systems were analyzed using a linear theory. The neglect of nonlinear effects was due to the fact that large optical fields could not be produced. With the experimental demonstration of the ruby laser by **Theodore Harold Maiman (1927–2007)** in July 1960, a light source became available that would produce nonlinear optical behavior (a Q-switched ruby laser is 10^{12} times as bright as a high-pressure mercury arc lamp).[1] The first nonlinear optics experiment was conducted by **Peter A. Franken (1928–1999)**, along with several other investigators, at the University of Michigan. The Michigan group initially demonstrated second-harmonic generation and, later, optical rectification. The field of nonlinear optics quickly developed, and today it is a large and active area of research.

The theory we have developed for optics has assumed a linear relationship between the applied electric field and the material's response, namely, the polarization

$$\mathbf{P} = \varepsilon_0 \chi \mathbf{E}.$$

Using a typical laser, Nd:YAG, we can generate 1 MW, 1 ns pulses at a 1 μm wavelength. A typical beam diameter of 1 mm^2 results in a peak electric field strength of 10^7 V/m. If we focus this beam to an area of approximately λ^2, the electric field strength can reach 10^{10} V/m. This is of the order of atomic field strengths and is too large to allow the relationship between **P** and **E** to be treated as linear. In this chapter, we will treat nonlinear effects by assuming that the relationship between **P** and **E** is described by a power series

$$P_i^{\omega} = P_i^0 + \sum_j \chi_{ij} E_j^{\omega} + \sum_{j,\ell} \chi_{ij\ell} \nabla_\ell E_j^{\omega} + \sum_{j,\ell} \chi_{ij\ell} E_j^{\omega_1} E_\ell^{\omega_2} + \sum_{j,\ell,m} \chi_{ij\ell m} E_j^{\omega_1} E_\ell^{\omega_2} E_m^{\omega_3} + \sum_{j,\ell} \chi_{ij\ell} E_j^{\omega_1} B_\ell^{\omega_2} + \ldots.$$

This means that we are assuming that the nonlinear effects are a small perturbation on the linear behavior we have described. Each of the terms in this expansion can be identified with observable phenomena in optics [1, 2].

1. The first term in the expansion is associated with the spontaneous DC ($\omega = 0$) polarization of a material. The connection of this term to optics is not immediately apparent, but there are several important optical applications utilizing this polarization.

Pyroelectrics are materials that exhibit an electric polarization when the temperature of the crystal is changed. The materials exhibiting this effect have polar unit cells, i.e., the unit cell of the crystal has a net dipole moment. Rochelle salt, wurtzite, and cane sugar are examples of pyroelectric materials. A subclass

[1] Lasers with intensities up to 10^{19} W/cm^2 have been produced in a number of laboratories as general research platforms.

Modern Optics. Second Edition. B. D. Guenther.

© B. D. Guenther 2015. Published in 2015 by Oxford University Press.

of pyroelectrics are the ferroelectrics, which we will find useful in harmonic generation. The temperature-induced polarization does not persist, but rather is neutralized by migration of charge to the crystal's surface. Thus, only changes in temperature are observable by monitoring the polarization.

A detector constructed from a pyroelectric material is only sensitive to dT/dt and can only respond to modulated, chopped, or pulsed radiation. To construct a detector, electrodes are attached to the pyroelectric crystal, with an orientation perpendicular to the axis of polarization. Radiation incident on the detector surface causes a temperature change of the crystal, which, through the pyroelectric effect, changes the spontaneous electric polarization. To neutralize the thermally induced polarization, a current is generated that is proportional to the change in the crystal's temperature. Pyroelectrics are used in optics as broadband radiation detectors and are found commercially in thermally activated light switches. A popular detector material is $LiTaO_3$.

Ferroelectrics are pyroelectric materials that exhibit long-range ordering of the dipole moments, creating a spontaneous polarization. The direction of spontaneous polarization can be reversed by an applied electric field. When plotted as a function of electric field, the polarization exhibits a hysteresis loop due to the presence of domains in the crystal, similar to the domains found in magnetic materials. The ferroelectric is therefore an electric equivalent of a ferromagnet. The prototypical members of the three major groups of ferroelectrics are shown in Table 15.1. Through rotation of the polarization of the individual domains, a spatial variation of the birefringence of a ferroelectric has been used to provide optical displays with nonvolatile storage.

Table 15.1 *Typical members of ferroelectric classes*

Name	Formula	Crystal group
Barium titanate	$BaTiO_3$	$m3m$
KDP	KH_2PO_4	$\bar{4}2m$
Rochelle salt	$NaKC_4H_4O_6.4H_2O$	222

2. The second term in the expansion is the normal linear optical response of a material.
3. The third term describes optically active materials.
4. The fourth term corresponds to the second-order processes listed in Table 15.2.
5. The fifth term corresponds to third-order processes listed in Table 15.3.
6. The sixth term corresponds to various magneto-optic effects. When $\omega_2 = 0$, the term describes the Faraday effect.

In this chapter, we will briefly examine some nonlinear processes and their applications. For more details, consult one of the several books available on nonlinear optics [3–6]. The theoretical development of nonlinear optics presented in this chapter is based on perturbation theory, introduced in Appendix 15A.

The polarization due to a nonlinear response of a material to an electromagnetic wave will be obtained from perturbation theory. The nonlinear behavior of the material will be

Table 15.2 *Second-order nonlinear processes*

Frequency		
Incident fields	Polarization	Process
ω_1, ω_2	$\omega_1 = \omega_1 + \omega_2$	Sum-frequency mixing
ω_1	$\omega = 2\omega_1$	Second-harmonic
$\omega_1, 0$	$\omega = \omega_1$	Pockels effect
ω_1, ω_2	$\omega = \omega_1 - \omega_2$	Difference-frequency mixing
ω_1	$\omega_1 = 0$	Inverse electro-optic effect, DC rectification

Table 15.3 *Third-order nonlinear processes*

Frequency		
Incident fields	Polarization	Process
ω_1	$3\omega_1$	Third-harmonic
ω_1, ω_2	$\omega = \omega_1 + \omega_2 - \omega_2$	Raman effect
ω_1	$\omega = \omega_1 + \omega_1 - \omega_1$	Optical Kerr effect
$\omega_1, \omega_2, \omega_3$	$\omega = \omega_1 + \omega_2 + \omega_3$	Three-frequency mixing
$\omega_1, \omega_2, \omega_3$	$\omega_3 + \omega_1 = \omega_1 + \omega_2$	Four-wave difference
ω_1	$\omega = \omega_1$	Phase conjugation
$\omega_1, 0$	$\omega = \omega_1$	Kerr effect

characterized through a parameter called the nonlinear dielectric susceptibility. A related parameter, called the nonlinear optical coefficient, is found to be more useful to experimentalists, so a relationship between the two parameters will be derived. The calculation of an effective nonlinear optical coefficient for one crystal class will be presented in Appendix 15C, while the coefficients for the other crystal classes will simply be listed in tabular form. The value of the nonlinear coefficient of a material can be estimated by using a rule to be discussed in Appendix 15B.

Maxwell's equations will be used to obtain the equation of motion for a wave propagating in a nonlinear medium. In its most general form, this equation involves waves of three frequencies. Conservation of energy and conservation of momentum restrict the values of the frequencies and propagation vectors of the three waves.

We will restrict our attention to the situation for which two of the frequencies are identical and equal to ω. Conservation of energy requires that the frequency of the third wave be 2ω. The nonlinear process involving these waves is called second-harmonic generation. We will discuss a number of methods for satisfying conservation of momentum for second-harmonic generation.

Third-order nonlinearities can be observed whenever symmetry conditions prevent second-order nonlinearities. The discussion of third-order nonlinearities will be limited to the process called phase conjugation. This effect will be discussed in terms of holography and will be interpreted as a dynamic holographic recording.

15.2 Nonlinear Polarization

The macroscopic polarization was defined in (8.19) as

$$P = Nex.$$

We will use the first-order perturbation calculation of the oscillator displacement x, for a forced oscillator, with a second-order nonlinearity, derived in Appendix 15A, (15A.6). We can write the resulting polarization as

$$\begin{aligned} P &= Nex^{(1)} \\ &= P(\omega_1) + P(\omega_2) + P(\omega_1 + \omega_2) + P(\omega_1 - \omega_2) + P(2\omega_1) + P(2\omega_2) + P(0). \end{aligned} \tag{15.1}$$

We will later learn that the individual terms of (15.1) occur separately, owing to conservation of momentum (which in nonlinear optics is called *phase matching*), allowing the effects of each polarization term to be treated individually.

We introduce a new parameter called the *dielectric susceptibility*

$$\begin{aligned} \chi &= \frac{\varepsilon}{\varepsilon_0} - 1 \\ &= n^2 - 1, \end{aligned} \tag{15.2}$$

which is the proportionality constant between the applied electric field and the induced polarization,

$$P(\omega_i) = \chi(\omega_i)\varepsilon_0 E_i. \tag{15.3}$$

In general, χ is a complex function, but, if the frequencies involved are far from resonance, as we will assume, it can be treated as a real function. To find the induced polarization $P(\omega)$ for a second-order nonlinearity, we will use the first-order perturbation results of Appendix 15A, i.e., the terms of $x^{(1)}$, (15A.16), to write susceptibilities for each of the frequency components.

The fundamental frequency term of the susceptibility is

$$\chi(\omega_i) = \frac{Ne}{\varepsilon_0 E_i} X_i. \tag{15.4}$$

We use (15A.17) to write

$$\chi^{(1)}(\omega_i) = \frac{Ne^2}{\varepsilon_0 m} \frac{1}{\sqrt{(\omega_i^2 - \omega_0^2)^2 + \gamma^2 \omega_i^2}}. \tag{15.5}$$

This is the *zeroth-order solution*, which is called the *linear susceptibility*, $\chi^{(1)}(\omega)$. It is a dimensionless number, independent of the system of units of **P** and **E**.

The second-order nonlinear components of the susceptibility are defined by the equation

$$\begin{aligned} P(\omega_i \pm \omega_j) &= P_{\mathrm{NL}}(\omega_3) \\ &= \chi^{(2)}(\omega_i \pm \omega_j)\varepsilon_0 E_i E_j. \end{aligned}$$

Here we denote the terms resulting from the first-order perturbation model as the second-order nonlinear susceptibility, $\chi^{(2)}$. We can use (15A.18) or (15A.19) to write the *sum-* or *difference-frequency susceptibility*,

$$\chi^{(2)}\left(\omega_i \pm \omega_j\right) = \frac{Ne}{\varepsilon_0 E_i E_j} X_{i+j}$$

$$= \frac{\dfrac{Ne^3 a_2}{\varepsilon_0 m^2}}{\sqrt{\left(\omega_i^2 - \omega_0^2\right)^2 + \gamma^2\omega_i^2}\sqrt{\left(\omega_j^2 - \omega_0^2\right)^2 + \gamma^2\omega_j^2}\sqrt{\left[\left(\omega_i \pm \omega_j\right)^2 - \omega_0^2\right]^2 + \gamma^2\left(\omega_i \pm \omega_j\right)^2}}. \quad (15.6)$$

This term describe a *parametric interaction*. (Parametric processes were defined in Chapter 14, during the discussion of the acousto-optic effect.) Whenever $\omega_1 = \omega_2$, the process is said to be *degenerate*. The physical processes described by this susceptibility are grouped under five separate categories:

1. The term *parametric amplification* is used to indicate that the transfer of power is from a pump wave at

   $$\omega_3 = \omega_1 + \omega_2$$

   to the signal and idler waves, at ω_1 and ω_2. If we place the material producing parametric amplification in an optical resonator (e.g., a Fabry–Perot cavity) tuned to the signal, idler, or both, then we will observe *parametric oscillation*.
2. If the energy flows into the harmonic frequency ω_3 from the signal and idler waves, the process is called *sum-frequency* or *difference-frequency generation*.
3. A high-intensity idler frequency ω_2 can be used to convert a low-level signal frequency ω_1 to the frequency ω_3 via *frequency up-conversion*. This process is identical to sum-frequency generation except for the relative intensities of the three waves.
4. For degenerate sum-frequency generation, where $\omega_1 = \omega_2$, the name *second-harmonic generation* is used to label the process. We can derive the susceptibility for second-harmonic generation by setting $\omega_2 = 0$ and by using the first term of (15A.20) in an equation similar to (15.4). We obtain for the second-harmonic component of the susceptibility,

   $$\frac{\dfrac{Ne^3 a_2}{2\varepsilon_0 m^2}}{\left[\left(\omega_1^2 - \omega_0^2\right)^2 + \gamma^2\omega_1^2\right]\sqrt{\left(4\omega_1^2 - \omega_0^2\right)^2 + \gamma^2 4\omega_1^2}}. \quad (15.7)$$

   If we define $\chi^{(2)}(2\omega)$ as the degenerate susceptibility calculated using (15.6), then (15.7) is equal to

   $$\frac{\chi^{(2)}(2\omega)}{2}.$$

   The factor of 2 occurs because in (15.7) only one fundamental wave is present, whereas in (15.6) there are two fundamental waves. $\chi^{(2)}(2\omega)$ has dimensions of inverse electric field intensity (in MKS units, this is m/V).

5. *Optical rectification* involves the zero-frequency component of the susceptibility, obtained by using (15A.21). Optical rectification can also be viewed as a special case of difference-frequency generation, where the difference frequency is zero. It is linked to the Pockels effect and may be thought of as an inverse Pockels effect.

The nonlinear susceptibility can be enhanced by operating near a resonance so that

$$\omega_i^2 - \omega_0^2 \approx 0.$$

It should be noted that χ in (15.6) is not only a function of the applied frequencies but also a function of the generated frequency. This means that $\chi(\omega_1, \omega_2, \omega_3)$ can be enhanced not only when ω_1 or ω_2 are near an absorption resonance but also when ω_3 is near an absorption frequency.

The units usually encountered in the literature are c.g.s. (Gaussian) units. To convert to MKS units, we use the fact that the polarization is given by

$$\begin{aligned} P(\text{c.g.s.}) &= Nex \leftrightarrow \frac{1}{\text{cm}^3} \cdot \text{statcoulomb} \cdot \text{cm} \\ &= \frac{\text{m}^3}{10^6\ \text{cm}^3} \cdot \frac{3 \times 10^9\ \text{statcoulomb}}{\text{coulomb}} \cdot \frac{10^2 \text{cm}}{\text{m}} \leftrightarrow P(\text{MKS}), \\ P(\text{c.g.s.}) &= \left(3 \times 10^5\right) P(\text{MKS}). \end{aligned} \tag{15.8}$$

From Appendix 2B, we obtain the relationship between the electric field in c.g.s. and MKS units, allowing us to write

$$\begin{aligned} \chi^{(n)}(\text{MKS}) &= \frac{\chi^{(n)}(\text{c.g.s.})}{\varepsilon_0 (3 \times 10^4)^n (3 \times 10^5)} \\ &\approx \frac{4\pi}{(3 \times 10^4)^{n-1}} \chi^{(n)}(\text{c.g.s.}). \end{aligned} \tag{15.9}$$

Some second-harmonic nonlinear susceptibilities are listed in Table 15.4.

Table 15.4 *Second-harmonic nonlinear susceptibility*

Material	Class	Element	$\chi^{(2)}(10^{-12}$ m/V)	$\lambda(\mu\text{m})$
Te	32	111	1.0×10^4	10.6
$LiNbO_3$	$3m$	222	6.14	1.06
		322	–11.6	
$BaTiO_3$	$4mm$	131	–34.4	1.06
		311	–36	
		333	–13.2	
KDP	$\bar{4}2m$	123	0.98	1.06
		312	0.94	
$LiIO_3$	6	331	–11.2	1.06
		333	–8.4	
CdSe	$6mm$	131	62	10.6
		311	57	
		333	109	
GaAs	$\bar{4}3m$	123	377	10.6

15.3 Nonlinear Optical Coefficient

The susceptibility χ is the quantity calculated by the theorist, but the experimentalist measures the *nonlinear optical coefficient* $\boldsymbol{d}$. This is defined by

$$P(2\omega) = d(2\omega)E^2 \cos(2\omega t - 2kx). \tag{15.10}$$

We will discuss the nonlinear optical coefficient in terms of second-harmonic polarization, but it can apply to any frequency component of the susceptibility. A more general expression for the nonlinear optical coefficient can be defined:

$$d(\omega_3) = \frac{ma_2\varepsilon_0^3\chi^{(1)}(\omega_1)\chi^{(1)}(\omega_2)\chi^{(1)}(\omega_3)}{N^2e^3},$$

which is expressed in terms of the three frequencies associated with the pump, signal, and idler waves.

Equating (15.7) and (15.10) will generate a relationship for the nonlinear optical coefficient in terms of the susceptibility:

$$d(2\omega) = \frac{\dfrac{Ne^3a_2}{2m^2}}{\left[\left(\omega^2-\omega_0^2\right)^2+\gamma^2\omega^2\right]\sqrt{\left(4\omega^2-\omega_0^2\right)^2+\gamma^2 4\omega^2}}, \tag{15.11}$$

or

$$2d(2\omega) = \chi^{(2)}(2\omega).$$

We can rewrite d in terms of the linear susceptibility at the fundamental and the second harmonic of the light wave, given by (15.5):

$$d(2\omega) = \frac{a_2m\varepsilon_0^3}{2N^2e^3}[\chi^{(1)}(\omega)]^2\chi^{(1)}(2\omega). \tag{15.12}$$

Using the definition of χ given by (15.2), we find that (15.12) states that materials with a high refractive index will also have a high nonlinear coefficient (see Table 15.5). It has been found empirically that the ratio of d to the two susceptibilities is approximately a constant for a wide range of materials. This fact, called *Miller's rule*, will be discussed in Appendix 15B.

The relationship between the nonlinear optical coefficient in c.g.s. and MKS units is obtained from (15.9):

$$d_{\text{MKS}}(2\omega) = (3.7\times10^{-15})d_{\text{cgs}}(2\omega). \tag{15.13}$$

Some authors define d without ε_0. With that definition, the constant used in (15.9) will also relate d between the two systems of units. We have included ε_0 in the values listed for d.

In the nonlinear optics literature, the value of $d(2\omega)$ is often stated with reference to $d_{36}(2\omega)$ for KDP, which is equal to

$$d_{36}(2\omega) = 4.42 \times 10^{-24} \text{ m / V}.$$

Some nonlinear optical coefficients referenced to KDP are shown in Table 15.6 in Section 15.7.

15.4 Symmetry Properties

We have treated the parameters χ and d as scalars, but in reality they are third-rank tensors, relating two vectors to a third. For example, the polarization along the x-direction, associated with a wave of frequency ω_3, is related to the electric field at ω_1 and ω_2 by the equation

$$\begin{aligned} P_x(\omega_3) = {} & d_{xxx}(\omega_3)E_x(\omega_1)E_x(\omega_2) + d_{xyy}(\omega_3)E_y(\omega_1)E_y(\omega_2) + d_{zzz}(\omega_3)E_z(\omega_1)E_z(\omega_2) \\ & + d_{xzy}(\omega_3)E_z(\omega_1)E_y(\omega_2) + d_{xyz}(\omega_3)E_y(\omega_1)E_z(\omega_2) + d_{xzx}(\omega_3)E_z(\omega_1)E_x(\omega_2) \\ & + d_{xxz}(\omega_3)E_x(\omega_1)E_z(\omega_2) + d_{xxy}(\omega_3)E_x(\omega_1)E_y(\omega_2) + d_{xyx}(\omega_3)E_y(\omega_1)E_x(\omega_2). \end{aligned}$$

In general a tensor of rank 3 has 27 components, but a number of symmetry arguments can be invoked to reduce the number of nonzero terms in the tensor associated with the optical nonlinear interaction.

(a) **Loss-free medium** In a lossless medium, we can use an argument similar to the one used in Chapter 13 to demonstrate that the order of writing E_j and E_k is immaterial and

$$d_{ijk} = d_{ikj}$$

for all combinations of i, j, and k; the frequencies must be permuted with the coordinates for this equality to hold. The equality allows the replacement of the last two indices of d and χ with one, as was done for the electro-optic coefficient [see Appendix 14A, (14A.1), to obtain the rule used in the replacement]. In matrix form, the polarization is given by

$$\begin{bmatrix} P_x(\omega_3) \\ P_y(\omega_3) \\ P_z(\omega_3) \end{bmatrix} = \begin{bmatrix} d_{11} & d_{12} & d_{13} & d_{14} & d_{15} & d_{16} \\ d_{21} & d_{22} & d_{23} & d_{24} & d_{25} & d_{26} \\ d_{31} & d_{32} & d_{33} & d_{34} & d_{35} & d_{36} \end{bmatrix} \begin{bmatrix} E_x(\omega_1)E_x(\omega_2) \\ E_y(\omega_1)E_y(\omega_2) \\ E_z(\omega_1)E_z(\omega_2) \\ E_y(\omega_1)E_z(\omega_2) + E_z(\omega_1)E_y(\omega_2) \\ E_x(\omega_1)E_z(\omega_2) + E_z(\omega_1)E_x(\omega_2) \\ E_x(\omega_1)E_y(\omega_2) + E_y(\omega_1)E_x(\omega_2) \end{bmatrix}. \tag{15.14}$$

(b) **Crystal symmetry** The crystal symmetry establishes the nonzero terms, d_{ijk}, of the tensor; for example, if the crystal has inversion symmetry, all the d_{ijk} are zero,

reducing the total number of point groups that must be considered from 32 to 20. The application of symmetry arguments yields a tensor with the same nonzero terms as the piezoelectric and Pockels effect tensors (see Appendix 14A).

The actual values of the elements of the three tensors—the piezoelectric, Pockels effect, and optical susceptibility tensors—differ because the physical origins of the processes they describe are different. The piezoelectric tensor describes the electrical behavior of a crystal when the ions are physically displaced. The optical susceptibility is due to the electronic polarizability, as is the Pockels effect, but dispersion causes the Pockels and susceptibility terms to differ.

(c) **Dispersion-free medium** The nonlinear optical coefficient tensor has additional symmetry, and is further simplified, if dispersion in the material under study can be neglected. If the nonlinear polarization is due only to electronic motion, and if there are no absorption resonances in the spectral region containing ω_1, ω_2, and ω_3, then the dispersion of the nonlinearity is negligible and all frequencies act in an equivalent manner. When the conditions for negligible dispersion are met, all elements, d_{ijk}, of the nonlinear optical coefficient tensor formed by permuting i, j, and k are equal. This is called *Kleinman's symmetry condition* [6].

We will simplify all further discussions by replacing the nonlinear optical coefficient tensor by a scalar parameter called the *effective* $\boldsymbol{d}$, $\boldsymbol{d}_{\text{eff}}$. The equations we derive using the

Table 15.5 *Effective nonlinear optical coefficients*

Class	Two extraordinary rays, one ordinary ray	Two ordinary rays, one extraordinary ray
6	0	$d_{15}\sin\theta$
4	0	$d_{15}\sin\theta$
6*mm*	0	$d_{15}\sin\theta$
4*mm*	0	$d_{15}\sin\theta$
622	0	0
644	0	0
$\bar{6}m2$	$d_{22}\cos^2\theta\cos 3\phi$	$-d_{22}\cos\theta\sin 3\phi$
3*m*	$d_{22}\cos^2\theta\cos 3\phi$	$d_{15}\sin\theta - d_{22}\cos\theta\sin 3\phi$
$\bar{6}$	$(d_{11}\sin 3\phi + d_{22}\cos 3\phi)\cos^2\theta$	$(d_{11}\cos 3\phi - d_{22}\sin 3\phi)\cos\theta$
3	$(d_{11}\sin 3\phi + d_{22}\cos 3\phi)\cos^2\theta$	$d_{15}\sin\theta + (d_{11}\cos 3\phi - d_{22}\sin 3\phi)\cos\theta$
32	$d_{11}\cos^2\theta\sin 3\phi$	$d_{11}\cos\theta\cos 3\phi$
$\bar{4}$	$(d_{14}\cos 2\phi - d_{15}\sin 2\phi)\sin 2\theta$	$-(d_{14}\sin 2\phi - d_{15}\cos 2\phi)\sin\theta$
$\bar{4}2m$	$d_{14}\sin 2\theta\cos 2\phi$	$-d_{14}\sin\theta\cos 2\phi$

effective $\boldsymbol{d}$ can be restored to a three-dimensional result by inserting the appropriate equation for $\boldsymbol{d}_{\text{eff}}$. The calculation of $\boldsymbol{d}_{\text{eff}}$ assumes two linearly polarized waves, incident upon a birefringent crystal. The equation for $\boldsymbol{d}_{\text{eff}}$ depends upon the crystal class and the waves' polarization and propagation vector orientation with respect to the optical axis. An example of the technique used to calculate $\boldsymbol{d}_{\text{eff}}$ is found in Appendix 15C, along with the geometrical identification of the angles θ and ϕ. Table 15.5 shows $\boldsymbol{d}_{\text{eff}}$ for materials where Kleinman's symmetry is valid; a more complete listing can be found in the book by Zernike and Midwinter [5].

15.5 Wave Propagation in a Nonlinear Medium

The effective nonlinear optical coefficient results in an effective nonlinear polarization (see Appendix 14C). This effective nonlinear polarization will be used to derive the equations for the electromagnetic radiation produced by the nonlinear interaction. The starting point of this calculation is Maxwell's equations. The constitutive relations, from Chapter 2, are modified to allow for a nonlinear polarization:

$$\begin{aligned} &\mathbf{B} = \mu\mathbf{H}, \quad \mathbf{J} = \sigma\mathbf{E}, \\ &\mathbf{D} = \varepsilon_0\mathbf{E} + \mathbf{P} \\ &\quad = \varepsilon_0\mathbf{E} + \varepsilon_0\chi\mathbf{E} + \mathbf{P}_{\text{NL}}. \end{aligned} \tag{15.15}$$

We will assume that the medium is homogeneous and nonmagnetic, allowing the parameters χ, σ, and μ to be treated as constants with respect to the ∇ operator. We can now use Maxwell's equations to develop the wave equation in much the same way as we did in Chapter 2.

The time derivatives of (2.3) and (2.4) are

$$\begin{aligned} \nabla \times \frac{\partial \mathbf{E}}{\partial t} &= -\mu \frac{\partial^2 \mathbf{H}}{\partial t^2}, \\ \nabla \times \frac{\partial \mathbf{H}}{\partial t} &= \varepsilon_0(1+\chi)\frac{\partial^2 \mathbf{E}}{\partial t^2} + \sigma\frac{\partial \mathbf{E}}{\partial t} + \frac{\partial^2 \mathbf{P}_{\text{NL}}}{\partial t^2}, \end{aligned} \tag{15.16}$$

and the curls of these same equations are

$$\begin{aligned} \nabla \times \nabla \times \mathbf{E} &= -\mu\nabla \times \frac{\partial \mathbf{H}}{\partial t}, \\ \nabla \times \nabla \times \frac{\partial \mathbf{H}}{\partial t} &= \varepsilon_0(1+\chi)\nabla \times \frac{\partial \mathbf{E}}{\partial t} + \sigma\nabla \times \mathbf{E}. \end{aligned} \tag{15.17}$$

Combining (15.16) and (15.17), we obtain

$$\nabla \times \nabla \times \mathbf{E} + \mu\varepsilon_0(1+\chi)\frac{\partial^2 \mathbf{E}}{\partial t^2} + \mu\sigma\frac{\partial \mathbf{E}}{\partial t} + \mu\frac{\partial^2 \mathbf{P}_{\text{NL}}}{\partial t^2} = 0, \tag{15.18}$$

$$\nabla \times \nabla \times \mathbf{H} + \mu\varepsilon_0(1+\chi)\frac{\partial^2 \mathbf{H}}{\partial t^2} + \mu\sigma\frac{\partial \mathbf{H}}{\partial t} = 0.$$

We are not interested in the equation involving the magnetic field **H**, so we will only simplify (15.18), using the vector identity (2A.12). The result of this manipulation of Maxwell's equations is the wave equation for a nonlinear medium:

$$\nabla^2\mathbf{E} = \mu\sigma\frac{\partial\mathbf{E}}{\partial t} + \mu\varepsilon\frac{\partial^2\mathbf{E}}{\partial t^2} + \mu\frac{\partial^2\mathbf{P}_{\mathrm{NL}}}{\partial t^2}. \tag{15.19}$$

To interpret the physical significance of this nonlinear wave equation, we will apply the paraxial approximation to evaluate the one-dimensional problem of three plane waves of frequencies ω_1, ω_2, and ω_3 propagating in the positive z-direction. The electric field E is composed of three plane waves of the form

$$E(\omega_i) = E_i = \frac{1}{2}\left[E_i(z)e^{i(\omega_i t - k_i z)} + E_i^*(z)e^{-i(\omega_i t - k_i z)}\right]. \tag{15.20}$$

(Note that the subscript i occurring in this equation labels the frequency associated with the wave and not one of the Cartesian coordinates.)

By substituting these three plane waves into the wave equation, we will discover the properties of the waves when they are solutions to the nonlinear wave equation. The left-hand side of (15.19) is evaluated using the assumption that the variation of the complex amplitude of the light waves with z is small, i.e.,

$$k_i\frac{\partial E_i}{\partial z} \gg \frac{\partial^2 E_i}{\partial z^2}.$$

The left-hand side of (15.19) then becomes

$$\nabla^2 E_i = -\frac{1}{2}\left(k_i^2 E_i + 2ik_i\frac{\partial E_i}{\partial z}\right)e^{i(\omega_i t - k_i z)} + c.c.,$$

where c.c. denotes the complex conjugate of the first term,

$$\text{c.c.} = -\frac{1}{2}\left(k_i^2 E_i - 2ik_i\frac{\partial E_i}{\partial z}\right)e^{-i(\omega_i t - k_i z)}.$$

The time derivatives of the electric field can be written by using (1.22). The only term of (15.19) that has not been evaluated previously involves P_{NL}. The definition of the nonlinear optical coefficient (15.10) can be generalized to the following expression for the nonlinear polarization due to the three waves:

$$\begin{aligned} P_{\mathrm{NL}} &= P_{\mathrm{NL}}(\omega_1) + P_{\mathrm{NL}}(\omega_2) + P_{\mathrm{NL}}(\omega_3) \\ &= d[E^*(\omega_2)E(\omega_3) + E^*(\omega_1)E(\omega_3) + E^*(\omega_1)E(\omega_2)]. \end{aligned}$$

Using $P_{\mathrm{NL}}(\omega_1)$ as an example, the second derivative with respect to time is

$$\frac{\partial^2 P_{\mathrm{NL}}(\omega_1)}{\partial t^2} = -(\omega_3 - \omega_2)^2 d\, E_2^* E_3 e^{-i[(\omega_3-\omega_2)t-(k_3-k_2)z]} + \text{c.c.} \tag{15.21}$$

The solution of the wave equation for the three plane waves would be quite easy if we could treat each frequency component separately, but P_{NL} involves the frequency combinations $\omega_1 + \omega_2$, $\omega_3 - \omega_2$, and $\omega_3 - \omega_1$. This prevents simplification of the equation unless

$$\omega_3 = \omega_1 + \omega_2.$$

When this equality holds, we can separate the wave equation into three coupled amplitude equations.

The coupled equation for E_1 is

$$-\frac{1}{2}\left(k_1^2 E_1 + 2ik_1\frac{\partial E_1}{\partial z}\right)e^{i(\omega_1 t - k_1 z)} + \text{c.c.} = (i\omega_1\mu\sigma_1 - \omega_1^2\mu\varepsilon_1)\frac{E_1}{2}e^{i(\omega_1 t - k_1 z)} + \text{c.c.}$$
$$-\left(\frac{\omega_1^2\mu d}{2}E_3 E_2^* e^{i[\omega_1 t - (k_3 - k_2)z]} + \text{c.c.}\right), \qquad (15.22)$$

where we have labeled ε and σ with the frequency label in case dispersion is important. If we multiply both sides of (15.22) by the plane wave

$$\frac{e^{-i(\omega_1 t - k_1 z - \pi/2)}}{k} = \frac{i}{k}e^{-i(\omega_1 t - k_1 z)}$$

and use the identity $k_1^2 = \omega_1^2\mu\varepsilon_1$, we can simplify the equation. Carrying out identical operations on all three equations yields

$$\frac{\partial E_1}{\partial z} = -\frac{\sigma_1}{2}\sqrt{\frac{\mu}{\varepsilon_1}}E_1 - \frac{i\omega_1}{2}\sqrt{\frac{\mu}{\varepsilon_1}}d E_3 E_2^* e^{-i(k_3 - k_2 - k_1)z}, \qquad (15.23)$$

$$\frac{\partial E_2}{\partial z} = -\frac{\sigma_2}{2}\sqrt{\frac{\mu}{\varepsilon_2}}E_2 - \frac{i\omega_2}{2}\sqrt{\frac{\mu}{\varepsilon_2}}d E_3 E_1^* e^{-i(k_3 - k_2 - k_1)z}, \qquad (15.24)$$

$$\frac{\partial E_3}{\partial z} = -\frac{\sigma_3}{2}\sqrt{\frac{\mu}{\varepsilon_3}}E_3 - \frac{i\omega_3}{2}\sqrt{\frac{\mu}{\varepsilon_3}}d E_1 E_2 e^{-i(k_1 + k_2 - k_3)z}. \qquad (15.25)$$

As was mentioned in Chapter 2, following (2.20), the ratio

$$\sqrt{\frac{\mu_0}{\varepsilon_0}} = 377 \text{ ohms}$$

is defined as the impedance of free space. The ratios appearing in the coupled equations (15.23)–(15.25) can be simplified by using this definition:

$$\sqrt{\frac{\mu}{\varepsilon}} \approx \frac{1}{n}\sqrt{\frac{\mu_0}{\varepsilon_0}} = \frac{377}{n}.$$

Equations (15.23)–(15.25) give the rate of change, with distance, of the wave amplitude at one frequency as a function of the wave amplitudes at two other frequencies. The equations, which are coupled through the nonlinear optical constant d, can be solved, but the solutions involve elliptic integrals [7]. A great deal about the nonlinear paramagnetic interaction can be learned without finding the complete solution to these equations.

The allowable frequencies are specified by the requirement that

$$\omega_3 = \omega_1 + \omega_2.$$

There is a phase difference between the wave at ω_3 and the waves at ω_1 and ω_2 given by

$$\Delta k = k_3 - k_2 - k_1.$$

This phase difference causes the amplitude of each wave to vary in a different sinusoidal fashion as the waves propagate along the z-direction. The term involving σ, the conductivity

of the medium, is equal to the absorption loss that may take place as the waves propagate in the z-direction.

The nonlinear interaction can be interpreted, in light of the discussion of acousto-optics in Chapter 14, as a scattering process. The requirement that $\omega_3 = \omega_1 + \omega_2$ is a statement of conservation of energy. The phase difference Δk indicates the momentum change in the scattering event. If the scattering event is elastic, then $\Delta k = 0$, and momentum is conserved. If the scattering event is inelastic, then $\Delta k \neq 0$. In Sections 15.6 and 15.7, we will examine the impact of the two conservation laws on nonlinear optical processes [8].

15.6 Conservation of Energy

In this section, we will assume that $\Delta k = 0$ and that the material is a perfect insulator, so $\sigma_1 = \sigma_2 = \sigma_3 = 0$. Using these assumptions and multiplying (15.23)–(15.25) by E_i^*, we obtain

$$E_1^* \frac{\partial E_1}{\partial z} = -\frac{i\mathcal{A}}{2} E_1^* E_2^* E_3 \omega_1 \sqrt{\frac{\mu}{\varepsilon_1}}, \tag{15.26}$$

$$E_2^* \frac{\partial E_2}{\partial z} = -\frac{i\mathcal{A}}{2} E_1^* E_2^* E_3 \omega_2 \sqrt{\frac{\mu}{\varepsilon_2}}, \tag{15.27}$$

$$E_3^* \frac{\partial E_3}{\partial z} = -\frac{i\mathcal{A}}{2} E_1 E_2 E_3^* \omega_3 \sqrt{\frac{\mu}{\varepsilon_3}}. \tag{15.28}$$

If we use the fact that

$$\frac{\partial}{\partial z}(E_i E_i^*) = E_i \frac{\partial E_i^*}{\partial z} + E_i^* \frac{\partial E_i}{\partial z},$$

we find that (15.26)–(15.28) lead to the identity

$$\frac{1}{\omega_1}\sqrt{\frac{\varepsilon_1}{\mu}}\frac{\partial}{\partial z}(E_1 E_1^*) = \frac{1}{\omega_2}\sqrt{\frac{\varepsilon_2}{\mu}}\frac{\partial}{\partial z}(E_2 E_2^*) = -\frac{1}{\omega_3}\sqrt{\frac{\varepsilon_3}{\mu}}\frac{\partial}{\partial z}(E_3 E_3^*). \tag{15.29}$$

The definition of the average Poynting vector (2.26) can be used to rewrite (15.29) as an energy conservation law. We discover the requirement that $\omega_3 = \omega_1 + \omega_2$ leads to an energy conservation law without the need to specify the type of interaction.

15.6.1 Manley–Rowe Relation

The conservation of energy law (15.29),

$$\frac{\text{change in power at } \omega_1}{\omega_1} = \frac{\text{change in power at } \omega_2}{\omega_2} = -\frac{\text{change in power at } \omega_3}{\omega_3},$$

is known as the *Manley–Rowe relation* (**John M. Manley, Harrison E. Rowe**) and is valid for all sum- or difference-frequency generation (mixing) processes. In words, it states that if waves at frequencies ω_1 and ω_2 are used to generate a wave at frequency ω_3, then the waves at frequencies ω_1 and ω_2 will lose the energy gained by the wave at frequency ω_3.

A quantum view of the Manley–Rowe relation can be obtained by noticing that EE^*/ω is a measure of the photon density:

$$\frac{EE^*}{\omega} = \frac{I}{\omega} = \frac{N\hbar\omega}{\omega} = N\hbar.$$

Two photons with energies $\hbar\omega_1$ and $\hbar\omega_2$ combine to produce a single photon with energy $\hbar\omega_3$; the number of photons is not conserved, but the energy is.

15.7 Conservation of Momentum

We now will return to (15.25) and find an approximate form for the variation of the light wave E_3 at frequency ω_3 by assuming the following:

1. $\omega_3 = \omega_1 + \omega_2$.
2. $\sigma = 0$; i.e., the nonlinear medium is a lossless medium.
3. The nonlinear material occupies the positive half plane, to the right of $z = 0$, the boundary of the nonlinear material.
4. $E_3 = 0$ at $z \leq 0$; i.e., outside of the nonlinear material, only the waves E_1 and E_2 exist.
5. E_1 and E_2 are constant along the z-direction; i.e., very little energy is transferred into the amplitude E_3 from E_1 and E_2.

With these assumptions, we may integrate (15.25) to find the field's amplitude at a distance $z = L$ into the nonlinear material:

$$E_3 = -\frac{i\omega_3}{2}\sqrt{\frac{\mu}{\varepsilon_3}}\,d \int_0^L E_1 E_2 e^{i\Delta kz}\,dz$$

$$= -\frac{\omega_3}{2}\sqrt{\frac{\mu}{\varepsilon_3}}\,\frac{d\,E_1E_2}{\Delta k}(e^{i\Delta kL} - 1). \tag{15.30}$$

We will use the result of this integration to calculate the Poynting vector for the wave at frequency ω_3. The Poynting vector will allow the significance of the phase difference Δk to be given a physical interpretation, in terms of its influence on energy flow. In addition, a figure of merit for evaluating nonlinear materials will be generated.

15.7.1 Poynting Vector

If we use the value of E_3 from (15.30) to calculate the Poynting vector of the wave at frequency ω_3, we will obtain the energy per unit area flowing across the plane at $z = L$ in the nonlinear medium:

$$S_3 = \frac{n_3}{2c\mu}\left(\frac{\omega_3^2\mu}{4\varepsilon_3}\,\frac{d^2}{\Delta k^2}E_1^2E_2^2\right)[(e^{i\Delta kL} - 1)(e^{-i\Delta kL} - 1)]. \tag{15.31}$$

We can use the three identities

$$\frac{1}{\varepsilon_3}\frac{\varepsilon_0}{\varepsilon_0} = \frac{1}{n_3^2\varepsilon_0}, \quad E_i^2 = \frac{2\mu c}{n_i}S_i, \quad \frac{\mu^2 c}{\varepsilon_0} \approx \sqrt{\left(\frac{\mu}{\varepsilon_0}\right)^3}$$

to simplify (15.31):

$$S_3 = \frac{\omega_3^2}{2n_1n_2n_3}\sqrt{\left(\frac{\mu}{\varepsilon_0}\right)^3}\frac{d^2L^2S_1S_2}{(\Delta kL)^2}[2 - e^{-i\Delta kL} - e^{i\Delta kL}].$$

The term in square brackets can be replaced by

$$4\sin^2(\Delta kL/2),$$

yielding the final result for the energy in the nonlinearly generated wave at frequency ω_3:

$$S_3 = \frac{\omega_3^2}{2n_1n_2n_3}\sqrt{\left(\frac{\mu}{\varepsilon_0}\right)^3}d^2L^2S_1S_2\left[\frac{\sin^2(\Delta kL/2)}{(\Delta kL/2)^2}\right]. \tag{15.32}$$

The instantaneous value of (15.32) has units of J/m^2, and the average value has units of W/m^2.

The factor d used in (15.32) is the effective nonlinear optical constant and must be replaced, in any calculation, with an expression derived using the method outlined in Appendix 15C. Thus, implicit in d is information about the direction of the polarization of the output wave as a function of the input waves' polarization and propagation direction, see Table 15.5.

The physical significance of the difference in propagation vectors, Δk, of the three waves can be discovered by examining (15.32):

1. When $\Delta k = 0$, the output power, contained in the wave of frequency ω_3, is proportional to the product of the input powers of the waves at ω_1 and ω_2. The output power is also proportional to the square of the propagation path length in the nonlinear medium.
2. **Figure of merit:** The energy in the nonlinearly generated wave is proportional to

$$S_3 \propto \frac{d^2}{n_1n_2n_3}.$$

We can use this ratio as a figure of merit for nonlinear materials (see Table 15.6):

$$\mathcal{M} = \frac{d^2}{n^3}.$$

Miller's rule, discussed in Appendix 15B, also suggests that the ratio d/n is an appropriate figure of merit. This is because a material with a large nonlinear coefficient will also have a large refractive index according to Miller's rule. By dividing d by n, we remove the weighting given to the nonlinear optical coefficient by the index of refraction.

Table 15.6 *Relative nonlinear coefficients and figure of merit*

Material	λ (μm)	n_o	n_e	d(ref. KDP)	$\mathcal{M}$ ($\times 10^{-46}$)
Te	5.3	4.86	6.3	$d_{11} = 1298$	2835
	10.6	4.8	6.25		
ADP	0.265	1.59	1.54	$d_{36} = 1.21$	0.08
	0.53	1.53	1.48		1.14
	1.06	1.51	1.47		
$LiNbO_3$	0.53	2.33	2.23	$d_{15} = 12.5$	3.03
	1.06	2.24	2.16		
$AgGaSe_2$	5.3	2.61	2.58	$d_{36} = 76$	8.58
	10.6	2.59	2.56		
$ZnGeP_2$	5.3	3.11	3.15	$d_{36} = 173$	146
	10.6	3.07	3.11		
$CdGeAs_2$	5.3	3.53	3.62	$d_{36} = 472$	810
	10.6	3.50	3.59		

3. **Coherence length:** When $\Delta k \neq 0$, the output power varies as

$$\text{sinc}^2(\Delta kL/2).$$

The energy in the nonlinearly generated wave, S_3, is a maximum at

$$L = \frac{\pi}{2\Delta k},$$

found by taking the derivative of (15.32) with respect to L and setting it equal to zero. We define this distance as the *coherence length*

$$\ell_c = \frac{\pi}{2\Delta k}. \tag{15.33}$$

In second-harmonic generation, it equals the length of a nonlinear material effective in generating second-harmonic radiation. Its size can be estimated by using the parameters associated with second-harmonic generation:

$$\omega_1 = \omega_2, \quad \omega_3 = 2\omega_1,$$
$$k_1 = k_2 = \frac{n_1\omega_1}{c}, \quad k_3 = \frac{n_3\omega_3}{c} = 2\frac{n_3\omega_1}{c}.$$

It is important to note that $k_3 \neq 2k_1$ because of dispersion:

$$\begin{aligned}\Delta k &= k_3 - k_2 - k_1 \\ &= \frac{2\omega_1}{c}(n_3 - n_1).\end{aligned}$$

The coherence length for second-harmonic generation is therefore

$$\ell_c = \frac{\lambda_1}{4(n_3 - n_1)}, \tag{15.34}$$

Table 15.7 *Second-harmonic coherence length*

Crystal	$\lambda(\mu m)$	ℓ_c(expt.) (μm)	ℓ_c (calc.) (μm)
KDP	0.694	18.5	18.8
	1.06	22	22
KD*P	0.694	20.6	
	1.06	21.2	
ADP	0.694	17.7	18.2
	1.06	21	20.6
$BaTiO_3$	1.06	5.8	

where λ_1 is the vacuum wavelength of the fundamental frequency. We can now use some real parameters to find a typical coherence length. We will double an infrared wavelength of 1 μm into the visible at 500 nm and will use KDP as the nonlinear material. For KDP (we will use the values for the ordinary ray),

$$\lambda_1 = 10^{-6}\text{m}, \quad n_1 = 1.50873,$$
$$\lambda_3 = 5 \times 10^{-7}\text{m}, \quad n_3 = 1.529833.$$

The coherence length is 1.18×10^{-5} m. This value is equal to the maximum useful crystal length for producing second-harmonic power when $\Delta k \neq 0$.

4. The coherence lengths for second-harmonic generation, shown in Table 15.7, are quite small. For second-harmonic generation to be useful, it is necessary to obtain larger coherence lengths by keeping $\Delta k \approx 0$. This leads to the question of how close a match must be obtained between n_1 and n_3 to generate a useful coherence length. To produce a coherence length of 1 mm for second-harmonic generation using 1 μm, (15.34) predicts that the index for the fundamental wavelength must equal

$$n_1 = n_3 \pm 0.00025.$$

In nonlinear optics, the process of reducing the phase difference Δk is called *phase matching*. If we view harmonic generation as a scattering process, then phase matching is equivalent to ensuring that momentum is conserved.

15.7.2 Phase Matching

We will try to visualize the problem of phase mismatch by following two waves along a linear array of eight atoms. We will assume that the index of refraction for the material at the fundamental frequency ω_1 is n_1 and the index at the harmonic wave ω_3 is $n_3 = \frac{16}{9} n_1$. To make the visualization easy, we assume that λ_1 is exactly equal to the atomic spacing. This requires that λ_3 be $\frac{8}{9}$ of the atomic spacing. The phase mismatch between these two waves as they propagate along the row of atoms is

$$k_3 - k_1 = \frac{\pi\, n_1}{4\lambda_1}.$$

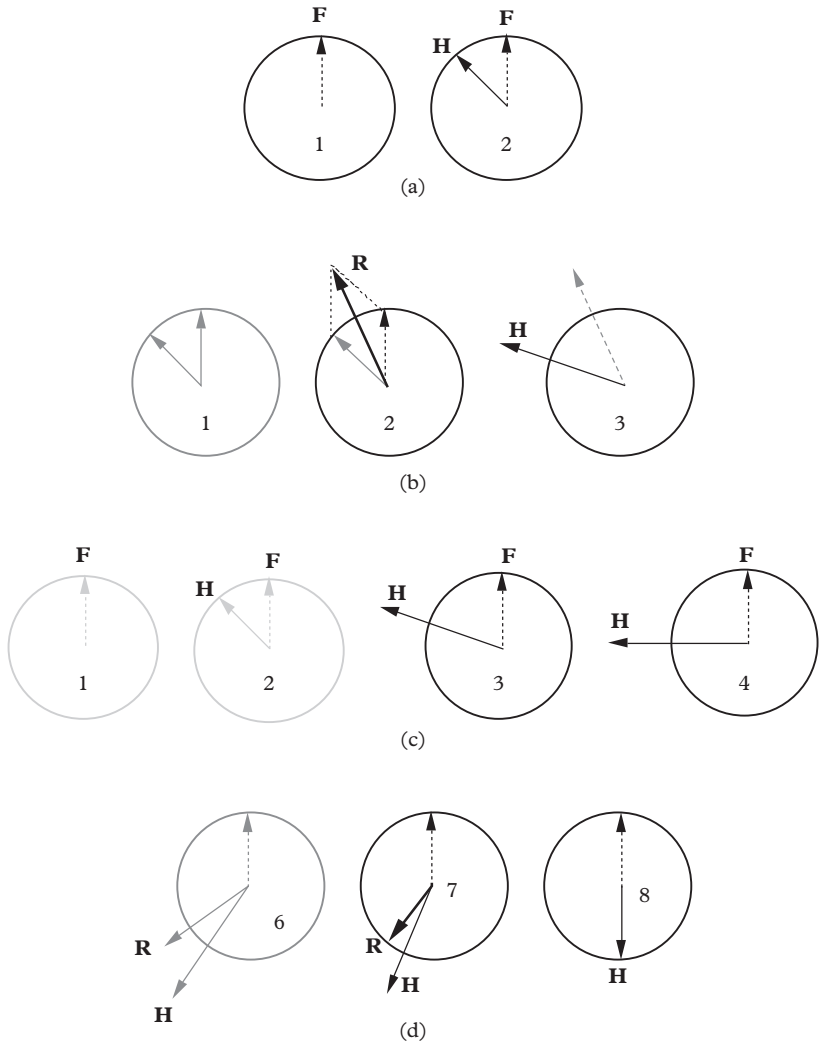

Figure 15.1 *(a)The first two atoms in a nonlinear material are located at positions 1 and 2. The electric field of the fundamental wave is denoted by* **F**. *It has the same phase at each atom. The polarization induced by* **F** *in atom 1 generates a harmonic wave* **H** *at atom 2. (b) Propagation of harmonic wave along the chain of atoms. (c) Four atoms in a nonlinear material. The fundamental and harmonic waves have reached atoms 3 and 4. Atoms 1 and 2 from (a) are shown for reference. (d) The fundamental and harmonic wave in the nonlinear crystal have reached atom 8. The harmonic wave is completely out of phase with the fundamental, so the resultant field is zero. The polarization, induced in atom 8 is therefore zero.*

The fundamental wave at a frequency ω_1 induces a nonlinear polarization that lags behind the fundamental wave by $\pi/4$. This polarization generates a harmonic wave at ω_3. As we move from atom to atom, we will add the harmonic wave generated by the polarization, at frequency ω_3, to the fundamental wave, at frequency ω_1, using the vector approach introduced in Chapter 4 (see Figure 4.1). The sum of these two waves will equal the local field experienced by the atom, and this will, in turn, determine the induced polarization.

At atom 1, the only wave present is the fundamental wave, we label its electric field **F** in Figure 15.1(a). At atom 2, the fundamental wave **F** is joined by the harmonic wave **H** produced by the polarization induced in atom 1. The harmonic wave lags the fundamental wave **F** by 45°, as shown in Figure 15.1(a). The resultant of the two waves **H** and **F** is

equal to a field of amplitude **R**. This resultant field induces a polarization in atom 2, which produces a harmonic wave at atom 3, again lagging the inducing polarization by $\pi/4$; see Figure 15.1(b). As the waves move on through the crystal, we reach atom 4, where the resultant of **H** and **F** reaches its maximum value; see Figure 15.1(c). The polarization induced by this wave is a maximum at atom 5. When we finally reach atom 8, the induced polarization due to the resultant formed by adding the fundamental **F** and the harmonic **H** is zero; see Figure 15.1(d). Atom 8 sees no field and therefore produces no harmonic wave.

This geometrical analysis agrees with the calculation of the coherence length using (15.33) and demonstrates that the coherence length is a measure of the distance over which the fundamental and harmonic waves propagate in phase through the nonlinear material.

15.8 Second-Harmonic Generation

In the derivation of (15.32), we assumed low harmonic conversion efficiency, i.e., E_1 and E_2 remain near their original value and E_3 is small relative to them. This assumption prevents the calculation of how energy flows from the fundamental to the harmonic. A simple example, involving the second harmonic, will allow an estimate of the energy flow between the fundamental and harmonic waves. We will assume the following:

1. Second-harmonic generation, $\omega_3 = 2\omega$, where $\omega_1 = \omega_2 = \omega$.
2. A perfect dielectric, $\sigma = 0$. We need not worry about loss in the medium.
3. The nonlinear material occupies the positive half-plane, $z \geq 0$.
4. $E_1 = E_2 = E(\omega)e^{i\varphi(\omega)}$ and $E(2\omega)e^{i\varphi(2\omega)}$.
5. There is no dispersion, so $\varepsilon_1 = \varepsilon_2 = \varepsilon_3 = \varepsilon$. This assumption allows perfect phase matching, $\Delta k = 0$.
6. $E_3 = 0$ and $E_1 = E_0 e^{i\varphi(\omega)}$ at $z = 0$, the boundary of the nonlinear material.

These assumptions allow us to rewrite (15.26) and (15.27) as

$$\frac{\partial E(\omega)}{\partial z} = -i\sqrt{\frac{\mu}{\varepsilon}}\,\frac{d\omega}{2}E(\omega)E(2\omega)e^{i\varphi(2\omega)}, \tag{15.35}$$

$$\frac{\partial E(2\omega)}{\partial z} = -i\sqrt{\frac{\mu}{\varepsilon}}\,d\omega E^2(\omega)e^{i[2\varphi(\omega)-\varphi(2\omega)]}. \tag{15.36}$$

For growth of the second-harmonic wave, we require

$$2\varphi(\omega) - \varphi(2\omega) = \frac{\pi}{2};$$

i.e., the phase of the generated wave must lag the polarization that creates it by 90°. When this occurs, (15.36) is a real positive function.

We also use the energy conservation law, to be proved in Problem 15.3. This conservation law states that the sum of the power densities of the fundamental and second-harmonic waves must be a constant over the propagation paths and allows us to rewrite (15.36) as

$$\frac{\partial E(2\omega)}{\partial z} = d\omega\sqrt{\frac{\mu}{\varepsilon}}\,[E_0^2(\omega) - E^2(2\omega)]. \tag{15.37}$$

By integrating (15.37) from $z = 0$ to $z = L$, we obtain an equation for the second-harmonic amplitude at a distance L into the nonlinear material:

$$E(2\omega) = E_0(\omega) \tanh\left[E_0(\omega) L d \omega \sqrt{\frac{\mu}{\varepsilon}}\right]. \tag{15.38}$$

The conservation law of Problem 15.3 permits the use of (15.38) to obtain the fundamental field's amplitude

$$E(\omega) = E_0(\omega) \operatorname{sech}\left[E_0(\omega) L d \omega \sqrt{\frac{\mu}{\varepsilon}}\right]. \tag{15.39}$$

Equations (15.38) and (15.39) are displayed in Figure 15.2. The initial slope of the second-harmonic curve is given by (15.32) with $\Delta k = 0$.

The simple theory predicts the possibility of obtaining 100% conversion of the fundamental wave into the second-harmonic wave. Our theory is too simple to figure out how efficient the doubling process will be. Doubling efficiencies of 80% have been reported in the literature. The quantum theory predicts that when the fundamental wave shrinks to the level of quantum noise, the energy flow will reverse and the fundamental wave will grow at the expense of the second harmonic. (These results have been derived for plane wave interactions. In practice, to increase the light fields, focused Gaussian beams are used [9].)

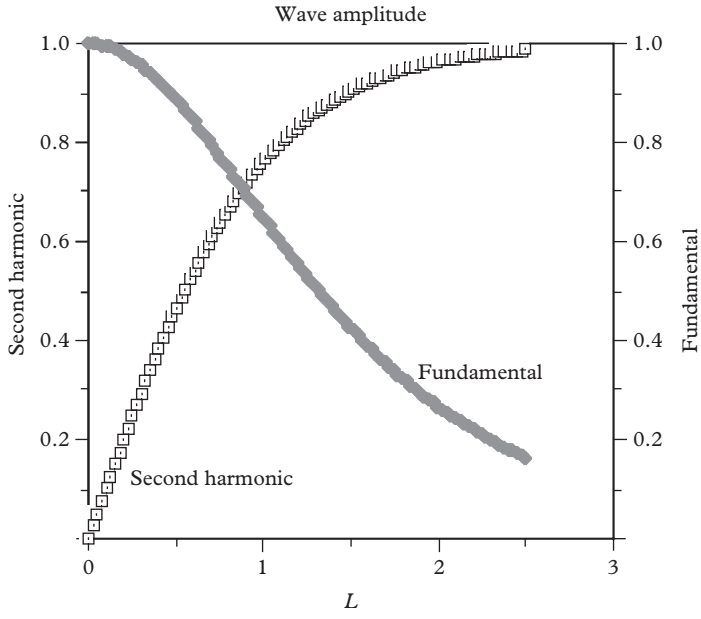

Figure 15.2 *Wave energy for the fundamental and second-harmonic waves as they travel into a nonlinear material.*

15.9 Methods of Phase Matching

A number of different ways of obtaining phase matching have been proposed. We will discuss a large number of these because the problem of phase matching is key to the utilization of the second-order nonlinearity in harmonic generation.

15.9.1 Quasi-Phase Matching (QPM)

If the phase difference between the harmonic and the fundamental waves is changed by 180°, after the waves have propagated one coherence length, we can prevent the energy from draining from the harmonic back into the fundamental wave. One way to accomplish this would be to stack a series of crystal plates or thin-film layers—each one a coherence length thick (see Figure 15.3). In this design, the index of refraction is assumed to be the same in each layer so that there are no reflections at the interfaces.

To understand this method, we initially assume there is no nonlinear interaction in the shaded layers of Figure 15.3: $d_2 = 0$. After propagating a coherence length in material one, with nonlinear optical coefficient d_1, the fundamental and harmonic are out of phase by π. If we did nothing, energy would begin to flow back from the harmonic to the fundamental. At this point, the two waves enter the second material. Because we assumed $d_2 = 0$, there is no nonlinear interaction in the second material; the two waves are not coupled and do not interact. After traveling a coherence length in the linear medium, the waves are again in phase. The in-phase waves again enter the nonlinear region with the nonlinear coefficient d_1, and additional energy is transferred from the fundamental to the harmonic wave. The first demonstration of this was by Franken, Peters, and Hill using quartz plates in 1961. Figure 15.4 is a copy of part of a viewgraph describing the unpublished work. Figure 15.5 compares the growth of the second harmonic for perfect phase matching and for QPM.

It is quite straightforward to show [11] that phase matching for difference-frequency mixing is obtained when

$$\Delta k = k_3 - k_1 + k_2 = \frac{(2m+1)\pi}{\ell},$$

where ℓ is the thickness of each plate and m is an integer constant. When $m = 0$, ℓ is equal to the natural coherence length. The output intensity using this technique is, at best (when $m = 0$), only 40% of the value obtained that would be obtained if perfect phase matching existed. This type of phase matching has been demonstrated in GaAs [13, 14].

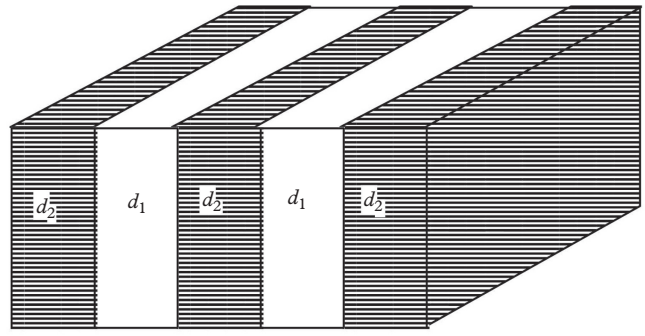

Figure 15.3 *Multilayers of nonlinear material. The sign of the nonlinear coefficient is periodically modulated, with the period of modulation being equal to the coherence length.*

It was difficult to construct a QPM structure until ferroelectric materials with alternating domains of a ferroelectric [14] were used for QPM. Reflections at the surfaces of the plates lowered the performance, and most investigators turned to other techniques for phase matching. In 1980, the first single crystal with periodically polled layers was grown [15]. The next major improvement was the growth of single-crystal fibers of ferroelectric crystals and ferroelectric waveguides in 1989. The materials can now be purchased commercially.

QPM provides the following advantages:

1. It allows the use of materials with insufficient birefringence for phase matching (e.g., GaAs).
2. It has the capacity to phase-match any frequencies in the transparency range.
3. It shows an enhanced capability for construction of optical parametric oscillators.
4. It allows noncritical (90°) phase matching.
5. It can be engineered to eliminate Poynting walkoff.
6. The largest nonlinear coefficient in a material can be selected (e.g., d_{33} in $LiNbO_3$).

15.9.2 Total Internal Reflection

We can use the fact that a wave undergoes a phase change during total internal reflection (see Figure 3.13) to obtain phase matching. Consider second-harmonic generation; the relative phase change on reflection is given by

$$\varphi = 2\delta(\omega) - \delta(2\omega),$$

where δ is obtained from either (3.54) or (3.55). The relative phase change between the fundamental and harmonic due to dispersion is

$$2\psi = [n(2\omega) - n(\omega)]\frac{2\omega L}{c},$$

where we have assumed a propagation distance L. This phase change is compensated for by proper adjustment of the internal reflection angle θ. Phase matching by total internal reflection has been observed using a CO_2 laser at $\lambda = 10.5915$ μm, with the geometry shown in Figure 15.6 [16].

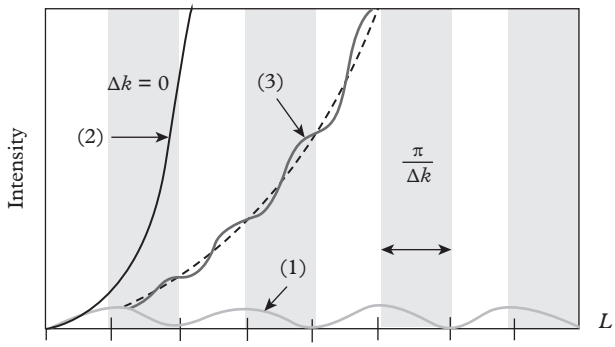

Figure 15.5 *Effect of phase matching on the growth of the second harmonic. The sinusoidal curve (1) is the behavior described in Figure 15.1. The curve (2) occurs when perfect phase matching is obtained, and the curve (3) is the behavior for quasi-phase matching.*

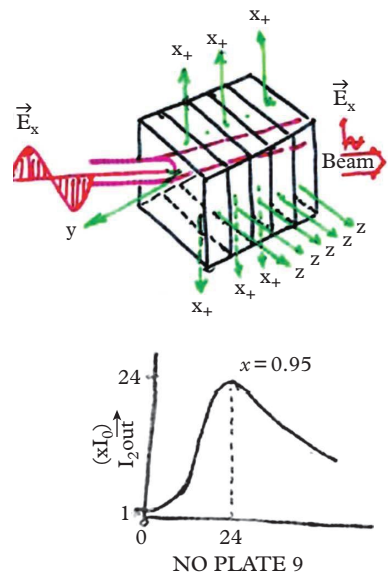

Figure 15.4 *Quasi-phase matching using quartz plates reported by Hill and mentioned by J.A. Giordmaine in a general interest article [10].*

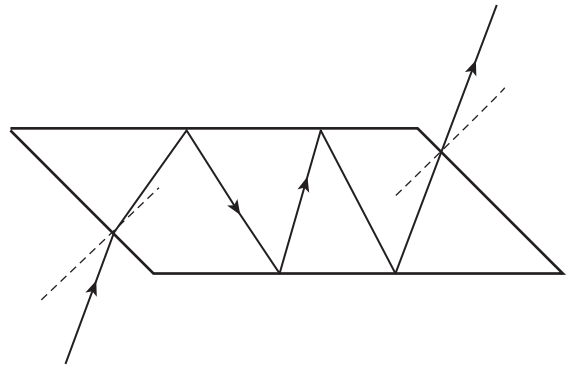

Figure 15.6 *Configuration used to obtain phase matching by total internal reflection.*

15.9.3 Dielectric Waveguide

The use of a waveguide for phase matching is a natural extension of the use of total internal reflection. Associated with each of the waveguide modes excited is a different effective index of refraction (see Chapter 5)

$$N = \frac{\beta}{k}. \tag{15.40}$$

The effective index can range between the value for the substrate and the bulk value for the guide material. A mathematical discussion of this type of phase matching can be found in a paper suggesting its use for operation in the submillimeter wavelength region of the spectrum [17].

15.9.4 Noncollinear Phase Matching

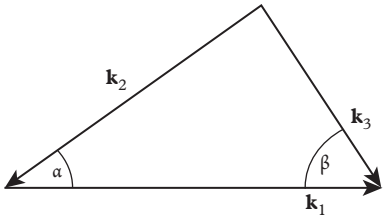

Figure 15.7 *Noncollinear phase matching. The vector sum of the propagation vectors, rather than the scalar sum, is set equal to zero.*

The previous techniques are called *collinear techniques* because the waves are propagating in the same direction. It is possible to perform phase matching by *noncollinear techniques* where the waves propagate at an angle with respect to one another. The concept of noncollinear phase matching is quite straightforward, as can be seen in Figure 15.7. Instead of requiring that the scalar momentum conservation equation be satisfied, a vector equation must be satisfied:

$$\Delta\mathbf{k} = \mathbf{k}_3 - \mathbf{k}_1 - \mathbf{k}_2 = 0. \tag{15.41}$$

The restrictions that phase matching place on the angle α between $\mathbf{k}_1$ and $\mathbf{k}_2$ and on the angle β between $\mathbf{k}_1$ and $\mathbf{k}_3$ can easily be derived by applying the law of cosines to Figure 15.7:

$$\begin{aligned} k_3^2 &= k_1^2 + k_2^2 - 2k_1k_2\cos\alpha, \\ \cos\alpha &= 1 - 2\sin^2\frac{\alpha}{2} \\ &= \frac{n_1^2\omega_1^2 + n_2^2\omega_2^2 - n_3^2\omega_3^2}{2n_1\omega_1 n_2\omega_2}. \end{aligned} \tag{15.42}$$

To evaluate the physical implications of this result, we will treat the case of difference-frequency generation, $\omega_1 - \omega_2 = \omega_3$. For simplicity, we make the physically realistic assumption that $n_1 \approx n_2 = n, n_3 = n + \Delta n$ and that $\Delta n^2 \approx 0$ (see Table 15.6, where index values for the case of second-harmonic generation are listed). With these assumptions about the index of refraction, the angle α is given roughly by

$$\sin^2 \frac{\alpha}{2} \approx \frac{\Delta n \omega_3^2}{2n\omega_1\omega_2}. \tag{15.43}$$

For small values of α (i.e., nearly collinear waves),

$$\alpha \approx \frac{\omega_3}{\sqrt{\omega_1\omega_2}} \sqrt{\frac{2\Delta n}{n}}.$$

Since α is real only if $\Delta n > 0$, noncollinear phase matching for difference-frequency generation can be produced only in regions of anomalous dispersion.

As we did for α, we can use the law of cosines to evaluate β:

$$\begin{aligned} \sin^2 \frac{\beta}{2} &\approx \frac{2n\Delta n\omega_1\omega_3 - 2n\Delta n\omega_3^2}{4n(n + \Delta n)\omega_1\omega_3} \\ &= \frac{\Delta n}{2(n + \Delta n)} - \frac{\Delta n\omega_3}{2(n + \Delta n)\omega_1}. \end{aligned}$$

From the geometry used in Figure 15.7, $\omega_3 < \omega_1$ and the second term is smaller than the first. If we also assume, as we did for α, that the waves are nearly collinear, $\sin(\beta/2) \approx \beta/2$, then the third frequency must be much smaller than the first, $\omega_3 \ll \omega_1$ and we may ignore the second term. With these approximations, the angle β is

$$\beta = \sqrt{\frac{2\Delta n}{n}}. \tag{15.44}$$

The angle β is, within the approximations used here, independent of frequency. It is the broadband behavior implied by (15.44) that is the major advantage of the noncollinear phase matching technique.

Examples of geometries that have been used for noncollinear mixing are shown in Figure 15.8.

A useful application of noncollinear phase matching is in the measurement of picosecond optical pulses using second-harmonic generation autocorrelation (see Figure 15.9 and Problem 15.7). Two samples of a picosecond pulse are obtained with a beamsplitter. One of the samples is delayed in time by propagating it over a longer optical path. The two samples are added together in a nonlinear crystal. The amount of second-harmonic radiation produced is determined by the temporal overlap of the two pulses; Figure 15.9(b). By varying the time delay, an autocorrelation of the picosecond pulse is produced. The temporal resolution is obtained by varying an optical path length, to vary τ, rather than through the temporal resolution of the detector.

Accidental noncollinear phase matching between the fundamental on-axis beam and energy scattered from the second wave can be observed in crystals where collinear phase matching occurs. In second-harmonic generation, this leads to interesting ring-shaped patterns [18]. The harmonics shown in Figure 15.10 were generated by a ferroelectric material that illustrates the degree of sophistication that has been obtained in optical phase matching.

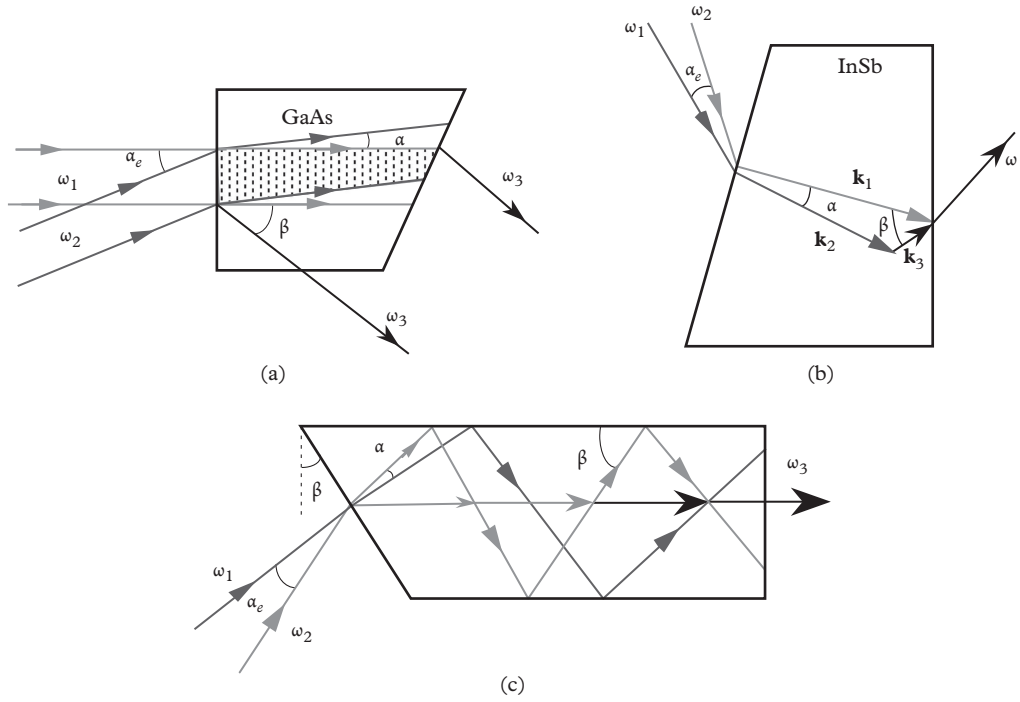

Figure 15.8 *Geometries used for noncollinear phase matching. The slanted faces are to allow efficient coupling. The guided wave geometry in the bottom figure is to increase the effective interaction length.*

15.9.5 Birefringent Phase Matching

While QPM technology spent a 30-year period developing a practical capability, the most popular method of phase matching utilized birefringence. The fact that in an anisotropic crystal, the refractive index depends both upon the wavelength and upon the polarization of a light wave makes it possible to find an operating condition where $\Delta k = 0$. We derived an expression for the index of refraction as a function of propagation direction for a uniaxial crystal in Appendix 13C. Using (13C.7), a plot of the extraordinary index of refraction as a function of the angle between the propagation direction and the optical axis is presented in Figure 15.11. It can be seen that the index of refraction can be adjusted to any value between n_e and n_o by varying the propagation direction. If the variation in the index of refraction due to birefringence is larger than the dispersive change in the index, then phase matching can be obtained. Phase matching is accomplished by using linearly polarized waves, propagating at the proper angle, to ensure that $n(2\omega) = n(\omega)$.

There are two methods of achieving the phase-matched condition using birefringence:

- *Type I*: The waves at frequencies ω_1 and ω_2 have the same polarization; i.e., both are ordinary or both are extraordinary waves. The third wave, at frequency ω_3, is polarized in an orthogonal direction.
- *Type II*: The waves at frequencies ω_1 and ω_2 are orthogonally polarized. The third wave, at frequency ω_3, can have its polarization direction parallel to either of the other waves.

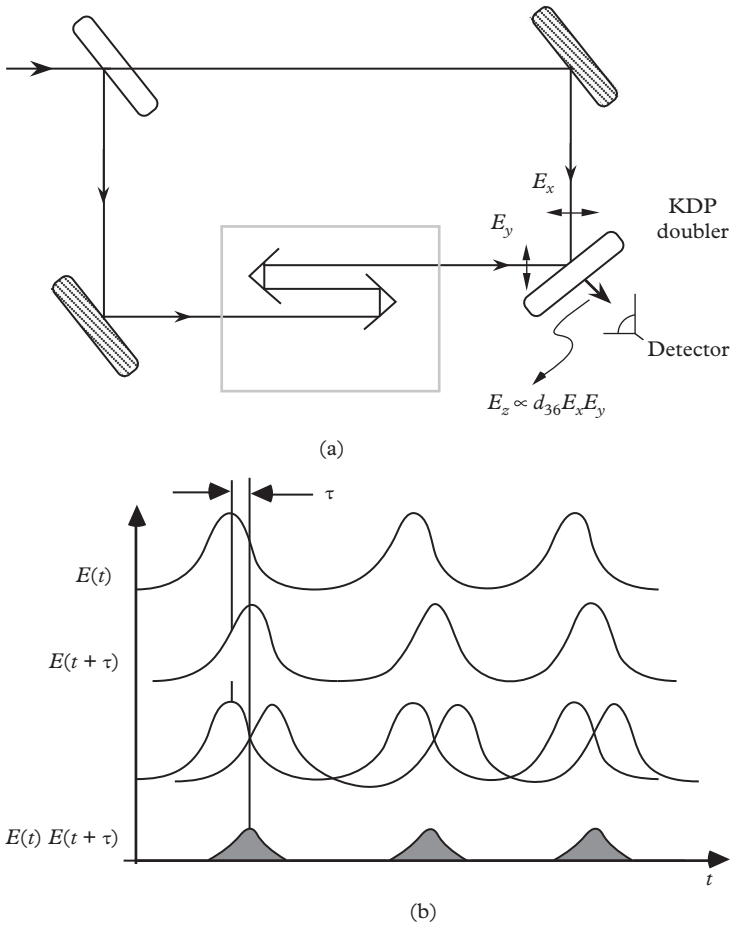

Figure 15.9 *(a) Picosecond pulse detection using the autocorrelation of two samples of a pulse. One sample is delayed by a time* τ *with respect to the other sample. The two pulses are mixed in a nonlinear crystal and integrated on a detector to give the autocorrelation function. (b) The two pulses are overlapped in space (second curve from bottom) by adjusting* τ*. The overlapping pulses produce the second-harmonic emission shown as the bottom curve. Only the area under the pulse at the second harmonic is detected. Temporal resolution is obtained by varying* τ

To demonstrate phase matching using birefringence, the phase matching condition for three uniaxial crystals will be determined. For collinearly propagating waves, the phase matching condition (15.42) reduces to

$$n_3\omega_3 = n_1\omega_1 - n_2\omega_2. \tag{15.45}$$

The indices of refraction depend on the type of phase matching and on the type of birefringent crystal—biaxial or positive or negative uniaxial. For uniaxial crystals, the phase matching equation becomes

	$n_e < n_o$	$n_e > n_o$
Type I	$n_e(\omega_3) = \frac{\omega_1}{\omega_3} n_o(\omega_1) + \frac{\omega_2}{\omega_3} n_o(\omega_2)$	$n_o(\omega_3) = \frac{\omega_1}{\omega_3} n_e(\omega_1) + \frac{\omega_2}{\omega_3} n_e(\omega_2)$
Type II	$n_e(\omega_3) = \frac{\omega_1}{\omega_3} n_e(\omega_1) + \frac{\omega_2}{\omega_3} n_o(\omega_2)$	$n_o(\omega_3) = \frac{\omega_1}{\omega_3} n_o(\omega_1) + \frac{\omega_2}{\omega_3} n_e(\omega_2)$

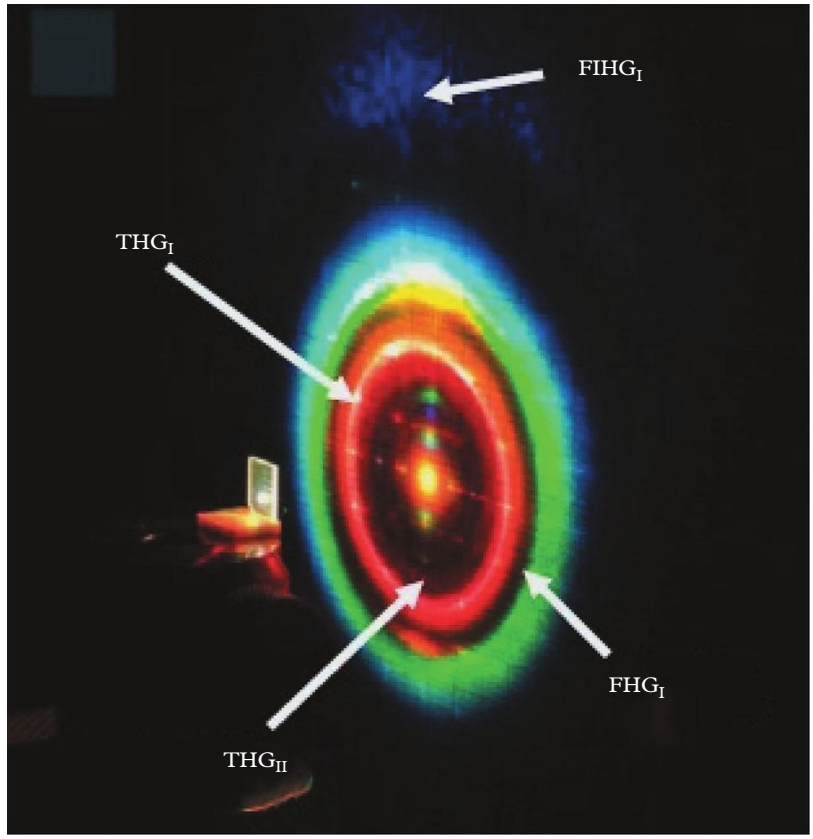

Figure 15.10 *Multicolor ring-shaped high-harmonic generation recorded in the far field from a $LiNbO_3$ photonic crystal. The fundamental wavelength was 2100 nm. Red, green, and blue conical emissions are due to frequency tripling, quadrupling, and quintupling of the fundamental wave. (Mateos, L., et al.,* Simultaneous generation of second to fifth harmonic conical beams in a two dimensional nonlinear photonic crystal. *Opt. Express, 2012. 20: p. 29940–29948. Courtesy Mariola O. Ramirez.)*

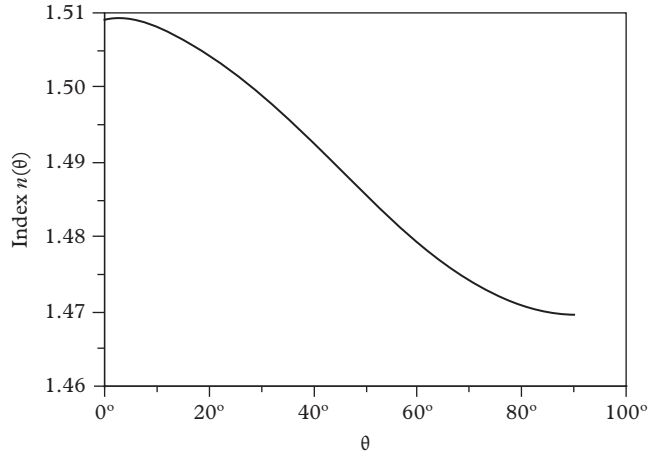

Figure 15.11 *Variation in the value of the extraordinary index of refraction with propagation angle in KDP at room temperature and 1 μm. The index varies from n_o at $\theta = 0°$ to n_e at $\theta = 90°$.*

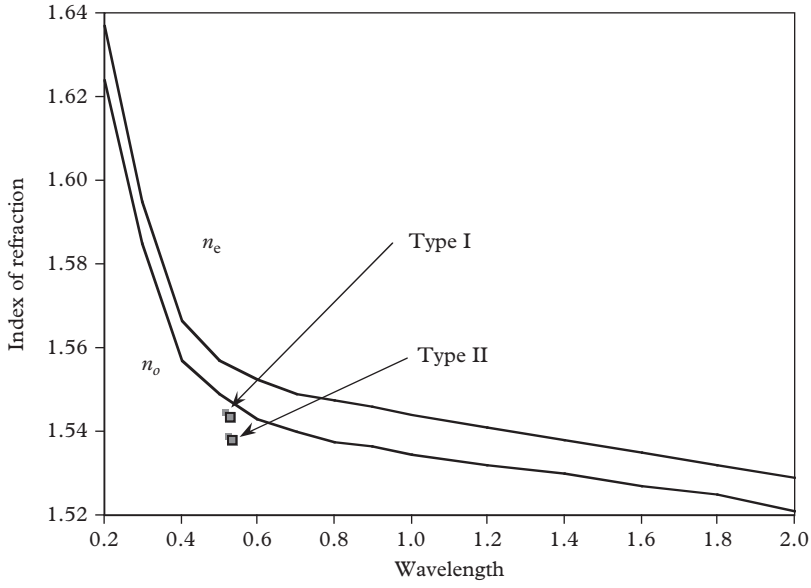

Figure 15.12 *Dispersion in quartz. The points labeled "Type I" and "Type II" are the indices that would have to exist if we could have phase matching in quartz for doubling 1.06 μm.*

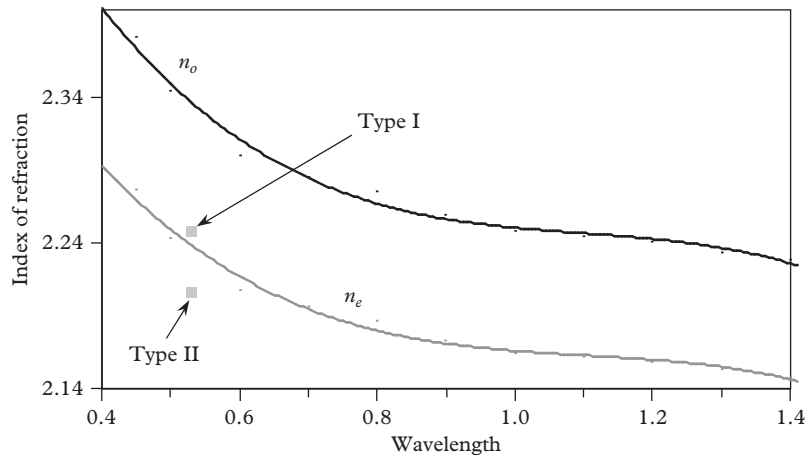

Figure 15.13 *Dispersion in lithium niobate. As can be seen, for doubling of 1.06 μm, only type I phase matching is possible.*

Figures 15.12–15.14 display the ordinary and extraordinary indices of refraction as functions of wavelength for three common birefringent crystals: quartz, $LiNbO_3$, and KDP. In addition to the dispersion curves for these crystals, points are plotted on the graphs indicating the phase matching conditions required to convert radiation of wavelength 1.06 μm to a wavelength of 530 nm.

Figure 15.12 shows the dispersion of the ordinary and extraordinary indices of quartz. These curves bound the indices of refraction that are accessible at each wavelength by varying the propagation direction. The points labeled "Type I" and "Type II" are the indices of refraction that must exist if phase matching is to occur for second-harmonic generation

with a fundamental wavelength of 1.06 μm. The indices that 530 nm light waves must have are smaller than any index available in quartz; therefore, phase matching is not possible. This is why Franken and Hill turned to QPM using quartz plates to try to get a detectable second-harmonic signal.

The dispersion curve in Figure 15.13 is for $LiNbO_3$. From the position of the required second-harmonic index for type II phase matching, we see that only type I phase matching can occur in $LiNbO_3$ for second-harmonic generation of 1.06 μm. In Figure 15.13, it is apparent that type I phase matching is approximately obtained when $\theta = 90°$. Exact phase matching at 90° can be obtained by adjusting the temperature of the crystal. Phase matching at 90° is called *noncritical phase matching. Critical phase matching* occurs in all other propagation directions.

Noncritical phase matching offers an advantage in second-harmonic generation. When the light wave propagates normal to the optic axis of a birefringent crystal, the extraordinary and ordinary waves propagate in a collinear direction. At all other angles, except 0°, birefringence is observed, and the two waves propagate at an angle with respect to each other. This is called Poynting vector walkoff, [see Problem 13.9 and (13.35)]. For a typical birefringent crystal, when the propagation direction makes an angle of $\theta = 45°$ with the optical axis, the Poynting walkoff angle is about 2°. It is often necessary to focus the incident light wave to increase the nonlinear interaction, Poynting vector walkoff causes the ordinary and extraordinary waves to separate after a distance called the *aperture length*

$$\ell_a = \frac{\sqrt{\pi} w_0}{\phi},$$

where ϕ is the Poynting vector walkoff angle, (13.35), and w_0 is the beam waist. By obtaining phase matching at 90°, we can eliminate Poynting vector walkoff and increase the aperture length for second-harmonic generation. Noncritical phase matching also offers the advantage of increasing the acceptance angle (i.e., the angular spread of the fundamental beam) by as much as an order of magnitude over the acceptance angle for critical phase matching.

KDP is a material that can have either type I or type II phase matching, as we can see in Figure 15.14. For type I phase matching, the phase matching angle is given by

$$\sin^2 \theta_m = \frac{\dfrac{1}{n_o^2(\omega)} - \dfrac{1}{n_o^2(2\omega)}}{\dfrac{1}{n_e^2(2\omega)} - \dfrac{1}{n_o^2(2\omega)}}, \tag{15.46}$$

and for type II phase matching,

$$\sin^2 \theta_m = \frac{\left[\dfrac{n_o(\omega)}{2n_o(2\omega) - n_o(\omega)}\right]^2 - 1}{\left[\dfrac{n_o(\omega)}{n_e(\omega)}\right]^2 - 1}. \tag{15.47}$$

In those materials that allow both types of phase matching, how do we decide which type to use? One basis for selecting the type of phase matching is the ability to operate with

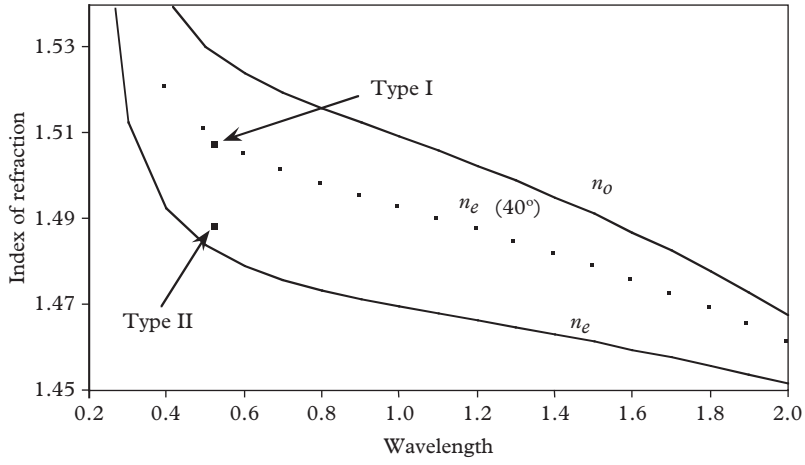

Figure 15.14 *Dispersion in KDP. The birefringence is large enough in KDP to allow both type I and type II phase matching for doubling of 1.06 μm. Note that the angle for type I phase matching is 42.4°.*

the waves propagating in a direction 90° with respect to the optical axis. A second reason for selecting one type of phase matching over another can be found in Table 15.5. The magnitude of d_{eff} is a function of the phase matching angle. For type I phase matching in KDP, we find from Table 15.5 that

$$d_{\text{eff}} = -d_{14} \sin\theta \sin 2\phi.$$

Once θ is fixed by the phase matching condition, we can maximize d_{eff} by selecting the direction of propagation so that it makes an angle of $\phi = 45°$ with respect to the x-axis of the crystal. In Table 15.5, we find for KDP that the selection of $\theta = 90°$ results in a d_{eff} equal to zero for type II phase matching, but results in the maximum value for d_{eff} for type I phase matching. To maximize d_{eff} for type II phase matching in KDP, we would select $\phi = 0°$ and select the phase matching angle to be $\theta \approx 45°$.

15.10 Phase Conjugation

A theoretical description of the third-order nonlinear properties of materials can be developed with the same procedures used to develop the second-order theory. In the second-order nonlinear theory, $\chi^{(2)}$ was found to exhibit both resonant and loss properties, similar to $\chi^{(1)} \cdot \chi^{(3)}$ exhibits the same resonant behavior. The imaginary part of $\chi^{(3)}$, corresponding to either energy gain or loss, describes Raman, Brillouin, and Rayleigh scattering, as well as two photon processes. The real part of $\chi^{(3)}$ describes the process of harmonic wave generation, the optical Kerr effect, and intensity-dependent changes in the index of refraction.

The nonlinear polarization is given by a number of terms of the form

$$[P_{\text{NL}}^{(3)}(\omega_4)]_i = \mathcal{D}\left[\sum_{jk\ell} \chi_{ijk\ell}^{(3)}(\omega_1, \omega_2, \omega_3, \omega_4) E_j(\omega_1) E_k(\omega_2) E_\ell(\omega_3) + \text{c.c.}\right], \tag{15.48}$$

where $\mathcal{D}$ is a numerical constant that depends on the values of ω_1, ω_2, ω_3, and ω_4 (see Table 15.8). $\chi^{(3)}$ is a fourth-rank tensor, relating one vector to three others.

Table 15.8 *Constants $\mathcal{D}$ in (15.48) for third-order nonlinear processes*

$\mathcal{D}$	ω_1	ω_2	ω_3	ω_4
$\frac{1}{4}$	ω	ω	ω	3ω
$\frac{3}{4}$	ω_1	ω_2	ω_1	$2\omega_1 + \omega_2$
$\frac{3}{2}$	ω_1	ω_2	ω_3	$\omega_1 + \omega_2 + \omega_3$
$\frac{3}{4}$	ω_1	ω_2	ω_1	$2\omega_1 - \omega_2$
$\frac{3}{2}$	ω_1	ω_2	ω_2	$\omega_1 + \omega_2 - \omega_2$
$\frac{3}{4}$	ω	ω	ω	$\omega + \omega - \omega$
3	ω	0	0	ω

Symmetry arguments can be applied to $\chi^{(3)}$, as they were to $\chi^{(2)}$, resulting in simplifications [19]. One important result of the symmetry arguments is that $\chi^{(3)}$ is nonzero for centrosymmetric systems (i.e., systems with inversion symmetry). The nonzero elements of the tensor are identified in Appendix 14A. Far from resonant conditions,

$$\mathcal{O}(\chi^{(3)}) = \begin{cases} 10^{-33} & \text{c.g.s.,} \\ 10^{-58} & \text{MKS.} \end{cases}$$

$\chi^{(3)}(\omega, 0, 0, \omega)$ is the susceptibility associated with the DC Kerr effect, discussed in Chapter 14. We will only examine one additional term of the third-order nonlinear polarization, $\chi^{(3)}_{ijk\ell}(\omega, \omega, \omega, \omega)$, which is associated with the optical Kerr effect. We will discover that the theory allows the effect to be interpreted as a holographic process. Some typical values of $\chi^{(3)}$ are shown in Table 15.9.

One of the processes associated with $\chi^{(3)}(\omega, \omega, \omega, \omega)$ is called *degenerate four-wave mixing* or *phase conjugation*. The mathematical details of the theory [20] are similar to the analysis of the second-order nonlinearity described earlier. The experimental geometry normally used in the development of the theory is shown in Figure 15.15.

Table 15.9 *Third-order nonlinear susceptibility*

Material	$\chi_{ijk\ell}$ ($\times 10^{-13}$ esu)[a]	$ijk\ell$
CS_2	2.7	1221
	3.9	1111
2-Methyl-4-nitroaniline	119	1111
Polydiacetylene	400	1111

[a]The c.g.s. units shown here are those normally found in the literature. To convert to MKS units for χ, use (15.9).

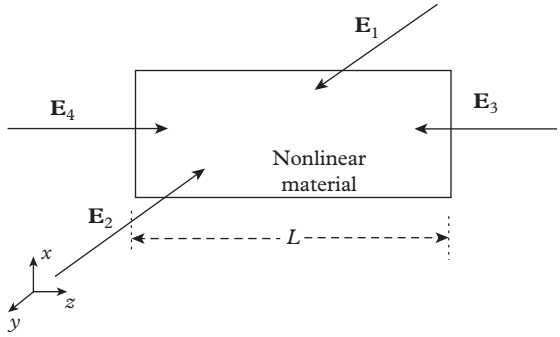

Figure 15.15 *Geometry for phase conjugation.*

The geometry of the experiment makes it possible to treat each wave separately, reducing the problem to the solution of a wave equation involving $P^{(3)}$. The fact that $\mathbf{k}_1 + \mathbf{k}_2 = 0$ in Figure 15.15 allows the problem to be reduced to one dimension. The orientation of the $\mathbf{k}$ vectors ensures phase matching at all times.

The wave equation to be solved is (15.19), with an applied electric field consisting of three waves, each described by (15.20). The nonlinear polarization will involve terms of the form

$$\chi^{(3)}_{ijk\ell} E_{1j} E_{2k} E^*_{3\ell} e^{i(\omega t - kz)}, \tag{15.49}$$

as well as terms involving 2ω. We will neglect the 2ω terms and give a justification for ignoring these higher-frequency terms later.

All of the waves are assumed to have the same polarization, so only one of the tensor components for $\chi^{(3)}$ enters into the calculation. This assumption allows the replacement of the tensor with a scalar: $\chi^{(3)}_{1111} \rightarrow \chi^{(3)}$. (This assumption is more restrictive than we need. We could relax the assumption and require that wave pair 1 and 2 and pair 3 and 4 each have the same polarizations. The susceptibility would still only contain one tensor component, $\chi^{(3)}_{1221} \rightarrow \chi^{(3)}$, and the susceptibility could continue to be treated as a scalar.) A further simplification can be obtained by assuming that

$$|E_3|, |E_4| \ll |E_1|, |E_2|.$$

Using an approach similar to the one used to derive (15.23)–(15.25), the wave equation for the complex amplitude of the wave generated by the nonlinear interaction can be written as

$$\frac{dE_4}{dz} = -i\frac{\omega\chi^{(3)}}{2}\sqrt{\frac{\mu}{\varepsilon}}\left(|E_1|^2 + |E_2|^2\right)E_4 - i\frac{\omega\chi^{(3)}}{2}\sqrt{\frac{\mu}{\varepsilon}}\,E_1 E_2 E_3^*. \tag{15.50}$$

The first term in (15.50) describes the optical Kerr effect. This term can be incorporated into the theory by modifying the propagation vector for wave 4 from k to

$$\check{k} = k + \frac{\omega\chi^{(3)}}{2}\sqrt{\frac{\mu}{\varepsilon}}\left(|E_1|^2 + |E_2|^2\right). \tag{15.51}$$

This new propagation constant can be included in the definitions of the complex amplitudes for the four waves by introducing a new complex amplitude of the form

$$\mathcal{A} = Ee^{-i\check{k}z}. \tag{15.52}$$

With this new definition, (15.50) becomes, for waves 4 and 3,

$$\frac{d\mathcal{A}_4}{dz} = -i\frac{\omega\chi^{(3)}}{2}\sqrt{\frac{\mu}{\varepsilon}}\,\mathcal{A}_1\mathcal{A}_2\mathcal{A}_3^*, \tag{15.53}$$

$$\frac{d\mathcal{A}_3^*}{dz} = -i\frac{\omega\chi^{(3)*}}{2}\sqrt{\frac{\mu}{\varepsilon}}\,\mathcal{A}_1^*\mathcal{A}_2^*\mathcal{A}_4. \tag{15.54}$$

We will not solve (15.50) for waves 1 and 2, but will, instead, treat them as "medium conditioners"and include their effects in a material constant defined by the equation

$$\kappa = \frac{\omega\chi^{(3)*}}{2}\sqrt{\frac{\mu}{\varepsilon}}\,\mathcal{A}_1^*\mathcal{A}_2^*. \tag{15.55}$$

This material constant is a spatially dependent index of refraction that will affect the propagation of the other waves.

The solution of (15.53) and (15.54) can easily be obtained. The nonlinear medium is assumed to occupy the positive half-plane with one edge at $z = 0$ and the other at $z = L$. As boundary conditions, we will assume that wave 4 is incident on the nonlinear medium from the left with a complex amplitude $\mathcal{A}_4(0)$ at the boundary. We assume that the wave with complex amplitude $\mathcal{A}_3$ is produced in the nonlinear medium; therefore, we must have $\mathcal{A}_3(L) = 0$ at the right boundary of the nonlinear medium. The solution of (15.54) for wave 3 is

$$\mathcal{A}_3(z) = \frac{\cos|\kappa z|}{\cos(|\kappa|L)}\mathcal{A}_3(L) + i\kappa^*\frac{\sin[|\kappa|(z-L)]}{|\kappa|\cos(|\kappa|L)}\mathcal{A}_4^*(0).$$

The solution of (15.53) is left as Problem 15.5.

At the front surface of the nonlinear medium, we have

$$\mathcal{A}_3(0) = -i\frac{\kappa^*}{|\kappa|}\mathcal{A}_4^*(0)\tan(|\kappa|L). \tag{15.56}$$

Equation (15.56) predicts that the third-order nonlinear medium will act as a mirror with the distinctive property of reflecting the conjugate of the incident wave. (See Chapter 12 for a discussion of conjugate waves.)The reflectivity of this strange mirror can be greater than 1 whenever

$$\frac{\pi}{4} \le |\kappa|L \le \frac{3\pi}{4}.$$

One of the interesting aspects of the phase conjugate system is the analogy with holography. Assume for the moment that κL is small so that $\tan\kappa L$ may be replaced by κL. Equation (15.56) describes the complex amplitude of the wave traveling to the left in Figure 15.16 as it leaves the nonlinear medium. For small κL, (15.56) becomes

$$\mathcal{A}_3(0) = -i\frac{\omega\chi^{(3)}}{2}\sqrt{\frac{\mu}{\varepsilon}}\,\mathcal{A}_1\mathcal{A}_2\mathcal{A}_4^*(0). \tag{15.57}$$

Because of the similarity with terms in (12.4), we treat the formation of $\mathcal{A}_3$ as the diffraction of $\mathcal{A}_1$, by a fringe system produced by interference between $\mathcal{A}_2$ and $\mathcal{A}_4^*$, as shown in Figure 15.16(a).

A second interpretation concerning the formation of $\mathcal{A}_3$ views it as a wave originating from the diffraction of wave 2 by a fringe system created through the interference of

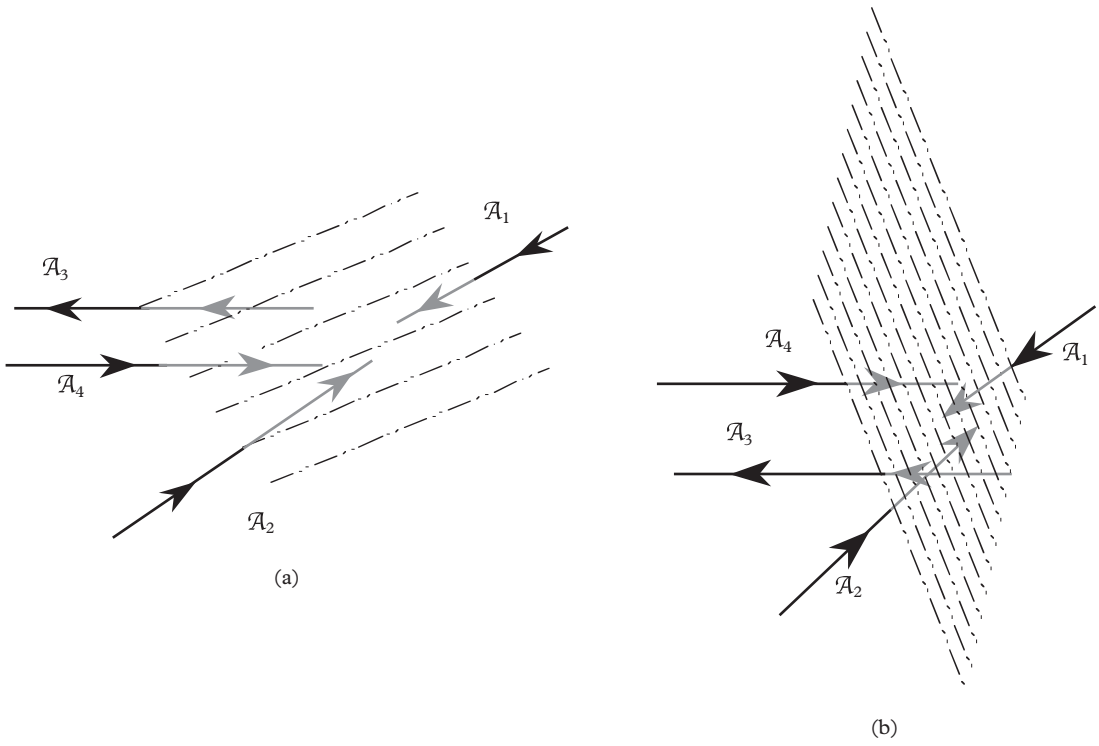

Figure 15.16 *Phase conjugation from a holographic point of view. (a) Beams 2 and 4 conjugate interfere to produce a set of fringes, and beam 1 diffracts off the fringes to produce beam 3. (b) Beams 1 and 4 conjugate interfere to produce a set of fringes, and beam 2 diffracts off the fringes to produce beam 3.*

$\mathcal{A}_1$ and $\mathcal{A}_4^*$; Figure 15.16(b). In this picture of phase conjugation, the term involving 2ω, which we ignored earlier, describes a set of moving fringes. If the nonlinear medium has a temporal response that is too slow to respond to the motion of the fringes, due to waves of frequency 2ω (a most probable condition), then it is proper to ignore the nonlinear term involving 2ω.

If the conjugate wave $\mathcal{A}_3 = \mathcal{A}_4^*$ is made to propagate back along the same path taken by $\mathcal{A}_4$ in reaching the conjugate medium, then $\mathcal{A}_3$, upon arriving at the source of $\mathcal{A}_4$, will have the same form as $\mathcal{A}_4$. This occurs no matter how much the wave is distorted by the medium along the path, as long as the distortion does not change with time. The first demonstration of distortion removal by phase conjugation was made by Herwig Kogelnik in 1965. The demonstration was made by producing the interference fringes of Figure 15.16 in a photographic plate. While this was an interesting demonstration of a novel application of holography, the fact that it did not occur in real time reduced its usefulness.

The ability to perform the same distortion removal but in real time makes the four-wave mixing we just described very appealing. Figure 15.17 is a demonstration of phase conjugation generated by Jack Feinberg of the University of Southern California. Figure 15.17(a) is the original undistorted image—a picture of a cat. The image was distorted by passing it

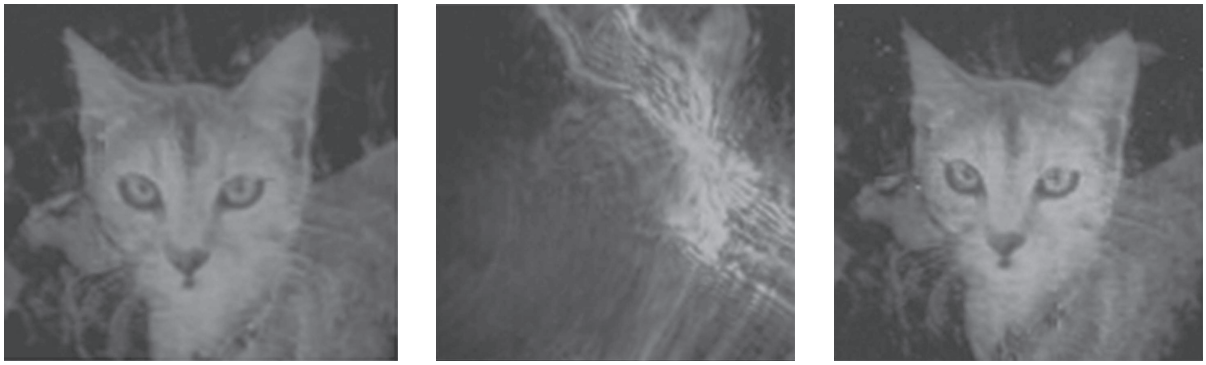

(a) (b) (c)

Figure 15.17 *Image restoration using phase conjugation. (a) Original image of a cat. (b) Distorted image of the cat. The distortion was produced by smearing glue on a microscope slide. (c) The distortion is removed and the image restored by the use of phase conjugation. Complete restoration has not been accomplished, because some of the distorted signal missed the phase conjugator. (Courtesy Jack Feinberg, University of Southern California.)*

through a microscope slide smeared with glue. The distorted image, the wave we will use as $\mathcal{A}_4$, is shown in Figure 15.17(b). Through the use of phase conjugation, the distorted image was returned to nearly its original form by generating the wave $\mathcal{A}_3$. The wave $\mathcal{A}_3$ from the phase conjugation process is shown in Figure 15.17(c).

Because the process shown in Figure 15.17 can be accomplished in real time, it appears to be quite useful, but the need for the two coherent light beams, $\mathcal{A}_1$ and $\mathcal{A}_2$, makes its implementation messy. Professor Feinberg discovered that by proper choice of materials and experimental conditions, only $\mathcal{A}_4$ is needed to perform phase conjugation. In fact, the images shown in Figure 15.17 were obtained using only $\mathcal{A}_4$. This process is called *self-pumped phase conjugation* [21].

To explain how and why self-pumped phase conjugation occurs requires the introduction of a new physical process and some modification to our theory. There is no space here to explore this subject. The reader should consult a very readable introduction by Professor Feinberg [22].

15.11 Summary

In this chapter, the effects of a large optical field were explored. The polarization induced by the optical field could no longer be treated as a linear function of the optical field, but was now described by a power series

$$P_i^{\omega} = P_i^0 + \sum_j \chi_{ij} E_j^{\omega} + \sum_{j,\ell} \chi_{ij\ell} \nabla_\ell E_j^{\omega} + \sum_{j,\ell} \chi_{ij\ell} E_j^{\omega_1} E_\ell^{\omega_2} + \sum_{j,\ell,m} \chi_{ij\ell m} E_j^{\omega_1} E_\ell^{\omega_2} E_m^{\omega_3} + \sum_{j,\ell} \chi_{ij\ell} E_j^{\omega_1} B_\ell^{\omega_2} + \dots ,$$

with the **dielectric susceptibility**

$$\chi = \frac{\varepsilon}{\varepsilon_0} - 1 = n^2 - 1$$

as the expansion parameter.

The **linear susceptibility**, defined by

$$P(\omega_i) = \chi^{(1)}(\omega_i)\varepsilon_0 E_i,$$

was obtained by neglecting nonlinear behavior:

$$\chi^{(1)}(\omega_i) = \frac{Ne^2}{\varepsilon_0 m} \frac{1}{\sqrt{(\omega_i^2 - \omega_0^2)^2 + \gamma^2\omega_i^2}}.$$

The second-order nonlinear polarization was defined as

$$P(\omega_i \pm \omega_j) = P_{\mathrm{NL}}(\omega_3) = \chi^{(2)}(\omega_i \pm \omega_j)\varepsilon_0 E_i E_j.$$

The second-order susceptibility was found by applying first-order perturbation theory. If each of the applied fields is at a different frequency, then the theory yields the **sum-** or **difference-frequency susceptibility**:

$$\chi^{(2)}(\omega_i \pm \omega_j) = \frac{Ne}{\varepsilon_0 E_i E_j} X_{i+j}$$

$$= \frac{\frac{Ne^3 a_2}{\varepsilon_0 m^2}}{\sqrt{(\omega_i^2 - \omega_0^2)^2 + \gamma^2\omega_i^2}\sqrt{(\omega_j^2 - \omega_0^2)^2 + \gamma^2\omega_j^2}\sqrt{[(\omega_i \pm \omega_j)^2 - \omega_0^2]^2 + \gamma^2(\omega_i \pm \omega_j)^2}}.$$

Experimentally, a parameter called the **nonlinear optical coefficient** is measured. It is defined by the equation

$$P(2\omega) = d(2\omega)E^2 \cos(2\omega t - 2kz).$$

For second-harmonic generation, we can write $\boldsymbol{d}$ in terms of the linear susceptibility at the fundamental and the second harmonic of the light wave:

$$d(2\omega) = \frac{a_2 m\varepsilon_0^3}{2N^2 e^3}[\chi^{(1)}(\omega)]^2 \chi^{(1)}(2\omega).$$

The wave equation for a nonlinear medium,

$$\nabla^2 \mathbf{E} = \mu\sigma \frac{\partial \mathbf{E}}{\partial t} + \mu\varepsilon \frac{\partial^2 \mathbf{E}}{\partial t^2} + \mu \frac{\partial^2 \mathbf{P}_{\mathrm{NL}}}{\partial t^2},$$

was derived in this chapter, but its general solution was not obtained. The one-dimensional form of the wave equation was examined for the case when $\Delta k = k_3 - k_2 - k_1 = 0$. The result was an energy conservation law called the **Manley–Rowe relation**:

$$\frac{1}{\omega_1}\sqrt{\frac{\varepsilon_1}{\mu}}\frac{\partial}{\partial z}(E_1 E_1^*) = \frac{1}{\omega_2}\sqrt{\frac{\varepsilon_2}{\mu}}\frac{\partial}{\partial z}(E_2 E_2^*) = -\frac{1}{\omega_3}\sqrt{\frac{\varepsilon_3}{\mu}}\frac{\partial}{\partial z}(E_3 E_3^*).$$

By assuming that the nonlinear interaction was weak, so that the two incident waves could be treated as constants, and by using the conservation of energy, the flux density of the nonlinearly generated wave was found to be

$$S_3 = \frac{\omega_3^2}{2n_1n_2n_3}\sqrt{\left(\frac{\mu}{\varepsilon_0}\right)^3}\, d^2L^2S_1S_2\left[\frac{\sin^2(\Delta kL/2)}{(\Delta kL/2)^2}\right].$$

Because the Poynting vector is proportional to d^2 and $1/n^3$, we define a **figure of merit** for nonlinear materials,

$$\mathcal{M} = \frac{d^2}{n^3}.$$

This figure of merit allows the performance of nonlinear materials to be compared.

If $\Delta k \neq 0$, then the fundamental waves at frequencies ω_1 and ω_2 travel at velocities that differ from the nonlinearly generated harmonic wave, at frequency ω_3. The waves get out of phase in a distance called the **coherence length**. For second-harmonic generation, the coherence length is equal to

$$\ell_c = \frac{\lambda_1}{4(n_3 - n_1)}.$$

Over a distance equal to the coherence length, energy is transferred from the fundamental waves to the harmonic wave. For distances between ℓ_c and $2\ell_c$, energy is transferred back from the harmonic wave to the fundamental waves. This cyclic transfer of energy continues as long as the waves remain in the nonlinear material. Whenever $\Delta k = 0$, the waves are phase-matched, and all of the energy is transferred from the fundamental waves to the harmonic wave. For example, the amplitude of the second-harmonic wave generated under phase-matched conditions at a position L into the nonlinear medium is

$$E(2\omega) = E_0(\omega)\tanh\left[E_0(\omega)Ld\,\omega\sqrt{\frac{\mu}{\varepsilon}}\right].$$

Phase matching can be produced in the following ways:

1. Periodic variation of the nonlinear coefficient.
2. Using the phase changes produced by total internal reflection.
3. Using the effective index of refraction for different modes in a dielectric waveguide.
4. Using nonparallel propagation vectors to create $\Delta\mathbf{k} = 0$.
5. Using the fact that the extraordinary index of refraction in a birefringent medium can be varied from n_e to n_o by modifying the propagation direction.

Phase matching using birefringence is produced by satisfying one of the following four equations:

	$n_e < n_o$	$n_e > n_o$
Type I	$n_e(\omega_3) = \frac{\omega_1}{\omega_3}n_o(\omega_1) + \frac{\omega_2}{\omega_3}n_o(\omega_2)$	$n_o(\omega_3) = \frac{\omega_1}{\omega_3}n_e(\omega_1) + \frac{\omega_2}{\omega_3}n_e(\omega_2)$
Type II	$n_e(\omega_3) = \frac{\omega_1}{\omega_3}n_e(\omega_1) + \frac{\omega_2}{\omega_3}n_o(\omega_2)$	$n_o(\omega_3) = \frac{\omega_1}{\omega_3}n_o(\omega_1) + \frac{\omega_2}{\omega_3}n_e(\omega_2)$

Only one third-order nonlinearity was discussed—the nonlinearity associated with phase conjugation. Third-order nonlinearities involve four waves; the complex amplitudes of waves 4 and 3 are given by the equations

$$\frac{d\mathcal{A}_4}{dz} = -i\frac{\omega\chi^{(3)}}{2}\sqrt{\frac{\mu}{\varepsilon}}\mathcal{A}_1\mathcal{A}_2\mathcal{A}_3^*,$$

$$\frac{d\mathcal{A}_3^*}{dz} = -i\frac{\omega\chi^{(3)*}}{2}\sqrt{\frac{\mu}{\varepsilon}}\mathcal{A}_1^*\mathcal{A}_2^*\mathcal{A}_4.$$

The effect of waves 1 and 2 is incorporated into the theory by the use of the coupling coefficient

$$\kappa = \frac{\omega\chi^{(3)*}}{2}\sqrt{\frac{\mu}{\varepsilon}}\mathcal{A}_1^*\mathcal{A}_2^*.$$

The complex amplitude of wave 3,

$$\mathcal{A}_3(z) = \frac{\cos|\kappa z|}{\cos(|\kappa|L)}\mathcal{A}_3(L) + i\kappa^*\frac{\sin[|\kappa|(z-L)]}{|\kappa|\cos(|\kappa|L)}\mathcal{A}_4^*(0),$$

is proportional to the conjugate of wave 4 at $z = 0$.

15.12 Problems

15.1. Show the steps leading to the more general expression for $d_{\text{eff}}(\omega_3)$ given in Chapter 15 that involves $\chi^{(1)}(\omega_1)$, $\chi^{(1)}(\omega_2)$, and $\chi^{(1)}(\omega_3)$. Equation (15.12) is a special case of this more general expression.

15.2. Find d_{eff} for the crystal class $\bar{4}3m$. Assume the medium has a negative birefringence. The result will apply to a large number of the II–IV and the III–V semiconductors such as GaAs.

15.3. Using (15.23) and (15.25) for second-harmonic generation, i.e., when $E_1 = E_2$ and $\omega_3 = 2\omega_1 = 2\omega_2$, show that the sum of the power densities of the fundamental waves and the second-harmonic wave is a constant with respect to the propagation path. Assume that the conductivities σ are zero and that we have phase matching.

15.4. Franken demonstrated second-harmonic generation by using quartz and a ruby laser operating at a wavelength of 694.3 nm. Was phase matching achieved? What is the coherence length for second-harmonic phase matching in quartz?

15.5. Find the complex amplitude $\mathcal{A}_4(z)$, using (15.53). Find the relationship between $\mathcal{A}_4(L)$ and $\mathcal{A}_4(0)$ using the boundary conditions used in Chapter 15 to find the relationship for $\mathcal{A}_3$.

15.6. Discuss the physical significance of the condition

$$|\kappa|L = \frac{\pi}{2}$$

from the theory of phase conjugation.

15.7. Examine noncollinear phase matching for second-harmonic generation. Derive expressions for the angles α and β defined in Figure 15.5.

Table 15.10 *Dispersion data for KDP*

Wavelength	n_o	n_e
200	1.6226	1.5639
300	1.5456	1.4982
400	1.5245	1.4802
500	1.5149	1.4725
600	1.5093	1.4683
700	1.5052	1.4656
800	1.5019	1.4637

15.8. In the autocorrelator shown in Figure 15.7(a), the length of one arm of the correlator must be varied to scan over a light pulse. Over what distance must the arm be varied to scan over a one-picosecond pulse? How might you create this variation?

15.9. Beta barium borate (β-BaB_2O_4) is a popular nonlinear material. It belongs to the point group 3. What does its second-order susceptibility tensor look like if Kleinman's symmetry condition holds?

15.10. Find an expression for d_{eff} for the negative uniaxial crystal β-BaB_2O_4 for both type I and type II phase matching.

15.11. If we use 10.6 μm radiation to generate, through difference-frequency mixing, 1.12 μm radiation, what is the maximum efficiency for the conversion, based upon the Manley–Rowe limit?

15.12. Calculate the phase matching angle for type I phase matching in KDP when the objective is to double 694 nm radiation. The dispersion data for KDP are given in Table 15.10.

15.13. In Problem 15.12, what is the Poynting walkoff angle?

15.14. The dispersion relationships for the ordinary and extraordinary waves in β-BaB_2O_4 are given by the Sellmeier relations

$$n_o^2 = 1.3416 + \frac{1.3812}{1 - \dfrac{0.015443}{\lambda^2}} + 0.00268\lambda^2,$$

$$n_e^2 = -0.1552 + \frac{2.5077}{1 - \dfrac{0.006745}{\lambda^2}} + 0.01438\lambda^2.$$

Calculate the phase matching angle for doubling 1 μm radiation using type I phase matching.

15.15. Using the dispersion relations in Problem 15.14, neglecting the λ^2 dependence, find the wavelength for noncritical phase matching.

15.16. We wish to frequency-double a one-picosecond pulse. If the fundamental and harmonic travel at different velocities, we have a temporal walkoff occurring as the wave propagates through the crystal. Calculate the temporal walkoff time per unit length for doubling of a 1 ps pulse at a wavelength of 1 μm in β-BaB_2O_4.

REFERENCES

1. Brewster, D., *On the effects of simple pressure in producing that species of crystallization which forms two oppositely polarised images, and exhibits the complementary colours by polarised light*. Phil. Trans. R. Soc. Lond., 1815. **105**: p. 60–64.
2. Mueller, H., *Theory of the photoelastic effect of cubic crystals*. Phys. Rev., 1935. **47**: p. 947–957.
3. Bloembergen, N., *Nonlinear Optics*. 4th ed. 1996: World Scientific.
4. Boyd, R.W., *Nonlinear Optics*. 3rd ed. 2008: Academic Press.
5. Zernike, F. and K.E. Midwinter, *Applied Nonlinear Optics*. 2006: Dover.
6. Shen, Y.R., *The Principles of Nonlinear Optics*. 1984: Wiley-Interscience.
7. Armstrong, J.A., et al., *Interactions between light waves in a nonlinear dielectric*. Phys. Rev., 1962. **127**: p. 1918–1939.

8. Bloembergen, N., *Conservation laws in nonlinear optics*. J. Opt. Soc. Am., 1980. **70**: p. 1492–1436.
9. Boyd, G.D. and D.A. Kleinman, *Parametric interaction of focused Gaussian light beams*. J. Appl. Phys, 1968. **39**: p. 3597–3639.
10. Giordmaine, J.A., *The interaction of light with light*. Scientific American, 1964. **210**(4): p. 38–49.
11. Yacoby, Y., R.L. Aggarwal, and B. Lax, *Phase matching by periodic variation of nonlinear coefficients*. J. Appl. Phys, 1973. **44**: p. 3180–3181.
12. van der Ziel, J.P. and M. Ilegems, *Optical second harmonic generation in periodic multilayer GaAs–$Al_{0.3}Ga_{0.7}As$ structures*. Appl. Phys. Lett., 1976. **28**: p. 437–439.
13. Pasiskevicius, V., et al., *Quasi-phase matched nonlinear media: progress towards nonlinear optical engineering*. Opt. Mater., 2012. **34**: p. 513–523.
14. Miller, R.C., *Optical harmonic generation in single crystal $BaTiO_3$*. Phys. Rev. Lett., 1964. **134**: p. 1313.
15. Feng, D., et al., *Enhancement of second-harmonic generation in $LiNbO_3$*. Appl. Phys. Lett., 1980. **37**: p. 607.
16. Boyd, G.D. and C.K.N. Patel, *Enhancement of optical second harmonic generation by reflection phase matching in ZnS and GaAs*. Appl. Phys. Lett., 1966. **8**: p. 313–315.
17. Thompson, D.E. and P.D. Coleman, *Step-tunable far infrared radiation by phase matched mixing in planar-dielectric waveguides*. IEEE Trans. Microwave Theory Tech., 1974. **MTT-22**: p. 955–1000.
18. Trebino, R., *Second harmonic generation rings and refractive index measurement in uniaxial crystals*. Appl. Opt., 1981. **20**: p. 2090–2096.
19. Birss, R.R., *Property tensors in magnetic crystal classes*. Proc. Phys. Soc. (Lond.), 1962. **79**: p. 946–953.
20. Yariv, A., *Optical Electronics in Modern Communications*. 5th ed. 1997: Oxford University Press.
21. Feinberg, J., *Self-pumped continuous-wave phase conjugator using internal reflection*. Opt. Lett., 1982. **7**: p. 486–487.
22. Feinberg, J., *Photorefractive nonlinear optics*. Phys.Today, 1988(October): p. 6–12.

Appendix 15A Nonlinear Optical Medium

15A.1 Introduction

To describe dispersion, in Chapter 7, the optical medium was modeled by a classical linear oscillator with a dissipative term, (7.26). The solution of the model's equation of motion was a damped sinusoidal wave (7.27). The behavior of the oscillator when it was driven by a simple periodic force was determined by assuming a linear response to the driving force, (7.28). In this appendix, we will develop a model of a nonlinear optical medium by modifying the linear model used in Chapter 7. The linear model is first generalized to describe the effects of an arbitrary light wave as the driving force. The linear theory is then expanded to include nonlinear response to the driving force, by the use of a generalized potential energy function.

The solution of the nonlinear equation will be obtained by the use of perturbation theory. A brief description of the steps used in the solution will demonstrate that the second- and third-order nonlinearities can be treated independently. This result will be used to obtain the equation for the displacement of a nonlinear harmonic oscillator driven by a force containing two frequencies.

15A.2 Generalized Linear Theory

To describe the behavior of materials in response to an arbitrary driving force, the simple harmonic function used in (7.28) is replaced by a generalized periodic function written as a Fourier series. This force is due to an applied electric field. The real electric field is written, using complex functions according to the notation

$$\mathcal{R}e\{\tilde{z}\} = \frac{\tilde{z} + \tilde{z}^*}{2},$$

as

$$\mathbf{E} = \frac{1}{2}\left(\tilde{\mathbf{E}}_1 e^{i(\omega_1 t - k_1 x)} + \tilde{\mathbf{E}}_1^* e^{-i(\omega_1 t - k_1 x)} + \ldots + \tilde{\mathbf{E}}_n e^{i(\omega_n t - k_n x)} + \tilde{\mathbf{E}}_n^* e^{-i(\omega_n t - k_n x)}\right). \tag{15A.1}$$

We will assume a one-dimensional problem to reduce the complexity of the derivation. The notation may be simplified by using the identity

$$E(\omega_{-n}) \equiv E(-\omega_n) = E^*(\omega_n) = \frac{1}{2}\tilde{E}_n^* e^{ik_n x}.$$

The generalized harmonic driving force of (15A.1) can now be written in the very compact form

$$F(t) = \frac{e}{m}\sum_{n=-\infty}^{\infty} E(\omega_n) e^{i\omega_n t}.$$

With the generalized driving force, the steady-state solution of the equation of motion, describing the oscillator's displacement, is a Fourier series, each term of which is identical to the solution obtained for a simple periodic driving force:

$$\begin{aligned} x &= \sum_{n=-\infty}^{\infty} X_n e^{i\omega_n t} \\ &= \sum_{n=-\infty}^{\infty} \frac{\frac{e}{m}E(\omega_n)}{\sqrt{(\omega_n^2 - \omega_0^2)^2 + \gamma^2\omega_n^2}} e^{i\omega_n t}. \end{aligned} \tag{15A.2}$$

There is a phase lag between the driving force and the nth ncomponent of the Fourier series describing the displacement, given by

$$\phi_n = \tan^{-1}\frac{\gamma\omega_n}{\omega_n^2 - \omega_0^2}. \tag{15A.3}$$

15A.3 Nonlinear Equation of Motion

The model for a linear system can easily be modified to explain nonlinear behavior by replacing the harmonic oscillator potential used in the linear theory with a power series

$$V(x) = V_0 + \frac{1}{2}\left(\frac{d^2V}{dx^2}\right)x^2 + \frac{1}{6}\left(\frac{d^3V}{dx^3}\right)x^3 + \frac{1}{24}\left(\frac{d^4V}{dx^4}\right)x^4 + \ldots. \tag{15A.4}$$

Figure 15A.1 shows a nonlinear potential constructed using an equation of the form

$$V(x) = \frac{1}{2}m\omega_0^2 x^2 + \frac{1}{3}ma_2 x^3 + \frac{1}{4}ma_3 x^4.$$

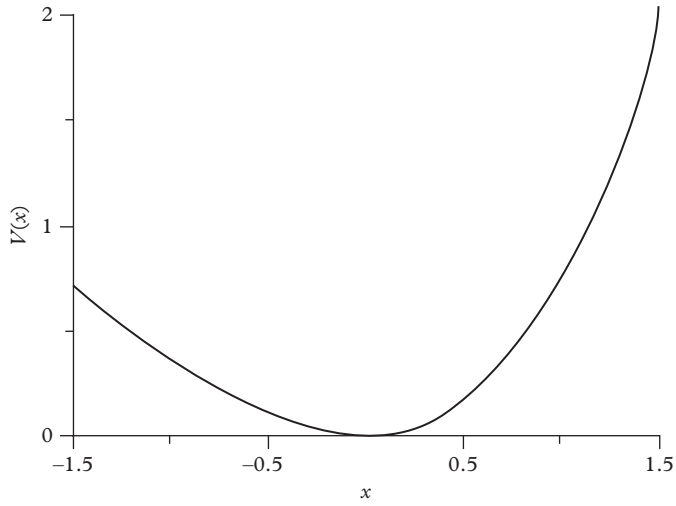

Figure 15A.1 *A possible nonlinear potential based upon (15A.4).*

In Figure 15A.1, the terms of this approximate potential were chosen to be

$$m\omega_0^2 = 1, \quad ma_2 = \frac{1}{2}, \quad ma_3 = \frac{1}{6}.$$

The powers of x in the expansion that are needed to describe the potential are determined by the symmetry in the material. For example, if the material has inversion symmetry, then $V(x)$ is an even function, and only even powers of x are found in the power series.

The nonlinear processes involved in a solid do not all have the same response speed. Electrons have the fastest response, while molecular motion is much slower. To handle both types of oscillators, we must replace the single coordinate x by coordinates for the electronic motion, q_e, and the ion motion, q_i. For example, the nonlinear term $ma_2\mathrm{x}^3$ would be replaced by four terms

$$Aq_i^3 + Bq_i^2 q_e + Cq_i q_e^2 + Dq_e^3.$$

In the simplified discussion presented here, we will ignore these complications. The nonlinear equation of motion that must be solved is therefore of the form

$$\frac{d^2x}{dt^2} + \gamma\frac{dx}{dt} + \omega_0^2 x + a_2x^2 + a_3x^3 = 0.$$

15A.4 Perturbation Technique

The application of the perturbation technique to the solution of the equation of motion for a nonlinear oscillator is based upon the assumption that each of the additional terms in (15A.4) is much smaller than those preceding it. The solution obtained by neglecting the additional term will therefore only need a small correction to satisfy the more complex potential.

In the description of the perturbation technique, a solution of the equation of motion of a nonlinear oscillator with no dissipation, $\gamma = 0$, will be obtained:

$$\frac{d^2x}{dt^2} + \omega_0^2 x + a_2 x^2 + a_3 x^3 = 0. \tag{15A.5}$$

The first step in the application of the perturbation technique involves neglecting the nonlinear terms in the potential energy function, by setting their coefficients equal to zero: $a_2 = a_3 = 0$. The resulting equation of motion describes a simple harmonic oscillator with a solution given by

$$x^{(0)} = X_1 \cos \omega_0 t. \tag{15A.6}$$

This solution is called the *zeroth-order approximate solution*.

The next step requires the substitution of the zeroth-order solution (15A.6) into (15A.5), to produce a first-order approximation to the nonlinear equation. It is necessary to replace ω_0 by ω_1 in (15A.6), because the nonlinear oscillator will have a resonant frequency that differs from the linear oscillator's frequency:

$$\frac{d^2x}{dt^2} + \omega_0^2 x = -a_2 X_1^2 \cos^2 \omega_1 t - a_3 X_1^3 \cos^3 \omega_1 t.$$

Use of the trigonometric identities

$$\cos^2 \theta = \frac{1}{2}(1 + \cos 2\theta),$$

$$\cos^3 \theta = \frac{1}{4}(\cos 3\theta + 3 \cos \theta)$$

will make the results easier to interpret. Substituting these identities into the equation of motion produces an equation involving harmonics of ω_1:

$$\frac{d^2x}{dt^2} + \omega_0^2 x = -\frac{1}{2} a_2 X_1^2 - \frac{3}{4} a_3 X_1^3 \cos \omega_1 t - \frac{1}{2} a_2 X_1^2 \cos 2\omega_1 t - \frac{1}{4} a_3 X_1^3 \cos 3\omega_1 t. \tag{15A.7}$$

The solution of this equation, called the *first-order approximate solution*, is assumed to be a finite harmonic series, containing the same frequencies as found in the driving force on the right-hand side of (15A.7):

$$x^{(1)} = X_0 + X_1 \cos \omega_1 t + X_2 \cos 2\omega_1 t + X_3 \cos 3\omega_1 t. \tag{15A.8}$$

To determine the values of the coefficients of the series when (15A.8) is as solution of (15A.7), we substitute (15A.8) and its derivatives into (15A.7):

$$(\omega_0^2 - \omega_1^2) X_1 \cos \omega_1 t - (\omega_0^2 - 4\omega_1^2) X_2 \cos 2\omega_1 t - (\omega_0^2 - 9\omega_1^2) X_3 \cos 3\omega_1 t + \omega_0^2 X_0$$

$$= -\frac{1}{2} a_2 X_1^2 - \frac{3}{4} a_3 X_1^3 \cos \omega_1 t - \frac{1}{2} a_2 X_1^2 \cos 2\omega_1 t - \frac{1}{4} a_3 X_1^3 \cos 3\omega_1 t.$$

Equating the coefficients of the cosine functions produces a set of equations specifying the form of the coefficients X_0, X_2, and X_3 in terms of X_1 when (15A.8) is a solution.

The coefficient X_0 is found by equating the terms without time dependence in the above equation. The time-independent (or DC) term in the first-order approximate solution must obey the equation

$$X_0 = -\frac{a_2 X_1^2}{2\omega_0^2}. \tag{15A.9}$$

The physical interpretation given to this result is that the second-order nonlinear coefficient a_2 of the potential function causes a shift of the equilibrium position of the oscillator. The shift is a function of the amplitude of the fundamental frequency of the oscillator, X_1.

The shift of the equilibrium position can be verified by constructing line segments parallel to the x-axis in Figure 15A.1, connecting points on the potential curve on either side of $x = 0$ at equal values of $V(x)$. The centers of the line segments move to the left as V(x) increases. This is the behavior predicted by (15A.9).

By equating terms involving cos ω_1t, we discover that the frequency of the nonlinear oscillator is not equal to the frequency of the linear oscillator. The change in the oscillator frequency is proportional to the third-order nonlinear coefficient:

$$\omega_1^2 = \omega_0^2 + \frac{3}{4} a_3 X_1^2. \tag{15A.10a}$$

The oscillator frequency is also modified by the second-order nonlinearity. By equating terms involving cos $2\omega_1 t$, we discover that a second change in oscillator frequency occurs, proportional to the second-order nonlinear coefficient of the potential:

$$\omega_1^2 = \frac{\omega_0^2}{4} - \frac{a_2 X_1^2}{8X_2}. \tag{15A.10b}$$

Both frequency changes are proportional to the square of the amplitude of the fundamental frequency of the oscillator. We would expect the frequency change associated with the second-order nonlinearity to dominate, because the second-order nonlinearity should be larger than the third-order nonlinearity.

Equation (15A.10b) can be solved for the functional form of the second-harmonic coefficient X_2:

$$X_2 = \frac{a_2 X_1^2}{2(\omega_0^2 - 4\omega_1^2)}.$$

Finally, equating terms involving cos $3\omega_1 t$ yields the functional form of the coefficient of the third harmonic, X_3:

$$X_3 = \frac{a_3 X_1^3}{4(\omega_0^2 - 9\omega_1^2)}.$$

We can now write the first-order solution of the nonlinear oscillator:

$$x^{(1)} = -\left(\frac{a_2}{2\omega_0^2}\right) X_1^2 + X_1 \cos\omega_1 t + \left(\frac{a_2}{6\omega_0^2}\right) X_1^2 \cos 2\omega_1 t$$

$$+ \left(\frac{a_3}{32\omega_0^2}\right) X_1^3 \cos 3\omega_1 t. \tag{15A.11}$$

The displacement predicted by (15A.11) is a function not only of the fundamental frequency of the oscillator, but also of the second and third harmonics. In examining $x^{(1)}$, we see that the DC and second-harmonic components are functions of the second-order nonlinear coefficient a_2 but not of the third-order coefficient a_3. The third harmonic of the oscillator frequency is only a function of the third-order nonlinear coefficient of the potential, a_3. This means that, to the accuracy of this first-order theory, we can treat each nonlinear term separately.

A second-order perturbation calculation can be obtained by substituting the first-order solution (15A.11) into (15A.5) to give a second-order approximation to the differential equation. We will not carry out the second-order calculation.

It is difficult to keep all of the approximations separated. Hopefully, the discussion has made clear the difference between the order of the solution of (15A.5) and the order of the approximate representation of the nonlinear potential (15A.4). Equation (15A.11) is the first-order perturbation solution of an equation involving a third-order expression of a nonlinear potential.

15A.5 Second-Order Nonlinearity

We have demonstrated that the second- and third-order nonlinear contributions to the potential can be treated separately. We will examine the second-order nonlinearity using first-order perturbation theory. The driving field **E** to be used in the calculation is given by the Fourier series (15A.1).

The zeroth-order solution of the differential equation

$$\frac{d^2x}{dt^2} + \gamma\frac{dx}{dt} + \omega_0^2 x + a_2x^2 = -\frac{e}{m}E$$

is $x^{(0)}$ given by (15A.2). The zeroth-order solution $x^{(0)}$ is used to rewrite the differential equation. The result will be the first-order approximation of the equation of motion of the nonlinear system:

$$\frac{d^2x}{dt^2} + \gamma\frac{dx}{dt} + \omega_0^2 x = -\frac{e}{m}\sum_n E(\omega_n)e^{i\omega_n t} - \frac{a_2e^2}{m^2}\sum_n\sum_m \frac{E(\omega_n)E(\omega_m)e^{i(\omega_n+\omega_m)t}}{(\omega_n^2-\omega_0^2+i\gamma\omega_n)(\omega_m^2-\omega_0^2+i\gamma\omega_m)}. \tag{15A.12}$$

To solve this equation, the solution is assumed to have the same form as (15A.8):

$$x^{(1)} = \sum_k X_k e^{i\omega_k t}. \tag{15A.13}$$

Substituting (15A.13) and its derivatives into (15A.12) generates the values of the coefficients X_n when (15A.13) is a solution. Whenever $\omega_k = \omega_n$, the coefficient of the nth harmonic must be

$$X_n = \frac{\frac{e}{m}E(\omega_n)}{\omega_n^2-\omega_0^2+i\gamma\omega_n}. \tag{15A.14}$$

When $\omega_k = \omega_n + \omega_m$, the coefficient of the $(n+m)$th harmonic must be

$$X_{n+m} = \frac{\frac{e^2 a_2}{m^2} E(\omega_n) E(\omega_m)}{(\omega_n^2 - \omega_0^2 + i\gamma\omega_n)(\omega_m^2 - \omega_0^2 + i\gamma\omega_m)[(\omega_n + \omega_m)^2 - \omega_0^2 + i\gamma(\omega_n + \omega_m)]}. \quad (15A.15)$$

The solution involves three frequencies (ω_n, ω_m, and $\omega_n + \omega_m$,) and the coefficients given above. It describes the behavior of the nonlinear oscillator for any pair of Fourier components of an arbitrary waveform. This result is too general to understand, so we will make some simplifications.

To make it easier to obtain a physically interpretation of (15A.15), we will limit the discussion to a nonlinear oscillator driven by two harmonic waves, with frequencies ω_1 and ω_2. Making use of $\mathcal{R}e\{\tilde{z}\} = \frac{1}{2}(\tilde{z} + \tilde{z}^*)$ and the relationship between various coefficients,

$$(X_{-n})^* = X_n, \quad (X_{-n-m})^* = X_{nm},$$

we can write the solution of the nonlinear oscillator equation when driven by two frequencies as

$$\begin{aligned} x^{(1)} = 2\{&|X_1|\cos\omega_1 t + |X_2|\cos\omega_2 t + 2|X_{1+2}|\cos(\omega_1+\omega_2)t \\ &+ 2|X_{1-2}|\cos[(\omega_1-\omega_2)t] + |X_{1+1}|\cos 2\omega_1 t + |X_{2+2}|\cos 2\omega_2 t \\ &+ |X_{1-1}| + |X_{2-2}|\}, \end{aligned} \quad (15A.16)$$

where we have assumed that ϕ_n, defined by (15A.3), may be neglected.

Each term of (15A.16) is associated with a different frequency. The coefficients associated with each frequency are written explicitly below:

1. The fundamental driving frequencies:

$$\frac{\frac{e}{m}E_1\cos(\omega_1 t - k_1 x)}{\sqrt{(\omega_1^2-\omega_0^2)^2 + \gamma^2\omega_1^2}} + \frac{\frac{e}{m}E_2\cos(\omega_2 t - k_2 x)}{\sqrt{(\omega_2^2-\omega_0^2)^2 + \gamma^2\omega_2^2}}. \quad (15A.17)$$

2. The sum frequency:

$$\frac{\frac{e^2 a_2}{m^2}E_1E_2\cos[(\omega_1+\omega_2)t - (k_1+k_2)x]}{\sqrt{(\omega_1^2-\omega_0^2)^2 + \gamma^2\omega_1^2}\sqrt{(\omega_2^2-\omega_0^2)^2 + \gamma^2\omega_2^2}\sqrt{[(\omega_1+\omega_2)^2-\omega_0^2]^2 + \gamma^2(\omega_1+\omega_2)^2}}. \quad (15A.18)$$

3. The difference frequency:

$$\frac{\frac{e^2 a_2}{m^2}E_1E_2\cos[(\omega_1-\omega_2)t - (k_1-k_2)x]}{\sqrt{(\omega_1^2-\omega_0^2)^2 + \gamma^2\omega_1^2}\sqrt{(\omega_2^2-\omega_0^2)^2 + \gamma^2\omega_2^2}\sqrt{[(\omega_1-\omega_2)^2-\omega_0^2]^2 + \gamma^2(\omega_1-\omega_2)^2}}. \quad (15A.19)$$

4. The second harmonics of the driving frequencies:

$$\begin{aligned} &\frac{\frac{e^2 a_2}{2m^2}E_1^2\cos(2\omega_1 t - 2k_1 x)}{[(\omega_1^2-\omega_0^2)^2 + \gamma^2\omega_1^2]\sqrt{(4\omega_1^2-\omega_0^2)^2 + \gamma^2 4\omega_1^2}} \\ &\qquad + \frac{\frac{e^2 a_2}{2m^2}E_2^2\cos(2\omega_2 t - 2k_2 x)}{[(\omega_2^2-\omega_0^2)^2 + \gamma^2\omega_2^2]\sqrt{(4\omega_2^2-\omega_0^2)^2 + \gamma^2 4\omega_2^2}}. \end{aligned} \quad (15A.20)$$

5. The DC terms:

$$\frac{\frac{e^2 a_2}{m^2} E_1^2}{\omega_0^2 \sqrt{(\omega_1^2 - \omega_0^2)^2 + \gamma^2 \omega_1^2}} + \frac{\frac{e^2 a_2}{m^2} E_2^2}{\omega_0^2 \sqrt{(\omega_2^2 - \omega_0^2)^2 + \gamma^2 \omega_2^2}}. \tag{15A.21}$$

Each of the terms discussed here can be treated separately, because of the need to require conservation of momentum and conservation of energy. The conservation laws restrict solutions through the equations

$$\omega_3 = \omega_1 \pm \omega_2, \quad \mathbf{k}_3 = \mathbf{k}_1 + \mathbf{k}_2.$$

The results of the perturbation solution are applied to the physical problem of calculating the macroscopic polarization of a nonlinear material in Chapter 15.

Appendix 15B Miller's Rule

R.C. Miller [1] observed that for second-harmonic generation, the ratio

$$\Delta = \frac{d(2\omega)}{[\chi^{(1)}(\omega)]^2 \chi^{(1)}(2\omega)\varepsilon_0^2} \tag{15B.1}$$

was a constant from material to material. Table 15B.1 displays some materials and their values of *Miller's coefficient* Δ. Examining the table, we see that for a large number of materials, Δ varies by a factor of five while the nonlinear coefficient varies by a factor of 10^3.

The classical theory derived in Chapter 15 yields an equation for Δ in terms of the nonlinear coefficient:

$$\Delta = \frac{m a_2}{2N^2 e^3}. \tag{15B.2}$$

Treating Δ as a constant implies that a_2/N^2 is also a constant. To obtain an estimate of the second-order nonlinear coefficient a_2, we assume that the second-order nonlinear term and harmonic term in the potential energy function are equal:

$$\omega_0^2 x = a_2 x^2.$$

Table 15B.1 *Miller's coefficient*

Material	d_{ij}(MKS) ($\times 10^{-22}$)	λ(μm)	Δ_{ij}(MKS) ($\times 10^9$)	Class
KDP	0.1	1.06	9.7	$\bar{4}2m$
ZnS	5.66	1.06	9.5	$\bar{4}3m$
Te	940	5.0	11.6	32
CdTe	29.6	10.6	18.9	$\bar{4}3m$
GaAs	65	10.6	10	$\bar{4}3m$
CdSe	9.6	10.6	13	$6mm$
$LiNbO_3$	9.25	1.06	24.3	$3m$

If we assume that x is of the order of the lattice spacing,

$$\mathcal{O}(x) = \frac{1}{N^{1/3}},$$

then we can write a_2 as

$$a_2 = \frac{\omega_0^2}{x} \approx \omega_0^2 N^{1/3}.$$

This rather crude estimate of a_2 can be used to calculate an order-of-magnitude value for Δ. A more exact estimate of a_2 can be obtained by introducing an analytic potential for the an harmonic oscillator [2], but the more complicated potential provides the same order-of-magnitude estimate for Δ:

$$\Delta \approx \frac{m\omega_0^2 N^{1/3}}{2N^2 e^3} = \frac{m\omega_0^2}{2e^3 N^{5/3}}. \tag{15B.3}$$

If $m = 10^{-30}$ kg, $\omega_0 = 2\pi \times 10^{15}$, and $N = 10^{29}$ m^{-3}, then

$$\Delta = 2.3 \times 10^9 \text{ m / V},$$

or

$$\Delta \approx 10^{-6} \text{ c.g.s. units.}$$

A quantum mechanical model of the nonlinear oscillator, assuming a two-level system, leads to similar results.

REFERENCES

1. Miller, R.C., *Optical harmonic generation in single crystal $BaTiO_3$*. Phys. Rev. Lett., 1964. **134**: p. 1313.
2. Garret, C.G.B. and F.N.H. Robinson, *Miller's phenomenological rule for computing nonlinear susceptibilities*. IEEE J. Quantum Electron., 1966. **QE-2**: p. 328.

Appendix 15C Nonlinear Polarization in the 32 Point Group

To demonstrate the procedure used to calculate the effective nonlinear coefficient d_{eff}, we will examine a crystal belonging to the crystal class 32. Examples of crystals in this class are tellurium and quartz.

We will assume that two linearly polarized plane waves, of the same frequency ω and with amplitudes E_o and E_e, are copropagating in a crystal belonging to the point group 32. The propagation vectors of the waves make an angle θ with respect to the optical axis, which is parallel to the z-axis (in crystallography, this is the c-axis). We will assume further that the plane containing the propagation vectors and the optical axis makes an angle ϕ with respect

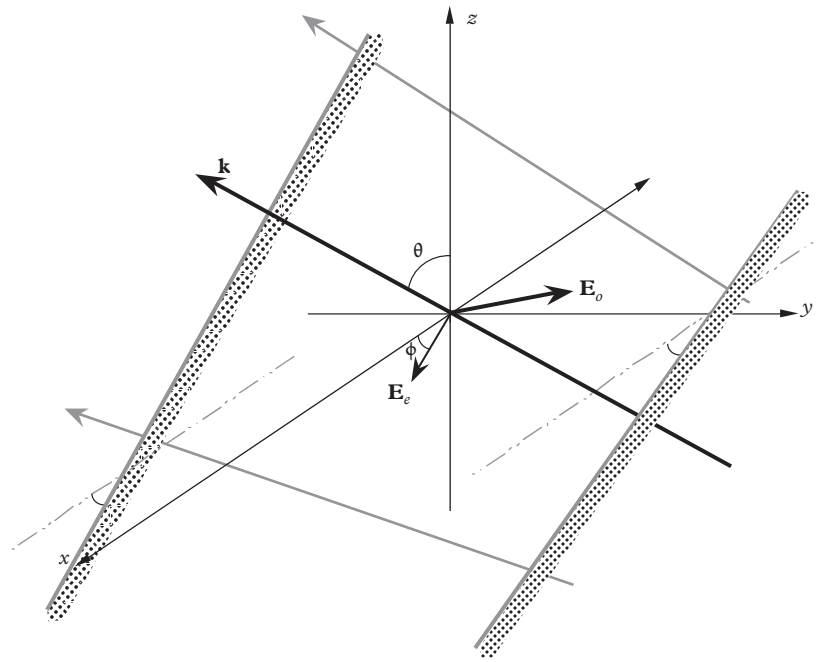

Figure 15C.1 *Geometry for calculation of effective nonlinear coefficient.*

to the x-axis (see Figure 15C.1). The polarization of E_e (the extraordinary wave) lies in this plane at an angle θ to the (x, y) plane, and the polarization of E_o (the ordinary wave) is perpendicular to this plane, lying in the (x, y) plane (see Figure 15C.2).

The nonlinear susceptibility matrix for a crystal, in the 32 symmetry group, can be found in Appendix 14A. The three components of the nonlinear polarization associated with the second harmonic are

$$\begin{aligned} P_x(2\omega) &= d_{11}E_{ex}E_{ox} - d_{11}E_{ey}E_{oy} + d_{14}E_{ey}E_{oz} + d_{14}E_{ez}E_{oy}, \\ P_x(2\omega) &= -d_{14}E_{ex}E_{oz} - d_{14}E_{ez}E_{ox} - d_{11}E_{ex}E_{oy} - d_{11}E_{ey}E_{ox}, \\ P_z(2\omega) &= 0. \end{aligned} \tag{15C.1}$$

The geometrical construction in Figure 15C.2 is used to obtain the field components:

$$\begin{aligned} E_{ex} &= E_e \cos\theta \cos\phi, & E_{ox} &= -E_o \sin\phi, \\ E_{ey} &= E_e \cos\theta \sin\phi, & E_{oy} &= E_o \cos\phi, \\ E_{ez} &= -E_e \sin\theta, & E_{oz} &= 0, \end{aligned} \tag{15C.2}$$

By substituting (15C.2) into (15C.1), we obtain the two components of P. These components are then used to calculate the polarization, normal to the plane and parallel to E_o:

$$\begin{aligned} P_\perp(2\omega) &= P_x \sin\phi - P_y \cos\phi, \\ P_\perp(2\omega) &= E_e E_o (d_{11} \cos\theta \cos 3\phi). \end{aligned}$$

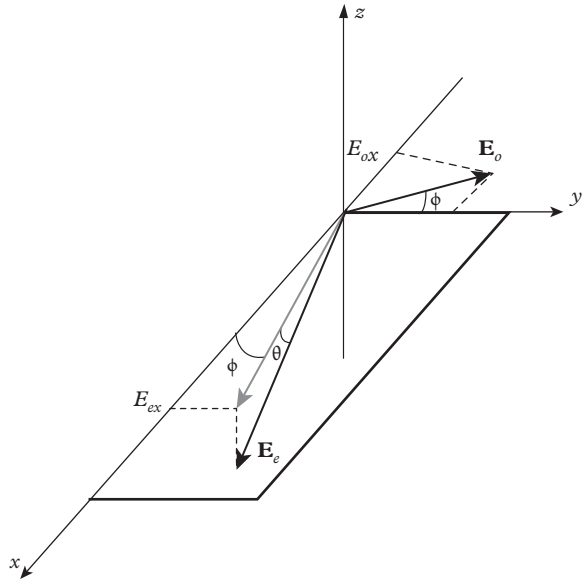

Figure 15C.2 *An enlarged view of Figure 15C.1, showing the projection of the electric fields for two orthogonally polarized waves onto the coordinate axis.*

The effective d for this polarization is

$$d_{\text{eff}} = d_{11} \cos\theta \cos 3\phi. \tag{15C.3}$$

The component of the polarization in the plane, and parallel to E_e, is

$$\begin{aligned} P_{\parallel}(2\omega) &= (P_x \cos\phi + P_y \sin\phi)\cos\theta + P_z \sin\theta \\ &= -E_e E_o (d_{11} \cos^2\theta \sin 3\phi + d_{14} \sin\theta \cos\theta). \end{aligned}$$

The effectived d for this polarization is

$$d_{\text{eff}} = d_{11} \cos^2\theta \sin 3\phi + d_{14} \sin\theta \cos\theta. \tag{15C.4}$$

The 3ϕ has its physical basis in the fact that members of this group have a z-axis with threefold symmetry.

Index

A

Abbe number (*see* V-number)
  Abbe value 255, 261, 264, 283, 300, 606
Abbe theory 417, 453
  image resolution 384, 520, 644
Abbe, Ernst 1840–1905 193
aberration 127, 137, 210
  astigmatism 206
    sagittal image plane 207
    tangential image plane 206
  chromatic aberration 298, 304
    longitudinal chromatic aberration 299
    secondary spectrum 304
  coma 202–203
  distortion 209, 210
    barrel distortion 209
    pincushion distortion 209–210
  field curvature 207
  off-axis aberrations 198, 205
  offense against sine 204
  ray-intercept 193, 304, 305
  spherical aberration 198, 203
    longitudinal spherical aberration 200–201, 212
  third-order aberration 193, 197, 211
absorption coefficient 42
acceptance angle (*see* numerical aperture)
achiral (*see* chiral: chirality)
achromat 301, 303
acoustic modulation (*see* modulator)
  acousto-optic tunable filter 643
    beam deflector 603, 644
    mode lock 646
acoustic wave 603
  phonon 635, 636
acousto-optic scattering 635–636, 656
  Bragg scattering 635, 637, 656
    Bragg angle 638, 659
  Brillouin's theory 634
afocal 188
Airy pattern 196, 397
  Airy disk 397, 398
  Airy formula 397
  circular aperture 394, 396, 469–477, 480
Airy, George Biddell 1801–1892 397
amplitude impulse response (*see* function: delta function)
Ampère's law 17
anisotropy 567
  optical indicatrix 199, 550, 564, 566–567, 590
    index ellipsoid 605
    Poinsot ellipsoid 567
  pleochroism 551
apodization 415, 432, 434
arrays 401, 442
atomic refractivity 288
  Gladstone and Dale 288

B

Babinet, Jacques 1794–1872 490
bandwidth 26, 47, 110, 265, 308–309, 338–340, 425, 429, 518–519, 531, 535, 548, 640–642, 645, 646, 648
  spatial bandwidth 425
bending (*see* Coddington shape)
Biot and Savart (*see* Ampère's law)
Biot, Jean Baptiste 1774–1862 551
birefringence 550, 559, 585, 603, 632, 688, 700
  biaxial 559, 595
  biradials 594
  extraordinary wave 549, 561
  fast axis 561
  ordinary wave 549, 585
  slow axis 561
Bloch, Felix 1905–1983 496
Bloch's theorem 524, 525
bokeh 434
boundary conditions
  Kirchhoff boundary conditions 379
  Maxwell equations 60
  reflection and refraction 53, 56, 58
    Fresnel's formula 58
  Sommerfeld 343
  Sommerfeld radiation condition 379
Bragg's law 512, 637
  diffraction grating 401
    grating equation 413, 511
    gratings, holographic 500
Brewster, Sir David 1781–1868 68
  kaleidoscope 68
cardinal points 186–187
  focal plane 140, 180, 186, 192–193, 196, 201–202, 207, 351, 369, 385, 388–391, 394, 398, 412, 414, 416–419, 422, 431, 434, 438, 469, 505–508, 521, 544–548, 643
    focal point 185–186, 211
  nodal 189
  principal plane 187
    principal point 187

C

Cauchy, Augustin Louis 1789–1857 255
Cauchy's equation 255
chief ray (*see* stop: aperture stop: principal ray)
chiral 578, 603
  chirality 578, 603
    Louis Pasteur 1822–1895 578
    optical activity 578, 580, 585
circular polarized 581
  dextrorotatory 578, 583
  levorotatory 578, 583
Clausius–Mossotti equation 288–289, 301
Coddington factors (*see* shape factor)
Coddington position 211
Coddington shape 210–211
coherence 307, 310, 331, 401
  coherence function 312, 315, 318
  coherence length 319, 329
    longitudinal coherence length 329
  coherence time 306, 318–319, 337, 338
  degree of coherence 311, 313, 316–318, 323, 327
    reduction property 333
  fringe visibility 316, 329, 336
  intensity interferometry 306–307, 332–334

coherence (*continued*)
interference spectroscopy (*see* interferometer)
retardation time 99, 323–324
spatial coherence 323, 329
Van Cittert–Zernike theorem 327
temporal coherence 318, 323
coherency matrix (*see* polarization)
coherent imaging (*see* Abbe theory)
coherent noise (*see* speckle noise)
conservation law
conservation of energy 84, 603, 666, 710
conservation of momentum 636, 640, 666–677, 710
constitutive relations 18, 24, 580, 673
constringence (*see* V-number: V-number, the constringence)
Cornu spiral 459, 466–468, 486, 488
Cotton, Amié Auguste 1869–1951 (*see* Mouton, Henri 1869–1935)
Cotton–Mouton effect 629
Cotton–Mouton coefficient 630

D

density 17, 24–25
current density 17, 286
energy density 24, 662
flux density 25
irradiance 25
number density 268, 272, 288, 653
density matrix 35, 39, 577
dichroic (*see* polarization)
dichroic materials 551, 568
dichroism 551, 580
difference-frequency (*see* nonlinear)
diffraction 132, 196, 342, 347, 365, 460
Babinet's principle 490
diffraction circular aperture 460
Fraunhofer diffraction 342, 356, 412
far-field pattern 365, 387–388
Fraunhofer diffraction pattern 384, 385, 391, 394, 414, 433, 643
Huygens–Fresnel integral 342
Fresnel diffraction 342, 343, 352, 473
Fresnel approximation 460
Young's two-slit experiment 79, 323, 325, 402, 505
dispersion (*see* Abbe number: Abbe value)
dispersion equation 11, 158, 161, 177–178, 256–257, 261
dispersion relationship (*see* Cauchy's equation)
mode dispersion 264, 265
Dollond, John 1706–1761 (*see* aberration)
Drude's theory 580, 583

E

elasto-optic effect 635
polarizability 631
electro-optic coefficient 605
polarization-optic coefficients 606

F

Fabry–Perot interferometer 106–107, 109, 112, 439
chromatic resolving power 107, 109
finesse 110, 111–112
Fabry–Perot resonator 141, 145, 178, 369
Fabry–Perot cavity (*see* photonic crystal)
stability condition 141, 369
Fermat's principle (*see* optical path length)
Hamilton's principle (*see* geometrical optics)
fibers 72, 127, 162
cladding 146, 149–151, 171, 173, 181–182, 264
core 146, 150, 173, 264
hollow core photonic 530, 531
V-number for fibers 155
filter
bandpass 160, 643
coatings 94
antireflection coating 94, 118, 120
dielectric coating 79, 116, 555
dielectric film 89
dielectric layer 90, 101, 437
high-pass filter 429
interference filters 116
low-pass filter 428
matched filter 547
spatial filter 428, 432, 437
Foucault knife-edge 434–435
wavelength-selective filter 114
Floquet theorem (*see* Bloch's theorem)
Foucault polarizer (*see* polarizer: Glan–Foucault)
Fourier theory 214
Fourier integral 222
Fourier transform properties 214
Fourier transform operator 412
Fourier series 215, 218, 223
Fourier coefficients 217
Parseval's theorem 252
Fraunhofer, Joseph von 1787–1826 384
Fraunhofer solar spectrum 279
Fresnel's mirrors (*see* interferometer: Lloyd's mirror experiment)
Fresnel–Kirchhoff diffraction formula 380
diffraction integral 347, 356
fringe 85, 307, 313, 320
Fizeau 91–92, 95, 113
Newton's rings 79, 95, 97
Haidinger's fringes (*see* interference)
fringe contrast (*see* coherence: fringe visibility)
function
Airy function 397
autocorrelation function 237, 238
Bessel functions 162, 245, 364, 542
comb function (*see* sampling)
convolution operation 241
convolution integral 244, 247, 354
convolution theorem 249, 442
correlation 237–238, 240
cross-correlation 237
delta function 230–231, 242, 454
Gaussian function 342, 359
Green's function 205, 215, 243–244, 248, 341
Lorentzian function 276
sinc 226–227, 393, 397

G

Gaussian beam (*see* Gaussian wave)
Gaussian distribution (*see* function: Gaussian function)
Gaussian parameter 370, 373–374
beam waist 342, 356, 360–361, 434
complex size parameter 360, 367
diffraction angle 362
Gaussian wave 344
Gouy phase shift 361, 381
Hermite–Gaussian 363
Laguerre–Gaussian waves 363
paraxial wave 357–358, 360

geometrical optics 171
ABCD matrix 127, 178, 183, 189
paraxial *ABCD* matrix 141
refraction matrix 139–141
thin-lens equation 186–187
image-matrix 187
imaging condition 183, 185, 188
Lagrangian formulation 127
Newtonian formalism 186
ray tracing 135, 136, 139
resonators 126, 356
sign convention 66, 136, 409
glass 95, 193, 299–300, 304–305
crown glass 300
dispersion in glass (*see* Abbe number: Abbe value)
flint glass 300
guided wave 127, 146, 159
coupling 149, 162–163, 165
end-fired coupling 149–150
evanescent wave coupling 164
cutoff condition 157, 161–162
guided wave modes 162
mode coupling (*see* guided wave: coupling)
prism coupling 164, 165
zigzag model 153

H

half-wave plate (*see* retarder)
half-wave retardation 617, 647
Hanbury Brown–Twiss intensity interferometer 333–334
harmonic motion 1, 3, 33
helicity 33
helical 578–579
Helmholtz equation 7, 11, 129, 342
Hermitian operator (*see* photonic structure)
hologram 496, 498, 501, 510, 516, 519, 639
absorption hologram 502
Fourier transform holograms 520, 545
image hologram 521
K-ratio 513, 535
off-axis hologram 501, 508
thick hologram 512
thin hologram 505, 513
holographic 502, 505
holographic grating 500
holographic image 499–500, 519
spatial frequency 535, 547
holographic optical element 501, 543
space-conjugate wave 505
homodyne (*see* mixing)
Huygens' principle 342, 345, 347, 372
Huygens wavelet 341–343, 372, 476, 481

I

illuminance (*see* density: flux density)
lux (*see* lumen/m^2)
image 134, 184–185, 188, 195, 205
image blur 539
image contrast 451
real image 191, 508
virtual image 504, 517
impulse response (*see* function: Green's function)
index of refraction 20, 27, 42, 84, 157
complex index of refraction 45, 73, 75, 117, 280–281, 294, 551, 559
effective guide 157
interference 83, 85
Fizeau 92, 310
Haidinger's 94
interference fringes (*see* fringe)
interference pattern 79, 196, 322, 391, 500
interferometer 98, 100
Fabry–Perot 106
Lloyd's mirror experiment 87
Mach–Zehnder interferometer 101
Michelson's interferometer 323
Michelson's stellar interferometer 307, 401
Twyman–Green interferometer 100

J

Jones calculus 577–578
Jones matrices 551, 585
Jones vector 39, 40, 577, 585

K

Kerr 604, 621, 623, 647, 694
Kerr effect 604–605, 610, 612, 666, 694
Kerr coefficient 605
Kerr tensors 651
Kerr modulator 621
Kerr, John 1824–1907 604
Kirchhoff theory 375, 383
Kirchhoff diffraction 341, 375–377, 379, 380
knife-edge test (*see* filter: spatial filter: Foucault knife-edge)

L

Lagrange invariant 185, 205
Lagrangian equation 166
pendulum 166
Larmor precession frequency 627
Larmor, Joseph 1857–1942 627
lens *f*/# 191
lens equation 184, 186–187
Gaussian form 186
lensmakers 185–186
Newtonian form 187
lens splitting 212
lens vertex 188
lens's system matrix 183
light-beating spectroscopy (*see* spectroscopy)
Lissajous figure 29–31
Lissajous, Jules Antoine 1822–1880 29
longitudinal chromatic 299
longitudinal color (*see* aberration: chromatic aberration: longitudinal chromatic aberration)
Lorentz, Hendrik Antoon 1853–1928 256
lumen/m^2 25

M

magneto-optic effect 604, 624, 647, 665
Faraday effect 578, 624–625, 627, 629–630, 647, 665
Faraday rotation 628
isolator 629
magneto-optic susceptibility 624
Manley–Rowe relation (*see* mixing)
Maxwell, James Clerk 1831–1879 15
Maxwell's equations 18–19, 59, 83, 121, 254, 341, 343, 522, 571, 579, 666
meridional rays 146, 152
Michelson interferometer 98
microscope 126, 317, 385, 426
dark-ground illumination microscopy 434
microscope objective 375
oblique illumination 426
phase contrast (*see* Zernike, Frits 1885–1966: Zernike phase contrast microscope)
mirror figure 111
mixing 501, 666, 677, 694, 699
four-wave mixing 501, 666, 694, 695, 697–698
photoelectric mixing 307

modulation 258, 261, 306, 500, 603
amplitude-modulated wave 258
carrier frequency 227, 261
carrier wave 259
Faraday isolator 629
frequency-modulated 641, 659
index modulation 500, 533
modulation transfer function 450, 485
modulator 612–613, 621–622, 629, 639, 643
chopper 602
electro-optic modulator 603, 621
Kerr modulation 615
Pockels modulator 621
Pockels cell 615
shutter 602, 621
monochromatic 310
Mouton, Henri 1869–1935 604

N

nanophotonics (*see* photonic crystal)
Newton, Isaac 1642–1727 1
noise, coherent (*see* speckle)
nonlinear 665–668, 670, 672–673, 676, 693, 705, 707
coupling coefficient 701
effective nonlinear coefficient 711–712
Kleinman's symmetry condition 672
Miller's rule 670, 678, 710
Raman effect 666
rectification 664, 666
second-harmonic 666, 668, 682, 692, 710
sum-frequency 666, 668
nonlinear optical coefficient 666, 670
nonlinear optical coefficient tensor 672
nonlinear optical constant 675, 678
nonlinear susceptibility 668, 712
nonpropagating (*see* wave: evanescent wave)
numerical aperture 151–152

O

obliquity factor (*see* diffraction: Huygens–Fresnel integral: Fresnel diffraction)
optical coherence tomography (see: microscope)
optical path length 84, 127, 130, 132–133, 191
optical sine theorem 204–205
Abbe sine condition 204

P

paraxial approximation (*see* geometrical optics)
paraxial ray 169, 179, 197, 200–201
paraxial theory 127, 136–137, 193, 195
Pasteur, Louis 1822–1895 (*see* chiral: chirality: optical activity)
Perot, Jean Baptiste Gaspard Gustave Alfred 1863–1925 (*see* Fabry–Perot interferometer)
Petzval sum 208
sagitta 207
Petzval, Josef Max 1807–1891 193
phase conjugation (*see* mixing: four-wave mixing)
phase hologram 502, 543
photonic crystal 111, 178, 522, 526, 531, 533, 539, 668
hollow-core photonic bandgap 530
one-dimensional photonic crystal 497, 527
three-dimensional photonic crystal 533
two-dimensional photonic crystal 528, 530
photonic structure 496, 533
band-gap 497, 527, 533
hollow-core photonic crystal fibers 530, 531
opal 533, 534
peacock 535
photons 26, 334–335, 524, 635
piezoelectric 606, 631
piezoelectric tensor 606, 650, 672
pinhole camera 484–485
single-Fresnel-zone pinhole 484
plasmon polaritons 72, 284–285
plasmonic-based optical systems 286
Pockels coefficient 605, 607–608
Pockels, Friedrich Carl Alwin 1865–1913 604
Poisson's spot (*see* diffraction: Huygens–Fresnel integral: Fresnel diffraction)
polaritons (*see* plasmon polaritons)
polarization 16
effective index 121, 157, 686, 700
left-circular polarization 39
p-polarized 558
Poincaré sphere 38
polarization by birefringence (*see* birefringence)
polarization by reflection 68
polarization ellipse 31, 37
s-polarized 558
polarized 33–34, 37, 39, 76, 83, 550, 578, 688
left-elliptically polarized 581
left-circularly polarized 34, 580, 585
right-circular 34–36, 582, 583, 585, 627
polarizer 36, 552, 554, 557
circular polarizer 585
Feussner polarizer 564
Glan–Foucault 563–564
Glan–Taylor 564
Glan–Thompson 564
Malus' law 614
Polaroid 68, 552
H-sheet 552–553, 556
J-sheet 552
K-sheet 552
Rochon polarizers 561
Wollaston 561, 562, 563
Poynting theorem 24
Poynting vector 24–25, 72, 550, 593
Poynting walkoff angle 587, 623, 692
Poynting, John Henry 1852–1914 24
pressure-broadened 315
Lorentzian spectral distribution 315
propagation 76
nondispersive 19, 260, 263
propagation constant 3, 42, 157, 158, 258
pupil 189–191, 195, 561
entrance pupil 190–191
exit pupil 190–191
pyroelectrics 664, 665

Q

q-parameter (*see* Gaussian parameter)
Q-switch 646
quarter-wave plate 572–573, 586

R

radiometry 25
Raman, C.V. 1888–1970 638
Raman–Nath scattering 638, 659–660
reflection 53, 56, 58, 71, 76, 127, 132, 342, 345
amplitude reflection coefficient 61
phase change 73
reflectance coefficient 63
reflected amplitude 61
reflected wave 54, 58, 69
reflectivity 65
refraction 53, 56, 58, 76, 127, 132–133, 166, 168–169
refractivities (*see* Clausius–Mossotti equation)
refringence (*see* refraction)

resolution criterion 442, 444, 519
  Rayleigh's criterion (*see* Abbe theory: image resolution)
  Sparrow criterion 446–447, 452–453
  Strehl ratio 196–197
retarder 551, 572, 576–577, 586
  Babinet compensator 575
  compensator 573
  quarter-wave plate 572–573, 586
  Rhomb 574–575
  Soleil–Babinet compensator (*see* retarder: Babinet compensator)
rotatory power (*see* specific rotation)
Royen (*see* Van Royen, Willebrord Snel 1580–1626)

S

sag (*see* Petzval sum: sagitta)
sagittal plane 194–195, 205, 207
sampling 231, 233–234, 237, 248
Savart (*see* Ampère's law)
Schlieren method (*see* filter: spatial filter: Foucault knife-edge)
second-rank tensor 550, 589, 630
Seidel coefficients 197
Seidel, Ludwig Philipp 1821–1896 193
SELFOC® fiber 179
  SELFOC® lens 175, 182
Sellmeier relation 256
Sellmeier, Wilhelm (1871) 256
shape factor 210
shift-invariant 242–243
skew ray 146, 151
specific rotation 583
speckle 306, 400, 455
speckle noise 306, 400–401, 454
spectrometer 317, 407
  Fourier transform spectroscopy 307, 312
  grating spectrometers 407
    Littrow configuration 411
spectroscopy 310, 312
stationarity (*see* shift-invariant)
stellar interferometer (*see* coherence)
Stokes vector 39, 40, 47, 77–78, 575, 577, 585
  degree of polarization 38, 47, 77, 555
  Mueller calculus 578
  Mueller–Stokes matrix 585
  Stokes parameter 36, 39
stop (*see* pupil)
  aperture stop 189
    principal ray 190–191, 194, 197, 201, 203
superluminal 292, 293
  Brillouin precursor 290
  precursor 290–291, 295
  Sommerfeld precursor 290
surface plasmon (*see* plasmon polaritons)
susceptibility 666–668, 670, 672

T

tangential 194, 198
  tangential field 206–207
  tangential focal plane 207
  tangential plane (*see* sagittal plane)
tangential rays 194, 203, 206–207
telegraph equations 41
tensor calculus 559
  electro-optic tensors 650
    Pockels tensor 606, 622, 650
  ellipsoid (*see* anisotropy: optical indicatrix)
  indicatrix 550, 564, 567, 606, 622, 630
tensor matrix 622
  electro-optic indicatrix 606
time-averaged flux density 25
  intensity 6, 26
total reflection 56, 71–73, 563, 686, 700
  critical angle 69, 71, 77
  frustrated total reflection 72
  phase change upon total reflection 73, 146
transforms 218, 222, 241, 244, 248, 327, 388, 392, 448
  cosine transform 224–225
  Fourier transform 223–225, 231, 239, 244, 248, 252
  sine transform 224, 327, 392
transmissivity 65

U

uniaxial (*see* birefringence)
unpolarized beam 561

V

V-number 299, 301
  V-number, the constringence 299
Van Cittert 327
Van Royen, Willebrord Snel 1580–1626 53
VanderLugt filter 544
velocity 4, 7, 16
  group velocity 255, 258, 260, 262, 293
  phase velocity 4, 7, 256, 260, 289
  velocity of propagation 265, 598
  velocity, superluminal propagation 289
velocity of light 15–16, 20, 290
Venant's hypothesis (*see* boundary conditions: Kirchhoff boundary conditions)
vignetting 191
visibility 104, 307, 316

W

waist (*see* Gaussian parameter: beam waist)
walkoff (*see* Poynting theorem: Poynting vector: Poynting walkoff angle)
wave 1, 4, 6, 16, 24, 45
  conjugate wave 504–505
  electromagnetic wave 16, 19, 29, 496, 536, 578, 665
  evanescent wave 72, 158, 285–286
wavefront 6–8
  plane wave 7–8, 16
  spherical wave 7, 9, 354
waveguide dispersion 264
waveguide mode 148–149, 153
wavelength 3, 55, 84
wavelet (*see* Huygens' principle: Huygens wavelet)
wavenumber (*see* propagation constant)
wavevector 8, 12, 57

Y

Young, Thomas 1773–1829 1, 79
Young's two-slit experiment 1, 79

Z

z-cut (*see* modulator: Pockels modulator)
Zeeman effect (*see* magneto-optic effect: Faraday effect)
Zeeman, Pieter 1865–1943 624
Zernike theorem (*see* coherence: spatial coherence: Van Cittert–Zernike theorem)
Zernike, Frits 1885–1966 307
  Zernike phase contrast microscope 384–385, 435
zone plate 459, 481–484, 488–489, 496, 513–517, 536–537
  chirped grating 516
  zone plate's resolution 484